Springer Proceedings in Energy

Yafang Han *Editor*

Advances in Energy and Environmental Materials

Proceedings of Chinese Materials Conference 2017

Springer

Springer Proceedings in Energy

More information about this series at http://www.springer.com/series/13370

Yafang Han
Editor

Advances in Energy and Environmental Materials

Proceedings of Chinese Materials Conference 2017

Springer

Editor
Yafang Han
Chinese Materials Research Society
Beijing
China

ISSN 2352-2534 ISSN 2352-2542 (electronic)
Springer Proceedings in Energy
ISBN 978-981-13-0157-5 ISBN 978-981-13-0158-2 (eBook)
https://doi.org/10.1007/978-981-13-0158-2

Library of Congress Control Number: 2018938382

Printed on acid-free paper

This Springer imprint is published by the registered company Springer Nature Singapore Pte Ltd.
part of Springer Nature
The registered company address is: 152 Beach Road, #21-01/04 Gateway East, Singapore 189721, Singapore

Preface

This is the proceedings of the selected papers presented at Chinese Materials Conference 2017 (CMC2017) held in Yinchuan City, Ningxia, China, July 06–12, 2017.

The Chinese Materials Conference (CMC) is the most important serial conference of Chinese Materials Research Society (C-MRS) and is held each year since the early 1990s. Chinese Materials Conference 2017 had 37 symposia covering four fields of Energy and environmental materials, Advanced functional materials, High-performance structural materials, and Design, preparation, and characterization of materials. More than 5500 participants attended the conference, and the organizers received more than 700 technical papers. By recommendation of symposium organizers and after peer-reviewing, 434 papers are published in the present proceedings, which are divided into four volumes of

Part 1: Advances in Energy and Environmental Materials

Part 2: High-Performance Structural Materials

Part 3: Advances in Materials Processing

Part 4: Advanced Functional Materials

This is the volume for Part 1 including 96 papers selected from eight symposia of A01: Energy conversion and storage materials; A02: Thermoelectric materials and devices; A03: Nuclear materials; A04: Solar energy materials and photovoltaic cell; A05: Minerals and oil and gas materials; B01: Photocatalytic materials for energy production; B02: Eco-materials; B03: Environmental engineering materials.

The editors would like to give the thanks to the symposium chairs and all the paper reviewers of this volume, and the thanks should be also given to Mrs. Yiming Jia and Mr. Yongzheng Zhang for their hard work of compilation and typesetting for each paper in this volume.

Beijing, China
March 2018

Yafang Han

Contents

Enhancement of Proton Conductivity of Polymer Electrolyte Membrane Enabled by Electrospun Nanofibers

Cuicui Dong, Zhimin Hao and Qiong Zhou

Abstract TiO_2 nanofiber with different diameters was synthesized by calcining electrospun polyacrylonitrile (PAN) nanofibers embedded with titanium precursors. The TiO_2 nanofibers was incorporated into sulfonated poly(ether ether ketone) (SPEEK) to preprare the proton exchange membrane (PEM). The incorporation of inorganic nanofiber can improve the performance of composite membrane. The conductivity of the SPEEK/TiO_2-130 composite membrane is 1.15 times higher than that of the pristine SPEEK membrane at 100% relative humidity and 25 °C. In addition, the stable fiber skeleton suppresses the swelling coefficient of PEM. Compared to pristine SPEEK membrane, the SPEEK/TiO_2 membranes exhibit higher comprehensive performance.

Keywords SPEEK · Composite membrane · Fuel cells · Proton exchange membrane

Introduction

Direct methanol fuel cells (DMFCs) have attracted worldwide interest in the fields of automobiles, portable devices and residential power sources [1, 2]. Proton exchange membrane (PEM) is vital component which determine the performance and lifetime of DMFCs. The Nafion series membrane have high proton conductivity and excellent chemical stability but their utilization for DMFCs is hampered by the

C. Dong · Z. Hao · Q. Zhou (✉)
Department of Materials Science and Engineering, China University of Petroleum-Beijing, Beijing 102249, China
e-mail: zhouqiong_cn@163.com

C. Dong
e-mail: shuiyuanzuo@126.com

C. Dong · Z. Hao · Q. Zhou
Beijing Key Laboratory of Failure, Corrosion, and Protection of Oil/Gas Facilities, China University of Petroleum-Beijing, Beijing 102249, China

Y. Han (ed.), *Advances in Energy and Environmental Materials*,
Springer Proceedings in Energy, https://doi.org/10.1007/978-981-13-0158-2_1

high cost. In the past two decades, many research groups have made continuing effort to find a ideal membrane material as substitute for Nafion. Sulfonated Poly (ether ether ketone) (SPEEK), a kind of low cost polymer material with excellent mechanical properties, exhibits great potential for DMFCs applications [3]. However, the conductivity of SPEEK is low owing to its narrower proton-conducting channels. This characteristic affect the overall DMFCs performance. It is worth noting that the incorporation of proton-conducting inorganic fillers for inter-connecting the proton-conducting channels within SPEEK is a facile and efficient approach to overcome this issue.

TiO_2 nanofiber is one of the most advanced nano-material used as additive to the SPEEK matrix for membrane electrolyte [4]. But, there are problems associated with the preparation of TiO_2 nanofiber. The conventional preparation methods of TiO_2 nanofiber would use various hazardous chemicals. In this study, a single spinneret electrospinning technique was used to prepare TiO_2 nanofiber [5]. The synthetic route is relatively simple, cost-effective and without any hazardous chemicals. We prepare a SPEEK/TiO_2 nanofiber composite membrane and evaluate the membrane by investigating the water uptake (WU), dimensional stability, proton conductivity, and methanol permeability.

Experimental Section

Materials and Chemicals. PEEK powder was purchased from Victrex, Titanium (IV) oxide acetylacetonate (TiOacac) was purchased from Alfa Aesar. N,N-Dimethylformamide (DMF), dimethyl sulfoxide (DMSO) and H_2SO_4 (98%) were purchased from Beijing Chemical Reagent Factory.

Synthesis of SPEEK. 20 g of the PEEK was dissolved in 200 ml of concentrated H_2SO_4 preheated to 25 °C. The blended solution was heated to 45 °C and stirred for 3 h, then poured the sulfonated polymer solution into ice water to terminate the reaction. The polymer precipitate was washed with deionized water until the pH was neutral, then dried under vacuum at 80 °C for 24 h to get SPEEK.

Preparation of Inorganic Nanofiber. TiO_2 nanofibers were prepared by a two-step process. Firstly, 0.5 g of TiOacac was dispersed into 3.0 g of DMF and 1.0 g of PAN was completely dissolved in 6.0 g of DMF under vigorous stirring. Then, mixed the solutions together and stirred until a homogenous solution was obtained. The single spinneret electrospinning technology was used to electrospun the blend solution. The PAN/TiOacac nanofiber with various diameters was prepared by changing electrospinning parameters. The light yellow color composite mat was obtained on a piece of aluminum foil. The TiO_2 nanofibers were prepared by calcining electrospun composites mat in a muffle roaster. The composite mat was heated from 30 to 250 °C and thermally stabilized at 250 °C for 1 h and then heating to 550 °C and stabilized at this temperature for 5 h. The TiO_2 nanofibers

with various diameters (130, 160 and 220 nm) were fabricated, named as TiO_2-130, TiO_2-160 and TiO_2-220, respectively.

Preparation and Characterization of The Blend Membranes. Various diameters of TiO_2-130, TiO_2-160 and TiO_2-220 were impregnated in SPEEK ionomer to prepare SPEEK/TiO_2 composite membrane by the following procedures. Certain weight of SPEEK and TiO_2 nanofiber was dissolved in DMSO, then cast onto a glass dish and dried at 90 °C for 24 h under vacuum. The microstructures of the membranes were analyzed using a FEI F20 transmission electron microscope (TEM) equipped with energy dispersive X-ray spectroscopic analyzer (EDS) and a FEI Quanta 200F scanning electron microscope (SEM) operated at 30 kV.

Evaluation of Water Uptake (WU), Swelling Ratio (SR) and Proton Conductivity. The WUs and swelling rates of the membrane samples were determined by comparing the mass and dimensional changes of the membranes between the water-saturated and dry states, as reported in a previous study. The proton conductivity measurements were performed on a CHI660D electrochemical workstation. The membrane sample was soaked in deionized water at a certain temperature ranging from 30 to 60 °C, as reported in a previous study.

Results and Discussion

Characterization of TiO_2 Nanofiber. The PAN/TiOacac nanofiber with various diameters was prepared by changing electrospinning parameters (such as the distance of needle to the collector, diameter of the needle and charge density). The morphology of the prepared TiO_2-128 nanofiber was observed by SEM and shown in Fig. 1. The surface of nanofibers are smooth without beaded. Furthermore, F1b shows the enlarged morphology, the result represents that the nanofibers are compact without void space.

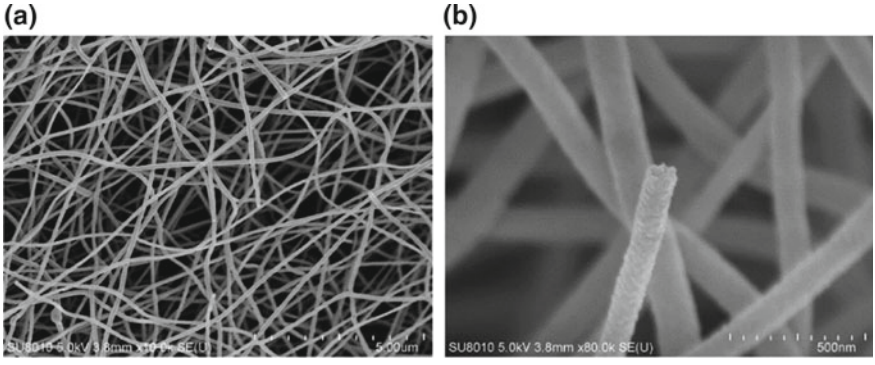

Fig. 1 **a** SEM image and **b** enlarged SEM image of TiO_2 nanofibers

The TEM (Fig. 2a–c) image illustrates the connections of the small particles forming the fiber structure. This structure is stable because the strong adsorption of particles.

STEM elemental mapping analysis of TiO_2 nanofiber was detected and shown in Fig. 2d–f. The elemental Ti (yellow color points in Fig. 2e) and O (blue color points in Fig. 2f) are clearly observed in the nanofibers. The element mapping photos exhibit the uniform dispersion of all elements, indicating the precursor are dispersible well in the fibers.

Characterization of Membranes. The cross-section morphology of plain SPEEK and hybrid membranes are shown in Fig. 3. The nanofibers are evenly dispersed in the composite membranes without phase separation or defects when the content of TiO_2 nanofibers is less than 1.0 wt%. Furthermore, TiO_2 nanofibers keep fiber structure without obvious destruction in the inner part of the composite membranes. This result proves that SPEEK does not affect the shape and status of the nanofibers. However, when nanofiber content is increased up to 1.5 wt%, the heterogeneous morphology and defects be found due to the stacking and aggregation of nanofibers.

The elemental mappings were utilized to further detect the dispersion of TiO_2 nanofiber in composite membrane. Figure 4 shows Ti, S and O elements in the SPEEK/TiO_2 composite membrane. The characteristic elements distribute evenly and continuously on the cross-section of the membrane. In summary, the dense and homogeneous composite membranes can be successfully prepared.

WU, SR and Proton Conductivity. The WU and SR of all samples were measured at 25 and 50 °C (Fig. 5). Compare to pristine SPEEK, all SPEEK/TiO_2 membrane

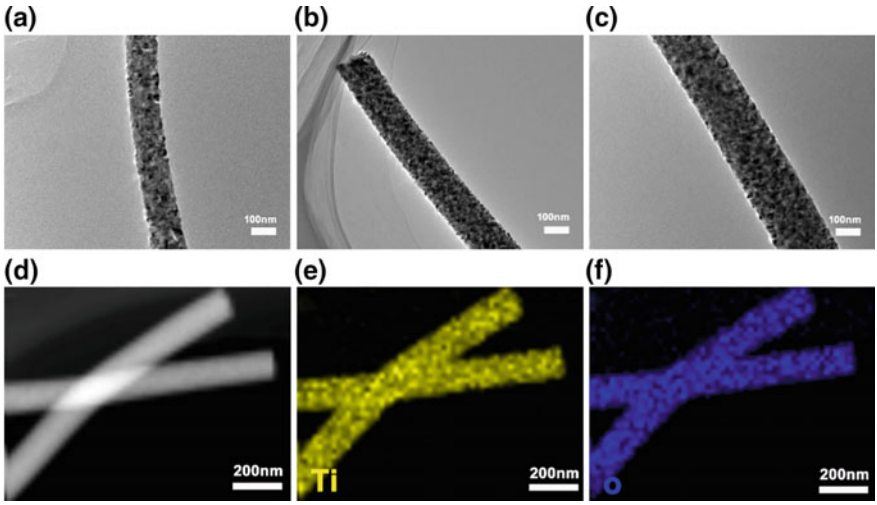

Fig. 2 TEM images of **a** TiO_2-128, **b** TiO_2-155 and **c** TiO_2-218; elemental mapping analysis of TiO_2 nanofiber; **d** bright field image, **e** Ti and **f** O

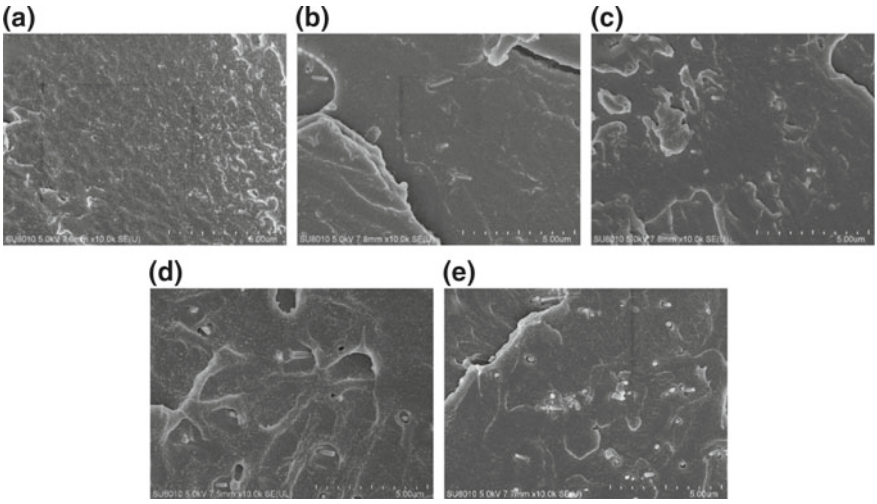

Fig. 3 SEM cross-section images of **a** SPEEK, **b** SPEEK/TiO_2-0.2 wt%, **c** SPEEK/TiO_2-0.5 wt%, **d** SPEEK/TiO_2-1.0 wt%, and **e** SPEEK/TiO_2-1.5 wt% membranes

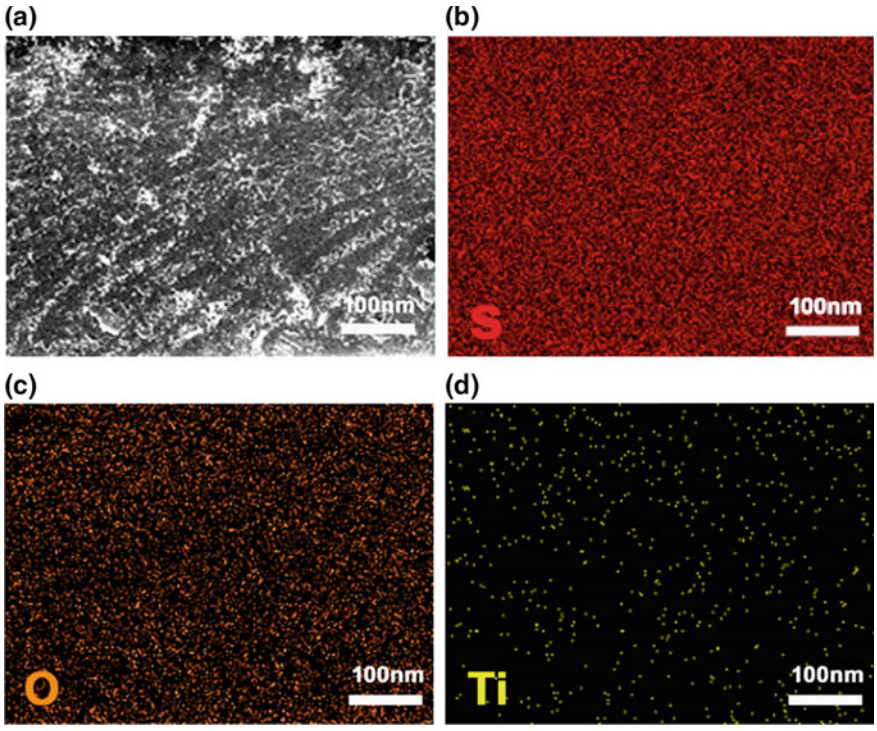

Fig. 4 SEM elemental mapping of cross section of SPEEK/TiO_2 membrane: **a** bright field image, **b** S, **c** Ti and **d** O

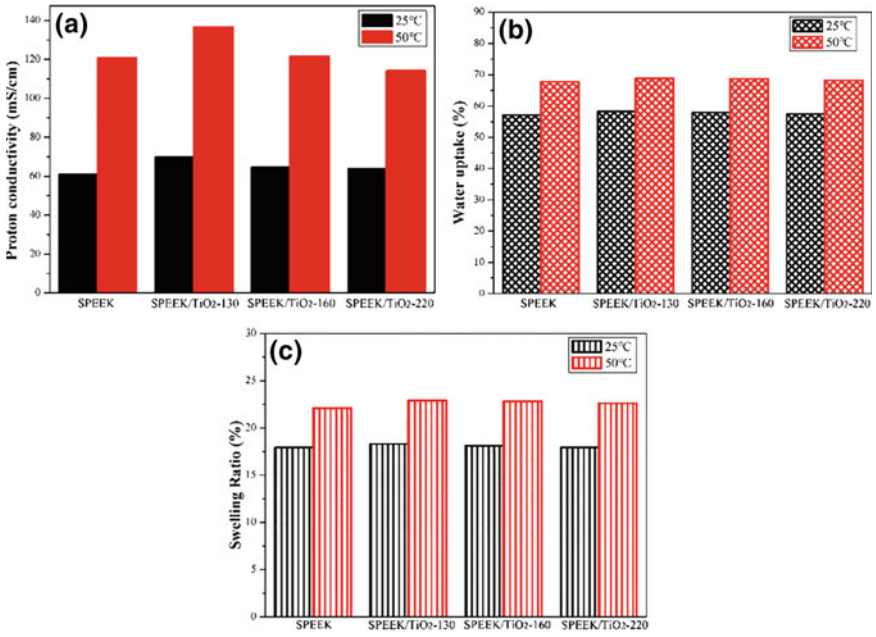

Fig. 5 **a** Conductivity, **b** WU and **c** in-plane swelling ratio of pristine SPEEK and SPEEK composite membranes

exhibits higher WU. This may be contribute to hydrophilic TiO_2 make hydrophilicity of membranes increase. With the decrease of TiO_2 diameter, the WU of membranes increases from 7.4 wt% in SPEEK/TiO_2-220 to 8.2 wt% in SPEEK/TiO_2-130 membrane at 25 °C. This may be due to the hydrophilicity of TiO_2 nanofiber decrease with the increasing nanofiber diameter.

The DR of the membrane also plays an important role in influencing the dimensional stability of PEM [6]. The tendency of DR is substantially in accordance with that of WU. But, the increment decreases after the nanofibers are incorporated. Because the stable fiber skeleton improve the dimensional stability of the composite membrane.

Compare to pristine SPEEK membrane (σ = 60.9 mS/cm, 25 °C), optimal proton conductivity of 69.8 mS/cm^{-1} is obtained on SPEEK/TiO_2-130. Hydrophilic TiO_2 promotes the membrane to absorb more water which facilitates proton transfer via "vehicle" mechanism. Moreover, TiO_2 nanofiber interconnect the ionic clusters and subtle regions in the SPEEK matrix, creating continuous proton transfer network to improve conductivity.

Conclusions

In this work, the various diameter of TiO_2 nanofibers were successfully prepared and incorporated into SPEEK to prepare SPEEK/TiO_2 composite membranes. The performances of the composite membranes are compared in terms of the diameter of incorporated nanofiber. The SPEEK/TiO_2-130 membrane has the highest conductivity of 69.8 mS/cm. All SPEEK/TiO_2 composite membranes show higher proton conductivities and better dimensional stability than the pure SPEEK membranes.

Acknowledgements This study was supported financially by the National Key Research and development Plan (Grant no: 2016YFC0303700); National Science and Technology Major Project (Research Index: 201505017-002).

References

1. S.D. Bhat, A.K. Sahu, A. Jalajakshi, S. Pitchumani, P. Sridhar, C. George, PVA-SSA-HPA mixed-matrix-membrane electrolytes for DMFCs. J. Electrochem. Soc. **157**, B1403–B1412 (2010)
2. C.-C. Yang, Y.J. Li, T.-H. Liou, Preparation of novel poly(vinyl alcohol)/SiO_2 nanocomposite membranes by a sol–gel process and their application on alkaline DMFCs. Desalination **276**, 366–372 (2011)
3. J.-C. Tsai, H.-P. Cheng, J.-F. Kuo, Y.-H. Huang, C.-Y. Chen, Blended Nafion®/SPEEK direct methanol fuel cell membranes for reduced methanol permeability. J. Power Sources **189**, 958–965 (2009)
4. Y. Jun, H. Zarrin, M. Fowler, Z. Chen, Functionalized titania nanotube composite membranes for high temperature proton exchange membrane fuel cells. Int. J. Hydrogen Energy **36**, 6073–6081 (2011)
5. K. Ketpang, B. Son, D. Lee, S. Shanmugam, Porous zirconium oxide nanotube modified Nafion composite membrane for polymer electrolyte membrane fuel cells operated under dry conditions. J. Membr. Sci. **488**, 154–165 (2015)
6. S. Zhong, C. Sun, Y. Gao, X. Cui, Preparation and characterization of polymer electrolyte membranes based on silicon-containing core-shell structured nanocomposite latex particles. J. Power Sources **289**, 34–40 (2015)

Effect of Co-Doping on the Structure, Magnetic and Hydrogen Absorption Properties of $Fe_{17}Dy_2$ Compound

Yongbin Guo, Lei Ma, Dao Wang, Xin Zhou, Lin Li and Jinliang Tang

Abstract The $Fe_{17}Dy_2Co_x$ (x = 0.0–0.15) compounds were prepared by arc melting method, and then annealed at 800 °C for 100 h. The effect of Co-doping on the structure, magnetic and hydrogen absorption properties was studied by X-ray diffraction (XRD) and vibrating sample magnetometer (VSM), and Pressure Concentration Temperature (PCT). The results show that the unit cell volume and lattice parameter a, b and c of $Fe_{17}Dy_2Co_x$ increase firstly and then decrease synchronously with the Co content. And $Fe_{17}Dy_2Co_x$ compounds still keep the Th_2Ni_{17}-type hexagonal crystal structure and ferromagnetism with the increase of Co content. For an applied field changed from 0 to 2T, the saturation magnetization (M_S) is tuned from 62.09 Am^2/kg at x = 0.0–84.3 Am^2/kg at x = 0.15. The content of hydrogen abstraction for $Fe_{17}Dy_2Co_x$ (x = 0.0, 0.05, 0.1, 0.15) compounds are 0.14, 0.027, 0.034 and 0.03 wt% respectively, which is a novel property in magnet and magnetic materials.

Keywords $Fe_{17}Dy_2$ compound · Hydrogen absorption · Magnetic properties

Introduction

Intermetallic compounds composed of rare-earth (R) and transition-metal (T) elements have an important role from technological and fundamental point of view [1–3]. So the R-T type compounds have attracted much attention in recent years as possible high-performance permanent magnetic materials [4–7]. R_2T_{17} compounds (T = Fe or Co) crystallize either in the rhombohedral structure (R-3m

Y. Guo · L. Ma (✉) · D. Wang · X. Zhou · L. Li · J. Tang
School of Materials Science and Engineering, Guilin University of Electronic Technology, Guilin 541004, China
e-mail: malei@guet.edu.cn

L. Ma · L. Li
Guangxi Key Laboratory of Information Materials, Guilin University of Electronic Technology, Guilin 541004, China

Y. Han (ed.), *Advances in Energy and Environmental Materials*,
Springer Proceedings in Energy, https://doi.org/10.1007/978-981-13-0158-2_2

space group, Th_2Zn_{17}-like with a single R site 6c and four different T sites 6c, 9d, 18f, and 18h) for light rare earths or in the hexagonal structure for heavy rare earths (P6/mmc space group, Th_2Ni_{17}-like with two R sites 2b and 2d and four T sites 4f, 6g, 12j, and 12k). The change of structure usually occurs at R = Gd and results from the lanthanide contraction [8]. The low Curie temperature and magnetic anisotropy of R_2Fe_{17} compounds make them the applications as permanent magnets [9–11]. Interests in this series compounds have been renewed since it was shown that insertion of light interstitial atoms such as hydrogen could raise usually the low Curie temperature of the ferromagnetic compounds. Substantial improvements in the magnetic properties were achieved by alloying the binary compounds with carbon [12–16], and more nitrides of R_2Fe_{17} prepared by gas-solid reaction of N_2 [17]. At same time the hydrides are also of interest. The ternary hydrides of formula $R_2Fe_{17}H_x$ are interesting materials to better understand the parent alloy properties and to improve the behaviour of the interstitial compounds $R_2Fe_{17}H_x$ ($0 < x < 5$). It may be useful to investigate the effects of hydrogenation on the structural and magnetic properties.

In this work, we report the structure and magnetic properties of the $Fe_{17}Dy_2Co_x$ alloys and corresponding hydrogenated compounds. The effect of Co doping on the structure, magnetic and hydrogen absorption properties of $Fe_{17}Dy_2$ compounds was investigated, and the optimum hydrogen absorption ratio was determined by adjusting the Co content.

Experimental

The $Fe_{17}Dy_2Co_x$ compounds were prepared by arc melting method. The purity of Fe, Co and Dy is better than 99.99%. In order to ensure the uniformity of the composition in the smelting process, the samples were repeatedly smelted 3 to 4 times. The ingots were wrapped in a tantalum foil, sealed in quartz tube filled argon, annealed at 800 °C for 100 h, and then quenched into ice-water. The X-ray diffraction (XRD) was carried out with PANalytical PIXcel^{3D} X-ray polycrystalline powder diffractometer using Cu $K\alpha_1$ radiation. The scans in 2θ were collected between 20° and 120° with steps of 0.026°. Analysis of XRD patterns was carried out with the Fullprof suite package. The magnetic measurements were performed using the vibrating sample magnetometer (VSM) (VSM are manufactured by Lake Shore 7400). The chemical homogeneity and microstructures were confirmed by a scanning electron microscopy (SEM, FEI Quanta 450 FEG) equipped with energy dispersive X-ray spectrometer (EDS, Oxford instruments X-Max20). The measurements of hydrogen absorption were carried out using the Pressure Concentration Temperature (PCT: PCTPro 2000).

Results and Discussion

Crystal Structure. The structure of $Fe_{17}Dy_2$ compound is a typical Th_2Ni_{17} hexagonal structure with P6/mmc space group. Figure 1 depicts the XRD patterns recorded for a powder specimen of $Fe_{17}Dy_2Co_x$ (x = 0.0, 0.05, 0.1, 0.15) compounds, and all the diffraction pattern peaks can be indexed as the Th_2Ni_{17}-type structure (hexagonal). When the Co-doping amount does not cause large distortion of the lattice, and lattice structure remains the same. Figure 2 shows the SEM image of $Fe_{17}Dy_2Co_{0.05}$ sample. It indicates that it is a good single phase, which is consistent with the results of Fig. 1. Based on XRD data and the model of $Fe_{17}Dy_2$ (Th_2Ni_{17}-structure), full profile Rietveld refinement showed good fits between experimental and calculated profiles for $Fe_{17}Dy_2Co_{0.05}$ compounds, as shown in Fig. 3. The lattice constants and cell volumes of $Fe_{17}Dy_2Co_x$ alloys are presented in Table 1. It can be seen that the unit-cell volume of $Fe_{17}Dy_2Co_x$ compounds firstly increase and then decrease with the content of Co.

Magnetic Properties. Figure 4a shows the magnetic hysteresis loops of $Fe_{17}Dy_2Co_x$ (x = 0.0, 0.05, 0.1, 0.15) compounds measured at 300 K. It indicates the compounds are soft magnetic materials. It can be seen that the magnetic moment of the $Fe_{17}Dy_2Co_x$ compounds are close to saturation at $\sim$0.5 T. The compounds remain ferromagnetic with the increase of Co contents, which indicates that the Co-doping does not change the magnetic-type of the compounds. Figure 4b shows the magnetization (M_S) dependence on Co concentration of $Fe_{17}Dy_2Co_x$ (x = 0.0, 0.05, 0.1, 0.15) compounds. The saturated M_S of $Fe_{17}Dy_2Co_x$ compounds can be tuned from 62.09 Am^2/kg at x = 0.0 to 84.3 Am^2/kg at x = 0.15. It indicated that Co doping can ingcrease the M_S of the $Fe_{17}Dy_2Co_x$ compounds, and does not increase the coercivity. This is because that the 3d electron layer of Fe is one

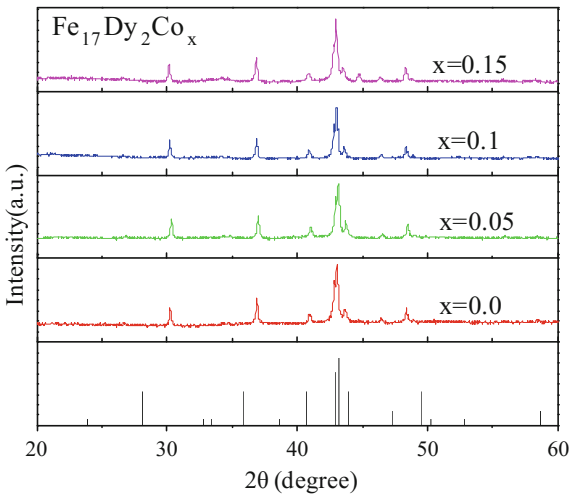

Fig. 1 XRD patterns of $Fe_{17}Dy_2Co_x$ (x = 0.0, 0.05, 0.1, 0.15) compounds annealed at 800 °C for 100 h

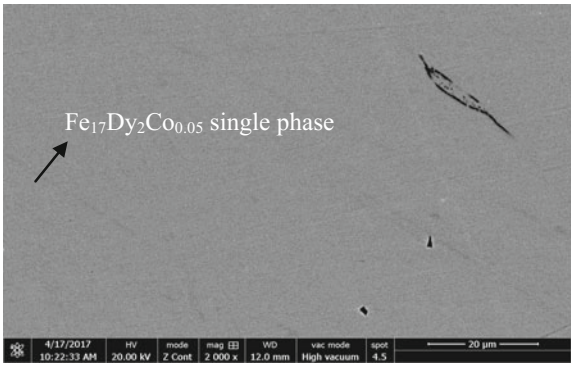

Fig. 2 SEM image of the $Fe_{17}Dy_2Co_{0.05}$ sample

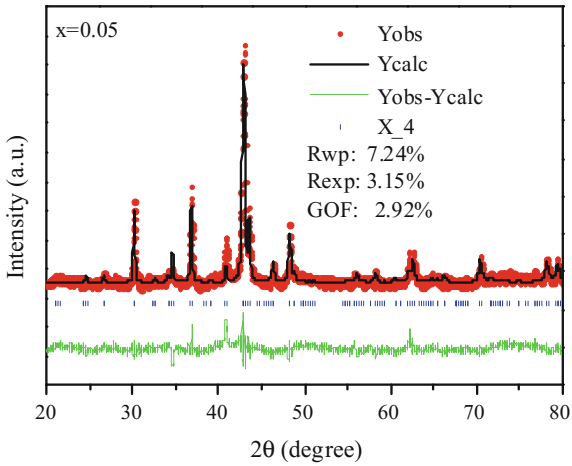

Fig. 3 Rietveld results of the XRD pattern of $Fe_{17}Dy_2Co_{0.05}$ compound

Table 1 Lattice constants a, b, c and unit-cell volume of $Fe_{17}Dy_2Co_x$ compounds

Alloy composition	a = b/nm	c/nm	V/nm^3
x = 0.0	0.845(6)	0.829(8)	0.513(9)
x = 0.05	0.846(1)	0.831(2)	0.515(3)
x = 0.1	0.845(8)	0.831(1)	0.514(9)
x = 0.15	0.845(5)	0.831(8)	0.514(9)

electron less than Co, and they are often ferromagnetic. When the doping of Co atoms occurs, the compounds exhibit ferromagnetic properties. And with the doping of Co atoms, the original Fe–Fe and Fe–Dy intermolecular interaction are gradually replaced by Co–Co, Co–Dy and Fe–Co between the ferromagnetic elements, and the exchange coupling effect of ferromagnetism is enhanced. So the performances of the series compounds are ferromagnetic.

Hydrogen Absorption Properties. It is interesting that hydrogen absorption properties were found in $Fe_{17}Dy_2Co_x$ (x = 0.05, 0.1, 0.15) compounds at 573 K,

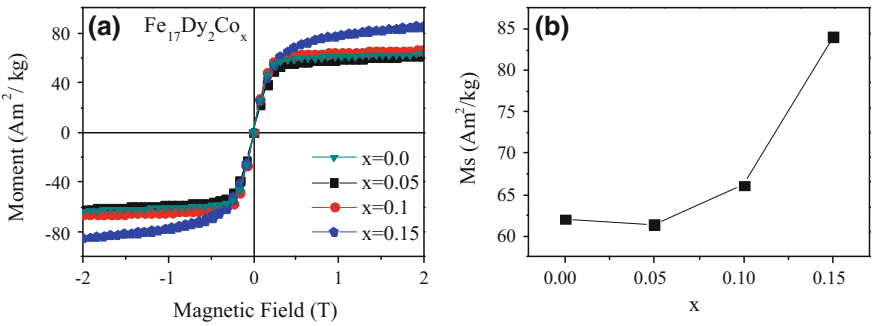

Fig. 4 Magnetic hysteresis loops of $Fe_{17}Dy_2Co_x$ compounds measured at 300 K (**a**) and saturation magnetization versus Co content of $Fe_{17}Dy_2Co_x$ compounds (**b**)

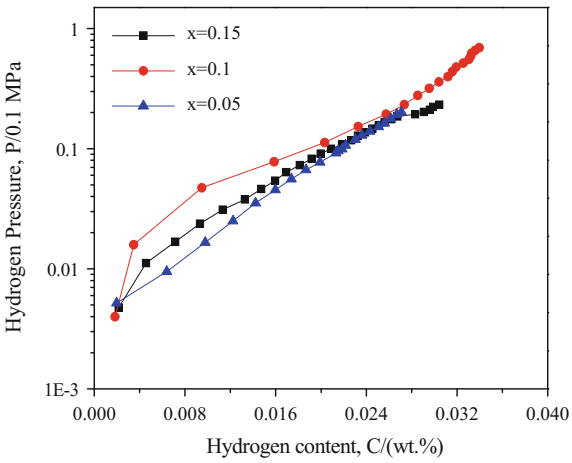

Fig. 5 PCT curves for $Fe_{17}Dy_2Co_x$ compounds measured at 573 K

which is a novel property in magnet and magnetic materials. Figure 5 shows the curves of hydrogen absorption content with Co contents for $Fe_{17}Dy_2Co_x$ compounds. Before making the PCT, the sample was activated 3 times at 573 K. From Fig. 5, the curves indicates that the hydrogen absorption content of $Fe_{17}Dy_2Co_x$ compounds increase firstly and then decrease with the doping of Co content. The content of hydrogen abstraction for $Fe_{17}Dy_2Co_x$ (x = 0.05, 0.1, 0.15) compounds are 0.027, 0.034 and 0.03 wt%, respectively. The addition of Co does not improve greatly the hydrogen absorption properties of the $Fe_{17}Dy_2Co_x$ compounds, but tunes the change in a certain range. In Fig. 4a, the ferromagnetic effect is enhanced with the increase of Co content. Therefore, it is deduced that the ferromagnetic enhancement is conducive to the increase of hydrogen absorption in this compounds. Further work is being studied.

Conclusions

The structure, magentic and hydrogen absorption properties of $Fe_{17}Dy_2Co_x$ (x = 0.0–0.15) compounds were investigated. The results show that $Fe_{17}Dy_2Co_x$ (x = 0.0–0.15) compounds always keep a typical Th_2Ni_{17} hexagonal structure, and the space group is P6/mmc. With the doping of Co content, the unit cell parameters and cell volume increase firstly and then decrease. The Fe17Dy2Cox compounds remain ferromagnetism and the MS can be tuned from 62.09 to 84.3 Am^2/kg with the increase of Co content. The maximum value of hydrogen uptake of $Fe_{17}Dy_2Co_x$ (x = 0.0, 0.05, 0.1, 0.15) compounds is 0.14 wt%, which decreases with the change of Co content. The material shows a novel characteristic in the properties of magnetism and hydrogen storage.

Ackonwledgements This work is supported by the National Natural Science Foundation of China (51461012), the Guangxi Key Laboratory of Information Materials (161011-Z, 161005-K, 151007-K) and the Guangxi Natural Science Foundation (2016GXNSFAA380030, 2016GXNSFGA380001).

References

1. K. Kobayashi, S. Suzuki, T. Kuno, K. Urushibata, N. Sakuma, M. Yano, T. Shouji, A. Kato, A. Manabe, The stability of newly developed (R,Zr)(Fe,Co)$_{12-x}$Ti$_x$ alloys for permanent magnets. J. Alloy. Compd. **694**, 914–920 (2017)
2. P. Rajasekhara, K. Deepak Kumar, G. Markandeyulu, Anomalous Hall effect studies on Tb-Fe thin films. J. Magn. Magn. Mater. **412**, 201–206 (2016)
3. K. Wada, R. Antos, K. Aoshima, K. Machida, K. Kuga, H. Ono, H. Kikuchi, N. Shimidzu, T. Ishibashi, Aperture-ratio dependence of the efficiency of magneto-optical first-order diffraction in GdFe stripe arrays with alternating perpendicular magnetizatio. Opt. Commun. **371**, 67–71 (2016)
4. A.G. Kuchin, W. Iwasieczko, S.P. Platonov, The magnetocaloric effect in R_2Fe_{17} intermetallics with different types of magnetic phase transition. Low Temp. Phys. **41**, 985 (2015)
5. Yu.G. Pastushenkov, K.P. Skokov, M.B. Lyakhova, E.S. Antonova, Domain structure of R_2Fe_{17} intermetallic compounds with planar-type anisotropy. Met. Sci. Heat Treat. **58**, 594–598 (2017)
6. Y.G. Pastushenkov, K.P. Skokov, E.S. Antonova, T.I. Ivanova, J.S. Bartolomé, Domain structure transformation and magnetic susceptibility of Ho_2Fe_{17} single crystals. J. Alloy. Compd. **689**, 894–898 (2016)
7. S. Charfeddine, K. Zehani, L. Bessais, A. Korchef, Structural, magnetic, magneto-caloric and Mossbauer spectral study of Tb_2Fe_{17} compound synthesized by arc melting. J. Solid State Chem. **238**, 15–20 (2016)
8. H.S. Li, J.M.D. Coey, in *Handbook of Magnetic Materials*, ed. by K.H.J. Buschow (North-Holland, Amsterdam, 1991), p. 6
9. D. Sanavi Khoshnoud, N. Tajabor, F. Pourarian, H. Salamati, Influence of Si and Co substitutions on magnetoelastic properties of R_2Fe_{17} (R=Y, Er and Tm) intermetallic compounds. J. Magn. Magn. Mater. **321**, 3847–3853 (2009)
10. H.Y. Chen, Y. Zhang, J.Z. Han, H.L. Du, C.S. Wang, Y.C. Yang, Magnetocaloric effect in R_2Fe_{17} (R=Sm, Gd, Tb, Dy, Er). J. Magn. Magn. Mater. **320**, 1382–1384 (2008)

11. A.G. Kuchin, N.V. Mushnikov, M.I. Bartashevich, O. Prokhnenko, V.I. Khrabrov, T. P. Lapin, Magnetic properties of the $Ce_2Fe_{17-x}Mn_x$ helical magnets up to high magnetic fields. J. Magn. Magn. Mater. **313**, 1–7 (2007)
12. X.Z. Wang, K. Donnelly, J.M.D. Coey, B. Chevalier, J. Etourneau, T. Berlureau, Hydrogen absorption and desorption in Nd_2Fe_{17} and Sm_2Fe_{17}. J. Mater. Sci. **23**, 329 (1988)
13. B. Rupp, G. Wiesinger, Magnetic and structural properties of a novel ternary hydride: $Nd_2Fe_{17}H_x$ ($0<x<5$). J. Magn. Magn. Mater. **71**, 269 (1988)
14. O. Isnard, S. Miraglia, J.L. Soubeyroux, D. Fruchart, A. Stergiou, Neutron diffraction study of the structural and magnetic properties of the $R_2Fe_{17}H_x(D_x)$ ternary compounds (R=Ce, Nd and Ho). J. Less-Common Met. **162**, 273 (1990)
15. D. Fruchart, S. Miraglia, Hydrogenated hard magnetic alloys from fundamental to applications. J. Appl. Phys. **69**, 5578–5583 (1991)
16. X.P. Zhong, R.J. Radwanski, F.R. de Boer, T.H. Jacobs, K.H.J. Buschow, Magnetic and crystallographic characteristics of rare-earth ternary carbides derived from R_2 Fe_{17} compounds. J. Magn. Magn. Mater. **86**, 333 (1990)
17. J.M.D. Coey, H. Sun, Improved magnetic properties by treatment of iron rare-earth intermetallic compounds in ammonia. J. Magn. Magn. Mater. **87**, L251–L254 (1990)

Preparation of Mechanical Alloying AlCuFe Alloy and Its Application in Li-Ion Battery Anode

Xiao Lan, Zhanhao Sun and Xunyong Jiang

Abstract Aluminum has high lithium storage capacity and poor cycle performance as one kind of new advanced material. In this paper, $Al_{64}Cu_{23.5}Fe_{12.5}$ alloy was prepared by mechanical alloying with pure Al, Cu, and Fe powder as the initial materials and the electrochemical lithium storage performance of AlCuFe ternary alloy was studied. The effects of different milling device and experimental parameters on the microstructure of the alloy were also studied. Magnetic measurement was performed on alloy under different MA state. The results of XRD show that the peak of the elemental phase widens with the increase of the grinding time. New phase appears at about 75 h. It is found that the magnetism of the alloy is weakened with the formation of the new alloy. The discharge capacity of AlCuFe increase with longer milling time. After a long milling time of 100 h in 500 rmp, $Al_{64}Cu_{23.5}Fe_{12.5}$ alloy exhibites the highest first discharge capacities of 314 mAh g^{-1}. Then the capacity gradually decays in the first 20 cycles and stabilizes at a range of 175–200 mAh g^{-1}, which corresponds to 68% of initial capacity. Compared with pure Al, AlCuFe alloy-show better cycle stability, this facile MA approach provides helpful synergistic effects.

Keywords Lithium ion battery · Anode material · Mechanical alloying AlCuFe

X. Lan · Z. Sun · X. Jiang (✉)
School of Materials Science and Engineering, Tianjin University of Technology, Tianjin, China
e-mail: jiangxunyong@tjut.edu.cn

X. Lan
e-mail: lanmiaosx@163.com

Z. Sun
e-mail: sunzhh_977@163.com

Y. Han (ed.), *Advances in Energy and Environmental Materials*,
Springer Proceedings in Energy, https://doi.org/10.1007/978-981-13-0158-2_3

Introduction

An increasing number of electric or plug-in hybrid vehicles, portable electronic devices, and power tool technologies require a significant increase of the energy density of Li-ion batteries [1]. As a result of small size, high capacity and long cycle life advantages, lithium-ion batteries are increasingly widely used in all aspects of life, such as mobile phones, computers and other electronic products [2]. Currently, commercial LIB technology generally employs synthetic graphite as an anode for LIB batteries due to its stable cycling performance. However, critical problems such as limited raw material resources, complicated synthetic process, and high-temperature synthesis is still unresolved, leading to high synthetic graphite production costs. In addition, another issue of carbon materials is their low theoretical specific capacity of 372 mAh g^{-1}, leading to poor energy storage performance [3]. Therefore, to improve the capacity of LIB, anode with high theoretical capacity should be used, such as metal-based materials. Aluminum has high lithium storage capacity. However, these material always suffer rapid capacity fading arising from structural degradation and electrical contact loss during cycling. Aluminum-based intermetallic compounds can improve the cycling performance of Al anode through reducing the volume change of electrode by adding inert element into Al substrate, such as AlCuFe,which preventing the severe volume expansion stress of metal-based materials [4, 5]. Generally, AlCuFe alloy was prepared by melting and casting method. When the battery is assembled, it is also necessary to grind the casting alloy into powder. The mechanical alloying method (MA) can use elemental powder as the raw material to obtain the alloy powder. Mitka and Wang successfully prepared AlCuFe alloy using mechanical alloying process [6, 7]. In this paper, $Al_{64}Cu_{23.5}Fe_{12.5}$ was prepared by mechanical alloying using pure Al, Cu and Fe powder as the starting materials. The influence of the milling conditions on the phase structure of the alloy was studied. The electrochemical storage performance of AlCuFe alloy was measured.

Experimental

Elemental powders (99.9 wt% purity, average particle size in the range of 8–55 μm) of Al, Cu and Fe were mechanically alloyed to prepare the $Al_{64}Cu_{23.5}Fe_{12.5}$ element. The milling experiments were performed in a planetary ball mill (RE-QM-2SP12) and a high-energy vibrating ball mill (MSK-SFM-3). A 100 ml stainless steel vial and 3–10 mm (in diameter) stainless steel balls were used. The powders were balanced to give the nominal composition of $Al_{64}Cu_{23.5}Fe_{12.5}$ (at.%) and mixed in a glove box under a purified Ar atmosphere. The mixed powders were then sealed into the stainless steel vial. The ball to powder weight ratio was maintained as 20:1. N-hexane is surfactant to prevent welding of powder on the wall of mill pot. Argon is filled in mill to prevent powder and oxidation. Magnetic

measurements were made using VSM magnetic performance meter. Electrochemical measurements were performed using coin cells (CR2032, Hohsen Corporation), which are consist of $Al_{64}Cu_{23.5}Fe_{12.5}$ as the anode, Li metal foil (Honjo Chemical, 99.8%) as the cathode, a 1.0 M LiPF6 solution in a mixture of ethylene carbonateedimethyl carbonate (1:1) as the electrolyte, and a porous polypropylene membrane (Celgard 2400) as the separator. The $Al_{64}Cu_{23.5}Fe_{12.5}$ electrodes were prepared on a Cu foil substrate (Nippon Foil, 18 μm) as the current collector using coating an-methyl-2-pyrrolidinone solvent (NMP, Aldrich) based slurry with a mixture of 80 wt% of active materials, 10 wt% PVDF as the binder, and 10 wt% acetylene black as the conducting material. The resultant electrodes were dried in an oven at 90 °C for 9 h. All coin cells were assembled in a high-purity argon-filled glove box with H_2O and O_2 contents less than 5 ppm. The discharge-charge tests carried out using a battery cycler system (WonATech Corp., WMPG 3000) in the potential range of 0.0–2.0 V (vs. Li/Li þ) at 25 °C in an incubator. The cycling stability was observed up to 100 cycles at a current density of 100 mAh g^{-1}. XRD was carried out using the D/Max2500pc Rigaku/Japan instruments with Cu Kα radiation, the scan scope was set from 10° to 90°.

Results and Discussion

Experimental parameters of MA process. In this paper, MA were performed with planetary ball mill (RE-QM-2SP12) and high-energy vibrating ball mill (MSK-SFM-3). The influence of different mill appraptus on the phase evolusion during MA process was studied, as shown in Fig. 1. Figure 1a is the XRD results of AlCuFe power prepared by planetary ball milling and high energy vibration ball milling. As grinding time increases, the diffraction peak tends to widen significantly, indicating that the particle size decreases gradually with time. But before and after the curve in addition to the peak and no other changes, indicating that in this process there is no new phase of the formation. We speculate that the reason why no quasicrystal is generated is that the energy during the reaction is not enough, and then the change in the reaction process can be observed by increasing the milling time and the rotation speed.. MA process of high-energy vibrating ball mill is faster than planetary ball mill, Compared with high-energy vibration ball milling, the planetary ball mill can simultaneously mill four sets of samples, high-energy vibration ball milling can only mill a group of samples. So we chose the planetary ball milling in the following the experiment.

The reason of incomplete alloying of $Al_{64}Cu_{23.5}Fe_{12.5}$ may come from in sufficient energy in the milling process. The rotation speed should be get a higher level. Figure 1b is the XRD results of $Al_{64}Cu_{23.5}Fe_{12.5}$ powders under different rotation speed. It can be see that the diffraction peak widened with 550 rmp compared with 500 rmp, which indicates the grain refinement. High speed can

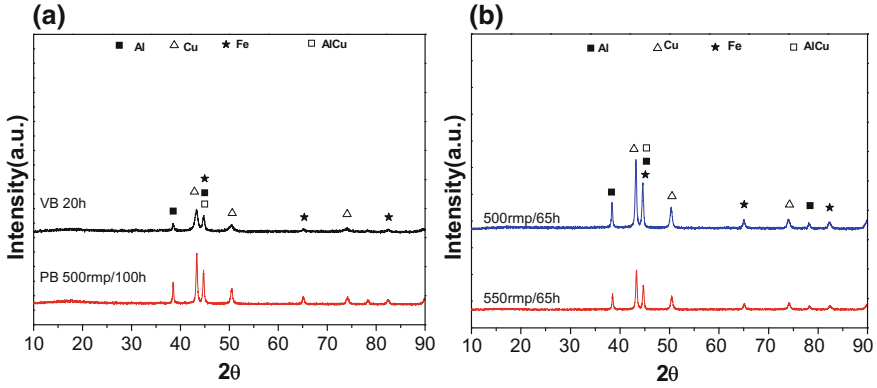

Fig. 1 **a** XRD patterns of $Al_{64}Cu_{23.5}Fe_{12.5}$ with different apparatus, planetary ball milling (PB), high-energy vibration ball milling (VB). **b** XRD patterns of the $Al_{64}Cu_{23.5}Fe_{12.5}$ powders under different rotation speed with planetary ball milling

promote the alloy formation of MA. But in line with the situation in Fig. 1b, it achieve part of the alloying.

Change of phase structure during MA. Figure 2a show XRD patterns of the as-milled $Al_{64}Cu_{23.5}Fe_{12.5}$ powder with various time intervals. The diffraction peaks obviously tend to broaden with increasing milling time, indicating the reduction of the powder size,and there no new phase was formed, but the peak of elemental aluminum, copper and iron decreased continuously. The XRD pattern reveals that the as-milled product after 65 h of MA consists of a new λ-Al(Cu, Fe) phase, β-Al(Cu, Fe) and the residual Al Fe and Cu. Since there is almost no interdiffusion between Cu and Fe [8], it is assumed that Al, Cu, Fe form a stable intermetallic compound AlCu and AlFe phase during the initial reaction. As the rest of the reaction progresses into the two phases, the Fe solid solution enters the AlCu phase or Cu enters the AlFe phase. During this process, the β phase and the γ phase play a transitional role as intermediate products, after which the AlCuFe alloy And doped some of the simple substance. In the experiment of this figure, perhaps because the speed is too high, the stress in the reaction process inhibits the reaction of the mesophase to the alloy phase, which hinders the solution reaction and quasi-crystal formation.

During the process for the production of lithium battery negative slurry with samples of different milling time, The magnetic stick was used. We found that the sample with short milling glue on the surface of magnetic stick. The sample with longer milling time did not show this phenomenon. This means that magnetic elemental Fe disappar during MA process. This is in accord with the XRD results (Fig. 2a). The diffraction peak of Fe gradually weakened with longer milling time. Magnetic measurements were performed on the AlCuFe powder with different milling time. The results are shown Fig. 2b. Curve *a* is milling 0 h samples, curves

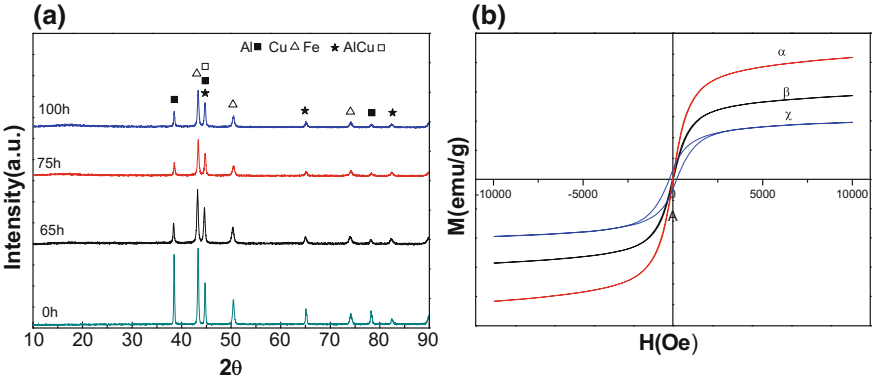

Fig. 2 **a** XRD patterns of the $Al_{64}Cu_{23.5}Fe_{12.5}$ powders with various MA time. **b** Magnetic property of $Al_{64}Cu_{23.5}Fe_{12.5}$ poeders after various MA times (α 0 h, β 10 h, χ 20 h)

b, *c* were samples milling 65, 100 h. With the increase of the milling time, the magnetism of the samples are getting weaker, indicating that the content of elemental Fe is gradually reduced during the process of milling. Fe element is dissolved in the other phase with the increase of the milling time, which leads to the weakness of the magnetism of samples. At this stage, part of the Fe element solid solution into the AlCu phase and the formation of AlCuFe alloy, the remainder is a mixture of Al, Cu, Fe powder and λ-Al_3Fe.

Electrochemical properties of $Al_{64}Cu_{23.5}Fe_{12.5}$ prepared by MA. A mixed powder of MA 100 h AlCuFe alloy [Al, Cu, Fe, λ-Al_3Fe, β-Al(Cu, Fe), AlCuFe] was prepared into a negative electrode sheet of a lithium ion battery and assembled into a lithium ion battery, followed by charge and discharge and a series of tests.

Figure 3a show the cycle-discharge specific capacity of AlCuFe alloy with different milling time. The first discharge capacity of the sample milling 100 h is 305 mAh g^{-1}, and the capacity is reduced to 190 mAh g^{-1} after 30 cycles. Milling 75 h samples also have similar circulatory trends, but it decays to a stable value of 180 mAh g^{-1} after 20 cycles. It can be seen that as the milling time of the sample increases, the discharge capacity of the sample increases.

Figure 3b shows the discharge capacity-cycle number of AlCuFe and pure Al. It can be seen that the first discharge capacity of pure Al is much larger, but its attenuation is extremely serious. After 20 cycle, the discharge capacity is almost zero. The samples of AlCuFe with 100 h milling were basically stable after 10 cycles, and the stable specific capacity reached 250 mAh g^{-1}, which was much higher than that of pure Al.

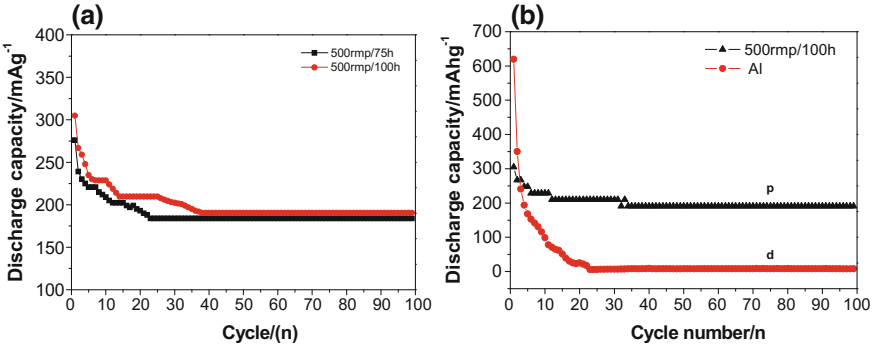

Fig. 3 **a** Cycling performance of different MA times. **b** Cycling performance of planetary ball mill 500 rmp MA 100 h (p) and pure Al (d) electrodes

Conclusion

In this paper, $Al_{64}Cu_{23.5}Fe_{12.5}$ was prepared by mechanical alloying using pure Al, Cu and Fe powder as the starting materials.

1. Changing the laboratory equipment, changing the milling time and speed can not achieve AlCuFe powder completely alloying. It is found that the fully alloyed of AlCuFe powder does not form directly from the milling process for a nominal composition of $Al_{64}Cu_{23.5}Fe_{12.5}$ powders, and a longer time milling results in the formation of part of alloying of AlCuFe after the MA treatment.
2. Under the condition of 500 rmp, the ferromagnetism of the material decreases with the increase of the milling time, and the peak value of the iron phase is greatly weakened, which indicates that the iron element may enter the other phase through solid solution.
3. The first specific discharge capacities are 308 and 278 mAh g^{-1} for 100, 75 h MA electrodes. With the increase of milling time and speed, the discharge capacity of lithium ion battery is obviously increased, and the stability is better. The optimised AlCuFe electrode shows improved lithium storage properties, outstanding cycling stability (198 mAh g^{-1} after 100 cycles). Compared with the negative electrode Al, AlCuFe alloy material has better stability, and the cycle performance, meanwhile the stability of the discharge capacity is higher.

Acknowledgements Project supported by Natural Science Foundation of Tianjin, No. 16JCTPJC51900.

References

1. S. Zheng, W. Yang, Y. Zhu, H. Zhou, J. Wang, J. Yang, In situ reduction and intercalation of graphite oxides for Li-S battery cathodes. J. Adv. Energy Mater. **1400482**, 5–9 (2014)
2. P.G. Bruce, B. Scrosati, J.-M. Tarascon, Nanomaterials for rechargeable lithium batteries. Angew. Chem. Int. Ed. **47**, 2930–2946 (2008)
3. M. Cao, M. Zhang, L. Xing, Q. Wang, X.-Y. Xue, One-step preparation of pomegranate-shaped Sn/SnO_x/nanocarbon composites for fabricating ultrafast-charging/long-life lithium-ion battery. J. Alloy. Compd. **694**, 30–39 (2017)
4. H. Liu, R. Hu, C. Huang, W. Sun, H. Zhang, M. Zhu, Toward cyclic durable core/shell nanostructure of Sn-C composite anodes for stable lithium storage by simulating its lithiation-induced internal strain. J. Alloy. Compd. **704**, 348–358 (2017)
5. R. Liu, W. Su, P. He, C. Shen, C. Zhang, F. Su, C.-A. Wang, Synthesis of SnO_2/Sn hybrid hollow spheres as high performance anode materials for lithium ion battery. J. Alloy. Compd. **688**, 908–913 (2016)
6. M. Mitka et al., Microstructure of mechanically alloyed and annealed $Al_{62}Cu_{25.5}Fe_{12.5}$ powder. J. Alloy. Compd. **653**, 47–53 (2015)
7. W. Yan, T. Ying et al., On phase transformations in mechanically alloyed and subsequently annealed $Al_{70}Cu_{20}Fe_{10}$. J. Intermetallics **16**, 121–129 (2008)
8. A.I. Salimon, A.M. Korsunsky, E.V. Shelekhov, T.A. Sviridova, S.D. Kaloshkin, V.S. Tcherdyntsev et al., Acta Mater. **49**, 1821–1833 (2001)

Pentabasic Thermoelectricity System Prepared by Powder Metallurgy Method and the Performance Thermoelectric Generator Modules

Ye Guo, Jiangduo Wang, Yuanfa Deng, Chulan Lu, Yiping Luo and Bin Lin

Abstract With the technological development and awareness of energy conservation and environmental protection, how to take advantage of waste heat has been concerned global. However, effective methods to recycle low temperature waste heat which is lower than 200 °C are still lacked. A kind of pentabasic thermoelectricity system which is prepared by smelting and powder metallurgy method is described in this paper. Thermoelectric generator (TEG) modules with different area and height ratio (A/H) p-n couples are assembled. At temperature gradient 100 K, the TEG module can obtain the biggest load power 2.39 W corresponding the module with A/H = 5.5 and load resistance 1.5 Ω.

Keywords Low temperature waste heat · Thermoelectric generator modules Area and height ratio · Load power

Introduction

Only no more than 40% energy is make good use by current energy conversion technologies and the other energy dissipate by style of waste heat primarily [1]. However, recycling low temperature waste heat distributing from 50 to 200 °C that have low thermal flux density is more challenging than high temperature waste heat in industry [2, 3].

Thermoelectric material and related technology, as a low-carbon energy conversion technique, can take advantage of automobile exhaust gas or industrial waste heat and then convert it to direct current [4–7]. The performance of thermoelectric material is related to its intrinsic properties which can be described by the

Y. Guo · J. Wang · Y. Deng · C. Lu · Y. Luo (✉) · B. Lin (✉)
Guangdong Leizig Thermoelectric Technologies Co., Ltd.,
Guangzhou 510470, Guangdong, China
e-mail: yale_guo@leizig.com

B. Lin
e-mail: tu_luo@leizig.com

Y. Han (ed.), *Advances in Energy and Environmental Materials*,
Springer Proceedings in Energy, https://doi.org/10.1007/978-981-13-0158-2_4

dimensionless figure of merit $ZT = \alpha^2\sigma/\kappa$, where α is the Seebeck coefficient, σ is the electrical conductivity, κ is the thermal conductivity, and T is the absolute temperature. This three parameters α, σ and κ are relate to each other [8–10].

In practical application, whether they are used for cool or generator, the modules were assembled in series by many p-n couples. Nevertheless, to acquire high performance TEG modules, both p-type and n-type require not only excellent ZT value but also good compatibility between them. The good compatibility mean the number and curve of Seebeck coefficient, electrical conductivity and ZT value are approximate and have similar varying tendency in their working temperature interval [11–18]. And similar electrical conductivity is the most important factor.

In this work, we introduce a pentabasic thermoelectricity system which is consisted of five elements Bi, Sb, S, Te and Se. P-type and n-type thermoelectric material can be obtained by adjusting the ratios of this five elements. It can be more easily to acquire good compatibility between p-type and n-type materials they have similar chemical constitution. TEG modules with different height p-n couples are assembled. The power output of open-circuit voltage, short-circuit current and the resistive load power of those TEG module were measured and discussed.

Experimental

Sample Preparation. P-type and n-type samples were synthesized by direct solid state reaction. High purity starting elements, Bi (99.999%), Sb (99.999%), S (99.999%), Te (99.999%) and Se (99.999%) were weighted out in stoichiometric ratios and added into quartz ampoules which were evacuated to <1 Pa. Then the evacuated ampoules were placed into a resistance melting furnace and heated with 2 °C/min to 650 °C and held at that temperature for 48 h. And then they were cooled to room temperature naturally. The resulting alloys were broken to powder and put into a stainless steel pots and ball milled for 60 min in full-directional planetary ball mill. Those ball-milled powders were cold pressed into a column with the pressure 900 Mpa and annealed under vacuum for 6 h at 400 °C. Then they were cooled to room temperature naturally with 1 °C/min to acquire final product.
Module Fabrication. The TEG modules with dimensions of 40 * 45 mm and different p-n couple height were fabricated by automatic die bonder. 127 pairs of p-n couples were assembled electrically in series with aluminium oxide ceramic substrates as electrical insulator foundation. The structure graph of our TEG modules is shown in Fig. 1. Nickel was chosen on TE materials as the diffusion barrier to inhibit element diffusions between the TE materials and the solder and copper was used as the electrode. The cross section area of all p or n leg is 1.7 * 1.7 mm^2. The height of p and n leg is 0.42, 0.52, 0.82, 0.92 and 1.00 mm. It means that the area and height ratio (A/H) of p-n legs is 6.80, 5.50, 4.62, 3.50, 3.12 and 2.89 respectively.

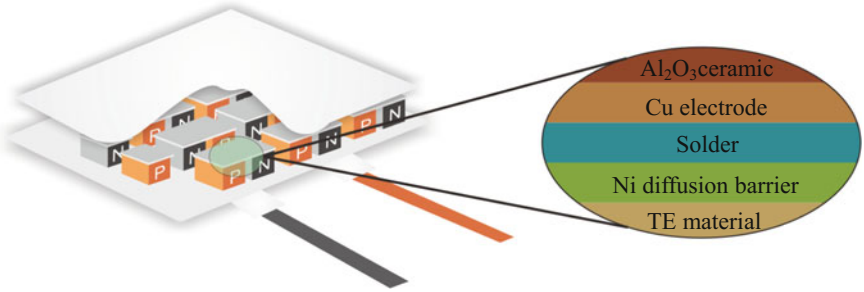

Fig. 1 Structure graph of TEG module

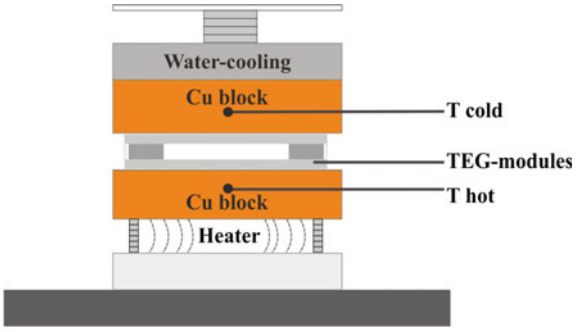

Fig. 2 Structure graph of homebuilt testing device

Testing. The Seebeck coefficient and electrical conductivity and at 298–473 K were measured using Linseis LSR-3/1100 under vacuum environment. Thermal conductivity at 298–473 K was calculated by multiplied the thermal diffusivity, heat capacity and sample density. The thermal diffusivity was measured at argon atmosphere using a laser flash method (FL4010, TA Co. Ltd.). The heat capacity was measured using DSC 200 F3 (Netzsch Co. Ltd.). The density was measured by Archimedes method. The power output of open-circuit voltage, short-circuit current, load voltage, load current and the resistive load power of the TEG module were measured by our homebuilt testing device (Fig. 2). Tow copper blocks were used to connect heater that can heat to 300 °C and circulating water cooling. The TEG module was placed between those two copper blocks. And load resistance is provided by DC Electronic Load (ITECH, IT8511+) which can change resistance easily and display load resistance, load current, load voltage and load power. Open-circuit voltage and short-circuit current were tested with temperature gradient from 10 to 130 K and resistive load characteristics were measured at temperature gradient 100 K.

Results and Discussion

Electric Properties of Materials. Figure 3a displays the temperature dependence of Seebeck coefficient p-type and n-type materials. The curve of those two materials have similar varying tendency in the temperature interval from 298 to 473 K (25–200 °C). Figure 3b shows the temperature dependence of electric conductivity of p-type and n-type samples from 298 to 473 K. Original electric conductivity of those tow material is about 50,000 S/m at 298 K and decline synchronously with temperature increasing. The temperature dependence of the thermal conductivity is shown in Fig. 3c. Thermal conductivity of p-type sample is lower than 0.75 $Wm^{-1}K^{-1}$ and n-type sample is lower than 0.90 $Wm^{-1}K^{-1}$. As shown in Fig. 4d, figure of merit ZT was calculated. The p-type sample has a good performance in ZT value which is 1.24 at 348 K and has an average value about 1. Although perfect compatibility electrical conductivity is acquired between p-type and n-type materials, ZT value of n-type materials isn't an ideal level obviously.

Electric Properties of TEG Modules. Modules resistance with A/H 6.80, 5.50, 4.62, 3.50, 3.12 and 2.89 are 0.72, 0.84, 0.91, 1.43, 1.59 and 1.42 Ω. The abnormal

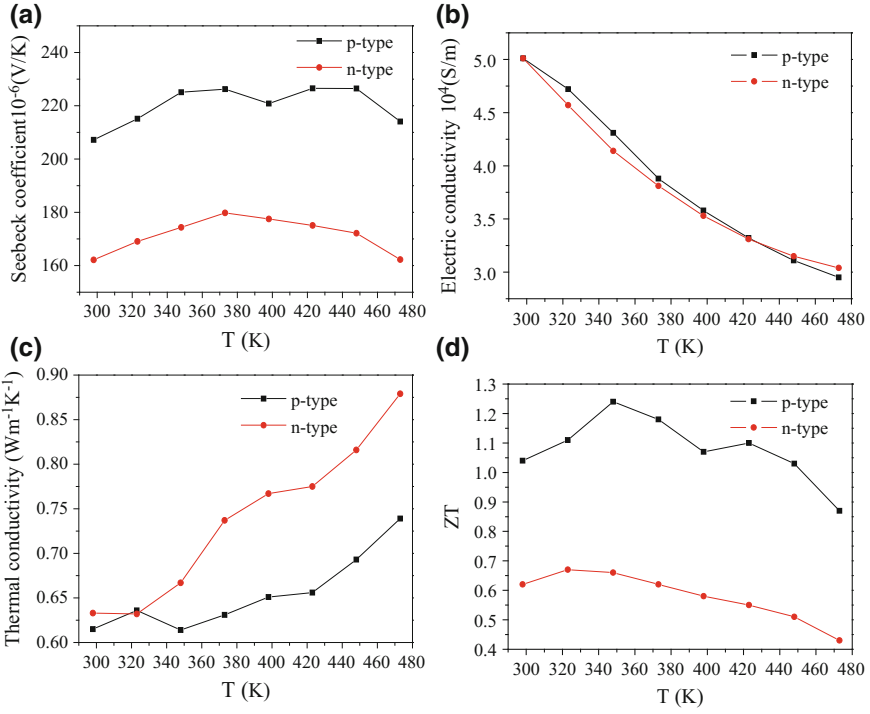

Fig. 3 Temperature dependence of **a** the Seebeck coefficient, **b** electrical conductivity, **c** thermal conductivity and **d** figure of merit ZT for p-type and n-type samples from 298 to 473 K

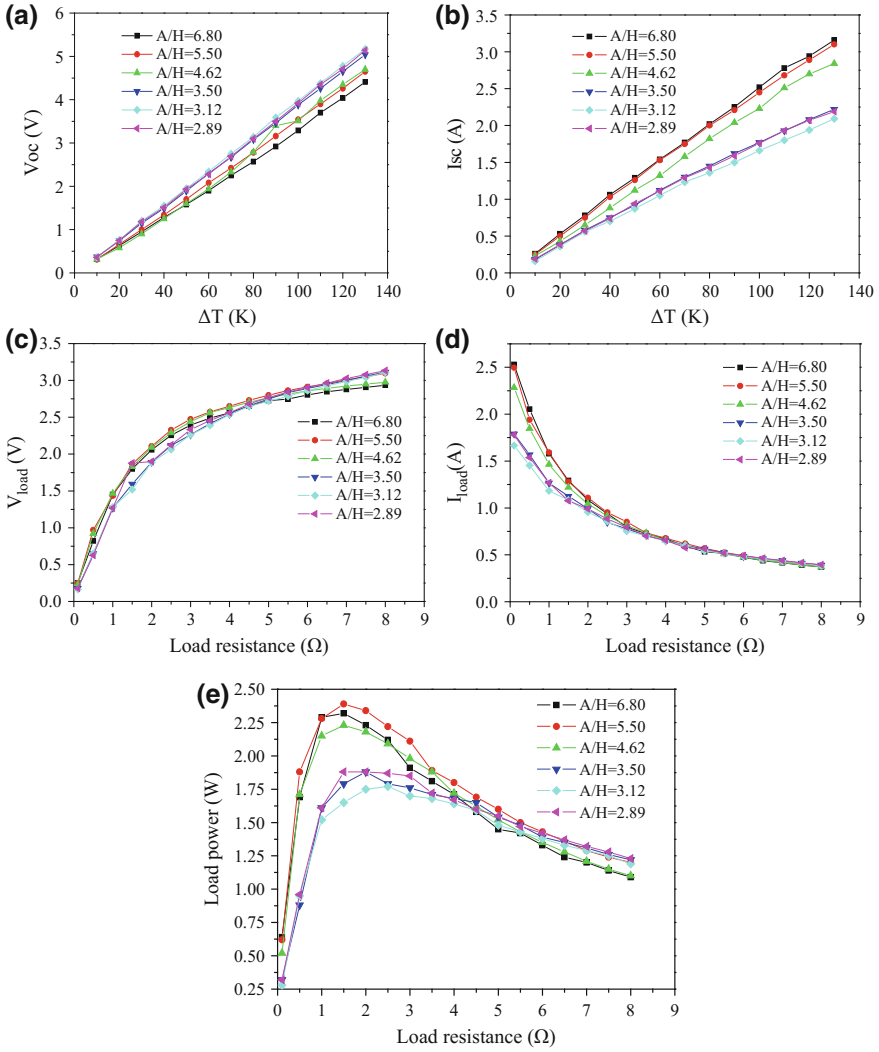

Fig. 4 Electric properties of TEG modules **a** temperature dependence of open-circuit voltage, **b** temperature dependence of short-circuit current, **c** load current temperature gradient 100 K, **d** load voltage temperature gradient 100 K and **e** load power temperature gradient 100 K

resistance for A/H = 2.89 is on account of the samples were experienced tow times cold pressing and sintering process. Figure 4a, b displays the open-circuit voltage and short-circuit current of TEG modules with a series of A/H respectively. Figure 4c–e shows load current, load voltage and load power with the load resistance range from 0.1 to 8 Ω. Electric properties of TEG modules, especially the current and the load power, increase with the A/H changing from 2.89 to 6.80. And the biggest load power is 2.39 W corresponding the module with A/H = 5.5 and

load resistance 1.5 Ω. Heat flux Q was obtained based on the one-dimensional Fourier's law [19, 20]: $Q = \kappa * A * \Delta T/L$ where κ and A are the thermal conductivity and the cross-sectional area, respectively. ΔT is the temperature difference measured by the thermocouples embedded in the two Cu block and L is the vertical distance between the two thermocouples. The cross section area of all p or n leg is 1.7 * 1.7 mm^2. It is obvious that the higher A/H can lead to lower L and higher Q. Although higher A/H and Q is good for achieving bigger output power, in actual application, heat dissipation potential on cold side must be considered.

Conclusion

In summary, p-type and n-type material with perfect compatibility on electrical conductivity were acquired by this method easily to realize mass production. The optimal ZT value for p-type material is 1.24 at 348 K. Electric properties of TEG modules increase with the A/H adding from 2.89 to 6.80 and the biggest load power is 2.39 W corresponding the module with A/H = 5.5 and load resistance 1.5 Ω at temperature gradient 100 K. However, in practical application, heat dissipation capacity on cold side must be considered to acquire ideal temperature gradient and output power.

Acknowledgements This work was supported by the Guangdong Leizig Thermoelectric Technologies Co., Ltd.

References

1. M. Zebarjadi, K. Esfarjani, M.S. Dresselhaus, Z.F. Ren, G. Chen, Perspectives on thermoelectrics: from fundamentals to device applications. Energy Environ. Sci. **5**, 5147 (2012)
2. D. Wang, X. Ling, H. Peng, L. Liu, L. Tao, Efficiency and optimal performance evaluation of organic Rankine cycle for low grade waste heat power generation. Energy **50**, 343 (2013)
3. Z. Wang, N. Zhou, J. Guo, X. Wang, Fluid selection and parametric optimization of organic Rankine cycle using low temperature waste heat. Energy **40**, 107–115 (2012)
4. J.W. Fergus, Oxide materials for high temperature thermoelectric energy conversion. J. Eur. Ceram. Soc. **32**, 525–540 (2012)
5. G.J. Snyder, E.S. Toberer, Complex thermoelectric materials. Nat. Mater. **7**, 105 (2008)
6. A.J. Minnich, M.S. Dresselhaus, Z.F. Ren, G. Chen, Bulk nanostructured thermoelectric materials: current research and future prospects. Energy Environ. Sci. **2**, 466–479 (2009)
7. M. Barati, S. Esfahani, T.A. Utigard, Energy recovery from high temperature slags. Energy **36**, 5440 (2011)
8. X.W. Wang, H. Lee, Y.C. Lan, G.H. Zhu, G. Joshi, D.Z. Wang, J.Yang, A.J. Muto, M.Y. Tang, J. Klatsky, S. Song, M.S. Dresselhaus, G. Chen, Z.F. Ren, Enhanced thermoelectric figure of merit in nanostructured n-type silicon germanium bulk alloy. Appl. Phys. Lett. **93**, 193121 (2008)

9. J.R. Sootsman, D.Y. Chung, M.G. Kanatzidis, New and old concepts in thermoelectric materials. Angew. Chem. Int. Edit. **48**, 8616–8639 (2009)
10. J.P. Heremans, V. Jovovic, E.S. Toberer, A. Saramat, K. Kurosaki, A. Charoenphakdee, S. Yamanaka, G.J. Snyder, Enhancement of thermoelectric efficiency in PbTe by distortion of the electronic density of states. Science **321**, 554–557 (2008)
11. Q.H. Zhang, X.Y. Huang, S.Q. Bai, X. Shi, C. Uher, L.D. Chen, Thermoelectric devices for power generation: recent progress and future challenges. Adv. Eng. Mater. **18**, 194–213 (2016)
12. D. Kraemer, J. Sui, K. McEnaney, H. Zhao, Q. Jie, Z.F. Renand, G. Chen, High thermoelectric conversion efficiency of MgAgSb-based material with hot-pressed contacts. Energy Environ. Sci. **8**, 1299–1308 (2015)
13. P.A. Zong, R. Hanus, M. Dylla, Y.S. Tang, J.C. Liao, Q.H. Zhang, G.J. Snyder, L.D. Chen, Skutterudite with graphene-modified grain-boundary complexion enhances zT enabling high-efficiency thermoelectric device. Energy Environ. Sci. **10**, 183–191 (2017)
14. Y.S. Park, T. Thompson, Y. Kim, J.R. Salvador, J.S. Sakamoto, Protective enamel coating for n- and p-type skutterudite thermoelectric materials. J. Mater. Sci. **50**, 1500–1512 (2015)
15. J.R. Salvador, J.Y. Cho, Z. Ye, J.E. Moczygemba, A.J. Thompson, J.W. Sharp, J.D. Koenig, R. Maloney, T. Thompson, J. Sakamoto, H. Wang, A.A. Wereszczak, Power-generation characteristics after vibration and thermal stresses of thermoelectric unicouples with $CoSb_3$/Ti/Mo(Cu) interfaces. Phys. Chem. Chem. Phys. **16**, 12510–12520 (2014)
16. H.S. Kim, W.S. Liu, Z.F. Ren, The bridge between the materials and devices of thermoelectric power generators. Energy Environ. Sci. **10**, 69–85 (2017)
17. T. Sakamoto, Y. Taguchi, T. Kutsuwa, K. Ichimi, S. Kasatani, M. Inada, Investigation of barrier-layer materials for Mg_2Si/Ni interfaces. J. Electron. Mater. **45**, 321–1327 (2016)
18. M. Gu, X.G. Xia, X.Y. Huang, S.Q. Bai, X.Y. Li, L.D. Chen, Study on the interfacial stability of p-type Ti/$Ce_yFe_xCo_{4-x}Sb_{12}$ thermoelectric joints at high temperature. J. Alloys Compd. **671**, 238–244 (2016)
19. F. Hao, P. Qiu, Y. Tang, S. Bai, High efficiency Bi_2Te_3-basedmaterials and devices for thermoelectric power generation between 100 and 300 °C. Energy Environ. Sci. **9**, 3120 (2016)
20. Q. Zhang, J. Liao, Y. Tang, M. Gu, C. Ming, P. Qiu, S. Bai, X. Shi, C. Uher, L. Chen, Realizing a thermoelectric conversion efficiency of 12% in bismuth telluride/skutterudite segmented modules through full-parameter optimization and energy-loss minimized integration. Energy Environ. Sci. **10**, 956–963 (2017)

The Influence of Al Content on the Thermoelectric Property of Al-Doped ZnO Thin Films

Ying-Zhen Li, Zhuang-Hao Zheng, Jing-Ting Luo, Fu Li, Guang-Xing Liang and Ping Fan

Abstract Direct current magnetron reactive sputtering was used to deposit Al-doped ZnO (AZO) thin films on BK7 glass substrates by using Zn–Al alloy target at room-temperature. Al contents of Zn–Al alloy target were changed and all AZO thin films were annealed at 773 K for 1 h. It can be found that all the AZO thin films were n-type semiconductor material, and have preferred orientation with the c-axis normal. The thermoelectric properties results show that the Seebeck coefficient of the AZO thin films with Al content of 4 wt% has higher Seebeck value of 64 μV/K in comparison with others. The electric conductivity and power factor of AZO thin films with Al content of 2 wt% have maximum values of that 5.30×10^4 S/m and 0.74×10^{-4} W/mK^2, respectively.

Keywords AZO thin film · Oxygen argon ratio · Thermoelectric properties Zn–Al alloy target

Introduction

Nowadays, there is a lot of waste heat in the social life and production. One of the ways which heat to electrical energy directly is using thermoelectric materials [1]. Thermoelectric device is a kind of the applications about renewable energy resource alternatives to fossil fuels [2]. The efficiency of thermoelectric device is decided by the merit (defined as $S^2T\sigma\kappa^{-1}$) of thermoelectric material [3]. ZnO has outstanding thermoelectric property and chemical stability, so it is considered to be one of the

Y.Z. Li · Z.H. Zheng (✉) · J.T. Luo · F. Li · G.X. Liang · P. Fan (✉)
Shenzhen Key Laboratory of Advanced Thin Films and Applications,
Institute of Thin Film Physics and Applications, College of Physics and Energy, Shenzhen University,
Shenzhen 518060, China
e-mail: zhengzh@szu.edu.cn

P. Fan
e-mail: fanping@szu.edu.cn

Y. Han (ed.), *Advances in Energy and Environmental Materials*,
Springer Proceedings in Energy, https://doi.org/10.1007/978-981-13-0158-2_5

best materials about thermoelectric application [4]. The large exciton binding energy of ZnO is 60 meV at room temperature and the wide band gap material with an energy gap is 3.3 eV [5]. ZnO film is one of n-type semiconductor material. Because there are oxygen vacancies and interstitial Zn in the ZnO film, electrical conductivity of ZnO thin film improves and the Seebeck on high temperatures keeps high [6]. ZnO thin film can be deposited by different of techniques, for example sputtering, chemical vapor deposition and so on [7]. In the paper, the deposition technique is direct current magnetron reactive sputtering using Zn–Al alloy target. And the thermoelectric properties of AZO films were investigated as the function of Al contents.

Experimental

AZO films were deposited on BK7 glass substrates with the size of 30 × 30 × 2 mm using direct current reactive magnetron sputtering by Zn–Al alloy target at room-temperature. Prior to thin film deposition, the BK7 substrates were ultrasonically cleaned in alcohol for 5 min and then in deionized water for 5 min. The background pressure reached 6.0×10^{-4} Pa. The work pressure was set to 0.5 Pa with 6 sccm of O_2 as the reactive gas and 40 sccm of Ar as the working gas. The sputtering power of Zn–Al remained 100 W. In order to remove contaminants and native oxides on the surfaces of the Zn–Al alloy target, a 10-min sputter cleaning process was performed. The deposition time was 30 min. After the films were deposited, the films were annealed at 773 K for one hour in the chamber pressure of 8.0×10^{-4} Pa. In order to study the influence of Al content on the thermoelectric properties of AZO films, Zn–Al alloy targets with Al content of 1, 2, 3 and 4 wt% were used for depositing the thin films.

The electric conductivity [defined as $\sigma = (R_s d)^{-1}$] of the thin films were tested by using the of four-probe technique to obtain the sheet resistance R_s and DEKTAK3 ST (RIGAKU ULTIMA4) surface-profile measurement system to obtain the thickness d. The Seebeck coefficient was obtained at by a Seebeck coefficient measurement system with the temperature from 313 to 553 K under air atmosphere. The microstructure was characterized by X-ray diffractometer technique (BRUKER DEKTAKXT). The surface morphology was obtained by using scanning electron microscope.

Results and Analysis

The electrical conductivities of the AZO films on different measuring temperature were changed, and the result is showed in Fig. 1a. The electrical conductivities of the films decrease with the increasing temperature, manifesting the behavior of metallic conduction. The thin film with 1 wt% Al content has low electrical

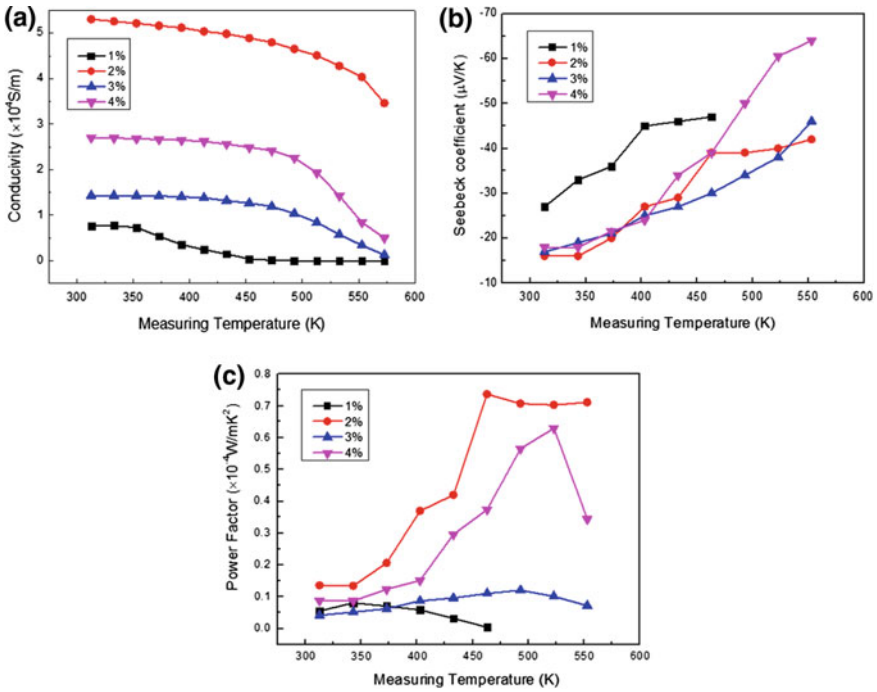

Fig. 1 Electrical conductivities, Seebeck coefficients and power factors of AZO films **a** electrical conductivities, **b** Seebeck coefficients, **c** power factors

conductivity, which is lower than 30 S/m when the measuring temperature is higher than 493 K. The electrical conductivity of the thin film with 2 wt% Al content is higher than others and the maximal value is 5.30×10^4 S/m. The electrical conductivity is defined as $\sigma = nev$. Because Al^{3+} ions replaces Zn^{2+} ions, the carrier density (n) increase when Al-doping content of AZO films increases. Meanwhile, the carrier mobility (v) decreased due to the scattering by ionized impurity [8].

The Seebeck coefficients of the AZO films on different measuring temperature are showed in Fig. 1b. All the Seebeck coefficients are negative, which illustrates that all of the films are n-type semiconductor. The Seebeck coefficient of the film with 1 wt% Al content is higher than others when the measuring temperature is lower than 463 K. However, it is unstable that the Seebeck coefficient transforms to positive and then changes to negative again when the measuring temperature is higher than 463 K, so the accurate measurement of the Seebeck coefficients can't be obtained in high temperature. That is why we did not provide the data over 463 K of this sample. The Seebeck coefficients (defined as $S = \gamma\text{-ln } n$) of the thin films increase with the increasing temperature. It explains that scattering factor (γ) increase with increasing of Al-doping content which may due to scattering process of Al^{3+} ions in high temperature. And the interaction between carrier and lattice vibration may also intensify in high temperature. The absolute values of the thin

films are similar to each other in the low measuring temperature, but when the measuring temperature is higher than 463 K, the Seebeck coefficient of the thin film with 4 wt% Al content is highest. Besides, the maximal absolute value is 64 μV/K.

The power factors of the AZO films on different measuring temperature are showed in Fig. 1c. When the measuring temperature is increases, the power factors of thin films increase. But they have a little decrease when the measuring temperature continues to rise. When the Al content of the films increases, the power factors of the films trend to rise firstly and then decrease. The maximal value of power factor is 0.74×10^{-4} W/mK^2 with the Al content of 2 wt%.

X-ray diffraction patterns of AZO films are shown in Fig. 2. The thin films with 2, 3 and 4 wt% Al content have two major diffraction peaks and the peaks locate at 34.4° and 72.5°. Which are indexed as the reflection from the diffraction of the ZnO (002) and (004) planes. It indicates that the AZO films have preferred orientation with the *c*-axis normal. The intensity of the (002) plane first increases and then decreases as the Al contents of thin films increase. The thin film with 4 wt% Al content has a relatively stronger intensity. However, the thin films with 1 wt% Al content have eight major diffraction peaks located at 31.8°, 34.4°, 36.3°, 47.5°, 56.6°, 62.9°, 38.0° and 72.5°, which are indexed as the reflection from the diffraction of the ZnO (100), (002), (101), (102), (110), (103), (112) and (004) planes. It indicates that the growth orientation of this thin film is various which may cause the weak intensity of planes with 1 wt% Al content. In addition, it may also cause that the thin film with 1 wt% Al content has a low electrical conductivity and an unstable Seebeck coefficient in high temperature. On the whole, the films with suitable Al-doping content have preferable crystallinity and stronger texture. Besides, the peak of Al or aluminium oxide measured in the XRD pattern is not exist. It infers that Al atoms have been combined in the lattice. And there is no elemental or oxide of Al in the films [9].

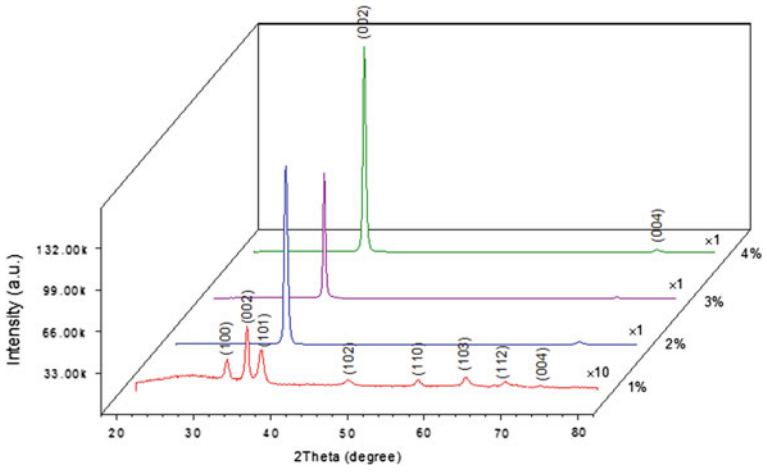

Fig. 2 XRD patterns of samples

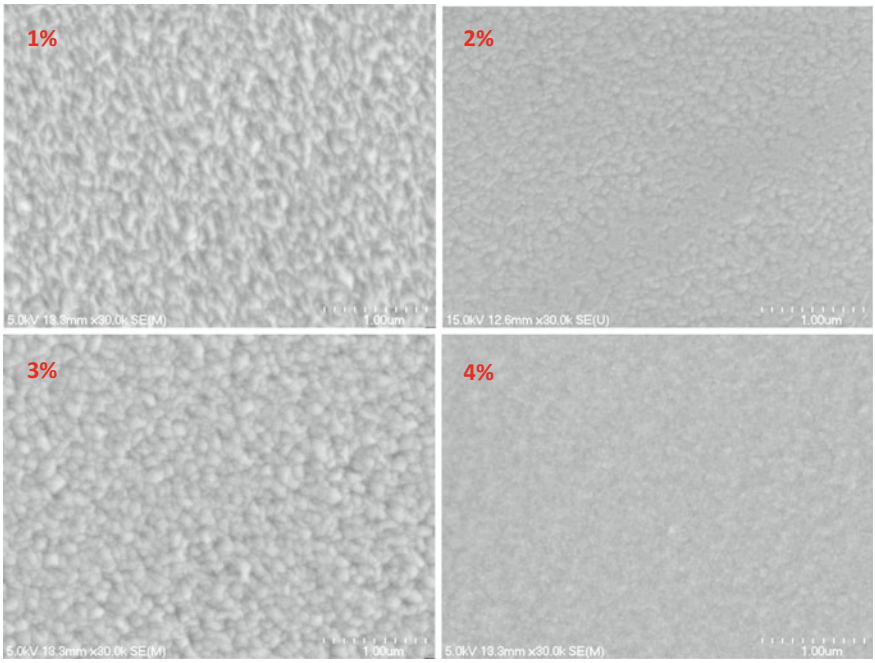

Fig. 3 The SEM of samples

The SEM of AZO films are shown in Fig. 3. It shows that the grain of AZO film with 1 wt% Al content is pointed. The electron transport of AZO films may be choked. As a results, the Seebeck coefficient become unstable and the electrical conductivity decrease [8]. The grains of films become round as the Al contents of thin films increase.

Conclusions

AZO films were obtained by using direct current reactive magnetron sputtering by Zn-Al alloy target with different Al contents at room temperature. And then thin films were annealed at 773 K for one hour. The XRD pattern illustrates that the film with Al content of 4 wt% has well crystallinity and higher Seebeck coefficient with the maximal absolute value of 64 μV/K. The electric conductivity and power factor of AZO films deposited by Zn-Al alloy targets with 2 wt% Al content are highest of all the samples, where the maximum value is 5.30×10^4 S/m and 0.74×10^{-4} W/mK^2, respectively. Therefore, appropriate Al doping-content can enhance thermoelectric properties of AZO films.

Acknowledgements This work is supported by Basical Research Program of Shenzhen (JCYJ20160307113206388), National Natural Science Foundation of China (No. 11604212 and 61404086).

References

1. P. Fan, Z.H. Zheng, Y.Z. Li, Q.Y. Lin, J.T. Luo, G.X. Liang, X.M. Cai, D.P. Zhang, F. Ye, Appl. Phys. Lett. **106**, 073901 (2015)
2. D.K. Seo, S. Shin, H.H. Cho, B.H. Kong, D.M. Whang, H.K. Cho, Acta Mater. **59**, 6743–6750 (2011)
3. Z.H. Zheng, P. Fan, J.T. Luo, X.M. Cai, G.X. Liang, D.P. Zhang, F. Ye, Thin Solid Films **562**, 181–184 (2014)
4. T. Tian, L.H. Cheng, J.J. Xing, L.Y. Zheng, Z.Y. Man, D.L. Hu, S. Bernik, J.T. Zeng, J. Yang, Y. Liu, G.Y. Li, Mater. Des. **132**, 479–485 (2017)
5. L. Li, L. Fang, X.M. Chen, J. Liu, F.F. Yang, Q.J. Li, G.B. Liu, S.J. Feng, Physica E **41**, 169–174 (2008)
6. C.L. Cramera, G.J. Jesus, P.S. Colasuonno, T.B. Holland, J. Eur. Ceram. Soc. **37**, 4693–4700 (2017)
7. A. Moustaghfir, E. Tomasella, A. Rivaton, B. Mailhot, M. Jacquet, J.L. Gardette, J. Cellier, Surf. Coat. Technol. **180–181**, 642–645 (2004)
8. P. Fan, Y.Z. Li, Z.H. Zheng, Q.Y. Lin, J.T. Luo, G.X. Liang, M.Q. Zhang, M.C. Chen, Appl. Surf. Sci. **284**, 145–149 (2013)
9. N.H. Sheeba, S.C. Vattappalam, G.S Okram, V. Sharma, P.V. Sreenivasan, S. Mathew, R. ReenaPhilip, Mater. Res. Bull. **93**, 130–137 (2017)

Effect of Working Pressure on the Structural and Thermoelectric Properties of Bismuth Telluride Thin Films Deposited by Magnetron Sputtering

Zhiwei Zhang, Yuan Deng, Yao Wang, Daming Zhu, Wenhui Yan, Zhigang Jia and Fen Wang

Abstract Highly (00l)-oriented bismuth telluride polycrystalline thin films were prepared on quartz glass by magnetron co-sputtering at appropriate working pressure. The effect of working pressure on the growth behavior, microstructure and electrical transport properties of Bi_2Te_3 thin films were studied. The results showed that increasing working pressure brought more particle scattering and also decreased the velocity of the sputtered particles. As a result, the nucleation rate of the crystal grains decreased and more sufficient growth along the in-plane direction was induced. When the working pressure was 2.0 Pa, the balance between nucleation rate and growth rate of the crystal grains reached, which brings highly (00l) crystal plane orientation in Bi_2Te_3 polycrystalline thin film. Compared with the Bi_2Te_3 thin film with certain (015) orientation deposited at 0.5 Pa, the

Z. Zhang (✉) · D. Zhu · W. Yan · Z. Jia · F. Wang
AECC Aero Engine Academy of China, Beijing 101304, China
e-mail: zzw704@163.com

D. Zhu
e-mail: damingzhu@126.com

W. Yan
e-mail: abuaa@163.com

Z. Jia
e-mail: jia2001720@126.com

F. Wang
e-mail: wafenng@163.com

Y. Deng · Y. Wang
Beijing Key Laboratory for Advanced Functional Materials and Thin Film Technology, School of Materials Science and Engineering, Beihang University, Beijing 100191, China
e-mail: dengyuan@buaa.edu.cn

Y. Wang
e-mail: wang-yao@buaa.edu.cn

Y. Han (ed.), *Advances in Energy and Environmental Materials*,
Springer Proceedings in Energy, https://doi.org/10.1007/978-981-13-0158-2_6

(00l)-oriented Bi_2Te_3 thin film had the double Seebeck coefficient, which was above -200 μV K^{-1} between 300 and 400 K and reached to the maximum value -225 μV K^{-1} at 360 K. Therefore the power factor of the thin film is greatly enhanced and reaches to above 38×10^{-4} W m^{-1} K^{-2} at 360 K, which is comparable to the value of the optimal $Bi_2Te_{2.7}Se_{0.3}$ bulk alloys.

Keywords Bismuth telluride · Thin film · Magnetron sputtering
Thermoelectric property

Introduction

Thermoelectric (TE) materials can achieve the direct conversion between heat and electricity and have been heavily investigated over the past few decades for solid state cooling and power generation [1–3]. Energy conversion efficiency of a TE material can be evaluated by the dimensionless figure of merit $ZT = S^2\sigma T/\kappa$, where S, σ, T and κ are the Seebeck coefficient, electrical conductivity, absolute temperature and thermal conductivity, respectively [4, 5]. Therefore, a good TE material should possess high electrical conductivity, high Seebeck coefficient and low thermal conductivity. However, because these parameters are coupled via band structures and scattering mechanisms, it is difficult to control them independently and the optimization of thermoelectric property is limited in bulk materials [6]. Recently, low dimensionality has been proved to be an effective way to improve ZT by increasing the Seebeck coefficient due to quantum confinement effect and simultaneously decreasing thermal conductivity owing to the enhanced phonon scattering at boundaries and interfaces [7–10].

Bismuth telluride based thermoelectric materials are still the best TE materials near room temperature, which is very suitable for cooling and refrigeration. Based on the rapid development of micro-cooling devices integrated with microelectromechanical systems (MEMS), the deposition of high performance Bi_2Te_3 based thin films is of great interest. Two dimensional thin films are also convenient for adjusting and optimizing the microstructure of TE materials [11]. Many techniques have been reported to prepare Bi_2Te_3 based thin films, such as physical evaporation, molecular beam epitaxy (MBE), pulsed laser deposition (PLD), and metal organic chemical vapor deposition (MOCVD) [12–15]. Compared with these methods, magnetron sputtering is more beneficial to deposit thin films with high density and large-scale fabrication. During deposition, working pressure is a very important parameter, which can affect the deposition rate, quality and microstructure of thin film. Therefore, it is necessary to study the effect of working pressure on the microstructure and thermoelectric properties of Bi_2Te_3 thin films particularly.

In this study, Bi_2Te_3 thin films were deposited by co-sputtering in order to control the composition of the films. The effects of working pressure on the microstructure and thermoelectric properties of Bi_2Te_3 thin films were investigated.

Experimental

Bismuth telluride thin films were deposited on polished quartz glass substrate by co-sputtering method, described in our previous work [16]. Hot-pressed Bi_2Te_3 target (99.99%) and Te target (99.99%) with 60 mm diameter were used and the distance between targets and substrates maintained at 90 mm. Bi_2Te_3 target was connected to a direct current power supplier with 20 W and Te target was connected to a radio frequency power supplier with 45 W. The deposition temperature and duration were fixed at 350 °C and 1 h, while the working pressure varied from 0.5 to 2.2 Pa.

X-ray diffraction (XRD) patterns of the products were taken on a Rigaku D/MAX 2200 PC automatic X-ray diffractometer. Morphologies and composition of the thin films were analyzed by field emission scanning electron microscopy (FE-SEM) (FEI Sirion 200) and energy dispersive X-ray spectroscopy (EDS). Carrier concentration and mobility were measured on a Hall effect measurement system (ECOPIA HMS-3000). In-plane electrical conductivity and Seebeck coefficient were simultaneously measured by ZEM-3 (Ulvac Riko, Inc.).

Results and Discussion

Figure 1 shows the XRD patterns of the Bi_2Te_3 thin films deposited at different working pressure. It can be found that the diffraction peaks of the samples are well assigned to the standard pattern of Bi_2Te_3 with rhombohedral structure (JCPDS 15-0863). For the Bi_2Te_3 thin film deposited at 0.5 Pa, certain (015) orientation is achieved. Along with the increase of working pressure, the film gradually converts to be highly (00l) oriented at 2.0 Pa, indicating the vital effect of working pressure on the microstructure of Bi_2Te_3 thin film.

The surface view and cross-sectional view of the Bi_2Te_3 thin films are shown in Fig. 2. From the surface view (Fig. 2a), it can be seen that the film deposited at 0.5 Pa consists of nanoscale grains with average size of about 600 nm. These grains are well crystallized, but not parallel to the substrate. From the cross-sectional view, it can be seen that the thin film has island growth mode with column structure, which are orderly stacked by nanoplates, as shown in Fig. 2b. This orientation is consistent with the result of XRD. As the working pressure increases, the films become more dense and flat composing of hexagonal crystals. As shown in Fig. 2g, h, the film deposited at 2.0 Pa is composed of 300 nm hexagonal crystals stacked orderly with the ab plane preferentially oriented to form columns normal to the substrate, which confirms the greatly enhanced intensity of (00l) peaks as shown in XRD. For magnetron sputtering, increasing working pressure would bring more particle scattering and also decrease the velocity of the sputtered particles. As a result, the nucleation rate of crystal grains is decreased and more sufficient growth along the in-plane direction is induced. When the working pressure is 2.0 Pa, the

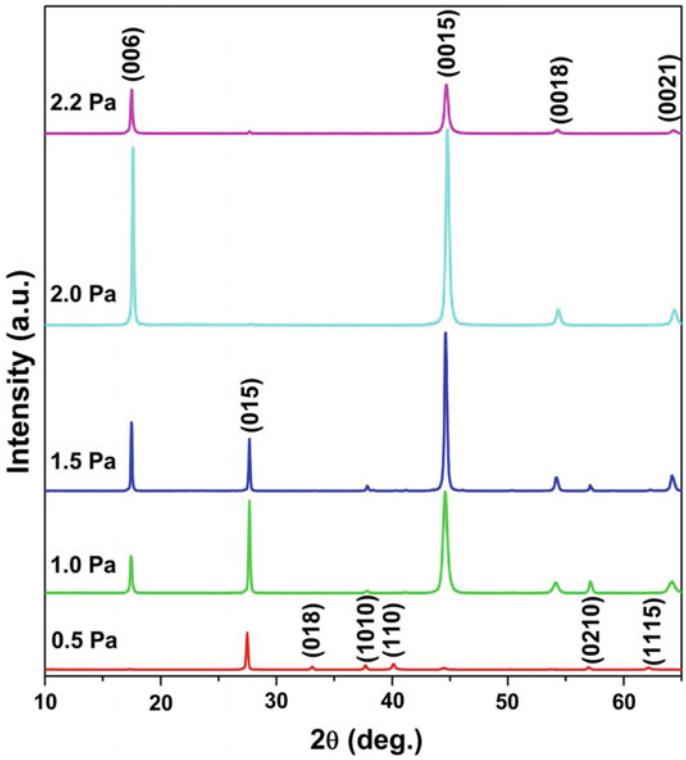

Fig. 1 XRD patterns of the Bi_2Te_3 thin films deposited at different working pressure

balance between nucleation rate and growth rate of crystal grains is reached, which brings highly (00 l) crystal plane orientation. All the films are stoichiometric with atomic ratio of ~2:3, as confirmed by EDS analysis (see Table 1 and the inset in Fig. 2).

Along with the structural characteristics, electrical transport properties of the Bi_2Te_3 thin films were also strongly affected by the working pressure, as shown in Fig. 3. Figure 3a shows the change of room temperature carrier concentration and mobility with working pressure. Along with the increase of working pressure, carrier concentration of the films decreases gradually, which is about -2.9×10^{20} cm^{-3} at 0.5 Pa and decreases to -1.0×10^{20} cm^{-3} at 2.0 Pa. As evidenced by the SEM results, the lower nucleation rate and ampler growth of the crystal grains along the in-plane direction at higher working pressure would bring lower defects in the film and thus decrease the carrier concentration. On the contrary, carrier mobility of the films increases with working pressure, which achieves 52 cm^2 V^{-1} s^{-1} at 2.0 Pa. The gradually formed layered nanostructure and enhanced (00l) plane orientation should constitute the transport passage for electrons. For the thin film deposited at 2.2 Pa, the weakened layered nanostructure and (00l) plane orientation cause the decrease of carrier mobility.

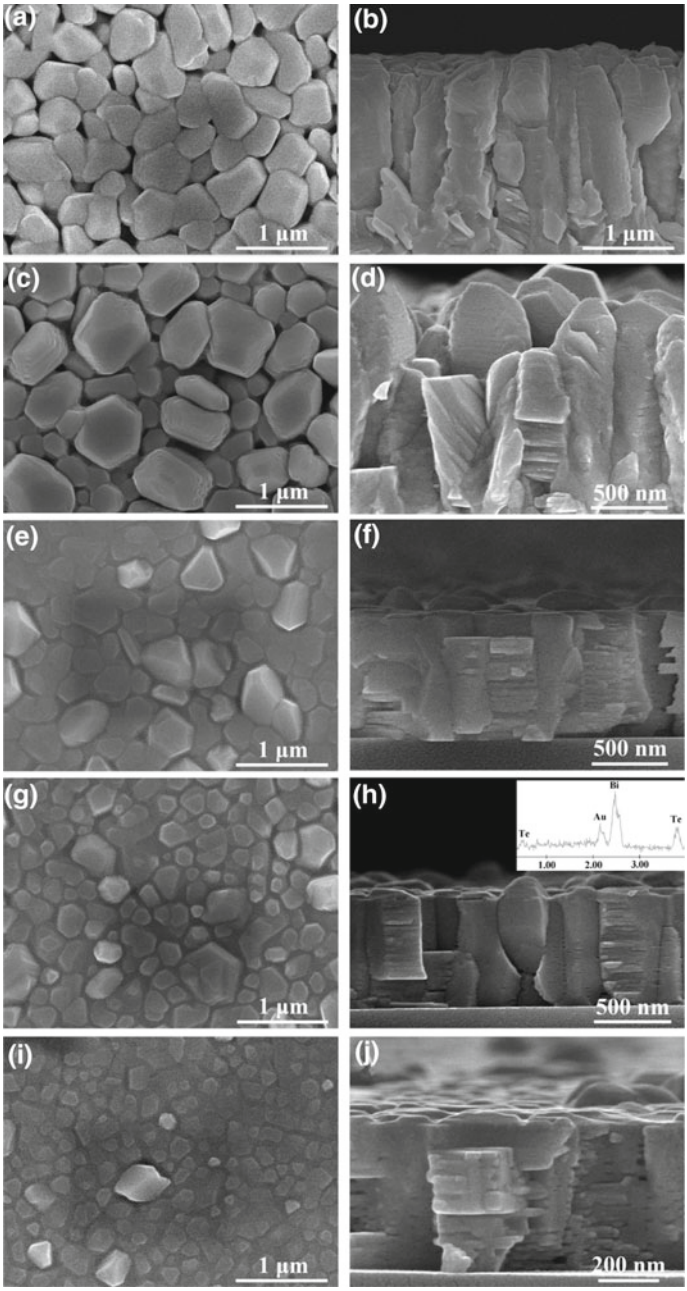

Fig. 2 Surface view and cross-sectional view of the Bi_2Te_3 thin films deposited at different working pressure: **a**, **b** 0.5 Pa; **c**, **d** 1.0 Pa; **e**, **f** 1.5 Pa; **g**, **h** 2.0 Pa; **i**, **j** 2.2 Pa

Table 1 Chemical composition of the thin films analyzed by EDS

Working pressure (Pa)	Bi content (at.%)	Te content (at.%)
0.5	39.9	60.1
1.0	40.1	59.9
1.5	40.1	59.9
2.0	39.9	60.1
2.2	39.8	60.2

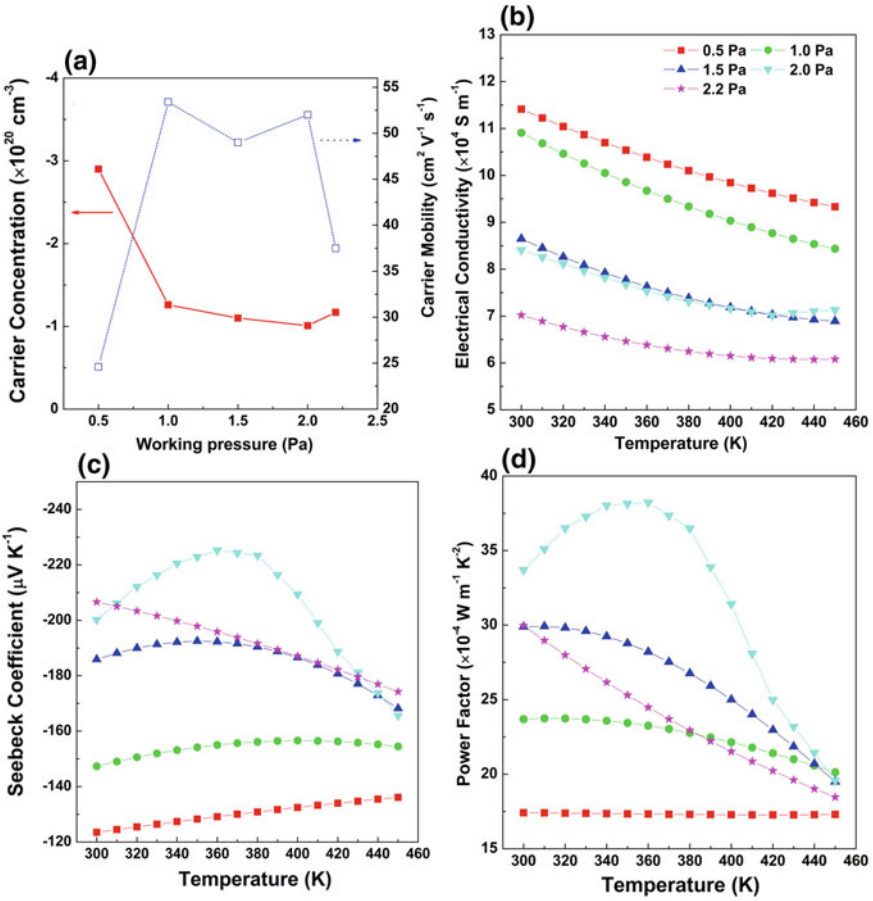

Fig. 3 Room temperature carrier concentration, carrier mobility (**a**) and the temperature dependence of electrical conductivities (**b**), seebeck coefficients (**c**) and power factors (**d**) of the Bi_2Te_3 thin films deposited at different working pressure with distinct microstructures

As shown in Fig. 3b, electrical conductivity decreases with the increase of working pressure. Electrical conductivity can be expressed with carrier concentration and mobility as $\sigma = ne\mu$, where n, μ, and e represent carrier concentration, carrier mobility, and the electronic charge, respectively. Therefore, the main reason is the decreased carrier concentration at higher working pressure. However, the electrical conductivity of the film deposited at 2.0 Pa is still comparable with the values of hot-pressed or SPS sintered Bi_2Te_3 based bulk materials, which is about 8.4×10^4 S m^{-1} at room temperature [17, 18].

Figure 3c shows the influence of working pressure on Seebeck coefficients of the thin films. All films have negative values of Seebeck coefficient, indicating the n-type transport behavior. With the rising working pressure, the absolute value of Seebeck coefficient increases and achieves the maximum value for the film deposited at 2.0 Pa, which is 200 μV K^{-1} at room temperature and 225 μV K^{-1} at 360 K. Because the carrier concentration and mobility of the films deposited between 1.0 and 2.0 Pa are nearly the same, the main reason should be the enhanced (00l) plane orientation and more obvious layered nanostructure. Based on Boltzmann distribution for the electrons, the Seebeck coefficient can be expressed as $S = k_B(s - \ln n)/e + C_1$, where k_B is the Boltzmann constant, s is the scattering parameter and C_1 is the proper constant [19]. As an approximation, the relaxation time can be expressed as $\tau = \tau_0 E^s$, where τ_0 is a constant and E stands for the energy of carriers. The preferential orientation of (00l) plane and layered nanostructure parallel to the substrate would prolong relaxation time and enlarges scattering parameter. Therefore, the film deposited at 2.0 Pa with complete (00l) plane orientation and obvious layered nanostructure has the maximum Seebeck coefficient.

The relationship between temperature and power factor for the films deposited at different working pressure is shown in Fig. 3d. For the film deposited at 2.0 Pa, the power factor is near 34×10^{-4} W m^{-1} K^{-2} and exceeds 38×10^{-4} W m^{-1} K^{-2}, which is even comparable with the reported maximum power factor of the n-type $Bi_2Te_{2.7}Se_{0.3}$ bulk material (35×10^{-4} W m^{-1} K^{-2}), indicating the superiority of magnetron sputtering for depositing (00l)-oriented Bi_2Te_3 based TE material [20].

Conclusion

In summary, highly (00l) plane orientation in Bi_2Te_3 thin film has been achieved by optimizing working pressure using a simple magnetron co-sputtering method. Higher working pressure brings more particle scattering and also decreases the velocity of the sputtered particles. As a result, the nucleation rate of the crystal grains is decreased and more sufficient growth along the in-plane direction is induced. When the balance between nucleation rate and growth rate of the crystal grains is reached, highly (00l) crystal plane orientation in Bi_2Te_3 polycrystalline

thin film is achieved. Due to this special nanostructure, the Seebeck coefficient and power factor of Bi_2Te_3 thin film can be greatly promoted. Preferential orientation of the optimum crystal plane is also applicable to other TE materials with anisotropy for enhancing thermoelectric property.

Acknowledgements This work was supported by the State Key Program of National Natural Science Foundation of China (Grant No. 61534001) and National Natural Science Foundation of China (Grant No. 51601005)

References

1. I. Chowdhury, R. Prasher, K. Lofgreen, G. Chrysler, S. Narasimhan, R. Mahajan, D. Koester, R. Alley, R. Venkatasubramanian, On-chip cooling by superlattice-based thin-film thermoelectrics. Nat. Nanotechnol. **4**, 235–238 (2009)
2. Q. Zhang, X. Huang, S. Bai, X. Shi, C. Uher, L. Chen, Adv. Eng. Mater. **18**, 194–213 (2016)
3. X. Hu, P. Jood, M. Ohta, M. Kunii, K. Nagase, H. Nishiate, M.G. Kanatzidis, A. Yamamoto, Power generation from nanostructured PbTe-based thermoelectrics: comprehensive development from materials to modules. Energy Environ. Sci. **9**, 517–529 (2016)
4. D.M. Rowe, *Thermoelectrics Handbook: Macro to Nano* (CRC Press, Boca Raton, 2005)
5. Y. Chen, M. He, B. Liu, G.C. Bazan, J. Zhou, Z. Liang, Bendable n-type metallic nanocomposites with large thermoelectric power factor. Adv. Mater. **29**, 1604752 (2017)
6. L.D. Zhao, V.P. Dravid, M.G. Kanatzidis, The panoscopic approach to high performance thermoelectrics. Energy Environ. Sci. **7**, 251–268 (2014)
7. Y. Pei, H. Wang, G.J. Snyder, Band engineering of thermoelectric materials. Adv. Mater. **24**, 6125–6135 (2012)
8. J.J. Urban, Prospects for thermoelectricity in quantum dot hybrid arrays. Nat. Nanotechnol. **10**, 997–1001 (2015)
9. Y. Liu, P. Sahoo, J.P.A. Makongo, X. Zhou, S.J. Kim, H. Chi, C. Uher, X. Pan, P.F. P. Poudeu, Large enhancements of thermopower and carrier mobility in quantum dot engineered bulk semiconductors. J. Am. Chem. Soc. **135**, 7486–7495 (2013)
10. D. Wu, L.D. Zhao, F. Zheng, L. Jin, M.G. Kanatzidis, J. He, Understanding nanostructuring processes in thermoelectrics and their effects on lattice thermal conductivity. Adv. Mater. **28**, 2737–2743 (2016)
11. M. Tan, Y. Deng, Y. Wang, Ordered structure and high thermoelectric properties of $Bi_2(Te, Se)_3$ nanowire array. Nano Energy **3**, 144–151 (2014)
12. M. Kashiwagi, S. Hirata, K. Harada, Y. Zheng, K. Miyazaki, M. Yahiro, C. Adachi, Enhanced figure of merit of a porous thin film of bismuth antimony telluride. Appl. Phys. Lett. **98**, 023114 (2011)
13. N. Peranio, M. Winkler, M. Dürrschnabel, J. König, O. Eibl, Assessing antisite defect and impurity concentrations in Bi_2Te_3 based thin films by high-accuracy chemical analysis. Adv. Funct. Mater. **23**, 4969–4976 (2013)
14. A. Li Bassi, A. Bailini, C.S. Casari, F. Donati, A. Mantegazza, M. Passoni, V. Russo, C.E. Bottani, Thermoelectric properties of Bi–Te films with controlled structure and morphology. J. Appl. Phys. **105**, 124307 (2009)
15. Z. Sun, S. Liufu, X. Chen, L. Chen, Enhanced thermoelectric properties of $Bi_{0.5}Sb_{1.5}Te_3$ films by chemical vapor transport process. ACS Appl. Mater. Interfaces **3**, 1390–1393 (2011)
16. Z. Zhang, Y. Wang, Y. Deng, Y. Xu, The effect of (00l) crystal plane orientation on the thermoelectric properties of Bi_2Te_3 thin film. Solid State Commun. **151**, 1520–1523 (2011)

17. L.P. Hu, X.H. Liu, H.H. Xie, J.J. Shen, T.J. Zhu, X.B. Zhao, Improving thermoelectric properties of n-type bismuth–telluride-based alloys by deformation-induced lattice defects and texture enhancement. Acta Mater. **60**, 4431–4437 (2012)
18. J.S. Son, M.K. Choi, M.K. Han, K. Park, J.Y. Kim, S.J. Lim, M. Oh, Y. Kuk, C. Park, S. J. Kim, T. Hyeon, Nano Lett. **12**, 640–647 (2012)
19. D.B. Hyun, J.S. Hwang, J.D. Shim, Thermoelectric properties of $(Bi_{0.25}Sb_{0.75})_2Te_3$ alloys fabricated by hot-pressing method. J. Mater. Sci. **36**, 1285–1291 (2001)
20. X. Yan, B. Poudel, Y. Ma, W.S. Liu, G. Joshi, H. Wang, Y.C. Lan, D.Z. Wang, G. Chen, Z.F. Ren, Experimental studies on anisotropic thermoelectric properties and structures of n-type $Bi_2Te_{2.7}Se_{0.3}$. Nano Lett. **10**, 3373–3378 (2010)

Quick Fabrication and Thermoelectric Properties of Doped Tetrahedrites

Ping Lv, Yun Yu and Xiaoya Li

Abstract In this paper, the effect of annealing time on the microstructure and thermoelectric properties of $Cu_{11.5}Mn_{0.5}Sb_4S_{13}$ tetrahedrite was studied, hoping to shorten the fabrication time of bulk doped tetrahedrites. The results show that $Cu_{11.5}Mn_{0.5}Sb_4S_{13}$ tetrahedrite phase formed in the melt during cooling. The ingot consisted of principal phase of $Cu_{11.5}Mn_{0.5}Sb_4S_{13}$ and secondary phases of Cu_3SbS_4, Cu_2S and $CuSbS_2$. Long time annealing could not eliminate the Cu_3SbS_4 and $CuSbS_2$ phases in $Cu_{11.5}Mn_{0.5}Sb_4S_{13}$ tetrahedrite. Sintering could eliminate Cu_2S phase. Long time annealing had slight effect on electrical resistivity, and negligible effect on Seebeck coefficient and thermal conductivity of $Cu_{11.5}Mn_{0.5}Sb_4S_{13}$ tetrahedrite. All the $Cu_{11.5}Mn_{0.5}Sb_4S_{13}$ samples had *ZT* in excess of 0.6 at above 650 K and the maximum *ZT* value obtained in this study was 0.74 for the un-annealed sample. Cobalt doped tetrahedrite $Cu_{11.5}Co_{0.5}Sb_4S_{13}$ fabricated by the un-annealed process could also obtain a *ZT* value of ~ 0.7. Based on the experimental results, the time for preparing doped tetrahedrites can be cut considerably.

Keywords $Cu_{11.5}Mn_{0.5}Sb_4S_{13}$ tetrahedrite · Annealing · Microstructure Thermoelectric properties

Introduction

With increasing energy consumption and intensifying environmental problems, the environment-friendly thermoelectric technology attracts wide attention as one of the alternative ways to tackle the above mentioned problems. Thermoelectric conver-

P. Lv · Y. Yu
School of Materials and Engineering, Jiangsu University of Technology, Changzhou 213001, China

P. Lv · X. Li (✉)
Shanghai Institute of Ceramics, Chinese Academy of Sciences, Shanghai 200050, China
e-mail: xyli@mail.sic.ac.cn

Y. Han (ed.), *Advances in Energy and Environmental Materials*,
Springer Proceedings in Energy, https://doi.org/10.1007/978-981-13-0158-2_7

sion efficiency depends on the Carnot efficiency and dimensionless figure of merit, the *ZT* value, defined as $ZT = \alpha^2 T/\rho\kappa$, where α, T, ρ and κ are the Seebeck coefficient, absolute temperature, electrical resistivity and thermal conductivity, respectively. The performance of thermoelectric materials has made great progress as the advancement of the theories of thermoelectric materials and synthetic preparation [1, 2]. However, the complicated and time- and energy-consuming fabrication process, high cost, toxic elements and the use of rare elements limit large-scale applications of thermoelectric materials.

Tetrahedrite ($Cu_{12}Sb_4S_{13}$) thermoelectric materials consist mainly of earth-abundant and environment-friendly elements copper and sulfur, moreover, natural mineral tetrahedrites can be used as direct source of the thermoelectric materials [3]. Researches on the low-cost, environment-friendly, high performance tetrahedrite thermoelectric materials are expected to create new opportunities of thermoelectric energy generation applications. Till now researches have been mainly focused on the enhancement of the thermoelectric performance of $Cu_{12}Sb_4S_{13}$ tetrahedrite by substitution Cu with Mn, Fe, Co, Ni, Zn and other elements. The highest *ZT* values reported for the Zn, Ni, Ni and Zn, Fe, Mn and Te doped tetrahedrites are 0.9 [3], 0.7 [4], 1.03 [5], 0.8 [3], 1.13 [6] and 0.92 [7], respectively. However, the preparation process of tetrahedrites is time and energy consuming. The melting time is about three days and the annealing time is two weeks [3]. In our previous work [8], a process was developed to prepare undoped tetrahedrite $Cu_{12}Sb_4S_{13}$ with good thermoelectric performance in a considerably reduced melting and annealing time. In this work, the effect of annealing time on the microstructure and thermoelectric properties of Mn doped tetrahedrite $Cu_{11.5}Mn_{0.5}Sb_4S_{13}$ was studied, hoping to shorten the fabrication time of bulk doped tetrahedrites. Results show that good thermoelectric performance doped tetrahedrite can also be obtained by a fast preparation process without annealing.

Experimental Procedures

Ten gram $Cu_{11.5}Mn_{0.5}Sb_4S_{13}$tetrahedrite ingots were prepared by a direct melting method. The starting materials, Cu shots (99.999%, Alfa-Aesar), Mn pieces (99.95%, Alfa-Aesar), Sb shot (99.9999%, Alfa-Aesar) and S pieces (99.999%, Alfa-Aesar), were weighed out in stoichiometric ratios and loaded into silica ampoules. The ampoules were evacuated to a pressure of 0.1 Pa and then sealed. The sealed ampoules were suspended in a vertical tube furnace, and heated to 923 K at a rate of 15 $Kmin^{-1}$ and held for four hours. Then the furnace was switched off, and the ampoules cooled down to room temperature.

To study the effect of annealing time on the microstructure and thermoelectric properties of $Cu_{11.5}Mn_{0.5}Sb_4S_{13}$ tetrahedrite, the ingots were crushed and ground into powders, and then cold pressed and placed into silica ampoules and a box furnace to anneal at 723 K for one day, 3, 7 and 14 days, respectively. The annealed pellets were ground into powders, loaded into graphite dies with a

diameter of 15 mm, and then hot pressed at 743 K and 62 MPa for 40 min. For comparison, a disc was also hot pressed under the same condition with the un-annealed powders. The sintered disks were cut for characterization of thermoelectric properties.

The samples were examined by powder X-ray diffraction (XRD, Rigaku Rint 2000, Cu K_α). The microstructure and phase composition of the ingot and sintered samples were also examined by SEM and EDS. The densities of the sintered samples were measured using the Archimedean method. The Seebeck coefficient and electrical resistivity were measured using the standard 4-probe method (LINSEIS LSR-3) in helium atmosphere. The thermal conductivity was calculated from the measured thermal diffusivity D, specific heat $C_{p,}$ and density d according to the relationship $\kappa = DC_pd$. Thermal diffusivity of the samples were measured by a laser flash method (LINSEIS LFA 1000) and the specific heat $C_p$of the samples was calculated using the Dulong-Petit law. The measurement errors for the electrical resistivity, the thermal conductivity and the Seebeck coefficient are ±5–7, ±5–7 and ±5%, respectively.

Results and Discussion

X-ray Diffraction Patterns. For the $Cu_{11.5}Mn_{0.5}Sb_4S_{13}$tetrahedrite powder samples are shown Fig. 1 The major peaks of the un-annealed sample match the $Cu_{12}Sb_4S_{13}$ phase, and a few peaks match Cu_3SbS_4, implying that the tetrahedrite phase forms in the melt during cooling, and the ingots consist of principal $Cu_{11.5}Mn_{0.5}Sb_4S_{13}$ tetrahedrite and secondary Cu_3SbS_4. The annealed samples also contain secondary phase Cu_3SbS_4. Wang [8, 9] and Chetty [10] and Suekuni [11] also observed the secondary phase Cu_3SbS_4 in the synthesized tetrahedrite materials. It seems long time annealing cannot eliminate the second phase Cu_3SbS_4 in tetrahedrites.

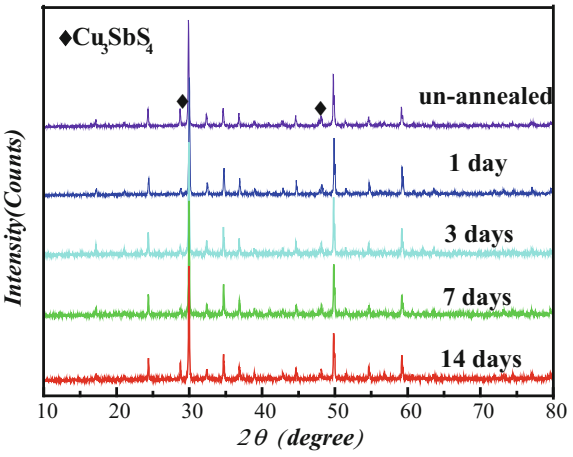

Fig. 1 X-ray diffraction patterns for the $Cu_{11.5}Mn_{0.5}Sb_4S_{13}$ tetrahedrite powder samples

SEM Back Scattering Images. of the $Cu_{11.5}Mn_{0.5}Sb_4S_{13}$ tetrahedrite ingot and sintered samples with powders before and after annealing for 1 day and 14 days are shown Fig. 2. It can be seen that the ingot consists of matrix and secondary phases in light grey, dark grey and white. EDS show they are $Cu_{11.5}Mn_{0.5}Sb_4S_{13}$, Cu_3SbS_4, Cu_2S and $CuSbS_2$, respectively. The sintered samples consist of matrix $Cu_{11.5}Mn_{0.5}Sb_4S_{13}$ and secondary Cu_3SbS_4 and $CuSbS_2$. The impurity phase $CuSbS_2$ is not found in the X-ray diffraction patterns (Fig. 1). The reason is likely that the content of impurity phase $CuSbS_2$ is too less to be detected, whose diffraction peak is obscured in comparison to the peaks of other phases. The impurity phase Cu_2S in the ingot disappears in the sintered samples, possibly due to the Cu_2S phase reacts further into other phase under high temperature and high pressure during the sintering process. In addition, the micro-porous area fraction of the sample sintered with the one day annealed powders is significantly less than that of the samples sintered with the powders before and after annealed for 14 days. As is known, the longer the annealing time the better the crystallization quality is for the annealed powders. And the better crystallization quality the poorer sintering property is for the annealed powders. This maybe the reason why the sample sintered with the one day annealed powders has less micro-porous in comparison to other samples.

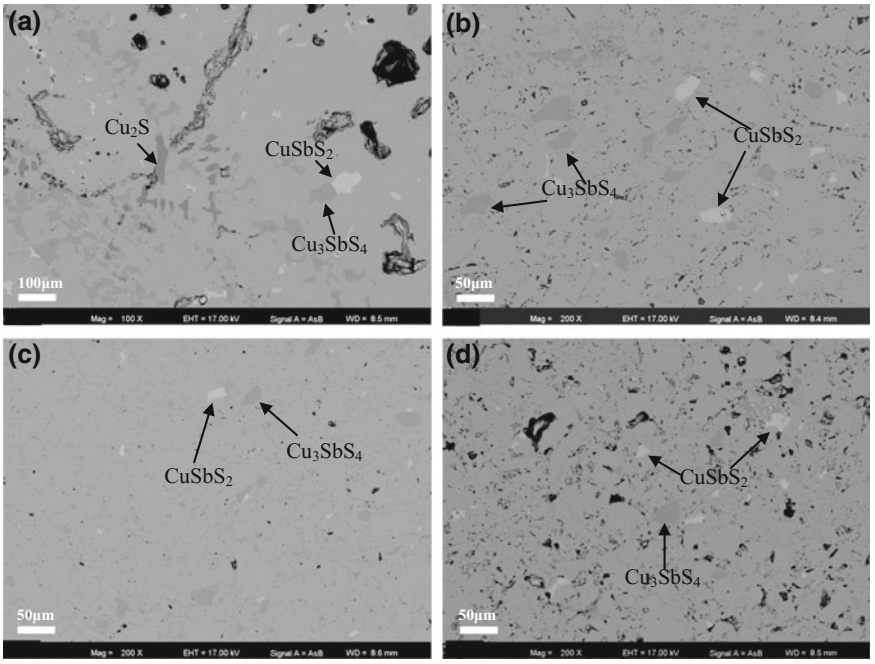

Fig. 2 Back-scattering images of the $Cu_{11.5}Mn_{0.5}Sb_4S_{13}$ Tetrahedrite ingot (**a**) and samples sintered with powder before (**b**) and after annealing for 1 day (**c**) and 14 days (**d**)

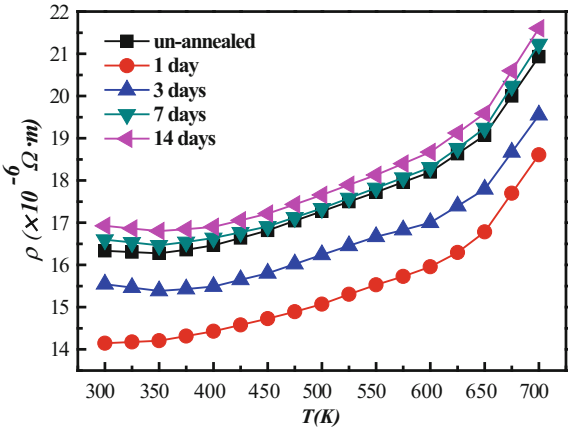

Fig. 3 Temperature dependence of the electrical resistivity for the$Cu_{11.5}Mn_{0.5}Sb_4S_{13}$ tetrahedrite samples sintered with powders before and after annealing

Electrical Conductivity. As a function of temperature for the $Cu_{11.5}Mn_{0.5}Sb_4S_{13}$ samples sintered with powders before and after annealing is shown Fig. 3. The electrical resistivity of all the samples of $Cu_{11.5}Mn_{0.5}Sb_4S_{13}$ increases with temperature. The tendency of the electrical resistivity change with temperature agrees with that reported by Wang [9] and Chetty [10]. The electrical resistivity of the samples decreases with increase of annealing time, and then increases with increasing annealing time when the annealing time exceeds one day. The electrical resistivity of the un-annealed sample is about 16.335–20.932 $\times$ 10^{-6} Ω m in whole temperature range. The electrical resistivity of the one day annealed sample drops to 14.145–18.608 $\times$ 10^{-6} Ω m, which is the lowest among the samples. And the electrical resistivity goes up to 15.542–19.548 $\times$ 10^{-6}, 16.597–21.228 $\times$ 10^{-6} and 16.928–21.603 $\times$ 10^{-6} Ω m for the 3, 7 and 14 days annealed samples, respectively. The trend of electrical resistivity change with annealing time is inconsistent with that of $Cu_{12}Sb_4S_{13}$ tetrahedrite [8], which goes down with increasing annealing time. The crystallization quality, homogeneity of the doped Mn (the real doping amount) and density combine to affect the electrical resistivity of the samples. As the annealing time increases, the crystallization quality and the homogeneity of the doped Mn are improved, and the density drops slightly under the same sintering condition. The electrical resistivity of the samples decreases with increasing of crystallization quality, and increases with increasing of real Mn doping amount and dropping of density. That's why the electrical resistivity of the samples drops at first, and then increase with increasing annealing time.

Seebeck Coefficient. As a function of temperature for the $Cu_{11.5}Mn_{0.5}Sb_4S_{13}$ tetrahedrite samples sintered with powders before and after annealing is shown in Fig. 4. The Seebeck cofficient of all the $Cu_{11.5}Mn_{0.5}Sb_4S_{13}$ tetrahedrite samples is positive and rises with temperature, which indicates the majority carriers are hole and the tetrahedrites exhibit p-type conduction. Although the seebeck coefficients of the sample is different, and the difference is small within the measurement error, which means that annealing time has a negligible effect on the seebeck coefficient.

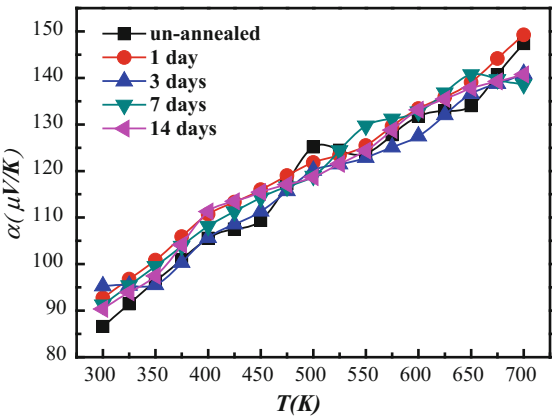

Fig. 4 Temperature dependence of the Seebeck coefficient for the $Cu_{11.5}Mn_{0.5}Sb_4S_{13}$ tetrahedrite samples sintered with powders before and after annealing

In the temperature range of 300–700 K, the seebeck coefficient of $Cu_{11.5}Mn_{0.5}Sb_4S_{13}$ tetrahedrite samples is between 86 and 150 μV/K, close to that of $Cu_{11.5}Mn_{0.5}Sb_4S_{13}$ tetrahedrites reported by Wang [9] and Chetty [10].

Thermal Conductivity. As function of temperature for the $Cu_{11.5}Mn_{0.5}Sb_4S_{13}$ tetrahedrite samples sintered with powders before and after annealing is shown in Fig. 5. The thermal conductivity of the samples rises with increasing temperature, and then drops slightly over the temperature range of 650–700 K, similar to those reported before [6, 9, 10]. It was attributed to a low lattice thermal conductivity resulting from complex crystal structure and strong lattice anharmonicity and dominant electronic thermal conductivity which increases with temperature according to Wiedemann-Franz law [7]. Among all the samples, the thermal conductivity of the one day annealed sample is the highest, 1.12–1.22 Wm^{-1} K^{-1}, over the temperature range of 400–700 K, while that of the un-annealed sample is the lowest, 0.96–1.00 Wm^{-1} K^{-1}. The thermal conductivity of the more than one annealed samples is very close, the difference of the thermal conductivity is within the measurement errors, indicating that prolonged annealing time has negligible effect on the thermal conductivity of $Cu_{11.5}Mn_{0.5}Sb_4S_{13}$ tetrahedrite.

Dimensionless Figure of Merit (*ZT*). As function of temperature for all the $Cu_{11.5}Mn_{0.5}Sb_4S_{13}$ tetrahedrite samples is calculated based on the above data and is presented in Fig. 6. It can be seen that the samples with different annealing time have similar *ZT* value in the temperature range of ~700 K, and the *ZT* value of the samples exceeds 0.6 at above 650 K. Theun-annealed sample has the largest *ZT* value of 0.74, which is very close to that of $Cu_{11.6}Mn_{0.4}Sb_4S_{13}$ tetrahedrite reported by Chetty [10]. This means it is unnecessary to prolong annealing to improve thermoelectric properties of $Cu_{11.5}Mn_{0.5}Sb_4S_{13}$tetrahedrite. Cobalt doped tetrahedrite $Cu_{11.5}Co_{0.5}Sb_4S_{13}$ was also prepared by the process of melting and hot press, without annealing. The *ZT* value of the tetrahedrite is ~0.7. It seems that preparation time of high performance doped tetrahedrite thermoelectric materials can be cut considerably.

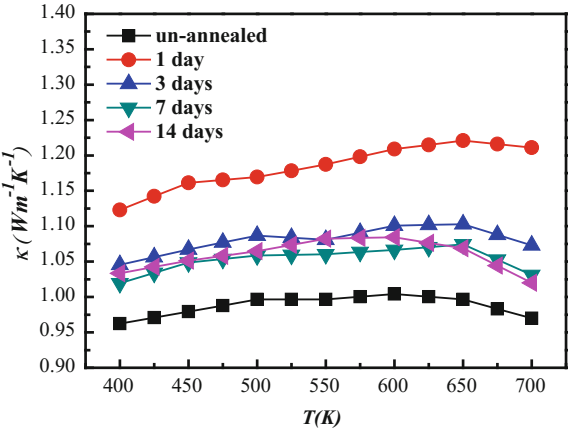

Fig. 5 Temperature dependence of the thermal conductivity for the $Cu_{11.5}Mn_{0.5}Sb_4S_{13}$ tetrahedrite samples sintered with powders before and after annealing

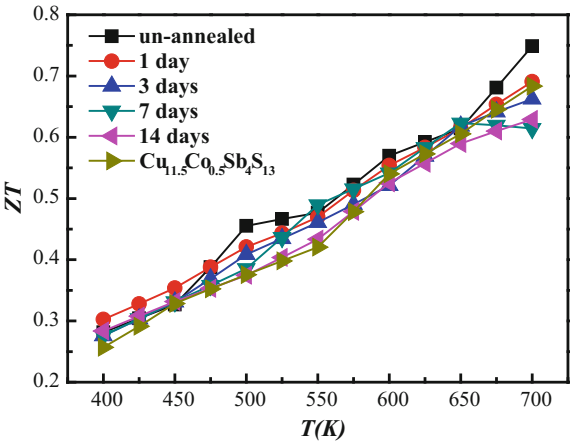

Fig. 6 Temperature dependence of the figure of merit for the $Cu_{11.5}Mn_{0.5}Sb_4S_{13}$ tetrahedrite and $Cu_{11.5}Co_{0.5}Sb_4S_{13}$ tetrahedrite samples

Summary

Manganese doped tetrahedrite $Cu_{11.5}Mn_{0.5}Sb_4S_{13}$ was fabricated by fast melting and annealing method. The $Cu_{11.5}Mn_{0.5}Sb_4S_{13}$tetrahedrite phase forms in the melt during cooling. The ingot consists of principal phase of $Cu_{11.5}Mn_{0.5}Sb_4S_{13}$ and secondary phases of Cu_3SbS_4, Cu_2S and $CuSbS_2$. Annealing has negligible effect on eliminating the Cu_3SbS_4 and $CuSbS_2$ phases in $Cu_{11.5}Mn_{0.5}Sb_4S_{13}$ tetrahedrite. Sintering can eliminate Cu_2S phase. Long time annealing has slight effect on electrical resistivity, and negligible effect on Seebeck coefficient and thermal conductivity of $Cu_{11.5}Mn_{0.5}Sb_4S_{13}$ tetrahedrite. All the $Cu_{11.5}Mn_{0.5}Sb_4S_{13}$ samples have *ZT* in excess of 0.6 at above 650 K and the maximum *ZT* value obtained in this study is 0.74 for the un-annealed sample. Cobalt doped tetrahedrite $Cu_{11.5}Co_{0.5}Sb_4S_{13}$ fabricated by the un-annealed process also obtained *ZT* value of

$\sim$0.7. Based on our experimental results, the time for preparing doped tetrahedrites can be cut considerably.

Acknowledgements This work is financially supported by Natural Science Foundation of China (51372261).

References

1. L.D. Zhao, H.J. Wu, S.Q. Hao, C.I. Wu, X.Y. Zhou, K. Biswas, J.Q. He, T.P. Hogan, C. Uher, C. Wolverton, All-scale hierarchical thermoelectrics: MgTe in PbTe facilitates valence band convergence and suppresses bipolar thermal transport for high performance. Energy Environ. Sci. **6**, 3346–3355 (2013)
2. Y.Z. Pei, X.Y. Shi, A. LaLonde, H. Wang, L.D. Chen, G.J. Snyder, Convergence of electronic bands for high performance bulk thermoelectrics. Nature **473**, 66–69 (2011)
3. X. Lu, D.T. Morelli, Y. Xia, F. Zhou, V. Ozolins, H. Chi, C. Uher, High performance thermoelectricity in earth-abundant compounds based on natural mineral tetradrites. Adv. Energy Mater. **3**, 342–348 (2013)
4. K. Suekuni, K. Tsuruta, M. Kunii, H. Nishiate, E. Nishibori, S. Maki, M. Ohta, A. Yamamoto, M.J. Koyano, High performance thermoelectric mineral $Cu_{12-x}Ni_xSb_4S_{13}$ tetradrites. J. Appl. Phys. **113**, 043712 (2013)
5. X. Lu, D.T. Morelli, Y. Xia, F. Zhou, V. Ozolins, Increasing the thermoelectric figure of merit of tetrahedrite by co-doping with nickel and zinc. Chem. Mater. **27**, 408–413 (2015)
6. J. Heo, G. Laurita, S. Muir, M.A. Subramanian, D.A. Keszler, Enhanced thermoelectric performance of synthetic tetrahedrites. Chem. Mater. **26**, 2047–2051 (2014)
7. X. Lu, D. Morelli, The effect of Te substitution for Sb on thermoelectric properties of tetrahedrite. J. Electron. Mater. **43**, 1983–1987 (2014)
8. J.Y. Wang, M. Gu, Y.F. Bao, X.Y. Li, L.D. Chen, Quick fabrication and thermoelectric properties of $Cu_{12}Sb_4S_{13}$ tetrahedrite. J. Electron. Mater. **45**, 2274–2277 (2016)
9. J.Y. Wang, X.Y. Li, Y.F. Bao, Thermoelectric properties of Mn doped $Cu_{12-x}Mn_xSb_4S_{13}$ tetrahedrites. Mater. Sci. Forum **847**, 161–165 (2016)
10. R. Chetty, P. Kumar, G. Rogl, P. Rogl, E. Bauer, H. Michor, S. Suwas, S. Puchegger, G. Giesterg, R. Mallik, Thermoelectric properties of a Mn substituted synthetic tetrahedrite. Phys. Chem. Chem. Phys. **17**, 1716–1727 (2015)
11. K. Suekuni, K. Tsuruta, T. Ariga, M. Koyano, Thermoelectric properties of mineral tetrahedrite $Cu_{10}Tr_2Sb_4S_{13}$. Appl. Phys. Exp. **5**, 05120 (2012)

Analysis and Characterization of the Microstructure Properties for U–Zr Series Alloys

Zhiyong Bai, Jiancheng Liu and Xuewei Zhang

Abstract The microstructure of alloy has an important influence on the application as fuel elements in the reactor. By spray casting the U–2, 4, 6, 8 and 10 wt% Zr series alloy are prepared. Alloy samples are treated through homogenization annealing. In the paper, the transformation law of microstructure and performance of the alloy under different conditions was studied and the thermal physical properties of U–Zr series alloy were also obtained. The results show it will provide technical basis for the application of the U–Zr alloy fuel.

Keywords Microstructure · Homogenization annealing · Thermal physical properties · U–Zr series alloy

Introduction

Zirconium has a relative low cross section of thermal neutron. Thus uranium alloys with Zr have excellent corrosion resistance and dimensional stability in the thermal cycling. These advantages make the U–Zr alloy becoming excellent choice of fuel in nuclear reactor. As early as 1985, three kinds of fuel U–10Zr, U–8Pu–10Zr, U–19Pu–10Zr were tested in the EBR-II in the United States. Results show that the addition of Zr increases the compatibility between the alloy fuel and cladding material [1]. And the irradiation stability of U–Zr alloy fuel is closely related to the composition, phase structure and microstructure uniformity.

Z. Bai (✉) · J. Liu · X. Zhang
China North Nuclear Fuel Co. Ltd., 456, Baotou 014035, Inner Mongolia, China
e-mail: bzyzlqnm@163.com

J. Liu
e-mail: 690226911@qq.com

X. Zhang
e-mail: 969647786@qq.com

Y. Han (ed.), *Advances in Energy and Environmental Materials*,
Springer Proceedings in Energy, https://doi.org/10.1007/978-981-13-0158-2_8

The phase composition of U–Zr alloy and the phase transformation law during the heat treatment greatly affect the application of alloy fuel in the reactor operation. So far, U–Zr alloy are used as reactor fuel in as-cast form commonly. The research about U–Zr alloy casting and subsequent processing has been rarely reported. Thus, the microstructures of a series of uranium zirconium alloy with different states were studied to provide theoretical basis for further development and application of U–Zr alloy fuel in this paper.

Experiments

Firstly a series of U–Zr alloy samples with the Zr content of 2, 4, 6, 8 and 10 wt% were prepared by spray casting. Homogenization heat treatment was carried out on the samples. Metallographic microscope, XRD, scanning electron microscopy (SEM), energy dispersive spectrometer (EDS) were used to detect and analyze the alloy. The microstructure of as-cast alloy and alloy with different heat treatment were studied. At the same time alloy density, heat capacity (specific heat), thermal conductivity, thermal expansion coefficient and other physical performance of the U–Zr series alloy have been inspected.

Metallographic Tests. The polished and corrosion state of U–Zr alloy with different heat treatments were analyzed by metallographic microscope. The universal research level automatic metallographic microscope was used in the research with the models AxioObserverZ1m. At the same time the alloy composition is analyzed by Scanning Electron Microscopy (SEM) spectrometer (Model VEGA3XMU).

Phase Structure Analysis. The phase structure of U–Zr alloy was analyzed by X-ray diffract meter (model D8 Da Vinci). The scanning mode is 2θ with scan range from 10° to 90°. The step interval is 0.02°. And each step acquisition time is 0.02 s. The source is standard Cu Kα with a wave length of 0.154 nm. The work voltage of the X ray tube is 40 kV and the current is 40 mA.

Physical Performance Tests. The tests sample size is Φ20 mm. The thermal conductivity tests are conducted on thermal conductivity detection instrument (LSA457). The STA449F3 synchronous heat analyzer was used to measure the specific heat. And the thermal expansion coefficient was tested by the DIL402CD thermal expansion coefficient meter.

Results and Discussion

Microstructure Analysis of the Spray as-cast Alloy Sample. As-cast alloy sample polished is observed by the metallographic microscope. Figure 1 shows the polished states of U–2 wt% Zr and U–8 wt% Zr alloy. The surface of the specimen

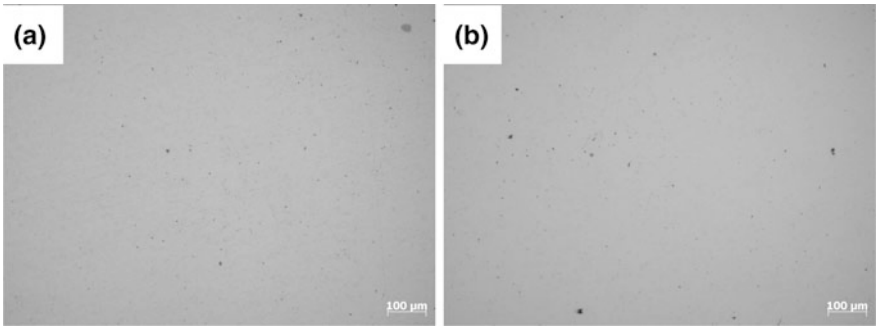

Fig. 1 Metallographic pictures of polished state for spray casting samples. **a** U–2 wt% Zr, **b** U–8 wt% Zr

is smooth. There are no obvious inclusion and incomplete fusion. The microstructure appearance of the other series alloy is similar as Fig. 1, which shows that the alloy prepared through the present melting process can be alloyed fully.

The corrosive states of the as-cast sample are shown in Fig. 2. Figure 2a is U–2 wt% Zr alloy. In the grey matrix there uniformly distributes small light phase. Figure 2b is U–4 wt% Zr alloys, the area light phase become bigger, with a fish-bone shape. And there is evident grain boundary. At the same time there appears some acicular structure within the grain boundary, which is similar to the acicular martensite. The states of U–6 wt% Zr and U–8 wt% Zr alloy are shown in Fig. 2c, d. The acicular structure is more visible in microscopic tissue. But it turns to be smaller. The microstructure of U–10 wt% Zr alloy appeared to be lath-like interleaved distribution. And the two phases show to be an alternative distribution. There are more and larger light color phase particles in U–10 wt% Zr alloy.

A spectral analysis of light phase of different alloys is shown in Fig. 3. The results show that it is U–56 wt% Zr. According to the phase diagram, during the cold process of melt, the Zr-rich phase will precipitate firstly, and then the structure of equilibrium is formed. The light colored parts of the alloy are considered to be Zr-rich phase, and the grey matrix is the α-U + δ phase (Fig. 4).

The acicular structure in the metallographic photograph is similar to that of the quenched α' phase in the U-rich alloy. In order to study the formation mechanism of acicular structure, the U–4 wt% Zr alloy sample was selected for quenching (metallographic pictures are shown in Fig. 5). And the acicular microstructure in the U–4 wt% Zr alloy after quenching is martensite. This is consistent with the microstructure of the as cast U–4 wt% Zr alloy sample. It shows that the cooling rate of melting in the mould is high in the spray molding process, which reaches the level of the quenching. In addition, with the further increase of Zr, acicular structure become small step by step until the microstructure of U–10 wt% Zr alloy reaching the lath-like interleaved distribution. It suggests that under the same process condition, the alloy phase transition resistance increases gradually and the metastable

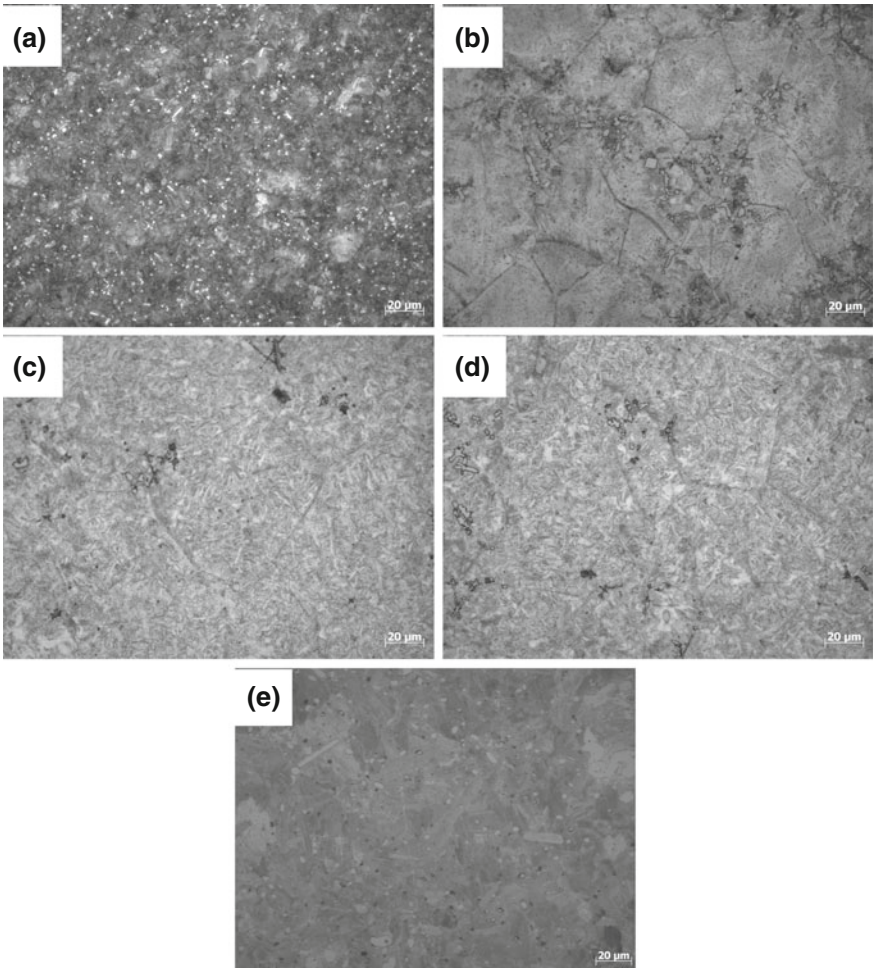

Fig. 2 Corrosive metallographic pictures of as-cast U–Zr alloy samples. **a** U–2 wt% Zr, **b** U–4 wt % Zr, **c** U–6 wt% Zr, **d** U–8 wt% Zr, **e** U–10 wt% Zr

organization increases. And the stability of the metastable organization in the alloy with high contents of Zr is improved.

X-ray tests are made on all alloys, as shown in Fig. 4. Most of components are α-U, and when the content of Zirconium reaches 10% there appeared α-U + δ phase.

Microstructure Analysis of the Alloy after the Homogenization Annealing. The sample of spray cast is treated with homogenization annealing. First, polish the sample. Then the microstructure of the sample is observed by the image analyzer.

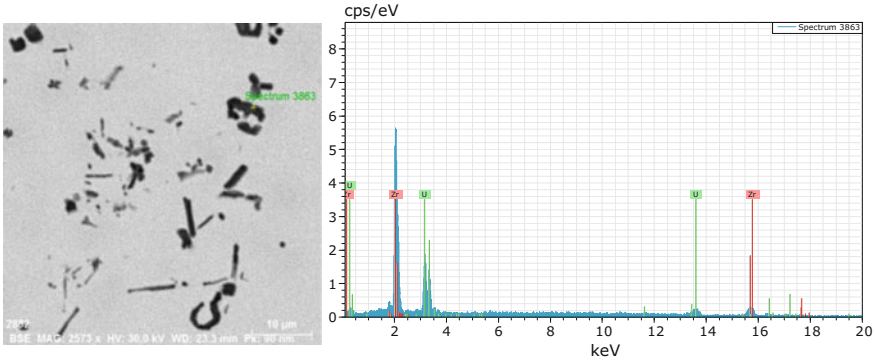

Element	Weigh percentage(%)	Atom percentage(%)
Zr	56.79	77.42
U	43.21	22.58

Fig. 3 Spectrum analysis of U–Zr alloy spray casting sample

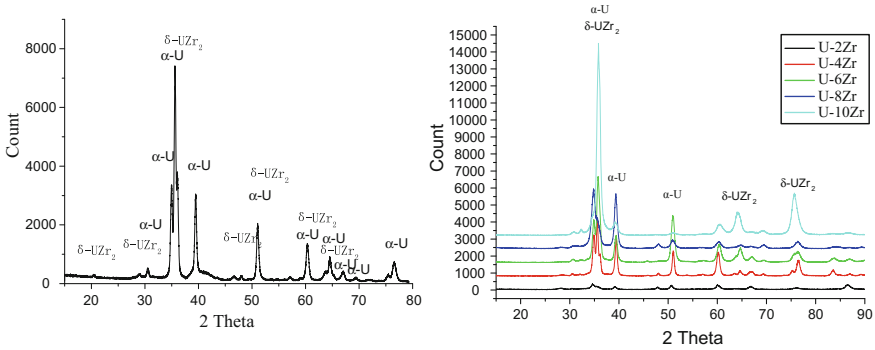

Fig. 4 XRD curve of as cast alloy samples

Fig. 5 Quenching metallographic picture of U–4 wt% Zr alloy sample

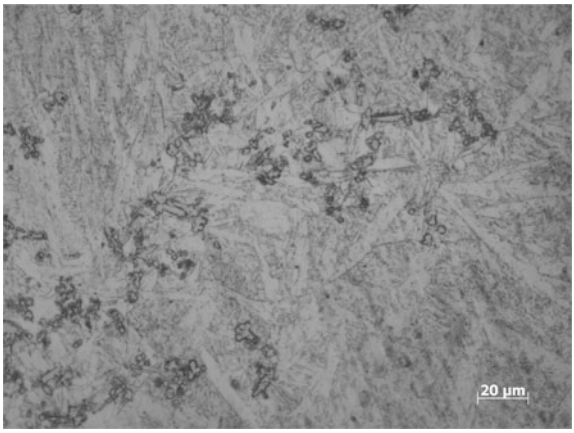

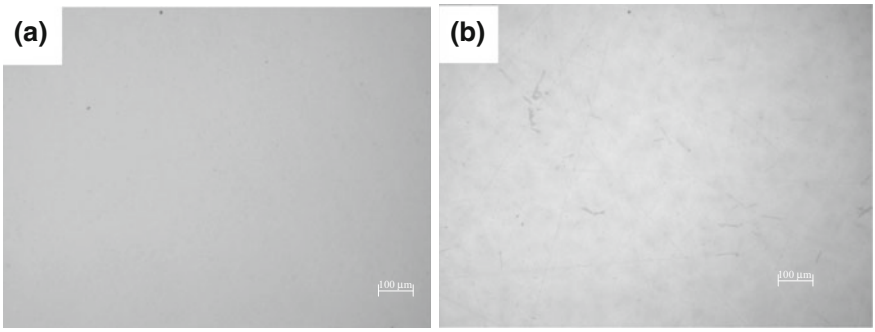

Fig. 6 Metallographic structure of U–Zr alloys after homogenization annealing. **a** U–2 wt% Zr, **b** U–10 wt% Zr)

Figure 6 is the pictures of polished U–2 wt% Zr and U–10 wt% Zr. The surface of the sample is smooth. And there are no obvious inclusion and incomplete fusions.

Figure 7 shows the metallographic picture after the Homogenization annealing of U–Zr alloy. Figure 7a, b show the U–2 wt% Zr, U–4 wt% Zr state respectively. The microstructure is layered, which is similar to the pearlite state of steel. And with the increase content of zirconium, layers of microstructure progressively refinement. Figure 7c is the metallographic photograph of U–6 wt% Zr alloy; the microstructure is shown as the lath-like interleaved distribution. With the content of Zr increased, the microstructure of U–8 wt% Zr alloy is similar to the twin structures in the pearlite (Fig. 7d). When the content of Zr is 10 wt%, the twin morphology of organization is more apparent and become finer (Fig. 7e).At the same time characteristic of pearlite is further weakened.

Homogenizing annealing is approximately equal to balance cooling. Figure 8 is equilibrium phase diagram of U–Zr alloy [2]. According to the phase diagram, the phase transformation of U–2–10 wt% of Zr alloy is from hypereutectoid to eutectoid transformation, and then the hypereutectoid transformation. The phase undergoes the transformation from a single γ phase to $\gamma' + \beta(U)$. As the temperature drops the phase become $\beta(U)$, $\alpha(U)$ and Zr-rich phase $\beta(Zr)$, finally it becomes $\alpha(U) + \delta$ phase at room temperature. With the content of Zr increases, it is difficult to undergo the solid diffusion transformation. And because of the pinning effect of Zr elements, microstructure transform in the form of twin change, Fig. 7e obviously shows the typical twin microstructure.

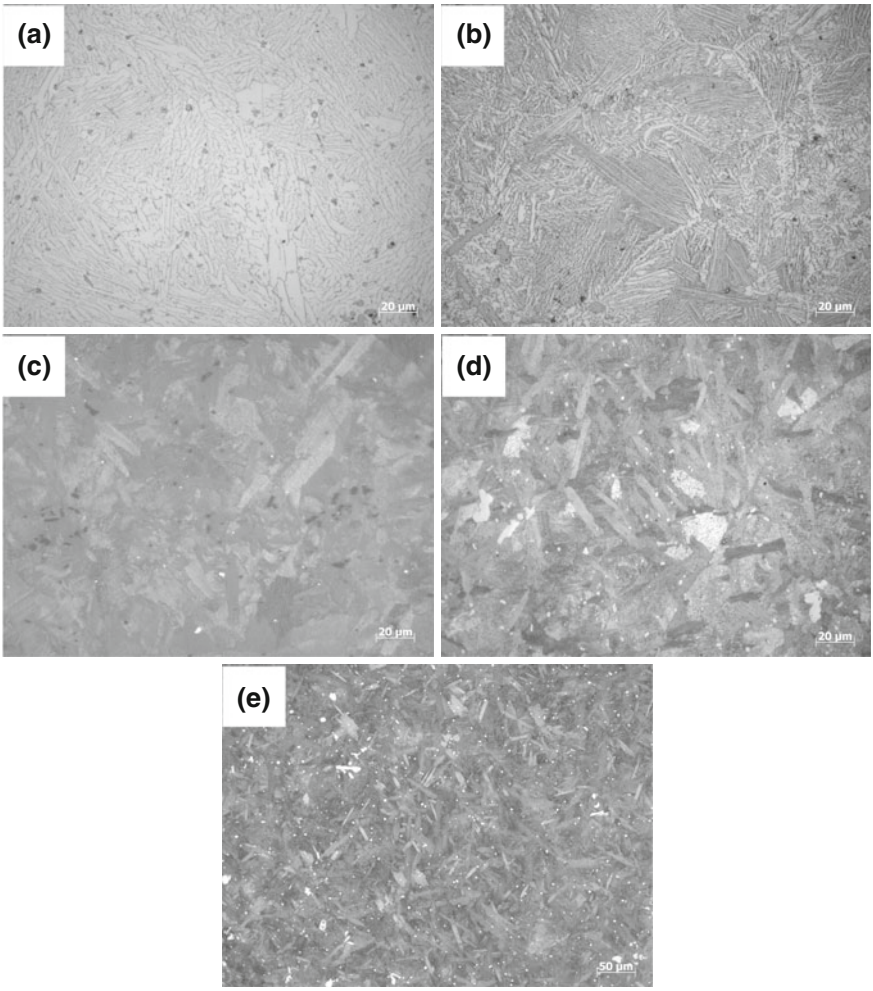

Fig. 7 Metallographic microstructure of U–Zr alloys after homogenization annealing. **a** U–2 wt% Zr, **b** U–4 wt% Zr, **c** U–6 wt% Zr, **d** U–8 wt% Zr, **e** U–10 wt% Zr

A spectral analysis of light objects is demonstrated in Fig. 9. The results show that it is U–75 wt% Zr. According to the phase diagram, during the cooling process of melting, the Zr-rich phase firstly precipitated, and then the structure of the near balance is formed. So the light colored parts of the alloy are considered to be Zr-rich phase and the grey matrix is the (α-U + δ) phase.

X-ray tests are made on all alloys, as shown in Fig. 10. Most of components are α-U, and when the content of Zirconium reaches 10% there appeared δ phase.

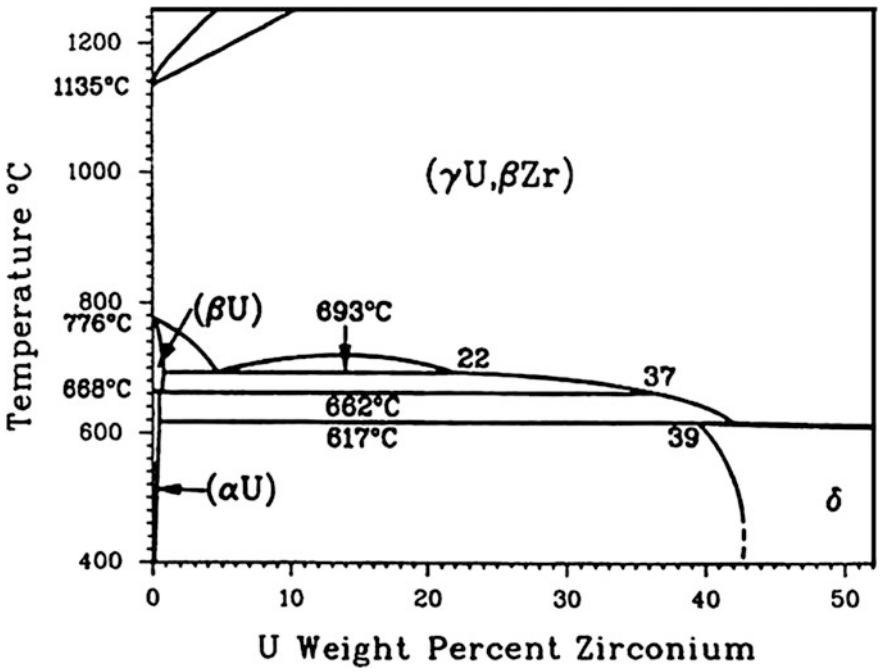

Fig. 8 Phase diagram of U–Zr alloy

Physical performance tests. The physical properties such as heat capacity (specific heat), thermal conductivity (heat conductivity) and thermal expansion coefficient are tested. A graph of data trends for different alloys is shown as follow.

As shown in the Fig. 11, with the increase of temperature the specific heat turn to slow down, and the lowest point is at 350 °C. Then it slowly rising, jump greatly at 700 °C. The whole process is relatively stable.

The thermal conductivity is obtained through multiplying the heat diffusion coefficient, density and the specific heat capacity, as shown in Fig. 12. From room temperature to 600 °C, the thermal diffusion coefficient increases as the temperature rises gradually. There has a little change when the temperature is a little higher than 600 °C. According to the phase diagram, at 612 °C $\alpha + \delta \rightarrow \alpha + \gamma 2$ transformation occurs, after that the phase transition also occurs at 659 °C and 688 °C. It is due to the fluctuation of thermal diffusion coefficient. When the temperature is higher than 720 °C it comes into single phase zone, and the thermal diffusion coefficient is rising fast.

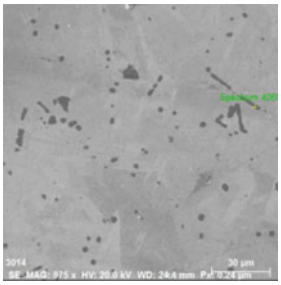

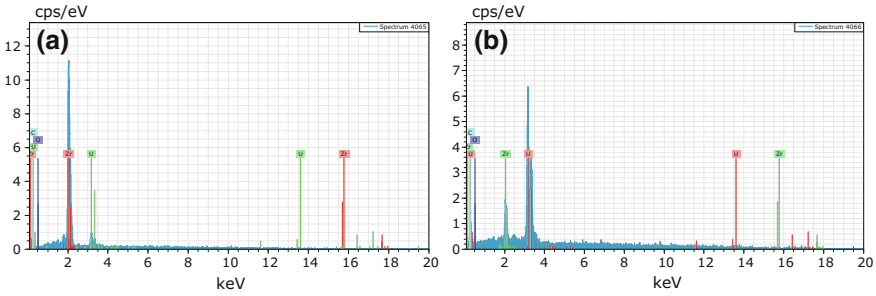

	data of Fig.a			data of Fig.b	
element	weigh percentage(%)	atom percentage(%)	element	weigh percentage(%)	atom percentage(%)
U	15.01	6.25	U	85.40	47.27
Zr	75.99	65.22	Zr	10.53	15.20

Fig. 9 Spectral analysis data of U–Zr alloy after annealing

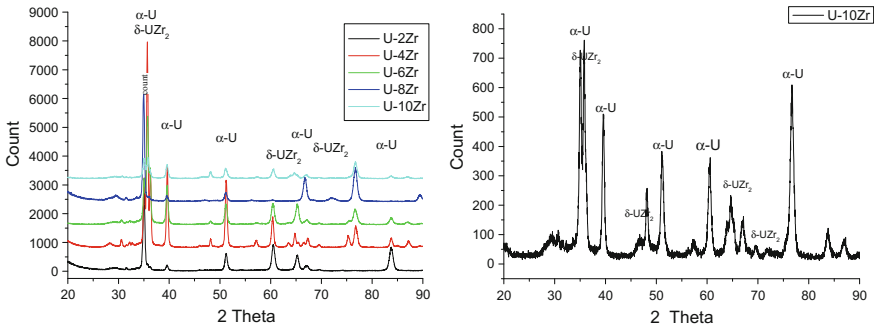

Fig. 10 XRD curve of U–Zr alloy after homogenization annealing

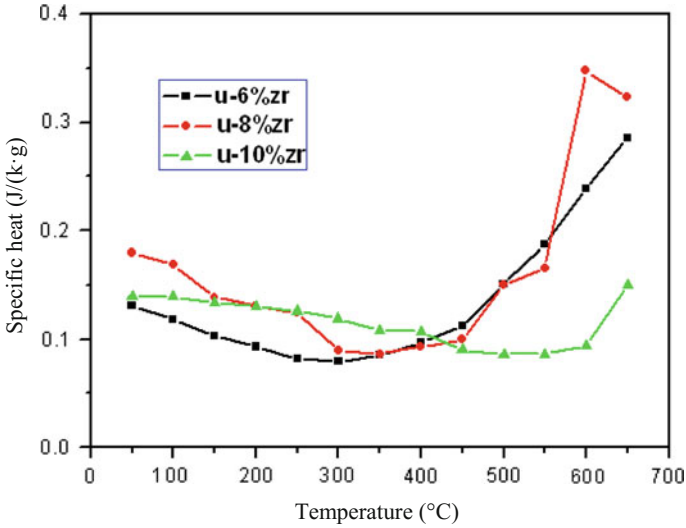

Fig. 11 Specific heat curves of U–Zr alloys

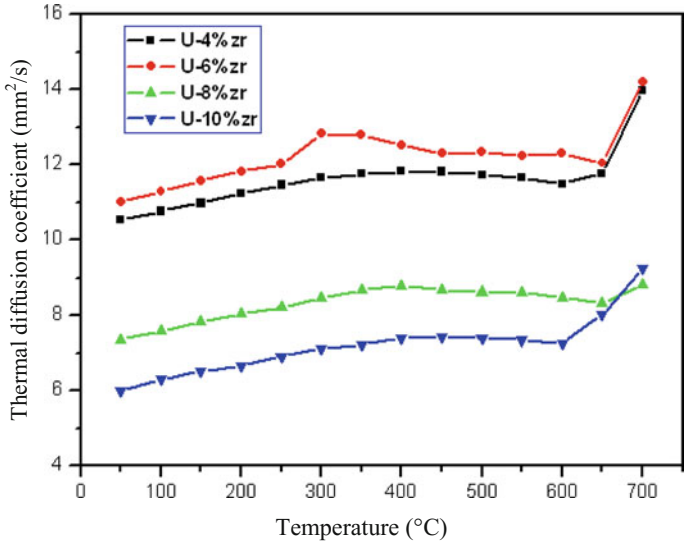

Fig. 12 Thermal diffusion coefficient of the U–Zr alloys

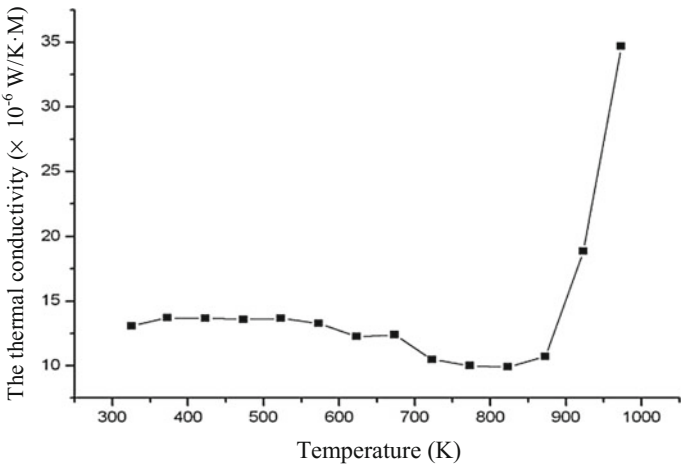

Fig. 13 Thermal conductivity-temperature curve of U–10 Zr

Based on heat diffusion coefficient, density and specific heat the thermal conductivity under different temperatures can be obtained (assuming that the density varies rarely with temperature). The thermal conductivity change process of U–10 Zr alloy is shown in Fig. 13. With the increase of temperature the alloy thermal conductivity firstly drops. After 900 K it rises rapidly.

As shown in Fig. 14, thermal expansion coefficient of U–10% Zr increases with the increase of temperature, at 700 °C it reaches the maximum: 18.57 × 10^{-6}/°C.

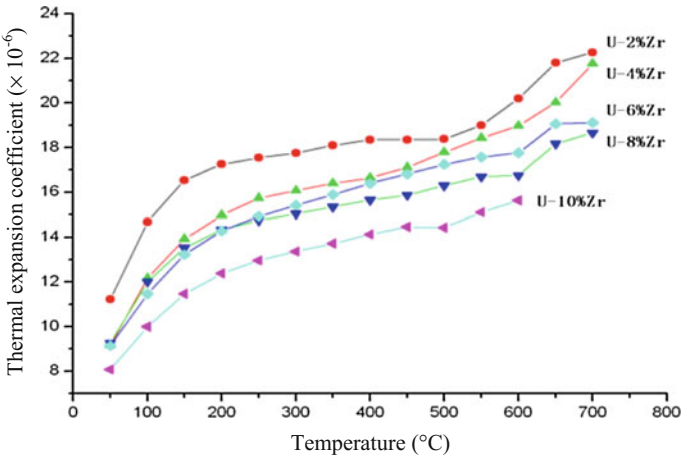

Fig. 14 Thermal expansion coefficient-temperature curve of U–Zr

Conclusions

When the cooling speed of U–Zr alloy is fast, as-cast microstructure morphology is characterized by liquid quenching microstructure, there is a clear grain boundary, at the same time the acicular structure characteristics is shown within the grain boundary. With the increase of Zr content, microstructure of acicular morphology is more apparent, but is relatively smaller. The microstructure of U–10 wt% Zr alloy is shown in the shape of the lath-like interleaved distribution, and in the interior of the lath-like microstructure two kinds of phase is interleaved by lamellar structure distribution. And the number and size of the rich-zirconium phase in the matrix are increasing gradually.

The microstructure of U–Zr alloy after homogenization annealing is layered, which is similar to the pearlite of steel. With the content of zirconium increases, the microstructure of layer is gradually refined. The microstructure of U–6 wt% Zr alloy is shown in the shape of the lath-like interleaved distribution. With the content of Zr increases, twin structures appear in the U–8 wt% Zr alloy which is similar to the pearlite. When the content of Zr is 10 wt%, the twin morphology of organization is more apparent and becomes finer. At the same time characteristic of pearlite is further weakened in the organization.

The specific heat slowly declines with the increase of temperature and reaches the lowest at 350 °C, and then slowly rises. From room temperature to 600 °C the thermal diffusion coefficient increases as the temperature rises gradually. Between 600 °C and 690 °C there are fluctuations. From 720 °C, thermal diffusion coefficient is rising fast.

References

1. L.C. Walters, Thirty years of fuels and materials information from EBR-II. J. Nucl. Mater. **270**, 39–48 (1999)
2. C.B. Basak, Microstructural evaluation of U-rich U–Zr alloys under near-equilibrium condition. J. Nucl. Mater. **416**, 280–287 (2011)

Influence of Layer Thickness of RPV Steel Samples Prepared by WEDM Technology

Chengliang Li, Guogang Shu, Xiaoying Wang and Wei Liu

Abstract Wire-cut electrical discharge machining (WEDM) technology has gradually become popular for preparing nuclear reactor pressure vessel (RPV) steel samples after neutron irradiation. The sample section in its polished state was characterized and analysed using metallographic microstructure observation, element energy spectrum analysis and the micro-region Vickers hardness (Hv) method. The experimental results show that the influence of the layer thickness of an RPV steel sample prepared by WEDM can be effectively distinguished by means of section micro-region Hv data, and the distance is approximately 120 μm to the sample surface, with a significant change in the range of 60 μm. This conclusion is also applicable to the preparation of other low-alloy steel samples with similar chemical composition, strength and toughness properties as well as heat treatment.

Keywords Wire-cut electrical discharge machining technology
Influence layer · Vickers hardness · Reactor pressure vessel steels

C. Li · W. Liu (✉)
School of Materials Science and Engineering, Tsinghua University,
Beijing 100084, China
e-mail: liuw@mail.tsinghua.edu.cn

C. Li
e-mail: lichengliang@cgnpc.com.cn

G. Shu
State Key Laboratory of Nuclear Power Safety Monitoring Technology and Equipment,
China Nuclear Power Engineering Co., Ltd., Shenzhen 518172, China
e-mail: shuguogang@cgnpc.com.cn

X. Wang
Institute of Materials, China Academy of Engineering Physics, Mianyang 621900, China
e-mail: wangxiaoying@caep.cn

Y. Han (ed.), *Advances in Energy and Environmental Materials*,
Springer Proceedings in Energy, https://doi.org/10.1007/978-981-13-0158-2_9

Introduction

EDM (electrical discharge machining) is based on the use of immersion in a working fluid between two generated pulse discharges and is an electric erosion special processing method for conductive materials. One of the common forms of EDM is the use of a moving thin metal wire as the tool electrode. Compared with traditional mechanical processing with a narrow slit, this material removal method features a higher utilization rate and processing accuracy, along with a high degree of automation, no need for special radiation protection measures, the production of less radioactive waste products and fewer requirements related to operator skills, leading it to gradually be applied in recent years for the determination of the physical and chemical properties of samples prepared after the neutron irradiation test of RPV steel, which is highly radioactive. On the other hand, electric spark cutting will induce carbonization, oxidation, remelting and water quenching to a certain extent, which will affect the microstructure and properties of the sample surface or near surface conditions and thereby the validity and accuracy of the experimental results [1–5]. At present, there is little research on the degree of influence, especially quantitative analysis, in the literature. This paper is based on experimental research on WEDM examining the degree of influence on the surface of the sample preparation technique of RPV steel samples to explore the influence of the layer (also called hardening layer) thickness range and provide a technical reference to counterparts carrying out experimental work.

Materials and Methods

The RPV steel used in this experiment is manganese nickel molybdenum alloy steel, French AFNOR brand 16MND5 steel, similar to the United States ASME brand SA508, GR 3 CL 1 steel. The chemical composition of the steel is shown in Table 1, the heat treatment process is shown in Table 2, and the mechanical properties are shown in Table 3.

A semi closed loop NC WEDM machine (DK7732F type) and the commercial DIC-206 (Dick brand) coolant medium were used for the electric spark cutting of the RPV steel. Samples with dimensions of 1 mm × 1 mm × 0.8 mm were prepared and inlaid and subjected to grinding, polishing and etching processes. Then, the sample section was polished again to carry out metallographic observation, X-ray analysis (EDS), and Vivtorinox (Hv) micro hardness and corrosion microstructure observations. The loading pressure of the hardness test was 50 gf, and the pressure was 15 s.

Table 1 Chemical composition of RPV steel (mass%)

C	Mn	Ni	Mo	P	S	Cr	Si	Cu	Al	Co	V	B	Fe
0.18	1.39	0.71	0.47	0.005	0.002	0.12	0.22	0.03	0.01	<0.02	<0.01	0.0002	Balance

Table 2 Heat treatment conditions of RPV steel

	Holding temperature/°C	Holding temperature/h	Heating rate/°C/h	Cooling method
Normalizing	920 ± 10	5	30 max[a]	Still air cooling
Quenching	890 ± 10	5	50 max[a]	Water spraying
Tempering	650 ± 10	10	60 max[a]	Still air cooling
SPWHT[b]	620 ± 5	16	55 max[a]	Still air cooling

Note [a]Above 350 °C, [b]*SPWHT* Simulated post-weld heat treatment

Table 3 Mechanical properties of RPV steel

Rm/MPa	$R_{p0.2}$/MPa	USE/J	RT_{NDT}/°C
591	460	335	−30

Note Rm ultimate tensile strength at room temperature, $R_{p0.2}$ yield strength at 0.2% offset at room temperature, *USE* upper shelf energy of KV transition curve, RT_{NDT} reference nil ductility transition temperature

Results and Discussion

The metallographic polished samples section observation optical images are shown in Fig. 1 and microstructure optical photographs (bright and dark fields) are shown in Fig. 2. Comparing Figs. 1 and 2, it is difficult to distinguish the influence of the thickness of the layer and the thickness of the cutting process. The image edge of the sample is different from the centre of the sample, but the main reason for the difference is the mechanical polishing of the sample longitudinal section and the cross section at the junction (under the surface of the sample, figure), forming a fillet and preventing the determination of the effect of the electric spark cutting layer.

Fig. 1 Metallographic microstructure of the sample section in polished state

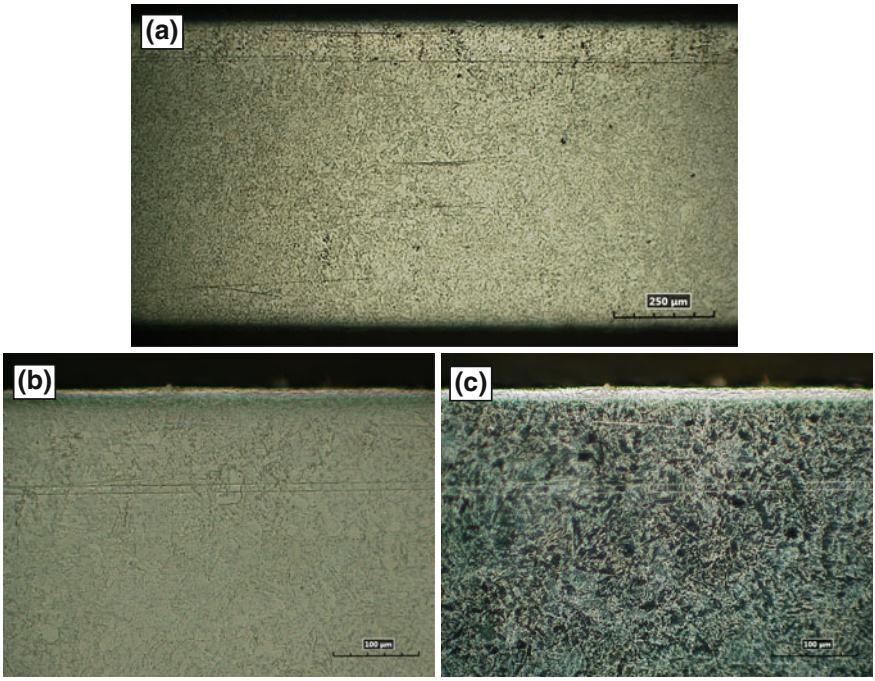

Fig. 2 Metallographic microstructure of the sample section in corroded state (**a** Zoom in 100 times with bright fields; **b** Zoom in 250 times with bright fields; **c** Zoom in 250 times with dark fields)

The results of the EDS analysis of the polished sample cross section are shown in Fig. 3. The results show the presence of oxygen, carbon, manganese, iron, cobalt, as well as five other element distribution lines, all showing different approximately flat values. There was no obvious turning point, so the results from the EDS analysis can effectively identify the effects of the electric spark cutting layer.

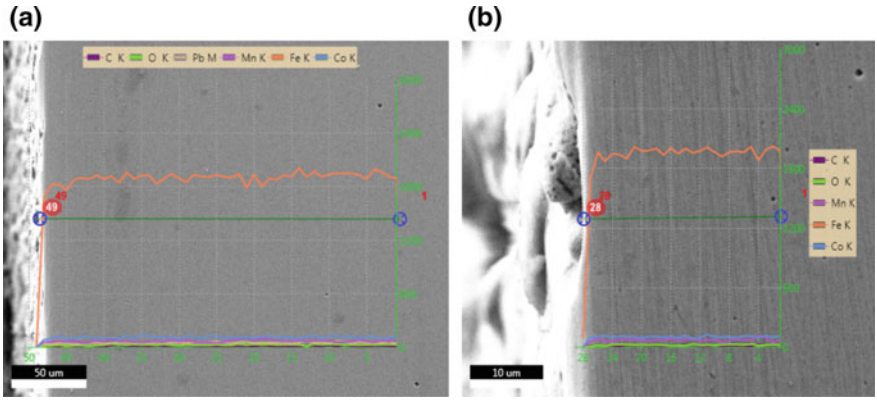

Fig. 3 EDS component distribution lines of the sample section in the polished state

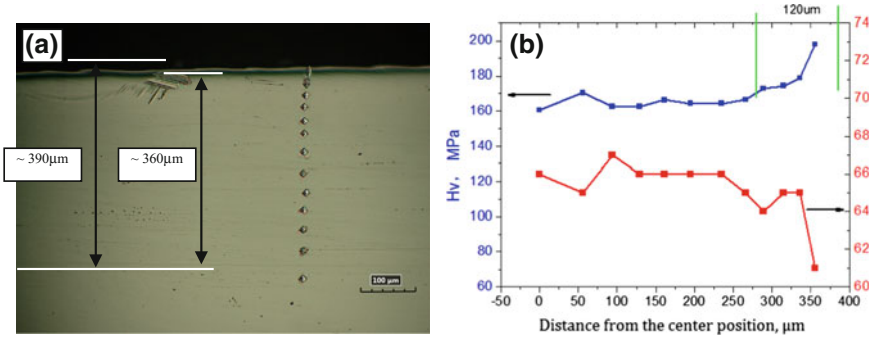

Fig. 4 Micro area Hv distribution line of the sample section in the polished state

The Hv test results of the polished sample cross section are shown in Fig. 4a is the reference point position coordinate diagram Fig. 4b, which is the test data of Hv. From graph Fig. 4a, the reference point is selected as the centre of the cross-section geometry, and the point is analysed from the point to the surface. The reference surface distance from the point is approximately 390 μm, and the final measuring point distance is approximately 360 μm. Diagram Fig. 4b shows that the maximum range of the thickness of the layer is approximately 120 μm, with a significant change in the thickness of approximately 60 μm. It is necessary to note that close to the near-surface test, the Hv quadrilateral head traces become asymmetric, showing that the vertical direction on the diagonal surface side gradually becomes shorter. This is because the initial analysis sample of the near-surface roughness may be poor due to pressure head loading near the tissue deformation, causing asymmetrical results. Hence, the horizontal direction is used, so the head loading is relatively uniform and symmetric. Figure 4b shows the diagonal length of the horizontal direction of the measuring point (a) as measured by the number of grid points. Two results are given to compare the effect of the thickness of the layer.

For the electric spark cutting heat effect of the preparation of the RPV steel samples, the samples along the cross-section of the temperature distribution information and quantitative characterization is difficult to achieve in the conventional experimental equipment, and under rapid heating, the water quenching process may also change, causing vacancy and dislocation generation, so the experiment may be temporarily unable to determine electric spark cutting of the micro phase. Dislocation and other possible defects may also affect the depth and extent, necessitating further experimental research.

Conclusion

(1) Through EDS analysis and metallographic section observation, polished sample tissue sections of the state polishing micro Hv test, determined from cross-sectional micro Hv test data, can effectively judge the EDM preparation of the RPV steel samples when the effect of the layer thickness is approximately

120 μm from the surface selection area, while the variation of the hardness of the 60 selection M depth is more significant.

(2) Therefore, in carrying out the relevant physical and chemical tests, especially micro experiments, such as TEM sample preparation, and nano-indentation hardness tests, such as the preparation technology of the RPV steel samples of WEDM, it is suggested that at least a 60 μm depth selection be considered, followed by grinding to remove the influence of the conventional process to avoid the influence, or layer of the affected areas, to ensure that the samples near the surface organization and performance test results when the data have validity and accuracy.

(3) The above conclusions are also applicable to other low-alloy steels (RPV) that are similar to those discussed in this paper, such as the chemical composition of materials, the mechanical properties of strength and toughness, and the heat treatment state.

References

1. G.P. Wang, W.Q. Liu, Y.L. Huang et al., Effects of sintering temperature on the mechanical properties of sintered NdFeB permanent magnets prepared by spark plasma sintering. J. Magn. Magn. Mater. **349**, 1–4 (2014)
2. K. Mouralova, J. Kovar, J. Mach, L. Klakurkova, J. Bednar, Analyzing the surface layer after WEDM depending on the parameters of a machine for the 16MnCr5 steel. J. Int. Meas. Confederation **94**, 771–779 (2016)
3. J. Zhang, Q. Li, H. Zhang, Investigation of micro square structure fabrication by applying textured cutting tool in WEDM. Micromachines **6**, 1427–1434 (2015)
4. P. Shandilya, P.K. Jain, N.K. Jain, Study on wire electric discharge machining based on response surface methodology and genetic algorithm. Adv. Mater. Res. **622**, 1280–1284 (2013)
5. E. Levashov, A. Kudryashov, E. Kharlamov et al., Formation of FGM coating by the new method of thermoreactive electrospark surface strengthening. Mater. Sci. Forum **308–311**, 262–270 (1999)

Simulations of Ion Irradiation Induced Segregation in RPV Model Alloys

Boyan Li, Ben Xu, Shenyang Hu, Chengliang Li, Qiulin Li, Jun Chen, Guogang Shu, Yuqing Weng and Wei Liu

Abstract In nuclear pressure vessel steels, some alloy elements, such as Mn, Ni and Cr, can improve the mechanical and radiation resistance performances. Experiments have shown, however, that these elements will segregate and lead to clusters in the matrix after neutron/ion radiation. These segregation/clusters will reduce the toughness in the material. In this work, we simulated the radiation-induced segregation (RIS) along the ion path in bcc Fe–1.4at.%Mn–0.7at.%Ni alloys and Fe–1.7% Cr–3.3%Ni alloys currently according to RPV steel, to study the ion irradiation induced segregation of Cr/Mn and Ni, using the framework of reaction rate-theory modeling. The simulation results are compared with experiment results and demonstrated that Cr, Mn, Ni segregate along the ion irradiation path. These results are consistent with both the theoretical simulation and experimental observations.

Keywords RPV model alloys · Ion irradiation · Segregation · Rate theory

B. Li · B. Xu (✉) · W. Liu (✉)
School of Materials Science and Engineering, Tsinghua University, Beijing, China
e-mail: xuben@mail.tsinghua.edu.cn

W. Liu
e-mail: liuw@mail.tsinghua.edu.cn

S. Hu
Pacific Northwest National Laboratory, Richland, WA, USA

C. Li · J. Chen · G. Shu
China Nuclear Power Engineering Co., Ltd., Shenzhen, China

Q. Li
Graduate School at Shenzhen, Tsinghua University, Shenzhen, China

Y. Weng
Central Iron & Steel Research Institute, Beijing, China

Y. Han (ed.), *Advances in Energy and Environmental Materials*,
Springer Proceedings in Energy, https://doi.org/10.1007/978-981-13-0158-2_10

Introduction

Neutron/ion irradiation induces additional defects in materials, such as excess vacancies and interstitials. These defects influence the transport of the alloy components in the matrix, and lead to changes in the local chemical composition. These radiation induced segregation (RIS) or clusters are very common in alloys under ion irradiation [1]. In nuclear pressure vessel steels, some alloy elements, such as Mn, Ni and Cr, can improve the mechanical and radiation resistance performances. Experiments have shown, however, that these elements will segregate and lead to clusters in the matrix after neutron/ion radiation. These segregation/clusters will reduce the toughness in the material [2]. Fe–Cr alloys, for example, ultimately form Cr-rich clusters after neutron/ion radiation in reactor environments. Some alloy elements in the matrix, such as Mn and Ni can accelerate the non-classical clustering [3]. Experiments and simulation results both show the segregation of these elements in RPV steel [4–8]. It turns out that these segregation or clusters lead to material property degradation. As to radiation resist alloys, these properties include many of their key features, embrittlement, the reduction of ductile to brittle transition temperatures, and the reduction of stress corrosion resistance for example [3]. Therefore, it is necessary to study the mechanism and evolutionary kinetics of neutron/ion radiation induced segregation and clustering. The simulation results can help to predict the mechanical properties change and protect from fracture risk, and guide the designing for advanced radiation resistant materials as well.

In general, the working environment of RPV steels contains neutron irradiation. However, experiments for neutron radiation are very expensive and take a long time (always several years). On the other hand, neutron irradiation samples have radioactivity and require a long cooling time. Considering these cost and safety reasons, ion irradiation is always used to simulate the effects of neutron irradiation. In this work, predictive modeling of RIS is performed in bcc Fe–1.4at.%Mn–0.7at.% Ni and Fe–1.7%Cr–3.3%Ni RPV model alloys under Fe ion irradiation, to study the radiation induced segregation of Cr/Mn/Ni along the ion irradiation path.

Description of the Model

Compared with materials at thermal equilibrium, ion irradiation brings much higher concentration of defects, such as vacancies and interstitials. These defects will influence the dynamics and thermodynamics in alloys, and therefore, microstructure and property evolutionary kinetics. In this model, we assume that (1) ion radiation induced defects do not influence the chemical potential energy of the system; (2) only single vacancies and interstitials induced by ion radiation are mobile; and (3) the diffusion coefficients of different elements only affected by vacancy concentration.

In accordance with these assumptions, we can set up a series of spatial depend variables to describe the microstructure evolution in ion radiated Fe–Mn–Ni (or Fe–Cr–Ni) alloys. In the system, Fe, Mn, and Ni (or Fe, Cr and Ni) can lie in both host lattice sites and interstitial sites. We use $C_m(r,t)$ $(m = Fe, Mn, Ni \text{ or } Fe, Cr, Ni)$ to describe the total molar fraction of different element at r point and evolution time t. On the other hand, we use $C_n(r,t)$ $(n = v, i)$ to describe the concentration of vacancy and interstitial at r point and evolution time t, respectively. Here, $C_i(r,t)$ is the total interstitial concentration, including Fe, Mn and Ni (or Fe, Cr and Ni) interstitial, and $C_i(r,t) = \sum C_i^m(r,t)$ $(m = Fe, Mn, Ni \text{ or } Fe, Cr, Ni)$. Where $C_i^m(r,t)$ represent the concentration of interstitial for $m = Fe, Mn, Ni \text{ or } Fe, Cr, Ni$ species. Interstitial atoms exist in the form of dumbbells in BCC Fe–Mn–Ni or Fe–Cr–Ni alloys. According to Ref. [9], the binding energies of Fe–Mn, Fe–Ni, and Fe–Cr dumbbells are −0.5, 0.1, −0.1 eV, respectively. Here, negative binding energy means attractive energy. That is to say, the Fe–Mn mixed dumbbells are stable, while the Fe–Ni dumbbells are highly unstable. Therefore, we can set the initial concentration of Ni interstitial to be 0 because of the instability of Fe–Ni mixed dumbbells. On the other hand, the binding energy of Fe–Mn mixed dumbbells are stronger than that of Fe–Fe mixed dumbbells (0 eV). So, the interstitial defects should contain Mn atoms rather than Fe atoms. Therefore, in the Fe–Mn–Ni system, we can set:

$$C_i(r,t) = C_{Mn}^i(r,t); \quad C_{Fe}^i(r,t) = 0; \quad C_{Ni}^i(r,t) = 0.$$

For the same reason, in Fe–Cr–Ni system, we can set:

$$C_i(r,t) = C_{Cr}^i(r,t); \quad C_{Fe}^i(r,t) = 0; \quad C_{Ni}^i(r,t) = 0.$$

Because of the very low concentration of $C_v(r,t)$ and $C_i(r,t)$, we assume that the sum of molar fraction of Fe, Mn, and Ni (or Fe, Cr and Ni) is 1 at *r* point and time t. Therefore, $C_{Fe}(r,t)$ is not an independent variable. It can be calculated by $C_{Fe}(r,t) = 1 - C_{Mn}(r,t) - C_{Ni}(r,t)$ or $C_{Fe}(r,t) = 1 - C_{Cr}(r,t) - C_{Ni}(r,t)$.

Kinetic model for chemical species evolution

Reaction rate theory has been extensively used to describe the microstructure evolution in ion irradiated alloys. Both experiments and simulation work show that the formation of ion radiation induced defects has a strong connection with spatial positions. The induced vacancies and interstitials have different distribution along the ion irradiation direction. Furthermore, matrix defects, such as dislocations and grain boundaries, are sinks for vacancies and interstitials. and lead to defect gradients around the matrix defects. Such distribution of defects will influence the chemical potential energy as well as the diffusion coefficient of the solute alloys, which may result in solute atoms segregation or clustering.

In order to describe the solute segregation with the effects of ion radiation induced defects, we take consideration of a spatially dependent reaction rate theory.

In this work, we consider a Fe–Mn–Ni (or Fe–Cr–Ni) ternary system, then the contribution of ion deposition in component fractions can be calculated as followed:

$$\Delta C_m(r,t) = \frac{C_m(r,t)}{1 + K_{Fe}\Delta t} - C_m(r,t) = \frac{-K_{Fe}\Delta t C_m(r,t)}{1 + K_{Fe}\Delta t}, \quad (m = Cr, Mn, Ni) \quad (1)$$

$$\Delta C_{Fe}(r,t) = \frac{C_{Fe}(r,t) + K_{Fe}\Delta t}{1 + K_{Fe}\Delta t} - C_{Fe}(r,t) = \frac{(1 - C_{Fe}(r,t))K_{Fe}\Delta t}{1 + K_{Fe}\Delta t} \quad (2)$$

$$\lim_{\Delta_t \to 0} \frac{\Delta C_m(r,t)}{\Delta t} = \begin{cases} -K_{Fe}C_m(r,t) & m = Cr, Mn, Ni \\ (1 - C_m(r,t))K_{Fe} & m = Fe \end{cases} \quad (3)$$

where K_{Fe} is the deposition rate of iron (atoms per second per lattice site), spatially depending on the distance from the radiated surface. With these equations, we can obtain the diffusion equations of each elements:

$$\frac{\partial C_m(r,t)}{\partial t} = -\nabla J_m - K_{Fe}C_m(r,t) \quad m = Cr, Mn, Ni \quad (4)$$

$$\frac{\partial C_{Fe}(r,t)}{\partial t} = -\nabla J_{Fe} + (1 - C_{Fe}(r,t))\, K_{Fe} \quad (5)$$

where J_m is the flux of the solute atoms for $m = Fe, Cr, Mn, Ni$. Here, we assume that the driving force of each solute atoms diffusion is proportional to their concentration gradient. Their equations can be found in Ref. [10]:

$$J_m = -\left[d_v^m C_v(r,t) + d_i^m C_i(r,t)\right]\nabla C_m(r,t) + C_m(r,t)\left[d_v^m \nabla C_v(r,t) - d_i^m \nabla C_i(r,t)\right] \quad m = Fe, Cr, Mn, Ni \quad (6)$$

where d_n^m is the diffusion coefficient of m element ($m = Fe, Cr, Mn, \text{or } Ni$), according to vacancy ($n = v$) diffusion mechanisms and interstitial ($n = i$) diffusion mechanisms, respectively.

Kinetic model for point defects evolution

The evolution equations for defects can be found in Ref. [10], and described as:

$$\frac{\partial C_i(r,\, t)}{\partial t} = -\nabla J_i(r,t) + K + K_{Fe} - R_f C_v(r,t)C_i(r,t) - k_i^2 D_i(r,t)\left(C_i(r,t) - C_i^e\right) \quad (7)$$

$$\frac{\partial C_v(r,t)}{\partial t} = -\nabla J_v(r,t) + K - R_f C_v(r,t)C_i(r,t) - k_v^2 D_v(r,t)\left(C_v(r,t) - C_v^e\right) \quad (8)$$

$$J_v = -D_v \nabla C_v(r,t) + \sum_{m=Fe,Mn,Ni\ (or\ Fe,Cr,Ni)} d_v^m C_v \nabla C_m(r,t) \tag{9}$$

$$J_i = -\nabla \left(\sum_{m=Fe,Mn,Ni\ (or\ Fe,Cr,Ni)} d_i^m C_m(r,t) C_i(r,t) \right), \quad m = Fe, Cu, Mn \tag{10}$$

In these equations, k_n^2 is the sink strength. C_n^e are the thermal equilibrium concentrations for different defects. D_n are the defect diffusion coefficients. J_v is the flux of vacancies, and J_i is the flux of interstitials.R_f is the recombination factor of the defects. The diffusion coefficients of vacancy $(n = v)$ and interstitial $(n = i)$ are described as $D_n(r,t) = \sum d_n^m C_m(r,t)$ (m = Fe, Mn, Ni or Fe, Cr, Ni).

Normalization

In the simulations, we can make the following normalizations:

$$r^* = \frac{r}{l_0},\ \nabla^* = \left(\frac{\partial}{\partial x^*}, \frac{\partial}{\partial y^*}, \frac{\partial}{\partial z^*} \right) = l_0 \nabla$$

$$d_{FeV}^* = \frac{d_{FeV}}{d_{FeV}} = 1,\ d_{Fei}^* = \frac{d_{Fei}}{d_{FeV}},\ d_{MnV}^* = \frac{d_{MnV}}{d_{FeV}},\ d_{Mni}^* = \frac{d_{Mni}}{d_{FeV}},\ d_{NiV}^* = \frac{d_{NiV}}{d_{FeV}},$$
$$d_{Nii}^* = \frac{d_{Nii}}{d_{FeV}}$$

$$d_{CrV}^* = \frac{d_{CrV}}{d_{FeV}},\ d_{Cri}^* = \frac{d_{Cri}}{d_{FeV}},\ D_V^* = \frac{D_V}{d_{FeV}},\ D_i^* = \frac{D_i}{d_{FeV}}$$

$$t^* = \frac{t}{t_0},\ t_0 = \frac{l_0^2}{d_{FeV}},\ R_f^* = \frac{l_0^2}{d_{FeV}} R_f,\ k_v^* = l_0 k_v,\ k_i^* = l_0 k_i$$

where l_0 is a unit length and d_{FeV} is the diffusion coefficient of Fe via vacancy mechanism at T = 565 K.

Simulation Results and Discussion

In the simulation, RIS simulations were carried out at 565 K for the Fe–1.7%Cr–3.3%Ni alloys irradiated by 3 meV Fe^{3+} ions and 373 K for Fe–1.4%Mn–0.7%Ni alloys irradiated by 3.5 meV Fe^{3+} with dose ranges from 10 to 30 dpa. The choice of the alloys and irradiation condition are considered to be compared with experiments results [11, 12]. The original profiles of radiation damage *K* and K_{Fe} along the projected range of metal ions were calculated with TRIM-2008 code, shown in Figs. 1 and 2. The smooth approximations of these depth profiles are used.

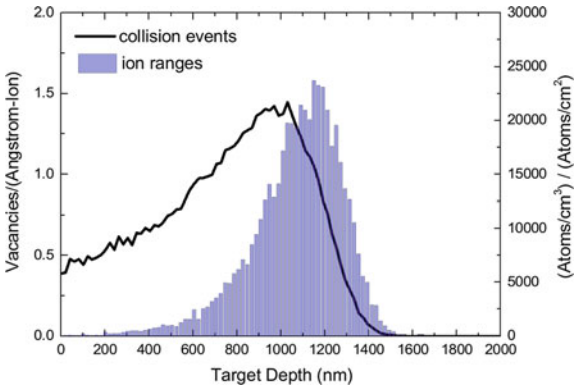

Fig. 1 Distribution of vacancies and injected ion ranges in Fe–1.7%Cr–3.3%Ni alloys irradiated by 3 meV Fe^{3+} ions

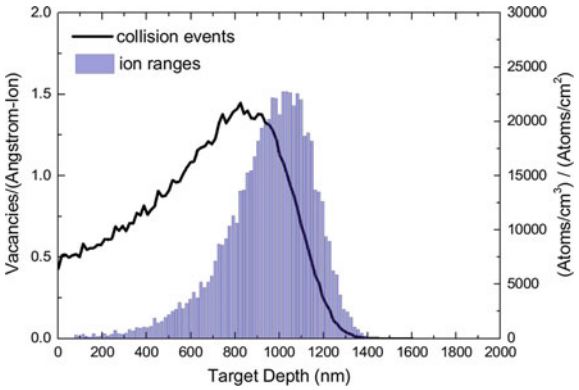

Fig. 2 Distribution of vacancies and injected ion ranges in Fe–1.4%Mn–0.7% Ni alloys irradiated by 3.5 meV Fe^{3+} ions

The evolution of the radiation defects, vacancies and interstitials, is first calculated by the equations proposed in Sect. "Description of the Model". The simulations were conducted in 1D with a physical size of $1000l_0$ for simplicity. We solve these evolution Eqs. (4–10) using a semi-implicit method in Fourier space [13, 14]. The diffusion coefficient of Fe, Cr, Mn and Ni by vacancy diffusion mechanisms are listed in Table 1, adapted from reference [15]. Other parameters needed in the model are listed in Table 2. According to the binding energy for forming different mixed dumbbells discussed in Sect. "Description of the Model", we can set $D_i^* = d_{Mni}^* = 1.0 \times 10^5$, and $d_{Nii}^* = d_{Fei}^* = 0$ for Fe–Mn–Ni system and $D_i^* = d_{Cri}^* = 1.0 \times 10^5$, and $d_{Nii}^* = d_{Fei}^* = 0$ for the Fe–Cr–Ni system. In accordance with the normalizations presented in the end of Sect. "Description of the Model", we normalized some parameters needed in the model and list them in Table 2. D_i^* and D_V^* can be influenced by the evolution temperature. These defects diffusion coefficients can be calculated by their migration energies. For BCC Fe matrix, the migration energies for vacancy and interstitial are 0.7 and 0.3 eV, respectively [16]. In consideration of a narrow evolution temperature range, they are assumed to be constant, for simplicity. On the other hand, the formation energies of vacancy and interstitial are 2.1

Table 1 Diffusion coefficients of different solute alloys in different temperatures

Element	$[m^2\ s^{-1}]$ (565 K)	$[m^2\ s^{-1}]$ (373 K)
Fe	5.1×10^{-29}	1.7×10^{-44}
Cr	2.8×10^{-26}	*
Mn	*	9.1×10^{-41}
Ni	1.7×10^{-28}	1.0×10^{-41}

Table 2 Parameters used in the model (starred values are normalized parameters)

Parameters	Value	Parameters	Value	Parameters	Value
l_0	2 nm	E_v^f	2.1 eV	R^*	3.2
D_V^*	5.0	E_i^f	4.0 eV	k_v^*	0
D_i^*	1.0×10^5	d_{Fei}^*	0	k_i^*	0
d_{Cri}^*	1.0×10^5	d_{Mni}^*	1.0×10^5	d_{Nii}^*	0

and 4 eV in BCC Fe matrix, respectively [17]. Thus, their equilibrium concentrations can be estimated by Arrhenius equation, about 10^{-20}, very low. Therefore, the initial concentration of vacancies and interstitials can be set as $C_v^e = C_i^e = 0$.

Figure 3 shows the results of ion irradiation induced segregation along the injected direction in Fe–1.7%Cr–3.3%Ni alloys for different times (damage doses 10–30 dpa) during 3 meV Fe^{3+} ion irradiation. Figure 4 shows the results in Fe–1.4%Mn–0.7%Ni alloys for different times (damage doses 10–30 dpa) during 3.5 meV Fe^{3+} ion irradiation.

With these results, we can see that ion irradiation can significantly influence the distribution of different elements along the injected direction, especially in the region of the maximum point defects generation rate. Another trend is that the

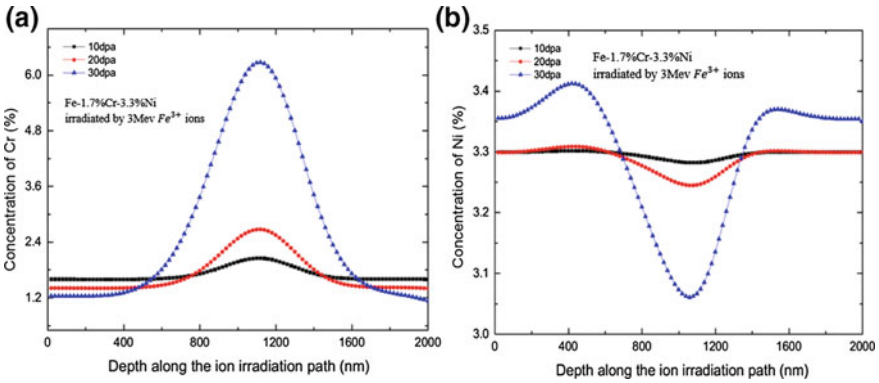

Fig. 3 Calculated RIS-produced profiles of Cr (**a**) and Ni (**b**) contents along the projected range of 3 meV Fe^{3+} ions in Fe–1.7%Cr–3.3%Ni for 10–30 dpa

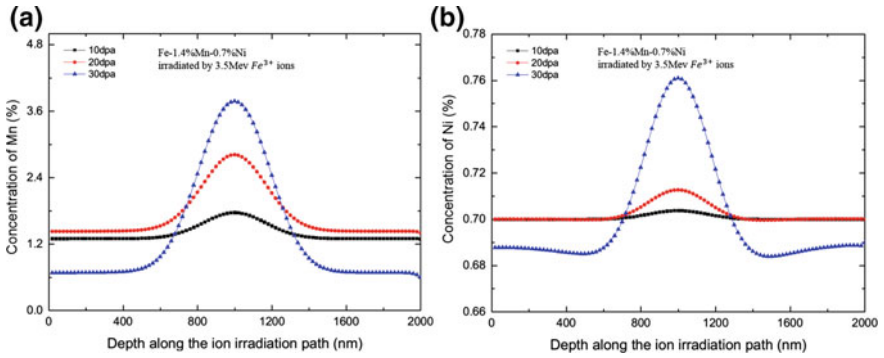

Fig. 4 Calculated RIS-produced profiles of Mn (**a**) and Ni (**b**) contents along the projected range of 3.5 meV Fe^{3+} ions in Fe–1.4%Mn–0.7%Ni for 10–30 dpa

continuously injected ions cause the changes in local composition near the surface of the sample. The radiation induced segregation increases with the increase of the evolution time (damage doses). The Ion radiation damage brings excess defects, vacancies and interstitials. These vacancy concentration gradient may enhance the mobility of different solute elements in the alloys, which accelerate the RIS. The difference between the Fe–Cr–Ni and Fe–Mn–Ni system are that segregation of Ni are in different position. This might because of the relative diffusion coefficient of Cr/Ni (>100) and Mn/Ni (<10) via vacancy diffusion mechanisms. This RIS results have been found in experiments as well, which will lead to irradiation induced hardening [11]. In Fe–Cr–Ni system, there are phase field model that confirm the chemical free energy gradient also help the segregation of Cr [18]. Phase field approach for Fe–Cu–Mn–Ni system also obtained the stable segregation or clustering of Cu/Mn/Ni [19–21]. These models demonstrated that the segregation of Mn/Ni/Cr are reasonable in the alloys. In this work, we just take into consider the influence of dynamics of solutes in the alloys for simplicity, without the effects of thermodynamics (chemical free energy gradient). We will expand this model to take into account both dynamics and thermodynamics in our future work.

Summary

In this work, we calculated the ion irradiation induced segregation along the ion path at 565 K for the bcc Fe–1.7%Cr–3.3%Ni alloys irradiated by 3 meV Fe^{3+} ions and 373 K for bcc Fe–1.4%Mn–0.7%Ni alloys irradiated by 3.5 meV Fe^{3+} with dose ranges from 10 to 30 dpa, using the framework of reaction rate-theory modeling. The simulation results are compared with experiment results and demonstrated that Cr, Mn, Ni segregate along the ion irradiation path, in consistent with the theoretical simulations and experimental results [10–12, 18–21]. The

continuously injected ions cause the changes in local composition near the surface of the sample, and the RIS increases with the increase of the evolution time (damage doses). This model just consider the influence of dynamics of solutes in the alloys, and we will take into account thermodynamics in our future work.

Acknowledgements We are grateful for the financial support provided by the National Natural Science Foundation of China (51301094), the National Magnetic Confinement Fusion Science programme of China under Grant (51471092) and China Nuclear Power Engineering Co., Ltd. (2013966003). The simulations were performed on TianHe-1(A), located in the National Supercomputer Center in Tianjin. This work is also supported by Tsinghua National Laboratory.

References

1. M. Nastar, F. Soisson, *Radiation-Induced Segregation* (2012), pp. 471–496
2. E.D. Eason, G.R. Odette, R.K. Nanstad, T. Yamamoto, A physically-based correlation of irradiation-induced transition temperature shifts for RPV steels. J. Nucl. Mater. **433**, 240–254 (2013)
3. G.R. Odette, G.E. Lucas, Recent progress in understanding reactor pressure vessel steel embrittlement. Radiat. Eff. Defects Solids **144**, 189–231 (2006)
4. M.K. Miller, K.F. Russell, Embrittlement of RPV steels: an atom probe tomography perspective. J. Nucl. Mater. **371**, 145–160 (2007)
5. M.K. Miller, K.F. Russell, M.A. Sokolov, R.K. Nanstad, APT characterization of irradiated high nickel RPV steels. J. Nucl. Mater. **361**, 248–261 (2007)
6. M.K. Miller, K.A. Powers, R.K. Nanstad, P. Efsing, Atom probe tomography characterizations of high nickel, low copper surveillance RPV welds irradiated to high fluences. J. Nucl. Mater. **437**, 107–115 (2013)
7. M.K. Miller, B.D. Wirth, G.R. Odette, Precipitation in neutron-irradiated Fe–Cu and Fe–Cu–Mn model alloys: a comparison of APT and SANS data. Mater. Sci. Eng., A **353**, 133–139 (2003)
8. A. Seko, N. Odagaki, S.R. Nishitani, I. Tanaka, H. Adachi, Free-energy calculation of precipitate nucleation in a Fe-Cu-Ni alloy. Mater. Trans. **45**, 1978–1981 (2004)
9. P. Olsson, T.P.C. Klaver, C. Domain, Ab initiostudy of solute transition-metal interactions with point defects in bcc Fe. Phys. Rev. B **81** (2010)
10. V.A. Pechenkin, I.A. Stepanov, Modeling the radiation-induced segregation of undersized solutes near grain boundaries. Mater. Sci. Forum **294**, 771–774 (1999)
11. J. Jiang, Y.C. Wu, X.B. Liu, R.S. Wang, Y. Nagai, K. Inoue, Y. Shimizu, T. Toyama, Microstructural evolution of RPV steels under proton and ion irradiation studied by positron annihilation spectroscopy. J. Nucl. Mater. **458**, 326–334 (2015)
12. X. Bai, S. Wu, P. Liaw, L. Shao, J. Gigax, Effect of heavy ion irradiation dosage on the hardness of SA508-IV reactor pressure vessel steel. Metals **7**, 25 (2017)
13. L. Zhang, L.-Q. Chen, Q. Du, Simultaneous prediction of morphologies of a critical nucleus and an equilibrium precipitate in solids. Commun. Comput. Phys. **7**, 674 (2009)
14. L. Zhang, L.-Q. Chen, Q. Du, Diffuse-interface approach to predicting morphologies of critical nucleus and equilibrium structure for cubic to tetragonal transformations. J. Comput. Phys. **229**, 6574–6584 (2010)
15. L. Messina, M. Nastar, N. Sandberg, P. Olsson, Systematic electronic-structure investigation of substitutional impurity diffusion and flux coupling in bcc iron. Phys. Rev. B **93** (2016)
16. C.-C. Fu, J.D. Torre, F. Willaime, J.-L. Bocquet, A. Barbu, Multiscale modelling of defect kinetics in irradiated iron. Nat. Mater. **4**, 68–74 (2004)

17. C. Domain, C.S. Becquart, Ab initio calculations of defects in Fe and dilute Fe-Cu alloys. Phys. Rev. B **65** (2001)
18. Y. Li, S. Hu, L. Zhang, X. Sun, Non-classical nuclei and growth kinetics of Cr precipitates in FeCr alloys during ageing. Modell. Simul. Mater. Sci. Eng. **22**, 025002 (2014)
19. T. Koyama, H. Onodera, Computer simulation of phase decomposition in Fe-Cu-Mn-Ni quaternary alloy based on the phase-field method. Mater. Trans. **46**, 1187–1192 (2005)
20. C. Zhang, M. Enomoto, Study of the influence of alloying elements on Cu precipitation in steel by non-classical nucleation theory. Acta Mater. **54**, 4183–4191 (2006)
21. C. Zhang, M. Enomoto, T. Yamashita, N. Sano, Cu precipitation in a prestrained Fe-1.5 wt pct Cu alloy during isothermal aging. Metall. Mater. Trans. A **35**, 1263–1272 (2004)

Influence of Orthogonal Heat Treatments on Mechanical Properties of HT-9 Ferritic/Martensitic Steel

Tingwei Ma, Xianchao Hao, Tian Liang, Bo Chen, Ping Wang, Yingche Ma and Kui Liu

Abstract A series of heat treatments by orthogonal experimental method were performed to study the mechanical properties of HT-9 ferritic/martensitic steel. The results show that the tempering temperature is the most important factor affecting the yield strength ($R_{p0.2}$) and elongation (EL%) of HT-9 steel. With the increments of tempering temperature, EL% increases and $R_{p0.2}$ decreases gradually. Both normalizing temperature and tempering temperature show influence on DBTT of HT-9 steel. Considering the tensile strength and impact toughness properties with no abrupt reduction of tensile strength, the optimal heat treatment regime is selected as follows: normalizing at 1000 °C for 0.5 h followed by oil cooling, and tempering at 760 °C for 1.5 h followed by air cooling.

Keywords Ferritic/martensitic steel · Orthogonal analysis · Tempering Ductile-to-brittle transition temperature

T. Ma · P. Wang (✉)
Key Laboratory of Electromagnetic Processing of Materials, Ministry of Education, Northeastern University, Shenyang 110004, China
e-mail: wping@epm.neu.edu.cn

T. Ma
e-mail: matingwe@163.com

X. Hao · T. Liang · B. Chen · Y. Ma · K. Liu
Institute of Metal Research, Chinese Academy of Sciences, Shenyang 110016, China
e-mail: xchao@imr.ac.cn

T. Liang
e-mail: tliang@imr.ac.cn

B. Chen
e-mail: bchen@imr.ac.cn

Y. Ma
e-mail: ycma@imr.ac.cn

K. Liu
e-mail: kliu@imr.ac.cn

T. Ma
Yingkou Institute of Technology, Yingkou 115014, China

Y. Han (ed.), *Advances in Energy and Environmental Materials*,
Springer Proceedings in Energy, https://doi.org/10.1007/978-981-13-0158-2_11

Introduction

9–12%Cr ferritic/martensitic steels (FMS) have been selected as the fuel cladding or core structures in Generation IV nuclear reactors because of their superior resistance to irradiation embrittlement and radiation-induced swelling, high thermal conductivity, low thermal expansion, as well as good oxidation and corrosion resistance at elevated temperatures [1–3]. HT-9 steel is one of the first generation heat-resistant steels with the nominal chemical composition Fe-0.2C-12Cr-1Mo-0.5W-0.3V. It was used primarily for structural applications in fossil power plants, such as tubing or piping [4, 5]. From 1970s, it was chosen as duct materials of sodium-cooled fast reactors and the performance under irradiation was investigated extensively. The main finding is that HT-9 steel was not susceptible to irradiation embrittlement during long term operation unlike austenitic steels [6–10], while exhibited an abrupt deceasing of impact toughness and increment of ductile-to-brittle transition temperature (DBTT). Neutron irradiation led to an increase in the temperature of the DBTT up to approximately 200 °C, and yielded a potential risk of rupture during long-term application [11, 12]. The reduction of DBTT and the increments of absorbed energy before irradiation is thought an effective method to improve the impact properties after irradiation. Though many factors had effects on impact properties, the modification of heat treatment parameters was a useful method to improve the impact toughness [13]. Precipitation behavior during normalizing, and tempering, and the influence of heating rates were investigated by researchers [14, 15]. The heat treatment of HT-9 steel proposed by Rowcliffe [16] was composed of austenization at 1050 °C for 1 h followed by air cooling and tempering at 780 °C for 2.5 h followed by air cooling.

With the developments of Generation IV nuclear reactors, more strict requirements have been proposed [11]. HT-9 steel for application in new-generation sodium-cooled reactors should have high-tensile strength, moderate ductility under ambient and elevated temperatures and low DBTT and high impact absorbed energy [3, 11]. Many researches focus on sole parameter of heat treatments [14, 15] to our own knowledge. Actually, normalizing, tempering and the cooling methods have interactive effects on the microstructure evolution and related mechanical properties. To separate their effects on yield strength, elongation and ductile-to-brittle transition temperature (DBTT), the orthogonal design method [17] is used in this paper. An optimal heat treatment is put forward based on the experimental results.

Materials and Experimental Procedure

HT-9 steel was melted in a 50 kg vacuum induction melting (VIM) furnace. The ingot was hot-worked at 1050 °C into plates with thickness of 14 mm. Plates were cut into about 60 mm long to prepare for the subsequent heat treatments and mechanical testing. The chemical composition is listed in Table 1.

Table 1 Chemical compositions of HT-9 [wt%]

C	Si	Mn	Cr	Mo	W	V	Ni	S	P	N	Fe
0.16	0.04	0.58	12.20	0.90	0.50	0.29	0.69	0.002	0.003	0.106	Bal.

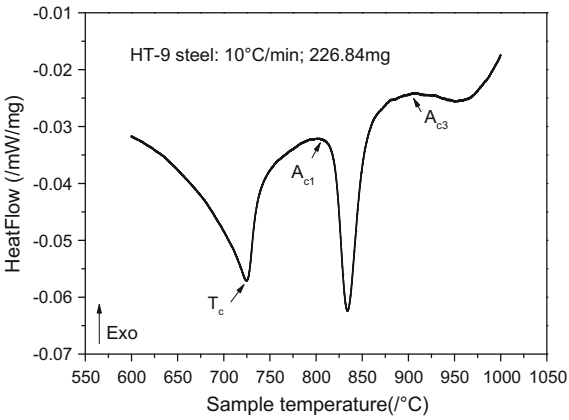

Fig. 1 A typical DSC trace obtained during heating schedule. T_c marks the magnetic transformation point, while A_{c1} and A_{c3} denote the austenite start and end temperatures, respectively

Table 2 Factors for orthogonal experiment in the present study

Factor	Designed level		
Normalizing[°C]	1000	1050	1080
Tempering[°C]	650	700	760
Cooling method	WQ[a]	OQ[b]	AC[c]

Note [a]water quenching; [b]oil quenching; [c]air cooling

The critical transformation temperature was studied by differential scanning calorimeter (DSC). Parameters for DSC analysis were as follows: rapidly heating to 500 °C, then heating to 1000 °C at a rate of 10 °C/min and holding for 20 min, followed by furnace cooling to 200 °C at a rate of 10 °C/min then rapidly cooling to the room temperature. The DSC result is shown in Fig. 1. The phase transformation temperatures of HT-9 steel in Table 1, i.e., A_{c1}, A_{c3} and T_c were 802, 904 and 725 °C, respectively.

The normalizing temperature should be higher than A_{c3}, and the tempering temperature should be lower than A_{c1} for 9–12%Cr steels. Based on the obtained critical temperatures and heat-treatment parameter proposed by Rowcliffe [16], the normalizing temperature, tempering temperature, and cooling method were chosen as orthogonal factors to design the orthogonal experiments, which is shown in Table 2. The holding time for normalizing and tempering were set at 0.5 and 2.5 h, respectively.

Standard Charpy V-notch specimens with dimension of 10 mm×10 mm×55 mm (length) were machined from tempered plates. Impact tests were conducted in the temperature range of −110 to 23 °C. Three specimens were prepared for each impact. The results were then screened and averaged. Hyperbolic tangent curves

were used for analyzing the DBTT and the upper stage energy (USE). Tensile tests were performed at room temperature on a hydraulic test system. Cylindrical tensile samples with diameter of 5 mm and gauge length of 25 mm were machined for tensile tests after tempering. Two specimens were prepared for tensile tests and the results were averaged.

Results and Discussion

Orthogonal Design Analysis. An orthogonal form of three factors and three levels in each factor was designed as shown in Table 2. The orthogonal tests results of HT-9 steel specimen are listed in Table 3. In this table, A, B and C stand for normalizing temperature, tempering temperature and cooling method, respectively. D is error column. $R_{p0.2}$ is the yield strength at room temperature, EL% is the elongation.

Orthogonal methods define the factors of $\overline{K_i}$, R, V, V_e and F to evaluate the effects of different parameters. $\overline{K_i}$ is the mathematic average value of any column on level number i. R is the value of subtraction between the maximum and the minimum of $\overline{K_i}$ in the same factor. V is variance. F is the value of F-test. V_e is variance of error. The values of $\overline{K_i}$, R, V and F have been calculated by the equations as follows, and are listed in Tables 4, 5 and 6.

$$\overline{K_{ij}} = (\overline{K_{1j}} + \overline{K_{2j}} + \overline{K_{3j}})/3. \tag{1}$$

$$R_j = \max(\overline{K_j}) - \min(\overline{K_j}). \tag{2}$$

$$f_j = factor\ numbers - 1 = m - 1. \tag{3}$$

Table 3 Results of orthogonal tests for heat treatment process and mechanical properties

Experimental No.	A	B	C	D	$R_{p0.2}$	EL	DBTT
	Normalizing/ [°C]	Tempering/ [°C]	Cooling method	4e	[MPa]	%	[°C]
1	1000	650	WQ	1	888.5	16.8	−12
2	1000	700	OQ	2	765.5	20	−9.5
3	1000	760	AC	3	591	24	−26
4	1050	650	OQ	3	938.5	18	−20.5
5	1050	700	AC	1	810.5	18.8	0
6	1050	760	WQ	2	638	22.5	−22
7	1080	650	AC	2	910	15.3	−5
8	1080	700	WQ	3	865	15	1
9	1080	760	OQ	1	643	21	−9

Table 4 Orthogonal design analysis of yield strength ($R_{p0.2}$)

	$\overline{K_1}$	$\overline{K_2}$	$\overline{K_3}$	R	f	S	V	F
Normalizing	748.3	795.7	806	57.7	2	5672.67	2836.3	5.0
Tempering	912.3	813.7	624	288.3	2	128845	64422.0	114.5
Cooling method	797.2	782.3	770.5	26.7	2	1071.17	535.58	1.0
Error					2	1125.5	562.75	
Total					8	136714		$F_{0.05}(2,2) = 19.0$

Table 5 Orthogonal design analysis of elongation (EL%)

	$\overline{K_1}$	$\overline{K_2}$	$\overline{K_3}$	R	f	S	V	F
Normalizing	20.3	19.1	17.1	3.2	2	15.3889	7.69	61.8
Tempering	16.7	17.9	21.8	5.1	2	43.0822	21.54	173.1
Cooling method	17.4	19.7	19.4	2.3	2	8.81556	4.41	35.4
Error					2	0.24889	0.12	
Total					8	67.5356		$F_{0.05}(2,2) = 19.0$

Table 6 Orthogonal design analysis of ductile-brittle transition temperature (DBTT)

	$\overline{K_1}$	$\overline{K_2}$	$\overline{K_3}$	R	f	S	V	F
Normalizing	−15.8	−14	−4.3	11.5	2	229.58	114.79	2.2
Tempering	−12.5	−2.7	−19	16.3	2	400.727	200.36	3.8
Cooling method	−11	−13	−10.2	2.8	2	12.3267	6.16	0.1
Error					2	104.927	52.46	
Total					8	747.56		$F_{0.05}(2,2) = 19.0$

$$S_j = \frac{1}{\mathrm{n}}\sum_{i=1}^{m}\left(\sum_{j=1}^{n} K_{ij}\right)^2 - \left(\sum_{i=a}^{m}\sum_{j=1}^{n} K_{ij}\right)^2 /mn. \tag{4}$$

$$S_T = \sum_{i=1}^{\mathrm{m}}\sum_{j=1}^{n} K_{ij}^2 - \left(\sum_{i=a}^{m}\sum_{j=1}^{n} K_{ij}\right)^2 /mn. \tag{5}$$

$$V_j = S_j/f_j. \tag{6}$$

$$F_j = V_j/V_e = (S_j/f_j)/(S_e/f_e). \tag{7}$$

where, m is the factors number, n is the experiment number of each factor, f is the degree of freedom, S is the sum of squares.

R manifests the relative influence on the objective function. The bigger the R value, the stronger the influence of factors on mechanical properties by orthogonal design analysis [18]. Because R is the subtraction between the max $\overline{K_i}$ and the

Table 7 Important influential levels of factors

	$R_{p0.2}$	EL%	DBTT
Normalizing [°C]	1080	1000	1000
Tempering/[°C]	650	760	760
Cooling method	WQ	OQ	OQ

min $\overline{K_i}$ in the same factor, it can be analyzed intuitively by $\overline{K_i}$. The level of factor is important if $\overline{K_i}$ is the max. For example, $\overline{K_3}$ is the maximum in the normalizing temperature in Table 4, which indicates that 1080 °C of normalizing temperature is more important level than 1000 and 1050 °C. In the same manner, $\overline{K_1}$ of 650 °C for tempering temperature is more greater than 700 and 760 °C, and $\overline{K_1}$ of WQ for cooling method is bigger than OQ and AC in yield strength. In Table 5, 1000 °C for normalizing temperature, 760 °C for tempering temperature and OQ for cooling method are important levels than the others in the same factor. 1000 °C, 760 °C and OQ are also important levels for DBTT as shown in Table 6. The important levels of factors in orthogonal experiments are shown in Table 7 based on $\overline{K_i}$.

Direct analysis through *R* is sample to affirm the optimum regime, but it is difficult to know whether it is significant effect on results of different factors experiments. Variance analysis is, therefore, employed in solving these problems by *F*-value. The larger the difference between *V* and *F*-value, the stronger the influence [18].

F-value for tempering temperature is 114.5 in Table 4, which is greater than that for normalizing temperature or cooling method. It is evident that tempering temperature is a significant factor on $R_{p0.2}$ at a 95% confidence limit through *F*-test. So, the most important influential factor on $R_{p0.2}$ is the tempering temperature, while the normalizing temperature or cooling method plays a negligible role. The influence order of factors on $R_{p0.2}$ with a decreasing sequence is tempering temperature, normalizing temperature and cooling method, the same order as *R*-test.

F-value for tempering temperature is 173.1 in the Table 5, which is the largest in the three factors. Although all three F-values are more than $F_{0.05}(2, 2) = 19.0$ with a 95% confidence, it is also evident that tempering temperature play the significant role on EL%. The influence order on elongation is tempering temperature, normalizing temperature and cooling method, with the same order from *R*-test in Table 5.

From the *F* analysis in Table 6, it is evident that although the relative influence order of heat treatment parameters on Charpy impact toughness is the same as that on $R_{p0.2}$ and elongation, the difference of *F*-values between normalizing temperature and tempering temperature is smaller. And both *F*-values are lower than $F_{0.05}(2, 2) = 19.0$. The influence of three factors should be re-evaluated from *R* as shown in Fig. 2. It is evident f that the fluctuated scope of tempering temperature is the most notable on $R_{p0.2}$ and EL% of HT-9 steel. The fluctuated scope of normalizing temperature is the middle of three effectors. The influence of normalizing and tempering parameters on DBTT are larger than that of cooling methods. However, the fluctuation of three factors for DBTT does not keep a monotone decreasing or increasing manner in Fig. 2c. It could be concluded that all three

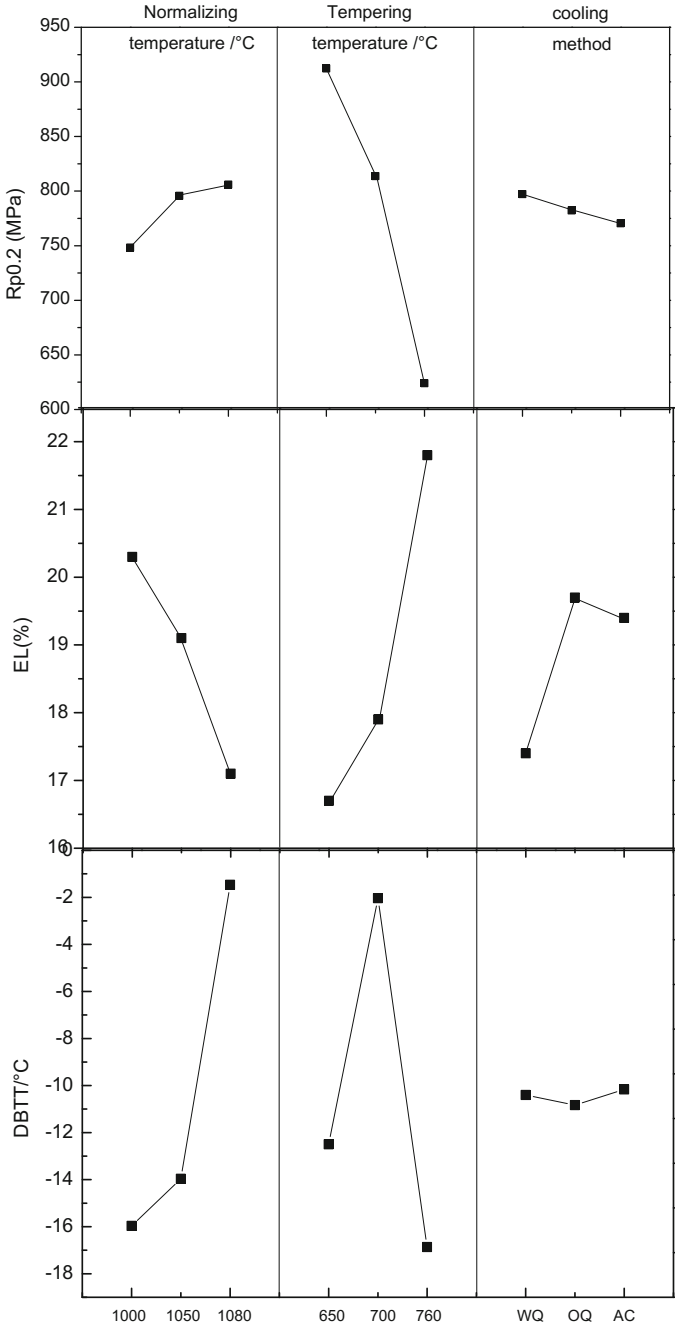

Fig. 2 Effects of normalizing temperature, tempering temperature and cooling method on **a** yield strength($R_{p0.2}$), **b** elongation (EL%) and **c** ductile-to-brittle transition temperature (DBTT)

factors show some interactive effects on DBTT of HT-9 steel. As for 9–12%Cr FMS [19–21], the reported influential factors on DBTT could be listed as follows: Prior austenitic grains, packet size, lath width, carbide morphology and distribution, dislocation density and its distribution. The controlling microstructure parameters for DBTT or impact toughness are not clear because of the multiple components and phases after heat treatments. Microstructural observation will be performed to evaluate the relationship between microstructure and the correlated Charpy impact properties in future which may provide some assistant for screening the significant factors as shown in Table 2.

Optimal Heat Treatment Regime. As discussed above, the cooling method is not a significant factor for mechanical properties of HT-9 steel. As shown in Fig. 2, the optimum values of $R_{p0.2}$, EL% and DBTT are obtained at the level parameter C1 (water quench), C2 (oil quench) and C2 (oil quench), respectively. So the optimal cooling method for HT-9 steel is recommended to be oil quenching after normalizing.

From Fig. 2, we could see that the highest yield strength, the maximum elongation and the lowest DBTT could be obtained when the normalizing temperatures were chosen as A3 (1080 °C), A1 (1000 °C) and A1 (1000 °C), respectively. The increment of yield strength ($R_{p0.2}$) could be attributed to the increased amount of alloying elements such as Cr, Mo, W, V in the matrix by the dissolution of carbides or nitrides. In practice a low normalizing temperature is used because the temperature of $M_{23}C_6$ carbide dissolution is usually lower than 1000 °C [22]. Though not be dissolved completely, nitrides or carbonitrides are used to pinning grain boundaries and decreasing the grain size. In this investigation, the optimal normalizing temperature is chosen as 1000 °C.

From the analysis of Tables 4 and 5, Fig. 2, the value of $R_{p0.2}$ decreased with increasing of tempering temperature, while the value of EL% increased with increasing of tempering temperature. For getting good material properties on $R_{p0.2}$ and EL%, tempering temperature can be chosen B1 (650 °C) and B3 (760 °C), respectively. The value of $R_{p0.2}$ is 591 MPa when HT-9 steel is temporized at 760 °C, which is sufficient to meet the demand of application. The value of DBTT is fittest when the temperature was set at 760 °C as shown in Table 3. In order to achieve optimum combination of $R_{p0.2}$, EL% and DBTT, tempering temperature is believed to be 760 °C.

Based on above analysis, the optimal heat treatment regime is: normalizing at 1000 °C for 0.5 h, followed by OQ, and tempering at 760 °C for 1.5 h followed by air cooling.

Conclusions

The effect of heat treatment to HT-9 steel on the mechanical properties has been investigated. The following conclusions could be based on the results obtained us:

(1) Tempering temperature is the most significant factor that influences the yield strength and elongation of HT-9 steel from the orthogonal design and analysis. The yield strength decreases and the elongation increases with the increasing of tempering temperature. Normalizing temperature and tempering temperature exhibit interactive influence on the impact toughness based on the R and F values.
(2) Cooling method is not a significant factor and plays little role in mechanical properties from the orthogonal analysis. Oil quenching is recommended for HT-9 steel after normalization.
(3) The optimal heat treatment regime for HT-9 steel is as follows: normalizing at 1000 °C for 0.5 h followed by oil quenching, and tempering at 760 °C for 1.5 h followed by air cooling. The steel can gain a good combination of strength, elongation and impact toughness through the heat treatment regime.

Acknowledgements This work was supported by the National Key Technology R&D Program, China (No. 149601A-A033).

References

1. F. Abe, T. Noda, H. Araki, M. Okada, Development of reduced-activation martensitic 9Cr steels for fusion reactor. J. Nucl. Sci. Technol. **31**, 279–292 (1994)
2. R.L. Klueh, D.R. Harries, in *American Society for Testing and Materials* (West Conshohocken, Pennsylvania, 2001)
3. R.L. Klueh, A.T. Nelson, Ferritic/martensitic steels for next-generation reactors. J. Nucl. Mater. **371**, 37–52 (2007)
4. K. Natesan, A. Purohit, S.W. Tam, *Materials Behavior in HTGR Environments* (U.S. Department of Commerce, National Bureau of Standards Special Technical Publication, Washington, 2003)
5. T.R. Allen, R.G. Lott, J.T. Busby, A.S. Kumar, in *Effects of Radiation on Materials, 22nd International Symposium*, ASTM STP1475, Boston 2004, pp. 99–105
6. F. Abe, T-U. Kern, R. Viswanathan, *Creep-Resistant Steels* (Woodhead, Boca Raton, 2008)
7. S. Sathyanarayanan, J. Basu, A. Moitra, G. Sasikala, V. Singh, Effect of thermal aging on ductile-brittle transition temperature of modified 9Cr-1Mo steel evaluated with reference temperature approach under dynamic loading condition. Metall. Mater. Trans. A. **44**, 2141–2155 (2013)
8. X. Hu, L. X. Huang, W. Yan, W. Wang, W. Sha, Y.Y. Shan, K. Yang, Evolution of microstructure and changes of mechanical properties of CLAM steel after long-term aging. Mater. Sci. Eng. A. **586**, 253–258 (2013)
9. W. L. Zhong, W. Wang, X. Yang, W. S. Li, W. Yan, W. Sha, W. Wang, Y. Y. Shan, K. Yang, Relationship between laves phase and the impact brittleness of P92 steel reevaluated, Mater. Sci. Eng. A. **639**, 252–258 (2015)

10. G. Sasikala, S.K, Ray, Evaluation of quasistatic fracture toughness of a modified 9Cr-1Mo (P91) steel. Master. Sci. Eng. A. **479**, 105–111 (2008)
11. P. Yvon, F. Carré, Structural materials challenges for advanced reactor systems. J. Nucl. Mater. **385**, 217–222 (2009)
12. K.L. Murty, I. Charit, Static strain aging and dislocation-impurity interactions in irradiated mild steel. J. Nucl. Mater. **382**, 217–222 (2008)
13. R.C. Wilcox, B.A. Chin, Austenitizing and microstructure of a HT-9 steel. J. Nucl. Mater. **17**, 285–298 (1984)
14. P.J. Ennis, A. Zielinska-Lipiec, O. Wachter, A. Czyrska-Filemonowicz, Microstructural stability and creep rupture strength of the martensitic steel P92 for advanced power plant original research article. Acta Mater **45**, 4901–4907 (1997)
15. T.C. Totemeier, J.A. Simpson, H. Tian, Effect of weld intercooling temperature on the structure and impact strength of ferritic-martensitic steels. Metall. Sci. Eng. A. **426**, 323–331 (2006)
16. A.F. Rowcliffe, J.P. Robertson, R.L. Klueh, K. Shiba, D.J. Alexander, M.L. Grossbeck, S. Jitsukawa, Fracture toughness and tensile behavior of ferritic-martensitic steels irradiated at low temperatures. J. Nucl. Mater. **258–263**, 1275–1279 (1998)
17. A.H. Cai, Y. Zhou, J.Y. Tan, Y. Luo, T.L. Li, M. Chen, W.K. An, Optimization of composition of heat-treated chromium white cast iron casting by phosphate graphite mold. J. Alloy. Compd. **466**, 273–280 (2008)
18. S.J. Kim, Y.G. Cho, C.S. Oh, D.E. Kim, M.B. Moon, H.N. Han, Development of a dual phase steel using orthogonal design method, Mater. Des. **30**, 1251–1257 (2009)
19. I. Calliari, M. Zanesco, M. Dabalà, K. Brunelli, E. Ramous, Investigation of microstructure and properties of a Ni–Mo martensitic stainless steel, Mater. Des. **29**, 246–250 (2008)
20. R.C. Fan, M. Gao, Y.C. Ma, X.D. Zha, X.C. Hao, K. Liu, Effects of heat treatment and nitrogen on microstructure and mechanical properties of 1Cr12NiMo martensitic stainless steel. J. Mater. Sci. Technol. **28**, 1059–1066 (2012)
21. C.H. Hsu, H.Y. Teng, S.C. Lee, Effects of heat treatment and testing temperature on fracture mechanics behavior of low-Si CA-15 stainless steel. Metall. Mater. Trans. A. **35**, 471–480 (2004)
22. T. Karthikeyan, V. Thomas Paul, S. Saroja, A. Moitra, G. Sasikala, M. Vijayalakshmi, Grain refinement to improve impact toughness in 9Cr-1Mo steel through a double austenitization treatment. J. Nucl. Mater. **419**, 256–262 (2011)

Microstructure Evolution During Fabrication of Zr–Sn–Nb Alloy Tubes

Zongpei Wu, Zhongbo Yang, Wei Yi and Wenjin Zhao

Abstract Zr–Sn–Nb alloy is an important field of Zirconium alloy for high burn-up Pressurized Water Reactors (PWRs). This article reports the microstructure evolution of Zr–0.5Sn–0.15Nb–0.75FeV alloy tube during fabrication. The morphologies of grain and second phase particles (SPPs), their shape, size and distribution have been studied in detail using optical microscopy (OM), scanning electron microscopy (SEM) and transmission electron microscopy (TEM). The microstructure evolution is as follows: lath martensite (β-quenching) → heterogeneous deformation structure and dynamically recrystallized grain (hot extrusion) → heterogeneous deformation structure (cold rolling) → heterogeneous recrystallized grain (intermediate annealing) → homogeneous deformation structure (finishing rolling) → homogeneous fully recrystallized structure (final annealing). SPPs in the hot extruded tubes tend to precipitate along the direction of deformation. With the processing and heat treatment of the alloy, the SPPs are distributed more dispersively. At last, homogeneous and fine SPPs are distributed on Zr matrix uniformly. It can be found that two kinds of SPPs exist in the products. One are ZrFeV SPPs without Nb and the other are ZrNbFeV SPPs containing a small amount of Nb. Fe/V in SPPs are similar to the Fe/V in addition of alloying element and the results show Fe and V can precipitate fully in the form of SPPs.

Keywords Zr–Sn–Nb alloy · Fuel cladding tubes · Processing and heat treatment Microstructure

Z. Wu (✉) · Z. Yang · W. Yi · W. Zhao
National Key Laboratory for Nuclear Fuel and Material, Nuclear Power Institute of China, Chengdu 610041, China
e-mail: wuzpxs@163.com

Y. Han (ed.), *Advances in Energy and Environmental Materials*,
Springer Proceedings in Energy, https://doi.org/10.1007/978-981-13-0158-2_12

Introduction

Zirconium alloys are the only cladding material used in the PWRs due to their excellent neutron economy, superior corrosion resistance and favorable mechanical properties under irradiation [1]. Among them, Zircaloy-4 alloy has been used as nuclear fuel cladding materials for several decades without any significant problem in PWRs. However, more advanced Zirconium alloys are recently required for the more severe operating conditions such as higher burn-up, increased operation temperature, and different pH operation conditions. Therefore, many works have been done for developing better Zr-based alloy, and Zr–Sn–Nb alloy is an important field for high burn-up PWRs. Many researches about Zr-2, Zr-4 and Zr–Nb alloy show that the processing and heat treatment can affect microstructure and strongly influence the properties [2–4]. However, the researches about the processing and microstructure of Zr–Sn–Nb alloys are rare. In this article, the microstructure evolution of Zr–0.5Sn–0.15Nb–0.75FeV alloy tubes has been studied in detail using OM, SEM and TEM.

Experimentation

The materials selected for experimentation were Zr–0.5Sn–0.15Nb–0.75FeV alloy tubes. They were prepared by following major stages: (a) forging ingot in the region of 900–1100 °C; (b) quenching the forged billets in the region of 1000–1050 °C; (c) extruding tubes in the region of 600–700 °C; (d) three passes cold rolling and processing annealing, which is called P1, P2, P3 cold rolling and processing annealing in this paper; (e) finishing rolling and final annealing. The process is shown briefly in the Fig. 1. In order to study microstructure evolution during fabrication of alloy tube, some specimens were selected from different processing stages.

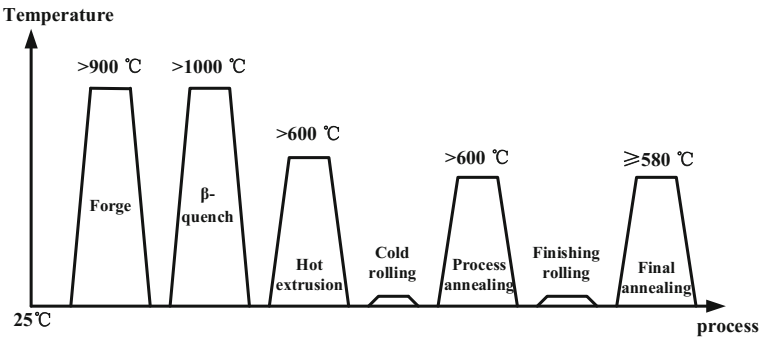

Fig. 1 Preparation of Zr–Sn–Nb alloy tubes

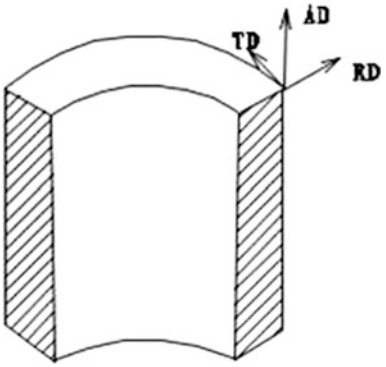

Fig. 2 AD-RD side and TD-RD side

A Leica MeF3A optical microscopy equipped with an optical polarizer was employed to characterize the morphologies of grain, and the observation surface is AD-RD side and TD-RD side, as is shown in Fig. 2. Before OM observation, specimens were mechanically ground using SiC paper (4000# in the final step) and etched in a mixed solution composed of 10% HF + 45% HNO_3 + 45% H_2O by rubbing for 30 s with a cotton wool and then electrolytic colored by 5% H_2SO_4.

A FEI Nova 400 field emission scanning electron microscopy analysis system (Channel 5, HKL Technology-Oxford Instruments) was employed to analyze shape, size and distribution of SPPs, and the observation surface is AD-RD side. Before SEM observation, specimens were mechanically ground using SiC paper (4000# in the final step) and etched in a mixed solution composed of 10% HNO_3 + 30% HF + 60% $C_3H_8O_3$ by rubbing for 5–10 s with a cotton wool and rinsed in HNO_3 to skim off the oil on the surface.

A JEOL-200CX transmission electron microscopy equipped with Energy dispersive X-ray spectroscopy (EDS) analysis system was employed to analyze shapes, distributions and composition of SPPs, and TEM specimens were prepared by electro-polishing in TENUPOL-2twin-jet electropolisher. The electropolishing solution consisted of $HClO_4$36 mL + CH_3CH_2OH 264 mL working at a voltage of 50 V and a temperature of −40 °C.

Results and Discussion

Metallographic Structure Evolution. Figure 3 shows the metallographic structure evolution during process after β-quenching. The metallographic image after β-quenching (Fig. 3a) shows a typical martensite structure. After homogenization treatment at β-region, Zr-based alloy was cooled in water. And cooling rate value was very high. So the martensitic transformation occurs [5]. There are three kinds of typical grain existing in the tubes obtained from hot extrusion (Fig. 3b). The first kind is fibrous grain paralleled to the rolling direction. These grains are thin and

long. The second kind is fine dynamic recrystallized grains. It shows that dynamic recrystallization occurs during the hot extrusion. The third kind is belt-shaped heterogeneous deformation structure. There are twins found in this kind of structure. The belt-shaped heterogeneous deformation structure and fibrous grains also are found in P1 and P2 cold rolled tubes (Fig. 3c, e). Main reason for heterogeneous deformation structure is as follows. At room temperature, the zirconium alloy is α-Zr, which is hexagonal close packed structure, and there are few independent enabled slip systems during the deformation process. It leads the anisotropy of mechanics. So the heterogeneous deformation structure appears frequently during the preparation of Zr-based alloy [6, 7]. The microstructure of P1 and P2 processing annealed tubes shows that most of grains are aquiaxed, but a small amount of belt-shaped deformation structure appears (Fig. 3d, f). This phenomenon is related to the recrystallization driving force. During the annealing process, recrystallization prefers to occur in structure with large deformation. But the number of the dislocations in heterogeneous deformation structure is very limited. It cannot provide enough energy for recrystallization. So recovery occurs during the annealing. Because the grain is broken and a large amount of crystal defects and deformation energy will be introduced, the average size of grains in P2 processing annealed tubes is less than the average size of grains in P1 processing annealed tubes. Microstructure of P3 cold rolled tubes and finishing rolled tubes show that a large number of fine fibrous grain appear, and heterogeneous deformation structure disappears (Fig. 3g, i). It indicates that the heterogeneous deformation structures are highly deformed under the strong continuous deformation during continuous cold rolling process.

Figure 4 shows the metallographic structures of AD-RD side and TD-RD side of the products. After a series of processing and heat treatment, a number of fine equiaxed crystal grains distribute uniformly. The well-recrystallized zirconium alloy tubes could be prepared by the present fabrication technology.

SPPs Evolution. The solid solutions in α-Zr of main alloy elements are very low, so the precipitation and growth of SPPs will occur in the preparation of Zr-based alloy tubes. Some researches suggest that corrosion resistance, grain growth behavior, mechanical properties and irradiation behaviors are strongly influenced by the behaviors of SPPs [8–10]. Figure 5 shows the morphologies of SPPs in every processing. The precipitations of SPPs mainly occur in the processing and heat treatment after β-quenching, so the hot extruded tubes is chosen as the initial stage. As is shown below, SPPs in the hot extruded tubes tend to precipitate along the direction of deformation. The process of SPPs precipitation may has some connection with the working temperature of hot extrusion. Because cold rolling produces rolling streamline structure, the distribution of SPPs also shows obvious belt-shaped distribution (Fig. 5b). After P1 processing annealing, the SPPs is slightly dispersed (Fig. 5c). With the processing and heat treatment of the alloy, the SPPs distribute more dispersively. At last, homogeneous and fine SPPs distribute in Zr matrix uniformly. This suggests that deformation can further improve microstructure uniformity of Zr-based alloy.

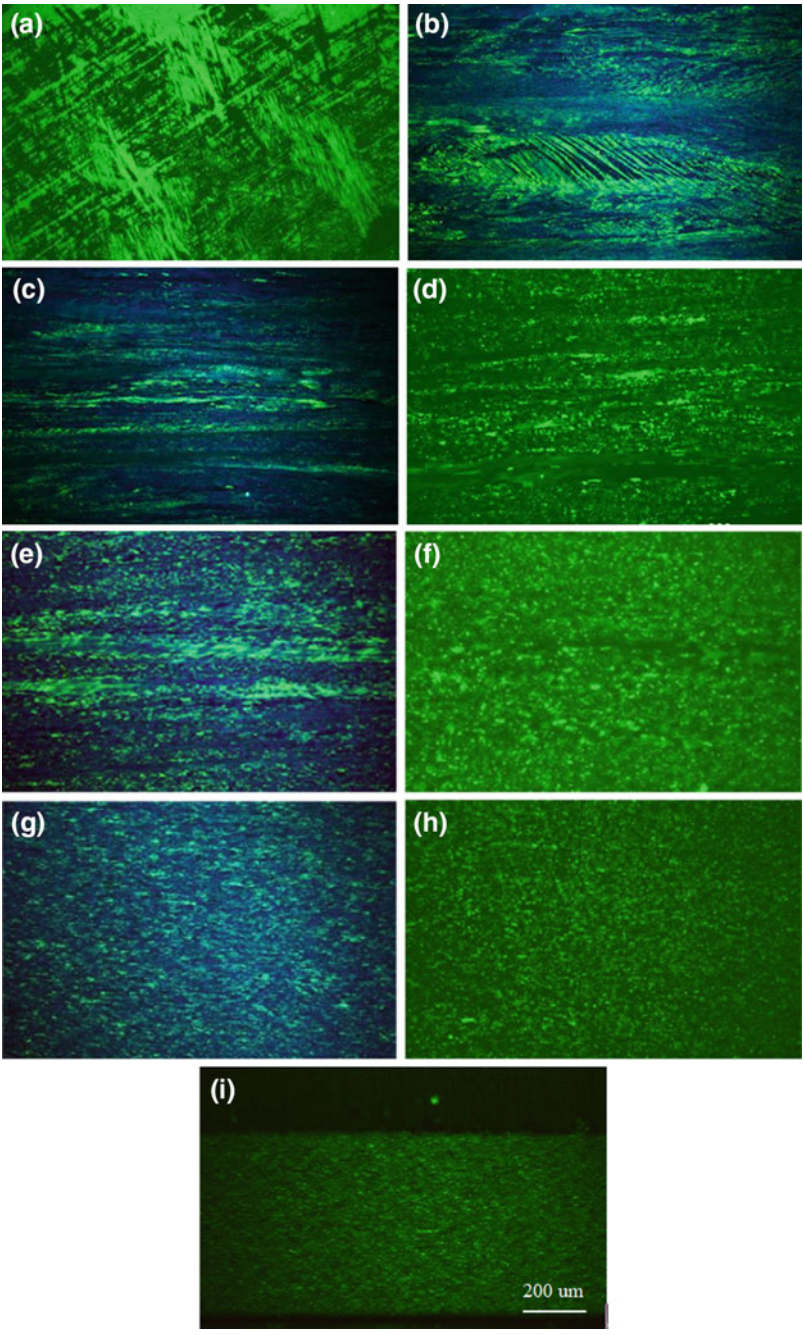

Fig. 3 Metallographic structure evolution of AD-RD side during fabrication: **a** β-quenching; **b** hot extrusion; **c** P1 cold rolling; **d** P1 processing annealing; **e** P2 cold rolling; **f** P2 processing annealing; **g** P3 cold rolling; **h** P3 processing annealing; **i** finishing rolling

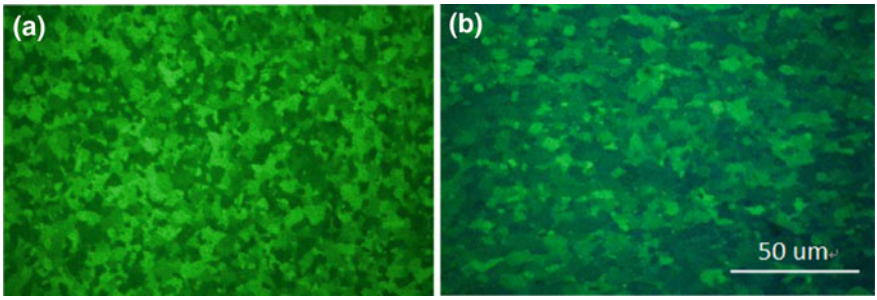

Fig. 4 Metallographic structure of products: **a** TD-RD side; **b** AD-RD side

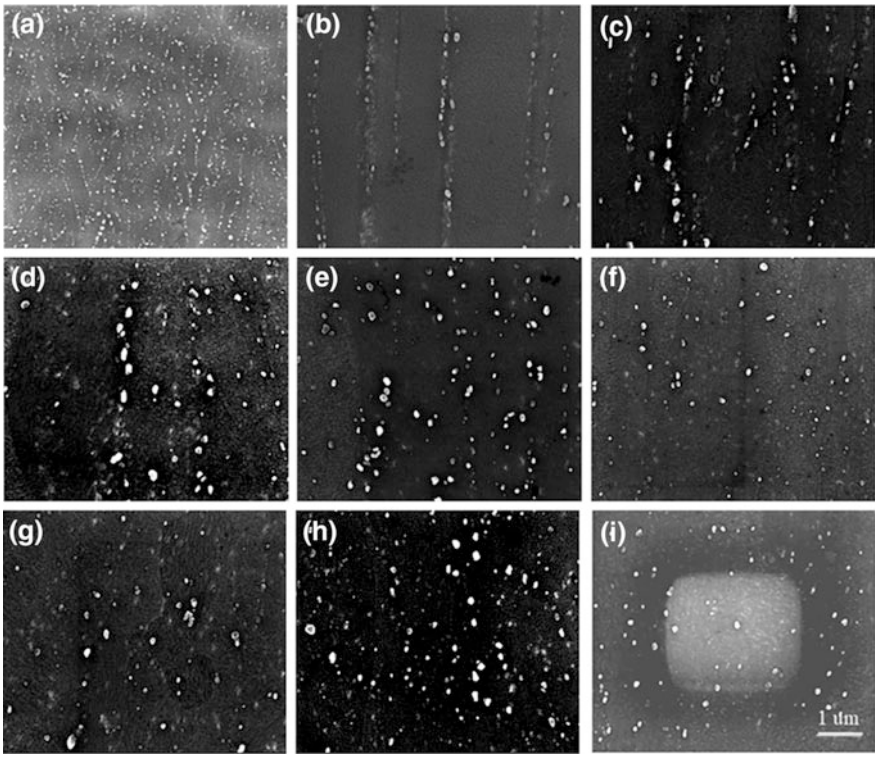

Fig. 5 Morphology evolution of SPPs: **a** hot extrusion; **b** P1 cold rolling; **c** P1 processing annealing; **d** P2 cold rolling; **e** P2 processing annealing; **f** P3 cold rolling; **g** P3 processing annealing; **h** finishing rolling; **i** final annealing

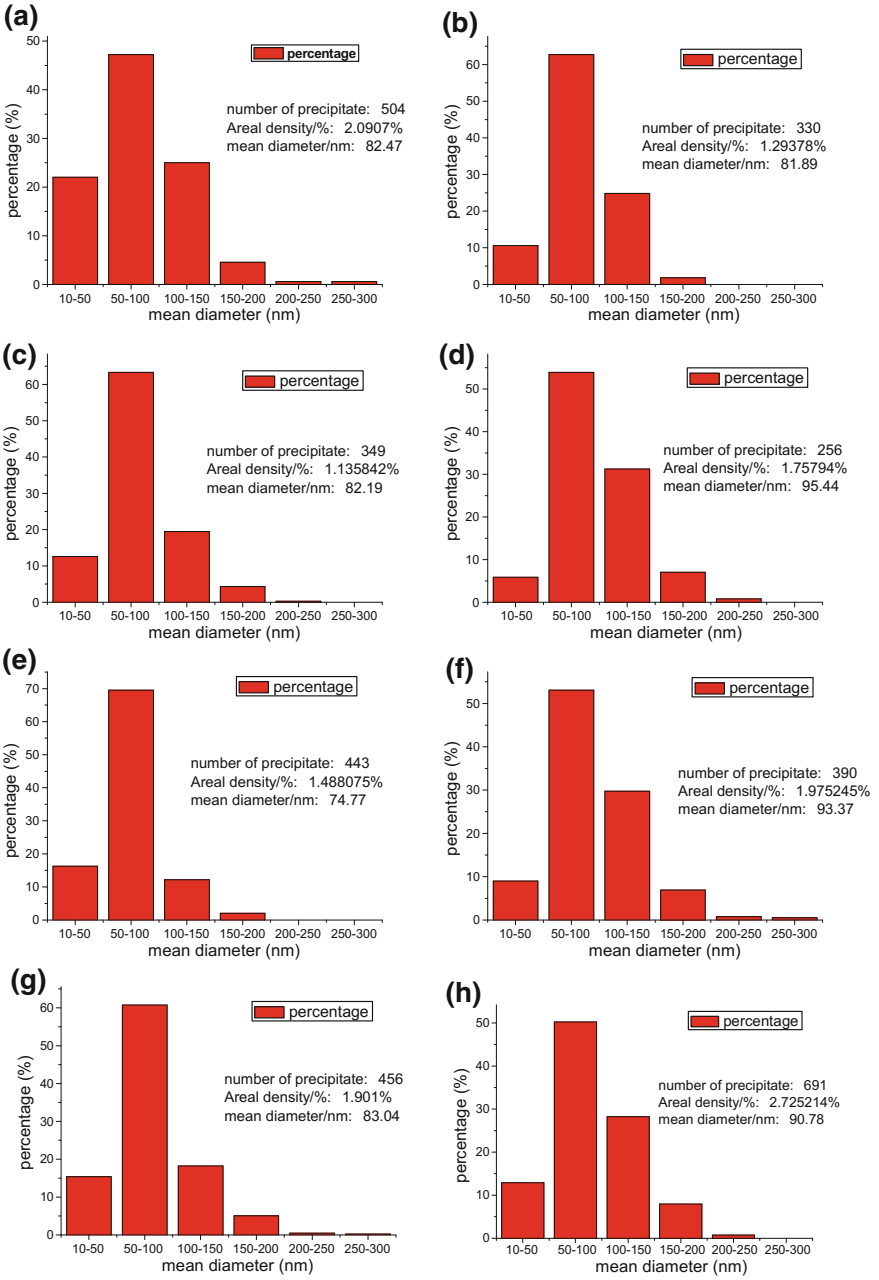

Fig. 6 Size distribution of SPPs in different processing stages: **a** P1 cold rolling; **b** P1 processing annealing; **c** P2 cold rolling; **d** P2 processing annealing; **e** P3 cold rolling; **f** P3 processing annealing; **g** finishing rolling; **h** final annealing

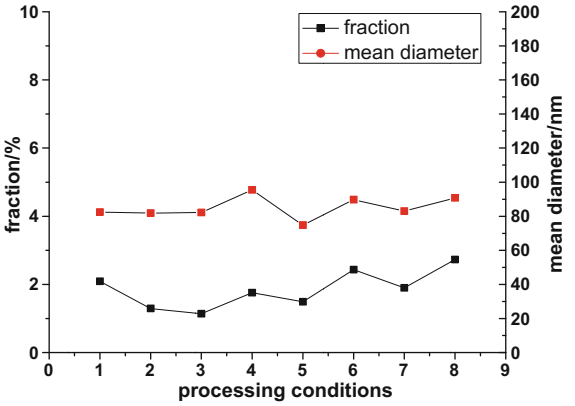

Fig. 7 Volume fractions and mean diameters of SPPs in different processing stages: 1-P1 cold rolling; 2-P1 processing annealing; 3-P2 cold rolling; 4-P2 processing annealing; 5-P3cold rolling; 6-P3 processing annealing; 7-finishing rolling; 8-final annealing

Micro image analysis system (MIAS) is used to analyze the size distribution of SPPs. Figures 6 and 7 show the results. The sizes of SPPs are distributed in the range of 10–150 nm mainly. The mean diameters are distributed in the range of 73–96 nm. This suggests that the whole process of processing can control the size of SPPs effectively. In addition, the volume fractions of SPPs maintain within a narrow range during the fabrication, all in the range of 1.13–2.73%. This shows that the SPPs have precipitated fully during the process. The average size of SPPs in the annealed tube is generally bigger than the SPPs in the cold-rolled tube. The number of the SPPs in the range of 10–50 nm has fallen and the number of the SPPs above 100 nm has risen. It indicates small SPPs will grow during the process of annealing.

Figure 8 shows the microstructure of products obtained from TEM. It's obvious that homogeneous and fine SPPs distribute on Zr matrix uniformly. The analysis of SPPs composition obtained from EDS, which is shown in Fig. 9, shows that two kinds of SPPs exist in the tubes. One is the ZrFeV SPPs without Nb, and the other is a ZrNbFeV SPPs containing a small amount of Nb. All the SPPs selected for EDS analysis contain V, which is related to the nature of V. Solubility of Fe, Cr and V in α-Zr are very low. These elements tend to form the second phase particles, and Fe/V in SPPs are similar to the Fe/V in addition of alloying element, and this shows that Fe and V precipitate fully in the form of SPPs.

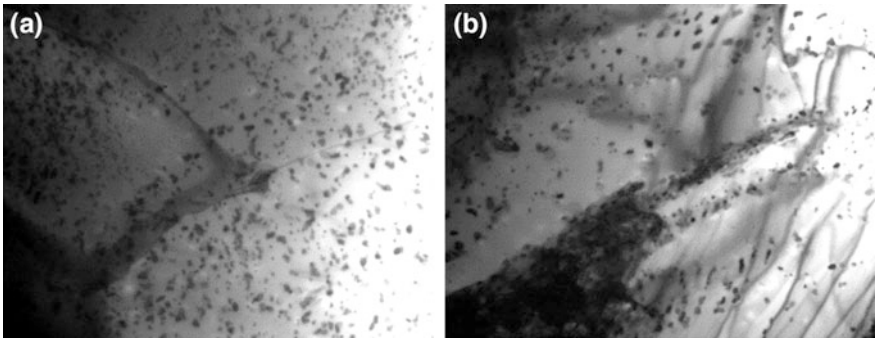

Fig. 8 Microstructure of products obtained from TEM **a** low magnification; **b** high magnification

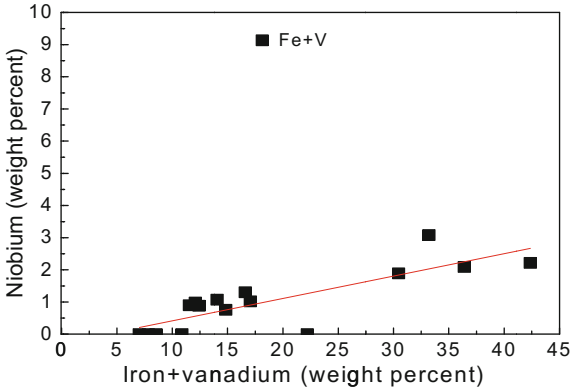

Fig. 9 The relation between Nb and other elements of SPPs in products

Conclusion

(1) The microstructure evolution of Zr–0.5Sn–0.15Nb–0.75FeV alloy tubes during fabrication is as follows: lath martensite (β-quenching) → heterogeneous deformation structure and dynamically recrystallized grain (hot extrusion) → heterogeneous deformation structure (cold rolling) → heterogeneous recrystallized grain (intermediate annealing) → homogeneous deformation structure (finishing rolling) → homogeneous fully recrystallized structure (final annealing).

(2) SPPs tend to precipitate along the direction of deformation after hot extrusion. With the processing and heat treatment of the alloy, the SPPs are distributed more dispersively. At last, homogeneous and fine SPPs are distributed on Zr matrix uniformly.

(3) There are two kinds of SPPs existing in the products. One are ZrFeV SPPs without Nb, and the others are ZrNbFeV SPPs containing a small amount of Nb. Fe/V in SPPs are similar to the Fe/V in addition of alloying element, and this shows Fe and V precipitate fully in the form of SPPs.

References

1. H.J Yong, K.O Lee, H.G. Kim, Correlation between microstructure and corrosion behavior of Zr–Nb binary alloy. J. Nucl. Mater. **302**(1), 9–19 (2002)
2. A. Miquet, D. Charquet, Solid state phase equilibria of Zircaloy-4 in the temperature range 750–1050 °C. J. Nucl. Mater. **105**, 132–141 (1982)
3. W. Zhao, B. Zhou, Z. Miao et al, Studies of new zirconium alloys. Rare Metal Mater. Eng. **30** (6), 19–23 (2001)
4. J.P. Mardon, D. Charquet, J. Senevat, Influence of composition and fabrication process on out-of-pile and in-pile properties of M5 alloy (2000)
5. R.A. Holt, The beta to alpha phase transformation in Zircaloy-4. J. Nucl. Mater. **35**, 322–334 (1970)
6. F. Wagner, N. Bozzolo, O. Van Landuyt, et al., Evolution of recrystallisation texture and microstructure in low alloyed titanium sheets. Acta. Mater. **50**, 1245–1259 (2002)
7. S.K. Sahoo, V.D. Hiwarkar, I. Samajdar, G.K. Dey, D. Srivastav, R. Tiwari, S. Banerjee, Heterogeneous deformation in single-phase Zircaloy 2. Scripta Mater. **56**, 963–966 (2007)
8. W. Liu, Q. Li, B. Zhou, et al., Effect of heat treatment on the microstructure and corrosion resistance of a Zr–Sn–Nb–Fe–Cr alloy. J. Nucl. Mater. **341**, 97–102 (2005)
9. J.Y. Park, B.K. Choi, Y.H. Jeong, et al., Corrosion behavior of Zr alloys with a high Nb content. J. Nucl. Mater. **340**, 237–246 (2005)
10. B.X. Zhou, M.Y. Yao, Q. Li, et al., Nodular corrosion resistance of Zr–Sn–Nb alloy. Rare Metal Mat. Eng. **36**, 1317–132 (2007)

Corrosion Resistance of Zr–0.8Sn–0.25Nb–0.35Fe–0.1 Cr–0.05Ge Alloy

Zhongbo Yang, Zongpei Wu, Shaoyu Qiu, Zhuqing Cheng, Jun Qiu, Ben Wang and Gaihuan Yuan

Abstract The samples of Zr–0.8Sn–0.25Nb–0.35Fe–0.1Cr–0.05Ge alloy, including stress relieving annealing (SRA) and recrystallization annealing (RXA) cladding tubes, were tested in static autoclave in 360 °C/18.6 MPa pure water, 360 °C/18.6 MPa/0.01 mol/L LiOH aqueous solutions and 400 °C/10.3 MPa steam. The microstructure characteristics were analyzed by Transmission Electron Microscope (TEM) and Scanning Electron Microscope (SEM). It was shown that the corrosion weight gain of RXA tube was lower than that of SRA tube in three different corrosive mediums. The fine precipitates in the alloys were mainly HCP-Zr (Nb, Fe, $Cr)_2$ and FCC-Zr_2 (Fe, Cr), which were homogeneous and dispersed. In the SRA tube, the average diameter of precipitates was relatively smaller, and a small amount of TET-Zr_3Ge was also observed. The cracks paralleling to the interface of oxide/metal were formed in the fracture surface of the oxide film, and the oxide film in the inner surface presented the "Cauliflower-like" morphology. As the corrosion time increased, there were more pores or cracks in the oxide film and the size of "Cauliflower-like" structure grew bigger.

Keywords Zr–0.8sn–0.25Nb–0.35Fe–0.1Cr-0.05Ge alloy · Corrosion Microstructure · Oxide films

Introduction

Zirconium alloys are extensively used to manufacture nuclear reactor components, such as fuel claddings, coolant channels, pressure tubes and other in-core structural components, due to the low neutron absorption cross section, superior corrosion

Z. Yang (✉) · Z. Wu · S. Qiu · Z. Cheng · J. Qiu
Science and Technology on Reactor Fuel and Materials Laboratory, Nuclear Power Institute of China, Chengdu 610213, China
e-mail: yangzhongb@mails.ucas.ac.cn

B. Wang · G. Yuan
State Nuclear Baoti Zirconium Industry Company, Baoji 721013, China

Y. Han (ed.), *Advances in Energy and Environmental Materials*,
Springer Proceedings in Energy, https://doi.org/10.1007/978-981-13-0158-2_13

resistance and high mechanical strength etc. As the nuclear reactor technology is gradually developing to the direction of higher burn-up, thermal efficiency, secure reliability, and lower fuel cycle cost, higher request for corrosion resistance of zirconium alloys are put forward. Many countries have carried out the research of new zirconium alloys cladding materials, and Nb-containing zirconium alloys is one of the main development direction, including M5, E635 and X5A, and so on [1–3], and their corrosion resistance in pile are obviously better than Zircaloy-4.

The corrosion resistance of Nb-containing zirconium alloys is closely related to alloy elements and precipitates. Research showed that in the Zr–Nb series alloys, when the Nb content in the matrix is close to the equilibrium solid solubility (0.2–0.3wt%), the corrosion resistance was the best in 200–400 °C water or steam [4]. As for Zr–Nb–Fe alloys, it's reported that when the amount of Nb and Fe elements was about 0.8wt%, the corrosion resistance became better if the Nb/Fe ratio decreased to about 1, due to the formation of more FCC-Zr_2 (Nb, Fe) precipitates [5]. So far, the effect and mechanism of Nb element on the corrosion resistance of zirconium alloy are not clear.

Zr–0.8Sn–0.25Nb–0.35Fe–0.1Cr–0.05Ge alloy(S alloy) is a new Nb-containing zirconium alloy developed by China. In this paper, to better understand the effect of Nb element and microstructure on the corrosion behavior of S alloy, specimens of stress relieving annealing (SRA) and recrystallization annealing (RXA) tubes were prepared respectively, and then corroded in static autoclave in 360 °C/18.6 MPa pure water, 360 °C/18.6 MPa/0.01 mol/L LiOH aqueous solutions and 400 °C/10.3 MPa steam. The corrosion kinetics and microstructure characteristics of S alloy, especially the precipitates and oxide films were analyzed. The mechanism of microstructure on the corrosion resistance of S alloy was discussed.

Materials and Methods of Research

The S alloy cladding tubes are provided by State Nuclear Baoti Zirconium Industry Company. The main process and heat treatment process included smelting of 1000 kg ingot, forging, homogenization of β phase and water quenching, hot extrusion at α phase region, four times cold rolling and final annealing, to obtain the cladding tubes with a diameter of Φ9.5 mm and wall thickness of 0.57 mm. The final annealing temperatures for stress and recrystallized cladding tubes were 450 and 560 °C respectively.

The specimens were corroded in static autoclave in 360 °C/18.6 MPa pure water, 360 °C/18.6 MPa/0.01 mol/L LiOH aqueous solutions and 400 °C/10.3 MPa steam, for 500 days. The corrosion kinetics curves were obtained through the measured corrosion weight gains in different stages. The microstructures before and after corrosion were analyzed using Field Emission Scanning Electron Microscope (FESEM), High Resolution Transmission Electron Microscope (HR TEM), and Scanning Transmission Electron Microscope (STEM).

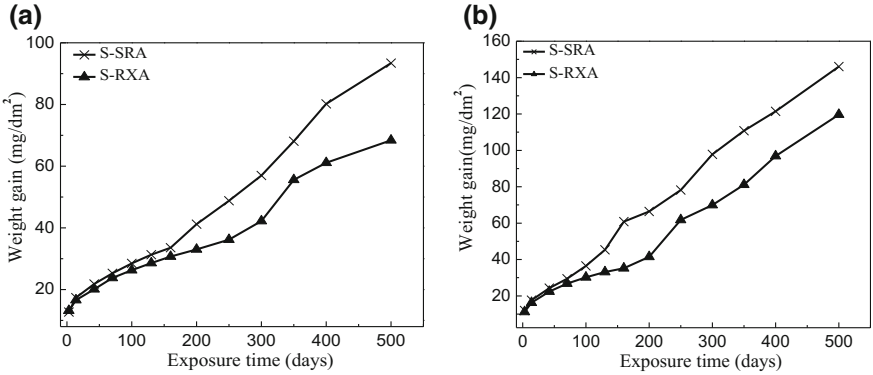

Fig. 1 Corrosion kinetics curves of Zr–0.8Sn–0.25Nb–0.35Fe–0.1Cr–0.05Ge alloys corroded in **a** 360 °C, 18.6 MPa pure water and **b** 360 °C, 18.6 MPa, 0.01 mol/L LiOH aqueous solution

Results and Discussion

Corrosion Kinetics. Figure 1 showed the corrosion dynamic curves of S alloys with SRA and RXA corroded in 360 °C/18.6 MPa pure water (Fig. 1a) and 0.01 mol/L LiOH aqueous solution (Fig. 1b). The corrosion transitions were found in both conditions, and the corrosion weight gain increased swiftly after corrosion transition, which representing that the corrosion rate speed up. In both corrosion conditions, the corrosion transition time of RXA alloy was later than that of SRA alloy, and the weight gain was also lower after long-term corrosion.

The corrosion transition happened at about 42 days when the alloys corroded in 400 °C/10.3 MPa superheated steam, After 500 days corrosion, the weight gain of RXA alloy was lower than SRA alloy, which was similar to that in pure water and LiOH aqueous solution (Fig. 2).

Microstructure of Cladding Tubes. The results of TEM analysis showed that in the SRA alloy there exist lath, high density dislocation, dislocation, subgrain morphologies, and so on, which indicated the microstructure is grain stress state, while the microstructure of the RXA alloy showed equiaxed grains, less deformation, and good recrystallization degree (Fig. 3). The results of SEM analysis showed that the second phase particles (SPPs) distribute uniformly (Fig. 4). The size of SPPs distributed as follows: smaller than 25 nm accounts for 1–11%, 25–75 nm for 20–46%, the number of particles decreased firstly and then increased slightly when the size became from 75–200 to 200–300 nm. Because of the higher final annealing temperature of RXA alloy, the average diameter (112 nm) of SPPs is relatively larger than that of SRA alloy (90 nm).

Usually, Sn is fully soluble in α-Zr, however, the solid solubility of Nb, Fe and Cr in α-Zr is very small. For example, the solid solubility of in α-Zr is only 120 ug/g at 820 °C. Therefore, most of the Nb, Fe, Cr in the alloy will precipitate and form intermetallic compounds. The TEM analysis results showed that the SPPs in SRA

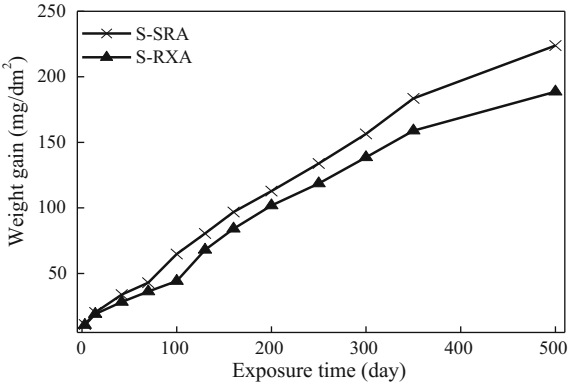

Fig. 2 Corrosion kinetics curves of Zr–0.8Sn–0.25Nb–0.35Fe–0.1Cr–0.05Ge alloys corroded in 400 °C, 10.3 MPa superheat steam

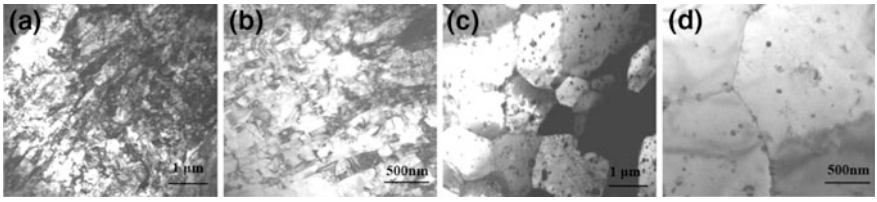

Fig. 3 TEM images of Zr–0.8Sn–0.25Nb–0.35Fe–0.1Cr–0.05Ge alloys, **a** SRA, **b** SRA, **c** RXA, **d** RXA

alloy were mainly ZrNbFeCr, ZrFeCr and ZrGe(Fe)Cr (Table 1). The ZrNbFeCr SPPs was Zr(Fe, Cr, Nb)$_2$ with a typical HCP structure (Fig. 5a). The SPPs containing Ge had very low Fe and Cr, which was Zr_3Ge with a tetragonal structure. In addition, there were a small amount of FCC ZrFeCr (Fig. 5b), whose Fe/Cr ratio was closed to 2.3–3.3.

The SPPs in RXA alloy were mainly HCP-Zr (Fe, Cr, Nb)$_2$, but less amount of tetragonal Zr_3Ge were observed (Fig. 5c), which was related to the higher diffusion rate of Fe and Ge atom at the higher temperature of the final heat treatment.

Microstructure of Oxide Film. Corrosion of zirconium alloys in different water chemical mediums is actually the process of the diffusion of O^{2-} or OH^- through the oxide film to the interface at the metal/oxide film, which reacts with Zr matrix to form ZrO_{2-y} (y = 0–2). In practice, the O^{2-} or OH^- production is attributed to anion vacancies diffusion to the opposite direction under the electric field function, and the anion vacancies will react with H_2O to form O^{2-} or OH^-. During the process of corrosion, the second phase particles and alloying elements dissolved in α-Zr will be oxidized finally, which will greatly affect the corrosion resistance of zirconium alloys [6, 7]. Figures 6, 7 and 8 showed the STEM images of oxide film and the selected area electron diffraction of precipitate characteristics of RXA alloys

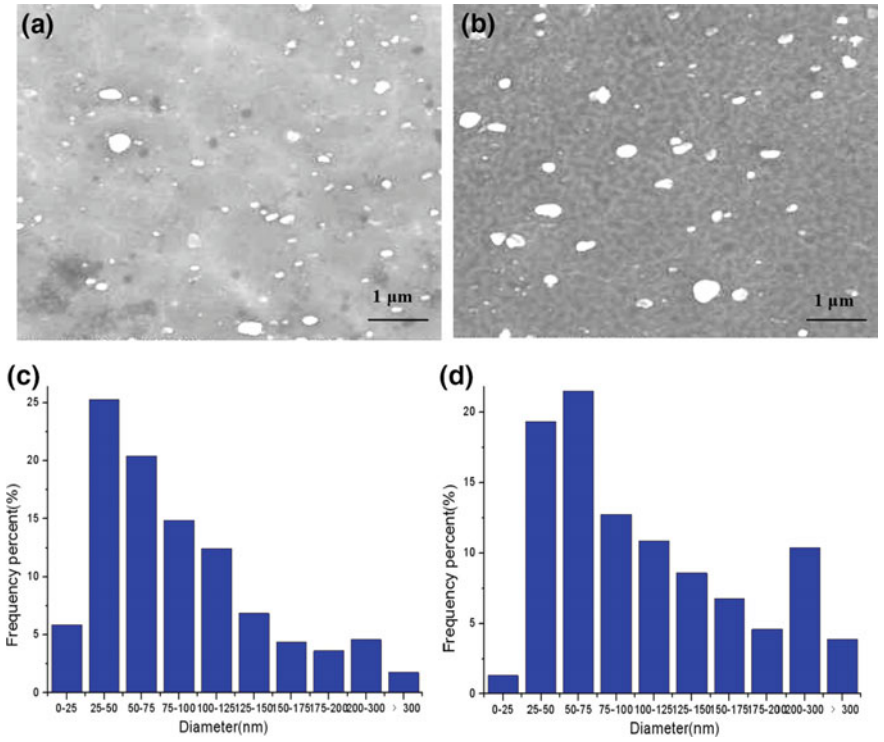

Fig. 4 SEM images and statistical results of precipitate characteristics of Zr–0.8Sn–0.25Nb–0.35Fe–0.1Cr–0.05Ge alloys, **a** SRA, **b** RXA, **c** SRA, **d** RXA

Table 1 The SPPs analysis results using TEM-EDS of Zr–0.8Sn–0.25Nb–0.35Fe–0.1Cr–0.05Ge alloy cladding tubes (wt%)

Alloy state	The type of SPPs	Nb	Fe	Cr	Ge	Zr	Nb/Fe
SRA	ZrNbFeCr	3.69	15.31	8.84	/	71.24	0.24
		2.24	8.31	5.79	/	83.65	0.27
	Zr(Fe)CrGe	/	/	1.42	7.18	90.06	/
		/	/	1.47	14.05	84.48	/
	ZrFeCr	/	21.01	6.34	/	66.85	/
		/	14.58	6.22	/	79.21	/
RXA	ZrNbFeCr	2.8	22.92	7.41	/	66.55	0.12
		5.06	23.45	8.64	/	62.85	0.22
	Zr(Fe)CrGe	/	0.73	1.6	11.96	85.71	/
		/	9.23	1.86	7.83	81.07	/
	ZrFeCr	/	16.51	7.05	/	75.32	/
		/	12.86	7.30	/	79.84	/

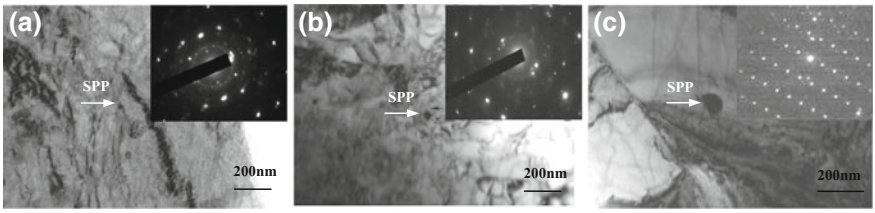

Fig. 5 TEM images and selected area electron diffraction of precipitates of Zr–0.8Sn–0.25Nb–0.35Fe–0.1Cr–0.05Ge alloys, **a** SRA, **b** SRA, **c** RXA

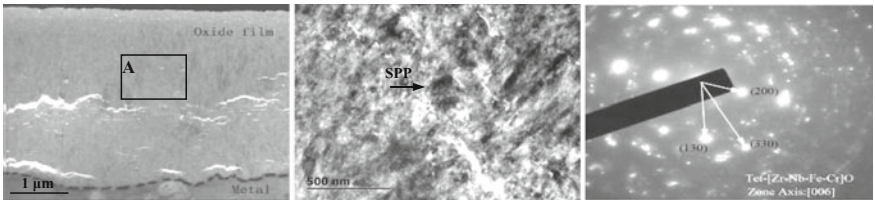

(a) Bright field image (b) A at high magnification (c) Diffraction pattern of SPP

Fig. 6 STEM images and selected area electron diffraction of precipitate characteristics of RXA-Zr–0.8Sn–0.25Nb–0.35Fe–0.1Cr–0.05Ge alloy oxide film corroded in 360 °C/18.6 MPa pure water

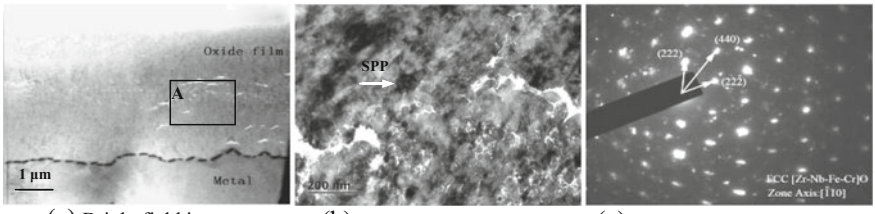

(a) Bright field image (b) A at high magnification (c) Diffraction pattern of SPP

Fig. 7 STEM images and selected area electron diffraction of precipitate characteristics of RXA-Zr–0.8Sn–0.25Nb–0.35Fe–0.1Cr–0.05Ge alloy oxide film corroded in 360 °C/18.6 MPa/0.01 mol/L LiOH aqueous solution

corroded in 360 °C/18.6 MPa pure water after 500 days, in 360 °C/18.6 MPa/0.01 mol/L LiOH aqueous solution after 300 days and in 400 °C/10.3 MPa superheated steam after 160 days. The corresponding average thickness of the oxide film were approximately 4.2, 4.7 and 5.5 μm, respectively. The interface between the oxide film and the metal substrate (O/M) was wavy, and the oxide film near the substrate was mainly composed of columnar crystal, and away from the substrate was mainly composed of fine equiaxed grains, which indicated that the growth of the oxide film is the evolution process from columnar to equiaxed.

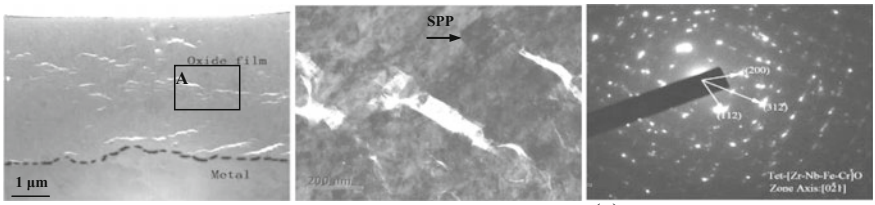

Fig. 8 STEM images and selected area electron diffraction of precipitate characteristics of RXA-Zr–0.8Sn–0.25Nb–0.35Fe–0.1Cr–0.05Ge alloy oxide film corroded in 400 °C/10.3 MPa steam

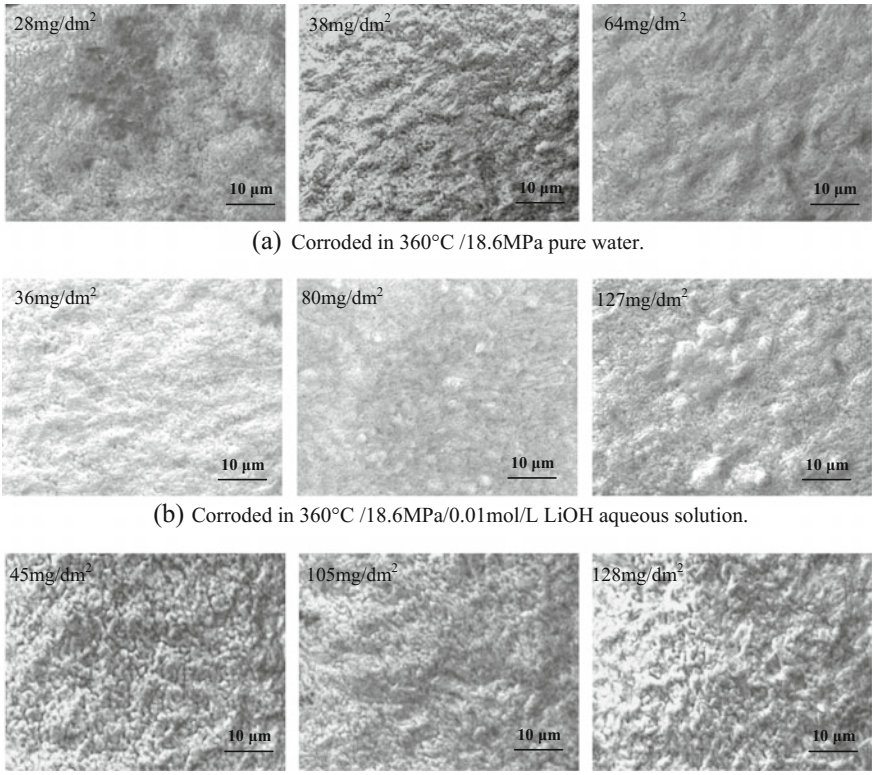

Fig. 9 Micrographs at the oxide film/substrate interface of RXA-Zr–0.8Sn–0.25Nb–0.35Fe–0.1Cr–0.05Ge alloys corroded in different corrosive mediums

In addition, the pores or cracks could be observed in oxide film after corroded in different chemical mediums, but near the interface of O/M it's difficult to be observed. The analysis results of precipitates near the pores or cracks showed that the precipitates are face centered cubic structure ZrNbFeCrO and tetragonal

ZrNbFeCrO. Although there are some oxygen in the precipitates, they still maintain a certain crystal structure. The pores or cracks in oxide film may come from the stress generated at the substrate/interface by the volume expansion of zirconium alloy matrix and oxidation of SPPs during the corrosion process. It's also possible that the amorphous oxidation of the matrix near the precipitates peel by ion beam bombardment using FIB, and then form the pores or cracks. The pores or cracks will provide channels for oxygen diffusion, which will improve the corrosion rate of alloy. The higher the corrosion weight gain is, the more the holes or flaws paralleling to the long axis of the oxide film are.

Figure 9 showed the micrographs at the oxide film/substrate interface of RXA Zr–0.8Sn–0.25Nb–0.35Fe-0.1Cr–0.05Ge alloy corroded in different corrosive mediums. The oxide films showed cauliflower-like structure, and the size was positive correlated with the corrosion weight gain, which was consistent with the results of studies [8]. For the possible reasons of the cauliflower-like protrusions, literature [9] explained with the relationship between pores, holes, cracks and corrosion process. It was shown that the formation of pore clusters in the oxide film and other defects promotes the diffusion of O^2, which made the oxide film advance to the metal substrate. With the oxidation process, a larger size of cauliflower will form at the oxide/substrate interface. Therefore, the size of protuberance and the fluctuation degree represented the growth rate of oxide film and uneven growth trend. When cracks and holes formed after corrosion transition, the diffusion rate of oxygen ions and the growth rate of oxide film then increased, leading to the growth inhomogeneity of oxide film become more obvious.

Conclusions

(1) For Zr–0.8Sn–0.25Nb–0.35Fe–0.1Cr–0.05Ge alloy, the corrosion weight gain of RXA alloy is lower than that of SRA alloy after 500 days corrosion test in three different corrosive mediums.
(2) The SPPs are dispersed evenly in the alloy, which are mainly HCP-Zr (Nb, Fe, Cr)$_2$ and FCC-Zr_2 (Fe, Cr). Compared with RXA alloy, the average diameter of precipitates in SRA alloy is relatively smaller, but the number of TET-Zr_3Ge is relatively more.
(3) The interface between the oxide film and the metal substrate (O/M) is wavy, and the oxide film near the O/M interface is compact and mainly composed of columnar crystal, while the oxide film away from the O/M interface mainly consists of fine equiaxed grains. A large number of different size of pores or cracks are observed.
(4) With the increasing of corrosion rate, there are more cracks or pores in the section of the oxide film and the size of cauliflower-like structure grew bigger.

References

1. A. Garner, A. Gholinia, P. Frankel, M. Gass, I. MacLaren, M. Preussl, The microstructure and microtexture of zirconium oxide films studied by transmission electron backscatter diffraction and automated crystal orientation mapping with transmission electron microscopy. Acta. Mater. **80**, 159–162 (2014)
2. P. Platt, P. Frankel, M. Gass, M. Preuss, Critical assessment of finite element analysis applied to metal–oxide interface roughness in oxidising zirconium alloys. J. Nucl. Mater. **464**, 313–318 (2015)
3. P. Platt, E. Polatidis, P. Frankel, M. Klaus, M. Gass, R. Howells, M. Preuss, A study into stress relaxation in oxides formed on zirconium alloys. J. Nucl. Mater. **456**, 415–421 (2015)
4. Y.H. Jeong, H.G Kim, T.H Kim. Effect of βphase, precipitate and Nb-concentration in matrix on corrosion and oxide characteristics of Zr-xNb alloys. J. Nucl. Mater. **317**, 1–12 (2003)
5. H.G. Kim, J.Y. Park, Y.H. Jeong, Ex-ractor corrosion and oxide characteristics of Zr–Nb–Fe alloys with the Nb/Fe ratio. J. Nucl. Mater. **345**, 1–10 (2005)
6. B. Gabory, Y. Dong, A.T. Motta et al., EELS and atom probe tomography study of the evolution of the metal/oxide interface during zirconium alloy oxidation. J. Nucl. Mater. **462**, 304–309 (2015)
7. A. Couet, A.T. Motta, B. de Gabory, Microbeam X-ray absorption near-edge spectroscopy study of the oxidation of Fe and Nb in zirconium alloy oxide layers. J. Nucl. Mater. **452**(1–3), 614–627 (2014)
8. J-L. Zhang, X-F. Xie, M.-Y. Yao, Study on the corrosion resistance of Zr–1Nb–0.7Sn–0.03Fe-xGe Alloy in Lithiated water at 360. Acta Metall. Sinica. **49**(4), 443–449, (2013)
9. J. Huang, M. Yao, C. Gao et al., The influence of second phase particles on the crack formation in oxide films formed on zirconium alloys. Corros. Sci. **99**, 172–177 (2015)

Effect of Grain Orientation on Surface Damage of Niobium Doped Tungsten with Helium Implantation

Yutian Ma, Junbiao Liu, Han Li, Long Cheng, Ying Zhang and Kaigui Zhu

Abstract Niobium doped tungsten was irradiated by helium ion implantation, and the effect of grain orientation on surface damage induced by helium sputtering was studied by X-ray photoelectron spectroscopy, scanning electron microscopy, atomic force microscopy and electron backscattered diffraction. Many cavities or pores caused by helium sputtering were observed on the surface of the samples, and the surface damage of tungsten by helium irradiation was aggravated by 1.0×10^{18} Nb/cm^2 doping. It was found that the surface damage of different crystal orientations was distinct under same helium implantation condition. The surface damage of grains with (1 1 0) orientation was worse than that of grains with (1 1 1) and (1 0 0) orientation. The result suggested that the surface damage induced by helium sputtering was closely related to helium implantation fluence and grain orientation.

Keywords Tungsten · Helium implantation · Sputtering · Grain orientation

Introduction

Tungsten, due to its unique low sputtering and erosion rate, is a candidate plasma-facing material for controlled fusion devices like ITER [1–3]. However, it is confined by the interaction between the activated plasma and the wall, since sputtering at tungsten surface may occur when the wall is irradiated by He produced by (n, α) reactions, leading to instability and reduction of the quality of the plasma. These effects are particularly crucial in the divertor of a tokamak reactor design. Another major consequence is the long-term gradation of the mechanical properties of the wall material.

Y. Ma · J. Liu · H. Li
Institute of Electrical Engineering, Chinese Academy of Sciences, Beijing 100190, China
e-mail: guangxima888@126.com

Y. Ma · L. Cheng · Y. Zhang (✉) · K. Zhu
Department of Physics, Beihang University, Beijing 100191, China
e-mail: zhyi@buaa.edu.cn

Y. Han (ed.), *Advances in Energy and Environmental Materials*,
Springer Proceedings in Energy, https://doi.org/10.1007/978-981-13-0158-2_14

In the field of materials for fusion, many studies focusing on helium blistering behavior in tungsten have already been performed [4–6], and the research for He sputtering of tungsten has turned up in recent years [7–11]. It is well-known that He has a strong tendency to precipitate into cluster in tungsten via a variety of possible diffusion mechanisms, and the coalescence and growth of clusters are able to produce swelling and blistering, which results in the surface damage. The He-induced surface damage caused by helium blistering and helium sputtering, which caused significant morphology changes in the surface of tungsten. Depending on the irradiation condition, different changes in the microstructure of tungsten occur, such as fuzz growth at elevated exposure temperature [10]. In addition, the grain orientation affected the He-induced surface damage has been reported in some literatures [12–15]. This is interesting as it may provide an approach to understand the helium behavior in tungsten. Recently, Hou et al. simulated the damage induced by helium implantation for crystalline tungsten with (1 0 0), (1 1 0) and (1 1 1) by the Binary Collision Approximation, and found that the He backscattering yields follow the same scaling: 8% on (1 1 0), 4% on (1 0 0), 3% on (1 1 1) [16]. Sefta et al. simulated (1 0 0) and (1 1 0) surfaces damage induced by helium ion exposure in the range of 300 eV–1 keV by Molecular Dynamics, and revealed that sputtering is higher for (1 1 0) surfaces relative to (1 0 0) surfaces [17]. Becquart et al. simulated formation energies for different configurations of the self-interstitial atoms in tungsten (1 0 0), (1 1 0) and (1 1 1) surfaces, and found that the (1 1 1) dumbbell to be the most stable in tungsten [18]. Based on the above theoretical research, the related experimental studies are necessary to investigate the effect of grain orientation on surface damage induced by helium ions.

Doping elements in tungsten could improve its property. Tungsten and niobium (Nb) could form solute solid and the addition of niobium in tungsten could improve mechanical property such as ductility and strength. In our previous work, two kinds of W materials, i.e. pure tungsten and niobium doped tungsten, were studied with helium ion implantation [19]. It was found that niobium doped tungsten had improved helium sputtering resistance compared to pure tungsten. Grain orientation effects in sputtering have been reported by Manova et al. [20, 21] and Michaluk, et al. [22]. In this work, niobium-doped tungsten samples were implanted with helium as previous [19], and the surface damage as a function of grain orientation was investigated. We found that grains with (1 1 0) orientation were most severely damaged by helium sputtering, and grains having (1 1 1) orientation were damaged the least. The relative height of grains as a function of surface orientation following He implantation was used to show the relation between surface damage and orientation.

Experiment Description

Pure tungsten plate was prepared by powder-metallurgy and hot-rolled reduction, with a purity of 99.99 wt%. Samples used in the experiments were cut into 10 mm $\times$ 10 mm $\times$ 3 mm-thick from the plates and polished on one side. Each

one was cleaned in an acetone ultrasonic bath before testing. Niobium was implanted into tungsten with an incident energy of 45 keV and fluence of 1.0×10^{18} Nb/cm^2 using an ion implanter equipped with Metal Vapor Vacuum Arc (MEVVA). The background pressure was lower than 1.0×10^{-5} Pa, and the working pressure of helium around the sample holder was 1 Pa. The incident energy of helium was about 40 keV with a flux of 1.5–2.0 $\times$ 10^{13} ion/cm^2/s and the incident fluence were varied via choosing different irradiation durations from 3.0×10^{16} to 3.6×10^{17} He/cm^2. During each implantation, the sample surface temperature was kept below 400 K by water cooling.

The surface compositions were analyzed by X-ray photoelectron spectroscopy (XPS) since the samples were implanted with niobium. The XPS spectra of Nb was measured at a pass energy of 20 eV and an energy step of 0.2 eV. The original surface was sputtered using 1 keV argon (Ar) ions for 1, 2, 4, 6, 8, and 10 min. The Ar ion etching rate is estimated to be 0.08 nm/s.

The surface damage of irradiated samples was observed with scanning electron microscope (SEM) and atomic force microscopy (AFM). Electron backscattered diffraction (EBSD) was employed to examine grain orientation.

Results and Discussion

Surface Composition. Figure 1 shows the XPS spectra of Nb 3d. The two peaks at 203 and 206 eV are due to the metallic state of Nb, i.e. Nb 3d5/2 and Nb 3d3/2, respectively. Moreover, two peaks near 210 and 207.5 eV in the case of no etching were observed, which correspond to the Nb 3d3/2 and Nb 3d5/2 bands in Nb_2O_5, respectively. However, Nb–W intermetallic compounds were not observed in the Nb 3d spectrum as shown in Fig. 1a, which indicates no formation of Nb–W intermetallic compounds during Nb implantation. Though the peak of Nb concentration reached 8.32 at% after 1.0 $\times$ 1018 Nb/cm^2 as shown in Fig. 1b, no

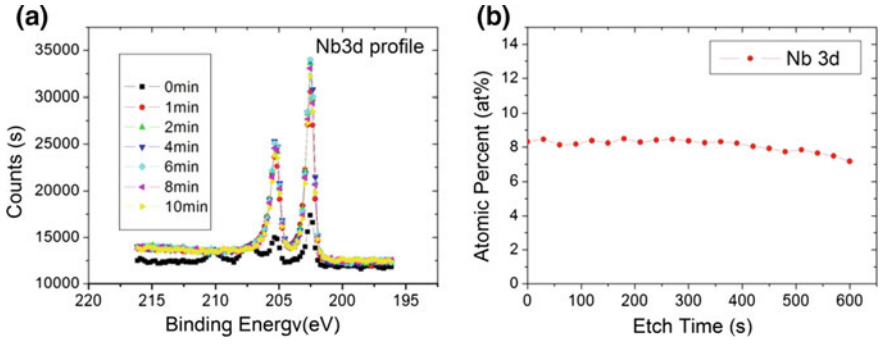

Fig. 1 Nb 3d spectra (**a**) and atomic percents of Nb as a function of sputtering time (**b**) in tungsten samples implanted with 1.0×10^{18} Nb/cm^2

Nb–W intermetallic compound was formed due to the low sample temperature. These results suggest that Nb is mainly a metal dopant in solution in tungsten.

Surface Damage. The surface morphology changes of Nb doped tungsten as a function of He implantation fluence is shown in Fig. 2. Compared with surface morphology of un-irradiated sample as shown in Fig. 2a, a lot of nano-size cavities were observed on the surface of sample irradiated with 3×10^{16} He/cm^2 as shown in Fig. 2b, which due to helium sputtering since the irradiation energy is much higher than the sputtering threshold of tungsten (50 eV). However, under higher irradiation fluence, the amount and density of cavities decreased and many pores appeared on surface of sample as shown in Fig. 2c, and the diameters of pores were in the range of 50–100 nm. With increasing He fluence, the average diameter of the surface pores increased and the cavities disappeared at the fluence of 1.2×10^{17} He/cm^2 as shown in Fig. 2d. Besides, these pores had a coalescence process and tended to form bigger pores with higher He fluence as shown in Fig. 2e [23]. These pores varied in shape during their coalescence process, from circle pore to long groove, which indicates that the coalescence happened under certain orientations at the fluence of 3.6×10^{17} He/cm^2, the evolution of coalescence resulted in the formation of "coral" type surface structures as observed in Fig. 2f. Similar surface morphology was reported previously [24]. In addition, the surface was strongly corrugated with protrusions arranged along parallel lines as shown in Fig. 2e and more obvious with higher He fluence as shown in Fig. 2f, which is similar to surface morphology reported by Manova [20]. From the result, the surface morphology changed obviously, and the change is closely related with the helium irradiation fluence.

The irradiated surfaces were also observed at a tilting angle of 70° and a special surface morphology by helium sputtering was observed at low magnification. At the

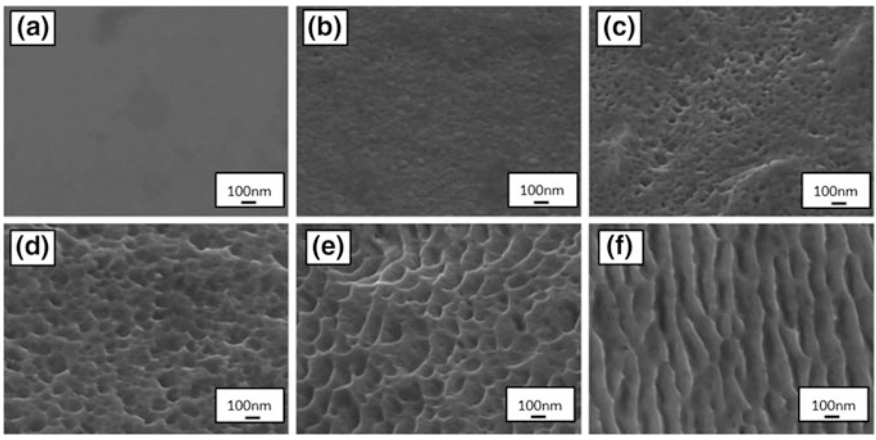

Fig. 2 Surface topographies of 1×10^{18} ions/cm^2 Nb doped tungsten samples irradiated by 40 keV He with various fluences: **a** 0, **b** 3.0×10^{16} He/cm^2, **c** 6.0×10^{16} He/cm^2, **d** 1.2×10^{17} He/cm^2, **e** 2.4×10^{17} He/cm^2, and **f** 3.6×10^{17} He/cm^2

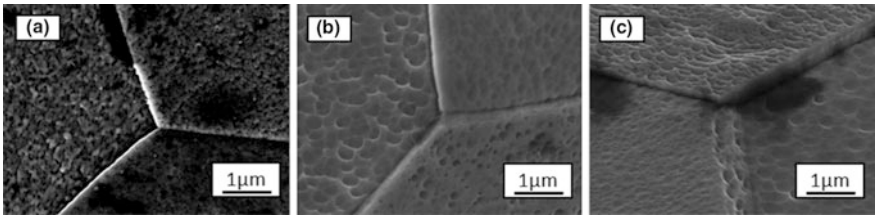

Fig. 3 Surface topographies of 1.0×10^{18} ions/cm^2 Nb doped tungsten samples irradiated by 40 keV He with various fluences: **a** 1.2×10^{17} He/cm^2, **b** 2.4×10^{17} He/cm^2, and **c** 3.6×10^{17} He/cm^2

fluence of 1.2×10^{17}, 2.4×10^{17} and 3.6×10^{17} He/cm^2, three adjacent grains demonstrate different heights as shown in Fig. 3. The grain height difference induced by He sputtering was prominent with increasing He implantation fluence as shown in Fig. 3a–c. Moreover, the difference in the surface morphology was observed, which changes thoroughly from grain to grain with very sharp grain boundaries, and the similar phenomenon has been reported in the literature [12]. The difference of surface morphology is not correlated with the direction of the ion beam as discussed in the literature [12], since an identical with implantation angle was used in this work. Thus, the surface damage is considered to be related to grain crystal orientation. However, this phenomenon was not observed in pure tungsten, 1.0×10^{16} Nb/cm^2 doped tungsten and 1.0×10^{17} Nb/cm^2 doped tungsten under same helium implantation condition in our previous work. According to the results of first-principle computations by Wu et al. [25], the phenomenon may attribute to the following reason: Nb as an impurity implanted into tungsten decreased the charge density and increased the binding energy, resulted in the aggregation of He atoms around the impurities, which enhanced the He damage in tungsten.

EBSD Analysis. The EBSD measurement was done in the area of 18×15 μm^2 with a scanning step of 0.5 μm/min on a hexagonal grid for samples shown in Fig. 3. The EBSD map of sample (same sample as in Fig. 3b) irradiated by 40 keV He ion beam with 2.4×10^{17} He/cm^2 was shown in Fig. 4. The individual grains were marked as a, b, c in both the SEM image and EBSD map. According to EBSD measurement, the three orientations of (1 0 0), (1 1 0) and (1 1 1) were present on the surface, and the grain orientation of a, b, c corresponds to (1 1 1), (1 0 0), and (1 1 0), respectively. It can be clearly seen that the height of grain with (1 1 0) orientation was lower than that of other two grains, and the height of grain with (1 1 1) orientation was the highest. In other words, the grain with (1 1 0) orientation was damaged worse than the other two grains, and the damage of grain with (1 1 1) orientation was the slightest. The EBSD result of the two other samples (same sample as Fig. 3a, c respectively) irradiated by He ion beam with 1.2×10^{17} and 3.6×10^{17} He/cm^2 as shown in Fig. 5a, b, respectively. Similar phenomenon was observed, which proved that there is a strong correlation between the surface damage and grain orientation. The surface height difference indicates that the

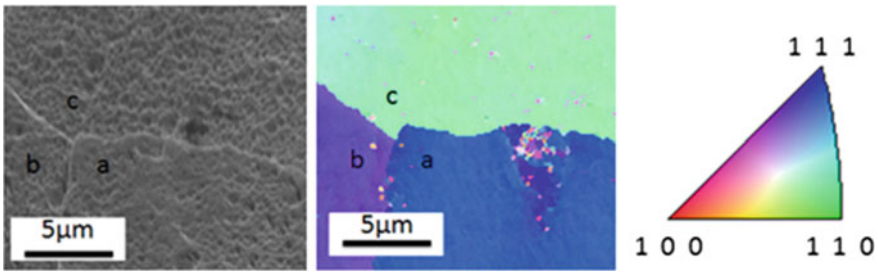

Fig. 4 EBSD map of sample irradiated by 40 keV He with 2.4×10^{17} He/cm^2

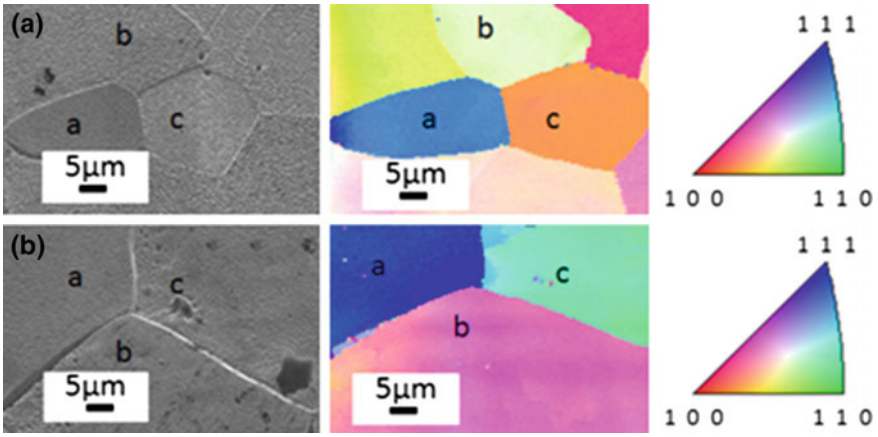

Fig. 5 EBSD map of sample irradiated by 40 keV He with **a** 1.2×10^{17} He/cm^2, **b** 3.6×10^{17} He/cm^2

helium sputtering yield of different crystalline planes $Y_{(UVW)}$ for tungsten, which can be calculated from the FIB experiment by the following formula [26]:

$$Y_{(UVW)} = \frac{N_{target}}{N_{ion}} = \frac{\frac{N_A \cdot V \cdot \rho}{m_{t\arg et}}}{\frac{i \cdot t}{e}} = \frac{e \cdot N_A \cdot A \cdot h_{(UVW)} \cdot \rho}{m_{t\arg et} \cdot i \cdot t} \quad (1)$$

where e is the elementary charge, N_A is the Avogadro constant, A is the sputtering area, $h_{(UVW)}$ is the erosion depth of a tungsten crystalline plane, ρ is the tungsten target density, mtarget is the tungsten atom weight, i is the ion beam current, and t is the sputtering time.

AFM Measurement. The step heights between the surfaces of different grain orientations discussed above were further measured with AFM scanning. Figure 6 shows the AFM images of the scanning results with the values of height difference between (1 0 0), (1 1 0), (1 1 1) orientations. The grain orientation of (1 1 1), (1 0 0), and (1 1 0) was marked as a, b and c, respectively. The height difference between (1 1 1) and (1 0 0) is marked as h_{ab}, the height difference between (1 1 1) and (1 1 0) was marked as h_{ac}, and the height difference between (1 0 0) and (1 1 0) was marked as h_{bc}. For Nb doped tungsten (same as Fig. 3a) irradiated with

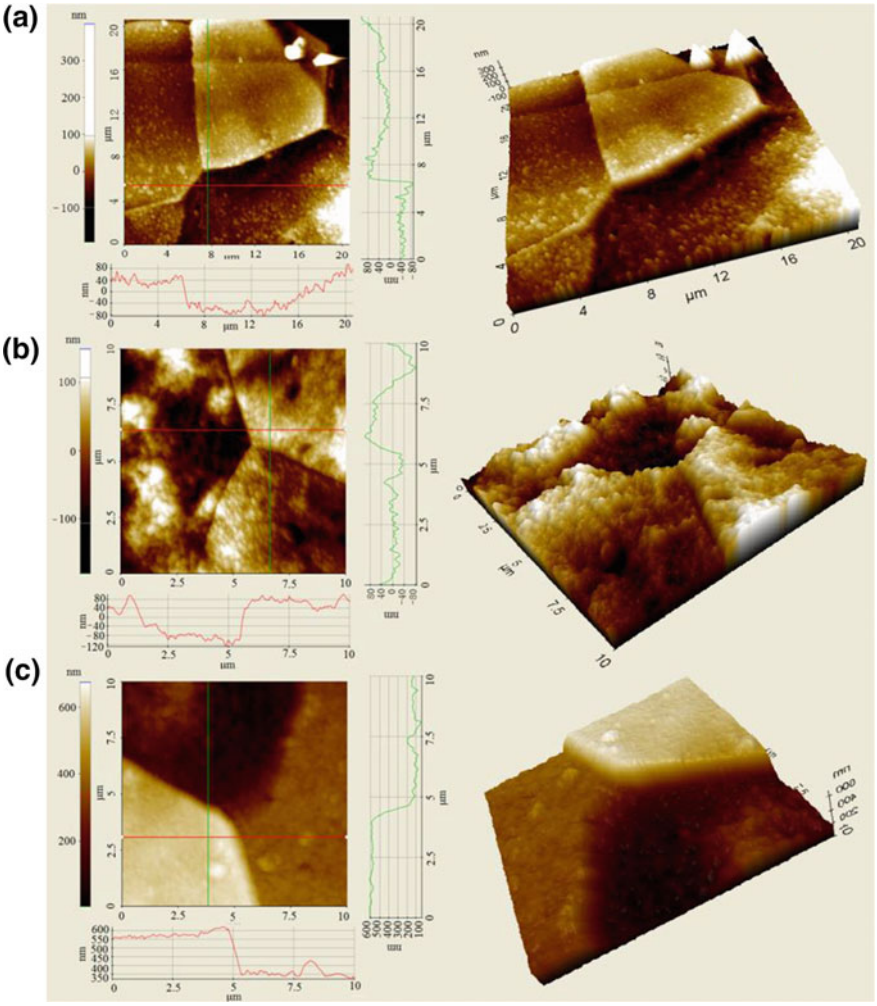

Fig. 6 2D and 3D AFM images of 1.0×10^{18} ions/cm^2 Nb doped tungsten samples irradiated by 40 keV He with various fluences: **a** 1.2×10^{17} He/cm^2, **b** 2.4×10^{17} He/cm^2, and **c** 3.6×10^{17} He/cm^2

1.2×10^{17} He/cm^2 as shown in Fig. 6a, h_{ab}, h_{bc} and h_{ac} was 40, 80 and 120 nm, respectively. Corresponding to the samples (same as Fig. 3b, c, respectively) as shown in Fig. 6b, h_{ab}, h_{bc} and h_{ac} is 80, 80 and 160 nm for 2.4×10^{17} He/cm^2, and in Fig. 6c, h_{ab}, h_{bc} and h_{ac} was 250, 250 and 500 nm for 3.6×10^{17} He/cm^2. This indicates that the helium sputtering rate of different crystal surface was different and the sputtering rate increases with the helium fluence increasing. In addition, the measured height of individual grains by AFM could be converted by Eq. (1) to obtain the sputtering yield for tungsten. The sputtering yield of (1 1 0) plane was the highest, followed by that of (1 0 0) plane, while that of (1 1 1) plane was the lowest. The results are agreed with the sputtering yield of molybdenum by Huang [26].

First-Principles Computation. The relationship between surface damage and grain orientation was studied with the first-principles computation. Density functional theory (DFT) calculations were performed with the Vienna Ab Initio Simulation Package (VASP) [27, 28]. The W-6 s 5d were treated as valence electrons, while the ionic cores were represented by the projector augmented wave (PAW) potentials [29]. The exchange and correlation interaction among electrons were described at the level of the generalized gradient approximation (GGA) using the Perdew–Burke–Ernzerhof (PBE) formula [30]. The kinetic energy cutoff for the plane-wave basis set was set to 400 eV, which kept the total energy errors below 1 meV. The first-order Methfessel–Paxton method [31] was used for the Fermi surface smearing, with a width of 0.2 eV. The convergence criteria for the electronic self-consistent iteration and the ionic relaxation loop were set to 10–5 eV and 0.01 eV/Å, respectively. As for the W bulk, the k-point sampling was chosen with $8 \times 8 \times 8$ net-grid which keeps the total energy errors below 10 meV. The calculated lattice constant 3.175 Å were agreed well with experimental value 3.165 Å. Three typical of low Miller index surfaces of W (1 0 0) (1 1 0) (1 1 1) were investigated here. Three surface models of W (1 0 0) (1 1 0) and (1 1 1) surface are shown in Fig. 7. The surface slabed models with a dimension of 3×3 for (100), 3×2 for (1 1 0) and 3×3 for (1 1 1) surface. The atom layer was chosen with 9

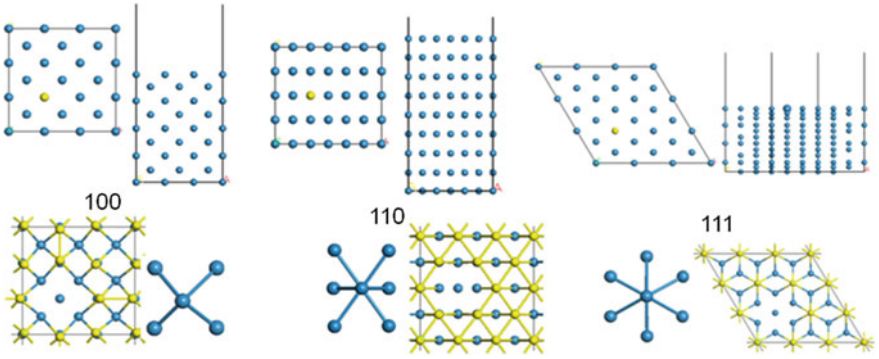

Fig. 7 Three surface models of W (1 0 0) (1 1 0) and (1 1 1) surface. The blue balls represent tungsten atoms, and the yellow balls in the surface will be taken away in the later

Table 1 Atomic surface density, surface energy and escape energy of different crystal

Crystal	Surface atomic density (atoms/Å2)	Surface energy (eV/Å2)	Escape energy (eV)
(1 0 0)	0.09919	0.247	10.470484
(1 1 0)	0.14028	0.201	12.845554
(1 1 1)	0.05726	0.217	11.469154

layers for (1 0 0) and (1 1 0), 12 layers for (1 1 1). The k-point sampling was chosen as 3 × 3 × 1 for (1 0 0) and (1 1 0), 2 × 2 × 1 for the (1 1 1) surface. Only the bottom atom layer was fixed to mimic the semi-infinite crystal for all calculations.

According to the first-principles computations, the atomic distance, surface atomic density, surface energy and escaping energy are listed in Table 1. The follow equation was used to calculate the escapeenergy: $Eesc = En_{-1} + Ew - En$, in which, Ew is the energy of one tungsten atom in bulk, En and En−1 are the energy of slab and the energy of slab with one atom taken away from the surface layer, respectively. The escaping energy is the energy needed to take away one surface atom which represents the stability of the surface. From Table 1, it is found that the escaping energy varied with the surface energy, that is, the lower the surface energy was, the higher the escaping energy. With physical intuitively, under the same irradiation condition, the surface damage would be more moderate with higher escaping energy, that is to say, the (1 1 0) surface would be have the slightest surface damage due to its highest escaping energy. While the (1 1 0) surface has the highest escaping energy and the smallest surface energy, but the (1 1 0) surface has the most serious surface damage under the He ions irradiation as shown in our experiments.

The surface atomic densities are calculated as following 0.05726/Å^2, 0.09919/Å^2 and 0.14028/Å^2 for (1 1 1), (1 0 0) and (1 1 0), respectively. The atomic surface density of (1 1 0) surface is the largest and it is almost triple time of (1 1 1) surface. The result of the atomic surface density calculation demonstrate different planar packing fraction (f) at different orientations, that is f (1 1 0) > f (1 0 0) > f (1 1 1). This agrees with the result from molybdenum, another bcc metal [26]. Difference of damage level at different orientations can be explained by the variation of the planar packing fraction. According to the literature [32, 33], the surface sputtering happens when atoms at sub-surface layer receive enough momentum via collision cascade events. At the orientation of the highest planar packing fraction the penetration of implantation particles suffers the greatest retarding based on the crystalline transparency model [34, 35]. The momentum transfer happens at the shallowest depth, compared with the other two orientations, resulting to the most severe damage on the surface [36]. With this notion, we can explain why (1 1 0) surface has the most serious damage, (1 0 0) takes second place and (1 1 1) has the slightest surface damage.

Conclusions

Helium ion implantation has been carried out on niobium doped tungsten. The surface damage induced by helium implantation was characterized and discussed. The Nb was implanted into tungsten and existed in atomic states on tungsten substrate. Many cavities or pores caused by helium sputtering were observed on the surface of sample, and the surface damage of tungsten by helium irradiation was aggravated by 1.0×10^{18} Nb/cm^2 doping. It was found that the surface damage is related with grain orientation. The damage of grain with (1 1 0) orientation is the most, while that of grain with (1 1 1) orientation is the slightest. The surface damage difference is owing to the atomic surface density in grain with different crystal orientation.

Acknowledgements This research is supported by the National Magnetic Confinement Fusion Programs with Grant No. 2013GB109003, and the National Natural Science Foundation of China with Grant No. 51171006, and Scientific Research equipment development project of Chinese Academy of Sciences (with Grant No. YZ201410).

References

1. J. Roth, E. Tsitrone, A. Loarte, et al., Recent analysis of key plasma wall interactions issues for ITER. J. Nucl. Mater. **390–391**, 1–9 (2009)
2. H. Bolt, V. Barabash, G. Federici, et al., Plasma facing and high heat flux materials—needs for ITER and beyond. J. Nucl. Mater. **307–311**, 43–52 (2002)
3. H. Bolt, V. Barabash, W. Krauss, et al., Materials for the plasma-facing components of fusion reactors. J. Nucl. Mater. **329–333**, 66–73 (2004)
4. K. Tokunaga, R.P. Doerner, R. Seraydarian, et al., Surface morphology and helium retention on tungsten exposed to low energy and high flux helium plasma. J. Nucl. Mater. **313–316**, 92–96 (2003)
5. D. Nishijima, M.Y. Ye, N. Ohno, et al., Incident ion energy dependence of bubble formation on tungsten surface with low energy and high flux helium plasma irradiation. J. Nucl. Mater. **313–316**, 1029–1033 (2004)
6. S.B. Gilliam, S.M. Gidcumb, N.R. Parikh, et al., Retention and surface blistering of helium irradiated tungsten as a first wall material. J. Nucl. Mater. **347**, 289–297 (2005)
7. M. Tomita, K. Masumori, Fluence- and temperature-dependence of sputtering yield by 25 keV He-ion bombardment on tungsten and niobium. Nucl. Instr. Methods B. **39**, 95–98 (1989)
8. M.J. Baldwin, R.P. Doerner, Formation of helium induced nanostructure 'fuzz' on various tungsten grades. J. Nucl. Mater. **404**, 165–173 (2010)
9. A. Lasa, K.O.E. Henriksson, K. Nordlund, MD simulations of onset of tungsten fuzz formation under helium irradiation. Nucl. Instr. Methods B. **303**, 156–161, (2013)
10. D. Nishijima, M.J. Baldwin, R.P. Doerner, et al., Sputtering properties of tungsten 'fuzzy' surfaces. J. Nucl. Mater. **415**, 96–99 (2011)
11. K. Katayama, K. Imaoka, T. Okamura, et al., Helium and hydrogen trapping in tungsten deposition layers formed by helium plasma sputtering. Fusion Eng. Des. **82**, 1645–1650 (2007)
12. B.M.U. Scherzer, in *Development of Surface Topography Due to Gas Ion Implantation*, ed. by R. Behrisch. Sputtering by Particle Bombardment, (Springer, Berlin, 1981) pp. 271–355

13. C. Li, H. Greuner, Y. Yuan, et al., Effects of temperature on surface modification of W exposed to He particles. J. Nucl. Mater. **455**, 201–206 (2014)
14. N. Ohno, Y. Hirahata, M. Yamagiwa, et al., Influence of crystal orientation on damages of tungsten exposed to helium plasma. J. Nucl. Mater. **438**, 879–882 (2013)
15. C.M. Parish, H. Hijazi, H.M. Meyer, et al., Effect of tungsten crystallographic orientation on He-ion-induced surface morphology changes. Acta Mater. **62**, 173–181 (2014)
16. M. Hou, C.J. Ortiz, C.S. Becquart, et al., Microstructure evolution of irradiated tungsten: crystal effects in He and H implantation as modelled in the binary collision approximation. J. Nucl. Mater. **403**, 89–100 (2010)
17. F. Sefta, N. Juslin, K. D. Hammond, et al., Molecular dynamics simulations on the effect of sub-surface helium bubbles on the sputtering yield of tungsten. J. Nucl Mater. **438**, 493–496 (2013)
18. C.S. Becquart, C. Domain, Ab initio calculations about intrinsic point defects and He in W. Nucl. Instr. Methods B. **255**, 23–26 (2007)
19. Y.T. Ma, Y. Zhang, G.H. Lu, et al., Effect of helium implantation on mechanical properties of niobium doped tungsten, Sci. Chin. Phys. Mech. Astron. **56**(7), 1396–1400 (2013)
20. D. Manova, M. Schreck, S. Mändl, et al., Orientation dependent sputter yield of aluminium. Surf. Coat. Technol. **151–152**, 72–75 (2002)
21. H.K. Zhang, D.M. Liu, H.B. Li et al., Study on the microstructure of high purity aluminum sputtering targets by EBSD method. J. Chin. Electr. Microsc. Soc. **27**(6), 491–494 (2008)
22. C.A. Michaluk, Correlating discrete orientation and grain size to the sputter deposition properties of tantalum. J. Electron Mater. **31**(1), 1–9 (2002)
23. S. Sharafat, A. Takahashi, K. Nagasawa et al., A description of stress driven bubble growth of helium implanted tungsten. J. Nucl. Mater. **389**, 203–212 (2009)
24. Q. Xu, N. Yoshida, T. Yoshiie, Accumulation of helium in tungsten irradiated by helium and neutrons. J. Nucl. Mater. **367–370**, 806–811 (2007)
25. X-B. Wu, X-S. Kong, Y-W. You, et al., First principles study of helium trapping by solute elements in tungsten. J. Nucl. Mater. **455**, 151–156 (2014)
26. H.S. Huang, C.H. Chiu, I.T. Hong, et al., Determining the sputter yields of molybdenum in low-index crystal planes via electron backscattered diffraction, focused ion beam and atomic force microscope. Mater. Charact. **83**, 68–73 (2013)
27. G. Kresse, J. Hafner, Ab Initio Molecular Dynamics for Liquid Metals. Phys Rev B. **47**, 558–561 (1993)
28. G. Kresse, J. Furthmüller, Efficiency of Ab-Initio total energy calculations for metals and semiconductors using a plane-wave basis set. Comp. Mater. Sci. **6**, 15–50 (1996)
29. G. Kresse, D. Joubert, From ultrasoft pseudopotentials to the projector augmented-wave method. Phys. Rev. B. **59**, 1758–1775 (1999)
30. J.P. Perdew, K. Burke, M. Ernzerhof, Generalized gradient approximation made simple. Phys. Rev. Lett. **77**, 3865–3868 (1996)
31. M. Methfessel, A.T. Paxton, High-precision sampling for Brillouin-zone integration in metals. Phys. Rev. B. **40**, 3616 (1989)
32. C. Michaluk, *Metallurgical Factors Affecting the Performance of Tantalum Sputtering Targets*, ed. by C. Culbertson. Proceedings of 41th International Symposium on Tantalum and Niobium. Brussels, Belgium: Tantalum–Niobium International Study Center, 2000, p. 75
33. R.S. Averback, T.D. Rubia, Displacement damage in irradiated metals and semiconductors. Solid State Phys. **51**, 281–402, (1997)
34. J.M. Fluit, P.K. Rol, J. Kistemaker, Angular-dependent sputtering of copper single crystals. J. Appl. Phys. **34**, 690–691 (1963)
35. A.L. Southern, W.R. Willis, M.T. Robinson, Sputtering experiments with 1- to 5-keV Ar + ions, J. Appl. Phys. **34**, 153–163 (1963)
36. G.D. Magnuson, C.E. Carlston, Electron ejection from metals due to 1- to 10-keV noble gas ion bombardment. I. polycrystalline materials. J. Appl. Phys. **34**, 3267–3273 (1963)

Classification Characterization and Data Mining Research on W Surface Modification Induced by Particle Fluxes: A Method Investigation

Chun Li, Shiyu Ma and Pengcheng Shi

Abstract Particle irradiation from the fusion plasma will lead to significant changes in W surface morphology. Imagery method and qualitative description are generally used to describe and classify these damage morphologies, which is not conductive to reveal the essential relationship between different damage structures and the influence rules of different irradiation conditions. Based on texture feature analysis, this work provides a classification and characterization method by selecting four feature structures, "hole" structure, "branch" structure, "blister" structure and "groove" structure, to analyze surface SEM images, to conduct a preliminary exploration by using data mining technology. The relationship between different feature structures and the effect significance level of different influence factors, including incident energy, incident flux, total incident fluence and exposure temperature has been obtained from the preliminary application in the research on W surface modification induced by He or D particles. With the increase of sample size and considered factors, this method is expected to provide more valuable reference for the mechanism researches on irradiation damage of material's surface.

Keywords Tungsten · Surface modification · Image analysis

C. Li (✉) · S. Ma · P. Shi
College of Mechanical and Materials Engineering, North China University of Technology, Beijing 100144, China
e-mail: lichun@ncut.edu.cn

S. Ma
e-mail: 18801292553@163.com

P. Shi
e-mail: 15001306272@163.com

Y. Han (ed.), *Advances in Energy and Environmental Materials*,
Springer Proceedings in Energy, https://doi.org/10.1007/978-981-13-0158-2_15

Introduction

During usage of Tokamaks, particle irradiation from the fusion plasma is expected to lead to performance degradation of plasma facing components due to the development of significant changes in surface morphology. Therefore, as a promising candidate plasma facing material, the surface modification of tungsten (W) induced by particle fluxes has caught extensive attentions in recent years [1–14]. Figure 1a shows several typical W surface modifications induced by He or D particle fluxes reported in references.

In the current studies, imagery method and qualitative description are generally used to describe and classify these damage morphologies with different shapes and sizes, such as a porous structure, a pitting structure, a fuzz structure, a grass-like structure, small pores, larger blisters, finer coral-like structures and so on. This situation easily covers the essential relationship between different damage structures, and is not conductive to reveal the influence rules of different irradiation conditions. For example, Fig. 1b summarizes 63 results reported in Refs. [1–8], and shows the observed relationship between He-induced surface modification, incident energy, total incident fluence and exposure temperature. Great difference can be seen among the damage surfaces under various irradiation conditions with different parameters. However, various and confused names of the morphologies make it

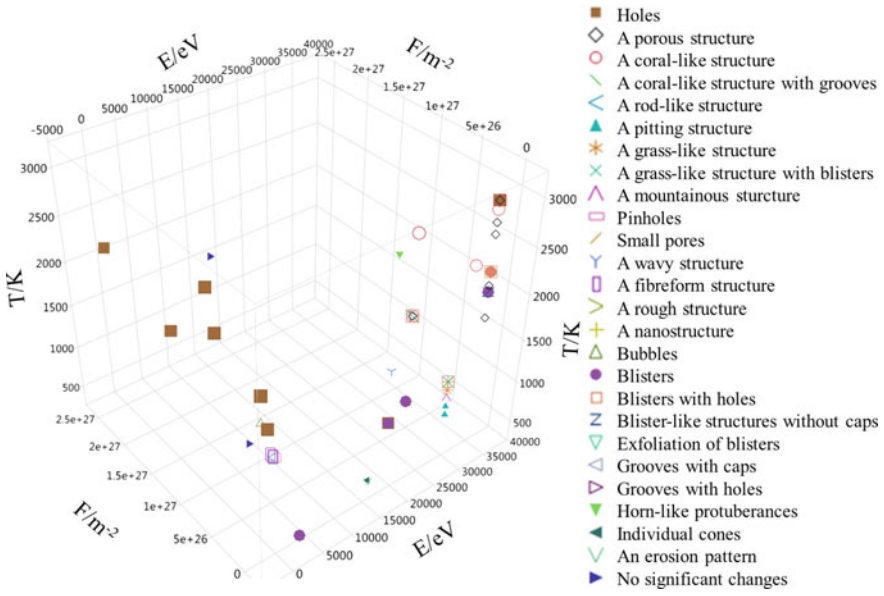

Fig. 1 Three dimensional scatter plot of the relationship between He-induced surface modification, incident energy, total incident fluence and exposure temperature (The original experimental data came from Refs. [1–8])

very difficult to search for the specific rules of the influence factors (energy, fluence and temperature) by using this kind of three dimensional scatter plot.

Therefore, the purpose of this study is to find out a relatively uniform method to describe and classify W surface different modifications induced by particle fluxes, and explore its preliminary application combining with data mining technology.

Methods

The local statistics characteristics of W surface damage morphologies induced by particle fluxes show approximately periodic variations, so in terms of image analysis, this kind of morphologies can be regarded as texture images. In the research of texture image, appropriate texture features are usually selected to serve image classification [15]. Thus borrowing this idea, based on texture feature analysis, four feature structures were selected in this study to serve the description and classification of W surface damage morphologies. They are "hole" structure, "branch" structure, "blister" structure and "groove" structure.

The "hole" structure includes "holes", "pinholes" and "pores" with different sizes. The commonly-used "porous structure" in references has this type of feature structure. The average diameter of the holes is used to characterize the structure size, and the area percentage of holes in surface SEM images (called "surface damage rate" in this study) is used to characterize the structure density. The situations that two kinds of "holes" with large size difference appear together and that "holes" and "blisters" or "grooves" appear together are both very common.

The "branch" structure includes "the coral-like structure", "the rod-like structure", "the grass-like structure", "the fibreform structure", "the fuzz structure", etc. The average width of independent branches is used to characterize the structure size, and similar as the "hole" structure, "surface damage rate" is used to characterize the structure density, which refers to "100%—the area percentage of branches in surface SEM images" for the "branch" structure.

The "blister" structure appears as bulges with domes or crescent-shaped gaps from the top view. Most are circular and a few show irregular shapes. The name for this type of feature structure in references is relatively unified. All the D-induced surface modifications summarized in this study are in this class. The average diameter of the blisters is used to characterize the structure size, and the area percentage of bulges in surface SEM images (surface damage rate) is used to characterize the structure density.

The "groove" structure is also called as "the pitting structure", etc. It is generally considered forming from ruptured blisters and blister cap exfoliation [6]. So in many reports, this type of feature structure is directly called "blister bursting" [9] or "blister-like structures without caps" [1]. This study also discussed the relationship between "blister" and "groove" structures, seen in the next section.

It should be noted that, when the incident energy is higher than the sputtering threshold, physical sputtering will cause different erosion patterns on W surface,

especially for He particles, such as "wave structures" or "individual cones" [5]. Erosion patterns are closely related to the local orientation of each individual grain, and in this study, they are not considered into any of the four feature structures.

In order to investigate the applied value of the above classification and characterization method, 66 He-induced W surface modification samples and 37 D-induced W surface blistering samples summarized from 14 references [1–14] were respectively analyzed and a preliminary exploration was conducted by using data mining technology.

Data mining technology is a kind of comprehensive technology to search from large amounts of data for useful information, such as hidden association or important factors, based on statistics theory and computer technology. With the advent of the era of big data, data mining technology has a great development. Many pieces of statistical exploration software have been developed, and widely applied in the field of market analysis or production control etc., which has acquired a great of achievements. It can be expected that, the application of this technology in the research on irradiation damage of material's surface, will provide a powerful tool to find inner links and reveal essential laws. The statistical exploration software JMP supplied by SAS company was used in this study.

Results and Discussion

Application on He-Induced Surface Modification

The Relationship between Different Feature Structures. Figure 2a shows some irradiation conditions of He fluxes, including incident energy (E), total incident fluence (F) and exposure temperature (T), under which the four feature structures

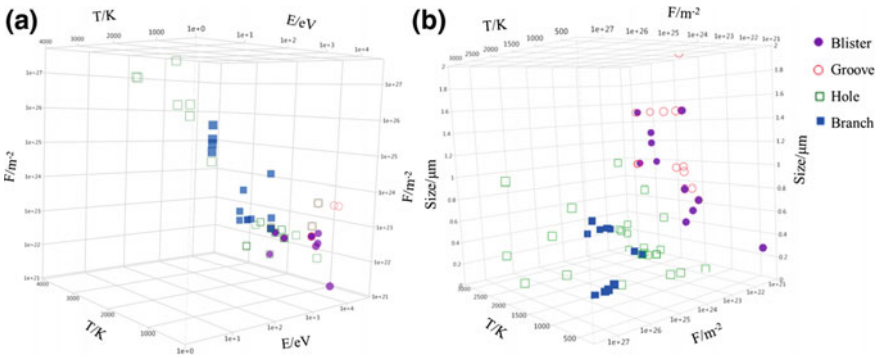

Fig. 2 Three dimensional scatter plots of **a** the relationship between the He-induced four feature structures ("hole" structures, "branch" structures, "blister" structures and "groove" structures) and irradiation conditions [incident energy (E), total incident fluence (F) and exposure temperature (T)]; **b** the sizes of different feature structures under corresponding T and F (The original experimental data came from Refs. [1–8])

were respectively observed on W surfaces, using a logarithmic scale for E and F. As shown, the four feature structures can be obviously divided into 2 groups, "blister versus groove" group and "hole versus branch" group, according to different irradiation conditions.

Compared with hole and branch structures, blister and groove structures are concentrated in high energy, low temperature and low fluence region, while the fluence for grooves is a little higher than that for blisters. In addition, Fig. 2b shows the sizes of different feature structures under corresponding T and F, (using a logarithmic scale for F). It can be seen that blister and groove structures are similar in size, generally in the scale of micron meters, while hole and branch structures are mostly much finer. The above results agree with the formation mechanism suggested in previous studies, i.e. ruptured blisters form grooves.

However, the hole and branch structures, especially the hole structure, are widely distributing in different energy, temperature and fluence regions, as seen in Fig. 2a. Interestingly, for high energy (keV) He-induced damage structure, branches appeared under higher temperature and higher fluence than holes; by contrast, for low energy (eV) He-induced damage structure, holes appeared under higher temperature and higher fluence than branches. This phenomenon is considered to be a result of the different formation mechanisms for damage structures under different energy He fluxes. Previous experimental studies suggested that, the branch structure induced by high energy He is the evolution of a hole structure [6], while the branch structure induced by low energy He forms from a swelling process as a consequence of the coalescence of the helium bubbles [3]. The analysis of surface damage rate also supports this speculation from another side, as shown in Fig. 3.

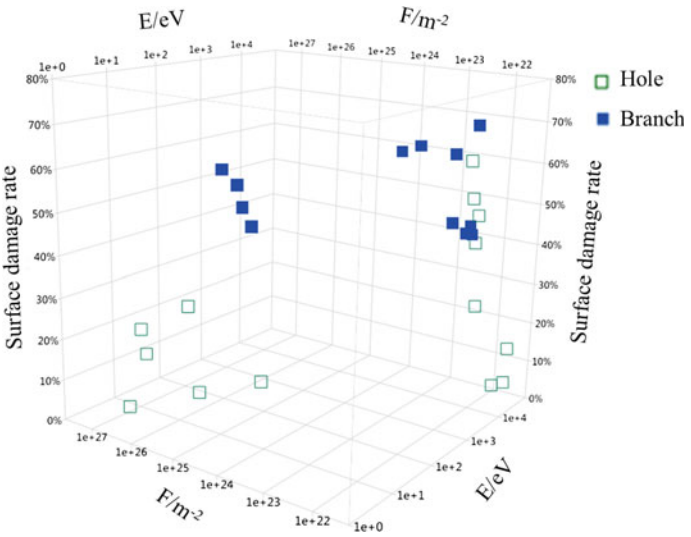

Fig. 3 Three dimensional scatter plot of the surface damage rate of He-induced "hole" structures and "branch" structures under corresponding incident energy (E) and total incident fluence (F) (The original experimental data came from Refs. [1–8])

For high energy He, the surface damage rate of branch structures is higher than that of hole structures, and the latter increases with increasing fluence till approaching the former. At this point, hole structures develop into branch structures. However, for low energy He, the surface damage rate difference between branch and hole structures is always obvious.

Influence Factors of Feature Structure Size. By using the response screening analysis of JMP, this study respectively investigated the effect of influence factors including incident energy (E), incident flux (f), total incident fluence (F) and exposure temperature (T) on the size of He-induced four feature structures. In order to make a comparison of the effect significance level between different factors, the factors E, f and F were transformed to LogWorth scale (lgE = log10(E), lgf = log10(f), lgF = log10(F)). Then the four parameters lgE, lgf, lgF, T were all normalized. The effect significance level can be judged according to p-value acquired through response screening analysis. Based on statistical principles, p-value 0.01, $0.01 < p\text{-value} \leq 0.05$, $0.05 < p\text{-value} \leq 0.1$ or $p\text{-value} > 0.1$ respectively suggest the factor has very significant effect, significant effect, little significant effect or no significant effect on the response. However if the factors have highly significant effects, the associated p-values will be so small that visualizing them graphically can be challenging. So p-value is often transformed to the LogWorth ($-\log10(p\text{-value})$) scale as the parameter "LogWorth" to show the results of response screening analysis.

As shown in Fig. 4a, temperature and energy have highly significant effect on the size of the "branch" structure, while flux and fluence have relatively significant effect on the size of both the "branch" and "hole" structures. Figure 4b shows the specific rules: the branch size increases with increasing temperature, increasing

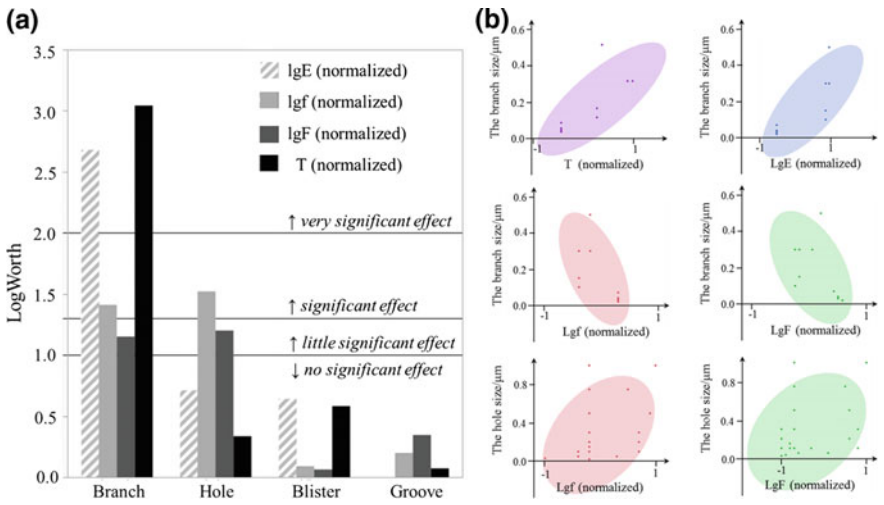

Fig. 4 **a** The effect significance level of different factors on He-induced feature structure size and **b** the specific rules (The original experimental data came from Refs. [1–8])

energy, decreasing flux or decreasing fluence; while the hole size increases with increasing flux or increasing fluence.

No factor with significant effect on the size of blisters or grooves was obtained in this work, probably because the effect of grain orientation has not been considered, which has been proved to be an important influence factor. In addition, interaction or polynomial effects were not considered neither, and the total sample size was still too small for statistical analysis. All above need to be improved.

Application on D-induced Blistering. For D-induced blistering of W, two kinds of "blisters" with large size difference often appear together on one sample. Therefore in this study, the sizes of large and small blisters are respectively indicated by D_L and D_S. If all the blisters on one sample are of similar size, let $D_L = D_S$. Thus the blister size for one sample is mainly reflected by D_L. A parameter D_S/D_L is introduced to reflect the homogeneity of blistering and surface damage rate is used to reflect the damage severity.

Similar as the above section, the response screening analysis of JMP were used to investigated the effect of incident energy (E), incident flux (f), total incident fluence (F) and exposure temperature (T) on D-induced blistering. The factors f and F were transformed to LogWorth scale (lgf = log10(f) and lgF = log10(F)). Then the four parameters E, lgf, lgF, T were all normalized. The results of response screening analysis are shown in Fig. 5a. D Energy has highly significant effect on the main blister size, and D flux has highly significant effect on the size of both the main and small blisters. Figure 5b shows the specific rules: the blister size increases

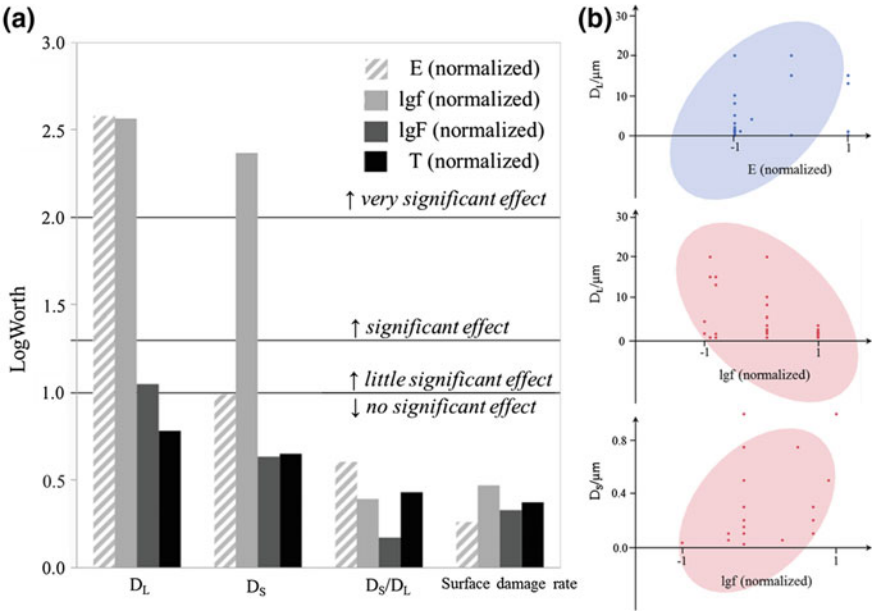

Fig. 5 **a** The effect significance level of different factors on D-induced blistering and **b** the specific rules (The original experimental data came from Refs. [9–14])

with increasing energy or decreasing flux. No factor with significant effect on blistering homogeneity or surface damage rate was obtained in this work, which should be attributed to the small sample size and needs further research.

Conclusions

Based on texture feature analysis, four feature structures, "hole" structure, "branch" structure, "blister" structure and "groove" structure, were selected in this work to serve the description and classification of materials' surface damage morphologies. This method can be used to analyze surface SEM images and create conditions for utilizing data mining technology.

Preliminary application in the research on W surface modification induced by He or D particles shows the relationship between different feature structures and suggests the effect significance level of different influence factors, including incident energy, incident flux, total incident fluence and exposure temperature. It has been found that temperature and energy probably have highly significant effect on the He-induced "branch" structure, while flux and energy may have highly significant effect on D-induced blistering.

However, these results only mean this classification and characterization method has applied value in irradiation damage researches, but may be not true or objective enough due to the limited sample size and unconsidered factors. With the increase of sample size and considered factors, this method is expected to provide more valuable reference for the mechanism researches on irradiation damage of material's surface.

Acknowledgements This work is supported by research start-up fund of North China University of Technology.

References

1. Y. Yuan, H. Greuner, B. Böswirth et al., Surface modification of molten W exposed to high heat flux helium neutral beams. J. Nucl. Mater. **437**, 297–302 (2013)
2. D. Nishijima, M.Y. Ye, N. Ohno et al., Formation mechanism of bubbles and holes on tungsten surface with low-energy and high-flux helium plasma irradiation in NAGDIS-II. J. Nucl. Mater. **329–333**, 1029–1033 (2004)
3. S. Kajita, W. Sakaguchi, N. Ohno et al., Formation process of tungsten nanostructure by the exposure to helium plasma under fusion relevant plasma conditions. Nucl. Fusion. **49**, 095005 (2009).
4. K. Tokunaga, S. Tamura, N. Yoshida et al., Synergistic effects of high heat loading and helium irradiation of tungsten. J. Nucl. Mater. **329–333**, 757–760 (2004)
5. H. Greuner, H. Maier, M. Balden, et al. Investigation of W components exposed to high thermal and high H/He fluxes. J. Nucl. Mater. **417** (2011) 495–498.

6. C. Li, H. Greuner, Y. Yuan et al., Effects of temperature on surface modification of W exposed to He particles. J. Nucl. Mater. **455**, 201–206 (2014)
7. C. Li, H. Greuner, X. Zhou et al., Surface modifications of rolled W during exposure to high heat loads with He. Nucl. Tech. **38**, 070604 (2015)
8. S.J. Zenobia, L.M. Garrison, G.L. Kulcinski, The response of polycrystalline tungsten to 30 keV helium ion implantation at normal incidence and high temperatures. J. Nucl. Mater. **425**, 83–92 (2012)
9. W.M. Shu, A. Kawasuso, Y. Miwa et al., Microstructure dependence of deuterium retention and blistering in the near-surface region of tungsten exposed to high flux deuterium plasmas of 38 eV at 315 K. Phys. Scr. **T128**, 96–99 (2007)
10. S. Lindig, M. Balden, V.Kh. Alimov et al., Subsurface morphology changes due to deuterium bombardment of tungsten. Phys. Scr. **T138**, 014040 (2009)
11. A.A. Haasz, M. Poon, J.W. Davis, The effect of ion damage on deuterium trapping in tungsten. J. Nucl. Mater. **266–269**, 520–525 (1999)
12. Y.Z. Jia, G. De Temmerman, G.-N. Luo, Surface morphology and deuterium retention in tungsten exposed to high flux D plasma at high temperatures. J. Nucl. Mater. **457**, 213–219 (2015)
13. Y. Zayachuk, M.H.J.'t Hoen, P.A. Zeijlmans van Emmichoven et al., Surface modification of tungsten and tungsten–tantalum alloys exposed to high-flux deuterium plasma and its impact on deuterium retention. Nucl. Fusion. **53**, 013013 (2013)
14. W. Wang, J. Roth, S. Lindig et al. Blister formation of tungsten due to ion bombardment. J. Nucl. Mater. **299**, 124–131 (2001)
15. J.X. Ge., *Study of Image Feature Extraction and Texture Classification Algorithm* (Tianjin University, Tianjin, 2010)

Development of GH3535 Alloy for Thorium Molten Salt Reactor

Man Wang, Qiliang Nai, Jun Qiu, Baoshun Wang, Chen Yang, Cheng Su and Jianping Liang

Abstract The GH3535 seamless pipe was developed by hot extrusion and cold rolling. The mechanical properties and corrosion resistance of GH3535 seamless pipe under molten salt environment were tested at different temperatures. The results showed that the extrudability of GH3535 alloy was fine at 1150–1250 °C, and the mechanical properties of hot-extruded GH3535 alloy pipe were excellent and the microstructure was uniform. The average grain size of GH3535 seamless pipe is about 67 μm. The yield strength of GH3535 alloy pipe is above 200 MPa at 650–700 °C, the tensile strength is above 480 MPa. The corrosion resistance of GH3535 alloy seamless pipe is also good in high temperature (700 °C) molten salt environment.

Keywords Thorium-based molten salt reactor · GH3535 alloy
Seamless pipe · Hot extrusion · Nickel-based

Introduction

Thorium molten salt reactor (TMSR for shot) is the ideal reactor type with thorium uranium fuel cycle which is included in the candidate fourth-generation advanced nuclear reactor [1, 2]. The major characteristic of the TMSR is the use of molten salt fuel and thorium 232 as raw material for proliferation [3–5]. However, it is very critical to select materials of the pipes, core cladding and structural components of

M. Wang (✉) · Q. Nai · J. Qiu · B. Wang · C. Yang · C. Su
Zhejiang JIULI Hi-Tech Metals Co.Ltd, Huzhou 313028, Zhejiang, China
e-mail: wangman@jiuli.com

Q. Nai
e-mail: naiqiliang@126.com

J. Liang
Shanghai Institute of Applied Physics, Chinese Academy of Sciences, Shanghai 201821, China

Y. Han (ed.), *Advances in Energy and Environmental Materials*,
Springer Proceedings in Energy, https://doi.org/10.1007/978-981-13-0158-2_16

the selection in TMSR system due to the corrosive environment of molten salt (650–850 °C).

Ni–Mo–Cr–based Hastelloy N alloy (GH3535) was listed as the candidate material of TMSR [6–8] in the "Advanced Nuclear Fission Energy" of the Chinese Academy of Sciences, which was launched in 2011 by the Chinese Academy of Sciences.

GH3535 alloy with FCC structure is a Ni–Cr–Mo superalloy by solution strengthening [9, 10]. The alloy has poor processability because of its high alloying degree. In the view of the lack of the reports about the researches and manufacture process of the GH3535 alloy seamless pipe at home and abroad, JIULI starts the GH3535 alloy seamless pipe research and development supported by Chinese Academy of Sciences Shanghai Institute of Applied Physics. JIULI successfully develops the sizes from Φ13.72 to Φ168 mm as per different specifications of seamless pipe, adopting the proper forming process of hot extrusion, cold processing technology and heat treatment process.

Materials and Experimental Procedure

Materials. The GH3535 alloy was smelted by vacuum induction melting and vacuum consumable arc remelting (VIM+VAR) method. The designed chemical composition (wt%) of GH3535 alloy is listed in Table 1. After the homogenization treatment, the smelted GH3535 alloy was hammer cogged to a round bar. The hot extrusion process of the GH3535 alloy was performed on a 42MN steel extruder with a glass lubricant. The temperature of hot extrusion process was between 1150 and 1250 °C. Then the cold rolling process of the GH3535 alloy seamless pipe was performed in the cold rolling mills such as LG180, LG60, LG15.

Experimental procedure. The microstructures of the GH3535 alloy were observed by Zeiss metallographic microscope and Hitachi-3400 N scanning electron microscope (SEM). The flattening test and the flaring test of the GH3535 alloy seamless pipe were performed according to GB/T 246 and ASTM B829 standards, respectively. The sample for flattening test was about 65 mm in length, and the flattening coefficient was 0.09. As for the flaring test, the dilution rate was 30% of the outer diameter and the flaring top cone angle was 60°. The tensile test of the GH3535 alloy seamless pipe was performed using a Zwick test machine.

The corrosion rate of the GH3535 alloy seamless pipe was measured by static molten salt corrosion test at 700 °C for 400 h. The weight loss per unit area of the sample and the diffusion depth of Cr were calculated. The relevant metal ion concentrations in the molten salt environment before and after corrosion were detected.

Table 1 Chemical composition of GH3535 alloy (wt%)

C	Cr	Mo	Fe	Si	Mn	Al + Ti	Co	Ni
0.04	8	18	3.5	0.5	0.8	0.3	0.02	Bal.

Results and Analysis

Microstructure Characteristics of GH3535 Alloy Round Steel. Figure 1 shows the organizations of the raw material. A great amount of precipitates could be observed in the matrix, which is distributed in stripes, as shown in Fig. 1a. Based on the energy dispersive spectrometer (EDS) analysis, as shown in Fig. 1b, c, it could be concluded that the precipitates are rich in Mo and Ni. This type of carbide is commonly named as M_6C phase, which is mainly formed in the liquid phase solidification process. The M_6C phase particles are mainly distributed in the grain boundaries or the dendritic grain boundaries [9–11].

Previous studies showed [12, 13] that the M_6C phase has a high recovery temperature. After the heat treatment at a high temperature (from 1220 °C to 1260 °C), the amount of M_6C carbides is significantly decreased. The precipitation of carbides would reduce the high temperature plasticity of the alloy and increase the deformation resistance.

Microstructure Characteristics and performance of GH3535 Alloy hot extrusion pipe. Figure 2 shows the phase precipitation characteristics curve of GH3535 alloy. The hot extrusion temperature is between 1150 °C and 1250 °C obtained from the characteristic curve.

Figure 3a shows the outside surface of hot extrusion pipe after pickling, no pits, scratches and other defects can be observed. Figure 3b shows the inner surface of hot extrusion pipe which has no cracks, folds and other defects. It follows that the hot extrusion temperature is reasonable between 1150 °C and 1250 °C. If the

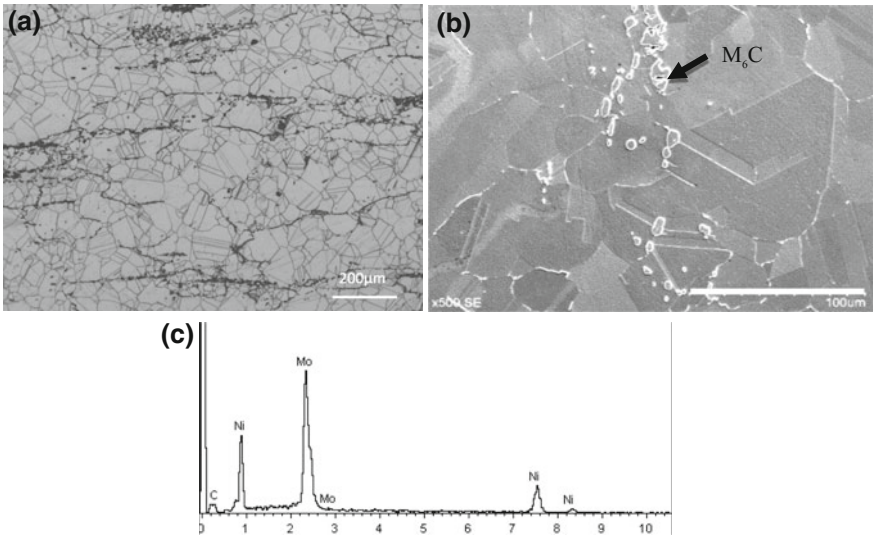

Fig. 1 Raw material organization: **a** Microstructure, **b** scanning electron microscope, **c** EDS analysis

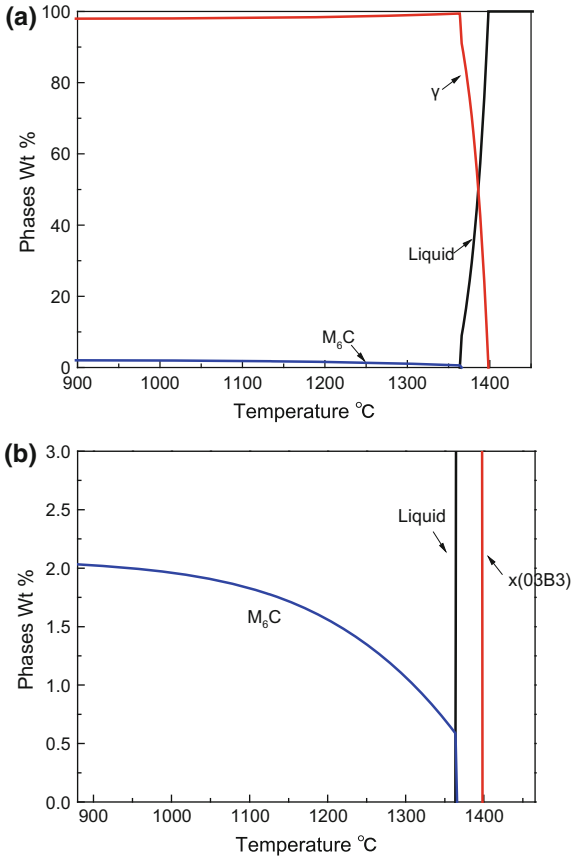

Fig. 2 Phase precipitation characteristics curve of GH3535 alloy: **a** phase diagram of GH3535 alloy, **b** local phase-portrait

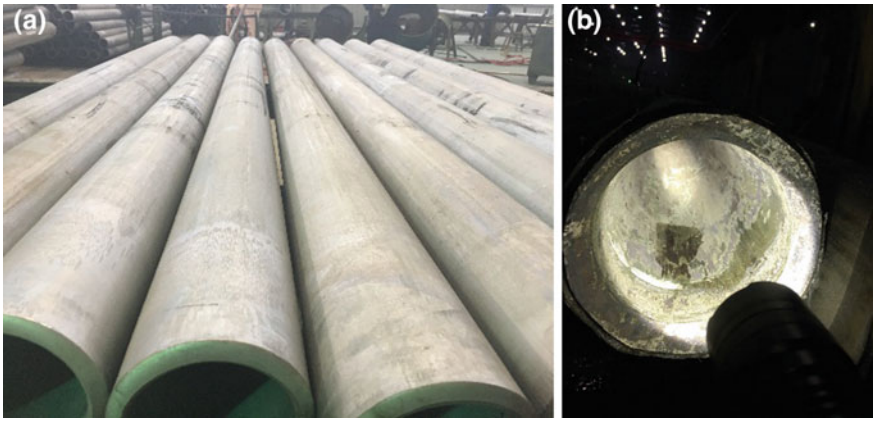

Fig. 3 Extrusion pipe morphology: **a** outside surface, **b** inner surface

temperature is lower than the specified value, the hot extrusion will be fail, otherwise, the hot extrusion pipe is stratified when the temperature is higher.

The good plasticity and excellent performance of finished pipes could be achieved by cold deformation after annealing treatment, based on the extruded pipe with a good tissue uniformity. Figure 4 shows the grain size map of the extrusion tube head, middle and stern. It seems that a full dynamic recrystallization has been occurred in the processing of extrusion, which has formed equiaxed grains and uniform organization. The average grain size of the tube head is about 37.5 μm, the middle is about 38 μm, and the end is about 67 μm.

Figure 5a shows the SEM image of extrusion pipe. It seems that large pieces of precipitation are in the longitudinal direction and a little precipitation in grain boundary. The precipitates are still rich in Mo, Ni phase as shown in Fig. 5b.

Annealing treatment of the extrusion pipe should be performed before the cold deformation for a good deformation performance. Figure 6 shows the comparison of extrusion pipe mechanical properties before and after annealing treatment. It seems that the tensile strength is lower, the yield strength decreases significantly and the elongation of Normal temperature to 600 °C changes a litter, but the elongation is significantly increased at 650–700 °C high temperature.

Microstructure of GH3535 alloy Seamless pipe. The GH3535 alloy seamless pipe has a uniform microstructure in the length direction as shown in Fig. 7. The average grain size is 37–70 μm among the head, middle and stern of the GH3535

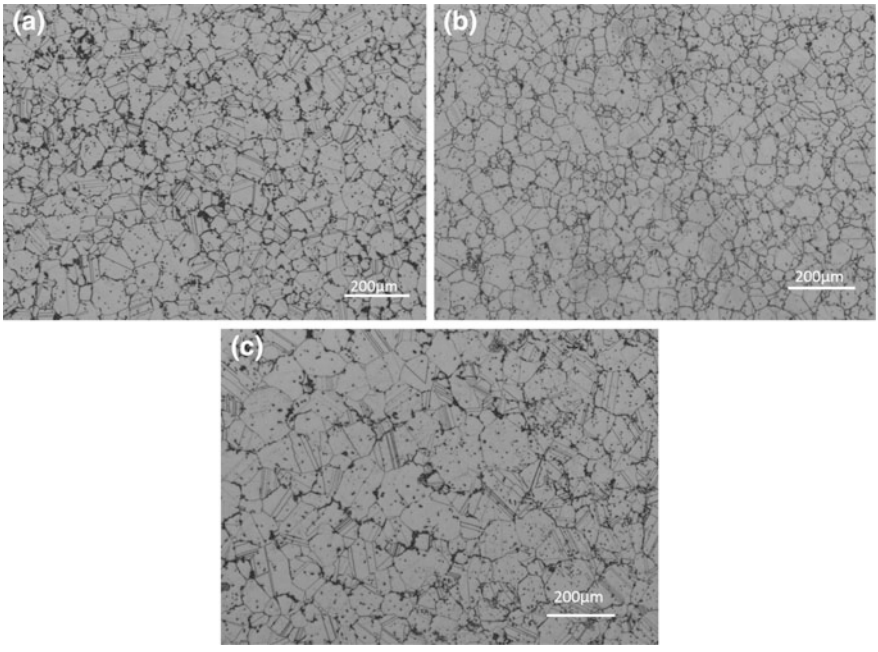

Fig. 4 Grain sizes of extrusion pipe indicate the area of head (**a**), middle (**b**), stern (**c**)

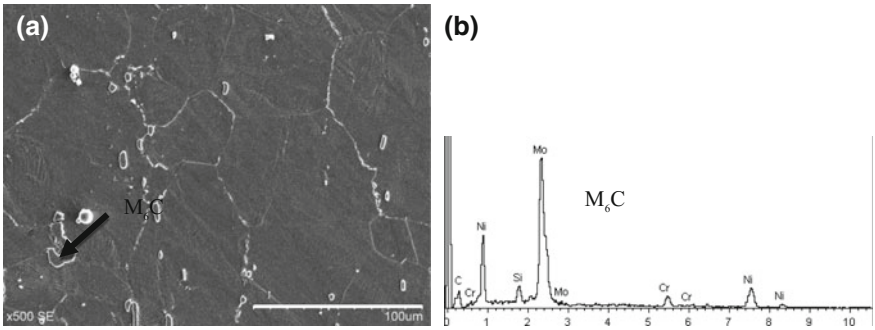

Fig. 5 SEM of extruded pipe (**a**) and EDS analysis (**b**)

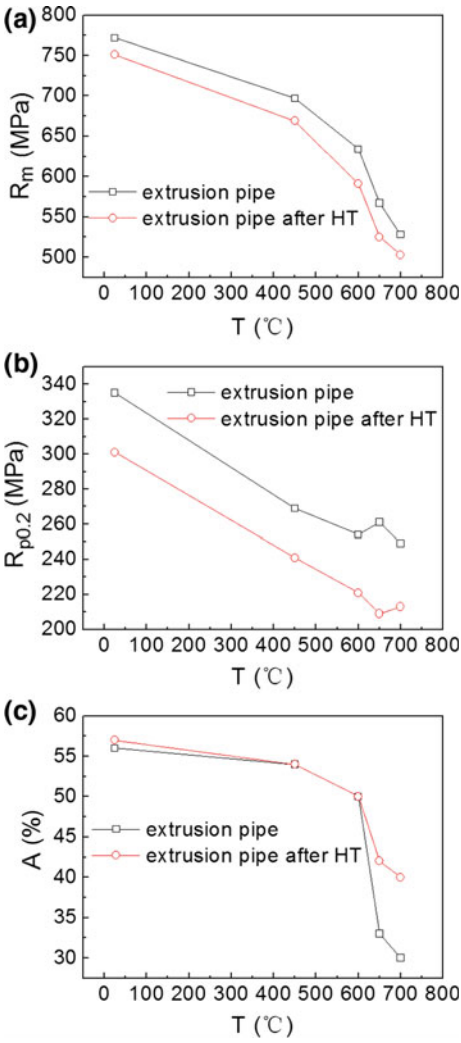

Fig. 6 Comparison of mechanical properties of the extrusion pipe before and after annealing treatment: **a** the tensile strength, **b** the yield strength, **c** the elongation

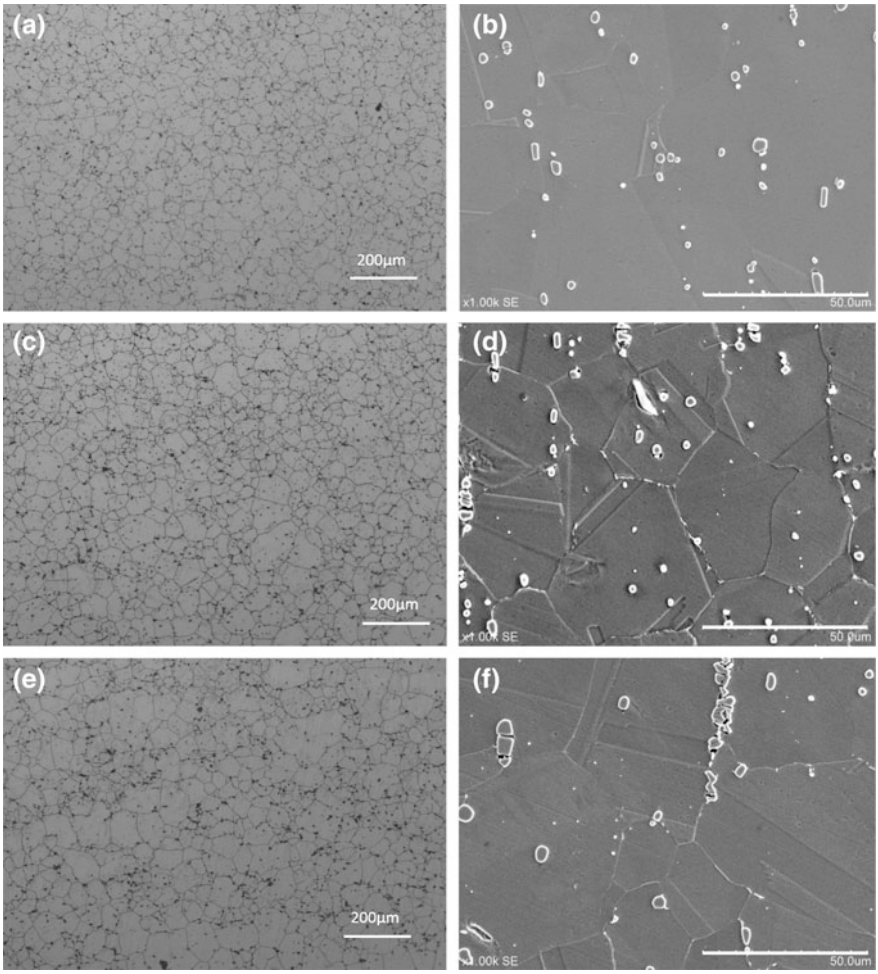

Fig. 7 Grain size of pipe head (**a**), middle (**c**), stern (**e**), the SEM of pipe head (**b**), middle (**d**), stern (**f**)

alloy pipe. On the other hand, the GH3535 alloy seamless pipe still has large pieces of precipitation in the longitudinal direction as the same as the matrix, as shown in Fig. 8. Although the primary carbides is hardly to dissolve, it plays a strengthening role with dispersed in transgranular. The grain boundary on the basic precipitation has no precipitation with strictly heat treatment.

Mechanical properties of GH3535 alloy Seamless pipe. Figure 8 shows the mechanical properties of different seamless pipes (Φ168, Φ76, Φ13.72 mm) at room temperature and high temperature (450 °C, 600 °C, 700 °C). It seems that as the test temperature increased, the tensile strength and yield strength are decreased a downward trend, and the elongation is also decreased. The tensile strength and yield

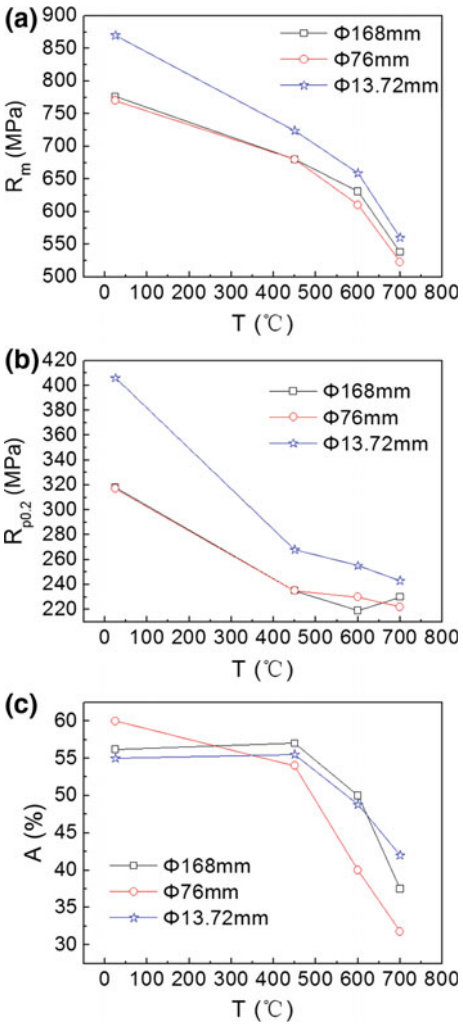

Fig. 8 Comparison of mechanical properties of the pipes: **a** the tensile strength, **b** the yield strength, **c** the elongation

strength has no difference, and the elongation is close among different seamless pipes. Furthermore, the pipes have a high yield strength at 600–700 °C temperature, and the elongation can reach more than 35%.

Besides, the GH3535 alloy seamless pipes have no cracks or openings after technological test such as flaring and flattening test. The seamless GH3535 alloy pipes have good processing performance such as tube plate welding, bending and other process requirements.

Corrosion resistance in molten salt of GH3535 alloy. Table 2 shows the content of Cr after the molten salt corrosion test and depth of diffusion for element Cr in the molten salt corrosion environment (FLiNaK) in a molten salt at 700 °C for

Table 2 the content of Cr after the molten salt corrosion test

No.	The content of Cr after the molten salt corrosion test/[ppm]	The diffusion depth of Cr element/[μm]
The original state	59	/
1#	148	7–8
2#	151	9–10
3#	143	8–9
4#	148	8–9

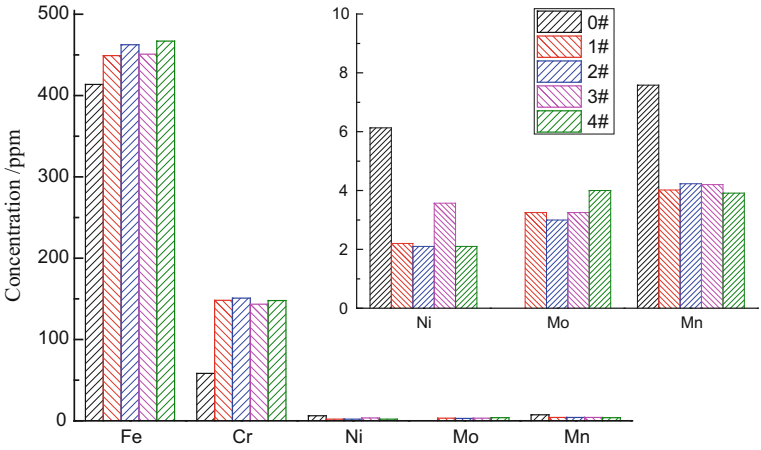

Fig. 9 Content of various elements after the molten salt corrosion test: 1#(Φ114.3 mm), 2#(Φ88.9 mm), 3#(Φ76 mm), 4#(Φ13.72 mm)

400 h. It can be seen that the GH3535 alloy seamless pipes have good corrosion resistance in the molten salt corrosion environment.

Figure 9 shows the content of various elements after molten salt corrosion test at 700 °C for 400 h. It seems that the content of the elements in the molten salt is not much difference after the corrosion. It confirms that there is no significant difference in the corrosion resistance of the GH3535 pipes in the molten salt corrosion environment.

Figure 10 shows the weight loss per unit area of sample of four kinds of pipes (Φ114.3, Φ88.9, Φ76, Φ13.72 mm) after the molten salt corrosion test. It can seem that the corrosion rate of the pipe is low, the weight loss per unit area is less than 0.05 mg/cm^2, except individual pipe is negative growth.

According to the activity of the elemental composition, the more active Cr can replace the Fe in the ionic state, and the Fe deposition on the surface of the alloy caused by the displacement reaction may cause the weight gain of the sample, and on the other hand some impurities adhered to the sample surface may cause weight gain, too. The specific reasons need to combine the other test data for analysis and evaluation.

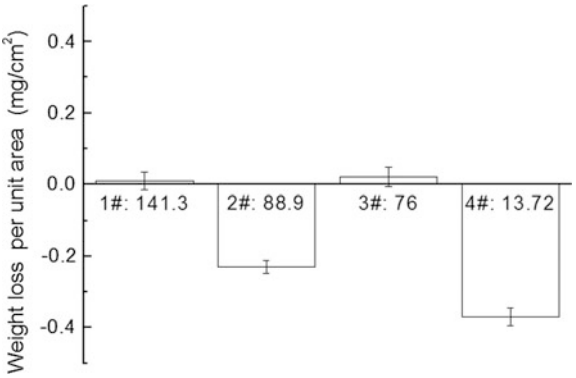

Fig. 10 Weight loss per unit area of sample after the molten salt corrosion test

Conclusion

The GH3535 seamless pipe was developed by the hot extrusion of the glass lubricant and multi-pass cold rolling between 1150 °C and 1250 °C.

The mechanical properties of GH3535 seamless pipe can be enhanced at room temperature, which the tensile strength can reach 800 MPa, the yield strength can reach 300 MPa, and the elongation is about 55%. Meanwhile, the yield strength of GH3535 seamless pipe is above 200 MPa and the elongation is more than 35% at 600–700 °C temperature.

The corrosion rate of the GH3535 alloy seamless pipe may be reduced, which the weight loss per unit area is less than 0.05 mg/cm^2, except individual pipe is negative growth. So the further research needs to be done.

References

1. T. Abram, S. Ion, Generation-IV nuclear power: A review of the state of the science. Energy Policy **36**(12), 4323 (2008)
2. M.M. Waldrop. Nature **492**, 26 (2012)
3. Committee U.S. DOE. *A Technology Roadmap for Generation IV Nuclear Energy Systems, GIF-002-00*. The gerneration IV international forum (2002)
4. R.C. Robertson, *MSRE Design and Operation Report, Part I, Description of Reactor Design, ORNL-TM-0728* (Oak Ridge National Laboratory, Oak Ridge, Tennessee, 1965)
5. R.E. Thoma, *Chemical Aspects of MSRE Operations, ORNL.4658* (Oak Ridge National Laboratory, Oak Ridge, Tennessee, 1971)
6. M.H. Jiang, H.J. Xu, Z.M. Dai, Advanced fission energy program—TMSR nuclear energy system. Bull. Chin. Acad. Sci. **27** (3), 366 (2012)
7. R.E. Gehlbach, H.E. McCoy, Phase instability in Hastelloy N Superalloys. Int. Symp. Struct. Stab. Superalioys **2**, 346–366 (1968)
8. J.H. Devan, R.B. Evans, *Corrosion Behavior of Reactor Materials in Fluoride Salt Mixtures, ORNLTM-0328* (Oak Ridge National Laboratory, Oak Ridge, Tennessee, 1962)

9. R.C. Briant, A.M. Weinberg, Molten fluorides as power reactor fuels. Nucl. Sci. Eng. **2**, 797–803 (1957)
10. H.E. McCoy Jr., *Status of Materials Development for Molten Salt Reactors, ORNL/TM-5920* (1978)
11. P. Hosnedl, O. Matal, *Development of Structural Material and Equipment for Molten Salt Technology, Pyrochemical Separations* (2001), p. 197
12. T. Liu, *The Study of Microstructure and Properties of a Corrosion Resistant Nickel—base GH3535 Superalloy* 64–66 (2015)
13. W. Zhang, Effect of solution heat treatment on microstructure and properties of GH3535 alloy. Rare Met. Mater. Eng. **45**(6) (2016)

Melting Technology for Uniformity Control of U–10Zr Alloy

Gang Zeng, Bin Su, Daoming Chen, Yuting Zhang, Jingyuan Liu and Jian Wu

Abstract U–Zr alloy has the advantages of high thermal conductivity and anti-radiation swelling performance, as a promising metallic nuclear fuel for its fast breeder reactor. In this paper, U–10Zr alloy was prepared by multi-induction melting method and chemical analysis, optical metallography, XRD and SEM were used to investigate the effects of melting technology on the distribution of Zr as well as the phase composition in U–10Zr alloy. The results show that the dissolution of Zr in U is more complete in the second smelting process. The chemical composition is homogeneous while distribution of U, Zr and C is different in different location. The first smelting by vacuum induction removes more impurity of the ingots. The distribution of zirconium and carbon in the transverse-direction of U–10Zr ingots is more uniform. U–10Zr alloy exists in an acicular martensite state along with small quantity of nonmartensitic α phase. The zirconium element is more easy to form carbide and nitride with the C and N elements than the uranium. The as-cast U–10Zr alloy is composed mainly of α phase and δ-UZr_2 phase.

G. Zeng · B. Su · D. Chen (✉) · J. Liu · J. Wu
Institute of Materials, China Academy of Engineering Physics,
Jiangyou 621908, Sichuan, China
e-mail: chendaominght@126.com

G. Zeng
e-mail: steelzun@139.com

B. Su
e-mail: subin@caep.cn

J. Liu
e-mail: liujingyuanhit@163.com

J. Wu
e-mail: wujian@caep.cn

Y. Zhang
Science and Technology on Surface Physics and Chemistry Laboratory,
Jiangyou 621908, Sichuan, China
e-mail: zhangyuting@caep.cn

Y. Han (ed.), *Advances in Energy and Environmental Materials*,
Springer Proceedings in Energy, https://doi.org/10.1007/978-981-13-0158-2_17

Keywords U–10Zr alloy · Uniformity · Vacuum induction melting
Impurity

Introduction

It is known that uranium alloyed with small quantity of elements such as molybdenum and zirconium can enhance its mechanical properties and corrosion resistance without greatly reducing its density. The U–Zr binary alloy is an important subsystem of the U–Pu–Zr ternary alloy, which has been recognized as a promising metallic nuclear fuel for its fast breeder reactor [1–5]. U–Zr as alloy in the uranium alloy system, combined with effective density design, can effectively control and solve the high temperature phase transition of metal uranium fuel, radiation swelling and many other issues [6]. U–Zr alloy has the advantages of high thermal conductivity and anti-radiation swelling performance as the promising metallic nuclear fuel for its fast breeder reactor with small quantity of zirconium added to uranium to produce fine grain alloy with good dimensional stability [7, 8]. The U–10Zr alloy in U–Zr system is the most promising metal fuel. Previous studies mainly focused on physical metallurgy, thermodynamics and kinetics of fuel phase stability as well as the evolution of U–10Zr alloy [9, 10]. However, owing to the high melting point and low density of zirconium, it is difficult to ensure the sufficient dissolution of zirconium during melting process. The zirconium element is easy to form carbide and nitride. The gathered impurity will cause inhomogeneity composition of alloy. The control of homogeneity of U–10Zr alloy that is melted by vacuum induction melting has few research. The knowledge of the uniformity of U–Zr alloy is required to evaluate stability in long-term storage and disposal of spent fuels and to stabilize the metal chip waste which is generated during its melting process. Previous studies revealed some differences in oxidation behavior between the electropolished and the mechanically polished uranium samples [11]. However, they ignored the importance of chemical composition on U–Zr properties. The uranium alloys with uniform composition and high quality is a prerequisite for the study of metallic nuclear fuel [12]. Thus, it is highly important to understand the distribution of zirconium and microstructures in the as-cast U–10Zr alloys.

Materials Preparation

Depleted uranium and zirconium bars were used for the preparation of U–10Zr alloy. The alloys were melt-cast twice in a ceramic crucible by vacuum induction melting. The zirconium bars were placed under the uranium ingots in the ceramic crucible. During the first melting process, the distribution of Zr in U–10Zr alloy was nonuniform, the zirconium alloying element was added to 10.3%. The zirconium alloying element was kept to 10% at the second melting process in order to

Table 1 The major melting technological parameters

Smelt times	Crucible	Temperature (°C)	Time (min)
1st	CaO Ceramic crucible	1600	30
2nd	CaO Ceramic crucible	1600	20
		1400	10
		1600	20

eliminate macro non uniformity. In addition, the samples were heated to 1600 °C in order to ensure homogeneity before cooling down to room temperature. The major melting technological parameters were presented in Table 1. For experimental characterization, the alloy ingots were cut into suitable shapes.

Chemical Composition and Property

The chemical composition of different parts of alloy ingots was analyzed. Standard metallographic techniques were used for grinding and polishing. 5% H_3PO_4 aqueous solution was applied for electroetching and constant 2 V DC bias was used for the etching. The samples were then repolished for XRD analysis. The XRD analysis was carried out using a Philips XRD vertical goniometer with Cu Kα radiation.

Results and Discussion

The U–10Zr alloy was melt-cast by vacuum induction melting. The alloy ingots were fused into cylinder with the size of φ80 mm × 150 mm. The samples were cut from ingots to analyze chemical composition of zirconium and carbon. Figure 1

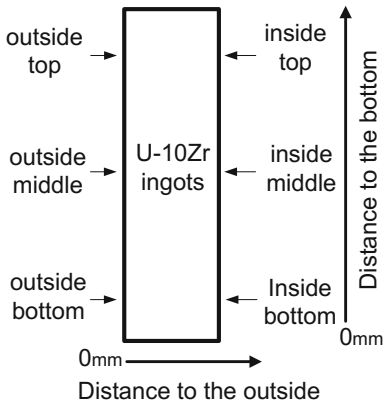

Fig. 1 Different sampling location of the as-cast U–10Zr alloys

shows the different sampling location of the as-cast U–10Zr alloy. In order to increase accuracy, the uniformity in the distribution of the alloying element was evaluated based on the different position of ingots.

Based on the analysis of constituents sampling from different locality in U–10Zr samples, the distribution of Zr and C were investigated. Figure 2 shows the chemical composition of zirconium and carbon with different distance to the bottom of U–10Zr cylinder. Zirconium was loaded on the bottom of CaO ceramic crucible, which helped to control the homogeneity of U–10Zr alloy. When the melting temperature was about 1600 °C, melting time was about 9 min, and the uranium ingots were melted totally. Zirconium bars were slowly dissolved into the liquid uranium. It showed that the general efficiency of the homogeneity controlling for Zirconium component and the carbon impurity decreasing of U–10Zr alloy were good. The first smelting by vacuum induction removes more inclusions of the ingots. The alloying effect of uranium and zirconium in the second smelting process is more complete.

Figure 3 shows the distribution of zirconium and carbon in the transverse-direction of U–10Zr ingots. The results showed that the both element Zr and C distributed evenly in the extent-direction and transverse-direction of U–10Zr ingots in the same condition. During the first melting process, the zirconium element was easy to form inclusions with carbon and nitrogen. The gathered impurity had lower density and floated up to the top of ingots. When the second melting process began, the C and N inclusions were removed. During the second melting process, the temperature should be lowered to 1400 °C after melting for 20 min at 1600 °C. Through controlling the power of induction furnace, the magnetic field had mixing effects on metal liquid. The zirconium alloying element showed no difference in distribution.

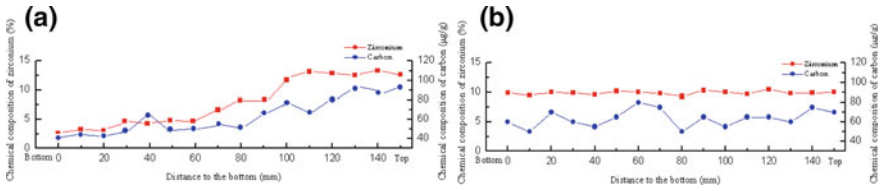

Fig. 2 Distribution of zirconium and carbon in the extent-direction of U–10Zr ingots **a** 1st smelt times, **b** 2nd smelt times

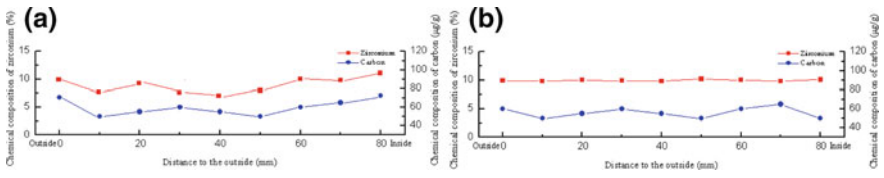

Fig. 3 Distribution of zirconium and carbon in the transverse-direction of U–10Zr ingots **a** 1st smelt times, **b** 2nd smelt times

Optical micrographs of as-cast U–10Zr alloy are presented in Fig. 4 and show that U–10Zr alloy is in an acicular martensite state along with small quantity of nonmartensitic α phase. The changes in the morphology of the U–10Zr alloy can be explained by the effects of Zr element. The martensitic plates in the samples were formed during the solidification process. In the process of alloying, uranium ingots melted slowly to avoid the rapid rise of the zirconium bars. During the first melting process, the alloy ingots were unable to dissolve zirconium bars completely. The distribution of zirconium element became uniform during the second melting process. Zirconium as alloying element caused constitutional supercooling during the cooling process, leading to the growth of dendritic microstructure. The micro-hardness of as-cast U–10Zr samples increased to 495 MPa compared with substrate uranium samples.

Scanning electron microscope (SEM) examinations of as-cast U–10Zr alloys are shown in Fig. 5. It is known to all that the microstructure contains martensitic α phase, and the dark places in Fig. 5 are composed of zirconium and its inclusions. During the melting process, zirconium as a kind of alloying element compounds with carbon inclusions. When the melting temperature rises to 1600 °C and melting time is extended to over 30 min, the zirconium inclusions are reduced.

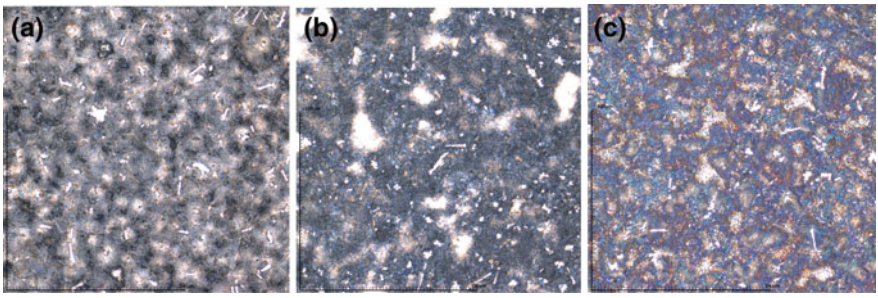

Fig. 4 Different sampling location of optical photomicrograph of the as-cast U–10Zr alloys; **a** top, **b** middle and **c** bottom

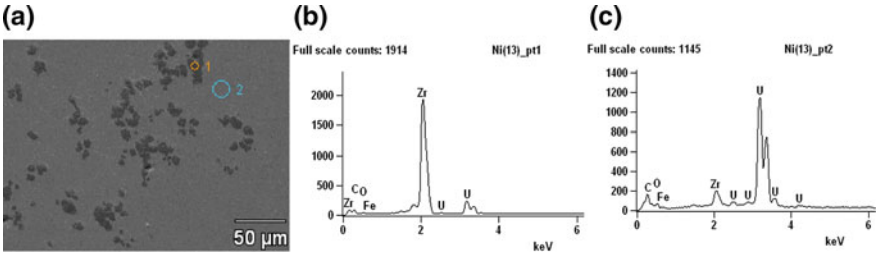

Fig. 5 SEM and EDS images of the as-cast U–10Zr alloys **a** SEM images, **b** EDS images of pt1 and **c** EDS images of pt2

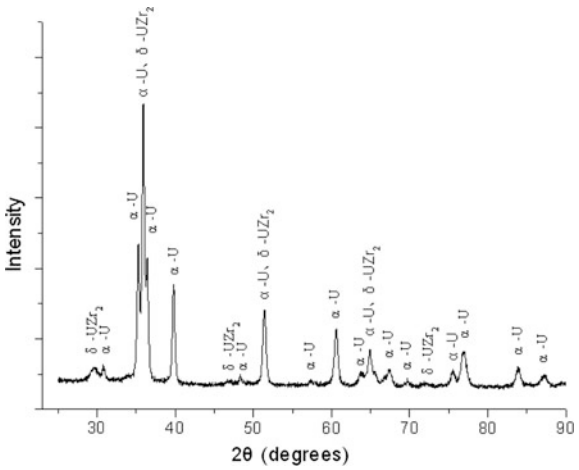

Fig. 6 XRD data of the as-cast U–10Zr alloys

Figure 6 presents the results of XRD measurements of as-cast U–10Zr alloy. It indicates that the U–10Zr alloy is mainly composed of α phase. According to Fig. 6, three weak peaks appear in the XRD experimental spectra at 29.6°, 46.9° and 72.0°. These peaks corresponding to the δ-UZr_2 phase indicates that the δ-UZr_2 phase exists in as-cast U–10Zr alloy. Previous studies have already found the formation of δ-UZr_2 phase in as-cast U–10Zr alloy by arc melting [9]. The present study reveals that the δ-UZr_2 phase still exists in the as-cast U–10Zr alloy by vacuum induction melting. The uniform distribution of zirconium element is propitious to the stabilization of δ-UZr_2 phase.

Summary

As-cast U–Zr alloys with a Zr content of 10 wt% have been characterized by chemical analysis, optical metallography, X-ray diffraction and scanning electron microscopy. The chemical composition of ingots by the multi-induction melting method is homogeneous. The element distribution of the transverse-direction of the ingot is more uniform. As-cast U–10Zr alloy predominately consists of α phase supersaturated with Zr and δ-UZr_2 phase. Moreover, the uniform distribution of zirconium element is propitious to the stabilization of δ-UZr_2 phase.

References

1. K.H. Kweon, H.K. Shin, K.J. Kim et al., Korean J. Chem. Eng. **15**(4), 439–444 (1998)
2. W. Carmack, D. Porter, Y. Chang, S. Hayes, M. Meyer, D. Burkes, C. Lee, T. Mizuno, F. Delage, J. Somers, J. Nucl. Mater. **392**, 139 (2009)

3. J. Kittel, B. Frost, J. Mustelier, K. Bagley, G. Crittenden, J. Van Dievoet, J. Nucl. Mater. **204**, 1 (1993)
4. R. Benedict, C. Solbrig, B. Westphal, T. Johnson, S. Li, K. Marsden, K. Goff, Adv. Nucl. Fuel Cycles Syst. (GLOBAL 2007) (2007)
5. D.E. Burkes, R.S. Fielding, D.L. Porter, D.C. Crawford, M.K. Meyer, J. Nucl. Mater. **389** (2009)
6. M. Kurata, Calphad **23**, 305 (1999)
7. A. Bagchi, G. Prasad, K. Khan, R. Singh, J. Mater. Sci. Eng. **2** (2013)
8. D.W. Brown, M.A.M. Bourke, R.D. Field, W.L. Hults, D.F. Teter, D.J. Thoma, S.C. Vogel, Mater. Sci. **421** (2006)
9. Y. Zhang, X. Wang, G. Zeng et al., J. Nucl. Mater. **471**, 59–64 (2016)
10. C. Basak, BARC Newsletter, p. 60 (2010)
11. L. Leibowitz, J.G. Schnizlein, L.W. Mishler et al., J. Electrochem. Soc. **108**, 1153 (1961)
12. C. Liu, M. Jiang, C. Yin, Nucl. Pow. Eng. **27**, 50–53 (2006)

Preparation and Characterization of Ni+Zn Composite Coating on U–Ti Alloy

Yanhui Bai, Bin Su, Qingfu Tang, Qingfu Wang, Wenpeng Li and Zhenhong Wang

Abstract Uranium and uranium alloys are a kind of important nuclear materials with unique physics and chemical properties. Unfortunately, it is eroded easily, especially in humid environment. In this paper, Ni coating and Ni+Zn composite coating were prepared on the surface of U–Ti alloy. The adhesion strength, phase structure and corrosion properties were characterized by tensile method, X-ray diffraction and electrochemical methods. The results showed that the Ni coating was a face centered cubic structure, while the anodic Ni+Zn composite coating was hexagonal structure. The average adhesion strength of composite coating was 16.0 MPa. The corrosion protection of composite coating was mainly due to the electrochemical protection of Zn coating and the physic barrier function of Ni coating.

Keywords U–Ti alloy · Electroplating · Ni+Zn composite coating

Y. Bai · B. Su · Q. Tang · Q. Wang · W. Li (✉) · Z. Wang
Institute of Materials, China Academy of Engineering Physics,
Mianyang 621908, China
e-mail: liwenpengim@163.com

Y. Bai
e-mail: baiyanhui@caep.cn

B. Su
e-mail: subin@caep.cn

Q. Tang
e-mail: tangqingfu@caep.cn

Q. Wang
e-mail: wangqingfu@caep.cn

Z. Wang
e-mail: wangzhenhong@caep.cn

Y. Han (ed.), *Advances in Energy and Environmental Materials*,
Springer Proceedings in Energy, https://doi.org/10.1007/978-981-13-0158-2_18

Introduction

Due to its unique properties, uranium and uranium alloy is widely used in many fields. However, uranium and its alloys corrode easily in various atmospheres because of their highly reactive [1]. To maintain its good properties and improve the corrosion resistance, a large number of methods have been tested in past years. Among them, electroplating is the most effective and widely used process [2, 3].

Meanwhile, the oxide film formed in air, which is disadvantage for coating adhesion, is difficultly eliminable [4]. In present literatures [5–16], most of the related studies were focused on Ni plating, Ni+Zn composite plating and Ni–Zn alloy coatings. Wang [17] studied the effects of pulse plating on the properties of Ni coating, the results revealed that crystal grain could be refined by pulse-plating. Meanwhile, the corrosion resistance of Ni plating could also be improved by pulse-plating. Dini [18] prepared Zn-10Ni alloy coatings on uranium alloy by electroplating. The results revealed that Zn–Ni alloy coatings provided good protection for uranium alloy in salt frog and in non-sealed moist-nitrogen. Weirick [19] studied the anti-corrosion properties of electroplated nickel coating, electroplated nickel-zinc composite coating and galvanized zinc coating with environmental unfriendly solutions. The results suggested that electroplated nickel offered only temporary protection whereas galvanized zinc and electroplated nickel-zinc provided long-lasting protection.

The aim of this work was to prepare Ni+Zn composite coating by electroplating methods with environmental friendly solutions, and the effect of coating species on corrosion properties was studied by means of polarization, impedance, XRD and adhesion testing.

Experimental

Sample Preparation. The samples φ20 mm × 5 mm cut from a U-0.75 wt% Ti ingot. The surface of the alloy samples was polished with Buehler silicon carbide paper up to 1200 grade. All the substrates were ultrasonically cleaned using ethanol, after cleaning the panels were performed immediately to minimize the effects of surface oxidation.

Uranium coupons were roughened by chemical methods of 1400 g/L ferric chloride, followed by washing with HNO_3 solution [12]. And then electroplating was carried out in nickel plating bath and Zn plating bath respectively. The bath temperature, composition and current densities used are listed in Tables 1 and 2 respectively. The coupons after plating were passivated by CrO_3 solution [4], and then washed with distilled water and dried in 80 °C for 1 h.

Table 1 Nickel plating bath

Composition	Experimental condition
$Ni(NH_2SO_3)_2.4H_2O$	400–450 (g/L)
H_3BO_3	30–35 (g/L)
$NiCl_2$	7–10 (g/L)
Temperature	45–50 (°C)
Current	2–2.5 (A/dm^2)

Table 2 Zinc plating bath

Composition	Experimental condition
ZnO	16–20 (g/L)
MERLIN agents	15–20 (mL/L)
NaOH	80–100 (g/L)
Temperature	Room temperature
Current	1.5–3 (A/dm^2)

Characterization. The corrosion resistance of the samples was studied via electrochemical impedance spectroscopy (EIS) using a PARSTAT 4000 electrochemical workstation. The experiments were performed at room temperature in a three electrode cell, where the uranium sample, platinum net, and a saturated calomel electrode (SCE) were the working, counter, and reference electrodes, respectively. All potentials were referred to the SCE (+0.215 V). A sample area of 1 cm^2 was exposed to 3.5 wt% NaCl solution. The measuring frequency of EIS ranged from 10^5–10^2 Hz, with a sinusoidal alternating potential signal of 10 mV. Scan rate of potentiodynamic polarization curves is 0.167 mV/s, and range from −0.25 V to 1.0 V. All tests conducted in room temperature.

The phase structure of the films was analyzed by XRD (Philips X'Pert Pro) with a Cu K_α (k = 0.15406 nm) source and the incident angle was about 2°. The adhesion intensity was tested by tensile method with E44 epoxy resin.

Results and Discussions

Phase Structure. Figure 1 shows the phase structure of Ni coating, Ni+Zn coating and Ni+Zn+chromate coatings. According to the XRD data, the Ni coating was face centered cubic with {111}, {200}, {220}, {311} orientations, and the preferred orientation is {200}. The phase structure of Ni+Zn coating was mainly hexagonal close packed with {101}, {102}, {103}, {200},{210}, {006}, {212}. The patterns difference between Ni+Zn coating and Ni+Zn+chromate coating was the intensity value. The reason of this difference might be the dissolution of {103} crystal plane. Unlabeled weak peaks in Fig. 1 were the thin zinc oxidation film. From XRD patterns, we found that the phase structure of the Ni+Zn composite coating was

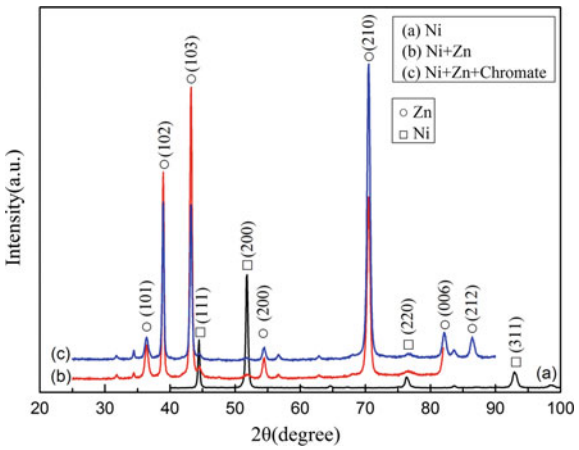

Fig. 1 XRD patterns of prepared coatings

mostly Zn, which revealed that the interface between Ni coating and Zn coating was just physical joint. Meanwhile, the XRD result revealed that composite coatings on U–Ti alloy exhibited typical sandwich structure.

Adhesion Test. Adhesion strength was tested by tensile method with E44 epoxy resin. Figure 2 shows the illustration diagram of testing process. Each sample was test three times at the same condition. The results were listed in Table 3.

From the test results, we found that the largest adhesive strength of different coating interface was very approximate. The Ni coating was slightly peeling off when tensile strength reached 16.5 MPa, and the same phenomenon also appeared on composite coating when tensile strength reached 17.1 MPa. These results indicated that the bonding type of U–Ti alloy/Ni coating interface was similar to

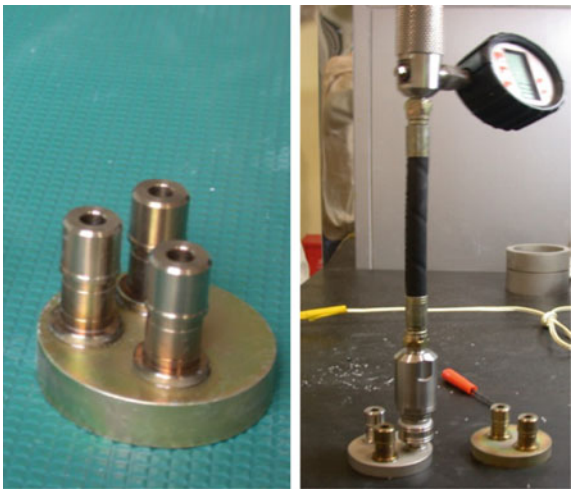

Fig. 2 Adhesives strength tests diagram

Table 3 Coating adhesive strength

Samples	Coatings	Strength (MPa)	Phenomenon
1	Ni	15.8	Epoxy debonding
2		14.7	Epoxy debonding
3		16.5	Some coating debonding
Average		15.7	
4	Ni+Zn+Chromate	17.1	Some coating debonding
5		15.2	Epoxy debonding
6		15.8	Epoxy debonding
Average		16.0	

that of Ni coating/Zn coating interface. And we could infer that the bonding style of U–Ti alloy/Ni coating interface might also be physical joint.

Corrosion Test. Corrosion protection properties of the electroplated coatings were estimated in 3.5 wt% NaCl by EIS and potentiodynamic methods.

Figure 3 present the impedance spectra obtained from U–Ti substrate, Ni coating and composites coating.

From Fig. 3a, we could observe that the EIS results showed well-defined capacity loop. Meanwhile, the impedance in the low frequency increased more than one order of magnitude between Ni coating and U–Ti substrate. However, the impedance value in the low frequency of composite coating (Ni+Zn+chromate) was much lower than that of U–Ti substrate.

In general, |Z| value during medium-high frequency region reflects the property of coatings, and |Z| value during low frequency region reflects the corrosion reaction of coatings [20]. From Fig. 3b, the Bode plots of U–Ti alloy was similar to Ni coating, but the |Z| value of U–Ti alloy was smaller than that of Ni coating sample, which revealed that the charge transfer resistance of U–Ti alloy was also smaller than that of Ni coating. During the low frequency zone (<1 Hz), the |Z|

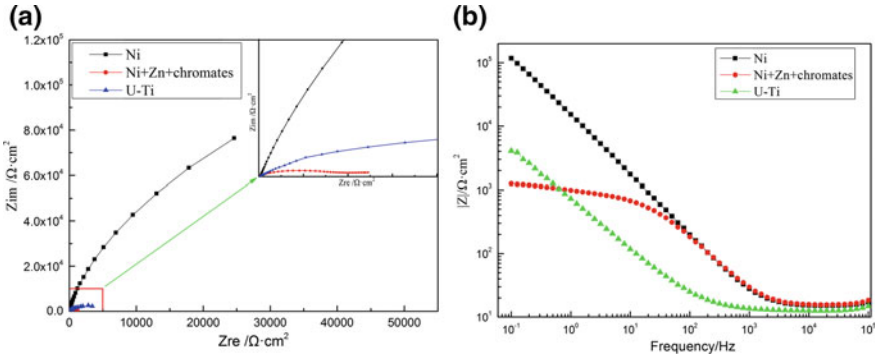

Fig. 3 EIS plots of electroplated samples. **a** Nyquist plot; **b** Bode plot

value of Ni coating was the largest, and then was the |Z| value of U–Ti alloy, and the |Z| value of composite coatings was the least. This phenomenon in low frequency related to anticorrosion property, which illustrated that the anticorrosion property of Ni coating was the best. However, when the frequency is larger than 1 Hz, the sequence of |Z| value was Ni > composite coating (Ni+Zn +chromates) > U–Ti. This phenomenon related to the property of coatings, and also revealed that electroplated layers on U–Ti alloy could provide corrosion protection.

Those results showed Zn coating played a sacrificial role in coating protective process, and Ni coating played a physics barrage role in anticorrosion process.

Figure 4 shows the polarization curves recorded on the bare U–Ti alloy and coating treated samples in 3.5 wt% NaCl solution. The corrosion current density (i_{corr}) values and corrosion potential are summarized in Table 4.

From Fig. 4 and the fit results in Table 4, we could observe that the corrosion potential of Ni coating increased by about one order of magnitude than that of bare alloy. Meanwhile, the i_{corr} of Ni coating decreased obviously. As i_{corr} is proportional to the corrosion rate [21], an obvious improvement in corrosion resistance was observed. These results suggest that the Ni coating is a cathodal plating film, and the anticorrosion property is due to its physic barrier function.

Compared to bare alloy, the corrosion potential of Ni+Zn composite coating was much lower. And the i_{corr} revealed the opposite change trend. Those results revealed that Zn coating was a sacrificial coatings and would dissolve firstly when exposure to corrosive environment. Its anticorrosion property was due to electrochemical protection.

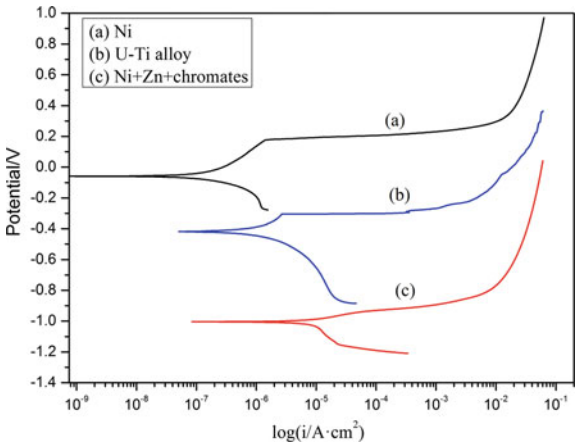

Fig. 4 Potentiodynamic polarization curves of samples

Table 4 Fit results obtained of potentiodynamic polarization curves

Samples	E_{corr} (mV)	i_{corr} (μA cm^{-2})
U–Ti alloy	−624	46.0
Ni coating	−27	0.0648
Ni+Zn+chromates coating	−947	57.5

Conclusion

Ni+Zn composite coating was prepared by electroplating. The adhesion strength of coating was up to 16.0 MPa. XRD was used to study the phase structure of the composite coating, and revealed that the interface of Ni coating/Zn coating was just physical joint. Meanwhile, the EIS and POD were used to study the anticorrosion properties, and the results showed that the composite coating provided the finest anticorrosion property. The anticorrosion property of composite coating was due to the physic barrier function of cathodal Ni coating and the electrochemical protection of anodic Zn coating.

References

1. L.Z. Luo, X.C. Lai, X.L. Wang, Recent advances in study of uranium surface chemistry in China. Radiochim. Acta. **102**, 27–39 (2014)
2. L.J. Weirick, C.T. Lynch, Corrosion resistant coatings for uranium and uranium alloys. (San Francisco, 1977)
3. L.J. Weirick, Protective coatings for uranium alloys, Sandia laboratories, pp. 949–1002 (1974)
4. A.L. Frederick, *Modern Electroplating*, 3rd edn. (Intersicence Publication, Newyork, 1974)
5. J.W. Dini, H.R. Johnson, Corrosion behavior, mechanical properties, and long-term aging of nickel-plated uranium, SAND 76-8035, 1976
6. K.G. James, R. Seegmiller, Surface treatments and electroplated coatings on uranium. Plating **3**, 215 (1963)
7. E.C. Dwight, Preparation and electroplating on uranium. Plating **4**, 363 (1962)
8. H.R. Johnson, J.W. Dini, Etching and plating of uranium alloys. Metal Finish. **3**, 37 (1976)
9. A.G. Gray, Nickel Plating Uranium. U.S. Patent 2894884, 14 July 1959
10. A.G. Gray, Copper Plating Uranium. U.S. Patent 2894885, 14 July 1959
11. P.R. Coronado, L.M. Berry, Pretreating Uranium. U.S. Patent 3341350, 12 Sept 1967
12. J.W. Dini, H.R. Johnson, Plating on some difficult-to-plate metal and alloys. Plat. Surf. Finish. **10**, 64 (1981)
13. J.W. Dini, H.R. Johnson, J.R. Helms, Nickel-pated uranium: bond strength. Plating **1**, 53–56 (1974)
14. P.B. Waldrop, M.J. Bezik, Uranium etchant and method. U.S. Patent 3573120, 30 Mar 1971
15. R. Brugger, *Nickel Plating* (Robert Draper LTD, Great Britain, 1970)
16. L.J. Weirick, D.L. Douglass, Effect of thin electrodeposited nickel coatings on the corrosion behavior of U-0.75Ti. Corrosion **32**, 209 (1976)
17. Q.F. Wang, Research of microstructure and properties of nickel pulse-plating coating on uranium, China Academy of Engineering and Physics, 2004
18. J.W. Dini, H.R. Johnson, Corrosion resistance of zinc-nickel plated uranium-0.75 titanium alloy. Met. Finish. 45–48 (1980)
19. L.J. Weirick, Corrosion and protection of uranium alloy penetrators. SAND 75-8243, 1975
20. Z.L. Zou, Preparation and properties of vanadate composite anti-fingerprint coatings, Harbin Institute of Technology, 2011
21. E. McCafferty, *Introduction to Corrosion Science* (Springer Science Business Media, New York, 2010

Numerical Simulation and Experimental Research of the Hydrostatic Extrusion Process of Pure Tungsten

Shengqiang Du, Kaijun Hong, Xiang Zan, Ping Li, Laima Luo, Yang Yu and Yucheng Wu

Abstract A finite element model (FEM) of the hydrostatic extrusion (HE) process with pressure load model is established in this paper. On this basis, the hot hydrostatic extrusion process of sintered pure tungsten under different temperatures (T), extrusion ratios (R) and die angles (α) are simulated by introducing the Johnson-Cook constitutive relation for material flowing behavior. The simulation results show that there is a negative correlation between the extrusion pressure (P) and T, a positive correlation between P and lnR. And during the increase of the α value, the P value decreases first and then increases. The die angle corresponding to the minimum P is different under different extrusion ratio. Furthermore, a

S. Du · X. Zan (✉) · P. Li · L. Luo · Y. Wu
School of Materials Science and Engineering, Hefei University of Technology, Hefei 230009, China
e-mail: zanx@hfut.edu.cn

S. Du
e-mail: 15255150652@163.com

P. Li
e-mail: li_ping@hfut.edu.cn

L. Luo
e-mail: luolaima@126.com

Y. Wu
e-mail: ycwu@hfut.edu.cn

K. Hong · P. Li · Y. Wu
Institute of Industry and Equipment Technology, Hefei University of Technology, Hefei 230009, China
e-mail: 2016170186@mail.hfut.edu.cn

X. Zan · L. Luo · Y. Wu
National–Local Joint Engineering Research Centre of Nonferrous Metals and Processing Technology, Hefei 230009, China

Y. Yu
School of Materials Science and Engineering, Harbin Institute of Technology—Weihai, Weihai 264209, China
e-mail: hityyang@hit.edu.cn

Y. Han (ed.), *Advances in Energy and Environmental Materials*,
Springer Proceedings in Energy, https://doi.org/10.1007/978-981-13-0158-2_19

tendency of internal cracking during the process can be found when the R value is relatively small. Based on the simulation results, the experiment of hot hydrostatic extrusion of sintered pure tungsten is carried out. The microhardness, microstructure and mechanical properties of the tungsten before and after the process are investigated. The results show that after the hot hydrostatic extrusion, the grain size of the tungsten is subdivided, the hardness is improved obviously and the mechanical properties is remarkable.

Keywords Pure tungsten · Hydrostatic extrusion · Finite element analysis
Microhardness · Microstructure · Mechanical properties

Introduction

Pure tungsten has the advantages of high melting point, high thermal conductivity, low sputtering rate and low vapor pressure etc., and is considered to be the primary candidate as plasma facing materials (PFM) used in the future nuclear fusion heap [1–4]. The ITER organization decided to develop the full tungsten divertor in 2011 [5, 6]. But tungsten materials have the disadvantages of the low intergranular combination degree, brittleness in low temperature or under irradiation, and high ductile-brittle transition temperature, leading to the great limitation of its application [7]. The plastic deformation process is an effective method to refine the tungsten grain size, increasing the density, so that the microstructure and the thermal conductivity can be improved. Furthermore, the ductile-brittle transition temperature can be reduced and the high temperature mechanical properties, and anti-radiation brittlement performance will be improved, either. Hydrostatic extrusion is a severe plastic deformation method (SPD) that forces the material to deform by hydrostatic pressure. During the forming process, the material is under hydrostatic compressive state which could greatly improve the formability of the material. It is one of the most effective methods to fabricate the refractory materials such as tungsten [8–10].

In recent years, finite element analysis (FEA) has gradually become an effective means to study the hydrostatic extrusion of tungsten. Through the research, it was found that there were obvious differences in the stress distribution under different extrusion temperature, extrusion ratio and die angle. Inappropriate selection of process parameters may lead to defects such as surface cracks and internal cracks [11]. Meanwhile, the temperature (T), the extrusion ratio (R) and the die angle (2α) were the three of most important parameters affecting the extrusion pressure [8, 12, 13]. Moreover, the shape of die contours could affect the extrusion pressure and the stress distribution to some extent [14]. By comparing the results of numerical simulation and corresponding experiments, some errors could be found, which were mainly caused by geometric errors, experimental statistical errors and too idealization and simplification of traditional finite element models [15].

So far, all FEA studies on the hydrostatic extrusion of pure tungsten were based on the simplified hydrostatic extrusion model with displacement loads and rigid

restraints, which did not reflect the hydrostatic pressure feature. In the present study, the FEA under hydrostatic pressure loads is designed and the constitutive relation of pure tungsten is introduced. The effect of parameter R and α on the hydrostatic extrusion under different temperatures is studied. Additionally, the hydraulic extrusion experiment is completed under the guidance of the simulation results, the microhardness, microstructure and mechanical properties of sintered pure tungsten before and after the extrusion are contrasted.

FEA Methods and Materials

Hydrostatic extrusion is a SPD method that forces the material to deform by means of liquid pressure (Fig. 1a). In the HE process, the billet is tapered to match the die geometry, the gap between the billet and the container is filled with pressure medium surrounding the billet and conveys the extrusion force of the moving punch onto it and the pressure medium is forced by its inherent pressure into the gap between the die and the billet generating excellent lubrication on the contact surface [16, 17]. Hydrostatic pressure and good lubrication conditions are beneficial for plastic deformation process of brittle materials, difficult-to-deformation materials [18]. While, in the conventional extrusion, the billet is pressed by the punch directly and so deformed (Fig. 1b).

Currently, displacement loads are used in almost all of the hydrostatic extrusion simulations [19, 20]. The displacement loads with even speed is directly applied on the upper surface of the billet (Fig. 2a). Thus, the extrusion force can be calculated by the reaction force. The lateral surface of the billet is constrained by rigid lines to ensure the materials cannot flow along the positive direction of the radius. The coefficient of friction over this region is set to 0 which represents the zero friction

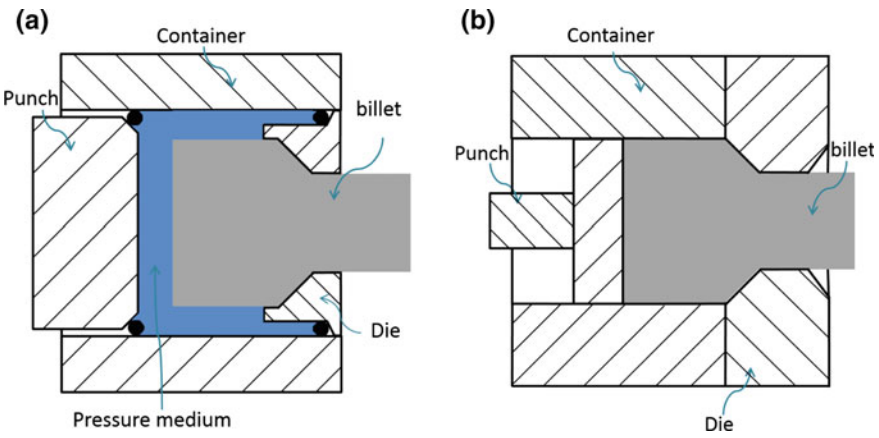

Fig. 1 Principle of **a** hydrostatic extrusion and **b** conventional extrusion

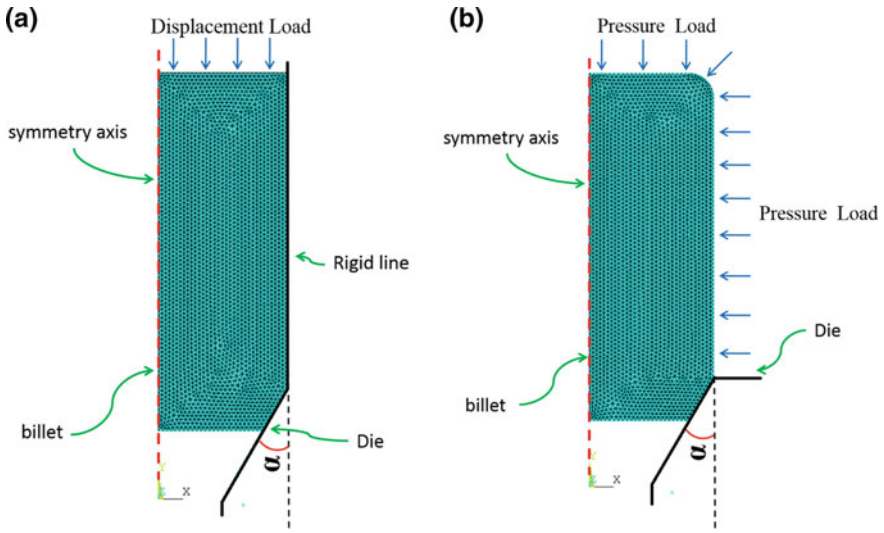

Fig. 2 Models of **a** displacement load and **b** pressure load

between billet and pressure medium. Only the rigid constraints and minimal friction coefficient cannot fully reflect all the advantages of the hydrostatic extrusion. Essentially, the displacement load model is a conventional extrusion model with near-zero friction between the billet and the die. According to the law of hydrostatic pressure, a static hydrostatic extrusion model is designed in this paper. The pressure load model is the model replacing the pressure medium as the boundary condition of the billet, modeling only its pressure properties. The pressure is set to increase linearly with the time, replacing the effect of the punch pushing the pressure medium. So, in this model, the punch is not needed because the billet is deformed by the increased pressure. In the pressure load model, the central axis of the billet is the symmetrical axis of both billet and die, and the pressure load only exists over the un-deformed outer surface of the billet (The fillet at upper right of the billet is built to verify the uniform distribution of the pressure load) [21]. Because the pressure medium used in the hot hydrostatic extrusion of pure tungsten is BN powder, so the friction coefficient is set to 0.05 [22].

A Johnson-Cook model of pure tungsten is determined by Jin et al. [23], and the equation can be described as

$$\sigma = (91.7110 + 235.8226\varepsilon^{0.2557})(1 + 0.0461\mathrm{In}\dot{\varepsilon}^{*})(1 - \mathrm{T}^{*0.5485}). \quad (1)$$

The true stress-strain curves of 1250, 1350, 1450, 1550 and 1650 °C are shown in Fig. 3. The density is 19.2 g/cm^3 and Poisson ratio is 0.28.

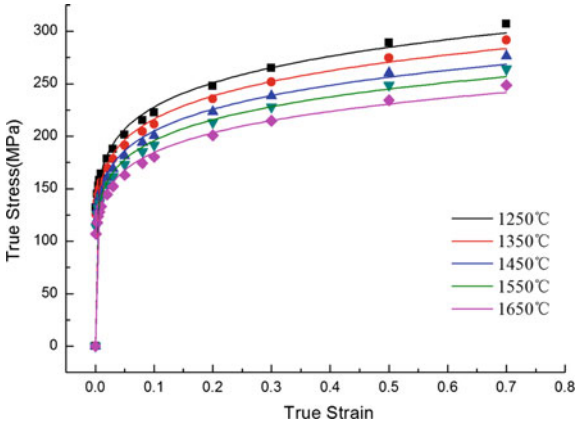

Fig. 3 True stress-strain curves under different temperature

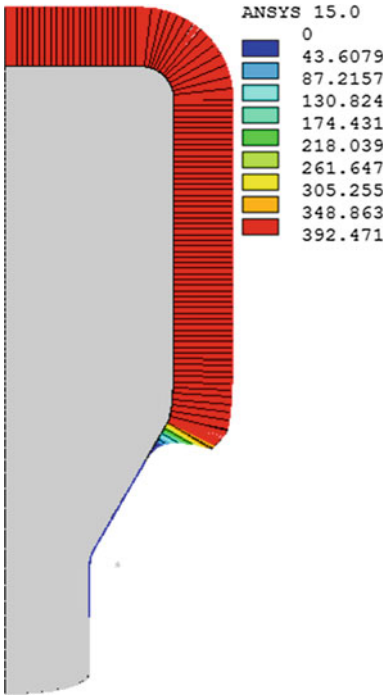

Fig. 4 Fluid pressure distribution

Finite Element Simulation Results and Discussion

The fluid pressure during the forming process can be observed in Fig. 4. Unique pressure is applied to the surface of the undeformed part and gradually decreases at the inlet zone. The existence of the hydrostatic pressure can also be confirmed by Von-Mises equivalent stress in Fig. 5. In the undeformed region, the Mises stress

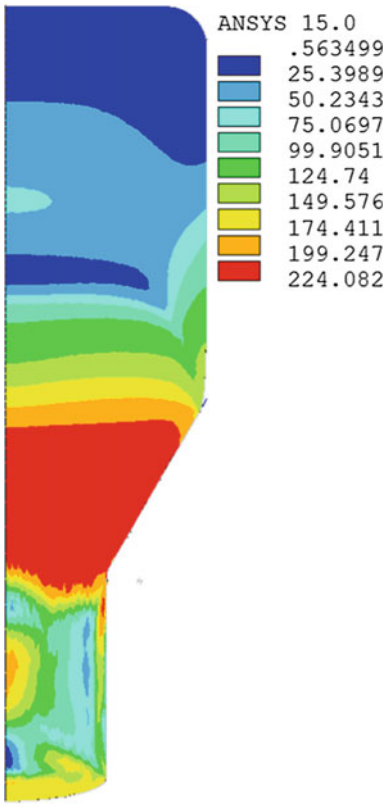

Fig. 5 Von-Mises stress distribution

value is close to zero due to the hydrostatic pressure. As the material flows to the deformation zone, the hydrostatic pressure environment disappears, the Von-Mises stress increases and the material gradually yields. The above indicates that the pressure loading method can restore the true hydrostatic extrusion process greatly.

When the half die angle $\alpha = 30°$, the region of tensile stress can be divided into 2 parts, one at the core and another at the surface (Fig. 6). Tensile stress area at the core gradually reduced when the extrusion ratio increases from 2.25 to 6.25. At the same time, under different extrusion ratios, there is a significant tensile stress distribution on the surface of the extruded part. The possible reason is, when the extrusion is relatively small, the material flow velocity at the core is slow, uneven deformation of the material leads to the existence of additional tensile stress at the central part, which is likely to cause cracks inside the material [11]. As the extrusion ratio increases, the velocity difference of the material decreases, and the additional tensile at the core gradually disappears. Meanwhile, the material flow behavior at the surface depends on the die contour shape and friction. When the extrusion ratio is too large, the friction resistance increases, the flow velocity of the material at surface is slower than that of the core. The additional tensile stress is transferred to the surface of the material, when it reaches the material tensile limit,

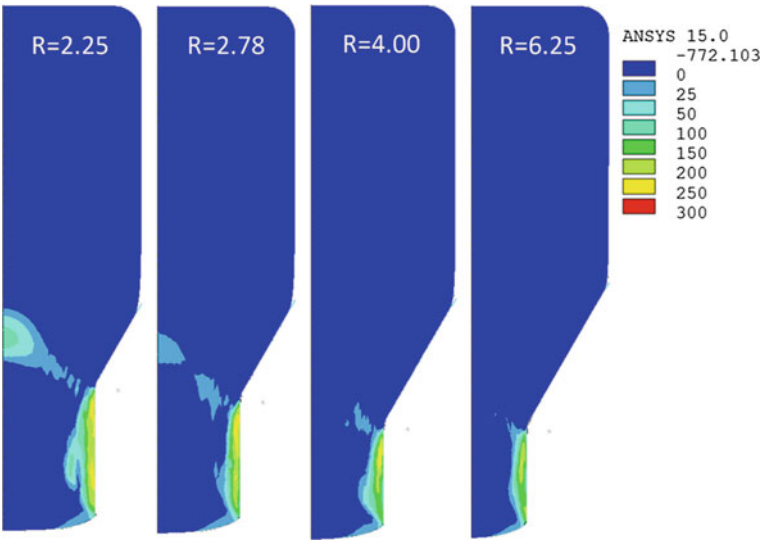

Fig. 6 Axial stress distribution under different extrusion ratios

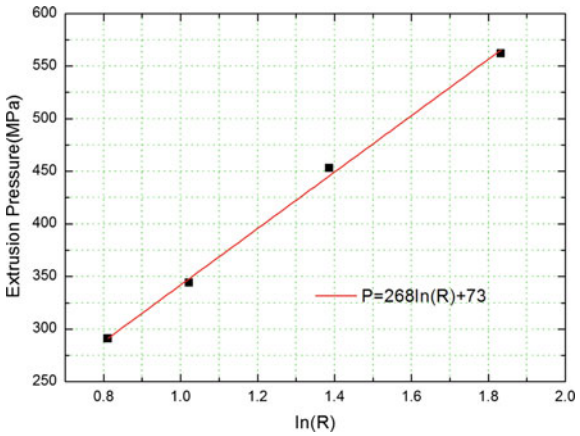

Fig. 7 Relationship between extrusion pressure (P) and extrusion ratio (R)

and then the longitudinal cracks may occur. Therefore, for the hydrostatic extrusion of pure tungsten, it is necessary to select an appropriate extrusion ratio to prevent internal and surface cracking defects.

The P value changes with the increased R and the linear relationship between P and lnR can be found as P = 268 lnR + 73 (Fig. 7), which theoretically indicates the extrusion ratio of pure tungsten can be infinite, but the R value must maintain a definite range because of material properties and device limit.

Von-Mises equivalent strain value rise as half die angle (α) respectively is 12.5°, 15°, 17.5°, 20°, 30°, 45°, 60° when R = 4.00. The large strain region extends from core to surface, a new large strain region appears near surface and expand to the

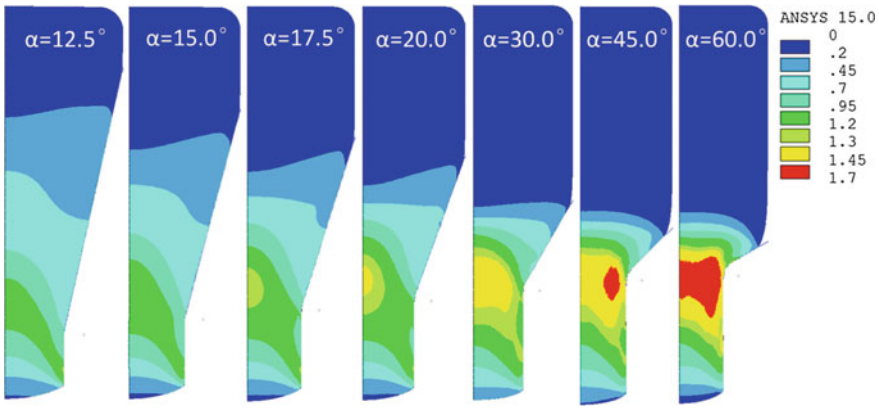

Fig. 8 Von-Mises equivalent strain under different half die angles

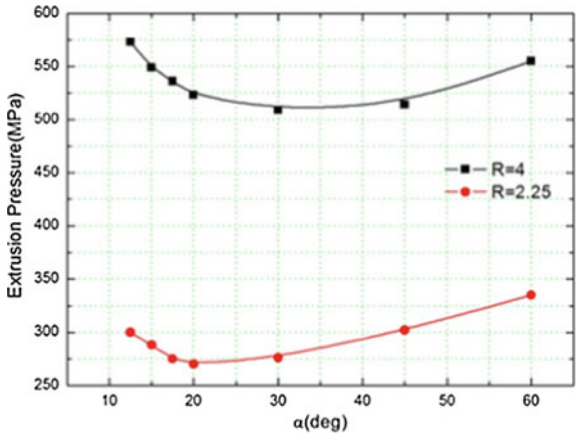

Fig. 9 Relationship between extrusion pressure (P) and half die angle (α)

core after 30° (Fig. 8). The uneven distribution of strain manifests the non-uniform deformation, and inhomogeneity intensifies after 30°.

The extrusion pressure under different angles also indicates this non-uniform deformation. P value decreases firstly then increases as α rises from 12.5° to 60°. The angle corresponding with the lowest P value is the optimal die angle, 40° when R = 2.25 and 60° when R = 4.00, respectively (Fig. 9). The magnitude of the optimal angle depends on the deformation redundant work and friction work. The redundant work is the extra work required to resist uneven deformation that rises when the die angle increases. At the same time, the change of the angle leads to the contact pressure, contact area changes, which directly affects the friction work. The two works together on the α—P relationship result in the existence of the optimal die angle. When R value changes, the redundant work, friction work is changed directly, resulting in the change of optimal angle. That is the reason why the optimal die angle is different under different extrusion ratio.

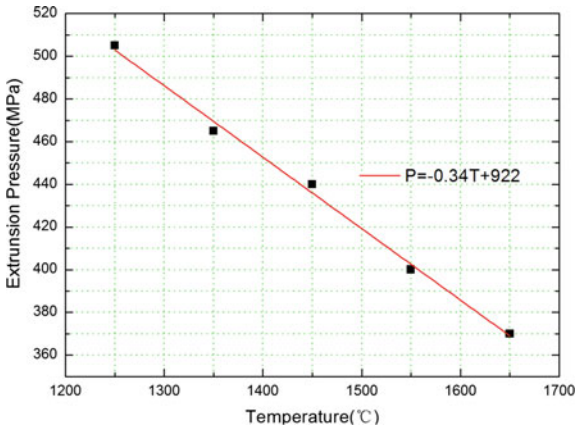

Fig. 10 Relationship between extrusion pressure (P) and temperature (T)

Figure 10 shows the effect of temperature on the extrusion force between 1250 and 1650 °C. When the half-mode angle is 30° and the extrusion ratio is 4.00, it can be found that the squeezing force P decreases linearly with the temperature T described as $P = -0.34\ T + 922$. Increasing the extrusion temperature can greatly reduce the extrusion pressure of the hydrostatic extrusion, prolong the life of the molder and complete larger deformation amount. But the high temperature will make the grain growth phenomenon more significant, which is not conducive to the refinement of tungsten grains and improvements of synthetical properties.

Experiments Results and Discussion

Based on the simulation results, the corresponding experiment of hot hydrostatic extrusion is carried out at 1550–1600 °C on the basis of practical operating conditions. The diameter of the billet is 50.0 mm (Fig. 11), the diameter of the product is 25.0 mm (Fig. 12) and the extrusion ratio is 4.00. The extruded tungsten with good surface quality can be found without any cracking defects, which proves that the simulation results have a certain guiding effect.

The microhardness on the transverse cross section of the material before and after extrusion is measured. The hardness distribution on the sintered billet is relatively uniform, as shown in Table 1. Hardness is basically same during central and edge area, about 367.83 $HV_{3.0}$. Compared to the sintered billet, the monolithic hardness of the extruded rod is significantly improved, which is due to the increasing density of dislocation caused by the deformation process. The hardness of the extruded tungsten rods shows a tendency of decrease during the radial direction (Fig. 13). The main reasons for this phenomenon can be concluded as below: uniform material flow during the extrusion process; low deformation ratio of the surface material due to the rapidly drop down of the surface temperature.

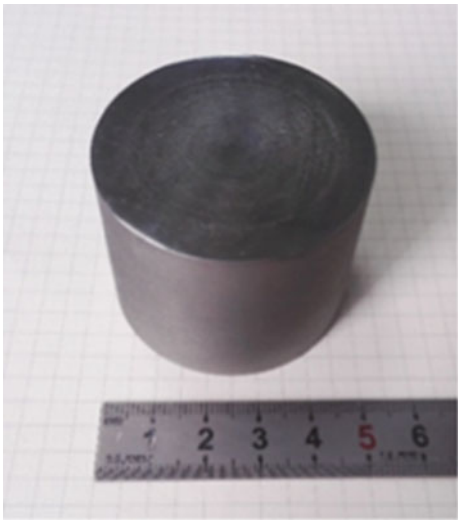

Fig. 11 Sintered tungsten billet

Fig. 12 Tungsten rod after hydrostatic extrusion

Table 1 Microhardness values of sintered tungsten billet of transverse cross section

Region	Vickers hardness ($HV_{3.0}$)					Mean ($HV_{3.0}$)
Center	364.8	376.9	364.8	378.4	361.8	369.3
Transition	372.3	370.7	361.8	368.4	368.3	367.6
Edge	370.7	372.3	360.4	366.2	363.8	366.6

The microstructure of the transverse cross section of the material before and after extrusion is observed by means of SEM (Fig. 14). The tungsten grains are greatly refined after hydrostatic extrusion. The microstructure of the extruded tungsten rod is observed during the transverse and longitudinal cross section (Fig. 15). In the transverse cross section, the grain shape is nearly circular, and the grain size is

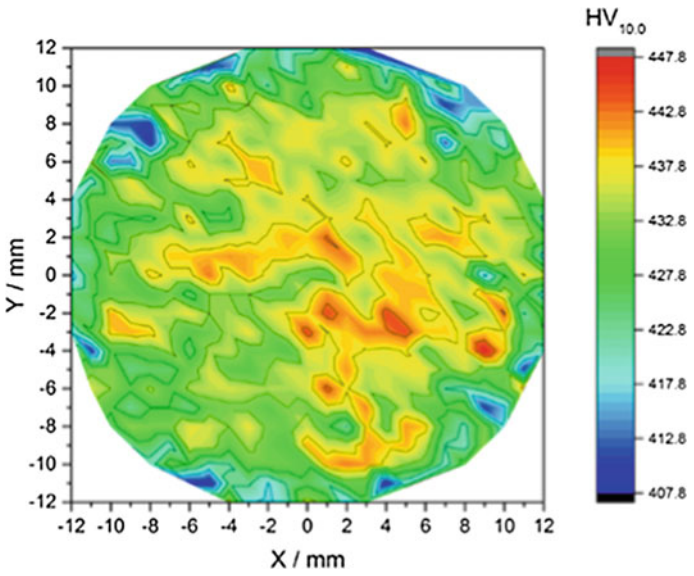

Fig. 13 Microhardness distribution of extruded rod during transverse cross section

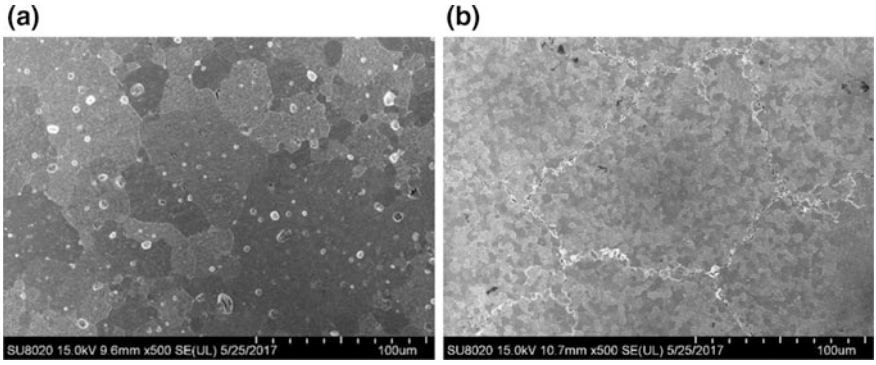

Fig. 14 Microstructure of sintered pure tungsten **a** before extrusion and **b** after extrusion

uniform. Meanwhile, its longitudinal section grain is stretched into an oval shape in the direction of the extrusion during the hydrostatic extrusion deformation.

The dynamic compression tests of sintered and hydrostatic extruded tungsten are carried out at room temperature and by means of the Hopkinson bar. The dynamic strain rate $\dot{\varepsilon} = 1200\,\mathrm{s}^{-1}$ is used and the true stress-strain curves are shown in Fig. 16. The yield strength of sintered tungsten is increased from about 1.3 GPa to the extruded 2.0 GPa. This is because tungsten grains are significantly refined during the extrusion process. Meanwhile, the hardening modulus of the material after extrusion is obviously reduced, and the work hardening phenomenon is not

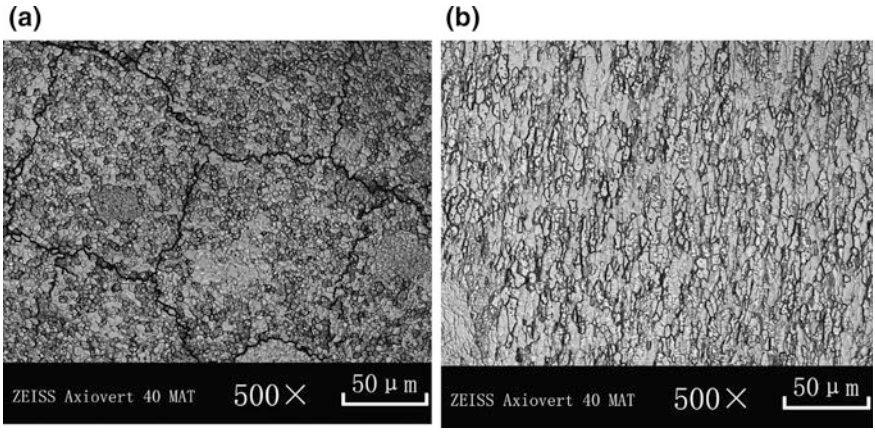

Fig. 15 Microstructure of extruded rod during **a** transverse cross section and **b** longitudinal cross section

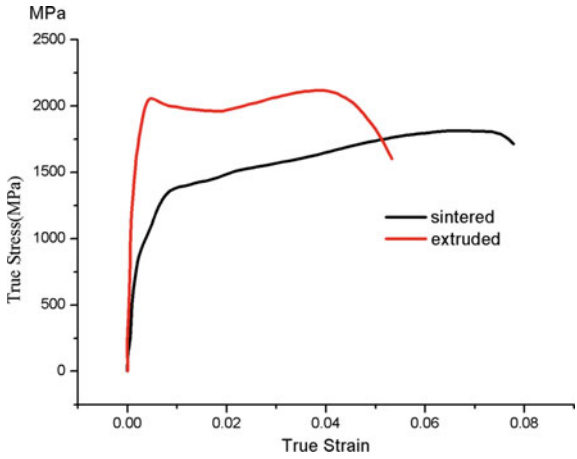

Fig. 16 True stress-strain curves of sintered billet and extruded rod

obvious. This is because during the deformation process, the dislocation density tends to saturate, and the strain hardening rate is gradually reduced. Oppositely, the initial dislocation density of the sintered tungsten is very low, so the rate of dislocation multiplication is faster than that of the dislocation recovery rate, leading to the lattice distortion energy increase, the dislocation movement is greatly resisted, the deformation resistance of the material is relatively large, the strain strengthening effect is obvious.

Summary

The hot hydrostatic extrusion process of sintered pure tungsten is studied by finite element analysis and related experiments. A finite element model of hydrostatic extrusion with hydrostatic pressure is designed. This model can better respond to the hydrostatic pressure effect compared with traditional displacement loading model. Further, the hydrostatic extrusion process under different R and α was simulated by this model during 1250–1650 °C. The results show that when the extrusion ratio R increases from 2.25 to 6.25, the tensile stress region at central region disappears gradually, meanwhile the extrusion pressure P increases, and the relationship between the P and R is P = 268 ln(R) + 73. When α increases from 12.5° to 60°, the P value first decreases and then increases. The optimal die angle is 40° when R is 2.25, 60° when R is 4.00, respectively. As temperature increases from 1250 to 1650 °C, the extrusion pressure decreases linearly. Based on the numerical simulation results, the hot hydrostatic extrusion experiment of pure tungsten is carried out. After the hydrostatic extrusion, the grain size refinement effect is obvious and the hardness is significantly improved. The dynamic compression experiment results show that the yield strength of tungsten after hydrostatic extrusion is improved from 1.3 GPa in sintered state to 2.0 GPa in extrusion state while the effect of strain hardening is weakened.

Acknowledgements This paper was supported by National Magnetic Confinement Fusion Program with Grant No. 2014GB121001 and National Natural Science Foundation of China with Grant No. 51575128.

References

1. H. Bolt, V. Barabash, G. Federici et al., Plasma facing and high heat flux materials—needs for ITER and beyond. J. Nucl. Mater. **307–311**, 43–52 (2002)
2. M. Merola, D. Loesser, A. Martin et al., ITER plasma-facing components. Fusion Eng. Des. **85**, 2312–2322 (2010)
3. V. Philipps, Tungsten as material for plasma-facing components in fusion devices. J. Nucl. Mater. **415**, S2–S9 (2011)
4. X.Y. Ding, L.M. Luo, L.M. Huang et al., Research progress in irradiation damage of tungsten and tungsten alloys for nuclear fusion reactor. Chin. J. Rare Met. **39**, 1139–1147 (2015)
5. T. Hirai, F. Escourbiac, S. Carpentier-Chouchana et al., ITER tungsten divertor design development and qualification program. Fusion Eng. Des. **88**, 1798–1801 (2013)
6. R.A. Pitts, S. Carpentier, F. Escourbiac et al., A full tungsten divertor for ITER: Physics issues and design status. J. Nucl. Mater. **438**, S48–S56 (2013)
7. M. Rieth, S.L. Dudarev, S.M.G.D. Vicente et al., Recent progress in research on tungsten materials for nuclear fusion applications in Europe. J. Nucl. Mater. **432**, 482–500 (2013)
8. F.C. Wang, *Hydrostatic Extrusion* (1st, National Defense Industry, Beijing, 2008)
9. Z.H. Zhang, F.C. Wang, S.K. Li et al., Deformation characteristics of the 93 W–4.9Ni–2.1Fe tungsten heavy alloy deformed by hydrostatic extrusion. Mater. Sci. Eng., A. **435–436**, 632–637 (2006)

10. Z.H. Zhang, F.C. Wang, Research on the deformation strengthening mechanism of a tungsten heavy alloy by hydrostatic extrusion. Int. J. Refract. Met. Hard Mater. **19**, 177–182 (2001)
11. А.Н. Колпашников, *Hot Liquid Extrusion of Metal Materials* (National Defense Industry, Beijing, 1988)
12. D.R. Li, Z.Y. Liu, Y. Yu et al., Numerical simulation of hot hydrostatic extrusion of W-40wt. % Cu. Mater. Sci. Eng., A. **499**, 118–122 (2009)
13. B. Manafi, M. Saeidi, Deformation behavior of 93 Tungsten alloy under hydrostatic extrusion. Int. J. Adv. Manuf. Technol. **76**, 28487–28492 (2014)
14. F.C. Wang, Z.H. Zhang, S.K. Li, Numerical simulation for the process of hydrostatic extrusion of 245 tungsten alloys with different die contours. Acta Armamentarii. **22**, 525–528 (2001)
15. R. Kopp, G. Barton, Finite element modeling of hydrostatic extrusion of magnesium. J. Technol. Plast. **28**, 1–12 (2003)
16. Q. Zhou, R.Q. Xu, Lubricating properties and development application of graphite materials. New Carbon Mater. 11–16 (1997)
17. J. Robertson, Method of and apparatus for forming metal articles, British Patent No. 19 356 (October 14, 1893), US Patent (1894) 504
18. H.L.D. Pugh, *The Mechanical Behaviour of Materials Under Pressure* (Elsevier, 1987), pp. 525–590
19. Z.H. Zhang, F.C. Wang, Y.M. Sun et al., Finite element analysis and experimental investigation of the hydrostatic extrusion process of deforming two-layer Cu/AI composite. J. Beijing Inst. Technol. (English Edition) **22**, 544–549 (2013)
20. A. Feuerhack, C. Binotsch, A. Wolff et al., A numerical criterion for quality prediction of bimetal strands. J. Mater. Process. Tech. **214**, 183–189 (2014)
21. S.Q. Du, X. Zan, P. Li et al., Comparison of hydrostatic extrusion between pressure-load and displacement-load models. Metals **7**, 78 (2017)
22. Q.L. Guo, The contrast between the effect of boron nitride and that of common solid lubricant additives on sliding friction. J. G Univ. Technol. (Nat Sci Ed) **26**, 41–46 (1997)
23. W. Jin, G.Q. Zhao, L. Chen et al., A comparative study of several constitutive models for powder metallurgy tungsten at elevated temperature. Mater. Des. **90**, 91–100 (2016)

Ceramic Coatings Formed on the Surface of $ZrH_{1.8}$ by Micro-arc Oxidation in Aluminate System

Pengfei Zhang, Shufang Yan, Shijiang Li, Yanhua Geng and Weidong Chen

Abstract The ZrO_2–Al_2O_3 ceramic layer was prepared by the micro-arc oxidation with $NaAlO_2$–NaOH–Na_2EDTA as electrolyte system under the constant voltage mode. The surface and cross-sectional morphologies, phase structures and chemical composition of the coatings were characterized by Field effect scanning election microscopy (FE-SEM), X-ray diffraction (XRD) and energy disperse spectroscopy (EDS). The results show that in Aluminate System under the applied conditions can obtain about 132 μm ceramic layer, the ceramic layer section is compact and uniform, the growth rate is about 13.2 μm/min. The EDS result shows that the ceramic layer contains Zirconium (Zr), Aluminum (Al) and oxygen (O), and the ceramic layer is mainly composed of aluminum oxide (α-Al_2O_3), monoclinic zirconia (m-ZrO_2), tetragonal zirconia (t-ZrO_2) and cubic zirconia (c-ZrO_2). The dense coating obviously enhances the hydrogen anti-permeation effects that the Permeation Reduction Factor value is improved about 16 times in contrast with the uncoated $ZrH_{1.8}$.

Keywords Zirconium hydride · Micro-arc oxidation · Aluminate Hydrogen permeation barrier

Introduction

Zirconium hydride ($ZrH_{1.8}$) has high hydrogen content, low thermal neutron absorption, favorable mechanical properties and negative temperature coefficient, which make an ideal moderator material in the nuclear power industry [1–5]. However, the moderating efficiency can decrease with changing environmental conditions, such as high temperature and high pressure. Generally, $ZrH_{1.8}$ is coated with hydrogen resistant ceramic coating to minimize the potential impact from hydrogen loss problem [6–8]. Using surface treatment technology for the

P. Zhang (✉) · S. Yan · S. Li · Y. Geng · W. Chen
College of Materials Science and Engineering, Inner Mongolia University of Technology, Hohhot 010051, China
e-mail: pfzhang.kk@foxmail.com

Y. Han (ed.), *Advances in Energy and Environmental Materials*,
Springer Proceedings in Energy, https://doi.org/10.1007/978-981-13-0158-2_20

preparation of hydrogen resistant ceramic coating, which based on its relatively low hydrogen permeation compared with matrix alloys, is one of the most effective methods to extend the service life of the zirconium hydride moderator [9, 10]. Some possible surface treatment technologies are available for zirconium and its alloys, including electroplating, sol-gel, plasma electrolytic oxidation (PEO) and physical vapor deposition [11]. Micro-arc oxidation (MAO) is developed from anodic oxidation. As a new surface modification technique, MAO has been used for surface treatment of some valve metals such as Mg, Al and Ti [12–14]. The ceramic coating prepared by MAO has the characteristics of high hardness, excellent corrosion resistance, high wear resistance and strong adhesion [15, 16].

The properties of MAO ceramic coating depend on the components of the electrolyte and the process parameters employed. In previous studies, Fabrication of ceramic layer on Zr and its alloys by MAO has been reported, but most of them were conducted in phosphate and silicate electrolyte system [17, 18]. Studies about the applications of aluminate as an electrolyte in MAO on zirconium alloys are scarce. Usage of the aluminate as the electrolyte has the advantage of high efficiency, green environmental protection and improves the compactness of the coating [19, 20]. In this study, MAO coatings were produced on zirconium hydride substrate in aluminate electrolyte. The structure characteristics of the coatings were observed and analyzed by X-ray diffraction (XRD) technique using Cu-Kα radiation and field effect scanning election microscopy (FE-SEM) with energy dispersive X-ray spectroscopy (EDS) to proposed operation parameters and theoretical guidance for preparation of MAO coating.

Experimental Details

The zirconium hydride ($ZrH_{1.8}$) circular column was cut to disc-shaped sample with the dimensions of Φ 20 mm × 2 mm. The sample was ground from 240 to 1000 grit SiC paper. After grinding, the sample was washed in distilled water, ultrasonically degreased in ethanol and acetone for 5 min before the experiment. In the MAO process, the $ZrH_{1.8}$ immersed in a solution of aluminate salt (18 g/L-$NaAlO_2$, 1.5 g/L-NaOH, 2 g/L-Na_2EDTA) was used as an anode, and the stainless steel plate was used as a cathode. The treatment was carried out under constant voltage mode at +350 V/–120 V for 10 min. The temperature of the electrolytes was kept under 25 °C by circulating water cooling system. After the MAO process, the sample was cleaned with distilled water and dried with the warm air.

The phase content of MAO coating was analyzed by an X'Pert PRO X-ray diffractometer (Cu Kα radiation) at 40 kV and 40 mA over a 2θ = 20° to 80° with a scanning speed of 1° min^{-1} and a step size of 0.05°. The coating surface was examined using FEI Quanta FEG 250 field effect scanning election microscopy (FE-SEM). A HITACHI SU-8010 FE-SEM was used to analyze its cross-section microstructure and element distributions. The anti-permeation influences was tested by the method of vacuum dehydrogenation experiment [21].

Results and Discussion

Surface Morphology of MAO Ceramic Coating. Figure 1 shows the surface morphology of the MAO coating on the $ZrH_{1.8}$ in aluminate electrolyte system. The ceramic coating exhibited the porous and rough microstructure with cracks and volcano crater-like features. The max micro pore is about 3.4 μm in diameter as shown in Fig. 1, which indicates that intense spark discharges were generated during the MAO treatment. Due to the uneven surface of the sample, the discharging always happened at the relative thin part of the layer with low dielectric breakdown resistance. Countless tiny sparks can be seen on the sample surface during the MAO treatment. When the spark discharges is over, the pore is left at the location of the reaction. The formation of the MAO ceramic coating consisted of three stages, the first stage is the creation of discharging channels, the second stage is melting and oxidation of metal alloys, and the third stage is cooling and deposition of the oxidized material. These steps are repeated during the MAO process, which results in the increase of the coating thickness.

Formation of these pores could be the result of the gas emission and melted metal-oxide thrown out of spark discharged channels. Some cracks were observed on the surface of ceramic coating, it can be ascribed to thermal stresses in discharge channels due to rapid cooling of molten materials on the surface.

Cross-sectional Morphology and EDS Analysis of MAO Ceramic Coating. Figure 2 illustrates the cross-sectional morphology of the ceramic coating formed in aluminate electrolyte system. The ceramic coating is composed of inner dense layer and outer loose layer. It can be seen that there are some small pores with different sizes in the loose layer, and the outermost ceramic layer has jagged shape, which is

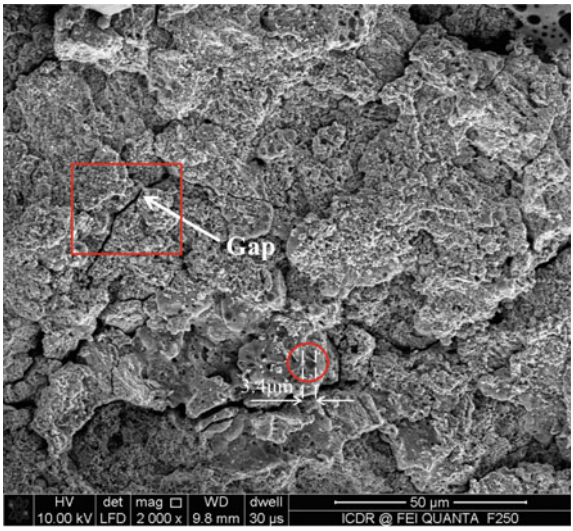

Fig. 1 Surface morphologies of the MAO coatings formed in the $NaAlO_2$ electrolyte on the surface of $ZrH_{1.8}$

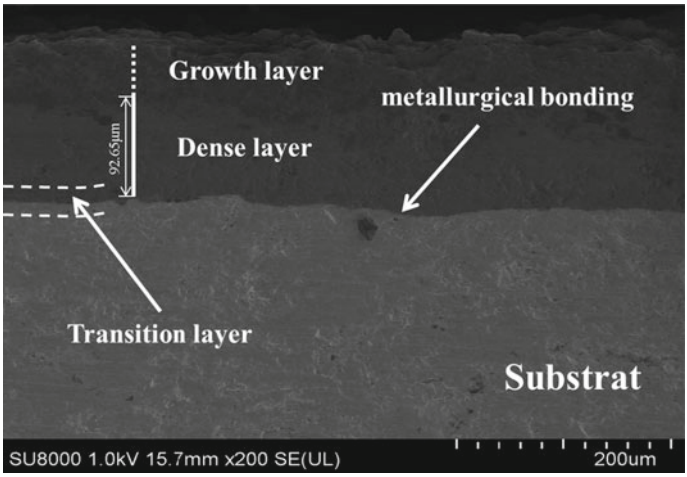

Fig. 2 Cross-section morphology of the MAO coatings formed in the $NaAlO_2$ electrolyte on the surface of $ZrH_{1.8}$

mainly because of the different growth rate and the product of the most recent discharges during coating growth. The thickness of the ceramic coating produced is about 132 μm with no apparent discontinuity between layer and substrate, the dense layer with high proportion accounts for 70% of total layer. It demonstrates the high growing speed of coating and high percentage of dense layer can be obtained in aluminate electrolyte system. Chikada [22] and his team found that hydrogen permeation resistance performance is related to the coating thickness as well as the density of the layer. Therefore, the preparation of a dense oxide layer with a certain thickness is the key to improve the performance of hydrogen permeation resistance.

EDS analyses selected over a larger area of the ceramic coating and the chemical composition of the coating assessed at the region are shown in Fig. 3, showing Al, Zr and O elements. This suggested that both Al^{3+} and Zr^{4+} compound formed ceramic coating. The oxidation and electrodeposition reactions during the MAO process were generalized as follows:

$$Zr^{4+} + 2O^{2-} = ZrO_2. \quad (1)$$

$$2Al^{3+} + 3O^{2-} = Al_2O_3. \quad (2)$$

The atomic rations of Al, Zr, and O in the EDS analysis also indicate the occurrence of the above reactions. Aluminum and its alloys exhibited superior mechanical properties and low hydrogen ion permeability [23–25]. It is considered that Al introduced into ceramic coating can improve the corrosion resistance and hydrogen permeation resistance. Furthermore, the elements in electrolyte participate in coating formation make it possible that the elemental component can be

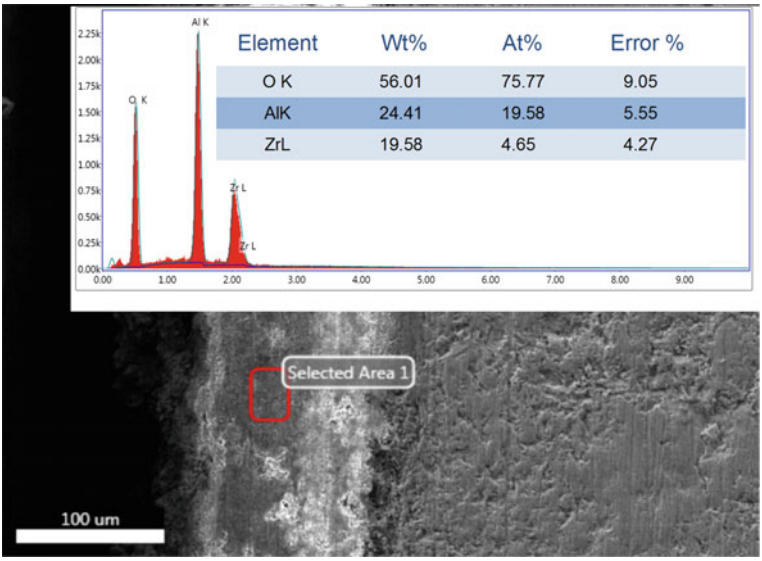

Fig. 3 EDS analysis of the MAO coatings formed in the $NaAlO_2$ electrolyte on the surface of $ZrH_{1.8}$

controlled by adjusting the electrolyte composition, so as to improve the capability of the ceramic coating.

Phase composition and Hydrogen Permeation Test of MAO Ceramic Coating. Figure 4 shows XRD pattern of the ceramic coating formed on $ZrH_{1.8}$ in aluminate electrolyte. The MAO coating is mainly composed of monoclinic zirconia (m-ZrO_2), tetragonal zirconia (t-ZrO_2), cubic zirconia (c-ZrO_2) and aluminum oxide (α-Al_2O_3). It is known that m-ZrO_2 is low-temperature phase, while the t-ZrO_2 and c-ZrO_2 are high-temperature phase. Moreover, the transition of monoclinic to tetragonal occurs at 1170 °C and the tetragonal to cubic occurs at 2370 °C [26]. When the MAO process occurs, the local temperature can rise up to 1×10^4 K [27], which is high enough to melt the metal and metal-oxide. With the temperature suddenly decrease, the different cooling rates of the molten ZrO_2 can be stabilized in various classes phase. Although t-ZrO_2 and c-ZrO_2 are high temperature phase, its stabilization at room temperature was attributed to several reasons such as reduction of grain size, residual compressive stresses and α-Al_2O_3 existence in the ZrO_2 phases.

The index of the permeation reduction factor (PRF) of MAO coating are shown in Fig. 5. The matrix treated in aluminate electrolyte enhances the hydrogen anti-permeation effect up to 16 times, particularly higher than uncoated $ZrH_{1.8}$ matrix. Therefore, the ceramic coating formed by technique on the surface of $ZrH_{1.8}$ manifest effective diffusion barrier to hydrogen.

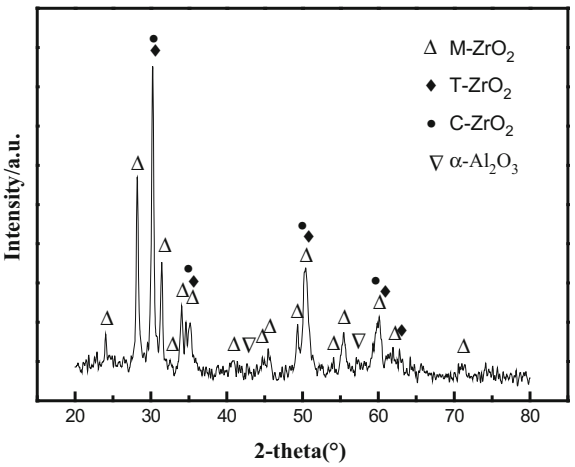

Fig. 4 XRD patterns of the MAO coatings formed in the $NaAlO_2$ electrolyte on the surface of $ZrH_{1.8}$

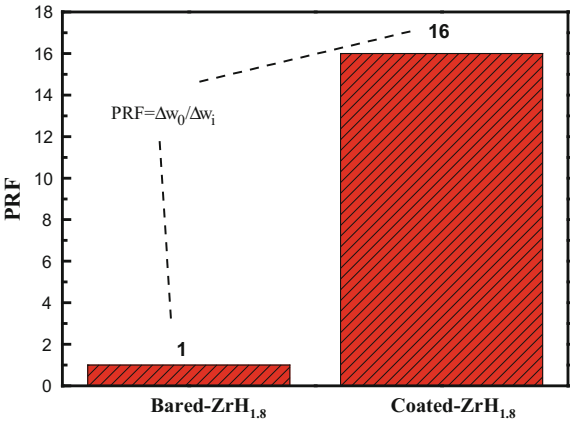

Fig. 5 Contrasted result of permeation reduction factor between coated $ZrH_{1.8}$ and uncoated $ZrH_{1.8}$

Conclusion

A compact and uniform ZrO_2 ceramic coating was fabricated on the $ZrH_{1.8}$ matrix in aluminate electrolyte by using technique of MAO. The ceramic coating synthesized in aluminate electrolyte with small pores presents excellent compactness. The XRD reveals that ceramic coating prepared in aluminate electrolyte consists of m-ZrO_2, t-ZrO_2, c-ZrO_2 and α-Al_2O_3, and the high temperature phase is stabilized at room temperature. The process of MAO significantly improves the hydrogen anti-permeation influences, as well as the PRF value is enhanced about 16 times compared with uncoated $ZrH_{1.8}$ matrix. It could be concluded that the ceramic coating demonstrated the excellent properties in hydrogen permeation resistance.

Acknowledgements This project was financially supported by the National Natural Science Foundation (No. 51164023 and 51364026), the Program for Young Talents of Science and Technology in Universities of Inner Mongolia Autonomous Region (No. NJYT-13-B10).

References

1. Y. Li, C. Zhu, S. Dai, Study of oxidation and sintering behavior of zirconium hydride alloy powder. Powder Metall. Technol. **30**, 225–259 (2012)
2. W. Chen, S. Yan, X. Zhong, J. Wang, Study on oxidation kinetics of zirconium hydride at 450–600 °C. Rare Met. Mater. Eng. **40**, 1038–1040 (2011)
3. K.A. Terrani, M. Balooch, D. Wongsawaeng, S. Jaiyen, D.R. Olander, The kinetics of hydrogen desorption from and adsorption on zirconium hydride. J. Nucl. Mater. **397,** 61–68 (2010)
4. T. Hayashi, K. Tobita, Y. Nakamori, S. Orimo, Advanced neutron shielding material using zirconium borohydride and zirconium hydride. J. Nucl. Mater. **386** 119–121 (2009)
5. P. Zhao, Q. Peng, X. Kong, C. Zou, Application of initiating condition and emergency action level in NPP at ATWS. Nucl. Power Eng. **27**, 62–65 (2006)
6. Q. Liu, L. Qin, Y. Chang, P. Zhao, Study on the hydrogen permeation barrier on the surface of the zirconium hydride by the method of CO_2. React. Surf. Technol. **34**, 32–34 (2005)
7. T.M. Adams, P. Korinko, A. Duncan, Evaluation of oxidation and hydrogen permeation in Al-containing stainless steel alloys. Mater. Sci. Eng. **424**, 33–39 (2006)
8. M.M. Krishtal, Effect of structure of aluminum-silicon alloys on the process of formation and characteristics of oxide layer in microarc oxidizing. Met. Sci. Heat Treat. **9**, 377–384 (2004)
9. H. Zhang, Q. Yang, Z. Wang, X. Liu, Study on hydrogen permeation barrier of zirconium hydride. At. Energy Sci. Technol. **39**, 83–87 (2005)
10. P. Zhao, X. Kong, C. Zou, Study on Hydrogen Barrier of Cr-C Alloy Fabricated by Electroplating upon Zirconium Hydride. Nucl Power Eng **26**, 576–613 (2005)
11. D. Sreekanth, N. Rameshbabu, K. Venkateswarlu, Effect of various additives on morphology and corrosion behavior of ceramic coatings developed on AZ31 magnesium alloy by plasma electrolytic oxidation. Sciverse ScienceDirect **38**, 4607–4615 (2012)
12. Y.C. Jung, K.R. Shin, Y.G. Ko, Shin DH, Surface characteristics and biological response of titanium oxide layer formed via micro-arc oxidation in K_3PO_4 and Na_3PO_4 electrolytes. J. Alloy. Compd. **1**, S548–S552 (2014)
13. J. Guo, R. Sun, Research progress of micro-arc oxidation process on some non-ferrous metals. Hot Working Technol. **42**, 28–32 (2013)
14. W. Jiang, G. Wang, Recent progress of microarc oxidation process for magnesium alloy. Electroplating Pollut. Control **30**, 1–4 (2010)
15. J. Zhao, Z. Zhang, Z. Wang, Structure and corrosion resistance of composite ceramic coating prepared by EASP/MAO on AZ91D magnesium alloy. Rare Met. **37**, 549–556 (2013)
16. M. Laleh, F. Kargar, S. Rouhaghdam, Investigation of rare earth sealing of porous micro-arc oxidation coating formed on AZ91D magnesium alloy. J. Rare Earths **30**, 1293–1297 (2012)
17. S. Wang, F. Guo, L. Liu et al., Effect of process parameters on thickness and morphology of micro-arc oxidation ceramic coating of zirconium alloy. Rare Met. Mater. Eng. **37**, 1466–1470 (2008)
18. W.B. Xue, Q. Jin, Q.Z. Zhu et al., Preparation and properties of ceramic coating formed by microarc oxidation on zirconium alloy formed by microarc oxidation on zirconium alloy. Trans. Mater. Heat Treat. **31**, 119–122 (2010)
19. K. Hao, J. Miao, Q. Chen, X. Dong, R. Wu, Z. Wei, Effect of sodium aluminate concentration on properties of micro-arc oxidation coatings on aluminum alloy 7075. **42**, 49–51 (2013)
20. D.R. Fang, J.H. Wang, J. Yang, Electrolyte optimization of microarc oxidation of magnesium alloy. Trans. Mater. Heat Treat. **25**, 1072–1075 (2004)

21. L.M. Chang, Growth regularity of ceramic coating on magnesium alloy by plasma electrolytic oxidation. J. Alloy. Compd. **468**, 462–468 (2009)
22. T. Chikada, A. Suzuki, T. Kobayashi, Microstructure change and deuterium permeation behavior of erbium oxide coating. J. Nucl. Mater. **41**, 1241–1244 (2011)
23. L. Sorokin, A. Sonnenberg, M. Aumailley, R. Timpl, P. Ekblom, Improvement to corrosion resistance of MAO coated 2519 aluminum alloy by formation of polypropylene film on its surface Corrosion-Resistance of MAO-Coatings on Al–Si Alloys. Surf. Coat. Technol. **232**, 674–679 (2013)
24. M. Jia, Y. Wang, H. Zhao et al., Effects of sodium aluminate on corrosion resistance of Mg-Li alloy micro-arc oxidation coating. Electroplating Pollut. Control **34**, 34–37 (2014)
25. S. Li, D. He, X. Liu, C. Zhang, Hydrogen Permeation Properties of Alumina Coating on 316L Stainless Steel. J. Inorg. Mater. **28**, 775–779 (2013)
26. E. Matykina, R. Arrabal, P. Skeldon et al., Plasma electrolytic oxidation of a zirconium alloy under AC conditions. Surf. Coat. Technol. **204**, 2142–2151 (2010)
27. J.L. Xu, Z.C. Zhong, D.Z. Yu, F. Liu, J.M. Luo, Effect of micro-arc oxidation surface modification on the properties of the NiTi shape memory alloy. J. Mater. Sci. Mater. Med. **23**, 2839–2846 (2012)

Irradiation Hardening and Indentation Size Effect of the 304NG Stainless Steels After Triple Beam Irradiation

Hailiang Ma, Ping Fan, Qiaoli Zhang, Yi Zuo, Tongyu Zhu, Yongnan Zheng, Ali Wen, Ruoyu Bai, Boqun Cui, Lihua Chen, Weisheng Jiang, Xinzhong Cao, Baoyi Wang, Shengyun Zhu and Daqing Yuan

Abstract The nuclear grade 304NG stainless steel (SS) has been developed in the past several decades as the new generation of internal material in light water reactors. The irradiation effects of domestic 304NG SS were simulated by the triple ion beam irradiation on the heavy ion, hydrogen and helium triple ion beam irradiation platform at China institute of Atomic Energy. The irradiation experiments were carried out with various doses (6, 15, 30 and 150 dpa at 300 °C) and temperatures (300, 350, 400, 450 °C with 6 dpa). The depth-dependent hardness and elastic modulus of the specimens before and after irradiation were measured by nanoindentation with the continuous stiffness measurement technique. For the specimens irradiated at 300 °C, the hardness generally increases with the increasing dose. The depth-dependent hardness in the micro-indentation region (indentation depth $h > 100$ nm) of those specimens with dose less than 30 dpa can be well explained by Nix & Gao formulae of the indentation size effect. For the specimens irradiated at different temperatures, the hardening effect can be observed for all specimens for indentation depth beyond 1 μm and the hardness decreases with increasing irradiation temperature. However, as the irradiation temperature elevates or the dose increases up to 150 dpa, the hardness for the indentation depth $h < 500$ nm deviates significantly from the projection of the Nix & Gao model. The surface morphology observed by SEM and the S parameters extracted from the slow positron annihilation Doppler broadening indicate that the drastic reduction of hardness those specimens with indentation depth $h < 500$ nm can be attributed to the change of surface morphology.

H. Ma · P. Fan · Q. Zhang · Y. Zuo · Y. Zheng · A. Wen · R. Bai · B. Cui
L. Chen · W. Jiang · S. Zhu · D. Yuan (✉)
China Institute of Atomic Energy, Beijing, China
e-mail: yuandq@ciae.ac.cn

T. Zhu
The 404 Company Limited, China National Nuclear Corporation, Lanzhou 732850, China

X. Cao · B. Wang
Institute of High Energy Physics, CAS, Beijing, China

Y. Han (ed.), *Advances in Energy and Environmental Materials*,
Springer Proceedings in Energy, https://doi.org/10.1007/978-981-13-0158-2_21

Keywords 304NG stainless steel · Triple beam irradiation · Nanoindentation
Indentation size effect · Slow positron doppler broadening

Introduction

The reactor internals (except fuel elements) are designed to support, align, and guide the reactor core components; direct coolant flow to and from core components; and guide and support the incore instrumentation [1]. Unlike the stainless steel components of fuel elements that are discharged and replaced after a few reactor cycles, the core support structure is intended to remain for the whole reactor life. The internal material must tolerate exposure to the coolant (high temperature water, liquid metals, gas, or liquid salts), stress, vibration, an intense field of high-energy neutrons, or gradients in temperature [2]. The integrity of internals not only is the safety mandate but also concerns the economics of current nuclear power plants through service life extension. Most light water reactor internals were fabricated with 304 and/or 316 stainless steels (SS).

Types 304 SS suffers from inter-granular stress corrosion cracking (IGSCC) in boiling water reactors (BWRs), due to the irradiation accelerated Cr-carbides precipitation along grain boundaries. Lower carbon 304L reduces IGSCC, as do the stabilized stainless steel grades such as 321 and 347 SS, which form TiC or NbC carbides to prevent Cr-carbide precipitation at grain boundaries. However, Type 304L has less strength than Type 304. Additions of nitrogen provide higher strength, higher resistance to strain-induced martensite formation and better localized corrosion properties [3–6].

In order to keep the strength of 304 SS, and possess the inter-granular corrosion resistant properties of 304L, meanwhile not deviate from the long term work of building the nuclear directive rules, the nuclear power industry has supported the development of nitrogen-strengthened nuclear grade (NG) stainless steels, by further limiting the contents of phosphorus and sulfur impurities. They are designated as 304NG (304 Nuclear Grade) in USA, ST2LN in Japan, Z2CN19-10 and Z3CN18-10 in France. In China, according to the requirement of nuclear reactor projects, similar grades designated as the nitrogen controlled 304 SS were developed [3]. The corrosion test showed that the domestic 304NG has better corrosion properties than the 321 SS [3, 4, 7].

The heavy-ion irradiation is a commonly used method in the simulation of neutron irradiation of materials in reactors [8, 9]. The heavy-ion irradiation can produce damage cascade in materials similar to fast neutrons. The damage rate of heavy-ion irradiation is usually 3–5 orders larger than that in thermo reactors. In addition, due to high Coulomb barriers, the bombardment of heavy-ions usually does not result in activation in specimens, so that there is no need of hot cell and cooling.

The neutron irradiation also produces transmutation products such as helium and hydrogen. They can couple with radiation damages and lead to the further degradation of material properties, the so called synergistic effect [10–12]. Investigation

of the synergistic effect is a currently hot topic in the study of structure materials particularly in the advanced nuclear systems. In order to simulate the actual environments for the structural materials in light water reactors, the triple beams, i.e. the heavy-ion, hydrogen and helium beams, have been used in this irradiation experiment. In the post irradiation examinations, the nanoindentation and slow positron Doppler broadening measurements were used to characterize the irradiation effect of the 304NG specimens.

Experimental Details

Specimen Preparation and Triple Ion Irradiation. The chemical composition and mechanical properties of domestic 304NG can be found in Refs. [3, 4]. Before the irradiation, the specimens with thickness of 0.5 mm were mechanically ground with the SiC abrasive papers (#800–3000) and diamond suspension (diameter $\sim$2.5 μm), until a mirror-like surface was reached.

The irradiation experiments were carried out on the triple ion beam irradiation platform at China institute of Atomic Energy. This platform consists of a 250 kV implanter with the mixed Hydrogen and Helium beams, the HI-13 tandem accelerator with the maximum acceleration voltage 13 meV, and an irradiation chamber with controlled temperature from room temperature to $\sim$1000 °C [12]. The Penning mixed-ion source is used in the implanter. The flux of mixed Hydrogen and Helium beams was controlled through the adjustment of each valve. In the chamber, the specimens were mounted on a slice of copper, which was brazed with a K-type thermocouple to monitor the temperature. A thermostat connected a heater and the thermocouple so that the target temperature can be adjusted automatically to a preset value with accuracy of $\pm$ 2 °C.

During the irradiation experiment, the 100 keV hydrogen and 200 keV helium beams from the implanters were simultaneously co-implanted into the specimens with the 80 meV Ni delivered by the HI-13 accelerator. In order to simulate the operating conditions of PWR, the 304NG SS specimens were irradiated up to 6, 15, 30, 150 dpa at typical coolant temperature 300 °C. For a 6 dpa specimen, the irradiation fluences were 3.23×10^{14} cm^{-2} for hydrogen, 2.36×10^{13} cm^{-2} for helium, and 7.42×10^{15} cm^{-2} for Ni ions, respectively. The ratio of hydrogen and helium was chosen to simulate the transmutation production ratio in thermo reactors [13]. The depth profiles of the implanted ions were calculated by the SRIM program [14, 15], shown in Fig. 1. The depth distributions of H and He are well overlapped from 300 to 500 nm. It should be noted that the dpa peak of energetic Ni ions lies around 7.0 μm beneath the specimen surface so that the irradiation damages in the triple-beam irradiated region are much smaller, a little more than 5 dpa at 500 nm depth.

Post Irradiation Examinations. The nanoindentation with continuous stiffness measurement technique [16] was performed with a nano indenter (MTS NanoIndenter XP) to investigate the hardness change after the irradiation. The

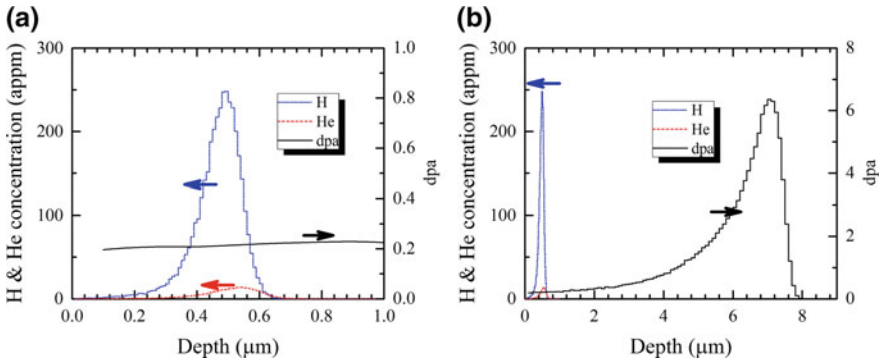

Fig. 1 Depth profiles of the implanted ions and radiation damages in irradiated 304NG steels. **a** Depth $h \leq 1.0$ μm, **b** full range, i.e. $h \leq 9.0$ μm

hardness around the irradiation center was measured for ten times and then averaged for each specimen. The total indentation depth was ~2.0 μm. The tip geometry (Berkovich type) was calibrated from indentation on a fused silica with the same indentation depth. The Poisson ratio of 0.25 was used to extract the Young's modulus.

Surface analysis of irradiated specimens was performed by a Zeiss GeminiSEM 300, using secondary electrons. The imaged area is chosen to be around the irradiation center of specimens.

The positron annihilation spectroscopy is a sensitive probe to the open-volume defects such as vacancy type of defects. The irradiation damage area induced by fast ions are limited, generally a few μm from the surface and spatially uneven distributed in irradiated materials. Slow positron Doppler broadening technique provides a method to detect the defect profile in irradiated materials. The slow positron Doppler broadening measurements were carried out with the slow positron beam facility at Institute of High Energy Physics [17]. The energies of the mono-energetic slow positron beams were tuned up to 20 keV which covers depth up to ~600 nm. The line-shape parameters S and W are defined as the ratio of counts in the central region and in the high-momentum region symmetrical to the annihilation gamma peak, respectively, to the total number of counts in the peak. In practice, the central and high-momentum region are defined as the gamma energies ranging from 510.2–511.8 keV and 513.6–516.9 keV, respectively, while the totals counts is defined in the range of 499.5–522.5 keV.

Results and Discussions

The indentation hardness of 304NG specimens before and after irradiation was shown in Fig. 2. It is seen from Fig. 2a that for the specimens irradiated at 300 °C, the hardness generally decreases with increasing indentation depth which usually

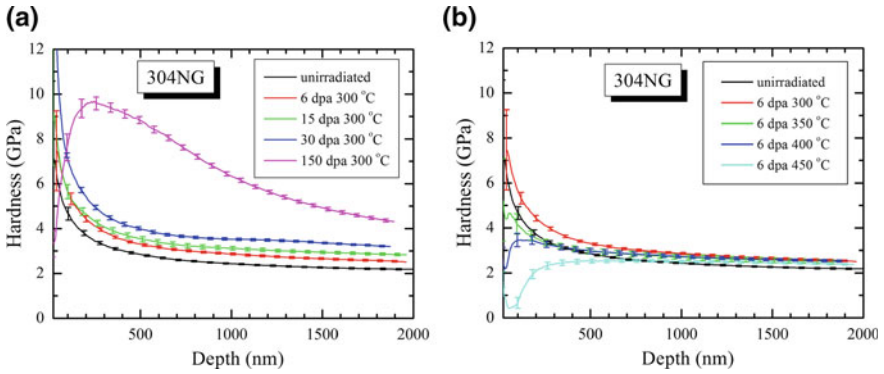

Fig. 2 The indentation hardness of unirradiated and irradiated specimens. **a** Different dpas at 300 °C, **b** different temperatures with 6 dpa peak damage

can be interpreted as the indentation size effect (ISE) [18, 19], and the hardness also generally increases with increasing damage level at all indentation depths. However, the hardness of the 150 dpa specimen is decreasing with decreasing indentation depth for $h < 200$ nm. For the specimens irradiated at different temperatures with 6 dpa damage level, it is seen from Fig. 2b that the hardness generally decreases with increasing irradiation temperature. Particularly, the marked decrease appears for the specimens irradiated at higher temperatures with $h < 500$ nm. The decreasing hardness is accompanied with the decreasing modulus in similar depths, see Fig. 3.

Based on the concept of geometrically necessary dislocations, Nix and Gao developed a model for the ISE [18], and proposed a depth profile of nano-hardness as follows

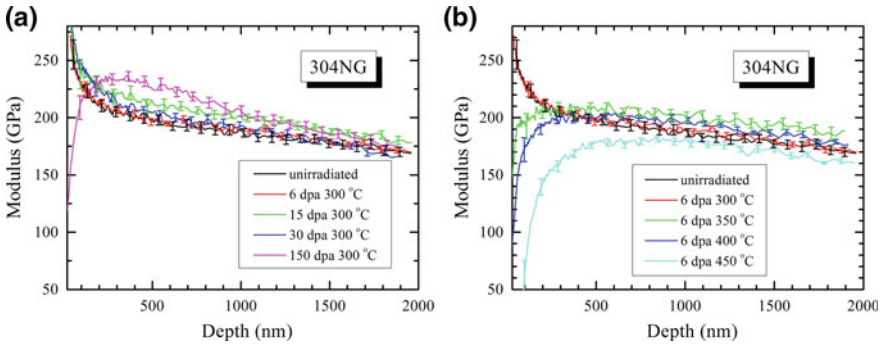

Fig. 3 The Young's modulus of unirradiated and irradiated specimens. **a** For different damage levels at 300 °C. **b** For different temperatures with 6 dpa peak damage

$$H = H_0\sqrt{1+\frac{h^*}{h}} \tag{1}$$

where H_0 is the macroscopic hardness (i.e., hardness at infinite depth), h^* the characteristic length which depends on the material and the shape of indenter tip.

The data in Fig. 2 are re-plotted as H^2 versus $1/h$, shown in Fig. 4. It is seen that for the specimens irradiated at 300 °C and to damage levels 6, 15, 30 dpa, the generally excellent linear relation between H^2 versus $1/h$ suggests that the validity of Nix & Gao formulae can extent to the micro-indentation region (indentation depth $h > 100$ nm). However for the specimen irradiated up to 150 dpa damage level at 300 °C, the relation between hardness and indentation depth deviates significantly from the Eq. (1) in the range of $h < 500$ nm. The deviation can also be observed in the specimens irradiated at temperatures higher than 300 °C, and the degree of deviation seems to increase with increasing temperature. The depth range $h < 500$ nm is largely coincident with the hydrogen and helium implantation region, which raises a question whether this phenomenon could be resulted from the synergistic effect of triple beam irradiation or other reasons.

The decreasing hardness with decreasing indentation depth was sometimes attributed to the reverse indentation size effect (RISE) [20, 21]. As is known the magnitude of ISE is very sensitive to surface preparation i.e., surface contamination, surface roughness and mechanical damage from surface preparation [22, 23], so should be the reverse indentation size effect. In order to clarify the reason behind the observed RISE in this experiment, we have examined the surface morphology of the specimens with a scanning electron microscope (SEM) and performed the slow positron annihilation Doppler broadening measurements.

The 30,000X magnified photos of the irradiated area are shown in Fig. 5. It is seen that the specimens irradiated at higher temperatures (350, 400, 450 °C) had accumulated some deposition on the irradiated area. For the specimens irradiated at

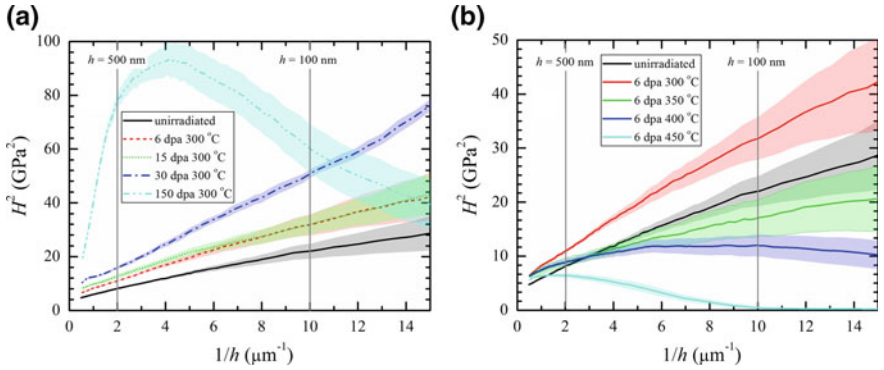

Fig. 4 A plot of H^2 versus $1/h$ for the 304NG specimens. The shaded areas indicate experimental errors. **a** For different damage levels at 300 °C. **b** For different temperatures with 6 dpa peak damage

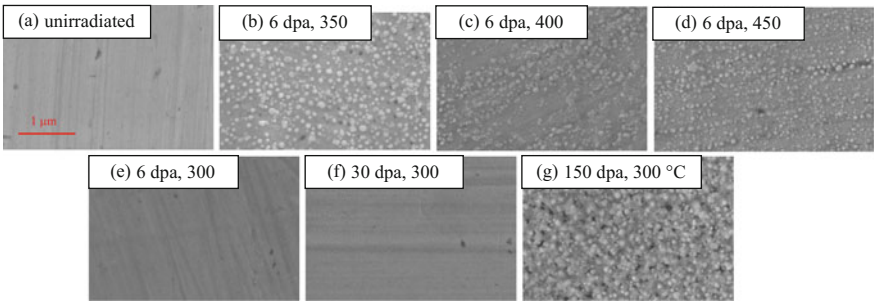

Fig. 5 The surface morphology of the 304NG specimens before and after irradiation. **a** unirradiated, **b**, **c**, **d** irradiated at 350, 400, 450 °C, respectively, with damage level of 6 dpa, **e**, **f**, **g** irradiated at 300 °C with damage level up to 150 dpa

300 °C, very minor deposition was observed for the those with damage level ≤ 30 dpa. For the 150 dpa specimen, it seems more deposition was accumulated than those 6 dpa specimens irradiated at higher temperatures. Our previous study with the Raman spectroscopy technique on the irradiated stainless steels shows that the deposition is mostly composed of amorphous carbon, forming two peaks, D (disorder) and G (graphite) peaks in the Raman spectrum.

The *S* parameters obtained from slow positron annihilation Doppler broadening measurements are shown in Fig. 6a. It is seen that for the specimens with strong RISE, i.e. the one irradiated at 450 °C to 6 dpa and the one irradiated at 300 °C to 150 dpa, the *S* parameters for the positron mean depth *R* less than ~ 50 nm are comparable but much larger than that the specimen irradiated at 300 °C to 6 dpa. Particularly, the *S* parameters of the specimen irradiated at 450 °C to 6 dpa become lower than those of the specimen at 300 °C to 6 dpa for the positron mean depth *R* larger than ~ 100 nm. That clearly shows that the RISE observed in this paper is mostly likely resulted from the degradation of surface morphology. As the positron energy increases to 15–20 keV, the penetration depth profile of positrons shown in Fig. 6b will largely overlap with the H and He concentration peak shown in Fig. 1a. The shift of *S* parameters of three specimens plotted in Fig. 6 is consistent with the nanoindentation hardness measurements.

It is also interesting to study if there is any difference in the structure of deposition for different irradiation conditions. We then plotted the *W*-*S* curve in Fig. 7, with a distinction of positron energies. The positron with energy less than 5 keV can be regarded as annihilated near the surface site. We can see that the *W*-*S* curves generally coincide for the specimens irradiated at 300 °C, although there is huge difference in the *S* curve and the surface morphology for the 6 dpa and 150 dpa specimens. However, for the positron energies less than 5 keV, the *W*-*S* curve of the specimen irradiated at 450 °C is somewhat different from those of the specimens irradiated at 300 °C. The above observations suggest that the defect type does not change in the 300 °C irradiations but differs between irradiations at different temperatures at least near the surface.

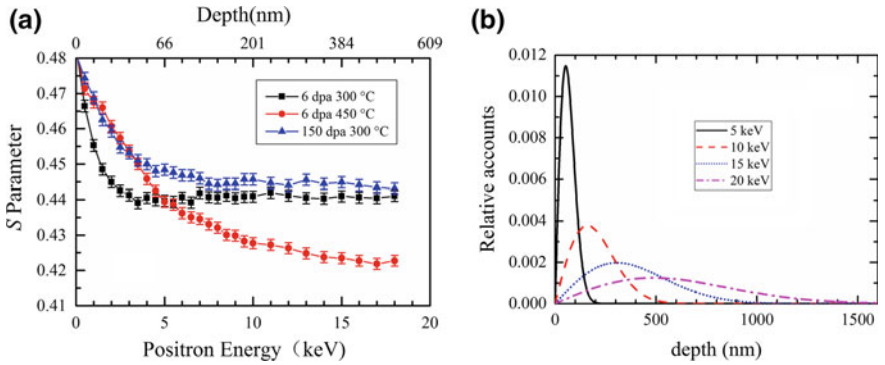

Fig. 6 **a** Depth profiles of *S* parameters for three irradiated specimens. The upper horizontal axis gives the calculated mean depth *R* from the surface for given incident positron energy, using the formulae $R = (40/\rho)E^{1.6}$, where ρ is the material density in the unit of g/cm^3, *E* the incident positron energy in keV, the calculated *R* is in the unit of nm. **b** The penetration depth profile of positron into steel. The formulae and parameters can be found in Refs. [24, 25]

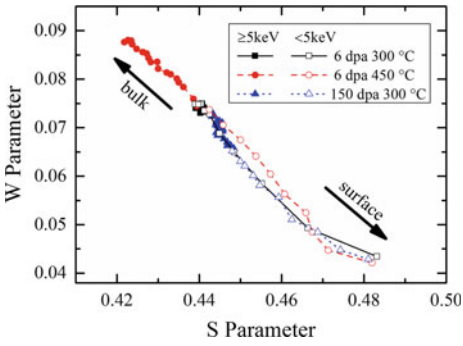

Fig. 7 The S-W plot for three irradiated specimens. The data where the positron energy is less than 5 keV were plotted with open symbols

Summary

In summary, the irradiation effects of domestic 304NG SS were simulated by the triple ion beam irradiation. The depth-dependent hardness and elastic modulus of the specimens before and after irradiation were measured by nanoindentation with the continuous stiffness measurement technique. For the specimens irradiated at 300 °C, the hardness generally increases with the increasing dose. The depth-dependent hardness of these specimens with dose less than 30 dpa in the micro-indentation region (indentation depth $h > 100$ nm) can be well explained by the Nix & Gao model of indentation size effect. For the specimens irradiated at different temperatures, the hardening can be observed for all specimens for indentation depth beyond 1 μm and the hardness decreases with increasing irradiation temperature. However, as the irradiation temperature elevates or the dose increases up to 150 dpa, the hardness for the indentation depth $h < 500$ nm deviates

significantly from the projection of the Nix & Gao model. The surface morphology observed by SEM and the *S* parameters extracted from the slow positron annihilation Doppler broadening suggest that the drastic reduction of hardness those specimens with indentation depth $h < 500$ nm can be attributed to the change of surface morphology. The detailed *W-S* curves indicate that the defect type near the surface is the same for the specimens irradiated at the same temperature, but alters for the specimens irradiated at different temperatures.

Acknowledgements The authors acknowledge the support from the National Science Foundation of China under Grant No. 11005158 and 9112600, and the National major project of science and technology under Grant No. 2012ZX06004-005-005.

References

1. H. Wolfgang, *Materials for nuclear plants: from safe design to residual life assessments* (Springer, London, 2013)
2. T. Allen, J. Busby, M. Meyer, D. Petti, Materials challenges for nuclear systems. Mater. Today **13**, 14 (2010)
3. Y. Wen, X.-P. Lai, Y.-G. Duan, E. Jiang, G.-F. Li, B. Xu, B. Gong, Research on application performance of nitrogen-containing stainless steel 304NG made in China. Nucl. Power Eng. **28**(z1), 40–43 (2007). (in Chinese)
4. Y.J. Wei, D.H. Xia, S.Z. Song, Detection of SCC of 304NG stainless steel in an acidic NaCl solution using electrochemical noise based on chaos and wavelet analysis. Russ. J. Electrochem. **52**, 560–575 (2016)
5. J.E. Alexander, et al., Alternative alloys for BWR piping applications, Final Report, NP-2671-LD, General Electric Company, October (1982)
6. R.W. Weeks, Stress-corrosion cracking in BWR and PWR piping, Proceedings of the International Symposium on Environmental Degradation of Materials in Nuclear Power Systems—Water Reactors: Myrtle Beach, South Carolina, August 22–25, (1983)
7. Q. Luo, Y. Chen, S. Liu, The studies on the corrosion behaviors of 316NG and 304NG nitrogen-containing stainless steels made in China. Procedia Eng. **27**, 1560–1567 (2012)
8. ASTM E521-16, Standard practice for investigating the effects of neutron radiation damage using charged-particle irradiation, ASTM International, West Conshohocken, PA, (2016). www.astm.org
9. G.S. Was, *Fundamentals of radiation materials science: metals and alloys* (Springer, Berlin, 2007)
10. E.H. Lee, J.D. Hunn, G.R. Rao, R.L. Klueh, L.K. Mansur, Triple ion beam studies of radiation damage in 9Cr-2WVTa ferritic martensitic steel for a high power spallation neutron source. J. Nucl. Mater. **271**, 385–390 (1999)
11. T. Tanaka, K. Oka, S. Ohnuki, S. Yamashita, T. Suda, S. Watanabe, E. Wakai, Synergistic effect of helium and hydrogen for defect evolution under multi-ion irradiation of Fe–Cr ferritic alloys. J. Nucl. Mater. **329–333**, 294–298 (2004)
12. D.-Q. Yuan, Y.-N. Zhen, Y. Zuo, P. Fan, D.-M. Zhou, Q.-L. Zhang, X.-Q. Ma, B.-Q. Cui, L.-H. Chen, W.-S. Jiang, Y.-C. Wu, Q.-Y. Huan, L. Pen, X.-Z. Cao, B.-Y. Wang, L. Wei, S.-Y. Zhu, Synergistic effect of triple ion beams on radiation damage in CLAM steel. Chin. Phys. Lett. **31**, 2012–2014 (2014)
13. L.R. Greenwood, F.A. Garner, Hydrogen generation arising from the 59Ni(n, p) reaction and its impact on fission–fusion correlations. J. Nucl. Mater. **233**, 1530 (1996)

14. J. Biersack, L. Haggmark, A Monte Carlo computer program for the transport of energetic ions in amorphous targets. Nucl. Instr. Meth. **174**, 257 (1980)
15. J.F. Ziegler, M.D. Ziegler, J.P. Biersack, SRIM—The stopping and range of ions in matter (2010). Nucl. Instr. Meth. Phys. Res. B **268**, 1818 (2010)
16. W.C. Oliver, G.M. Pharr, An improved technique for determining hardness and elastic modulus using load and displacement sensing indentation experiments. J. Mater. Res. **7**, 1564 (1992)
17. B.Y. Wang, X.Z. Cao, R.S. Yu et al., The slow positron beam based on beijing electron-positron collider. Mater. Sci. Forum **445–446**, 513–515 (2004)
18. W.D. Nix, H.J. Gao, Indentation size effects in crystalline materials: a law for strain gradient plasticity. J. Mech. Phys. Solids **46**, 411–425 (1998)
19. G.M. Pharr, E.G. Herbert, Y. Gao, The indentation size effect: a critical examination of experimental observations and mechanistic interpretations. Annu. Rev. Mater. Res. **40**, 271–292 (2010)
20. H. Zhang, C. Zhang, Y. Yang, Y. Meng, J. Jang, A. Kimura, Irradiation hardening of ODS ferritic steels under helium implantation and heavy-ion irradiation. J. Nucl. Mater. **455**, 349–353 (2014)
21. X. Bai, S. Wu, P.K. Liaw, L. Shao, J. Gigax, Effect of heavy ion irradiation dosage on the hardness of SA508-IV reactor pressure vessel steel. Metals (Basel) **7**, 1–11 (2017)
22. Y. Liu, A.H.W. Ngan, Depth dependence of hardness in copper single crystals measured by nanoindentation. Scr. Mater **44**, 237–241 (2001)
23. Z. Wang, Influences of sample preparation on the indentation size effect and nanoindentation pop-in on nickel. Ph.D. dissertation, University of Tennessee, 2012
24. M.J. Puska, R.M. Nieminen, Theory of positrons in solids and on solid surfaces. Rev. Mod. Phys. **66**(3), 841–897 (1994)
25. A. Vehanen, K. Saarinen, P. Hautojärvi, H. Huomo, Profiling multilayer structures with monoenergetic positrons. Phys. Rev. B **35**, 4606 (1987)

Preparation of ZrO_2–Al_2O_3 Composite Gel Film by Sol-Gel

YanHua Geng, WeiDong Chen, PengFei Zhang, ShuFang Yan and Zhao Li

Abstract In this paper, ZrO_2–Al_2O_3 composite sol prepared by zirconium oxynitrate and isopropanol aluminum precursor was fabricated by sol-gel method. ZrO_2–Al_2O_3 composite gel film was prepared on the surface of zirconium hydride in turns by dip-coating and heat treatment. The morphology and phase structure of the composite gel film were analyzed by scanning electron microscopy (SEM), confocal laser scanning microscope (CLSM) and X-ray diffraction (XRD). Differential scanning calorimetry and thermogravimetry (DSC-TG) analysis were performed to investigate the behavior of composite sol in the heat treatment. The results show that ZrO_2–Al_2O_3 composite gel film with about 20 μm in thickness is uniform, continuous and compact on the surface of zirconium hydride. There is substantial weight loss in the TG curve before 500 °C. After that, TG curve is flat. The total weight loss of ZrO_2–Al_2O_3 composite sol is 74.2% in the heat treatment. Composite gel has amorphous structure at 600 °C, and it is mainly composed of T-ZrO_2 between 700 and 800 °C. The aim of crystal stabilizer alumina is to inhibit phase transformation of zirconia.

Keywords Sol-Gel · Zirconium hydride · Composite gel film · Crystal stabilizer

Y. Geng · W. Chen (✉) · P. Zhang · S. Yan · Z. Li
College of Materials Science and Engineering, Inner Mongolia University of Technology, Inner Mongolia, Hohhot 010051, China
e-mail: weidongch@163.com

Y. Geng
e-mail: 1149399750@qq.com

P. Zhang
e-mail: pfzhang.kk@foxmail.com

S. Yan
e-mail: ysfch@163.com

Z. Li
e-mail: 806038023@qq.com

Y. Han (ed.), *Advances in Energy and Environmental Materials*,
Springer Proceedings in Energy, https://doi.org/10.1007/978-981-13-0158-2_22

Introduction

Moderator is required to prevent neutron leakage in nuclear reactors. Zirconium hydride is the preferred moderator materials in nuclear reactor with high hydrogen density, good thermal conductivity, low neutron capture cross section, negative temperature coefficient [1–5]. However, zirconium hydride is easy to be affected by hydrogen loss at high reactor working temperature according to H-ZrH_x balance reaction, resulting in the decrease of H/Zr atomic ratio, then moderating efficiency and service life of zirconium hydride would be shortened [6]. Thus, in order to reduce the leakage of hydrogen, anti-hydrogen penetration barrier film is prepared on the surface of the zirconium hydride without affecting the moderating ability of the solid moderator [7].

At present, barrier films, such as aluminum, titanium, carbide, oxide, are extensively studied [8]. In these films, zirconia film is the most promising hydrogen barrier materials due to its good chemical stability, low thermal conductivity, and thermal expansion coefficient that is close to the zirconium hydride [9]. At present, such film on the surface of $ZrH_{1.8}$ is prepared by physical vapor deposition (PVD) [10], chemical vapor deposition (CVD) [11], electroplating [12], Sol-Gel method and so on. However, it's difficult to control the composition of films, and deposited rate is low for PVD. It requires higher deposited temperature for CVD. In the field of research and application on penetration barrier films, sol-gel method has some advantages, such as the reaction is easy to be controlled, the process is simple, economical and feasible to prepare dense, uniform composite gel film [13, 14]. But, zirconia is prone to occur phase transformation during the heat treatment by sol-gel, which is converted from tetragonal phase to monoclinic phase. Along with the transformation, cracks in the film result from changes of lattice parameter and volume [15]. Therefore, the effective way to solve cracks of zirconia film is to add crystal stabilizer, such as Al_2O_3, Y_2O_3, SiO_2 and so on. It is known from literature [16] that the addition of Al_2O_3 can effectively hinder phase transformation of zirconia, and Al_2O_3 film is an excellent anti-hydrogen permeation material [17, 18]. Therefore, ZrO_2–Al_2O_3 composite gel film is expected to be the ideal hydrogen barrier film for zirconium hydride.

In this research, ZrO_2–Al_2O_3 composite gel film was fabricated on the surface of zirconium hydride by sol-gel method. The surface morphology, cross-sectional morphology, chemical compositions of composite gel film were characterized by field emission scanning electron microscopy (FE-SEM), confocal laser scanning microscope (CLSM) and X-ray diffraction (XRD).

Experimental

Experimental Materials. $ZrH_{1.8}$ samples provided by General Research Institute for Nonferrous Metals, Beijing, were used as the substrate material. The shape with Φ 20 mm × 2 mm in dimension was polished by various grades of SiC sand paper, and then cleaned by acetone, ethanol and distilled water, at last dried for later sol-gel experiment.

Preparation of ZrO_2–Al_2O_3 Composite Sol. Zirconium oxalate sol (sol A) was fabricated by zirconium oxychloride and oxalic acid as raw materials at 95 °C. Boehmite sol (sol B) was prepared by dissolving isopropanol aluminum in n-propanol, and then chelating with acetyl acetone and isopropyl alcohol at 90 °C. Adhesive was added to the sol A and sol B respectively. At last, sol A was polymerized with sol B to prepare ZrO_2–Al_2O_3 composite sol with mole ration of n(Zr):n(Al) = 2:1.

Analysis of ZrO_2–Al_2O_3 Composite Gel Film. Differential scanning calorimetry and thermogravimetry (DSC-TG, Model STA 409 PC Luxx) were performed to investigate the decomposition behavior of ZrO_2–Al_2O_3 composite sol. The phase composition and structure of ZrO_2–Al_2O_3 composite gel were analyzed with APD-10 automatic powder diffraction made by PILIPS (Cu target, electricity 35 mA, voltage 40 kV, step scan 0.02°). The morphology of ZrO_2–Al_2O_3 composite gel film was observed by Sigma 500 SEM and CLSM.

Results and Discussion

DSC-TG Analysis of Composite Sol. Thermal analysis results of composite sol with heating rate of 10 °C/min in air are shown in Fig. 1. In the DSC curve, endothermic peaks of ZrO_2–Al_2O_3 composite sol are detected at near 90 and 155 °C, these peaks are believed to correspond to the volatilization of small molecule organic solvents, absorbed water and hydrochloric acid. Endothermic peak at near 200 °C demonstrates that zirconium oxalate hydrate removes crystal water. There is an endothermic peak that results from decomposition of $ZrOC_2O_4$ and AlOOH, combustion of organic matter between 270 and 500 °C, at the same time, there is substantial weight loss in the TG curve. After that, TG curve is flat. The total weight loss of ZrO_2–Al_2O_3 composite sol is 74.2% in the heat treatment. Endothermic peak exists due to phase transformation of zirconia between 600 and 700 °C.

XRD Analysis of Composite Gel. XRD analysis results of composite gel are shown in Fig. 2. Composite gel has amorphous structure at 600 °C. From 700 to 800 °C, composite gel keeps the same diffraction pattern of tetragonal zirconia, no diffraction peaks of monoclinic zirconia and alumina. Moreover, with the increase of heat treatment temperature from 700 to 800 °C, the intensity of diffraction peak increases and the width of diffraction peak decreases gradually, indicating that crystal structure becomes integrity and the grain sizes grow gradually. XRD

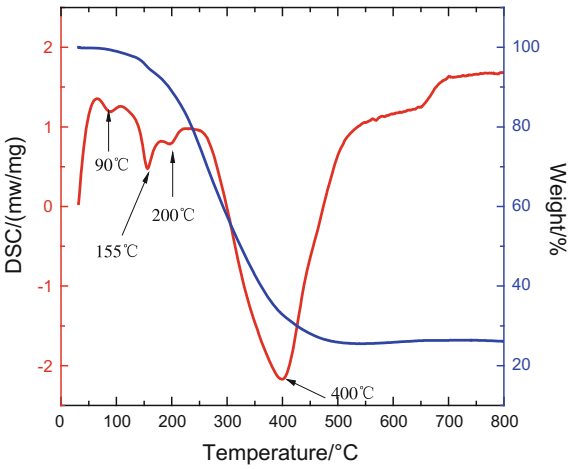

Fig. 1 TG-DSC curves of the composite sol

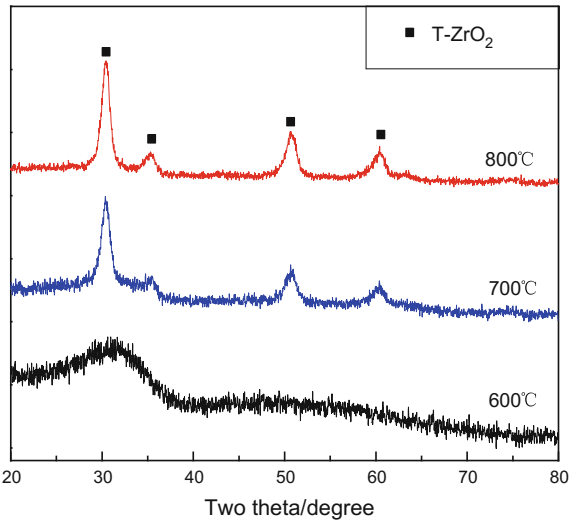

Fig. 2 XRD patterns of the composite gel

analysis results are consistent with DSC-TG analysis results. The process only occurs phase transformation of zirconia, and has very little weight loss between 600 and 800 °C. It is known from the literature [19] that zirconia prepared by sol-gel method has monoclinic phase at 600 °C, and with the increase of heat treatment temperature, the proportion of monoclinic zirconia is increasing. However, in this research, composite gel doesn't appear monoclinic zirconia. It can be concluded that the addition of Al_2O_3 restricts phase transformation of zirconia.

Morphology Analysis of ZrO_2–Al_2O_3 Composite Gel Film. Figure 3 shows the surface morphology of ZrO_2–Al_2O_3 composite gel film on $ZrH_{1.8}$. It can be seen that the surface of ZrO_2–Al_2O_3 composite gel film is smooth, it also has no cracks

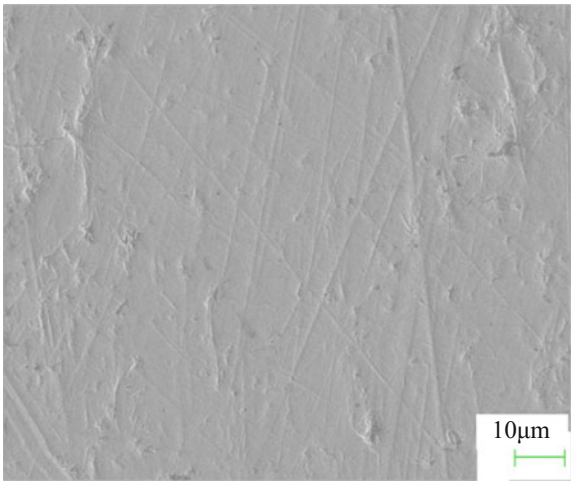

Fig. 3 Surface morphology of ZrO_2–Al_2O_3 composite gel film on $ZrH_{1.8}$

and no shedding phenomenon, but composite gel film has scratches which are caused by sandpaper grinding, the main reason is that the thickness of composite gel film is thin.

The surface morphology of ZrO_2–Al_2O_3 composite gel film on $ZrH_{1.8}$ is presented in Fig. 4. It can be seen from the Fig. 4 that ZrO_2–Al_2O_3 composite gel film is uniform, the difference of height between the highest point and the lowest point is 1.649 μm, and the roughness of composite gel film is 0.243 μm. In this study, acetyl acetone in boehmite sol acts as catalyst. When zirconium oxalate sol is mixed with boehmite sol, acetyl acetone takes two –C=O groups to form steric hindered effects which make repulsion among colloidal particles, effectively preventing colloidal particles to grow, and avoiding agglomeration of colloidal particles, as a result, the stability of mixed sol is improved [20]; On the other hand, mixed sol

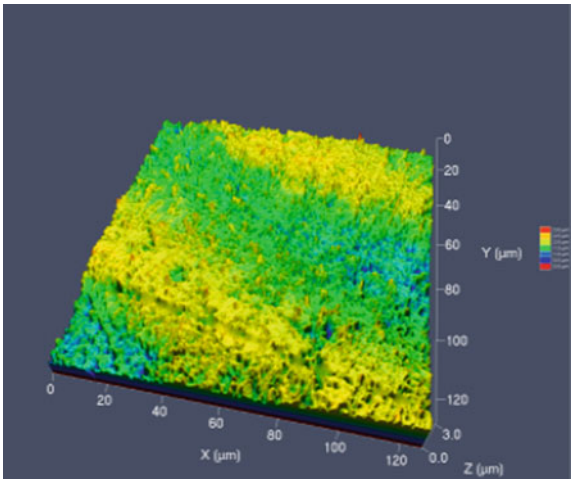

Fig. 4 Surface morphology of ZrO_2–Al_2O_3 composite gel film on $ZrH_{1.8}$

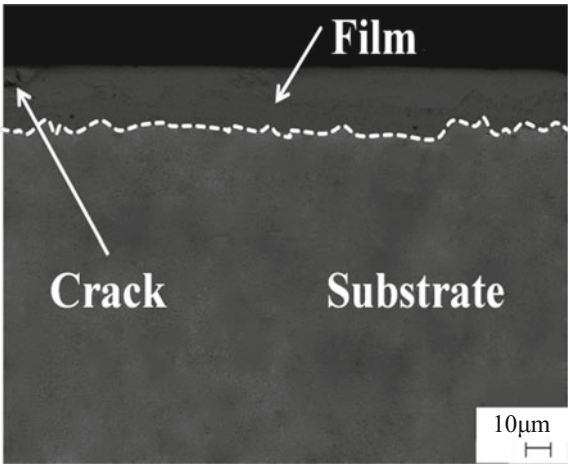

Fig. 5 Cross-sectional morphology of ZrO_2–Al_2O_3 composite gel film on $ZrH_{1.8}$ surface

contains OH carried by the organic alcohol which can be associated with water, absorbing on the surface of mixed sol, reducing the surface tension of this system, resulting in the better stability of mixed sol [21]. Consequently, the surface quality of ZrO_2–Al_2O_3 composite gel film is enhanced.

Figure 5 shows cross-sectional morphology of ZrO_2–Al_2O_3 composite gel film on $ZrH_{1.8}$ surface. From the cross-sectional view of composite gel film, the thickness of ZrO_2–Al_2O_3 composite gel film which is continuous, uniform and tightly connected to the substrate is about 20 μm. The reason is that the addition of Al_2O_3 inhibits phase transformation of ZrO_2, the cross-sectional quality of gel film is improved. However, cracks exist due to the mismatch stress. The stress may be originated from the capillary force or thermal expansion mismatch [22].

Conclusion

Composite gel has amorphous structure at 600 °C and the phase structure of composite gel is mainly composed of tetragonal zirconia from 700 to 800 °C. The addition of Al_2O_3 inhibits transformation of ZrO_2 from the tetragonal phase to the monoclinic phase, the way which stabilizes phase transformation of ZrO_2. The XRD analysis results are consistent with DSC-TG analysis results. The total weight loss of ZrO_2–Al_2O_3 composite sol is 74.2% in the heat treatment. ZrO_2–Al_2O_3 composite gel film with about 20 μm in thickness formed by sol-gel method is smooth, uniform, continuous and compact.

References

1. M.M. Yao, F. Li, W. He, A novel method for preparing nano- and microcomposite Al_2O_3–ZrO_2 ceramic coatings. J. Dispersion Sci. Technol. **29**, 482–484 (2008)
2. M.P. Puls, S.Q. Shi, J. Rabier, Experimental studies of mechanical properties of solid zirconium hydrides. J. Nucl. Mater. **336**, 73–80 (2005)
3. S. Yamanaka, K. Yoshioka, M. Uno, M. Katsura, H. Anada, T. Matsuda, S. Kobayashi, Thermal and mechanical properties of zirconium hydride. J. Alloys Compd. **293–295**, 23–29 (1999)
4. M. Uno, K. Yamada, T. Maruyama, H. Muta, S. Yamanaka, Thermophysical properties of zirconium hydride and deuteride. J. Alloys Compd. **366**, 101–106 (2004)
5. J.W. Wang, L.J. Wang, W.D. Chen, J.D. Zhang, Effect of Nb on cracking and hydrogen content of zirconium hydride. Rare Met. **36**, 61–63 (2012)
6. H.F. Zhang, Q.F. Yang, Z.D. Wang, X.Z. Liu, Study on hydrogen permeation barrier of zirconium hydride. At. Energy Sci. Technol. **39**, 83–87 (2005)
7. M. Wu, Y. Chen, J.Q. Peng, G.Q. Yan, Y.P. Sun, J.D. Zhang, S.L. Zhang, L.J. Wang, Hydrogen permeation resistance and characterization of Si–Al and Si–Zr composite sol oxide coating on surface of zirconium hydride. Rare Met. **36**, 55–60 (2017)
8. L.A. Cai, H.X. Liu, W.J. Zhang, An overview on hydrogen permeation barrier development. Hot Working Technol. **43**, 10–13 (2014)
9. Z.G. Wang, W.D. Chen, S.F. Yan, X.J. Fan, Z.G. Xu, Characterization of ZrO2 ceramic coatings on $ZrH_{1.8}$ prepared in different electrolytes by micro-arc oxidation. Rare Met., 1–8 (2015)
10. T. Chikada, A. Suzuki, T. Kobayashi, H. Maier, T. Terai, T. Muroga, Microstructure change and deuterium permeation behavior of erbium oxide coating. J. Nucl. Mater. **417**(1–3), 1241–1244 (2011)
11. S. Ruppi, Deposition, microstructure and properties of texture-controlled CVD α-Al2O3 coatings. Int. J. Refract Metal Hard Mater. **23**(4–6), 306–316 (2005)
12. S.J. Kim, K.Y. Kim, Electrochemical hydrogen permeation measurement through high-strength steel under uniaxial tensile stress in plastic range. Scripta Mater. **66**(12), 1069–1072 (2012)
13. N.R. Yang, G.Y. Yu, The basic principle and process of sol-gel method. B. Chin. Ceram. Soc., 56–63 (1993)
14. Z.J. Wang, W.W. Ji, H. Du, X.Y. Li, J.H. Gong, J.H. Ma, J. Xu, J. Sol-Gel Sci. **72**, 511–517 (2014)
15. Y.X. Hao, J.S. Li, X.J. Yang, X. Wang, L.D. Lu, Preparation of ZrO_2–Al_2O_3 composite membranes by sol-gel process and their characterization. Mater. Sci. Eng., A **367**, 243–247 (2004)
16. L. Gao, Q. Liu, J.S. Hong, Phase transformation in the Al_2O_3–ZrO_2 system. J. Mater. Sci. **33**, 1399–1403 (1998)
17. J. Feng, M. Dan, F.Y. Jin, M.Y. Chen, L.R. Shen, H.H. Tong, G.K. Zhang, Preparation and properties of alumina coatings as tritium permeation barrier by plasma electrolytic oxidation. Rare Met. Mat. Eng. **45**, 315–320 (2016)
18. A. Perujo, K.S. Forcey, Tritium permeation barriers for fusion technology. Fusion Eng. Des. **28**, 252–257 (1995)
19. M. Tahmasebpour, A.A. Babaluo, M.K.R. Aghjeh, Synthesis of zirconia nanopowders from various zirconium salts via polyacrylamide gel method. J. Eur. Ceram. Soc. **28**, 773–778 (2008)
20. M. Wu, Y. Chen, J.Q. Peng, G.Q. Yan, Y.P. Sun, L.J. Wang, Performance of silica sol coating on $ZrH_{1.8}$ with different component contents. Rare Met. **40**, 1145–1153 (2016)
21. J.L. Hu, Y.G. Luo, J.Q. Luo, Q. Liu, X.Y. Tian, Preparation and characterization of alumina zirconia composite powders by alcohol–water method. B. Chin. Ceram. Soc. **35**, 3669–3673 (2016)
22. Y. Hao, J. Li, X. Yang, X. Wang, L. Lu, Preparation of ZrO2–Al2O3 composite membranes by sol-gel process and their characterization. Mater. Sci. Eng., A **367**(1–2), 243–247 (2004)

Influence of Substrate Temperature on Optical Properties of Antimony Selenide Films by Thermal Evaporation

Shenglan Wu, Rui Leng, Jing Zhang, Chunlin Fu and Kunlun Wu

Abstract Antimony selenide is a binary single-phase semiconductor material with suitable optical band gap, large absorption coefficient, low cost and low toxicity and so on, and it is propitious for preparing absorption layer of a solar cell. In this work, Sb_2Se_3 thin films were prepared by the thermal evaporation. The crystal structure and surface morphology of the thin films were characterized by X-Ray diffraction (XRD) and atomic force microscope (AFM). The transmittance was measured by UV spectrophotometer, and then the optical band gap was calculated. The influence of substrate temperature on the optical properties of the thin films was studied. The grain distribution of the Sb_2Se_3 thin films is relatively uniform density, no crack, and the particle diameter is about 0.25 μm. With the increase of the substrate temperature, the crystallization of the thin films is higher and higher, the thin films' transmittance is only 10–18% in visible region, and the average thickness of the thin films is 4.1576 μm. Through calculation, the average optical band gap of the film is 1.69 eV, while the short circuit photocurrent and the open circuit voltage are 0.0648 mA and 0.8359 V respectively.

Keywords Antimony selenide · Thin film · Thermal evaporation
Substrate temperature · Optical performance

S. Wu · R. Leng · J. Zhang · C. Fu (✉)
School of Metallurgy and Materials Engineering, Chongqing University of Science and Technology, Chongqing, China
e-mail: chlfu@126.com

S. Wu
e-mail: 17725022665@163.com

R. Leng
e-mail: 1091307947@qq.com

J. Zhang
e-mail: 1181807264@qq.com

K. Wu
Chongqing Ceprei Industrial Technology Research Institute, Chongqing, China
e-mail: wisekl5@163.com

Y. Han (ed.), *Advances in Energy and Environmental Materials*,
Springer Proceedings in Energy, https://doi.org/10.1007/978-981-13-0158-2_23

Introduction

With the global demand for energy increased, people pay more attention on the development of green energy [1], especially solar cells. In the solar cells, except silicon-based solar cells [2, 3], the development of thin film solar cells is the most remarkable. It has advantages such as high efficiency, low cost and performance stability. Copper zinc tin sulfur (CZTS), cadmium telluride (CdTe) and copper indium gallium selenide (CIGS) solar cells achieve excellent solar energy conversion efficiencies of 12.6% [4], 20.4% [5] and 20.8% [6], respectively. But CZTS and CIGS contains four elements, which can easily produce mixed phase to generating defects. What's more, they contain toxic elements of cadmium, indium and tellurium, a high price element gallium. Therefore, they are not widely used. In latest years, the perovskite solar cells conversion efficiency could be able to achieve 22.1% [7], nothing but the stability of it is not well. There is an urgent need to find non-toxic, abundant, low-cost elements of the earth. Sb_2Se_3 which is a binary compound with high saturation vapor pressure, rich resources and direct band-gap is suitable to prepare solar cell. The absorption coefficient of the short-wave visible light is $>10^5$ cm^{-1}, and the theoretical photoelectric conversion rate of single junction cell is above 30% [8]. The ideal single-junction solar cell maintains a band gap range between 1.10 eV and 1.70 eV [9]. So far most relevant work focused on the characterization of Sb_2Se_3 thin films produced from chemical bath deposition (CBD) [10, 11], electrodeposition [12–14], solution method, rapid thermal evaporation (RTE) [15], and sputtering [16].

In this paper, we report the preparation of Sb_2Se_3 thin films by vacuum deposition and annealing. Five different substrate temperatures were employed in the thin films preparation. The surface topography, crystal structure, and optical properties of the thin films were investigated.

Experiment

The Sb_2Se_3 thin films were prepared by vacuum evaporation system (500C-G, China). Before deposition, fluorine doped tin oxide (FTO) substrates were cleaned by sequential sonication in 2% detergent solution, acetone, alcohol, followed by immersion in alcohol. In order to obtain better quality thin films, the 99.99% pure antimony selenide particles were ground in agate mortar, then putting them in the molybdenum crucible. And the chamber was pumped to a pressure of less than 3×10^{-3} Pa before evaporation. The deposition rate is controlled by adjusting the resistance current applied to the filaments. The resistance current was 80 A. The distance of the evaporation source and the sample holder (planar, 110 mm diameter) was 15 cm. The evaporation source was preheated for 10 min before opening the shutter to deposit Sb_2Se_3 thin films. Deposition was carried out at different substrate temperatures (100, 150, 200, 250, and 600 °C) to investigate the effect of the substrate to the properties of Sb_2Se_3 thin films separately and lasted for 30 min.

Afterward, the shutter was closed and the samples were cool down to room temperature naturally, and then annealed at 200 °C.

The crystal structures of the Sb_2Se_3 were measured by X-ray diffraction (XRD: SmartLab-9, Japan) with Cu Kα radiation. The morphology was researched by atomic force microscope (AFM: NTEGRA Prima, Russia). The transmittance was measured by ultraviolet and visible spectrophotometer (TU1810, China), and the optical band gap of the thin films were calculated through the transmittance spectrum of the thin film. The thickness of the thin films was measured by the step profiler (VEECO Dektak 150, America). The *I-V* curves was tested by the solar cell test system (*I-V* Test Station 2000, America).

Results and Discussion

Surface Topography. In this work, we chose 200 °C as the annealing temperature, and heat preservation time was 1 h. However, all the prepared thin films were cracked. The thin films that the substrate temperatures were 100 and 150 °C fell off completely, meanwhile a part of the thin films were peeled off when substrate temperature at 200 °C. We speculated whether the substrate was not cleaned entirely or contaminated, leading the adhesive force decreasing. Based on the above speculation, we carried out the following work: re-cleaning the substrate, the cleaning step unchanged, but the cleaning time of each step extended for 15 min. Before the next cleaning, the substrate all were put in deionized water to be washed, and the number of cleaning was increased from three to five.

The newly prepared thin films are not much different from the previously prepared thin films. But when the substrate temperature was 200 °C, the thin films were no longer crack, the degree of shedding of the 100 and 150 °C all relieved. The surface morphology of the thin films was further characterized by AFM (scan range is 3 μm, scan rate 1 Hz) in Fig. 1. With the substrate temperature improved, the crystallinity and flatness of the films are raised. However, when the temperature is too high, the deposited film may undergo secondary evaporation even though molten, thus the roughness of the films decreases.

Crystal Structure. XRD was applied to characterize Sb_2Se_3 thin films deposited at different substrate temperatures. There is no sharp diffraction peak of the non-annealed Sb_2Se_3 thin films, and there are many miscellaneous peaks, as shown in Fig. 2. This indicates that the thermal evaporated thin films were still amorphous. After annealed at 200 °C, comparing the XRD pattern of the annealed thin films to the standard card (JCPDS 15-0861) (Fig. 2), the major peaks of the three samples (200, 250, and 600 °C) are roughly the same as the orthorhombic Sb_2Se_3, and there is a second phase (Se element) here. The reason for the Se peak may be that selenium has not been removed absolutely in the tube before annealing. With the increase of the substrate temperature, the crystallization of the thin films is higher and higher.

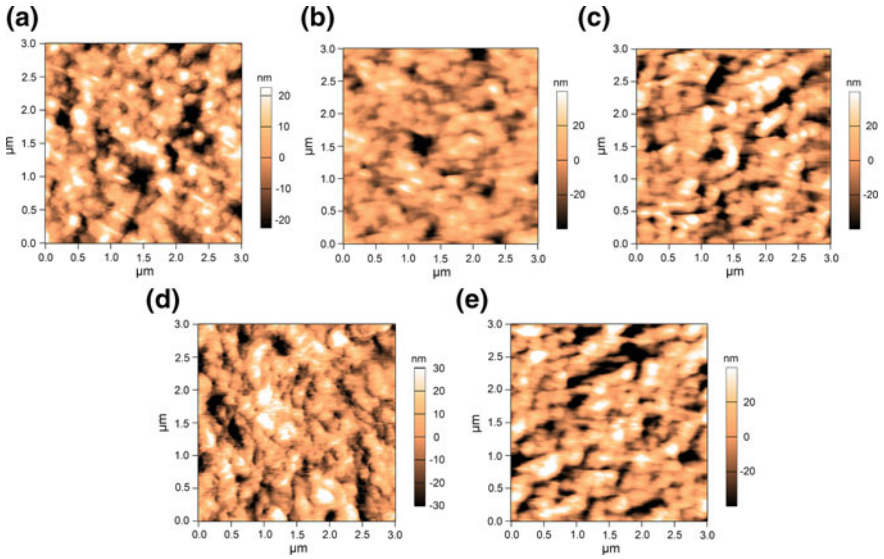

Fig. 1 AFM of the Sb_2Se_3 films at different substrate temperatures: **a** 100 °C, **b** 150 °C, **c** 200 °C, **d** 250 °C, **e** 600 °C

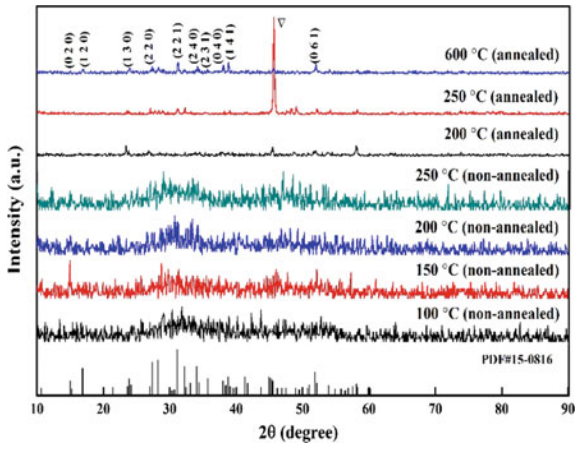

Fig. 2 XRD pattern of thin films prepared at different substrate temperatures

The lattice constant can be calculated from Bragg and orthorhombic d-spacing equation:

$$2dsin\theta = n\lambda \tag{1}$$

where d is the interplanar spacing, θ is the diffraction angle, n is the number of interplanar spacing, λ is the wavelength of X-rays (0.154 nm). Based on standard card (JCPDS 15-0861), the lattice constants were calculated by the Eq. (1). As

Table 1 The lattice constant of Sb_2Se_3 thin films

	a (nm)	b (nm)	c (nm)	$\alpha = \beta = \gamma$ (°)	Grain size (nm)
Thin films	1.1774	1.1820	0.3950	90	62.0
Powders	1.1619	1.1764	0.3984	90	79.3

shown in Table 1, the cell parameters of the 600 °C thin films and the powders is approximate.

Optical Property. The ultraviolet and visible spectrophotometer was used to measure the transmittance spectrum of the Sb_2Se_3 thin films. The spectral range and step width were 200–900 and 1 nm, respectively. The transmittance of the non-annealed thin films with different substrate temperatures was similar in Fig. 3a. In contrast to the ultraviolet region, there is a lower transmittance of the Sb_2Se_3 thin films in the visible region, it's just about 5%. After annealing, the transmittance of the thin films is slightly elevated in both ultraviolet and visible areas, particularly 600 °C. Nevertheless, the thin films' transmittance is still only 10–18% in visible region (except 600 °C). In contrast, the transmittance of near infrared area is lightly reduced.

The absorption coefficient and band gap of the thin films can be gained by the transmittance spectra.

The equation for the absorption coefficient α of the thin films is:

$$\alpha = \frac{\ln\left(\frac{1}{T}\right)}{d} \tag{2}$$

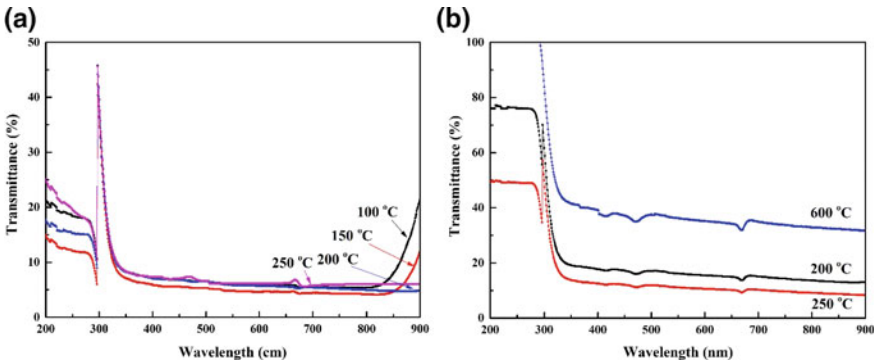

Fig. 3 Transmittance of the thin films prepared at different substrate temperatures: **a** non-annealed, **b** annealed

Table 2 The thickness of thin films at different substrate temperatures

Substrate temperate (°C)	100	150	200	250	600
Thickness (μm)	4.331	4.007	4.235	4.118	4.102

where α is the absorption coefficient, T is the transmittance, d is the thickness. When the thin films were prepared, the masks were used to cover the substrates and eventually form a step on the thin films. The thickness of Sb_2Se_3 thin films were tested by step profiler respectively, and the result is shown in Table 2. The average thickness is 4.1576 μm probably.

The optical band gap of thin films can be calculated by the Tauc equation:

$$(\alpha hv) = A\left(hv - E_g\right)^n \tag{3}$$

where $v = c/\lambda$ is corresponding to the frequency of the wavelength, c is the speed of light, λ is wavelength, h is the Planck constant, A is constant, E_g is an optical band gap. The values of n are 1/2, 2, 3/2, or 3, respectively, the corresponding ones are direct and indirect allowable transition, direct prohibition of transition and indirect prohibition of transition. The thin film of Sb_2Se_3 is directly allowed to transition, so $n = 1/2$, which can be taken into the formula:

$$(\alpha hv)^2 = A^2\left(hv - E_g\right) \tag{4}$$

It can be obtained $(\alpha hv)^2$-hv curve, as shown in Fig. 4. The optical band gap of the Sb_2Se_3 thin films can be obtained by the curve tangent of the extrapolation method. The optical band gap values of different substrate temperatures are listed in Table 3. The prepared thin films' average optical band gap is 1.69 eV. This result is disparity from the results reported in the relevant literature. The reason may be that the thin films' crystallinity is not high enough and there is impurity phase leading to the number of the internal defects add. At the same time, because of the existence of selenium in the thin films, the selenium/antimony ratio is higher than the standard selenium antimony material. And the increase in selenium content will lead to increasing optical band gap [17], so the band gap is greater than the ideal 1.2 eV.

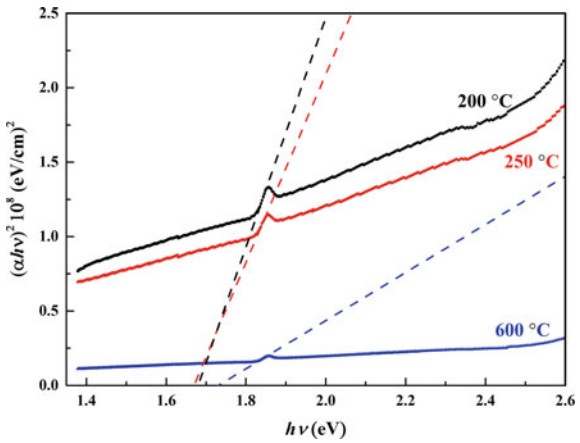

Fig. 4 $(\alpha hv)^2$-hv of the Sb_2Se_3 thin films prepared at different substrate temperatures

Table 3 The optical band gap of Sb_2Se_3 thin films at different substrate temperatures

Substrate temperature (°C)	Optical band gap (eV)	Average optical band gap (eV)
200	1.67	1.69
250	1.68	
600	1.73	

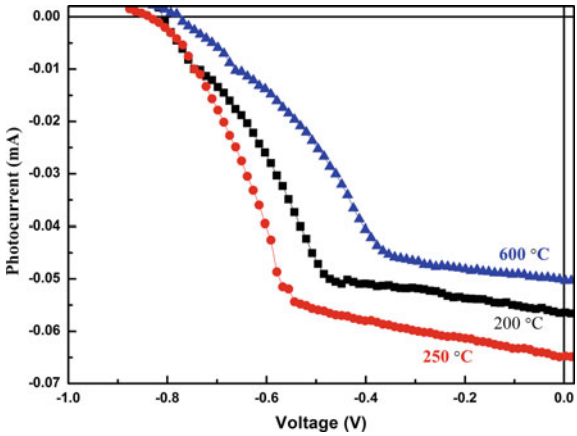

Fig. 5 *I-V* curves of the Sb_2Se_3 thin films prepared at different substrate temperatures

In order to further characterize the photoelectric properties of the films, the photovoltaic curves of the films were tested (the top electrode area is 0.0028 cm^2) as shown in Fig. 5 and the specific data is shown in Table 4. The short circuit photocurrent (I_{sc}) and the open circuit voltage (V_{oc}) were largest when the substrate temperature is 250 °C, followed by 200 and 600 °C respectively. It can be seen that, as the substrate temperature increases, the optical performance improves first and then is declines. The reason for this phenomenon may be that with the substrate temperature increases, the band gap and the transmittance both decreases first and then rises. So the absorption spectrum range and the absorbance show the same and the opposite trend respectively. Therefore, the number of carriers is affected, and the quantity is increased and then decreased, so the short circuit photocurrent and the open circuit voltage enhances fist and then reduces.

Table 4 The short circuit current and the open circuit voltage at different substrate temperatures

Substrate temperature (°C)	Short circuit current (mA)	Open circuit voltage (V)
200	0.0565	0.8090
250	0.0648	0.8359
600	0.0503	0.7759

Conclusion

Sb_2Se_3 thin films were prepared by thermal evaporation method. The influence of the substrate temperature on the crystal structure, the surface morphology, the thickness, the optical band gap and photovoltaic performance were studied, then the relation between the substrate temperature and crystal structure, size and the optical performance were found. The main conclusions are as follows:

(1) The grain distribution of Sb_2Se_3 thin films is relatively uniform density, no crack, and the particle diameter is about 0.25 μm the average thickness is 4.1576 μm.
(2) With the increase of the substrate temperature, the roughness of the thin films is decreasing, and the degree of crystallization is higher and higher, however the transmittance of the thin film is increasing too.
(3) The optical band gap of the prepared Sb_2Se_3 thin film is 1.69 eV, while the best short circuit photocurrent and the open circuit voltage are 0.0648 mA and 0.8359 V respectively.

Acknowledgements This work was supported by the National Natural Science Foundation of China (51372283), the Program for Innovation Teams in University of Chongqing, China (Grant No. CXTDX201601032), the Program of Science and Technology Innovation of Chongqing University of Science & Technology (YKJCX1620214).

References

1. M. Mehrabankhomartash, M. Rayati, A. Sheikhi et al., Practical battery size optimization of a PV system by considering individual customer damage function. Renew. Sust. Energ. Rev. **67**, 36–50 (2017)
2. U.C. Matur, S. Akyol, N. Baydogan, et al., The characteristic behaviors of solgel-derived CIGS thin films exposed to the specific environmental conditions, in *Energy systems and management* (Springer International Publishing, Cham, 2015), pp. 179–191
3. M.A. Mughal, R. Engelken, R. Sharma, Progress in indium (III) sulfide (In_2S_3) buffer layer deposition techniques for CIS, CIGS, and CdTe-based thin film solar cells. Sol. Energy **120**, 131–146 (2015)
4. W. Wang, M.T. Winkler, O Gunawan, et al., Device characteristics of CZTSSe thin-film solar cells with 12.6% efficiency. Adv. Energy. Mater. **4**(7), 403–410 (2014)
5. Information on http://investor.firstsolar.com/releasedetail.cfm?ReleaseID=828273
6. M.A. Green, K. Emery, Y. Hishikawa et al., Solar cell efficiency tables (version 43). Prog. Photovolt: Res. Appl. **22**, 1–9 (2013)
7. S.Y. Kim, H.J. Jo, S.J. Sung et al., Perspective: Understanding of ripening growth model for minimum residual PbI_2 and its limitation in the planar perovskite solar cells. APL Mater. **4**, 10–875 (2016)
8. D.J. Xue, H.J. Shi, T. Jiang, Recent progress in material study and photovoltaic device of Sb_2Se_3. Acta. Phys. Sin-CH Ed. **64** (2015)
9. A. Goetzberger, C. Hebling, H.-W. Schock, Photovoltaic materials, history, statusand outlook. Mat. Sci. Eng. A-Struct. **40**, 1–46 (2003)

10. H. Maghraoui-Meherzi, T.B Nasr, M. Dachraoui, Synthesis, structure and optical properties of Sb_2Se_3. Mat. Sci. Semicon. Pro. **16**, 179–184 (2013)
11. Y. Rodríguez-Lazcano, Y. Peña, M.T.S. Nair et al., Polycrystalline thin films of antimony selenide via chemical bath deposition and post deposition treatments. Thin Solid Films **493**, 77–82 (2005)
12. Y. Lai, Z. Chen, C. Han et al., Preparation and characterization of Sb_2Se_3, thin films by electrodeposition and annealing treatment. Appl. Surf. Sci. **261**, 510–514 (2012)
13. X. Shi, X. Zhang, Y. Tian et al., Electrodeposition of Sb_2Se_3, on indium-doped tin oxides substrate: nucleation and growth. Appl. Surf. Sci. **6**, 2169–2173 (2012)
14. T.T. Ngo, S. Chavhan, I. Kosta et al., Electrodeposition of antimony selenide thin films and application in semiconductor sensitized solar cells. Acs. Appl. Mater. Int. **6**, 2836 (2014)
15. Y. Zhou, L. Wang, S. Chen et al., Thin-film Sb_2Se_3 photovoltaics with oriented one-dimensional ribbons and benign grain boundaries. Nat. Photonics **9**, 409–415 (2015)
16. C. Yuan, X. Jin, G. Jiang et al., Sb_2Se_3, solar cells prepared with selenized dc-sputtered metallic precursors. J Mater. Sci-Mater Electron. **27**, 8906–8910 (2016)
17. A. Solieman, A.A. Abu-Sehly, Modelling of optical properties of amorphous selenium thin films. Phys. B Phys. Condens. Matter **405**, 1101–1107 (2010)

Preparation and Optoelectronic Properties of CuI Films by Pulling and Chemical Vapor Deposition

Weilin Shi, Qiang Wang and Xiying Ma

Abstract Copper iodide (CuI) is a wide band gap semiconductor of I-VII group with excellent hole-transporting properties that has great potential uses in photoelectronic field. We present the preparation and optoelectronic properties of CuI films by pulling and chemical vapor deposition (CVD) methods. The former was deposited on ITO conductive glass substrate with the continuous pulling method, while the latter was grown on Si and quartz wafers by CVD deposition. The influences of deposition conditions on the structure, morphology and optoelectronic properties of CuI films have been studied using the measurement of X-ray diffraction (XRD), UV spectrophotometer and Hall Effect instrument. We found that the CuI films prepared by pulling 20 times or deposition 20 min have smooth surface morphology and good optoelectronic properties. Moreover, The CuI films prepared by CVD have better crystallinity, good current-voltage (*I-V*) property and stronger absorption in Ultraviolet band of light than that of CuI films by pulling method. Both CuI films have high absorptivity in ultraviolet band and high transmission in visible light range that show CuI film is more suitable as a window layer for solar cells to enhance the efficiency of solar cells.

Keywords CuI · Pulling method · Chemical vapor deposition
Morphology · *I-V* property

W. Shi · Q. Wang · X. Ma (✉)
Suzhou University of Science and Technology, Suzhou 215009, Jiangsu, China
e-mail: 291740901@qq.com

W. Shi
e-mail: goldlionwl@163.com

Q. Wang
e-mail: 954896802@qq.com

Y. Han (ed.), *Advances in Energy and Environmental Materials*,
Springer Proceedings in Energy, https://doi.org/10.1007/978-981-13-0158-2_24

Introduction

CuI, an I-VII group semiconductor with broad band energy gap and high conductivity, is an excellent hole-transporting material and become the hot topics in recent years due to the optical and electrical properties [1–5]. CuI thin films show great potential applications in perovskite solar cells, polymer solar cells, heterojunction solar cells and other fields [6–9]. As the hole-transporting material, CuI is very cheap, good conductivity, and little environmental pollution, which will largely low the cost of the perovskite solar cells and expand their applications. For example, Christians et al. [10] used CuI film as the anode transport layer to replace spiro-OMeTAD in the perovskite solar cell structure, because spiro-OMeTAD is difficult to preparation, the yield is very low, and the price is very expensive about ten times higher than that of gold. In addition, CuI is a kind of molecular crystal, no residual stress and interface states. It can fabricate good interference in the heterojunction of CuI and Si [11]; and it can be inserted in the interferences of ZnO/Si to reduce interface states of heterojunction and enhance the conductivity. Moreover, it is found that CuI film based perovskite solar cells have high photoelectric conversion efficiency [12], and the short-circuit current of it is more steady for continuously irradiate 2 h. Therefore, as the transport layer and window layer for perovskite solar cells CuI film has great uses.

So far, the preparation of CuI films have many approaches, such as thermal evaporation method [11], spin coating method [13] and spray method [14]. However, the CuI films prepared by these methods have large roughness, which influences the application of CuI in the devices. Therefore, reproducibility mature technology with simple process and low price to prepare high quality CuI films is an important hot issue in the perovskite solar cells production of the word. Herein, we present the continuous pulling method and chemical vapor deposition (CVD) for high quality CuI films. Pulling and CVD preparations are simple and scalable methods for rapid preparation large area film materials. The surface morphology, structure, *I-V* properties and light absorption properties of the prepared CuI films were systemically studied and analyzed.

Material and Preparation

Purity analysis copper iodide (CuI) powder as the raw material was bought in Shanghai shengxiang Chemical Reagent Co., Ltd.). ITO transparent conductive glasses with a square resistance of 300–500 Ω/□ are used as the substrates. Acetone, Absolute ethanol and deionized water were used as solvent and cleaner to clean substrates and beaker other tools; silver nitrate ($AgNO_3$) was used as dopant to doping CuI film for improving the conductivity of the films.

Pulling Method. CuI saturated solution was prepared by using analytical grade 10.000 g CuI powder dissolved in 200 mL deionized water for stirring 20 min at room temperature. Then the solution was doped with Ag ions by slowly dropped a $AgNO_3$ solution that was previously dissolved 0.2 g $AgNO_3$ in 20 ml deionized water in a large beaker, by which Ag ions was incorporated into CuI self-assembly in situ. After doping, CuI thin films were deposited via pulling method on ITO substrates that were ultrasonically cleaned with deionized water, dried at 80 °C in a drying oven, and washed with deionized water for several times to move the loose CuI particles. Finally, CuI thin film samples were completed by repeating this pulling-drying procession 10–30 times according the thickness requirements and annulled at 350 °C in the atmosphere of Ar in a large horizontal quartz tube furnace.
Chemical Vapor Deposition. CuI film samples were fabricated by a liquid phase chemical vapor deposition process. The growth system is composed of a large horizontal quartz tube furnace, a vacuum system, a gas meter, and a temperature controller. For uniform growth, cleaned Si (111) substrates with a resistivity of 3–5 Ω/cm were placed at the center of the furnace. Prior to the fabrication, the furnace was pumped to high vacuum and heated to 100 °C and kept at this temperature for 2 h to remove any water moisture from the mixture. Then the furnace was heated to the growing temperature of 300 °C. The above prepared CuI saturated solution was put in a conical flask that was positioned in a water bath with a constant temperature of 75 °C. Argon (Ar) gas was flows into CuI saturated solution, and CuI molecules were carried into the tube by Ar gas and pass through the furnace with a constant velocity. They took a chemical reaction and condensed on the substrates. The growth process was carried out for 10–30 min and then annealed in situ at 350 °C for 30 min. Finally, the samples were removed form the furnace when the system was cooled down to room temperature.

The morphology of the products was investigated by an atomic force microscope (AFM). The composition was analyzed by X-ray diffraction (XRD) on a RINT2000 vertical goniometer with Cu $K\alpha$ radiation (λ = 0.1541 nm). The electrical properties of the samples were analyzed by a Hall Effect Measurement System (HMS-3000, Ecopia, Anyang, South Korea) at room temperature. The optical absorption spectra of the samples were investigated by a UV-visible spectrophotometer (Shimadzu UV-3600).

Results and Discussion

The crystal structures of the samples were characterized by XRD. The XRD patterns of the CuI films deposited by pulling method are illustrated in Fig. 1a. A_1, A_2, and A_3 denote CuI film samples prepared by 10, 20, and 30 pulling times, respectively. three samples has a wide diffraction band appearing at 25° in the spectrum, belongs to the (111) planes of cubic CuI according to the X-Ray standard card (24-0363), indicating that CuI films are mainly composed by amorphous phase CuI particles even the samples were annealed at 350 °C in Ar atmosphere. The half

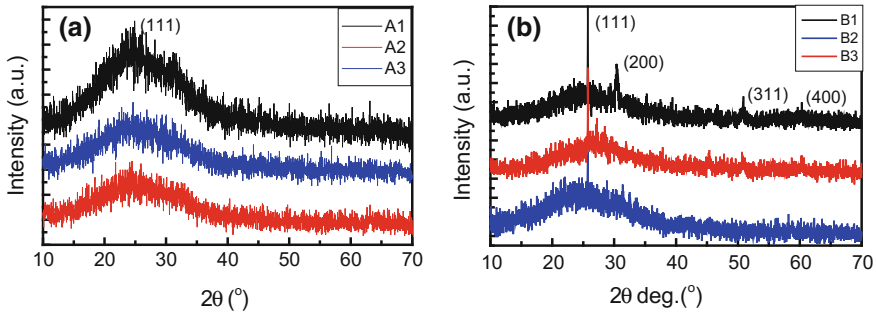

Fig. 1 The XRD patterns of the CuI films. **a** A_1, A_2, and A_3 samples by pulling method; **b** B_1, B_2, and B_3 samples by CVD method

width of height (FWHM) is up to 17°. The diffraction intensity of the samples increases with the pulling times because the thickness of the CuI films increases.

Figure 1b shows the XRD pattern of CuI films deposited by CVD. B_1, B_2, and B_3 denote the CuI film samples deposited by CVD deposition with 10, 20, and 30 min, respectively. Clearly, a sharp diffraction peak is located at 24.9°, corresponding to the (111) crystal planes of CuI, which shows that the CuI films have good crystal structures. Specially, for B_3 sample, beside the strong peak of 25°, there are other three small peaks located at 30.5°, 50.9°, and 60.2°, corresponding to (200) and (311) crystal planes of CuI. The FWHM of the peak at 25° is less than 1°, indicating that the B_3 sample is consisted of tiny CuI nanoparticles and their preferred in (111) crystal plane. In addition, the diffraction intensity of (111) plane is stronger with deposition time. Compared the XRD results of pulling and CVD methods, CuI films deposited by CVD have good crystallinity.

Figure 2a shows the AFM image of the CuI film A_3 sample obtained by pulling method for 30 times on ITO glass. Here only shows the morphology of A_3 sample because the surface morphologies of the three samples are very similar. The film shows a continuous and compact film with small wave and some nanoparticles are scattered on top layer. Figure 2b shows the AFM picture of B_3 sample by CVD on quartz crystalline slides for 30 min. Also, the surface morphologies of B_1, and B_2 samples are very similar to B_3 except the thickness. We can see many CuI quantum dots around 100 nm in diameter are uniformly distributed on the surface of the sample. Under the quantum dots, the film is homogeneous and continuous, with a uniform color and a thickness of about 100 nm. This growth mode will be the layer-quantum dot mode, corresponds to the cubic crystalline structure of CuI.

The surface *I-V* properties of the CuI samples measured by a Hall Effect measurement system, as shown in Fig. 3. In Fig. 3a the voltages between two electrodes in A_1, A_2, and A_3 samples show a fluctuate linear dependency on the applied current, indicating that the CuI films by pulling have weak electrical conductivity because of the films were composed by many amorphous phase CuI particles and CuI itself with large energy band gap. We note that the *I-V* properties of the samples become better with the pulling time increasing; A_3 sample has good linear

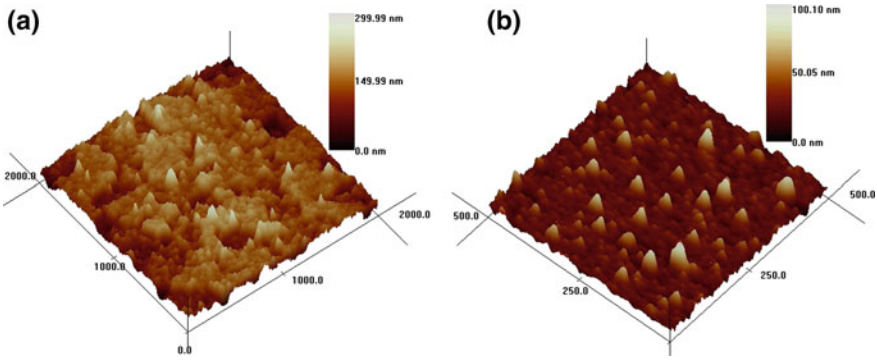

Fig. 2 The AFM images of the CuI films. **a** A_1, A_2, and A_3 samples by pulling method; **b** B_1, B_2, and B_3 samples by CVD method

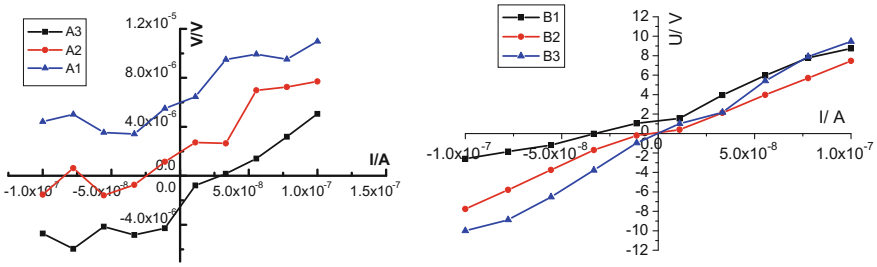

Fig. 3 The surface *I-V* properties of the CuI films. **a** A_1, A_2, and A_3 samples by pulling method; **b** B_1, B_2, and B_3 samples by CVD method

relationship because it has continues film with few defect. The *I-V* behaviors in Fig. 3b show a approximate linear dependence of the B_1, B_2, and B_3 samples, showing that they have good conductivity resulting from the samples constituted by CuI nanoparticles with few surface defects or impurities. Among three samples, B_3 sample has the best *I-V* property due to it has continues film and good crystalline from AFM picture and XRD pattern.

Figure 4a and b show the UV-vis absorption spectra of the CuI samples in the wavelength region of 250–500 nm. CuI films by two methods have a strong optical absorption peak at 300 nm, and the optical absorption covers the wavelength region of 280–310 nm, consistent with the previously reported findings. Over 320 nm, the absorptivity of the films decreases quickly, and no other absorption peaks are observed, indicating that the CuI films are transparent to visible light range. The absorption intensity in Fig. 4a for pulling samples is almost the same height, and the bandwidth of them is about 22 nm. While the absorption intensity in Fig. 4b for CVD samples increases with deposition time; and the bandwidth is a little wide, about 25 nm. The absorption intensity of CuI film by CVD is almost two times than

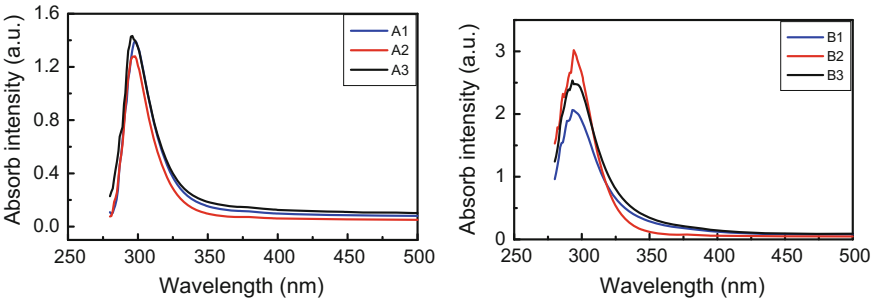

Fig. 4 The optical absorb properties of the CuI films. **a** A_1, A_2, and A_3 samples by pulling method; **b** B_1, B_2, and B_3 samples by CVD method

that of by the pulling method. The absorption spectra show that CuI film is more suitable to be a window layer for solar cells, due to its high transmission to visible light and high absorptivity in ultraviolet band that is beneficial for the improvement the efficiency of solar cells.

Summary

CuI films were prepared by pulling method and chemical vapor deposition (CVD) methods on ITO conductive glass, Si and quartz substrate. The influences of deposition condition on the structure, morphology and optoelectronic properties of CuI films were studied. We find that CuI films have smooth surface morphology, better crystallinity, and optoelectronic properties by CVD deposition of 20 min. Moreover, the prepared CuI films have strong absorption in 300 nm Ultraviolet band of light and high transmission in visible light range, showing that CuI film is more suitable as a window layer for solar cells to enhance the efficiency of solar cells.

Acknowledgements This work is supported in parts by the National Natural Science Foundation of China (No. 31570515), the Scientific Project Program of Suzhou City (No. SYN201511) and the USTS Cooperative Innovation Center for Functional Oxide Films and Optical Information.

References

1. S. Murugesan, Structural and electrical properties of CuI–Ag_2O–MoO_3–WO_3 glassy-crystalline composite solid electrolyte system. J. Non-Cryst. Solids **396–397**, 8–12 (2014)
2. L. Liu, H. Zhang, J. Li, Y. Shen, C. Wang, L. Qiu, Y. Yuan, A. Xie, Porous Fe_3O_4/CuI/PANI nanosheets with excellent microwave absorption and hydrophobic property. Mater. Res. Bull. **53**, 58–64 (2014)

3. Y. Xu, D. Chen, X. Jiao, PAM-assisted synthesis of single-crystalline CuI nanorods. Mater. Lett. **63**, 1859–1861 (2009)
4. P.M. Sirimannea, T. Sogab, M. Kunst, Observation of microwave conductivity in copper iodide films and relay effect in the dye molecules attached to CuI photocathode. J. Solid State Chem. **178**, 3010–3013 (2005)
5. P. Gao, M. Gu, X. Liu, B. Liu, S. Huang, X-ray excited luminescence of cuprous iodide single crystals: on the nature of red luminescence. Appl. Phys. Lett. **95** 221904(1–3) (2009)
6. Y. Zhou, T. Taima, T. Miyadera, T. Yamanari, M. Kitamura, K. Nakatsu, Y. Yoshida, Glancing angle deposition of copper iodide nanocrystals for efficient organic photovoltaics. Nano Lett. **12**, 4146–4152 (2012)
7. W. Sun, H. Peng, Y. Li, W. Yan, Z. Liu, Z. Bian, C. Huang, Solution-processed copper iodide as an inexpensive and effective anode buffer layer for polymer solar cells. J. Phys. Chem. C **118**, 16806–16812 (2014)
8. I. Konovalov, L. Makhova, Valence band offset at interfaces between CuI and indium sulfides. J. Appl Phys. **103** 103702(1–7) (2008)
9. S. Das, J. Choi, T.L. Alford, P_3HT: $PC_{61}BM$ based solar cells employing solution processed copper iodide as the hole transport layer. Sol. Energy Mater. Sol. Cells **133**, 255–259 (2014)
10. J.A. Christians, R.C.M. Fung, P.V. Kamat, An inorganic hole conductor for organo-lead halide perovskite solar cells. Improved hole conductivity with copper iodide. J. Am. Chem. Soc. **136**, 758–764 (2013)
11. W. Sun, H. Peng, Y. Li, W. Yan, Z. Liu, Z. Bian, C. Huang, Solution-processed copper iodide as an inexpensive and effective anode buffer layer for polymer solar cells. J. Phys. Chem. C **118**, 16806–16812 (2014)
12. H. Iimori, S. Yamane, T. Kitamura, K. Murakoshi, A. Imanishi, Y. Nakato, High photovoltage generation at minority-carrier controlled n-Si/p-CuI heterojunction with morphologically soft CuI. J. Phys. Chem. C **112**, 11586–11590 (2008)
13. S. Inudo, M. Miyake, T. Hirato, Electrical properties of CuI films prepared by spin coating. Phys. Status Solidi Appl. Mater. **210**, 2395–2398 (2013)
14. Y. Yan, Y. Liu, L. Fang, Z. Lu, Z. Li, S. Zhou, Growth of CuI buffer layer prepared by spraying method. Trans. Nonferrous Met. Soc. China **21**, 359–363 (2011)

A Thermodynamic Database of Drill Pipe Steel and Its Application in High Strength Drill Pipe Design

Shuliang Wang, Xiaohui Su, Lujiang Zhou, Chaozheng Fu, Jing Yuan, Chunyan Fu, Xin Wang and Yixiong Huang

Abstract A thermodynamic database for drill pipe steel, including Fe, Al, C, Cr, Cu, Mn, Mo, N, Nb, Ni, Si, Ti, V elements, has been developed by the calculation of phase diagrams (CALPHAD) method. The Gibbs free energies of the liquid phases were described by subregular solution model. The Gibbs free energies of the interstitial solid solution (bcc, fcc, cub, cbcc, hcp) and various types of carbonitrides were modeled by sublattice model. The thermodynamic database has been applied to calculate A3 temperature of five drill pipe steel cases, to analyze the phase equilibria and to simulate the secondary phase particles in drill pipe steel. The calculated results show that the present thermodynamic database can provide critical information for heat treatment and components design of drill pipe steel.

S. Wang · X. Su · L. Zhou · C. Fu · J. Yuan · C. Fu (✉) · X. Wang (✉)
School of Materials Science and Engineering, Southwest Petroleum University, 610500 Chengdu, China
e-mail: fcyan1975@126.com

X. Wang
e-mail: xin.wang@swpu.edu.cn

S. Wang
e-mail: wsliang1465@126.com

X. Su
e-mail: xhsu92@qq.com

L. Zhou
e-mail: 1306352897@qq.com

C. Fu
e-mail: fchzh1992@126.com

J. Yuan
e-mail: 308199148@qq.com

S. Wang · Y. Huang
College of Materials and Fujian Provincial Key Laboratory of Materials Genome, Xiamen University, 361005 Xiamen, China
e-mail: hyx@xmu.edu.cn

Y. Han (ed.), *Advances in Energy and Environmental Materials*,
Springer Proceedings in Energy, https://doi.org/10.1007/978-981-13-0158-2_25

Keywords Drill pipe steel · CALPHAD · Thermodynamic database
Heat treatment

Introduction

Drill pipes are main tools for oil and gas drilling. With the increase of well depth, the work conditions are becoming more and more harsh, and the drill pipe will bear more load during operation. The failure accident of oil drill pipe occurred frequently in such a harsh drilling environment, and hence caused a different degree of downtime and greater economic losses. Therefore, higher strength is required for the drill pipe materials to ensure the drilling quality and safety as well as the work efficiency [1]. At present, ordinary API (American Petroleum Institute) steel pipes have been unable to meet the requirements under these conditions [2]. Developing new high-strength drill pipes steel is very necessary.

The development of most traditional high-strength drill pipe steel uses "trial-and-error" method, which expends a lot of manpower and material resources. Moreover, the research and development cycle is relatively long, with high cost and inefficiency. In June 2011, the United States proposed "Materials Genome Initiative for Global Competitiveness" [3], in which, building a database based on the basic data such as thermodynamic and kinetic parameters and reducing reliance on physical experiments through powerful computational analysis can greatly shorten the development cycle of new materials. Method of CALPHAD [4] is based on thermodynamics, and maximizes the use of experimental data. More complex phase diagram can then be calculated by using the computer technology. The advantage of CALPHAD is that it can predict complex system by studying simple analogues, using mathematical processing such as extrapolation. It can also easily calculate various phase diagrams, such as steady-state phase diagram, metastable phase diagram, thermodynamic phase diagram, e.t. At present, steel metallurgy is one of the most successful applications of CALPHAD method.

In this study, a thermodynamic database (Fe–Al–C–Cr–Cu–Mn–Mo–N–Nb–Ni–Si–Ti–V) for drill pipe steel has been developed by collecting a large amount of thermodynamic evaluation data using the CALPHAD method. Based on this thermodynamic database, the related simulation calculation was carried out. By comparing with the experimental results of the heat treatment process of drill pipe steel materials as well as the precipitation of the second phase particles, it is further proved that this thermodynamic database can be used as an effective guide for the development of drill pipe steel material.

Development of Thermodynamic Database for Drill Pipe Steel

In this study, the thermodynamic database (Fe–Al–C–Cr–Cu–Mn–Mo–N–Nb–Ni–Si–Ti–V) for drill pipe steel covers all Fe–X (Al, C, Cr, Cu, Mn, Mo, N, Nb, Ni, Si, Ti, V) binary systems, some important ternary systems and multivariate systems, as shown in Table 1. The thermodynamic information of the binary, ternary and multivariate systems contained in the database is derived from the relevant evaluation literature. The Gibbs free energy function of the pure component involved in this study is taken from the SGTE pure component thermodynamic database [5].

In this alloy system, the Gibbs free energies of the liquid phases were described by subregular solution model [6]. Considering the solid solubility of C and N atoms, the free energy of the solid solution phases (bcc, fcc, cub, cbcc, hcp) [7] and the non-stoichiometric carbon-nitrogen compounds M(C, N) and M_2(C, N) containing solid solution were described by double sub-lattice model [8]. For the phases of cementite, Ksi carbides, M_3C, M_3C_2, M_5C_2 and M_7C_3, the Gibbs free energies were described by double sub-lattice models, whereas those of the $M_{23}C_6$ phase [9] and M_6C phase [10] were described by three sub-lattice and four sub-lattice model respectively. Table 2 shows the thermodynamic model of each major phase in the alloy system.

Table 1 Thermodynamic database of drill pipe steel

Systems	Elements (X)
Fe–X binary	Al, C, Cr, Cu, Mn, Mo, N, Nb, Ni, Si, Ti, V
Fe–C–X ternary	Cr, Cu, Mn, Mo, N, Nb, Ni, Si, Ti, V
Fe–Ni–X ternary	Cu, Mo, Nb, Si, Ti, V
Fe–Cr–X ternary	Mn, N, Nb, Ni, V
Fe–N–X ternary	Mn, Nb, Ti, V
Fe–Ti–X ternary	Nb, V
Fe–Mn–X ternary	Nb, Si
Fe–Cr–C–X quaternary	V, Mo Ni, Mn
Fe–Cr–Mn–X quaternary	V, Nb
Fe–Ti–C–X quaternary	Nb
Fe–Mn–Nb–X quaternary	N
Fe–Al–Mn–X quaternary	Si
Multicomponent	Fe–Nb–Ti–C–N

Table 2 Thermodynamic model of each major phase in the alloy system

Phases	Thermodynamic models
Liquid	(Fe, Al, C, Cr, Cu, Mn, Mo, N, Nb, Ni, Si, Ti, V)$_1$
bcc	(Fe, Al, Cr, Cu, Mn, Mo, Nb, Ni, Si, Ti, V)$_1$(C, N, Va)$_3$
Fcc, M(C, N)	(Fe, Al, Cr, Cu, Mn, Mo, Nb, Ni, Si, Ti, V)$_1$(C, N, Va)$_1$
cbcc, cub	(Fe, Al, Cr, Mn, Nb, Ni, Si, Ti, V)$_1$(C, N, Va)$_1$
Hcp, M_2(C, N)	(Fe, Al, Cr, Cu, Mn, Mo, Nb, Ni, Si, Ti, V)$_1$(C, N, Va)$_{0.5}$
Ksi	(Fe, Cr, Mo)$_3$(C)$_1$
Cementite	(Fe, Cr, Mn, Mo, Nb, Ni, V)$_3$(C)$_1$
M_3C_2	(Fe, Cr, Mn, Mo, V)$_3$(C)$_2$
M_5C_2	(Fe, Mn, Nb, V)$_5$(C)$_2$
M_7C_3	(Fe, Cr, Mn, Mo, Nb, Ni, V)$_7$(C)$_3$
$M_{23}C_6$	(Fe, Cr, Mn, Nb, Ni, V)$_{20}$(Fe, Cr, Mn, Mo, Nb, Ni, V)$_3$(C)$_6$
M_6C	(Fe, Ni)$_2$(Mo)$_2$(Fe, Mo, Ni)$_2$(C)$_1$

Application of Thermodynamic Database for Drill Pipe Steel

Drilling rods are subjected to alternating stress of drilling rigs and rock formations during drilling operations. Thus, the toughness of drill pipe materials is a prerequisite for ensuring the safety and service life of drill pipe. The microstructure of the drill pipe is an important factor affecting the mechanical properties of the drill pipe. At present, most of the micro-organizations of drill pipe products are tempered sorbite, and the heat treatment process is quenching together with high temperature tempering. In order to obtain a higher strength, some manufacturers use a quenching and low temperature tempering heat treating, where the low-carbon martensite/bainite (austenite, ferrite, etc.) duplex microstructure are obtained.

Design of Heat Treatment Process. This study obtained some typical high-strength drill pipe steels composition and heat treatment process parameters from literature [11–13], as shown in Table 3. The value of A3 temperature of the drill pipe in Table 3 was calculated by the phase diagram calculation software-Pandat [14] using the thermodynamic database of the drill pipe established in this study. Because that phase transition is always carried out under non-equilibrium conditions in practical heat treatment process, there are generally different degrees of hysteresis. That is to say, the actual phase change temperature Ac3 at the time of heating is higher than the equilibrium phase transition temperature Ac3. For the alloy steel, because the diffusion of alloying elements in the austenite is difficult than carbon, the quenching temperature is generally 50–100 °C above Ac3 [15]. It can be seen from Table 3 that the calculated results obtained from the thermodynamic database established in this study can provide very effective guidance for the heat treatment process design of drill pipes. For example, according to the phase diagram calculated from the database, the heat treatment of

Table 3 Chemical composition (wt%), quenching temperature [11–13] and calculated A3 temperature of high-strength drill pipe cases

Drill pipe case	C (%)	Si (%)	Cr (%)	Mn (%)	Mo (%)	Ni (%)	V (%)	Nb (%)	Ti (%)	Al (%)	N (%)	Quenching temperature (°C)	A3 calculated temperature (°C)
1#	0.34	0.21	0.04	1.55	–	0.016	0.098	–	0.026	–	0.006	850	775
2#	0.32	0.21	0.04	1.54	–	0.015	0.045	–	–	–	0.007	850	775
3#	0.25	0.32	1.12	1.02	0.98	–	0.09	0.03	–	–	–	920	820
4#	0.26	0.27	1.02	1.00	0.34	–	0.07	–	–	–	–	880	800
5#	0.20	0.24	0.85	0.82	0.45	–	0.10	–	–	–	–	910	830

quenching, tempering and other temperatures can be designed. Composition of materials with different performance requirements can also be designed. As well as the process reference provided the design for new materials.

Martensite-ferrite duplex steel is based on ferrite, in which martensite disperses in the matrix. Compared with other high-strength steel, duplex steel has excellent strength and toughness matching. The structure of the drill pipe material can be adjusted by the complexation treatment to obtain the optimal strength and toughness.

Luo et al. [16, 17] studied complexation treatment on S135 drill pipe through the sub-temperature quenching heat treatment, and obtained a dual phase structure. Compared with the original tempered sorbite structure, the strength of drill pipe after complexation treatment has a significant improvement, while the impact toughness has only a slight decrease. In this study, the equilibrium phase diagram of drill pipe steel with containing Fe-0.32 wt% C-0.24 wt% Si-0.85 wt% Mn-1.02 wt% Cr-0.06 wt% Ti-0.06 wt% Cu [16, 17] and the precipitation process of each phase with temperature were calculated by using the above-obtained thermodynamic database, as shown in Figs. 1 and 2. From the calculated results, it can be seen that the temperatures of A1 and A3 are 723 and 785 °C respectively, while the temperatures of Ac1 and Ac3 of the drill pipe material in literatures [16, 17] are 743 and 813 °C,

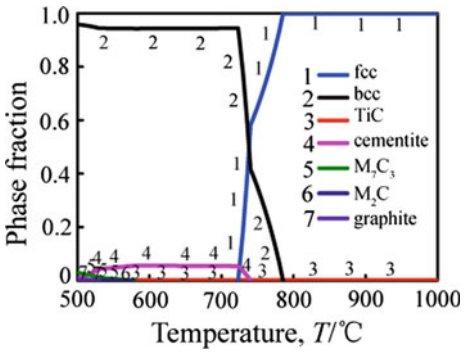

Fig. 1 Calculated thermodynamic equilibrium phase diagram of S135 drill pipe steel

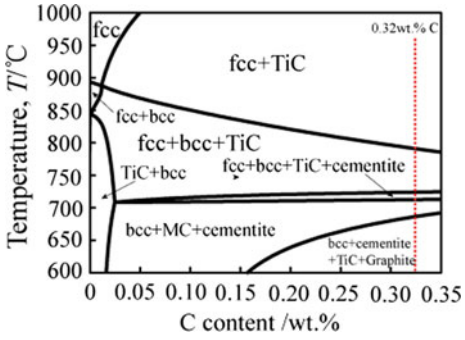

Fig. 2 Temperature dependence of the precipitation of phases in S135 drill pipe steel

respectively. Taking into account the actual heating conditions and the different degree of hysteresis, the calculated results are in rather acceptable accordance with experimental results, and can provide a theoretical reference for the complexation design of the drill pipe. It is also seen from Figs. 1 and 2 that a small amount of the second phase carbide particles existing in the two-phase region of the austenite and ferrite, which is due to the fact that the addition of trace element Ti in the steel and the element is liable to form a second phase particles with high melting point and good stability [18].

Analysis of the Precipitation of the Second Phase Carbonitride Particles. Trace alloy elements (Ti, V, Nb, etc.) can easily form small carbonitride with C and N atoms, which can effectively prevent the growth of austenite grain and refine the organization, and grain as well as facilitate the precipitation. Taking account the strengthening effect of trace alloy, drill pipe steel often requires the addition of Ti, V, Nb and other trace elements to improve the strength. Zhu et al. [11] studied the precipitation of the second phase carbonitride particles of V and Ti in the drill pipe alloy. The composition of the test steel is shown in Table 3 as the #1 and #2 samples. #1 test steel contains Ti and V, and #2 test steel only contains V.

Based on the composition of #1 and #2 test steels in Table 3, the thermodynamics calculation of #1 and #2 test steels was carried out by using the thermodynamics database for drill pipe alloy. Figure 3 is the temperature dependence of phase precipitation quantity of the tested steel in reference [11]. The calculated results show that there is no difference in the phase change between #1 and #2, and the calculated value of A3 is 775 °C. Moreover, it can be seen from Fig. 3 that the two test steels have second phase carbonitride particles in a large temperature range.

Figure 4 shows the temperature dependence of the Ti, V, C, N contents in the M(C, N) carbonitrides. It can be seen that the M(C, N) carbonitrides in the #1 test steel are (Ti, V)(C, N) particles. As the temperature increases in the austenite region, the content of Ti and N in the M(C, N) carbonitride increased, whereas the

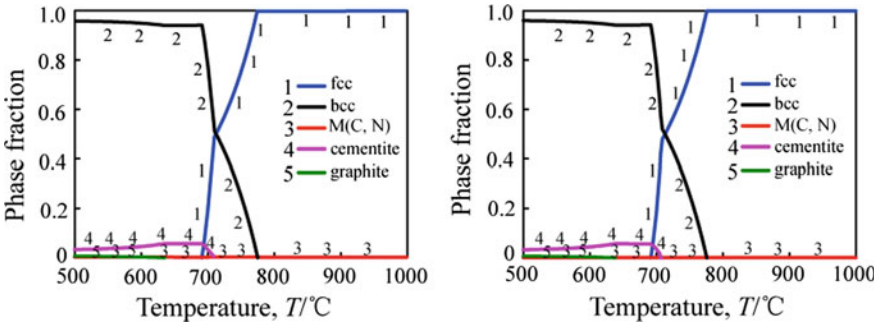

Fig. 3 Temperature dependence of the phase precipitation quantity of tested steel in Ref. [13]

content of V and C decreased. This is due to the low stability of vanadium-rich carbon and nitrogen compounds, which will dissolve in the austenite region with high temperature, while Ti(C, N) is highly stable and difficult to dissolve [18]. And it can be seen from Fig. 4b that the M(C, N) carbonitrides in the #2 test steel are V (C, N) particles. As the temperature increases, the content of N in the M(C, N) carbonitride increased, whereas the content of C decreases and the content of V basically remains unchanged. This is due to the large difference in solubility between VC and VN in austenite. The solubility product of VC is two orders of magnitudes larger than that of VN [18], therefore VC is easier to dissolve when temperature increases.

Figure 5 is the temperature dependence of the carbonitrides quantity in #1 and #2 test steel. As can be seen from Fig. 5, the #1 test steel contains obviously more carbon-nitrogen compound particles than the #2 test steel at the same temperature, and the content of carbonitride in both test steels gradually reduced with the increase of temperature. The carbonitrides particles in the #1 test steel appear to have higher melting temperatures. This is because the more the microalloying element (V, Ti) content, the greater the number of second-phase particles in the steel. Besides, in the austenitizing heating process, the second phase of carbonitride particles will be dissolved. The content of Ti, V and C in the #1 test steel is higher than that of the #2 test steel. Therefore, it is concluded that the carbonitride content in the #1 test steel is high. Since the stability of V(C, N) is much lower than that of (Ti, V)(C, N), it can be dissolved at a relatively lower temperature [11, 18]. When the temperature increases, the carbonitrides in both #1 test steel and #2 test steel are decreased, while the Ti(C, N) compounds with high thermal stability remained in the #1 test steel. This explains the existence of a small amount of carbonitride phase in the high temperature austenite region.

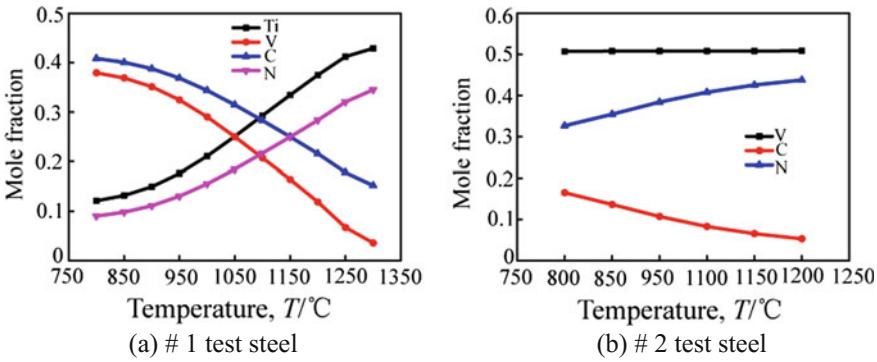

Fig. 4 Temperature dependence of the Ti, V, C, N contents in the M(C, N) carbonitrides

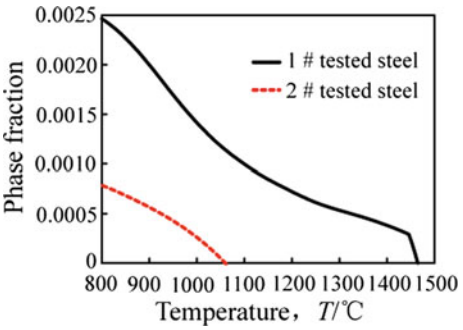

Fig. 5 Temperature dependence of the carbonitrides quantity in #1 and #2 test steel conclusions

Conclusions

A thermodynamic database for drill pipe steel, including Fe, Al, C, Cr, Cu, Mn, Mo, N, Nb, Ni, Si, Ti, V has been developed by using the calculation of phase diagrams (CALPHAD) method. The Gibbs free energies of liquid phase, solid solution phase and carbonitride phase were described by a reasonable thermodynamic model. Compared with those of the drill pipe cases, the calculation results of the thermodynamics database were found to be able to provide a very effective theoretical guide for the heat treatment process of the steel material for the drill pipe. The thermodynamic database established in this study provides an important theoretical guidance for the further development and design of new high strength drill pipe, including the composition of high strength drill pipe and heat treatment process.

Acknowledgements This work was supported by the Innovative training program (KSZ16121) of Southwest Petroleum University, and open fund of Fujian Provincial Key Laboratory of Materials Genome (Xiamen University) and National Natural Science Foundation of China (51374180). The authors acknowledge funding from the Department of Education of Sichuan Province (17ZA0419) as well as scientific research starting project funding (2017QHZ020) of Southwest Petroleum University.

References

1. Z.Q. Li, S.L. Lv, C.X. Yang, Preventing high strength casing from facture and standardization. Phys. Test. Chem. Anal. (Part A: Physical Testing) **50**, 903–906 (2014)
2. API SPEC 5DP-2009, Specification for drill pipe, 5th edn, Washington DC, (2001)
3. Materials Genome Initiative for Global Competitiveness. USA National Science and Technology Council, (2011)
4. L. Kaufman, H. Bernstein, *Computer calculation of phase diagram* (Academic Press Inc., New York, 1970)
5. A.T. Dinsdale, SGTE Data for Pure Elements. Calphad **15**, 317–425 (1991)
6. O. Redlich, A.T. Kister, Algebraic representation of thermodynamic properties and the classification of solutions. Ind. Eng. Chem. **40**, 345–348 (1948)

7. M. Hillert, L.I. Staffansson, The regular solution model for stoichiometric phases and ionic melts. Acta Chem. Scand. **24**, 3618–3626 (1970)
8. A. Kroupa, J. Havránková, M. Svoboda, M. Coufalová, J. Vřešt'Ál, Phase diagram in the iron-rich corner of the Fe-Cr-Mo-V-C system below 1000 K. J. Phase Equilib. **22**, 312–323 (2001)
9. C. Qiu, An analysis of the Cr-Fe-Mo-C system and modification of thermodynamic parameters. ISIJ International **32**, 1117–1127 (1992)
10. J.O. Andersson, A thermodynamic evaluation of the Fe-Cr-C system. Metallurgical Transactions A **19**, 627–636 (1988)
11. M.Y. Zhu, Z.F. Lu, F. Huang et al., Effect of secondary phase particles on V-Timicroalloy steel of oil country tubular goods (OCTG) mechanical properties. Heat Treatment of Metals **36**, 70–73 (2011)
12. P. Zhao, J. Yu, China Patent CN201410558878, (2015)
13. Y. Jiang, C.Y. Zhang, J.X. Zhou, et al., China Patent CN201010286595, (2011)
14. S.L. Chen, S. Daniel, F. Zhang et al., The PANDAT software package and its applications. Calphad **26**, 175–188 (2002)
15. Z.Y. Cui, Y.C. Tan, *Metallurgy and heat treatment*, 2nd edn. (Mechanical Industry Press, Beijing, 2013)
16. S.J. Luo, R. Wang, K. Zhao, Effect of dual phase treatment on microstructure and mechanical properties of S135 drill pipe steel. Trans. Mater. Heat Treat. **34**, 118–122 (2013)
17. S.J. Luo, R. Wang, L.L. Huang et al., Effect of subcritical quenching on microstructure and mechanical properties of drill pipe steel. Mater Mech. Eng. **37**, 35–38 (2013)
18. R. Lagneborg, T. Siwecki, S. Zajac et al., The role of vanadium in microalloyed steels. Scandanavian J. Metall. **28**, 186–241 (1999)

Effect of Shape of Pore Forming Agent on Structure and Properties of Aluminum Foams

Bensheng Huang, Xing Zhao, Chenglong Gong and Ziyu Wang

Abstract The aluminum foams was prepared by powder sintering method. Internal pores were made of spherical urea particles or bar-shaped urea particles, and the influence of this factor was studied. The internal structure and composition of the aluminum foams were measured by SEM and XRD, then the effects of the shape of pore forming agent on the porosity, compressive property and energy absorption efficiency were researched. Finally, the micro-residual stress in the aluminum foams was calculated. The results show: the porosity of the aluminum foams is slightly lower than the volume fraction of urea particles after the sintering process; the maximum micro-residual stress of aluminum foams with spherical urea particles is 47.22 MPa and the maximum micro-residual stress of aluminum foams with bar-shaped urea particles is 57.38 MPa; the aluminum foams with spherical urea particles is more stable than the others, the compressive strength of the aluminum foams with spherical urea particles is also stronger; when entering the platform area, the energy absorption efficiency of aluminum foams with spherical urea particles is obviously higher, and its maximum efficiency of energy absorption is 71.9%.

Keywords Aluminum foams · Urea particle · Compression properties
Micro residual stress

B. Huang (✉) · X. Zhao · C. Gong · Z. Wang
School of Materials Science and Engineering,
Southwest Petroleum University, Chengdu, China
e-mail: hbslxp@163.com

X. Zhao
e-mail: 344633353@qq.com

C. Gong
e-mail: gcllyh1992@qq.com

Z. Wang
e-mail: 602298017@qq.com

Y. Han (ed.), *Advances in Energy and Environmental Materials*,
Springer Proceedings in Energy, https://doi.org/10.1007/978-981-13-0158-2_26

Introduction

Foam metal is a new materials which consists of metal frameworks and pores. Compared with the dense metal, it has many advantages, including high porosity, good acoustic properties, good resistance of impact, high specific surface area and great damping properties. In the 1940s, S. Sonik had researched foam metal at first, with the development of foam metal, it has been widely used in aerospace, automobile manufacturing, biomedicine, field of energy and so on [1–3]. Among the foam metal, aluminum foams is a new type with rapid developing in recent years [4], it also has many advantages, such as lower density, strong capacity of energy absorption, great corrosive resistance and so on [5]. There are many preparation methods to manufact aluminum foams, including foaming method of molten aluminum, electrodeposition, casting, powder sintering method [6–8]. Powder sintering process is simpler comparing with these methods, because the shape and size of pores can be acquired by adding the corresponding pore forming agent. Therefore, the aluminum foams was prepared by powder sintering method in this paper. The effects of different shapes of pore forming agent (urea particles) on the stability of structure were studied, and the porosity, compressive properties, internal micro—residual stress and energy absorption efficiency were measured.

Materials and Experiments

Materials. The base metal is industrial pure aluminum, purity $\geq 99\%$, the particle size is 325 mesh; there are two different shapes of urea particles acting as pore forming agent: the diameter of spherical urea particles is about 1.60–2.00 mm; the length of bar-shaped urea particles is about 1.50–2.10 mm, the width is about 0.40–0.70 mm.

Experiments. At first, the urea particles are dried, then mix aluminum powder with spherical urea (denoted by S) and bar-shaped urea (denoted by B) at different ratios of volume, as shown in Table 1.

Three specimens were prepared under each parameter, the parameter of agitators was 100 r/min; the mixed powder was filled into a mold and its size is Φ40 mm 40 mm, then the mixed powder was pressed on a hydraulic machine, the pressure is 300 MPa; the green was placed into water (80 °C) for 4 h. In addition, the water was replaced every 1 h; finally, the performs were vacuum sintered (1×10^{-2}, 580 °C) for 1 h.

Table 1 Volume ratio of urea (%)

No	1	2	3	4	5	6
Type	S	S	S	B	B	B
Volume	50	60	70	50	60	70

The porosity of aluminum foams was measured by density method, the equation as follows:

$$\theta = \frac{1}{\rho}\left(1 - \frac{m}{v}\right) \times 100\% \tag{1}$$

(θ: the porosity; m: the quality of aluminum foams; v: the volume of aluminum foams; ρ: the density of pure aluminum, 2.70 g/cm^3).

The pore morphology of *No*. 1 and *No*. 4 specimens was observed by SEM; the phase was analyzed by XRD; the maximum micro residual stress can be used to measure the stability of aluminum foams, the highest diffraction peak was found in XRD, taking the corresponding diffraction angle, two sets of specimens were estimated by Eq. (2), as shown below:

$$\sigma_{\text{micro}} = \frac{E\pi\beta\text{ctg}\theta}{180^\circ \times 4} \tag{2}$$

(β: Half-width of Spectrum Widening; E: Elastic modulus of the material; θ: diffraction angle).

Finally, the specimens were worked θ and its size was Φ30 mm × 30 mm, *No*. 1 and *No*. 4 specimens were compressed by universal materials testing machines (the loading speed: 2 mm/min), then stress-strain curve was acquired; the compressive properties of materials can reflect its capability of energy absorption, the energy absorption efficiency was indicated by E in engineering [9], the equation of energy absorption efficiency is as follows:

$$E = \frac{\int_0^l \sigma d_\varepsilon}{\sigma_{\max} l} \tag{3}$$

(E: energy absorption efficiency; l: the maximum value of strain; $\sigma_{\max}$: the maximum value of stress).

Results and Discussion

The Results of Porosity. The porosity is an important parameter to measure the structure and properties of aluminum foams, the value of porosity will directly affect properties of aluminum foams, such as compression properties, energy absorption efficiency and electrical conductivity [10]. According to Eq. (1), the porosity was measured. The test results are averaged, and the results are shown in Fig. 1.

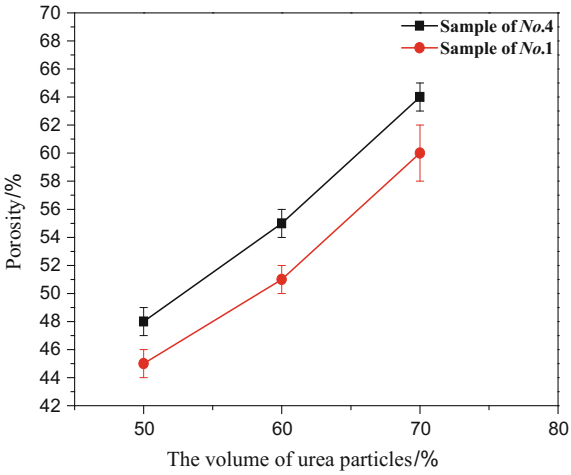

Fig. 1 Porosity change curve

It can be found from Fig. 1 that the porosity of the two specimens was slightly lower than the volume of pore forming agent, which indicated that the volume change of aluminum powder was less than the volume change of urea particles after pressing process. The compressive strength of urea particles is lower than that of aluminum powder, so it is more smoothly to deform. With the larger volume ratio of urea particles, the larger the ΔV value (that is the difference between the volume ratio of the initial urea particles and the porosity). When the amount of urea particles increases, it means that the content of the base metal would reduce, since the compressive strength of the urea particles is lower than that of aluminum powder. There is not enough supporting effect of the base aluminum powder, when the pore forming agent is removed, the tendency of pores collapse is serious and the porosity will decrease. In the case of adding the same amount of urea particles, the porosity of specimens which added bar-shaped is higher than the porosity of specimens which added spherical urea particles. During the pressing process, the force area of spherical urea particles is larger than bar-shaped urea particles. Meanwhile, the bar-shaped urea particles tend to be placed in parallel in the mixing process. The deformation of spherical urea particles is larger in the case of same pressure, so the porosity of aluminum foams which be formed by spherical urea particles is lower.

Microstructure. The structure of *No*. 1 specimen and *No*. 4 specimen had been observed by SEM technology, the direction of observation is perpendicular to pressing direction, the results show in Fig. 2.

The microstructure of specimen which was formed by spherical urea particles as shown in Fig. 2a, it can be found that the shape of pores is elliptical, while the reason is that the spherical urea particles are deformed during the pressing process. In sintering process, the urea particles were heated and the gas produced by decomposition escaped matrix, so the smaller pores occurred in wall. It can be found from Fig. 2b that the pores which was formed by bar-shaped urea particles

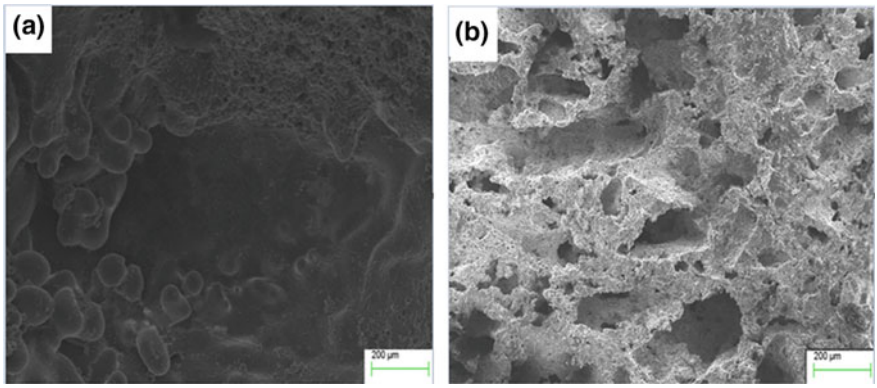

Fig. 2 SEM micrographs of aluminum foams. **a** Specimen of *No*. 1; **b** Specimen of *No*. 4

are irregular or bar-shaped, but the bar-shaped pores are more than irregular pores. This phenomenon means that the bar-shaped urea particles tend to be placed in parallel in mixing process, the size of bar-shaped pores is close to the size of bar-shaped urea particles, and the production of irregular pores is due to the factor that the bar-shaped urea particles are broken off by pressure.

Phase and Micro Residual Stress. The phase of *No*. 1 specimen and *No*. 4 specimen had been analyzed by XRD technology, the results shown in Fig. 3.

By comparing the standard PDF card, it shows that the main phase of *No*. 1 specimen and *No*. 4 specimen are Al and Al_2O_3, indicating that a part of matrix has been oxidized, in addition, urea do not remain inside the matrix after sintering process. It can be seen form Fig. 3 that there are lots of diffraction peaks in XRD patterns, it means that the dense sintered body does not be completed after sintering process, there are still some aluminum powder inside, the grain orientation is different, when the Bragg equation is satisfied, the diffraction peaks will appear.

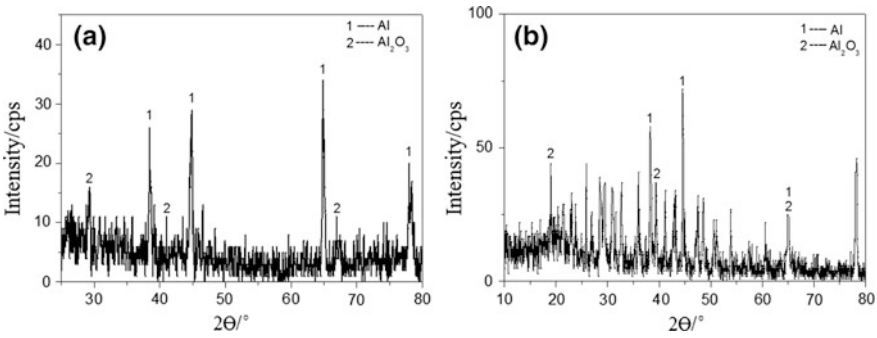

Fig. 3 XRD analysis of the samples. **a** Sample of *No*. 1; **b** Sample of *No*. 4

Due to the existence of micro residual stress, it can change interplanar distance and X-ray diffraction line is broadened. Taking the diffraction angle which corresponds to the highest diffraction peak, the maximum micro residual stress was calculated by Eq. (2) [11]. The results show that the maximum micro residual stress of *No*. 1 specimen is 47.22 MPa, the maximum micro residual stress of *No*. 4 specimen is 57.38 MPa. It indicates that the force loading at spherical urea particles is more uniformly, the bar-shaped urea particles tend to be placed in parallel. Therefore, the force area of bar-shaped urea particles is smaller and the pressure consumption of spherical urea particles is more by changing volume. In addition, there are lots of sharp corners in bar-shaped urea particles, it is easy to produce stress concentration. The stability of specimens which be formed by spherical urea particles is stronger in the case of same pressure.

Compression Properties and Energy Absorption Efficiency. Aluminum foams is considered a reliable structural material, and compression properties is an important index of its mechanical properties. The *No*. 1 specimens and *No*. 4 specimens (each specimen contains three parallel testing group) had been tested, the results were averaged, the stress-strain curve as shown in Fig. 4.

It can be seen from Fig. 4 that the two sets of curves are roughly divided into three regions: elastic region, platform region and dense region. When the specimens are in elastic region, it produces elastic deformation; with the increasing pressure, the base structure of aluminum foams begins to deform, the stress-strain curve begins to show a non-linear rising; entering the dense region, the base structure has been destroyed, the pores have collapsed and densified, the stress-strain curve has risen sharply, these three stages are not completely separate. It can be seen from Fig. 4 that the curve is not smooth and likes a jagged, it indicates that compression process is collapse–dense–dense. In compression process, the transmission of pressure has time difference, and the pressure will be consumed in the aluminum foams. This factor must cause pressure fall, the pressure will gradually decline from

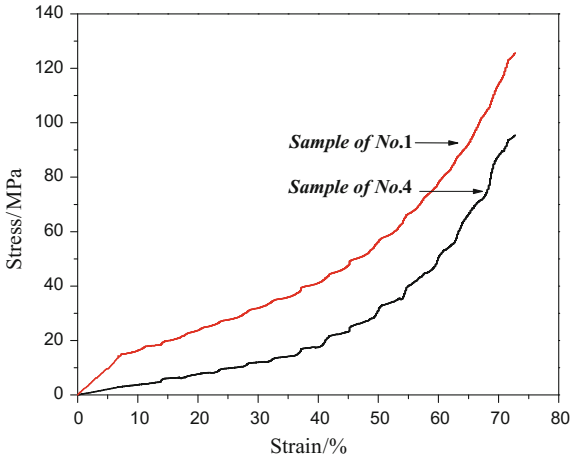

Fig. 4 Stress-strain curve of the *No*. 1 specimens and *No*. 4 specimens

surface to interior, so the curve likes s jagged. From Fig. 4, it can be found that elastic deformation peak of aluminum foams which was formed by spherical urea particles is higher than the others. According to Fig. 1, the porosity of the aluminum foams which was formed by spherical urea particles is lower. When the porosity reduces, the pores in matrix reduces accordingly, and the bearing capacity of aluminum foams becomes stronger, therefore, a greater stress can be required. This is a reason that the stress-strain curve of aluminum foams which was formed by spherical urea particles is located above. According to Fig. 2, the internal structure of aluminum foams which was formed by spherical urea particles is more smooth. Through the calculation of the maximum micro residual stress, it shows that the maximum micro residual stress of aluminum foams which was formed by spherical urea particles is lower and its stability is stronger.

At present, the application of aluminum foams in the field of energy absorption has gradually increased. In the 1980s, Gibson [12] had proposed that mechanical properties of aluminum foams has important influences in matrix materials properties, relative density and the structure of pores. Ginson and Ashby [13] found that the pores orientation, the distribution of the solid phase in the matrix materials, the density gradient, the defects in the matrix and the nonconformity of the pores have a significant effect on the mechanical properties of foam metal by establishing the mechanical model. The energy absorption mechanism of aluminum foams is through the yield and deformation of its own pores structure to absorb external energy, so the energy absorption properties of aluminum foams is built on the its mechanical properties.

According to the Eq. (3), the *No*. 1 specimen and *No*. 4 specimen (each specimen contains three parallel testing groups) have been tested to establish its energy absorption efficiency, the results show in Fig. 5.

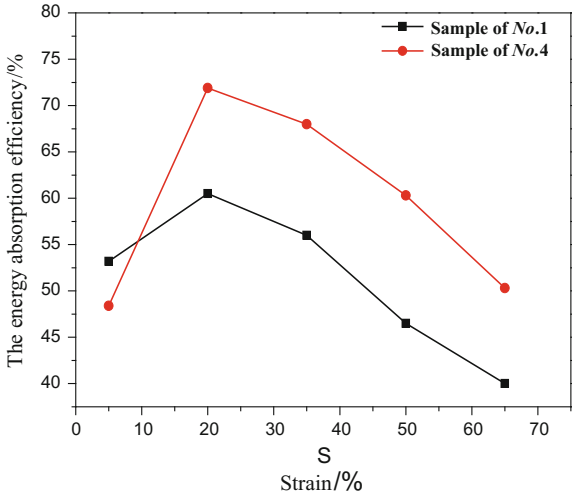

Fig. 5 Energy absorption efficiency curve

It can be seen from Fig. 5 that the energy absorption efficiency of aluminum foams which was formed by spherical urea's particles is lower than the aluminum foams which was formed by bar-shaped urea particles when the amount of deformation is 5%. There is a crossing point in both curves when the amount of deformation is between 5 and 20%, and the energy absorption efficiency curve of the aluminum foams which was formed by spherical urea particles is rising faster. The deformation type of aluminum foams is elastic deformation, meanwhile, the main factor is the content of matrix metal at this time. According to the previous analysis, it shows that the porosity of aluminum foams which was formed by bar-shaped urea particles is slightly higher when the volume ratio is the same, this factor is conducive to the capacity of energy absorption, so its energy absorption efficiency is higher. Increasing the amounts of deformation is, the curve enters to the platform area, the deformation type of aluminum foams is not elastic deformation but plastic deformation at the moment. Due to the micro residual stress of the aluminum foams which was formed by bar-shaped urea particles is higher and the stability of the pores structure is low, therefore, the pores are easy to collapse when the plastic deformation occurs. In contrast, the micro residual stress of the aluminum foams which was formed by spherical urea particles is lower and the stability of oval pores is better, it is conducive to the capacity of energy absorption, so the energy absorption efficiency curve of the aluminum foams which was formed by spherical urea particles is rising faster. When the amounts of deformation is larger than 20%, it can be seen that the energy absorption efficiency curve of the both curves is drastically decreasing, the reason is that the internal pores of aluminum foams is gradually collapsed.

Conclusions

(1) The porosity of aluminum foams is slighter lower than that of the initial volume ratio of urea particles. When the volume ratio of urea particles is the same, the porosity of aluminum foams formed by bar-shaped urea particles is slightly higher than that of aluminum foams formed by spherical urea particles;
(2) The maximum micro residual stress of aluminum foams which was formed by spherical urea particles is 47.22 MPa, while the maximum micro residual stress of aluminum foams which was formed by bar-shaped urea particles is 57.38 MPa;
(3) The compression properties of aluminum foams formed by spherical urea particles is greater than those of aluminum foams formed by bar-shaped urea particles. When the curve is entering the platform area, the energy absorption efficiency of aluminum foams formed by spherical urea particles is significantly higher, the peak of the energy absorption efficiency is 71.9%.

Acknowledgements This work was financially supported by Key Laboratory of Ministry of Education of Oil & Gas Equipment (Fund Number OGE201402-02) and Key Projects of Sichuan Provincial Education Department (Project Number 15ZA0057).

References

1. H. Tang et al., Effect of pore structure on performance of porous metal fiber materials. Rare Metal Mater. Eng. **44**(8), 1821–1826 (2015)
2. L.-P. Lefebvre, J. Banhart, D.C. Dunand, Porous metals and metallic foams: current status and recent developments. Adv. Eng. Mater. **10**(9), 775–787 (2008)
3. S. Benjamin, U.S. Patent 2,434,775, 1948
4. L. Wang et al., Study on preparing techmque of the open pores foam aluminum using investment casting process. Foundry **20**(1), 8–10 (1999)
5. P. Liu et al., Applications of porous metal materials. J. Funct. Mater. **32**(2), 12–15 (2001)
6. S. Wang, Analysis of production process and application of foamed aluminum. Nonferrous Metals Proc. **3**, 11–13 (2016)
7. B. Jiang, Y. Liu, Y. Si, Properties of open cell aluminum foams prepared by space-holder method. Heat Treat. Metals. **32**(3), 33–35 (2007)
8. A. Antenucci et al., Improvement of the mechanical and thermal characteristics of open cell aluminum foams by the electrodeposition of Cu. Mater. Des. **59**, 124–129 (2014)
9. Q.Z. Wang et al., Compressive behaviors and energy-absorption properties of an open-celled porous Cu fabricated by replication of NaCl space-holders. J. Mater. Process. Tech. **211**(3), 363–367 (2011)
10. N. Nciri, Cellular metals manufacturing. Am. Machinist **6**(3), 117–126 (2014)
11. B.D. Cullity, W.W. John, Elements of X-ray diffraction. Am. J. Phys. **25**(6), 394–395 (1957)
12. F. Han, Z. Zhu, The mechanical behavior of foamed aluminum. J. Mater. Sci. **34**(2), 291–299 (1999)
13. J. Hunt, U.S. Patent 4,258,889, 1981

Corrosion Inhibition Performance of Special Brass Alloy with Different Heat Treatment

Zhou Fan, Ziyu Wang, Chunfeng Yang, Taiyu Huang and Minan Ren

Abstract In the process of oil and gas extraction and production, a large amount of corrosive ion water containing $H_2S\backslash CO_2\backslash Cl$ is often produced in oil and gas wells, causing serious corrosion to the oil casing. The release of electrons by the activity of metals, improve the nature of the produced water, electrochemical corrosion protection is one of the effective anti-corrosion methods, research on new anti-corrosive alloy material to prevent oil casing corrosion, has important theoretical and practical significance. Electrochemical tests and Scanning electron microscopy (SEM) used in this article to were studied the properties and morphology of the samples. The polarization curves and impedance spectra of N80 steel under different experimental conditions were tested. The microstructure after corrosion and the effect of new special brass alloy on the corrosion of N80 steel in oil and gas field production were studied. And the difference of corrosion inhibition effect of special brass in different heat treatment state was investigated. The result shows that the new special brass alloy can improve the corrosion potential of N80 steel in oil and gas field production water, reduce the corrosion current density and the phenomenon of surface pitting. It can be found that special brass alloy can effectively mitigate the corrosion of N80 steel. In addition, the solid solution alloy is more beneficial to retard the corrosion of N80 steel.

Z. Fan (✉) · Z. Wang · T. Huang · M. Ren
School of Materials Science and Engineering,
Southwest Petroleum University, Chengdu, China
e-mail: fanzhou505@163.com

Z. Wang
e-mail: 602298017@qq.com

T. Huang
e-mail: 361799368@qq.com

M. Ren
e-mail: 1282513310@qq.com

C. Yang
Journal Center, Southwest Petroleum University, Chengdu, China
e-mail: 15940049385@163.com

Y. Han (ed.), *Advances in Energy and Environmental Materials*,
Springer Proceedings in Energy, https://doi.org/10.1007/978-981-13-0158-2_27

Keywords Special brass · Solution treatment · Oilfield produced water
N80 steel · Polarization curve · Impedance spectroscopy

Introduction

Corrosion can cause oil pipeline leakage in the normal production of oil field, and huge economic loss, even caused huge security problems [1–4]. The main forms of corrosion include: chemical corrosion, electrochemical corrosion and bacteria corrosion, etc. In the industrial developed countries, the annual economic loss caused by pipeline corrosion accounts about 3% of the gross national product [5], so the corrosion and protection problem has become the research focus in the oil field development [6–9]. At present, anticorrosion means main include: using corrosion resistant materials, corrosion inhibitor, anticorrosion coating, cathodic protection technology, etc. Due to the potential difference between alloy material components, cathodic protection can be realized by using alloy, to achieve the purpose of corrosion mitigation. Previous studies showed that copper alloy not only has significant anti fouling ability, also has the anticorrosion ability, and the advantages of energy saving, low cost, long service life, wide application prospects, but the current theoretical research on this aspect is still not perfect, and the application in oil field area is relatively small. In this work, using special brass alloy containing Ni, Sn, Ce and other alloy elements, based on a certain oil field output water corrosion medium, using electrochemical workstation and scanning electron microscopy to study the effect of special brass alloy on corrosion of N80 pipeline steel, and heat treated special brass, to study the effect of heat treatment on corrosion inhibition of special brass alloy. Provide reference for the application of alloy in pipeline corrosion protection.

Materials and Methods

Compositions of Produced Water And Special Brass Alloy. The special brass alloy for the experiment was smelted by high frequency induction melting furnace, and the chemical compositions of alloy were shown in Table 1. The parameters of produced water were shown in Table 2.

Specimen Preparation. Before experiment, the special brass alloy was machined by wire cut electrical discharge machining into the dimension of 10 mm × 10

Table 1 Chemical compositions of alloy

Elements	Cu	Zn	Ni	Sn	Mn	Ti	Al	Pb	Si	Mg	Ce
Content (wt%)	67.10	21.60	4.70	2.40	1.10	1.10	0.80	0.10	0.80	0.60	0.12

Table 2 Parameters of produced water

Ion	Na^+	Mg^{2+}	Ca^{2+}	K^+	HCO_3^-	SO_4^{2-}	Cl^-
Content (*g*/L)	2.2242	0.5923	3.0824	13.6592	0.7077	0.17728	22.5601

mm × 10 mm for preparation, and then drilling on the surface. The specimens were divided into three groups, each group contains four specimens, selected a set of specimens for heat treatment, heat treatment temperature is 750 °C, treating one hour.

Oil Field Produced Water Treatment. Special brass alloy used as electrochemical catalyst, could provide electronic to solution system, made the solution produce electrochemical action, weakening the oxidation of solution to metal, inhibit the corrosion of the metal. Therefore, put special brass alloy in the produced water for 3 days, make it react adequately with ions.

Electrochemical Tests. The corrosion behavior of the specimens under investigation were monitored using DC polarization techniques and EIS, using with treated and untreated produced water in room temperature as corrosive medium, respectively. Before each test, the working surface was polished with abrasive paper. And rinsed with deionized water, then swabbed with petroleum ether to remove the oil, finally cleaned the stains with anhydrous ethanol, the surface was dried by hair dryer, and mounted in an epoxy resin, leaving an exposed area about 1 cm^2. The polarization experiments and EIS, were carried out using a standard electrochemical workstation (PGSTAT 302 N) with a three-electrode cell, auxiliary electrodes are platinum electrode, reference electrodes are saturated calomel electrode, and N80 steel as the working electrode, the experiments were using a scan rate of 1 mV/s. After testing, the polarization curves and impedance spectroscopy were fitting by the analysis software.

Surface Morphology Observation. The morphologies of specimens which after removing the corrosion products under different conditions were observed by Scanning Electron Microscopy (SEM, ZEISS-EV0-MA15).

Results and Discussion

Electrochemical corrosion test results of N80 steel in produced water under different conditions were investigated. The polarization curves of N80 steel were determined by the different processing conditions, the final results were presented in Fig. 1. The calculation results of the corrosion current density (i_{corr}) and the corrosion potential (E_{corr}) were shown in Table 3.

In a typical polarization curve, a lower corrosion current density (i_{corr}) and a higher corrosion potential (E_{corr}) are related to a better corrosion resistance [10–13]. As shown in Fig. 1 and Table 3, E_{corr} obviously increase from −0.90 V to −0.66 V, the N80 steel in untreated produced water doesn't appear obvious anode passivation

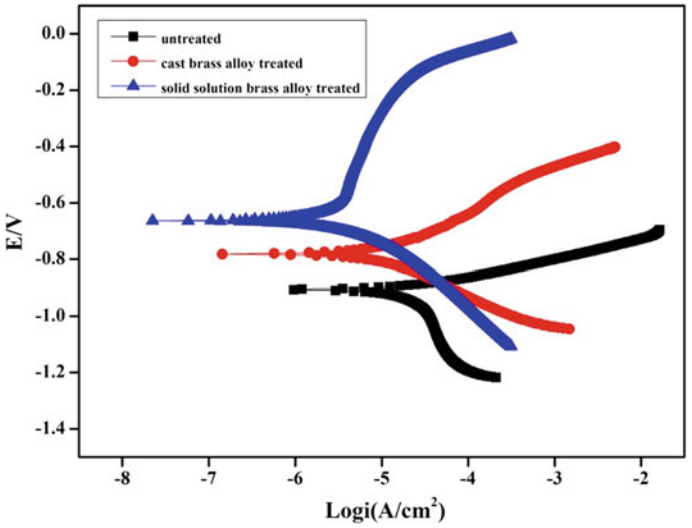

Fig. 1 Polarization curves of N80 steel in different treating conditions

Table 3 Electrochemical parameters of N80 steel in different treating conditions

Electrochemical parameters	Experimental conditions		
	Untreated	Cast brass alloy treated	Solid solution brass alloy treated
i_{corr} (A/cm^2)	7.65×10^{-6}	5.84×10^{-6}	2.09×10^{-6}
E_{corr} (V)	−0.90	−0.78	−0.66

region, but observed in produced water which under different treated conditions, and the passivation degree in produced water which treated by solid solution brass alloy is the most obviously, moreover, the E_{corr} were all increased in a certain range. The i_{corr} of N80 steel in the solid solution brass alloy treated produced water (2.09×10^{-6} A/cm^2) is much lower than the other experiment in this work.

By the second law of Faraday, the corrosion rate of N80 steel gradually increased with the rise of i_{corr}, therefore, the results suggested that the corrosion degree of N80 steel in untreated produced water is the most serious, on the contrary, in produced water which treated by solid solution brass alloy, the degree is the lightest.

According to the corrosion process of steel in carbon dioxide [14], the product was $Fe(HCO_3)_2$, but it was unstable, under certain conditions would be decomposed to $FeCO_3$, and the corrosion degree of N80 steel would increase with the decrease of pH value. Because of special brass alloy contains Cu, zinc elements, these elements can form a galvanic cell on the surface, and generated galvanic cell reaction, got OH^-, which could neutralizing H^+ in produced water, thereby reduced the production of Fe^{2+} and $FeCO_3$. Moreover, if the pH value increases, the

difficulty of dissolving $FeCO_3$ increases, which is beneficial to the formation of product film, then covered the surface of N80 steel, slowed down the corrosion rate [15, 16]. Taken as a whole, special brass alloy could lower the corrosion of N80 steel, and the solid solution special brass alloy has the most obviously effect in this experiment.

All spectrums were analyzed and fitted in the terms of the equivalent circuit provided in Fig. 2 by using the software. In this experiment, the fitted results of EIS data obtained from Fig. 3 were given in Table 4. The equivalent circuit consists of the solution resistance (R_s) connected in series with parallel-connected elements, in which included a constant phase element (CPE) and the charge transfer resistance (R_{ct}).

From Fig. 3, a depressed loop from the medium to high frequency region for all tested specimens is observed. It is seen that specimens in treated produced water exhibit higher resistance compared with the specimens in untreated produced water, moreover, the specimen in solid solution brass alloy treated produced water has the highest resistance.

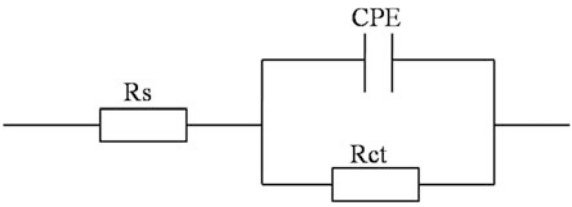

Fig. 2 Equivalent circuit

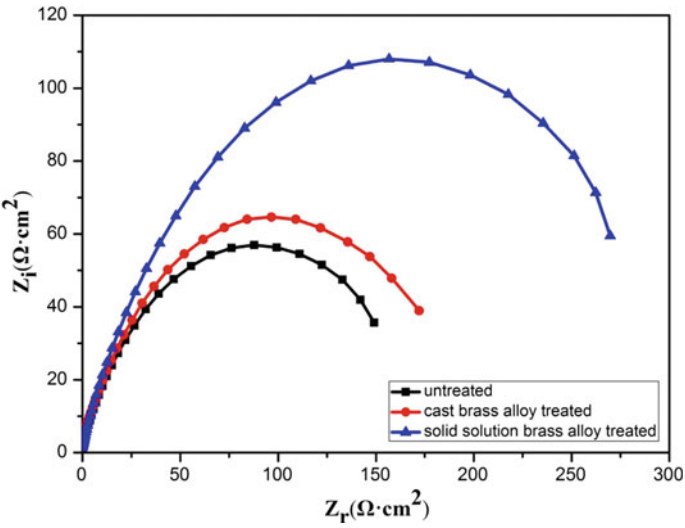

Fig. 3 EIS spectra presented as Nyquist plot at different produced water

Table 4 Fitting parameters of the experimental steels obtained from EIS spectra

Produced water treated conditions	$R_S/(\Omega.cm^2)$	$CPE/(F{\cdot}cm^{-2})$	$R_{ct}/(\Omega.cm^2)$
Untreated	6.125	0.0003152	151.7
Cast brass alloy treated	6.975	0.0003147	174.9
Solid solution brass alloy treated	12.39	0.0001458	276.8

In oil field produced water, as the corrosion progressed, the corrosion product film was formed on the steel surface, which could prevent the further increase of the corrosion rate [17]. As can be seen from the foregoing, special brass alloys could increase pH value, let the corrosion products easily deposited on the surface of N80 steel, so that N80 steel surface covering more corrosion products, greatly reduce the corrosion rate and increase the value of R_{ct}. Therefore, special brass alloys can effectively slow down the corrosion rate of N80 steel in produced water, and the corrosion resistance of N80 steel in solid solution brass alloy treated produced water is the most obviously, this is consistent with the polarization curve test.

As shown in Fig. 4, the surface morphology of specimen was observed by SEM photograph. The N80 steel in the produced water without treatment (Fig. 4a) was

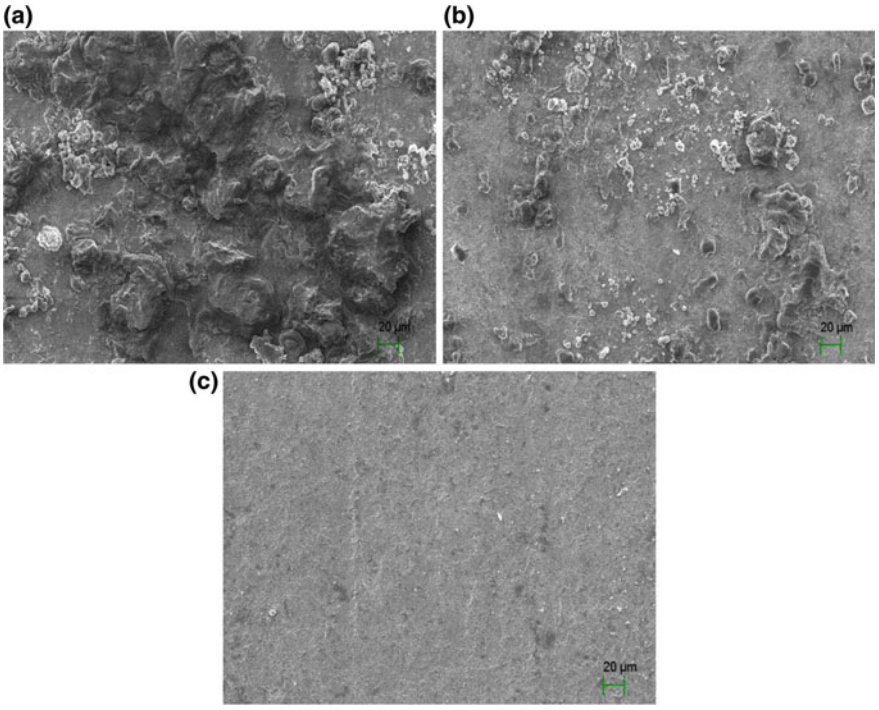

Fig. 4 Surface morphology of the N80 steels after corrosion test: **a** untreated produced water, **b** produced water after cast brass alloy treated, **c** produced water after solid solution brass alloy treated

observed that a lot of protrusions and cracks prevail over the entire surface, the degree of corrosion is very serious. However, in the produced water with alloy treated, the surface morphology of N80 steels is quite different from the last one (Fig. 4b–c), and the protrusions and cracks are reduced, the degree of corrosion has also been reduced. Thus, special brass alloys can significantly slow the corrosion of N80 steel in the produced water, and the effect of the solid solution special brass alloy to reduce the corrosion is better than the other experiment, this is consistent with the previous experimental results.

Conclusions

The result shows that special brass alloy can increase pH value in oilfield produced water, and reduce the solubility of corrosion products. Therefore, in this experiment, the electrochemical test results of N80 steel in different corrosive medium are obviously different. In the corrosive medium which after alloy treated, the self-corrosion voltage of N80 steel is increased from −0.90 V to −0.66 V, and the corrosion current is reduced to 2.09×10^{-6} A/cm^2. Moreover, the results of scanning electron microscopy shows that the corrosion products covered on the surface of N80 steel is reduced, it means that the corrosion degree of N80 steel is obviously reduced, that is, the special brass alloy can play the role of corrosion inhibition. Taken as a whole, special brass alloy can effectively slow down the corrosion of N80 steel, and solid solution special brass alloy corrosion inhibition effect is better.

Acknowledgements This work was financially supported by Innovative Entrepreneurship Training for Southwest Petroleum University, (No. 201610615086).

References

1. Y. Liu et al., Electrochemical polarization study on crude oil pipeline corrosion by the produced water with high salinity. Eng. Fail. Anal. **60**, 307–315 (2016)
2. C.-H. Peng, Z.-Y. Liu, X.-Z. Wei, Failure analysis of a steel tube joint perforated by corrosion in a well-drilling pipe. Eng. Fail. Anal. **25**, 13–28 (2012)
3. J.L. Alamilla et al., Failure analysis and mechanical performance of an oil pipeline. Mater. Des. **50**, 766–773 (2013)
4. C.I. Ossai, B. Boswell, I.J. Davies, Pipeline failures in corrosive environments–a conceptual analysis of trends and effects. Eng. Fail. Anal. **53**, 36–58 (2015)
5. W. Ma, H. Sun, D. Kang et al., Introduction to steel skeleton plastic clad pipe. Oil-Gasfield Surf. Eng. **21**(1), 35–35 (2002)
6. J. Zhang, Y. Ling, H. Zhang, Corrosion prevention strategy for oil refining device. (2008)
7. N. Lin, J. Zou, H. Zhou, Reaserch status of CO_2 corrosion on N80 oil casing tube steel. Mater. China **28**(2), 14–18 (2009)

8. Z. Li, Y. Cheng, H. Bi, Dong Youzhi, Research progress of CO_2/H_2S corrosion and inhibitor techniques in oil and gas fields. CIESC J. **65**(2), 406–414 (2014)
9. S. Zhu, H. Liu, Z. Bai, Dynamic corrosion behavior of P110 steel in stimulated oil field CO_2/H_2S environment. Chem. Eng. Oil Gas **38**(1), 65–68 (2009)
10. J. Han et al., Etching and heating treatment combined approach for superhydrophobic surface on brass substrates and the consequent corrosion resistance. Corros. Sci. **102**, 251–258 (2016)
11. A.O. Yüce, G. Kardaş, Adsorption and inhibition effect of 2-thiohydantoin on mild steel corrosion in 0.1 M HCl. Corros. Sci. **58**, 86–94 (2012)
12. M. Ko et al., In situ synchrotron X-ray diffraction study of the effect of microstructure and boundary layer conditions on CO_2 corrosion of pipeline steels. Corros. Sci. **90**, 192–201 (2015)
13. R. Mishra, R. Balasubramaniam, Effect of nanocrystalline grain size on the electrochemical and corrosion behavior of nickel. Corros. Sci. **46**(12), 3019–3029 (2004)
14. Q. Yuan, Q. Liu, Y. Bi, Z. Niu, Y. Wang, He Zhiyong et al., CO_2 corrosion mechanism and corrosion method in oil and gas field development. Nat. Gas Oil **33**(2), 78–81 (2015)
15. H. Ma et al., Inhibition of copper corrosion by several Schiff bases in aerated halide solutions. J. Appl. Electrochem. **32**(1), 65–72 (2002)
16. D. Shi, J. Zhang, F. Kuang, X. Cao, Zheng Chu, The current research status of temperature under high pressure CO_2 corrosion. Chem. Eng. Equip. **11**, 129–131 (2010)
17. Y. Liu et al., Electrochemical polarization study on crude oil pipeline corrosion by the produced water with high salinity. Eng. Fail. Anal. **60**, 307–315 (2016)

CO_2 Precipitation Approach in Preparation of White Carbon Black

Yuying Zhang, Lingxin Peng, Yujiao Guo and Shengming Jin

Abstract The white carbon black powders were prepared through carbonation of water glass. The UV-vis spectra and ^{29}SiNMR were used to characterize the configuration of silicon atoms before and after polymerization of silicic acid. The results indicated that the luminousness decreased as the reaction progress. The polymerization process was divided into three stages which include slow polymerization, fast polymerization and the end of polymerization. The signals of ^{29}SiNMR demonstrated that the silicate of raw material was in a ring multimer. In the fast polymerization phase, ^{29}SiNMR signal was split into 5 peaks which indicated there were a complex configuration resulted from silicon atom in different chemical environment including monomers, multimers and hydrated ions. After completion of polymerization, the ^{29}SiNMR signal presented a single peak at −113 ppm with two shoulder at −98 and −93 ppm, indicating that the silicic acid polymerized to form homogeneous Q^4 configuration. TEM images revealed that the white carbon black powders were spherical particles resulted from homogeneous polymerization of ring nucleus. The effects of pH value, temperature on polymerization rate of silicic acid were studied as well. In alkaline system, the polymerization rate of silicic acid

Y. Zhang · L. Peng · Y. Guo · S. Jin (✉)
School of Minerals Processing and Bioengineering, Central South University, Changsha 410083, China
e-mail: shmjin@126.com

Y. Zhang
e-mail: 155612087@csu.edu.cn

L. Peng
e-mail: wysplx@163.com

Y. Guo
e-mail: 15273110133@163.com

Y. Zhang · L. Peng · Y. Guo · S. Jin
Key Laboratory for Mineral Materials and Application of Hunan Province, Central South University, Changsha 410083, China

Y. Han (ed.), *Advances in Energy and Environmental Materials*,
Springer Proceedings in Energy, https://doi.org/10.1007/978-981-13-0158-2_28

decreased with the increase of pH value. Higher the reaction temperature, shorter the gelation time of silicic acid. The growth kinetics of hydrated silica was investigated and the apparent activation energy of particle growth of hydrated SiO_2 was 43.377 kJ/mol in the first polymerization stage.

Keywords Sodium silicate · White carbon black · Carbonation
Growth kinetics

Introduction

Tunable size and specific surface area of white carbon black (WCB) powders, which was well-dispersed powders and rich of surface –OH groups, exhibited superior performance for various applications, such as rubber, plastic, coating, sealing carrier, food and pharmaceutical industries, etc. [1, 2]. In a typical synthesis, the polymerization reaction between inorganic acid and water glass occurred in a suitable pH ranges. After filtering, washing and pulping, the precipitates were collected after acidification treatment. Subsequent drying, the traditional white carbon black powders were obtained [3]. However, many problems appeared in the traditional production process. Namely, large amounts of waste effluent were produced owing to used H_2SO_4 or HCl as precipitant in the typical process, which contained sulphate and chloride resulted in difficult recycling water. The discharge of CO_2 not only wastes natural resources but also harms the environment, ecological balance and people's health because of the consumption of Na_2CO_3, coal or natural gas during the process of produce WCB. Compared with traditional methods, carbonation method used CO_2 precipitant instead of the traditional inorganic acid to react with water glass to form $mSiO_2{\cdot}nH_2O$ [4]. The wastewater contained Na_2CO_3 and $NaHCO_3$ could be used to prepare water glass after crystallization. Therefore, the circulation utilization rate of sodium salt were improved in the entire production process of WCB powders. Besides, the carbonation method also can reduce the emissions of CO_2 and wastewater containing salts. Much attention was paid to structure control of WCB powders through carbonation of water glass recently. Some scholars [5, 6] introduced supercritical CO_2 as the reactant to generate WCB powders with controllable morphologies and properties via adjusting pressure of CO_2 and temperature. Meanwhile, the CO_2 is not only a reaction agent, but also a modifier of the product. Cai et al. [7] reported an interesting method approach to prepare WCB via precipitation method, which used the $Na_2O{\cdot}SiO_2{\cdot}9H_2O$ as a raw material, CO_2 as precipitant, and polyethylene glycol (PEG6000) as non-ionic dispersant. The reaction mechanism was shown in Eq. (1).

$$2NaOH \cdot SiO_2 + CO_2 = Na_2CO_3 + 2SiO_2 \downarrow + H_2O \quad (1)$$

The effects of temperature, reaction time, concentration of water glass and polyethylene glycol on the conversion rate and the average particle size were

studied under the atmospheric pressure of 0.2 MPa. Kai et al. reported that WCB powders were prepared through reaction of Na_2SiO_3 aqueous and CO_2 precipitation from lime-kiln gas [8]. Lee et al. reported that WCB powders were formed through carbonation of water glass in which CO_2 come from decomposing NH_4HCO_3 and $CO(NH_2)_2$ [9]. Compared with the traditional acid precipitation method, carbonation process has lots of advantages including low consumption of raw materials, friendly environment, controllable structure and particle size [10].

Nevertheless, WCB powders from carbonization method still suffers from poor stability of CO_2 acidification and hydrolysis equilibrium of salt existed in this system. According to results of silicic acid and its salt reported by Chen [11], a series of experiments indicated a certain relationship between salt concentration and gelation time. With the modulus increase, the polymerization degree of silicate increased owing to the weak interaction between sodium and silicic acid in aqueous solution. High Coordination compound existed on the polysilicic acid surface could accelerate the polymerization rate of silicic acid. Therefore, the polymerization rate of Na_2SiO_3 with high modulus could be adjusted by the salts due to colloidal polysilicic acid. In contrast, the low-polymeric silicic acid composed of low polysilicate ions was not sensitive to additives [12]. In this work, the change of luminousness with polymerization degree was studied. The configurations of silicon atoms during carbonation were characterized by ^{29}SiNMR method and the polymerization kinetics of silicic acid was investigated as well.

Experimental Section

Sodium silicate (M=3.5, SiO_2: 22.87%.) was purchased from Zhuzhou Xinglong Chemical Co. Ltd, and sodium hydroxide (NaOH, AR) was provided by XiLong Chemical Co. Ltd. In a typical procedure, mixed gases (N_2 and CO_2) were successively passed through a solution of sodium silicate under magnetic stirring. When the pH value of solution in a suitable pH ranges, solution weaned from ventilation and collosol was formed by polymerization of silicic acid. According to the optical properties of collosol, the light mainly happened scattering owing to the diameter of the colloidal particles is smaller than wavelength of the light when the light passes through the colloid solution [13]. Therefore, we could estimate the volume change of the collosol though determining the scattering intensity change in the process of forming the collosol. For the colloidal particle radius less than 47 nm, Rayleigh derived formula of calculated scattering intensity according to Eq. (2).

$$I = \frac{9\pi^2 V^2 C}{2\lambda^4 l^2}\left(\frac{n^2 - n_0^2}{n^2 + 2n_0^2}\right)^2 \left(1 + \cos^2\delta\right) I_0 \tag{2}$$

where C is the number of particles per unit volume; V is the volume of particles; λ is the wavelength of incident light; l is the distance of between observer and

scattering center; n is the dispersed phase refractive index; n_0 is the dispersion medium refraction index; I_0 is the incident intensity; and δ is the scattering angle.

According to the formula of Rayleigh, it can be deduced that scattering intensity is proportional to volume square of the particle. Therefore, the volume of the colloidal particles is positively related to polymerization degree for spherical nucleus due to approximate growth velocity of hydrated SiO_2 and similar density of the colloidal particles. A measure and analysis method of polymerization degree in the polymerization process of silicic acid was reported by Xu. and Liu et al. [14, 15]. Based on their research, a relationship formula between average polymerization degree and measured scattering intensity of system was established as Eq. (3).

$$\frac{1 - T_0}{1 - T_i} = \frac{m_0}{m_i} \tag{3}$$

where T_0 is the initial transmittance; T_i is the transmittance when polymerization degree is m_i; m_0 is the initial average degree of polymerization; m_i is the average degree of polymerization at a certain time.

The chemical environment of Si atoms in polymerized silicic acid were determined using ^{29}SiNMR spectrum on an infinity plus 300 nuclear magnetic resonance spectrometer (Varian Corporation, USA). In different stages of polymerization, the sample was took out to transfer to the freezers immediately. It can reduced the polymerization of surface –OH groups and maintained the stability of the Si chemical environment.

Results and Discussion

The Effect of the Polymerization Degree on Transmittance. Figure 1a shows the relationship between the transmittance of the solution and the time at different temperature when the end pH of 9.38 was adjusted by CO_2. The results indicated that the curve could be divided into three stages according to the change of the slope. In the first stage, the profiles of curves were similar with linearity relationship between the change of transmittance (%) and time (min). In the second stage, the profiles of curves illustrates that value of transmittance with time (min) changed very quickly. And then, the transmittance decreased slowly again, indicating that the particle growth completed in the three stage. Inflection point appeared between two stages. Mutation time of slope increased with decrease of temperature. When temperature was more than 60 °C, mutation point of slope was not obvious. As we known, the transmittance of system was corresponding to the volume of particles which was related to growth velocity of hydrated SiO_2 with respect to polymerization rate of silicic acid. Consequently, the polymerization rate increased with increase of the reaction temperature.

In order to well understand the growth mechanism of hydrated SiO_2, the volume of particles was calculated at different stage based on Rayleigh formula. The

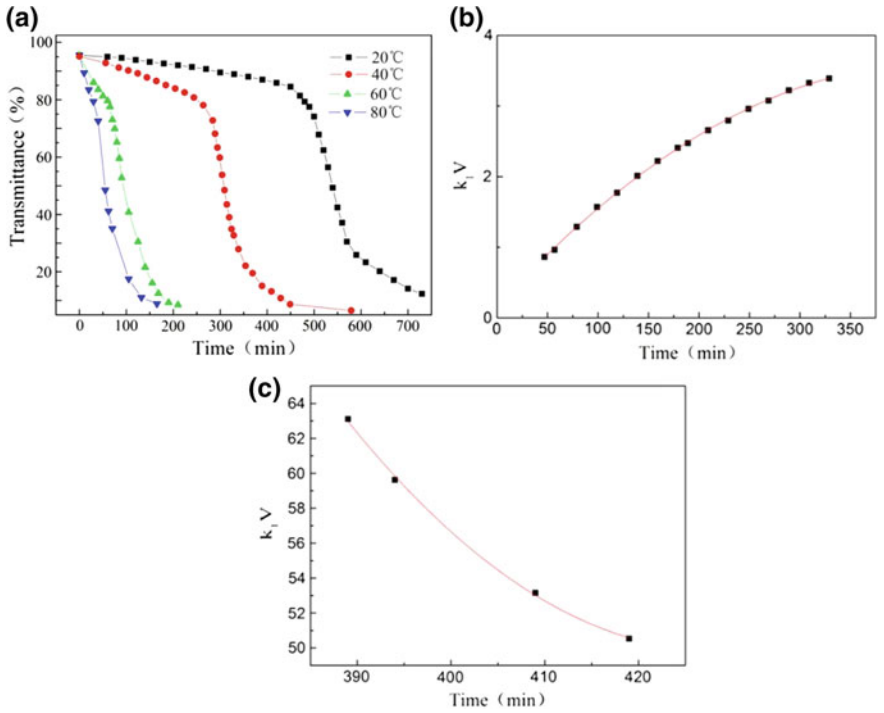

Fig. 1 **a** Plots of transmittance value of poly-silicic acid against time. **b** Plot of k_1V value against time in the first stage. **c** Plot of KV value against time in the second stage

relationship of volume change of hydrated SiO_2 versus reaction time showed in Fig. 1b, c. Under the certain reaction conditions and particle size, the Rayleigh formula the following equations could be deduced according to Rayleigh formula as Eqs. (4–6):

$$I = k_1 V^2 \tag{4}$$

$$I = (1 - T) * I_0 \tag{5}$$

$$T = k_2 t + b \tag{6}$$

where the I is scattering intensity; k_1 is a constant; V is the volume of hydrated SiO_2 particles; T is the transmittance; I_0 is the incident intensity; k_2, b are the constants of linear equations; and t is the reaction time.

In the first stage of the reaction, as Fig. 1b, the volume of the particles increased with increase of the reaction time. The curve gradually tended to a steady state, indicating that the growth rate of particles volume were slow down. Obviously, the change of the volume of silica particles conformed to the deduced formula from Rayleigh. In the first stage, and the monomer and dimer reacted with multimer

nucleus to form the poly-silicic acid clusters. The polymerization of silicic acid accorded with a linear variation with the change of reaction time. However, as Fig. 1c, the volume of the particle decreased with increase of reaction time. It was obvious that the variation of particle volume was no longer consistent with Rayleigh equation. Perhaps, the degree of polymerization failed to be completely determined by the volume of particles because of the complex polymerization environment.

In the second stage, There were many reactants, for example, some of monomer, dimer and multimer of silicic acid, co-existed in this stage. The species polymerized each other to form large particles, which resulted in the change of transmittance away from Rayleigh equation.

The ^{29}SiNMR Spectra of Poly-Silicic Acid at Different Reaction Stages. Because of the complicated configuration of silicon atoms in aqueous solution or polymeric state, the structure of silicic acid ions should be characterized by ^{29}SiNMR spectrum [16]. In different stages of polymerization, the sample was transferred to the freezers immediately in order to minimize the effect of ambient temperature on polymerization degree of silicic acid. Figure 2 shows the ^{29}SiNMR spectra of silicic acid in different reaction stage. The result of ^{29}SiNMR spectrum of silicic acid in first stage exhibited a chemical shift at −72.23, −80.43, −82.38, −88.85 and −97.5 ppm corresponding to Q^0, Q^1, Q^2, Q^3 configuration of silicon atoms in aqueous silicic acid, respectively. Q^0 configuration denotes free single silicic acid molecules indicating that free silicic acid monomer existed in glass water with modulus of 3.5. Silicon atoms with chemical shift at −80 to −83 ppm were assigned to Q^1 configuration which was dimer of silicic acid. It was interesting that ^{29}SiNMR signal was split into 3 peaks and a separated shift at −82.38 ppm, indicating that silicic acid dimers were surrounded by hydrated sodium resulted in change of electron cloud density of silicon atom or Si–O structural unit at the edge of silicic trimer. Q^2 configuration correspond to chain-like structural or ring-like

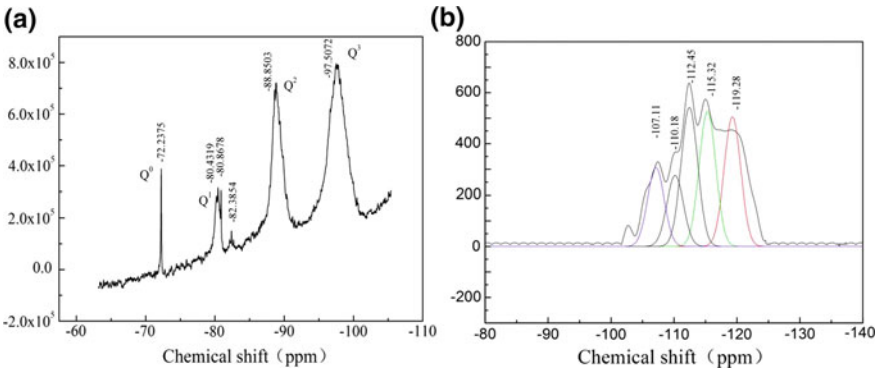

Fig. 2 **a** ^{29}SiNMR spectrum of the silicic acid in the first stage. **b** ^{29}SiNMR spectrum of the silicic oligomeric structure in the second stage

structural units, which contains the single and double chains or rings. Q^3 configurations maybe contain the structure of double chain multimer and laminated structure. Therefore, it was obvious that the silicic acid ions were mostly in oligomeric state, in the first stage, indicating that the structure of layered and chained were mainly included. The initial average degree of polymerization was 6 according to Rayleigh equation, which was in the oligomeric state.

In the second stage of polymerization reaction, the ^{29}SiNMR spectrum of silicic oligomeric showed in Fig. 2b. The chemical shift of silicon atoms were in a certain range from −105 to −125 ppm. All the spectra were simulated and separated using the Gaussian-Lorentzian model. Five NMR lines at −107, −110, −112, −115 and −119 ppm appear in ^{29}SiNMR spectrum of silicic oligomeric at the second stage. Chemical shift at −102 ppm was a separated line, which were belonged to Q^3 configurations at the edge of silicic oligomeric colloid particles. According to TO_4 structural characteristics in silicate, chemical shift of −102 to −129 ppm could assign to Q^4 configurations. Therefore, the loose hydrated SiO_2 particles in second stage were dominated in the basic SiO_4 units of Q^4 configuration, which split into many resonance peaks resulted in unstable strength of Si–O–Si bonds. It was reasonable that the structure of three-dimensional network is gradually formed by the silicic acid clusters [17].

Figure 3 shows the ^{29}SiNMR spectrum of hydrated SiO_2 in the endpoint of reaction. The chemical shift of Si atom presented a single peak at −113 ppm with two shoulders at −92 ppm and −98 ppm, indicating that the chemical environment of Si atom was in Q^4 configurations and a few Q^2 configurations at the edge of particles. Meanwhile, the results also illustrated that the bonding strength of –Si–O–Si–O– in hydrated SiO_2 was homogeneous and stable [18]. A homogeneous gelation state could be obtained in the end of silicic acid polymerization.

In order to further understanding the polymerization mechanism of hydrated SiO_2 particles, the TEM image was observed in Fig. 4 obtained on transmission electron microscopy (TECNAI G2 60-300, FEI, USA). The morphologies of the

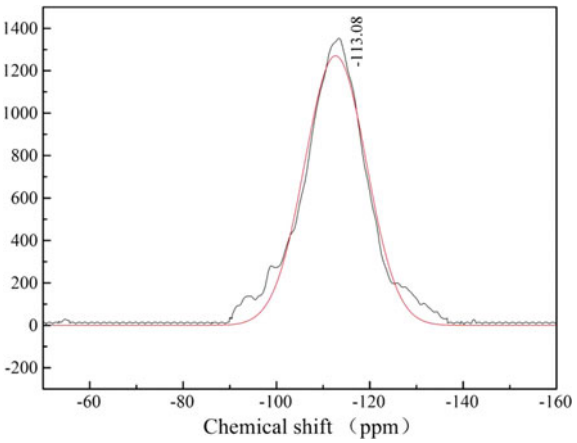

Fig. 3 ^{29}SiNMR spectrum of the hydrated SiO_2 colloid particles at the last stage

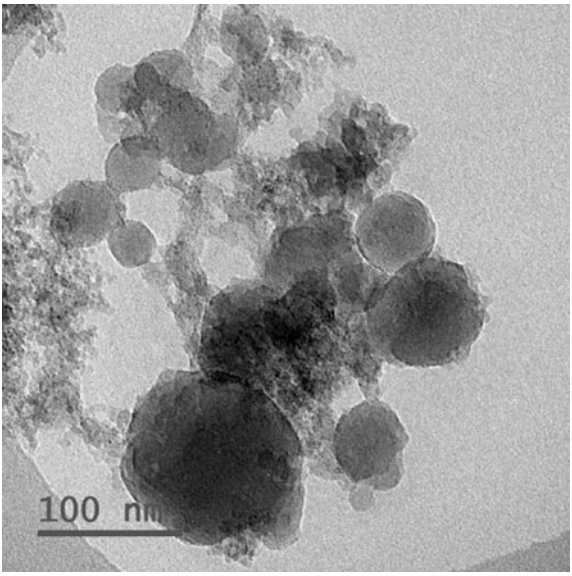

Fig. 4 TEM image of the SiO_2 precipitation after polymerization

particles were spherical or cubic with different sizes, which indicate that the polymerization rate of silicic acid was homogenous in a ring-like or double-chains-like nucleus of multimer silicic acid and the particles with corresponding morphologies were formed eventually.

The initial average polymerization degree of silicic acid was approximately equal to 6 according to Rayleigh equation. After the activation, the pH value of the solution were in a certain range from 9 to 9.5. According to the theory of acid

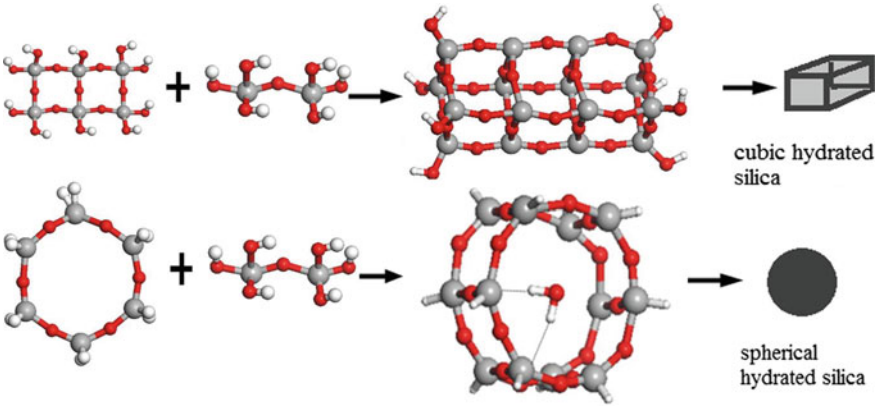

Fig. 5 Polymerization mechanism of hydrated silica

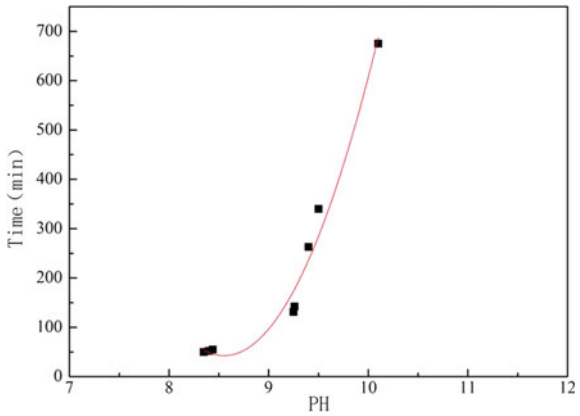

Fig. 6 Plot of gelation time of polysilicic acid against pH

strength and molecular structure [19], the ^{29}SiNMR spectra illustrated that the main state of polymerization of silicic acid were rings and double chains. Consequently, It was evidenced that the mechanism model of silicic acid presented in Fig. 5.

Effects of pH Value on Polymerization of Silicic Acid in Alkaline solution. Figure 6 shows the relationship of gelation time of polysilicic acid against pH when the modulus of water glass is 3.5. The gelation time increased with the increases of pH value when the end point of acidification pH value was more than 7.0, indicating that the rate of polymerization of silicic acid decreases with the value of pH increased. According to the theory of silicic acid polymerization, the relationship between the polymerization time and the pH value are similar to "N" curves with the change of pH value [20]. However, only one half of the curve of pH vs gelation time appeared in CO_2 carbonation of water glass solution.

The acidified solution mainly contained sodium carbonate, which was the salt of weak acid. Therefore, the buffer solution of carbonate system formed and resulted in the range of pH > 8. The left of the "N" shape curve (pH < 8) couldn't be achieved in this experiment.

Effects of Temperature on Silicic Acid Polymerization. Figure 7 shows the relationship of gelation time of silicic acid against temperature when the modulus of water glass is 3.5 and about pH 9.3. It was clear that the temperature had a great impact on the rate of polymerization of silicic acid ions. The lower the temperature of solution, the slower the polymerization rate of silicic acid and the longer the gelation time. With the temperature rising, the kinetic energy of silicic acid ions increases. The rate of molecular motion increased, which improved the probability of collision between molecules. Therefore, the polymerization was promoted, which speed up the rate of gelation.

Growth Kinetics of Hydrated SiO_2 Particles. The complexity of condensation reaction derived from diversity of silicate ions. It was difficult to establish the kinetic model of silicic acid polymerization. However, a simplified kinetic model could be established through Rayleigh equation. In polymerization process of silicic acid, homogeneous growth rate in all directions was assumed to hydrated SiO_2. The

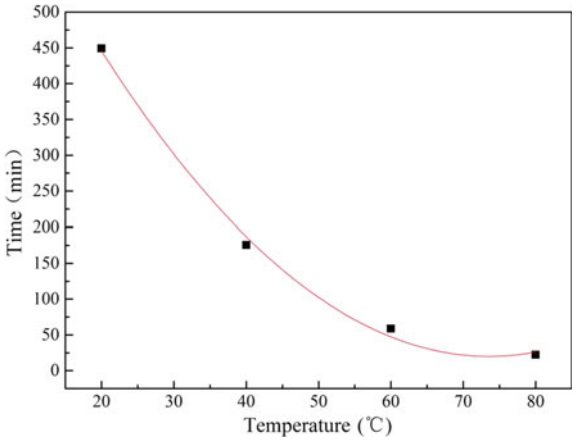

Fig. 7 Plot of gelation time of polysilicic acid against temperature

reaction kinetics of silicic acid was equivalent to the relationship of volume of hydrate SiO_2 particles vs reaction time. It was reasonable that the kinetic equation was written as Eq. (7) in the first stage of polymerization.

$$r = k_3 dV/dt \tag{7}$$

where r denotes growth rate of hydrated SiO_2; V is the volume of hydrated SiO_2; t is reaction time of silicic acid. Substitution of Eq. (4) into Eq. (7) gives

$$r = k_3 d\left(\sqrt{\frac{1}{k_1}}\right)/dt = \frac{(k_3 {k_1}^{0.5}) d\sqrt{I}}{dt} = Kd\sqrt{I}/dt \tag{8}$$

where $K = k_3 k_1^{0.5}$.

Therefore, K at different temperature could be obtained from Fig. 1a. A plot of lnK against 1/T shows in Fig. 8. There was a good linear relationship between 1/T and lnK.

According to the Arrhenius equation (Eq. 9), the E_α/R ratio is only with respect to the reaction temperature. Therefore, the relationship between reaction mechanism and rate of polymerization could be reflected by the activation energy quantitatively [21].

$$\ln K = \left(-\frac{E\alpha}{R}\right)\frac{1}{T} + \ln A \tag{9}$$

where K is the constant of reaction rate, A is the pre-exponential factor, R is the ideal gas constant, T is the absolute temperature, and E_α is the apparent activation energy.

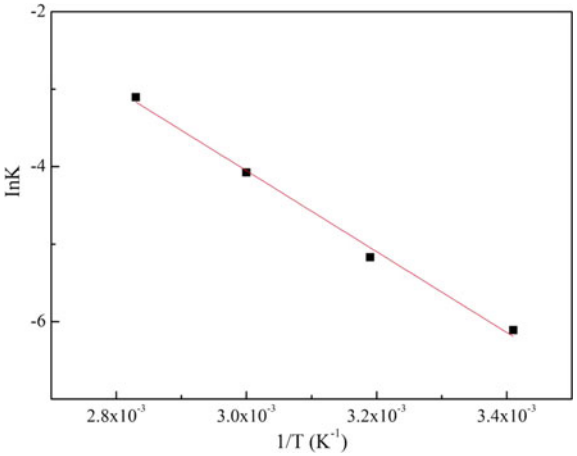

Fig. 8 Plot of lnK against 1/T

Therefore, according to the Arrhenius equation and Fig. 8, the apparent activation energy, 43.377 kJ/mol, of the silicic acid polymerization at first stage could be calculated by the slope of the curve.

Conclusions

White carbon black powders were prepared through the reaction of CO_2 precipitant and water glass of 3.5 modulus. In alkaline system, the polymerization of silicic acid can be divided into three stages. In the first stage, the growth of hydrated SiO_2 particles accords with linear mode. Loosing poly-silicic acid clusters are at the second stage, and stabilization of hydrated SiO_2 is at the third stage. ^{29}SiNMR spectra verifies that ring-like silicic acid exists in the water glass. The TEM image and ^{29}SiNMR spectra illustrates that there are two kinds of silicate polymerization mechanism derived from ring-like nucleus and double-chains-like nucleus and result in spherical and cubic white carbon black powders. A kinetics model at the first condensation stage is established based on the Rayleigh equation. The apparent activation energy of 43.377 kJ/mol is calculated at the first polymerization stage.

References

1. Y.H. Jin, A. Li, S.G. Hazelton, S. Liang, C.L. John, P.D. Selid, D.T. Pierce, J.X. Zhao, Amorphous silica nanohybrids: synthesis, properties and applications. Coordin. Chem. Rev. **253**, 2998–3014 (2009)
2. F. Marquez-Linares, R.M. Roque-Malherbe, Synthesis and characterization of large specific surface area nanostructured amorphous silica materials. J. Nanosci. Nanotechnol. **6**, 1114 (2006)

3. T. Tarutani, Polymerization of silicic acid. A Rev. Anal. Sci. **5**, 245–252 (1989)
4. U.K.H. Bangi, A.P. Rao, H. Hirashima, A.V. Rao, Physico-chemical properties of ambiently dried sodium silicate based aerogels catalyzed with various acids. J. Sol-Gel. Sci. Technol. **50**, 187–197 (2009)
5. P. Chattopadhyay, R.B. Gupta, Supercritical CO_2-based formation of silica nanoparticles using water-in-oil microemulsions. Ind. Eng. Chem. Res. **42**, 465–472 (2003)
6. J. Zhang, Z. Liu, B. Han, Y. Wang, Z. Li, G. Yang, A simple and inexpensive route to synthesize porous silica microflowers by supercritical CO_2. Micropor. Mesopor. Mater. **87**, 10–14 (2005)
7. X. Cai, R.Y. Hong, L.S. Wang, X.Y. Wang, H.Z. Li, Y. Zheng, D.G. Wei, Synthesis of silica powders by pressured carbonation. Chem. Eng. J. **151**, 380–386 (2009)
8. H.E. Kai, H.G. Chen, Preparation of white carbon black with lime-kiln gas by carbonization. Chin. J. Process. Eng. **6**, 554–559 (2006)
9. J.W. Lee, R. Li, Integration of fossil energy systems with CO_2 sequestration through NH_4HCO_3 production. Energ. Convers. Manage. **44**, 1535–1546 (2003)
10. M.G. Gordienko, A.M. Katalevich, S.I. Ivanov, N.V. Men'Shutina, M.Z. Zhurinov, A.Z. Abil'Magzhanov, Evaluation of the significance of the factors influencing the microstructure of silicic acid gels. Glass. Ceram. **72**, 465–468 (2016)
11. R. Chen, J. Wang, H. Liu, A. Dai, Studies on silicic acid and its salt(XIV). J. Nanjing. Univ. Nat. Sci. Ed. **401**, 1084–1086 (1983)
12. A. Dai, R. Chen, M. Ji, Q. Dai, X. Zhang, B. Wang, Studies on silicic acid and its salt(IX). J. Nanjing. Univ. Nat. Sci. Ed. **1**, 82–97 (1964)
13. R.V. Nauman, P. Debye, Light-scattering investigations of carefully filtered sodium silicate solutions. J. Phys. Coll. Chem. **55**, 1–9 (1951)
14. R. Xu, G. Yu, X. Yu, The measurement of average degree of polymerization of silicate ions in water glass. J. Jilin. Univ. Nat. Sci. Ed. **2**, 107–111 (1980)
15. L. Liu, The measuring and analyzing of polymerization degree of silicic acid in the course of gelation of water glass. J. Harbin. Univ. Civil. Eng. Arch. **3**, 78–84 (1986)
16. H.C. Marsmann, 29 Si NMR. Ency. Encycl. Spectrom. 2539–2549 (1999)
17. C.T. Knight, R.J. Balec, S.D. Kinrade, The structure of silicate anions in aqueous alkaline solutions. Angew. Chem. Int. Edit. **46**, 8148–8152 (2007)
18. S. Jin, G. Qiu, F. Xiao, Y. Chang, C. Wan, Investigation of the structural characterization of mesoporous molecular sieves MCM-41 from sepiolite. J. Am. Ceram. Soc. **90**, 957–961 (2007)
19. Y. Mao, G. Wang, R. Chen, A. Dai, Studies on silicic acid and its salt(XX). J. Nanjing. Univ. Nat. Sci. Ed. **03**, 106–110 (1987)
20. A. Dai, R. Chen, T. Zhu, Studies on silicic acid and its salt(VII). J. Nanjing. Univ. Nat. Sci. Ed. **03**, 20–29 (1963)
21. P. Gao, H. Wang, Z. Jin, Kinetic study on sol-gel transition and application of SiO_2 sol. Acta Materiae Compositae Sin. **20**, 122–127 (2003)

Grains Growth Kinetics of Al Doped Nano-$LiMn_2O_4$

Xiaolan Song, Ying Zhang, Haibo Wang, Dongfeng Liu and Minchao An

Abstract Nano-$LiMn_2O_4$ was synthesized by co-precipitation method and doped with Al ion in this study. This kind of material was characterized by X-ray diffraction, transmission electron microscope and energy dispersive spectrometer. Effects of doped Al content (0.1, 0.2 0.3 and 0.4), calcination temperatures (600, 650, 700, 750, 800 and 850 °C) and calcination times (4, 6, 8, 10 and 12 h) on crystallinity and grain size of materials were studied. Results indicated that Al doping did not change the spinel structure. Calcination temperature and time both showed positive correlations with the grain size. Grain growth kinetics of $LiMn_2O_4$ nanocrystal was simulated with a conventional model and a novel model respectively. Simulation results exhibit that the novel model is suitable to fit with data, meaning the important roles of diffusion and surface reaction.

Keywords Nano-$LiMn_2O_4$ · Al doped · Co-precipitation · Grain growth kinetics

X. Song (✉) · Y. Zhang · H. Wang · D. Liu · M. An
School of Mineral Processing and Bioengineering, Central South University, Changsha 410083, China
e-mail: xlsongtg@126.com

Y. Zhang
e-mail: zymissyou777@163.com

H. Wang
e-mail: whbcsu@126.com

D. Liu
e-mail: dongfengliu2008@126.com

M. An
e-mail: anminchao@163.com

X. Song · Y. Zhang · H. Wang
Key Laboratory for Mineral Materials and Application of Hunan Province, Central South University, Changsha 410083, China

Y. Han (ed.), *Advances in Energy and Environmental Materials*,
Springer Proceedings in Energy, https://doi.org/10.1007/978-981-13-0158-2_29

Introduction

With the rapid development of modern society, lithium-ion battery has become one ideal device for energy storage. Due to its low price, environment-friendliness and good security, lithium manganite ($LiMn_2O_4$, mainly structure as spinel type) is an important cathode electrode material of lithium battery [1]. However, $LiMn_2O_4$ has a serious problem about capacity fading during the charging-discharging process and impedes its wide application [2], especially when the temperature is higher than 55 °C.

In recent years, in order to solve the capacity fading problem of $LiMn_2O_4$ electrode material, researchers have taken a series of studies [3, 4]. Here is a widely accepted explanation named "Jahn-Teller effect" for this fading phenomenon [5]. According to Jahn-Teller effect, there is a lattice distortion of spinel $LiMn_2O_4$ crystal during charging-discharging process, leading to change of unit cell volume and crystalline conversion from cubic lattice system to tetragonal lattice system. In this case, it is harmful for transmission of lithium ion in electrode material, increasing the impedance and reducing the capacity. To improve the electrochemical performance of $LiMn_2O_4$ electrode material, one efficient method as doping modification is usually used. In $LiMn_2O_4$ crystal, the doped ions could replace the weak Mn–O bond, improving the stability of $LiMn_2O_4$ crystal and limiting the Jahn-Teller effect. At present, doped ions mainly include main group metal elements (Mg, Al) [6], transition metal elements (Ti, Cd, Dy, Tb, Cr) [7, 8] and nonmetal elements (S) [9]. Thirunakaran et al. [10] prepared the spherical $LiMn_2O_4$ using phthalic acid by sol-gel method, with particle size of less than 100 nm. The spherical $LiMn_2O_4$ electrode showed initial capacity of 145 mAh/g, but was with severe capacity fading. After doped by Cr ion, the capacity fading of material has been suppressed. Cras et al. [11] studied the Li–Mn–O material system and found that after doped by Al ion via solid-state dissolution, the Jahn-Teller effect was attenuated in the $LiAl_xMn_{2-x}O_4$ material.

For grain growth kinetics in calcination process of solid material, there is a classical theory named Hillert theory, considering the diffusion influence for the growth of micron grains. However, for nanocrystalline, with large specific surface area and strong surface activity, the Hillert model is not suitable. It is necessary to develop a new kinetic model for nanocrystalline. Based on the preliminary basis of our group, we developed a novel kinetic theory [12], considering the diffusion of influence and surface reaction for nanocrystalline.

In this work, co-precipitation method was used to synthesize Al-doped nano $LiMn_2O_4$ material. The structure and properties of materials were investigated by series of characterizations. The grain size was calculated by the Scherer equation. Then the conventional kinetics model and novel kinetics model for grain growth were studied.

Materials and Methods

Preparation. According to our report [13], $LiOH{\cdot}H_2O$ (Kermel, AR) and $Mn(CH_3COO)_2{\cdot}4H_2O$ (Kermel, AR) were used to prepare 50 mL of LiOH solution at 0.525 mol/L and 100 mL of $Mn(CH_3COO)_2$ solution at 0.5 mol/L. Then LiOH solution was added into $Mn(CH_3COO)_2$ solution at 60 drops per minute in water bath at 60 °C, with stirring speed of 400 r/min. Residue was dried at 100 °C for 12 h. Subsequently, it was pre-sintered at 400 °C for 2 h, and then calcined at different temperatures (600, 650, 700, 750, 800 °C) for different times (4, 6, 8, 10 and 12 h). Finally, after cooled and grinded, the $LiMn_2O_4$ product was obtained.

For the doping of Al ion, the 100 mL of $Mn(CH_3COO)_2{\cdot}4H_2O$ solution was changed as 100 mL of mixture solution as $Mn(CH_3COO)_2{\cdot}4H_2O$ and $AlCl_3{\cdot}6H_2O$ (Kermel, AR), with molar ratio of $Mn(CH_3COO)_2/AlCl_3$ = (2−x):x (x = 0.1, 0.2, 0.3 and 0.4). The following steps were the same as above, and the end product would be $LiAl_xMn_{2-x}O_4$.

Characterization. Crystalline structures of samples were analyzed using an X-ray diffractometer (Rigaku, D/max-2550). The X-ray diffraction (XRD) pattern was obtained at 40 kV and 250 mA, using Cu Kα radiation (λ = 0.154 nm), in range of 10–85° (2θ) with a step width of 0.02°. Surface morphologies were examined by using a transmission electron microscope (TEM) (Philip, Tecnai 220AEM), with the accelerated voltage of 20 kV. Besides, the energy dispersive spectrometer (EDS) was taken on the TEM to calculate the relative contents of elements. The grain size D (nm) was calculated according to the Scherrer formula (Eq. 1) [14]:

$$D = K\lambda/(\beta\cos\theta) \tag{1}$$

where K is the Scherrer constant of 0.89; β is the integral half-height width (rad); λ is the X-ray wavelength of 0.154 nm; θ is the diffraction angle.

Results and Discussion

Effect of Doped Al Content. Figure 1 shows the XRD patterns of $LiAl_xMn_{2-x}O_4$ (x = 0.1, 0.2, 0.3, 0.4) calcined at 700 °C for 6 h with different Al contents. It could be seen that pure $LiMn_2O_4$ and $LiAl_xMn_{2-x}O_4$ were both spinel-type structures [15], with characteristic peaks of (111), (311) and (400). There was no visible change for diffraction peak after doping Al, indicating that the doped Al^{3+} had completely entered into the spinel $LiMn_2O_4$ lattice without obvious distortion of crystalline structure. One reason was that the radius of Al^{3+} was smaller than Mn^{3+}, so Al^{3+} could substitute Mn^{3+} and form the Al–O bond. Gong et al. [16] prepared Al-doped spinel $LiMn_2O_4$, the results showed that the spinel structure was very stable when the doping Al content was less than x = 0.2. Among these different

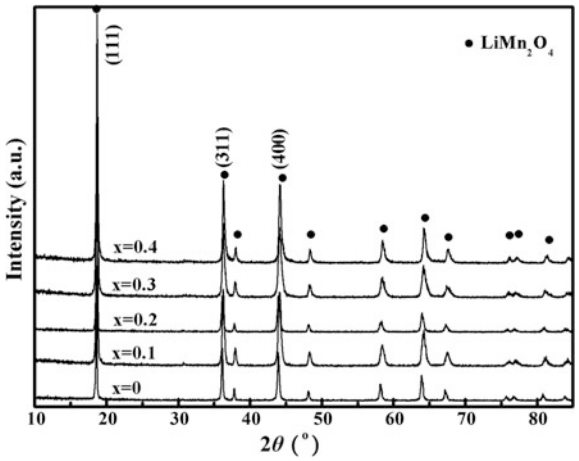

Fig. 1 XRD patterns for $LiAl_xMn_{2-x}O_4$ nanocrystallines calcined at 700 °C for 6 h

doping Al samples, the diffraction intensity of $LiAl_{0.1}Mn_{1.9}O_4$ was the largest and its Al content was less than x = 0.2. Therefore, the sample of $LiAl_{0.1}Mn_{1.9}O_4$ was chosen to compare with pure $LiMn_2O_4$ in subsequent kinetics study.

Effect of Temperature. Figure 2 is the XRD pattern of materials after calcinations at different temperatures for 6 h. It could be seen that the sample had characteristic peaks of cubic spinel $LiMn_2O_4$ [15]. The doped Al did not change the characteristic peaks of $LiMn_2O_4$, indicating that the doped Al^{3+} entered into the spinel lattice, forming the $LiAl_{0.1}Mn_{1.9}O_4$ nanocrystalline. Under low calcination temperature, the diffraction peaks displayed relatively weak intensity and wide width, suggesting the relatively small grain size of nano $LiAl_{0.1}Mn_{1.9}O_4$. With the increasement of calcination temperature, these diffraction peaks were strong and sharp, signifying that the grain size of nano $LiAl_{0.1}Mn_{1.9}O_4$ became larger and the crystallinity became more complete.

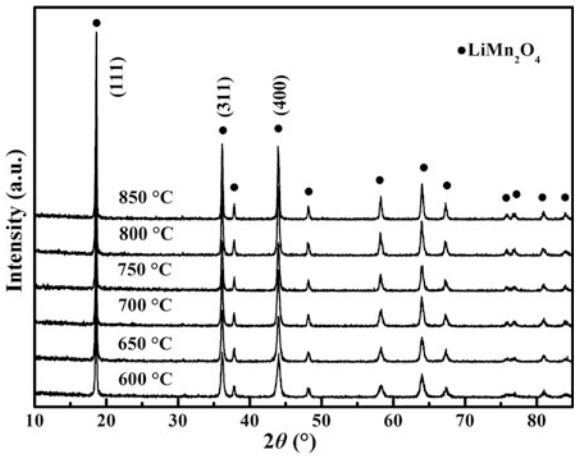

Fig. 2 XRD patterns of $LiAl_{0.1}Mn_{1.9}O_4$ nanocrystallines calcined at different temperatures for 6 h

Table 1 Grain sizes of $LiAl_{0.1}Mn_{1.9}O_4$ nanocrystal at different calcination temperatures for 6 h

T (°C)	600	650	700	750	800	850
D (nm)	28.4	30.7	33.6	37.4	43.2	50.1

The values of grain size from Scherrer formula for nano $LiAl_{0.1}Mn_{1.9}O_4$ are shown in Table 1. Results showed that calcination temperature displayed the positive correlation on grain size of $LiMn_2O_4$. At relatively low temperature, the diffusion speed was slow, so the growth of lattice nucleus was difficult, leading to the small grain size. While the calcination temperature increased, the diffusion speed also increased, so the nanocrystalline became large. From 600 to 850 °C, the grain size increased from 28.4 to 50.1 nm.

Effect of Time. The XRD pattern of nano $LiAl_{0.1}Mn_{1.9}O_4$ calcined at 700 °C for different times are shown in Fig. 3. From the pattern, these five materials all displayed the characteristic peaks of spinel $LiMn_2O_4$ [15]. And doped Al^{3+} did not change the crystal structure. At short calcination time, the diffraction peaks were weak and wide, implying the small grain size of sample. While at long calcination time, the pattern exhibited strong and sharp diffraction peaks, indicating the larger grain size and complete crystallinity of $LiAl_{0.1}Mn_{1.9}O_4$.

Table 2 shows the grain size values from Eq. (1) of nano $LiAl_{0.1}Mn_{1.9}O_4$. It could be found that there was also a positive correlation between calcination time and grain size. When the time was short, the growth and development of lattice nucleus were not complete, resulting in the small nanocrystalline. With the prolongation of calcination time, nanocrystalline developed and became large. From 4 to 12 h, the grain size increased from 31.2 to 39.7 nm. Moreover, the increasing percentage for grain size of calcination time was less than temperature.

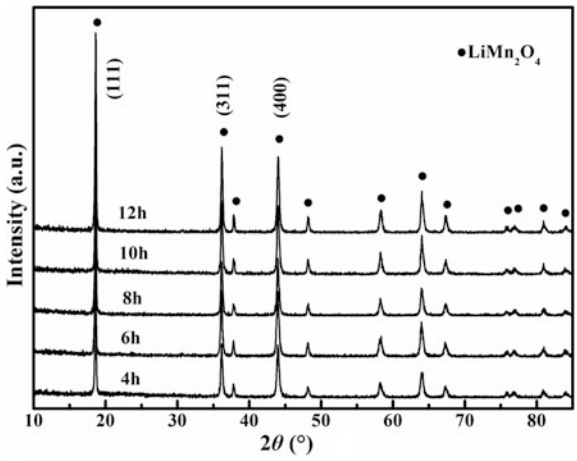

Fig. 3 XRD patterns of $LiAl_{0.1}Mn_{1.9}O_4$ nanocrystallines calcined for different time at 700 °C

Table 2 Grain sizes of $LiAl_{0.1}Mn_{1.9}O_4$ nanocrystal at different calcination times at 700 °C

t (h)	4	6	8	10	12
D (nm)	31.2	33.6	35.0	37.7	39.7

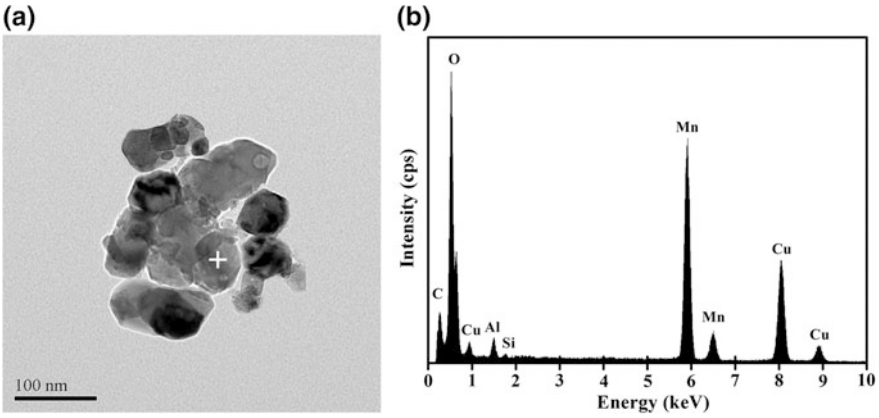

Fig. 4 **a** TEM image and **b** EDS of $LiAl_{0.1}Mn_{1.9}O_4$ at 700 °C for 6 h

TEM and EDS Analysis. Figure 4a is a TEM photo of $LiAl_{0.1}Mn_{1.9}O_4$ sample at 700 °C for 6 h. As can be seen, the sample displayed complete crystallinity and slight agglomeration. And the grain size of this sample was about 30–40 nm, confirming the inference from XRD patterns.

Figure 4b is an EDS of "+" in TEM. It could be seen that the sample contains Mn, O and Al elements, suggesting that Al ions successfully enter into the $LiMn_2O_4$ lattice. In addition, C, Cu and Si were observed from TEM instrumentation during the test.

Grain Growth Kinetics. According to Hillert model, here is a kinetics equation (Eq. 2) [17]:

$$D^n = k_0 t \exp(-E/(RT)) = kt \tag{2}$$

where n is reaction order, k_0 is grain growth rate constant, t is time, E is reaction activation energy, T is Kelvin temperature, k is equation constant.

When the temperature T is constant, the Eq. (2) is changed as Eq. (3); while the time t is constant, the Eq. (2) is changed as Eq. (4).

$$n\ln D = \ln k + \ln t \tag{3}$$

$$n\ln D = \ln(k_0 t) - E/(RT) \tag{4}$$

From the grain size D values in Table 2, the value of n calculated by regression using the least squares method was 6.36 by Eq. (3) at 700 °C, meaning the reaction order of 6. Then according to grain size D values in Table 1, the activation energy E via the least squares method was calculated as 120.66 kJ/mol. And the regression of conventional model is shown in Fig. 5a. There was a linear relationship between ln D and $1/T$, with the correlation coefficient R^2 of 0.978.

Based on our previous report, a novel kinetics model was given as Eq. (5) [12]:

$$1/D = A + B/T \tag{5}$$

where A was defined as $t^{-1/n}$, B was defined as $t^{-1/n}E'/nR$, E' is the new activation energy.

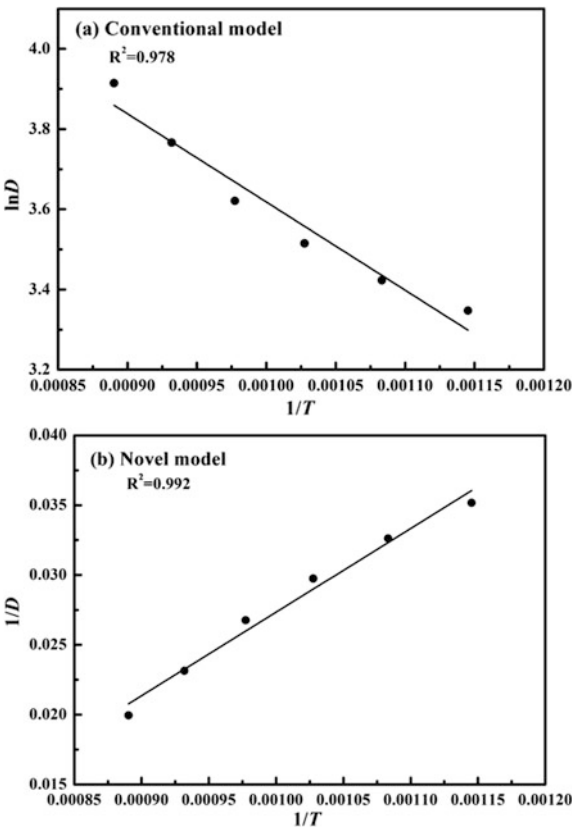

Fig. 5 Regression of kinetics equations for **a** conventional model, **b** novel model

Due to reaction order of 6 and grain size values in Table 1, the values of A and B could be calculated from the linear regression of Eq. (5). It displayed the values as: $A = t^{-1/n} = 0.0361$, $B = t^{-1/n}E'/nR = 58.712$. In this case, the value of E' was calculated as 81.13 kJ/mol. And the regression of novel model is displayed in Fig. 5b. There was a linear relationship between $1/D$ and $1/T$, with the correlation coefficient R^2 of 0.992.

Comparing with two kinetics models, it could be found that our novel model exhibited the higher correlation coefficient than conventional model, indicating it was more suitable for $LiAl_{0.1}Mn_{1.9}O_4$ nanocrystalline. For nanocrystalline, it showed large specific surface area and strong surface activity. Except for diffusion influence, surface reaction should also be considered. Thence, the activation energy of nanomaterial was less than micron material.

Conclusions

$LiMn_2O_4$ nanocrystal was prepared by co-precipitation method, and Al ion was doped to obtain $LiAl_xMn_{2-x}O_4$ material. The XRD patterns display that $LiAl_{0.1}Mn_{1.9}O_4$ shows the strong diffraction intensity and stable structure. Calcination temperature and time both had significant influences on grain sizes. With temperature increased from 600 to 850 °C, the grain size increases from 28.4 to 50.1 nm. While with time increased from 4 to 12 h, the grain size increases from 31.2 to 39.7 nm. Grain growth kinetics is simulated with two models. The novel model is more suitable to fit with experimental data of grain sizes than the conventional one, indicating that both diffusion and surface reaction play the important roles during grain growth process.

Acknowledgements This work was supported by Fundamental Research Funds for Central Universities of Central South University (2017zzts108) and Innovative Projects for Students of Central South University.

References

1. H.W. Lee, P. Muralidharan, R. Ruffo et al., Ultrathin spinel $LiMn_2O_4$ nanowires as high power cathode materials for Li-ion batteries. Nano Lett. **10**, 3852–3856 (2010)
2. K. Chung, H. Lee, W. Yoon et al., Studies of $LiMn_2O_4$ capacity fading mechanism at elevated temperature using in situ synchrotron X-ray diffraction. J. Electrochem. Soc. **153**, A774–A780 (2006)
3. Y. Liu, L. Tan, L. Li, Tris(trimethylsilyl) borate as an electrolyte additive to improve the cyclability of $LiMn_2O_4$ cathode for lithium-ion battery. J. Power Sources **221**, 90–96 (2013)
4. Y.J. Wei, L.Y. Yan, C.Z. Wang et al., Effects of Ni doping on [MnO_6] octahedron in LiMn2O4. J. Phys. Chem. B. **108**, 18547–18551 (2004)
5. W. Tang, Y. Hou, F. Wang et al., $LiMn_2O_4$ nanotube as cathode material of second-level charge capability for aqueous rechargeable batteries. Nano Lett. **13**, 2036–2040 (2013)

6. Y.L. Ding, J. Xie, G.S. Cao et al., Enhanced elevated-temperature performance of Al-doped single-crystalline $LiMn_2O_4$ nanotubes as cathodes for lithium ion batteries. J. Phys. Chem. C **115**, 9821–9825 (2011)
7. P. Ram, A. Gören, S. Ferdov et al., Improved performance of rare earth doped $LiMn_2O_4$ cathodes for lithium-ion battery applications. New J. Chem. **40**, 6244–6252 (2016)
8. M. Jeong, M. Lee, J. Cho et al., Surface Mn oxidation state controlled spinel $LiMn_2O_4$ as a cathode material for high-energy Li-Ion batteries. Adv. Energy Mater. **5**, 1500440 (2015)
9. W. Wen, B. Ju, X. Wang et al., Effects of magnesium and fluorine co-doping on the structural and electrochemical performance of the spinel $LiMn_2O_4$ cathode materials. Electrochim. Acta **147**, 271–278 (2014)
10. R. Thirunakaran, A. Sivashanmugam, S. Gopukumar et al., Phthalic acid assisted nano-sized spinel $LiMn_2O_4$ and $LiCr_xMn_{2-x}O_4$ (x = 0.00 − 0.40) via sol-gel synthesis and its electrochemical behaviour for use in Li-ion-batteries. Mater. Res. Bull. **43**, 2119–2129 (2008)
11. F.L. Cras, D. Bloch, M. Anne et al., Lithium Intercalation in Li–Mg–Mn–O and Li–Al–Mn–O Spinels. Solid State Ionics **89**(3–4), 203–213 (1996)
12. X.L. Song, D. Liu, Y. Zhang et al., Grain growth kinetics of SnO_2 nanocrystals synthesized by precipitation method. J. Wuhan Univ. Technol. **25**, 929–934 (2010)
13. X.L. Song, Y. Zhang, Y.X. Zhou et al., Grain growth kinetics of $LiMn_2O_4$ nanocrystals during calcining process. Integr. Ferroelectr. **178**, 35–41 (2017)
14. A.V. Potapenko, S.I. Chernukhin, I.V. Romanova et al., Citric acid aided synthesis, characterization, and high-rate electrochemical performance of $LiNi_{0.5}Mn_{1.5}O_4$. Electrochim. Acta **134**, 442–449 (2014)
15. F.Y. Shih, K.Z. Fung, Effect of annealing temperature on electrochemical performance of thin-film $LiMn_2O_4$ cathode. J. Power Sources **159**, 179–185 (2006)
16. J. Gong, J.H. Yang, C.Z. Wang et al., Effects of Al doping on the spinel structure of Li[Mn (Al)]$_2O_4$. Chem. J. Chin. Univ. **23**, 2322–2324 (2002)
17. K.J. Song, Y.H. Wei, K. Fang et al., Cellular automaton-based study of factors that affect dynamic solid phase transformation kinetics. Appl. Math. Model. **39**, 5058–5072 (2015)

Novel Semi-interpenetrating Polymeric Networks with Multiple Shape Memory

Shishan Xue, Yuanpeng Wu, Haiyan Zhang, Xin Wang, Zhaohui Zheng and Xiaobin Ding

Abstract Multiple shape memory polymers can memory multiple shapes and they are useful in many fields. In this work, poly(methyl methacrylate)/poly (dimethylsiloxane-b-ethylene oxide) methyl terminated (PMMA/PDMS-PEO) semi-interpenetrating polymeric networks (semi-IPNs) with broadened glass transition were prepared through ultraviolet-initiated radical polymerization. These novel semi-IPNs can provide many transition temperatures for multiple-step shape fixation and recovery and thus can realized dual, triple, and quadruple shape memory effects in a shape memory cycle.

Keywords Shape memory polymers · Multiple shape memory
Polymeric networks · Poly(methyl methacrylate)

S. Xue · Y. Wu (✉) · H. Zhang · X. Wang
School of Materials Science and Engineering,
Southwest Petroleum University, Chengdu 610500, China
e-mail: ypwu@swpu.edu.cn

S. Xue
e-mail: xueshishancarol@163.com

H. Zhang
e-mail: haiyanwin@126.com

X. Wang
e-mail: xin.wang@swpu.edu.cn

Z. Zheng · X. Ding
Chengdu Institute of Organic Chemistry, Chinese Academy
of Sciences, Chengdu 610041, China
e-mail: zhzheng@cioc.ac.cn

X. Ding
e-mail: xbding@cioc.ac.cn

Y. Han (ed.), *Advances in Energy and Environmental Materials*,
Springer Proceedings in Energy, https://doi.org/10.1007/978-981-13-0158-2_30

Introduction

Shape memory polymers (SMPs) are well-known intelligent materials with promising applications such as sensors, self-healing materials, biomedical devices and smart textiles [1]. SMPs can change their shapes in a predefined way from temporary to permanent shape when exposed to stimulus like heat, electricity, light and magnetic field [2–5]. Generally, SMPs have one transition temperature (T_{trans}) that permits the fix of only one temporary shape, showing dual shape memory behaviors. Recently, multiple SMPs having two or more T_{trans}'s have been reported and attracted growing attentions [6]. Unlike those with single T_{trans}, SMPs with multiple T_{trans}'s can memorize two or more temporary shapes and sequentially recover to their original shape from two or more temporary shapes under controlled stimulus, making them suitable candidates for applications in adjustable complex shapes, such as smart implants, surgical catheter and bio-medical actuator [7]. These promising potentials in application motivate the research of novel multiple-SMPs [8].

Broadening glass transition is an effective way for achieving multiple SMPs [2, 9]. Our group have previously prepared multiple SMPs from PMMA/poly (ethylene glycol) semi-IPNs and PMMA/poly(ε-caprolactone) co-networks with broadened glass transition [10–12]. Although the shape memory effects of these SMPs are good, the polymer preparation, notably heat-induced radical polymerization, is less efficient. Herein, PMMA/PDMS-PEO semi-IPNs with broadened glass transition were prepared by a timesaving technology, i.e. ultraviolet (UV)-initiated radical polymerization. PDMS-PEO was chosen because the flexible PDMS chains can broaden the thermal transition of semi-IPNs whereas PEO segments can decrease the micro-phase separation between the copolymer and PMMA [10].

Experimental

The semi-IPNs were prepared through UV-initiated polymerization. PDMS-PEO (20:80 (molar ratio), Mw = 3000) was dissolved in methyl methacrylate (MMA) under stirring. Ethylene glycol dimethacrylate (EGDMA) and UV initiator (2-hydroxy-2-methyl propiophenone, HMP) were then added. The mixture was poured into a mould and polymerized with UV irradiation for 1.5 h. The feeding weight ratios of MMA to PDMS-PEO were varied at 20:1, 20:2, 20:3, 20:4 and 20:5. The corresponding polymers were donated as PMMA/PDMS-PEO-x, where x = 1, 2, 3, 4, 5 for different feeding ratio. EGDMA and HMP were kept at 2 and 0.2 wt% of MMA and PDMS-PEO.

Differential scanning calorimetry (DSC) was performed on a TA Q200 instrument from −60 to 120 °C at heating and cooling rates of 10 °C/min. Dynamic mechanical analysis (DMA) was effected at a heating rate of 10 °C/min on a TA Q800 instrument.

Results and Discussion

Thermal Properties of PMMA/PDMS-PEO. The thermal behaviors of PMMA/PDMS-PEO of different compositions were studied by DSC and DMA. DSC was performed from −60 to 120 °C at heating and cooling rates of 10 °C/min. The temperature was selected in this range due to the chains of the polymers can be crystallized at low temperature and the heating history of the polymer can be eliminated at high temperature. Figure 1a presents the DSC curves obtained from the second cooling scan with temperature from −55 to 55 °C. The distinct exothermic peak at about −20 °C for pure PDMS-PEO is attributed to the crystallization of the copolymer [10, 13]. The crystallization temperature gradually despaired with increasing PDMS-PEO content for the composites. This may be related to the steric effect of PMMA networks on the formation of PDMS-PEO crystal, suggesting a fully miscible and homogeneous amorphous phase in these composites particularly for PMMA/PDMS-PEO-3, -4 and -5 semi-IPNs [11].

DMA results for the determination of thermal transition and T_g (defined as the peak maxima in tan δ traces) of semi-IPNs are shown in Fig. 1b. The T_g of semi-IPNs decreased with growing PDMS-PEO content due to the introduction of flexible PDMS-PEO segments into PMMA networks, indicating a homogeneous amorphous phase formed in the semi-IPNs [12]. It can also be observed that these semi-IPNs exhibited remarkably broadened thermal transitions which can be tuned by weight fraction of the two precursors. It is noted that PMMA/PDMS-PEO-3 possessed a thermal transition region from 40 to 160 °C. The region is obviously broader than that of common SMPs [14]. This may be ascribed to the homogeneous amorphous phase formed by the crosslinking of PMMA with PDMS-PEO. The two domains are restricted to small phase in the semi-IPNs, supressing their glass transition to gradually approach and turned into a broadened thermal transition region eventually [15]. Because of that, many separated T_{trans} can be chosen within the thermal transition region and utilized for multiple shape memory effects (SMEs).

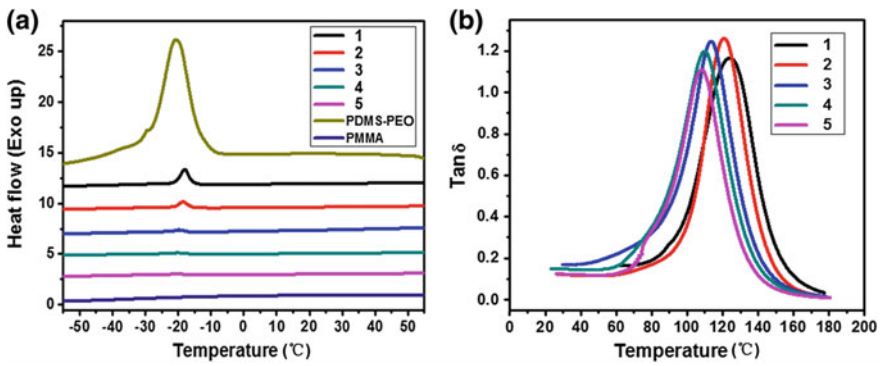

Fig. 1 **a** DSC thermograms and **b** DMA results of PMMA/PDMS-PEO-1 (1), PMMA/PDMS-PEO-2 (2), PMMA/PDMS-PEO-3 (3), PMMA/PDMS-PEO-4 (4), PMMA/PDMS-PEO-5 (5) semi-IPNs and pure PDMS-PEO, PMMA

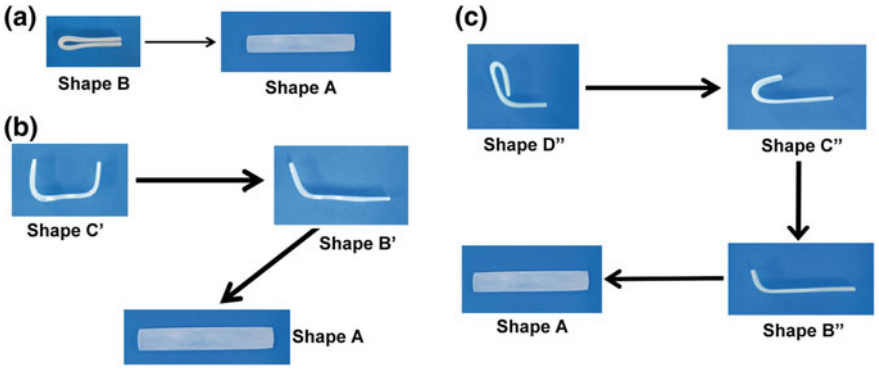

Fig. 2 Images of **a** Dual, **b** triple and **c** quadruple shape memory of PMMA/PDMS-PEO semi-IPNs

Multiple SEMs of PMMA/PDMS-PEO. PMMA/PDMS-PEO-3 was selected as an example model to describe the multiple SMEs. The permanent shape A was bent at 170, 150, 130, 110, 80 °C to temporary shape B and cooled to 25 °C. When the external force was removed, shape B was fixed and the fixity rates (R_f) measured by angle method [10] were 99.8, 99.4, 99.1, 98.7 and 98.6%, respectively. Figure 2a shows the dual shape recovery process. Shape B was reheated to 170, 150, 130, 110, 90 °C and thus shape A was obtained with recovery rates (R_r) [10] of 99.2, 98.6, 98.4, 98.5 and 98.1%.

In order to achieve triple SMEs, two T_{trans}'s within the broad thermal transition are required [15]. Herein, two T_{trans}'s at 170 and 90 °C were chosen to accomplish the triple SMEs. PMMA/PDMS-PEO-3 with permanent shape A was deformed at 170 °C to shape B′ under external force. Then it was cooled to 90 °C and the first temporary shape B′ with $R_{f(A-B')}$ equal to 80.5% was obtained. Subsequently, shape B′ was deformed to shape C′ and fixed at 25 °C with $R_{f(B'-C')}$ of 89.6%. Figure 2b depicts the recovering procedure of triple SMEs. When shape C′ was heated to 90 °C, shape B′ with $R_{r(C'-B')}$ of 93.4% was recovered. Then the sample was reheated to 170 °C and the permanent shape A with $R_{r(B'-A)}$ of 96.2% was achieved. Interestingly, the triple SMEs can also be realized if two other T_{trans}'s in the thermal transition range are chosen. Typically, if 160 and 80 °C are selected as T_{trans}, the fixation and recovery for triple SMEs can also be realized. In fact, there are many combinations of T_{trans} that can implement triple SMEs, although the R_f and R_r may be different. This indicates that the glass transition region of this polymer is sufficiently broad to memorize three shapes [16, 17]. Theoretically, a broad glass transition region can be considered as an infinite number of transitions, leading to multiple SMEs in the range [18, 19].

Furthermore, quadruple SMEs are achieved by selecting three T_{trans}'s (170, 110 and 75 °C). PMMA/PDMS-PEO-3 with permanent shape A was heated to 170 °C

and deformed to shape B″. The temperature was decreased to 110 °C and the first temporary shape B″ was fixed. Then, shape B″ was deformed to shape C″ and cooled to 75 °C for fixation. Finally, shape C″ was changed to shape D″ and cooled to 25 °C to fix temporary shape. Figure 2c demonstrates the recovery of quadruple SMEs. By heating to 75 °C, shape C″ was recovered. When reheated to 110 and 170 °C, shape B″ and permanent shape A were obtained subsequently. Using the angle method, $R_{f(A-B'')}$, $R_{f\ (B''-C'')}$ and $R_{f\ (C''-D'')}$ were determined as 81.3, 78.2 and 76.8%, while $R_{r(D''-C'')}$, $R_{r(C''-B'')}$, and $R_{r(B''-A)}$ were calculated to be 89.5, 88.7 and 91.6%. Similar to triple SMEs, any other three T_{trans}'s in the transition temperature range can also be chosen to accomplish the quadruple SMEs without changing the compositions of the polymer [20]. In other words, by tuning the T_{trans} in the thermal transition, we can achieve a series of multiple SMEs without the necessity of changing the chemical structure or composition of the semi-IPNs. This may help to develop essential methods for fabricating multiple functional materials [21, 22].

Mechanism of Multiple SEMs. Based on the results of multiple SMEs and molecular structure of the semi-IPNs, a possible mechanism is proposed [23]. In the semi-IPNs, the cross-linking PMMA chains and linear PDMS-PEO chains are forcedly interlocked. This makes the glass transition span a broader temperature interval that allows numerous T_{trans}'s for multiple SMEs [14, 24]. When at T_{trans}, high, all polymer chains are flexible and the polymer is readily deformable. When cooled to T_{trans}, middle, the first temporary shape B is fixed because the polymeric segments in the amorphous PMMA/PDMS-PEO mixed phase are partially vitrified and the stored energy can fix the temporary shape. After the shape is deformed at $T_{trans,\ middle}$ and cooled to $T_{trans,\ low}$, the second temporary shape C is obtained because the whole amorphous PMMA/PDMS-PEO phase is now in a completely glassy state at this temperature, and the polymeric chains are frozen and the energy stored at this step fixes the temporary shape. When the SMP is heated from low to high temperature step by step, the frozen polymeric chains are activated subsequently. The stored energy is thus released from $T_{trans,\ low}$ to $T_{trans,\ middle}$, $T_{trans,\ high}$ and triple SMEs is achieved [25]. The above proposed mechanism for triple SMEs is illustrated in Fig. 3. The molecular mechanism of quadruple-SME can be analogically deduced from the proposed mechanism.

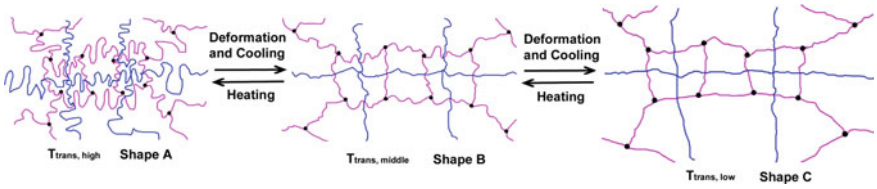

Fig. 3 Mechanism of multiple shape memory effects of PMMA/PDMS-PEO semi-IPNs. Magenta: PMMA chains, blue: PDMS-PEO chains, and black: cross-links

Conclusions

In conclusion, novel PMMA/PDMS-PEO semi-IPNs with broad thermal transition region were prepared through UV-initiated polymerization. The polymers can realize multiple SMEs without breaking or re-synthesizing the polymeric semi-IPNs. The versatile dual, triple to quadruple SMEs can be effectively adjusted by selecting suitable T_{trans} within the broadened thermal transition range. Importantly, the broader transition range makes these semi-IPNs promising candidates in complex applications especially in medical and aerospace fields.

Acknowledgements The research was financially supported by National Nature Science Foundation of China (No. 51304166), Foundation of Science and Technology Bureau of Chengdu (No. 12DXYB191JH-002), Foundation of Sichuan Youth Science and Technology (2016JQ0036) and Department of Education (No. 16CZ0007) of Sichuan Province.

References

1. J. Leng, X. Lan, Y. Liu, S. Du, Prog, Thermo- and pH-sensitive shape memory polyurethane containing carboxyl groups, Mater. Sci. **56**, 1077–1135 (2011)
2. H. Koerner, G. Price, N.A. Pearce, M. Alexander, R.A. Vaia, Remotely actuated polymer nanocomposites-stress-recovery of carbon-nanotube-filled thermoplastic elastomers, Nat. Mater. **3**, 115–120 (2004)
3. M.R. Ramdas, K.S.S. Kumar, C.P.R. Nair, Click polymerizations: encouraging route for shape memory polymers. Mater. Lett. **172**, 216–221 (2016)
4. Y. Chen, Z.Y. Zhao, K. Alamgir, et al., Shape memory of microscale and nanoscale imprinted patterns on a supramolecular polymer compound. Macromol. Rapid. Comm. **37**, 1932–1938 (2016)
5. X.Y. Chen, K. Alexey, S.S. Bao, B. Marcela, Y. Lin, Plasma immersion ion implantation of polyurethane shape memory polymer: surface properties and protein immobilization. Appl. Surf. Sci. **416**, 686–695 (2017)
6. H. Du, X. Liu, Y. Yu, Y. Xu, Y. Wang, Z. Liang, Microwave-induced poly(ionic liquid)/poly (vinyl alcohol) shape memory composites. Macromol. Chem. Phys. **217**, 2626–2634 (2016)
7. Y. Li, Y. Zhou, Y. Zhou, Q. Yu, J. Zhu, N. Zhou, Dynamic furan/maleimide bond-incorporated cyclic polymer for topology transformation. React. Funct. Polym. **116**, 41–48 (2017)
8. G. Yang, X. Liu, T. Yoong, L. Vitali, Body temperature-responsive two-way and moisture-responsive one-way shape memory behaviors of poly(ethylene glycol)-based networks. Polym. Chem. **8**, 3833–3840 (2017)
9. Q. Zhao, M. Behl, A. Lendlein, Shape-memory polymers with multiple transitions: complex actively moving polymers. Soft Mater. **9**, 1744–1755 (2012)
10. J. Li, T. Liu, S. Xia, Y. Pan, Z. Zheng, X. Ding, et al., A versatile approach to achieve quintuple-shape memory effect by semi-interpenetrating polymer networks containing broadened glass transition and crystalline segments. J. Mater. Chem. **21**, 12213–12217 (2011)
11. J. Li, T. Liu, Y. Pan, S. Xia, Z. Zheng, X. Ding, et al., A versatile polymer co-network with broadened glass transition showing adjustable multiple-shape memory effect. Macromol. Chem. Phys. **213**, 2246–2252 (2012)

12. Y. Wang, J. Li, X. Li, Y. Pan, Z. Zheng, X. Ding, et al., Relation between temperature memory effect and multiple-shape memory behaviors based on polymer networks, RSC Adv. **4**, 20364–20370 (2014)
13. S. Senta, W. Mattias, H. Hendrik, Bio-inspired hierarchical micro- and nano-wrinkles obtained via mechanically directed self-assembly on shape-memory polymers. Soft Matter **13**, 4328–4334 (2017)
14. R. Hu, V.L. Dimonie, M.S. El-Aasser, R.A. Pearson, A. Hiltner, S.G. Mylonakis, et al., Multicomponent latex IPN materials: 2. Damping and mechanical behavior. J. Polym. Sci. Pol. Phys. **35**, 1501–1514 (1997)
15. S. Chatani, C. Wang, M. Podgorski, C.N. Bowman, Triple shape memory materials incorporating two distinct polymer networks formed by selective thiol-michael addition reactions, Macromolecules. **47**, 4949–4954 (2014)
16. Y. Shao, C. Lavigueur, X.X. Zhu. Multishape memory effect of norbornene-based copolymers with cholic acid pendant groups. Macromolecules, **45**, 1924–1930 (2012)
17. D. Sherif, O. Osman, Characterization of superelastic shape memory alloy fiber-reinforced polymer composites under tensile cyclic loading. Mater. Design **111**, 504–512 (2016)
18. L. Wang, X. Yang, H. Chen, T. Gong, W. Li, G. Yang, Design of triple-shape memory polyurethane with photo-cross-linking of cinnamon groups. ACS Appl. Mater. Inter. **5**, 10520–10528 (2013)
19. Y. Sun, S. Cai, J. Ren, N. Hani, Room temperature deformable shape memory composite with fine-tuned crystallization induced via nanoclay particles. J. Polym. Sci. Pol. Phys. **55**, 1197–1200 (2017)
20. X. Li, Y. Pan, J. Lai, R. Wu, Z. Zheng, X. Ding, Design of well-defined shape memory networks with high homogeneity: towards advanced shape memory polymeric materials. Polym. Chem. **8**, 3867–3873 (2017)
21. K. Kratz, U. Voigt, A. Lendlein, Temperature-memory effect of copolyesterurethanes and their application potential in minimally invasive medical technologies. Adv. Funct. Mater. **22**, 3057–3065 (2012)
22. Q. Tan, L. Liu, F. Li, X. Lan, Y. Liu, Strength property analysis for fiber-reinforced shape memory polymer composite laminate. J. Mat. Syst. Str. **28**, 1627–1639 (2017)
23. O. Adebola, J. Chen, Reprogrammable Chemical 3D Shaping for Origami, Kirigami, and Reconfigurable Molding. Angew. Chem. Int. Edit. **56**, 8250–8253 (2017)
24. S. Mohammad, B. Masoud, R. Mohammadreza, Thermally and electrically triggered triple-shape memory behavior of poly(vinyl acetate)/poly(lactic acid) due to graphene-induced phase separation. ACS Appl. Mater. Inter. **9**, 24061–24070 (2017)
25. Y. Shi, R.A. Weiss, Sulfonated poly(ether ether ketone) ionomers and their high temperature shape memory behavior. Macromolecules. **47**, 1732–1740 (2014)

Corrosion Resistance of Epoxy Resin Paint Modified by Hybrid Silica Sol in Simulated Oilfield Produced Water

Xia Wang, Xingxing Ji, Feiyu Wang, Hui Wang and Shuaifei Ren

Abstract Using organic-inorganic hybrid silica sol as modifier to prepare the modified epoxy resin paint, and the corrosion resistance of epoxy resin paint in simulated oilfield produced water was studied by electrochemical impedance spectroscopy test (EIS) and autoclave test, with scanning electron microscope (SEM) and energy dispersive spectrometer (EDS) as ancillary analyses. The results showed that when the paint coat was soaked for 7 days at different temperatures, the coating resistance could reach 10^7–10^8 Ω. When the temperature is 50 °C, the maximum resistance of coating is about 8.073×10^7 Ω, and the corrosion resistance property is the best. In addition, when the resin paint is soaked in the condition of T = 100 °C and P (CO_2) = 2 MPa with high-temperature autoclave for two days, the surface of resin paint has no foaming and shedding phenomenon. The SEM and EDS analysis show that the corrosion resistance of the coating in simulated oilfield produced water is improved significantly.

Keywords Organic-inorganic hybrid silica sol · Epoxy resin · Oilfield produced water · Electrochemical test

X. Wang (✉) · X. Ji · F. Wang · H. Wang · S. Ren
School of Material Science and Engineering,
Southwest Petroleum University, Chengdu 610500, China
e-mail: swpi_wx@126.com

X. Ji
e-mail: Jxx_swpu@163.com

F. Wang
e-mail: 422064796@qq.com

H. Wang
e-mail: awanghuideyouxiang@126.com

S. Ren
e-mail: duh1478@163.com

Y. Han (ed.), *Advances in Energy and Environmental Materials*,
Springer Proceedings in Energy, https://doi.org/10.1007/978-981-13-0158-2_31

Introduction

Oilfield produced water is the by-product in the extraction of oil and gas. The high temperature and salinity can lead to serious corrosion of steel [1]. When in the environment of oil field produced water, coating the pipes in service is one of the important means to retard the causticity [2]. Epoxy resin coating has excellent corrosion and chemical resistance, which has extensive application prospect and significant application value [3]. But due to the pure epoxy resin is three-dimensional network structure after solidified, the crosslinking density is high and there are large internal stress, resulting in hard and crisp texture. The poor thermal stability and easy decomposed property can be obvious limit to the application of epoxy resin coating [4, 5]. Organic-inorganic hybrid silicon can effectively improve the dispersion of nano-SiO_2 particles in epoxy resin [6–8]. Moreover, organic-inorganic hybrid silicon materials also have the properties of nanoparticles, which can enhance the toughness, temperature-resistance and corrosion resistance of epoxy resin coating [9–12], so it is an important research direction of epoxy resin coating modification [13]. Chou [14] and Zandi-Zand [15] studied the corrosion behavior of organic-inorganic hybrid coatings, which are deposited on the surface of metal matrix. The results showed that the corrosion potential of the coated metal system is increased. The corrosion current density decreased about 3–4 orders of magnitude, which proved that the hybrid membrane enhanced the corrosion resistance of the metal matrix.

Experimental

Experimental Drugs and Instruments. Tetraethoxysilane (TEOS), saline coupling agent (KH-560), isopropyl alcohol, xylene, n-butanol, cyclohexanone, sodium hydroxide, zinc powder, barium sulfate, titanium dioxide, talc powder, De-foaming agents and levelling agents; epoxy resin, polyamide 650. Type *pgstat302n* electrochemical workstation, Eco-Chemic Holland; *Cambridge S250 MK3* scanning electron microscopy, England. *WHF-2.5* high temperature autoclave, *Weihai* automatic control reactor Co Ltd.

Preparation of Modified Epoxy Resin Paint. Preparation of organic-inorganic hybrid silica sol. The appropriate amount of TEOS, KH-560 and isopropyl alcohol mixed evenly and adjust the pH to 10 with NaOH, the mixed with deionized water and isopropyl alcohol slowly added, the reaction after 2 h heated to 70 °C reaction 6 h, to obtain a light yellow transparent non-floc organic-inorganic hybrid silica sol [16].

Preparation of Modified Epoxy Resin Paint. Modified silica sol and epoxy resin in accordance with the mass ratio (5:4) mixed to obtain hybrid modified epoxy resin. A component (as shown in Table 1) was mixed uniformly, and after 3 h, the B component was added. Wherein the mixed solvent composition in the A and B

Table 1 A, B two-component paint coating formulation

Component	Material name	Quality percentage
A component	Hybrid modified epoxy resin	36
	Zinc powder	16
	Talc	1.6
	Titanium dioxide	1.6
	Barium sulfate	4.8
	Mixed solvent	16
B component	Polyamide resin 650	16
	Mixed solvent	8

Table 2 Simulated oilfield produced water

Reagent	$CaCl_2$	$MaCl_2$	KCl	Na_2SO_4	NaCl	$NaHCO_3$
Concentration (g/L)	10.945	3.08	0.445	0.46	43.595	3.34

components is (xylene: n-butanol: cyclohexanone mass ratio of 3:1:1), continue to stir in the magnetic 2 h, in the course of which, add 5‰ leveling agent and defoamer, to be modified epoxy resin paint. X65 steel sheet by hand brushing (before brushing on the surface of the sample treatment, X65 steel was polished with 280 #, 320 #, 400 #, 600 # metallographic sandpaper, and then degreased with acetone, ethanol was used to remove the water). After the sample was dry, it was cured in an electric blast oven for 4 h. Simulated oil field composition of water in Table 2, the temperature is 40 °C.

Results and Discussion

EIS Test of Paint Coats in Simulated Oilfield Produced Water. The prepared paint was sealed with 704 silica gel, leaving only one side of the coating. The coated samples were all immersed in 40, 50 and 60 °C simulated oilfield produced water. After 7 days of immersion, the samples were taken and sealed with paraffin, 1 cm^2 area for electrochemical impedance spectroscopy test (EIS). The test frequency range was 10^{-2}–10^5 Hz, the increase was 20 mV, and the saturated calomel electrode was used as the reference electrode, the platinum wire electrode was used as the privacy electrode, the X65 steel sheet was used as working electrode, and the corrosive medium was the simulated oilfield produced water. The Nyquist map and Bode pattern after immersion in simulated oilfield produced water for 7 days are shown in Fig. 1.

The radius of the first arc of the Nyquist curve at 60 °C is less than 40 and 50 °C, as compared to the semi-circular arc of the Nyquist curve, which is soaked in simulated oilfield produced water at 40, 50 and 60 °C for 7 days. However, in the

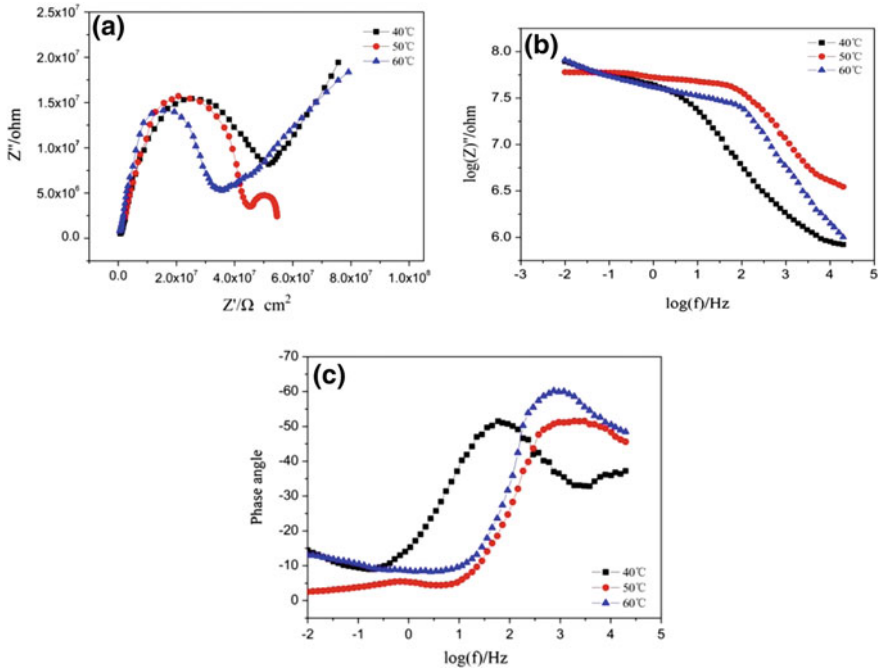

Fig. 1 Impedance spectrum after immersion 7 days at different temperature

high frequency region, the Nyquist curve for 7 days immersion at 50 ° C shows a smaller half-circular arc with a smaller radius, significantly different from the 40 and 60 ° C immersion for 7 days. The Nyquist curve is a trailing curve with a slope of 45° [17].

Figure 1b and c are the Bode diagrams of paint coats soaked 7 days at different temperatures. The impedance in the low frequency region is minimum after soaking at 50, but at 3 temperatures, the impedance decreases to a lesser extent. At three temperatures, the impedance of the coating in the low frequency region can reach 10^7–10^8, which shows that the paint coating has excellent corrosion resistance and great stability.

It can be seen from Fig. 1c that the curves at three temperatures have two time constants [18]. The Nyquist curves of the samples soaked at 40 and 60 °C were similar to those obtained by ZSIMPWIN software, and the fitting was obtained by fitting the circuit [19] as shown in Fig. 2a. The fitting circuit of the sample at 50 °C is shown in Fig. 3b.

It can be concluded from Table 3, the maximum coating resistance of the coating Rc after soaking 7 days is 8.073×10^7 Ω at 50 °C, and the minimum coating resistance Rc is 1.616×10^7 Ω at 60 °C. Indicating that the coating performance at 50 °C is better than 60 and 40 °C.

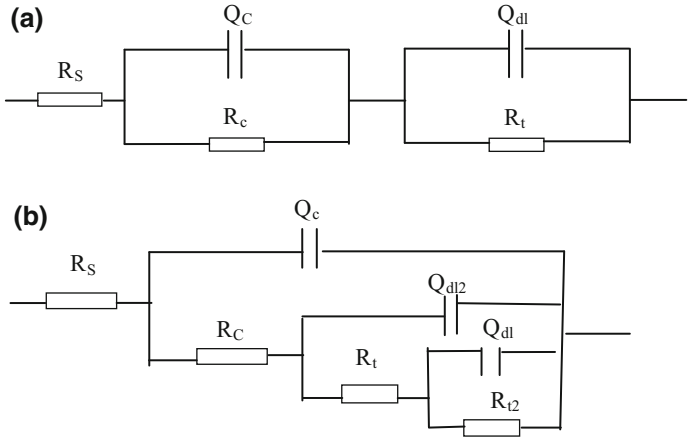

Fig. 2 **a** Equivalent circuit of the paint coats after immersion 7 days at 40 and 60 °C; **b** Equivalent circuit of the paint coats after immersion 7 days at 50 °C

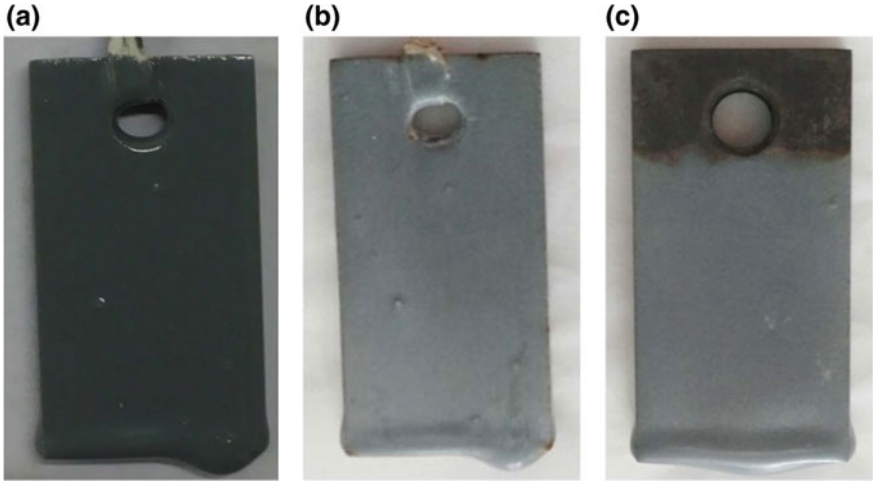

Fig. 3 Paint macro-photo before and after soaking 2 days in P (CO_2) = 2 MPa, T = 100 °C high temperature autoclave **a** Sample before corrosion; **b** Sample after corrosion; **c** The upper part of the exposed specimen

Corrosion Resistance of Paint in High Temperature and Pressure. The use of high-temperature autoclave on the preparation of hybrid modified epoxy resin paint in more stringent conditions for corrosion experiments [20, 21]. First, nitrogen is removed to remove the oxygen from the simulated oilfield produced water and the reactor. Then, CO_2 is removed by nitrogen, heated to 100 °C, and then CO_2 is fed to the desired pressure. Corrosion tests were carried out on the prepared paint coatings at T = 100°C, P (CO_2) = 2 MPa. The prepared paint coating was subjected to a

Table 3 Fitting data of 40, 60 °C after soaking 7 days

Temperature (°C)	40	50	60
R_S (Ω cm^{-2})	0.01	0.01	0.02
Q_C ($\Omega^{-1}sncm^{-2}$)	9.929E−10	9.197E−7	3.244E−8
n1	0.8569	0.3106	0.3174
R_c (Ω cm^{-2})	3.381E7	8.073E7	1.616E7
Q_{dl} ($\Omega^{-1}sncm^{-2}$)	4.398E−8	6.31E−12	8.224E−11
n2	0.2945	1	0.8763
Rt (Ω cm^{-2})	4.429E8	1.231	2.822E7
Q_{dl2} ($\Omega^{-1}sncm^{-2}$)		7.572E−5	
n3		0.0654	
R_{t2} (Ω cm^{-2})		4.116E7	

corrosion test at 100 °C and 2 MPa CO_2. X-ray diffraction (XRD) and scanning electron microscopy (SEM) were used to analyze the corrosion resistance of the paint coating after.

The macroscopic morphology of the specimen before and after the high temperature and high pressure experiment is shown in Fig. 3. Figure 3a shows the macroscopic photograph of the organic-inorganic hybrid modified paint before etching, which has a deep color and a strong light intensity. Figure 3b shows the macroscopic morphology of the sample after 2 days of immersion in simulated oilfield water at T = 100 °C, P (CO_2) = 2 MPa, and its surface has lost its brightness and the color of the coating becomes shallow. Probably because the surface of the coating of Zn reacts with the corrosive medium, resulting in a layer of lighter colour of the film, its material by XRD analysis shows that $ZnCO_3$ and $Zn_5(CO_3)_2(OH)_6$. Figure 3c is a macroscopic photograph of the corroded steel sheet. The sample is characterized by the fact that some of the steel sheets in the upper half are not painted, and it can be seen that the X65 steel sheet at the coating is not corroded. The corrosion of the exposed steel sheet is serious, not only is comprehensive corrosion, in some parts there are pits, the above description of paint in the high temperature autoclave after soak 2 days the corrosion resistance is good. **XRD Analysis**. Figure 4a can be drawn, the coating composition before the corrosion is relatively simple, the 2θ of 36.408°, 39.108°, 43.325° and 54.427° of the characteristic peaks of Zn, The characteristic peaks of BaSO4 at 2θ of 20.597°, 22.928°, 25.987°, 32.940°, 42.729°, 48.734°, 56.655°. Figure 4b shows that the organic inorganic hybrid paint has a certain change after 2 days corrosion reaction in the high temperature autoclave with the condition of T = 100 °C, P (CO_2) = 2 MPa. The 2θ of 25.256°, 32.786°, 38.923°, 46.845°, 53.968°, 62.332° of the characteristic peaks of $ZnCO_3$, The 2θ of 30.525° and 63.246° of the characteristic peaks of $Zn_5(CO_3)_2(OH)_6$, It is shown that Zn powder is involved in electrochemical reaction and plays a certain role in the cathodic protection of sacrificial anode. At the same time, $ZnCO_3$ and Zn_5 $(CO_3)_2$ $(OH)_6$ are the products

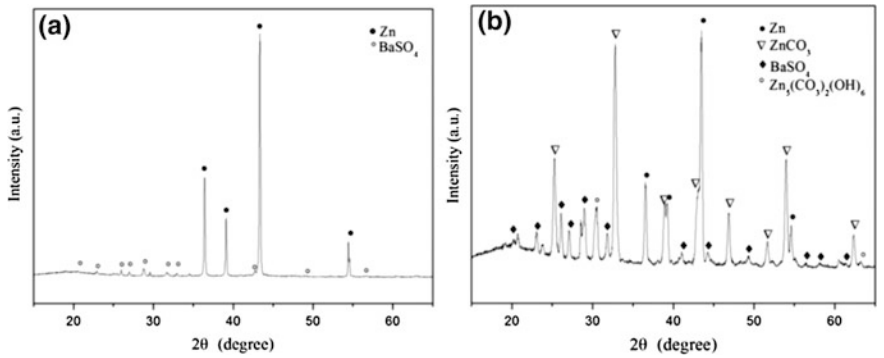

Fig. 4 XRD spectra of paint coats before and after 2 days reaction in P (CO_2) = 2 MPa, T = 100 °C high temperature autoclave. **a** XRD spectra before corrosion; **b** XRD spectra after corrosion

of corrosion deposition of zinc powder, these products can play the role of shielding protection. At the same time, because the product is $ZnCO_3$, $Zn_5(CO_3)_2(OH)_6$ is the product of corrosion deposition of zinc powder, it can play a shielding role. In addition, SiO_2 in the paint because there is no crystallization, it was not measured in the XRD, but the SiO_2 particles to fill the part of the structure of the hole, played a better anti-corrosion effect.

SEM and EDS Analysis. Figure 5 is SEM images of organic-inorganic hybrid silica sol modified epoxy resin after soaked 2 days in high temperature autoclave with the condition of T = 100 °C, P (CO_2) = 2 MPa. The figure can be seen in the white dot-like material and a very small number of black pinhole. The white dot-like substance is the crystal of the partial salt in the corrosive medium, and the black pinhole is a defect that occurs during the etching process. There are a few pinholes on the surface of the coating, but less overall defects.

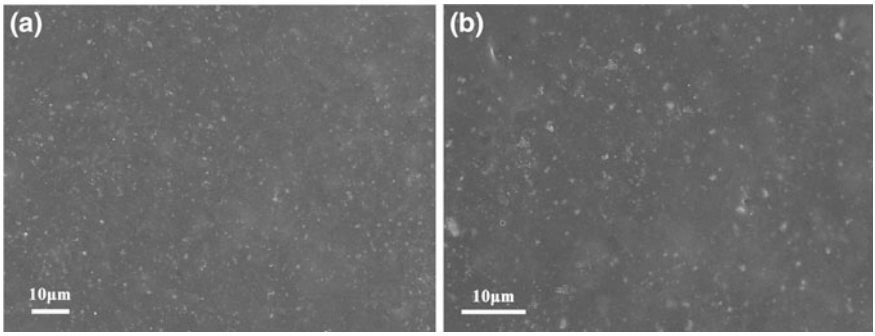

Fig. 5 SEM test of paint coats before and after 2 days reaction in P (CO_2) = 2 MPa, T = 100 °C high temperature autoclave. **a** 1000 times SEM after corrosion; **b** 2000 times SEM after corrosion

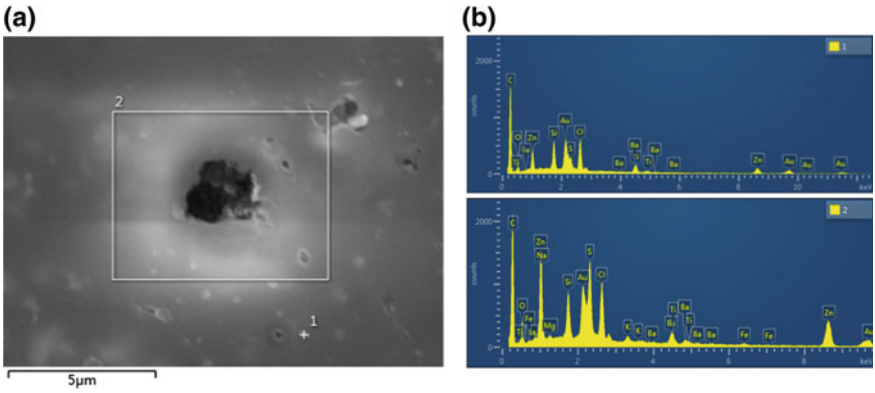

Fig. 6 EDS test of paint coats after 2d reaction in P (CO_2) = 2 MPa, T = 100 °C high temperature autoclave. **a** EDS scan 20,000 times magnification; **b** components of 1 and 2 position

Figure 6 shows the EDS spectra of the paint coats after 2 days reaction in the high temperature autoclave with condition of P (CO_2) = 2 MPa and T = 100 ° C. It can be found that pinhole is present at 1 and its diameter is about 2 μm. From Fig. 6b, it can be concluded that there are Fe elements at position 2, indicating that corrosion has occurred on the metal surface. In addition, there is no Fe element at position 1, indicating that the corrosion pits are formed soon, the corrosion is not serious, and the coating is not completely damaged and still in the state of protecting the metal matrix. Si element appears in the energy spectrum, XRD can not detect the corresponding Si, indicating that the resulting SiO_2 is amorphous, further proof of amorphous SiO_2 particles to fill part of the structural pores, excellent resistance for the paint from the anti-corrosion effect To a certain role.

Mechanism of Corrosion Resistance. According to XRD analysis, the paint coating in the high temperature autoclave reaction 2 days with a basic zinc carbonate generated, which is because the coating in the coating to play a certain sacrificial anode cathodic protection, to protect the higher potential of the Fe, Zn powder corrosion of the original battery reaction, the formation of basic zinc carbonate can effectively protect the X65 steel, the corrosion product structure is dense, and is difficult to dissolve stable compounds. At the same time, due to the presence of organic-inorganic hybrid silicon particles, the transmission of corrosive media has been a certain hindrance. The nanoparticles in epoxy resin can fill the "structural pores" which can not be avoided by organic coating, To prevent the infiltration of corrosive media. Therefore, the prepared anti-corrosion mechanism of paint is the shielding effect and cathodic protection.

Conclusions

Organic-inorganic hybrid silica sol modified paint was immersed in simulated oilfield water at 40, 50 and 60 °C for 7 days. The resistance values of the coatings at three temperatures can reach 10^7–$10^8\Omega$ in the low frequency region. The maximum resistance Rc of the coating is $8.073 \times 10^7\Omega$ at the 50 °C. The results show that the corrosion resistance of the paint coating is excellent and the stability is great. In the high temperature autoclave, the corrosion resistance of the modified modified epoxy resin paint is studied, and the results are shown in SEM and EDS. The paint corrosion resistance is good, and its anti-corrosion mechanism can be explained by the shielding effect and cathodic protection.

References

1. J. Qiu, M. Du, Y.Lu , Y. Zhang, H.J. Guo , C.J. Li, The study of X65 carbon steel in simulated oil field water by production of cathodic protection. J. China J. Corros Prot **34**, 333–338 (2014)
2. S.N. Zhao, *Study on the Influence of Oil and Water Components on the Corrosion Performance*. (South China University Technology, 2010)
3. B. Chen, The application status and development of epoxy resin coatings. J. Chem. Eng. Manage. **33**, 72–73 (2015)
4. N. Elhalawany, M.M. Saleeb, M.K. Zahran, Novel anticorrosive emulsion-type paints containing organic/inorganic nanohybrid particles. J. Prog Org Coat **77**, 548–556 (2014)
5. D.R.Xin, *The Failure Mechanism of Interface and Mechanical Properties of Epoxy Resin in the Hydrothermal Environment* (Research of South China University Technology, 2013)
6. V.D. Ramos, H.M. Dacosta, V.L.P. Soares, R.S.V Nascimento, Modification of epoxy resin: a comparison of different types of elastomer. J. Polym. Test. **24**, 387–394 (2005)
7. Z.P. Zhang, A.J. Gu, G.Z. Liang, P.G. Ren, J.Q. Xie, X.L. Wang, Thermo-oxygen degradation mechanisms of poss/epoxy nanocomposites. J. Polym. Degrad. Stab. **92**, 1986–1993 (2007)
8. P.A. Charpentier, K. Burgess, L. Wang, R.R. Chowdhury, A.F. Lotus, G. Moula, Nano-TiO_2/polyurethane composites for antibacterial and self-cleaning coatings. J. Nanotechnol **23**, 425–436 (2012)
9. R. Zandi-zand, L.A. Ershad, A. Rahimi, A. J. Progr. Org. Coat. **53**, 286–291 (2005)
10. T.L. Metroke, J.S. Gandhi, A. Apblett, Corrosion resistance properties of Ormosil coatings on 2024-T3 aluminum alloy. J. Progr. Org. Coat. **50**, 231–246 (2004)
11. Y. Liu, D.Z. Sun, H. You, J.S. Chung, J. Appl Surf. Sci. **246**, 82–89 (2005)
12. W.L .Li, S.M. Yang,S.H. Zhi, Preparation and performance analysis of J. coating industry new silica sol modified epoxy coatings 41 (2011) 4–8
13. F. Zhang, *The Study of Organic and Inorganic Hybrid Epoxy Resin Coating Materials* (Wuhan University of Technology, 2011), pp. 1–5
14. T.P. Chou, C. Chandrasekaran, S.J. Limmer,S. Seraji,Y. Wu, M.J. Forbes, C. Nguyen, G.Z. Cao, Organic-inorganic hybrid coatings for corrosion protection. J. Non-Cryst. Solids **290**, 153–162 (2001)
15. R. Zandi-zand, L.A. Ershad, A. Rahimi, Silica based organic-inorganic hybrid nano-composite coatings for corrosion protection. J. Progr. Org. Coat. **53**, 286–291 (2005)
16. X. Wang , S.C. Shi, Y.X. Chen, Y.C. Wu, X.X. Ji, Organic inorganic hybrid silica sol modified epoxy resin coating preparation and properties. J. Mat. Rev. **30**, 335–339 (2016)

17. X. Zhao, *Characteristics of Electrochemical Impedance Spectroscopy in Deterioration Process of Organic Coating* (Ocean University of China, 2007)
18. J.C. Chen, X.D. Wang, D.B. Sun, Penetration of chlorine ion in organic coating and deterioration process by electrochemical impedance spectroscopy. J. Mat. Eng. **6**, 56–57 (2011)
19. X. Yuan, *Theoretical and Experimental Study on Corrosion Failure Behavior of Coating/Metal System* (Northwestern Polytechnical University, 2016)
20. C.H. Jiang, R.P, Jing, Y.W. Jiang, W. Chen, X.F. Wang, J. Corros. Protect. **9**, 460–463 (2006)
21. J. Guo, *Applicability Evaluation of Inner Coating in Oil Pressure Vessel* (Xi'an Petroleum University, 2015)

Conductivity and Electromagnetic Shielding Effectiveness of Flaky Ni/Ni–Cu–La–B-Coated Glass Fiber/Acrylic Resin Composite Shielding Coating

Denggao Guan, Yang Liu, Dehao Hu, Zehang Dai, Caiwen Wu, Rundong Zhou, Jiayun Cao, Xinghong Pu and Li Cheng

Abstract Flaky Ni/Ni–Cu–La–B-coated Glass Fiber/Acrylic resin composite coatings were prepared using the flaky nickel powders and glass fibers and as fillers and Acrylic resin as binder. The results show that the appropriate content of Ni–Cu–La–B-coated glass fibers is 6 wt% in the composite filler and the optimum ratio of the filler to acrylic resin is 4:1. The electrical conductivity of the coating with a thickness of 300 μm has a minimum value of 0.68 Ω cm and the shielding effectiveness of the coatings is up to 47.78–64.28 dB in the frequency range of 0.3–1000 MHz. This offers a new idea to enhance the added value of the glass fibers and raise the level of electromagnetic radiation protection.

Keywords Electromagnetic shielding coating · Electromagnetic shielding effectiveness · Glass fiber · Electromagnetic environmental pollution Electromagnetic radiation protection

Introduction

Electromagnetic radiation pollution is the world's fourth kind of pollution after air, water, noise pollution with the science and technology progress and people's living standards continue to improve [1]. The new pollution, which is known as the silent killer and a great public hazard of modern society, can produce electromagnetic

D. Guan (✉) · Y. Liu · D. Hu · Z. Dai · C. Wu · R. Zhou · J. Cao · X. Pu · L. Cheng
College of Materials and Chemistry and Chemical Engineering, Chengdu University of Technology, Chengdu 610059, Sichuan, China
e-mail: gdg@cdut.edu.cn

D. Guan
Mineral Resources Chemistry Key Laboratory of Sichuan Higher Education Institutions, Chengdu 610059, Sichuan, China

Y. Han (ed.), *Advances in Energy and Environmental Materials*,
Springer Proceedings in Energy, https://doi.org/10.1007/978-981-13-0158-2_32

information leaks, electromagnetic interference, electromagnetic environment pollution [2, 3]. Electromagnetic shielding and absorbing and filtering technology can effectively restrain electromagnetic radiation. Among them, electromagnetic shielding coatings has become one of the main material of control electromagnetic radiation pollution because of its cost-effective, simple process equipment, convenient and flexible application. Hence, the research and development of cost-effective electromagnetic shielding coatings has practical significance.

Electromagnetic shielding fillers are key determinants of electromagnetic shielding coating performance factors. But traditional electromagnetic shielding fillers with conductive performance, high cost, great density and low chemical stability are mainly metal powder such as gold, silver, copper, nickel, etc., followed by nonmetal powder with bad conductivity, low cost, small density and low chemical stability such as carbon black, graphite, tourmaline, etc. [1, 3–5]. These fillers has certain limitations in the engineering application of electromagnetic wave shielding coating. Therefore, to research and develop various efficient electromagnetic shielding fillers have become one of the important topics in research of materials. Electroless plating is a kind of low cost, green environmental protection, widely used metal surface modification methods, preparation of coating uniformity, strong and composition is easy to control. At present, with plastic, fiber fabric, glass beads and metal powder etc. as the substrate, using chemical plating technology has been successfully prepared a variety of new type of electromagnetic shielding fillers [6–8].

Insulator glass fiber can be fabricated into a novel Ni–Cu–La–B-coated glass fiber with high conductivity by electroless plating to improve its added value and broaden its application scope. Inexpensive Ni–Cu–La–B-coated glass fiber can be used for prevention and control of electromagnetic wave pollution at low costs. In this paper, a novel electromagnetic shielding composite coating with high performance was prepared using the Ni–Cu–La–B-coated glass fibers and flaky nickel powders as fillers and Acrylic resin as binders. Furthermore, the conductivity and electromagnetic shielding effectiveness of flaky Ni–Cu–La–B-coated glass fiber/Acrylic resin composite coatings were studied. This provides a new thought and method to improve the added value of the glass fiber and electromagnetic shielding coatings research and development of low cost.

Experimental

Materials. SEM image of flaky nickel powders (99.90 wt% of Ni, Chengdu Nuclear 857 New Materials co., LTD) is shown in Fig. 1; SEM image of Ni–Cu–La–B-coated glass fibers (29.50 wt% of Ni and 0.84 wt% of Cu and 0.5 wt% of La and 0.5 wt% of B, Homemade) is shown in Fig. 1; Moreover, Acrylic resin, dedicated thinner, additive etc. are all homemade.

Preparation of Electromagnetic Shielding Material. The main preparation methods of a novel flaky Ni–Cu–La–B-coated glass fiber/Acrylic resin composite

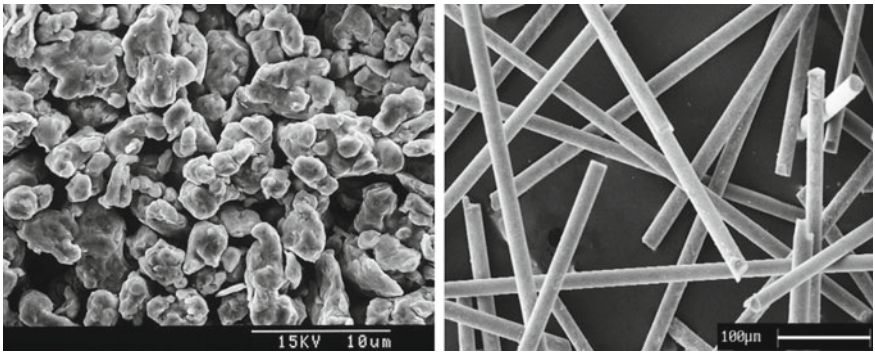

(a) Flaky nickel powders (b) Ni-Cu-La-B-coated glass fibers

Fig. 1 SEM images of the fillers of electromagnetic shielding composite coatings. **a** Flaky nickel powders, **b** Ni–Cu–La–B-coated glass fibers

coatings are as follows: (1) Coupling surface treatment of filler particles. In order to improve the dispersion of composite filler particles in the resin and coating quality, the surface of flaky micro-nickel powders and Ni–Cu–La–B-coated glass fiber (fillers) was modified by titanate coupling agent (3 wt% of the fillers). (2) Formula design, counting, weighing and mixing. The composition of the electromagnetic shielding coating and preparation process were optimized by means of orthogonal experiment. The weight ratio of filler to resin in the shielding coating is 4:1. The prepared filler samples contain 0, 1, 2, 3, 4, 5, 6, 7 and 8 wt% of Ni–Cu–La–B-coated glass fibers respectively. Acrylic resin was used as binder of the coating. (3) Coating viscosity adjustment. Finally, a new type of flaky Ni/Ni–Cu–La–B-coated Glass Fibers/Acrylic resin composite coating was prepared by counting and weighing, mixing, coating viscosity adjustment, etc. The coating viscosity was adjusted with thinner in about 30 s. (4) Spray coating. The coating was sprayed over the surface of PVC plastic substrate, whose outside diameter measured 115 mm and inner hole diameter measured 10 mm. The thickness of PVC plastic substrate was 2 mm. The film thickness was 300 μm. (5) Drying and curing of coating. After surface drying, the substrate was put into the oven in 80–100 °C drying after 30 min. And then take out to dry at room temperature for 24 h.

Properties Testing of Electromagnetic Shielding Material. The resistance of the electromagnetic shielding coating was tested with a digital multimeter. The test of shielding effectiveness of the shielding coating followed the standard SJ20524-95, i.e., "Measuring Methods for Shielding Effectiveness of Materials". The shielding effectiveness was tested by coaxial flange test device which was developed by Southeast University in China. Schematic diagram of the coaxial flange test device of shielding effectiveness of the shielding coating is shown in Fig. 2. The operating frequency of coaxial testing device is in the range of 0.3–1500 MHz, and its impedance is 50 Ω. The value of tested shielding effectiveness is higher than 100 dB dynamic range.

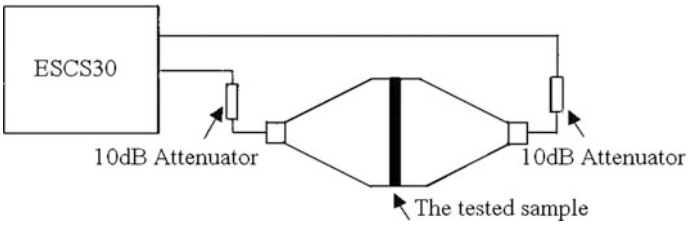

Fig. 2 Schematic diagram of shielding effectiveness test device of the shielding coating

Adhesion test of the shielding coating was performed according to the standard GB/T 9286-1988 "Paints and Varnishes-cross Cut Test for Films" (China). Pencil hardness was tested according to the standard GB/T 6739-1996 "Determination of Film Hardness by Pencil Test" (China). Impact resistance determination of the shielding coating was conducted according to the standard GB/T 1732-1993 "Determination of Impact Resistance of Film" (China). Wear resistance was tested following the standard GB/GB1768-1979 "Method of Test for Abrasion Resistance of Paint Films" (China). Drying time test of the shielding coating was conducted according to the standard GB/T 1728-1979 "Methods of Test for Drying Time of Coatings of Paints and Putties" (China).

Results and Discussion

Conductivity of the Electromagnetic Shielding Material. The effect of Ni–Cu–La–B-coated glass-fiber content in the composite filler effect on the resistivity of the flaky Ni/Ni–Cu–La–B-coated Glass Fiber/Acrylic resin composite coating is shown in Fig. 3.

Fig. 3 Effect of Ni–Cu–La–B-coated glass-fiber content on the coating resistivity

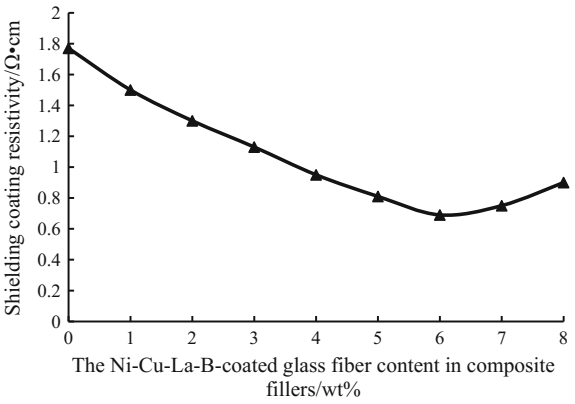

In Fig. 3, the coating resistivity decreases with the increase of Ni–Cu–La–B-coated glass fibers content in the composite filler when the content of fibers is less than 6 wt%. Nevertheless, the coating resistivity increases when the content of fibers is higher than 6 wt%. A low resistivity is desirable for a shielding coating to ensure its high electrical conductivity. So, the appropriate content of Ni–Cu–La–B-coated glass fibers is 6 wt% in the composite filler. According to the conductive theory of filled conductive composite shielding coating, This is due to the conductivity of the coating that mainly depends on high-quality conductive network which is formed through the interaction between Acrylic resin and flaky nickel powders and Ni–Cu–La–B-coated glass fibers. The dense high-quality conductive network is based on the synergy between nickel powders and an appropriate amount of Ni–Cu–La–B-coated glass fibers [8]. The coating conductivity decreases due to the decline in the coating's liquidity and dispersing ability as a result of the excessive adding Ni–Cu–La–B-coated glass fibers. In summary, the appropriate content of Ni–Cu–La–B-coated glass fibers is 6 wt% in the composite filler, the coating resistivity with a thickness of 300 μm has a minimum value of 0.68 Ω cm.

Shielding Effectiveness of Electromagnetic Shielding Material. A high electrical conductivity is desirable for a coating to ensure its high electromagnetic shielding effectiveness. A higher electrical conductivity of the coating will attenuate more incident electromagnetic wave energy by electromagnetic shielding coatings, and the shielding effectiveness of the coating is better according to the theory of electromagnetic shielding [8]. Therefore, in this study only the shielding effectiveness of two kinds of flaky Nickel/Acrylic resin electromagnetic shielding coatings with or without 6 wt% of Ni–Cu–La–B-coated glass fibers were tested. The test results of shielding effectiveness of the coatings are shown in Table 1.

Table 1 shows that shielding effectiveness of the coating containing 6 wt% of Ni–Cu–La–B-coated glass fibers dramatically increases compared with that of the coating without the Ni–Cu–La–B-coated glass fibers. This is because in the absence of Ni–Cu–La–B-coated glass fiber bridging, flake nickel powder has less chances of

Table 1 Shielding effectiveness of the shielding coatings (dB)

Frequency (MHz)	Without Ni–Cu–La–B-coated glass fibers (dB)	Containing 6 wt% of Ni–Cu–La–B-coated glass fibers (dB)
0.3	48.92	59.63
5	50.85	64.28
30	49.74	52.00
50	51.24	56.61
100	49.87	50.86
200	49.72	50.11
300	45.89	47.78
500	40.55	48.00
800	40.76	48.02
1000	40.13	49.60

Table 2 Physical properties of the coatings containing 6 wt% of Ni–Cu–La–B-coated glass fibers

Test items	Test standard	Test results
Adhesion/level	GB/T9286-1988	1
Pencil hardness/H	GB6739-1986	5
Impact strength (kg cm)	GB/T1732-1993	50
Abrasion resistance/(gravity, g/cm^2)	GB1768-1979	0.001
Surface dry time, min (25 °C)	GB/T1728-1979	30
Bone dry time, h (25 °C)	GB/T1728-1979	12

contact between particles, the conductive network of the coating without Ni–Cu–La–B-coated glass is not dense and the conductivity of the coating is poorer. Electromagnetic waves can get through the loose conductive network. This reduces the loss of the electromagnetic wave reflection and absorption. Therefore, the electromagnetic wave reflection and absorption losses is small, accordingly, the coating of the shielding effectiveness is poorer. In contrast, the coating containing 6 wt% of Ni–Cu–La–B-coated glass fibers has the densest conductive network and the best electrical conductivity. The coating has the optimal attenuation effect on the incident electromagnetic wave energy when the content of Ni–Cu–La–B-coated glass fibers is 6 wt%. In summary, flaky Nickel/Acrylic resin electromagnetic shielding coatings achieved satisfactory electrical conductivity and electromagnetic shielding effectiveness if 6 wt% of Ni–Cu–La–B-coated glass fibers were added. Hence, electromagnetic wave pollution of the environment got effective control by the conductive shielding coatings.

Physical Properties of Electromagnetic Shielding Material. The test results of environmental performance of the coatings containing 6 wt% of Ni–Cu–La–B-coated glass fibers is shown in Table 2.

Thus it can be seen that these main physical properties and environmental performances of the flaky Nickel/Acrylic resin electromagnetic shielding coatings containing 6 wt% of Ni–Cu–La–B-coated glass fibers achieve the requirements of the military standard GJB 2604-1996 “Military Electromagnetic Shielding Coatings General Specification”.

Conclusion

A novel material, flaky Ni(filler)/Ni–Cu–La–B-coated glass fibers(filler)/Acrylic resin(binder) composite shielding coating, is prepared following processes such as counting, weighing, mixing, paint viscosity adjustment, etc. The applicable content of Ni–Cu–La–B-coated glass fibers is 6 wt% in the filler and the optimum ratio of the filler to Acrylic resin is 4:1 with a coating layer thickness of 300 μm, when the coating has the optimal conductivity and electromagnetic shielding effectiveness, and the resistivity of the coating is as low as 0.68 Ω cm. Besides, the shielding

effectiveness is up to 47.78–64.28 dB in the frequency range of 0.3–1000 MHz. The main physical properties and environmental performances of the coating are in accordance with the military standard GJB 2604-1996. This offers a new idea to enhance the added value of the glass fibers and raise the level of electromagnetic radiation protection.

Acknowledgements This work was financially supported by the Key Research Projects of Science and Technology Department of Sichuan Province of China (2017GZ0392), and the Science and Technology Huimin Projects of Science and Technology Bureau of Chengdu of Sichuan Province of China (2015-HM01-00387-SF).

References

1. D.G. Guan, G.L. Xu, Y. Sun, et al., Russ. J. Appl. Chem. **87**, 1171–1174 (2014)
2. S.J. Genuis, Pub. Heal. **122**, 113–124 (2008)
3. J.Z. Wang, J. Ma, H. Zhi, et al., Rar. Met. Mater. Eng. **46**, 73–77 (2017)
4. J. Lee, B.M. Jung, S.B. Lee, et al., Appl. Sur. Sci., **415**, 99–103 (2017)
5. W.H. Zhang, Y. Chen, D.Q. Lu, et al., China Prev. Med., **10**, 1033–1034 (2009)
6. D.G. Guan, Y. Sun, G. Xu, et al., Appl. Mech. Mater. **395–396**, 37–40 (2013)
7. Y.W. Gao, H.L. Zhu, Adv. Mater. Res. **610–613**, 33–738 (2013)
8. D.G. Guan, C.M. Sun, Y. Sun, et al., Chengdu Univ. Techno. (Natur. Sci. Ed.), **37**, 216–220 (2010)

Acid Leaching Process in Extracting Vanadium from Blast Furnace Slag in Panzhihua Vanadium Titanium Magnetite

Zehang Dai, Denggao Guan, Yang Liu, Dehao Hu, Rundong Zhou, Jiayun Cao, Li Cheng and Xinghong Pu

Abstract Vanadium titanium magnetite is a multi-element-coexistent iron ore which contain mainly iron, titanium, and vanadium. With present techniques, nearly all the iron but a small amount of vanadium were able to extracted from the magnetite. The V-bearing blast furnace slags cause the release of harmful substances into the environments as well as a waste of the vanadium resources. In this paper, the extraction of vanadium from blast furnace slag was studied by direct roasting and hydrochloric acid leaching techniques. The effects of processing parameters were studied on the extraction of vanadium. The results showed that the leaching rate of vanadium reached about 85.94% under the optimum conditions: mineral size of 200 meshes, the roasting temperature of 873 K, the roasting time of 120 min, the HCl concentration of 27.75%, the solid to liquid to ratio of 1:4 g/mL, the leaching temperature of 363 K, and the leaching time of 180 min. The obtained results in this study will have great impact on recycle and reuse of the vanadium resources from blast furnace slag.

Keywords Vanadium titanium magnetite · Blast furnace slag · Vanadium Resource utilization · Extraction rate

Z. Dai (✉) · D. Guan · Y. Liu · D. Hu · R. Zhou · J. Cao · L. Cheng · X. Pu
College of Materials and Chemistry and Chemical Engineering,
Chengdu University of Technology, Chengdu 610059, Sichuan, China
e-mail: daizehang0419@163.com

D. Guan
e-mail: gdg@cdut.edu.cn

D. Guan
Mineral Resources Chemistry Key Laboratory of Sichuan Higher Education Institutions,
Chengdu 610059, Sichuan, China

Y. Han (ed.), *Advances in Energy and Environmental Materials*,
Springer Proceedings in Energy, https://doi.org/10.1007/978-981-13-0158-2_33

Introduction

China is the largest country of vanadium reserves in the world. More than 10 provinces possess the vanadium minerals, Sichuan have accounted for 62.2% [1]. In the natural world, vanadium is found in various minerals, among which vanadium-titanium (V-Ti) magnetite is the most important raw material for vanadium extraction, 98% of the proved vanadium reserves are found in vanadium-titanium magnetite. More than 90% of China's vanadium-titanium magnetite is concentrated in Panxi area [2–4]. At present, the main method of V making is extracted from their ores, steelmaking slags, petroleum soot and spent catalyst [5]. The blast furnace slag if not processed, not only takes up a lot of land resources and pollutes the soil, atmosphere and water environment, but also wastes the vanadium resources [6]. Therefore, extracting vanadium from blast furnace slag has extensive exploitive foreground based on decrease the resource losing and environment polluting. Acid leaching is a widely used process for extracting vanadium because of its high rate of lixiviation and strong applicability to the slag [7]. Most of the vanadium in blast furnace slag exists in the lattice of aluminosilicate minerals, or adsorbed in organic matters or aluminosilicate minerals [8, 9]. The traditional technology of vanadium extraction from blast furnace slag is leaching calcium vanadate from the ore phase with sulfuric acid.

In this paper, we use vanadium-titanium-magnetite blast furnace slag in Panzhihua as raw materials, direct leaching with hydrochloric acid after oxidation roasting [10]. Hydrochloric acid has the strongest permeability and it is easily reacted with the vanadium oxide in the crystal lattice. Process parameters such as the mineral size, the calcination temperature, the calcination duration, the acid concentration, the solid to liquid ratio, the leaching temperature and the leaching duration on the leaching rate of vanadium were assessed.

Experiment

Raw Materials. The blast furnace iron-making slags used in this experiment were collected from a steel factory in Panzhihua. The slags show a dark blockpartly covered with yellow foam solid.

Experimental Procedure. The slags were grinded and screened to obtain the powder. A muffle furnace was employed in the roasting process. The sample was taken out and cooled at room temperature after the roasting process was completed. In all the leaching experiment, 5 g of roasted slag was leached with the 20 mL HCl solution under certain conditions. The slurry was separated via vacuum filtration, and the residue was washed three times by distilled water. The raw materials and the residue*s* were direct dissolved with nitric acid, hydrochloric acid and hydrofluoric acid by electric heating plate digestion. The leaching rate of vanadium (μ) was obtained according to Eq. (1).

$$\mu = (R_0 - R)/R_0 \quad (1)$$

where R_0 is the total vanadium, R is the content of vanadium in leaching residue. **Characterization**. The phase compositions of the slag were measured by X-ray diffraction (XRD), the chemical compositions were determined by using an X-ray fluorescence spectrometer (XRF), the morphologies were analyzed by scanning electronic microscope (SEM), the content of vanadium was measured by using a Inductively Coupled Plasma Optical Emission Spectrometer (ICP-OES).

Results and Discussion

Chemical Composition of the Slag. The XRF analysis results showed that the composition of slag were calcium oxide (26.98 wt%, vol or atm), silicon dioxide (24.82%), titanium dioxide (16.89%), aluminum oxide (13.57%), magnesium oxide (7.61%), iron oxide (1.39%) and vanadium pentoxide (1.06%).

Phase Composition of the Slag. The XRD pattern of the sample measured showed in Fig. 1 that the main mineral components of slag are pertovskite, titanium diopside, magnesia-alumina spinel, titanium rich diopside, etc. The diffraction peak of V is not obvious because of the low vanadium content. The slag is mainly composed of oxygen, calcium, silicon, titanium, magnesium, aluminum, iron and vanadium, etc.

Microstructures of the Slag. The SEM image of the slag sample was given in Fig. 2a, and that of the slag after crushing into 200-meshes, roasting at 873 K for 120 min and leaching in 27.75% HCl at 363 K for 180 min was given in Fig. 2b. Figure 2a shows the slag has a compact massive structure. There is no cracks and holes on slags. The block structure was grindedto the maximum extent possible to make the H^+ get in, so that to improve the leaching rate. Figure 2b shows a large number of slits and pores appeared after crushing, roasting and acid leaching.

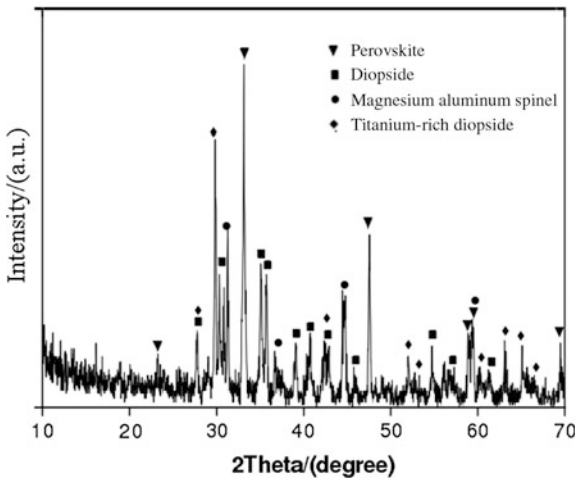

Fig. 1 XRD pattern of the blast furnace slag

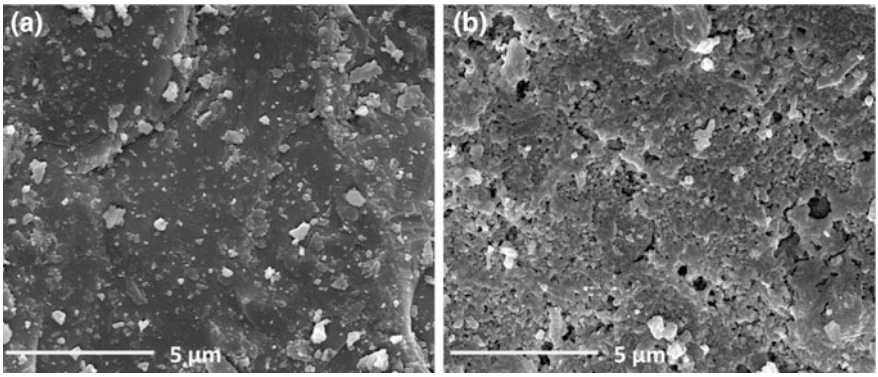

Fig. 2 SEM images of **a** the blast furnace slag; **b** the blast furnace slag after crushed, roasted, and leached

Effect of Mineral Size. The effect of mineral size on the extraction of vanadium was conducted from 80 to 200 meshes while keeping a fixed roasting temperature of 873 K for 120 min. The subsequent leaching experiments were carried out under the following conditions: HCl concentration of 27.75%, solid to liquid ratio of 1:4 g/mL, leaching temperature of 363 K, and leaching time of 180 min.

The results are investigated in Fig. 3. It can be observed that the leaching rate of vanadium increased gradually and reached a maximum value of 85.96% at 200 meshes. The area of mineral contact with acid increases with decreasing particle size of the slag, and lead the smaller barrier to capture H^+ and energy, which is good for H^+ to enter the mineral lattice and destroy the crystal lattice, releasing the

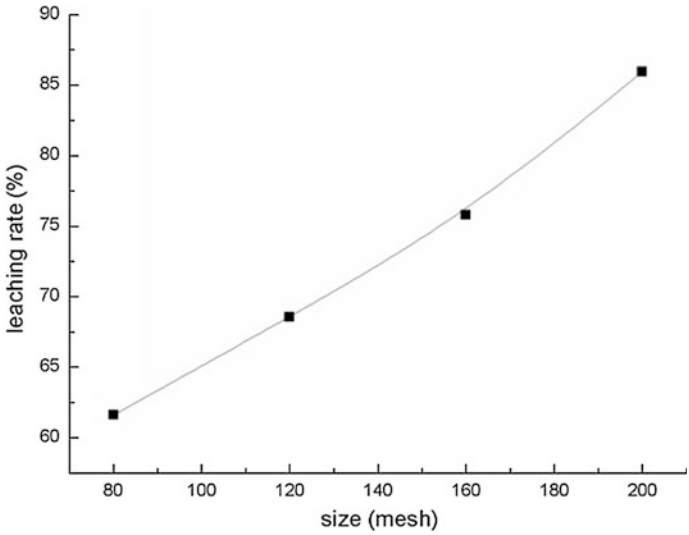

Fig. 3 Leaching rate of vanadium versus particle size

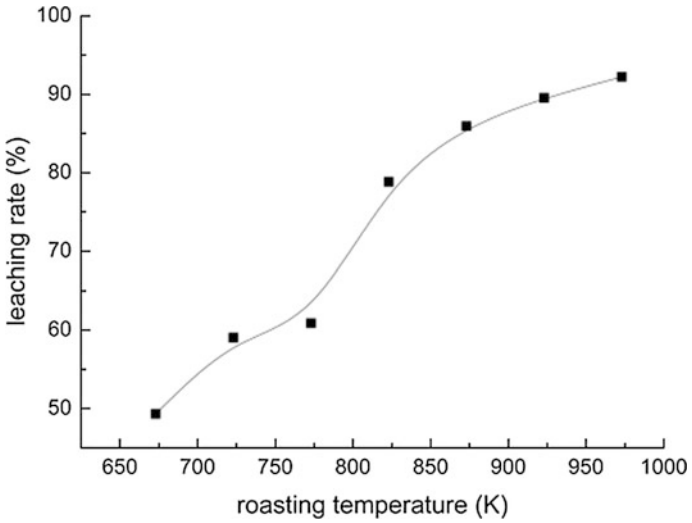

Fig. 4 Leaching rate of vanadium versus roasting temperature

vanadium into the solution. Theoretically, the smaller the size of the mineral, the more beneficial to the leaching of vanadium, but in the actual production process, with the reduction of mineral size, the operation process will be complicated, so we choose the 200-meshes.

Effect of Roasting Temperature. To study the effect of roasting temperature on the extraction of vanadium, the roasting temperature was varied from 673 to 973 K, while the other conditions were kept constant. The effects of calcination temperature on the leaching rate of vanadium were investigated in Fig. 4.

According to Fig. 4, the leaching rate increased significantly with increasing roasting temperature. However, with a further increase in roasting temperature to 923 K, the leaching rate is slow growth. The possible reason is that the vanadium is enwrapped by sintered matters [11].

Effect of Roasting Time. The effect of roasting time on the extraction of vanadium was conducted from 60 to 240 min while keeping other conditions constant. The results are shown in Fig. 5. It can be indicated that the leaching rate reached 85.96% at 120 min, then it started to low growth even decrease. That's might because the low valence vanadium cannot be oxidized completely when the roasting time is too short, and the sample was sintered when the roasting time increasing.

Effect of HCl Concentration. The effect of hydrochloric acid concentration on the extraction of vanadium was investigated from 18.5 to 29.6% (mass fraction). The results are shown in Fig. 6. The leaching rate of vanadium increased from 70.7 to 86.55% when the HCl concentration varied from 18.5 to 29.6%. It is possible that leaching reactions take place quickly in a higher HCl concentration, which facilitated the infiltration of H^+ into the lattice and destroyed the mineral, made the

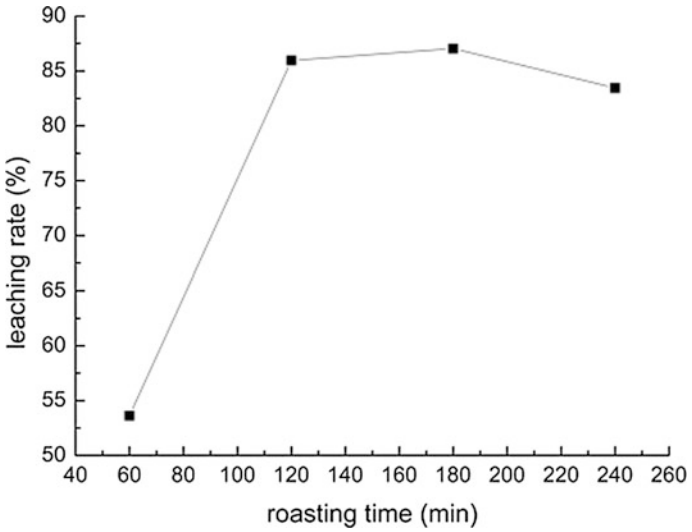

Fig. 5 Leaching rate of vanadium versus roasting time

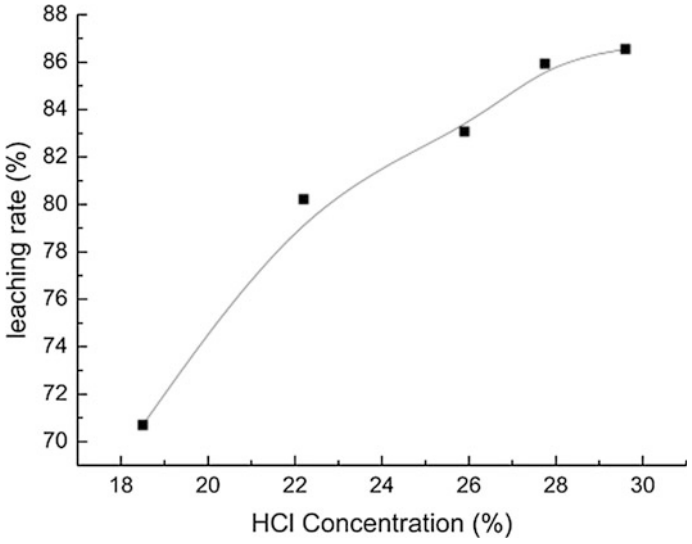

Fig. 6 Leaching rate of vanadium versus HCl concentration

leaching rate of V increased. But the leaching rate tendency was gradually constant with the increasing of HCl concentration. Increasing the concentration is not economical, so the optimum concentration is 27.75%.

Effect of Solid to Liquid ratio. The effect of solid to liquid ratio on the extraction of vanadium was examined from 1:1 to 1:5 g/mL.

The Fig. 7 shows that the leaching rate of vanadium increased with an increase in solid to liquid up to 1:4 g/mL. However, when the solid to liquid ratio was varied from 1:4 to 1:5 g/mL, the leaching rate of vanadium was not greatly changed.

Effect of Leaching temperature. The leaching temperatures were set from 293 to 363 K. The result was investigated in Fig. 8.

It showed that the leaching rate of vanadium increased with increasing leaching temperature. Hence, the leaching temperature should be as high as possible in practice. The leaching rate of vanadium reached a peak value of 85.94% at 363 K. With increasing temperature, molecular thermodynamic movement speeded-up and the reaction activity of the leaching agent was also enhanced, which makes the leaching process easier. Therefore, considering the cost and energy saving, 363 K is used as the optimum value in the following study.

Effect of Leaching Time. The effect of leaching time on the extraction of vanadium was studied from 60 to 360 min, the results shown in Fig. 9 indicate that the leaching rate gradually increased with leaching time up to 180 min. With a longer leaching time, the leaching rate of vanadium had no obvious change.

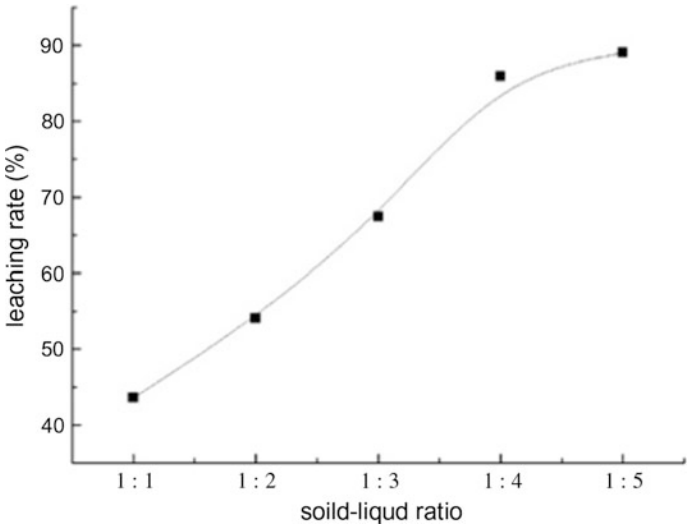

Fig. 7 Leaching rate of vanadium versus solid-liquid ratio

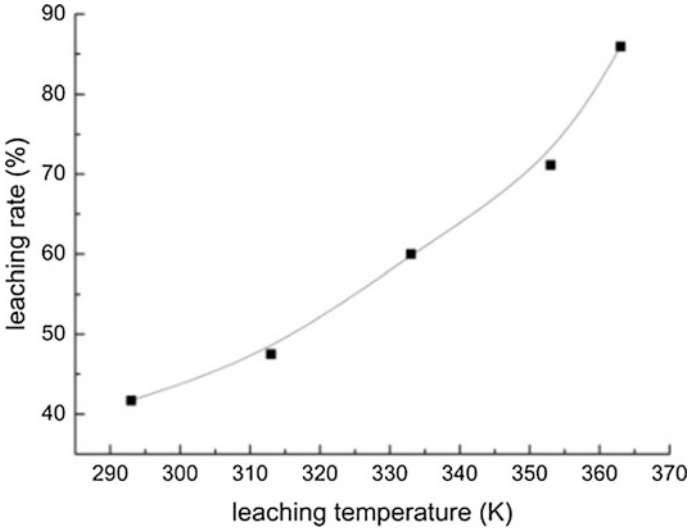

Fig. 8 Leaching rate of vanadium versus leaching temperature

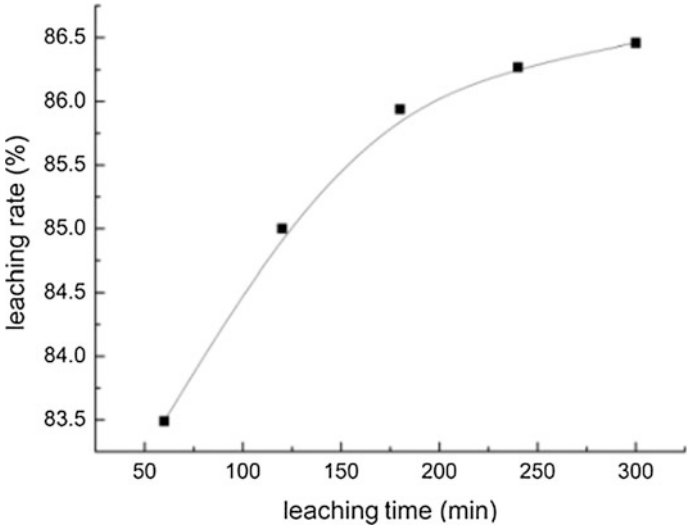

Fig. 9 Leaching rate of vanadium versus leaching time

Conclusions

In this paper, a direct roasting and hydrochloric acid leaching process was carried out to extract vanadium from blast furnace slag. During the oxidation roasting process, the low valence vanadium was completely oxidized into a high valence soluble vanadate. And the hydrochloric acid thoroughly broke down vanadium-bearing titanium diopside and other silicoaluminate minerals to generate K^+, Mg^{2+} and Al^{3+}, and vanadium was release into the leachate. Under the optimum conditions (mineral size of 200 meshes, the roasting temperature of 873 K for 120 min, HCl concentration of 27.75%, solid to liquid ratio of 1:4 g/mL, and leaching temperature of 363 K for 180 min), the leaching rate of vanadium reached 85.94%. The main impurities were remained in the leach residue. The leaching rate of vanadium increased rapidly with the increase of mineral size, hydrochloric acid concentration, leaching temperature and time. It is proved as an effective method for the recycle of vanadium from blast furnace slag.

Acknowledgements This work was financially supported by the Key Research Projects of Science and Technology Department of Sichuan Province of China (2017GZ0392), and the Science and Technology Huimin Projects of Science and Technology Bureau of Chengdu of Sichuan Province of China (2015-HM01-00387-SF).

References

1. S.X. Zhuang, *A new non-pollution technology of extracting vanadium from siliceous navajoite* (Central South University, Hunan Province, 2007).
2. Y.C. Dong, X.R. Wu, L. Yu, L.S. Li, Fundamental research on vanadium recovering from V-bearing steelmaking slag. J. Eng. Sci. **09**, 63–68 (2007)
3. S.L. Yang, Vanadium titanium material (Beijing Metallurgical Industry Press, Beijing, 2007)
4. L. Duan, Q.H. Tian, X.Y. Guo, Review on production and utilization of vanadium resources in China. J. Hunan Nonferrous Metals **22**, 17–20 (2006)
5. J.F. Hu, *A New Process of Recover Vanadium from Spent Petrochemical Catalysts* (Kunming University of Science and Technology, Yunnan Province, 2006)
6. A.R. Zhou, P. Lu, Study on the track and recycle of vanadium in the titanium extraction from blast furnace slag. J. Iron Steel Vanadium Titanium **36**, 63–67 (2015)
7. J. Cao, *A Study on the New Production Process of Extracted Vanadium from Stone Coal* (Hunan University, Hunan Province, 2011)
8. H.W. Ge, *Study on New Process of Leaching Vanadium from Vanadium Containing Tailings* (Kunming University of Science and Technology, Yunnan Province, 2008)
9. S.J. Min, *Study on Vanadium Extracting Technology from Vanadium-Titanium-Magnetite Tailings* (Chengdu University of Technology, Sichuan Province, 2009)
10. Y. Huang, X. Jia, H. Liu, Effect of hydrochloric acid on vanadium recovery from vanadium tailings. J. Technol. Wind **16**, 127–127 (2016)
11. X. Li, B. Xie, Extraction of vanadium from high calcium vanadium slag using direct roasting and soda leaching. Int. J. Min. Metall. Mat. **19**, 595–601 (2012)

The Effect of Vermiculite Loaded with MnO_2 on Adsorption of Heavy Metal Pb(II) in Wastewater

Caiwen Wu, Denggao Guan, Yinghui Cui, Dehao Hu, Yang Liu, Li Cheng, Xinghong Pu and Jiayun Cao

Abstract The modified vermiculite with MnO_2 was prepared by direct precipitation method using vermiculite, $MnSO_4$ and $KMnO_4$ as raw materials. The composition, structure and morphology of raw-vermiculite and modified-vermiculite were analyzed. The effect of the amount of vermiculite, the time of adsorption and the pH of heavy metal ion solution on the adsorption performance of Pb(II) in wastewater were compared. The results showed that modified vermiculite adsorbed heavy metal ions in water better than natural vermiculite. The maximum removal of lead ions from the aqueous solution reaches 99.148% at 60 min and pH 6 with 0.25 g modified vermiculite. At this point, the adsorption rate of modified vermiculite to Pb(II) is increased by about 30%. The results of this study have practical value in improving the value of vermiculite and the comprehensive treatment to lead wastewater.

Keywords Vermiculite · MnO_2 · Modification · Adsorption

Introduction

With the development of industry, heavy metal pollution is more and more serious. Heavy metal pollution is one of the most harmful water pollution problems, and heavy metal pollution in water has become an environmental problem in the world, and the issue of water pollution has been paid worldwide attention. One of the most

C. Wu (✉) · D. Guan · Y. Cui · D. Hu · Y. Liu · L. Cheng · X. Pu · J. Cao
Academy of Materials, Chemistry and Chemical Engineering, Chengdu University of Technology, 610059 Chengdu, Sichuan Province, China
e-mail: 990578245@qq.com

D. Guan
e-mail: gdg@cdut.edu.cn

D. Guan
Chemical Mineral Resources, Sichuan Province Key Laboratory of Colleges and Universities, Chengdu University of Technology, Chengdu, China

Y. Han (ed.), *Advances in Energy and Environmental Materials*,
Springer Proceedings in Energy, https://doi.org/10.1007/978-981-13-0158-2_34

hazardous heavy metals is Lead (Pb) which can be found in 0 and +2 oxidation state in aqueous solutions [1]. The presence of lead in water comes from the discharge of processing industrial effluents, namely electroplating, coatings, pigments, basic steel industry, textile industry, metal surface treatment and batteries in batteries [2]. Lead is a heavy metal and non-essential element to the human body, and excessive intake of the metal can damage the bones, nerves, circulation enzymes, endocrine functions and the immune systems of those exposed to it. Even small amounts of lead can cause neurological and reproductive problems, cardiovascular and developmental disorders, which a serious problems in children including slowed motor responses, decreased IQs, and hypertension [1, 3]. Therefore, the study of modified vermiculite removal of lead in wastewater is of great significance.

At present, the heavy metal ion treatment methods of wastewater mainly including reverse osmosis, electrodialysis, reduction, membrane separation, chemical precipitation and adsorption, etc. [4]. These methods have many shortcomings of high cost, large chemical requirement and incomplete treatment [5]. The most commonly used adsorbent material is activated carbon. However, the high cost of activated carbon is not widely used. Therefore, it is very necessary to find the adsorbent materials with low cost and good adsorption effect [6]. Vermiculite is a pore-connected layered silicate mineral with a layered structure comprising two silicon tetrahedra and one aluminum oxide octahedron. It has a large surface area and cation exchange, rich in reserves in China, cheap. So, it is a new type of adsorbent with great potential. At present, the modification method is the key to improve the adsorption performance of vermiculite [5, 7]. In recent years, the adsorption of manganese dioxide adsorbent has become a research hotspot, such as MnO_2 modified zeolite, bentonite, sand, diatomaceous and d-MnO_2 loaded weakly basic anion exchange resin D301, d-MnO_2-loaded graphene, manganese oxide was dispersed in cellulose gel beads [8–14].

The main purpose of the work is to investigate the effect of MnO_2 formed by $MnSO_4$ and $KMnO_4$ was supported on the vermiculite surface to obtain MnO_2 modified vermiculite. Effect of MnO_2-modified-vermiculite on Pb(II) adsorption efficiency in wastewater were investigated from the aspects of modified vermiculite dosage, adsorption time and pH value of heavy metal solution.

Experiment

Material. The raw vermiculite used in the tests collected from Lingshou County, Hebei Province, and crushed, over 100 mesh sieve, the size is about 0.15 mm. The experimental drugs used in the tests were all analytically pure. Manganese dioxide was prepared using potassium permanganate and manganese sulfate. Pure $Pb(NO_3)_2$ was used to prepare the working lead stock solution for the adsorption experiments.

Sample Preparation. 20 g of the deodorized 100 mesh vermiculite was weighed and added to a 250 mL Erlenmeyer flask containing 100 mL of $KMnO_4$ solution and a certain amount of $MnSO_4$ solution was added to the conical flask. When the violet-like powdery solid was formed on a conical flask, the mixture was gelled at 25 °C for 120 r/min for 2 h. And then removed, aging 24 h, with absolute ethanol and distilled water rinse vermiculite, until the solution pH is neutral, and then into the 70 °C drying box for drying, that is, MnO_2 modified vermiculite samples, sealed with a sealed bag, spare.

Lead Ions Adsorption Properties Test. At room temperature, a certain amount of ore vermiculite was added to 100 mL heavy metal Pb(II) solution with initial ion concentration of 50 mg/L. The concentration of Pb(II) in simulated wastewater was determined by ICP-OES method, and the adsorption rate of Pb(II) solution was calculated by the amount of vermiculite. The removal efficiency was calculated according to the following equation:

$$Sorption = \frac{C_0 - C_e}{C_0} \times 100\% \quad (1)$$

where: C_0 is the initial lead ion concentration (mg/L), C_e is the concentration of lead ion in equilibrium (mg/L).

Experimental Results and Analysis

The Chemical Composition of Vermiculite. The XRF results indicated that the vermiculite was composed of a variety of substances. The main chemical components were silica (44.97%), alumina (18.34%), iron oxide (14.12%), magnesium oxide (12.04%) and potassium oxide (5.80%), calcium oxide (2.38%), titanium dioxide (1.54%). There are a small amount of NaO, MnO, P_2O_5 and other oxides.

It can be seen from Fig. 1, raw vermiculite and modified vermiculite sample characteristics similar to the diffraction peak, modified vermiculite main mineral phase is still quartz, calcium and feldspar, but the diffraction peak broad and peak intensity becomes low. After the modification, the crystallinity is deteriorated. The reason may be that the effect of sulfuric acid on the vermiculite structure during the formation of MnO_2.

Microstructures of Vermiculite. The SEM photographs given in Fig. 2a, b shows the surface morphology of vermiculite and MnO_2 modified vermiculite.

As seen from the image in Fig. 2a, Vermiculite has a distinct layered mechanism with a massive and large particle structure on its surface, and there are many small holes and channels in these particles. Vermiculite unique layered structure and good ion exchange, making it an extraordinary significance in the treatment of waste water.

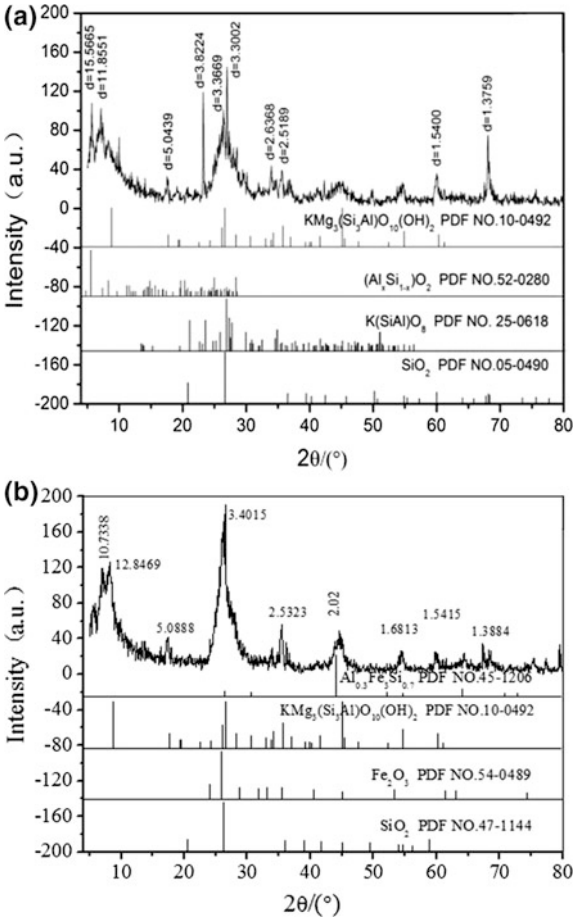

Fig. 1 XRD patterns of vermiculite before **a** and after **b** modification

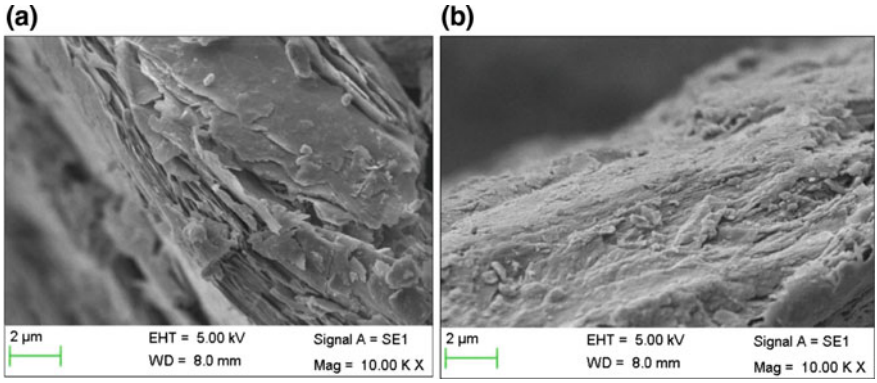

Fig. 2 **a** SEM image of vermiculite, **b** SEM image of MnO_2-Vermiculite

From Fig. 2b, the surface of manganese oxide-modified vermiculite is rugged, and there are more small particles, it's lamellar structure has not changed. The surface of manganese oxide modified vermiculite is relatively uniform and smooth.

Analysis of adsorption effect of vermiculite on Pb(II). The effect of vermiculite on the adsorption of heavy metal ions Pb(II) was discussed from the amount of vermiculite, the adsorption time and pH value of heavy metal solution, and the optimum adsorption conditions were obtained.

Effect of the vermiculite dosage. The initial solubility of lead ions is 50 mg/L, 100 mL, the adsorption time is 120 min, the amount of vermiculite is 0.05, 0.1, 0.25, 0.5, 1 g.

It can be seen from Fig. 3, the dosage of vermiculite is positively correlated with the adsorption rate of Pb(II). When the vermiculite was 0.1 g, the adsorption rate of unmodified vermiculite and modified vermiculite to Pb(II) was the highest, which was 98.42 and 99.024% respectively. The adsorption rate of Pb(II) between vermiculite 0.05 to 0.25 g is faster than that of 0.25–1 g. This is because when the amount of vermiculite 0.05 g less, vermiculite adsorption point is limited, with the vermiculite input increased from 0.05 to 1 g, vermiculite adsorption points increased, and vermiculite layer the amount of interchangeable cations also increases, so the adsorption efficiency increases [15]. As the amount of adsorbent increases, the active site on the adsorbent increases and the adsorption rate increases. When the adsorption of heavy metal ions Pb(II) on the vermiculite surface reaches dynamic equilibrium, the amount of vermiculite is increasing and the collision and aggregation effect of vermiculite particles are enhanced, and the adsorption point of vermiculite surface is not significant, At this time an additional increase in the amount of vermiculite can't effectively increase its adsorption effect. Among them, when the amount of vermiculite is 0.25 g, the adsorption rate of modified vermiculite to Pb(II) is about 15% higher than that of unmodified vermiculite.

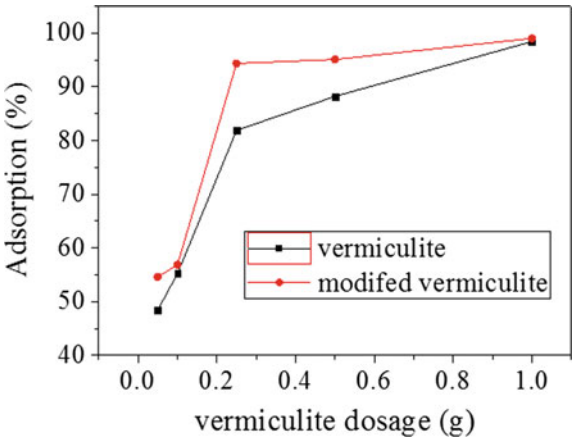

Fig. 3 Effect of dosage on adsorption rate of Pb (II)

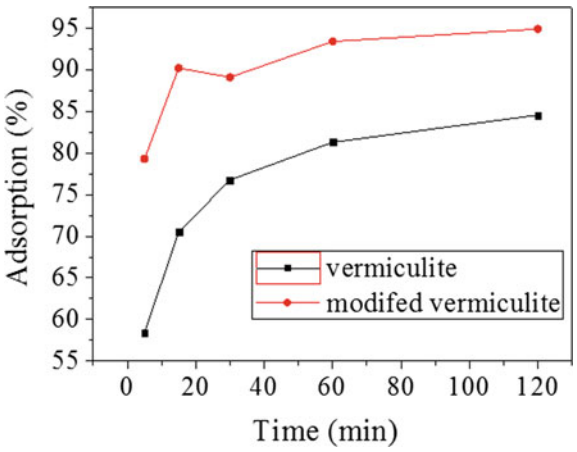

Fig. 4 Effect of adsorption time on adsorption rate of Pb(II)

Effect of contact time. The effect of the adsorption time on the adsorption efficiency was studied at initial concentrate of lead ion solution 50 mg/L, volume 100 mL, vermiculite 0.25 g. As seen in Fig. 4, the removal rate of Pb(II) ions by modified vermiculite increased with the increase of adsorption time and the adsorption rate was the highest at 120 min.

Vermiculite adsorption of metal ions is divided into two stages: rapid adsorption stage and adsorption equilibrium stage. This indicates that in the stage of rapid adsorption, vermiculite adsorbed more points on the surface and inside, and heavy metal ions migrated to the adsorption sites to be adsorbed. In the adsorption equilibrium stage, the active site decreases, the concentration of the solution decreases, and the kinetic energy of the hydrated ions increases, resulting in a dynamic equilibrium adsorption [16]. When the contact time is 15 min, the adsorption rate of modified vermiculite to Pb(II) is about 30% higher than that of unmodified vermiculite. Therefore, the modified vermiculite at a specific time on the adsorption of heavy metal ions have greatly improved.

Effect of pH. The adsorption rate of vermiculite was 1.78% at pH 2, increased to 6, and the adsorption rate increased to 96.066%. When the pH is 4, the adsorption rate of modified vermiculite to Pb(II) is about 15% higher than that of unmodified vermiculite. The adsorption rate of MnO_2 modified vermiculite was increased from 7.84% at pH 2 to 99.148% at pH 6. From the above data, pH is the main factor affecting the adsorption effect. The effect of pH can be explained taking into account the surface charge on the vermiculite. The reason is that the negative charge source of vermiculite is two parts, one is the permanent structure charge, mainly from the silicon tetrahedron Al^{3+} on Si^{4+} in the same phase, and has nothing to do with the pH value. Second, due to the pH value of the variable charge, due to the existence of a large number of vermiculite –Al–OH, –Si–OH and other groups, these groups through the association of H^+ variable surface charge.

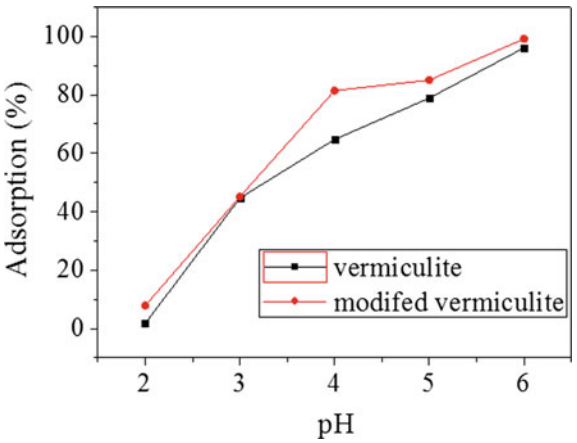

Fig. 5 Effect of pH value on adsorption rate of Pb(II)

From Fig. 5, When the pH is too low, the adsorption rate is lower because of the higher concentration of H^+ in the solution, which competes with Pb^{2+} for exchange of cations between vermiculite layers. With the increase of pH, the concentration of OH^- increases and the competitive exchange ability of H^+ weakens. At the same time, OH^- binds with H^+ in groups such as –Al–OH and –Si–OH to make the number of active sites on vermiculite surface and Negative charge increased, the adsorption rate increased. In the weakly acidic or neutral conditions, the heavy metal ion Pb(II) is hydrolyzed and the exchange affinity of the hydrolyzate Pb–OH+ is greater than that of the heavy metal Pb(II).

Conclusions

In this study, vermiculite is a layered structure of ferrous aluminosilicate minerals containing iron. The SEM showed that vermiculite is a layered structure with strong adsorption. Manganese oxide modified Vermiculite has many small particles. The adsorption of heavy metals was improved.

In addition, the effect of adsorbent dosage, adsorption time, pH, the adsorption of Pb(II) on natural vermiculite and modified vermiculite increased with the increasing of time, reached equilibrium within 60 min. The pH is the most important factor affecting the adsorption of vermiculite. Acidic conditions are not conducive to the adsorption of Pb(II) on vermiculite, but weak acid and neutral environment, the adsorption rate of Pb(II) in vermiculite was improved obviously.

When the concentration of dosage of vermiculite was 0.25 g, contact time was 60 min, pH was 6, the adsorption rate of Pb(II) was better. Compared with the removal rate of Pb(II) by raw vermiculite material was about 30% at 15 min, the manganese dioxide modified vermiculite shows a good removal.

Acknowledgements The study was strongly funded by the Key Research Projects of Science and Technology Department of Sichuan Province of China (2017GZ0392), and the Science and Technology Huimin Projects of Science and Technology Bureau of Chengdu of Sichuan Province of China (2015-HM01-00387-SF).

References

1. H.N. Kim, W.X. Ren, J.S. Kim et al., Fluorescent and colorimetric sensors for detection of lead, cadmium, and mercury ions. J. Cheminform. **41**(8), 3210 (2012)
2. S.T. El-Wakeel, R.S. El-Tawil, H.A.M. Abuzeid et al., Synthesis and structural properties of MnO_2, as adsorbent for the removal of lead (Pb^{2+}) from aqueous solution. J. Taiwan Inst. Chem. Eng. **72**, 95–103.
3. Z. Li, Z. Ma, T. van der Kuijp et al., A review of soil heavy metal pollution from mines in China: pollution and health risk assessment. J. Sci. Total Environ. **468–469**, 843–853 (2014)
4. W.X. Zhou, D.G. Guan, Y. Sun et al., Removal of Nickel (II) Ion from wastewater by modified maifanite. J. Mater. Sci. Forum. **814**, 371–375 (2015)
5. O. Duman, S. Tunç, T.G. Polat, Determination of adsorptive properties of expanded vermiculite for the removal of C. I. Basic Red 9 from aqueous solution: kinetic, isotherm and thermodynamic studies. J. Appl. Clay Sci. **109–110**, 22–32 (2015)
6. X. Yu, C. Wei, L. Ke, Development of organovermiculite-based adsorbent for removing anionic dye from aqueous solution. J. Hazard. Mater. **180**, 499–507 (2010)
7. F.S. Hashem, M.S. Amin, S.M.A. El-Gamal, Chemical activation of vermiculite to produce highly efficient material for Pb^{2+}, and Cd^{2+}, removal. J. Appl. Clay Sci. **115**, 189–200 (2015)
8. E. Eren, B.A. Fsin, Y. Onal, Removal of lead ions by acid activated and manganese oxide-coated bentonite. J. Hazard. Mater. **161**, 677–685 (2009)
9. R. Han, W. Zou, Z. Zhang, J. Shi, J. Yang, Removal of copper(II) and lead(II) from aqueous solution by manganese oxide coated sand I. characterization and kinetic study. J. Hazard. Mater. **137**, 384 (2006)
10. W. Zou, R. Han, Z. Chen, J. Zhang, J. Shi, Kinetic study of adsorption of Cu(II) and Pb(II) from aqueous solutions using manganese oxide coated zeolite in batch mode. J. Colloids Surf., A **279**, 238–246 (2006)
11. L. Dong, Z. Zhu, H. Ma, Y. Qiu, J. Zhao, Simultaneous adsorption of lead and cadmium on MnO_2-loaded resin. J. Environ. Sci. (English) **22**, 225 (2010)
12. F. Sagara, B.N. Wang, Isao Yoshida & Keihei Ueno, Preparation and adsorption properties of λ-MnO_2-cellulose hybrid-type lon-exchanger for lithium ion. application to the enrichment of lithium ion from seawater. J. Sep. Sci. Technol. **24**, 1227–1243 (1989)
13. M.F. Tutunju, The feasibility of using diatomite and Mn-diatomite for remediation of Pb, Cu, and Cd from water. J. Sep. Sci. Technol. **35**, 2299–2310 (2000)
14. A. Sarı, M. Tüzen, Adsorption of silver from aqueous solution onto raw vermiculite and manganese oxide-modified vermiculite. J. Microporous Mesoporous Mater. **170**, 155–163 (2013)
15. K. Ayse, Removal of phenol and 4-chlorophenol by surfactant-modified natural zeolite. J. Hazard. Mater. **144**, 307–315 (2007)
16. N.A. Badawy, A. El-Bayaa, E.A. Alkhalik, Vermiculite as an exchanger for copper(II) and Cr(III) ions, kinetic studies. J. Ionics **16**, 733–739 (2010)

Effect of Current Density on the Structure and Properties of Micro-arc Oxidation Coatings on Titanium Alloy Drill Pipe

Xiaowen Chen, Yu Tang, DeFen Zhang, Renpu Li, Wenxian Chen, Bo Zou, Li Jiang and Sheng Liang

Abstract TiO_2 ceramic coatings were prepared on the surface of titanium alloy drill pipe with different current density by pulsed DC micro-arc oxidation. The morphology, structure, composition, hardness, friction and wear properties and corrosion resistance of the coatings were analyzed by SEM, XRD, micro-sclerometer, ball-on-disk wear tester and electrochemical workstation respectively. The results show that with the increase of current density, the thickness and hardness of the coating increasing, the wear resistance and corrosion resistance first increase and latter reduce. At different current density, the phase structure of the film is mainly composed of rutile TiO_2 and anatase TiO_2, and also contains a small amount of Al_2TiO_5 crystal and amorphous SiO_2. The microstructure analysis shows that with the increase of current density, the density of the film increases and the roughness decreases, but when the current density continues to increase, the hole increases and the roughness increases. Under the

X. Chen (✉) · Y. Tang · D. Zhang · R. Li · W. Chen · B. Zou · L. Jiang · S. Liang
School of Materials Science and Engineering, Southwest Petroleum University, Chengdu 610500, China
e-mail: xwchen5188@163.com

Y. Tang
e-mail: 379981949@qq.com

D. Zhang
e-mail: zhangdefen0304@163.com

R. Li
e-mail: 1021920541@qq.com

W. Chen
e-mail: 943285696@qq.com

B. Zou
e-mail: 814523834@qq.com

L. Jiang
e-mail: 1182970490@qq.com

S. Liang
e-mail: 314323179@qq.com

Y. Han (ed.), *Advances in Energy and Environmental Materials*,
Springer Proceedings in Energy, https://doi.org/10.1007/978-981-13-0158-2_35

experimental conditions, when the current density is 10 A/dm^2, the combination property of the micro-arc oxidation layer is better.

Keywords Titanium alloy drill pipe · Micro-arc oxidation · Current density Structure · Properties

Introduction

With the rapid development of modern oil industry, oil well drilling technology put forward higher requirements to drilling tools. In order to meet the drilling requirements of special craft wells, a series of drilling tools and equipment have been developed, for example the titanium drill pipe is a new variety developed in recent years [1, 2]. Titanium alloy drill pipe has the advantages of high flexibility, small structural stress, fatigue resistance, corrosion resistance and light weight. It has wide application prospect in drilling application of high curvature wellbore. However, the hardness and wear resistance of the titanium alloy are poor, it is prone to adhesion in the wear process, so that the early failure of components occur in the working process. The surface treatment of titanium alloy technology includes nitriding treatment, chemical deposition and electrodeposition, surface electrophoresis coating, surface nano-treatment, laser surface strengthening, surface oxidation, etc. Micro-arc Oxidation (MAO) is a new type of surface treatment technology. Through the combination of electrolyte and the corresponding electrical parameters, aluminum, magnesium, titanium and its alloy surface rely on the arc discharge generate with the high instantaneous temperature and high instantaneous pressure and grow out metal oxide ceramic layer [3, 4]. There are many studies on the preparation and properties of micro-arc oxidation coatings on aluminum alloys and magnesium alloys [5–8], and titanium alloy in the field of biomedical research and application are very common [9–11], but titanium alloy application in the field of oil rarely report. In order to further improve the excellent surface properties of titanium alloy drill pipe and develop its application prospect in the field of petroleum and natural gas, Ti_6Al_4V titanium alloy was used as the matrix material to study the effect of current density on the structure and properties of micro-arc oxidation film and the practical application of titanium alloy drill pipe provide a scientific basis.

Test Materials and Methods

The Ti_6Al_4V titanium alloy drill pipe was selected as the experimental material. 15 samples are cut with cnc edm wire cutting machine, and the size is 40 mm × 15 mm × 0.8 mm. The chemical composition (wt%) of Ti_6Al_4V titanium alloy drill pipe is 5.5–6.8 Al, 3.5–4.5 V, $\leq$0.3 Fe, $\leq$0.1 C, $\leq$0.015 H, $\leq$0.2 O, the rest

is Ti. The micro-arc oxidation experiment was carried out in XDL20-6 device. The cathode was stainless steel plate and The electrolyte was Na_2SiO_3 + Na_3PO_4 + $NaAlO_2$ with frequency of 90 Hz, duty cycle of 70% and oxidation time of 30 min. The current density were 6, 7, 8, 10, 14 A/dm^2 respectively. Before the experiment, the sample was polished with 400 #, 800 #, 1000 # waterproof abrasive paper to light, then clean with ethanol and distilled water. After the test, the sample was washed with water. The thickness of the film was tested by TT230 digital cladding thickness gauge. Five points were randomly selected on the surface of the film, and the average value was taken as the thickness value of the film. The hardness of the film was measured with a digital microhardness HXD-2000TM/LCD. The load was 50 g and the loading time was 10 s. The surface layer of the sample was analyzed by X-ray instrument. The tube voltage was 40 kV, the tube current was 30 mA, and the diffraction angle was 10–80°, step 0.02°, 0.5 s per step, comparing with the standard card to calibrate Characteristic peaks. The morphology and uniformity, particle size and roughness of the micro-arc oxide film of Ti_6Al_4V titanium alloy were observed by ZEISS EVOMA15 SEM, and the types and contents of the elements in the film were measured by EDS. The friction and wear test was carried out on a disk friction tester with a steel ball of diameter of 6.35 mm and a load of 0.3 kg. The speed of the carrier was 200 r/min, the radius of rotation was 4 mm and the wear time was 10 min, after the test, brush to powder of wear, and weigh the quality of the sample after wear. Polarization curve was measured by SZF5 type electrochemical workstation, sample exposure area is 100 mm^2, the solution is 3.5% NaCl solution, the temperature is 30 °C.

Test Results and Analysis

Effect of Current Density on Hardness and Thickness of Micro-arc Oxidation Film of Ti_6Al_4V Titanium Alloy. The variation law of thickness and hardness of micro-arc oxidation film at different current densities is shown in Fig. 1. It can be seen from the curve (a) that the current density increase from 6 to 10 A/dm^2, the thickness of the film change from 21.0–28.7 μm, and then continue to increase the current density, the film thickness remain. The reason for this phenomenon is that with the current density increases, the energy per unit area of the film increases and promote film growth. At the same time, these energies make the discharge reaction more intense, break out more discharge ion channels, and expand the diameter of the discharge channel, which facilitates the plasma reaction of solute ions and molten matrix metal in the electrolyte, but when the current density continue to increase, the oxide melt more, and the thickness increase is not obvious. From the curve (b) can be seen: the current density increases, the film hardness increases. The current density increase from 6 to 8 A/dm^2, the hardness of the film increase from 832.4 HV to 1251.1 HV. The current density increase from 8 to 14 A/dm^2, the hardness of the film increase from 1251.1 HV to 1296.3 HV, the increase rate slows down. The reason why the hardness of the film increases with the current density:

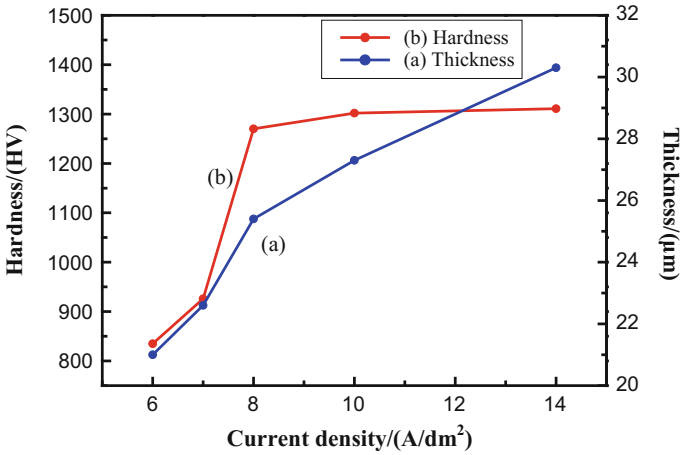

Fig. 1 Effect of current density on film hardness and thickness

increasing the current density increase the energy of the output, amorphous TiO_2 and anatase TiO_2 are converted to rutile TiO_2, and the hardness of the film increases; When the current density increases from 10 to 14 A/dm^2, although the density of the film decreases, the effect of the increase of rutile TiO_2 on the hardness of the film is greater than that of the decrease of the density. Dense layer discharge channel less, less defects, rutile TiO_2 content is high, so the hardness of the film with the dense layer thickness increases.

Effect of Current Density on Morphology of Micro-arc Oxidation Films of Ti_6Al_4V Titanium Alloy. The effect of current density on micro-morphology of micro-arc oxide film is shown in Fig. 2. It can be seen from Fig. 2a, b that the surface of the film is distributed with round particles, and the size distribution of the particles is not uniform. It can be seen that the holes with large diameter and shallow depth are distributed above the film. It can be seen from Fig. 2c that the micro-arc oxidation film has a larger area and smaller blocky-shaped particles with a diameter of about 30 μm. Different sizes of pits are distributed in the film. Compared with Fig. 2a, the blocky-shaped particles disappear showing sheet structure, in the 500 × SEM plot, no holes were observed, and in the 4000 × SEM plot, it was observed that fine pores were evenly distributed on the surface of the film. As can be seen from Fig. 2e, f, there are larger diameter blocky-shaped particles and densely pack deep pores. The roughness of Fig. 2a, e is significantly larger than that in Fig. 2c. The reason for this phenomenon is that as the current density increases (the current density increases from 7 to 10 A/dm^2), the energy acting on the film increases, the local temperature increases, and more of the melt ejects the discharge channel and solidify into small particles on the surface. These small particles are joined together to form the sheet structure in Fig. 2d, covering the surface pores, increasing the density and reducing the roughness. With the further increase of the current density, the spark discharge on the film is intense, the

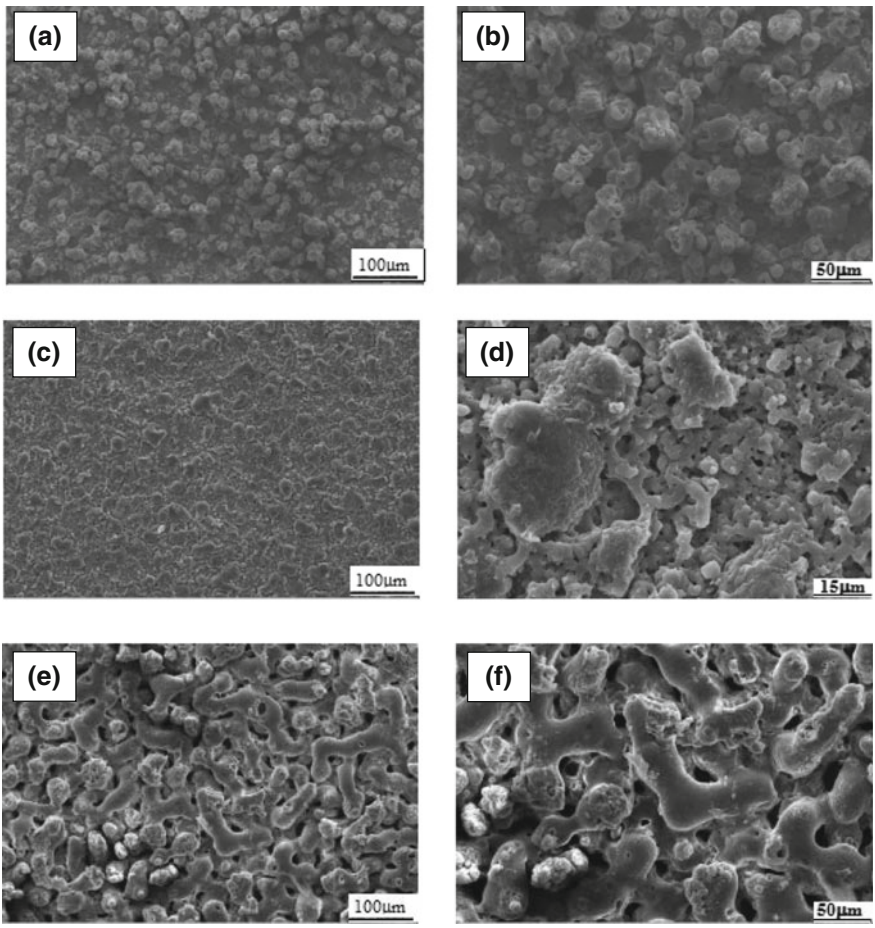

Fig. 2 Effect of current density on micro–morphology of micro-arc oxidation films **a**, **c**, **e** 7, 10, 14 A/dm^2(500×); **b**, **f** 7, 14 A/dm^2(1000×); **d**10 A/dm^2(4000×)

larger diameter of the melt combine to form strip shaped particles so that the degree of roughness increases.

The effect of current density on the elemental content of the film is shown in Fig. 3. It can be seen from Fig. 3 that the Si element content is greater than the P element and Al element content because of the different adsorption capacity of the micro-arc oxidation film, the adsorption capacity of SiO_3^{2-} ion on the film is the strongest, and the AlO_2^{2-} ion on the film is the weakest. silicon-containing persad more easy to occur chemical deposition in the film surface. When the current density increase from 7 to 14 A/dm^2, the Ti element content decreased from 25.91

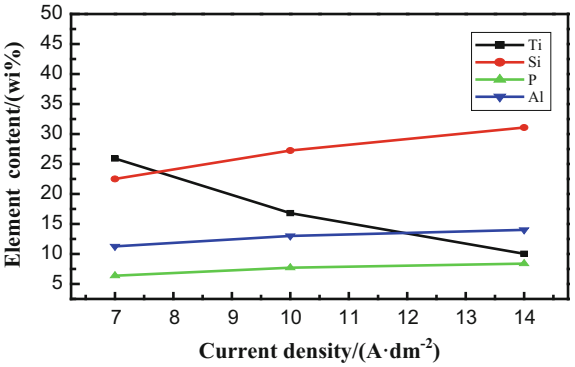

Fig. 3 Effect of current density on element content in film

to 10.03 wt%, the Si element content increase from 22.51 to 31.08 wt%, the P element content increase from 6.37 to 8.39 wt% and the Al element content increase from 11.27 wt% to 14.02 wt%. According to Ohm's law, increasing the current density, the resistance is almost constant, the voltage between the boards increases, so the amount of electrolyte ions migrating to the anode increases and the amount of electrolyte ions increases on the film.

Effect of Current Density on Microstructure of Micro-arc Oxidation Films of Ti_6Al_4V Titanium Alloy. The effect of current density on composition of the film is shown in Fig. 4 the effect of current density on the composition of the film is shown in figure. By analyzing the diffraction peak, we can see that the thickness of the film increases with the increase of the current density. Under the three different process parameters, the diffraction peak of anatase TiO_2 is not obvious, only two strong peaks appear. The diffraction peak intensity of rutile TiO_2 increases with the increase of current density, which is an explanation of the increase of the former hardness value provide the basis.

Effect of Current Density on Wear Resistance of Micro-arc Oxidation Films of Ti_6Al_4V Titanium Alloy. The effect of current density on the friction coefficient of the micro-arc oxidation film is shown in Fig. 5. The average coefficient of friction of Ti_6Al_4V titanium alloy is reduced from 0.119 to 0.0376 by increasing the current density. It can be seen from Fig. 5a that the coefficient of friction of the sample at a current density of 7 A/dm^2 is always in the running-in period and there is no stable phase. The friction coefficient of the film increases with the friction time, and the amplitude is larger. The Fig. 5b is the curve of the coefficient of friction of the sample at a current density of 10 A/dm^2. At the beginning of the friction, the friction is in the running-in period, the ball constantly grind the "convex" of surface of the film, and the contact area of the film increase resulting in increasing friction coefficient. the maximum reach 0.1. When the friction to 3 min, the loose layer reach the fatigue limit and peeling occur, the friction coefficient decrease sharply. The Fig. 5c is the curve of the coefficient of friction of the sample at a current density of 14 A/dm^2. The dense layer of the film is thicker, the running-in period

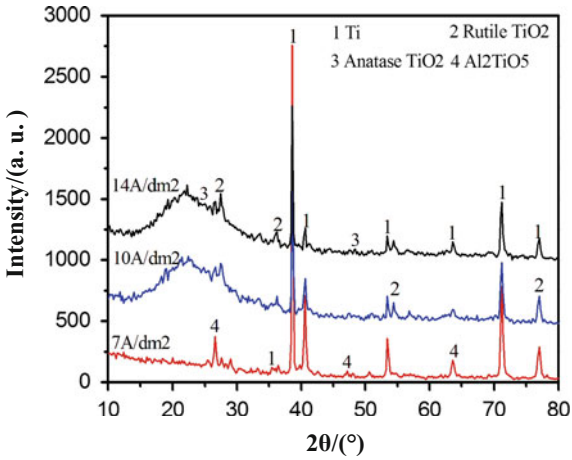

Fig. 4 XRD patterns of samples at different current densities

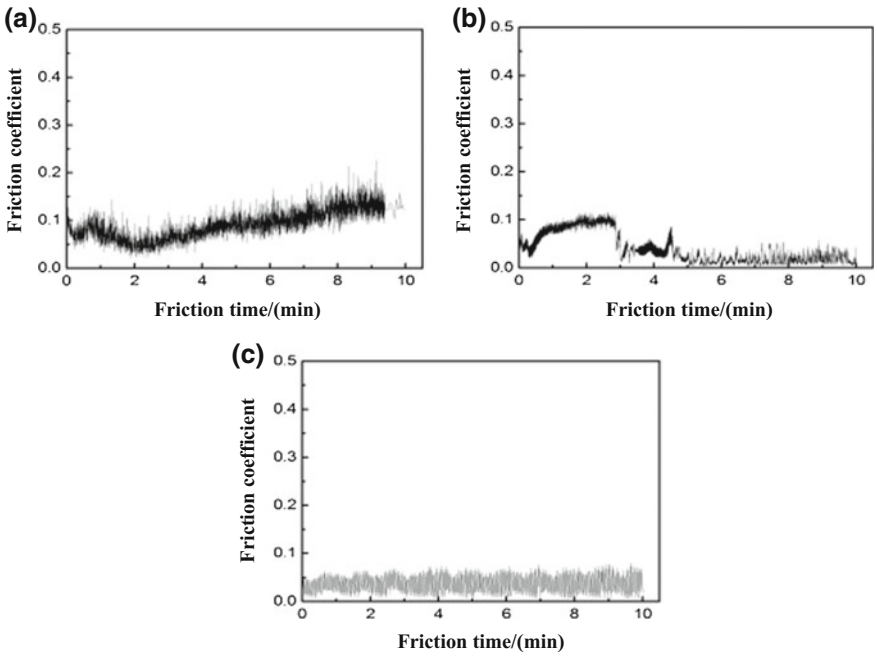

Fig. 5 Effect of current density on friction coefficient **a** 7 A/dm^2; **b** 10 A/dm^2; **c** 14 A/dm^2

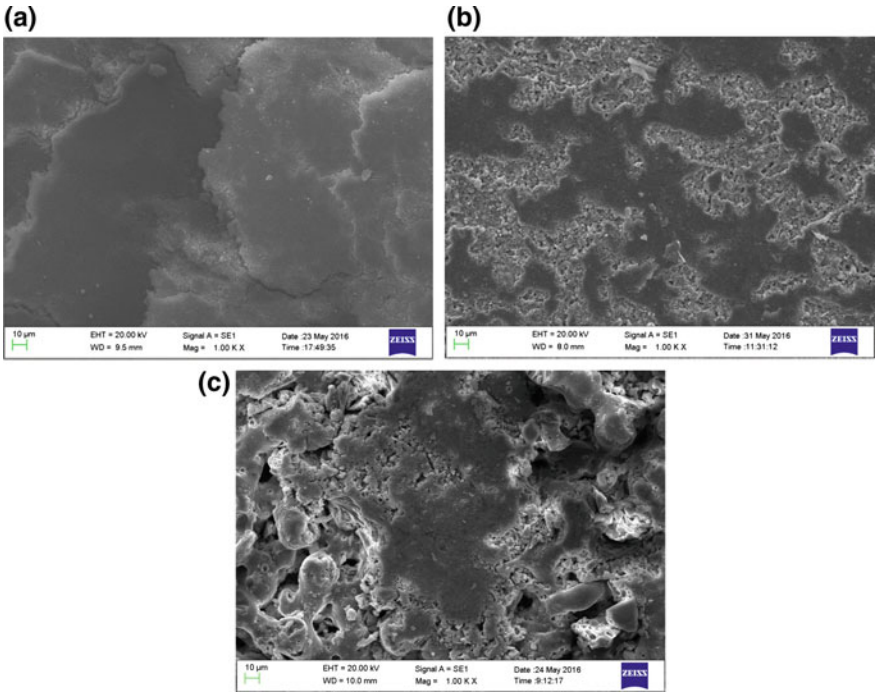

Fig. 6 Effect of current density on microstructure of film wear **a** 7 A/dm^2; **b** 10 A/dm^2; **c** 14 A/dm^2

will soon end, and then the curve into the stable stage, the friction coefficient has remain at 0.03 or so, comparing with the current density of 10 A/dm^2, the friction coefficient of the film in the stable stage the friction coefficient is greater, and the amplitude is more intense.

Figure 6 shows the micro-wear morphology of the sample with a current density of 7 A/dm^2. It can be seen from Fig. 6a that the frictional contact area is fish-scale and is accompanied by cracks, which is a typical abrasive wear characteristic. Because the steel ball cut the "convex" of the sample surface and press it into the pores of the film. The abrasive dust exerts compressive stress on the surrounding film, causing the surrounding film into plastic deformation, and when the plastic deformation accumulates to a certain extent, the crack occurs and the crack expand. It can be seen from Fig. 7 that when the Fe element content reaches 28 wt% in the film layer, adhesive wear occurs between the film and the steel ball. Figure 6b is the micro-morphology of current density of 10 A/dm^2 of sample in the 1000× SEM plot. Comparing with Fig. 6a, the abrasive wear phenomenon is weak. When the current density is 10 A/dm^2, the degree of film layer increase, and the increase of the hardened phase in the film reduces the plastic deformation, resulting in reducing the actual contact area and enhancing wear resistance of the film. Figure 6c is the

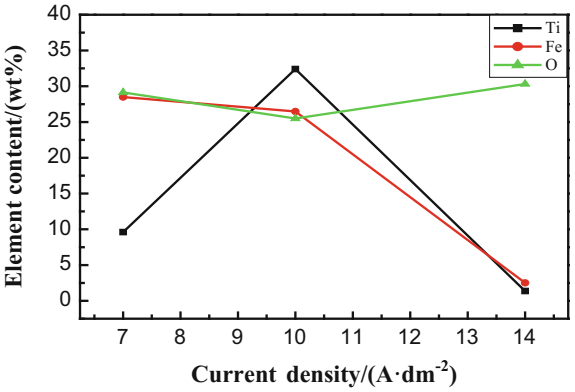

Fig. 7 Elemental content of frictional contact area of sample at different current densities

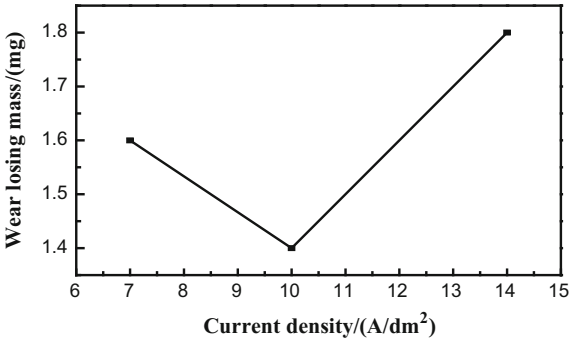

Fig. 8 Effect of current density on weightlessness of wear

micro-morphology of current density of 14 A/dm^2 of sample in the 1000× SEM plot. Comparing with Fig. 6b, the abrasive wear phenomenon is weak. It can be seen from Fig. 7, Fe element content is only 4%, which indicates that abrasive wear occurs mainly.

The effect of current density on weightlessness of wear is shown in Fig. 8 When the current density increase from 7 to 10 A/dm^2, the weightlessness of wear decrease from 1.6 to 1.4 mg, the hardness and the density of the film are increasing and the abrasion resistance improve. When the current density increase from 10 to 14 A/dm^2, the weightlessness of wear increase from 1.4 to 1.8 mg, and the density of the film and the abrasion resistance increase.

Effect of Current Density on Corrosion Resistance of Ti_6Al_4V Titanium Alloy Micro-arc Oxidation Film. The effect of current density on the corrosion resistance of the film is shown in Fig. 9. The values of self-corrosion current and self corrosion potential obtained by Tafel extrapolation are shown in Table 1. It can be seen from the table that the change trend of the corrosion current is not obvious. When the current density increases from 7 to 10 A/dm^2, the self-corrosion current decreases from 3.87 × 10^{-7} to 9.39 × 10^{-8} A/cm^2, the corrosion resistance improve. When

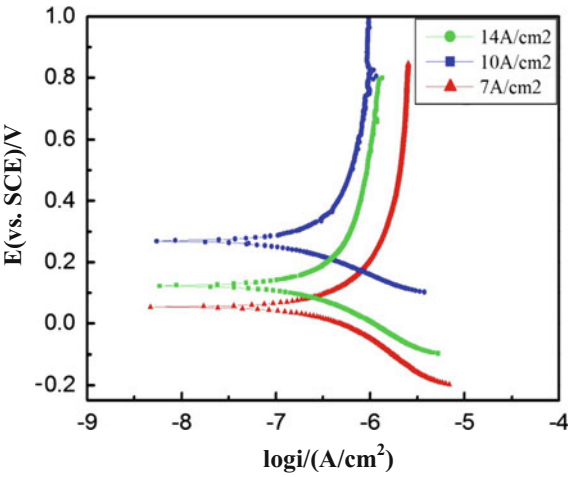

Fig. 9 Effect of current density on the polarization curve of film

Table 1 self-corrosion current and self corrosion potential at different current density

Current density (A/dm^2)	Self-corrosion potential (V)	Self-corrosion current (A/cm^2)
7	0.045	3.87×10^{-7}
10	0.276	9.39×10^{-8}
14	0.138	1.43×10^{-7}

the current density increase from 10 to 14 A/dm^2, the self-corrosion current increase from 9.39×10^{-8} to 1.43×10^{-7} A/cm^2, the self-corrosion current increases and the corrosion resistance decrease. The reason for this phenomenon is that the increase of the thickness, the decrease of the porosity and the increase of the corrosion resistance phase increase the corrosion resistance of the film. When the current density is in the range of $7A/m^2$–$10A/dm^2$, the increase of the current density decreases the number of holes in the sample, the surface of the film is denser and the corrosion resistance of the film increases. When the current density is in the range of $10–14A/dm^2$, the diameter of the micro-arc oxidation becomes larger and the number increases, but the thickness increases. When the effect of the thickness on the film is less than the effect of the density, the corrosion resistance of the film decreases. In addition, the increase of the current density of the sample from the structure of the anatase TiO_2 into the relatively dense structure of rutile TiO_2, the sample corrosion resistance enhance.

Summary

1. With the increase of the current density, the thickness and hardness of the film increase, but the wear resistance and corrosion resistance of the film increase first and then decrease.
2. At different current densities, the phase structure of the film is mainly rutile TiO_2 and anatase TiO_2, and also contains a small amount of Al_2TiO_5 crystal and SiO_2 amorphous state. Microstructure analysis shows that with the increase of current density, the density of the film increases and the roughness decreases, but with the current density continues to increase, the pores increase and the roughness increases.
3. Under the experimental conditions, when the current density of 10 A/dm^2, the integrated performance of micro-arc oxidation film is better.

References

1. Y.X. Wang, C.T. Zhang, B. Zhang, New type of titanium and aluminum alloy drill pipe of finite element analysis. Oil Field Equip. (2010)
2. D. She, W. Yue, Z. Fu et al., Effects of nitriding temperature on microstructures and vacuum tribological properties of plasma-nitrided titanium. Surf. Coat. Technol. **264**, 32–40 (2015)
3. W. Yang, B.L. Jiang, H.Y. Shi, Formation and growth mechanism of microarc oxidation coating on LY12 aluminium alloy. Chin. J. Nonferrous Metals **20**, 1949–1954 (2010)
4. H.Y. Wang, R.F. Zhu, Y.P. Lü et al., Research status of microarc oxidation process effect on ceramic coating characteristic of titanium and its alloys. Trans. Mater. Heat Treat. **33**, 1–6 (2012)
5. F. Chen, H. Zhou, B. Yao et al., Corrosion resistance property of the ceramic coating obtained through microarc oxidation on the AZ31 magnesium alloy surfaces. Surf. Coat. Techno **201**, 4905–4908 (2007)
6. Y. Shen, H-Xng Wang, Effect of Nano-MoS_2 particles on properties of micro arc oxidation coating prepared on surface of aluminum alloy drill pipe in offshore platform. Ship Eng. **38**, 89–93 (2016)
7. M.L. Kang, U.L. Byung, Evaluation of plasma temperature during plasma oxidation processing of AZ91 Mg alloy through analysis of the melting behavior of incorporated particles. Electrochim. Acta **67**, 6–11 (2012)
8. Y. Cheng, Z. Xue, Q. Wang et al., New findings on properties of plasma electrolytic oxidation coatings from study of an Al–Cu–Li alloy. Electrochim. Acta **107**, 358–378 (2013)
9. J.Q. Qiao, F.B. Wang, Fracture mechanics of composite ceramic coating prepared by micro-arc oxidation on biomedical titanium alloy. Plat. Finish. **34**, 18–22 (2012)
10. J.M. Zhang, Z.H. Wang, B.L. Jiang, Study of microarc oxidation ceramic coatings formed on titanium alloy based on biological treatment. Foundry Technol. **28**, 1063–1066 (2007)
11. F.B. Wang, D.I. Shi-Chun, Formation mechanism of micro-arc oxidation medical coating on titanium alloy surface. Corros. Prot. **33**, 400–403 (2012)

Formation Mechanism of 6009 Aluminum Alloy Joint by Laser-MIG Arc Hybrid Welding

Defen Zhang, Jinli Han, Xiaowen Chen, Yang Yang and Yu Tang

Abstract An investigation of the influence of different position for laser and arc on the formation mechanism of 6009 aluminum alloy joint by laser-MIG arc hybrid Welding was dealt with in this paper. As a result of stronger laser-arc coupling with laser at the front, the formability of joint which was welded with laser at the front is better than that of joint which was welded with arc at the front. Due to mechanical rabbling of arc, the grain size of upper weld is smaller than that of lower weld; There is softening zone in the heat affected zone of hybrid welding joint. In trailing MIG torch arrangement, the hardness of upper joint is less than that of lower joint for tempering of arc. While, the hardness of upper joint for leading MIG torch setup is higher than that of lower joint, owing to the secondary remelting of solidified metal by laser. That second phases at HAZ coarsens and grows has great influence on the mechanical property of the hybrid weld joint. Grooving before welding is beneficial to enhance the mechanical properties of joint. The tensile fracture of hybrid welding joint has typical dimples feature. The formation of dimples is associated with second phase particles.

Keywords 6009 aluminum alloys · Fiber laser-MIG arc hybrid welding
Formation mechanism

D. Zhang (✉) · J. Han · X. Chen · Y. Yang · Y. Tang
School of Material and Engineering, Southwest Petroleum University, Chengdu 610500, Sichuan, China
e-mail: zhangdefen0304@163.com

J. Han
e-mail: 2474298422@qq.com

X. Chen
e-mail: 879559431@qq.com

Y. Yang
e-mail: 985828158@qq.com

Y. Tang
e-mail: 379981949@qq.com

Y. Han (ed.), *Advances in Energy and Environmental Materials*,
Springer Proceedings in Energy, https://doi.org/10.1007/978-981-13-0158-2_36

Introduction

With the development of materials technology, the materials used in automobile is presenting lightweight tendency. Kim et al. [1] demonstrated the aluminum alloy, a low-density material, is frequently applied to automobile manufacture in recent years, which provides with a series of advantages, such as high strength rate, excellent corrosion resistance and formability, strong thermostability. Benedyk [2] reviewed the technological progress in lightweighting automotive vehicles from US, European, and Japanese automobile companies, and Raugei et al. [3] summarized the use of aluminum alloys in automobile manufacture is a important lightweighting strategy. Kohar et al. [4] investigated the behavior for vehicle lightweight design of aluminum framework during the transport of passengers. In the early 1970s, Americans has developed 6000-series aluminum alloys, acting as a material for auto body. And this aluminum alloys have been made full of various limousine [5].

The weldability of 6000-series aluminum alloys is key problem to limit its use. The welded joint by traditional welding technology, such as gas shielded welding, argon arc welding, usually has multiple defect and poor quality, which cannot meet the demands of industrial manufacture [6]. Now, aluminum alloy is mainly welded by Metal-inert Gas Welding(MIG). Nevertheless, the weld joint of MIG has many insuperable problems, like softening, gas holes, deformation, excessive penetration, misalignment, etc. [7]. Compared with traditional welding technology, welding aluminum alloy by fiber laser-MIG arc hybrid welding posses efficient, defect-little and other advantages of which the welding process is steadier [8]. Yang et al. [9] reported multiple defects exist in aluminum alloy joints welded by laser weld, due to high reflectivity of laser to aluminum alloy. Katayama [10] also summarized the cause and control measure of weld defect with aluminium alloy welded by laser weld. The hybrid welding avoids the shortcoming of single laser welding and electric-arc welding, and may assembles the bridging ability of the electric-arc welding and the deep fusibility of the laser welding, which generates the synergistic effect of "1 + 1 > 2". Compared with single laser welding, the fiber laser-MIG arc hybrid welding is provided with higher utilization rate of laser [11]. Guen et al. [12] found the coupling between laser and arc reduces markedly reflectivity of laser. Cai et al. [13] demonstrated that the laser accelerates droplet transferred steadily, which improves weld quality. Therefore, the study that 6009 aluminum alloy is welded by the fiber laser-MIG arc hybrid welding have the great significance. Recently, the study about microstructure and mechanical property of 6009 aluminum alloy is often reported, while the formation mechanism of joint and the weldability analysis about the fiber laser-MIG arc hybrid welding of 6009 aluminum alloy is less studied.

The fiber laser-MIG arc hybrid welding is put in use in vehicle, shipbuilding, petroleum pipeline and other industry, mainly adapts for welding materials which have high reflectivity, such as steel plate of medium thickness, magnesium-aluminum alloy, and other materials [14]. In this paper, the effect of changing

welding parameters on formability, microstructure and property of 6009 aluminum alloy joint by fiber laser-MIG arc hybrid welding is analyzed, and formation mechanism of joint is investigated in detail, for providing reference data for practical industrial production.

Experimental Materials and Experimental Methods

6009 aluminum alloy sheets with thicknesses of 6 mm were taken as the test material. The joint of 6009 aluminum alloy were made from two 150 mm × 60 mm × 6 mm plates connected via V-groove or I-groove with 1.6 mm gap sizes. The base metal has the 305 MPa tensile strength and the 13% elongation.

The experimental platform of the fiber laser-MIG arc hybrid welding machine, made up of fiber laser, pulse MIG welding machine, ABB robot and other parts, from the welding laboratory in Southwest Jiaotong University was employed in experimental welding equipment. A KEMPPI Pulse-450 welding system and IPG YLS-4000 multimode fiber laser system were used in the welding tests. The maximum output power of the IPG YLS-4000 is 4 kW with a laser wavelength of 1.07 μm. In welding process, the defocusing amount is zero, with pure argon gas protecting. The angle between the axis of the welding wire and horizontal plane was approximately 65°. The laser beam was inclined 10 degrees forwards to prevent any possible damage to the optical component by reflected light. Figure 1 shows the schematic of laser-MIG hybrid welding, where L_{DF} refers to the defocusing amount, L_{LA} is the distance between the laser and the electric arc, and L_{TBWD} is the vertical distance between the welding gun and the surface of workpiece. The 1.6 mm-diameter welding wire of which model number is ER5356 was take in this

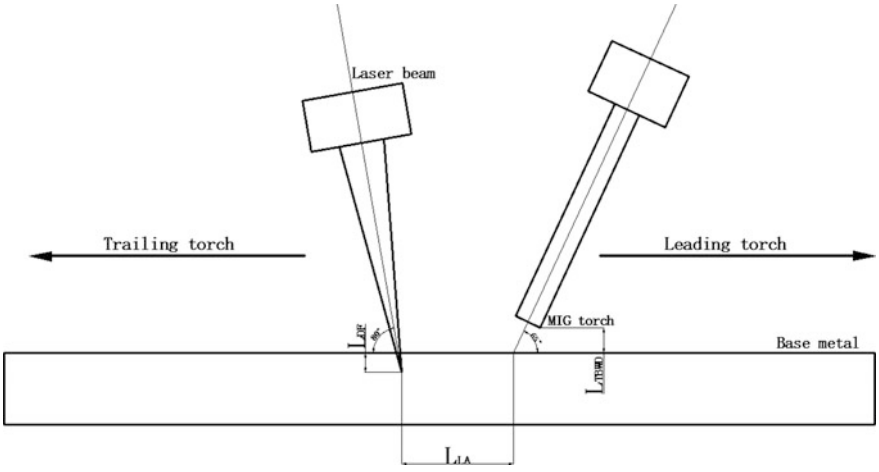

Fig. 1 Schematic of laser-MIG hybrid welding

Table 1 Welding parameters

Piece number	Laser and electric arc location	L_{LA}/(mm)	Laser power/(KW)	Welding current/(A)	Welding speed/(mm/min)	Wire feed rate/(m/min)
1	LL	2	4	185	900	12
2	AL	2	4	185	900	12
3	LL	2	4	185	900	12
4	LL	3	4	185	900	12
5	LL	4	4	185	900	12

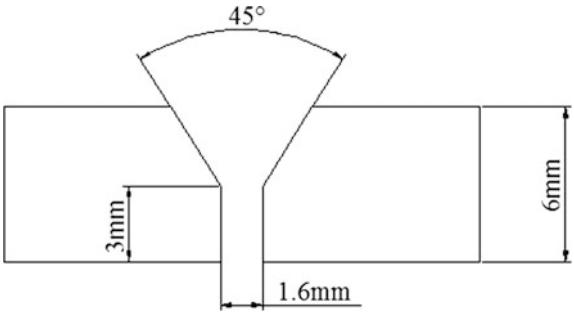

Fig. 2 Schematic diagram of welding groove

Table 2 Chemical composition of 6009 aluminum alloys and ER5356 welding wire

Grades	Si	Fe	Cu	Mn	Mg	Cr	Zn	Ti	Al
6009	0.6–1.0	0.5	0.15–0.6	0.2–0.8	0.4–0.8	0.1	0.25	0.1	Bal
ER5356	0.00346	0.168	0.0007	0.141	4.88	0.132	–	0.105	Bal

welding test. Table 1 lists detailed hybrid welding procedure, where No. 3 is only grooved in five welding samples, as shown in Fig. 2. In Table 1, LL refers to the laser leading, while AL refers to the arc leading, Table 2 lists the chemical composition of 6009 aluminum alloy and ER5356 type welding wire.

Workpieces were removed their superficial oxidation film by mechanical grind. Then workpieces, fixture and worktable were scrubbed by acetone before welding. Joint samples were cut out in perpendicular to welding direction to do metallographical test, hardness test and tensile test. Figure 3 shows the schematic diagram of tensile specimen's size. The microcomputer control electron universal testing machines of which model number is WDW-1000 was taken to do tensile test. The VMD-P300B type optical metallographic microscope was used to observe the joint microstructure. The joint hardness testing was measured in sectional horizontal and vertical direction by means of the HXD-1000TMB type digital microscopic hardness meter using 100 gf load with 15 s holding time. The EVO/MA15 type scanning electron microscope made in German was taken to analyze the tensile fracture.

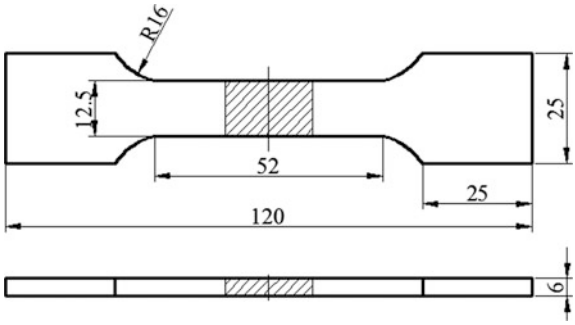

Fig. 3 Schematic diagram of tensile specimen's size

Test Results and Analysis

Joint Formability. Figure 4 shows cross-sectional photograph of hybrid welding joint of which laser is at the front and arc is at the front. As shown in Fig. 4a, b, weld width and weld depth of hybrid welding joint of which the laser is at the front are larger than that of which arc is at the front, so are penetration and formability. Moreover, lack of penetration appears at foot of hybrid weld of which arc is at the front. The reason can be that arc brings about increased weld width at the top part of hybrid welding joint, while laser bring about increased weld depth, as generating keyhole at fusion depth direction [15, 16]. In trailing MIG torch arrangement, laser plasma was diluted by succedent arc plasma, which enhances the transmissive efficient of laser energy with base metal heated, so that absorptivity of base metal in laser is enhanced, which increases weld depth. In addition, that metal vapor resulted

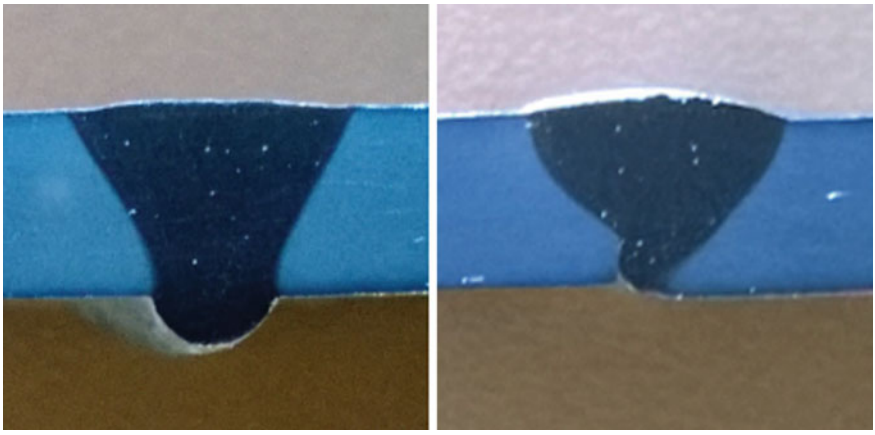

(a) Laser at the front. (b) Arc at the front.

Fig. 4 Cross-sectional photograph of hybrid welding joint

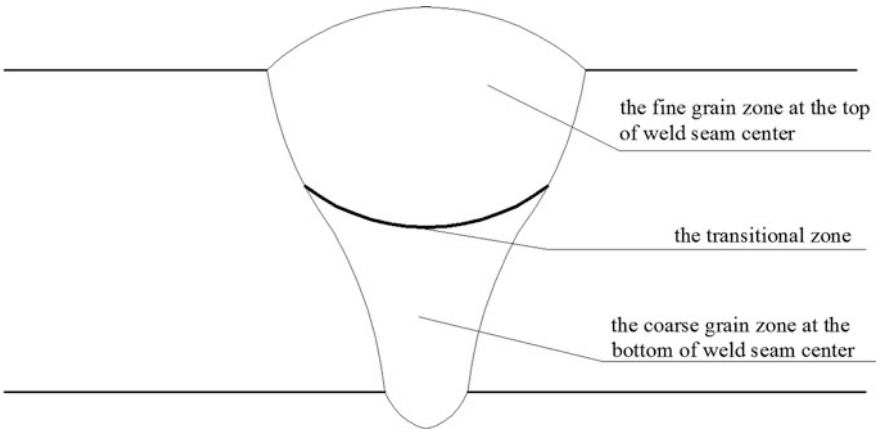

Fig. 5 Dividing of welding bead in the hybrid weld

from laser enters into arc zone enhances energy utilization ration of arc, which increases weld width at the top of weld [17]. In leading MIG torch arrangement, arc energy is mainly applied to fuse base metal, and subsequent laser impact on the top of weld pool. The absorptivity of laser for liquid metal in weld pool is enhanced. However, the utilization rate of arc energy isn't enhanced, which results in lesser total energy utilization ration, so that the weld width at the top of weld is less larger than these of which laser is at the front, and the weld width at the bottom of weld is very small.

Combined with back observation on microstructure, the fine grain zone at the top of weld seam enter, the transitional zone and the coarse grain zone at the bottom of weld seam enter are divided. Figure 5 shows region division from microstructure of the hybrid welding joint.

Microstructure. Figure 6 shows microstructure of the laser-MIG arc hybrid welded joint and parent metal microstructure in trailing MIG torch arrangement. It can be seen from Fig. 6d that parent metal is ribbon structure. As is shown in Fig. 6a, b, the fine and uniform grain is at the top of weld seam center, while the coarse grain is at the bottom of weld seam center. The reason is mainly that arc force of MIG acting on the top of weld pool and impact force of molten drop have mechanical rabble impact on weld pool, which benefits obtaining the fine grain at the top of weld [17]. Moreover, the arc source has the post thermal treatment influence on weld seam, which also benefit acquiring the uniform and fine grain. It can be seen from Fig. 6c that grain transits from the fine to the coarse, with depth accelerated in penetration direction. As shown in Fig. 6e, f, the width of fusion region of the fine grain zone at the top of weld is wider than that's at the bottom of weld. The reason is that the fine region at the top of weld gets the double function from laser and arc, and great thermal input leads molten metal region wider, the recrystallization grain growing more quickly, while the coarse grain zone at bottom of weld is precisely the opposite for only function of laser.

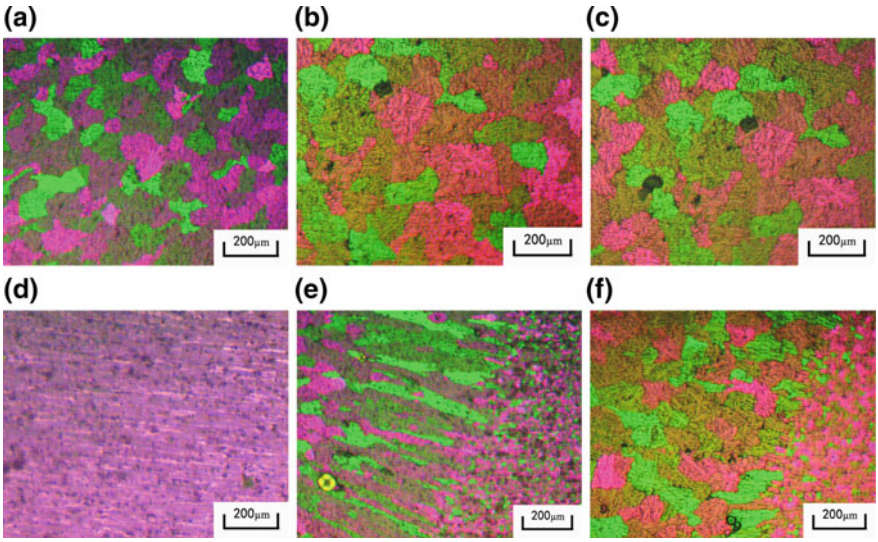

Fig. 6 Microstructure of welded joints and base metal. **a** Microstructure of upper weld seam center. **b** Microstructure of lower weld seam center. **c** The transitional zone. **d** Base meta. **e** Fusion region in upper weld and HAZ. **f** Fusion region in lower weld and HAZ

Joint precipitated phase. Figure 7 shows scanning electron micrographs of different sectional precipitated phase of the laser-MIG arc hybrid welding joint. Whether laser passes first or arc passes first, the size of precipitated phase of upper weld seam is all smaller than those of lower weld seam, as shown in Fig. 7a, b, d, e. When the laser is at the front, arc force of MIG acting on the top of weld pool and impact force of molten drop have strong mechanical rabble impact on weld pool, which benefits structure refinement. When arc is at the front, succedent laser thermal source exerts secondary remelting to hot metal on the upper weld pool, which benefits structure refinement. It can be seen from Fig. 7c, f that precipitated phase at heat affected zone (HAZ) grows obviously. Combining with microhardness distribution curves and the location of tensile break, that the second phase at HAZ coarsens and grows has great influence on the mechanical property of the hybrid weld joint.

Microhardness. Figure 8 shows the microhardness distribution curves of five groups of hybrid welding parameters. It can be seen from Fig. 8a that the minimum hardness region locates at HAZ, and the problem of soften appears at HAZ. The main reason is that over-aging is taken place at HAZ for elevated temperature during welding. Second phase precipitates from HAZ, assembles and grows, which appears softened problem for over-aging [18]. The weld hardness is about 59 HV, while the parent metal hardness is about 65 HV. As is shown in Fig. 8b, the hardness of upper weld is higher than that of lower weld for the sample No. 2, while

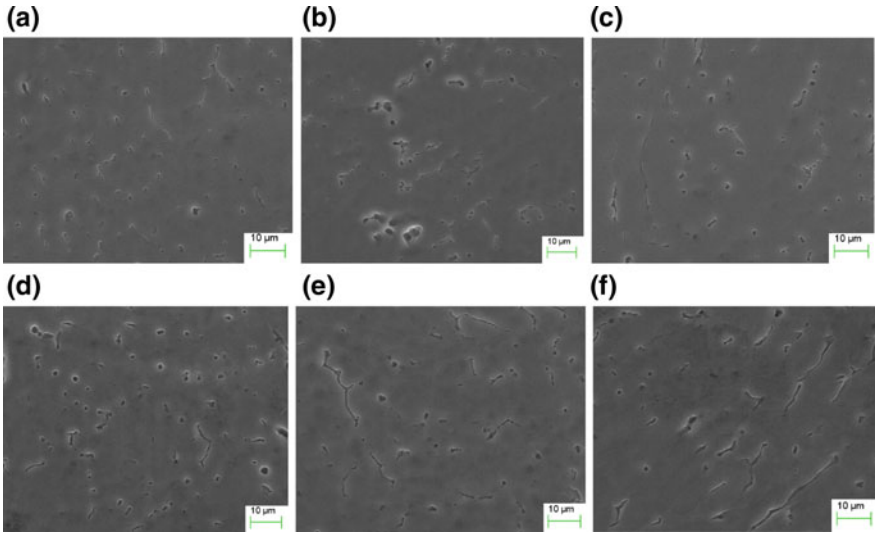

Fig. 7 Second phase appearance of hybrid welding joint. **a** Upper weld precipitated phase in trailing MIG torch arrangement. **b** Lower weld precipitated phase in trailing MIG torch arrangement. **c** Precipitated phase at HAZ in trailing MIG torch arrangement. **d** Upper weld precipitated phase in leading MIG torch arrangement. **e** Lower weld precipitated phase in leading MIG torch arrangement. **f** Precipitated phase at HAZ in leading MIG torch arrangement

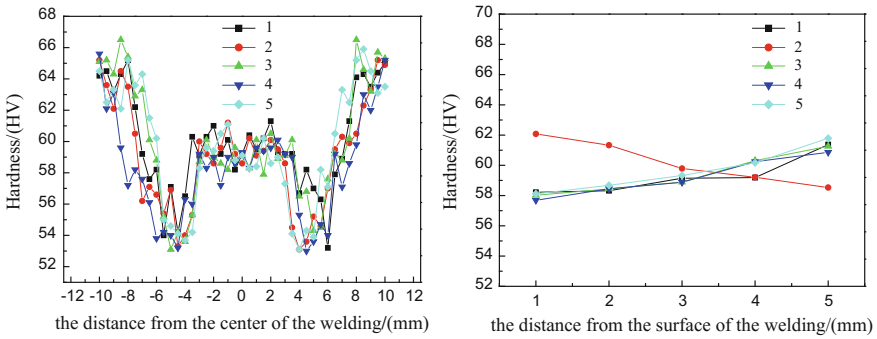

(a) Horizontal microhardness distribution curves of weld section.

(b) Vertical microhardness distribution curves of weld section.

Fig. 8 Distribution of microhardness in the hybrid welded joint

other samples are reverse. For leading laser setup, filled element overburns very seriously, with subsequent arc heat source drawing temper on upper weld, so that, the hardness of upper weld is lower than that of lower weld. However, solidified metal is remelted by laser beam, for leading arc setup, which refines structure, and enhances hardness of upside, as shown in Fig. 7d.

Table 3 Tensile properties of the hybrid welded joint

Piece number	Tensile strength/MPa	The elongation/%	Fracture position
1	194	5.4	HAZ
2	198	6.1	HAZ
3	200	7.3	HAZ
4	191	5.2	HAZ
5	196	5.8	HAZ

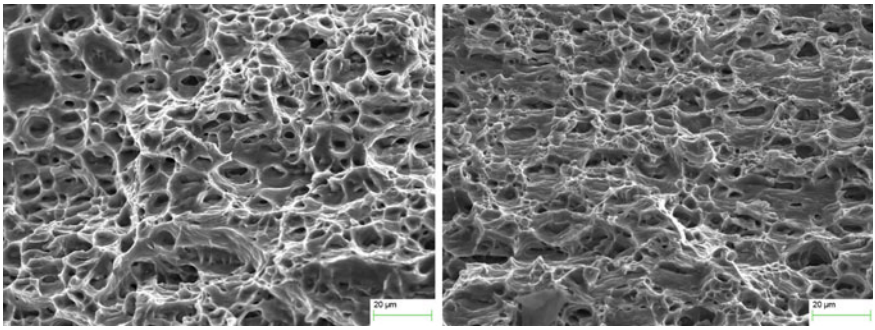

(a) Tensile fracture with laser at the front. (b) Tensile fracture with arc at the front.

Fig. 9 The fractographs of joint tensile specimens by two different welding processes

Tensile property. Table 3 lists tensile information of hybrid welding joints. Their tensile strength exceeds 62% of the base metal, and the maximum reaches 65% of the base metal. The analysis of microhardness reveals that soften region of joints locates at HAZ, so all samples breaks at HAZ. The excellent mechanical property is the sample No. 3, because grooving before welding benefits decreasing the tendency of air hole and crack. It can be seen from Table 3 that the tensile property of the sample No. 2 is better than that of the sample No. 1, which illustrates the truth that the tensile property of joint in leading MIG torch arrangement is slightly better than that in trailing MIG torch arrangement, but the welding formability in leading MIG torch is poor, as can be seen from the foregoing analysis of the joint formability.

Tensile Fracture Morphology. Figure 9 shows tensile fracture morphologies of joints under two kinds of process that laser is at the front and arc is at the front. It can be seen from Fig. 9a, b that deeper dimples of more uniform distributes uniformly in trailing MIG torch arrangement, while shallower dimples have the distinct feature of shear fracture in leading MIG torch arrangement. These two different tensile fracture all belongs to the typical dimple fracture, and obvious particles exists inside dimples which are generated for formation of microvoids during fracture, which illustrates that relative location of laser and arc has weak impact on the fracture mechanism of joints during welding in this welding test. Figure 10

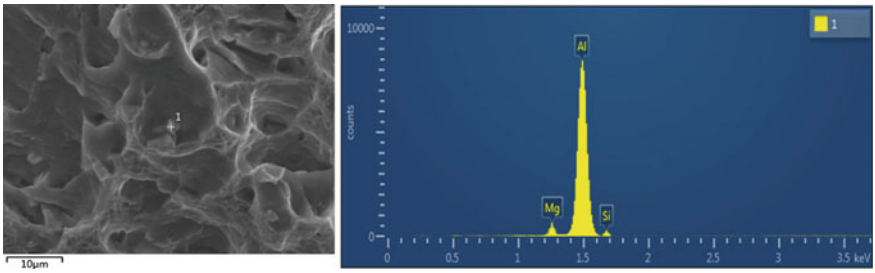

(a) Dimple morphology. (b) The composition of the second phase.

Fig. 10 The morphology of fracture and the analysis of composition

Table 4 The composition analysis of second phase particle

Element	Mg	Si	Al
wt%	4.39%	2.13%	Other

shows the EDS analysis of particle inside dimple under high power. Table 4 lists the detailed composition of the second phase. Table 4 suggests that major components of the second phase particle inside dimple is Al, Mg, and Si, among which the level of Mg is the highest, which illustrates that the formation of dimple relates to the second phase particle.

Summary

Formation mechanism of 6009 aluminum alloy joint by laser-MIG arc hybrid welding was investigated by the joint analysis of formability, microscopic structure, precipitated phase, microhardness, tensile property and tensile fracture morphology. The main conclusion are summarized as follow:

1. As a result of stronger laser-arc coupling with laser at the front, the welding formability of joint with laser at the front is better than that of arc at the front. The weld depth and width of joint with laser at the front are larger than that of arc at the front.
2. In trailing MIG torch arrangement, the refine and uniform grains locates on upper weld seam center, while the coarse grains locates on lower weld seam center, due to mechanical rabbling of arc.
3. The hybrid welding joint exists the soften region. The second phase at HAZ coarsens and grows has great influence on the mechanical property of the hybrid weld joint. Owing to the secondary remelting of solidified metal by laser, the microhardness of upper weld is greater than that of lower weld in leading MIG torch arrangement, while the joint with laser at the front is reverse for tempering of arc.

4. Grooving before welding benefits enhancing the joint mechanical property, when 6009 aluminum alloy plates with thicknesses of 6 mm are welded.
5. The tensile fracture of hybrid welding joint has typical dimples feature. The formation of dimples relates to second phase particles.

Acknowledgements This work was supported by of National Natural Science Foundation Project (Grant No. 51774249), The Foundation Sichuan Provincial Department of Education (Grant No. 15ZA0048) and Open Experimental Project In Southwest Petroleum University (Grant No. KSZ14113).

References

1. K.J. Kim, R.H. Rhee, B.I. Choi, C.W. Sung, C.P. Han, K.W. Kang, S.T. Won, Development of application technique of aluminum sandwich sheets for automotive hood. Int. J. Precision Eng. Manuf. **10**, 71–75 (2009)
2. J.C. Benedyk, 3–Aluminum alloys for lightweight automotive structures. Mater. Des. Manuf. Lightweight Veh. 79–113 (2010)
3. M. Raugei, D. Morrey, A. Hutchinson, P. Winfield, A coherent life cycle assessment of a range of lightweighting strategies for compact vehicles. J. Cleaner Prod. **108**, 1168–1176 (2015)
4. C.P. Kohar, A. Zhumagulov, A. Brahme, M.J. Worswick, R.K. Mishra, K. Inal, Development of high crush efficient, extrudable aluminium front rails for vehicle lightweighting. Int. J. Impact Eng. **95**, 17–34 (2016)
5. Y. Muraoka, H. Miyaoka, Development of an all-aluminum automotive body. J. Mater. Process. Technol. **38**, 655–674 (1993)
6. W.S. Miller, L. Zhuang, J. Bottema, A.J. Wittebrood, P.D. Smet, A. Haszler, A. Vieregge, Recent development in aluminium alloys for the automotive industry. Mater. Sci. Eng A. **280**, 37–49 (2000)
7. H.K. Lee, K.S. Chun, S.H. Park, C.Y. Kang, Control of surface defects on plasma-MIG hybrid welds in cryogenic aluminum alloys. Int. J. Naval Architect. Ocean Eng. **7**, 770–783 (2015)
8. M. Ono, Y. Shinbo, A. Yoshitake, M. Ohmura, Development of laser-arc hybrid welding. Nkk Tech. Rev. **86** (2002)
9. J. Yang, X.Y. Li, S.L. Gong, L. Chen, F. Xu, Typical joint defects in laser welded aluminium-lithium alloy. Lasers Eng. **2**, 337–350 (2011)
10. S. Katayama, 12–Defect formation mechanisms and preventive procedures in laser welding. Handb. Laser Weld. Technol. 332–373 (2013)
11. D. Petring, 18–Developments in hybridisation and combined laser beam welding technologies. Handb. of Laser Weld. Technol. 478–504 (2013)
12. E.L. Guen, R. Fabbro, M. Carin, F. Coste, P.L. Masson, Analysis of hybrid Nd: Yag laser-MAG arc welding processes. Opt. Laser Technol. **47**, 1155–1166 (2011)
13. C. Cai, J. Feng, L. Li, Y. Chen, Influence of laser on the droplet behavior in short-circuiting, globular, and spray modes of hybrid fiber laser-MIG welding. Opt. Laser Technol. **83**, 108–118 (2016)
14. C. Thomy, 10–Hybrid laser–arc welding of aluminium. Hybrid Laser-Arc Weld. 216–269 (2009)
15. Z. Gao, J. Huang, L.I. Yaling, W.U. Yixiong, Effect of relative position of laser beam and arc on formation of weld in laser-MIG hybrid welding. Trans. China Weld. Inst. (2008)

16. S. Liu, Y. Li, F. Liu, H. Zhang, H. Ding, Effects of relative positioning of energy sources on weld integrity for hybrid laser arc welding. Opt. Lasers Eng. **81**, 87–96 (2016)
17. S. Liu, J. Li, G. Mi, C. Wang, X. Hu, Study on laser-MIG hybrid welding characteristics of A7N01-T6 aluminum alloy. Int. J. Adv. Manuf. Technol. **87**, 1–10 (2016)
18. X. Li, X. Wang, Z. Lei, H. Yang, Investigation on softening of welded joint of side walls of high speed train of 6N01 aluminum alloy. Hanjie Xuebao/Trans. China Weld. Inst. **36**, 95–98 (2015)

Effect of Nb on Microstructure and Mechanical Properties of High-Strength Low-Alloy Welding Layer

Tengyang Xiong, Bin Wang, Yiwen Hu, Jing Hu and Senfeng Zhang

Abstract Using Q345 steel as a substrate, six kinds of high-strength low-alloy welding layers with different Nb contents were obtained by manual arc welding and chemical composition transition of electrode coating, and the effect of Nb on microstructure and properties of welding layers were investigated. The results showed that with the increase of Nb content, the microstructure was gradually uniform and the grains were obviously refined. The lath bainite in the welding layers gradually changed into granular bainite and when Nb content is 0.11%, the microstructure showed a whole granular bainite with no lath bainite. Furthermore, with Nb content increasing, NbC precipitates appeared on grain boundaries and decreased the grain size of M/A structure when the NbC precipitates increased. As Nb content varied from 0.0041 to 0.26 wt%, the yield strength increased from 560 to 751 MPa, and tensile strength increases from 630 to 815 MPa. The yield ratios are similar for both cases, while the elongation decrease slightly. At the temperature of −20 and −40 °C, the impact energy significantly increases from 30.2 and 13.0 J to 166.7 and 138.1 J, respectively. The hardness increases first, then decreases, and increases slowly again.

Keywords Nb · High-strength low-alloy welding layer · NbC
Microstructure · Mechanical properties

T. Xiong · B. Wang (✉) · Y. Hu · J. Hu · S. Zhang
School of Materials Science and Engineering, Southwest Petroleum University, Chengdu 610500, China
e-mail: 1013271031@qq.com

B. Wang
Welding Engineering Technology Research Center, Chengdu 610500, Sichuan, China

Y. Han (ed.), *Advances in Energy and Environmental Materials*,
Springer Proceedings in Energy, https://doi.org/10.1007/978-981-13-0158-2_37

Introduction

Metallurgical technology is developing rapidly. However, the performance of the available steels couldn't meet the requirements in various environments and at the same time, the cost is relatively high. In recent years, with the deep understanding of the mechanism of micro-alloying in steel and the rise of surfacing welding technology, the steel added alloying elements and surface surfacing with the required properties of the deposited metal have become the most direct and effective cost-saving way.

Microalloying elements mainly include Nb, V, Ti and so on. A large number of experiments have shown that the interaction between microalloying elements and iron, carbon or other microalloying elements can change the internal structure of the alloy [1–3], while Nb has the most optimum fine-grained strengthening effect of all the microalloying elements [4]. In the late 1950s and early 1960s, the microalloying technology of niobium develops rapidly and is gradually applied in microalloyed steels. In order to reduce the carbon content in ordinary carbon steel and improve toughness, the niobium element is added into steels [5, 6]. Niobium in the steel generally has the following effects. Firstly, it can inhibit the recrystallization of deformed austenite. Secondly, it can prevent grain growth. Thirdly, it can produce precipitates to achieve the effect of precipitation strengthening [7–9]. Niobium is a very important microalloying element, which has been used in various steels [10]. In most niobium-containing steels, niobium mainly exists as carbonitrides. Y. F. Bao et al. have shown that the addition of niobium in welding state can result in different size and quantities of niobium carbonitrides on the substrate and grain boundaries [11].

At present, there are many scholars starting the studies of Nb in welding layer, but there are limited researches using low-alloy steel manual arc electrode coating method to prepare the surfacing welding layer. In the existing studies, the analysis are mainly focused on pure mechanical properties or microstructure of welding layer, however, the effect of Nb on mechanical properties of high-strength low-alloy welding layer has not been studied comprehensively. Therefore, this experiment are mainly preparing the high-strength low-alloy welding layer on substrates with different niobium content, researching the microstructure observation, meanwhile conducting the tensile, impact and microhardness tests, in order to investigate the effect of Nb on microstructure and mechanical properties of high-strength low-alloy welding layer.

Materials and Methods

Materials. Q345 steel plate is used as the test substrate with size of 280 mm 160 mm × 18 mm, its chemical compositions are shown in Table 1. The type of low-alloy electrode is CHE607GX. By adding six different contents of ferroniobium

Table 1 Chemical compositions of Q345 steel

Element	C	Si	Mn	P	S	Al	V
Content (%)	<0.02	<0.55	1.0–1.6	0.030	0.030	>0.015	0.02–0.15

Table 2 Content of ferroniobium in the electrode CHE607GX (wt%)

Number	Addition of ferroniobium (g)	Content of ferroniobium in coating (%)
1#	0	0
2#	0.5	0.48
3#	1.0	0.92
4#	1.5	1.43
5#	2.0	1.91
6#	2.5	2.38

Table 3 Chemical compositions of welding layer (wt%)

Number	C	Mn	Si	P	S	Cr	Ni	Mo	Nb
1#	0.085	1.33	0.27	0.010	0.0042	0.042	1.50	0.0063	0.0041
2#	0.082	1.24	0.26	0.010	0.0039	0.039	1.44	0.0058	0.046
3#	0.082	1.34	0.32	0.010	0.0044	0.044	1.45	0.0060	0.11
4#	0.082	1.28	0.33	0.010	0.0040	0.040	1.44	0.0065	0.17
5#	0.085	1.27	0.28	0.010	0.0041	0.041	1.40	0.0065	0.19
6#	0.091	1.30	0.35	0.011	0.0040	0.041	1.33	0.0061	0.26

in the coating and using the same process to prepare the electrode used in this experiment, the addition amount of ferroniobium during preparation and the content of ferroniobium in covered electrode are shown in Table 2. The welding workpieces with size of 200 mm × 25 mm × 20 mm are prepared on the substrate by manual arc welding, and the welding process is completed by the same welder. DCEP operation is used in this experiment, where the current I is 170 A, welding speed v is 18–20 cm/min, and heat input is about 12.75–14.17 kJ/cm. The chemical compositions of different welding layers after welding are shown in Table 3. The welding layers are numbered as 1#, 2#, 3#, 4#, 5# and 6# respectively according to the Nb content.

Methods. The metallographic sample with size of 20 mm × 10 mm × 10 mm is cut from a welding workpiece using wire cutting machine, then mechanical grinding, polishing, eroding with 3% nitric acid alcohol solution, rinsing and drying are carried out. Microstructure observation is implemented with XJG-05 metallographic microscope and EVO MA15 scanning electron microscope. Further analysis of the location and size of precipitates in the welding layer is implemented by JEOL 2010 transmission electron microscopy. The welding sheet with thickness of 0.5 mm is cut by the wire cutting machine and then thinned to 50 μm by sandpaper.

The welding disc with diameter of 3 mm is prepared using a punching machine, and the TEM sample is prepared by twin-jet electropolishing. The electrolyte is 7% perchloric acid anhydrous glacial acetic acid solution, the twin-jet voltage is 28–30 V, and the current is 72–80 mA. The standard rod-shaped tensile test specimen with the diameter of 10 mm and the gauge length of 50 mm is prepared according to the standard ISO 5178 "Destructive tests on welds in metallic materials—Longitudinal tensile test on weld metal in fusion welded joints", and the CMT 6104 tensile test machine is used for tensile performance test, wherein the tensile speed is 2 mm/min. The standard V-notch impact specimen of 55 mm × 10 mm × 10 mm is prepared according to the standard ISO 9016 "Destructive test on welds in metallic materials—Impact tests". The bottom of the specimen is required to be smooth and have no obvious scratches lying in the same direction as the sample. The sample is cooled to the temperature of −20 and −40 °C respectively in a CDW-60 impact test cryostat, and then subjected to the impact test on a JB-300B impact tester. The observation of impact fracture is carried out by an EVO MA15 scanning electron microscope. The microhardness of each welding layer is measured by an HV-1000 microhardness tester, wherein the loading weight is 1000 kgf and the loading time is 10 s with 1 mm intervals on each sample. Six sample points are taken and averaged as the microhardness test result.

Microstructure Analysis of Different Nb Content in Welding Layer

The metallographic and SEM microstructure of six different Nb content in welding layer are shown in Fig. 1. It can be known that microstructure of different Nb content in welding layer is mainly bainite, ferrite and M/A components. With the increase of Nb content, quasi-polygonal ferrite (QPF) gradually increases, the lath bainite (LB) gradually reduces and transforms to granular bainite (GB) until the LB disappearing; the microstructure gradually becomes uniform and refined, the grain size reduces significantly. When Nb content is 0.0041 and 0.046%, the microstructure of welding layer is mainly bainite, ferrite and M/A components. According to the observation under metallographic microscope, the LB is black and gray lath-shaped, while the white part is QPF, the grain is relatively large, the microstructure distribution is uneven and the size is significantly different, as shown in Fig. 1a–d. When Nb content is 0.11%, the microstructure of welding layer is composed of LB and a small amount of GB, QPF and M/A components. Compared to the content of 0.0041 and 0.046%, the number of LB significantly reduces, while the distribution of QPF is more uniform and the grain size significantly reduces, shown in Fig. 1e–f. When Nb content is 0.17–0.26%, the welding layer mainly contains a small amount of GB, QPF and M/A components. The LB disappears, the distribution of microstructure present a relatively uniform state, and the size of grains is decreasing, as illustrated in Fig. 1g–l.

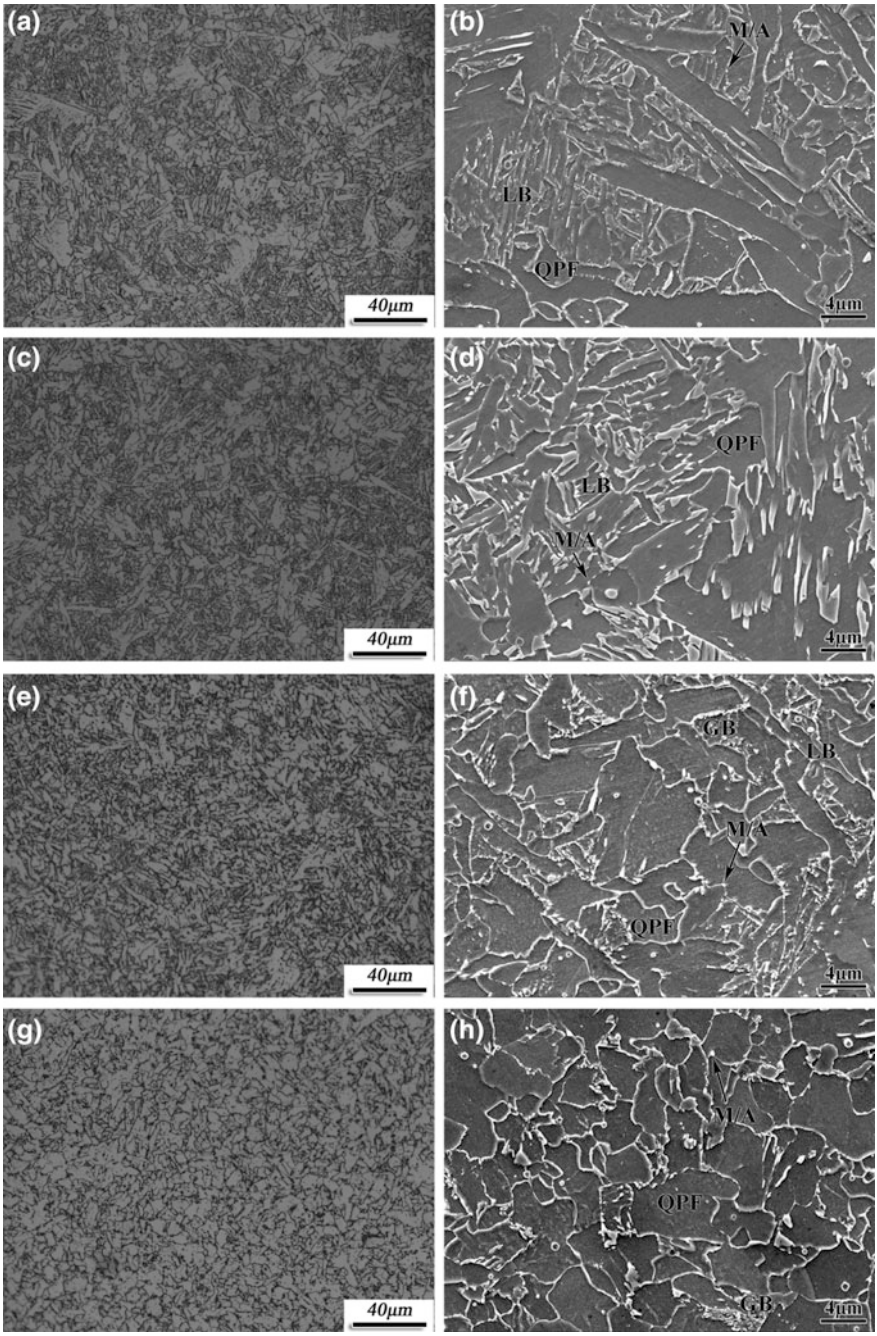

Fig. 1 Metallographic and SEM microstructure of welding layer with different Nb content. **a–b** ω(Nb) = 0.0041%; **c–d** ω(Nb) = 0.046%; **e–f** ω(Nb) = 0.11% **g–h** ω(Nb) = 0.17%; **i–j** ω(Nb) = 0.19%; **k–l** ω(Nb) = 0.26%

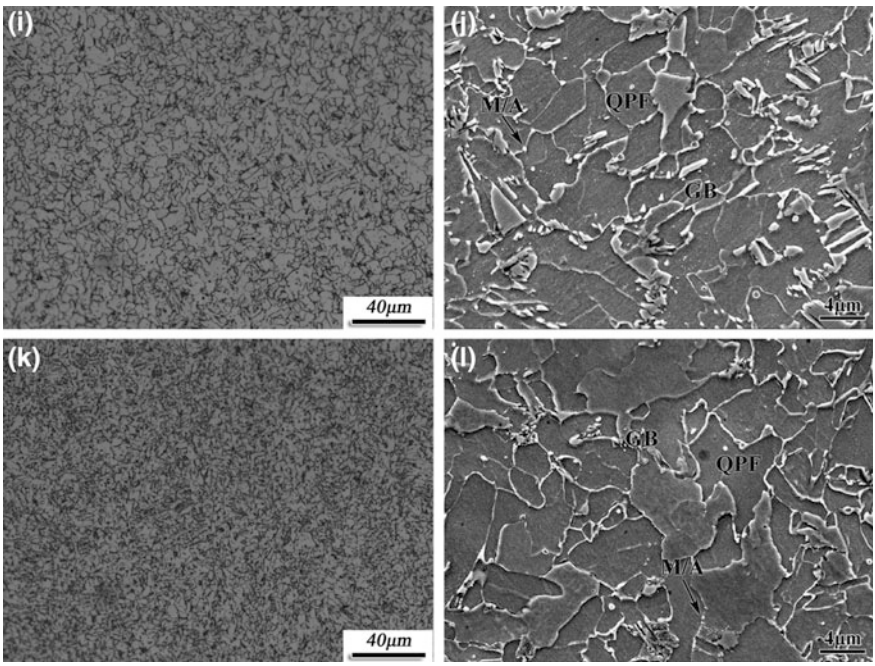

Fig. 1 (continued)

To further analyze the morphology and size of precipitates in welding layer, TEM observation in welding layer is carried out, the results are shown in Fig. 2. When the content of Nb is 0.0041%, the width of LB in welding layer is about 100–250 nm; The dislocations mainly distribute in the interior of LB and at the grain boundaries; The hard phase M/A mainly distribute in the interior and boundaries of grain, the size at grain boundaries is about 100 nm, while the size of grain interior is relatively large, about 300 nm. NbC is not observed in the sample of the welding layer because of the comparatively low Nb content, as shown in Fig. 2a–c. When Nb content is 0.11%, the welding layer mainly contains LB, ferrite, M/A components and NbC precipitates. M/A components with size of 100 nm are distributed at the interface between ferrite and LB, while granular NbC precipitated within grain interior and on the grain boundaries of ferrite is about 10 nm. There are plenty of dislocations intertwined on the grain boundaries, presuming the pinning effect of NbC on dislocations, shown in Fig. 2d–f. When Nb content is 0.19%, no LB is found in the welding layer, the size of M/A component obviously reduces and the dislocation density is higher than 0.0041 and 0.11%, because there are more precipitation of NbC in the welding layer which pinning lots of dislocations; at the same time, the NbC about 25 nm is comparatively large to 0.0041 and 0.11%, as shown in Fig. 2g–h. Therefore, with the increase of Nb content, the dislocation density in the welding layer gradually increases, the number of precipitates NbC gradually increases and the size of NbC becomes larger, while the hard phase M/A components gradually decrease.

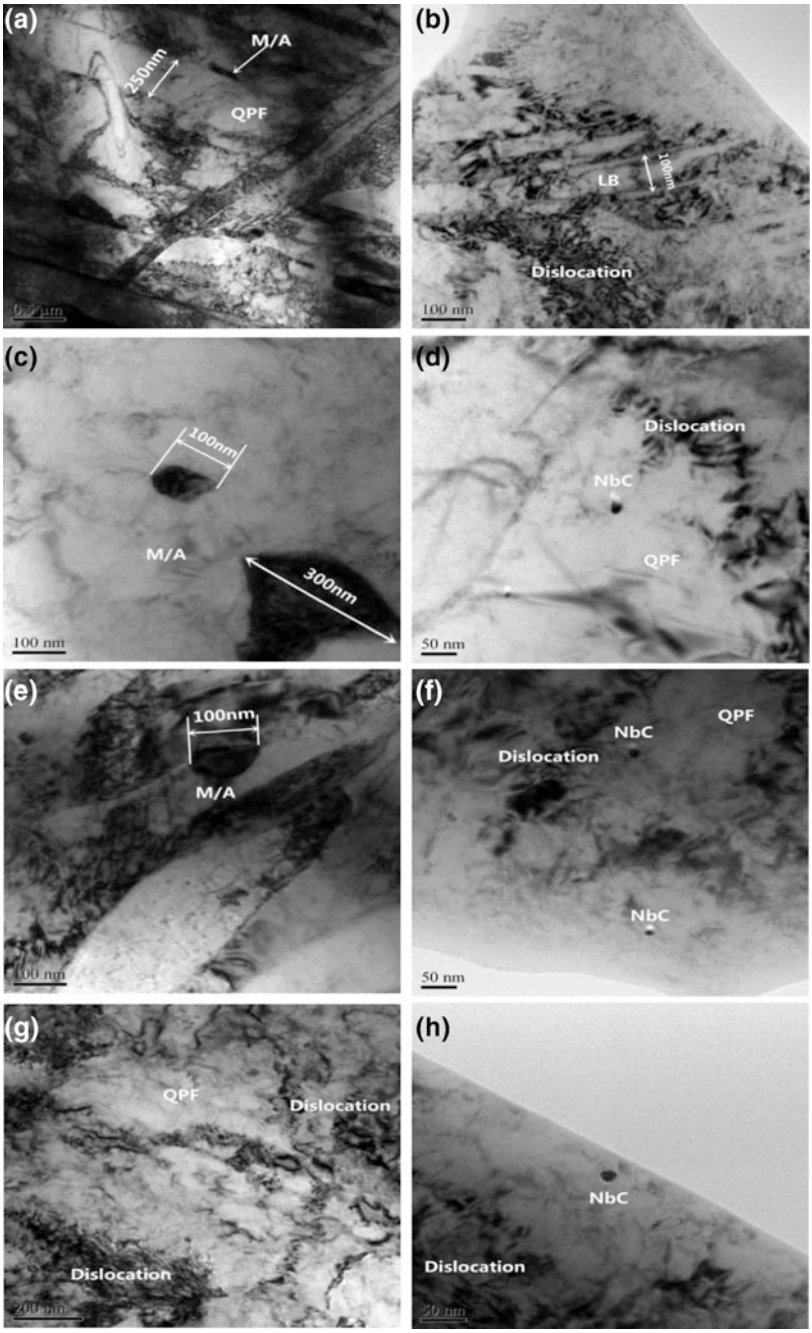

Fig. 2 TEM morphology of welding layer with different Nb content. **a–c** ω(Nb) = 0.0041%; **d–f** ω(Nb) = 0.11%; **g–h** ω(Nb) = 0.19%

Mechanical Properties Analysis of Welding Layer with Different Nb Content

Tensile Test Results. The tensile tests of six different Nb content in welding layers are carried out on a universal stretching machine. The test results are shown in Table 4. With the increase of Nb content, the yield strength and tensile strength of the welding layer gradually increase. As Nb content is 0.26%, the yield strength of the welding layer increases by 34% and the tensile strength increases by 29% compared with 0.0041%. Although the yield strength and the tensile strength increase greatly, the yield ratios remain the same which are around 0.9, indicating that the sharp increase of intensity has a small influence on the plasticity reserve of welding layer. However, the elongation shows a tendency of decreasing slowly, demonstrating that the plastic deformation ability of welding layer decreases slowly with the increase of Nb content. From the above analysis, the strength of the welding layer can be improved greatly, meanwhile ensure good plastic deformation ability with the increasing of Nb content.

As the Nb content increasing, it can be found that the volume fraction of LB gradually decreases, and a small amount of GB appears in the microstructure. Although the content of LB decreases, the increase of Nb content could promote the precipitation of carbonitride, mainly the carbide precipitation. Not only can enhance the effect of precipitation strengthening, pinning effect can also inhibit the dislocation sliding and form high-density dislocations at the grain boundaries, thereby significantly improving the strength of the welding layer. The higher the Nb content, the higher the content of precipitates, the greater the contribution to the strength of the welding layer. At the same time, the higher the Nb content, the more homogeneous the layer microstructure, the smaller the grain size, making the welding layer strength is further improved.

Impact Test Results and Impact Fracture Observation. The impact absorbing energy of each welding layer at the temperature of −20 and −40 °C is shown in Fig. 3. It is found that with the increase of Nb content, the low temperature impact toughness of the welding layer has been improved remarkably, and the impact energy at −20 °C has increased from 30.2 to 166.7 J, meanwhile the impact energy with content of 0.26% is 5 times of that with 0.0041%. However, the impact energy

Table 4 Tensile test data of different Nb content welding layers

Number	Yield strength $R_{t0.5}$ (MPa)	Tensile strength R_m (MPa)	Yield ratio ($R_{t0.5}/R_m$)	Elongation (%)
1#	560	630	0.889	28.0
2#	642	720	0.892	23.8
3#	682	758	0.900	23.3
4#	698	778	0.897	21.8
5#	709	792	0.895	21.8
6#	751	815	0.921	19.5

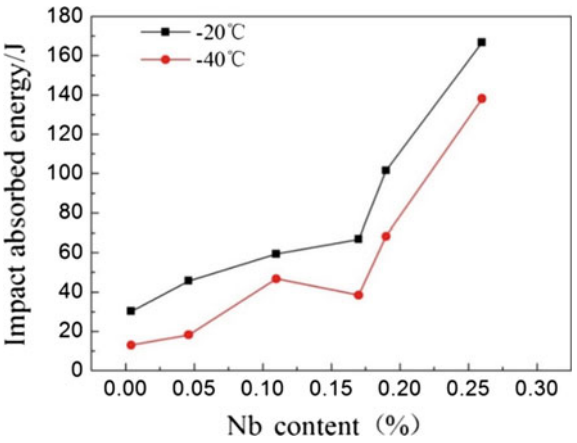

Fig. 3 Low-temperature impact absorbing energy of welding layers with different Nb content

at −40 °C has increased from 13.0 to 138.1 J, increasing nearly 10 times. Fine-grain strengthening is the only strengthening method that can improve the material strength and toughness at the same time. The Nb element can be dissolved in the ferrite matrix, thus segregation on the dislocation line and inhibit the nucleation process of recrystallization, which makes high-temperature recrystallization process delayed so that to obtain fine austenite grains. Meanwhile, Nb can precipitate second-phase particles such as niobium carbon and niobium nitride in the welding layer, and these fine carbonitride precipitates can play the role of pinning dislocations to prevent the grain growth and achieve the effect of grain refinement. Therefore, under the combined effect of the above two conditions, with the increase of Nb content, the grain size of microstructure gradually decreases, and the precipitates can be observed at the grain boundaries. When the Nb content increases from 0.0041 to 0.11%, the grain size decreases slightly, while the size of the hard phase M/A components is larger and the number is more, resulting in a slower growth of impact toughness. When the Nb content reaches 0.17%, the LB in the welding layer almost disappears, the microstructure is obviously homogenized, and the grain is obviously refined. Although the size of NbC precipitates increases with maximum size of about 25 nm, its damage to impact toughness is small, so the impact absorbing energy shows a significantly increasing trend (Figs. 4 and 5).

Hardness Test Results. The Micro Vickers Hardness of the welding layers with different Nb content is shown in Fig. 6. When the content of Nb is 0.0041–0.11%, the hardness value of the welding layer increases as Nb content increases. Although the LB in the welding layer reduces, a large amount of Nb-containing carbonitrides form in the welding layer, which is hard phase and dispersed in the matrix. And the higher Nb content, the greater the number of hard phases, thereby significantly increasing the hardness of the welding layer. When the Nb content reaches 0.17%, the hardness of the welding layer no longer increases, but declines instead. When the Nb content is too large, quantities of carbides form in the welding layer, causing the carbon in the matrix taken away. It is generally believed that the higher the

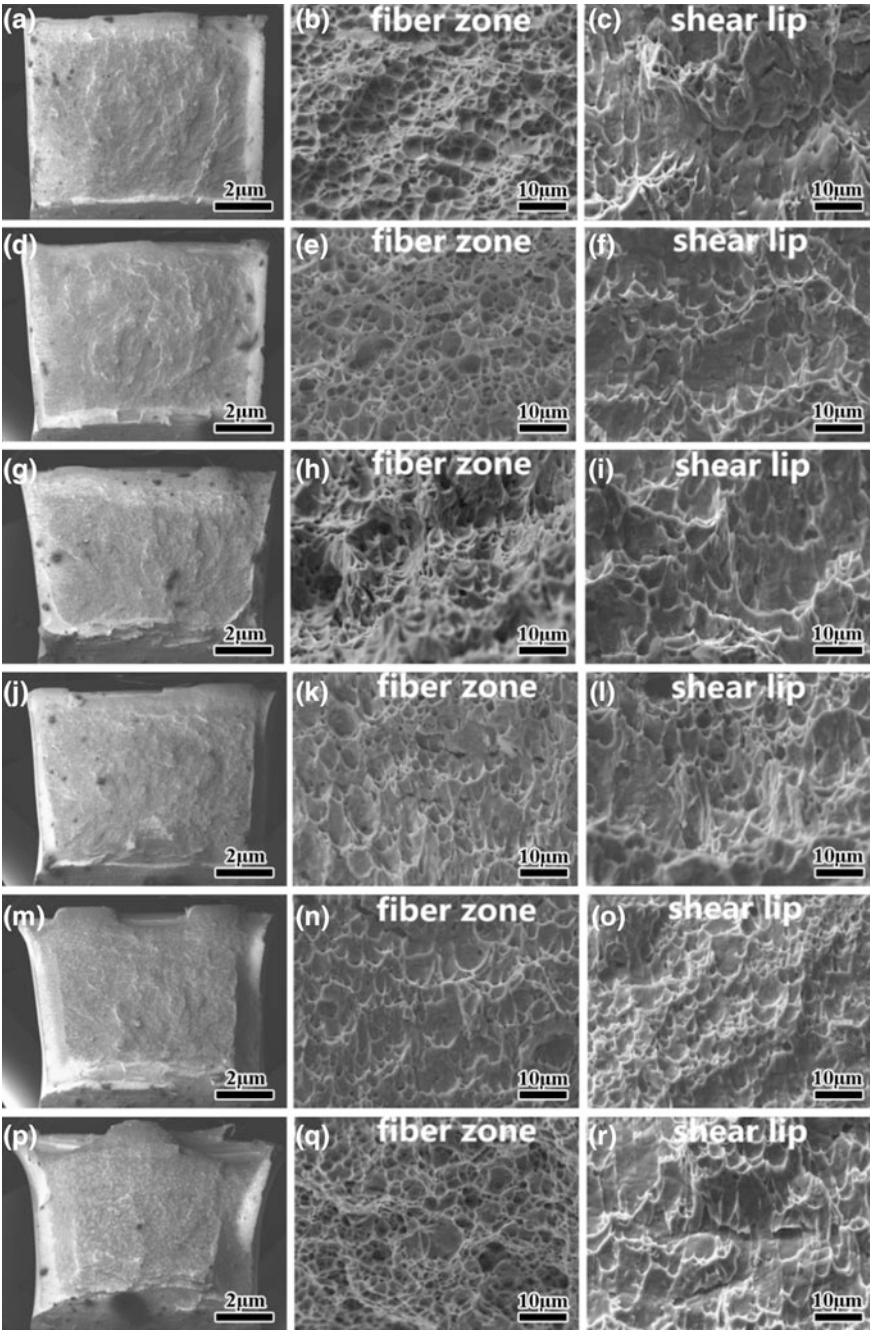

Fig. 4 Macro- and micro-structure of impact fracture in welding layers with different Nb content at −20 °C. **a–c** ω(Nb) = 0.0041%; **d–f** ω(Nb) = 0.046%; **g–i** ω(Nb) = 0.11%; **j–l** ω(Nb) = 0.17%; **m–o** ω(Nb) = 0.19%; **p–r** ω(Nb) = 0.26%

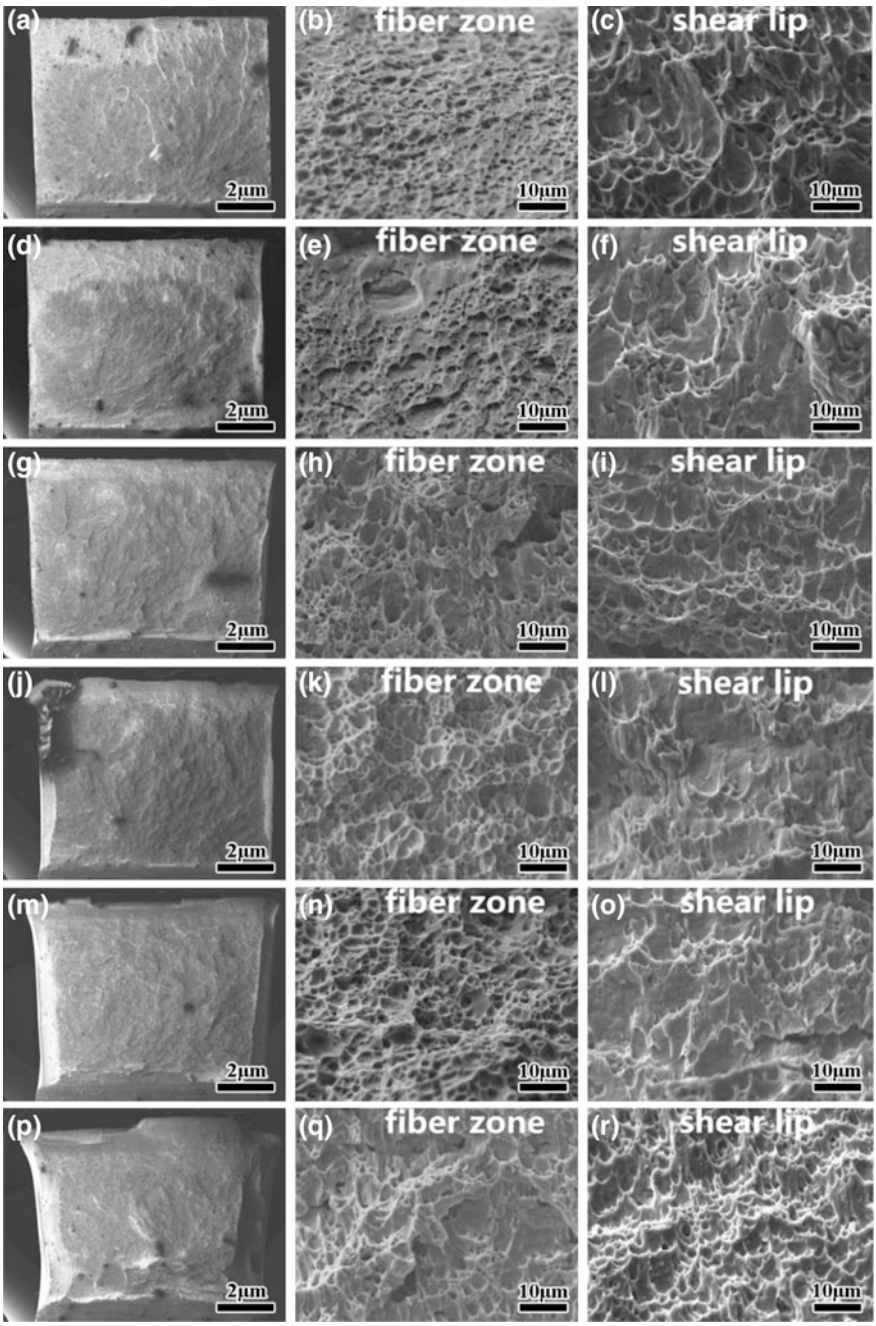

Fig. 5 Macro- and micro-structure of impact fracture in welding layers with different Nb content at −40 °C. **a–c** ω(Nb) = 0.0041%; **d–f** ω(Nb) = 0.046%; **g–i** ω(Nb) = 0.11%; **j–l** ω(Nb) = 0.17%; **m–o** ω(Nb) = 0.19%; **p–r** ω(Nb) = 0.26%

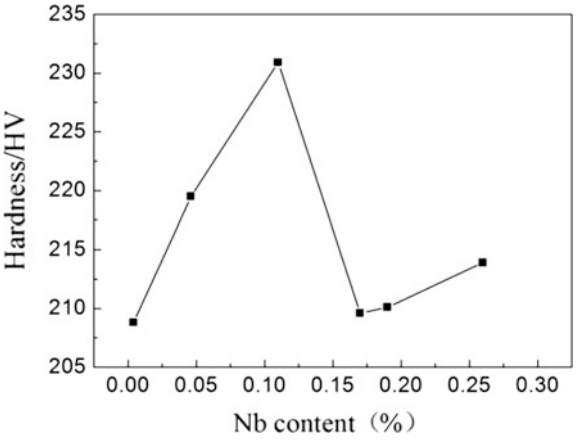

Fig. 6 Microhardness of welding layers with different Nb contents

carbon content, the higher the hardness. The reduction of carbon content in the matrix results in the formation of much ferrite matrix, which makes welding layer soft. Therefore, although lots of hard phases are formed, the hardness of welding layer decreases sharply with the content of 0.11–0.17%. Continue to increase the Nb content to 0.26%, the hardness value increases slowly from 209.6 HV to 213.9 HV, the analysis may be due to the following two reasons. First, with the increase of Nb content, the number of NbC in the welding layer is increasing, so that the hardness value increases slowly. Second, since the hardness test value usually fluctuates within a certain range, the difference between the tested data is small, and normal experimental error can also cause a slow increasing trend.

Conclusions

(1) With the increase of Nb content, the LB in the welding layer decreases, the ferrite increases, and the size of M/A components decreases. The microstructure gradually becomes uniform, and the grains are obviously refined. When the content of Nb is very low, no precipitate is observed in the welding layer, then by continuing to increase the Nb content, NbC appeared as a precipitation phase in the deposition layer. The number and size of precipitates are increase over time.

(2) With the increase of Nb content, the yield strength and tensile strength increases from 560 and 630 MPa to 751 and 815 MPa respectively. Although the yield ratio is about 0.9 for all cases, the elongation decreases from 28.0 to 19.5%, indicating that the plasticity decreases slowly. The impact energy increases from 30.2 and 13.0 J to 166.7 and 138.1 J respectively. The micro-hardness value increases rapidly when Nb content fall at the range of 0.0041 to 0.11 wt%, then drop sharply, and increases slowly at 0.17–0.26 wt%.

(3) The refined grain of Nb and the strengthening effect of NbC precipitates have significant influence on the microstructure and properties of high-strength low-alloy welding layers.

References

1. Y.Y. Ren, G.S. Zhang, S.Z. Wei et al., The development and prospect of China's surfacing technology. J. Weld. Technol. **41**, 1–4 (2012)
2. X.Y. Han, Functions of Nb, V and Ti in micro-alloyed steel. J. Wide Heavy Plate. **12**, 39–41 (2006)
3. Z.Y. Dong, Q.Y. Huang, in *Proceedings of the Eighth National Conference on welding*. Development status of surfacing welding in China and abroad (Machinery Industry Press, Beijing, 1997)
4. T.F. Wei, L.J. Gan, Q.D. Wang, Effect of Nb on microstructure and properties of low carbon microalloyed steel. J. Therm. Process. Technol. **14**, 126–128 (2015)
5. J.Y. Fu, Nb microalloying and niobium-containing steel development and technological progress. J. Iron Steel. **40**, 1–6 (2005)
6. J.J. Qi et al., *Micro-Alloyed Steels* (Metallurgy Industry Press, Beijing, 2006)
7. Q.L. Yong, H.Z. Pei, J.G. Tian et al., Physical data of niobium in steel. J. Iron Steel Res. **10**, 66–69 (1998)
8. S. Traint, A. Pichler, R. Sierlinger et al., Low-alloyed TRIP-steels with optimized strength, forming and welding properties. J. Steel Res. Int. **77**, 641–649 (2006)
9. H. Hu, G. Xu, L. Wang et al., The effects of Nb and Mo addition on transformation and properties in low carbon bainitic steels. J. Mater. Design. **84**, 95–99 (2015)
10. J.Y. Fu, F.M. Meng, Technology and development of Nb-containing steel for automobile industry. J. Automot. Process Mater. **6**, 26–31 (2004)
11. K. Yang, Q. Yang, Y.F. Bao, Formation of carbonitride precipitates in hardfacing alloy with niobium addition. J. Rare Metals. **32**, 52–56 (2013)

Preparation of Diatomite-Based Porous Ceramics

Li Zhang, Kaige Ma, Huan Luo, Xue Jin, Junfeng Li and Longshan Li

Abstract Porous ceramics have been attracted attention extensively because of their excellent chemical and thermal stability, excellent permeability, high specific surface area, extremely low electrical and thermal conductivity, energy saving, heat resistance and corrosion resistance. In this paper, diatomite-based porous ceramics were prepared using diatomite as main raw material and calcite as pore-forming agent. The effect of calcite were studied by thermal analysis, XRD, SEM, and porosity. The calcite decomposed at 600–800 °C and $CaSiO_3$ was synthesized in situ though the reaction of CaO from the calcite and SiO_2 from the diatomite. At sintering temperature of 1050 °C, the porous ceramic with 20% calcite addition reserved sub-micrometer pore structure of raw material diatomite as well as a relative high porosity (about 60%), which showed potential application in filtration.

Keywords Pore-forming agent · Diatomite · Porous ceramic · Calcite

L. Zhang (✉) · K. Ma · H. Luo · X. Jin
College of Materials and Chemistry and Chemical Engineering,
Chengdu University of Technology, Chengdu 610059, China
e-mail: zhanglixmu@163.com

K. Ma
e-mail: 1715578827@qq.com

H. Luo
e-mail: 804493630@qq.com

X. Jin
e-mail: 1196421368@qq.com

J. Li
Institute of Materials Science and Technology,
Chengdu University of Technology, Chengdu 610059, China
e-mail: ljfcdut@163.com

L. Li
Sichuan Konkasnow New Materials Co., Ltd., Post-Doctor Innovative
Practice Base, Yaan 625400, China
e-mail: konkasnow@vip.163.com

Y. Han (ed.), *Advances in Energy and Environmental Materials*,
Springer Proceedings in Energy, https://doi.org/10.1007/978-981-13-0158-2_38

Introduction

Porous ceramic materials present great interest due to its unique properties in a wide temperature range, such as high thermal shock resistance, high permeability, high surface area, chemical stability, low thermal conductivity, etc. [1]. These properties make the porous ceramic susceptible to a variety of applications, such as catalyst supports, filters, membranes, gas sensors, low weight structural materials, thermal insulators, biomaterials and other related applications [2]. For such applications, porous ceramics are designed to have different size distributions and porosity.

Several methods have been proposed to prepare porous ceramics, trying to obtain materials with complex geometry and projected microstructure for specific applications [3]. Regarding to the preparation of porous ceramics, the incorporation of organic materials into the composition of ceramic materials has been one of the most widely used methods [4]. Those organic materials are removed during the sintering process, leaving pores of different sizes depending on the particle size of the organic material. However, the mechanical properties of porous ceramics always deteriorate with the removal of organic materials, particularly when the pore size and porosity is large enough. The inorganic materials such as carbonate, sulfate, nitrate are also applied to the production of porous ceramics, which decompose at high temperature and leave pores in the partial densification porous ceramics. Therefore, it is possible to obtain a microstructure with different pore sizes, which can vary over a wide range of size from nanometers to millimeters.

Usually, the widely used porous ceramics are made of titania [5], zirconia [6], alumina and silica [7], alumina [8], etc. As the synthesized raw materials and high sintering temperature (usually as high as above 1300 °C), these porous ceramic products are expensive. The diatomaceous earth, also known as diatomite, is a naturally occurring, soft, siliceous sedimentary rock, with silica composition as high as 80–90%. Moreover, the specific surface area and porosity in the natural diatomite is large, which is beneficial to porous ceramics [9, 10]. In this study, experimental results regarding to the use of calcium carbonate as pore generating agent in diatomite-based porous ceramics is reported.

Experimental Procedure

The commercial natural powder of Diatomite (Jilin Changbai Diatomite Co., Ltd, China), Kaolinite (Zhangzhou Shengdi Kaolinite Co., Ltd, China) and Calcite (Sichuan Konkasnow New Materials Co., Ltd, China) were used as raw materials. Four formulations were used in this study, as shown in Table 1. Each formulation was mixed in a cylindrical wet ball mill for 60 min, then the slurry obtained was filtered and dried in an oven at 100 °C for 6 h. Further, each dried formulation was humidified with 2 wt% polyvinyl alcohol solution and then granulated in a 100 mesh sieve. Finally, the powders were uniaxially pressed in a press machine using a

Table 1 Formulations used in the study (wt%)

Composition	A	B	C	D
Diatomite	85	85	85	85
Kaolinite	15	15	15	15
Calcite	0	20	50	100

steel die with diameter of 35 mm at a pressure of 31 MPa. The green bodies were heat treated at 900, 950, 1000 and 1050 °C for 3 h with the heating rate of 5 °C/min in a muffle furnace.

The chemical composition of the raw material powders were analyzed using X-ray fluorescence spectrometry (XRF, XRF-1800, Shimadzu, Japan). Differential thermal analysis (DTA) and thermogravimetric analysis (TG) of the employed formulations was determined by a thermal gravimetric analyzer (STA-409-PC, Netzsch, Germany). Samples were heated to 1000 °C in flowing air (20 ml/min) at 15 °C/min. The phase analysis of the calcined samples was conducted by X-ray diffraction (XRD) using an X-ray diffractometer (DX-2700, Dangdong fangyuan Instrument Co., Ltd, China) with CuK_{α} radiation (40 kV, 30 mA) in the $2\theta = 10°–80°$ range. The sample was transversely cut and coated with a thin layer of a gold film for the microstructure evaluation in a scanning electron microscope (SEM, TM 3000, Hitachi, Japan), at an accelerating voltage of 10 kV. The specific gravity and apparent porosity of calcined porous ceramics was determined by density determination kit (AE124J, Shanghai Sunny Hengping Scientific Instrument Co., Ltd, China), using Archimedes' Principle at 20 °C with water as medium.

Results and Discussion

The chemical compositions of raw materials analyzed by XRF were shown in Table 2. The main oxides of diatomite is 92.28% silica, with 2.43% alumina and 2.27% alkaline oxides as major impurities, which was attributed mostly to clay minerals. The impurities content in calcite were relative low, indicating the high quality of the raw materials.

The thermal analysis of sample A was shown in Fig. 1. The mass loss was merely 1.5%, which was due to the decomposition of Kaolinite at 400–600 °C. With addition of 50% calcite, the mass loss of sample C reached 22.7% at 650–800 °C (Fig. 2), meanwhile, an endothermic peak at 783 °C was observed at

Table 2 Chemical composition of raw materials by XRF analysis (wt%)

Composition	SiO_2	Al_2O_3	Na_2O	K_2O	Fe_2O_3	CaO	MgO	TiO_2	Others
Diatomite	92.28	2.43	1.63	0.64	1.26	1.01	0.32	0.19	0.24
Kaolinite	58.16	38.73	0.16	0.77	0.70	0.07	–	0.06	1.35
Calcite	0.26	0.13	0.08	0.02	0.04	58.96	–	0.03	40.48

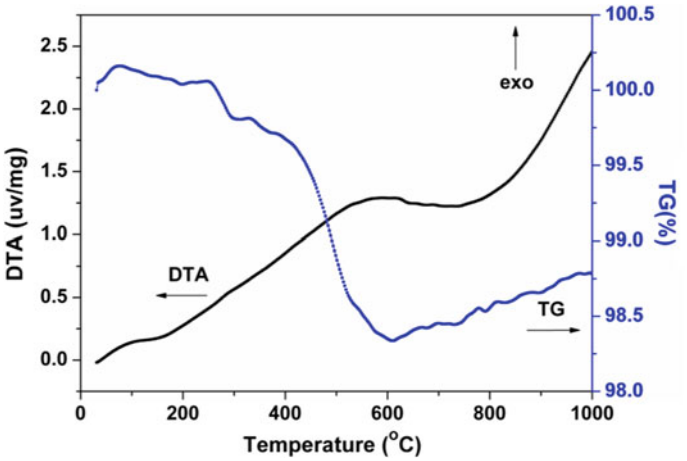

Fig. 1 TG-DTA curve of sample A (without $CaCO_3$)

DTA curve, confirming the decomposition of calcite (reaction 1). Another endothermic peak at 920 °C was ascribed to the solid reaction of CaO from calcite and SiO_2 from the diatomite (reaction 2), because of the negligible mass loss on the TG curve, and further confirmed product of $CaSiO_3$ by the XRD results. The reaction formulas were as follows:

$$CaCO_3 \rightarrow CaO + CO_2. \quad (1)$$

$$CaO + SiO_2 \rightarrow CaSiO_3. \quad (2)$$

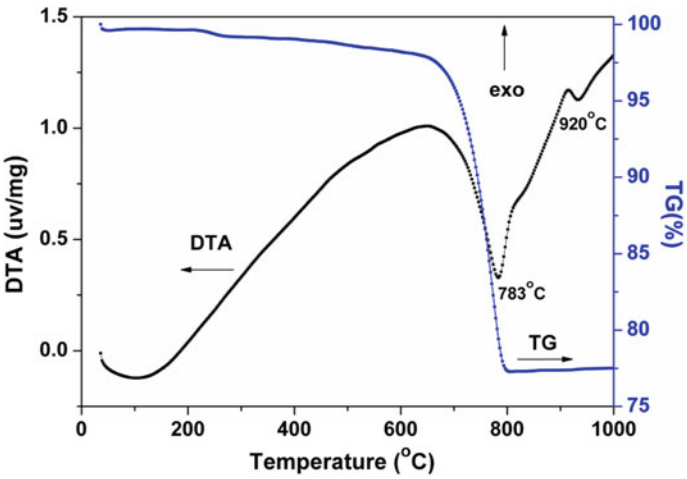

Fig. 2 TG-DTA curve of sample C (with 50% $CaCO_3$)

Table 3 Chemical composition of sample A, B, C and D(wt%)

Sample	Residual SiO_2	Al_2O_3	MgO	Na_2O	K_2O	$CaSiO_3$
A	87.77	8.02	0.28	1.44	0.67	1.83
B	66.87	7.17	0.25	1.30	0.60	23.81
C	42.80	6.21	0.21	1.13	0.52	49.13
D	14.79	5.08	0.17	0.95	0.43	78.58

The effect of the presence of calcium carbonate in the formulations must be considered and, for this, Table 3 showed the main chemical composition of the formulations used in this work calculated based on the raw materials. According to the reaction (2) and the CaO and SiO_2 content in the raw materials, the resultant content of $CaSiO_3$ and residual silica can be decided. Obviously, the amount of product $CaSiO_3$ increased with the calcite content in the green body, and the results were in accordance with the XRD results.

Figure 3 showed the XRD patterns of the samples calcined at 1050 °C. The major phase was cristobalite (PDF No: 39-1425) in formula without calcite, because the silica content was as high as 87.77% in sample A (Table 3). With 20% calcite addition, the wollastonite (PDF No: 42-0550) was detectable in sample B, and the diffraction peak intensities of wollastonite were obviously enhanced with the amount of calcite, at the expense of cristobalite. In the sample C and D, wollastonite was the major phase, indicating that most of SiO_2 reacted with CaO.

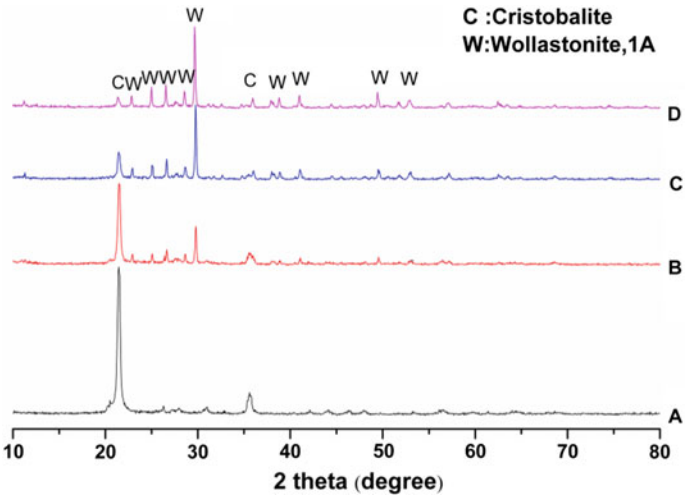

Fig. 3 XRD patterns of sample A, B, C, D calcined at 1050 °C for 3 h

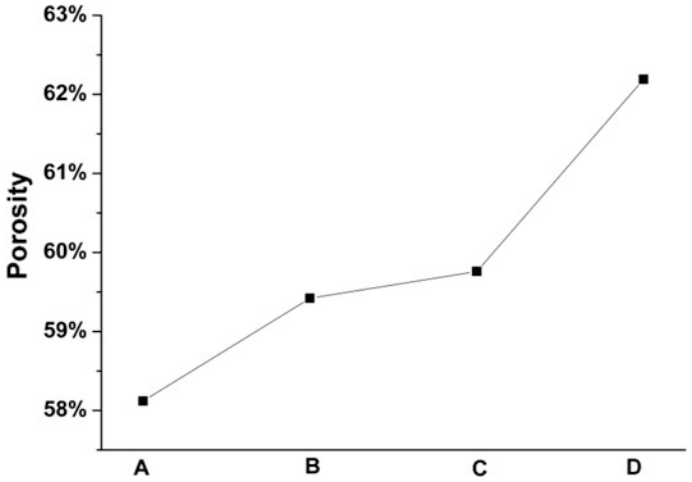

Fig. 4 The porosity of sample A, B, C, D calcined at 1050 °C for 3 h

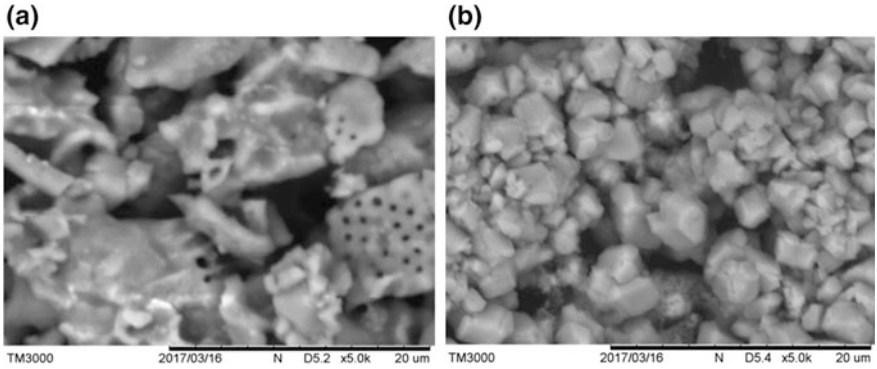

Fig. 5 SEM micrographs of **a** sample B and **b** sample D calcined at 1050 °C for 3 h

Figure 4 showed the porosity of the samples calcined at 1050 °C. The porosity of sample A was 58%, in which the pores of diatomite particles were remained. With the pore generator calcite addition, the porosity of sample calcined was enhanced, due to the CO_2 expansion at high temperature. However, the sub-micrometer pore structure of diatomite disappeared, especially in the sample D, whereas remained in sample B, as shown in Fig. 5a, b, respectively. The micro-structural evolution was coincide with the XRD results, in which silica from diatomite was major phase in sample B, compared with that $CaSiO_3$ in sample D. To obtain the better filtration effect in practical application, such as removal of bacteria, the sub-micrometer pore of original diatomite should be retained, thus the formula B was optimum in this study.

Conclusions

The influence of the calcium carbonate addition to a ceramic composition of diatomite was studied. The results showed that calcite addition causes a porosity increasing in the investigated formulations due to the generation of pores by the process of calcium carbonate degassing between about 650 and 800 °C. With 20% addition of calcite, the sub-micrometer pores of diatomite can be remained in the porous ceramic body and the porosity is as high as about 60%, showing potential application in filtration porosity.

Acknowledgements This work was financially supported by the National Natural Science Foundation of China (No. 51402028), Project of CDUT Innovation Team (Utilization of Rare Earth Resource and New Materials), and Sichuan Panxi Strategic Mineral Resource Innovation and Development Experimental Area 3rd Significant Science and Technology Project (No. CDWA2016ZC3-1).

References

1. E. Litovsky, M. Shapiro, A. Shavit, Gas pressure and temperature dependences of thermal conductivity of porous ceramic materials: part 2, refractories and ceramics with porosity exceeding 30%. J. Am. Ceram. Soc. **79**, 1366–1376 (1996)
2. H. Xinyou, M. Xu, W. Xuan, S. Qi, Current situation of preparation and application of porous ceramic materials. China Ceram. **51**, 5–8 (2015)
3. M. Fukushima, Y. Yoshizawa, P. Colombo, Fabrication of highly porous silica thermal insulators prepared by gelation-freezing route. J. Am. Ceram. Soc. **97**, 713–717 (2014)
4. L. Ya-ru, L. Ru-tie, X. Xiang, Preparation and application of porous ceramics with micron and sub-micron pore size. J. Synth. Cryst. **45**, 2300–2305 (2016)
5. E. Chevereau, N. Zouaoui, L. Limousy, P. Dutournié, S. Déon, P. Bourseau, Surface properties of ceramic ultrafiltration TiO_2 membranes: effects of surface equilibriums on salt retention. Desalination **255**, 1–8 (2010)
6. C.C. Coterillo, T. Yokoo, T. Yoshioka, T. Tsuru, M. Asaeda, Synthesis and characterization of microporous ZrO_2 membranes for gas permeation at 200 °C. Sep. Sci. Technol. **46**, 1224–1230 (2011)
7. A. Cheraitia, A. Ayral, A. Julbe, V. Rouessac, H. Satha, Synthesis and characterization of microporous silica-alumina membranes. J. Porous Mater. **17**, 259–263 (2010)
8. H. Qi, S. Niu, X. Jiang, N. Xu, Enhanced performance of a macroporous ceramic support for nanofiltration by using α-Al_2O_3 with narrow size distribution. Ceram. Int. **39**, 2463–2471 (2013)
9. T. Qian, J. Li, X. Min, Y. Deng, W. Guan, L. Ning, Diatomite: a promising natural candidate as carrier material for low, middle and high temperature phase change material. Energ. Convers. Manage. **98**, 34–45 (2015)
10. H. Liang, S. Zhou, Y. Chen, F. Zhou, C. Yan, Diatomite coated with Fe_2O_3 as an efficient heterogeneous catalyst for degradation of organic pollutant. J. Taiwan Inst. Chem. E. **49**, 105–112 (2015)

High-Strength Titanium Alloy Oil Well Pipe Material with High Hardness and Anti-galling Property

Shuliang Wang, Chaozheng Fu, Jing Chen, Chunyan Fu, Xin Wang and Yixiong Huang

Abstract Titanium alloys are usually used as the material of oil well pipes in the petroleum industry for its high specific strength, excellent corrosion resistance, high and low temperature resistance performance and high fatigue strength. However, due to inadequate strength and hardness, titanium alloy oil well pipes often suffer from thread galling during casing makeup. In this paper, the phase transformations in titanium alloys were described. Combined with the microstructural and strengthen mechanism of titanium alloys, the concepts for the research and development of anti-galling titanium alloy oil well pipe materials were also discussed.

Keywords Titanium alloys · Oil well pipe · Thread galling
Phase transformation · Strength

S. Wang · C. Fu · J. Chen · C. Fu (✉) · X. Wang (✉)
School of Materials Science and Engineering,
Southwest Petroleum University, Chengdu 610500, China
e-mail: fcyan1975@126.com

X. Wang
e-mail: xin.wang@swpu.edu.cn

S. Wang
e-mail: wsliang1465@126.com

C. Fu
e-mail: fchzh1992@126.com

J. Chen
e-mail: 917166390@qq.com

S. Wang · Y. Huang
College of Materials and Fujian Provincial Key Laboratory
of Materials Genome, Xiamen University, Xiamen 361005, China
e-mail: hyx@xmu.edu.cn

Y. Han (ed.), *Advances in Energy and Environmental Materials*,
Springer Proceedings in Energy, https://doi.org/10.1007/978-981-13-0158-2_39

Introduction

Recently, in the process of oil and gas exploitation, some complex environments including HPHT (high pressure high temperature), high content of CO_2, H_2S, Cl^- containing corrosive medium are emerging. The number of deep and ultra-deep wells is gradually increasing. For instance, The vertical depth of most wells in the Mexico Bay area are as high as 9 km, with the pressure at the bottom more than 140 MPa and the temperature over 200 °C [1]. In China, 70% of gas fields in Sichuan and Chongqing contain H_2S and CO_2. Plus, there are HPHT and corrosive environment in well drilling and completion operations for a variety of gas fields including Dabei gas field in Tarim Basin, Longgang gas field, Longmenshan gas field of Sichuan, and Xushen gas field of Daqing etc. [2].

Presently, the main materials for oil well pipe are carbon steel, stainless steel and nickel based alloy. However, in ultra-deep, HPHT and corrosive environment, these oil well tube materials have some disadvantages as drill tools in ultra-deep wells, for instance, limited use temperature and sulfide stress cracking resistance, high density [3]. Titanium (Ti) alloys are especially superior for drilling under HPHT environment for their excellent performance. But they also suffer from thread galling problems during assembling and disassembling [4]. In this paper, the thread galling causes were analyzed, and the phase transformations in titanium alloys were described. Moreover, the concepts for the research and development of anti-galling titanium alloy oil well pipe materials were discussed.

Characteristics of Titanium Alloy Oil Well Tube

Titanium alloy possesses high specific strength, outstanding corrosion resistance, high and low temperature resistance performance. Titanium has a density of 4.5 $g \cdot cm^{-3}$, is 43% lighter than any kinds of stainless steels and nickel base alloy, which makes titanium alloy pipe obviously advantageous for drilling applications in short radius horizontal wells, deep and ultra-deep water wells [5]. The fatigue life of titanium is ten times longer than that of steel. Thus even with a temperature of over 260 °C, titanium still has high strength. Besides, its modulus of elasticity and coefficient of thermal expansion is 1/2 and 2/3 of nickel base alloy, respectively, which is beneficial for the permanent seating of titanium alloy oil and well pipe under different working conditions without exceeding its minimum yield strength [6].

However, titanium alloys pipe will suffering from thread galling during thread assembling and disassembling. Thread-galling is a cold welding between metals. The causes of thread-galling come from two aspects. As for oil pipe materials, the allowable stress is related to its strength and hardness. It is possible to have plastic deformation and wear when the force applied to the material exceeds the allowable stress, then the cold-welding and gluing will form between the contact surfaces. Besides, the high-torque and unreasonable design of the thread structure will trigger

stress concentration and the distribution of stress are affected, which will increase the tendency of thread-galling [4].

Thus, in order to improve the anti-galling property of titanium alloys oil well pipe, the mechanical properties such as the strength, hardness and wear resistance should be increased, which needs to modify the microstructure of the materials. In this way, even those materials are under stresses during usage and processing, they would not easily be abraded and damaged by plastic formation due to their high performance.

Main Phase Transformations in Titanium Alloys

The properties of alloys are determined by their microstructure, which depends on the phase transformation in the alloy system. Therefore, in order to improve the properties of titanium alloy, it is necessary to understand the phase transformation processes.

Phase Transformations in Titanium Alloys during Quenching. According to the difference of the content of β phase stable element in titanium alloys, martensite (α′ or α″), ω_{ath} or metastable β phase can be obtained during quenching.

In general, when aTi alloy with less β stable elements is quenched from the β phase region or slightly below the temperature of β/α phase transition point, the β phase could be transformed into α′ martensite (hcp, acicular morphology), and the high temperature β phase will be transformed into α″ martensite (orthorhombic structure, acicular morphology) when the β stabilizer content is increased [7]. The martensitic transformation is non-diffusive. The atoms in the β phase displace regularly during phase transition. The atom displacement is larger and the lattice is easy to be reorganized when the alloy element content is low, so α′ phase can be obtained during quenching. Otherwise, α″ can be obtained. Lattice distortion will appear in martensite containing many elements, and make the hardness and strength of the alloy increased. However, owing to α″ phase with an orthorhombic structure, the hardness of α″ is lower than α′ phase with a hcp structure [7, 8].

With the increase of the β stabilizer in titanium alloy, the onset temperature of the martensitic transition (M_S point) will be decreased. When M_S decreased to room temperature, the content of the elements is then called the critical content. When the β stabilizer reaches the critical content, the ω_{ath} phase can be obtained during quenching from β phase region. The ωphase is the highest hardness solution phase in Ti alloys [9]. The strength and hardness will be increased sharply when the ω phase existing in the Ti alloys, but the plasticity and toughness will be decreased. The distribution of a certain amount of ω particles in the β matrix can improve the mechanical properties of the alloy, such as the yield strength, hardness and elastic modulus, and the plasticity and fracture toughness, etc. However, if the content of ω phase is too high, the plasticity will be greatly compromised [9, 10]. When the content of β phase stable element in titanium alloy exceeds the critical content, the β phase will be transformed into metastable β phase during quenching.

Phase Transformations of Titanium Alloys during Aging. The transitional phases obtained during quenching can be decomposed into different products, which depend on the composition and temperature during aging.

The α′ phase usually formed in alloy containing β phase eutectic elements (Mo, V, Ta, Nb) or β phase eutectoid elements(Cr, Mn, Fe, W), so the decomposition product of α′ phase during aging is related to the alloy system. In the β phase eutectic alloys, α′ phase can be directly decomposed to form stable α + β phases during aging. In the β phase eutectoid alloys, α′ phase can be decomposed into the stable α phase and intermetallic compounds [11]. Currently, the decomposition processes of α″ phase are categorized as the following [12].

(1) The metastable β phase precipitated from α″ phase during initial aging stage, and then the α″ phase gradually transformed into α′ phase with the depression of β stabilizer in α″ phase, and finally transformed into the stable α + β phases. The whole process is: $\alpha'' \rightarrow \beta_{meta} + \alpha''_{lean} \rightarrow \beta_{meta} + \alpha' \rightarrow \alpha + \beta$.
(2) The stable α phase precipitated from α″ phase during initial aging stage, then the α″ gradually transformed into metastable β phase with the increment of β stabilizer in α″ phase, and further transformed into the stable α + β phases. The whole process is: $\alpha'' \rightarrow \alpha + \alpha''_{rich} \rightarrow \beta_{meta} + \alpha \rightarrow \alpha + \beta$.
(3) During initial aging stage, the α″ phase is separated into one β stabilizer-rich region and another β stabilizer-poor region, and then the former gradually transformed into metastable β phase. Finally, stable α + β phases would be obtained. The whole process is: $\alpha'' \rightarrow \alpha''_{lean} + \alpha''_{rich} \rightarrow \beta_{meta} + \alpha''_{lean} \rightarrow \alpha + \beta$.

In the titanium alloys with higher content of β stabilizer, the metastable β phase can be obtained by quenching. During the subsequent aging process, the decomposition process of the metastable β phase is different, which also depends on the composition and aging temperature. At low aging temperature, the metastable β phase may be separated into two regions with low or high content of solute atoms, respectively. Finally, the stable α + β phases can be obtained with the increase of aging temperature or time. The complete process is $\beta_{meta} \rightarrow \beta + \beta' \rightarrow \beta + \alpha$ [8]. The β′ cannot significantly improve the strength of the Ti alloys. Therefore, it is very rare to study the β′ phase.

When the aging temperature is slightly high, the metastable β phase may be decomposed into the isothermal ω phase(ω_{iso}) and the stable β phase. The aging temperature of the ω_{iso} transition varies with the composition of alloys, usually in the range of 100–500 °C. The morphology of the ω_{iso} phase particles is related to the misfit between the ω phase and matrix. When the misfit is high, the morphology of the ω_{iso} particles is cubical and controlled by the decrease of the elastic strain of the matrix. In low misfit alloys, the ω_{iso} particle morphology is ellipsoid and controlled by the reduced surface energy [9]. So the ω_{iso} phase morphology can be controlled by adding different alloying elements. The hardness of ω_{iso} phase is as high as ω_{ath}, but its formation rate is not as fast as the ω_{ath} phase, which usually needs several or even dozens of hours to fill precipitate [13]. Therefore, the aging

time can be controlled in order to control the volume fraction of the isothermal ω phase, so that the excellent mechanical properties of the Ti alloys could be obtained.

The metastable β phase can be directly decomposed into the stable α + β phases during aging at high temperature, and the feature of α phase is dependent on the composition. Generally, they are 1α (lamellar morphology, having the burgers orientation relationship with the β matrix) and 2α (cluster α particles or lamellar morphology like a lens, having no burgers orientation relationship with matrix), respectively. The crystal structures of 1α and 2α phase are both hcp structure. It has been shown that the strengthening effect of 2α on Ti alloy is higher than that of 1α [8, 10].

Concepts for the Research and Development of Anti-galling Titanium Alloy Oil Well Pipe Materials

The alloying elements in Ti alloys are usually substitutional elements and the solid solution strengthening efficiency is limited. Therefore, the quenching and aging heat treatment are usually taken to strengthen the Ti alloys. As mentioned earlier, the metastable phases are likely to precipitate β′, ω and α (including 1α and 2α) during aging. The β′ phase cannot significantly improve the strength and hardness of the alloy, but the ω phase and α phase can, especially ω phase. If the volume fraction of the ω phase in the alloy is fitly controlled, excellent performance could be obtained. Otherwise, the properties of the alloy is poor. Therefore, it is very important to explore a kind of Ti alloys oil well pipe materials using ω phase as the hardening phase.

It is possible to control the volume fraction of ω_{iso} phase, but not the ω_{ath} phase. Therefore, it is feasible to utilize the ω_{iso} phase as the hardening phase, so that the strength and hardness of the Ti alloys can be improved. The ω_{iso} phase is generally obtained by means of aging the metastable β phase under proper temperature. In order to obtain the metastable β phase, the content of the β stable elements in the alloy must reach a certain content and appropriate heat treatment is needed. Accordingly, it is the key problem for the designers to know how to design the composition and heat treatment process to obtain the appropriate amount of ω_{iso} phase.

As for the research and development of new materials, most of the traditional methods are “trial method”, which has a long cycle, high cost and a lot of man-power and material resources would be wasted. The phase diagram is also called the ‘guide book’ of material designers, and the ‘map’ of metallurgical workers. It is an indispensable theoretical basis for the research and development of alloy materials. Thermodynamic database, model and phase diagram calculation software are the three elements of CALPHAD (calculation of phase diagrams). Particularly, the establishment of thermodynamic database is the most critical part. The general calculation and application processes are as follows. First, based on the

experimental data, thermodynamic data and the first principles calculation data and all the phases in the system are optimized by adopting appropriate model using CALPHAD software. Then, thermodynamic parameters of each phase in the low-component system are obtained. Finally, thermodynamic database of multi-component system can be established, and the phase diagram, freezing curve, thermodynamic properties can be concluded to guide the composition and process design of a new materials [14].

At present, the CALPHAD technology plays an important role in the development of a new materials. Wu et al. [14] calculated the adiabatic combustion temperature of pure metal and titanium alloy by using of the CALPHAD technology, which provided a basis for the selection of new type flame retardant titanium alloy. In the same way, Avraham et al. [15] designed the magnesium alloy with better creep performance, and optimized the aging heat treatment process.

Therefore, the CALPHAD technology can be applied to the development of new type high strength, high hardness and anti-galling titanium alloy tube. In this way, the development cycle, the raw materials and the costs can be saved.

Conclusion

The current industrial Ti alloys are designed using α phase as the hardening phase, however, in practice, there are still some problems such as inadequate strength and hardness, which could not meet the requirements. Therefore, it is necessary to research a new type of Ti alloys oil well pipe materials which use ω as the hardening phase, then the tendency of galling could be reduced to ensure the oil and gas exploration work carried out smoothly. Although the toughness of the Ti alloys will be decreased after being strengthened by ω phase, excellent performance could be obtained by means of correct controlling the volume fraction of the ω phase in the Ti alloys. As to how to design the alloy composition and thermally treat to obtain appropriate volume fraction of the ω phase, the CALPHAD technology can be used to assist the design and experiment. In addition, it is necessary to further study the effects of the volume fraction of the ω phase on the performance of alloys, the effects of alloying elements on the type of quenching phase and precipitation capacity of ω phase. In a word, there are many basic theories and processes need to be studied in depth, including the mechanism of phase transformation, thermodynamic and kinetic conditions in titanium alloys, heat treatment, etc.

Acknowledgements This work was supported by the Innovative training program (KSZ16113) and Scientific Research Foundation and Opening Foundation (X151516KCL23) of Southwest Petroleum University, and open fund of Fujian Provincial Key Laboratory of Materials Genome (Xiamen University). Xin Wang acknowledges a funding from the Department of Education of Sichuan Province (17ZA0419) as well as scientific research starting project funding (2017QHZ020) and start-up funding from Southwest Petroleum University.

References

1. A. Shadravan, M. Amani, HPHT 101-What petroleum engineers and geoscientists should know about high pressure high temperature wells environment. Energy Sci. Technol. **4**, 36–60 (2012)
2. D.S. Ye, Y. Ren, B. Guan, C.B. Yin, Difficulty and strategy of reservoir stimulation on abnormal-high temperature and high pressure wells in the Tarim basin. Natur. Gas Ind. **29**, 77–79 (2009)
3. B. Craig, Materials for deep oil and gas well construction. Adv. Mater. Process. **166**, 33–35 (2008)
4. U. Wiklund, I.M. Hutchings, Investigation of surface treatments for galling protection of titanium alloys. Wear **251**, 1034–1041 (2001)
5. K. Bybee, Titanium-drillpipe development for short-radius drilling. J. Petrol. Technol. **52**, 50–53 (2015)
6. R.D. Kane, S. Srinivasan, B. Craig, K.M. Yap, *A Comprehensive Study of Titanium Alloys for High Pressure High Temperature (HPHT) Wells, Corrosion 2015. NACE International* (Omnipress, Houston, 2015)
7. L. Zeng, T.R. Bieler, Effects of working, heat treatment, and aging on microstructural evolution and crystallographic texture of α, α′, α″ and β phases in Ti–6Al–4V wire. Mater. Sci. Eng, A **392**, 403–414 (2005)
8. I. Lonardelli, N. Gey, H.R. Wenk, M. Humbert, S.C. Vogel, L. Lutterotti, In situ observation of texture evolution during $\alpha \rightarrow \beta$ and $\beta \rightarrow \alpha$ phase transformations in titanium alloys investigated by neutron diffraction. Acta Mater. **55**, 5718–5727 (2007)
9. S. Nag, R. Banerjee, R. Srinivasan, J.Y. Hwang, M. Harper, H.L. Fraser, ω-Assisted nucleation and growth of α precipitates in the Ti-5Al-5Mo-5V-3Cr-0.5Fe β titanium alloy. Acta Mater. **57**, 2136–2147 (2009)
10. O. Yasuya, O. Toshitaka, N. Kiyomichi, K. Sengo, Effects of ω-phase precipitation on $\beta \rightarrow \alpha$, α″ transformations in a metastable β titanium alloy. Mater. Sci. Eng., A. **312**, 182–188 (2001)
11. X.K. Ma, F.G. Li, J.H. Li, J. Cao, P. Li, J.Z. Dong, Effect of heat treatment on the microstructure and micro-mechanical behavior of quenched Ti-6Al-4V alloy. J. Mater. Eng. Perform. **24**, 1–12 (2015)
12. Y.Z. He, W.X. Zhang, H.W. Zhou, Y.F. Lu, Z.P. Xi, Decomposition of orthorhombic martensite in TC21 alloy during aging treatment. Rare Metal. Mat. Eng. **41**, 800–804 (2012)
13. Z.B. Zhou, J.S. Li, H.C. Kou, Z.S Zhu, B. Tang, H. Chang, Aging response of TB-13 titanium alloy. Mater. Sci. Forum. **654**, 859–862 (2010)
14. B. Wu, J.J. Shen, J. Sun, Z. Zhang, S.S. Hui, Application of CALPHAD technology in development of advanced titanium alloys. Acta Metall. Sin. **38**, 644–649 (2002)
15. S. Avraham, Y. Maoz, M. Bamberger, Application of the CALPHAD approach to Mg-alloys design. CALPHAD **31**, 515–521 (2007)

Cracking Failure Analysis of X70 Pipeline Steel Weld

Bin Wang, Senfeng Zhang, Cui Zhou, Nan Liu, Liang Wang and Xiaoyu Tian

Abstract The weld defects were detected by Nondestructive Testing Technology (NTT). The microstructure and microhardness were examined by optical microscope(OM), scanning electron microscopy (SEM) equipped with EDS and Vicker microhardness tester to identify the reasons of cracking failure in X70 pipeline steel weldment. As a result, the microstructure in the root layer and filling layer of the weld presents ferrite and pearlite while it is ferrite and bainite in the covering layer, but the morphology and distribution as well as the content of ferrite and pearlite in the root layer are different from which in the filling layer; the cracks initiate at the root of the weld and propagate towards filling layer, and the C, O, S segregation is serious, which contribute to the initiation and propagation of the crack in the weld; the hardness decreases sharply around the crack tip, which exhibits lower strength.

Keywords Microstructure · Cracks · Segregation

B. Wang · S. Zhang · L. Wang
School of Materials Science and Engineering, Southwest Petroleum University, Chengdu 610500, China
e-mail: 18280383558@163.com

C. Zhou
Shanghai Jianke Engneering Consulting Co. Ltd, Shanghai 200032, China
e-mail: 1479390503@qq.com

B. Wang (✉)
Sichuan Provincial Research Center of Welding Engineering Technology, Chengdu, China
e-mail: 1247514463@qq.com

N. Liu
Sichuan Petroleum and Natural Gas Construction Engineering Co. LTD, Chengdu, China
e-mail: 1208959694@qq.com

X. Tian
One Two Project Management Co. LTD, Chengdu, China
e-mail: 304441738@qq.com

Y. Han (ed.), *Advances in Energy and Environmental Materials*,
Springer Proceedings in Energy, https://doi.org/10.1007/978-981-13-0158-2_40

Introduction

Currently, the increasing demand for oil and natural gas has forced energy industries to look for these resources in harsh environment. There is no doubt that steel pipelines are often used to carry these resources for long distances. The most important damage style in pipeline steels is crack in the weld which will lead to leakage and result in enormous losses. Also, the leakage or rupture of these pipelines can always pose a potential threat to humans and environment. So it is important to investigate the reasons of crack in the weld of pipelines in order to occupy a high quality weld.

Meresht [1] investigated the causes of stress corrosion cracking of API 5L X60 steel gas pipeline that was installed in the northern regions of Iran concluding that possible susceptibility to Stress Corrosion Cracking(SCC) failures of such pipelines was resulted from active defects on external surface. Mohtadi-Bonab [2] studied the mechanism of failure by hydrogen induced cracking in an acidic environment for API 5L X70 pipeline steel, and found that the role of high angle grain boundaries and type of fracture would be important in crack propagation. Welding process is a nonequilibrium thermodynamics process, often introducing several defects in the welding process, which will have a strong impact on servicing safety of pipeline steels. Based on this concept, a lot of works are done by scholars. Azevedo [3] investigated the transversal cracking of a seamed API 5L X46 steel tube belonging to a crude oil pipeline, considering the nucleation of the primary crack was associated to the presence of welding defects and corrosion pits. Fu [4] analyzed the cracking in girth weld of pipeline used in gasfield gathering system, concluding that the mechanically lined pipe crack initiated from outer carbon steel, and propagated in intergranular mode along the weld-fusion line. In order to identify causes of an incident taken place after an operation to repair a leak in an interstate natural gas pipeline, Farzadi [5] conducted a failure analysis which concluded that hydrogen-assisted cracking, wrong design of branch connection, paint coating, and pipeline operating conditions were major factors contributing to the failure.

The cracking failure may cause pollution, loss of production and even life danger. So it is necessary to deeply investigate the failure or defects reasons in the weld of the pipelines. The objective of this paper is to analyze the cracking failure reasons of girth weld in X70 pipeline steel.

Background of the Failure

The failed two segments of the X70 weld were shown in Fig. 1 containing inner pipe (a, c); and outer pipe (b, d). The cracking failed girth weld in X70 pipeline was firstly detected by X-ray detectoscope, and the results were shown in Fig. 2. It was found from Fig. 2 that three places of crack points appeared in the weld, and the three places of crack points were circled out in Fig. 1.

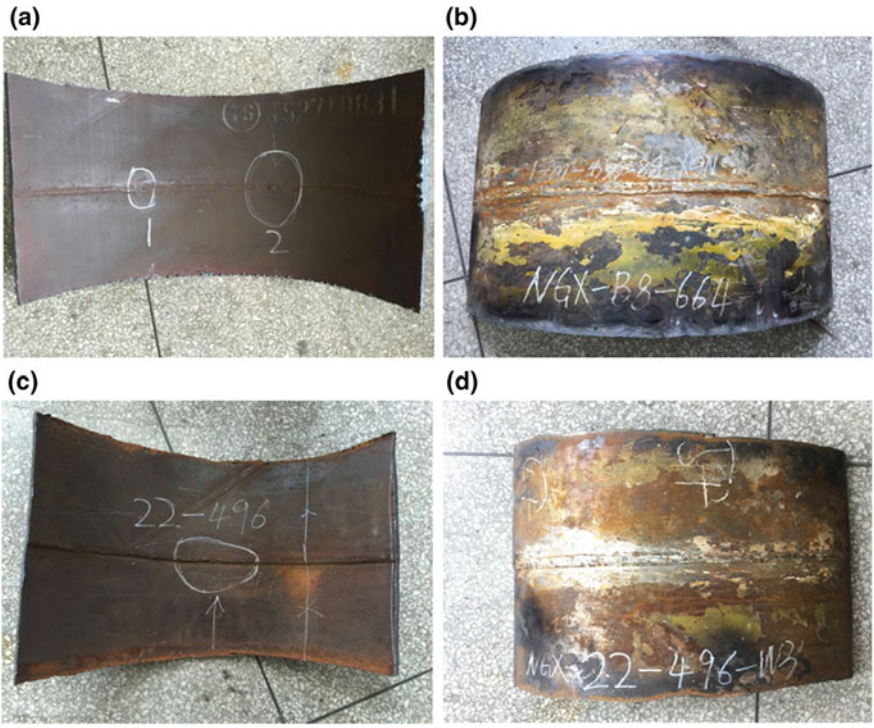

Fig. 1 Profile of failed segments; **a** two defects in the weld of one inner pipe; **b** outer profile of **a**; **c** one defect in the weld of the other inner pipe; **d** outer profile of **c**

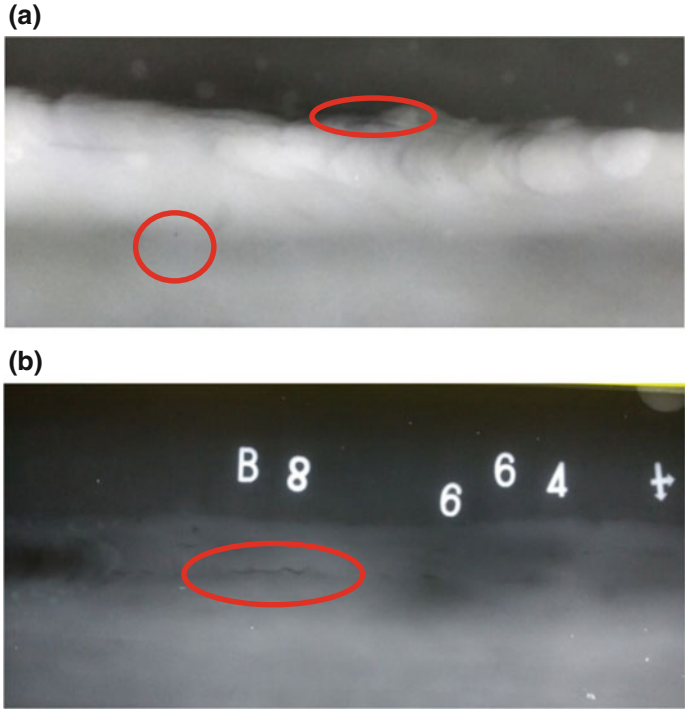

Fig. 2 Defects detected by X-ray detectoscope near failed girth weld; **a** detected result of Fig. 1a; **b** detected result of Fig. 1c

Failure Description and Analysis

Failure Description. In order to further exact the locations of detected defects, a Multi-function Ultrasonic Phased-array Detection System (SYNCSCAZ 16PT) was used to the three failure points. Then the three defects were extracted from the base metal using and were marked 1#, 2#, 3#, respectively. Specimen were prepared from the transverse cross section of the weld.

Morphology characterization of three defects in the weld of X70 pipeline steel was shown in Fig. 3. It was obvious that arc crater, excessive grind and a lower thickness of weld which compared to base metal all existed in 1# and 2#; lots of spatter on the back of the weld appeared in 1#, and also, serious undercut as well as spatter existed in 3#. These defects in the weld surface will introduce stress concentration, and induce crack initiation in the defects places [6]. The three specimen were cut by Wire cut Electrical Discharge Machining (WEDM) according to the

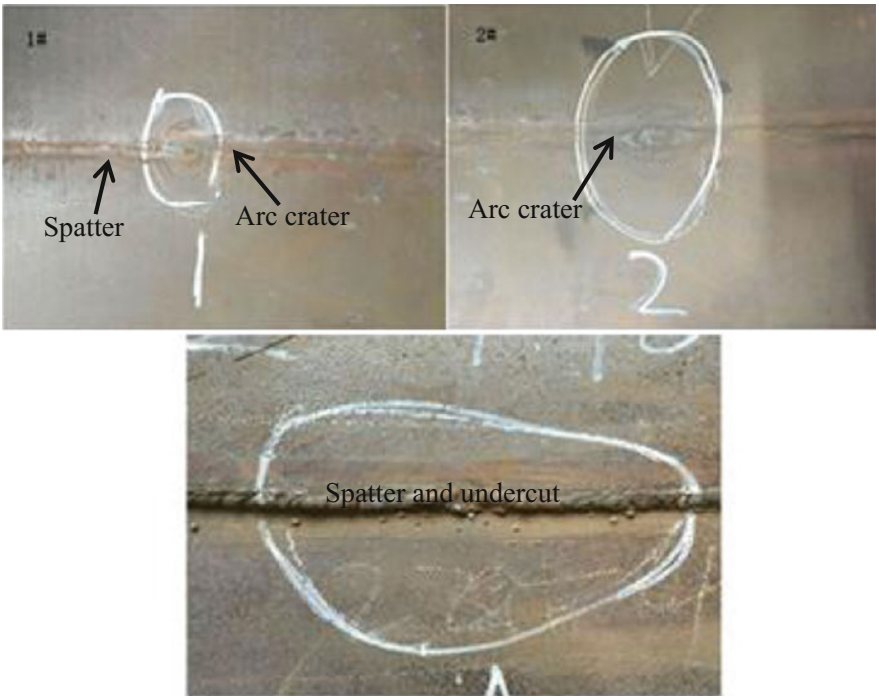

Fig. 3 Morphology characterization of the weld surface

Multi-function Ultrasonic Phased-array Detection System and prepared by grinding using 150, 240, 600, 1000, 2000, 3000 and 5000 grits of SiC paper and polished, then etched by nitric acid alcohol solution(4%). The microstructure features were studied using optical microscope (OM), and the results were shown in Fig. 4. It is obvious that there are three porosities locating in the filling layer in 1#, while it is a crack in the weld in 2#, and the crack initiates from central position of the weld root, extends towards filling layer and ends at the filling layer. When it comes to 3#, however, the crack initiates from undercut position of the weld root, circuitously extends towards filling layer and ends at the filling layer.

To sum up, the cracks all initiate from the weld root, and extend towards filling layer, which may relate to the different microstructure, composition of the weld. So microstructure investigations, EDS analysis as well as microhardness test were conducted in order to better understand the reasons of the weld cracking in X70 pipeline.

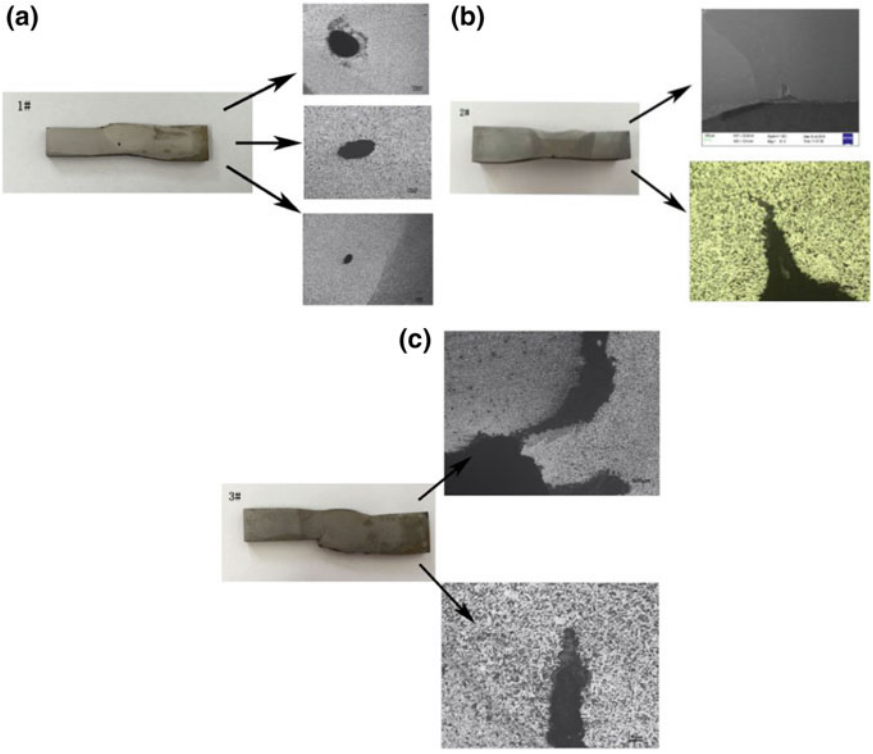

Fig. 4 OM observation results of 1#, 2#, 3#

Failure Analysis

Microstructure Observation. It is observed that there are three porosities locating in the filling layer in 1# and the enlarged morphology is shown in Fig. 5. The microstructure of the layer where porosities are located in is shown in Fig. 6. It can be confirmed from Fig. 6a that the irregular porosity which may result from the incomplete cleaning of the weld, is located in the filling layer and is adjacent to the root layer. The existence of irregular porosity will reduce force bearing area, contribute to stress concentration and then promote the formation and extension of crack [6, 7]. Figure 6b–d are microstructure of root layer, filling layer, and covering layer; respectively; it is a mixture of ferrite and pearlite in root layer and filling layer while some bainite structure formed in the covering layer; however, as the root welding process has a similarly effect with preheat on the filling welding, it formed more pro-eutectoid ferrite and less pearlite in filling layer compared with the root layer.

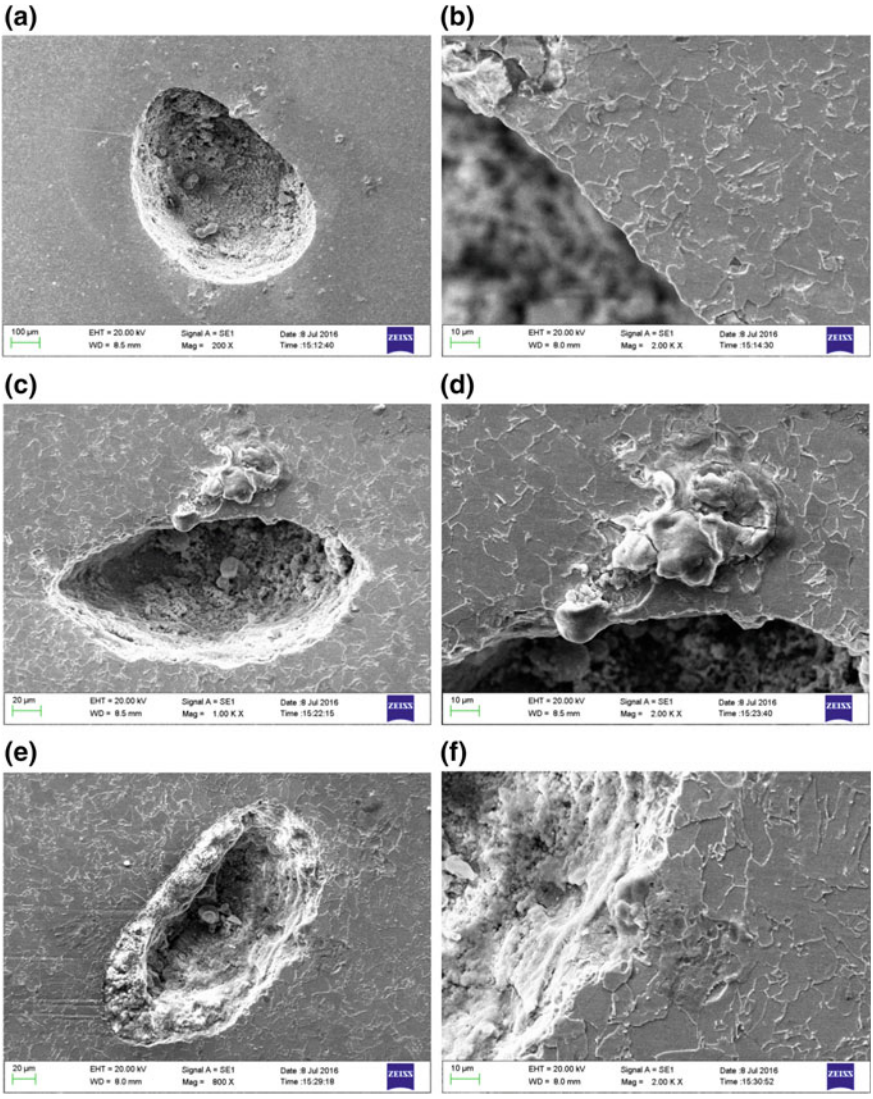

Fig. 5 **a**, **c**, **e** are three porosities locating in the filling layer in 1#, while **b**, **d**, **f** are enlarged one, respectively

The observed result of 2# is crack formed in weld. Figure 7 shows the microstructure of the weld where the crack is located in. The microstructure of each layer in 2# is similar to 1# because of the same welding process. There is an obvious notch in the root weld according to Fig. 7a, which may be the result of excessive grind to the weld reinforcements after welding process. This notch destroyed integrity and consistency of the weld, leaving a local damage on the

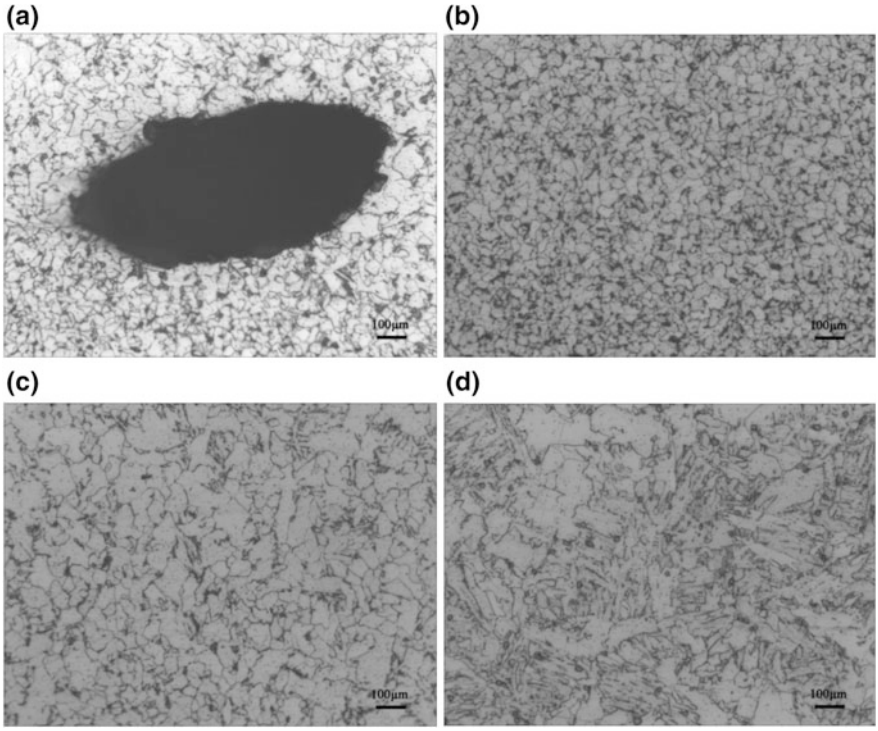

Fig. 6 Microstructure in the weld of 1# **a** morphology of porosity; **b–d** are microstructure of root layer, filling layer, and covering layer, respectively

surface and resulting in stress concentration [8], thus it will promote the original crack beside the notch extend to the weld with the comprehensive effect of flowing petroleum and natural gas in the pipeline, corrosion, etc. The crack originated from the weld root, then propagated irregularly and tortuously towards filling layer. In order to further investigate the crack propagation, a SEM observation was conducted. The result is shown in Fig. 8. It can be seen from Fig. 8a that the crack is located in the root layer and propagate irregularly and tortuously along a path shown in Fig. 8b. From Fig. 8c, there formed inclusion in the crack tip, and the inclusion has an effect on the crack propagation that the crack is arrested here. It can be speculated as the following views: firstly, ferrite can sustain some deformation [9] because of its excellent plasticity, then some stress can be released; secondly, as the inclusion has higher strength, the crack propagation can be effectively restrained.

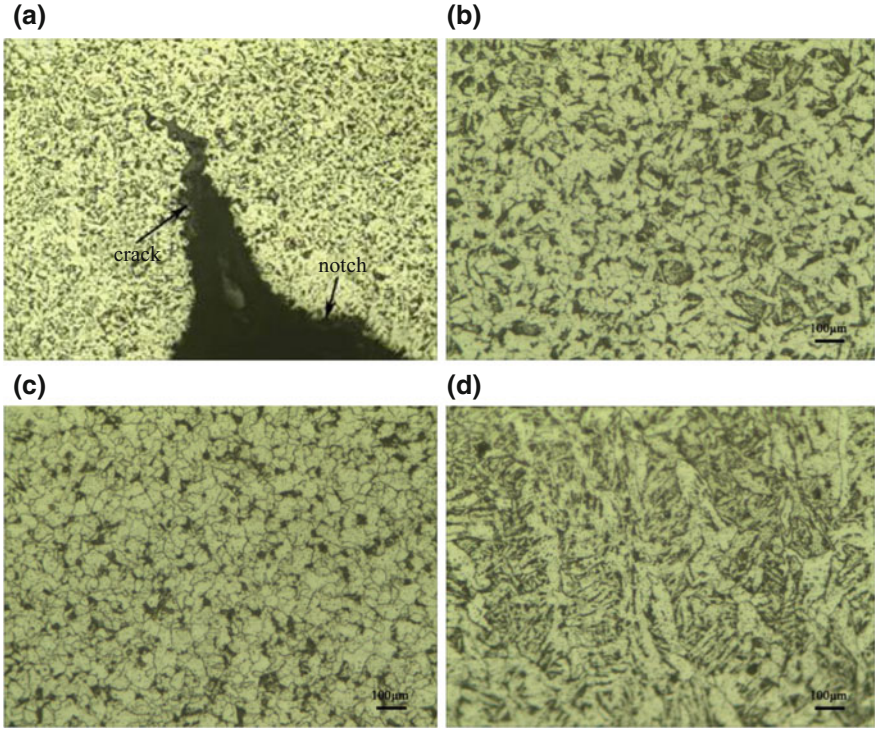

Fig. 7 Microstructure of the weld in 2#; **a** morphology of crack; **b**, **c**, **d** are microstructure of root layer, filling layer, and covering layer, respectively

The microstructure of each layer of 3# is shown in Fig. 9. The observation results indicate that the microstructure is mainly ferrite and pearlite. Figure 9a shows that crack originates from the undercut area and propagate towards weld center along the fusion line. The main reason is that edge offset exceed the technological procedure, which increased stress concentration and prompted the crack initiation. Besides, the heat affected zone experienced most serious edge offset, contained most serious stress centration, resulted in crack initiation and propagation under service environment. The crack width increased during propagation from fusion line to root weld center, and stopped at the filling layer. For one thing, the microstructure in heat affected zone refined a lot compared with root layer according to Fig. 9b, e; for another, although some stress was released, there were still stress concentration existed in the weld, and this prompted the crack propagated to coarse grain of root welding layer, then stopped with the comprehensive effect of some inclusion and ferrite as well as pearlite.

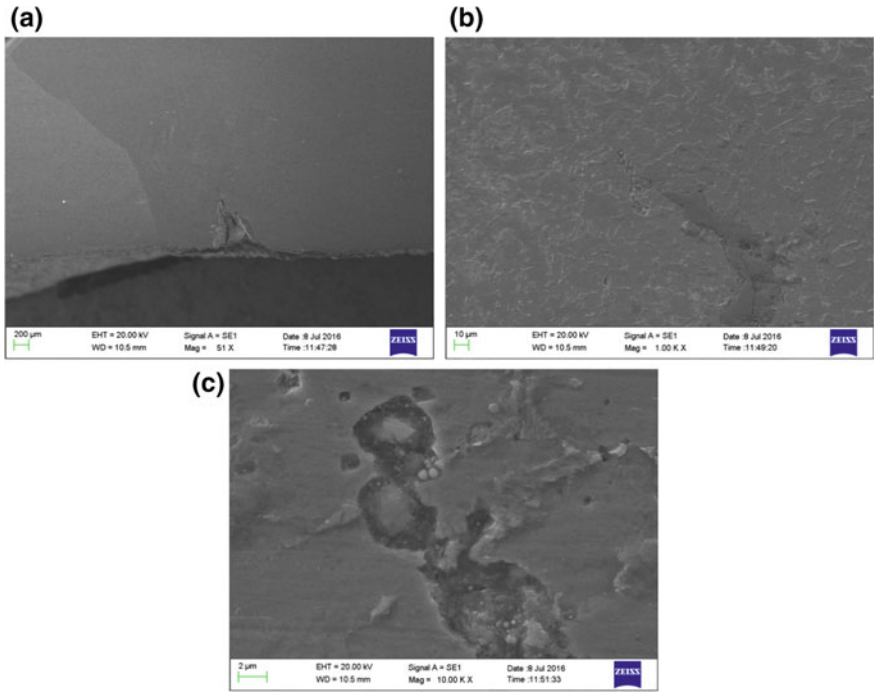

Fig. 8 SEM observation results of 2#; **a** macroscopic characteristic of notch and crack; **b** crackpropagation path; **c** crack tip in (b) with red circle

Element Distribution Analysis. In order to further investigate the reason of crack initiation and propagation, EDS analysis was conducted.

Figure 10 shows the surface scan result of porosity in 1#. The observation results show that there is more O element distributing along the crack edge alongside the porosity, which indicates that the crack may result from the oxide.

Figure 11 shows the point scan and surface scan results of crack in 2#. It can be concluded that element segregation is serious during welding process, and it is easy to form brittle inclusions [10]. On one hand, these brittle inclusions can not deform effectively to release stress; on another hand, they can also constrain crack propagation. Figure 11f shows the surface scan result of crack tip of 2#. It indicates that the beneficiation of C, S and O is serious.

Figure 12 shows the point scan and surface scan results of crack tip in 3#. It is also a beneficiation of C, S and O elements. These two elements can easily form brittle inclusion together with Si, Cr,Mn, Ti. As an oxidation environment can significantly accelerates crack growth rates, rather than temperature alone [11]. So it is important to control those elements like O, S.

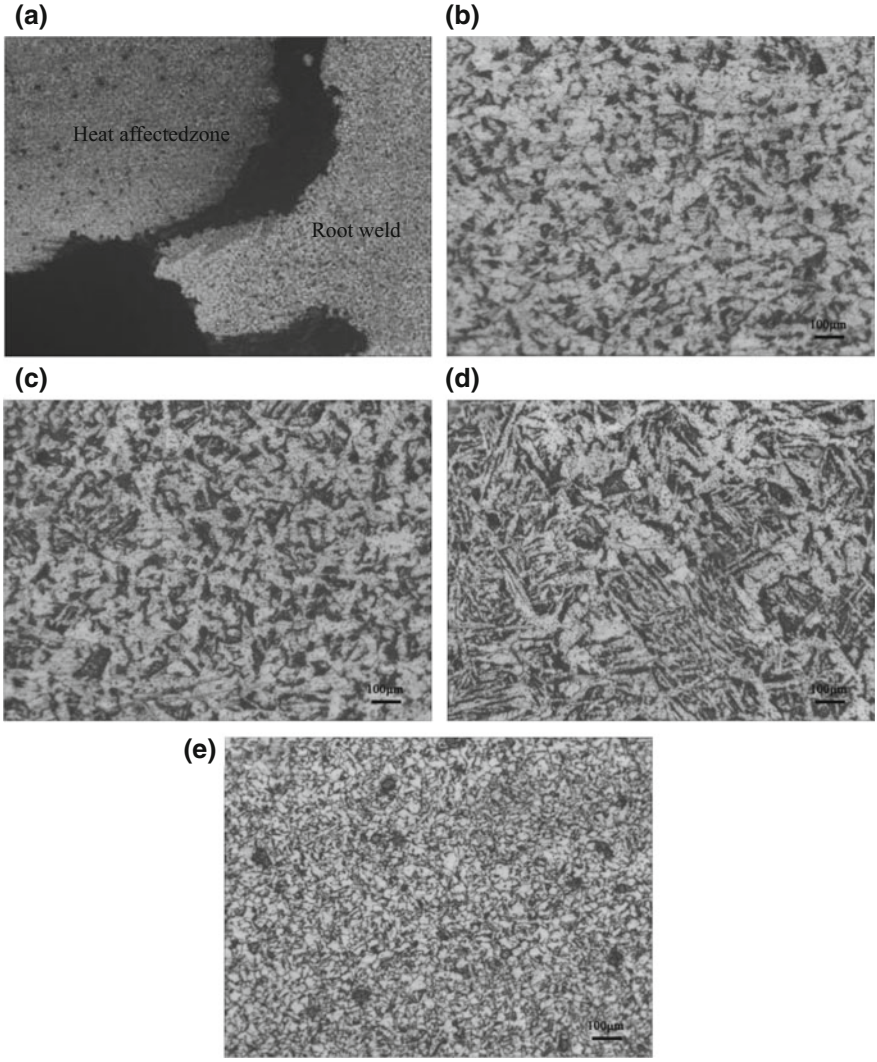

Fig. 9 Microstructure of the weld in 3#; **a** crack initiation position and propagation direction; **b**, **c**, **d** are microstructure of root layer, filling layer, and covering layer, respectively; **e** microstructure of crack initiation position

Microhardness Analysis. Microhardness test was conducted by tester HVD-2000TM/LCD at room temperature. 1# and 3# are selected for testing. As those defects are mainly distributed at filling layer, so the selected position is filling layer. The results are shown in Fig. 13. It can be clearly seen that the microhardness distribution is almost the same for the weldments with 1# and 3# that the

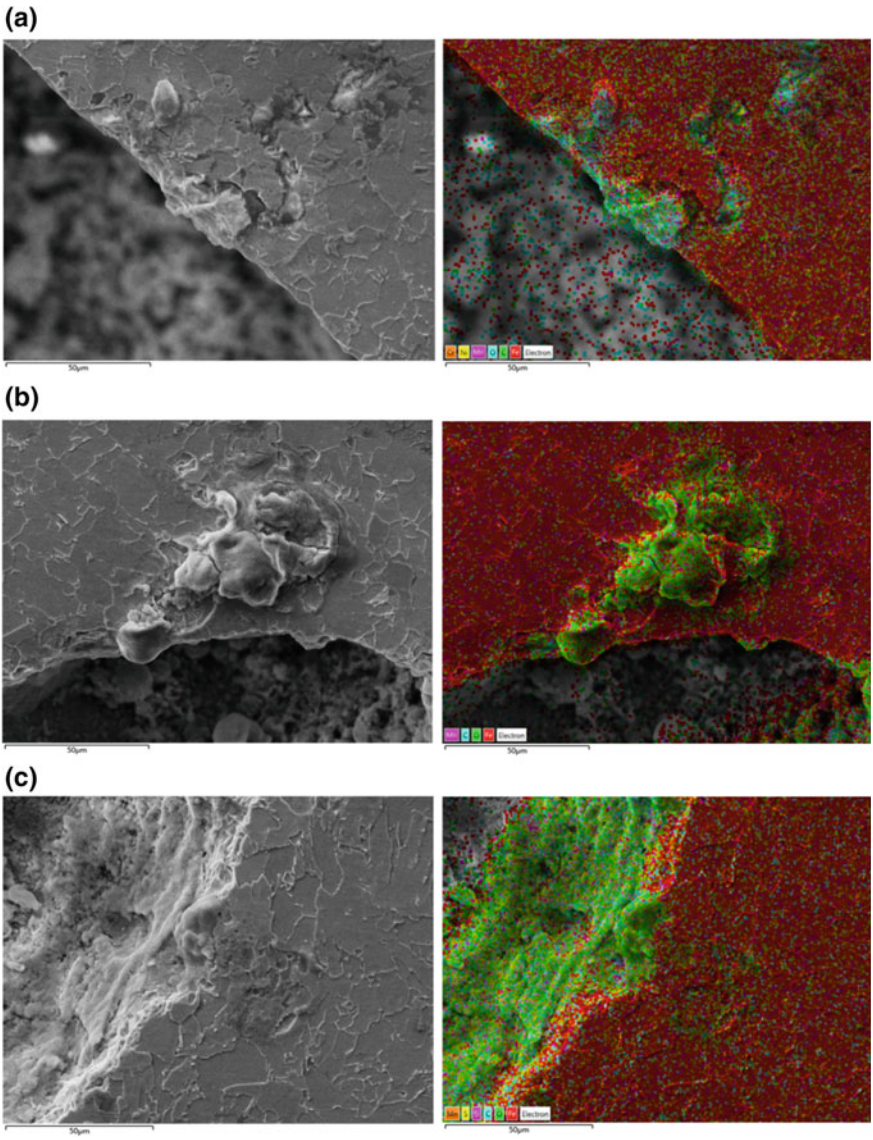

Fig. 10 Surface scan result of porosity in 1#

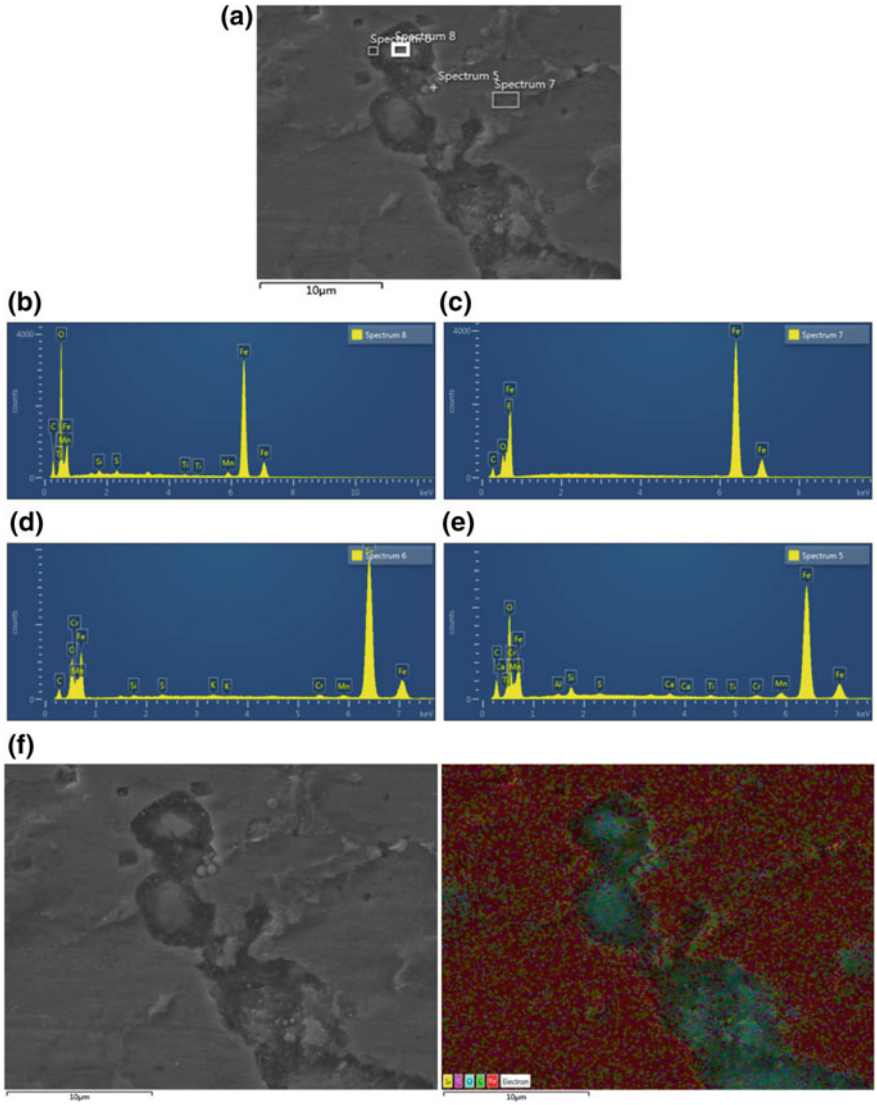

Fig. 11 EDS analysis of crack tip in 2#

microhardness values in the weld are all lower than base metal. The grain size in the weld is more coarse than heat affected zone and base metal, leading to a lower microhardness value in the weld. So it is important to control the grain size by controlling heat input and interpass temperature during welding process.

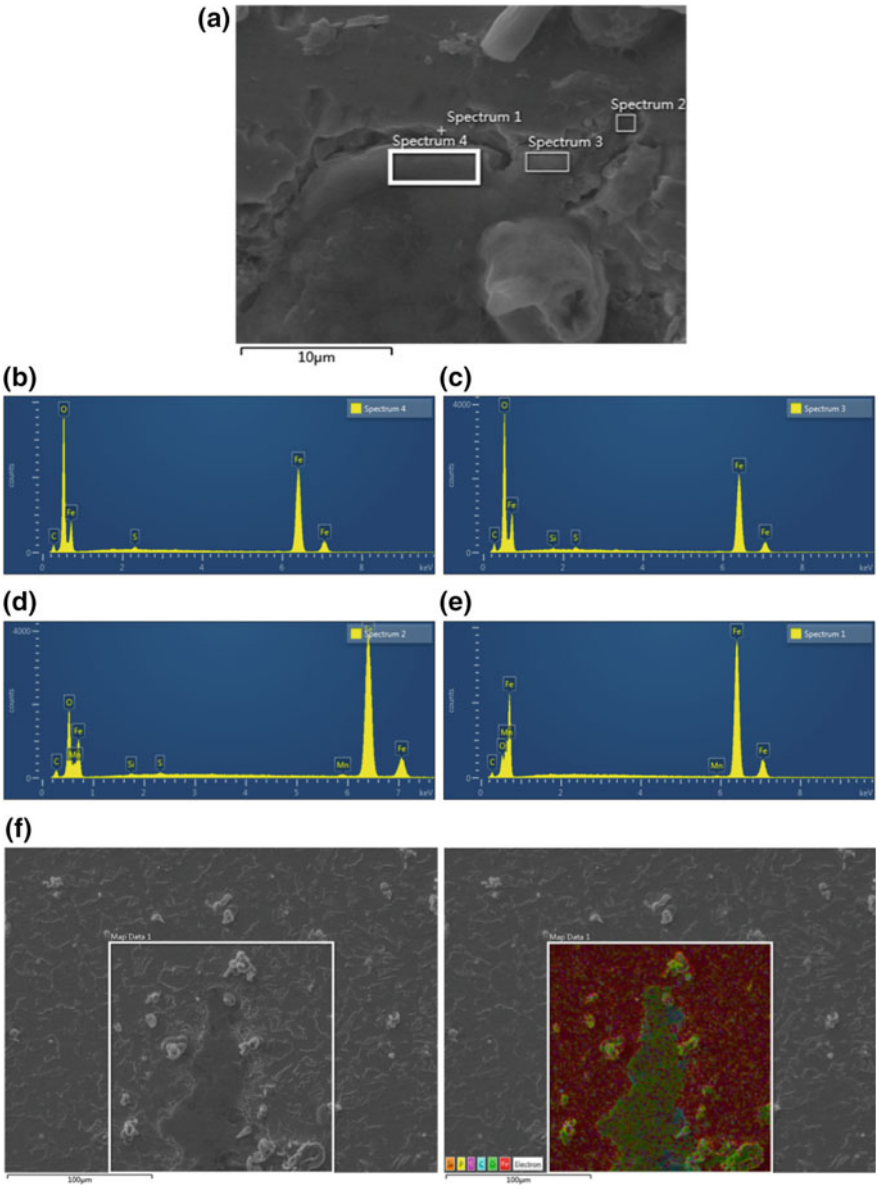

Fig. 12 EDS analysis of crack tip in 3#

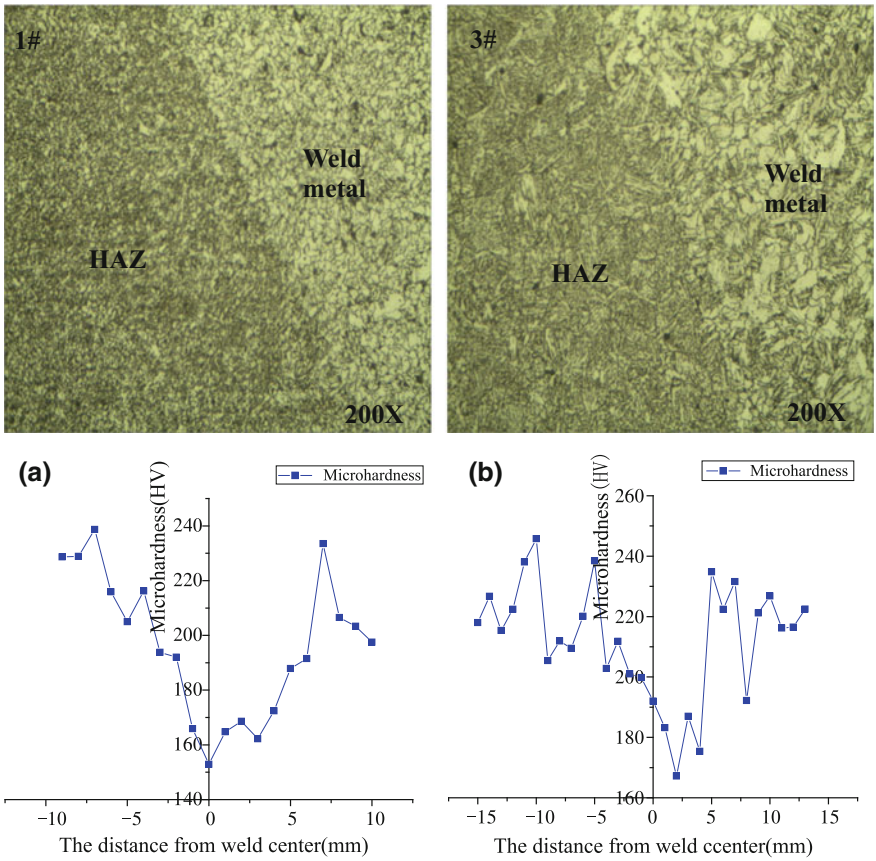

Fig. 13 Microhardness profile; **a** 1#; **b** 3#

Conclusion

The microstructure and microhardness were investigated to better elucidate the reason of cracking failure of X70 pipeline steel weld. The following conclusions can be made based on the aforementioned results:

1. The microstructure in the weld of X70 pipeline shows different distribution of ferrite and pearlite in root layer and filling layer, which is resulted different welding thermal cycle.
2. The enrichment of C, O, S in the crack position is serious which will contribute to the growth of crack.
3. The grain size can deeply influence the microhardness value, so the methods such as heat input and interpass temperature should be taken to control the grain size.

References

1. E.S. Meresht, T.S. Farahani, J. Neshati, Failure analysis of stress corrosion cracking occurred in a gas transmission steel pipeline. J. Eng. Fail. Anal. **18**, 963–970 (2011)
2. M.A. Mohtadi-Bonab, J.A. Szpunar, R. Basu et al., The mechanism of failure by hydrogen induced cracking in an acidic environment for API 5L X70 pipeline steel. J. international journal of hydrogen energy. **40**, 1096–1107 (2015)
3. C.R.F. Azevedo, Failure analysis of a crude oil pipeline. J. Eng. Fail. Anal. **14**, 978–994 (2007)
4. A.Q. Fu, X.R. Kuang, Y. Han et al., Failure analysis of girth weld cracking of mechanically lined pipe used in gasfield gathering system. J. Eng. Fail. Anal. **68**, 64–75 (2016)
5. A. Farzadi, Gas pipeline failure caused by in-service welding. J. Pressure Vessel Technol. **138**, 011405 (2016)
6. H. Alipooramirabad, A. Paradowska, R. Ghomashchi et al., Investigating the effects of welding process on residual stresses, microstructure and mechanical properties in HSLA steel welds. J. Manuf. Process. **28**, 70–81 (2017)
7. F. Shen, B. Zhao, L. Li et al., Fatigue damage evolution and lifetime prediction of welded joints with the consideration of residual stresses and porosity. Int. J. Fatigue. **163**, 272–279 (2017)
8. T. Łagoda, P. Biłous, Ł. Blacha, Investigation on the effect of geometric and structural notch on the fatigue notch factor in steel welded joints. Int. J. Fatigue **101**, 224–231 (2017)
9. Wang A, Shi Y, Chen C, Effect of aging-deformation-treatment on the formation of intragranular ferrite in V-microalloyed steel. J. Mater. Sci. Technol. 1–6 (2017)
10. Natividad C, García R, López VH et al. Metallurgical characterization of API X65 steel joint welded by MIG welding process with axial magnetic field. J. Mater. Res. 8–17 (2017)
11. R. Jiang, S. Everitt, N. Gao et al., Influence of oxidation on fatigue crack initiation and propagation in turbine disc alloy N18. J. Int. Fatigue. **75**, 89–99 (2015)

Preparation of MMT/MVQ Foam Material

Bin Xiang, Zhaoping Deng and Qiyi Gan

Abstract MMT/MVQ composites material was prepared by mechanical blending, and the silicone rubber foam was successfully prepared by supercritical carbon dioxide foaming method. The results show that the content of MMT is 5–10 phr, the effect of reinforce is best, and the cell morphology of silicone rubber foam is optimal.

Keywords MMT/MVQ composites material · Supercritical carbon dioxide Reinforce

Introduction

Silicone rubber foam is a porous polymer elastic material which includes the characteristics of silicone rubbers and foam materials [1]. It combines the excellent characteristics of silicone rubber material and foam. Not only does the silicone rubber foam have low toxicity, flexibility, reliability, and good reliability, but also exhibits low density, sound insulation and buffer shock absorption, etc. [2–4]. Hence, silicone rubber foam has been widely used in the fields of electronics industry, chemical industry, aerospace, etc. [5, 6].

The mechanical properties of silicone rubber foam are related to the cell density, cell distribution and cell morphology, which in turn, depending on the foaming methods [7, 8] and process conditions [9]. Traditional preparing methods of the

B. Xiang · Z. Deng (✉)
College of Materials and Chemistry and Chemical Engineering,
Chengdu University of Technology, Chengdu 610059, China
e-mail: 1581026467@qq.com

B. Xiang
e-mail: xiangbinvanilla@163.com

Q. Gan
Chengdu High-Tech Zone Technical Innovation Service Center,
Chengdu 610041, China
e-mail: 554121730@qq.com

Y. Han (ed.), *Advances in Energy and Environmental Materials*,
Springer Proceedings in Energy, https://doi.org/10.1007/978-981-13-0158-2_41

rubber foam can be divided into solvent foaming method and chemical foaming method [10, 11]. It is too difficult to control the cell size and cell distribution in the chemical foaming. In addition, the chemical residues of the blowing agent have an important effect on the properties of silicone rubber foam. Moreover, the chemical blowing agent will lead to environmental pollution. On the other hand, solvent foaming method has a low preparative efficiency. Compared with traditional foaming methods, supercritical foaming technology exhibits a number of superiorities, such as improving mechanical properties of foams, reducing the warping and residual stress of products [12–15]. Furthermore, supercritical carbon dioxide ($scCO_2$), as a green physical blowing agent, also avoids environmental pollution generated by chemical blowing agents [16, 17].

Recently, some literature has been pain on preparing silicone rubber foam with $scCO_2$. For example, Lee et al. [18] investigated the effect of the curing degree before foaming on the final cell size of silicone rubber foams, and the microcellular liquid silicone rubber foam with a cell size of 12 μm was successfully obtained. Song et al. [19] also made preliminary attempt to uncover the effect of the pre-curing time on foam morphology and density. They firstly reported that the high temperature vulcanized (HTV) silicone rubber foam was prepared with $scCO_2$. Liao et al. [20] investigated that the viscoelastic properties of silicone rubber play a vital role in the $scCO_2$ foaming process. Yang et al. [21] prepared the microcellular HTV silicone rubber foam by controlling the foaming parameters, and the smallest cell size could reached to 9.8 μm. However, in previous studies, it is focused on how to obtain the microcellular silicone rubber foam with the supercritical fluid technology.

It is well known that the mechanical properties of silicone rubber matrix are too weak to directly use. Hence, the silicone rubber matrix must be reinforced by a great deal of fillers. Silica is often used to reinforce the silicone rubber matrix, [22] But silica easy to reunite, and easy to breathe in operation, affecting health. MMT as a new type of reinforcing filler is widely used in rubber systems, such as SSBR, EPDM, NR and so on. At present, there is little research on the effect of MMT on the properties of silicone rubber.

In this work, we investigate the effect of the montmorillonite on the rheological properties and mechanical properties of the silicone rubber composites. Then, the cellular morphology of microcellular silicone rubber foam was prepared by $scCO_2$.

Experiment

Materials. The methyl vinyl silicone rubber (VMQ) with 0.22% vinyl (110-2) was supplied by NaNjingDongjue Silicone Group Co. Ltd, China. The molecular weight of the silicone rubber was about 450,000–700,000. Hydroxyl silicone oil (GY-209-3) was supplied by Chenguang Research Institute of Chemical Industry, China. The modified fumed silica (R812S) was obtained from DEGUSSA

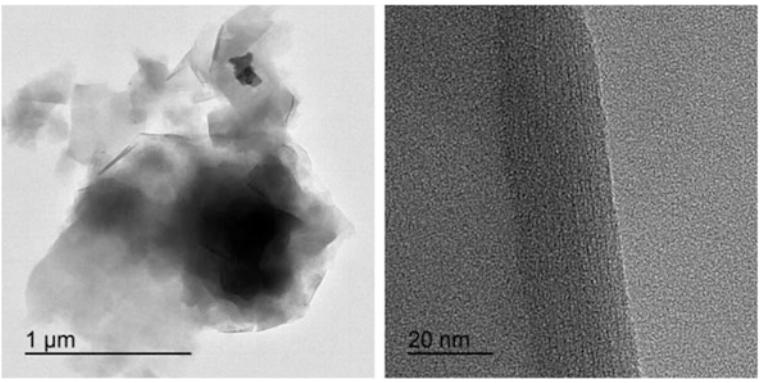

Fig. 1 TEM photograph of MMT

Corporation, Germany. Montmorillonite (MMT, DK-4),TEM image of the DK-4 are shown in Fig. 1. Dicumyl peroxide (DCP) was provided by Shanghai QianxiShanpu Chemical Co. Ltd, China.

Preparation of Silicone Rubber Composites. Firstly, methyl vinyl silicone rubber (VMQ), fumed silica, different contents of MMT and hydroxy silicone oil were put into an internal mixer (HAAKE, PolyLab OS-RheoDrive 7) at 105 °C for 30 min to obtain a rubber composite. The formulation of the silicone rubber composites was shown in Table 1 Secondly, the rubber composite and dicumyl peroxide (DCP) were thoroughly mixed in the mixer at 30 °C for 15 min.

Rheological Measurement. Silicone rubber composites were scanned by Rubber Process Analyzer (RPA2000). Measure viscoelastic response of the storage modulus (G') and viscosity (η^*) during the curing reaction for observing the curing behavior of the silicone rubber mixture at 160 °C, the frequency was 1 Hz.

TEM. Montmorillonite (DK-4) samples were dispersed into alcohol with an ultrasonic bath. The dispersion was then dropped onto a copper mesh with carbon supporting film. The TEM observation was performed with a Zriss Libra 200 electron microscope at an accelerating voltage of 200 kV.

SEM. The silicone rubber composites cellular structures of foamed samples were analyzed by an SH-5000 M scanning electron microscope (SEM).

Mechanical Properties. The composites mechanical properties (stress and strain) test by the solid rheometer (RSA G2) of TA company.

Table 1 Formulations of the silicone rubber composites

	MVQ	SiO_2	MMT	DCP
SiO_2/MVQ(30:100)	100	30	0	1
MMT-SiO_2(5:30)/MVQ	100	30	5	1
MMT-SiO_2(10:30)/MVQ	100	30	10	1
MMT-SiO_2(15:30)/MVQ	100	30	15	1

Results and Discussion

Rheological Properties of Silicone Rubber Composites. Figure 2 shows the effect of mmt content on the rheological properties of the silicone rubber composites. From Fig. 2, it is seen that the silicone rubber composites with different mmt content have the similar rheological behavior. Both the storage modulus (G') and the viscosity (η^*) are higher than the silicone rubber without mmt. And the content of mmt increases from 5 to 10 phr, the cure curves remains the same. But the G' and η^* are decrease when the content of mmt increases from 10 to 15 phr. This means that montmorillonite has a reinforcing effect on silicone rubber, With the increase of the content of montmorillonite, the reunion is serious and the reinforcement effect is decreased. In addition, with the increase of mmt content, the turning point of the viscosity curve was advanced, which means that the curing reaction of silicone rubber composites is advanced because of the increase in the content of mmt. The reason is that MMT has a adsorption effect and adsorption part of the curing agent.

The vulcanizing parameters of the silicone rubber composites were showed in Table 2. The scorching time (t_{10}) of silicone rubber composites decrease due to the addition of mmt, in contrast, the optimum cure time (t_{90}) of silicone rubber composites increased. That is to say, mmt is added to promote initial crosslinking. Meanwhile, with the growth of the content of mmt, the maximum storage torque (S'_{max}) of the silicone rubber composites gradually increases. Das et al. [23] believe that the maximum torque is the rubber molecular chain between the cross-linking density and filler on the rubber matrix reinforcement effect of the combined effect. That is, the strength of the characterization, the maximum torque has decreased, indicating that MMT and silicone rubber compatibility is poor. In the amount of MMT added 5 phr to achieve the best reinforcement effect.

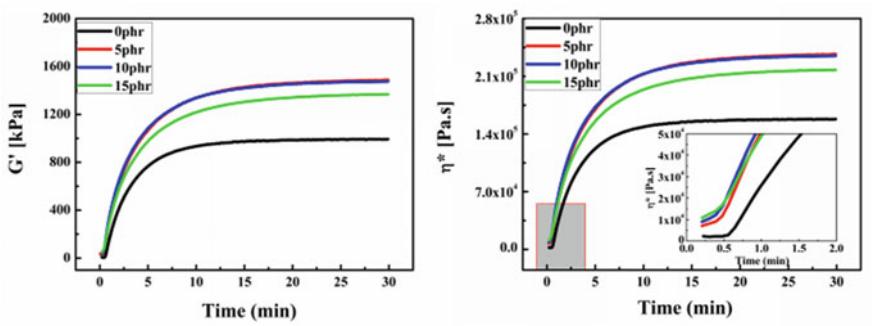

Fig. 2 Cure curves of composites with different content of MMT

Table 2 Vulcanization characteristics of composites

	t_{10} (min)	t_{90} (min)	S'_{min} (dNm)	S'_{max} (dNm)	$\Delta S'$ (dNm)
SiO_2/MVQ(30:100)	0.83	7.94	0.06	12.72	12.66
MMT-SiO_2(5:30)/MVQ	0.69	10.14	0.37	19.07	18.7
MMT-SiO_2(10:30)/MVQ	0.64	9.76	0.49	18.89	18.4
MMT-SiO_2(15:30)/MVQ	0.69	10.74	0.62	17.52	16.9

Mechanical Properties. Figure 3 can be seen, MMT added to a certain extent can improve the rubber composite stress and strain, when the mmt content of 15 phr, the stress decreased. This is due to the combining capacity between mmt lamellar and MVQ, which increases the tensile strength of the material in the fracture system. At the same time, the mmt lamellar plays a role in the physical cross-linking point in MVQ and improves the properties of the silicone rubber composite material Tensile Strength. When the MMT exceeds 15 phr, the tensile strength decreases, and the analysis indicates that this has reached the limit of the MMT intercalation MVQ. When the MMT content exceeds this limit, the MMT lamellae are agglomerated in the MVQ matrix, reducing their dispersion in MVQ. Therefore, the increase in the MMT content causes the tensile strength of the composite material to decrease. When the MMT exceeds 15 phr, the tensile strength decreases, and the analysis indicates that this has reached the limit of the MMT intercalation MVQ. When the MMT content exceeded, the MMT lamellae are agglomerated in the MVQ matrix, reducing their dispersion in MVQ. Therefore, the increase in the MMT content causes the tensile strength of the composite material to decrease.

Cell Morphology. Figure 4 shows the obtained morphologies of foamed silicone rubber by the supercritical carbon dioxide foaming process. From Fig. 4, when the content of MMT is 0 phr (that is, only silica is in the system), the silicone rubber foam with the same size and uniform in shape. At present, a few literature reported silica/silica rubber composites foams prepared by supercritical carbon dioxide, and the cell morphology can controlled by different process conditions.

With the incorporation of MMT, the cell structure changed significantly. The incorporation of MMT foam forms two different cell structures. That is to say, the MMT acts as a nucleating agent in supercritical foamed silicone rubber composites.

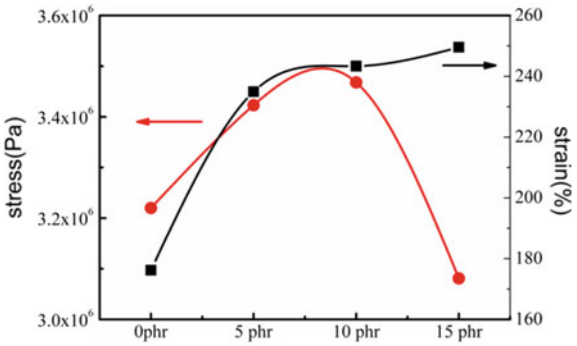

Fig. 3 Stress and strain curve with different MMT contents

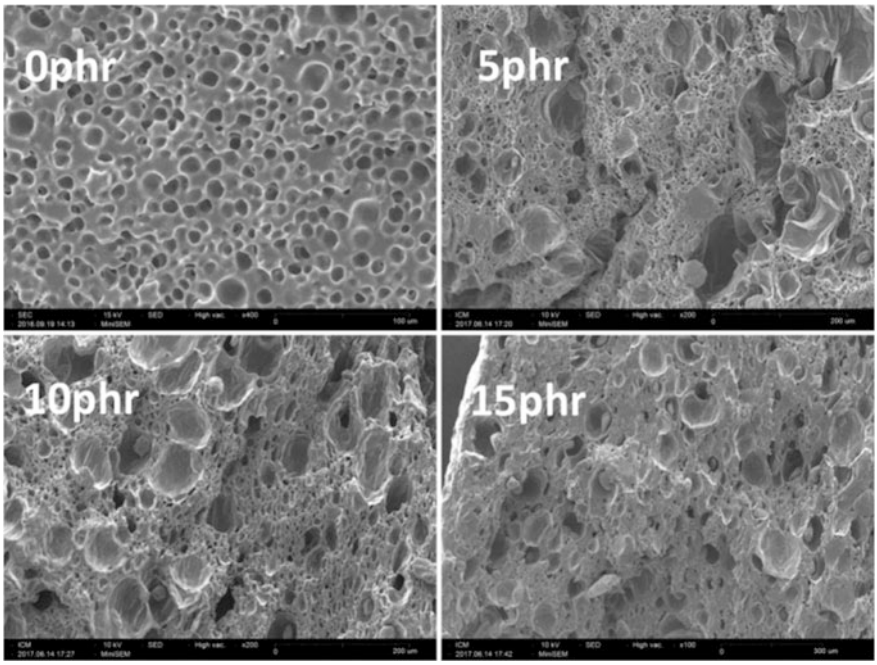

Fig. 4 SEM photographs of silicone rubber foams with the different content of MMT

As the content of MMT increases, the irregular cells formed tend to be regular and the cell size decreases. When the content of MMT is 15 phr, the cell density decrease, and cell size decrease. Hu et al. [24] study the effect of MMT content on CO_2 solubility and diffusion in PP/MMT composites, and to obtain the effect of nucleating agent content on cell quality. The composite material with the increase of the content of laminar MMT, to prevent the movement of its molecular chain, free volume reduction, help to reduce cell rupture. Exceeding this limit will inhibit cell nucleus growth and reduce cell mass.

Conclusions

1. The content of MMT is 5 phr, the reinforcement effect is the best, continue to increase, agglomeration is serious, making the reinforcement weakened.
2. The addition of montmorillonite improves the mechanical properties of the silicone rubber composites. When the content of montmorillonite is 10 phr, the stress and strain are the best.
3. MMT as a nucleating agent has been successfully used in supercritical carbon dioxide foam silicone rubber composite materials.

Acknowledgements This work is financially supported by a major frontier project of Sichuan Province, (Grant No. 2017JY0101).

References

1. N.L. Zhou, *Introduction of Silicone Polymer* (Science Press, Beijing, 2000)
2. R.W. Hergenrother, X.H. Yu, S.L. Cooper, Blood-contacting properties of polydimethyl siloxane polyurea-urethanes. Biomaterials **15**(8), 635–640 (1994)
3. Y.B. Kim, D. Cho, W.H. Park, Fabrication and characterization of TiO_2/poly(dimethyl siloxane) composite fibers with thermal and mechanical stability. J. Appl. Polym. Sci. **116**(1), 449–454 (2010)
4. R. Hernandez, J. Weksler, A. Padsalgikar, In vitro oxidation of high polydimethylsiloxane content biomedical polyurethanes: correlation with the microstructure. J. Biomed. Mater. Res. **87**(2), 546–556 (2008)
5. E.-S. Park, Mechanical properties and antibacterial activity of peroxide-cured silicone rubber foams. J. Appl. Polym. Sci. **110**, 1723–1729 (2008)
6. A.H. Landrock, *Glossary-Handbook of Plastic Foams*. (1995), pp. 456–481
7. P. Liu, D. Liu D, H. Zou, Structure and properties of closed-cell foam prepared from irradiation crosslinked silicone rubber. J. Appl. Polym. Sci. **113**(6), 3590–3595 (2009)
8. J.B. Grande, A.S. Fawcett, Anhydrous formation of foamed silicone elastomers using the Piers–Rubinsztajn reaction. J. Mclaughlin. Polym. **53**(15), 3135–3142 (2012)
9. J. Ling, W. Zhai, W. Feng, Facile preparation of lightweight microcellular polyetherimide/graphene composite foams for electromagnetic interference shielding. Appl. Mater. Interfac. **5**(7), 2677–2684 (2013)
10. K.A. Arora, A.J. Lesser, T.J. Mccarthy, Preparation and characterization of microcellular polystyrene foams processed in supercritical carbon dioxide. Macromolecules **31**(14), 4614–4620 (1999)
11. J.J. Chruściel, E. Leśniak, Preparation of flexible, self-extinguishing silicone foams. J. Appl. Polym. Sci. **119**(3), 1696–1703 (2010)
12. L.J.M. Jacobs, M.F. Kemmere, J.T.F. Keurentjes, Sustainable polymer foaming using high pressure carbon dioxide: a review on fundamentals, processes and applications. Green Chem. **10**(7), 731–738 (2008)
13. A. Gandhi, N. Asija, K.K. Gaur, S.J.A. Rizvi and V. Tiwari, Ultrasound assisted cyclic solid-state foaming for fabricating ultra-low density porous acrylonitrile–butadiene–styrene foams. Mater. Lett. **94**(94), 76–78 (2013)
14. W. Yao, D. Zhu, J. Liu, X. Yu and X. Ma, Silicone rubber as a novel insulating material for manufacturing cylindrical glass carbon fiber electrodes. Mater. Lett. **79**(23), 159–162 (2012)
15. H. Cochrane, C.S. Lin, The influence of fumed silica properties on the processing, curing, and reinforcement properties of silicone rubber. Rubber Chem. Technol. **66**(1), 48–60 (1993)
16. B. Krause, G.H. Koops, N. Vegt, Ultralow-k dielectrics made by supercritical foaming of thin polymer films. Adv. Mater. **14**(15), 1041–1046 (2002)
17. K.A. Seeler, V. Kumar, Tension-tension fatigue of microcellular polycarbonate: initial results. J. Reinf. Plast. Compos. **12**(3), 359–376 (1993)
18. I.K. Hong, S. Lee, Microcellular foaming of silicone rubber with supercritical carbon dioxide. Korean J. Chem. Eng. **31**(1), 166–171 (2014)
19. L. Song, A. Lu, P. Feng, Z. Lu, Preparation of silicone rubber foam using supercritical carbon dioxide. Mater. Lett. **121**(121), 126–128 (2015)
20. X. Liao, H. Xu, S. Li, C. Zhou, G. Li, C.B. Park, The effects of viscoelastic properties on the cellular morphology of silicone rubber foams generated by supercritical carbon dioxide. RSC Adv. **5**(129), 106981–106988 (2015)

21. Q. Yang, H. Yu, L. Song Y. Lei, F. Zhang, A. Lu, T. Liu, Solid-state microcellular high temperature vulcanized (HTV) silicone rubber foam with carbon dioxide. J. Appl. Polym. Sci. **134**(20) (2017)
22. H. Cohrane, C.S. Lin, The influence of fumed silica properties on the processing, curing and reinforcement properties of silicone rubber. Rubber Chem. Technol. **66**(1), 48 (1993)
23. A. Das, F.R. Costa, U. Wagenknecht, Nanocomposites based on chloroprene rubber: effect of chemical nature and organic modification of nanoclay on the vulcanizate properties. Eur. Polym. J. **44**(11), 3456–3465 (2008)
24. D. Hu, C. Jie, S. Sun, Solubility and diffusivity of CO_2 in isotactic polypropylene/nanomontmorillonite composites in melt and solid states. Ind. Eng. Chem. Res. **53**(7), 2673–2683 (2014)

Effect of Interface Layer on Compressive Deformation of SiCp/7075 Composites

Xiaohong Wang, Hailun Wang, Shilong Tang, Yuanhua Lin, Shu Wang and Zhengwei Peng

Abstract The oxidation or electroless nickel plating of SiC particles are two modification processes to improve the wettability of SiCp/Al interface. Studying the effects of this interface layer on compressive deformation of SiC particle reinforced aluminum matrix composites is helpful to optimising this compression process. In this paper, Deform-3D software was used to simulate the compression deformation behavior of 6.5% vol SiCp/7075 composites with SiO_2 or Ni interface layer. And the effects of interface layer materials on the temperature field, stress field, strain field and damage factor happening in the compression process were also analyzed. Simulation results show that, the maximum temperature, tensile stress, maximum effective strain and the damage factor of the Al matrix with Ni interface material are 0.6206 °C, 53 MPa, 5.70% and 0.0124 respectively more than the Al matrix with SiO_2 interface layer respectively. The simulation results are good agree with the experimental result.

Keywords SiCp/7075 composites · SiO_2 (SiC)/Al · Ni (SiC)/Al Finite element analysis

X. Wang (✉) · H. Wang · S. Tang · Y. Lin · S. Wang · Z. Peng
Department of Materials Science and Engineering,
Southwest Petroleum University, Chengdu 610500, China
e-mail: xhwang3368@swpu.edu.cn

H. Wang
e-mail: 386160742@qq.com

S. Tang
e-mail: 1105541696@qq.com

Y. Lin
e-mail: yhlin28@163.com

S. Wang
e-mail: 13085639509@163.com

Z. Peng
e-mail: 201521000670@stu.swpu.edu.cn

Y. Han (ed.), *Advances in Energy and Environmental Materials*,
Springer Proceedings in Energy, https://doi.org/10.1007/978-981-13-0158-2_42

Introduction

Particle reinforced metal matrix composites (PMMCs), which have a wide range of applications, generally have a higher specific strength and specific stiffness than the matrix material. In particular, silicon carbide particles reinforced aluminum matrix composites (SiCp/Al), which has a variety of characteristics, such as high specific strength, good thermal stability, high wear resistance, low density and so on, owns the largest potential in the field of oil drilling [1–3]. Because of the nonwettability of the SiC/Al interface, the oxidation or electroless nickel plating of SiC particles are two modification process to improve the wettability of SiCp/Al interface [4, 5]. It can effectively improve the SiC/Al interface wettability [6]. Moreover, moderate interface reaction can improve the elastic modulus of the composites [7], and the nickel-plated layer which has a high strength can be chemically bonded to the matrix [8].

In this paper, the microstructure compression process of two different interface materials is simulated. And analysis of the effect of interfacial layer materials on temperature, stress, strain and damage is also conducted. Finally, using an experiment verify the accuracy of this simulation results. The purpose of this simulation is to study the effect of interface layer material on compressive deformation.

Finite Element Molding

Geometric Model. The model is designed by PRO-E software, shown in Fig. 1. Considering the symmetry of deformation in the SiCp/7075 composites microstructure, we establish the 1/2 models. And the SiCp/7075 composites microstructure is compressed between two primary dies and one bottom die.

This part are assembled as shown in Fig. 2. In the process of simulation, the elastic deformation of matrix and interface layer is much smaller than that of plastic deformation, so that the matrix and interface layer are made of plastic, while the die and particle are made of rigid. Firstly, the overall temperature is set with 400 °C [9]. Secondly, the mesh is divided into two parts, one is the matrix mesh that is

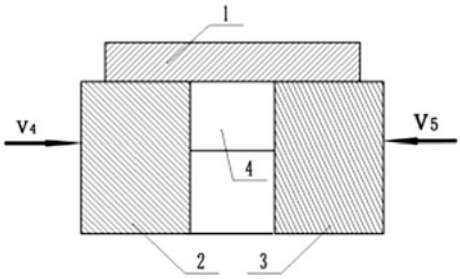

Fig. 1 The geometric model. 1-bottom die, 2, 3-primary die, 4-SiCp/7075 composites microstructure

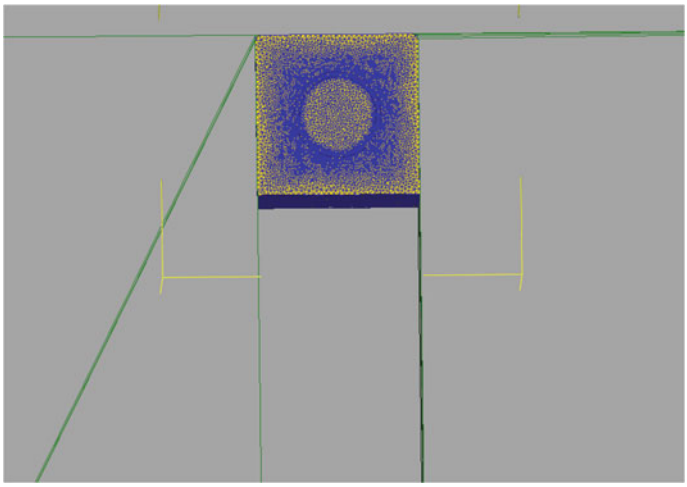

Fig. 2 The finite element model

quadrilateral and its number is 80,000, another one is the interface layer that is quadrilateral mesh and its number is 25,000. Thirdly, we adopted the Lagrangian-Euler finite element method. Fourthly, the convection coefficient between the matrix and air is 0 $N{\cdot}s^{-1}{\cdot}mm^{-1}{\cdot}C^{-1}$ and the interface layer is sticking condition to the matrix and the particles, with heat transfer coefficient of 11 $N{\cdot}s^{-1}{\cdot}mm^{-1}{\cdot}C^{-1}$ and no friction [10, 11]. There is no friction and no heat exchange between the matrix and the die [10, 11]. Finally, the compression rate is $0.03{\cdot}s^{-1}$. In order to ensure the accuracy of calculation, the step length is 1/3 matrix minimum grid constant.

The assumptions in this simulation process as follows: the connection between particles and matrix is ideal [12], the connection between particles and interface layer is ideal [12], and interface layer reaction is ignored.

Material Model. In the simulation, all calculation were carried out by using deform-3D software. The material used in this simulation was 7075 aluminum alloy which flow stress models is given by [13]:

$$\dot{\varepsilon} = 1.3769 \times 10^{12}[\sinh(0.013546\sigma)]^{6.71533}\exp\left[-193.692 \times 10^{3}/8.314(RT)\right] \quad (1)$$

for flow stress models, where $\dot{\varepsilon}$ is Strain rate, σ is Flow stress, R is Gas constant and T is Deformation of absolute temperature.

For this material, its young's modulus is 68,900, poisson's ratio is 0.3, thermal conductivity is 180.175 and heat capacity is 0.96, respectively [14].

The Damage model is given by [15, 16]:

$$C = \int^{\bar{\varepsilon}_F} \frac{\sigma^*}{\bar{\sigma}} d\bar{\varepsilon} \tag{2}$$

for Damage model, where C is Damage factor, $\bar{\sigma}$ is equivalent stress, $\bar{\varepsilon}$ is equivalent strain, $\bar{\varepsilon}_F$ is the equivalent strain at break and σ^* is Maximum principal stress.

SiO_2 and Ni are used as interface layer material. The flow stress models of SiO_2 and Ni are given by the existing literature [17, 18]:

$$\bar{\sigma} = \left(1200 + 891\bar{\varepsilon}^{0.2}\right)\left(1 + 0.02\ln\left(\frac{\dot{\bar{\varepsilon}}}{\dot{\bar{\varepsilon}}_0}\right)\right)\left(1 - \left(\frac{T-20}{1712}\right)^{0.64}\right) \tag{3}$$

$$\bar{\sigma} = \left(1200 + 891\bar{\varepsilon}^{0.2}\right)\left(1 + 0.02\ln\left(\frac{\dot{\bar{\varepsilon}}}{\dot{\bar{\varepsilon}}_0}\right)\right)\left(1 - \left(\frac{T-20}{2115}\right)^{0.64}\right) \tag{4}$$

flow stress models, where $\bar{\varepsilon}$ is Strain rate, $\dot{\bar{\varepsilon}}_0$ is Initial average strain rate, $\dot{\bar{\varepsilon}}$ is Average strain rate and T is Deformation of absolute temperature.

For Ni as the interface layer material, the thermal conductivity is 90 and heat capacity is 0.46, while the thermal conductivity is 16.7 and heat capacity is 0.71 of SiO_2 as the interface layer material [14].

Simulation Results and Discussion

Effect of Interface Material on the Temperature Field. Figures 3 and 4 show the microstructure temperature field of the interface layer material for Ni and SiO_2 6.5%, SiCp/7075 composite, respectively. As is shown in pictures, for the Ni interface material, with the matrix near the interface layer part, the maximum temperature located in parallel with the direction of compression position reaches at 403.7373 °C, and the minimum temperature is located in vertical with the direction of compression reaches at 403.7370 °C. On the interface layer, the maximum temperature located in parallel with the direction of compression position reaches at 403.4521 °C, and the minimum temperature located in vertical with the direction of compression reaches at 403.4516 °C. For the SiO_2 interface material, with the matrix near the interface layer part, the maximum temperature located in parallel with the direction of compression position reaches at 403.1097 °C, and the minimum temperature located in vertical with the direction of compression reaches at 403.1050 °C. On the interface layer, the maximum temperature located in parallel with the direction of compression position reaches at 397.2620 °C, and the

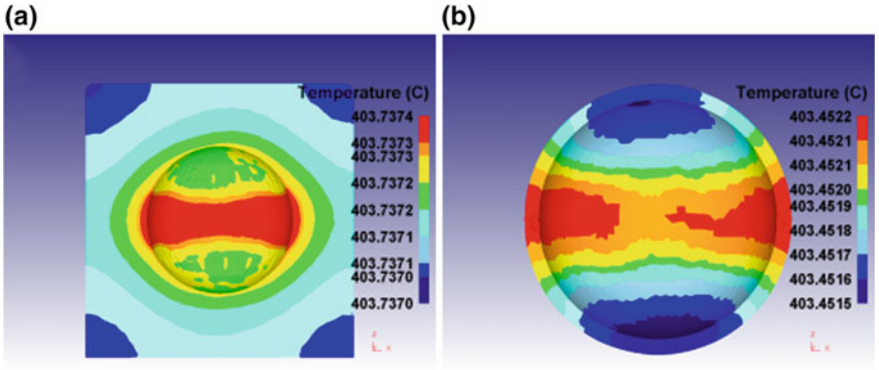

Fig. 3 For the Ni interface material, the temperature distribution of 6.5%SiCp/7075 composite microstructure. **a** matrix, **b** interface layer

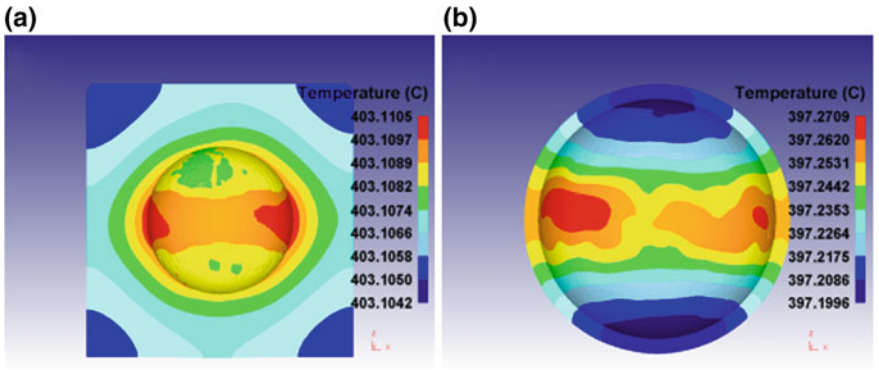

Fig. 4 For the SiO_2 interface material, the temperature distribution of 6.5%SiCp/7075 composite microstructure. **a** matrix, **b** interface layer

minimum temperature located in vertical with the direction of compression reaches at 397.2086 °C (Fig. 4).

Because of the thermal conductivity different on the interface layer, the temperature of matrix near the interface layer parts is higher. This is similar to the result that the effect of Continuous-distribution Inter-phase on the thermal conductivity of SiCp/Al Composites by using Numerical Simulation Method [19]. At the same time, Ding et al. found that temperature is one of the factors influencing the breaking limit of 7075 Aluminum Alloy [20].

Effect of Interface Material on Maximum Principal Stress. Figures 5 and 6 show the microstructure maximum principal stress distribution of the interface layer material for Ni and SiO_2 6.5%SiCp/7075 composite, respectively. As shown, the change of interface material does not affect the maximum principal stress of the

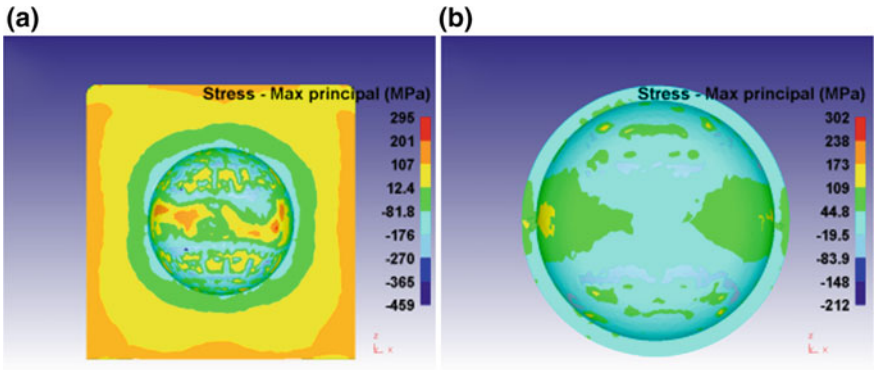

Fig. 5 For the Ni interface material, the maximum principal stress distribution of 6.5%SiCp/7075 composite microstructure. **a** matrix, **b** interface layer

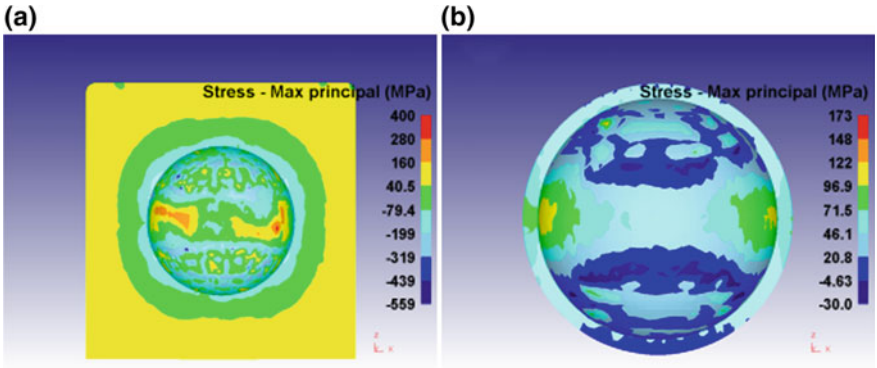

Fig. 6 For the SiO_2 interface material, the maximum principal stress distribution of 6.5%SiCp/7075 composite microstructure. **a** matrix, **b** interface layer

ring. For the Ni interface material, the maximum principal stress of the matrix near the interface layer is mainly tensile stress, which the maximum reaches at 107 MPa. However, the maximum of SiO_2 interface material is higher than the Ni interface material to reach 160 MPa. It can be seen that the change of interface material has a great influence on the maximum principal stress in the interface layer. For the Ni interface material, the maximum principal stress in the interfacial layer is mainly tensile stress, which the maximum reaches at 109 MPa. But for the SiO_2 interface material, the maximum principal stress in the interfacial layer is mainly compressive stress, which the maximum reaches at 4.63 MPa.

This is mainly caused by the difference in the heat capacity of the interfacial materials. Moreover, the results are similar to the effects of interfacial properties on the thermal residual stress of the metal matrix composites [21]. The residual stress is tensile stress in the interfacial layer that will result in radial crack initiation [22].

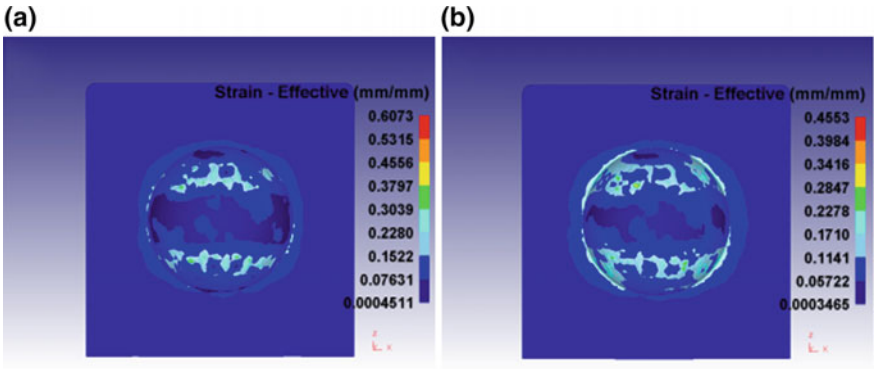

Fig. 7 The maximum effective strain distribution of 6.5%SiCp/7075 composite microstructure, **a** with Ni/Al interface layer, **b** with SiO_2/Al interface layer

Effect of Interface Material on Effective Strain. In the compression process of microstructure molding, the strain distribution on matrix is not uniform. Figure 7a and b reveal the microstructure effective strain distribution of the interface layer material for Ni and SiO_2 6.5%SiCp/7075 composite, respectively. For the Ni interface material, the maximum effective strain of the matrix is 0.2280 mm·mm^{-1}, which is located near the the interface of the matrix and 45° in the compression direction. For the SiO_2 interface material, the maximum effective strain of the matrix is 0.1710 mm·mm^{-1}, which is located near the the interface of the matrix and 45° in the compression direction. It is obvious that the maximum effective strain of the Ni interface material is 0.0570 mm·mm^{-1} higher than SiO_2 interface material. This is mainly because that the maximum principal stress is compressive stress, and the value of stress is larger, in that position. The result is similar to simulation of the strain rate sensitive flow behavior of SiC-particulate reinforced aluminum metal matrix composites [23].

Effect of Interface Material on Damage Factor. Figure 8 shows the damage factor distribution of the interface layer material for Ni and SiO_2 6.5%SiCp/7075 composite, respectively. As is shown in pictures, for the Ni interface material, the maximum damage factor of the matrix near the interface part reaches at 0.04865, and for the SiO_2 interface material, the maximum damage factor of the matrix near the interface part reaches at 0.03625. It is obvious that the damage factor of the Ni interface material is 0.01240 higher than SiO_2 interface material. And from the center to the surface, the damage will reduce gradually.

For the Ni interface material, the temperature, the tensile stress, and the effective strain of the matrix near the interface is 0.6206 °C, 53 MPa, and 0.0570 mm·mm^{-1} than that of the interface material is SiO_2. With the number of dislocation produced in the process of compression increased, the damage factor under the comprehensive process is bigger, so that the damage factor is 0.01240 than that of the interface material is SiO_2. This result is basically consistent with the study of Ding et al. about the high temperature deformation and breaking limit of 7075 aluminum alloy [20].

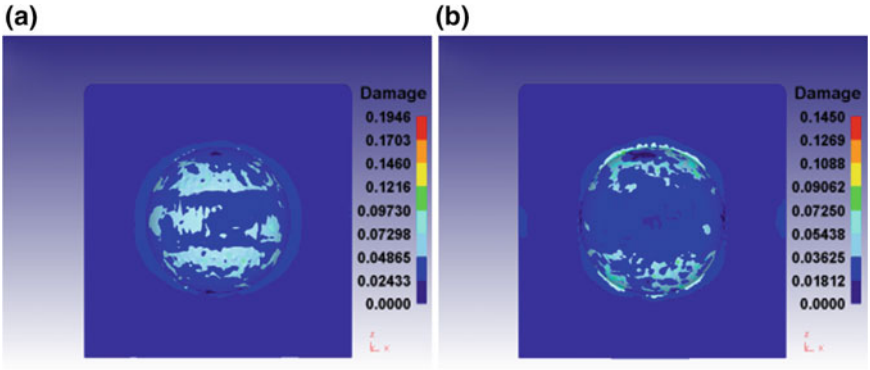

Fig. 8 The damage factor distribution of 6.5%SiCp/7075 composite microstructure, **a** with Ni/Al interface layer, **b** with SiO_2/Al interface layer

Experimental Work

To verify the simulation results, the high temperature compression tests were carried out using INSTRON 8801 testing machine. The material of the compression tests samples is 6.5%vol SiCp/7075 composites-ingot with SiO_2/Al or Ni/Al interface layer which is same with the material used in the simulation calculation. The further details of the SiCp/7075 composites plate preparation process are described by [24, 25]. The compression specimens are cylindrical with a diameter 8.15 mm and the length of 10 mm, which are cut from composite ingot without casting defects. The compression testing were carried out at 400 °C under the constant strain rate 0.03 s^{-1} until the compression ratio is up to 60%. All the parameter of the compression testing were agree with the simulation calculation.

Figure 9 shows the stress-strain behavior of the two materials obtained by the high-temperature compression experiment. Considering these diagrams, the sample of SiO_2(SiC)/7075 has the highest amount of compressive strength which is 403 MPa. As is shown in picture, the compressive strength of the SiO_2(SiC)/7075 composite is higher than that of Ni(SiC)/7075 composite, which indicates that SiO_2(SiC)/7075 composite can withstand the larger compressive stress. Figure 10 shows the morphology of the compressed samples. As is shown above, for the Ni interface material, the surface has three obvious cracks, one of them is 5 mm long and 0.3 mm wide and another crack is 3.5 mm long and 0.5 mm wide, and the third crack is 3 mm long and 0.7 mm wide. However, for the SiO_2 interface material, the surface has two obvious cracks, one crack is 3.5 mm long and 0.2 mm wide and the other one is 2 mm long and 0.15 mm wide. The results obvious that when the interface layer is SiO_2, the cracks is small, which is consistent with the simulation results.

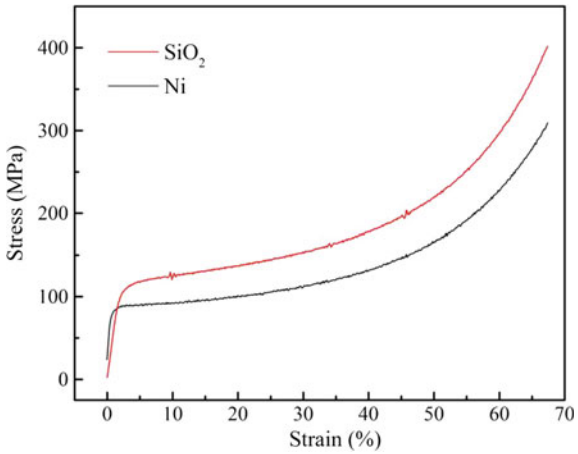

Fig. 9 Stress-strain curve of the compression sample with Ni/Al or with SiO_2/Al interface layer

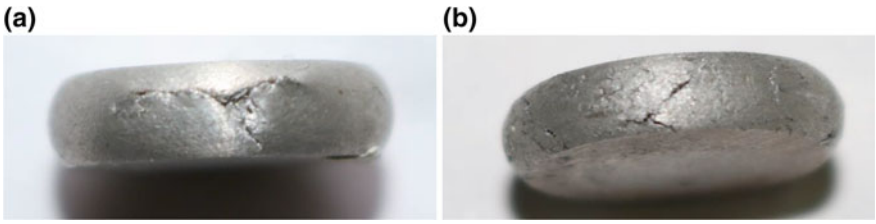

Fig. 10 Morphology of the compressed samples, **a** the compression sample with Ni/Al interface layer, **b** the compression sample with SiO_2/Al interface layer

Conclusions

Under comprehensive analysis, the damage factor of the Al matrix with Ni/Al interface layer is 0.0124 more than the Al matrix with SiO_2 interface layer under the same simulation conditions. And the compressed sample with Ni/Al interface layer has more cracks than that with SiO_2/Al interface layer and the depth of these cracks of the compressed sample with Ni/Al interface layer deeper than that with SiO_2/Al interface layer under the same compression conditions. The simulation results are agreed with the results of the compression testing. The SiCp/7075 composites with SiO_2/Al interface layer has better anti-cracking performance during the compressive deformation.

References

1. M.K. Surappa, Aluminium matrix composites: challenges and opportunities. Sadhana **28**(1–2), 319–334 (2003)
2. R.Q. Wang, J.P. Xie, W.J. Wu et al., Influence of SiCp pretreatment on microstructure and performance of SiCp/Al–Si composite. Powder Metall. Ind. **24**(6), 33–36 (2014)
3. W.J. Wu, A.Q. Wang, R.Q. Wang, Domestic research progress of Al–Si matrix composites reinforced by SiC particles. Powder Metall. Ind. **06**, 54–57 (2014)
4. J. Narciso, C. García-Cordovilla, E. Louis, Reactivity of thermally oxidized and unoxidized SiC particulates with aluminium–silicon alloys. Mater. Sci. Eng. B **15**(2), 148–155 (1992)
5. Trespaillébarrau P, Suéry M, Microstructural and mechanical characterisation of aluminium matrix composites reinforced with Ni and NiP coated SiC particles via liquid processing. Mater. Sci. Technol. **10**(6), 497–504 (2013)
6. X.H. Wang, Y. Ye, S. Wang et al., Research progress on wettability of SiC/Al interface layer in aluminum matrix. New Technol. New Process (4), 1–6 (2017)
7. Y. Cui, Effect of a slight interfacial reaction on the young's modulus of SiCp/6061A1 composite. Acta MateriaeCompositaeSinica **5**(1), 74–77 (1998)
8. L.B. Li, M.Z. An, G.H. Wu, Study on adhesion mechanism of SiC_p/Al composites and electroless nickel coating. Chin. J. Inorg. Chem. **21**(7), 982–986 (2005)
9. Dr. C.M. William, Dr. C.M. William. Implement Russian aluminum drill pipe and retractable drilling bits into the USA volume I: development of aluminum drill pipe in Russian. Off. Sci. Tech. Inf. Tech. Rep. (1999)
10. Reference to a book: ISBN 978-7-122-01224-1
11. X.K. WU, *Aluminium Profiles Extrusion Applied Technical Manual* (Middle and Southern University press, Changsha, 2006)
12. F. Xu, Y.L. Li, W.G. Guo et al. Influences of Particle Shape, Volume Fraction and Matrix Materials. Acta Materiae Compositae Sinica **20**(6), 36–41 (2003)
13. Z.Y. Li, *Research On Fracture In Multi-Way Loading Forming Process Of 7075 Aluminum* (Northwestern Polytechnical University, Xi'an, 2010)
14. Information on DEFORM-3D material library
15. H.J. Mcqueen, S. Yue, N.D. Ryan et al., Hot working characteristics of steels in austenitic state. J. Mater. Process. Technol. **53**(1–2), 293–310 (1995)
16. C.M. Sellars, W.J. Mctegart, On the mechanism of hot deformation. Acta Metall. **14**(9), 1136–1138 (1966)
17. W.U. Ong-Dan, H. Zhang, S. Chen et al., Trans. Nonferr. Metals Soc. Chin. **25**(3), 692–698 (2015)
18. G.Q. Wei, Y.J. Guan, L.H. Zhu, et al., Study on numerical simulation of hot extrusion process of automobile's hollow front Axle. Modern Manuf. Technol. Equip. (6), 81–83 (2016)
19. A.H. Zou, X.L. Zhou, X.Z. Hua et al., J. Inorg. Mater. **30**(12), 1283–1290 (2015)
20. L. Ding, J. Chen, K. Zheng, et al., J. Plast. Eng. (6), 157–161 (2016)
21. M.N. Yuan, Y.Q. Yang, B. Huang, et al., Effect of interfacial properties on thermal residual stress in metal matrix composite. Trans. Mater. Heat Treat. **33**(6), 174–178 (2012)
22. S.G. Warrier, D.B. Gundel, B.S. Majumdar et al., Metall. Mater. Trans. A. **27**(7), 2035–2043 (1996)
23. İ. Tirtom, M. Güden, H. Yıldız, Comput. Mater. Sci. **42**(4), 570–578 (2008)
24. Y.C. Guo, C. Cao, J.P. Li et al., Research on high temperature oxidation behavior of SiC and interface of al based composite. Hot Work. Technol. (8), 131–134 (2016)
25. Y. Ye, *Study on the Dispersity and Interface Behavior of Reinforced Phase of Sicp/Al–Cu–Mg Composites* (Southwest Petroleum University, 2017)

Mechanical Properties and Microstructure of Oil Well Cement Stone Reinforced with Potassium Titanate Whiskers

Jiaming Yu, Ming Li, Xihui Hu, Jianhua Guo and Quan Cao

Abstract The cement base material is one of the brittle materials. Under the complex downhole stress this kind of material easily failed and the sealing integrity was decreased. In this case the potassium titanate whiskers (PTW) improved the mechanical properties and microstructure of oil well cement. Scanning electron microscope (SEM) analysis and the mechanical testing were carried out. The result shows that the compressive, splitting tensile and flexural strength increased by 27.5, 110.5 and 30.7% respectively with the addition of 1.5% PTW after curing for 7 days. And the whisker pullout, crack deflection and whisker bridging are regarded as the effective mechanisms for the addition of potassium titanate whiskers to improve the mechanical properties and microstructure of oil well cement.

Keywords Oil well cement · Potassium titanate whiskers · Mechanical properties Microstructure · Toughening mechanism

J. Yu · M. Li (✉)
School of Materials Science and Engineering,
Southwest Petroleum University, Chengdu 610500, China
e-mail: 18555440762@126.com

J. Yu
e-mail: 770556948@qq.com

X. Hu · J. Guo · Q. Cao
Engineering Technology Institute of Petro China Southwest Oil and Gas Field Company, Chengdu, China
e-mail: huxihui@cnpc.com.cm

J. Guo
e-mail: guojianhua@cnpc.com.cn

Q. Cao
e-mail: caoquan@cnpc.com.cn

Y. Han (ed.), *Advances in Energy and Environmental Materials*,
Springer Proceedings in Energy, https://doi.org/10.1007/978-981-13-0158-2_43

Introduction

The property of cement sheath is a key factor of which affect the resources exploitation and storage in the oil well engineering [1]. With the exploitation of oil and gas gradually moving to deep, low permeability ocean and unconventional, the demand for the properties of cement stone goes higher and higher. The cement-based materials are one of the brittle materials, of which has a high compressive strength and elastic modulus and lower tensile strength, which results in the relatively obvious brittle characteristic in the fracture failure process. The stress from perforation and fracturing brings lot of micro-cracks in cement, leading to the destruction of the cementing integrity [2–4]. Many domestic scholars have found that whisker can improve the mechanical properties of cementitious composites [5, 6]. Various organic whisker used in the current well cementing engineering, such as calcium carbonate and magnesium borate whisker, to improve the toughness of cement stone to some extent, and they have advantages of low cost [7, 8]. PTW is a kind of single crystal fibrous material that grows in single crystal form, which length-diameter ratio is greater than ten and the size is much smaller than the short fiber. PTW has both the characteristics of mineral powder and fibers, and good compatibility with cement-based materials [9, 10]. Therefore, PTW is considered to be a promising reinforcing material because of its unique physical property. This research was to assess the influence of PTW on the mechanical properties and microstructure of oil well cement stone, and discuss the toughening mechanism.

Experimental Materials and Methods

Raw materials. The cement class is used class G oil-well cement, of which the chemical composition presented in Table 1. PTW were commercially available material from Nantong Auxin Electronic Technology Co. Ltd., Nantong, China. Other admixture such as fluid loss agent G33S and dispersant SXY-2 commercially obtained in China.

Experimental methods. Electronic hydraulic testing machines from Beijing Haizhi Technology Co. Ltd was used to measure tensile and compressive properties at a crosshead speed of 600 N/s. Motorized bending testers from Wuxi Jianyi Instrument & Machinery Co. Ltd was used to measure flexural properties with

Table 1 Chemical composition of class G oil-well cement as analyzed by X-ray fluorescence (XRF)

Composition	SiO_2	Al_2O_3	Fe_2O_3	CaO	MgO	K_2O	SO_3	MnO_2	Loss on ignition
Content (wt %)	22.7	3.39	4.81	65.5	0.9	0.37	1.21	0.09	0.25

3-point-bending with span and crosshead speed of 100 mm and 0.02 mm/min. Furthermore, the scanning electron microscope (SEM, JSM-6510LV) from Japan JEOL was used to observe the microstructure of the PTW and the fracture surface of the specimens.

Results and Discussion

Fractured surface morphology. The structure of oil-well cement stone formed is connected with the hydration and its products during the hardening process. As the schematic diagram shown below, Fig. 1a shows the virgin cement after curing for 7 days, it can see clearly the photo that the matrix structure was relatively loose and a lot of gap. This un-compacted structure frequently affects the cement matrix strength. Figure 1b shows the 1.5% PTW in reinforced cement after curing for 7 days, from the photos can be clearly seen the surface of cement matrix inlaid a large amount of tiny PTW, and there were little PTW pulling out from the surface of cement matrix. Therefore, there were no clear gap between cement matrix and PTW. As shown in the figure, the PTW embedded in cement matrix and a certain amount of fractured PTW pulling out can be observed, indicating that PTW might improve pull-out drag from cement matrix because of their higher length/diameter ratio, leading to increase the absorption and consumption of energy during the process of cement matrix damage. From these morphological analyzed above, PTW has better miscible or compatible with cement. Strong ability of adhesion formed between PTW and cement matrix will promote preferable stress transfer from the breakdown matrix to the PTW.

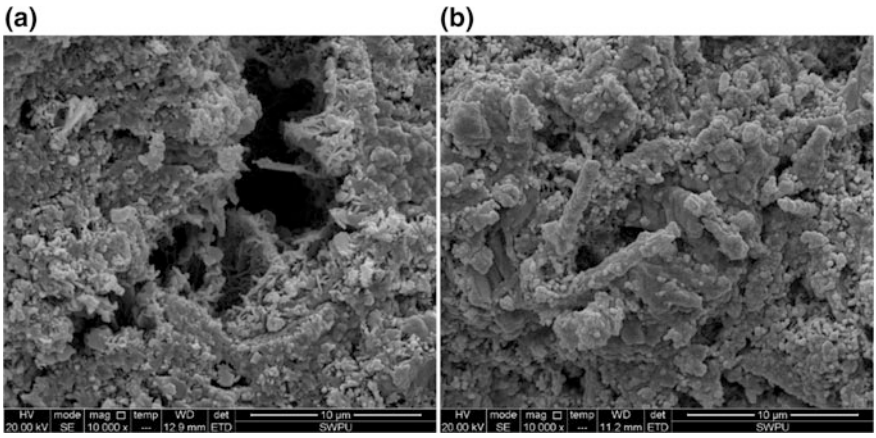

Fig. 1 The scanning electronic microscope photography of virgin cement sample

Mechanical properties. The effects of PTW content on the mechanical properties of cement solidification body under the different aging time at 3d and 7d (curing temperature of 60 °C) are shown in Fig. 2a–c respectively. From the figures can be seen that the strength of the virgin cement and whiskers reinforced cement show stable increase with the increase of hydration time. The decrease of the strength at 2% attributed to PTW dispersion is poor in cement leaded to PTW turn into a source of defect in the matrix. When the cement hydration time at 7 days, compared with virgin cement specimens, the average compressive strength, splitting tensile strength and flexural strength of the reinforced cement improve from 24.4 to 31.3 Mpa, 1.9 to 4 Mpa, 6.5 to 8.5 Mpa, increased by 27.5, 110.5 and 30.7% respective. Similar literature reported for mechanical properties of PTW in cement-based materials [11]. By increasing the content of PTW means there is more PTW exists within the cement matrix pullout from the fractured surfaces, which results in preferable stress transfer ability of cement matrix. With all property improvements comprehensively considered, the most effective dosage of PTW was 1.5%.

Toughening mechanism. The microstructure of oil cement stone analyzed by SEM, the microscopic mechanism of reinforcement by PTW consists of whisker bridging, crack deflection and whisker pullout. Observation under microscopy shows that PTW embedded in cement matrix with PTW (Fig. 3a–d). When a crack

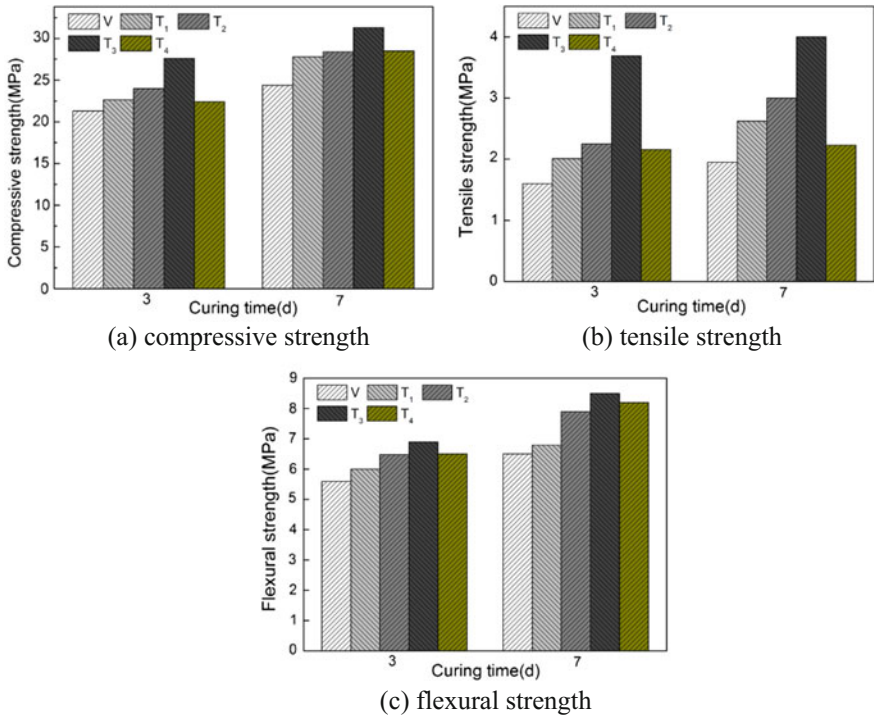

Fig. 2 **a** compressive strength **b** tensile strength **c** flexural strength

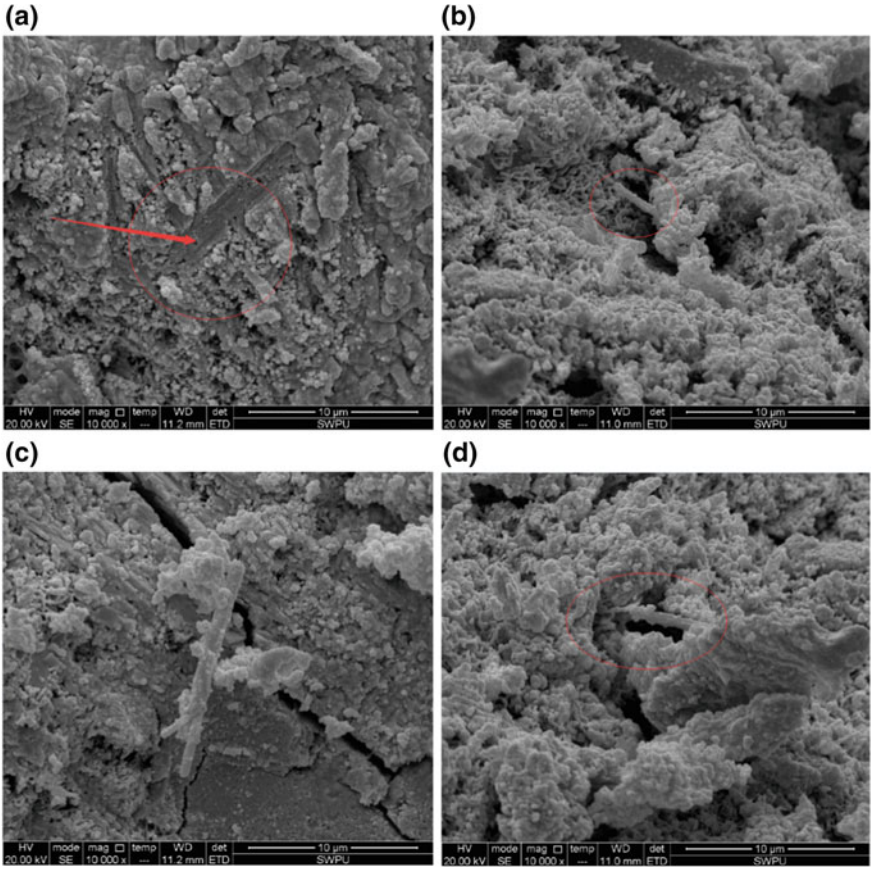

Fig. 3 The scanning electronic microscope photography of cement composites

extends to a whisker, since the whisker higher in mechanical strength, withstands the external load and bridges the opposite sides of the crack, the crack would need to consume more power to propagate further. Because the whisker and cement matrix are different in mechanical properties and there is an interface between them, when the shear stress acted on the whisker is greater than the whisker-matrix interface bond, the whisker will be pulled out (Fig. 3a–b), the stripping and rubbing of the whisker and matrix interface will prevent the crack propagation. When a crack extends to the area of PTW (Fig. 3c), the original crack propagation direction is limited, because of the weakness of whisker-cement interface, the crack will extend along the interface, due to the increase of crack propagation path, and the energy damaging cement will be consumed, leading to the enhancement in cement stone strength and toughness. At the same time, in the process of crack propagation if the whiskers span the sides of the crack (Fig. 3d), because of the pinning effect of the whisker in the cement matrix to consume more energy.

Conclusions

Potassium titanate whiskers (PTW) have a slightly influence on the compressive strength and significant influence on flexibility, tensile strength and microstructure of the oil-well composites. The cementitious composites containing PTW had the better interfacial adhesion and denser microstructure, therefore it included a few harmful holes. With the content of PTW increases from 0 to 2%, the mechanical properties of oil well cement obvious improvement. When the content of PTW is 1.5%, the reinforced cement splitting tensile strength reached the maximum value and the mechanical properties of oil well cement can be improved, and the compressive, tensile and flexibility increase by 27.5, 110.5 and 30.7% with 7 days of curing respectively. The whisker pullout, crack deflection and the whisker bridging are the effective mechanisms for the addition of potassium titanate whiskers to improve the toughening of oil well cement. The improvement of the mechanical strength may be important for application of PTW in oil well cement. The further research will be carried out.

References

1. Z. Li, K. Zhang, X. Guo, J. Liu, X. Cheng, J. Du, J. Nat. Gas Sci. Eng. **31**, 331 (2016)
2. L Sierra, M. Mayerhofer, C.J Jin, *Society of Petroleum Engineers*, SPE-163833-MS
3. M. Li, M. Liu, Y. Yang, Z. Li, X. Guo, Pet. Explor. Dev. **42**, 104 (2015)
4. D. Su, X. Yao, Drill Fluid Compl Fluid. **24**, 40 (2007)
5. M. Li, Y. Yang, M, Liu, X. Guo, S. Zhou, Constr. Build Mater **93**, 995 (2015)
6. M. Li, S. Deng, Y. Yu, J. Jin, Y. Yang, X. Guo, Constr. Build. Mater. **135**, 59 (2017)
7. M. Cao, C. Zhang, H. Lv, L. Xu, Constr. Build. Mater. **66**, 89 (2014)
8. C. Lou, X. Yao, G. Gu, P. Wang, S. Zhou, Drill. Fluid Compl. Fluid **32**, 77 (2015)
9. F. Cheng, Q. Jiang, Z. Zhang, Eng. Plast. Appl. **12**, 123 (2014)
10. G.S. Zhuang, G.X. Sui, H. Meng, Z.S. Sun, R. Yang, Comp. Sci. Technol. **67**, 1172 (2007)
11. X. Cheng, Q. Dong, Z. Li, X. Guo, W. Duan, J. Adhes. Sci. Technol. **34**, 343 (2017)

Slag Gelled Material for Cementing Slurry System Research

Qiwei Mu, Ming Li, Lu Liu and Jianzhang Hao

Abstract A slag cementing slurry was investigated in this study, which based on the slag MTC technology, drilling fluid technology and multifunctional curable liquid separation technology. According to the downhole temperature of different depth section, the impact of the solidified body strength performance was examined at temperature of 30, 50, 70, 90, 120 °C. The results indicated that the slag cementing fluid application temperature was from 30 to 90 °C, the density range was 1.30–1.60 g/cm^3, and the retarder HX-31L could be used to adjust thickening time. High cementing quality of this system had been obtained in the oilfield. The engineering behavior of fluid loss, stabilization and compatibility with drilling fluid were meet the engineering needs. The high temperature hydration products of slag solidified body were analyzed by the aid of SEM, XRD and EDS. Under the condition of 90 °C, the hydration products of slag solidified body are mainly a honeycombed or spherical C–S–H gel. The small contact surface of the hydration products results in poor cementing quality. The high Ca to Si value will produce the crystal shape shift and form in the internal stress, resulting the micro crack initiation and poor stability.

Keywords Slag · Gelled material · Cementing slurry system

Q. Mu · M. Li (✉) · L. Liu
School of Materials Science and Engineering,
Southwest Petroleum University, Chengdu 610500, China
e-mail: 185440762@126.com

Q. Mu
e-mail: 493101612@qq.com

L. Liu
e-mail: 519626160@qq.com

J. Hao
State Key Laboratory for Comprehensive Utilization of Vanadium and Titanium Resources,
Pangang Group Research Institute Co., Ltd, Panzhihua 617000, China
e-mail: 201294569@qq.com

Y. Han (ed.), *Advances in Energy and Environmental Materials*,
Springer Proceedings in Energy, https://doi.org/10.1007/978-981-13-0158-2_44

Introduction

Low density cement slurry is mainly used the microsphere, beads as light-weight-additives material [1, 2]. However, microsphere slurry density affected by pressure lead to system instability and easy to appear high pressure suppress pump phenomenon will increase the risk [3]. The drilling fluid and cement slurry have the different physical and chemical properties, the contact will produce different degrees of pollution and unable to guarantee the safe cementing [4]. A complete set of cement admixture has high price. Although previous research and development of new cement additive to improve cement properties and the cementing operation process, it still has not been achieved mud displacement efficiency and reinforced cement annulus packer capacity between the layers [5]. Therefore, development a stable system, good compatibility, low cost of low density cementing fluid to apply the low pressure easy leakage strata, long cementing section, free casing cementing, and filling cementing, will be a very necessary to research work [6–8]. To reduce the cementing cost and improve the quality of well cementing, this paper uses slag replace oil well cement as cementing material by reference the MTC technology and spacer solidified technology to form a low density slag cementing fluid and part to replace the current low density cement slurry [9–12].

Experiments and Methods

Material. Slag was obtained from the Shandong Yingan Environmental Protection Material Technology Ltd (Table 1). Other materials such as dispersant natural polymer Sodium Carboxymethyl Cellulose (formula for $C_8H_{11}O_7Na$, hereinafter referred to as CMC), activator JHQ, retarder HX-31L, and dispersant SMT were commercially obtained in Chengdu Kelong Chemical Reagent Factory.

Specimen preparation. Slag cementing slurries were prepared and cured according to the Chinese standard GB/T 19139-2012. This experiment selected the CMC of 0.5% as a suspending agent of slag cementing slurry system. In order to obtain the best comprehensive properties of slag solidified body, this slag cementing slurry choose the JHQ as activator of slag cementing slurry, the optimum mixing ratio of 5%. The slag cementing slurries were cast into steel molds with dimensions of φ 25 mm (inside diameter) × 25 mm and φ 50 mm (inside diameter) × 25 mm. Following this, slag cementing slurries were kept in standard curing molds at 30, 50, 70, 90, 120 °C with 100% relative humidity.

Table 1 Chemical composition of slag by XRF

	SiO_2	Al_2O_3	Fe_2O_3	CaO	MgO	TiO_2	MnO	Other
Slag	32.27	13.88	0.37	36.90	9.26	0.96	0.39	5.97

Testing procedure. The stability and fluidity of the slag cementing slurries were investigated according to Chinese standard GB/T 19139-2012. The compressive strengths and the tensile strengths of the slag solidified body were tested using an electronic-hydraulic pressure testing machine at a rate of 400 N/s (YA-300, Beijing Haizhi Science and Technology Development Center, China). All slag solidified body specimens were desiccated and gold-sputtered before characterization by SEM and EDS (JSM-6490LV, JEOL, Ltd.). The slag solidified body specimens were analyzed using XRD (DX-1000, Dandong Fangyuan Instrument Co., Ltd.).

Results and Discussion

Slag cementing fluid density range and formula design. In this paper, we study on the cementing fluid is mainly used in low pressure easy leakage formation, free casing of non-target zones filling and cementing operation. According to the density of the additive, preparation for measured slag cementing slurries formula and the basic properties are shown in Table 2.

Table 2 shows that the slag cementing slurries density is in the range of 1.3–1.6 g/cm^3.

Under the condition of low temperature, the cement paste early strength are rapidly developed.

Thickening time. After a great deal of data investigation, laboratory tests, and comprehensive analysis, this work chooses the production of HX-31L as a slag cementing fluid retarder. We evaluated the different amount of retarder HX-31L effect on the performance of slag cementing fluid. The working liquid formulas are shown in Table 3. The results are shown in Table 4.

As illustrated of the Tables 3 and 4, Retarder HX-31L make the slurries flowing better. HX-31L had a certain dispersion effect of slurry and good compatibility with other admixture of cementing fluid. When 0.5% of HX-31L added to cementing fluid, the thickening time increased 67 min. The thickening curve presents as a right

Table 2 Different density cementing fluid formula and the basic performance

The cementing fluid density [g/cm^3]	1.3	1.4	1.5	1.6
The temperature [°C]	30	30	30	30
The base slurry [g]	184	130	97	75
Slag [g]	100	100	100	100
Activator of JHQ [g]	5	5	5	5
Dispersant of SMT [g]	0	0	0	0.5
Thickening time [min]	103	94	69	48
Atmospheric pressure strength of 24 h [MPa]	3.24	5.12	8.56	10.92

Table 3 Different amount of retarder working fluid formulation

Number	Formula
1#	500 g water + 2.5 g CMC + 750 g slag + 37.5 g JHQ
2#	500 g water + 2.5 g CMC + 750 g slag + 37.5 g JHQ + 0.5% HX-31L
3#	500 g water + 2.5 g CMC + 750 g slag + 37.5 g JHQ + 1.0% HX-31L
4#	500 g water + 2.5 g CMC + 750 g slag + 37.5 g JHQ + 1.5% HX-31L
5#	500 g water + 2.5 g CMC + 750 g slag + 37.5 g JHQ + 2.0% HX-31L

Table 4 Retarder HX-31L effect on the properties of slag cementing fluid

Number	Retarder amount [%]	Fluidity [cm]	Thickening time [min]	Compressive strength [Mpa]	
				1d	3d
1#	0	18	48	12.6	15.1
2#	0.5	19	115	11.2	14.7
3#	1.0	19.5	179	10.5	14.5
4#	1.5	20.5	247	10.1	14.3
5#	2.0	21	301	9.4	14.1

angle by adding the retarder. With the increase of the amount of HX-31L, slag cementing fluid flow degree increase, the flow ability can get better, the thickening time of the cementing fluid increases linearly with the amount of retarder. From the compressive strength results, the amount of retarder has little impact on the strength development of the slag solidified body. Above all, HX-31L retarder can effectively adjust the slag cementing fluid's thickening time, and has little influence to other performance. This system good cementing quality had been obtained in the oilfield. The engineering behavior of fluid loss, stabilization and compatibility with drilling fluid were meet the engineering needs.

Mechanical properties. Slag cementing slurry was cured in the temperature of 30, 50, 70, 90 and 120 °C water bath to 1d, 3d, 7d. The compressive strength test results are shown in Fig. 1.

Figure 1 shows that the compressive strength of slag solidified body are range 10.95–15.5 MPa after 1 day, the high early strength can ensure the stable pressure formation.

Under the environment of 70 and 90 °C, the compressive strength of samples reached 15.54 and 14.64 MPa. Under the same conditions of temperature, the strength of the solidified body increases with the curing time. At the temperature of 70 °C, the solidified body reached the highest value of the compressive strength. The compressive strength of samples, reached to 24.8 and 25.12 MPa after 3d, 7d curing age, respectively. When the temperature exceeded 70 °C, the compressive strength of solidified body has a tendency to decline. The strength of samples curing at 90 °C for 7d is 21.12 MPa, declined by 15.9% relative to 70 °C. At 120 °C, the strength of the solidified body has intensity of the recession reached 53.4% relative to 70 °C.

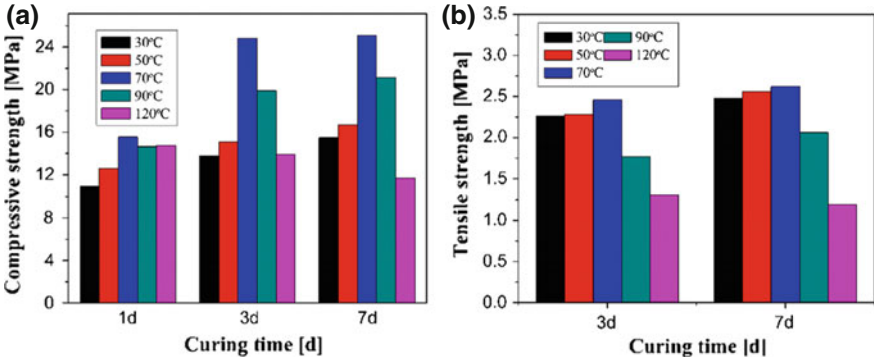

Fig. 1 Mechanical properties. **a** Tendency of the compressive strength **b** Change trend of tensile strength

Compared with the trend of the development of compressive strength, the slag solidified body under the condition of low temperature tensile strength was slightly higher than the high temperature strength. After curing at 30 °C for 3 days, the tensile strength of samples is 2.26 MPa. With the increase of temperature, the tensile strength of the solidified body fell slightly. The tensile strength is only 1.31 MPa at 120 °C. Under the same conditions of temperature, the longer of the curing time lightly increases the tensile strength of the solidified body.

The hydration products of slag cementing slurry. The XRD, SEM, EDS were used to investigate the phase and microstructure of slag solidified body types at 90 °C.

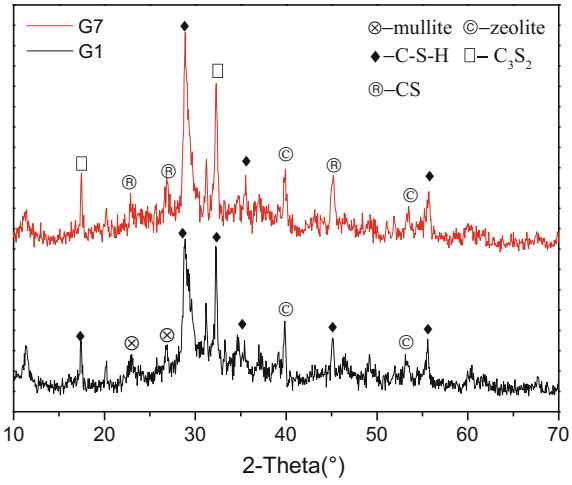

Fig. 2 Slag solidified body XRD spectrum

The XRD test results of slag solidified body after 1, 7 days curing time were shown in Fig. 2. Figure 2 illustrates the XRD patterns of slag solidified body after 1, 7 days curing time. As can be seen, slag hydration products mainly was C–S–H gel, mullite, zeolite minerals, and calcium silicate. Initial slag hydration, hydration products mainly was C–S–H gel and a small amount of mullite, zeolite minerals. With the increase of hydration period, hydration products of C–S–H gel diffraction peak became wider, shows that the products had more C–S–H gel, and early emergence of mullite diffraction peak disappears, meanwhile rankinite and wollastonite diffraction peak appeared.

Experiments observed the slag micro morphology of the solidified body by scanning electron microscope. Figure 3 illustrated the microstructure of the slag samples curing at 90 °C for 3d, 7d. Hydration for three days, hydration products mainly exist in the fibrous and amorphous shape C–S–H, and some irregular shape of zeolites. Small amounts of slag particles was embedded in the hydration

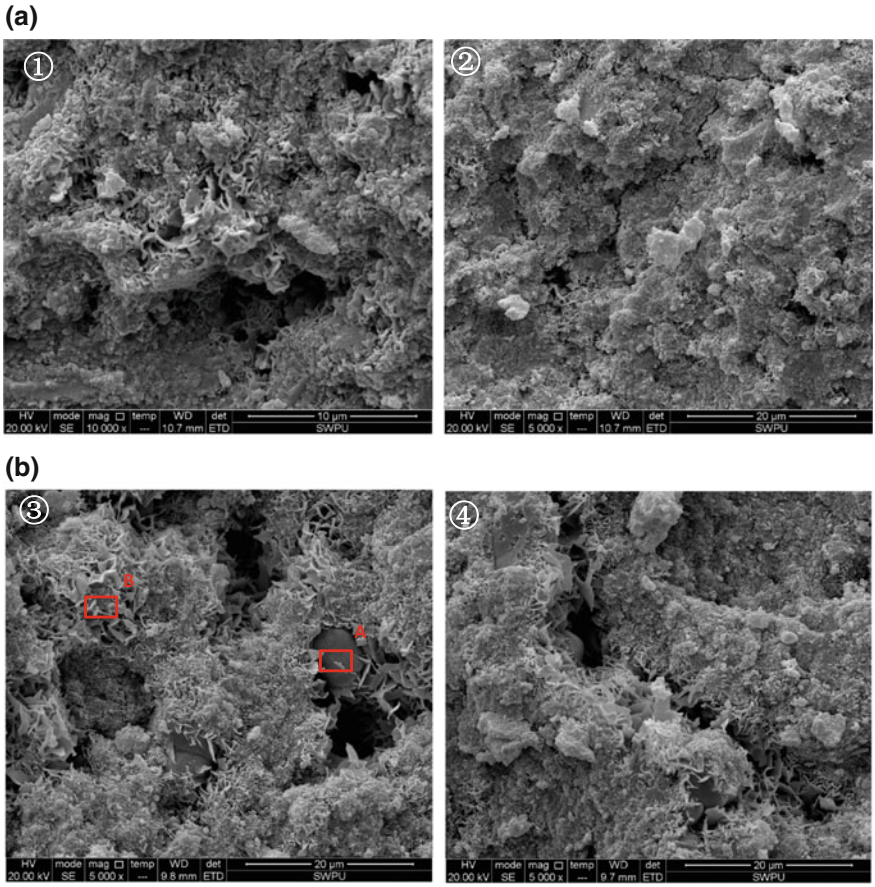

Fig. 3 Microscopic morphology. **a** Hydration for three days. **b** Hydration for seven days

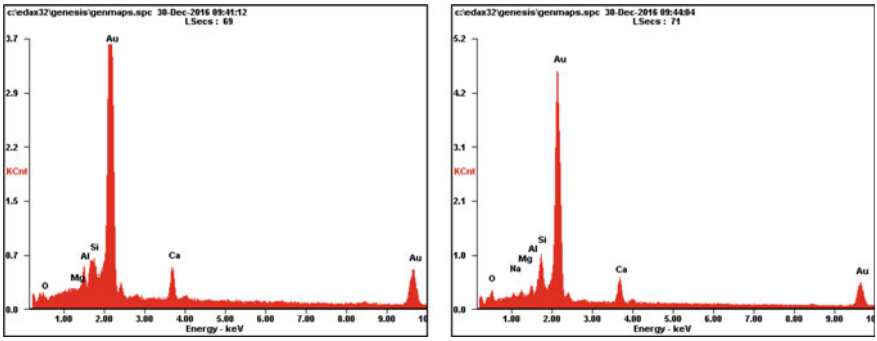

Fig. 4 EDS spectrum

products, formed a relatively dense structure. The existence of a small amount of micro cracks, cracks inside and around the hydration products were fibrous C–S–H gel. After seven days of hydration, the honeycombed C–S–H gel increased. The hydration products formed more dense structure by mutual connection, entwining together. When the temperature exceeds 90 °C, the strength of the solidified body attenuation phenomenon and the surface different degree of crack appeared. Increase the curing temperature and curing time, curing body crack become more obvious.

Two typical of hydration products area were choose to analysis the composition of hydration products phase by EDS spectrum. Hydration products tested EDS spectrum (red area), the main element analysis results were shown in Fig. 4 and Table 5. It can be seen that the hydration products main elements were Ca, Si and O, Al and Mg. This was because the slag containing Al and Mg, Al replace Si into the C–S–H gel formed same C–A–S–H gel. When the C–S–H gel Ca to Si ratio between 1 and 2, gel will present the phenomenon of dehydration, result in the structure prone to damages [13–15]. The honeycombed C–S–H gel molar ratio of Ca to Si was 0.72, but the Spherical C–S–H gel molar ratio of Ca to Si was 1.26. The high Ca to Si ratio of C–S–H generated hydration crystal structure transformation and the larger internal stress generated in the solidified body, causing the solidification structure damaged and cracked.

Table 5 Elemental analyses

Element types	Atomic number percent [%]	
	A	B
Ca	26.29	14.43
Mg	00.97	3.39
Al	12.94	4.35
Si	20.92	20.00
Na	–	3.56
O	38.88	54.27

Conclusions

1. A set of slurry with the range from 1.30 to 1.60 g/cm^3 was formed as low density of the slag cementing fluid gel material. Slurries had good rheological property, low fluid loss, good retro-gradation, thickening time controllable strength development, low temperature quickly and high long-term strength and were suitable for low pressure and leakage formations, a long cementing section for the purpose layer filling, cementing operation.
2. The application temperature range of the slurry is 30–90 °C.
3. With the increase of curing temperature and curing time, slag solidified body of compressive strength is a growing trend.
4. When the temperature exceeds 90 °C, the strength of the solidified body presents attenuation phenomenon and the surface has different degree of crack. Compared with the solidified body curing at 70 °C for 7d, the strength of samples curing at 90 °C declines by 15.9%, and at 120 °C the recession is 53.4%.
5. The high temperature hydration products of slag solidified body are mainly a honeycombed or spherical C–S–H gel, causing the micro crack initiation and poor stability.

Acknowledgements The authors would like to acknowledge the co-financial support by the National Science and Technology Major Project (NO. 2016ZX05020004-008 and 2016ZX05052) and Applied basic research project of Sichuan Province (2017JY0042) for the financial support.

References

1. M.A. Chunxu, Z. Duan, Z. Liu et al., Study and application of low density cement slurry containing artificial micro bead. Drill. Fluid Compl. Fluid. **43**, 15–18 (2016)
2. T. Sugama, B. Lipford, Hydrothermal light-weight calcium phosphate cements: use of polyacrylnitrile-shelled hollow microspheres. J. Mater. Sci. **32**, 3523–3534 (1997)
3. M.D. Alvarez, R. Fuentes, M.D. Olivares et al., Thermorheological characteristics of chickpea flour slurry as affected by moisture content. J. Food Eng. **136**, 9–18 (2014)
4. S. Liu, K. Zheng, C. Zhang et al., An experimental study on the prevention of cement slurry contamination during deep or ultradeep well cementing at Sichuan and Chongqing oil/gas fields. Nat. Gas Ind. **30**, 51–54 (2010)
5. D. Janssen, J.V. Aken, T. Scheerlinck et al., Acta Orthopaedica. **80**, 319–324 (2009)
6. C.L. Wang, W. Ni, S.Q. Zhang et al., Preparation and properties of autoclaved aerated concrete using coal gangue and iron ore tailings. Constr. Build. Mater. **104**, 109–115 (2016)
7. Y. Liu, Q. Zhang, C. Xie et al., Application of low-density and high-strength cement slurry in Kazakhstan. Drill. Fluid Compl. Fluid. **27**, 68–70 (2010)
8. B. Zhang, Research and application of low density and high strength cementing slurry. Fault Block Oil Gas Field. **30**, 59–62 (2009)
9. M. Codina, C. Cau-dit-Coumes, P. Le Bescop, J. Verdier, J.P. Ollivier. Design and characterization of low-heat and low-alkalinity cements. Cem. Concr. Res. **38**, 437–448 (2008)

10. F. Cassagnabere, M. Mouret, G. Escadeillas, Early hydration of clinker-slagmetakaolin combination in steam curing conditions, relation with mechanical properties. Cem. Concr. Res. **39**, 1164–1173 (2009)
11. N. Robeyst, E. Gruyaert, C.U. Grosse, N. De Belie. Monitoring the setting of concrete containing blast-furnace slag by measuring the ultrasonic p-wave velocity. Cem. Concr. Res. **38**, 1169–1176 (2008)
12. H.M. Dyson, I.G. Richardson, A.R. A combined 29Si MAS NMR and selective dissolution technique for the quantitative evaluation of hydrated blast furnace flag cement blends. J. Am. Ceram. Soc. **90**, 598–602 (2007)
13. A.A.M. Neto, M.A. Cincotto, W. Repette Drying and autogenous shrinkage of pastes and mortars with activated slag cement. Cem. Concr. Res. **38**, 565–574 (2008)
14. J.L. Vilaplana, F.J. Baeza, O. Galao et al. Mechanical properties of alkali activated blast furnace slag pastes reinforced with carbon fibers. Constr. Build. Mater. **116**, 63–71 (2016)
15. M.K. Ferber, A.A. Wereszczak, D.H. Hansen et al. Evaluation of interfacial mechanical properties in SiC fiber-reinforced macro-defect-free cement composites. Compos. Sci. Technol. **49**, 23–33 (1993)

Preparation of Crystal Quartz by Hydrothermal Synthesis

Songxia Li, Siqi Wang, Qi Xue, Jin Zhang and Ping Fan

Abstract Adopting high-purified $SiCl_4$ as raw material and taking Na_2CO_3 as mineralizer, crystallized SiO_2 was prepared with hydrothermal process. Particularly, the effect of processing temperature, precursor concentration and pH on the crystallization of SiO_2 were taken into consideration. To analyze the growing mechanism, the structure and morphologies of hydrothermal product were studied with XRD and SEM. The results showed three factors, including synthesis temperature, precursor concentration and pH, influenced the crystallization and morphologies of crystalline SiO_2 significantly. Proper hydrothermal processing, 220 °C hydrothermal environment, 1.2 mol/L precursor, pH 10.5 and Na_2CO_3 mineralizer, resulted in 8 μm well-crystallized columnar grain crystal. The crystallization process of SiO_2 followed the "dissolution-precipitation" mechanism in the hydrothermal synthesis and contained the aggregation-growth.

Keywords Hydrothermal process · Crystallized SiO_2 · Precursor concentration Temperature · pH

S. Li (✉) · S. Wang · Q. Xue · J. Zhang · P. Fan
School of Materials Science and Engineering,
Southwest Petroleum University, Chengdu 610500, China
e-mail: lisongxiay@163.com

S. Wang
e-mail: 346806743@qq.com

Q. Xue
e-mail: qxue01@163.com

J. Zhang
e-mail: jzhang@swpu.edu.cn

P. Fan
e-mail: 214692970@qq.com

Y. Han (ed.), *Advances in Energy and Environmental Materials*,
Springer Proceedings in Energy, https://doi.org/10.1007/978-981-13-0158-2_45

Introduction

As for the typically optical characters, thermal stability, inertia and irradiation performance, transparent SiO_2 was widely used in semi-conduct and astronavigation [1]. Limited by the shortage of raw material, smelting crystal was replaced by crystallized SiO_2 gradually.

The high-purity SiO_2 can be roughly divided into two categories: the inartificial one and the synthesis one, for which the former was purified with silica sand. Meanwhile, there were two ways to synthesize high-purity SiO_2: dry processing and wet processing (precipitation and hydrothermal). Wet processing was prior to the dry method in cost and security. The less soluble and immiscible material in closed container would be soluble if high temperature or high pressure, or both, were applied in the vessel which was stuffed with water, then material went through dissolution-crystallization [2]. In 1990s, researchers made SiO_2 by hydrothermal method which cost less, however, crystallized well, agglomerate slightly. This way was introduce to industrial crystal production [3]. With the research and development of hydrothermal processing, it became a competitive preparation processing to obtain oxide powders [4]. However, reports of the hydrothermal SiO_2 were mainly about crystalline ones rather than the powder ones.

In this paper, crystallized SiO_2 was prepared with hydrothermal processing by adopting high-purity $SiCl_4$ as raw material and taking Na_2CO_3 as mineralizer. The effects of these factors, including synthesis temperature, precursor concentration and pH, on the crystallization, particle the size and profile of SiO_2 were specifically studied. Based on the data, the growing mechanism was discussed.

Experimental

Rectification $SiCl_4$, $NH_3{\cdot}H_2O$(AR), Na_2CO_3 (AR), NaOH(AR) and deionized water were used in the experiment.

(1) Preparing crystal quartz with hydrolyzed $SiCl_4$. Firstly, $SiCl_4$ was hydrolyzed in $NH_3{\cdot}H_2O$. Then purging the precursor and drying it in 90 °C heating furnace. The certain pH liquor, stuffed reactor 80% volume, was consisted of Na_2CO_3 and hydrolyzed $SiCl_4$ which acted as mineralizer and precursor respectively. The reactor was heated under 140, 180, 220 and 260 °C respectively for a period of time then chilled in room temperature. Finally, cleaning the products with 1wt% hydrochloric acid and drying the sample under 90 °C again.
(2) Preparing the crystal quartz with the remnant hydrothermal liquor. To observe the crystallization, we vapored the remnant hydrothermal liquor to enrich

solution. The hydrothermal condition applied in the reactor as follows: 220 °C temperature, 30 h reacting time, pH 10.5 and 80% filling. Finally, cleaning the products with 1wt% hydrochloric acid and drying the sample under 90 °C.

(3) Analyzing the structure of specimen with XRD(DX-2000); Observing the micro-profile of sample by SEM(TM-1000).

Results and Discussion

Effect of Temperature on the Hydrothermal Reaction. Temperature was directly related to the powder quantity in practically manufacture was essential within the factors working on the hydrothermal system. Therefore 4 different temperature, 140, 180, 220 and 260 °C, were applied in the experiment. Figure 1 showed the XRD pattern of product derived from those series of hydrothermal temperature. When produced at 100 °C, the diffraction peaks of α-SiO_2 (PCPDF 65–0466) began to be detected. The diffraction peaks, however, showed typical characteristics of amorphous as they were lower and broader. Increasing the processing temperature up to 140 °C, the diffraction peaks of crystal α-SiO_2 were stronger and narrower. It meant that the crystallinity of the α-SiO_2 were better and higher than that of the 100 °C -produced sample. Further increasing the temperature, the diffraction pattern showed the similar multiple orientations of (100), (101), (110), (112), and (211) with the improvement of the intensity. It should be noted that when prepared at 260 °C, the intensity of the diffraction peaks decreased in comparison with the 220 °C -produced sample. Consequently, the crystal quartz grew in size and perfected in crystallization with rising temperature. But the size of crystal were thinned which resulted in the impairment of diffraction peak.

The morphologies of crystal quartz synthesized with different temperature were shown in Fig. 2. Increasing temperature, the boundary of quartz grain became sharp and clear, and the quartz revealed obvious columnar outline and perfected

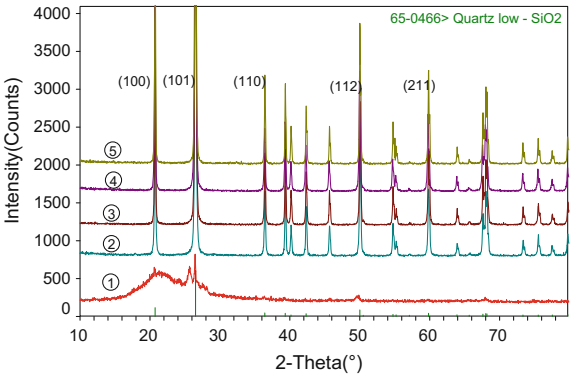

Fig. 1 XRD patterns of SiO_2 crystal obtained from different reaction temperature. ① 100 °C, ② 140 °C, ③ 180 °C, ④ 220 °C, ⑤ 260 °C

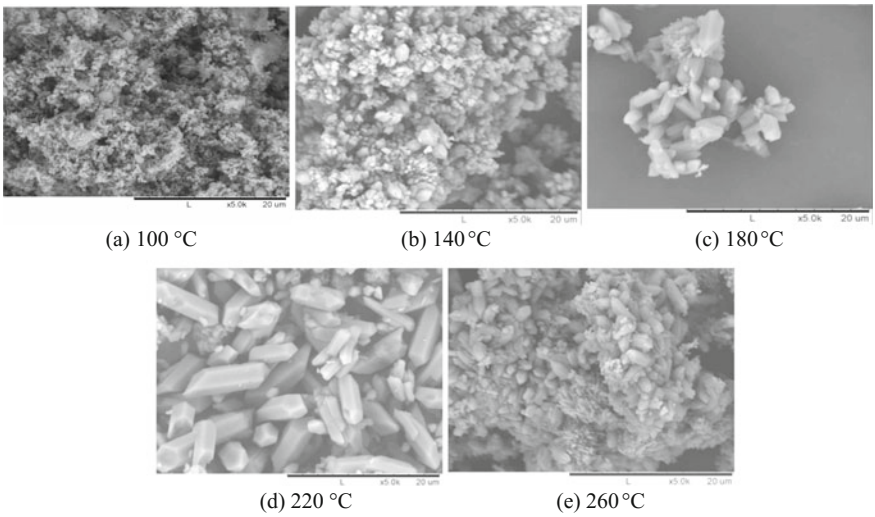

Fig. 2 SEM images of SiO_2 crystal obtained from different reaction temperature. **a** 100 °C **b** 140 °C **c** 180 °C **d** 220 °C **e** 260 °C

crystallization. Large bulk crystal SiO_2 enriched. On the other side, the thinned SiO_2 particles aggregated seriously as temperature was more than 220 °C. It can be interpreted as follows: rising temperature accelerated the dissolve rate of precursor and benefited the free energy of hydrothermal system, which attributed to the diffusion of Si–O directly and led to nucleation outweighing growth of particles indirectly [5]. All in all, 220 °C was the proper temperature for hydrothermal processing.

Effect of Precursor Concentration on the Hydrothermal Reaction. It was reported that the precursor concentration exerted a significant influence on the hydrothermal reaction [6]. To explore the influence of precursor concentration on the crystallization of quartz, different utility of precursor were adopted in the experiment with 30 h 220 °C treatment. The morphologies of products for each precursor concentration, were shown in Fig. 3. The crystal quartz seemed to be columnar shape as precursor concentration ranging from 0.8 to 1.4 mol/L. But the surface of the sample, 0.8 mol/L precursor concentration, disclosed numerous defects which may result from inadequate precursor. The crystal quartz particles thinned and aggregate seriously as precursor concentration ranging from 1.6 to 1.8 mol/L. And the outline of these particles was spherified. The reason for the phenomenon above was follows: Precursor concentration increase accelerated the growth rate of quartz. However, increasing precursor concentration was corresponded to rising viscosity of the liquid which impeded the diffusion of Si–O and impaired the dissolution of precursor, and all of these lessen the growth rate of quartz.

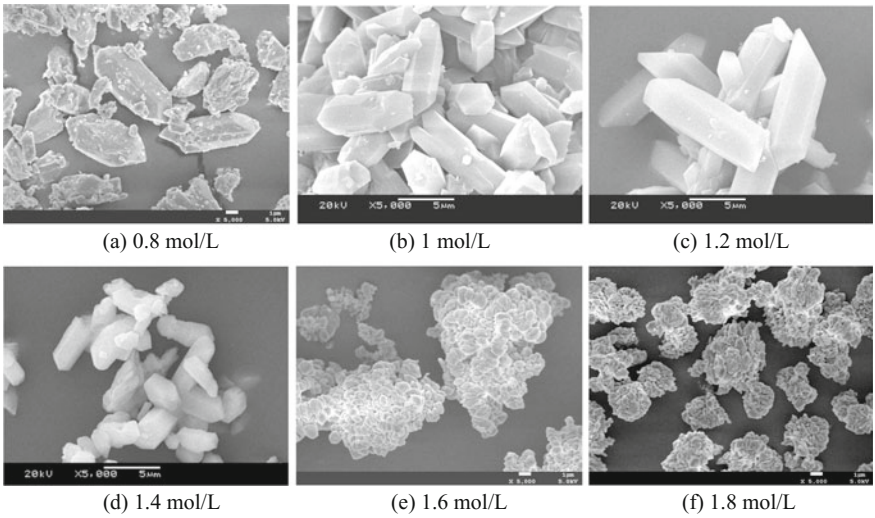

Fig. 3 SEM images of quartz prepared with different precursor concentration

Effect of pH on the Hydrothermal Reaction. The crystal SiO_2 was prepared by taking 1 mol/L precursor, stuffing 80% volume, using Na_2CO_3 as mineralizer in the experiment to find out proper pH. The specimen was accustomed to 30 h 220 °C heat and the adopted pH was set as pH9.5, pH10.5, pH11.5 and pH12.5, respectively. The morphologies of each product were scanned as Fig. 4. Low pH led to the weakness of SiO_2 solubility which resulted in thinning and pinning particles [7]. On the other side, high pH led to the obvious increase of precursor dissolution, thus the viscosity of liquid was improved, which greatly impacted on the crystallization of quartz [8]. Therefore pH needs to be controlled about 10.5.

Discussion on Crystallization Mechanism. There were two theories about the crystallization mechanism of hydrothermal processing, in situ crystallization and dissolution-crystallization. HERTL [9] prepared $BaTiO_3$ who considered crystal $BaTiO_3$ followed in situ crystallization. However, PINCELOUP [10] and Xu Hua-rui [11] who studied on the $BaTiO_3$ powder put forward dissolution-crystallization theory, and pointed out that bottleneck structure of particle was essential to the dissolution-crystallization progress. Weizhuo Zhong [12] insisted that the precursor dissolve in alkaline solution formed tetrahedron $Si(OH)_4$ and it nucleated and grew up with the supersaturation, which was obviously in favor of dissolution-crystallization theory. Moreover, the bottleneck theory, in Fig. 5, supported that crystallization just followed the rule of dissolution-crystallization. Otherwise, according to the Fig. 3a, b, the columnar quartz was derived from the gathering of amount small particles which made sense that aggregation growth also existed during the crystallization [13].

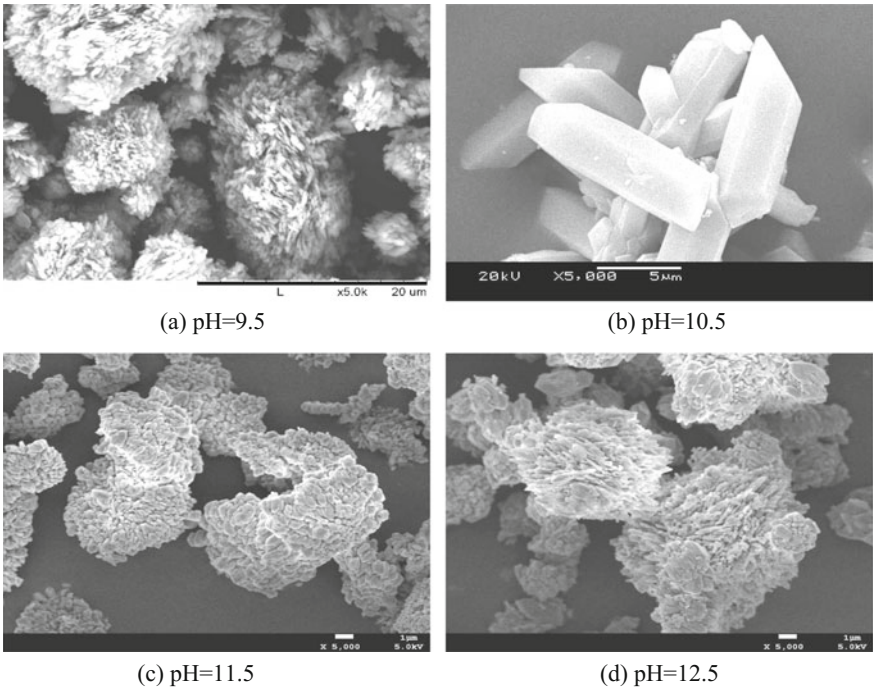

(a) pH=9.5 (b) pH=10.5

(c) pH=11.5 (d) pH=12.5

Fig. 4 SEM images of quartz prepared with different pH

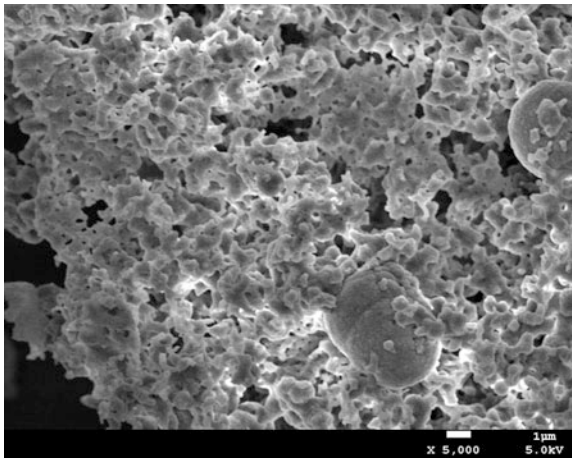

Fig. 5 SEM image of quartz prepared with remnant liquor

Conclusions

1. There are three factors, including synthesis temperature, precursor liquor concentration and pH, significantly involve the particle size and profile of crystalline SiO_2. Rising temperature was contributed to the size of columnar crystallized quartz. The particle size decreases and crystallization becomes non-columnar while the temperature is below 220 °C. The well-crystallization concentration of precursor is about 1.2 mol/L. Lower precursor concentration leads to defect of crystallization while higher concentration results in agglomeration. It is critical to keep the hydrothermal liquor pH 10.5. More or less pH will impair the crystallization of quartz and turn into small columnar crystallized quartz.
2. Taking Na_2CO_3 as mineralizer, hydrolyzing $SiCl_4$ as "Si source", the crystal quartz grows up under 140 °C or above. The growth of crystal follows the "dissolution-crystallization" rules, and sort of agglomeration either.

Acknowledgements This work was supported by the Scientific Research Foundation and Opening Foundation (X151517KCL52) of Southwest Petroleum University.

References

1. D.B. Jin, X.M. Zhang, W.W. Zhou. Study on Processing Technology of High Purity Quartz. J. Chin. Nonferr. Metals Ind. **4**, 44–48 (2004)
2. W.E. Shi, C.T. Xia, B.G. Wang, et al. Development and application of hydrothermal method. J. Inorg. Mater. **11**, 193–206 (1996)
3. Byrappa K, Yoshimura M. *Handbook of Hydrothermal Technology* (William Andrew, 2012)
4. Yanagisawa K, Zhu Y, Onda A, et al. Hydrothermal synthesis of mono-dispersed quartz powders. J. Mater. Sci. **39**, 2931–2934 (2004)
5. B.C. Zhang, Q. Xue, J. Zhang et al, Synthesis of high purity micron-sized quartz from SiCl4 by hydrothermal method. Inorg. Chem. Ind. **45**, 33–35 (2013)
6. R.R. Xu. *Inorganic Synthetic Chemistry* (Higher Education Press, Beijing, 1991) pp. 221–223
7. X. Chen, X.Y. Qu, L.W. Qiu et al., Hydrothermal experiment research on characteristics and mechanisms of quartz dissolution. Bull. Mineral. Pet. Geochem. **34**, 1027–1033 (2015)
8. S. Nangia, B.J. Garrison, Reaction rates and dissolution mechanisms of quartz as a function of pH. J. Phys. Chem. A. **112**, 2027–2033 (2008)
9. W. Hertl, Kinetics of barium titanate synthesis. J. Am. Ceram. Soc. **10**, 879–883 (1988)
10. P. Pinceloup, C. Courtois, J. Vicens et al., Evidence of a dissolution—precipitation mechanism in hydrothermal synthesis of barium titanate powders. J. Europ. Ceram. Soc. **19**, 973–977 (1999)
11. H. Xu, L. Gao, New evidence of a dissolution—precipitation mechanism in hydrothermal synthesis of barium titanate powders. Mater. Lett. **57**, 490–494 (2002)
12. W.Z. Zhong, G.Z. Liu, S.K. Hua et al., Formation mechanism of the growth forms of SiO_2 and SnO_2 under hydrothermal conditions. J. Synth. Cryst. **23**, 1–7 (1994)
13. W.E. Shi, C.T. Xia, B.G. Wang, et al. Aggregation growth in ceramic powders prepared by hydrothermal method. Sci. Chin. (Series E) **27**, 126–133 (1997)

Effect of Cold Deformation on the Microstructures, Mechanical Properties and Corrosion Behavior of IF Steel in Simulated H_2S Solutions

Wenzhu Shen, Gangqiang Wang, Long Chen, Xi Xu, Bo Yang and Chunfu Li

Abstract Expandable tubular technology is a new technology in oil industry. Interstitial-free (IF) steel has potential application as expandable tubular steel because of its excellent non-aging property and extra-deep drawing quality. In this study, the effects of cold deformation on the microstructures, mechanical properties, and corrosion behavior of IF steel in simulated H_2S solutions were investigated. Results showed that when the cold reduction rate was up to 60%, the grains tended to form a fibrous tissue. Hardness, yield strength, and tensile strength of IF steel increased with increasing cold reduction rates, whereas elongation decreased. Although the cold reduction rate increased up to 80%, the remaining elongation was beyond 10%, which was suitable for the expandable tubular application. With increasing cold reduction rate, the corrosion rate increased, and the "hardening" effect expanded.

Keywords Expandable tubular technology · Interstitial-free steel
Cold deformation · Microstructures · Mechanical properties · Simulates H_2S corrosion

W. Shen (✉) · G. Wang · L. Chen · X. Xu · B. Yang · C. Li
School of Material Science and Engineering,
Southwest Petroleum University, Chengdu 610500, China
e-mail: wenzhupinger@163.com

G. Wang
e-mail: 1026885825@qq.com

L. Chen
e-mail: a529328669@qq.com

X. Xu
e-mail: 2375884297@qq.com

B. Yang
e-mail: 2859588279@qq.com

C. Li
e-mail: lichunfu10@163.com

Y. Han (ed.), *Advances in Energy and Environmental Materials*,
Springer Proceedings in Energy, https://doi.org/10.1007/978-981-13-0158-2_46

Introduction

Expandable tubular technology is a new technology in oil industry that can distinctly reduce drilling and completion cost. This technology involves running the special expansion pipe string into the hole and the using a drive head to produce permanent deformation and expansion by either hydraulic or mechanic method, thus effectively enlarging the internal diameter size of the tubing or casing [1, 2].

Expandable tubular materials should have high plasticity, high strength, and high work-hardening rate. In the past, material selections were confined to the standard of the American Petroleum Industry (API), such as J55 steels [3]. However, the materials within the scope of API were not suitable for large expanding deformation. The deformation rate for J55 steels tubular is only 25%. Many studies were focused on unconventional steels that were not commonly used in oil and gas fields. Li et al. [3] from Southwest Petroleum University attempted to select twinning-induced plasticity (TWIP) steel, duplex stainless steel, and interstitial-free (IF) steel as alternative materials. IF steel is selected because of its suitable properties, such as non-aging property and extra-deep drawing quality. It is used to form some automobile parts that are difficult to shape [4, 5].

The expandable tubular will experience large deformation when it is used in oil and gas wells. A large expanding deformation is a plastic deformation that affects material properties. This study focuses on cold deformation effects on microstructures and mechanical properties. In oil and gas wells, corrosion issues are worthy of attention. Many oil and gas wells in Southwest China are high H_2S-containing environments [6–8]. The H_2S corrosion behavior of IF steel and the accompanying hydrogen brittleness are also investigated.

Experimental Aspects

The materials used in this investigation were IF steel. The chemical compositions (wt%) of the IF steel are as follows: 0.0012 C, 0.11 Si, 0.14 Mn, 0.007 P, 0.031 S, 0.04 Cu, 0.02 Ni, 0.091 Ti, 0.005 N, and Fe balance. The as-received IF steel was a hot-rolled annealing plate, which was size rolled to fabricate a 12 mm-thick plate, from the ingot. It was homogenized for 1 h at 700 °C and then furnace cooled.

In cold deformation processing, the samples were cut directly from hot-rolled steel plate in a lath measuring 20 mm × 100 mm and then cold-rolled to sheets with several passes by a roller mill. Cold deformation rates were 20, 40, and 60%. Standard specimens (ASTM A370) of the cold-rolled samples with various cold reductions were cut longitudinally in the rolling direction and subjected to tensile testing using an MTS machine.

Metallographic observations were carried out using an optical microscope. Details of the microstructural characteristics of some chosen cold and annealing samples were investigated using transmission electron microscopy (TEM). Thin foil

specimens for TEM observation were prepared using a twin-jet polisher in a 12 vol%$HClO_3$ + 88 vol% C_2H_5OH solution at −30 °C and 20–30 V. TEM observations were performed using a JEM-200CX at an accelerating voltage of 160 kV. The micro-hardness was measured using a Temin-HXD-2000TM/LCD micro-hardness tester with 500 g load.

The corrosion performance of IF steel samples in saturated hydrogen sulfide (H_2S) solutions were investigated by immersion test. The saturated H_2S solution was a vicarious solution by mixing 5%NaCI + 0.5%CH_3COOH + 10^{-3}mol/L$Na_2S_2O_3$. The weight loss method was adopted to investigate the corrosion rates of the samples. Samples were rinsed with distilled water and carefully dried before taking weight change measurements. The corresponding corrosion rates (r) in mils per year (mpy), based on weight loss measurements, were calculated using the following equation:

$$r = \frac{8.76 \times \Delta m}{s \times t \times \rho} \tag{1}$$

where Δm is the weight loss in gm (g), ρ is the density of steel g/cm^3, s is the total surface area (cm^2), and t is the total exposure time in hours. The effects of absorbed hydrogen during corrosion on mechanical properties were characterized by the change of hardness (HV).

Result and Discussion

Figure 1 shows the optical micrographs of hot-rolled annealing IF steel plate. The grains of hot-rolled annealing sample were equiaxial in shape with an average grain size of 35 μm. The hot-rolling annealing microstructure of IF steel did not exhibit any preferred orientation. The hot-rolled annealing IF steel had an approximate yield strength of 200 MPa, tensile strength of 345 MPa, hardness of approximately 93 HV, and approximate elongation of 54%.

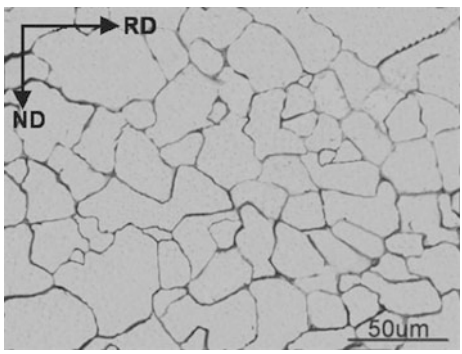

Fig. 1 Optical micrograph of the as-received hot-rolled annealing steel plate

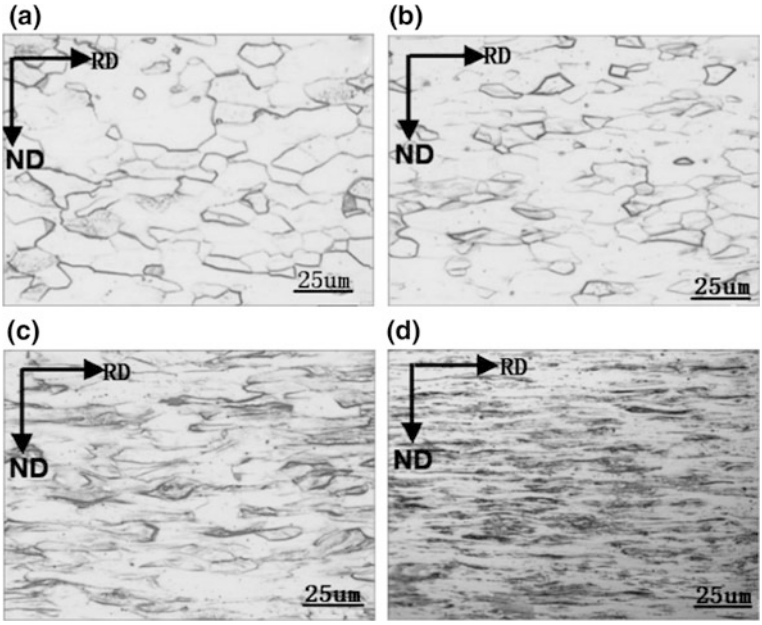

Fig. 2 Optical micrographs of the cold-rolled IF steels with various CR_s: **a** 20%, **b** 40%, **c** 60%, and **d** 80%

Figure 2 shows the optical micrographs of cold-rolled IF steel with various cold reduction rates. Cold rolling caused grain deformations. When the cold reduction rate was 20%, some grains presented deformation state, but most of grains still retained their equiaxed shape. With increasing cold reduction rate, more deformed grains appeared. When the cold reduction rate reached 60%, the grains tended to form a fibrous tissue, and large amounts of shear bands formed inner grains. At the cold reduction rate of 80%, the deformation of grains became very serious, and grain boundary could not be distinguished.

Figure 3 shows the microstructures of the chosen cold-rolled IF steels observed through TEM. The deformation shear band microstructures of the samples were not significant, and the main feature was a high density of dislocations in grains for the cold reduction rate of 20%. In some grains, the dislocations tended to form dislocation cells. With increasing cold rolling reduction rate, dislocation density increased, and deformation band microstructures could also be observed. During the cold deformation process, the grains were subjected to tensile and rotational stresses by the action of tensile and shear stresses. Hence, the grains were elongated along the rolling direction. With the increase of cold rolling deformation, the shapes of the grains gradually changed from polygon to long strip, flat, and fibrous grains.

Figure 4 shows the effect of cold-rolled deformation on properties of IF steel. The hardness and strength, including yield and tensile strengths of IF steel gradually increased with increasing cold reduction rates. Elongation of IF steel

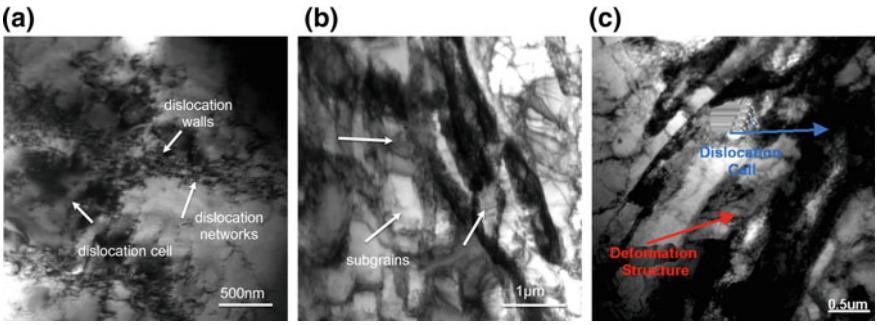

Fig. 3 TEM micrographs of cold-rolled IF steels with various CR_s **a** 20%, **b** 40%, and **c** 60%

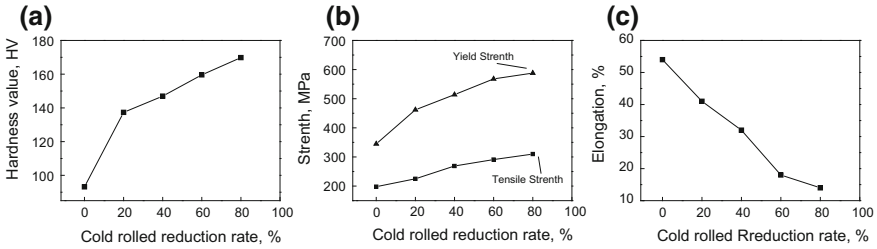

Fig. 4 Effect of cold deformation on **a** hardness, **b** strength, and **c** elongation of IF steel

decreased with increasing cold-rolled reduction rate. Cold deformation caused the "hardening effect." Work hardening effect means that when materials are subjected to external force, edge dislocation cannot cause a cross-slip to increase the resistance of dislocation movement because of the interaction of multi-slip systems and cross-slip. With increasing strain, dislocation density increases. Therefore, the materials increase hardness at the macroscopic level. The inner dislocation of IF steel increases gradually with increased cold-rolling deformation. The materials cause dislocation pile-up, and deformation stress storage energy is formed with dislocation movement. In the figure, when the cold-rolled reduction rate reached 80%, yield and tensile strengths increased to approximately 310 and 590 MPa, respectively. Importantly, the remaining elongation was beyond 10%, which is suitable for the application of expandable tubular.

Figure 5 shows corrosion rates (mpy) of various cold reduction rates of IF steel samples after immersion in saturated vicarious H_2S solutions for 30 days based on weight loss measurements. The figure presents the effect of cold-rolled deformation on corrosion rates of IF. The cold deformation had an acceleration effect on the corrosion of IF steel. The lowest corrosion rate (0.21 mpy) was obtained in as-received samples, but the lowest corrosion rate for 20% cold reduction rate samples was 0.25 mpy. Similarly, for 60% cold reduction rate samples, the lowest corrosion rate (0.30 mpy) was obtained. With increasing cold reduction rate, the

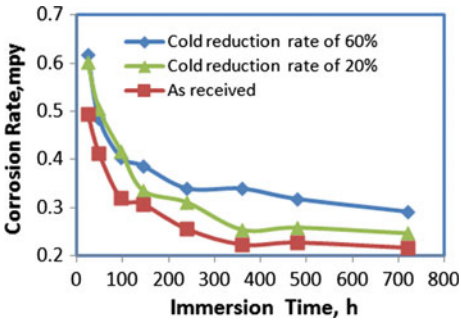

Fig. 5 Corrosion rates (mpy) of various CR samples after immersion in saturated vicarious H_2S solutions for 30 days based on weight loss measurements

corrosion rate increased. This trend may be related to the large number of defects in the deformed grains, such as slip-band inner grains.

Figure 6 shows the relationship between the hardness of cold-rolled IF steels and depth of grinding under different immersion times. After 24 h of immersion hardness, the values of steels increased, and the maximum hardness value was achieved after polishing 20 mm in thickness. Continuous polishing increased the hardness values. At 24 h immersion time, the change in hardness was not significant, especially for as-received steel and steel under the cold reduction rate of 20%. With increasing immersion time, the change in hardness became increasingly obvious. This trend is reflected not only in the increased magnitude of hardness, but also in the influence of the "hardening" range for materials. At 96 h immersion time, the increased magnitude of hardness was approximately 40 HV for cold-deformation steels but that for as-received steel was 30 HV. The "hardening" range expanded with increasing cold reduction rates.

When steels were immersed in acidic solution, especially in H_2S solutions, steels underwent anodic and cathodic reactions. Therefore, when IF steels were immersed in H_2S solutions, the consequent influences occur: (1) the surface in contact with

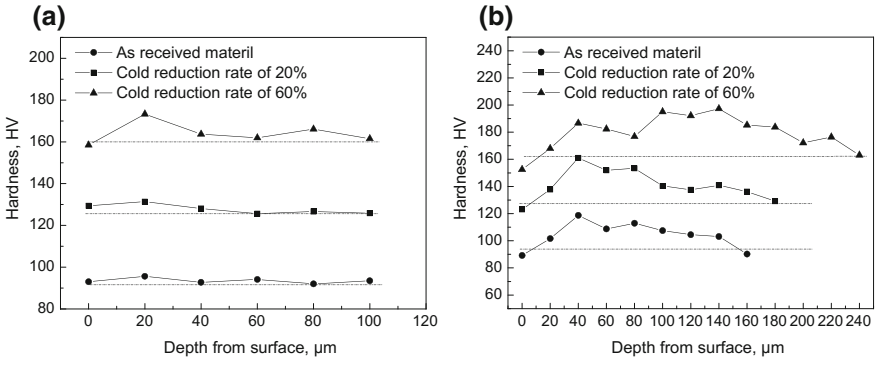

Fig. 6 Relationship between the hardness of IF steels and the depth of grinding under different immersion times: **a** 24 h and **b** 98 h

the solution generated a corrosion product, such as FeS; and (2) sulfide ion "poisoned" the hydrogen atoms, causing a cathodic reaction. Then, the hydrogen atoms are enriched on metal surfaces and permeated into the metal, causing hydrogen embitterment [9]. When immersion time was short, the permeability time of hydrogen atoms for metals was insufficient. This phenomenon caused a narrow hydrogen embitterment effect layer. With prolonged immersion time, the corrosion layer thickness increased; however, hydrogen atoms had sufficient time to permeate into the metals through the corrosion layer, thereby causing the increased thickness of the hydrogen embitterment effect layer. For cold-deformation steels, the process was more likely to capture more hydrogen atoms because of the large number of deformed defects. Therefore, hardness magnitude and "hardening" effect were higher and larger than those of as-received steel.

Conclusion

(1) With increasing cold reduction rate, more deformed grains appear. When the cold reduction rate is up to 60%, the grains tend to form a fibrous tissue.
(2) Dislocations and dislocation cells are the main characteristics in low cold reduction rate. However, with increasing cold reduction rate, dislocation density increases obviously, and deformation band microstructures can be observed.
(3) Hardness, yield strength, and tensile strength of IF steels increase with increasing cold reduction rates, whereas the elongation decreases. Even if the cold reduction rate is higher at 80%, the remaining elongation is beyond 10%.
(4) When IF steels are immersed in H_2S solutions, weight loss occurs because of the corrosion and hydrogen embitterment by permeated hydrogen.
(5) With increasing cold reduction rate, the corrosion rate increase and the influence "hardening" expands.

Acknowledgements This work was financially supported by the Extracurricular Opening Experiment Project of SWPU (KSZ16098), the General Project of Educational Commission of Sichuan Province (14ZB0055) and the Natural Science Foundation of SWPU (2013XJZ018).

References

1. R. Li, X. He, J. Liu, et al., Expansion pipe technology and its application in drilling and production. Chin. Pet. Mach. **30**, 66–68 (2002)
2. M. Chen, Q. Cui, Current research status and progress of hydrogen sulfide corrosion mechanism and protection. Pet. Eng. Constr. **36**, 1–6 (2010)
3. C.F. Li, K.H. Song, W.Z. Shen, P.Y. Luo. A prospect of the application of high-strength steel material in oil and gas industry. Chin. Pet. Mach. **39**, 60–66 (2011)

4. J.X. Li, Z.Y. Liu, C.R. Gao, Evolution of texture in interstitial free steel during multiple cold rolling and annealing, J. Mater. Process Technol. **167**, 132–137 (2015)
5. X.Y. Han, Rolling of IF steel in ferrite region. Steel Roll. **24**, 48–50 (2007)
6. Z.L. Li, T. Chen, Z.H. Zeng, Hydrogen and its diffusion coefficient in stainless steels during electrochemically induced annealing. J Beijing Univ. Chem. Technol. **32**, 60–63 (2005)
7. J.M. Zhai, Study of fatigue reliability on H_2S corroded metallic materials, Doctoral dissertation, Beijing University of Technology, 2013
8. Z.Y. Liu, X.Z. Wang, R.K. Liu, C.W. Du, X.G. Li, Electrochemical and sulfide stress corrosion cracking behaviors of tubing steels in a H_2S/CO_2 annular Environment. J. Mater. Eng. Perform. **23**, 1279–1287 (2014)
9. J.M. Zhai, X.Y. Li, M.Y. Wu, Y.L. Zhang, Corrosion behavior of 45# steel in hydrogen sulfide solutions. Corros. Prot. **34**, 1013–1018 (2013)

Effect of Isothermal Annealing on the Structure and Property of Different Types of Cr13 Stainless Steels

Chunyan Fu, Gaoxian Zhu, Qi Xue, Wenzhu Shen and Shuliang Wang

Abstract As one of the important stainless varieties of major steel production, Cr13 stainless steel is used widely in the world. The annealing treatment of the metal is important in the production and processing, and good annealed is helpful to mechanical processing and subsequent heat treatment of steel. The isothermal annealing and fully annealing treatment were carried out in the different types of Cr13 stainless steels respectively, and their structures and mechanical properties were compared in this study. The results show that the structure with the annealing treatment is even and fine. With the increase of carbon content, the hardness of the annealed Cr13 stainless steel increases. Fully annealed Cr13 stainless steel has lower hardness and greater elongation than that isothermal annealed.

Keywords Isothermal annealing · Microstructure · Mechanical properties

Introduction

The phase equilibrium microstructure of Cr13 stainless steel at room temperature is consisted of ferrite and carbide. In quenching state, it features good hardness and corrosion resistance, and is thus widely applied [1–6]. But Cr13 stainless steel is

C. Fu · G. Zhu · Q. Xue · W. Shen · S. Wang (✉)
School of Material Science and Engineering, Southwest Petroleum University, Chengdu 610500, Sichuan, China
e-mail: wsliang1465@126.com

C. Fu
e-mail: fcyan1975@126.com

G. Zhu
e-mail: 772162402@qq.com

Q. Xue
e-mail: qxue01@163.com

W. Shen
e-mail: 6305493@qq.com

Y. Han (ed.), *Advances in Energy and Environmental Materials*,
Springer Proceedings in Energy, https://doi.org/10.1007/978-981-13-0158-2_47

produced generally by adopting techniques of hot rolling or hot drawing after smelting. Temperature differences in the smelting often cause segregation and then inhomogeneous composition. And stress and non-uniform speed rate in the rolling cause uneven microstructure. Those disadvantages undoubtedly increase difficulty in processing and use. It is hoped that the material is less hard when machined and more ductile in the deformation processing. Before thermal refining, it is hoped that the metallic material features suitable grain size and more uniform microstructure. And these properties are realizable by annealing heat treatment. The ordinary annealing requires longer cooling time, making for low production efficiency. In recent years, the isothermal annealing process has realized isothermal microstructure transformation and greatly shorten the processing cycle by accurate control of the isothermal temperature and time as well as of subcooling for transformation, thus earning wide application [7, 8]. In this paper, both conventional and isothermal annealing treatments are applied to the processing of Cr13 steels, and the metallographic structure and mechanical properties of Cr13 steels respectively treated by two annealing processes have been tested and discussed.

Test Materials and Methods

The test steel is Cr13, and its main chemical components are shown in Table 1.

The samples of the metallographic observation were machined wit dimensions of 20 mm × 20 mm × 8 mm (length, width, thickness). The standard tensile specimen is machined with the thickness of 5 mm and parallel section width of 10 mm. Notched impact specimen is machined by standard.

Specimens are divided into two groups, respectively for conventional annealing treatment and isothermal annealing treatment, and then are given with quenching treatment after annealing processes. The conventional annealing process: after 960 °C × 40 min, furnace cooling to 200 °C and then air cooling; the isothermal annealing process: after 860 °C × 40 min, forced air cooling to 720 °C and then furnace cooling to 200 °C before air cooling; the quenching process: oil cooling after 960 °C × 40 min; the tempering process: 400 °C × 120 min.

After heat treatment processes above, the specimens are ready for the metallographic observation and tensile test. OLYMPUS GX51 optical metallographic microscope is used to observe the annealed structure and normalized structure; WDW200 electronic tensile testing machine is used to perform the tensile property

Table 1 Chemical components of Cr13 stainless steel (wt%)

	C	Mn	Si	P	S	Cr	Ni	Cu	Mo	V	Al
1Cr13	0.105	0.240	0.46	0.026	0.017	11.90	0.18	0.07	0.022		
2Cr13	0.210	0.330	0.36	0.025	0.005	12.25	0.15				
3Cr13	0.300	0.425	0.35	0.028	0.005	12.35	0.29	0.08	0.150	0.08	0.015

test of the quenched specimen; JBS-300 impact testing machine is used for impact test of the quenched specimen.

Test Results and Analysis

Figures 1, 2, 3, 4, 5, 6, 7, 8 and 9 respectively show the microstructure of 1Cr13, 2Cr13 and 3Cr13 after 960 °C × 40 min quenching and 400 °C × 120 min tempering for original state, full annealing state and isothermal annealing state, magnified 500 times.

After being quenched and tempered, the microstructure of Cr13 stainless steel in the annealing state is dominated by troostite structure with a small amount of pearlites. The cementite augments with increase in carbon content. The microstructure of the original state and the annealing state before quenching and tempering processes are compared. It can be observed that the microstructure in the annealing state before quenching and tempering has significantly decreased carbide

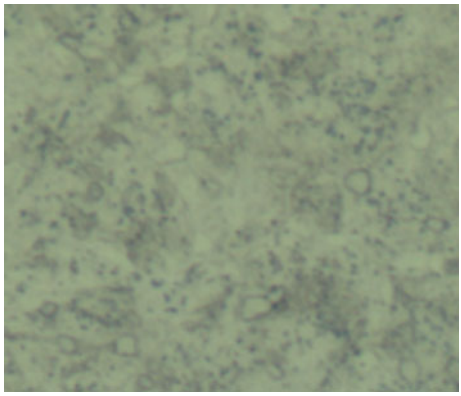

Fig. 1 Quenched 1Cr13 in the original state, 500×

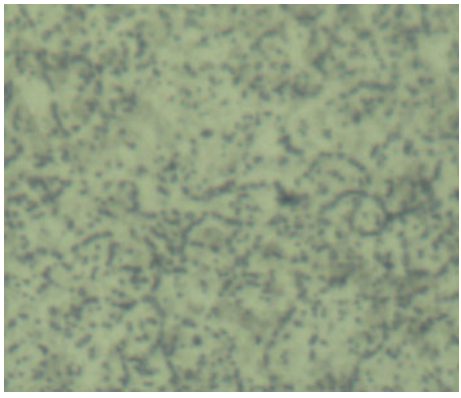

Fig. 2 Quenched 2Cr13 in the original state, 500×

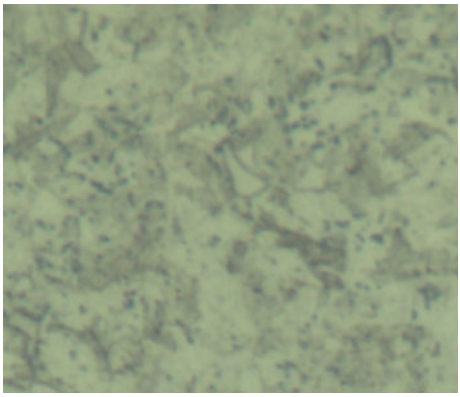

Fig. 3 Quenched 3Cr13 in the original state, 500×

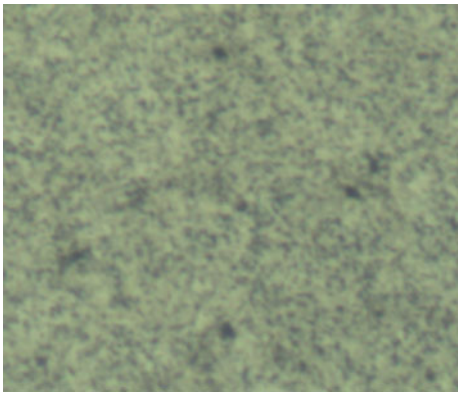

Fig. 4 Quenched 1Cr13 in the full annealing state, 500×

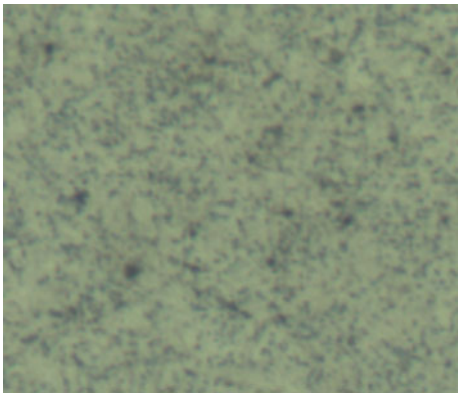

Fig. 5 Quenched 2Cr13in the full annealing state, 500×

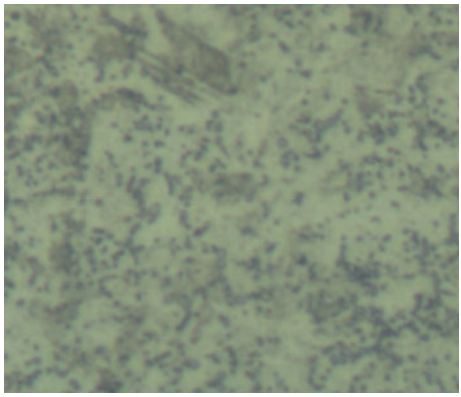

Fig. 6 Quenched 3Cr13 in the full annealing state, 500×

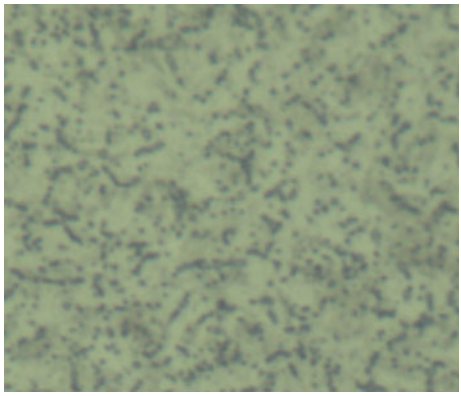

Fig. 7 Quenched 1Cr13 in the isothermal annealing state, 500×

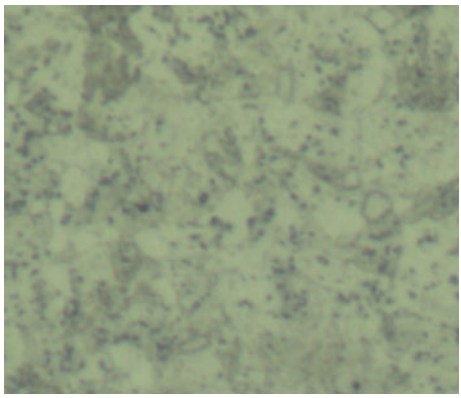

Fig. 8 Quenched 2Cr13 in the isothermal annealing state, 500×

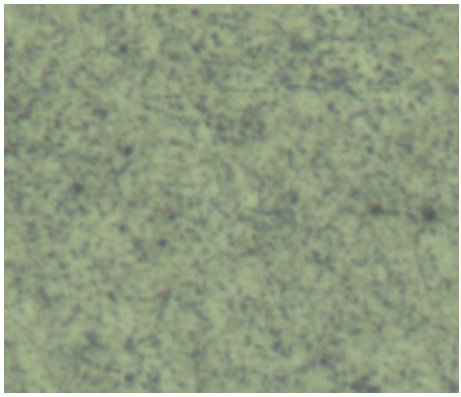

Fig. 9 Quenched 3Cr13 in the isothermal annealing state, 500×

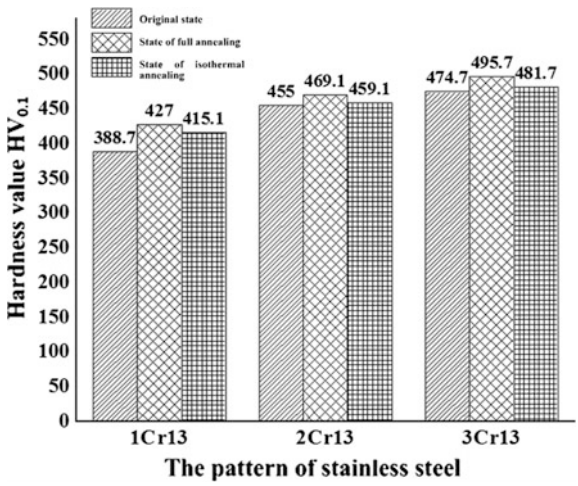

Fig. 10 Hardness of Cr13 stainless steel in the original state, the full annealing and the isothermal annealing before quenching and tempering

in both size and number, which indicates that annealing diffuses alloy elements, realizing improvements both in microstructure from the original state and in composition from inhomogeneous state.

Hardness of Cr13 stainless steel in the different initial states before quenching and tempering is shown in Fig. 10.

From comparison of hardness of the original state and annealing state before quenching and tempering, Cr13 stainless steel after annealing treatment can reach higher hardness on equal heat treatment conditions, which is helpful for hardening of the stainless steel. From comparison of hardness of the isothermal annealing state and full annealing state before quenching and tempering, the full annealing makes the hardness of Cr13 stainless steel increased greatly, especially for 1Cr13, up to 9.85%, but it does not mean the higher hardness is better and cooperation between hardness and toughness is also taken as a factor. With the increase in carbon content, Cr13 stainless steel hardness values corresponding increase.

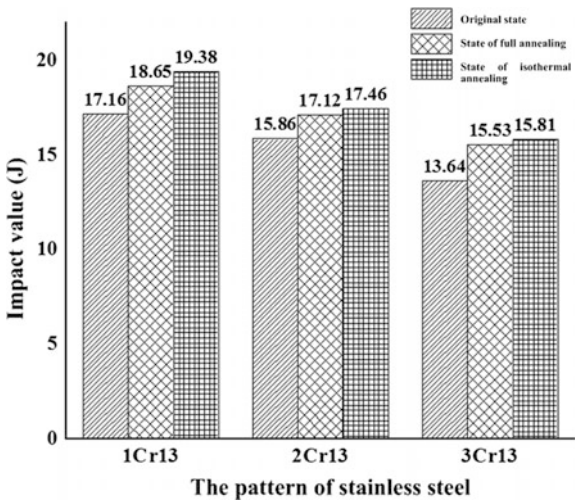

Fig. 11 Impact absorbing energy of Cr13 stainless steel in the original state, the full annealing state and the isothermal annealing state before quenching and tempering

Impact energy of Cr13 stainless steel in the different initial states before quenching and tempering is shown in Fig. 11.

From carbon content and the impact energy value, with the increase of carbon content, Cr13 stainless steel becomes less tough after quenching and tempering. From comparison of the impact energy value in the original state and annealing state before quenching and tempering, the value from annealing treatment before quenching and tempering is larger than that from direct quenching and tempering treatment, which indicates that annealing treatment can improve the toughness by quenching and tempering. From comparison of the impact energy value of the isothermal annealing state and full annealing state before quenching and tempering, the full annealing process makes the toughness of Cr13 stainless steel increased greatly by quenching and tempering, especially for 3Cr13, up to 15.91%.

From the hardness and impact energy value of the isothermal annealing state and full annealing state before quenching and tempering, and according to the cooperation of hardness and toughness in the practical use, hardness of the isothermal annealing state before quenching and tempering is better. This indicates that the isothermal annealing treatment contributes in a greater degree to the improvement of comprehensive mechanical property of Cr13 stainless steel after quenching and tempering.

Conclusions

The Cr13 stainless steel by the isothermal annealing has better comprehensive mechanical property than that by full annealing before quenching and tempering. With the increasing of the carbon content, the hardness of Cr13 stainless steel after

quenching and tempering increases, while the toughness decreases [9]. According to the actual demand, full annealing process is most preferred for machining of Cr13 stainless steel, while the isothermal annealing process is the best choice before quenching and tempering treatment.

References

1. S. Yao, J. Duan, Experimental study on optimization of heat treatment process of 2Cr13 steel rotating seat. Ship Sci. Technol. **30**(6), 127–130 (2008)
2. S. Cao, X. Sun, Quenching and tempering treatment of 2Cr13 steel. Heat Treat. **25**(1), 67–69 (2010)
3. H. Lai, L. Wang, Microstructure and performance of 2Cr13 steam turbine blades after laser alloying. Appl. Laser. **29**(6), 507–510 (2009)
4. P. Wang, B. Wang, J. Song, Effect of quenching temperature on microstructure and mechanical properties of 2Cr13 stainless steel. Hot Work. Technol. **37**(4), 71–73 (2008)
5. X. Zhu, Q. Dai, Influence of tempering temperature on stress corrosion cracking and mechanical hysteresis of 2Cr13 stainless steel. Trans. Mater. Heat Treat. **30**(1), 11–14 (2009)
6. X. Zhu, Q. Dai, Heat treatment improvement of martensite stainless steel receivers used in vehicle scale. Mech. Eng. Mater. **32**(6), 74–77 (2008)
7. Y. Liu, H. Wang, C. Ji et al., A new forge residual heat isothermal normalizing technique to improve the product quality and save energy. J. Changchun Univ. Technol. Nat. Sci. Ed. **28** (S0), 49–53 (2007)
8. R. Jin, Improvement of isothermal annealing process for 22CrM0H steel gear forgings. Heat Treat. Metals. **28**(12), 61–63 (2003)
9. P. Zhang, S. Zhou, Effect of heat treatment on microstructure and properties of Cr13 stainless steel. Spec. Steel Technol. **13**(3), 11–17 (2007)

Low Damage Fracturing Fluid in Low Water Bearing Coal Bed Based on Micro Mechanism of Foam

Xiaogang Li, Binyu Xu, Ping Zhang, Danqiong Li, Zhaozhong Yang, Zhiling Zhou and Zhichao Song

Abstract Coal bed methane (CBM) reservoir in Eastern-Yunnan and Western-Guizhou area generally has the problems of low water content, sensitive to external fluid, so it is promoted to use the foam fracturing fluid in hydraulic fracturing application. The change of bubble size and shape had been observed by using the long focal length zooming microscope and the environmental scanning electron microscope. The distribution and adsorption of additives had been studied by Cryo-SEM. With the experimental results, we can reveal the relation of the macroscopic properties of the foam fracturing fluid and microstructure of foam. Based on these, a low damage and enhanced desorption foam fracturing fluid suitable for low water bearing coal bed has been developed. The research shows that the film self-repair function determines the foam stability of the foam fracturing fluid, surfactant polarity on its important influence in the adsorption on coal surface, it is positive to select the appropriate surfactant for reducing the adsorption damage

X. Li (✉) · B. Xu · Z. Yang · Z. Song
State Key Laboratory of Oil and Gas Reservoir Geology and Exploitation,
South West Petroleum University, Chengdu 610500, Sichuan, China
e-mail: swpuadam@126.com

B. Xu
e-mail: 393184626@qq.com

Z. Yang
e-mail: yzzycl@vip.sina.com

Z. Song
e-mail: 455913065@qq.com

P. Zhang · D. Li
China United Coalbed Methane Corporation, Ltd, Beijing 100011, China
e-mail: zp_zcy@163.com

D. Li
e-mail: lidq14@cnooc.com.cn

Z. Zhou
College of Materials and Chemistry & Chemical Engineering,
Chengdu University of Technology, Chengdu, Sichuan 610059, China
e-mail: 34913755@qq.com

Y. Han (ed.), *Advances in Energy and Environmental Materials*,
Springer Proceedings in Energy, https://doi.org/10.1007/978-981-13-0158-2_48

and enhancing the foam stability of the fracturing fluid. The foam fracturing fluid developed in this study has a foam quality of 78% and a half-time of 1110 s. According to the SEM and damage experiment, the damage rate of the fluid to coal core is negative, and some secondary micro-fractures generated in the coal after soaking with the foam fracturing fluid. Thus, there is a field application value for the foam fracturing fluid which be studied in this paper.

Keywords Coal bed methane (CBM) · Foam fracturing fluid · Microanalysis Performance optimization

Introduction

With the unceasing adjustment of the country's energy structure, the proportion of clean energy, such as natural gas, is rising [1, 2]. As a kind of unconventional natural gas, CBM is a strategic supplement to conventional energy resources. The Eastern-Yunnan and Western-Guizhou area is one of the most abundant area of CBM resources in China [3], the development of CBM resources in this area can reduce or even avoid the gas accident, and can avoid the greenhouse effect caused by coal mine gas drainage, but also can reduce the air pollution caused by coal burning. But the permeability of coal reservoir in target area is low [4, 5], so stimulation is needed. Hydraulic fracturing is one of the important means of stimulation in coal reservoir. Moreover, the coal bed in this area are different from those in Qinshui and other places where they have been developed on a large scale. The hydrogeological features of this area are complex, and most of them are low water bearing coal bed or the dry coal bed. In the last stimulation of the reservoir in this area, the fracturing fluid such as linear adhesive has been used, which is easy to adsorb and difficult to flow back, that lead to that the effect of the stimulation is not ideal [6]. Therefore, the fracturing fluid with low damage and easy flow back is needed for the fracturing operation in this area.

Compared with conventional water based fracturing fluid, the foam fracturing fluid has the advantages of small amount of liquid to entry the well, reducing the damage to the reservoir, complementing the formation energy, assisting the fluid to flow back [7] and improving the desorption rate of methane in coal bed [8–12]. It can be used in the stimulation of low water bearing coal bed in this area. According to the gas in the foam, the foam fracturing fluid is divided into carbon dioxide foam fracturing fluid and nitrogen foam fracturing fluid. When CO_2 dissolved in water, the solution was acidic. There was some higher corrosion and safety requirements for the underground pipe column, fracturing equipment and tools with the CO_2 foam fracturing fluid, these will improve the cost. But the nitrogen foam fracturing fluid does not have this feature, it is recommended to use nitrogen foam fracturing fluid in the stimulation of coal bed. At the same time, macromolecule or polymer cannot be used as foam stabilizer in order to reduce the adsorption damage caused by additives. That is to say, when the low water bearing coal bed is fractured in the

area, it is necessary to adopt foam fracturing fluid with certain stability and without macromolecule or polymer stabilizer. The buried depth of coal bed in the target area is generally between 250–1500 m and the reservoir temperature is low [4, 6]. Therefore, the low damage foam fracturing fluid can be prepared with the synergism with surfactants.

As one of the important indexes for evaluation of fracturing fluid, the sand carrying capability of foam fracturing fluid relate to the stability of foam: only when the bubbles which supporting the proppant are deformation or rupture, and a channel foamed in the bubbles, proppant sinking will occur. According Doctor Fei (2017) [13], foam stability can be divided into three mechanisms (i.e., drainage, coarsening and rupture). These mechanisms include foam drainage caused by gravity [14], coarsening caused by gas transfer between bubbles [15], and bubble coalescence caused by rupture of liquid films [16]. On account of foam drainage influences the fraction of liquid in the foam, which determines both coarsening and coalescence of bubbles, a possible strategy for enhancing foam stability involves reducing the foam drainage is increasing the viscosity of fluid [17, 18]. For rheology, the transition of the form of surfactant micelle from spherical micelle to worm-like micelle equivalent to a dramatic increase in the fluid elasticity and viscosity [13]. The addition of electrolyte is propitious to transform from spherical micelles to worm-like micelles [19]. On the one hand, the thickness of ion-atmosphere of the head group of surfactant will be compressed by the counter ion, the repulsion between the head group of surfactants will be reduced, the density of surfactant which adsorbed on the surface will be increases, the surface tension will be further reduce, the foaming volume will be increases; on the other hand, the electrolyte will compress the electrical double layer, neutralize the charge, the electric repulsion between surfactants which adsorbed on both sides of the film between two bubbles will be weakened, the thickness of film will be thinned, the stability of foam will be declined [20]. Therefore, the concentration of inorganic salt must be screened so as to reduce its influence on foam stability. Increasing the concentration of surfactant can also improve the stability of foam, but when the concentration is greater than CMC, the stability of foam will decrease. Thus, the concentrations of surfactants also need to be screened. Improving foam quality, in order to make bubbles to contact and interfere with each other, the film will be shaped the most ideal form—hexagonal—the angle of boundary is 120°, at this point, the pressure is minimum, and the rate of drainage is decreases, which is beneficial to foam stability. Moreover, the uniform size and fine structure of foam can also reduce the rate of drainage and increase the stability of the foam [21].

The coal in the target area are amphiphilic, and the adsorption of surfactant on the surface of coal will aggravate the hydrophilic property of coal. This will increases the adsorption of surfactant on the surface of coal, and increases the water content in pores and fractures. The increase of water content will have a negative effect on desorption, diffusion and seepage of methane molecules in coal bed [22]. For changing the wettability of coal, reducing the damage caused by surfactant adsorption and water lock, and improving the ability of desorption and diffusion of methane, the fluorocarbon surfactant is added into the foam fracturing fluid as the

desorption agent [23, 24]. Because the fluorine are hard to be polarized, the polarity of fluorocarbon chain is smaller than that of hydrocarbon chain, so that the hydrophobic effect of fluorocarbon chain is much stronger than that of hydrocarbon chain, and the oil is also dispersed (the oil means hydrocarbon). In addition, the lower polar brings weaker interactions between fluorocarbon chains, which makes the fluorocarbon surfactant molecules are more inclined to oriented accumulate to form molecular film at the air/liquid interface than other surfactants. That can significantly reduce the surface tension, is conducive to the formation and stability of foam.

So the selective additives of foam fracturing fluid, should be free of macromolecules or polymer foam stabilizing agent; can reduce the surface tension; can increase the viscosity of liquid. In the system, two or more surfactants can form synergism. Foam quality should be at around 74% (the effect of foam quality on foam stability is the most active). The size of the foam should as uniform as possible. If there must to add inorganic salt, its effects on the foam should be as small as possible.

Experimental Section

Materials. Cocamido propyl betaine (XN-QPJ-A) were provided as solution by Chengdu Kehongda Technology Co., Ltd., China (30 ± 2 wt% active content). Cocamido propyl betaine is a betaine-type zwitterionic surfactant. Sodium alpha-olefin Sulfonate (XN-WPJ-1) were provided as solid power by Chengdu Kehongda Technology Co., Ltd., China (30 ± 2 wt% active content). Hexadecyl trimethyl ammonium bromide (XN-QPJ-B), sodium dodecyl benzene sulfonate (XN-QPJ-D), sodium dodecyl sulphate (XN-QPJ-E) and Sodium lauryl sulfonate (XN-WPJ-2) were provided as solid power by Chengdu Kelong Co., Ltd., China (90 wt% active content). KCl (XN-NT-20), $CaCl_2$, $MgCl_2$ and NaCl were provided as solid power by Chengdu Kelong Co., Ltd., China (99.5 wt% active content). N, N-Dimethyl-1-dodecylamine N-oxide (XN-QPJ-C) were provided as liquid by Chengdu Kelong Co., Ltd., China (95 wt% active content). Zwitterionic/composite/cationic/non-ionic fluorocarbon surfactant (XN-ZJX-1/2/3/4) were provided as solution by Chengdu Kehongda Technology Co., Ltd., China (50 ± 2 wt% active content). 20/40 mesh size ceramic proppant were provided by State Key Laboratory of Oil and Gas Geology and Exploitation, South West Petroleum University, China. All these chemicals were used without further purification. Deionized water was used in all the experiments. All working solutions were prepared immediately prior to each experiment at 27 ± 1 °C. In the damage experiment, the coal core is drilled from a large block of coal from the 3# layer of LC mine in Eastern-Yunnan.

Sample Preparation. These agents were added to 100 mL of deionized water using a glass rod to dissolve the powder with gentle stirring to avoid bubble formation in all cases. In the experiment of proppant sedimentation, the proppant

were introduced into the solution after all agents were dissolved. Once all additives were entirely dissolved or mixed, high-speed homogenization of the chemical mixture at 8000 rpm for 1 min using entrained air was performed to produce the foam (Waring-Blender method). This method could primely control mixing rate and mixing time, and had better repeatability.

Experimental Procedure. After the foaming was completed, the foam was immediately transferred to a 500 mL graduated cylinder. During the experiments, the total foam volume and half-time of foam were recorded (V_0 is the total foam volume, $t_{1/2}$ is the half-time). Then, the morphologies of the selected foam sample were imaged using a long focal length zooming microscope (Carl Zeiss, Germany) and a Quanta 450 environmental scanning electron microscope (FEI, America). The sample for zooming microscope were prepared by pouring same foam into a surface dish to observe the change of foam. These samples for scanning by SEM were prepared by freezing a small drop of foam or liquid on a clean wafer with liquid nitrogen to maintain the microstructures of the mixtures. Next, the rheological properties of the foam samples was investigated using a HAAKE MARS III Rheometer (Thermo Scientific, Germany). A double concentric cylinder (DG41) was used to carry out the steady rheological measurements. The apparent viscosity was measured by continuous shearing for 60 min at 42 °C. The entire process was performed at a constant shear rate of 170 s^{-1}. The same foam was mixed with 1 wt % ceramic proppant with a 20/40 mesh size (Equivalent diameter Dp = 700 mm) and density was equal to 2000 kg/m^3. A 500 mL graduated cylinder was applied to ensure that the diameter of graduated cylinder was at least 25 times larger than the diameter of the proppant to minimize the wall effect on the settling velocity. In the damage experiment of coal core with the foam fracturing fluid, firstly displacing the standard brine (2%KCl + 5.5%NaCl + 0.45%$MgCl_2$ + 0.55%$CaCl_2$) from one side, then driving the fracturing fluid (not foaming) from another side, and displacing the standard brine as the first time. When the standard brine is being driven, there should be at least three or more points of the value of permeability approximately equal or equal.

Results and Discussion

Foamability and Foam Stability. The total foam volume and half-time are the two key parameters to evaluate the foam fracturing fluid. The total foam volume represents the foamability of fracturing fluid, and the half-time represents the stability of foam. First, the effects of the kind and concentration of surfactant on the foamability and foam stability were studied. There is no correlation between the total foam volume and half-time, so in order to visually contrast foamability and foam stability with diverse surfactants, the integrated values can be used to compare.

Table 1 The data of the total foam volume, foam quality, half-time and integrated value for five surfactants in three concentrations respectively

Code	Concentration [%]	Total foam volume [V_0, mL]	Foam quality [%]	Half-time [$t_{1/2}$, s]	Integrated value [mL s]
XN-QPJ-A	0.5	330	70	323	106590
	1	420	76	1065	447300
	1.5	425	76	1138	483650
XN-QPJ-B	0.5	330	70	362	119460
	1	410	76	921	377610
	1.5	420	76	935	392700
XN-QPJ-C	0.5	420	76	294	123480
	1	470	79	369	173430
	1.5	505	80	410	207050
XN-QPJ-D	0.5	425	76	301	127925
	1	470	79	365	171550
	1.5	510	80	362	184620
XN-QPJ-E	0.5	460	78	300	138000
	1	470	79	322	151340
	1.5	435	77	298	129630

Selection of Foaming Agent. In Table 1, these data are shown as the total foam volume, foam quality, half-time and integrated value for five surfactants in three concentrations respectively. The integrated values of XN-QPJ-A are larger than any other surfactants in the concentration of 1 and 1.5% respectively. The increase of the value of the total foam volume and half-time are slackened when the concentration raise from 1 to 1.5%. Therefore, in consideration of economic efficiency, XN-QPJ-A with a concentration of 1% should be recommended as the foaming agent.

Selection of Foam Stabilizer. In order to avoid the adsorption damage caused by macromolecules or polymers, the surfactants which can form synergism with the foaming agent can be added as foam stabilizer. In Table 2, these data are shown as the total foam volume, foam quality, half-time and integrated value for two surfactants compounded with XN-QPJ-A in three concentrations respectively. The result of foaming and stability are better when XN-WPJ-1 compounded with XN-QPJ-A. But the increase of the value of the total foam volume and half-time are slackened when the concentration raise from 0.5 to 1%. Therefore, in consideration of economic efficiency, XN-WPJ-1 with a concentration of 0.5% should be recommended as the foam stabilizer.

Selection of Desorption Agent. The adding of desorption agent will have a problem of compatibility with foaming agent and foam stabilizer, so it is necessary to test the foaming and stabilizing ability of the fracturing fluid after adding the desorption agent. The concentration of those desorption agents are 0.5% uniformly, and the screening process is not discussed in this paper. On the basis of Table 3, both of integrated value and half-time are the largest when XN-ZJX-1 compounded

Table 2 The data of the total foam volume, foam quality, half-time and integrated value for two surfactants compounded with XN-QPJ-A in three concentrations respectively

Code	Concentration [%]	Total foam volume [V_0, mL]	Foam quality [%]	Half-time [$t_{1/2}$, s]	Integrated value [mL s]
XN-WPJ-1	0.1	420	76	1264	530880
	0.5	440	77	1765	776600
	1	460	78	1932	888720
XN-WPJ-2	0.1	435	77	1214	528090
	0.5	440	77	1300	572000
	1	430	77	1415	608450

Table 3 The data of the total foam volume, foam quality, half-time and integrated value for four desorption agents compounded with XN-QPJ-A and XN-WPJ-1 respectively

Code	Total foam volume [V_0, mL]	Foam quality [%]	Half-time [$t_{1/2}$, s]	Integrated value [mL s]
XN-ZJX-1	440	77	1783	784520
XN-ZJX-2	485	79	988	479180
XN-ZJX-3	450	78	936	421200
XN-ZJX-4	425	76	1329	564825

Table 4 The rate of anti-swelling of XN-NT-20 under different concentrations

No.	Liquid	Volume of clay [mL]	Rate of anti-swelling [%]
1	Deionized Water	3.95	/
2	Kerosene	0.56	/
3	0.5%XN-NT-20	0.91	89.68
4	1%XN-NT-20	0.69	96.17
5	1.5%XN-NT-20	0.59	99.12
6	2%XN-NT-20	0.61	98.53

with XN-QPJ-A and XN-WPJ-1, and the foam quality is 77%. So XN-ZJX-1 with a concentration of 0.5% should be recommended as the desorption agent in the foam fracturing fluid system.

Selection of Clay Stabilizer. In the earlier study, it was found that the anti-swelling effect of XN-NT-20 against at room temperature was the best, and the test data of its rate of anti-swelling under different concentrations are showing in Table 4. According to this table, the rate of anti-swelling of XN-NT-20 reaches a maximum, when the concentration reaches 1.5%. However, considering the rate of anti-swelling and economic factors, it is recommended that the maximum concentration shall not exceed 1%.

Nevertheless, XN-NT-20 is inorganic salt, the addition of it will impact on foaming and stabilizing ability of foam. Table 5 shows that the addition of

Table 5 The effect of XN-NT-20 on foaming and stabilizing ability of foam with different concentrations

Concentration [%]	Total foam volume [V_0, mL]	Foam quality [%]	Half-time [$t_{1/2}$, s]	Integrated value [mL s]
0.5%	455	78	1110	505050
1%	425	76	899	382075

Table 6 The eventually system of the foam fracturing fluid

No.	Agent	Type	Code	Concentration [%]
1	Foaming agent	Betaine-type zwitterionic surfactant	XN-QPJ-A	1
2	Foam stabilizer	Alpha-olefin sulfonate	XN-WPJ-1	0.5
3	Desorption agent	Zwitterionic fluorocarbon surfactant	XN-ZJX-1	0.5
4	Clay stabilizer	Inorganic salt	XN-NT-20	0.5

XN-NT-20 will reduce the half-time of the foam, and the greater of the concentration, the more of the depression. Though, the total foam volume of the system with 0.5% XN-NT-20 is increasing on the contrary. It proves that the addition of XN-NT-20 will debase the surface tension of the foam fracturing fluid, this is conducive to the formation of foam, but not conducive to the stability of foam. As the concentration increases to 1%, the volume of foam decreases to under no salt. The rate of anti-swelling of 1%XN-NT-20 is only about 10% larger than that of 0.5%XN-NT-20, but whereas the average content of clay in coal is about 10%, the disparity between the two will be further diminished, and therefore the recommended concentration of XN-NT-20 is 0.5%.

Based on the preceding screening, a foam fracturing fluid system has been formed, as shown in Table 6 The subsequent experiments will proceed with this system.

Stability and Microstructure of Foam Fracturing Fluid System. The foam was observed by the long focal length zooming microscope, and the magnification is 4×10. During the observation, the foam is unceasing changing. In Fig. 1a, the shape of the foam is micro round and regular, and the bubbles with different sizes are distributed evenly, the rate of drainage at this time is slow. As time goes on, the rate of drainage increases, the liquid film thin, and some of the bubbles coarsen, rupture and coalesce. When approaching to the half-time of the foam (Fig. 1c), the angles between the partial bubbles are close to 120°. These bubbles tend to stabilize, and the rate of drainage of those bubbles slow down. Figure 1d shows that, more angles close to or reach 120°, the liquid films are thinner and even can be observed the structure of underpart foam through the films. Throughout the observation, the rate of change of the foam (i.e., the rate of drainage) is slow-fast-slow, and fast turning point of the rate changes from fast to slow appearing before the half-time.

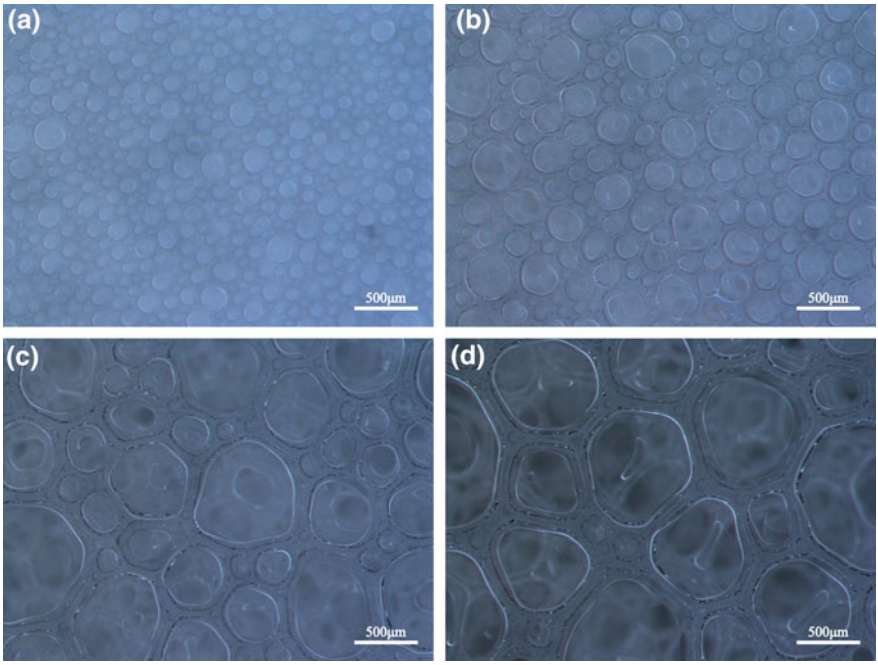

Fig. 1 Images captured by the long focal length zooming microscope. **a** The structure of foam at 60 s, **b** 341 s (5min 41 s), **c** 1035 s (17 min 15 s) and **d** 2377 s (39 min 37 s)

Figure 2a shows the honeycomb structure of foam, each bubble has a similar size and shape. The partial boundary angle is close to 120° (shown in Fig. 2b), and the surfactant molecules are dispersed evenly in the foam structure, this is propitious to the stabilization of foam.

Figure 2c–d shows the distribution of surfactants in the fluid, there are some worm-like micelles formed by surfactants and a chain consisting of surfactants between micelles. These are beneficial to improve the viscosity of liquid. In all experiments, the viscoelastic phenomenon was not observed in the liquid, that means the spatial structure of the worm-like micelles are weak, they are easily to disintegrate and disperse under shearing. It can avoid the damage caused by prolonged half-time in coal bed.

Rheology. The experimental result shows that the apparent viscosity of the fracturing fluid increases firstly and then decreases between 54–89 MPa s in 1 h at the shear rate of 170 s^{-1} and 90 °C. It means that the foam fracturing fluid has enough viscosity to transport the proppant under the influence of temperature and shear, so it can meet the demand of fracturing (Fig. 3).

Proppant Sedimentation. In addition to the viscoelastic effect of liquid, the suspension mechanism in foam is more determined by packaging and supporting the

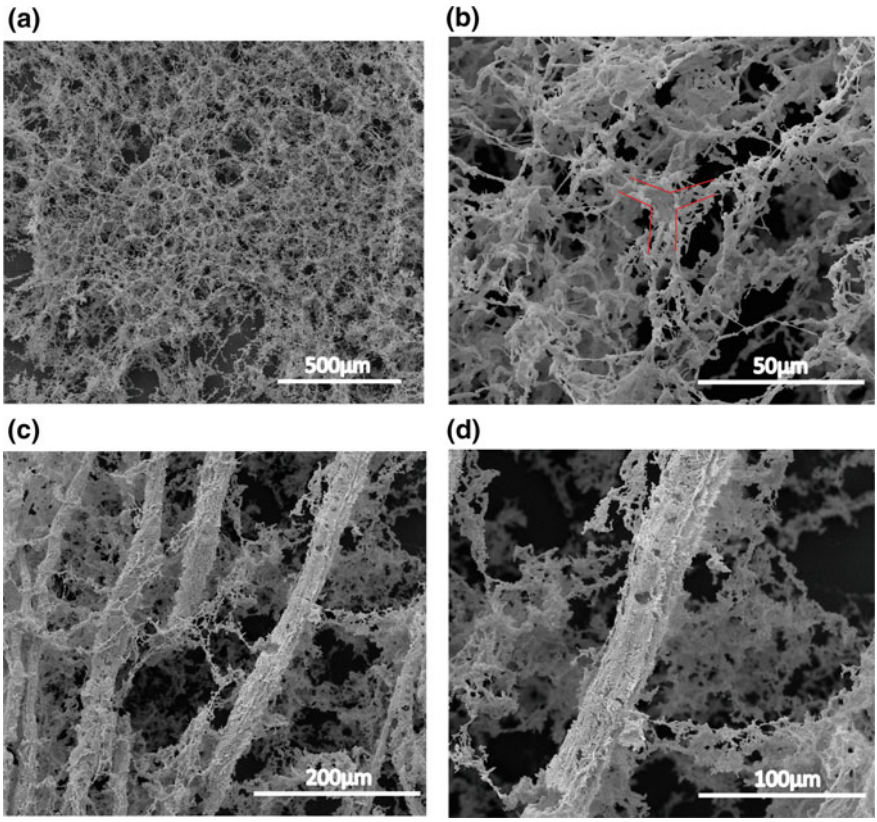

Fig. 2 Cryo-SEM images of frozen aqueous foams and fluid captured by Quanta 450 environmental scanning electron microscope. **a** The structure of foam at 150 times and **b** at 2000 times. **c** The distribution of surfactants in the fluid at 500 times and **d** at 1000 times

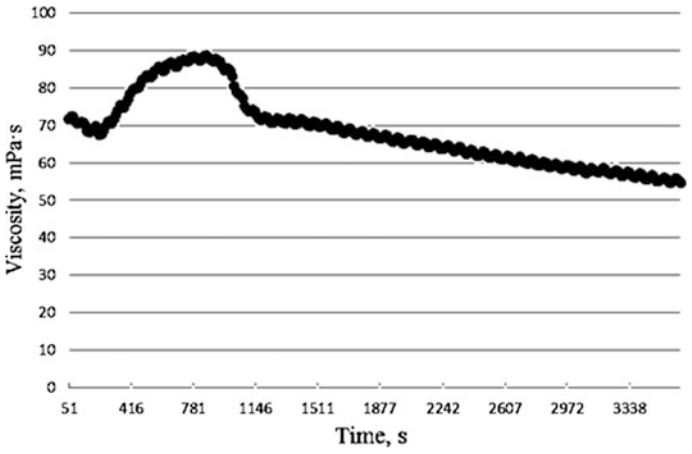

Fig. 3 Apparent viscosity as a function of time at a shear rate of 170 s^{-1} and 90 °C

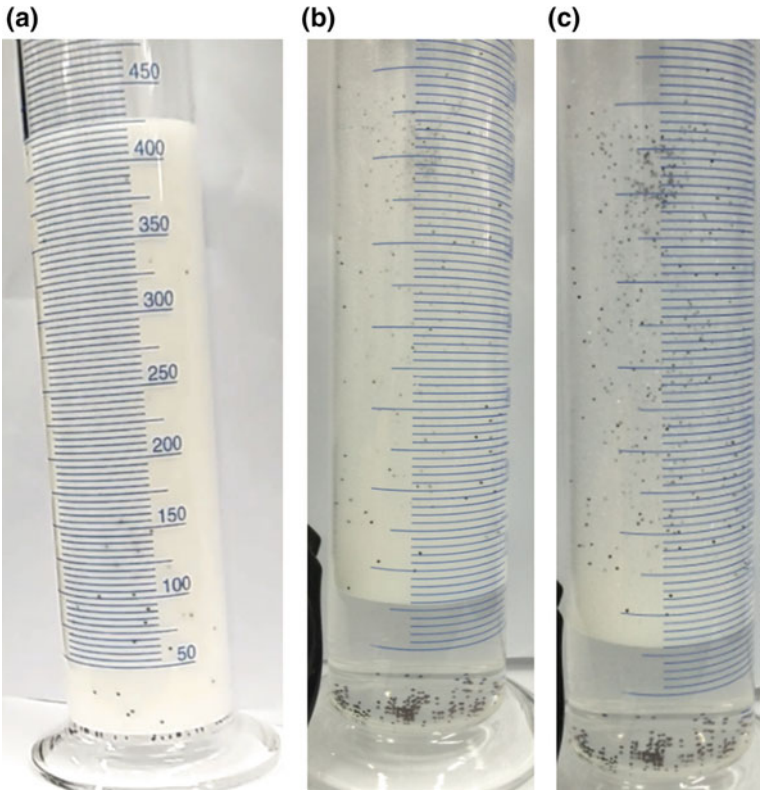

Fig. 4 Snapshots of the proppant sedimentation experiments from 0 to 80 min. **a** The proppant is dispersed evenly in the foam at initially. **b** 2160 s 36 min. **c** Most of the proppant remained suspended in the foam at 4800 s (80 min)

proppant by the bubbles. The proppant will settle only when the bubbles which acting on the proppant are seriously deformed or ruptured.

Through the observation, at the time of pouring the foam into a measuring cylinder after foaming, the distribution of proppant is uniform in the foam, and just a small amount of proppant are settled due to the contact with the bottom of the cylinder. With the experiment, the bubble deform and rupture faster when it close to the parting of the foam and liquid, and proppant settling faster. The proppant in the foam where they are far away from the boundary will not settle down, but will go up with the coalescence of bubbles. After 80 min, a majority of the proppant are still suspended in the foam, which shows that the foam fracturing fluid has better suspension performance and meets the requirements of fracturing (Fig. 4).

Damage to Coal Core. As the permeability showing in Table 7, there is a marked decline while the standard brine is displaced into the coal core for the first time, which suggests that the coal core has other sensitivities. After driving the foam

Table 7 Process and data of foam fracturing fluid on damaging coal core

No.	Process of displacement	Permeability [mD]	Rate of damage [%]
1	First displacing standard brine	0.0071	/
2		0.0059	
3		0.0056	
4		0.0044	
5		0.0045	
6		0.0045	
7	Driving the fracturing fluid	/	/
8	Second displacing standard brine	0.0049	−9.70
9		0.0048	−7.46
10		0.0048	−7.46
11		0.0048	−7.46
12		0.0048	−7.46

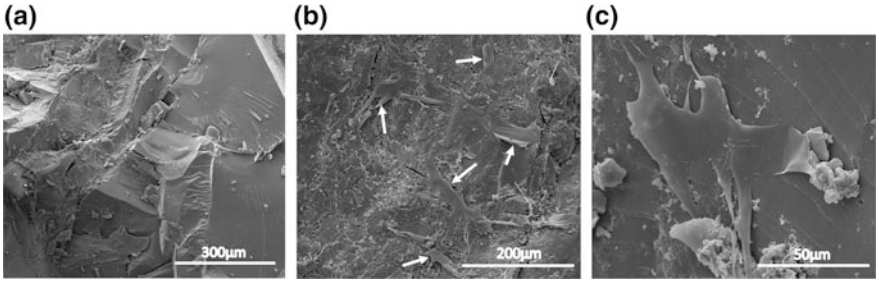

Fig. 5 SEM images of the coal without and with immersed in the fluid. **a** The image of the coal which was untreated by the fluid at 300 times. **b** and **c** The images of the coal which was treated by the fluid at 500 and 2000 times

fracturing fluid and immersing for 6 h, the permeability is measured by the displacing standard brine for the second time is larger than the first time, and the rate of damage is negative. It may be the sensitivity damages were partially lifted by the fracturing fluid, or some new seepage channels are possibly formed in the coal core after driving and immersing by the fracturing fluid.

According to Fig. 5, it can be known as that there are few fracture in the untreated coal (Fig. 5a). Oppositely, there are some secondary micro-fracture generated in the coal after immersing. Moreover, the areas where the secondary micro-fracture generated are the areas which adsorbed more surfactants (Fig. 5b). The areas there is no secondary micro cracks are less adsorbed (Fig. 5c). Adsorption occurred on the surface of coal and no adsorption was observed into the micro-fracture. The occurrence of secondary micro-fractures may be the cause of the negative rate of damage in the experiments.

Conclusions

The stimulation of CBM in Eastern-Yunnan and Western-Guizhou area require the fracturing fluid which had such benefits as strong proppant carrying capacity and low damage. Based on experimental observation, the foam fracturing fluid contains free of macromolecules or polymer but good foam stability, without crosslinking agent but strong proppant carrying capacity is the optional type of fracturing fluid for fracturing in this area.

The basic measures for controlling foam stability include screening the type and concentration of agent, optimizing foaming process and parameters, and controlling microstructure of foam.

The foam fracturing fluid obtained in this study has a foam quality of 78% and a half-time of 1110 s. The proppant carrying capacity of foam has been enhanced and the damage rate of the system to coal core is negative.

In this paper, there are still some phenomena that cannot be concluded, for example, the mechanism and influencing factors of secondary micro-fracture generated in the coal after soaking with the foam fracturing fluid need to be further study.

Acknowledgements The authors acknowledge the financial support provided by the National Science and Technology Major Project (2016ZX05044004002).

References

1. Ministry of Land and Resources People's Republic of China, *China Mineral Resources* (Geological Publishing House, Beijing, 2015), p. 4
2. Ministry of Land and Resources People's Republic of China, *China Mineral Resources* (Geological Publishing House, Beijing, 2016), p. 5
3. D. Gao, Y. Qin, T. Yi, Geological condition, exploration and exploitation strategy of coal-bed methane resources in Guizhou. Coal Geol. Chin. **21**, 20–23 (2009)
4. H. Xu, S. Sang, T. Yi, X. Zhao, H. Liu, L. Li, Control mechanism of buried depth and in-situ stress for coal reservoir permeability in Western Guizhou. Earth Sci. J. Chin. Univ. Geosci. **39**, 1507–1516 (2014)
5. Z. Chen, D. Tang, H. Xu, S. Tao, B. Zhang, J. Cai, C. Meng, The pore system properties of coalbed methane reservoirs and recovery in Western Guizhou and Eastern Yunnan. J. Chin. Coal Soc. **35**, 158–163 (2010)
6. X. Meng, S. Liu, G. Shi, L. Zhu, X. Feng, Results of CBM testing and remoulding of reservoir in Eastern Yunnan and Western Guizhou and related problems and suggestions. Chin. Coalbed Methane. **3**, 31–34 (2006)
7. D. Oussoltsev, I. Fomin, K.K. Butula, K. Mullen, A. Gaifullin, A. Ivshin, D. Senchenko, I. Faizullin, Foam fracturing: new stimulation edge in Western Siberia. SPE Russian Oil and Gas Technical Conference and Exhibition, Moscow, 2008, SPE 115558
8. R. Puri, D. Yee, Enhanced Coalbed Methane Recovery. SPE Annual Technical Conference and Exhibition, New Orleans, 1990, SPE 20732

9. C. W. Byrer, H. D. Guthrie, Appalachian coals: potential reservoirs for sequestering carbon dioxide emissions from power plants while enhancing CBM production. Proceedings of the International Coalbed Methane Symposium, University of Alabama, Tuscaloosa 1999
10. S. Stevens, CO_2 injection for enhancing coalbed methane recovery: project screening and design. Proceedings of the 1999 International Coalbed Methane Symposium, University of Alabama, Tuscaloosa, 1999
11. L. E. Arri, D. Yee, W. D. Morgan, M. W. Jeansonne, Modeling Coalbed Methane Production With Binary Gas Sorption. SPE Rocky Mountain Regional Meeting, Wyoming, 1992, SPE 24363
12. C.R. Clarkson, R. M. Bustin, Binary gas adsorption/desorption isotherms: effect of moisture and coal composition upon carbon dioxide selectivity over methane. Int. J. Coal Geol. **42**, 241–271 (2000)
13. Y. Fei, J. Zhu, B. Xu, X, Li, M. Gonzalez, M. Haghighi, J. Ind. Eng. Chem. 50, 190–198 (2017)
14. J. Angarska, C. Stubenrauch, E. Manev, Drainage of foam films stabilized with mixtures of non-ionic surfactants. Colloids Surf. A Physicochem. Eng. Asp. **309**, 189–197 (2007)
15. A. Maestro, E. Rio, W. Drenckhan, D. Langvevin, A. Salonen, Foams stabilised by mixtures of nanoparticles and oppositely charged surfactants: relationship between bubble shrinkage and foam coarsening, Soft Matter. **10**, 6975–6983 (2014)
16. R.I. Saye, J.A. Sethian, Multiscale modeling of membrane rearrangement, drainage, and rupture in evolving foams. Science. **340**, 720–724 (2013)
17. S. Guignot, S. Faure, M. Vignes-Adler, O. Pitois, Liquid and particles retention in foamed suspensions. Chem. Eng. Sci. **65**, 2579–2585 (2010)
18. J. Wang, A.V. Nguyen, Foam drainage in the presence of solid particles Soft. Matter. **12**, 3004–3012 (2016)
19. A. Sambasivam, A.V. Sangwai, R. Sureshkumar, Self-assembly of nanoparticle—surfactant complexes with Rodlike Micelles: a molecular dynamics study. Langmuir. **32**, 1214–1219 (2016)
20. J. Yang, *Principle and Application of Surfactants* (Southeast University Press, Nanjing, 2012)
21. X. Wang, Z. Wang, F. Wang, Y. Lu, *Theory and Practice of Carbon Dioxide Foam Fracturing Technology* (Petroleum Industry Press, Beijing, 2016)
22. Z. Yang, J. Han, Q. Fu, X. Li, J. Zhang, Nat. Gas Geosci. **26**, 951–957, 985 (2015)
23. Y. Kondo, N. Yoshino, hybrid fluorocarbon/hydrocarbon surfactants. Curr. Opin. Colloid Interface Sci. **10**, 88–93 (2005)
24. T. Yoshimura, A. Ohno, K. Esumi, Equilibrium and dynamic surface tension properties of partially fluorinated quaternary ammonium salt gemini surfactants. Langmuir. **22**, 4643–4648 (2006)

Fracture Conductivity Model Based on Proppants with Different Sizes

Zhaozhong Yang, Liyong Zhu, Ping Zhang, Danqiong Li, Xiaogang Li and Fangxuan Tang

Abstract Proppants for hydraulic fracturing usually refer to quartz sand, ceramic proppants and their modified products as well. Importantly, the fracture conductivity varies with the performance and properties of different proppants. However, there are still some uncertainties between the material properties and fracture conductivity. To this end, a numerical model was established based on the distribution of proppant particle size, material properties, fractal dimension of pore structure, elastic deformation, proppant embedment according to fractal theory and principle of elastic-plastic mechanics as well, which is used to predict fracture conductivity under multi-factor. The results show that fracture conductivity is directly related to material properties between proppant and reservoir rock. The Young's modulus of rock has a significant effect on the conductivity of the propped fracture. And, the influence of Poisson's ratio is weak. The fracture conductivity increases with the increase of pore fractal dimension.

Keywords Hydraulic fracturing · Fracture conductivity · Proppant Material properties · Fractal geometry · Elastic-plastic mechanics

Z. Yang · L. Zhu (✉) · X. Li · F. Tang
State Key Laboratory of Oil & Gas Reservoir Geology and Exploitation, Southwest Petroleum University, Chengdu 610500, Sichuan, China
e-mail: 807299627@qq.com

Z. Yang
e-mail: yzzycl@vip.sina.com

X. Li
e-mail: swpuadam@foxmail.com

F. Tang
e-mail: 277357741@qq.com

P. Zhang · D. Li
China United Coalbed Methane Corporation, Ltd., Beijing 100011, China
e-mail: zhangping30@cnooc.com.cn

D. Li
e-mail: lidq14@cnooc.com.cn

Y. Han (ed.), *Advances in Energy and Environmental Materials*,
Springer Proceedings in Energy, https://doi.org/10.1007/978-981-13-0158-2_49

Introduction

With the development of low permeability reservoirs in recent years, the hydraulic fracturing technique has been widely used as an effective reservoir stimulation method for shale gas, tight sandstone gas, coal-bed methane and other unconventional reservoirs The theory of hydraulic fracturing technique [1] can be concluded as follow.

Firstly, high viscosity fracturing fluid above the formation breakdown pressure is injected into the underground by the ground high pressure pumps. When the pressure is larger than the near borehole pressure and reaches the rock tensile strength, the fractures begin to propagate; Secondly, to make the fracture gradually extends as expected, the fracturing fluid are expected to be injected, where the carrying fluid mixed with proppants are delivered too, resulting in the fracture extended and filled with proppants. When the pump stops, long and wide enough, high conductivity propped fractures are formed underground, which makes sure the success of hydraulic fracturing. The fracture conductivity is the product of fracture permeability and fracture width, which determines the reconstruction effect of hydraulic fracturing treatment. The conductivity is controlled by the proppant, reservoir properties and many other factors, how to predict the propped fracture conductivity this issue has caused wide attention of scholars domestic and overseas. Zhirong [2, 3] found out the influence of different particle size combination of proppant by experiment, it turns out that big size proppant portfolio formation of the cracks in the diversion ability is significantly higher than small size proppant combination to form cracks. Lacy and Qingzhi [4–7] has evaluated the influence of proppant embedment, the research reveals that proppant embedment would cause a huge decline in conductivity, and the influence of proppant types, reservoir properties, paved-sand content and closure pressure has been discussed as well. Yongming [8] has built proppant embedded depth calculation model, on this basis, Zhifan [9] has matched out the relation between proppant embedment depth and fracture conductivity. Jinzhou [10] has established proppant embedment calculation model which considered of wall deformation, quantitatively analyzed how the closure pressure and reservoir Young's modulus affect proppant embedment depth while compared to the experiment results. Guotao [11, 12] has established the fracture conductivity prediction model considering the proppant embedment, study the proppant pave layers influence to the conductivity.

These experiments and theories researches have offered some references to the conductivity prediction. However, restrictions of the experimental conditions and excessive simplification of the models make the forecast results and actual situation a large deviation. Besides, existing fracture conductivity prediction models have all simplified the proppant particle as diameter spheres, which ignores the small particle size of proppant grain filling effect of pore space. This article is based on *fractal theory*, the *elastic-plastic mechanics of materials*, *Carman-Kozeny equation* and the *particle spatial arrangement basic theory*, established the fracture conductivity analytical mode which considering the proppant size distribution,

proppant and rock wall elastic deformation, proppant embedment, the fractal dimension of pore structure and the layer number of sanding, offering some theory basis for proppant selection and fracturing fluid design.

Model

The Fractal Characteristics of Fracture'S Pores. The scholars home and abroad found that when the pore space formed by the accumulation was filled up step by step, the proportion of radius reduced is not a constant, and the pore has obvious quasi self-similar structure [13].

According to the fractal geometry, proppant particles formed by the accumulation propped fracture pores satisfies the following scaling law [14]:

$$N(\varepsilon \geq \lambda_{\min}) = (\frac{\lambda_{\max}}{\lambda_{\min}})^{D_f}. \tag{1}$$

where N is the number of pores or capillaries, ε is the length scale and D_f is fractal dimension. Previous studies have shown that the fractal dimension of pore formed by closely packed particle is between 1.2619 and 1.6309, estimated 1.4649. Because the proppant particles randomly distribute in the fracture, apparently maximum pore size and minimum pore size are related to the smallest diameter and the largest diameter of proppant particles respectively. Further speaking, the smallest diameter of pore λ_{min} and the largest diameter of pore λ_{max} can be obtained from following expression by three dimensional geometry.

$$\lambda_{\min} = \left(\frac{2\sqrt{3} - \pi}{2\pi}\right)^{\frac{1}{2}} d_{\min}. \tag{2}$$

$$\lambda_{\max} = \left(\frac{2\sqrt{3} - \pi}{2\pi}\right)^{\frac{1}{2}} d_{\max}. \tag{3}$$

where d_{min} is the smallest diameter of proppant particles and d_{max} is the largest diameter of proppant particles. In Eqs. 2 and 3, the parameters d_{min} and d_{max} need to be solved based on the microstructures of proppant particles.

According to self-similar fractal geometries that is derived from Boming Fracture porosity is described by following expression [14]:

$$\phi = \left(\frac{\lambda_{\min}}{\lambda_{\max}}\right)^{d_E - D_f}. \tag{4}$$

where φ is the porosity of fracture and d_E is the Euclidean dimension.

Equations 1–4, the basis parameters of propped fracture pores, are used to derive fractal permeability model.

Based on Hagen-Poiseulle capillary model, Boming derived the fractal permeability which is expressed as [15–18]

$$K = \frac{\pi L_0^{1-D_T}}{128A} \frac{D_f}{3 + D_T - D_f} \lambda_{\max}^{3+D_T}. \tag{5}$$

where L_0 is the representative length, D_T is tortuosity fractal dimension and A is total cross sectional area.

The total cross sectional area A can be obtained by simplifying the pore cross section as circles. Specifically, the total cross sectional area A is expressed as

$$A = \frac{\int_{\lambda_{\min}}^{\lambda_{\max}} \frac{\pi}{4} \lambda^2 (-dN)}{\phi} = \frac{1-\phi}{\phi} \frac{\pi D_f \lambda_{\max}^2}{4\left(2 - D_f\right)}. \tag{6}$$

Due to the high porosity and high permeability characteristics of propped fracture, capillary can be simplified as straight capillary ($D_T = 1$). Combining Eqs. 1–6, fractal permeability of propped fracture can be expressed as:

$$K = \frac{(2\sqrt{3} - \pi)(2 - D_f)}{64\pi(4 - D_f)} \frac{\beta^{d_E - D_f}}{1 - \beta^{d_E - D_f}} d_{\max}^2. \tag{7}$$

where $\beta = \frac{d_{\min}}{d_{\max}}$ is the ratio of the smallest diameter of proppant particles and the largest diameter of Proppant particles.

Elastic Deformation. Assuming that proppant is homogeneous spherical, homogeneous isotropic materials, completely elastic, regardless of the interface friction resistance, the binding surface between the proppant particles can be considered as the combination of the curved surface, and the binding surface between the particles and fracture surface can be considered as the combination of the curved surface and the flat surface, which satisfies the Hertz's law. When two balls internally or externallly contact with stress, due to the elastic deformation of material, the contact point expanded into a circle with a radius of R_0 by extending around [19, 20]. According to elastic mechanics theory, the contact circle radius can be expressed as

$$R_0 = \left[\frac{3}{4} F \left(\frac{1 - \upsilon_{r_1}^2}{E_{r_1}} + \frac{1 - \upsilon_{r_2}^2}{E_{r_2}} \right) \frac{r_1 r_2}{r_1 \mp r_2} \right]^{\frac{1}{3}}. \tag{8}$$

where F is normal contact pressure, υ_{r_1} and υ_{r_2} are the Poisson's ratio of the two spheres respectively, E_{r_1} and E_{r_2} are the Young's modulus of the two individual spheres, and r_1 and r_2 are the circle radius of the two spheres.

The Deformation between Proppant Particles. Considering large size proppants prop main fracture and according to the theory of elastic mechanics, the contact circle radius which is between proppant particles can be expressed as

$$R_1 = \frac{3}{8}\pi p_c d_{\max} \frac{1-\upsilon_p^2}{E_p}. \tag{9}$$

where p_c is closure pressure, υ_p is the Poisson's ratio of proppants and E_p is the Young's modulus of proppants.

According to Hertz elastic theory, the effective diameter reduction between proppant particles is descripted as

$$\Delta d_1 \approx R_1^2/d_{\max}. \tag{10}$$

The Deformation between Proppant and Wall. Considering contact between proppant and wall, the reduction of proppant diameter is expressed as

$$R_2 = \frac{3}{8}\pi p_c d_{\max}\left(\frac{1-\upsilon_p^2}{E_p} + \frac{1-\upsilon_r^2}{E_r}\right). \tag{11}$$

where υ_r is the Poisson's ratio of formation and E_r is the Young's modulus of formation.

Similarly, the effective diameter reduction which is used to calculate fracture width is descripted as

$$\Delta d_2 \approx R_2^2/d_{\max}. \tag{12}$$

Proppant Embedment. After contacting with the rock wall, the proppant embedment phenomenon will happen under the closure pressure. The embedment of proppants would reduce fracture width and then lower the proppant fracture conductivity. The amount of embedment is expressed as [9]

$$h = \frac{1}{2}d_{\max} - \left\{\frac{d_{\max}^2}{4} - \frac{1}{6}\left[\frac{3\pi p_c d_{\max}^3}{4}\left(\frac{1-\upsilon_p^2}{E_p} + \frac{1-\upsilon_r^2}{E_r}\right)\right]^{\frac{2}{3}}\right\}^{\frac{1}{2}}. \tag{13}$$

Propped Fracture Width. According to the theory of particle accumulation, proppant particles with different arrangements in the fracture have different coordination numbers and porosity [21], and directly affect the propped fracture width. Under the closure pressure, proppant particles tend to be closely packed (rhombohedron filled), the fracture width expression is:

$$w = \frac{\sqrt{6}n}{3} d_{\max} - \frac{\sqrt{3}(n-1)}{2} \Delta d_1 - 2\Delta d_2 - 2h. \tag{14}$$

Proppant Fracture Conductivity Prediction Model. Combining the Eqs. 7 and 14, the proppant fracture conductivity prediction model considering distribution of proppant particle size, material properties, fractal dimension of pore structure, closure pressure and paved layers is expressed as

$$F_{RCD} = C \frac{\beta^{d_E - D_f}}{1 - \beta^{d_E - D_f}} \cdot [2\sqrt{6}nd_{\max} - 3\sqrt{3}(n-1)\Delta d_1 - 12\Delta d_2 - 12h] \cdot d_{\max}^2. \tag{15}$$

where $C = \frac{(2\sqrt{3}-\pi)(2-D_f)}{384\pi(4-D_f)}$ is a constant that is related to fractal dimension.

Equation 15 shows that proppant fracture conductivity is closely related to the proppant distribution characterization, fractal dimension of pore structure, closure pressure and paved layers.

Results and Discussions

Material Properties of Proppant and Mechanical Properties of Rock. As is shown in Fig. 1, different rock Poisson's ratio gives almost the equal fracture conductivity curves which indicate that fracture conductivity will increase with the increase of the Poisson's ratio, but the increase rate is not obvious. This is due to the increase of rock Poisson's ratio leads to the enhancement of lateral extension of rock. Correspondingly, the fracture conductivity slightly increases. What's more, the larger Young's modulus, the smaller elastic deformation and embedment, the larger the fracture conductivity.

Figure 2 shows the fracture conductivity versus Young's modulus at different Poisson's ratio of proppant. It can be seen clearly that the fracture conductivity increases with the increase of proppants' Young's modulus, and that the larger proppant Poisson's ratio, the larger the fracture conductivity. What's more, both effects of proppant Young's modulus and Poisson's are small.

According to the method in this paper, we plot the fracture conductivity figure that can show the matching relationship between the material properties of proppants and mechanical properties of rocks (Figs. 3 and 4). Thus, optimization of fracturing fluid and the proppant with low embedment degree (such as coated ceramsite proppant) is recommended to maintain the fracture conductivity in the soft coal reservoirs with low Young's modulus (usually <10 GPa). There are many

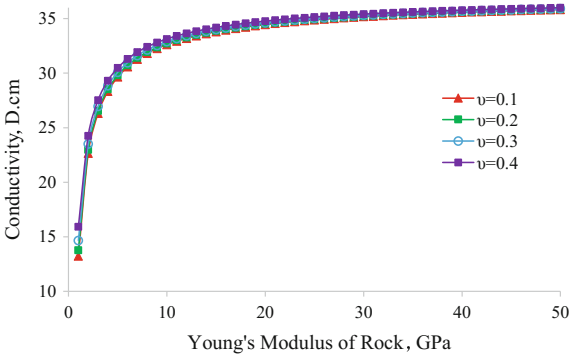

Fig. 1 The relationship between the fracture conductivity and Young's modulus of formation

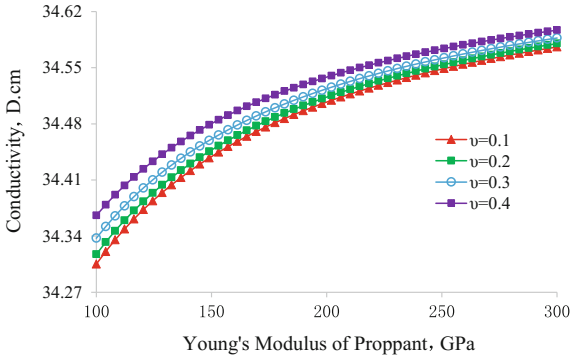

Fig. 2 The relationship between the fracture conductivity and Young's modulus of proppant

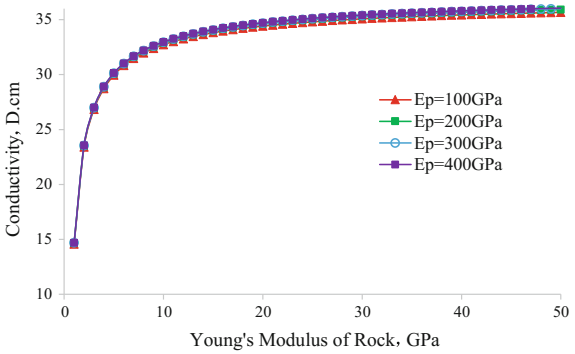

Fig. 3 The characteristic between the fracture conductivity and Young's modulus' matching relationship

small particle size, high strength proppants (such as ceramsite) available for tight sandstone reservoirs (Young's modulus 30–50 GPa, Poisson's ratio 0.10–0.15) and high stress reservoirs to achieve the effective prop of the dynamic fracture to ensure the fracture conductivity.

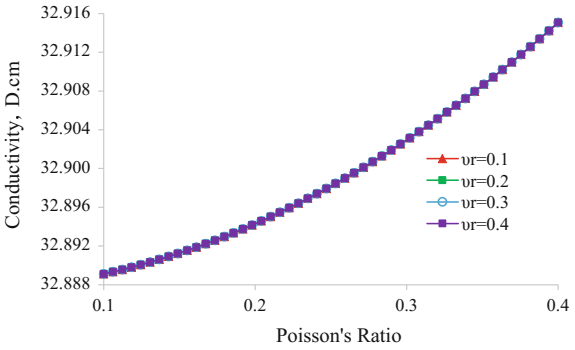

Fig. 4 The characteristic between the fracture conductivity and Poisson's ratio's matching relationship

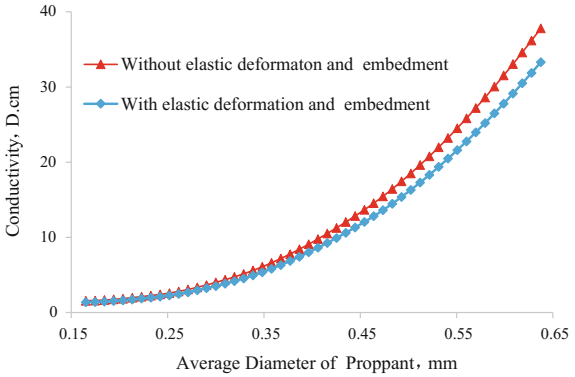

Fig. 5 The relationship between the fracture conductivity and the average particle size of the proppant

Distribution of Proppant Particle Size. Figure 5 shows the fracture conductivity increases rapidly with the increase of the average particle size of the proppant. It's obvious that the fracture which is propped by the large particles, has higher conductivity than propped by the small particles. For example, with elastic deformation and proppant embedment, fracture conductivity is 33.31 D cm when fracture is propped by 20–40 mesh proppants. However, fracture conductivity is 4.17 D cm, which is down by 87.48%.

Fractal Dimension. Fracture permeability expression Eq. 7 which is derived by fractal geometry theory with capillary model is closely related to size of fracture porosity microstructure and fractal dimension of pore structure. Thus, the fracture conductivity varies with the fractal dimension of propped fracture's pore structure (Fig. 6). It can be seen clearly that the larger the fractal dimension D_f, the more complex the pore structure, the larger fracture conductivity. It means that the fractal dimension is an important parameter for fracture conductivity. With elastic deformation and proppant embedment, fracture conductivity is 32.88 D cm at $D_f = 1.4649$.

Closure Pressure. Closure pressure is an important parameter characterizing the environment in which the proppant is located. Figure 7 shows the fracture

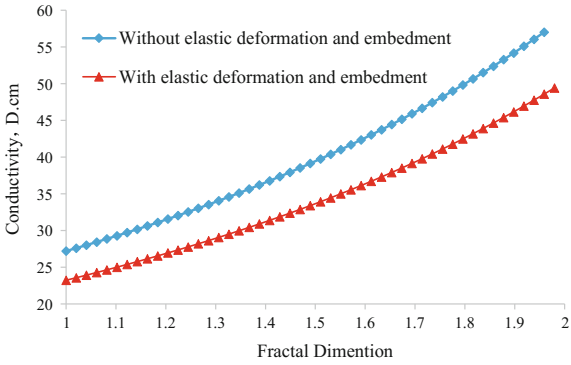

Fig. 6 The relationship between the fracture conductivity and the fractal dimension of pore structure

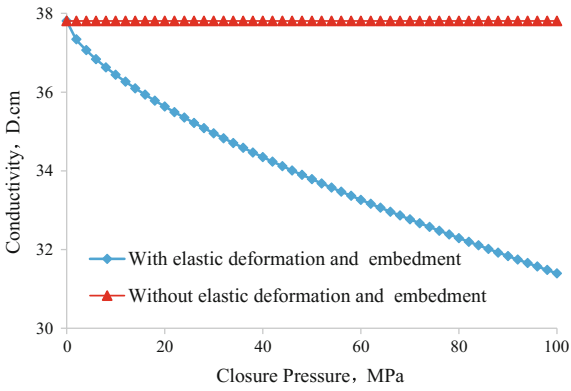

Fig. 7 Effects of closure pressure on fracture conductivity and embedment

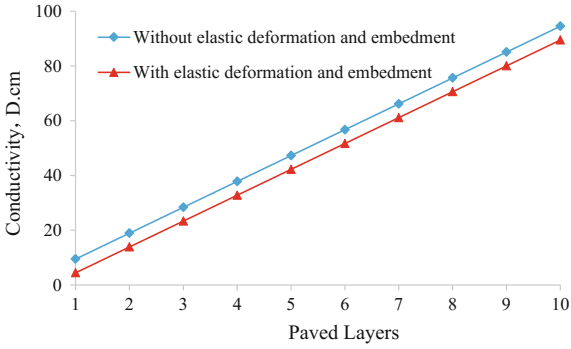

Fig. 8 Effect of paved layers on fracture conductivity

conductivity decreases with the increase of the closure pressure. In another word, the elastic deformation and embedment of proppants that located in high stress formation are serious, which lead to a decrease in fracture conductivity.

Paved Layers. Figure 8 is presented to illustrate importance of paved layers to fracture conductivity. The results show that fracture width rapidly increases with the

increase of the paved layers, and the conductivity of the propped fracture is increased. Correspondingly, the propped fracture conductivity will be slightly reduced when elastic deformation and proppant embedment are taken into account.

Conclusions and Recommendations

In this paper, a new analytical model which is associated with distribution of proppant particle size, material properties, fractal dimension of pore structure, closure pressure and paved layers was established based on the fractal geometry theory, elastic-plastic material mechanics and Carman-Kozeny equation. The fracture permeability in analytical model established in this paper is more closely related to the microstructures in propped fracture such as pore structure fractal dimension and pore size.

This work only focuses on initial propped fracture conductivity which is deposited by proppant with different particle sizes. The analytical expression for fracture width considering elastic deformation and proppant embedment reveals the principles of matching relationship between the proppant material and formation. A long-term propped fracture conductivity prediction model considering the effects of both proppant size distribution and proppant particles dissolution is expected to be presented on our future work.

Acknowledgements This work was supported by the National Science and Technique Major Project through subject number 2016ZX05044004002.

References

1. L. Yingchuan, *Production Engineering* (M. Petroleum Industry Press, 2009)
2. J. Zhirong, G. Jianchun, J. Zhao, W. Jinfang, Z. Zhihongm, K Dan, Experimental study on the influence of different particle size proppant combination on fracture conductivity. J. Pet. Geol. Eng. **21**, 88–90 (2007)
3. W. Lei, Z. Shicheng, Z. Wenzong, W. Qingzhi, Conductivity of the proppant combination with different grain sizes in complex fracture. J. Nat. Gas Ind. **25**, 64–66 (2005)
4. L.L. Lacy, A.R. Rickard, D.M. Bilden, Fracture width and embedment testing in soft reservoir sandstone. J. Spe Drill. Compl. **13**, 25–29 (1998)
5. W. Qinzhi, Z. Shicheng, W. Lei, Y. Liu, Influence of proppant embedment on fracture long time flow conductivity. J. Nat. Gas Ind. **25**, 65–68 (2005)
6. L. Cong, G. Jianchun, W. Wenyao, D. Yan F. Deng. Experimental research on proppant embedment and it's damage to fracture conductivity. J. Nat. Gas Ind. **28**, 99–101 (2008)
7. S. Haicheng, X. Yun, J. Jianfang, T. Zhuhong, L. Se, Influence of embedment of propping agent to conductivity of fracture created by hydraulic fracturing. J. Well Test. **18**, 8–10 (2009)
8. L. Yongming, L. Yan, J. Jizhong, Z. Jinzhou, G. Yang, Research on quantitative calculation model of proppant embedment. J. Southwest Pet. Univ. **33**, 94–97 (2011)

9. H. Zhifan, L. Yuan, Y. Xiangyi, X. Yang, L. Qin, Z. Wei, Fengying L, Under the condition of single sanding closure pressure affecting proppant embed depth study. J. Sci. Tech. Eng. **14**, 232–234 (2014)
10. Z. Jinzhou, H. Xianjie, L. Yongming, Acaculation model of proppant embedment depth. J. Oil Gas Tech. **36**, 209–212 (2014)
11. W. Guotao, X. Yun, Y. Zhenzhou, Y. Lifeng, Z. Jing, Numerical simulation considering the impact of proppant and its embedment degree on fracture flow conductivity. J. Nat. Gas Ind. **33**, 65–68 (2013)
12. Ya M, L. Zhiping, G. Zhenzhen, Calculation model of fracture conductivity in coal reservoir and its application. J. Chin. Coal Soc. **39**, 1852–1856 (2014)
13. Y. Tiesheng, Z. Zhenghong, Study on the fractal structure of close arrangement pattern of particles. J. Basic Sci. Eng. **2**, 152–156 (1994)
14. Y. Bomin, L.J. Lee, H. Cao, A fractal in-plane permeability model for fabrics. J. Polym. Compos. **23**, 201–221 (2002)
15. P.C. Carman, Permeability of saturated sands, soils and clays. J. Agric. Sci. **29**, 262–273 (1939)
16. J. Kozeny, Ueber Kapillare Leitung des Wassers im Boden. J. Sitzungsber Akad. Wins, Wien. **136**, 271–306 (1927)
17. Y. Bomin, P. Cheng, A fractal permeability model for bi-dispersed porous media. J. Int. J. Heat Mass Transf. **45**, 2983–2993 (2002)
18. X. Peng, Y. Boming, Developing a new form of permeability and Kozeny–Carman constant for homogeneous porous media by means of fractal geometry. J. Adv. Water Res. **31**, 74–81 (2008)
19. T. Hongliang, X. Yuan, T. Chen, Z. Jinhua, Z. Yi, Z. Chunhua. Contact problem between two spheres considering surface roughness and geometrical curvature. J. Xi'an Jiaotong Univ. **50**, 1–7 (2016)
20. X. Lun, *Elasticity* (Higher Education Press, 2006)
21. G. Guosheng, *Powder Engineering* (Tsinghua University Press, 2009)

Influences of the Synthesis Procedure on the Photocatalytic Property of Nanostructured Ceria Supported on SiO_2

Yongyi Ding, Ning Fang, Chengbao Liu and Zhigang Chen

Abstract Nanostructured ceria supported on SiO_2 catalysts were synthesized using four different preparation procedures: (1) cerium nitrate adsorption, (2) ammonia precipitation, (3) citric acid-ammonia complexing method (4) citric acid sol-gel method. Thermogravimetry-differential scanning calorimetry (TG-DSC) was used to analyze the weight loss and crystallization behavior of the precursors made by four synthesis procedures during heat treatment. The synthesis effects on the size, dispersion, crystallinity and photocatalytic properties of ceria supported on SiO_2 were characterized by X-ray diffraction (XRD), high-resolution transmission electron microscope (HRTEM), ultraviolet-visible absorption spectra (UV-Vis), photoluminescence spectra (PL) and photocatalytic degradation of methylene blue. The results show that ceria supported SiO_2 catalyst synthesized by sol-gel method has the best dispersity and photocatalytic performance, lowest crystallinity, smallest grain size and band gap.

Keywords Synthesis · Photocatalysis · CeO_2 · SiO_2

Y. Ding · N. Fang · Z. Chen (✉)
School of Material Science and Engineering, Jiangsu University,
Zhenjiang 212013, China
e-mail: czg@ujs.edu.cn

Y. Ding
e-mail: ding_yongyi@163.com

C. Liu · Z. Chen
School of Chemistry, Biology and Materials Engineering, Suzhou University of Science and Technology,
Suzhou 215009, China

C. Liu · Z. Chen
Jiangsu Key Laboratory for Environment Functional Materials,
Suzhou 215009, China

C. Liu · Z. Chen
Jiangsu Collaborative Innovation Center of Technology and Material for Water Treatment, Suzhou 215009, China

Y. Han (ed.), *Advances in Energy and Environmental Materials*,
Springer Proceedings in Energy, https://doi.org/10.1007/978-981-13-0158-2_50

Introduction

Ceria is a kind of rare-earth oxide material which has excellent thermal and mechanical resistance [1]. Due to its propensity to non-stoichiometry and oxygen storage capacity (OSC) [2], CeO_2 has been widely used as an efficient catalyst in various reactions such as, automotive emission control [3] and solid oxide fuel cell applications [4], especially in photocatalysis such as water splitting [5] and degradation of dyes [6]. However, the catalytic efficiency of ceria will be heavily deactivated if it is exposed to high temperatures over 900 °C and this is mainly due to thermal sintering [7].

There are various new methods to synthesis CeO_2 composite with other oxides in order to improve the thermal stability and the OSC of ceria [8–10]. Among these oxides, silica (SiO_2) has been widely studied because of its properties such as high surface area, thermal stability, nontoxicity and low cost [11]. Several studies have been carried out on the CeO_2–SiO_2, especially with ceria supported on silica, the data shows that the overall function of the catalyst has been improved when ceria is supported on silica [12].

Though there is high interest in developing new synthesis procedures to make high efficiency of CeO_2–SiO_2 compounds, the effects of the different preparation procedures on the properties of the catalyst have not been intensively investigated. In this paper, CeO_2–SiO_2 catalysts were synthesized by four preparation methods: (1) cerium nitrate adsorption, (2) ammonia precipitation, (3) citric acid sol-gel method and (4) citric acid-ammonia complexing method. The weight loss and crystallization behavior of the precursors were characterized by thermogravimetry-differential scanning calorimetry (TG-DSC). The crystallinity and dispersion of CeO_2 supported on SiO_2 were investigated by X-ray diffraction (XRD) and high-resolution transmission transmission electron microscope (HRTEM). The photocatalytic properties were characterized by ultraviolet-visible absorption spectra (UV-Vis), photoluminescence spectra (PL) and photocatalytic degradation of methylene blue.

Experimental

Material. Cerium nitrate ($Ce(NO_3)_3{\cdot}6H_2O$), citric acid ($C_6H_8O_7{\cdot}H_2O$), ammonia water ($NH_3{\cdot}H_2O$) were from Sinopharm Chemical Reagent Co. Ltd. of China. Silica-gel (500–800 mesh) was supplied by Qindao Bangkai Co. and was calcined in air at 800 °C for 4 h prior to impregnation.

Cerium Nitrate Adsorption Method (CS). $Ce(NO_3)_3{\cdot}6H_2O$ (26.05 g, 0.06 mol) was dissolved in 200 ml deionzed water, then SiO_2 (36.05 g, 0.6 mol) were added to the solution for impregnation.

Ammonia Precipitation Method (CNS). The precursor was prepared by precipitation from a suspension of $Ce(NO_3)_3{\cdot}6H_2O$ (0.06 mol) and SiO_2 (0.6 mol) by adding $NH_3{\cdot}H_2O$ to pH = 10.

Citric Acid-Ammonia Complex Method (CCNS). $Ce(NO_3)_3{\cdot}6H_2O$ (0.06 mol) and $C_6H_8O_7{\cdot}H_2O$ (0.06 mol) were dissolved in 200 ml deionzed water, then $NH_3{\cdot}H_2O$ was added until pH = 10 to get a clear solution. After that SiO_2 (0.6 mol) were added to the solution for impregnation.

Citric Acid Sol-Gel Method (CCS). $Ce(NO_3)_3{\cdot}6H_2O$ (0.06 mol) and $C_6H_8O_7{\cdot}H_2O$ (12.61 g, 0.06 mol) were dissolved in 200 ml deionzed water, then SiO_2 (0.6 mol) were added to the solution for impregnation.

All the suspension get from the above mentioned procedures were kept at 60 °C under magnetic stirring to evaporate solvent. After that, the dried precursors were calcined at 500 °C for 4 h. In the photocatalytic experiment, three samples were added to make comparison. One is the pure silica gel calcined at 800 °C, one is a mix of CeO_2 (prepared by sol-gel method as CCS) and pure silica gel corresponds to a Ce: Si = 0.1 atomic ratio, named Mixing. Considering the visible light can make contribution to the degradation of MB, a photocatalytic experiment with no catalyst named Blank was added to make comparison.

Characterization. XRD patterns were recorded on BRUKER D8 ADVANCE diffractometer with Cu Kα radiation at 40 kV and 40 mA. Thermogravimetry-differential scanning calorimetry (TG-DSC) was performed on a SDT Q600 thermal analyzer at a heating rate of 10 °C/min under air flow. Transmission electron microscopy (TEM) of the samples was performed using a JEM-2100 electron microscope operating at an accelerating voltage of 200 kV. The UV-Vis spectra were measured with Shimadzu UV 3600 plus spectrometer. The photoluminescence (PL) spectra were recorded on a Varian Cary-Eclipse 500 of which excitation wavelength was 325 nm.

Photocatalytic Activity Measurement. 250 ml of methylene blue (MB) solution (initial concentration: 30 mg/L) was used in the presence of 100 mg of catalyst under the visible light radiation provided by 500 W xenon lamp. Prior to irradiation, the solution was magnetically stirred in dark for 40 min to achieve adsorption equilibrium then 10 ml H_2O_2 solution was added. After every 20 min, about 5 ml of solution was pipette out and centrifuged. The absorbance of the clear supernatants at 663 nm wavelength determined the concentration of methylene blue. The catalytic degradation efficiency (%) for catalysts was calculated according to the equation:

$$\text{Efficiency of degradation}(\%) = 100\left(\frac{A_0 - A_t}{A_0}\right) \quad (1)$$

where A_0 = the absorbance of methylene blue solution before illumination, At = the absorbance of methylene blue solution after illumination time t.

Results and Discussion

TG-DSC Analysis. TG and DSC curves of the procedures synthesized by different procedures are shown in Fig. 1. In TG curve, the weight remain steady after 300 °C, indicating that the impurity substance in the precursor have been combusted completely and the CeO_2–SiO_2 binary oxide is quite stable. In that case, the calcination temperature of the catalysts can be set at 500 °C to remove the organic impurities. The total weight loss of the catalyst prepared by citric acid-ammonia complexing method (42%) and precipitation method (40%) are quite close, so are the adsorption method (30%) and the sol-gel method (29%). The weight loss before 200 °C can be ascribed to the evaporation of physically adsorbed water and the combustion of organic substances. The weight drop sharply in the range of 200–260 °C which may correspond to the decomposition or combustion of the CeO_2 procedures.

In DSC curve, the material prepared by adsorption method has an obvious endothermic peak at 220 °C, which indicates the decomposition of $Ce(NO_3)_3{\cdot}6H_2O$. In contrast, the catalyst prepared by citric acid-ammonia complexing method has an exothermic peak at 220 °C, with sol-gel method a little higher at 260 °C. These exothermic peaks indicate that the catalyst had crystallization behavior during the heating process. It can be seen that compared with the complexing method, sol-gel method can raise the crystallization temperature of ceria.

X-ray Diffraction and TEM Analysis. All the prepared powders were characterized by X-ray diffraction (XRD) (Fig. 2). Diffraction patterns specific to CeO_2 crystalline phase [13] can be identified in all the samples. The diffraction peaks at 28.6°, 33.07°, 47.48°, 56.34°, 59.1°, 69.4°, 76.7° and 79.0° are corresponding to the (111), (200), (220), (311), (222), (400), (331) and (420) planes of CeO_2 (JCPDS 34-0394). The peak intensity of the catalyst prepared by sol-gel method is the lowest. It can be calculated that catalyst prepared by sol-gel method has the smallest

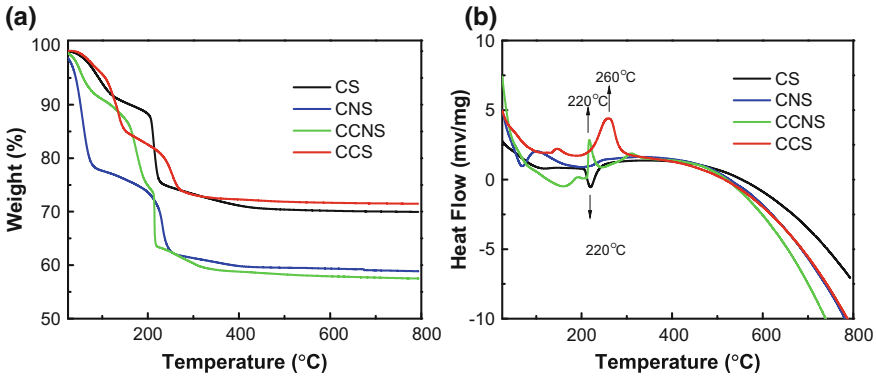

Fig. 1 TG **a** and DSC **b** curves of the procedures synthesized by different procedures

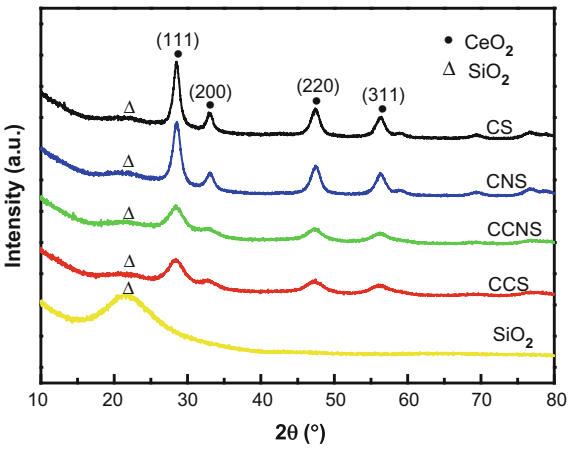

Fig. 2 XRD patterns of the catalysts synthesized by different procedures

crystallite size (4.3 nm) in lattice plane (111) of CeO_2 with complexing method, precipitation method and adsorption method coming the second (4.5 nm), third (7.1 nm) and the fourth (8.3 nm). The crystallinity of plane (111) of CeO_2 can also be calculated by the Reference Intensity Ratio (RIR) method. The calculated results showed that the crystallinity of the catalyst made by sol-gel method is the lowest (15%). The crystallinity of plane (111) of CeO_2 in complexing method (17%), precipitation method (41%) and adsorption method (43%) increased gradually coincide with the increase of the crystallite size of plane (111) of CeO_2. In addition, the average grain size of the catalysts can also be calculated and the average grain size of each catalyst is 3.2 nm, 3.9 nm, 9.2 nm, 13.6 nm respectively.

In this paper, the intensity of SiO_2 was represented by the relative peak area (23°) [14] of SiO_2. The relative peak area of SiO_2 can be calculated by the percentage of the diffraction peak area of SiO_2 in each sample relative to the diffraction peak area of pure SiO_2, as shown in Table 1. The catalyst made by sol-gel method has the lowest relative peak area of SiO_2 (7.2%) with complexing method, precipitation method and adsorption method coming the second (8.5%), third (10.34%) and fourth (11.25%), as shown in Table 1. This means the CeO_2 in the catalyst synthesized by sol-gel method has the best dispersion on the surface of SiO_2. All the data mentioned above are listed in Table 1.

Table 1 Structural properties of catalysts synthesized by different procedures

Sample	Crystallite size of plane (111) of CeO_2 (nm)	Crystallinity of plane (111) of CeO_2 (%)	Average grain size (nm)	Relative peak area of SiO_2 (%)
CS	8.3	43	13.6	11.2
CNS	7.1	41	9.2	10.3
CCNS	4.5	17	3.9	8.5
CCS	4.3	15	3.2	7.2

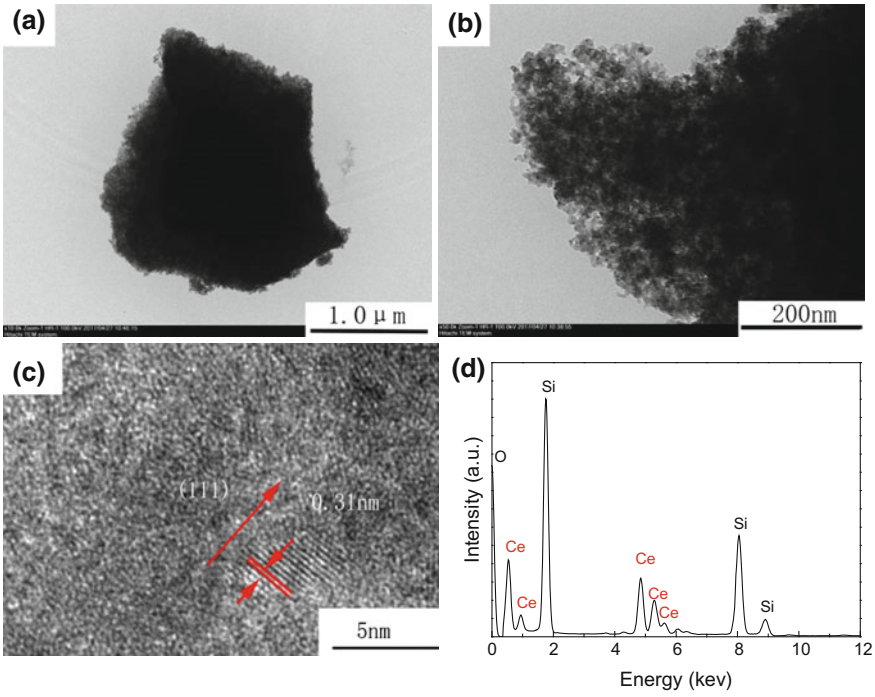

Fig. 3 TEM pictures of the catalyst made by sol-gel method **a** the morphology of the catalyst **b** the interface of the catalyst **c** the HRTEM picture of the particles on the support **d** the EDS spectra

Figure 3a shows the morphology of the catalyst synthesized by sol-gel method. Figure 3b shows that the CeO_2 particles dispersed on the SiO_2 support are homogenous and their crystallite size of plane (111) of CeO_2 is small which is in accordance with the XRD result. Figure 3c shows that the particles supported on the SiO_2 have a clear lattice line with a 0.31 nm spacing, corresponding to the crystal surface (111) of CeO_2. Additionally, energy dispersive X-ray spectroscopy (EDS) confirms the formation of CeO_2–SiO_2 composite, which was composed of the element Ce, Si, O as shown in Fig. 3d. The good dispersion of the metal oxide on the support is beneficial to improve photocatalytic performance of catalyst [15].

UV–Vis, PL and Photocatalytic Experiment Analysis. In Fig. 4, all the catalysts have strong absorption of light of when the wavelength was below 500 nm and the catalyst made by sol-gel method has the highest absorption of the four. Complexing method, precipitation method, absorption method come second, third and fourth. The band gap of the catalyst made by sol-gel method is the smallest (2.82 eV) with complexing method, precipitation method and adsorption method coming the second (2.88 eV), third (3.03 eV) and fourth (3.06 eV), as shown in Table 2, obtained from the equation:

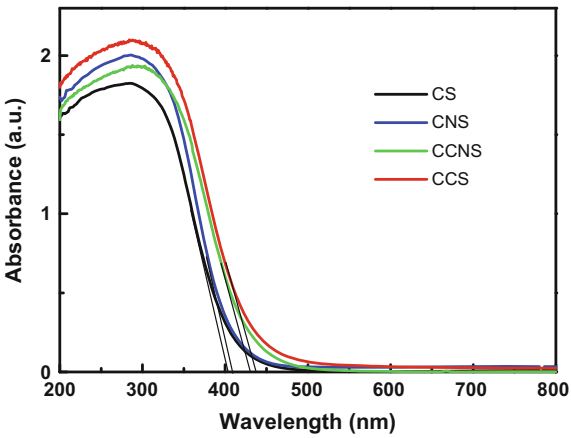

Fig. 4 UV-Vis spectra of the catalysts

Table 2 Photocataltic properties of sample CS, CNS, CCNS, CCS

Sample	Band gap (ev)	Intensity of the emission peak of PL at 467 nm (a.u.)	Removal efficiency (%)
CS	3.06	2.27×10^6	34.6
CNS	3.03	2.35×10^6	26.2
CCNS	2.88	2.51×10^6	19.3
CCS	2.82	2.54×10^6	16.5
SiO_2	–	–	13.2
Mixing	–	–	20.1
Blank	–	–	6.1

$$\mathrm{Eg} = 1240/\lambda\mathrm{g} \tag{2}$$

where E_g = the band gap of the catalyst, λ_g = the wavelength of the absorbed light by intercept method.

This result may be attributed to the fact that the sample prepared by sol-gel method has the smallest particle size and good distribution (as shown in Table 1) [16].

In Fig. 5, the intensity of the emission peaks ranging from 350 nm to 675 nm increase gradually from sol-gel method, complexing method, precipitation method to adsorption method. The highest emission peak is at around 467 nm, the catalyst prepared by sol-gel method has the lowest intensity (2.27×10^6), with complexing method (2.35×10^6), precipitation method (2.51×10^6) and adsorption method (2.54×10^6) coming the second, third and fourth, as shown in Table 2. One explanation for this is that the catalyst synthesized by sol-gel method has the lowest crystallinity of plane (111) of CeO_2 (15%) as shown in Table 1. The low crystallinity increases the crystal defects, and the defects of the crystal is beneficial to hinder the recombination of the photogenerated electrons and holes. In that case, the poor crystallinity of CeO_2 may reduce intensity of the emission peak [17].

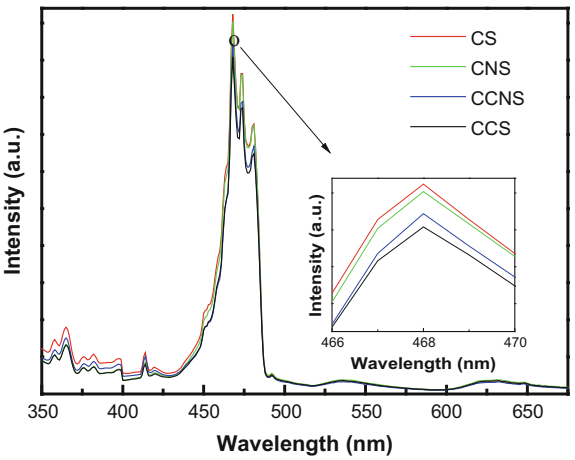

Fig. 5 PL spectra of the catalysts synthesized by different procedures

In Fig. 6, the catalyst synthesized by sol-gel method had the highest methylene blue (MB) removal efficiency up to 34.6% with complexing method and precipitation method coming second (26.2%) and third (19.3%).The catalyst prepared by absorption method had the lowest MB removal efficiency (16.5%), higher than the samples of SiO_2 (13.2%) and Blank (6.1%). It can be found that the silica supported cerium oxide enhanced its photocatalytic activity. Figures 4 and 6 show that the difference of the light utilization efficiency among samples has little effect on their photocatalytic capacity. Instead, the difference of photocatalytic properties is mainly affected by their light absorption capacity and structure, as shown in Figs. 2, 5 and 6. By comparing the removal efficiency of sample CCS and sample Mixing (20.1%), it can be seen that the photocatalytic activity of ceria can be improved by supported on SiO_2.

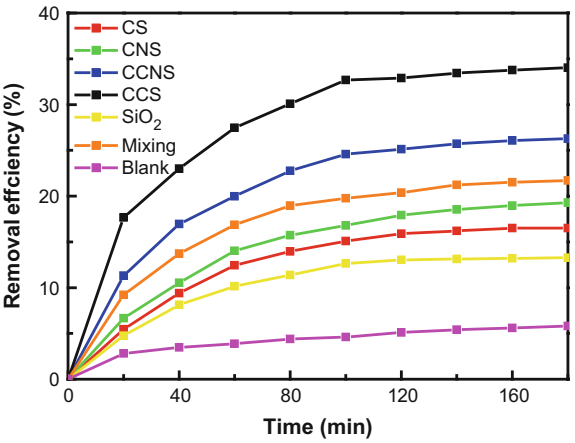

Fig. 6 Photocatalytic degradation properities of methylene blue of the catalysts

Conclusions

In this paper, influences of the synthesis procedure on the photocatalytic property of nanostructured ceria supported on SiO_2 were investigated. Cerium nitrate adsorption, ammonia precipitation, citric acid-ammonia complexing method and citric acid sol-gel method were used to synthesis the catalysts. The catalyst synthesized by sol-gel method has the smallest average grain size and the best dispersity on the SiO_2 support. UV–visible spectra show that the catalyst prepared by sol-gel method has the highest light absorption efficiency and the smallest band gap. The PL spectra show the catalyst prepared by sol-gel method has lowest photoluminescence efficiency which means the best effective separation of electron hole pairs. The photocatalytic properties of samples prepared by four methods are mainly affected by their light absorption capacity and structures. In addition, by comparing with the sample mixed by pure SiO_2 and CeO_2 in which CeO_2 powder was prepared in the same synthesis procedure, it can be seen that the photocatalytic activity of ceria can be improved by supported on SiO_2.

Acknowledgements This work was supported by the National Natural Science Foundation (NSF) of China (21407111, 21377090 and 51403148).

References

1. S. Sameshima, T. Ichikawa, M. Kawaminami et al., Thermal and mechanical properties of rare earth-doped ceria ceramics. Mater. Chem. Phys. **61**(1), 31–35 (1999)
2. E. Rocchini, M. Vicario, J. Llorca et al., Reduction and oxygen storage behavior of noble metals supported on silica-doped ceria. J. Catal. **211**(2), 407–421 (2002)
3. Q. Wang, B. Zhao, G. Li et al., Environ. Sci. Technol. **44**(10), 3870–3875 (2010)
4. L. Adijanto, A. Sampath, A.S. Yu et al. Synthesis and stability of Pd@ CeO_2 core–shell catalyst films in solid oxide fuel cell anodes. ACS Catalysis **3**(8), 1801–1809 (2013)
5. A. Primo, T. Marino, A. Corma et al., Efficient visible-light photocatalytic water splitting by minute amounts of gold supported on nanoparticulate CeO_2 obtained by a biopolymer templating method. J. Am. Chem. Soc. **133**(18), 6930–6933 (2011)
6. D. Channei, B. Inceesungvorn, N. Wetchakun et al., Photocatalytic degradation of methyl orange by CeO_2 and Fe–doped CeO_2 films under visible light irradiation. Sci. Rep. **4**, 5757 (2014)
7. C,. Wang, C. Zhang, X. Shen et al., *The Effect from CeO_2 to W-2 High-temperature Enamel Coating's Microstructure and Coefficient of Thermal Expansion* (2015)
8. V.V. Galvita, H. Poelman et al., Structural and kinetic study of the reduction of CuO–CeO_2/Al_2O_3 by time-resolved X-ray diffraction. Catal. Lett. 1–10 (2012)
9. M.C. Ribeiro, R.C. Rabelo-Neto, L.V. Mattos et al., A relationship between the production of oxygenates from ethanol/steam mixtures and the oxygen mobility in transition metal oxide doped CeO_2·SiO_2 catalysts. J. Phys. Chem. C **118**(48), 28007–28016 (2014)
10. F.L. Pissetti, M.S.P. Francisco, R. Landers et al., Phosphoric acid adsorbed on silica-ceria matrix obtained by sol-gel method: studies of local structure, texture and acid property. J. Braz. Chem. Soc. **18**(5), 976–983 (2007)
11. S. Tsoi, E. Fok, J.C. Sit et al., Superhydrophobic, high surface area, 3-D SiO_2 nanostructures through siloxane-based surface functionalization. Langmuir **20**(24), 10771–10774 (2004)

12. J. Strunk, W.C. Vining, A.T. Bell. Synthesis of different CeO_2 structures on mesoporous silica and characterization of their reduction properties. J. Phys. Chem. C **115**(10), 4114–4126 (2011)
13. J. Rebellato, M.M. Natile, A. Glisenti, Influence of the synthesis procedure on the properties and reactivity of nanostructured ceria powders. Applied Catalysis A: General, **339**(2), 108–120 (2008)
14. J.W. Kaczmar, K. Pietrzak, W. Włosiński, The production and application of metal matrix composite materials. J. Mater. Process. Technol. **106**(1), 58–67 (2000)
15. P. Ji, J. Zhang, F. Chen et al., J. Phys. Chem. C **112**(46), 17809–17813 (2008)
16. W. Zhang, W. Hu, W. Zhai et al., Novel Ag_3PO_4/CeO_2 p-n hierarchical heterojunction with enhanced photocatalytic performance. Mat. Res. **19**(ahead), 2016
17. M.A. Subhan, T. Ahmed, N. Uddin, Synthesis, structure, PL and photocatalytic activities of $La_2O_2CO_3{\cdot}CeO_2{\cdot}ZnO$ fabricated by co-precipitation method. Spectrochimica Acta Part A Mol. Biomol. Spect. **138**, 827–833 (2015)

Metal Ion–Induced Synthesis of Hierarchical ZnO Architectures with Various Morphologies and Their Photocatalytic Performances

Xinmei Liu, Shibo Yao, Yao Liu, Wenkang Zhang, Fengming Fu and Haiyan He

Abstract Three-dimensional (3D) hierarchical ZnO nanostructures were synthesized on zinc-electroplated Cu foil in one kind of metal salt-ammonia hydrothermal system. The morphologies, structures, components and spectra of the as-prepared products were characterized with SEM, XRD, EDS and UV-vis-DRS. The results showed the morphology of hierarchical ZnO architectures changed with varying the kind of metal salts added in the hydrothermal system, while the hexagonal wurtzite structure of ZnO kept constant. The photocatalytic experiment showed that different hierarchical ZnO films showed different photocatalytic activities for degrading methyl orange aqueous solution under ultraviolet irradiation, which was attributed to the difference of specific surface area, porous channel properties and light scattering effect from different hierarchical ZnO architectures. The inherent characteristics of metal ions, involving ionic radius, solubility and crystal structure of its oxide or hydroxide precipitates, and so on, was speculated to play an important role in the change of morphology of hierarchical ZnO architectures.

Keywords ZnO · Hierarchical architecture · Morphology change
Photocatalysis · Hydrothermal method

Introduction

ZnO is a promising candidate for photocatalysis due to a wide band gap of 3.37 eV, a large exciton binding energy of 60 meV, excellent catalytic and photochemical properties and low cost [1, 2]. The nanoscale ZnO is being increasingly used as photocatalysts in the degradation of dye wastewater under appropriate light irradiation [3, 4] due to its larger specific surface area-to-volume ratio and higher photocatalytic performance than that of bulk materials. Three-dimensional (3D)

X. Liu (✉) · S. Yao · Y. Liu · W. Zhang · F. Fu · H. He
College of Biological and Chemical Engineering, Guangxi University of Science and Technology, Liuzhou, Guangxi 545006, China
e-mail: xinmeiliu628@163.com

Y. Han (ed.), *Advances in Energy and Environmental Materials*,
Springer Proceedings in Energy, https://doi.org/10.1007/978-981-13-0158-2_51

hierarchical ZnO nanostructured powder using lower dimension nanocrystals such as nanoparticles, nanorods and nanosheets as the building blocks has exhibited an enhanced photocatalytic performance compared with its initial nanostructure [5, 6]. However, the deposition of 3D hierarchical ZnO nanostructure on suitable substrates are more desirable for photocatalytic applications because the novel film constructed by 3D hierarchical structure is not only helpful to improve catalytic activity due to its possessing the high specific surface area and the steric effect of "house of cards" of the hierarchical ZnO architecture, but also to overcome the agglomeration problem of conventional powdered ZnO photocatalyst and improve the recycling of photocatalyst [6, 7]. Further, the hierarchical assembly of nano-building-blocks also is a direction of material multifunction through structure assembly.

It is well known that the size and morphology is related to the photocatalytic properties of ZnO. Therefore, the synthesis of hierarchical ZnO nanostructures varied their morphology on suitable substrate is urgently developed for exploring the potentials of ZnO in photocatalysis.

Many researchers have been devoted to constructing hierarchical ZnO powdered architectures [6–8]. But very few reports are available to fabricate the hierarchical ZnO nano- or microstructured film, let alone the preparation of morphology controlled hierarchical ZnO structure.

Herein, we present a simple hydrothermal approach to synthesize hierarchical ZnO architectures with different morphologies on Cu foil. The morphology of hierarchical ZnO architecture was dependent on the kind of metal salt added in the hydrothermal system. The effect of metal salt on the morphology change of hierarchical ZnO architectures has been primarily discussed. The photocatalytic activities of various hierarchical ZnO nanostructure films for the degradation of methyl orange (MO) aqueous solution under UV irradiatio have been investigated.

Experimental Section

The Preparation of ZnO Nanostructure

The zinc-electroplated Cu foil was prepared by electrodeposition with Zn sheet (99.9%) as cathode, copper sheet (99.9%, $20 \times 40 \times 0.1$ mm^3) as anode, the mixture of zinc chloride, potassium chloride, boric acid and gelatin as electrolyte, similar to the approach described earlier. [9–11].

The obtained zinc-electroplated copper sheet was used for the following hydrothermal reaction: 40 mL of 0.001 mol/L metal salt aqueous solution was firstly added into a Teflon beaker in a stainless steel autoclave, and a little amount ammonia (28%) was added to a concentration of 0.25 mol/L. Next, the copper sheet was placed in Teflon beaker. Then, the stainless steel autoclave was placed in dry oven and maintained at a setting temperature for 9 h. After the completion of reaction, the film product was taken out from the autoclave. The distilled water as

well as absolute ethanol was used to washed the product. The as-obtained product was named as M/ZnO, M referred to the metal ion added in the hydrothermal reaction.

Characterization

The X-ray diffraction (XRD) analysis was performed on D/max-γB equipped with Cu Kα radiation over a range from 30° to 80°. The scanning electron microcopy (SEM) was carried out on SIRION 200, FEI equipped with an energy dispersive X-ray analysis (EDS). The absorption spectroscopy was obtained using an Ocean Optics Maya 2000 Pro optical fiber spectrometer, equipped with an integrating sphere, and $BaSO_4$ was used as the reference standard.

Photocatalytic Activity Test

The discoloration of the MO solution was investigated using the as-prepared film products as the catalysts. In a typical experiment, a 80 mL of MO solution with 10 mg/L of concentration was added into a quartz reactor and the film was hung on. The photocatalytic reaction was used a 300 W high pressure mercury lamp (HSX-F300, Beijing NBeT Group Corp) as the irradiation source. After the solution stirred for 30 min in the dark, the UV light was turned on and the reaction started. During the process of reaction, 3 mL of aliquots were collected from the reactor at 30-min intervals. Then, the solution was analyzed on a UV–vis spectrophotometer (UV-2000, Shanghai unique).

Results and Discussion

Figure 1 is shown the SEM image of the Zn plating on Cu substrate. A layer of dense caky Zn microplatelets (MPs) with ∼10 μm of diameters was observed on the Cu foil. The FESEM image showed the Zn MP had a protuberant centre, presenting a stepped increase of thickness from the margin to the center, and the spiral dislocation growth was used to described to the above behavior of Zn plating as discussed early [9]. The FESEM images of different hierarchical ZnO nanostructures are also shown in Fig. 1, which were prepared under the following hydrothermal conditions: 0.001 mol/L of different metal salt, 0.25 mol/L ammonia aqueous, 90 °C and 9 h. The differences of the morphology of the hierarchical ZnO architectures after the hydrothermal reaction were reflected in Fig. 1, all of which were composed of Zn MPc arrays covered by an outer layer of ZnO nanostructure arrays. The ZnO nanostructure arrays in all samples except for the samples of Zn/

ZnO and Mg/ZnO showed good 2-fold-symmetrical geometry with respect to the growth substrate of Zn MP. The ZnO nanostructures showed the same needle-like shape but different length and diameter in samples Zn/ZnO, Mg/ZnO, Ba/ZnO, Sr/ZnO, and Bi/ZnO. The ZnO nanostructure growing sparsely and randomly on both surfaces of Zn MPs was observed in sample Co/ZnO, showing a cone-shape with non-uniform diameter and length. The ZnO nanostructures in samples La/ZnO and Nd/ZnO showed a sheet-shape with high length and diameter ratio, being compact, uniform and symmetrical on both surfaces of Zn MPs. Most of the ZnO nanowires in Zn/ZnO sample growed laterally on the surface of Zn MPs, resulting in less symmetry with respect to Zn MP substrate. For Mg/ZnO sample, the ZnO nanowire grew disorderly on Cu foil. the 3D hierarchical morphology of ZnO was not clear. The outline of the Zn MP substrate had also vanished due to the complete dissolution for the growth of ZnO nanowires. Obviously, the differences in morphology of the hierarchical architectures were attributed to the differences in the shape, length, diameter, density and symmetry of ZnO nanostructures in different samples.

The mechanism of the growth of ZnO on Zn MPs on Cu substrate in a metal salt-free ammonia hydrothermal system has been discussed in our previous publication [10, 11]. The mechanism of metal ion-dependent morphology evolution was

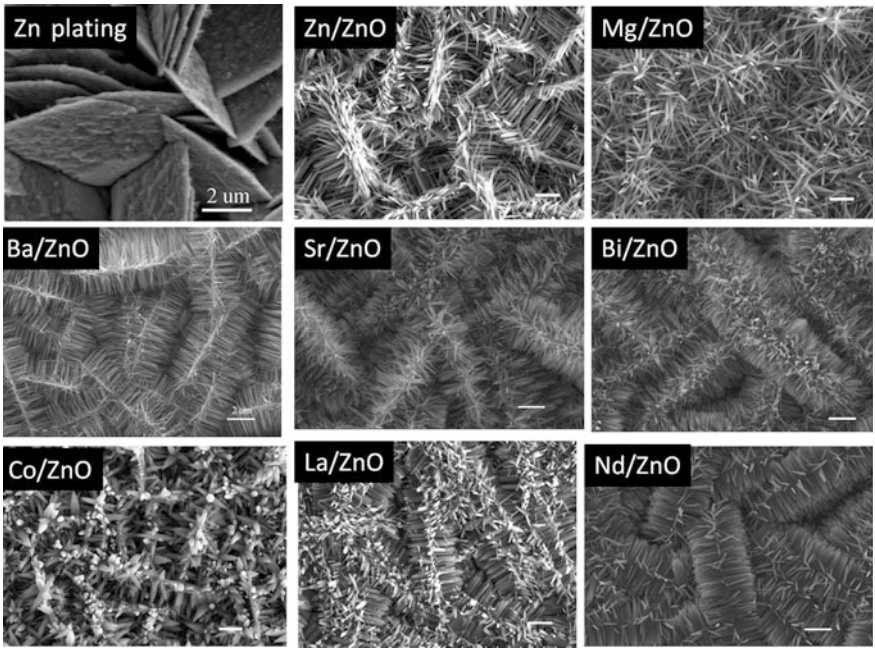

Fig. 1 SEM image of Zn-plated on Cu substrate under –0.40 V of cathode potential for 30 min (labeled as Zn Plating) and SEM images of the different hierarchical ZnO architectures synthesized under the following hydrothermal conditions: 90 °C, 9 h, 0.25 mol/L ammonia and 0.001 mol/L metal ion, which were marked as M/ZnO, M was the added metal ion. The bar in each image was 2 um

somewhat different. In metal ion-ammonia hydrothermal system, a layer of dense metal oxide or hydroxide precipitates instead of ZnO seed was firstly formed as nuclei covering the surface of Zn MPs in the initial nucleation stage, which induced a burst of heterogeneous nucleation of ZnO followed by the growth of a layer of dense ZnO nanocrystals on surfaces of Zn MP. During a prolonged hydrothermal reaction, the gradual dissolution of Zn MP gradually dissolve to offer the Zn source for the continuous growth of ZnO nanowires. The differences in solubility of different metal oxide or hydroxide precipitates led to the formation of different amounts of nuclei, which directly determined the density of ZnO nanocyrstal on the surface of Zn MPs. Furthermore, the differences in radius of metal ions and crystal structure of nuclei had an impact on the morphology of ZnO nanocrystals. The exact impact was not clear now. More experiments with the addition of other metal ions in hydrothermal reaction had been finished and the corresponding hierarchical ZnO nanostructures with different morphologies were also obtained. Their SEM images were not provided in the paper. Based on these facts, as a tentative conclusion, we were inclined to think that the metal ion, which could form metal oxide or hydroxide precipitates in ammonia aqueous solution, could induce this kind of heterogeneous nucleation and growth of ZnO and promote the formation of the hierarchical ZnO architecture with specific morphology.

The XRD patterns of different hierarchical ZnO architectures, involving Zn/ZnO, Mg/ZnO, La/ZnO, Sr/ZnO and Co/ZnO, are shown in Fig. 2. All peaks were well-indexed to wurtzite ZnO structure (JCPDS No. 36-1451) except for the peaks related to the Zn plating (JCPDS No. 04-0831) and Cu foil (JCPDS No. 04-0836), and the five samples showed no difference, indicating that neither the structural change of the ZnO nor the formation of element or oxide of the corresponding metal was found, suggested ZnO nanostructures with high purity on the copper foil.

The elemental analysis on the as-synthesized hierarchical ZnO films were identified by EDS. The typical EDS spectrum was shown in Fig. 3, which was

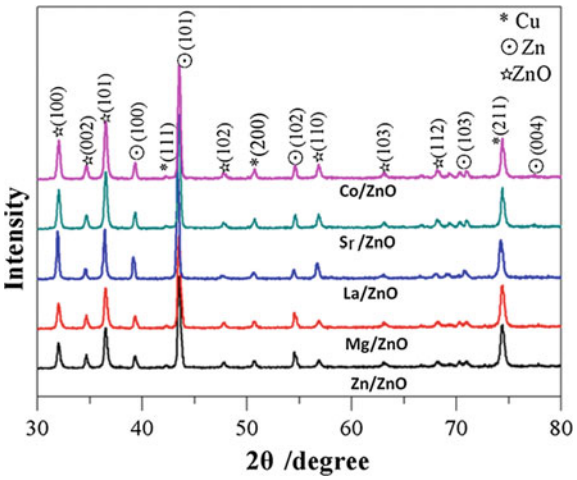

Fig. 2 XRD patterns of the different hierarchical ZnO nanostructure films

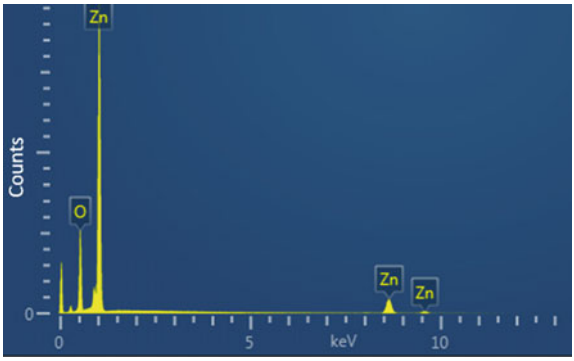

Fig. 3 Typical EDS spectrum of the hierarchical ZnO nanostructures

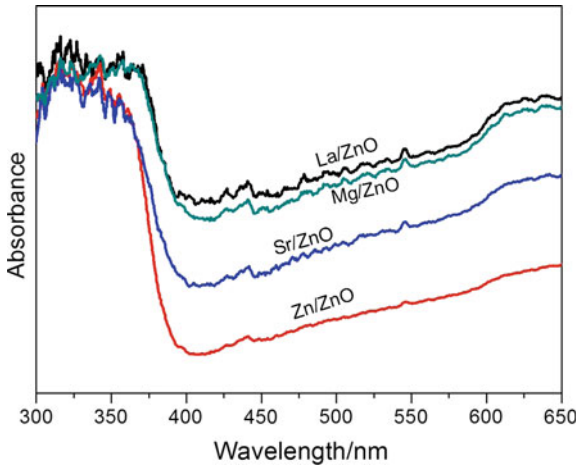

Fig. 4 UV–Vis-DRS spectra of La/ZnO, Sr/ZnO, Zn/ZnO and Mg/ZnO film samples

independent of metal salts added in hydrothermal system. It was observed that only Zn and O peaks clearly present in EDS spectrum. No peaks related to the metal element added was found in EDS spectrum, which could be attributed to the trace addition of metal salt.

Figure 4 is shown the UV–Vis-DRS spectra of La/ZnO, Sr/ZnO, Zn/ZnO and Mg/ZnO samples. A strong and broad absorption band was observed in the UV region, exhibiting a sharp absorption edge around 390 nm, which was the intrinsic band gap absorption of ZnO. In addition, the visible light absorption of ZnO was caused by light-scattering effect of ZnO nanowires, which was associated with the size, porous channel properties and packing density of ZnO nanostructures. As shown in Fig. 4, the light-scattering effect increased the efficiency of light harvesting in the following order: La/ZnO > MgZnO > Sr/ZnO > Zn/ZnO in the visible light range. In addition, the absorption edge La/ZnO and Mg/ZnO samples exhibited a slight red shift compared with Zn/ZnO and Sr/ZnO samples. The red shift should be considered to be related with the increase of concentration of defects, especially oxygen vacancies [12].

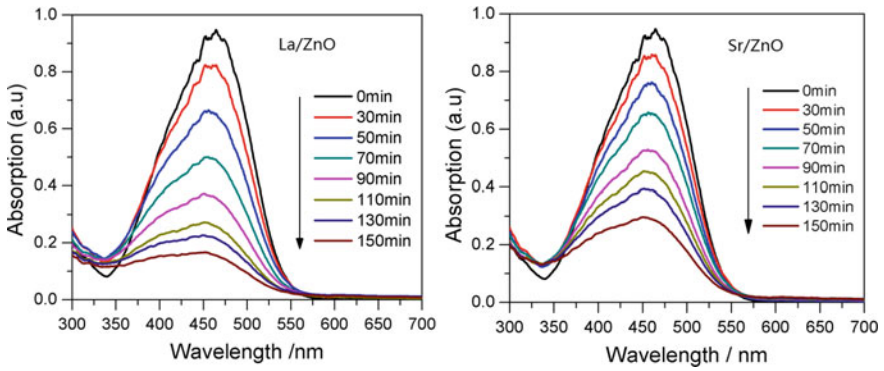

Fig. 5 UV–vis spectral changes of MO solution over the La/ZnO and Bi/ZnO film samples over UV illumination time

The as-prepared La/ZnO and Sr/ZnO film samples were selected to evaluate the photocatalytic activities of hierarchical ZnO nanostructure films by measuring the decomposition of MO as a model reaction. The absorption spectra of MO aqueous solution over UV illumination time using the hierarchical La/ZnO and Sr/ZnO films as catalysts, respectively, during the photocatalytic reaction are provided in Fig. 5. When La/ZnO sample as catalyst, a major absorption peak of the MO dye was at 452 nm, gradually decreased when the light illumination time were prolonged, and completely disappeared after 150 min. This variation of absorbance was consistent with the color varied from orange to nearly transparent, owing to the destruction of the chromophoric structure of the MO. Figure 5 also showed the photocatalytic activity of La/ZnO was slightly higher than that of Sr/ZnO sample. Two factors may be contributed to the higher photocatalytic activity of La/ZnO, one was its higher specific surface area, which would provide the more photocatalytic active sites to anchor target molecules and generate photoinduced electron–hole pairs. Another was related to the increase of the response of optical absorption in the UV–visible region, which arised from the bandgap of the ZnO product due to metal ion depant into the lattice of ZnO.

The degradation efficiencies of MO aqueous solution over the different hierarchical ZnO films after 150 min of UV irradiation are shown in Fig. 6. The different hierarchical ZnO nanostructured films exhibited different photocatalytic activities, but the differences of the photocatalytic performance are not significant, which was attributed to the difference in porous surface structure, specific surface area, morphology and crystalline quality in different hierarchical ZnO 3D architectures,which was consistent with the above disscussion.

The experiments of the photocatalytic stability were carried out in order to investigate the cycle life. The comparison of degradation of MO over the different recycled ZnO products (i.e. Co/ZnO, Bi/ZnO, La/ZnO and Mg/ZnO) during four recycling runs was shown in Fig. 7. The results from all the four ZnO film simples showed similar decrease of the photocatalytic activities as the number of runs. The

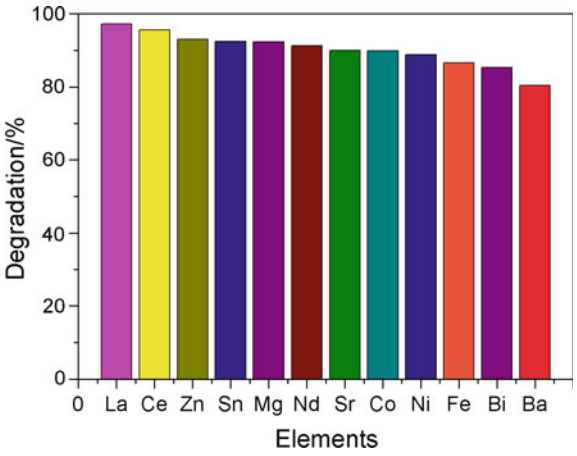

Fig. 6 The degradation efficiencies of MO aqueous solution after 150 min UV irradiation over different hierarchical ZnO nanostructured films. The elements on the horizontal axis represented the corresponding products synthesized with the addition of the metal salts

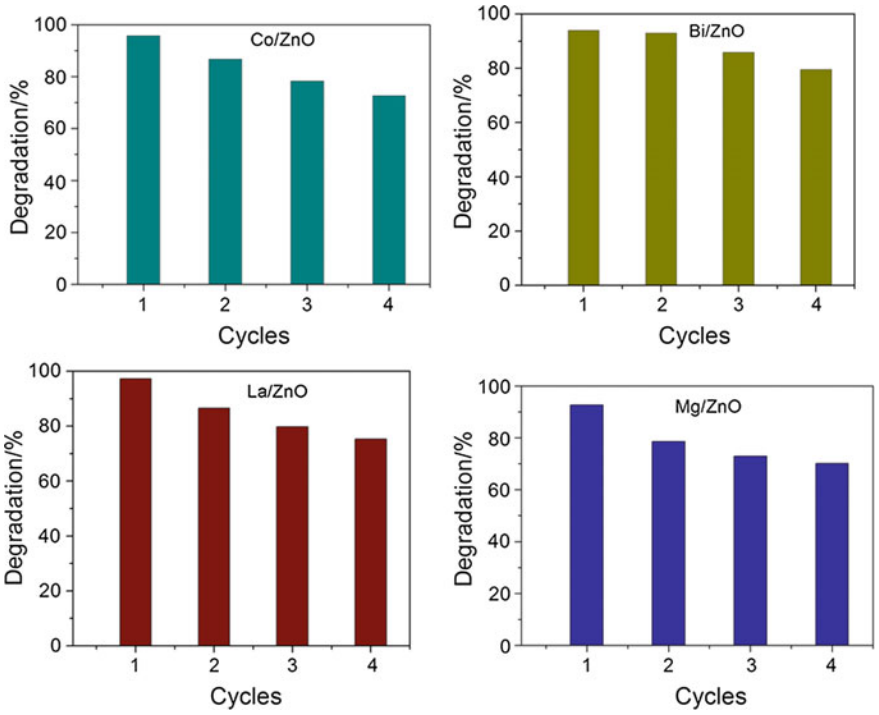

Fig. 7 The reproducibility of the experiments of different hierarchical ZnO nanostructured films

observed catalyst inactivation should be attributed to the following factors. One is the intermediate from the degradation of MO during illumination, which could be absorbed on the surface of ZnO nanowires, hampering active sites to absorb the UV light as well as electrons to transfer among the active sites for photocatalysis. In addition, the possible photo-dissolution of the ZnO occured in MO solution also led to the decrease of photocatalytic activity. In contrast, Bi/ZnO sample showed the best photocatalytic stability.

Summary

In summary, a facile hydrothermal method was developed for changing the morphologies of hierarchical ZnO architectures on Cu foil in large scale. The addition of different metal ions was used to regulate the morphologies of the hierarchical ZnO architecture. The different hierarchical ZnO architectures exhibited different photocatalytic activities for the degradation of MO under UV irradiation, which is attributed to the differences in porous surface structure, specific surface area, morphology and crystalline quality of hierarchical ZnO architectures.

Acknowledgements The research was supported by the National Natural Science Foundations of China (No. 21261003), and the Natural Science Foundation of Guangxi Zhuang Autonomous Region (No. 2013GXNSFAA019027), and the Guangxi University of Science and Technology (No. 12Z06).

References

1. S. Maa, R. Li, C. Lv, W. Xu, X. Gou, Facile synthesis of ZnO nanorod arrays and hierarchical nanostructures for photocatalysis and gas sensor applications. J Hazard. Mater. **192**, 730–740 (2011)
2. T.-H. Hsieh, J.-Y. Chen, C.-W. Huang, W.-W. Wu, Observing growth of nano-structured ZnO in liquid. Chem. Mater. **28**, 4507e-4511 (2016)
3. G.R.S. Andrade, C.C. Nascimento, E. C. Silva Jr. et al., ZnO/Au nanocatalysts for enhanced decolorization of an azo dye under solar, UV-A and dark conditions. J. Alloy. Compd. **710**, 557–566 (2017)
4. C. Tian, Q. Zhang, A. Wu et al., Cost-effective large-scale synthesis of ZnO photocatalyst with excellent performance for dye photodegradation. Chem. Commun. **48**(23), 2858–2860 (2012)
5. F. Lu, W.P. Cai, Y.G. Zhang, ZnO hierarchical micro/nanoarchitectures: solvothermal synthesis and structurally enhanced photocatalytic performance. Adv. Funct. Mater. **18**, 1047–1056 (2008)
6. J.C. Sin, S.M. Lam, K.T. Lee, A.R. Mohamed, Preparation of rare earth-doped ZnO hierarchical micro/nanospheres and their enhanced photocatalytic activity under visible light irradiation. Ceram. Int. **40**, 5431–5440 (2014)
7. H.B. Lu, S.M. Wang, L. Zhao, J.C. Li, B.H. Dong, Z.X. Xu, Hierarchical ZnO microarchitectures assembled by ultrathin nanosheets: hydrothermal synthesis and enhanced photocatalytic activity. J.Mater.Chem. **21**, 4228–4234 (2011)

8. A.J. Wang, Q.C. Liao, J.J. Feng, P.P. Zhang, A.Q. Li, J.J. Wang, Apple pectin-mediated green synthesis of hollow double-caged peanut-like ZnO hierarchical superstructures and photocatalytic applications. Cryst. Eng. Commun. **14**, 256–263 (2012)
9. X.Z. Lan, Y. Jiang, X.M. Liu, W.J. Wang, B.B. Wang, D. Wu, C. Liu, Y.G. Zhang, H.H. Zhong, Large-scale growth of a novel hierarchical ZnO three-dimensional nanostructure with preformed patterned substrate. Cryst. Growth Des. **11**(9), 3837–3843 (2011)
10. X.M. Liu, W.Y. Huang, G.X. Huang, F.M. Fu, H. Cheng, W.M. Guo, J.S. Li, H.D. Wu, Synthesis of bilayer ZnO nanowire arrays: Morphology evolution, optical properties and photocatalytic performance. Ceram. Int. **41**, 11710–11718 (2015)
11. X.M. Liu, W.Y. Huang, H. Cheng, B.B. Huang, D.W. Bai, F.M. Fu, H.D. Wu, L.J. Li, In-situ observation of hydrothermal growth of ZnO nanowires onpatterned Zn substrate and their photocatalytic performance. Appl. Surf. Sci. **356**, 240–248 (2015)
12. X. Liu, W. Huang, Hao Cheng et al., In-situ observation of hydrothermal growth of ZnO nanowires on Patterned Zn substrate and their photocatalytic performance. Appl. Surf. Sci. **356**, 240–248 (2015)

Eco-friendly Selective Synergistic Extraction Rare-Earths from Waste CRT Phosphor Powder Sulfuric Acid Leachate with Imidazolium-Based Ionic Liquid [OMIm] [PF_6] and Extractant Cyanex272

Xiangmiao Tian, Yufeng Wu, Xiaofei Yin, Yu Gong, Kaihua Zhang and Yu Fu

Abstract Considering the benefits of resource, environment and economy, recycling secondary rare earth resources is becoming an extremely significant resource regeneration way. In this paper, we reported a novel synergistic extraction system combining ionic liquid [OMIm] [PF_6] and extractant Cyanex272 to separate and purify the REE from the leachate of waste CRT phosphor powder. Some extraction parameters were studied including extraction acidity, the ratio of organic phase to aqueous phase, the ratio of Cyanex272 and [OMIm] [PF_6], extraction time and extraction temperature. The optimal parameters of the extraction process was obtained as extraction acidity 0.2 mol/L, the ratio of organic phase to aqueous phase 1:5, the ratio of Cyanex272 and [OMIm]PF_6 X_C = 0.4, extraction time 10 min and extraction temperature 25 °C. Under these conditions, REE is successfully and efficiently extracted and separated with zinc and aluminum, which revealed a potential application for REE separation and purification from electronic waste.

Keywords Ionic liquid extraction · Rare earth · CRT phosphor powder

X. Tian · Y. Wu (✉) · X. Yin · Y. Gong · K. Zhang · Y. Fu
Institute of Circular Economy, Beijing University of Technology,
No. 100, Pingleyuan Street, Chaoyang District, Beijing 100124, China
e-mail: wuyufeng3r@126.com

X. Tian
e-mail: popcorn555@126.com

Y. Han (ed.), *Advances in Energy and Environmental Materials*,
Springer Proceedings in Energy, https://doi.org/10.1007/978-981-13-0158-2_52

Introduction

Rare earth (REE) is an important strategic resource due to its unique optical, electronic and magnetic properties which has been widely applied in the vital fields of defense industry, aerospace vehicle, photoelectric display [1]. However, as it is difficult to replace in industries, a long-term of irrational exploitation, a crisis of REE has emerged in recent years [2, 3]. However, in the other hand, with the rapid development of display technology, cathode ray tube (CRT) display has been replaced by other types of display such as LCD, LED etc. What happened in China can be a good example, more than 30 million of scrap CRTs is generated only the year of 2013 [4]. Generally speaking, waste CRT is disposed by conventional treatments such as incineration, landfill as municipal refuse, which can cause massive pollution and damage to the environment by polluting the soil, water and air, and then endangering public health [5–7].

CRT is mainly composed of panel glass, funnel glass, electron gun, deflection coil and phosphor layer, usually, about 0.15–1 g REEs contained in the phosphor layer are yttrium and europium as luminescent material [8]. Therefore, large amounts of REE resources abandoned can be recovered and reused [9]. At present, as for the recycling of REEs from the CRT phosphor powder, the general process is "acid leaching- oxalate precipitation- calcination", providing the disadvantage of complicated technology, high energy consuming and high pollution [10–12] Ionic liquid (IL) is a rising reagent has widely used the field of separation and purification is the reason that it is an efficient and green reagent [13–17]. Noticeably, it is also applied in the separation of REEs, Rout and Binnemans used Cyanex923 with ionic liquid extracted the trivalent rare-earth ions showed that the combines extraction system had the great ability of separating the rare-earth and the mechanism of trivalent rare-earth ions was ion-exchange [18]. Zhu et al. utilized the ionic liquid tricaprylmethyl-ammonium nitrate and the extractant di(2-ethylhexyl) 2-ethylhexyl phosphonate to extract REE nitrates, their research results indicated the synergistic system they developed was help for the separation of light REEs from heavy REEs [19].

In this paper, based on our previous study, a novel IL-based synergistic extraction method is proposed for the separation of REE from the waste CRT phosphor powder sulphuric leachate (WCPL) by using ionic liquid 1-octyl-3-methylimidazolium hexafluorophosphate and extractant Bis(2,4,4-trimethylpentyl) Phosphinic acid (Cyanex272) [20]. The parameters investigated are acidity, the ratio of organic phase to aqueous phase, the ratio of Cyanex272 and [OMIm] [PF_6], exaction time and extraction temperature. In conclusion, we firstly develop a novel, efficient, green IL-based REE extraction technology employed in the recycling of REEs from the waste CRT phosphor powder, and this technology is a feasible to separate and recycle REEs from WCPL directly which can avoid high energy consuming process and achieve high purity secondary REE resources.

Experimental

Materials and Reagents. Phosphor powder was obtained from Shenzhen Green Eco-Manufacture Hi-tech Co., which was mixed with different kinds of scrap CRT phosphor powder. It was firstly sieved by 200 mesh to remove bulky solid impurity substance, and ball-milled 12 h by ball grinder under the rotation rate of 250 r/min for the purpose of well-distributed pretreatment. Afterwards, waste phosphor powder was leached by sulphuric acid according to our preliminary leaching investigations, then it was filtrated for subsequent extraction investigations.

All of other chemicals and reagents used in this research were of Analytical grade, and all of them without further purification in using process. Sulphuric acid ($\geq 95\%$) and hydrogen peroxide were purchased from Beijing Chemical Works. All of extractants used in our research were di-(2-ethylhexyl) phosphate (P204), Phosphonic acid (2-ethylhexyl)-mono (2-ethylhexyl) ester (P507), Tributyl phosphate (TBP), Tri-alkyl phosphine oxide (TRPO), Bis(2,4,4-trimethylpentyl) Phosphinic acid (Cyanex 272), 260# solvent oil, trialkyl-phosphine oxides (Cyanex 923), both of them were purchased from Shanghai Rare-earth Chemical Co. Ltd. Both of selected Ionic Liquids (ILs) were: [OMIm] [PF_6] (1-octyl-3-methylimidazolium hexafluorophosphate >99%), [BMIm] [BF_4] (1-butyl-3-methylimidazolium tetrafluoroborate, >99%), [BMIm] [PF_6] (1-butyl-3-methylimidazolium hexafluorophosphate, >99%) were purchased from Center of Green-chemistry and Catalysis, Lanzhou Institute of Chemical Physics. Y, Eu, Zn and Al (1000 mg/L, HNO_3) standard solutions were purchased from National Center of Analysis and Testing for Nonferrous Metals and Electronic Materials, General Research Institute for Nonferrous Metals, China.

Instrumentations. HJ-6A multiposition magnetic stirrer hotplate (Guohua) applied to achieve mixing uniformly in the process of extraction. The PH measurements carried out by a PB-10 digital PH-meter (Sartorius, German). Optima 8000 inductively coupled plasma-optical emission spectrometer (ICP-AES) (PerkinElmer, USA) was performed to determine the concentration of metals in the aqueous phase before and after extraction. All extraction experiments performed by three times to ensure the reproducibility of the values, and relative standard deviations were to be within $\pm 1\%$.

Extraction Procedures. Firstly, to determine which kind of extractant and ionic liquid is efficient to extraction Y, Eu and Zn, Al from phosphor powder acid leaching solution, different organic extractants and ionic liquids were extracted selectively for 4 major metals respectively. It was performed at room temperature with a mechanical shaker at a medium speed for 10 min and employed a 20:1 of phase ratio of aqueous phase to IL phase under pH = 2.5. After the extraction process reached equilibrium, the ion concentration of four major metals in the aqueous phase were measured by ICP-AES with triplicates. After extractant and IL were determined, a series of experiments about the effect of acid concentration in leaching liquor, phase ratio, extraction temperature, the volume fraction of

extractant and IL, extraction time. The extraction percentage (E%), distribution ratio (D), synergistic enhancement coefficient (R) and separation factor (α) could be written using the following equations:

$$D = \frac{[M]_{IL}}{[M]_{aq}} = \frac{[M]_i - [M]_f}{[M]_f} \times \frac{V_{aq}}{V_{IL}} \quad (1)$$

$$E\% = \frac{[M]_i - [M]_f}{[M]_i} \times 100 \quad (2)$$

$$R = \frac{D_{C+I}}{D_C + D_I} \quad (3)$$

$$\alpha = \frac{D_1}{D_2} \quad (4)$$

where $[M]_i$ and $[M]_f$ (mol/L) represents the metal concentration in the aqueous phase before and after extraction, respectively. V_{aq} and V_{IL} (mL) are the volumes of the aqueous phase and ionic liquid phase, respectively. D_{C+I}, D_C and D_I are the distribution ratios of M metal with Cyanex 923-[OMIm] [PF_6], Cyanex 923 and [OMIm] [PF_6], respectively. D_1 and D_2 are represents the distribution of metal 1 and 2.

Results and Discussion

The Determination of Extraction System. Firstly, we investigated the effect of different ionic liquids [OMIm] [PF_6] and [BMIm] [PF_6], different extractants P204, P507, Cyanex272, Cyanex923, TBP, TRPO and solvent soil extraction on the valuable metals from the leachate in a single system. As shown in Fig. 1, as for ionic liquid, whether [OMIm] [PF_6] or [BMIm] [PF_6], the extraction rate both less than 20%, and the extraction performance of [BMIm] [PF_6] was better than [OMIm] [PF_6]; However, besides TBP, TPRO and solvent soil, other extractants particularly P507 and Cyanex272 has a superior extraction ability. An important phenomenon was showed that both ionic liquid and extractant has not extraction ability to Al element. Next, we combined different ionic liquids with extractants for common extraction for valuable metals, from Fig. 2, we can see that P507, Cyanex272, Cyanex923, TRPO in two ionic liquids has not shown obvious difference for 4 elements, for P204 has little extraction ability on Zn, however, TBP has any extraction effect on any element. Considering the purpose of excellent extraction on Y and Eu, but has a little extraction effect on Zn, [OMIm] [PF_6] and Cyanex272 were determined as our extraction system for further research.

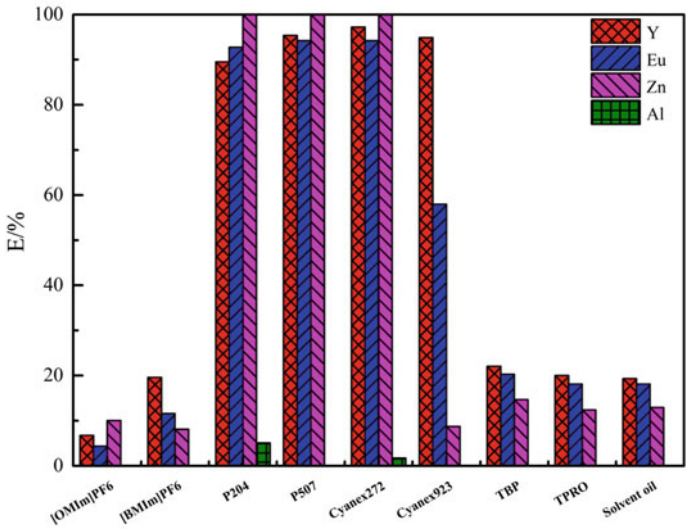

Fig. 1 Effect of extraction of different ion liquids and extractants extraction on the major metal elements of REEs from the leachate of waste CRT phosphor

The Effect of Balanced Acidity. The concentration of 0.1, 0.2, 0.3, 0.4, 0.5, 0.6, 0.7, 0.8, 1, 1.5, 2, 2.5, 3 mol/L leaching liquor were prepared, and then 10 ml leachate was taken, 1 ml [OMIm] [PF_6] and 1 ml Cyanex272 was added for extraction experiments. From Fig. 3a, it is clearly shows that acidity has a notable influence on extraction rate, as acidity increases from 0.1 up to 0.2 mol/L, except Al element, the extraction ratio of Y, Eu, Zn increase sharply from 4, 50, 0 to 96, 92, 37%, and then decrease rapidly with acidity increasing, Fig. 3b shows the relationship of distribution ratio between acidity concentration, which indicates same trend with extraction ratio. The determined system has initially realized the separation of REE elements with Zn and Al elements, therefore, the optimal acidity was selected at 0.2 mol/L.

The Effect of the Ratio of Organic Phase to Aqueous Phase. Another important factor has great influence on extraction is the ratio of organic phase to aqueous phase. As shown in Fig. 4, when the phase ratio is of 1:1, the extraction ratio of Y, Eu and Zn is 100, 97 and 65%, separately. Y element is almost not affected by phase ratio increasing to 1:50, the extraction ratio is still as high as 98%, however, the extraction of Eu and Zn elements both reduce with dwindling phase ratio levels, but the degree of decline in the Zn than Eu, thus, improving phase ratio to some extent can achieve preferable separating effect REE elements with Zn, notably particularly the decided phase ratio can' t be too high as a result of recovering Eu to an extreme. As a result, the best phase ratio is decided at 1:5.

The Effect of the Ratio of Cyanex272 and [OMIm] [PF_6]. Based on the different affinity of Cyanex272 and [OMIm] [PF_6] to each element in extraction process,

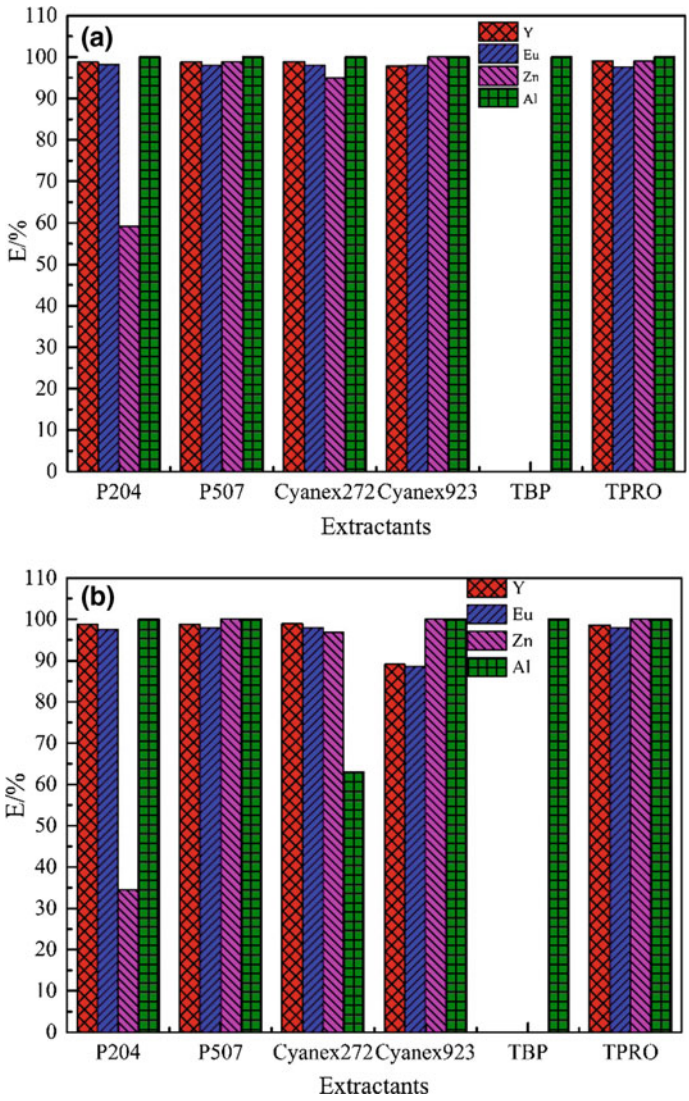

Fig. 2 Effect of extraction of ion liquids of [OMIm] [PF_6] and [BMIm] [PF_6] synergistic extraction on the major metal elements of REEs et al. from the leachate of waste CRT phosphor with different extractants, **a** ion liquid of [OMIm] [PF_6], **b** ion liquid of [BMIm] [PF_6]

consequently, it is necessary to investigate the effect of the ratio of them (the volume of Cyanex272 and [OMIm] [PF_6] to total volume are expressed as X_C and X_O independently). The analysis is demonstrating in Fig. 5, a very clearly tendency is suggested that Y, Eu, Zn has shown a different speed increase trend with the increase of the addition volume of Cyanex272, while [OMIm] [PF_6] exhibits the reverse result. When X_C increased from 0 to 0.3, the extraction rate of Y and Eu rise

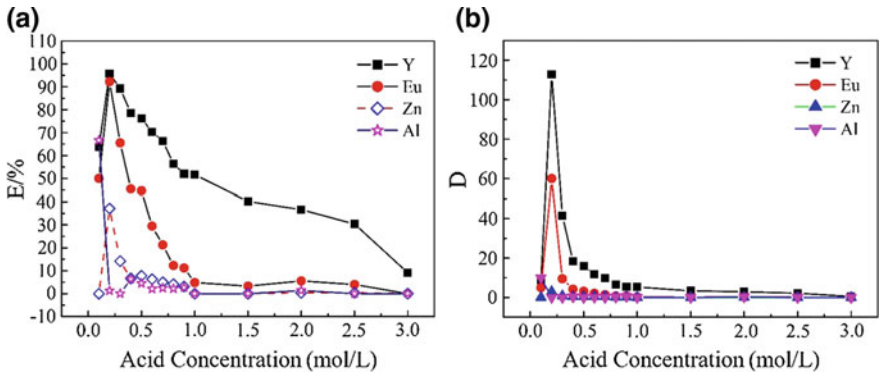

Fig. 3 Variation of the extraction rate and the distribution ratio of the major metal elements for synergistic extraction with [OMIm] [PF_6] and Cyanex272 as a function of the sulphuric acid concentration in the aqueous phase, **a** extraction rate, **b** distribution ratio

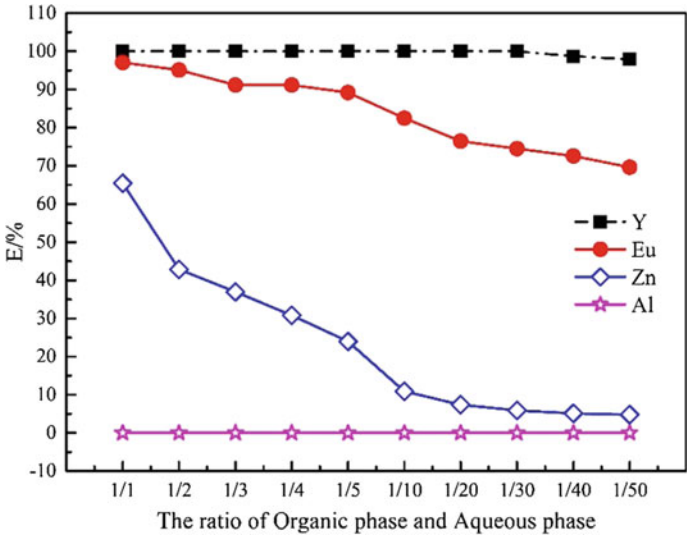

Fig. 4 Variation of the extraction rate of the major metal elements for synergistic extraction with [OMIm] [PF_6] and Cyanex272 as a function of the ratio of organic phase to aqueous phase

quickly to 100 and 94% respectively, however, Zn only increases up to 19%, Al rate reduces from 20 up to 13%; as the X_C increases, Y can be extracted completely, a little increase to Eu and a fast increase to Zn at nearly 40% extraction rate under the X_C is 1; as far as Al is concerned, it cannot be extracted entirely with the X_C up to 0.4. Further analysis found that Cyanex272 plays a dominant role in the extraction process with affinity order is Y < Eu < Zn < Al, while [OMIm] [PF_6] exhibits a strong selective effect which can reduce Cyanex272 affinity to zinc.

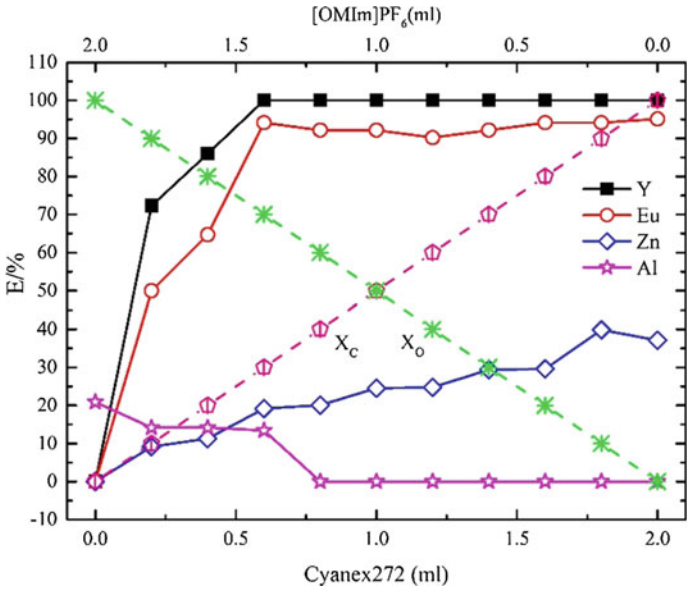

Fig. 5 Variation of the extraction rate of the major metal elements for synergistic extraction with [OMIm] [PF_6] and Cyanex272 as a function of the volume ratio of [OMIm] [PF_6] and Cyanex272

Considering a good extraction effect for Y and Eu and repellency for Zn and Al, the final phase ratio is selected at $X_C = 0.4$ and $X_O = 0.6$.

The Effect of Extraction Time. The effect of extraction time on four valuable elements are displayed in Fig. 6, it can be seen that extraction time plays a minor effect on extraction ratio, the extraction rate of Y and Eu rises with the increase of extraction time, when the extraction time increased from 1 min to 60 min, the extraction rate of Y and Eu only increased by 17 and 17% respectively, but Zn appears to be opposite trend that when the extraction time increased from 1 min to 30 min, the extraction rate of Zn only declines 4%, while the extraction time becomes 60 min, the extraction rate of Zn turns into 0. Al never extracted no matter how extraction time changes. As a consequence, the extraction Y and Eu is greatly influenced by extraction time, however, Zn is slightly affected by extraction time. When the time reaches a certain limit, a small amount of Zn is also released under the equilibrium move. Sufficient REE extraction rate, reduction extraction of Zn and time-saving are taken into comprehensive consideration, the optimum extraction is suggested to be 10 min.

The Effect of Extraction Temperature. Figure 7 is a description of the relationship of different elements extraction rate between extraction temperature. From the graph, it is concluded that extraction temperature has a little influence on Y extraction with only 3% increase when the extraction temperature changed from 25 to 55 °C, a greater effect on Eu and Zn with an increase of 22 and 27%,

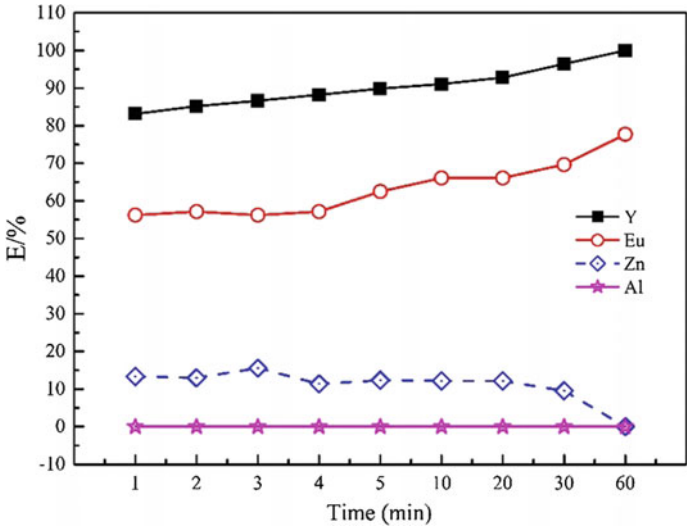

Fig. 6 Variation of the extraction rate of the major metal elements for synergistic extraction with [OMIm] [PF_6] and Cyanex272 as a function of the volume ratio of [OMIm] [PF_6] and Cyanex272

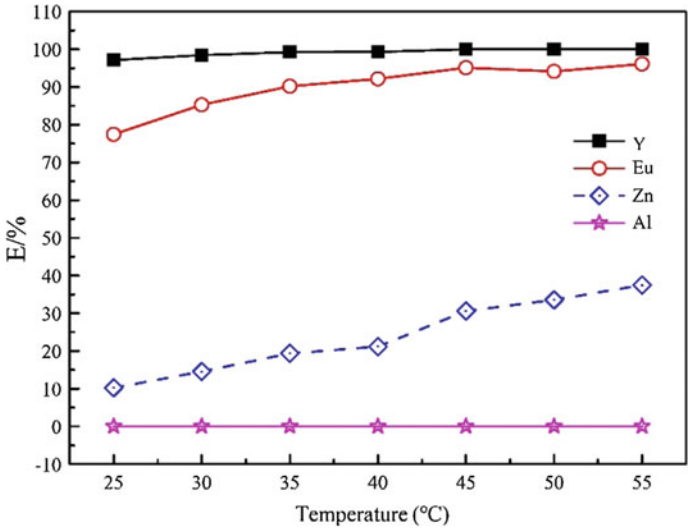

Fig. 7 Variation of the extraction rate of the major metal elements for synergistic extraction with [OMIm] [PF_6] and Cyanex272 as a function of the extraction time

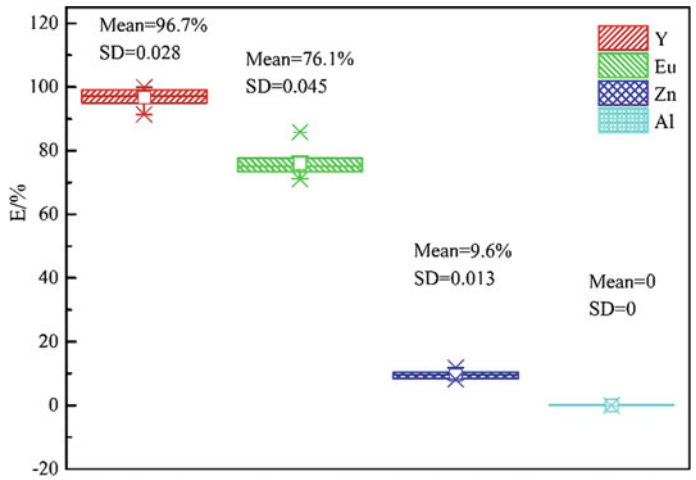

Fig. 8 Variation of the extraction rate of the major metal elements for synergistic extraction with [OMIm] [PF_6] and Cyanex272 under optimal parameters

Table 1 Distribution coefficients of REEs to Zn and synergistic extraction coefficients of Y, Eu, and Zn under the extraction system of [OMIm] [PF_6] and Cyanex272

Separation factor (β)	Synergistic extraction	[OMIm] [PF_6]	Cyanex272
$\beta_{Y/Zn}$	265.84	2.77	0.17
$\beta_{Eu/Zn}$	17.95	1.50	0.08
$\beta_{(Y+Eu)/Zn}$	141.90	2.14	0.13
elements	Y	Eu	Zn
R	4.74	1.35	0.003

respectively. Given that decreasing interference from impurities and reducing energy consumption, the extraction temperature is set as 25 °C (room temperature).

Extraction Experiments under the Optimal Extraction Parameters. The results of parallel experiments under optimal extraction parameters are expressed in Fig. 8 has indicated that the average extraction rate of Y, Eu, Zn is 96.7, 76.1, 9.6%, separately, and Al not be extracted completely. By calculating separation factor REE with Zn under single Cyanex272 system, single [OMIm] [PF_6] system and synergistic extraction system, conclusion can be made that the separation factor in dual extraction system heavily higher than single extraction system, which illustrates that selected extraction system has higher extraction selectivity to Y and Eu compared with Zn and Al. Simultaneously, calculating synergistic enhance factor is listed in Table 1 has indicated that the synergistic enhance factor of Y and Eu is 4.74 and 1.35 which is extremely greater than 1 suggesting synergistic extraction existed in the extraction process of Y and Eu, while for Zn, the factor 0.003 is far less than 1 which is demonstrating there is no synergistic extraction existed in the

extraction process of Zn. Although the extraction rate of Eu is not very high and about 9.6% Zn is still extracted after extraction once, the Y and Eu can be thoroughly extracted with the purity is as high as 99.99% and no any phenomenon of co-extraction generated.

Conclusions

The extraction behavior of Y, Eu, Zn, Al with a novel ionic liquid, [OMIm] [PF_6], and extractant Cyanex272 was investigated. Cyanex272 exhibited a higher affinity to Zn and Al than Y and Eu, while [OMIm] [PF_6] exhibited a higher selectivity to REE than Zn and Al. the optimal extraction parameters for the [OMIm] [PF_6] and Cyanex272 extraction system, were obtained as extraction acidity of 0.2 mol/L, extraction phase 1:5, the addition volume ratio of ionic liquid and extractant 0.6, extraction time 10 min, extraction temperature 25 °C. Under these conditions, REE is separated fully with Zn and Al after 3 times extraction. The whole process is a green, efficient and energy-saving method for separation and recycling REEs, which can be applied in the REE recycling field of waste CRT electrical and electronic equipment.

Acknowledgements This work was financially supported by Beijing Nova Program (Z1511000003150141), National Natural Science Foundation of China (2174068), Academician Workstation in Yunnan Province and Key Discipline for Resource, Environment & Circular Economy of Beijing (Q5104001201503).

References

1. K. Binnemans, P.T. Jones, B. Blanpain, T. Van Gerven, Y. Yang, A. Walton, M. Buchert, Recycling of rare earths: a critical review. J. Clean. Prod. **51**, 1–22 (2013)
2. S. Massari, M. Ruberti, Rare earth elements as critical raw materials: focus on international markets and future strategies. Resour.Policy **38**, 36–43 (2013)
3. X.J. Yang, A. Lin, X. Li, Y. Wu, W. Zhou, Z. Chen, China's ion-adsorption rare earth resources, mining consequences and preservation. Environ. Dev. **8**, 131–136 (2013)
4. Q. Xu, G. Li, W. He, J. Huang, X. Shi, Cathode ray tube (CRT) recycling: current capabilities in China and research progress. Waste Manage. **32**, 1566–1574 (2012)
5. I.C. Nnorom, O. Osibanjo, M.O.C. Ogwuegbu, Global disposal strategies for waste cathode ray tubes. Resour. Conserv. Recycl. **55**, 275–290 (2011)
6. Q. Song, J. Li, A systematic review of the human body burden of e-waste exposure in China. Environ. Int. **68**, 82–93 (2014)
7. S. Sthiannopkao, M.H. Wong, Handling e-waste in developed and developing countries: initiatives, practices, and consequences. Sci. Total Environ. **463–464**, 1147–1153 (2013)
8. X.T. Yu-Gong, Y. Wu, L.L. Zhe-Tan, Recent development of recycling lead from scrap CRTs: A technological review. Waste Manage. **57**, 176–186 (2016)

9. F. Ardente, F. Mathieux, M. Recchioni, Recycling of electronic displays: analysis of pre-processing and potential ecodesign improvements. Resour. Conserv. Recycl. **92**, 158–171 (2014)
10. L.V. Resende, C.A. Morais, Process development for the recovery of europium and yttrium from computer monitor screens. Miner. Eng. **70**, 217–221 (2015)
11. V. Innocenzi, I. De Michelis, F. Ferella, F. Beolchini, B. Kopacek, F. Vegliò, Recovery of yttrium from fluorescent powder of cathode ray tube, CRT: Zn removal by sulphide precipitation. Waste Manage. **33**, 2364–2371 (2013)
12. V. Innocenzi, I. De Michelis, F. Ferella, F. Vegliò, Recovery of yttrium from cathode ray tubes and lamps' fluorescent powders: experimental results and economic simulation. Waste Manage. **33**, 2390–2396 (2013)
13. A. Rout, S. Wellens, K. Binnemans, Separation of rare earths and nickel by solvent extraction with two mutually immiscible ionic liquids. RSC Adv. **4**, 5753–5758 (2014)
14. A. Rout, K. Binnemans, Separation of rare earths from transition metals by liquid-liquid extraction from a molten salt hydrate to an ionic liquid phase. Dalton Trans. **43**, 3186–3195 (2014)
15. R. Martínez-Palou, R. Luque, Applications of ionic liquids in the removal of contaminants from refinery feedstocks: an industrial perspective. Energ. Environ. Sci. **7**, 2414 (2014)
16. X. Sun, Y. Dong, Y. Wang, Y. Chai, The synergistic extraction of heavy rare earth elements using EHEHP-type and BTMPP-type functional ionic liquids. RSC Adv. **5**, 49500–49507 (2015)
17. Y. Shen, W. Li, J. Wu, S. Li, H. Luo, Solvent extraction of lanthanides and yttrium from aqueous solution with methylimidazole in an ionic liquid. Dalton Trans. **43**, 10023–10032 (2014)
18. A. Rout, K. Binnemans, Influence of the ionic liquid cation on the solvent extraction of trivalent rare-earth ions by mixtures of Cyanex 923 and ionic liquids. Dalton Trans. **44**, 1379–1387 (2015)
19. M. Zhu, J. Zhao, Y. Li, N. Mehio, Y. Qi, An ionic liquid-based synergistic extraction strategy for rare earths. Green Chem. **17**, 2981–2993 (2015)
20. X. Tian, X. Yin, Y. Gong, Y. Wu, Z. Tan, P. Xu, Characterization, recovery potentiality, and evaluation on recycling major metals from waste cathode-ray tube phosphor powder by using sulphuric acid leaching. J. Clean. Prod. **135**, 1210–1217 (2016)

Life Cycle Assessment of Representative Individual Light Rare Earth Chloride Production from Bastnaesite in China

Wenjuan Chen, Zhihong Wang, Xianzheng Gong, Boxue Sun, Feng Gao, Yu Liu and Zuoren Nie

Abstract Rare earth elements (REEs) have been applied in various economic fields e.g., metallurgy, automotive, electronics, aerospace and agriculture. China is the largest producer and exporter of rare earth in the world. Bastnaesite is an important category of light rare earth minerals. Light rare earth chlorides typically consist of lanthanum chloride, cerium chloride, praseodymium chloride and neodymium chloride. As the public concern on the issues of emission reduction and energy saving during the past decades, it is valuable to evaluate and analyze the comprehensive environmental impact caused by the rare earth industry. A standard LCA study on light rare earth chlorides was conducted in this paper. Allocation was carried out based on the actual situation of the technology currently employed in rare earth industry in China, and the function unit was defined as 1 kg of individual light rare earth chloride. The major part of the life cycle inventory (LCI) was compiled via an investigation on a rare earth enterprise in Sichuan province, located in southwest China, and the absent information were obtained through interviews with experts and published literature. The results indicated that the environmental impact of praseodymium chloride production was much severer than those of the production of lanthanum chloride, cerium chloride and neodymium chloride. The dominant environmental impact categories were fossil depletion potential (FDP), particulate matter formation potential (PMFP) and global warming potential (GWP). The environmental impacts were mainly caused by energy use. PMFP was mostly generated from the indirect production processes. Ammonia, sodium silicate and hydrochloric acid were the cardinal contributors to the aspect of materials consumption.

Keywords Rare earth chloride · Bastnaesite · Life cycle assessment Allocation

W. Chen (✉) · Z. Wang · X. Gong · B. Sun · F. Gao · Y. Liu · Z. Nie
Center of National Materials Life Cycle Assessment, College of Materials Science and Engineering, Beijing University of Technology,
No. 100 Pingleyuan, Beijing, China
e-mail: chenwenjuan@bjut.edu.cn

Y. Han (ed.), *Advances in Energy and Environmental Materials*,
Springer Proceedings in Energy, https://doi.org/10.1007/978-981-13-0158-2_53

Introduction

Rare earth elements (REEs) are a group of 17 elements contained lanthanide series, scandium and yttrium [1], which have been applied in fields of metallurgy, automotive, electronics, aerospace, agriculture etc. [2, 3]. China is the largest producer and exporter of rare earth in the world. Rare earth reserves in China is 23% of the world [4], nevertheless, China supplied nearly 90% rare earth demand of the world [5]. In 2013, bastnaesite output was 25878 t REO, which was 32% of the total concentrates [6].

Life cycle assessment (LCA) is used to evaluate the environmental impact of the product system. ISO 14040:2006 describes the principles and framework for LCA, which includes definition of the goal and scope, life cycle inventory analysis (LCI), life cycle impact assessment (LCIA) and life cycle interpretation.

There has been some emphasis on environmental analysis of REO production. George G. evaluated the environmental impacts and resource intensity of producing rare earth oxides (REO) from the Bayan Obo rare earth ores located in Inner Mongolia, China [7]. Ehsan Vahidi presented the LCA of in situ leach mining of REEs from ion adsorption clays in southern China, in which the function unit was defined as 1 kg mixed rare earth oxides [8]. This paper was the first LCA study of light rare earth chloride, including lanthanum chloride, cerium chloride, praseodymium chloride and neodymium chloride, which produced from bastnaesite located in Sichuan province, in China.

Methods

In this paper, LCA methodology was used to compare the environmental impact of producing 1 kg lanthanum chloride, cerium chloride, praseodymium chloride and neodymium chloride. The processes were from cradle to gate, which covered the entire production chain of these four rare earth chlorides, from raw ores mining, beneficiation, smelting to extraction separation.

One of the difficulties encountered in LCA is data availability. We created the life cycle inventory (LCI) based on rare earth enterprise (code name A) located in Sichuan province, in southwest area of China. Lack data were from experts interviews and literature sources.

In life cycle impact assessment (LCIA) stage, ReCiPe Version 1.08 model was selected to evaluate the environmental impact. This model included 14 impact categories: freshwater eutrophication (FEP), marine eutrophication (MEP), global warming (GWP), ozone depletion (ODP), terrestrial acidification (AP), photochemical oxidant formation (POFP), particulate matter formation (PMFP), ionising radiation (IRP), land occupation (LOP), natural land transformation (LTP), water depletion (WDP), metal depletion (MDP), fossil depletion (FDP), toxicity (TP).

In life cycle inventory analysis section, life cycle inventory was discussed. Open-pit mining was the major mining method of bastnaesite in Sichuan province [9].

Gravity-magnetic-flotation separation was the major beneficiation technology in concentrate production process [10]. After that, oxidation roasting-acid leaching and extraction separation was used to individual rare earth chloride production [11].

In open-pit mining process, 1 t rare earth ore mining consumed 3.93 kg diesel oil, 0.003 kg explosives, 0.01 kwh electricity. In beneficiation process, large particles of rare earth were collected by gravity separation, middle particles of rare earth were collected by magnetic separation, little particles of rare earth were collected by flotation separation. Recovery rate of REE was 75%. Based on the expert interview and calculation, 1 t REO rare earth concentrates production consumed 27 t raw ore, 0.67 kg H205, 75 kg sodium silicate, 0.67 kg pine oil, 887 kwh electricity and 8 t water.

In smelting process, oxidization roasting-hydrochloric acid leaching- extraction separation was the major technology used in concentrates smelting. Rare earth recovery rate was 96.58% in hydrochloric acid leaching and 99.88% cerium went into the leaching residue [12]. Therefore, CeO_2 contained in leaching residue was calculated according to the cerium content in bastnaesite concentrates [13]. Based on the data from experts interview, rare earth elements amounts in each stage could be calculated, which were shown in Fig. 1.

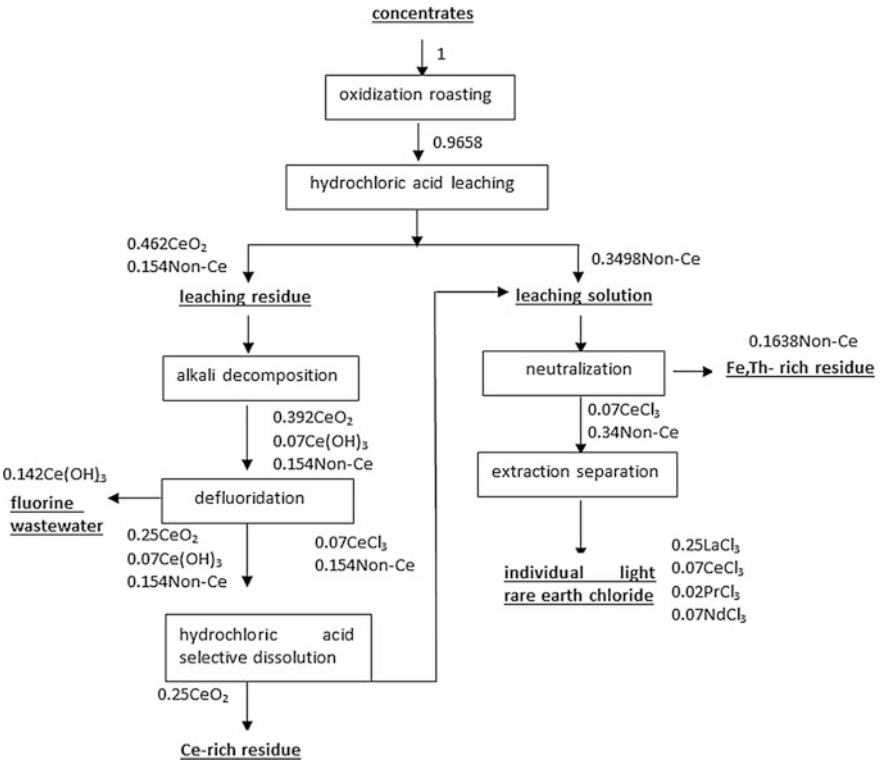

Fig. 1 Mass flow of rare earth elements in each production stage

Based on the experts interview, calculation and literature, life cycle inventory of 1 t rare earth concentrates (REO) in smelting process was obtained, the products were $LaCl_3$, $CeCl_3$, $PrCl_3$, $NdCl_3$ and Ce-rich residue. Energy and materials consumption and pollutant emission were allocated to the above five products. Allocation method were introduced as follows.

Coal, Water and Electricity. Coal was used in oxidization roasting stage, water was used in hydrochloric acid leaching, defluoridation, hydrochloric acid selective dissolution, extraction separation stage. Electricity was used in the whole stages, therefore, they were allocated to $LaCl_3$, $CeCl_3$, $PrCl_3$, $NdCl_3$ and Ce-rich residue based on the mass of products.

Hydrochloric Acid. Hydrochloric acid was used in hydrochloric acid leaching, hydrochloric acid selective dissolution and extraction separation stage.

In hydrochloric acid leaching stage, according to the chemical reaction equation, hydrochloric acid amount was calculated, which was allocated to $LaCl_3$, $CeCl_3$, $PrCl_3$, $NdCl_3$ and Ce-rich residue based on the mass of products. In hydrochloric acid selective dissolution stage, dissolution products were $CeCl_3$ and non-Ce chlorides. According to the chemical reaction equation, hydrochloric acid amount was calculated, then it was allocated to $LaCl_3$, $CeCl_3$, $PrCl_3$, $NdCl_3$ and Ce-rich residue based on the mass of products. In extraction separation stage, hydrochloric acid consumed in this stage was calculated by total consumed amount minus hydrochloric acid consumed in above two stages. The first separated product was neodymium chloride, then praseodymium chloride, the last were lanthanum chloride and cerium chloride. Allocation rule was based on the separation order and the mass of extraction separation products.

Ammonia, P507 and Kerosene. Calculation method of consumed amounts of ammonia, P507 and kerosene was similar with hydrochloric acid consumed in extraction separation stage.

SO_2, Smoke, NOx and CO. SO_2 and smoke were from direct and indirect emission. NOx and CO were from indirect emission. Direct emission amount was obtained from literature [14]. Indirect emission was caused by coal combustion, which was calculated according to the formula in literature [15].

CO_2. CO_2 was from direct and indirect emission. Direct emission amount was calculated by chemical reaction equation. Indirect emission was caused by coal combustion, which was calculated according to the formula in literature [16].

Dusk, Coal Slag, SS, F- and Calcium Fluoride. Dusk, coal slag, SS, F^- and calcium fluoride were from direct emission, the amounts were obtained from literature [6].

According to the research above, life cycle inventory of $LaCl_3$, $CeCl_3$, $PrCl_3$, $NdCl_3$ and Ce-rich residue in smelting process were obtained. Combined with mining process and concentration process, direct consumption and emission in whole life cycle were calculated. Indirect consumption and emission were caused by energy

and the main raw material production, such as coal, electricity, diesel oil and kerosene, the life cycle data of energy were from the research results of Beijing University of Technology. The life cycle data of ammonia, sodium silicate, hydrochloric acid were cited from Simapro 8 software.

Results and Discussion

Based on the above calculation, we listed the life cycle inventory of the rare earth products in Table 1.

Table 1 Life cycle inventory of the rare earth products

	Unit	$LaCl_3$	$CeCl_3$	$PrCl_3$	$NdCl_3$	Ce-rich residue
Input						
Raw coal	kg	1.38E+04	1.36E+04	3.49E+04	1.78E+04	1.33E+04
Raw oil	kg	1.61E+03	2.75E+03	8.94E+03	2.61E+03	7.41E+02
Natural gas	m^3	1.30E+03	4.01E+02	7.17E+02	2.41E+02	3.45E+01
Rare earth ore	t	1.08E+02	3.78E+02	1.35E+03	3.78E+02	1.08E+02
Explosive	kg	3.24E–01	1.13E+00	4.05E+00	1.13E+00	3.24E–01
Water	t	2.35E+02	3.17E+02	6.27E+02	3.08E+02	2.20E+02
NaOH	t	–	–	–	–	1.12E+00
H205	kg	2.68E+00	9.38E+00	3.35E+01	9.38E+00	2.68E+00
P507	kg	8.60E+00	1.20E+01	2.00E+01	7.20E+00	–
Pine oil	kg	2.68E+00	9.38E+00	3.35E+01	9.38E+00	2.68E+00
Output						
$LaCl_3$	t REO	1				
$CeCl_3$	t REO		1			
$PrCl_3$	t REO			1		
$NdCl_3$	t REO				1	
Ce-rich residue	t REO					1
CH_4	kg	6.40E–02	6.90E–02	5.90E–01	1.75E–01	6.28E–02
N_2O	kg	7.78E–02	7.05E–02	7.38E–01	2.17E–01	7.64E–02
NMVOC	kg	2.87E–01	3.18E–01	1.84E+00	6.12E–01	2.83E–01
PM	kg	1.93E+00	1.88E+00	1.60E+01	4.90E+00	1.90E+00
As	kg	5.32E–04	9.74E–04	2.60E–03	9.70E–04	5.24E–04
Cd	kg	3.38E–06	6.20E–06	1.65E–05	6.17E–06	3.33E–06
Cr	kg	4.49E–05	8.22E–05	2.20E–04	8.19E–05	4.42E–05
Hg	kg	2.33E–05	4.28E–05	1.14E–04	4.26E–05	2.30E–05
Ni	kg	6.66E–05	1.22E–04	3.26E–04	1.22E–04	6.56E–05
Pb	kg	4.66E–04	8.54E–04	2.28E–03	8.50E–04	4.59E–04
V	kg	7.66E–04	1.40E–03	3.75E–03	1.40E–03	7.55E–04

(continued)

Table 1 (continued)

	Unit	$LaCl_3$	$CeCl_3$	$PrCl_3$	$NdCl_3$	Ce-rich residue
Zn	kg	6.39E–04	1.17E–03	3.12E–03	1.17E–03	6.29E–04
COD	kg	2.57E–01	2.19E–01	2.74 E+00	7.82E–01	2.52E–01
Inert gas	Bq	1.59E+05	1.36E+05	1.70E+06	4.86E+05	1.56E+05
Tritium	Bq	1.80E+05	1.53E+05	1.92E+06	5.47E+05	1.76E+05
SO_2	kg	8.41E+01	7.68E+01	3.23E+02	1.30E+02	7.91E+01
Smoke	kg	4.91E+02	4.84E+02	4.88E+02	4.84E+02	4.91E+02
Dusk	kg	3.58E+02	3.06E+02	3.79E+03	1.08E+03	3.51E+02
Coal slag	kg	2.05E+03	2.04E+03	2.06E+03	2.21E+03	2.05E+03
CO_2	kg	2.82E+04	2.60E+04	6.67E+04	3.29E+04	2.36E+04
CO	kg	7.59E+01	7.38E+01	1.26E+02	8.51E+01	7.58E+01
NOx	kg	1.02E+02	1.00E+02	2.74E+02	1.36E+02	1.00E+02
SS	kg	1.05E+03	1.05E+03	1.05E+03	1.05E+03	–
F^-	kg	9.76E+01	9.76E+01	9.75E+01	9.76E+01	–
CaF_2	kg	2.93E+02	2.93E+02	2.93E+02	2.93E+02	–
Beneficiation Tailings (including water)	t	1.20E+02	4.20E+02	1.50E+03	4.20E+02	1.20E+02
Chloride	kg	5.60E+01	7.51E+01	1.17E+02	4.99E+01	1.69E+01
Sulfate	kg	8.18E+01	3.18E+01	1.96E+02	7.01E+01	2.15E+01
Phosphate	kg	2.30E–01	8.10E–01	2.90E+00	8.10E–01	2.30E–01
Potassium, ion	kg	6.40E–01	2.25E+00	8.03E+00	2.25E+00	6.40E–01
Calcium	kg	7.77E+00	8.16E+00	1.94E+00	7.80E–01	–

Table 2 Characterization results of the rare earth products

Impact categories	Unit	$LaCl_3$	$CeCl_3$	$PrCl_3$	$NdCl_3$	Ce-rich residue
GWP	DALY	3.95E–02	3.64E–02	9.37E–02	4.61E–02	3.31E–02
POFP	DALY	1.47E–07	1.45E–07	2.99E–07	2.99E–07	1.47E–07
PMFP	DALY	9.75E–02	8.36E–02	1.00E+00	2.88E–01	9.54E–02
HTP	DALY	8.82E–08	1.62E–07	4.31E–07	1.61E–07	8.69E–08
FDP	$	1.38E+03	1.43E+03	3.93E+03	1.67E+03	1.03E+03
AP	species.yr	8.19E–07	7.70E–07	2.77E–06	1.20E–06	7.85E–07
FEP	species.yr	3.37E–09	1.19E–08	4.25E–08	1.19E–08	3.37E–09
FETP	species.yr	9.91E–12	1.82E–11	4.85E–11	1.81E–11	9.76E–12
METP	species.yr	1.82E–12	3.34E–12	8.92E–12	3.34E–12	1.80E–12
TETP	species.yr	1.95E–32	3.58E–32	9.56E–32	3.58E–32	1.92E–32

Table 3 Normalization results of the rare earth products (p^{-1} yr^{-1})

Impact categories	$LaCl_3$	$CeCl_3$	$PrCl_3$	$NdCl_3$	Ce-rich residue
GWP	2.92E–01	2.70E–01	6.94E–01	3.41E–01	2.45E–01
POFP	1.09E–06	1.07E–06	2.21E–06	2.21E–06	1.09E–06
PMFP	7.22E–01	6.19E–01	7.43E+00	2.14E+00	7.07E–01
HTP	6.53E–07	1.20E–06	3.20E–06	1.19E–06	6.43E–07
FDP	5.61E+00	5.83E+00	1.61E+01	6.81E+00	4.19E+00
AP	8.93E–04	8.40E–04	3.02E–03	1.31E–03	8.56E–04
FEP	3.67E–06	1.29E–05	4.63E–05	1.29E–05	3.67E–06
FETP	1.08E–08	1.98E–08	5.28E–08	1.98E–08	1.06E–08
METP	1.99E–09	3.64E–09	9.73E–09	3.64E–09	1.96E–09
TETP	2.13E–29	3.90E–29	1.04E–28	3.90E–29	2.10E–29

Life cycle impact assessment was the necessary procedure in LCA study. Characterization factors, normalization factors and weighting factors were cited from ReCiPe Model. Characterization results, normalization results were listed in Tables 2 and 3.

Table 3 showed the normalization results. Normalization factors were cited from ReCiPe Endpoint Hierarchist world. Normalization results reveal the relative value of the environmental impact categories, which have the identical unit and can be compared between each other. Table 3 indicated that FDP, PMFP and GWP were the major environmental impacts of the rare earth products. Among the five rare earth products, the largest normalization results were from $PrCl_3$.

FDP was the most severe impact category in the whole $PrCl_3$ life cycle. Massive primary energy consumption in the concentrates production stage was the main contribution, the next one was the electricity consumption. PMFP was the second severe impact category, which was caused by the dusk and SO_2, which were mainly from the indirect emissions. The emission from production of energy, such as coal, electricity, kerosene and diesel oil was the main contribution for the PMFP. The proportion of impact category of rare earth products were shown in Fig. 2.

Based on the weighting factors in ReCiPe Version 1.08 model, the weighting results were obtained, which were shown in Table 4. Among the five rare earth products, $PrCl_3$ had the most significant influence. The weighting result of Ce-rich residue was the smallest. The impact of 1 kg $PrCl_3$ was 4.7 times of the Ce-rich residue, 3.6 times of $LaCl_3$, 3.6 times of $CeCl_3$, 2.6 times of $NdCl_3$ (Fig. 3).

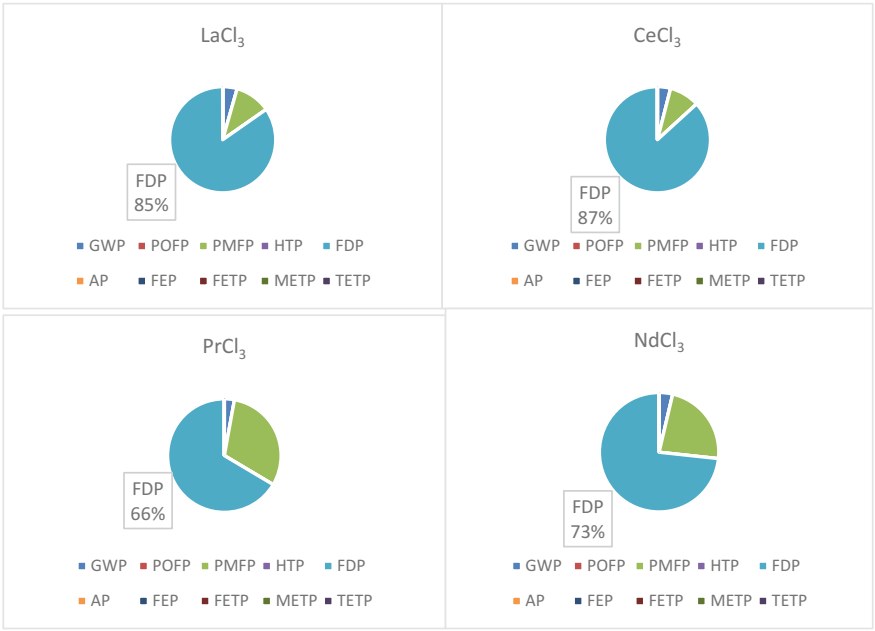

Fig. 2 Proportion of normalization results

Table 4 Weighting results of the rare earth products

	$LaCl_3$	$CeCl_3$	$PrCl_3$	$NdCl_3$	Ce-rich residue
Results	1.99E+03	2.02E+03	7.25E+03	2.79E+03	1.54E+03

Fig. 3 Weighting results of the rare earth products

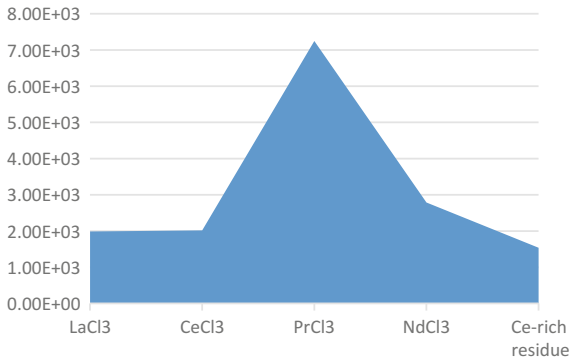

Conclusion

This study evaluated the environmental impacts of extracting representative individual light rare earth chloride production from bastnaesite in China from the perspective of life cycle. Life cycle inventory data were investigated from a typical rare earth enterprise in Sichuan province, China, and some lacking data were obtained via interviews with experts and published literature. ReCiPe model (Version 1.08) was used for impact assessment. The allocation procedure, individually determining the environmental impact of each type of rare earth chloride, was carried out based on the actual situation of the technology currently employed by rare earth industry.

The results showed that the production of $PrCl_3$ caused the severest environmental impact among different chlorides under consideration. The impact due to the production of 1 kg of $PrCl_3$ was as 4.7 times, 3.6 times, 3.6 times, 2.6 times as much as the impact due to the production of the same function unit of Ce-rich residue, $LaCl_3$, $CeCl_3$, and $NdCl_3$. The major environmental impacts were FDP, PMFP and GWP. The environmental impacts were mainly caused by energy use. FDP was due to the massive consumption of energy. PMFP was mainly caused by the indirect emissions, i.e., emissions generated in the production processes of coal, electricity, kerosene and diesel.

Ammonia, sodium silicate and hydrochloric acid were the major contributors to the aspect of materials consumption. The production of the above-mentioned three types of raw materials consumed a large amount of primary energy, which also significantly contributed to the indicator of FDP. This study revealed the causes of the environment impact due to the production of typical individual light rare earth chloride, which will be useful for engineers and policy makers who focus on that topic, and attention should be paid by future studies to technical methods that can increase the environment-friendliness of the rare earth industry in China.

Acknowledgements This study was supported by National Key Research and Development Plan (2016YFF0204403), Beijing municipal science & technology commission project (D161100002416001), National Key Research and Development Program (2016YFF0201501).

References

1. G.X. Xu, *Rare Earths*, 2nd edn. (Beijing, 2013)
2. X.W. Huang, Y.Q. Zhang, H.W. Li, Development trend and research progress of rare earth extraction in China. Sci. Found. China **3**, 134–137 (2011)
3. G.H. Liu, *Rare Earth Materials Science* (Chemical industry press, Beijing, 2011)
4. *White Papers of the Chinese Rare Earth Condition and Policy* (Beijing, 2012)
5. Z.W. Liu, D.F. Xue, *Transition of China Rare Earth*. Annual Academic Conference of the Chinese Society of Rare Earths (2017)
6. *The Editorial Board of CSRE Yearbook* (China Society Rare Earth yearbook, Beijing, 2013)

7. G.G. Zaimes, B.J. Hubler, S. Wang, V. Khanna, Environmental life cycle perspective on rare earth oxide production. ACS Sustain. Chem. Eng. **3**, 237–244 (2015)
8. E. Vahidi, J. Navarro, F. Zhao, An initial life cycle assessment of rare earth oxides production from ion-adsorption clays. Resour. Conserv. Recycl. **113**, 1–11 (2016)
9. X.W. Huang, H.W. Li, *Rare Earth of China* (Metallurgical industry press, Beijing, 2015)
10. C.H. Wang, Z. Hu, X.Y. Qiu, H.W. Li, T. Wang, Experimental study on a novel combined beneficiation technique for bastnaesite type RE ore using magnetic-gravity-flotation separation. Chin. J. Rare Metals **1**, 1–11 (2017)
11. Q.S. Yang, T. Yang, Study on new smelting process of bastnaesite. Rare Metals. Cemented Carbides **1**, 1–4 (2014)
12. W.Y. Wu, X. Bian, *Rare Earth Metallurgy Technology* (Science press, Beijing, 2012)
13. M.H. Wang, M. Zeng, L.S. Wang et al., Catalytic leaching process of bastnaesite with hydrochloric acid after oxidation roasting pretreatment. J. Chin. Soc. Rare Earths **2**, 148–154 (2013)
14. Analysis of production technology of rare earth separation products from Sichuan bastnaesite. Sichuan Rare Earth **3**, 24–27 (2007)
15. Information on http://www.eiafans.com/thread-16213-1-1.html
16. F. Gao, Research on life cycle assessment and the application in China magnesium industry, Doctoral Dissertation, 2008

Life Cycle Assessment of LFP Cathode Material Production for Power Lithium-Ion Batteries

Jun Xie, Feng Gao, Xianzheng Gong, Zhihong Wang, Yu Liu and Boxue Sun

Abstract To cope with the world energy crisis and global climate change, the governments of the world attach great importance to the development of new energy industry. The production and application of power lithium-ion battery also attract much attention. Based on the life cycle model we built for the lithium iron phosphate (LFP) cathode materials production, the resources and energy consumption inventory of LFP cathode production was calculated. The environmental impacts of LFP production for a power lithium-ion battery were analyzed. The results showed that the synthesis process of LFP production was the key production stage and accounted for 52.93% of the accumulated environmental burden, followed by Li_2CO_3 preparation, $(NH_2)_2HPO_4$ preparation and Fe_3O_4 preparation, which accounted for 20.90, 18.90 and 7.27% of overall environmental burdens respectively. The key impact categories of LFP production were human toxicity, fossil depletion, climate change and acidification, which accounted for 77.62, 6.36, 5.21 and 4.19% of total environmental impact, respectively. The climate change potential of LFP production in different stages was compared emphatically. The Li_2CO_3 preparation was the key stage for the climate change potential, which accounted for 50.59% of greenhouse gases emissions. The optimized synthesis

J. Xie (✉) · F. Gao · X. Gong · Z. Wang · Y. Liu · B. Sun
Center of National Materials Life Cycle Assessment, College of Materials Science and Engineering, Beijing University of Technology,
No. 100 Pingleyuan, Beijing, China
e-mail: xiejun@emails.bjut.edu.cn

F. Gao
e-mail: gaofeng@bjut.edu.cn

X. Gong
e-mail: gongxianzheng@bjut.edu.cn

Z. Wang
e-mail: wangzhihong@bjut.edu.cn

Y. Liu
e-mail: liuyu@bjut.edu.cn

B. Sun
e-mail: sunboxue@bjut.edu.cn

Y. Han (ed.), *Advances in Energy and Environmental Materials*,
Springer Proceedings in Energy, https://doi.org/10.1007/978-981-13-0158-2_54

process could be conducive to reduce the greenhouse gas emissions and decrease the environmental burden caused by the production of lithium iron phosphate.

Keywords Power lithium-ion battery · Cathode material · Lithium iron phosphate Life cycle assessment

Introduction

In the context of global climate change and environment protection, the development of the new energy industry has attracted widespread attention from governments, which also was one of the most driving force for the rapid development of electric vehicles. China's new energy industry has entered a stage of rapid development. The Chinese government has vigorously supported the use of power lithium-ion batteries as 'clean' energy applications in the automotive industry. With the improvement of power lithium-ion battery production technology, the scale of the power battery industry in China is rapidly expanding.

According to statistical data of the cathode material products shipments of China in 2016 [1], lithium iron phosphate (LFP) production grew by 76% than that in 2015, up to 57 thousand tons. Lithium cobalt nickel manganese (NCM) production grew by 67.1%, reaching 61 thousand tons. The substantial growth of LFP and NCM were mainly driven by power batteries which were mostly applied to electric vehicles. Lithium manganese oxide (LMO) shipments decreased by 47%, and lithium cobalt oxide (LCO) shipments decreased by 16.7%. Figure 1 showed the shipments of lithium-ion batteries cathode materials from 2013 to 2016. The output of LFP accounted for 35.2% of all cathode materials shipments in 2016, more than 1/3 of the total amount. As the good safety performance and charging characteristics of LFP compared with the traditional cathode materials, its output will improve continuously.

More cathode materials for power lithium-ion batteries have been applied to the automotive industry, and the environmental problems caused by them have also been paid much attention. Yajuan Yu studied the environmental impacts of LFP batteries and conventional batteries, and developed a professional software of life cycle environmental impact assessment for conventional lead-acid batteries and

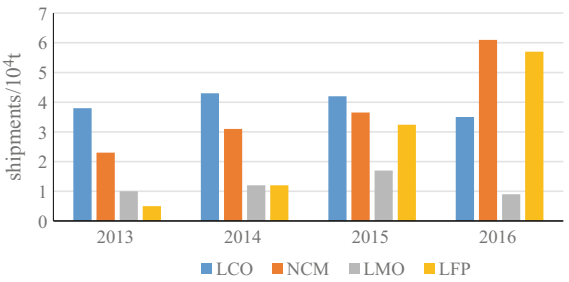

Fig. 1 Shipments of lithium-ion batteries cathode materials from 2013 to 2016

lithium iron phosphate batteries [2, 3]. Yuhan Liang studied the optimized design of lithium ion secondary batteries using combination of carbon footprints and life cycle assessment, the research indicated that the greenhouse gas emissions of LFP cathode material was 4.46 kg CO_2-eq [4]. Majeau et al. used the ReCiPe methodology to compare the environmental impacts of nickel hydrogen batteries, NCM batteries, LFP batteries and cathode materials. The study selected the use stage energy storage 50 MJ as functional unit, and evaluated the environmental impacts of each part of each product. The NiMH technology was found to have the highest environmental impact, followed by NCM and then LFP, for all categories considered except the ozone depletion potential [5]. Anna Stamp et al. applied the LCA methodology to assess the environmental impacts of the production of Li_2CO_3 from natural brine. The results showed that greenhouse gas emission of the currently-dominant production chain for 1 kg of Li_2CO_3 from brine was 2.02 kg CO_2-eq [6]. Notter et al. built a detailed life cycle inventory of lithium iron phosphate cathode material and provided a basis for more detailed environmental assessments of lithium iron phosphate. The study showed that major contribution to the environmental burden was the supply of metal material for the LFP [7].

Many researches of the environmental impact assessments for power lithium-ion batteries were carried out early [8–11]. However, the environmental impacts analyses of cathode materials for the power batteries associated with Chinese situation of resources and energy have been reported less. In this study, the life cycle assessment of LFP cathode material was carried out, nine environmental impact categories were mainly considered and the climate change potential was analyzed emphatically. This research was aimed to present the environmental hot spots for Chinese LFP cathode material production, and was beneficial to the prediction of environmental improvement potential for optimized technologies implementation.

Methodology and Data

Goal and Scope Definition. In this study, the functional unit was defined as 1 kg of LFP cathode material of the power lithium-ion battery. The system boundary included the ore mining, precursor preparation and synthesis of cathode materials and the energy generation. The synthesis methods of LFP cathode materials can be divided into two categories, solid phase synthesis and liquid phase synthesis. Solid phase synthesis mainly includes high temperature solid phase method and carbothermal reduction method. The high temperature solid phase method is one of the most common methods for the production of cathode materials [12–14].

In this study, the synthesis process of high temperature solid phase method was selected as production model, showed in Fig. 2. Firstly, the lithium source, the iron source and the phosphorus source were fully mixed and evenly dispersed. The mixture was fully ground with the organic solvent used as dispersing agent, and was decomposed at lower temperature in an inert atmosphere, and then was sintered and crushed in high temperature to get the LFP products.

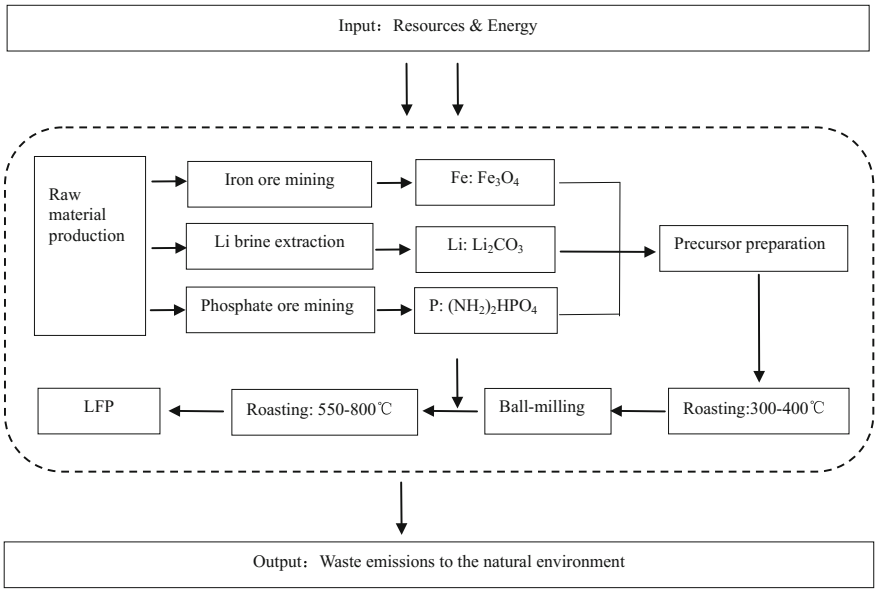

Fig. 2 System boundary of this study

Data Source and Calculation. The energy consumption for the raw materials production and the precursor synthesis process of the LFP cathode material was collected through the literature review and enterprise investigation. Lithium carbonate was produced by lithium brine of Saline Lake. The data were derived from SQM facility in Salar de Atacama, Chile [15–17]. Fe_3O_4 was the iron source for the LFP preparation, the data sources of which were collected from the reference [18]. $(NH_{2)2}HPO_4$ was an important raw material for the preparation of LFP, the data of which were derived from life cycle assessment of phosphate production in China Study [19]. The synthetic process for preparing lithium iron phosphate was based on data from a factory in Qingdao, China, that produces cathode materials for lithium batteries. As for the sources of background data, the inventory data of some other chemical reagents, such as organic solvent and alcohol, were obtained from the Ecoinvent database.

The pollutants emission data of the processes were obtained from the internal measurement values of the enterprises and also refer to the literature [20]. The CO_2 emissions of fossil energy combustion were taken from the reference [21]. The inventory data of electric power generation were derived from the research outcome of Sino-Center database in Beijing University of Technology (CNMLCA, 2013) [22], which were updated based on the literature (Di et al., 2007) [23]. The input and output of 1 kg of LFP production using the solid phase synthesis method was listed in Table 1.

Table 1 Inventory of 1 kg of LFP production by solid phase synthesis method [values are presented per functional unit]

Item	Input/Output	Unit	Amount				
			Li_2CO_3	Fe_3O_4	$(NH_2)_2HPO_4$	Synthesis	Sum
Material consumption	Li brine	kg	1.28E+00				1.28E+00
	Na_2CO_3	kg	5.80E–01				5.80E–01
	CaO	kg	2.11E–02				2.11E–02
	HCl	kg	9.36E–03				9.36E–03
	Organic solvent	kg	4.68E–03				4.68E–03
	H_2SO_4	kg	1.17E–02				1.17E–02
	Alcohol	kg	1.66E–04				1.66E–04
	Iron ore	kg		1.64E+00			1.64E+00
	Phosphate ore	kg			1.71E+00		1.71E+00
	Liquid ammonia	kg			1.84E–01		1.84E–01
	Sulfur	kg			3.59E–01		3.59E–01
	Calcium carbonate	kg			3.09E–04		3.09E–04
	Fresh water	kg	3.34E+00	2.41E–01	6.84E+00	2.60E+00	1.30E+01
Energy consumption	Electric power	kWh	1.45E–05	4.45E–02	2.64E–01	7.40E–01	1.05E+00
	Coal	kg	2.06E–01	5.32E–02	4.26E–05		2.59E–01
	Natural gas	m^3	8.90E–03	1.15E–03	9.98E–04		1.10E–02
	Crude oil	kg	2.59E–01	1.38E–02	8.11E–03		2.81E–01
Emissions	CO_2	kg	1.03E+00	1.73E–01	2.18E–01	6.10E–01	2.03E+00
	CH_4	kg	2.93E–05	2.92E–06	2.92E–06	8.10E–06	4.32E–05
	N_2O	kg	1.10E–05	2.49E–06	4.00E–06	1.12E–05	2.87E–05
	CO	kg	1.69E–04	7.34E–05	3.06E–04	8.58E–04	1.41E–03
	SO_2	kg	6.10E–04	3.27E–04	1.48E–03	4.14E–03	6.55E–03
	NOx	kg	4.66E–04	2.11E–04	1.00E–03	2.81E–03	4.49E–03
	NMVOC	kg	1.55E–05	3.22E–06	8.03E–06	2.25E–05	4.92E–05
	PM	kg	5.97E–05	2.11E–05	8.24E–05	2.31E–04	3.94E–04
	As	kg	1.02E–07	8.03E–08	4.11E–07	1.15E–06	1.75E–06

(continued)

Table 1 (continued)

Item	Input/Output	Unit	Amount				
			Li_2CO_3	Fe_3O_4	$(NH_2)_2HPO_4$	Synthesis	Sum
	Cd	kg	6.44E–09	2.16E–09	2.62E–09	7.34E–09	1.86E–08
	Cr	kg	5.27E–08	1.91E–08	3.47E–08	9.74E–08	2.04E–07
	Hg	kg	3.06E–08	1.08E–08	1.81E–08	5.06E–08	1.10E–07
	Ni	kg	5.32E–08	2.17E–08	5.16E–08	1.45E–07	2.71E–07
	Pb	kg	5.12E–07	1.92E–07	3.61E–07	1.01E–06	2.08E–06
	V	kg	1.28E–07	1.10E–07	5.93E–07	1.66E–06	2.49E–06
	Zn	kg	9.72E–07	2.90E–07	4.95E–07	1.39E–06	3.14E–06

Life Cycle Impact Assessment Methodology. This paper adopted the ReCiPe method, which is one of the most widely used assessment systems, to assess the environmental impacts of the LFP cathode material production process. Nine environmental impact types were considered including Marine eutrophication (MEP), Climate change (GWP), Terrestrial acidification (AP), Photochemical oxidant formation (POFP), Particulate matter formation (PMFP), Metal depletion (MDP), Fossil depletion (FDP), Human toxicity (HTP) and Marine ecotoxicity (METP) [24, 25]. Life cycle modeling and data processing and analysis of the LFP cathode material production were carried out using the SimaPro 7.2.2® (PRé Consultants, 2013) software developed by PRé Consultants in the Netherlands.

Results and Discussion

As shown in Table 2, the characterization for nine environmental impact types of 1 kg of LFP production were calculated. The characterization results for GWP, AP, MEP, POFP, PMFP, MDP, FDP, HTP and METP were 2.04 kg CO_2-eq, 9.07 kg SO_2-eq, 1.75 kg N-eq, 4.61 kg NMVOC, 2.69 kg PM10-eq, 1.94 kg Fe-eq, 4.65 kg oil-eq, 5.16 kg 1,4-DB-eq and 1.57 kg 1,4-DB-eq, respectively.

With the analysis of greenhouse gas emissions, was released by LFP production. The greenhouse gases emission for 1 kg of LFP cathode material production was 2.04 kg CO_2-eq, which was nearly half of the result calculated by Yuhan Liang (2016), which was 4.46 kg CO_2-eq. The difference was because of the transportation was not considered in this research, which caused some greenhouse gases emission. In the preparation stage of raw materials, most of the greenhouse gas emissions were from the energy consumption of Li_2CO_3 preparation, which released 1.03 kg CO_2-eq greenhouse gas. Followed by synthesis process, $(NH_2)_2HPO_4$ preparation and Fe_3O_4 preparation, that released 6.13 kg CO_2-eq,

Table 2 Characterization results of 1 kg of LFP production [values are presented per functional unit]

GHG	Unit	Li_2CO_3 production	Fe_3O_4 production	$(NH_2)_2HPO_4$ production	Synthesis process	Total
GWP	kg CO_2 eq	1.03E+00	1.73E−01	2.20E−01	6.13E−01	2.04E+00
AP	kg SO_2-eq	8.71E−04	4.45E−04	2.04E−03	5.71E−03	9.07E−03
MEP	kg N-eq	1.82E−05	8.21E−06	3.91E−05	1.10E−04	1.75E−04
POFP	kg NMVOC-eq	4.89E−04	2.17E−04	1.03E−03	2.87E−03	4.61E−03
PMFP	kg PM10-eq	2.84E−04	1.33E−04	5.98E−04	1.68E−03	2.69E−03
MDP	kg Fe-eq	5.13E−06	1.76E−06	3.30E−06	9.24E−06	1.94E−05
FDP	kg oil-eq	2.04E−01	4.74E−02	5.65E−02	1.57E−01	4.65E−01
HTP	kg 1,4-DB-eq	9.52E−02	3.72E−02	1.01E−01	2.83E−01	5.16E−01
METP	kg 1,4-DB-eq	2.90E−05	1.13E−05	3.07E−05	8.60E−05	1.57E−04

2.20 kg CO_2-eq and 1.73 kg CO_2-eq greenhouse gas. The greenhouse gas emissions of Li_2CO_3 preparation was the key stage accounting for 50.59% of greenhouse gases emissions. The preparation stage of raw materials was much higher than that of LFP synthesis process. The results about CO_2 equivalent of LFP production are shown in Table 3.

As shown in Figs. 3 and 4, the environmental impacts of LFP production were analyzed. The synthesis process of LFP production was the key production stage, which accounted for 52.93% of the environmental burden. Followed by Li_2CO_3 preparation process, $(NH_2)_2HPO_4$ preparation and Fe_3O_4 preparation accounted for 20.90, 18.90 and 7.27% of overall environmental burden, respectively. The key

Table 3 CO_2 equivalent emission of 1 kg of LFP production [values are presented per functional unit]

GHG	Unit	Li_2CO_3 production	Fe_3O_4 production	$(NH_2)_2HPO_4$ production	Synthesis process	Total
CO_2	kg CO_2-eq	1.03E+00	1.73E−01	2.18E−01	6.10E−01	2.03E+00
CH_4	kg CO_2-eq	7.32E−04	7.31E−05	7.31E−05	2.03E−04	1.08E−03
N_2O	kg CO_2-eq	3.29E−03	7.43E−04	1.19E−03	3.33E−03	8.56E−03
Sum	kg CO_2-eq	1.03E+00	1.73E−01	2.20E−01	6.13E−01	2.04E+00

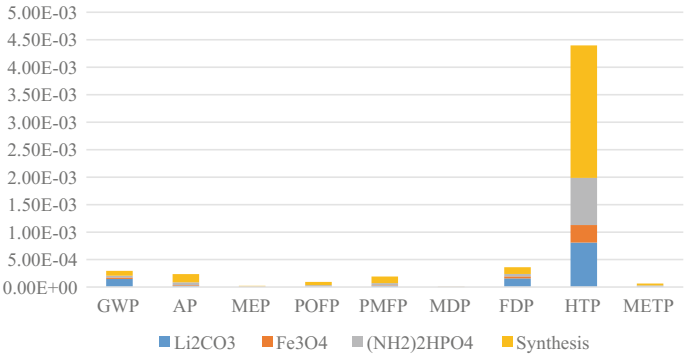

Fig. 3 Environmental impacts of 1 kg of LFP production

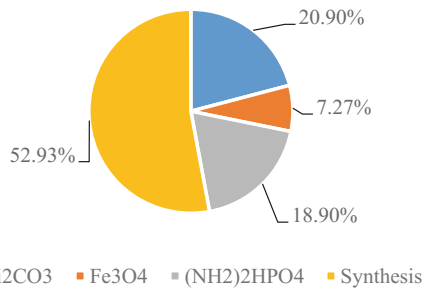

Fig. 4 Normalization results of 1 kg of LFP production in different stages

impact categories of LFP production were human toxicity, fossil depletion, climate change and acidification, which accounted for 77.62, 6.36, 5.21 and 4.19% of total environmental impact. In conclusion, the human toxicity was the main contributor to the total environmental impact, and the synthesis process was the major contributor to the environmental impacts of the whole production process.

Conclusions

The environmental burdens of LFP production have been identified and quantified by LCA in the context of material consumption, energy consumption, energy extraction and waste emissions. Nine environmental impact types were mainly considered in this paper, and the climate change potential for different production stages of LFP cathode materials was emphatically analyzed. The main conclusions can be drawn as follows.

(1) The normalization results show that the human toxicity is the largest environmental impact (77.62%) and synthesis process contributes most to overall environmental burdens (52.93%).
(2) The synthesis process of LFP production is the key production stage, accounted for 52.93% of the environmental burden, followed by Li_2CO_3 preparation, $(NH_2)_2HPO_4$ preparation and Fe_3O_4 preparation.
(3) The greenhouse gas emissions caused by synthesis process are higher than the $(NH_2)_2HPO_4$ preparation and Fe_3O_4 preparation. The synthesis process stage accounted for 30.11% of overall greenhouse gases emissions.
(4) In the production stages of LFP cathode materials, the Li_2CO_3 preparation releases 1.03 kg CO_2-eq greenhouse gas, is higher than other preparation stages for LFP.
(5) For the industrial energy saving and emission reduction, optimizing the technology of synthesis process will be conducive to reduce the greenhouse gas emissions, and to decrease the environmental burden caused by the production of LFP cathode material.

Acknowledgements This study was supported by National Key Research and Development Program (2016YFF0201501, 2017YFF0211501), Beijing municipal science & technology commission project (D161100002416001), and National Natural Science Foundation of China (NSFC, Project No. 51304009).

References

1. Information on http://www.battery.com.cn
2. C. Wang, B. Chen, Y.J. Yu, Carbon footprint analysis of lithium ion secondary battery industry: two case studies from China. J. J. Clean. Prod. **13**, 1–11 (2016)

3. Y.J. Yu, X. Wang, Environmental characteristics comparison of Li-ion batteries and Ni-MH batteries under the uncertainty of cycle performance. J. J. Hazard. Mater. **230**, 455–460 (2012)
4. Y.H. Liang, J. Su, Life cycle assessment of lithium-ion batteries for greenhouse gas emissions. J. Resour. Conserv. Recycl. **31**, 340–349 (2016)
5. G. Majeau, T.R. Hawkins, Life cycle environmental assessment of lithium-ion and nickel metal hydride batteries for plug-in hybrid and battery electric vehicles. J. Environ. Sci. Technol. **10**, 4548–4554 (2011)
6. S. Anna, Environmental impacts of a transition toward e-mobility: the present and future role of lithium carbonate production. J. J. Clean. Prod. **23**, 104–112 (2012)
7. D.A. Notter, M. Gauch, Contribution of Li-ion batteries to the environmental impact of electric vehicles. J. Environ. Sci. Technol. **44**, 6550–6556 (2010)
8. J.L. Sullivan, L. Gaines, Status of life cycle inventories for batteries. J. Energy Convers. Manage. **58**, 134–148 (2012)
9. J. Matheys, W. Autenboer, Influence of functional unit on the life cycle assessment of traction batteries. J. Life Cycle Assess. **12**, 191–196 (2007)
10. J. Matheys, J.M. Timmermans, Comparison of the environmental impact of five electric vehicle battery technologies using LCA. J. Int. J. Sustain. Manuf. **3**, 318–329 (2009)
11. C. Spanos, D.E. Turney, Life-cycle analysis of flow-assisted nickel zinc-, manganese dioxide-, and valve-regulated lead-acid batteries designed for demand-charge reduction. J. Renew. Sustain. Energy Rev. **43**, 478–494 (2015)
12. J.B. Dunn, L. Gaines, J.C. Kelly, The significance of Li-ion batteries in electric vehicle life-cycle energy and emissions and recycling's role in its reduction. J. Energy. Environ. Sci. **8**, 158–168 (2015)
13. D. Kushnir, Multi-level energy analysis of emerging technologies: a case study in new materials for lithium ion batteries. J. Clean. Prod. **19**, 1405–1416 (2011)
14. B. Reuter, Assessment of sustainability issues for the selection of materials and technologies during product design: a case study of lithium-ion batteries for electric vehicles. J. Int. J. Interact. Des. Manuf. **10**, 217–227 (2016)
15. K. Duncan, The time dimension and lithium resource constraints for electric vehicles. J. Resour. Policy **37**, 93–103 (2012)
16. O. Luis, M. Maarten, Key issues of lithium-ion batteries from resource depletion to environmental performance indicators. J. J. Clean. Prod. **108**, 54–362 (2015)
17. P. Swart, Resource demand for the production of different cathode materials for lithium ion batteries. J. J. Clean. Prod. **9**, 2–5 (2014)
18. J.Y. Hu, F. Gao, Z.H. Wang, Life Cycle Assessment of Steel Production. J. Materials Science Forum. **787**, 102–105 (2014)
19. F.F. Zhang, Life cycle assessment of ammonium phosphate production, Master's thesis, Shandong University, 2016
20. The first national census data compilation committee. In *Manual of Pollution Discharge Coefficient of the Pollution Source Census* (Beijing, 2011)
21. B.X. Sun, Z.R. Nie, Y. Liu, X.Z. Gong, F. Gao, Z.H. Wang, Research on life cycle CO_2 emissions of energy carriers in China. J. Mater. Res. Innovations **18**, 56–61 (2014)
22. Information on http://cnmlca.bjut.edu.cn/database
23. X.H. Di, Z.R. Nie, B.R. Yuan, T.Y. Zuo, Life cycle inventory for electricity generation in China. J. Life Cycle Assess. **12**, 217–224 (2007)
24. C. Shiau, C. Samaras, Impact of battery weight and charging patterns on the economic and environmental benefits of plug-in hybrid vehicles. J. Energy Policy **37**, 2653–2663 (2009)
25. F. Peters, M. Baumann, The environmental impact of Li-ion batteries and the role of key parameters—a review. J. Renew. Sustain. Energy Rev. **67**, 491–506 (2017)

Detailed Explanation on Scoring Items of Assessment Guidelines for Green Building Materials (Trail)—Heat Insulating Materials

Shiwei Ren, Yi Liu, Chunzhi Zhao and Quan Jiang

Abstract In October 2015, the Assessment Guidelines for Green Building Materials (Trail) (hereinafter referred to as "Guidelines") jointly printed and issued by the Ministry of Housing and Urban-Rural Development (MOHURD) and the Ministry of Industry and Information Technology (MIIT) of the People's Republic of China specifies the assessment requirements for seven categories of building materials including heat insulating materials. The Guidelines came into force in March 2016 and the assessment work on the seven categories of materials also successively proceeded henceforth. For the purpose of deepening implementation of the Guidelines issued by two Ministries, the specific performance indicators of different heat insulating materials are analyzed in detail and indicators such as heat conductivity coefficient and combustion performance are interpreted in five parts, i.e., energy-saving, emission reduction, safety, convenience and recyclability based on the principles for formulation of the Guidelines.

Keywords Assessment · Guidelines · Heat insulating materials Explanation

Introduction

Buildings are the basis of the people's livelihood and the building materials are the root of buildings. In February 2017, the Ministry of Housing and Urban-Rural Development issued the 13th Five-year Plan on Building Energy Saving and Green Building Development, aiming at establishing an energy-saving, low-carbon, green-ecological, intensive and efficient building energy-saving system. The Plan puts forward that, up to 2020, the energy efficiency of new urban buildings will improve by 20% than 2015, the proportion of green buildings will exceed 50% among

S. Ren (✉) · Y. Liu · C. Zhao · Q. Jiang
China Building Material Test & Certification Group Co., Ltd., 100024 Beijing, China
e-mail: 2829294538@qq.com

Y. Han (ed.), *Advances in Energy and Environmental Materials*,
Springer Proceedings in Energy, https://doi.org/10.1007/978-981-13-0158-2_55

the new urban buildings and the application proportion of green building materials will exceed 40%. Various green building materials, including environmental-friendly building material, ecological building material, healthy building material, etc., emerge in response to this development trend. Green Building Material Evaluation—Evaluation Certification [1] points out that: Green building materials may be defined as the environmental-friendly building materials which minimize the consumption of natural resources at the links of raw materials acquiring, production and application according to the life circle assessment (LCA), provided that the service performance is fulfilled, and are renewable or recyclable, and generate minimum environmental load after abandoned. Whether the product is green is subjected to comprehensive assessment on resource consumption and environmental impact throughout the whole life cycle from "cradle" to "grave". In order to provide scientific guidance and standardize the assessment and marking of green building materials in China, accelerate the popularization and application of green building materials, and promote the development of green buildings, the Assessment Guidelines for Green Building Materials (Trail) (hereinafter referred to as "Guidelines") was jointly formulated and issued by the Ministry of Housing and Urban-Rural Development (MOHURD) and the Ministry of Industry and Information Technology (MIIT) of the People's Republic of China, which specifies the assessment criteria for seven categories of products including heat insulating materials. This text will make detailed interpretation on major assessment indicators of heat insulating materials.

The Guidelines defines heat insulating materials as: building materials and products used to improve the heat insulating performance of building envelope, including organic and inorganic heat insulating materials. Organic heat insulating materials mainly include polyurethane foam, polystyrene board (molding and extrusion molding), phenolic foam and their products; inorganic heat insulating materials mainly include rock wool, slag wool, glass wool, aluminum silicate wool and their products, etc.

Energy-Saving

Production Energy Consumption per Unit Product and Energy Management System. Energy refers to the resources that provide available energy required by the human being directly or through conversion. *Law of the People's Republic of China on Conserving Energy* defines energy as coal, petroleum, natural gas, biomass energy, heating power and other resources that provide available energy directly or through processing and conversion [2]. Energy is the important material basis for development of national economy and society. In China, the shortage of resources and energy has become the key factor that restricts the sustainable development of national economy. At present, we are still at the stage of extensive economy; the low energy utilization efficiency and high energy consumption result in severe

waste; while the shortage of energy brings about enormous pressure on the inadequate resources and environmental governance in China.

Energy-saving is a very systematic and comprehensive work. The energy management will be out of line due to the lack of interconnected, interinhibitive and mutually promoting scientific energy management concept, mechanism and method, leading to absence of energy use standards, distribution quota, assessment criteria, management plan, loss supervision, energy-saving measures, waste supervision, etc. Some advanced organizations established energy management team and gradually realized that, in energy management, developing and applying energy saving technology and equipment are merely one aspect of energy saving and reliance on energy saving technology only cannot solve the energy supply and demand contradiction. Employing the systematic management methods to reduce consumption, improve utilization efficiency and propel behavior energy saving and construct energy management system is key to energy management. Applying the energy saving measures and technology into practice in a planned way to enable the organization reduce energy consumption continuously and improve energy utilization efficiency has not only accelerated the creation of systematic energy management concept, but also propelled the development and application of many national standards on energy management system.

The Guidelines specifies that the energy consumption per unit product is the energy consumed for producing a unit product during the statistical period (converted to standard coal). Corresponding national standard on energy consumption limits is formulated for rock wool and slag wool products. By comparing the energy consumption per unit product of enterprise with those specified in GB 30183 *The Norm of Energy Consumption per Unit Product of Rock Wool, Slag Wool and Their Products* [3] (Table 1), if both the comparable energy consumption and comparable fused coke consumption reach the required admission value, 80 is scored; if either of them fails to reach the admission value, 0 is scored. If both reach the advanced value, 100 is scored; if either of them fails to reach the advanced value, the lowest point is counted into the final score.

Since no corresponding energy consumption limits are stipulated for other heat insulating materials, e.g., polyurethane and EPS heat insulating materials, the energy consumption level per unit product for products manufactured by the enterprise in recent three years is taken as the indicator to assess their energy consumption.

Table 1 Influence of building products on resources, energy consumption and environmental emission

Energy consumption	Admission value	Advanced value
Comparable comprehensive energy consumption per unit product of rock wool, slag wool and their products/(kgce/t)	≤ 490.0	≤ 450.0
Comparable fused coke consumption per unit product of rock wool, slag wool and their products/(kgce/t)	≤ 260.0	≤ 240.0

The concept of energy management system stems from the concern about energy problems. The development of world economy has brought about energy restriction problems to all countries at varying degrees. The contradiction between development demand and energy restriction has awakened and strengthened people's awareness of energy crisis. People also realize that purely developing energy saving technology and equipment is just one aspect of energy saving work, so they begin to focus on systematic energy saving problems, such as industrial energy saving and building energy saving, research the low-cost or zero-cost methods, and employ systematic management means to reduce energy consumption and improve energy utilization efficiency.

China Standard Certification Center affiliated with China National Institute of Standardization launched the research on energy management system standards early in 2002, gradually exploring to establish the national series standards on energy management system. China Building Material Test & Certification Group Co., Ltd. has assessed over 70 building material enterprises since it launched green building material assessment in May 2016, but only one enterprise passed the energy management system certification. It reflects that the popularization of energy management system is not extensive, which provides the original intention for formulation of the Guidelines, i.e., driving the establishment of management system and perfecting the management mechanism.

Energy Consumption from Transportation of Raw Materials. The transportation of raw materials is at the upstream in the life cycle of production of heat insulating materials. According to the relevant information, the energy consumed in the exploitation and processing of building materials accounts for 37.5% of the total energy consumption of the building [4], and its carbon emission exerts great influence on the total carbon emission of the building. Energy consumption by transportation of raw materials is specially added in the Guidelines. Raw materials refer to various raw materials, main materials and auxiliary materials with shape or property changed through processing during the production and constituting the primary part of products. The category of raw material and its transportation mode will exert different influences on the environment.

The score for transportation of raw materials is the sum of scores in Tables 2 and 3, but the total score shall not exceed 100.

Heat Conductivity Coefficient. Energy-saving heat insulation is the fundamental national policy of China. Along with the deepening research on building techniques in China, the building heat insulation industry has developed sufficiently. While the heat insulating materials are extensively applied, their quality is varied; under the context of weak market regulation and fierce market competition, many merchants have reduced the cost. To make things worse, the employers lack sufficient knowledge of heat insulating materials and site construction, especially the organic heat insulating materials, leading to occurrence of fire accidents one after another. Great attention shall be paid to this. Heat conductivity coefficient and fireproof

Table 2 Accumulative transportation mode and proportion of raw materials (I)

Accumulative transportation proportion (Radius $\leq$ 500 km)	60% $\leq$ X < 70%	70% $\leq$ X < 80%	80% $\leq$ X < 90%	X $\geq$ 90%
Score	40	60	80	100
Accumulative transportation (radius > 500 km and by railway or steamship)	–	70% $\leq$ X < 80%	80% $\leq$ X < 90%	X $\geq$ 90%
Score	–	20	40	60

Table 3 Scoring for heat conductivity coefficient of heat insulating materials

Heat conductivity coefficient λ, W/(m·K)	Score
0.060 < λ $\leq$ 0.065	10
0.055 < λ $\leq$ 0.060	20
0.050 < λ $\leq$ 0.055	30
0.045 < λ $\leq$ 0.050	40
0.040 < λ $\leq$ 0.045	50
0.035 < λ $\leq$ 0.040	60
0.030 < λ $\leq$ 0.035	70
0.025 < λ $\leq$ 0.030	80
0.020 < λ $\leq$ 0.025	90
λ $\leq$ 0.020	100

performance are the important indicators for judging the quality of heat insulating materials.

Heat conductivity coefficient is an important indicator for assessing the heat-insulating performance. It is represented by λ and has the following physical meaning: the heat transferred in 1 m^2 of 1 m-thick material with the thermodynamic temperature difference on surfaces of two sides being 1 k under steady heat transfer, in W/(m K). The lower heat conductivity coefficient of materials indicates better heat-insulating performance. According to GB/T 4132-2015 Definitions of Terms Relating to Thermal Insulating Materials [5] and GB/T 10299-2011 Test Method for Hydrophobic Nature of Thermal Insulation [6], materials with T $\leq$ 350 °C, λ $\leq$ 0.12 W/(m K) are heat insulating materials [3].

Generally speaking, the dry apparent density, composition and structure of materials will directly affect the heat conductivity coefficient. The organic high polymer material has lower heat conductivity coefficient than inorganic material, that is to say, the organic high polymer material is superior to inorganic material in heat-insulating performance. For instance, the polyurethane foam and polystyrene foam heat insulating materials perform better than glass wool and rock wool heat insulating materials [7].

The scoring proportion specified in the Guidelines for this item is 0.16%, i.e., the full score is 16. The organic material possesses innate advantage.

Emission Reduction

Foaming Agent and Fire Retardant. The common heat insulating materials are classified into organic and inorganic categories, and organic foaming heat insulating material is one type among them, such as EPS, XPS and PURF.

EPS is polystyrene foam plastic sheet produced by prefoaming the expandable polystyrene beads by heating and then hot forming in mold, with closed cell structure and service temperature not exceeding 75 °C. It is widely applied in the field of house buildings in forms of color steel sandwich panel, steel wire (plate) grid, light-weight composite plate, etc.

XPS is heat-insulating extruded polystyrene foam, also known as extruded sheet. It is rigid foam plastic plate produced by hot mixing the raw material of polystyrene resin with other auxiliary materials and polymer and meanwhile adding foaming agent and fire retardant, and then molding by extrusion. XPS has perfect closed-pore honeycomb structure with the percentage of close area up to 99% above. Therefore, the heat conductivity coefficient and water absorbability are excellent.

PURF is made through polymerization and foaming of isocyanate and hydroxyl compound. It can be classified into soft and rigid types by degree of hardness. Generally, room-temperature foaming is adopted for PURF and the forming process is simple [8]. The soft type, mostly open-pore, is characterized by low density, air permeability, noise absorption, heat insulation and good rebound resilience.

At present, the universally applied foaming agents in market are mainly classified into physical foaming agent and chemical foaming agent; the former includes aliphatic hydrocarbon, hydrochloric ether, chlorofluorocarbon (CFC) and carbon dioxide foaming agents, while the latter mainly includes azo compounds, such as azodicarbonamide. Since 1950s, fluoro trichloromethane (CFC-11) has been widely applied as the preferred polyurethane foaming agent. However, it damages the atmospheric ozone layer. To protect the ecological environment on earth, CFCS compounds must be prohibited. Currently, HCFC, HFC and CO_2 foaming agents are the main substitute products in market, among which, HCFC and HCFC are just transitional products. The use of HCFC agents has been prohibited in EU, America and Japan. In China, the deadline is the year of 2030. The use of CFC foaming agent is not encouraged in China. Therefore, it is in response to this development trend that the Guidelines grants 50 scores for heat insulating material manufacturer who does not use CFC foaming agent.

Besides, the Guidelines proposes that the heat insulating material manufacturer who does not use hexabromocyclododecane fire retardant can also obtain 50 scores.

Fire retardant, which is also called uninflammable agent, fire-resistant agent or fire-proofing agent, is an important additive for synthetic organic heat insulating materials. Its function is to bestow the uninflammable, self-extinguishing and smoke-abatement characteristics to synthetic materials. It is classified into addictive and reactive types by application mode. Additive fire retardant is directly mixed with resin or adhesive and it is the primary application type with the advantages of convenient processing and wide scope of application. Reactive fire retardants are mostly the organic halogen and organophosphorus monomers containing reactive functional group, which are characterized by small influence on product property and persistent fire-retardant effect [9].

The current worldwide development trend of fire retardant is non-halogenation and ultra fining. The increasingly higher environmental protection requirements and stricter enforcement of environmental protection laws and regulations have affected the sales of chlorine-containing, fluorine-containing and bromine-containing fire retardants in European and American markets. The inorganic fire retardants occupy the primary proportion in foreign market, e.g., 55% above in European market, and the major fire retardant products are aluminum hydroxide and magnesium hydroxide. China is late in starting R&D and production of fire retardants. Bromine-containing fire retardant still takes a great proportion. The application proportion of aluminum hydroxide and magnesium hydroxide is only 10%, far below the foreign level in the corresponding period. Therefore, in order to encourage the application of bromine-free fire retardant and follow the development trend of green building materials, the enterprise not using hexabromocyclododecane fire retardant can obtain corresponding bonus point as encouragement.

Product Certification and Assessment. ISO defines product certification as a process that a third-party determines whether an enterprise's product, process or service meet the specific requirements and whether it is capable of continuously and stably producing products which comply with the standard requirements, through assessment of quality management system and type test on samples and offers written certificate for qualified enterprise. It is known from the definition that product certification includes product inspection and assessment of enterprise management system.

In developed countries, the development of green building materials is basically propelled through assessment and certification work and environment protection marks. Early in 1990s, Germany issued the world first environmental certification mark—"DER BLAUE ENGEL". In recent years, the EU nations such as the UK adopted green building material development strategies, including environmental mark for building products, environmental-friendly building product statement and enterprise in charge of procurement, through which the green development of building materials is effectively promoted. Other countries like Singapore and Australia also successively established environment-friendly product marks which involve various building materials such as tiles, flooring, masonry blocks and

stones, which played a significant role in driving the green development of those materials.

The existing product certification in China includes compulsory certification and non-compulsory certification. China compulsion certification, also referred to as CCC certification, is a product assessment system implemented by Chinese government according to laws and regulations for the purpose of protecting the health and safety of consumers, the environment and national security. It requires that the products must meet the national standards and relevant specifications. CCC certification is to carry out compulsory inspection and factory inspection on products listed in the developed CCC products Catalogue according to implementation rules for compulsory product certification. Any product listed in the CCC Catalogue that is not certified by designated certification authority or affixed with certification mark as required shall not be delivered, sold, imported or applied in other business operations. Non-compulsory certification is applicable to products not listed in the Catalogue. It is a voluntary act of the enterprises. At present, the popular certifications in China include China Environmental Labelling, CE (Conformite Europeenne), UL (Underwriter Laboratories Inc.), etc.

China Environmental Labelling is the most authoritative certification for green products and environment-friendly products. It is also called Ten-ring Certification, representing the official approval of the product's quality and environmental protective performance. Ministry of Environmental Protection designates China Environmental United Certification Center (CEC) as the sole certification authority to determine whether the product meets the national environmental protection requirements through multiple criteria assessment in three stages of document review, on-site inspection and sample testing. CE mark is the safety mark applied in European common market which claims that the product meets the relevant EU code. It is valued as the manufacturer's passport to open and enter into the European market. Products affixed with "CE" mark are allowed to sell in all EU members without the necessity to meet the requirements of each member. In this way, the free circulation of products is realized in the wide circle of EU members. Using CE mark for products in market is the compulsory requirement by EU members. CE is a qualification mark on safety rather than on quality. For the products sold in the market of European economic area (EU, EFTA members, excluding Switzerland), being affixed with CE mark represents that the product meets the requirements of a series of European Directives on safety and health, environmental protection and consumer protection, equivalent to CCC certification in China. UL is short for Underwriter Laboratories Inc., which was founded in 1894. UL is a private institution engaged in safety test and assessment, which is most cathedratic in America and relatively large in the World. It is an independent non-profit institution specialized in public safety testing. It employs scientific test methods to research whether the materials, devices, products, equipment and buildings are hazardous to life and property and the degree of hazard, if any; determines, compiles and issues the corresponding standards and materials helpful to reduce and avoid the loss of life and property; carries out truth investigation.

The enterprise can obtain bonus point if its application product passes relevant assessment or certification.

Safety

Standardization of Safety Production. Notice of the State Council on Further Enhancing the Production Safety Work of Enterprises (GUO FA [2010] No. 23) points out that it shall proceed in full swing to reach the standard of safety. For enterprises failing to reach the standard within the time specified, production license and safety production license shall be withheld according to law and they shall be ordered to shut down for rectification. On April 15, 2010, the State Administration of Work Safety published the industry standard regarding safety production (i.e. Basic Norms for Work Safety Standardization of Enterprises) in the No. 9 Announcement of 2010, which was implemented on June 1, 2010, with Standard No. AQ/T 9006-2010.

According to the requirements of Management Measures for Reviewing the Safety Production Standardization of Enterprises (Trail) issued by the State Administration of Work Safety, the standard grade of enterprise safety production standardization is divided into three levels ranging from the highest to the lowest. For enterprises with safety production standardization reaching Level I, the State Administration of Work Safety will release an announcement and confirm the review unit to issue the certificate to Level I enterprises; Level II enterprises are managed by provincial safety supervision and management departments and Level III enterprises by county-level safety supervision and management departments [10].

Therefore, enterprises shall at least meet Level III requirements specified in AQ/T 9006 Basic Norms for Work Safety Standardization of Enterprises and safety production standardization certificate within the validity period shall be provided.

Fireproof Performance. GB 8624 Classification on Burning Behaviour for Building Materials [11] specifies that the materials are classified into Grade A incombustible materials and Grade B combustible materials; Grade A is subdivided into homogeneous incombustible material and composite sandwich incombustible material while Grade B is subdivided into Grade B1 difficult-combustible, Grade B2 combustible and Grade B3 easily-combustible.

Main heat insulating materials with Grade A combustion performance include rock (mine) wool, foam glass, inorganic heat-insulating mortar, etc. Main heat insulating materials with Grade B1 combustion performance include phenolic aldehyde, adhesive polystyrene granule, etc. Main heat insulating materials with Class B2 combustion performance include molded polystyrene board (EPS), extruded polystyrene board (XPS), polyurethane (PU), polyethylene (PE), etc. From this we can tell that inorganic heat insulating material has innate advantage in fireproof performance and can obtain full score in this item.

Convenience. According to the Guidelines, convenience refers to the matching degree of the production, application and construction of products with the regional construction, as well as the influence on the economic development and environment of the application region.

The quality stability, modular design, complete set of configuration and prefabricated construction are main indicators to assess the convenience degree of heat insulating materials. Experts give comprehensive scores by inspecting whether the enterprise's products are included in catalogue of recommended excellent products, whether the production process meets the relevant laws and regulations, standards and codes in the application region, etc.

Recyclability. Sustainable development is a new development mode proposed in response to the increasingly severe scarcity of resources and environmental pollution in the development process of human society. Green building materials, which belong to environmentally-friendly materials, shall possess environmental compatibility and realize the sustainable development of ecological environment through recycling of resources.

Heat insulating materials consume massive amount of non-renewable resources. In *Selection Technology of Material for Green Building* [7], three common heat insulating materials (polystyrene board, rock wool board and polyurethane board) are assessed with LCA method, i.e., checklist analysis and characterization calculation are carried out on consumption of non-renewable resources (ADP), consumption of non-renewable energy (PED), greenhouse effect (GWP), acidification effect (AP) and eutrophication (EP) in the life cycle of unit quality (kg) product, the result shows that polystyrene board is notable in consumption of non-renewable resources, reaching 52.72 kg Coal-R equivalent/kg board, which is consistent with the phenomenon that the score of polystyrene board is generally lower than other heat-insulating products in practical assessment according to the Guidelines.

Conclusion

At present, the application and management of green building materials are still at the starting stage in China; many policies need further study and discussion. Accelerating the production and application of green building materials is the only way to drive green consumption, guide green development, accelerate structure optimization and speed up transformation and upgrading, and is also the urgent need for integrative development of green building material and green building industries. Assessment Guidelines for Green Building Materials (Trail) specifies the assessment requirements for seven major building materials including masonry material, heat insulating material, premixed concrete, building energy-saving glass,

ceramic tile, sanitary pottery and premixed mortar. The second batch of guidelines which covers water-proof sealing material, architectural coating, artificial board, composite metal decoration material, plastic pipe for building and flooring is also under preparation. Formulation of assessment requirements for other materials will also proceed in an organized way and the existing assessment requirements will be completed to jointly make contribution to the development of green building materials.

References

1. Q. Jiang, C. Zhao, L. Ma, Y. Liu et al., *Green building material evaluation—evaluation certification M* (Beijing, Chemical Industry Press, 2012), pp. 18–19
2. G. Ma, Analysis on energy management system construction and application, J. Suppl. Popular Utilization. Electr. **1**, 17–21 (2016)
3. GB 30183-2013 The norm of energy consumption per unit product of rock wool, slag wool and their products S
4. Q. Jiang, C. Zhao, Y. Liu, L. Ma et al., *Selection technology of material for green building M* (Beijing: Chemical Industry Press, 2015), pp. 86–92
5. GB/T 4132–2015 Definitions of terms relating to thermal insulating materials S 385
6. GB/T 10299-2011 Test method for hydrophobic nature of thermal insulation S
7. X. Chang, J. Zhang, X. Wang et al., Research on relation between density and heat conductivity coefficient of common heat insulating materials J. Res. Explor. **27**(2), 66–70 (2009)
8. Y. Geng, D. Qi, Introduction to several existing common heat insulating materials for building J. Liaoning Build. Mater. **9**, 44–45 (2009)
9. X. Zhang, Q. Lu, Production status and development prospect of fire retardant J. China Plast. Ind. **39**(4), 1–5 (2011)
10. G. Han, J. Yin, C. Guan et al., Interpretation of assessment guidelines for green building materials (Trail). J. Spec. Focus, 34–37 (2016)
11. GB 8624 Classification on burning behaviour for building materials S

Building 3D Printing: The Anisotropy Mechanical Properties and Printing Time

Penghao Xin, Ziming Wang, Wenbo Xi, Jingying Peng, Huan He and Ruifeng Tang

Abstract Three-dimensional technology is different from the traditional construction in process, which has many advantages like personal customization, reduced energy, rapid manufacturing. Therefore, to study the performance and test methods of 3D printing cement-based materials has significance effects on research and promotion of building three-dimensional technology. In this paper, addictive manufacturing and mould cast were used to manufacture samples. The results show that compressive strength of the printing samples is about 14 MPa at 1 day, 17 MPa at 3 days and 26 MPa at 7 days, which are about 55, 61 and 53% of the mould cast; the compressive strength of printing samples is anisotropy in the vertical and parallel directions for the printing direction, and the difference decreases with the flowbility increasing; the bonding layer gets weaker with the printing time increasing, especially at 10 min initially.

Keywords Three-dimensional technology · Cement-based materials
Anisotropy · Compressive strength

Introduction

3D printing technology, commonly called additive manufacturing [1], sets most advanced technology of software architecture, mechanical engineering, materials science, laser technology in one [2]. 3D printing is also known as "The important tool of production in the third industrial revolution [3]". It applies in industrial design, art design, mold manufacturing, jewelry, bio-engineering, aerospace, metal manufacturing, scientific research, cultural relics protection and other rapid devel-

P. Xin · Z. Wang (✉) · W. Xi · J. Peng · H. He · R. Tang
Colloge of Material Science Engineering, Beijing University of Technology, Beijing 100124, China
e-mail: wangziming@bjut.edu.cn

P. Xin
e-mail: xphnewsun@163.com

Y. Han (ed.), *Advances in Energy and Environmental Materials*,
Springer Proceedings in Energy, https://doi.org/10.1007/978-981-13-0158-2_56

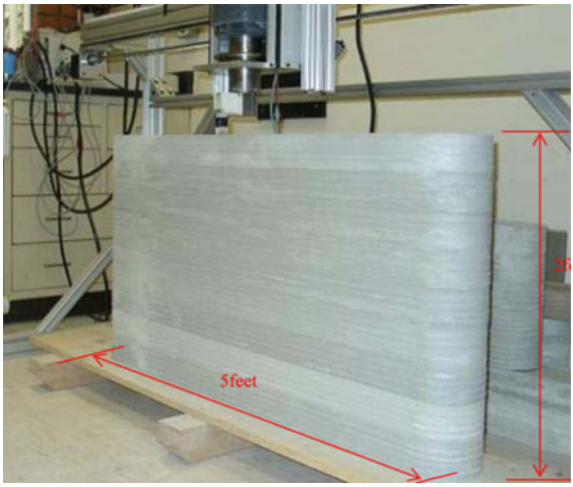

Fig. 1 Concrete wall completed by contour crafting

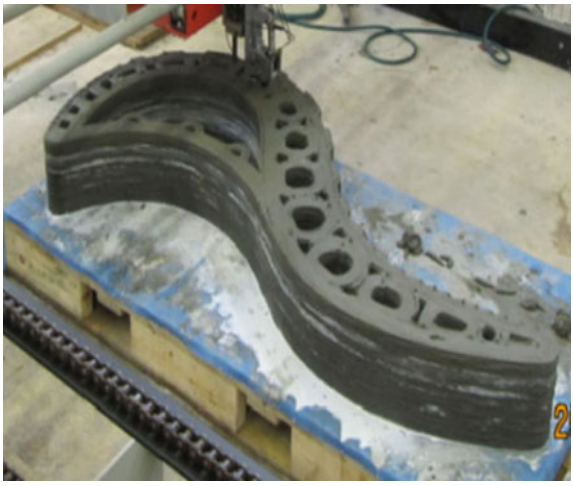

Fig. 2 Printed bench by concrete printing

opment fields. In recent years, its development of architecture has aroused the interest of scholars both at home and abroad.

Building 3D printing is a way to extrude cement-based materials through a nozzle, which uses a layer stacking technology to build components of construction. Professor B Khoshnev is from University of Southern California, invented the Contour Crafting (CC) [4]. The CC machine printed a hollow wall structure troweled by side trowels firstly and filled the inside space with concrete, shown in Fig. 1. Professor R. Buswell of Loughborough University in the United Kingdom has developed Concrete Printing [5], which extruded concrete filament continuously through a 9 mm diameter nozzle to build layer-by-layer structural components in a printing process, shown in Fig. 2.

Building 3D printing research also starts in many international commercial company. In June 2016, China Yingchuang successfully built an office in Dubai using 3D printing technology, which covers an area of 250 m^2. The building uses a special cement mixture as a printing material. In July 2016, Tongzhou District in Beijing, the first 3D printing villa completed. The villa, which covers an area of 400 m^2, has two floors. The giant printing machine used special reinforced concrete to build the villa with only 45 days. In December 2016, a Spanish Civil Engineering Company named Acciona, printing a concrete bridge with a length of 12 and 1.75 m wide, was put into use.

Due to the forming process, layer-by-layer, mechanical properties of specimens may have some differences in various direction [6]. Lin studied the mechanical properties of 3D printing samples in vertical and transverse [7]. In addition, the bond strength between the layers may also be the weakness point for printing specimens. This paper studies the anisotropy of the 3D printing specimen and the relationship between the interval time and the inter-layer strength.

Materials and Method

Materials. Cement tape P.I 42.5, fly ash, silica fume were formed the binder component. An agent that accelerates early strength and reduce drying shrinkage was used. Besides, accelerator formed by sulphuric, aluminium salt and diethanolamine was also maxed in to control setting time. Polycarboxylate superplasticizer was added to change flowability of mortar.

Cement: Reference cement was produced by China United Cement Group Corporation, the performances of the cement are shown in Tables 1 and 2.

Sand: Standard sand was adopted.

Additive: Superplasticizer: The Polycarboxylate superplasticizer was produced by Beijing Construction Engineering Research Institute Co., Ltd.

Table 1 The chemical compositions of Portland cement [%]

Name	SiO_2	Al_2O_3	Fe_2O_3	CaO	MgO	SO_3	Na_2Oeq	f-CaO	C_3S	C_2S	C_3A	C_4AF
Percentage	22.06	4.25	3.39	64.95	2.98	0.46	0.69	0.85	56.87	20.33	6.32	10.18

Table 2 The physical performance of cement

Fineness 0.08 [%]	Specific surface area [m^2/Kg]	Setting time [min′]		Bending strength [MPa]		Compressive strength [MPa]	
		Initial	Final	3d	28d	3d	28d
0.8	338	138	215	6.4	8.3	29.7	54.5

Table 3 The mix proportions

Number	Cement: fly ash: silica fume	Water/ binder ratio	Binder/ sand ratio	Dosage of superplasticizer [%]	Dosage of accelerator [%]	Dosage of fiber [Kg/m^3]	Dosage of HPMC [%]
C1	7:2:1	0.26	0.67	0.50	4.00	1.2	0.20
C2	7:2:1	0.26	0.67	0.75	4.00	1.2	0.20
C3	7:2:1	0.26	0.67	1.00	4.00	1.2	0.20

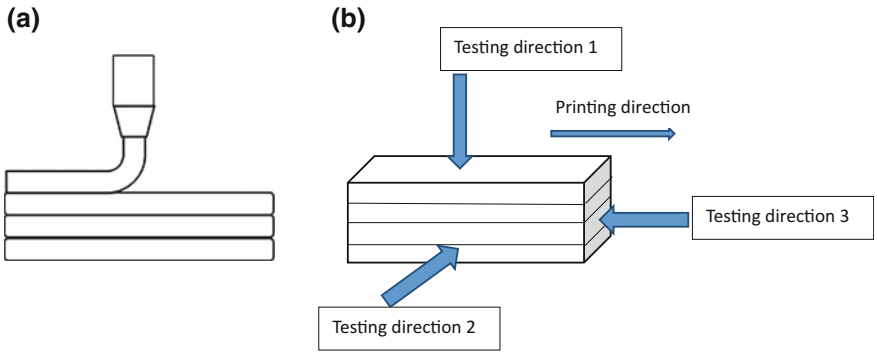

Fig. 3 Process in 3D printing (**a**) and testing directions (**b**)

Accelerator: The accelerator were made of sulphuric, aluminium salt and diethanolamine.
Fiber: The polypropylene micro fibers have length of 9 mm and diameter of 20 μm.
Mix proportions: In this paper, the dosage of superplasticizer was changed to adjust the motor flowability. The mix proportions are shown in Table 3.
Experimental Procedures. The preparation of cement mortar was manufactured according to GB/T17671-1999 [8], and samples were curing in standard curing box for 1 day, 3 days and 7 days. The flowability of the mortar was determined according to GB/ T2419-2005 [9]. The setting time of mortar was tested with JGJ70-90 [10]. The bonding strength of layers was testing by LBY-VI drawing test instrument.

The specimens were manufactured in both mould-cast and printed states. According to the mix design (number C1, C2, C3), the specimens made in mould were named M1, M2, M3, and printed specimens were named P1, P2, P3. The printed samples were manufactured with mortar-gun layer-by-layer, shown in Fig. 3a, then saw into 40 mm × 40 mm × 40 mm cubes for strength test. The compression surfaces were divided into three based on three-dimensional space like Fig. 3b. So, depending on the different compression surfaces, the printed samples were numbered P11, P12, P13, P21, P22, P23, P31, P32, P33.

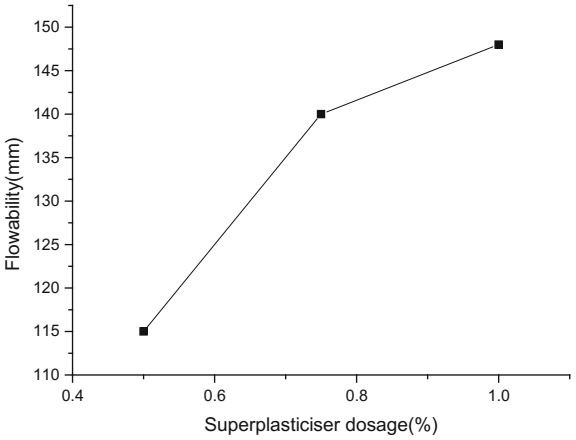

Fig. 4 Effect of superplasticiser on flowability

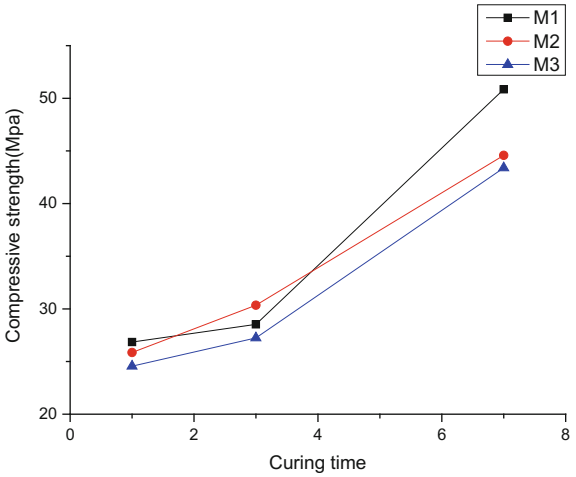

Fig. 5 Effect of superplasticiser on compressive strength

Results and Discussion

Flowability. The water reducing agent had the characteristic of changing fluidity when the water/cement ratio is constant. When the water/binder ratio was unchanged, the amount of effective component of water reducing agent was 0.5, 0.75 and 1% respectively. In this regard, the printing motor has good performance to be printed. The sample fluidity and compressive strength are shown in Figs. 4 and 5.

As shown in Fig. 5, the samples had early strength, and the strength of the M1 at 1 day was as high as 26.85 MPa. Cause of early strength agent, the early strength of the material was high resulting in 1 day. And relative to the strength of 3 days, the growth of strength was not so much. In the case of the same water/cement ratio,

with the amount of the water/reducing agent increasing, the fluidity of the mortar was obviously increased, but the compressive strength of the test piece was reduced.

The Effect of the Printing Process. The compressive strength of the molded samples and printed samples in three mix proportions at 1 day, 3 days and 7 days are shown in Fig. 6. It can be seen from the Fig. 6, the compressive strength of printed samples was lower than the normal molded samples, and for different compressive surface, the compressive strength was different. The strength of the direction 1 in vertical was the highest. The strength of P11 was 72.5% of the mold forming at 3 days, and the compressive strength of direction 3 was 56.19%. During the whole curing process, the strength of direction 2,3 were almost the same. But they were about 2–14% lower than the strength of direction 1. It is there are more pores or weaker point between the layers, resulting in different compressive strength in every direction, that is, printed samples have anisotropy of mechanical properties. During the test, the bonding strength between layers became weakness, as shown in Fig. 7.

The Effect of Flowability on Materials Mechanical Properties. The compressive strength of 1 day, 3 days, and 7 days for the different flowability mortars is shown in Fig. 8.

With the flowability of the mortar increasing, the difference of the compressive strength in three directions for the printed samples was reduced, as shown in Fig. 8. Compared with the standard mould formed samples, the maximum strength of C1 in the printed sample was 7.27% and the maximum strength of C3 was 5.49%. The maximum strength difference of C1 was 13.79%, the strength of C3 was 5.36% at 7 days. The results confirmed that with the increase of the water reducing agent, the flowability of the mortar increases and the interlaminar adhesion increases, so that the anisotropy difference between the different directions surfaces decreases.

The Effect of Time between Layers on Bonding Strength. During the printing process, there was an interval between the layers. The printing speed is too slow or process have a large intermission between every layer, will cause the bond strength of printing layers decreased, even cold joints and other issues, so that the mechanical properties of the specimens will be impacted.

It can be seen from the Fig. 9 that the bond strength of the inter-layer decreased as the interval time increased. At 5 min, the bond strength can reach 58.77% of the contrast sample, the loss strength was fast and large. Between 10 and 20 min, the inter-layer bond strength was roughly the same, the strength was mainly depending on the fresh cement slurry which was not completely set. After 20 min the bond strength decreased rapidly, and the bond strength became lower.

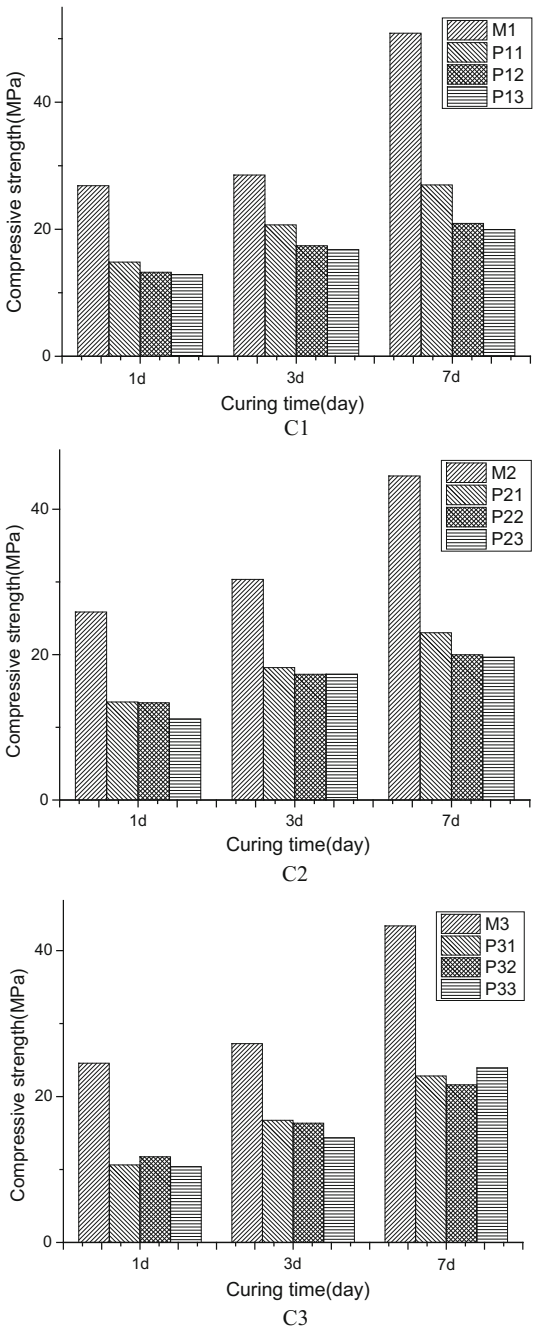

Fig. 6 The anisotropy caused of printing for three mix proportions

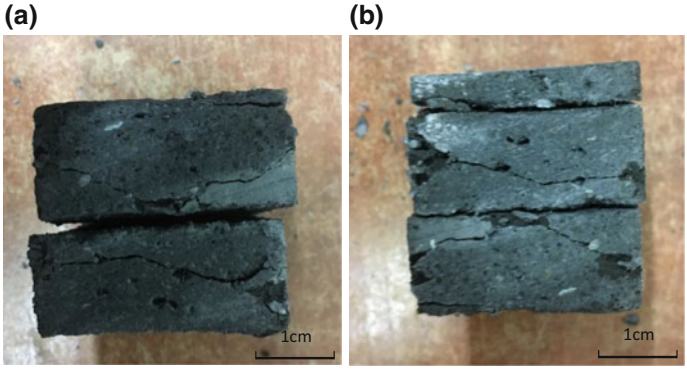

Fig. 7 The destruction in direction 2 (**a**) and direction 3 (**b**)

Fig. 8 Effect of flowability on compressive strength

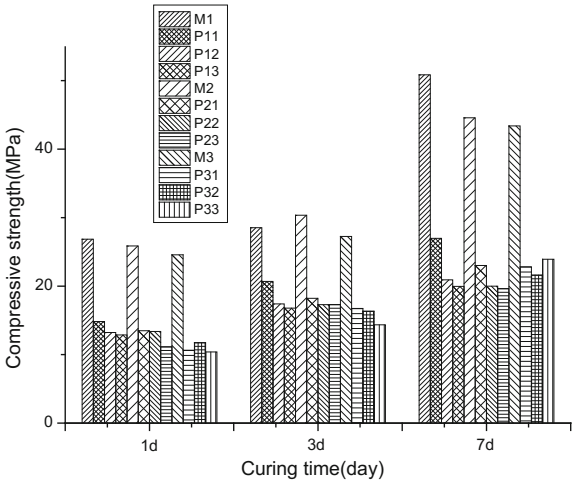

Fig. 9 Effect of printing time between layers on bonding strength of layers

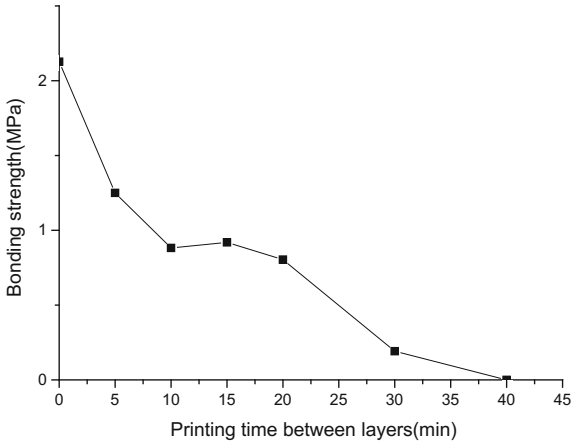

Conclusion

Building 3D printing has the characteristics of no mould forming, which is quite different from traditional construction, so its mechanical properties will be some differences. The strength of building 3D printing samples compared to the traditional mold specimens is lower, and the mechanical strength shows anisotropy, but the anisotropy decreases with the increasing of mortar fluidity. With the increase of the interval between layers, the bonding strength of layers is decreasing, so the appropriate interval interval is one of the important conditions to ensure the mechanical properties of the specimen.

References

1. B. Mueller, *Additive Manufacturing Technologies—Rapid Prototyping to Direct Digital Manufacturing* (Springer, US, 2012)
2. Z. Wang, W. Liu, 3D printing technology and its application in construction field. J. China Concr. **1**, 50–57 (2015)
3. P. Walters, K. Davies, 3D Printing for artists: research and creative practice. J. **1**, 12–15 (2010)
4. D. Hwang, B. Khoshnevis, D.J. Epstein, Concrete wall fabrication by contour crafting. J. ISARC Proceedings (2004)
5. T.T. Le, S.A. Austin, S. Lim et al., Mix design and fresh properties for high-performance printing concrete. J. Mater Structur. **45**, 1221–1232 (2012)
6. T.T. Le, S.A. Austin, S. Lim et al., Hardened properties of high-performance printing concrete. J. Cem. Concr. Res. **42**, 558–566 (2012)
7. X. Lin, T. Zhang, Preparation, properties and application of cement-based building 3D printing materials. J. The 2nd China International Conference on Solid Waste Ulitization & Eco-materials, 009, 55–66 (2016)
8. Z. Tang, Cement mortar strength test method (ISO method) standard has been approved. J. China Build. Mater. (1999)
9. C. Liu, B. Yan, X. Wang et al., "Cement mortar fluidity measurement method" GB/T2419 revision profile. J. Constr. Technol. **33**, 64–65 (2004)
10. Shanxi Provincial Institute of Architectural Science and Design, *Construction Mortar Basic Performance test Method: JGJ 70–90* (China Construction Industry Press, 1991)

Life Cycle Assessment of Typical Sanitary Ceramic Products in China

Yanjing Wang, Yu Liu, Xianzheng Gong, Zhihong Wang and Feng Gao

Abstract The ceramic sector contributes significantly to the consumption of resources and energy, as well as the impact to the natural environment in China. In this study, the environmental impact of sanitary ceramic products was quantified and analyzed using life cycle assessment methodology with a "cradle to gate" perspective. The results showed that fossil depletion (FDP) were the most serious environmental impacts which account for the total damage (62.02%), followed by global warming potential (GWP) (28.75%) and particulate matter formation (PMFP) (8.12%). In addition, the energy production phase was the stage that resulted to the major environment load due to natural gas production and power generation. The natural gas and coal consumption, as well as CO_2 emissions represented significant contribution to the total impact which account for 37.06, 18.92 and 28.44%, respectively. Moreover, it was indicated that the sensitivity of natural gas and electricity consumption to sanitary ceramics were greater than other substances. Therefore, reducing the consumption of natural gas, electricity and resin are the effective way to achieve energy saving and emission reduction in sanitary ceramic industry.

Keywords Sanitary ceramics · Life cycle analysis · Energy saving and emission reduction

Y. Wang · Y. Liu (✉) · X. Gong · Z. Wang · F. Gao
College of Materials Science and Engineering, Beijing University of Technology, No. 100 Ping Le Yuan, Chaoyang District, Beijing 100124, China
e-mail: liuyu@bjut.edu.cn

Y. Wang
e-mail: 291802146@emails.bjut.edu.cn

X. Gong
e-mail: gongxianzheng@bjut.edu.cn

Z. Wang
e-mail: wangzhihong@bjut.edu.cn

F. Gao
e-mail: egaofeng@bjut.edu.cn

Y. Han (ed.), *Advances in Energy and Environmental Materials*,
Springer Proceedings in Energy, https://doi.org/10.1007/978-981-13-0158-2_57

Introduction

In the past thirty years, the ceramic industry in China has developed rapidly driven by the domestic economy development and the technology innovation. China has become the largest ceramic producer in the world, the ceramic products were exported to more than 150 countries and regions. However, With the increasing concern from the government and the public about the environmental issues as well as the related energy consumption and emission standards become increasingly stringent. The large amount of energy consumption and resource consumption, as well as the pollution emission have become the main obstacles to the sustainable development of ceramic industry in recent year. According to statistics, the annual consumption of mineral production was over 140 million tons in building sanitary ceramics industry. In addition, more than 16 million tons of diesel and over 32 billion kWh electricity were consumed each year [1]. Therefore, it is an urgent task to speed up the implementation of energy-saving and emission reduction in Chinese ceramic industry.

In the field of energy saving and emission reduction of the ceramic industry, a large number of studies have been done which were basically based on the life cycle assessment (LCA) method. Bovea et al. (2005, 2007) [2, 3] established the ceramic tile packaging process and red clay mining process inventory data. The processes that involved the movement of clay within the mine that made the greatest contribution to impact categories for pollutant emissions. Ibáñez-Forés [4] set up a life cycle assessment model for ceramic tiles from raw material extraction to final waste recycling. The stage of the life cycle with the greatest environmental impact is the manufacture of the tile. Giudice et al. [5] evaluated the decorative ceramic plate environmental hot spots, the damage was due to the huge electricity consumption required for the ceramics manufacturing. In particular, electric kiln was at very high temperature during the first and second firing. Pini [6] discussed the life cycle assessment of decorative ceramic plates, the results demonstrated that the greatest environmental impact mainly affects the respiratory inorganics impact category due to base slip production (27.62%), caused by the transport of the raw materials.

On the other side, numerous LCA studies have been carried out in China. Tang [7] quantified the environmental impact of building ceramics, it was shown that the sintering process produced the largest amount of emissions which was derived from the combustion of fuel and the grinding of raw materials. Xie et al. [8] analyzed the environmental impact of the two different technologies by comparing the ceramic tiles and ceramic thin plates. In term of non-renewable resources, primary energy consumption and eutrophication indicators, ceramic plate were significantly better than ceramic tiles. Xia [9] made the list analysis of the daily ceramics in different decoration process and calculated the environmental impact potential of each stage of the life cycle. The firing and roasting production process emission amount of gas pollutants. However, there are few studies on life cycle assessment of sanitary ceramics in China. Chen [10] quantified environmental impact assessment of

pollutant emissions and noise in the production of sanitary ceramics, but not involved the energy and resource consumption.

In this study, the life cycle analysis model was set up to evaluate the environment burden of typical sanitary ceramics products during the life cycle in China. Hoping to provide a reference for the assessment of sanitary ceramics production and effective advice for energy conservation and emission reduction.

Data and Method

The functional unit of this study was defined as the "1t sanitary ceramic products". The system boundary was shown in Fig. 1, including the following life cycle process: acquisition of raw materials, transportation and ceramic manufacturing (from "cradle to gate").

Foreground Data Investigation. The foreground data included raw material consumption, energy consumption, pollutants emission in the ceramic production phase. The foreground data were collected by total amount in 2016 and calculated and presented by functional units, as shown in Tables 1 and 2.

Major pollutant emissions were illustrated in Table 3. The amount of PM emission was derived from monitor. However, the amount of the other pollutants were calculated, according to the amount of natural gas and diesel consumption, the

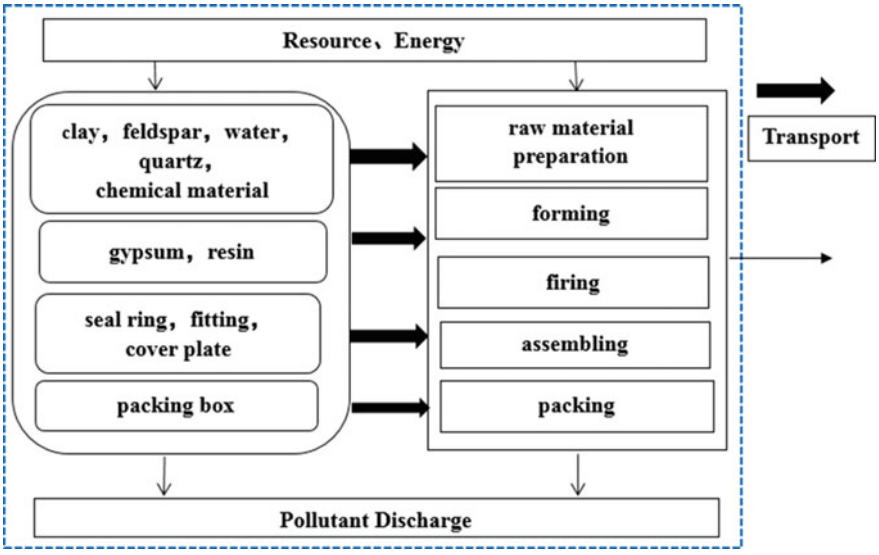

Fig. 1 System boundary of LCA

Table 1 Raw material consumption of sanitary ceramic products per functional unit

Items	Amount	Unit	Transportation/distance [km]
Feldspar	3.20E+02	kg/F.U.	Railway, 800
Clay	5.12E+02	kg/F.U.	Railway, 600
Quartz	4.18E+02	kg/F.U.	Highway, 300
Chemical material	2.00E+01	kg/F.U.	Highway, 250
Packing box	1.49E−02	kg/F.U.	Highway, 100
Seal ring	3.47E−03	kg/F.U.	Highway, 100
Fitting	1.74E−02	kg/F.U.	Highway, 7
Cover plate	2.78E−02	kg/F.U.	Highway, 8
Resin	1.05E+01	kg/F.U.	Railway, 1000
Gypsum	6.70E+01	kg/F.U.	Railway, 800
Water	1.38E+01	kg/F.U.	–

F.U. function unit

Table 2 Energy consumption survey data per functional unit

Items	Amount	Unit
Natural gas	2.05E+02	m^3/F.U.
Electricity	4.10E+02	kWh/F.U.
Diesel	1.74E−02	kg/F.U.

default calorific value were taken from China Energy Statistical Yearbook and the emission factors were derived from IPCC [11] and EEA Report [12].

Background Data Collection. The background data including their sources, time representation, geographical representation and technical representation were shown in Table 4. The data were obtained from the *Eco-invent* database [13] and the *Sinocenter* database [14].

Impact Assessment Method. According to the characteristics of environmental burden during sanitary ceramics production, seven different impact categories which were related to the sanitary ceramic were chosen for life cycle impact assessment, it included marine eutrophication (MEP), climate change (GWP),

Table 3 Major pollutant emissions of sanitary ceramic products per functional unit

Items	Amount	Unit	Data sources
CO_2	4.10E+02	kg/F.U.	Estimated
SO_2	5.08E−03	kg/F.U.	Estimated
NO_X	5.41E−01	kg/F.U.	Estimated
CO	2.12E−01	kg/F.U.	Estimated
NMVOC	1.68E−01	kg/F.U.	Estimated
PM	2.63E−05	kg/F.U.	Investigated
CH_4	7.31E−03	kg/F.U.	Estimated
N_2O	7.52E−04	kg/F.U.	Estimated

Table 4 Background data collection and description

Classification	Unit process	Data sources	Time representation	Geographical representation	Technical representation
Raw material acquisition	Feldspar	*Eco-invent*	2009	Europe	Average
	Clay	*Sinocenter*	2010	China	Average
	Quartz	*Eco-invent*	2009	Europe	Average
	Chemical material	*Eco-invent*	2009	Europe	Average
	PPMA	*Eco-invent*	2009	Europe	Average
	Resin	*Eco-invent*	2009	Europe	Average
	Gypsum	*Sinocenter*	2013	Europe	Average
	Packing box	*Eco-invent*	2009	China	Average
	Seal ring	*Eco-invent*	2008	Europe	Average
Energy production	Electricity	*Sinocenter*	2006	China	Average
	Natural gas	*Sinocenter*	2008	China	Average
	Diesel	*Sinocenter*	2008	China	Average
Transportation	Railway	*Sinocenter*	2010	China	Average
	Highway	*Sinocenter*	2010	China	Average

terrestrial acidification (AP), photochemical oxidant formation (POFP), particulate matter formation (PMFP), fossil depletion (FDP), human toxicity (HT). The characteristic factors applied to each impact category were those put forward by the Recipe 2008 method [15].

Result and Discussion

Contribution Analysis of Environmental Impact. The comparison between different environmental impact indicator were shown in Fig. 2. The contribution of production stage to each environmental impact were shown in Fig. 3. Firstly, the results highlighted that the fossil depletion played the major role in all the environment impact categories, which accounted for 62.02% to the total environment impact. A large amount natural gas were consumed during the firing process of ceramic, due to the high temperature requirement for the production of sanitary ceramics. The primary energy were consumed energy production stage (86.08%)

and raw material acquisition stage (12.62%). Secondly, global warming contribute 28.75% to the environmental impact. The combustion of natural gas during the ceramic production and coal during power generation discharged a large amount of greenhouse gas. Therefore, the products manufacture and energy production phase were the stages for this kind of impact, which accounted for 46.07 and 45.32%, respectively. Thirdly, the particulate matter formation impact category was affected by releasing particulate matter in air (8.12% of the total impact) mainly generated from the energy production process. Moreover, the human toxicity accounts for 1.19% of the environmental impact, mainly due to heavy metals released during the energy production phase.

Contribution of Unit Process Analysis. Comparison and contribution analyze of each stage were shown in Figs. 4 and 5. The results indicated that 73.02% of the total environment impact were caused in the energy production stage. Moreover, ceramic production stage contributed to 13.93% of the total environmental impact, the highlight impact category was global warming potential which contributed 95.11% to the environmental impact in this process. In addition, raw material acquisition consumed resources, energy and released particulates, account for 11.64% to the total environmental impact.

Contribution of Substance Analysis. The contribution of each substance to the single indicator was shown in Fig. 6. Natural gas and coal consumption, as well as CO_2 emission contributed greatest to the final results, accounting for 37.06, 18.92, 28.44%, respectively. Natural gas was mainly consumed in the production phase.

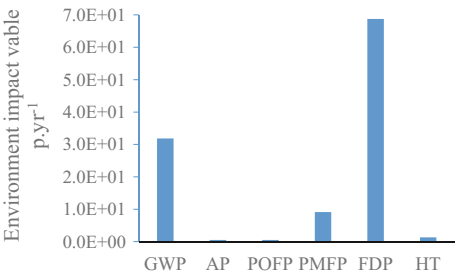

Fig. 2 Comparative environmental impact result

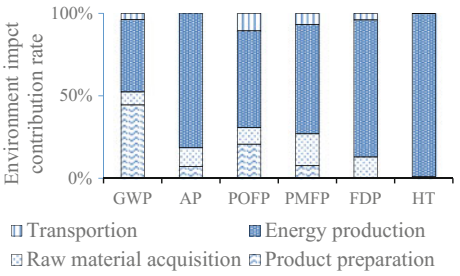

Fig. 3 Contribution of environmental impact

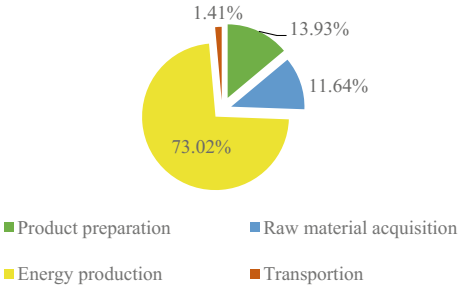

Fig. 4 Comparative of process to damage

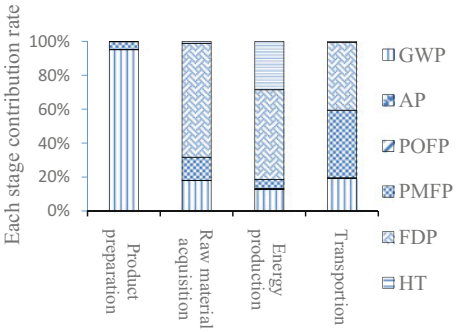

Fig. 5 Influence of each stage to environment impact

The raw coal was mainly consumed in the power production stage. In addition, the emission of CO_2 mainly came from the stage of product preparation and energy production. Moreover, the contribution rate of crude oil consumption, NO_X, SO_2 and particulate matter emissions were 6.04, 3.15, 3.13 and 1.84%, respectively.

Sensitivity Analysis of Parameter. The raw materials and energy consumption can be controlled by the manufacturer. The environmental impact reduction potential of each input substance was identified by sensitivity analysis. In sensitivity analysis,

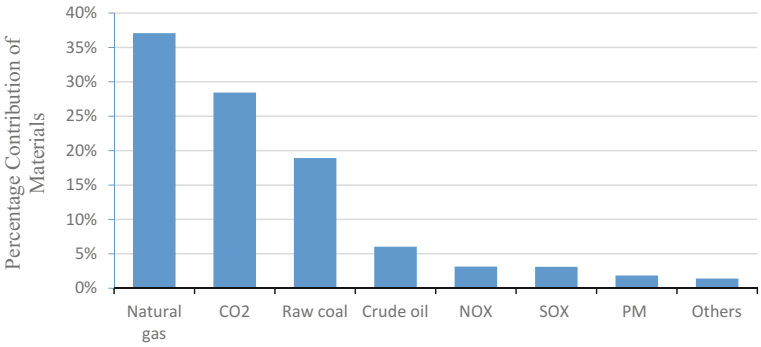

Fig. 6 Contribution analysis of substance to environment impact

the total environmental value was calculated when each input parameter was reduced and increased by 5%, respectively. The sensitivity analysis results were shown in Figs. 7 and 8. The results revealed that the sensitivity of natural gas consumption, electricity production and resin use to the total damage were greater than other substances. When the input of natural gas, power and resin decreased by 5%, the single score decreased by 2.66, 1.69 and 0.35% respectively. Therefore, reducing the consumption of natural gas, electricity and resin were the effective way to energy saving and emission reduction of sanitary ceramic products.

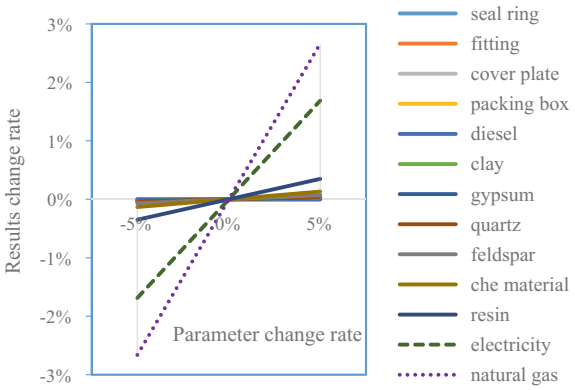

Fig. 7 Sensitivity of material input

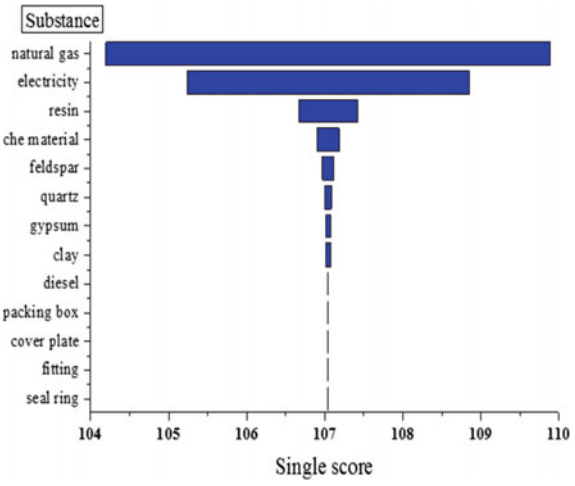

Fig. 8 The effect of input on single indicator

Conclusion

This study quantitatively calculated the energy consumption, resource consumption, and pollutant emission of typical sanitary ceramics products from "cradle to gate". It provided an effective basis of energy-saving and emission reduction for sanitary ceramics industry which is based on the sensitivity analysis. This study was beneficial to achieve energy saving and emission reduction for enterprises. The following conclusions are drawn and recommendation are made:

(1) The environmental impact contribution analysis shows that fossil depletion plays a significant role to the total environmental impact (accounted for 62.02%), so it is necessary to reduce the energy consumption per unit of product.
(2) The process contribution analysis shows that the energy production phase contributes the highest environmental burdens (accounted for 73.02%). There is a direct correlation between the environmental impact and the high level of energy consumption (mainly natural gas and electricity production), as well as, high pollutant emission caused by energy combustion.
(3) The substance contribution analysis shows that the natural gas, CO_2 and coal have the greatest contribution to single indicator, accounting for 37.06, 28.44 and 18.92%, respectively.
(4) The sensitivity analysis shows that consumption of natural gas, electricity and resin use results in the greatest impact on the decline in environmental impact, so reducing the consumption of natural gas and electricity, as well as resin are the most effective ways to achieve environmental performance reduction.

Acknowledgements This work was financially supported by the Beijing Natural Science Foundation (Grant No. 2164056), National Key Research and Development Plan (2016YFF0204403-02). Moreover, this work is financed by Beijing municipal science and technology commission project (D161100002416001), National Key Research and Development Program (2016YFF0201501).

References

1. B. Nie, Three major factors affect the development of China's construction and sanitary ceramics industry. Ceramics, 9–11 (2013)
2. M.D. Bovea, J. Serrano, G.M. Bruscas, A. Gallardo, Application of life cycle assessment to improve the environmental performance of a ceramic tile. Packag. Syst. Packag Technol. Sci. **19**, 83–95 (2005)
3. M.D. Bovea, U. Saura, J.L. Ferrero, J. Giner, Cradle-to-gate study of red clay for use in the ceramic industry. Int. J. Life Cycle Assess **12**(6), 439–447 (2007)
4. V. Ibáñez-Forés, M.-D, Bovea, A. Simó, Life cycle assessment of ceramic tiles. Environmental and statistical analysis. Int. J. Life Cycle Assess **16**, 916–928 (2011)
5. A.L. Giudice, C. Ingrao, M.T. Clasadonte, Life cycle assessment for highlighting environmental hotspots in the Sicilian traditional ceramic sector: the case of ornamental ceramic plates. J. Cleaner Prod. **142**, 225–239 (2017)

6. M. Pini, A.M. Ferrari, R. Gamberini, P. Neri et al., Life cycle assessment of a large, thin ceramic tile with advantageous technological properties. Int. J. Life Cycle Assess **19**, 1567–1580 (2014)
7. L. Tang, S. Dai, M. Yang, Application of life cycle assessment in energy saving evaluation of building ceramics. J. Wuhan Univ. **32**(4), 149–152 (2010)
8. A. Xie, H. Wang, Comparative analysis of ceramic wall tiles and ceramic slabs based on life cycle assessment. Chem. Eng. Equip. **5**, 208–211 (2013)
9. G. Xia, J. Zuo, Jingdezhen household China life cycle evaluation (LCA) **31**(4), 617–622 (2010)
10. Peixi Chen, Environmental impact assessment of sanitary ceramics life cycle. Sci. Technol. Innov. **18**, 50–51 (2015)
11. D.R. Gómez (Argentina), J.D. Watterson (UK), *IPCC Guidelines for National Greenhouse Gas Inventories* (2006)
12. L. Ntziachristos, Z. Samaras, *EMEP/EEA Air Pollutant Emission Inventory Guidebook 2016* (European Environment Agency)
13. Eco-invent Database v2.2, *Eco-invent* center. Swiss Centre for Life Cycle Inventories: 2010. http://www.ecoinvent.org/database/. Accessed 24 Sep 14 (2010)
14. Sinocenter, *Materials Life Cycle Inventory Database*. cnmlca.bjut.edu.cn
15. M.A.J. Huijbregts, Z.J.N. Steinmann, P.M.F. Elshout et al., ReCiPe2016: a harmonised life cycle impact assessme at midpoint and endpoint level (Springer-Verlag Berlin Heidelberg, 2016)

Strength Properties of Phosphogypsum Based Composite Filling Materials

Maohui Li and Zhijie Chen

Abstract The experimental research of new composite filling cementitious materials that could replace the cement has been carried out, which uses the phosphogypsum as the basic material, the lime, slag powder and other solid waste as auxiliary materials. The researchers use the orthogonal experiment to study the role of phosphogypsum addition for the strength of new composite filling cementitious materials. The strength rule function of new composite filling cementitious materials was obtained based on the phosphogypsum by genetic programming. The regression function was optimized using the genetic algorithms. Though analysing the hydration mechanism of the new composite filling cementitious materials by SEM and XRD, the C–S–H gel and ettringite are turned out as the mainly hydration products. The results are shown: the ettringite and brushite are mainly hydration products of the new composite filling cementitious materials. Comparing with the contrast test of cement, the hydration products of new composite filling cementitious materials based on the phosphogypsum have more ettringite than cement. With increasing of curing time, the hydration products are growing and constantly filled in the pore. Sodium hydroxide is added to accelerate the speed of hydration, and enhance the filling body age compressive strength. The strength of new composite filling cementitious materials based on the phosphogypsum can meet the requirement of Jinchuan Mine when the content of lime is 4.48%, phosphogypsum is 32.42%, glauber is 2.35%, sodium hydroxide is 2.5% and slag powder is 58.3% respectively.

Keywords Phosphogypsum · Composite filling materials · Strength performance Optimization algorithm · Hydration mechanism

M. Li
College of Materials Science and Engineering, North Minzu University, Yinchuan 750021, China
e-mail: lmnlmb@126.com

Z. Chen (✉)
China Highway Engineering Consulting Corporation, Beijing 100089, China
e-mail: Archi-cj@hotmail.com

Y. Han (ed.), *Advances in Energy and Environmental Materials*,
Springer Proceedings in Energy, https://doi.org/10.1007/978-981-13-0158-2_58

Introduction

Phosphogypsum is the elimination of calcium sulfate solid castoff during the production process of wet-process phosphoric acid. The production of 1 t of wet phosphoric acid produces about 4–5 t phosphogypsum. The statistics show that China's accumulation of phosphogypsum has more than 200 Mt. Phosphogypsum contains phosphorus, fluorine and many other harmful impurities, which makes it cannot be used directly for the production of gypsum building materials, and also difficult to processing and utilize [1, 2]. A large number of phosphogypsum is treated in a stacking manner. Traditional methods not only caused serious pollution to the surrounding ecological environment, but also lost the economic interests of the phosphate companies, and make a waste of land resources at the same time. Therefore, the corresponding study of comprehensive utilization of phosphogypsum is a mission of shouldering heavy responsibilities.

China has made some research on the problem of comprehensive utilization of phosphogypsum. Zhang [3], Zhang [4] and other researchers have laid a foundation for the comprehensive utilization of phosphogypsum by studying the physical and mechanical parameters of phosphogypsum.

Ma et al. [5] made a study on phosphogypsum-based composite cementitious materials by pretreatment of phosphogypsum with different temperature calcination, but the calcination pretreatment increased the utilization cost of phosphogypsum.

Hou et al. [6] used phosphogypsum and slag cement to carry out the experimental study of phosphogypsum base polymer and achieved good results, but the high economic cost of low gelling materials limited the extensive use in the process of mine filling.

In this paper, orthogonal experiments were carried out on the gypsum-based composite cementitious materials based on the Rod-mill tailings. The functional relationship between the compressive strength and the activator was analyzed by genetic programming [7, 8], and the regression function of constrained optimization by the genetic algorithm [9]. Taking Jinchuan Mine as an example, the optimal amount of phosphogypsum in the new composite cemented gelling material is obtained, which provides the theoretical basis for the comprehensive utilization of phosphogypsum and reduces the cost of mining filling.

Raw Materials and Test Methods

Raw Materials. Phosphogypsum-based composite filling cementing material mainly consists of filling aggregate, cementing material, admixture, water and other materials. The main components of cementitious materials are phosphogypsum, quick lime, slag powder and rod-mill tailing as filling aggregate in this test.

(1) Rod-mill tailing: producing area in Jinchang, specific gravity is 2.67 t/m^3, coefficient of uniformity is 8.2.
(2) Phosphogypsum: producing area in Jinchang, main component is $CaSO_4 \cdot 2H_2O$, density is 2.29 g/cm^3, surface area is 2582.6 cm^2/g.
(3) Quick lime: main components are CaO and MgO, density is 2.32 g/cm^3, surface area is 2662 cm^2/g.
(4) Slag Powder: density is 2.88 g/cm^3, surface area is 3663 cm^2/g.

Physicochemical Characteristics. The physical and chemical properties of the raw materials were obtained through the chemical composition and particle size distribution of phosphogypsum, lime, slag powder and rod-mill tailing. The results are shown in Table 1 and Fig. 1 [(a) is the particle size curve of the phosphogypsum, and (b) is the particle size curve of the slag].

From the analysis results, the main components of phosphogypsum are SO_3, CaO and P_2O_5, which are weak acid materials; the content of CaO and MgO in lime is about 82% of the total, which is a strong alkaline material and provides the main alkaline source in the composite filling cementitious material; the basicity coefficient of slag powder is 1.04, which belongs to acid slag, the main components are CaO, SiO_2 and Al_2O_3, and the slag mass fraction is 1.726, which has excellent activity.

Strength Test. The mortar ratio of the cemented gypsum-based composite cemented material was 1:4 and the mass fraction was 80%. At the same time, the ordinary portland cement control specimen was prepared and used for the comparison of the test results. The size of the specimen was 70.7 mm × 70.7 mm 70.7 mm. After the molding, the specimens were placed in a standard maintenance box with a humidity of 95% and a temperature of 20 °C. Compressive strength tests were performed at 3d, 7d and 28d age.

Neural Network. Based on the orthogonal test and the results of the difference analysis, the artificial neural network model was established based on MATLAB, and the training data were trained, studied and predicted, which laid the foundation for the follow-up optimization.

Table 1 Physicochemical of raw materials

Sample	Content/%							Density/ gcm^{-3}	Average particle size/um
	CaO	SiO_2	Al_2O_3	MgO	Fe_2O_3	P_2O_5	SO_3		
Phosphogypsum	28.6	–	0.36	2.44	0.48	1.47	49.07	2.29	31.01
Quick lime	73.05	1.07	–	9.88	2.32	–	–	2.32	14.07
Slag powder	41.35	35.52	12.14	8.15	–	–	–	2.88	24.31
Rod-mill tailings	1.39	63.6	5.96	3.68	3.44	–	–	2.67	291

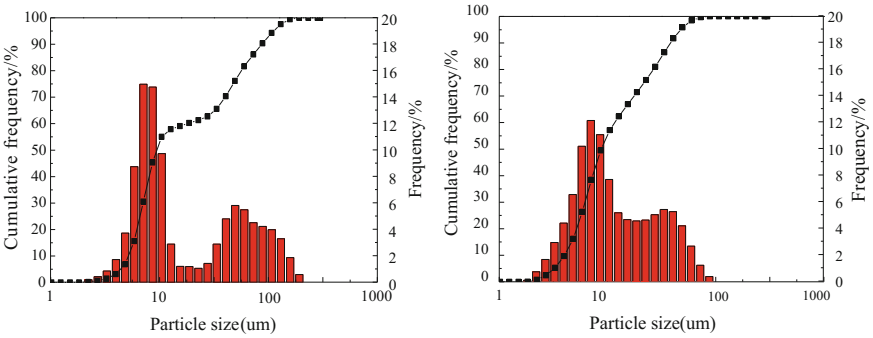

Fig. 1 Particle size of phosphogypsum and slag powder. **a** Phosphogypsum **b** Slag powder

Genetic Programming. In order to obtain the fitting function formula of the strength and proportion of the composite filling cementitious material, the genetic programming program was written by MATLAB.

Genetic Algorithm. Based on the three regression formulas obtained by genetic programming, combined with the actual parameters of compressive strength and shrinkage rate of 3d, 7d and 28d age of Jinchuan mine, the genetic algorithm optimization program was compiled with MATLAB.

XRD and SEM Test. The mineral phases of hydration products were determined by X-ray diffraction (XRD). The morphologies of hardened paste were determined by scanning electron microscope (SEM).

Results and Discussion

Range Analysis. Compressive strength tests are shown in Table 2. Based on the orthogonal test results, the influence of different factors on the strength of composite cemented gelled material was evaluated by the difference value, and the ratio of composite cementitious materials was determined. The range analysis results are shown in Table 3 and Fig. 2.

The best combination of lime, phosphogypsum and mirabilite is 4, 30 and 1% when the ratio of the quick lime, phosphite gypsum and mirabilite is 1.00:1.67:1.00 at the curing of 3d age.

The best combination of lime, phosphogypsum and mirabilite is 6, 40 and 1% when the ratio of the quick lime, phosphite gypsum and mirabilite is 3.67:5.07:1.00 at the curing of 7d age.

Table 2 Orthogonal test results of phosphogypsum cementitious materials

Numbering	Quick lime/%	Phosphogypsum/%	Mirabilite/%	Slag powder/%	Compressive strength/MPa			Shrinkage/%		
					3d	7d	28d	3d	7d	28d
B1	4	30	1	65	0.379	2.96	12.73	13.21	10.1	9.48
B2	4	35	3	58	0.25	2.53	9.74	11.15	10.86	6.29
B3	4	40	5	51	0.14	2.08	9.01	12.10	10.18	8.52
B4	6	30	3	61	0.622	3.36	10.81	11.5	12.46	7.12
B5	6	35	5	54	0.223	2.85	9.66	6.75	8.65	7.15
B6	6	40	1	53	0.209	2.27	9.77	10.05	12.68	10.85
B7	8	30	5	57	0.263	4.25	12.26	12	13.95	10.91
B8	8	35	1	56	0.159	3.39	8.77	12.23	12.14	9
B9	8	40	3	49	0.189	2.57	6.95	10.49	9.25	5.07
32.5 Cement					**1.65**	**2.61**	**5.1**	**7.19**	**8.12**	**8.55**

Table 3 Variance and weight analysis results of the orthogonal experimental

Curing age	Parameters	Quick lime	Phosphogypsum	Mirabilite
3d	Range (Rj)	0.15	0.24	0.14
	Relative weight	1.06	1.67	1.00
	Optimal proportion	4%	30%	1%
7d	Range (Rj)	0.88	1.22	0.24
	Relative weight	3.67	5.07	1.00
	Optimal proportion	6%	40%	1%
28d	Range (Rj)	1.17	3.36	1.26
	Relative weight	1.00	2.88	1.08
	Optimal proportion	4%	35%	1%

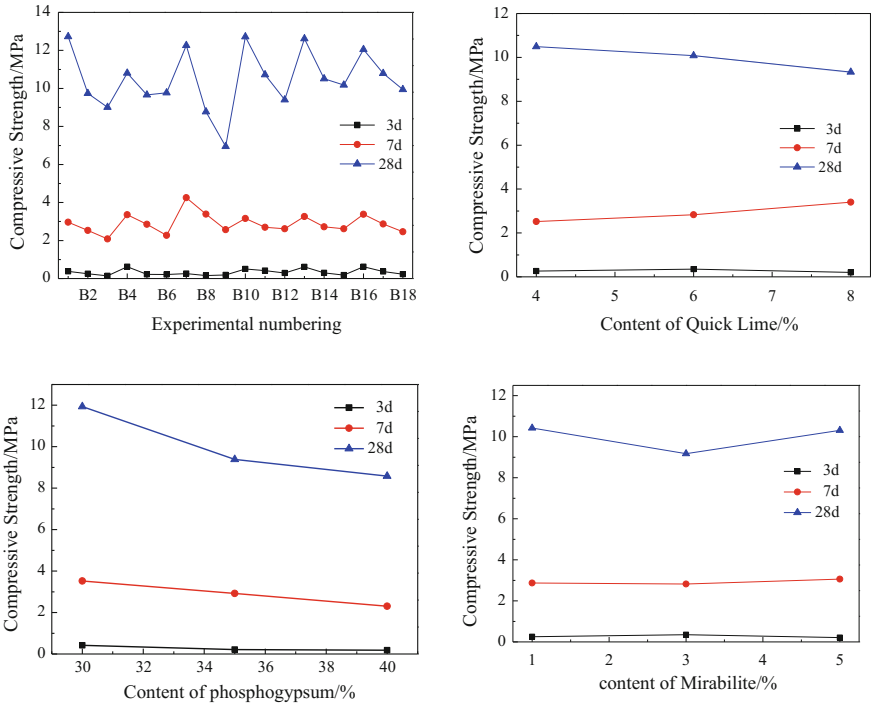

Fig. 2 Curve of compressive strength with orthogonal factors

The best combination of lime, phosphogypsum and mirabilite is 4, 35 and 1% when the ratio of the quick lime, phosphite gypsum and mirabilite is 1.00:2.73:1.07 at the curing of 28d age.

Comprehensive analysis of the results, quick lime, phosphogypsum and mirabilite should be selected about 5, 35 and 1%. The compressive strength of the

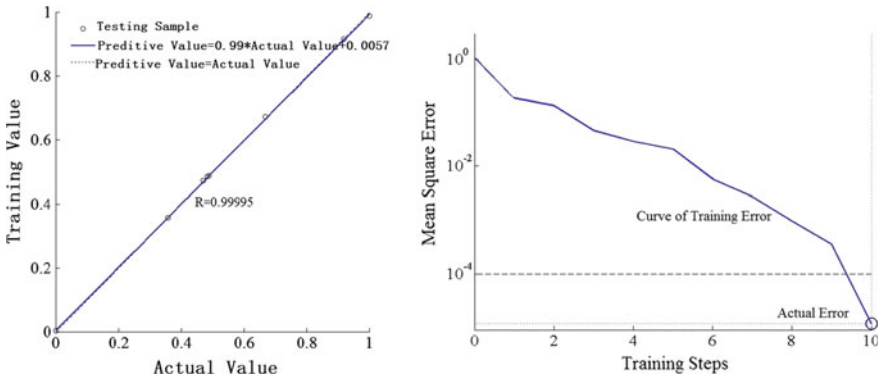

Fig. 3 Parameters graph of neural network

filling body at 3d age cannot meet the requirements of the compressive strength of the Jinchuan mine, so it is necessary to optimize the experimental ratio.

Training Results of Neural Network. The correlation coefficient between compressive strength and shrinkage is higher than 99%, the relative error is less than 5% as shown Fig. 3. So the neural network programs can be used to predict compressive strength and shrinkage of the phosphogypsum-based cementitious material. The prediction results of Compressive and shrinkage by the neural network are shown in Table 4.

Fitting Results of Genetic Programming. Tables 2 and 4 data as the sample, B1–B17 as the training samples, B18 as the validation of samples, the compressive strength genetic planning the best individual tree have been obtained according to Table 5 genetic planning method parameters to select. The fitting function formula of the strength and proportion of the composite filling cementitious material can be obtained by the Genetic programming. The best individual tree of 3d curing age is shown in Fig. 4.

Taking the test sample data into the resulting expression and comparing the prediction with actual compressive strength, the relative error of the predicted value of genetic planning is less than 5%, which can accurately reflect relationship between compressive strength and materials ratio. The formula for compressive strength is as follow:

$$R_{3d} = (X3 + (X4 + (2 * X3 + X4)/(X3 + 2 * X4))/(X1 + X2 + X4 - \exp(\exp(X3)) + X2 * X3))/(X1 * X3) \quad (1)$$

$$R_{7d} = (X1 + X2 + X4 + (2 * X1 - X2 + X3 + \exp(X3) + (2 * X1)/X2 + 1)/X2 + X1/(X2 + 1/X2))/X2 \quad (2)$$

Table 4 Results of neural network training

Numbering	Quick lime/%	Phosphogypsum/%	Mirabilite/%	Slag powder/%	Compressive strength/MPa			Shrinkage/%		
					3d	7d	28d	3d	7d	28d
B10	4.5	30	0.5	65	0.50	3.16	12.72	13.20	9.95	9.96
B11	4.5	35	1	59.5	0.42	2.70	10.72	13.09	12.09	10.67
B12	4.5	40	1.5	54	0.29	2.62	9.40	11.41	12.33	10.71
B13	5	30	1	64	0.61	3.26	12.62	13.19	9.46	9.72
B14	5	35	1.5	58.5	0.30	2.72	10.51	12.86	11.50	10.11
B15	5	40	0.5	54.5	0.18	2.62	10.18	11.17	11.61	10.83
B16	5.5	30	1.5	63	0.62	3.38	12.05	13.14	9.93	9.32
B17	5.5	35	0.5	59	0.37	2.87	10.79	13.13	11.72	10.51
B18	5.5	40	1	53.5	0.23	2.46	9.94	10.62	12.61	10.79

Table 5 Control parameters of genetic programming

Parameters	Value
Target	Relationship between compressive and various parameters
Terminators set	X_1–X_8
Functions set	+, –, ×, /, exp
Population size	91
Crossover probability	Dynamic
Mutation probability	Dynamic
Selection method	Competitive method
Stop criterion	Maximum times of allowable
Maximum times of allowable	51
Maximum depth of mutation	17
Method of initial group generation	Mixed method

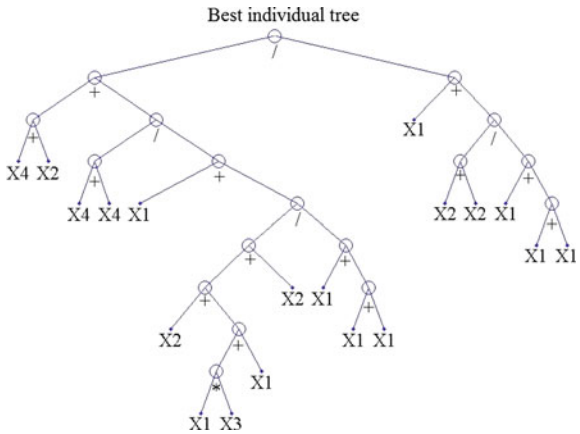

Fig. 4 Best individual tree genetic programming model obtained

$$R_{28d} = X1 + (X4 - X3 - X1 + (X4 \wedge 2 + X4 - X1 + X2 - X3)/(X1 + 2 * X2) + X4 \wedge 2)/(X1 * (2 * X2 + X4)) \quad (3)$$

In the formula, R3d, R7d, R28d, X1, X2, X3 and X4 are respectively represent the compressive strength(3d, 7d and 28d), quick lime, phosphogypsum, mirabilite and slag powder.

Optimization Results of Genetic Algorithm. The objective function of Genetic Algorithm is as follow:

$$
\begin{aligned}
R_{min} &= (R_{28d} - y_{28d})^2 + (R_{7d} - y_{7d})^2 + (R_{3d} - y_{3d})^2 \\
&= (X1 + (X4 - X3 - X1 + (X4 \wedge 2 + X4 - X1 + X2 - X3)/(X1 + 2 * X2) + X4 \wedge 2)/(X1 * (2 * X2 + X4)) \\
&\quad - 1047/100) \wedge 2 + ((X1 + X2 + X4 + (2 * X1 - X2 + X3 + \exp(X3) \\
&\quad + (2 * X1)/X2 + 1)/X2 + X1/(X2 + 1/X2))/X2 - 289/100) \wedge 2 \\
&\quad + ((X3 + (X4 + (2 * X3 + X4)/(X3 + 2 * X4))/(X1 + X2 + X4 - \exp(\exp(X3)) \\
&\quad + X2 * X3))/(X1 * X3) - 33/100) \wedge 2
\end{aligned} \tag{4}
$$

In the formula, y3d, y7d and y28d are respectively represent the mean compressive strength of 3d, 7d and 28d ages in orthogonal test. The constraints of objective function are as follows:

$R28d \geq 5$ MPa, $R7d \geq 2.5$ MPa, $R3d \geq 1.5$ MPa, $0 \leq X1 \leq 8$, $25 \leq X2 \leq 45$, $0 \leq X3 \leq 5$, $0 \leq X4 \leq 65$

The objective function obtains the minimum value when X1 = 4.48, X2 = 32.42, X3 = 2.35 and X4 = 60.74, R3d, R7d and R28d are 0.63 MPa, 3.06 MPa and 11.23 MPa respectively.

Results of Verification Test. The results show that the compressive strength at 3d of the filling body does not meet the filling strength of Jinchuan mine, but the compressive strength at 7d and 28d is much larger than the required filling strength. Therefore, the rate of hydration reaction of composite filling body at 3–7d age is much higher than that of 0–3d age. In order to improve the hydration reaction speed of 0–3d of the filling body and enhance the compressive strength of its 3d age, the sodium hydroxide has been added on the basis of optimizing the proportion. Results of verification test are as follows (Table 6):

Table 6 Results of verification test

Numbering	Quick lime/%	Phosphogypsum/ %	NaOH/ %	Mirabilite/ %	Slag powder/ %	Compressive strength of 3d/ MPa
C1	4.0	30	2	1.5	62.5	1.46
C2	4.0	32	3	2	56	1.80
C3	4.0	34	4	2.5	49.5	1.36
C4	4.5	30	3	2.5	59.5	2.73
C5	4.5	32	4	1.5	54.5	2.27
C6	4.5	34	2	2	51	1.43
C7	5.0	30	4	2	58	1.05
C8	5.0	32	2	2.5	54.5	1.65
C9	5.0	34	3	1.5	49.5	1.80
Mean value	4.5	32	3	2	55	1.73

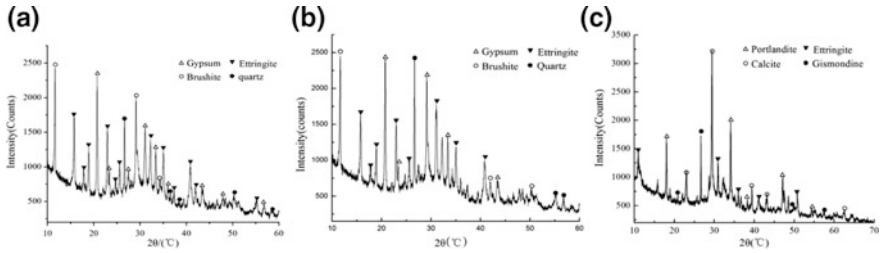

Fig. 5 XRD patterns of the hydration products

XRD Results. The XRD pattern of the phosphogypsum-based cementitious material and cement material at 28d age is shown in Fig. 5(a), (b) are the hydration pattern of phosphogypsum, and (c) is the hydration XRD pattern of cement).

The mainly hydration products of the phosphogypsum-based cementitious material are ettringite (Ca_6Al_2 $(SO)_3$ $(OH)_{12}{\cdot}26H_2O$), brushite ($CaPO_3$ (OH) $\cdot 2H_2O$), quartz (SiO_2) and dihydrate gypsum ($CaSO_4{\cdot}2H_2O$). The main hydration products of cement materials are mainly ettringite, calcium-calcium zeolite ($CaAl_2Si_2O_8{\cdot}4H_2O$), calcite ($CaCO_3$) and hportlandite (Ca $(OH)_2$).

The diffraction peak intensity of ettringite in the XRD pattern of the phosphogypsum-based cementitious material is significantly higher than that of the ettringite in the cement materials, so that the compressive strength of phosphogypsum-based cementitious material is higher than the compressive strength of cement materials.

Since $CaSO_4{\cdot}2H_2O$ is the main component of phosphogypsum, about 30% of phosphogypsum is added to the phosphogypsum-based cementitious material. $CaSO_4{\cdot}2H_2O$ is provided in the material more than $CaSO_4{\cdot}2H_2O$ consumed in the process of hydration. So a large amount of $CaSO_4{\cdot}2H_2O$ diffraction peak appears in the XRD pattern of the phosphogypsum-based cementitious material. As the slag powder contains about 35% of the SiO_2 that does not completely digest SiO_2 in hydration reaction, so in the XRD spectrum also appears SiO_2 diffraction peak.

SEM Results. The SEM results of the phosphogypsum-based cementitious material and cement material at 3d, 7d and 28d age are shown in Figs. 6, 7, 8 [(a) is the highest intensity ratio of orthogonal test, (b) is the optimized ratio, (c) is SEM for cement].

The hydration reaction of slag is relatively sufficient, and a small amount of unhydrated slag particles can be seen. Corresponding to the results of XRD analysis, the hydration products are mainly massive ettringite and C–S–H gels in massive ettringite, and the surface of the filling body is wrapped with dense hydration products. With the increase of hydration age, gradually formed a large number of hydration products, the internal structure of the slurry constantly dense, and improve the strength of the material.

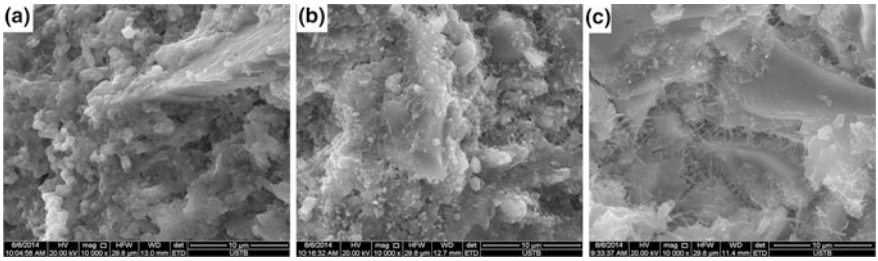

Fig. 6 SEM images of the hydration products in 3d

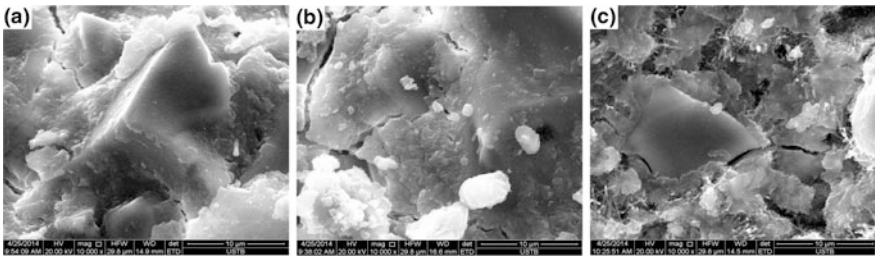

Fig. 7 SEM images of the hydration products in 7d

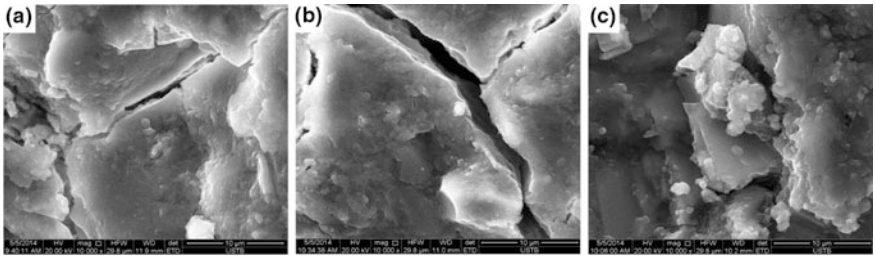

Fig. 8 SEM images of the hydration products in 28d

Phosphogypsum is involved in the hydration process during the hydration reaction. Since the phosphogypsum contains a large amount of $CaSO_4 \cdot 2H_2O$, the slag is always hydrated in the saturated sulphate solution. In the alkaline environment, CaO and Al_2O_3 and other active substances of slag continue to dissolve into the solution to produce the calcium trisulphoaluminate hydrate (AFt), which improves the affinity of the phosphogypsum and the hydration product interface, combines closely phosphogypsum and hydrated products. At the same time, due to the micro-expansion effect of hydrated phosphogypsum, with the extension of hydration age, the surface of the filling body appeared fine cracks, which was consistent with the decrease of shrinkage rate in Table 2.

Conclusions

The phosphogypsum contains a certain amount of P_2O_5 that is unfavorable for the formation of filling body strength. In the phosphogypsum-based cementitious material added to the excess of phosphogypsum, the compressive strength of the filling body decreases with the rise in phosphogypsum.

Through the optimization algorithm, the compressive strength of 7d and 28d age are able to meet the needs of mine filling strength respectively for Quick Lime, Phosphogypsum, Mirabilite and Slag Powder were 4.48, 32.42, 2.35, 60.74%. But the compressive strength of 3d age is lower.

On the basis of optimizing the ratio, NaOH is added as the catalyst to provide the alkali environment for the reaction of the material. The results showed that the compressive strength of the phosphogypsum-based cementitious material after NaOH addition was improved. NaOH can promote the dispersion of vitreous particles of slag powder, promote the hydration reaction rate of phosphogypsum and slag powder, and effectively improve the early compressive strength of the filling body.

The main hydration products of phosphogypsum - based cementitious materials are ettringite ($Ca_6Al_2(SO)_3(OH)_{12}\cdot 26H_2O$) and calcium phosphate ($CaPO_3(OH)\cdot 2H_2O$). Compared with the amount of ettringite in the hydration product of cement filling body, the hydration of phosphogypsum-based cementitious material is more complicated, coarse and compact. A large amount of ettringite and calcium phosphate are formed, laying the foundation for the growth of compressive strength. The strength performance of phosphogypsum-based cementitious material is better than that of cement-filled cementitious material under the same conditions.

References

1. Z. Yang, L. Xiang, Review of comprehensive utilization of phoshgogypsum. Norganic Chem. Ind. **01**, 8–10 (2007)
2. X. Zeng, Z. Shui, S. Ding et al., Influence of curing conditions on the performance of persulphated phosphogypsum-slag cement mortar. Concrete **2**, 110–113 (2015)
3. C. Zhang, C. Yang, K. Yu, et al., Study on physico-mechanical characteristics of phosphogypsum. Rock and Soil Mech. **28**(3), 461–466 (2007)
4. G. Zhang, Z. Yang, Q. Gao et al., Metal Mine **03**, 194–198 (2015)
5. Y. Ma, Y. Gao, N. Ye et al., Water resistance of composite binder based on phoshogypsum. J. Wuhan Univ. Technol. **34**(3), 29–33 (2012)
6. J. Hou, F. Mei, H. Xia, Models for strength law of phosphgypsum consolidation materials. J. Wuhan Univ. (Nat. Sci. Ed) **59**(4), 336–342 (2013)
7. S. Zhai, Q. Gao, J. China Coal Soc. **32**(3), 239–242 (2007)
8. B. Yang, L. Kuang, Z. Sun et al., Prediction of reservoir water saturation by genetic programming. J. Chengdu Univ. Technol. (Sci. Technol. Ed.) **33**(2), 209–213 (2006)
9. A.G. Niu, *Study on Improvement and Application of Genetic Programming* (University of Science and Technology of China, Hefei Shi, 2006)

Raman Spectroscopy of Graphene by the Method of Oxidization-Reduction

Bo Liang, Fenglan Han, Jintao Wang and Qi Luo

Abstract Graphene, a monolayer of carbon atoms packed into a two-dimensional crystal structure, attracted intense attention owing to its unique structure and optical, electronic properties. In this study, graphite oxide (GO) was prepared using flake graphite by an improved Hummers method. Hydrazine hydrate as reducing reagent was added to prepare reduced graphene oxide (RGO). GO and RGO were characterized by XRD, SEM and Raman. According to the peak position and intensity of the D, G and G′ band in Raman spectra, the influence of $KMnO_4$, H_2O_2 and hydrazine hydrate on the structure of graphene was studied. The results show that the I_D/I_G value is the minimum when the amount of $KMnO_4$ is 7.5 g; the I_D/I_G value is the least when the amount of H_2O_2 is 15 ml; the I_D/I_G value is the smallest and the G′ band obviously appears when the amount of hydrazine hydrate is 12 ml, which shows that the defects of graphene are the minimum and the number of graphene layers is the least.

Keywords Oxidization-reduction · Graphene · Defects · Raman spectroscopy

Introduction

Graphene, a monolayer of carbon atoms packed into a two-dimensional crystal structure of hexagonal honeycomb, is the basic part of the construction of other sp^2 allotropes of carbon [1]. As a kind of ideal two-dimensional crystals [2], graphene

B. Liang (✉) · F. Han · J. Wang · Q. Luo
School of Material Science and Engineering, North Minzu University, Yinchuan 750021, Ningxia Hui Autonomous Region, China
e-mail: lbscu@126.com

F. Han
e-mail: 625477897@qq.com

J. Wang
e-mail: wjt1986120@163.com

Q. Luo
e-mail: 656724657@qq.com

Y. Han (ed.), *Advances in Energy and Environmental Materials*,
Springer Proceedings in Energy, https://doi.org/10.1007/978-981-13-0158-2_59

with high electronic and thermal conductivity [3], large theoretical surface area, high Young's modulus and tensile strength, has a broad application prospect in the fields such as micro-or nano-electronic devices, photoelectric detection and conversion materials, the reinforced composite materials of structure and function, and energy storage materials [4].

At present, the method of oxidation-reduction is widely used to prepare graphene. Stankovich et al. [5] prepared graphene for the first time by the method of oxidation-reduction, and the reduced graphene with polymer coating was evenly dispersed in water. For the moment, Hummers method is well-known and widely used to create graphene sheets [6]. Graphite oxide and graphene have similar planar structure. If a suitable reduction method is applied to the graphite oxide, the functional groups on the surface of GO can be removed and graphene is obtained. For example, Zhang et al. [7] found that the functional groups on the surface of GO can be gradually eliminated and the graphene was obtained in the concentrated KOH (NaOH) solution. At present, oxidation-reduction has become an important method for the production of graphene on a large scale. However, graphene sheets prepared by this method are more prone to wrinkling or folding. And because the functional groups can not be completely eliminated, the thickness of graphene is too large.

Raman spectroscopy, which has high resolution, is a fast and nondestructive method for characterizing the crystal structure, electron band structure, phonon energy dispersion and electron phonon coupling [8]. It is one of the most popular characterization techniques in fullerene, carbon nanotube and diamond. It has played an important role in the development of carbon materials. Since the discovery of graphene, Raman spectroscopy has become one of the most important characterization techniques in the study of graphene. The structural defects of graphene (D peak), the in-plane vibration (G peak) and the interlayer stacking modes (G′ peak) of carbon atoms are well represented in Raman spectra [9, 10]. In this paper, graphite oxide (GO) was prepared by an improved Hummers method, and then graphene was obtained by reduction of GO with hydrazine hydrate. The morphology and structure of graphite oxide and graphene were characterized by X ray diffraction (XRD), scanning electron microscopy (SEM) and laser Raman spectroscopy (Raman). The defect degree of graphene was characterized and analyzed by Raman spectra. Finally, the relationship between the structure of graphene and the main process parameters was determined.

Experimental

Materials. Natural graphite flakes (100 mesh particle size) was acquired from Sigma Aldrich. Concentrated sulfuric acid (98%), potassium permanganate, hydrogen peroxide, hydrazine hydrate, hydrochloric acid and ammonia were purchased from Tianjin Kermel Chemical Reagent Co. Ltd. All chemicals used in the experiment are analytic reagents (AR).

Preparation of GO and Graphene Sheets. Graphite flake (1.5 g) was added to a mixed solution consisting of concentrated H_2SO_4(6 mL), $(NH_4)_2S_2O_8$(1.25 g) and P_2O_5(1.25 g) at 80 °C for 4.5 h. The mixture was washed and filtered with deionized water to remove the residual acid and dried at room temperature to obtain pre-oxidized graphite. The pre-oxidized graphite was mixed with concentrated H_2SO_4(60 mL) in an ice bath. $KMnO_4$ was added slowly to the suspension. Then the above mixture was stirred at 35 °C for 2 h. Afterwards, deionized water and 30% H_2O_2 were added gradually, and the color of the mixture turned from black to brilliant yellow along with bubbling. After cooling to room temperature, the mixture was centrifuged and washed with 5% HCl and then deionized water for several times. Water-soluble GO was synthesized.

Graphene sheets were synthesized via chemical reduction of the as-prepared GO. GO (0.3 g) was uniformly dispersed in deionized water(500 ml) with the help of ultrasonication. Then hydrazine hydrate ($H_4N_2{\cdot}H_2O$) and ammonia ($NH_3{\cdot}H_2O$) were added into the suspension of GO with vigorous agitation for a few minutes and the temperature was maintained at 95 °C for 1 h. After reaction, reduced graphene oxide (RGO) was centrifuged and washed with deionized water for several times, and then dried under vacuum.

Characterization. The phase structures of graphite and graphene were measured by X ray diffraction (XRD-6000, Shimadzu) with the scanning range of 10°–35°. The morphology of graphite flakes and graphene sheets was observed by scanning electron microscopy (SS-550, Shimadzu). Raman spectra were obtained on a renishaw invia raman microscope equipped with a 514.5 nm He–Ne laser line as the excitation source.

Results and Discussion

Characterization of Graphite, Graphite Oxide and Graphene. The XRD patterns of graphite flakes, graphite oxide and graphene are showed in Fig. 1. The graphite has a strong diffraction peak at about $2\theta = 26°$. However, this peak disappears in GO and the graphene show basal reflection peak at about $2\theta = 24°$. The figure shows the intensity of graphite is greater with a sharp and strong diffraction peak compared with that of graphene. High intensity with a sharp peak at about $2\theta = 26°$ shows the characteristic graphitic materials. A dramatically decrease in the intensity peak of graphene is caused by the decrease of thickness of graphite due to the break of inter-planar carbon within graphite structure during chemical reduction of the GO. There was no other apparent crystal plane diffraction peak observed in graphene indicates that there are no existence of oxygen or other functional groups in graphene sheets. From SEM images of graphite and graphene in Fig. 3a and b, the graphene sheets appear to be smaller in size and thinner in thickness with semi-transparent graphene sheets.

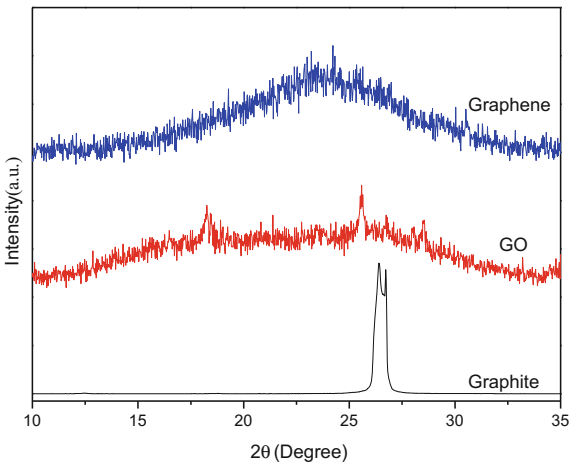

Fig. 1 XRD patterns of graphite, GO and graphene

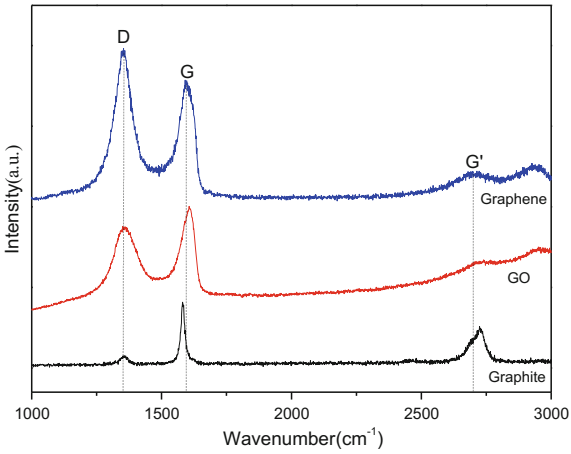

Fig. 2 Raman spectra of graphite, GO and graphene

Raman spectroscopy is a powerful tool to study the structures of carbon materials. Figure 2 shows the Raman spectra of graphite flakes, graphite oxide and graphene. The appearance of D band signal ($\sim$1350 cm^{-1}) gives the evidence about the presence of defects on graphite structure before oxidation begin with high G band ($\sim$1581 cm^{-1}) and moderately intense G′ band ($\sim$2697 cm^{-1}). These three bands clearly show the characteristic of graphitic materials (Fig. 3).

When GO is chemically reduced, the intensity of the D bands increased, which could be caused by introducing defects into the graphene sheets during preparation [10–12]. At the same time, the D/G intensity ratio of graphene sheets is higher than that of the GOs, which confirm the formation of numerous new graphitic domains after chemical reduction of GOs [12, 13].

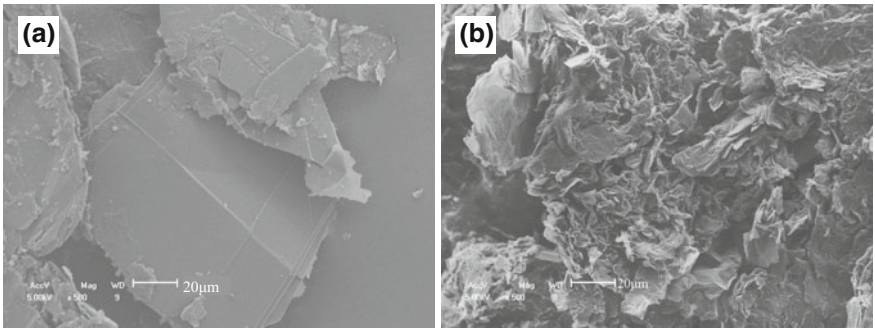

Fig. 3 SEM images of graphite (**a**) and graphene (**b**)

The Effect of Potassium Permanganate on Graphene. The Raman spectra of graphene with different amount of $KMnO_4$ are showed in Fig. 4. As can be seen in Fig. 4, Raman spectra of graphene were very similar. Two first-order bands of GO and graphene were observed: the D band at $\sim$1350 cm^{-1}, which correspond to the vibrations of carbon atoms at defect sites; the G band at $\sim$1590 cm^{-1}, which correspond to the vibrations of carbon atoms in the ideal graphitic lattice [14, 15]. The G′ band ($\sim$2697 cm^{-1}) represents the interlayer stacking of carbon atoms, which is used to determine the number of graphene layers [16]. From Raman spectra in Fig. 4, the D/G intensity ratio of graphene sheets is showed in Table 1.

The ratio of the intensity of the D band to that of the G band (I_D/I_G) is usually used as an important parameter to describe the defect density in graphene [17]. Assuming that the defect in graphene is a point defect and the average distance between two points is L_D, L_D can be quantified by calculating I_D/I_G from the Raman spectrum, $I_D/I_G \propto 1/L_D^2$. Thus we can estimate the density of defects in graphene. The smaller the value of I_D/I_G is, the fewer defects are in graphene.

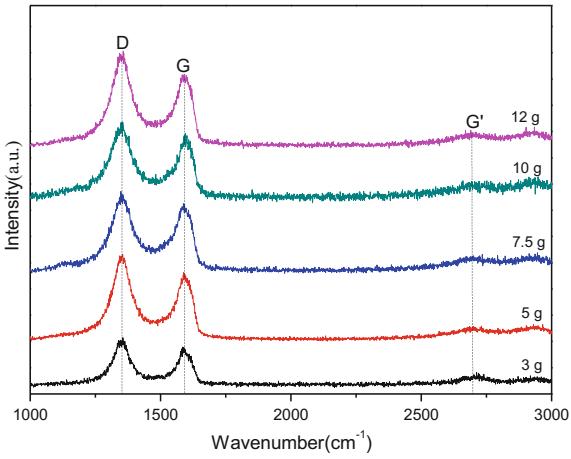

Fig. 4 Raman spectra of graphene with different amount of $KMnO_4$

Table 1 The I_D/I_G of graphene with different amount of $KMnO_4$

$KMnO_4$ [g]	D	G	I_D/I_G
3	(1350, 495)	(1592, 432)	1.146
5	(1350, 1296)	(1592, 1133)	1.144
7.5	(1350, 1846)	(1592, 1783)	1.035
10	(1350, 2521)	(1592, 2384)	1.057
12	(1350, 3210)	(1592, 3022)	1.062

As can be seen from the table, when the amount of $KMnO_4$ increases from 3 to 7.5 g, the I_D/I_G value reduces from 1.146 to 1.035. When the amount of $KMnO_4$ continues to increase to 12 g, the I_D/I_G value increases from 1.035 to 1.062. Therefore, when the amount of $KMnO_4$ is 7.5 g, the intensity ratio is minimum, at this time, the graphene has the least defects. $KMnO_4$ is an oxidant, although the more the amount, the more it can deepen the degree of oxidation of graphite, but at the same time it will also increase its defects and bring difficulties to the reduction.

The Effect of Hydrogen Peroxide on Graphene. The Raman spectra of graphene with different amount of H_2O_2 are showed in Fig. 5. From Raman spectra in Fig. 5, the D/G intensity ratio of graphene sheets are showed in Table 2.

As can be seen from the table, when the amount of H_2O_2 increases from 5 ml to 15 ml, the I_D/I_G value reduces from 1.307 to 1.049. When the amount of H_2O_2 continues to increase, the I_D/I_G value increases. Therefore, when the amount of H_2O_2 is 15 ml, the intensity ratio is minimum, at this time, the graphene has the least defects. H_2O_2 is an oxidizing agent, although the more the amount, the more it can deepen the degree of oxidation, but it also increases its defects.

The Effect of Hydrazine Hydrate on Graphene. The Raman spectra of graphene with different amount of hydrazine hydrate are showed in Fig. 6. From Raman spectra in Fig. 6, the D/G intensity ratio of graphene sheets is showed in Table 3.

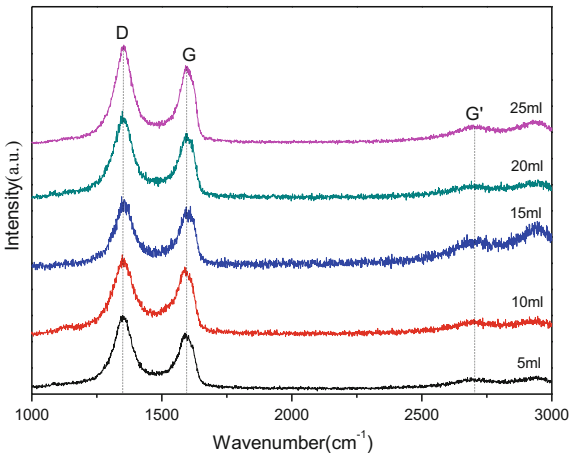

Fig. 5 Raman spectra of graphene with different amount of H_2O_2

Table 2 The I_D/I_G of graphene with different amount of H_2O_2

H_2O_2 [ml]	D	G	I_D/I_G
5	(1350, 745)	(1597, 570)	1.307
10	(1350, 1271)	(1597, 1170)	1.086
15	(1350, 1846)	(1597, 1759)	1.049
20	(1350, 2635)	(1597, 2447)	1.077
25	(1350, 3310)	(1597, 3110)	1.064

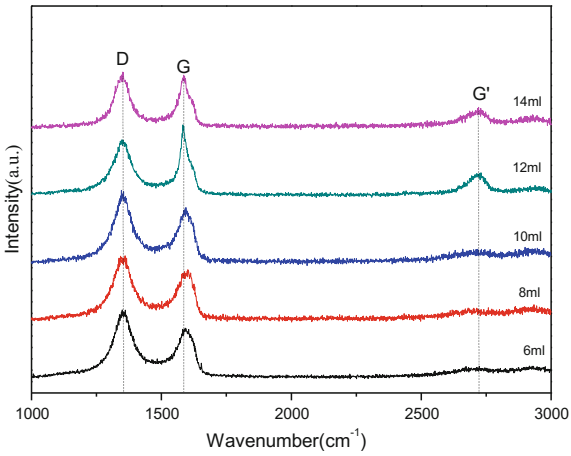

Fig. 6 Raman spectra of graphene with different amount of hydrazine hydrate

Table 3 The I_D/I_G of graphene with different amount of hydrazine hydrate

Hydrazine hydrate [ml]	D	G	I_D/I_G
6	(1350, 695)	(1587, 556)	1.25
8	(1350, 1188)	(1587, 1039)	1.143
10	(1350, 1740)	(1587, 1603)	1.085
12	(1350, 2212)	(1587, 2327)	0.951
14	(1350, 2787)	(1587, 2764)	1.008

As can be seen from the table, when the amount of hydrazine hydrate increases from 6 to 12 ml, the I_D/I_G value reduces from 1.25 to 0.951. When the amount of hydrazine hydrate continues to increase, the I_D/I_G value increases. Therefore, when the amount of hydrazine hydrate is 12 ml, the intensity ratio is minimum, at this time, the graphene has the least defects. It is worth noting that the G′ band of graphene sheets obviously appears, which shows that the number of graphene layers is the least with hydrazine hydrate of 12 ml.

Conclusions

In summary, the graphene sheets were prepared by the method of oxidation-reduction. The I_D/I_G values under different synthetic conditions were calculated from the Raman spectrum and the effect of oxidant and reducing agent on the structure of graphene was investigated. Firstly, the D/G intensity ratio of graphene sheets is higher than that of the GOs, which confirms the formation of numerous new graphitic domains after chemical reduction of GOs. The graphene sheets appear to be smaller in size and thinner in thickness with semi-transparent graphene sheets from SEM images. Secondly, $KMnO_4$ and H_2O_2 are two kinds of oxidants, although the more the amount, the more it can deepen the degree of oxidation, but at the same time it will also increase the defects of graphite and bring difficulties to the reduction. Finally, the I_D/I_G value is the smallest and the G′ band obviously appears when the amount of hydrazine hydrate is 12 ml, which shows that the defects of graphene are the minimum and the number of graphene layers is the least.

Acknowledgements The authors gratefully acknowledge the key research project of North Minzu University, China (Grant No. 2015KJ26), Research start-up fee of North Minzu University, China (Grant No. 4400302523) and Ningxia Autonomous Regional Level Undergraduate Innovation Program, China (Grant No. NXCX2016190) for financial support.

References

1. X. Ling, L.M. Xie, Y. Fang et al., Can graphene be used as a substrate for Raman enhancement. Nano Lett. **10**, 553–561 (2010)
2. Z.H. Ni, Y.Y. Wang, T. Yu et al., Raman spectroscopy and imaging of graphene. Nano Res. **1**, 273–291 (2008)
3. X. Du, I. Skachko, A. Barker et al., Approaching ballistic transport in suspended graphene. Nat. Nanotechnol. **3**, 491–495 (2008)
4. D. Sun, G. Aivazian, A.M. Jones et al., Ultrafast hot-carrier-dominated photocurrent in graphene. Nature Nanotechnology **7**, 114–118 (2012)
5. S. Stankovich, R.D. Piner, X.Q. Chen et al., Stable aqueous dispersions of graphitic nanoplatelets via the reduction of exfoliated graphite oxide in the presence of poly(sodium 4-styrenesulfonate). J. Mater. Chem. **16**, 155–158 (2006)
6. W.S. Hummers, R.E. Offeman, Preparation of graphitic oxide. J. Am. Chem. Soc. **80**, 1339–1339 (1958)
7. X.B. Fan, W.C. Peng, Y. Li et al., Deoxygenation of exfoliated graphite oxide under alkaline conditions: a green route to graphene preparation. Adv. Mater. **20**, 4490–4493 (2008)
8. D.L. Mafra, J. Kong, K. Sato et al., Using gate-modulated Raman scattering and electron-phonon interactions to probe single-layer graphene: a different approach to assign phonon combination modes. Phys. Rev. B **86**, 195434 (2012)
9. A.C. Ferrari, D.M. Basko, Raman spectroscopy as a versatile tool for studying the properties of graphene. Nat. Nanotechnol. **8**, 235–246 (2013)
10. A. Gupta, G. Chen, P. Joshi et al., Raman scattering from high-frequency phonons in supported n-graphene layer films. Nano Lett. **6**, 2667–2673 (2006)
11. Z.H. Ni, H.M. Wang, Y. Ma et al., Tunable stress and controlled thickness modification in graphene by annealing. ACS Nano **2**, 1033–1039 (2008)

12. H.L. Guo, X.F. Wang, Q.Y. Qian et al., A green approach to the synthesis of graphene nanosheets. ACS Nano **3**, 2653–2659 (2009)
13. S. Stankovich, D.A. Dikin, R.D. Piner et al., Synthesis of graphene-based nanosheets via chemical reduction of exfoliated graphite oxide. Carbon **45**, 1558–1565 (2007)
14. J.P. Tessonnier, M.A. Barteau, Dispersion of alkyl-chain-functionalized reduced graphene oxide sheets in nonpolar solvents. Langmuir **28**, 6691–6697 (2012)
15. A. Sadezky, H. Muckenhuber, H. Grothe et al., Raman microspectroscopy of soot and related carbonaceous materials: spectral analysis and structural information. Carbon **43**, 1731–1742 (2005)
16. A.C. Ferrari, D.M. Basko, Raman spectroscopy as a versatile tool for studying the properties of graphene. Nat. Nanotechnol. **8**, 235–246 (2013)
17. B. Li, L. Zhou, D. Wu et al., Photochemical chlorination of graphene. ACS Nano **5**, 5957–5961 (2011)

Effects of Functional Chelator and Mineral Admixture on the Salt Freeze-Thaw Resistance of Cement-Based Materials

Ruiyang Wang, Jianying Yu, Yagang Zha, Feng Yin and Zhilei Wang

Abstract The effects of functional chelator and mineral admixture on the salt freeze-thaw (F-T) resistance of cement-based materials were investigated. The salt F-T resistance of mortar was evaluated by mass loss, compressive strength loss and total porosity change. The results indicated that the properties of mortar with functional chelator are significantly superior to those of ordinary mortar after the salt F-T cycle test. Compared with the ordinary mortar, after 100 salt F-T cycles, the mass loss and the compressive strength loss of the mortar with 0.5% functional chelator were reduced by 23.6 and 26.7%, respectively. Moreover, the salt F-T resistance of the mortar with functional chelator and mineral admixtures was further promoted. As for mortar with 0.5% functional chelator and 20% slag grinding, the mass loss and the compressive strength were reduced by 24 and 11.3% than the mortar only with 0.5% functional chelator after 100 salt F-T cycles. Meanwhile, the total porosity of the mortar with 0.5% functional chelator and 20% fly ash was 24.3% less than the mortar only with 0.5% functional chelator after 100 salt F-T cycles. According to the SEM analysis, the mineral admixtures could fill the pores of the mortar, and the functional chelator could repair the crack of mortar after salt F-T cycles.

R. Wang · J. Yu (✉) · Y. Zha
State Key Laboratory of Silicate Materials for Architectures, Wuhan University of Technology, Wuhan 430070, China
e-mail: jyyu@whut.edu.cn

R. Wang
e-mail: 18202719663@163.com

Y. Zha
e-mail: zhayagang1023@163.com

F. Yin · Z. Wang
Inner Mongolia High-Grade Highway Construction and Development Co. Ltd, Hohhot 010020, China
e-mail: nmgyinfeng@163.com

Z. Wang
e-mail: 107932186@qq.com

Y. Han (ed.), *Advances in Energy and Environmental Materials*,
Springer Proceedings in Energy, https://doi.org/10.1007/978-981-13-0158-2_60

Keywords Functional chelator · Mineral admixture · Salt freeze-thaw
Cement based-materials

Introduction

In the snowy seasons, the surface of concrete pavement is always covered with snow and ice, and results in a lot of traffic inconveniences such as road slipper, slow driving, etc. With respect to this problem, chlorine salt is normally employed to de-ice and thaw snow due to its effect on the decreasing freezing point of the ice [1]. When the concrete road is permeated with the melting snow and chlorine salt, the concrete would be subjected to freeze-thaw (F-T) cycles and chloride ion erosion. This salt F-T will exacerbate the internal structural damage, leading to the rapid loss of concrete strength, the serious shortening of the concrete service life [2, 3].

The destruction of concrete by salt F-T is a special form, while the combined action of F-T and salt is more severe than pure F-T destroy. It may be the result of the hygroscopic effect and water holding capacity of the deicing salt greatly increase the concrete saturation degree and shorten saturation time. For instance, concrete specimens can only be saturated at 77% relative humidity in the NaCl solution. Moreover, it will be difficult to removal moisture in concrete, so that the concrete is in a saturated state for a long time, which could increase the extent of F-T damage of concrete [4–6].

In order to solve the destroy of salt F-T, a great deal of research has been reported. Marchand [7] investigated the salt F-T resistance of three kinds of concrete with the water cement ratio of 0.25, 0.35 and 0.45, the results indicated that the smaller the water cement ratio was, the less the denudation of concrete surface was under salt John [8] discovered that the air bubble spacing was controlled to 250–300 μm, the salt F-T resistant of concrete is the best. When the air bubble spacing is larger than the critical value, the ability of salt F-T resistance would decrease. Pigeon [9] observed the microscopic structure of concrete found that the density of concrete could be improved by fly ash, when the FA content is less than 30%, it is beneficial to the frost resistance of concrete. Although these methods can improve the salt F-T resistant ability of concrete, the frost resistance could hardly be controlled. Therefore, it is important to choose a ideal method to control salt F-T damage on concrete. Recently, some researchers have used functional chelator to improve the internal pores and heal internal cracks of concrete [10]. However, there is few work on the application of functional chelator to the salt F-T resistance of concrete.

This paper mainly investigated the effects of the function chelator and mineral admixture on the salt F-T resistance of cement mortar. The salt F-T resistance of mortars was evaluated by mass loss, loss of compressive strength and change of total porosity. The microstructure of mortars with function chelator and mineral admixture after salt F-T cycles was observed by scanning electron microscope (SEM).

Experimental

Materials. Ordinary Portland cement (PO 42.5) was provided by Huaxin Cement Co. LTD. River sand with fineness modulus 2.37. Functional chelator was prepared in our laboratory. Slag grinding (SG) was purchased by Wuhan Wuxin new type building materials Co. LTD. FA (first grade) was supplied by Yangluo power plant.
Preparation of Mortar. The mortar was prepared with the proportion in Table 1, the mortars were cast in molds with dimensions of 70.7 mm × 70.7 mm × 70.7 mm which were used for mass loss, compressive strength and total porosity test respectively. 18 samples were tested before salt F-T and 72 samples were tested during the salt F-T, a total of 90 samples was prepared.
Salt F-T Cycles Test. The sample was cured in the standard curing room for 24 day with a controlled temperature of 20 ± 2 °C and a RH 95%. After 24d, the curing mortar was absorbed in the NaCl solution of 3% mass fraction for 4d and then F-T experiment began. The level of the soaking liquid above the sample surface was kept at least 20–30 mm.

Salt freezing test was carried out by "quick freezing method", the sample was put in a plastic box before freeze-thaw, 3% NaCl was injected into the box, and kept the liquid level altitude was 1–2 cm higher than the top of the sample, then a plastic box was placed in low temperature; the time of freeze-thaw cycle was 4–8 h, the F-T time would not be less than 1–2 h. In this process, the lowest temperature of sample center had to be controlled at −18 ± 2 °C, the highest temperature was 15 ± 2 °C. The salt F-T test was a 100-time-cycles, the sample was tested every 25 cycles.

Table 1 Proportions of the mortar mixes

Cement (g)	Water (g)	Sand (g)	Chelator (g)	SG (g)	FA (g)
400	200	1200	–	–	–
400	200	1200	0.8	–	–
400	200	1200	2	–	–
320	200	1200	2	80	–
320	200	1200	2	–	80
400	200	1200	4	–	–

Properties Test

Mass Loss Rate. The ratio of mass loss can be calculated via Eq. 1.

$$\Delta W_{ni} = (W_{0i} - W_{ni})/W_{0i} \times 100\%. \quad (1)$$

where, W_{0i} is the mass of the samples without salt F-T; W_{ni} is the mass after N times of salt F-T cycles; ΔW_{ni} is the mass loss rate.

Compressive Strength Loss. The percentage of compressive strength decreased can be calculated via Eq. (2).

$$\Delta f_c = (f_{c0} - f_{cn})/f_{c0} \times 100\%. \quad (2)$$

where, f_{c0} is the compressive strength of samples without salt F-T cycles; f_{cn} is the compressive strength after N time of salt F-T cycles; Δf_c is the compressive strength loss rate.

Total Porosity. The determination of porosity using "saturated water dosages method", It means put the mortar in water and place 10 h to fully saturated, weighing the quality of sample, and then weighing the drying quality of the sample which under 105 °C (12–14 h) drying to constant weight [11, 12]. The total porosity of mortar can be calculated via Eq. (3).

$$\rho = (M_0 - M_i)/\rho_w V \times 100\%. \quad (3)$$

where, M_0 is fully saturated mortar mass; M_i is after drying of mortar mass; V is mortar volume ρ_w is density of water, ρ is total porosity. Moreover, the percentage of total porosity growth can be calculated via Eq. (4).

$$\rho^* = (\rho_n - \rho_0)/\rho_0 \times 100\%. \quad (4)$$

where, ρ_0 is the total porosity which without salt F-T cycle; ρ_n is total porosity after the N times of salt F-T cycle; ρ^* is total porosity growth rate.

SEM. The SEM was used to investigate the microstructure of mortars before and after salt F-T cycles. Small pieces of mortar specimens with the dimension of 5 mm × 5 mm × 5 mm were stored in 105 °C oven for a day to remove moisture. The specimen was sputter coated with Pt, and the prepared specimens were observed using QUANTA FEG 450 SEM.

Results and Discussion

Effect of Functional Chelator on Salt F-T Resistance of Mortar

Mass loss. Figure 1 shows the mass loss of mortars without or with functional chelator during salt F-T cycles. It can be seen from Fig. 1, when the dosage of functional chelator is 0.5%, the effect of salt F-T resisting is the best. After 100 salt F-T cycles, the ordinary mortar loss rate is 14.45%, and the mass loss rate of the mortar with 0.5% functional chelator is only 11.03%, which compared with the ordinary mortar decrease by 23.7%.

Compressive Strength Loss. Compressive strength of mortar with functional chelator at curing 28 days is shown in Fig. 2. It can be seen from Fig. 2, the compressive strength of mortar with functional chelator is stronger than the ordinary mortar, the mortar with 0.5% functional chelator compressive strength is 39.3 MPa, and the ordinary mortar compressive strength is only 31.7 MPa.

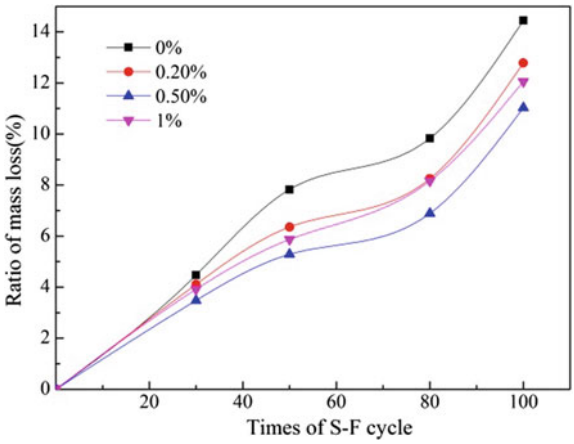

Fig. 1 Mass loss of mortars with functional chelator during salt F-T cycles

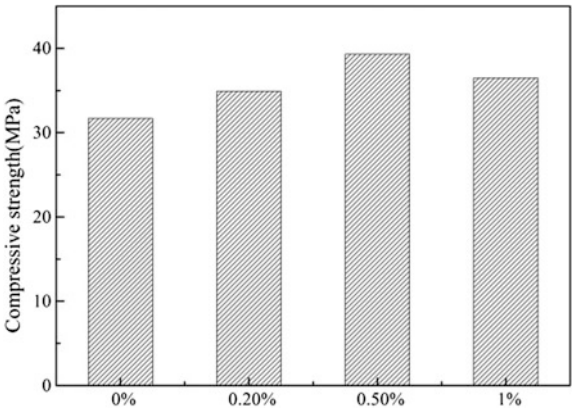

Fig. 2 Compressive strength of mortars with functional chelator

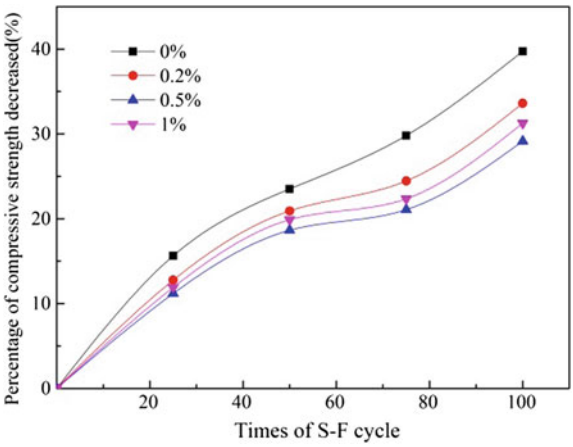

Fig. 3 Compressive strength loss of mortars with functional chelator during salt F-T cycles

Figure 3 displays the compressive strength loss of mortars without or with functional chelator during salt F-T cycles. The functional chelator can effectively reduce the compressive strength loss of mortar in the salt F-T cycles. After 100 salt F-T cycles, the ordinary mortar compressive loss rate is 39.74%, and the mortar with 0.5% functional chelator loss rate is 29.13%.

Total Porosity Change. The total porosity of mortars with functional chelator after curing 28 days is presented in Fig. 4. As can be seen from Fig. 4, the total porosity of mortar with functional chelator is significantly lower than the ordinary mortar. In a certain range, the total porosity will decrease when the dosage of functional chelator is increased, but the porosity will increases when the functional chelator is 1%. The dosage of functional chelator is 0.5%, the total porosity is 13.37%, which compared with the ordinary mortar decrease by 28%.

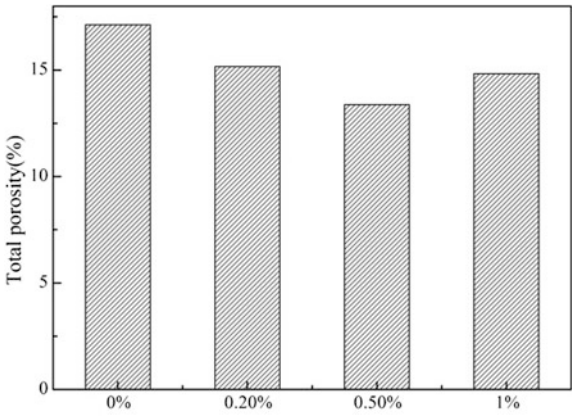

Fig. 4 Total porosity of mortars with functional chelator

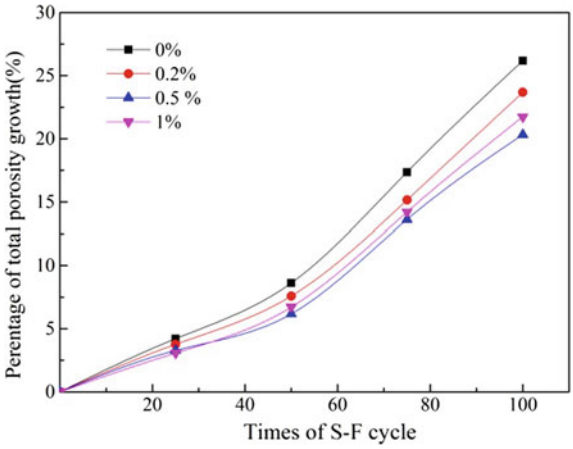

Fig. 5 Total porosity growth of mortars with functional chelator during salt F-T cycles

Figure 5 shows the total porosity growth of mortars without or with functional chelator during salt F-T cycles. As can see from Fig. 5, the mortar with functional chelator in the growth of total porosity is less than the ordinary mortar. The mortar with 0.5% functional chelator has strong ability to resist the salt F-T. After 100 salt F-T cycles, the mortar with 0.5% functional chelator that total porosity increases rate is 20.33%, and the ordinary mortar that total porosity increases rate is 26.18%.

Effect of Functional Chelator and Mineral Admixtures on Salt F-T Resistance of Mortar

Mass Loss. Figure 6 shows the mass loss of mortars with functional chelator and mineral admixtures during salt F-T cycles. As can be seen from Fig. 6, the combination of functional chelator and mineral admixtures has better effect on the mass loss of mortar. The mortar with functional chelator and SG can effectively slow

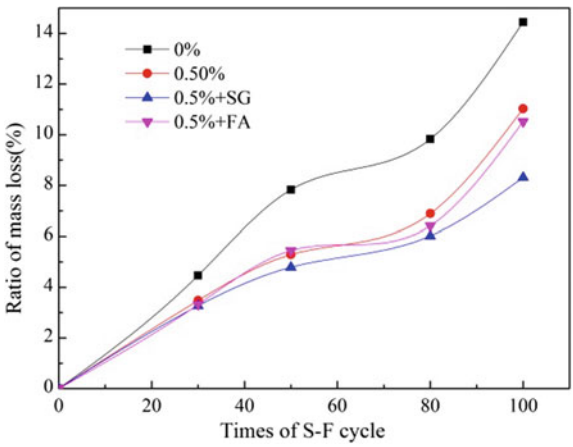

Fig. 6 Mass loss of mortars with functional chelator and mineral admixtures during salt F-T cycles

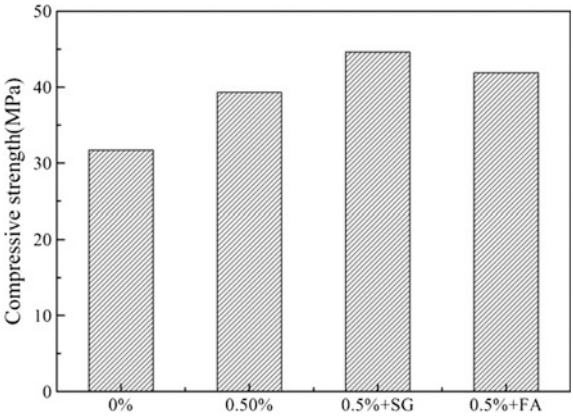

Fig. 7 Compressive strength of mortars with functional chelator and mineral admixtures

down mass loss in salt F-T cycles. After 100 salt F-T cycles, the mass loss rate of mortar with functional chelator and SG is only 8.31%, and the ordinary mortar mass loss rate is 14.45%.

Compressive Strength Loss. Figure 7 shows the compressive strength of mortars with functional chelator and mineral admixtures at curing 28 days. It is found that mortars with functional chelator and mineral admixtures have higher compressive strength. The compressive strength of mortar with functional chelator and SG is the strongest. The mortar with functional chelator and SG compressive strength reached 44.6 MPa, which compared with the ordinary mortar decrease by 40.7%. FA gives lower compressive strength than SG, this is because there are many harmful pores in the mortar that affect the compressive strength, and the ability of filling this pores with FA is weaker than that of SG.

Figure 8 displays the compressive strength loss of mortars with functional chelator and mineral admixtures during salt F-T cycles. As can be seen from Fig. 8, the mortar with functional chelator and mineral admixtures has higher compressive

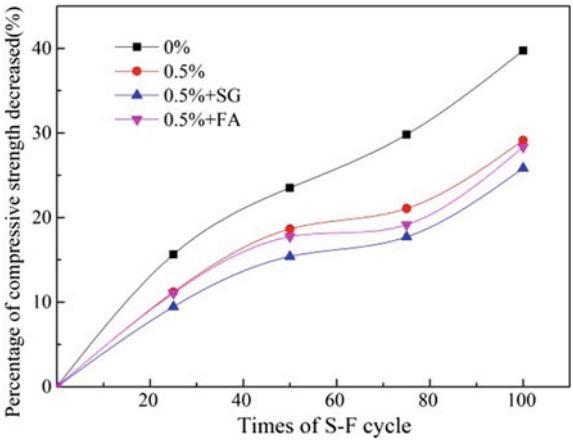

Fig. 8 Compressive strength loss of mortars with functional chelator and mineral admixtures during salt F-T cycles

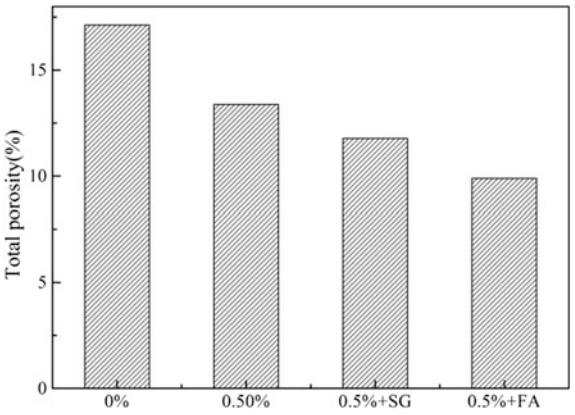

Fig. 9 Total porosity of mortars with functional chelator and mineral admixtures

strength than the mortar only with functional chelator after salt F-T cycles. The compressive strength loss rate of mortars with functional chelator and SG, FA is 25.84 and 28.33% respectively after 100 salt F-T cycles. FA gives higher strength loss than SG, this is because the harmful pores filled with FA is less than the SG, the mortar is not dense inside, the internal of mortar is easy to occur F-T damage.

Total porosity change. Figure 9 shows the total porosity of mortars with functional chelator and mineral admixtures at curing 28 days. As can see from Fig. 9, the mortar with functional chelator and mineral admixtures have lower total porosity, especially the mortar with functional chelator and FA. The total porosity of mortars with functional chelator and FA is only 9.89%, which compared with the ordinary mortar decrease by 42%.

Figure 10 shows the total porosity growth of mortars with functional chelator and mineral admixtures during salt F-T cycles. As can see from Fig. 10, the mortar with functional chelator and mineral admixtures resulted in relatively small change

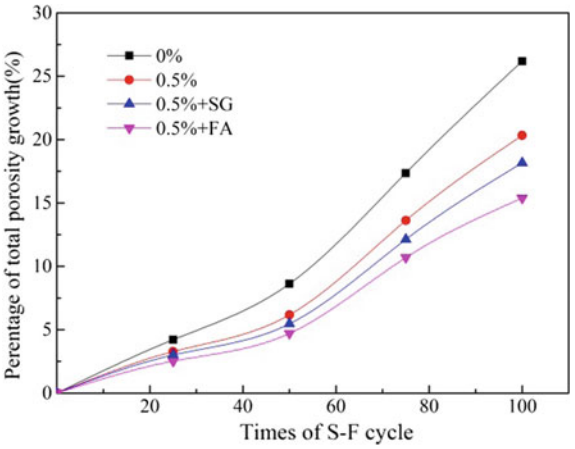

Fig. 10 Total porosity growth of mortars with functional chelator and mineral admixtures

in total porosity after salt F-T cycles. The total porosity growth ratio of mortar with functional chelator and SG, FA is 18.17 and 15.39% after 100 salt F-T cycles. Due to the FA is thinner than cement, it can enhance salt F-T resistance of mortars by the improvement of the internal pore structure.

Microstructure of Mortar after Salt F-T Cycles. The SEM images of mortars after 100 salt F-T cycles are shown in Fig. 11. As can see from Fig. 11, the ordinary mortar has appeared a clear and smooth crack with nothing in the middle of it. The

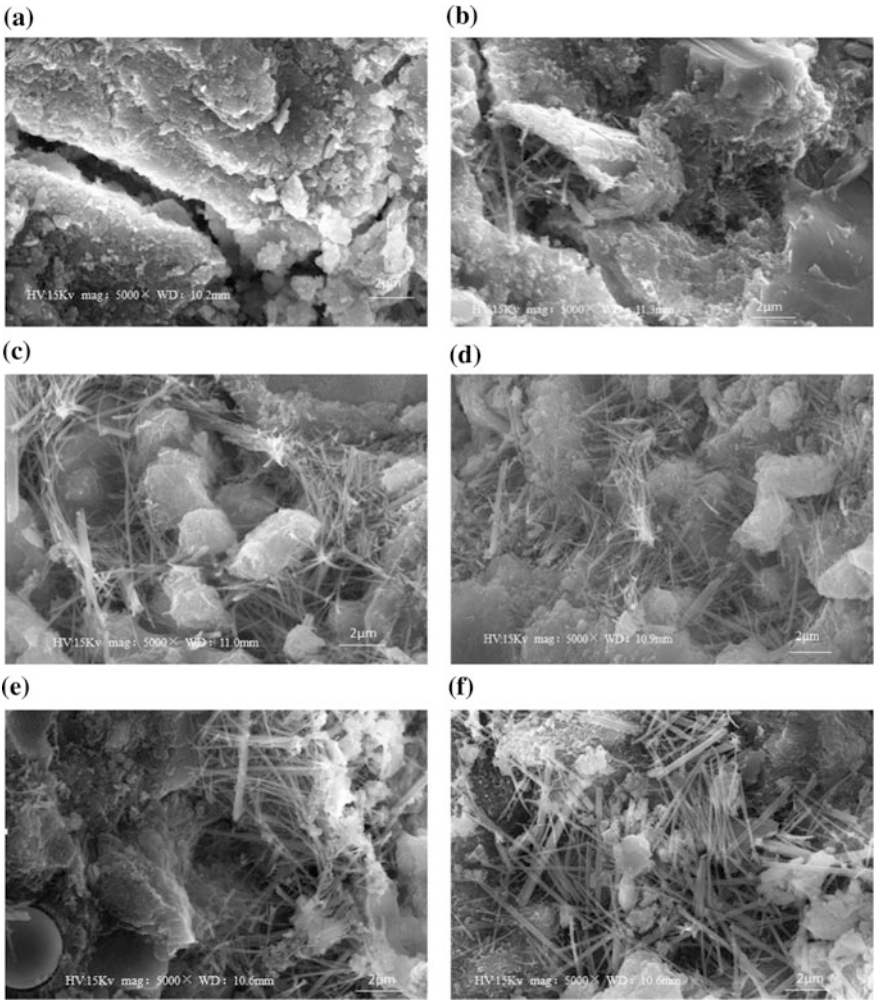

Fig. 11 SEM images of mortars with functional chelator and mineral admixtures **a** ordinary mortar; **b** mortar containing 0.2% chelator; **c** mortar containing 0.5% chelator; **d** mortar containing 0.5% chelator and 20% SG; **e** mortar containing 0.5% chelator and 20% FA; **f** mortar containing 1% chelator

mortar with functional chelator has smaller cracks internal and the crystalline is formed to repair the cracks. The crack of the mortar with 0.5% functional chelator was surrounded by lots of crystalline needle. The crystalline of the mortar with functional chelator and SG, FA is more than the mortar only with functional chelator.

Conclusion

The function chelator can improve the salt F-T resistance of mortar. Comparing with ordinary mortar, the mass loss of mortar with 0.2, 0.5 and 1% function chelator has reduced 11.5, 23.7 and 16.5% respectively after 100 salt F-T cycles. Moreover, after salt 100 F-T cycles, the compressive strength loss of ordinary mortar is 39.74%, but that of mortar with 0.2, 0.5 and 1% function chelator is 33.61, 29.13 and 31.27% respectively. From above analysis, the mortar with 0.5% functional chelator has better F-T resistance.

The salt F-T resistance of mortar can be further improved by function chelator and mineral admixtures. For the total porosity growth during 100 salt F-T cycles, addition of SG and FA dropped the mortar with the function chelator, 11.9 and 24.3% respectively relative to the mortar only with function chelator.

From the SEM analysis, the functional chelator and mineral admixtures can improve microstructure of mortars. The mineral admixtures can fill the pores of the mortar, and the crystal could repair the crack of mortar to make the interior structure denser after salt F-T cycles.

Acknowledgements This work is supported by the National Key R&D Program of China (No. 2017YFB0309905). The authors gratefully acknowledge financial support.

References

1. Z.H. Li, H.J. Ba, Study on the freeze-deicing salt resistance of the pavement concrete. J Sichuan Univ. **74**(10), 911–918 (2008)
2. J. Marchand, R. Pleau, M. Pigeon, Precision of tests for assessment of the deicer salt scaling resistance of concrete. Cem. Concr. Aggregates **18**(2), 85–91 (1996)
3. Q.B. Yang, Factors influencing the pressure of ice formation in NaCl solution. J. Build. Mater. **8**(5), 495–498 (2005)
4. J. Marchand, M. Pigeon, D. Bager et al., Influence of chloride solution concentration on deicer salt scaling deterioration of concrete. Aci Mater. J. **96**(4), 429–435 (1999)
5. J.J.V. Ii, G.W. Scherer, A review of salt scaling: II. Mechanisms. Cem. Concr. Res. **37**(7), 1022–1034 (2007)
6. M.A. Glinicki, M. Zielinski, Frost salt scaling resistance of concrete containing CFBC fly ash. Mater. Struct. **42**(7), 993–1002 (2009)
7. J. Marchand, M. Pigeon, D. Bager et al., Influence of chloride solution concentration on deicer salt scaling deterioration of concrete. Aci Mater. J. **96**(4), 429–435 (1999)

8. J.J.V. Ii, G.W. Scherer, A review of salt scaling: I. Phenomenology. Cem. Concr. Res. **37**(7), 1007–1021 (2007)
9. M. Pigeon, C. Talbot, J. Marchand et al., Surface microstructure and scaling resistance of concrete. Cem. Concr. Res. **26**(10), 1555–1566 (1996)
10. M. Roig-Flores, S. Moscato, P. Serna et al., Self-healing capability of concrete with crystalline admixtures in different environments. Constr. Build. Mater. **86**(6), 1–11 (2015)
11. V.T. Ngala, C.L. Page, L.J. Parrott et al., Diffusion in cementitious materials: II, further investigations of chloride and oxygen diffusion in well-cured OPC and OPC/30% PFA pastes. Cem. Concr. Res. **25**(4), 819–826 (1995)
12. V.T. Ngala, C.L. Page, Effects of carbonation on pore structure and diffusional properties of hydrated cement pastes. Cem. Concr. Res. **27**(7), 995–1007 (1997)

Physical and Chemical Properties of Rejuvenating Aged Binder with Waste Cooking Oil and Its Bioasphalt

Guiwen Wan, Meizhu Chen, Shaopeng Wu, Dong Zhang, Jingxiang Liu and Siqing Liu

Abstract WCO-based bioasphalt is prepared from waste cooking oil (WCO) by filter, deodorant, viscosity reduction, methyl ester and distillation. The objective of this study was to investigate the properties of rejuvenating aged asphalt binder with WCO-based bioasphalt and waste cooking oil. The materials used for this study included one virgin asphalt, aged asphalt (from virgin asphalt by thin film oven test and pressure aging vessel), waste cooking oil and its bioasphalt with five percentages (0, 3, 5, 7 and 9% of aged asphalt). The physical and rheological properties of these rejuvenated asphalts were tested including penetration, softening point, ductility, rotational viscosity, complex modulus and phase angle, creep stiffness (S) and creep rate (m-value). The chemical characteristics were evaluated using Fourier Transforms Infrared Spectroscopy (FTIR). The results indicate the physical and rheological properties of rejuvenate asphalts are closed to that of virgin asphalt with the dosages increased. Besides, the low temperature performance of rejuvenated asphalts is better compared with the aged asphalt while the high temperature anti-rutting performance need to be further improved. The carbonyl and sulfoxide indexes of rejuvenated asphalts are significantly lower than that of aged asphalt. In addition, the regenerated asphalts containing waste cooking oil show better performance than the ones containing WCO-based bioasphalt at the same

G. Wan · M. Chen (✉) · S. Wu · D. Zhang · J. Liu · S. Liu
State Key Laboratory of Silicate Materials for Architectures, Wuhan University of Technology, Wuhan 430070, China
e-mail: chenmzh@whut.edu.cn

G. Wan
e-mail: wanguiwen@whut.edu.cn

S. Wu
e-mail: wusp@whut.edu.cn

D. Zhang
e-mail: pytmac@whut.edu.cn

J. Liu
e-mail: liujingx@whut.edu.cn

S. Liu
e-mail: liusiqing@whut.edu.cn

Y. Han (ed.), *Advances in Energy and Environmental Materials*,
Springer Proceedings in Energy, https://doi.org/10.1007/978-981-13-0158-2_61

condition. Thus, the light components can be separated from the waste cooking oil and used for other purposes, which makes the waste cooking oil have a reasonable use and broaden the application way.

Keywords Asphalt binder · Aging · Rejuvenating · Waste cooking oil
WCO-based bioasphalt · Property research

Introduction

With the increasing of environmental consideration and materials costs, reclaimed asphalt pavement materials have been widely promoted because of the environmental benefits and costs reduction. It is reported that there are 500 million tons of asphalt produced in USA [1]. At present, the materials for the asphalt recycling are soft asphalt, foam asphalt, asphalt emulsion, rejuvenators. Among them, the regeneration is generally composed by the distillation products of crude oil and other mineral oil rich in aromatic hydrocarbon or resin. Many researchers have investigated the effects of these rejuvenators on the performance of asphalt binder and made some achievements [2]. Recently, waste products such as recycled waste cooking oil (WCO) were applied to rejuvenate aged asphalts [3]. According to the asphalt rejuvenating theory [3], WCO, low viscosity oil, is similar to the light oil components of asphalt and can be used as the rejuvenator of aged asphalts.

There are some researches about using the WCO to modify and regenerate asphalt. Su [4] researched the possibility of using microcapsules containing WCO to rejuvenate asphalt. The results indicate WCO can rejuvenate aged asphalt and has good thermal stability. Chen [5] investigated the physical, chemical and rheological properties of waste edible vegetable oil rejuvenated asphalt. The results indicate that waste edible vegetable oil can be used to regenerate asphalt but should be at a reasonable dosage of waste oil. Luo [6] investigated the properties of asphalt with WCO and polymer. The results indicate that asphalts containing WCO and polymer have better storage stability and can be used in pavement. Asli [3] investigated the physical properties of aged asphalt with WCO. The results indicate that that WCO can restore the physical properties of aged asphalt and the properties of rejuvenate asphalts are better than that origin asphalt.

But in some cases, the WCO has not been fully used. The study found that the WCO produced in China is about 5–7.5 million tons every year and only 4 million tons can be collected as a recycled resource [7]. The WCO-based bioasphalt was produced by WCO through filter, deodorant, viscosity reduction, methyl ester and distillation. There are some researches that WCO-based bioasphalt was used to modify asphalt and found that it has better performance. And bioasphalts from different sources have different effects on the petroleum asphalt [8]. Gong [9] used the sessile drop device (SDD) and atomic force microscopy (AFM) to research the bioasphalt. Then, the results indicate that bioasphalt be added into asphalt would produce different impacts on surface properties for different base asphalts. Han [10]

investigated the properties of asphalt binder when the rice hush and bio-oil was added and its optimum content, which indicates that the modified asphalt has a better performance. There are also some other bioasphalts obtained from rice husk ash and use it to rejuvenator asphalt [11].

In view of the research above, little information is available comparing the effect of WCO and WCO-based bioasphalt to aging asphalt. The WCO-based bioasphalt is heavy components of the WCO. In this study, the properties of rejuvenated asphalt by WCO-based asphalt were studied and compared with WCO. So that it makes us have a deeper understanding about the application of WCO and also can expand the way of application. Besides, the light components were separated from WCO and could be used for other purposes, which not only increases the utilization of WCO but also makes it have a rational application.

Materials and Experimental Methods

Materials

Waste Cooking Oil and Its Bioasphalt. WCO was collected from restaurant in this study, which was processed using a simple filtering. The WCO-based bioasphalt was produced by WCO through the filter, deodorant, viscosity reduction and methyl ester treatment, which is the heavy component of WCO. The viscosity values (25 °C) of WCO and WCO-based bioasphalt are 0.046 and 2.76 Pa s, respectively. The components of WCO and WCO-based bioasphalt were analyzed using the Fourier Transforms Infrared Spectroscopy (FTIR) tests and SARA (saturates, aromatics, resins and asphaltenes) fractions. The result indicates that WCO contains a lot of fatty acids and it is aromatic oil, Table 1 shows the SARA (saturates, aromatics, resins and asphaltenes) fractions of WCO and its bioasphalt. Figure 1 shows that WCO is yellow but WCO-based bioasphalt is black because some of the light components in the WCO-based bio-asphalt have been fractionated.

Table 1 SARA fractions of WCO and its bioasphalt

Content (%)	Saturates	Aromatics	Resins	Asphaltenes
WCO	4.60	65.18	27.03	3.19
Bioasphalt	3.34	20.06	67.05	9.57

Fig. 1 WCO (left) and WCO-based bioasphalt (right)

Table 2 Properties of virgin asphalt

Asphalt binder	Asphalt grade	Penetration (25 °C, 0.1 mm)	Softening point (°C)	Ductility (15 °C, cm)	Brookfield viscosity (135 °C, Pa s)
70#	60–80	62	48.3	>500	0.45

Virgin Asphalt. One asphalt binder 70# was used in this study, which is extensively utilized in China. Its basic properties were tested and shown in Table 2.

Aged Asphalt Binder. The aged asphalt was prepared by virgin asphalt using the thin film oven test (TFOT) and pressurized aging vessel (PAV) test. TFOT, stimulating short term aging of asphalt, was conducted at 165 °C for 5 h. PAV, stimulating long term aging of asphalt, was conducted at 100 °C for 20 h. The aged asphalt binder was obtained from virgin asphalt aged by PAV after TFOT.

Experimental Plan. Rejuvenated asphalt binders were prepared as the following process. Firstly, the aged asphalt was heated to 135 °C. And then WCO with different dosages was added to the aged asphalt, which is the WCO rejuvenated asphalts. Similarly, WCO-based bioasphalt was added to the asphalt with different dosages, which are the WCO-based bioasphalt rejuvenated asphalts. The dosages of WCO and WCO-based bioasphalt were 0, 3, 5, 7, 9 wt%, respectively. Figure 2

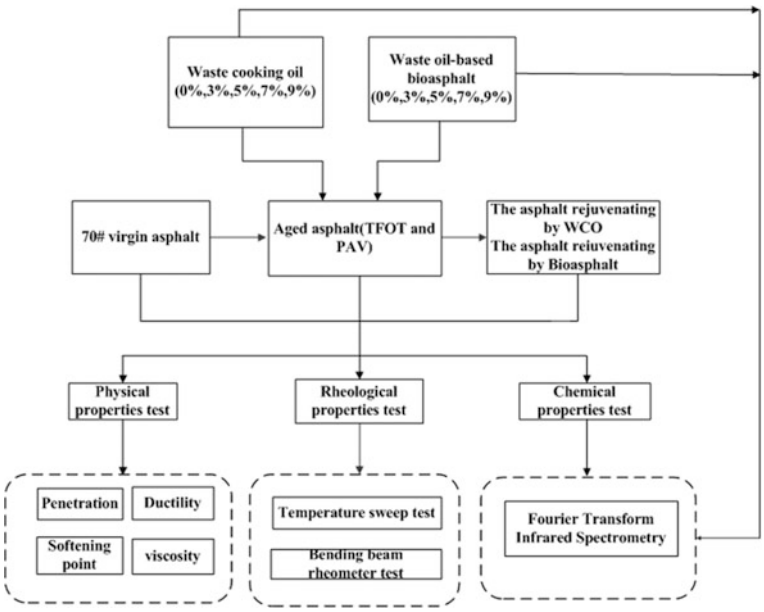

Fig. 2 The flow chart of the experimental program

shows the experimental plan and the logical relationship between materials, experiment and performance clearly.

Test Methods

Conventional Physical Properties Test. The conventional physical properties of asphalt were evaluated using penetration, softening point, ductility and rotational viscosity, in accordance with JTG E20T0604, JTG E20 T0606, JTG E20 T0605, JTG E20 T0625, respectively. The temperature to test the penetration and ductility are 25 and 15 °C, respectively. At the same time, the temperature to test viscosity is 135 °C.

Rheological Properties Test. The rheological properties of asphalt were evaluated using dynamic shear rheometer (DSR) and bending beam rheometer (BBR) tests. In this paper, the DSR test conditions are 25 mm diameter plates and 1 mm gap. The complex modulus and phase angle obtained from the temperature sweep tests at the temperature range from −10 to 80 °C [12]. The creep stiffness (S) and creep rate (m-value) obtained from the BBR tests at −12 °C [13].

Chemical Properties Test. The chemical properties and the structure of the asphalts were explored using fourier transform infrared (FTIR) in this study and the wavenumber ranged from 4000 cm −1 to 500 cm −1. The asphalt sample was dissolved by carbon disulfide on the KBr pellet and then it was measured on the FTIR.

Results and Discussions

Physical Properties

Penetration. The penetration of asphalt can indicate the soft and hard degree of asphalt. The asphalt is harder with smaller penetration value. Figure 3 indicates that the penetration values at 25 °C of rejuvenated asphalt with different regenerators and different dosages. It can be clearly observed from the Fig. 3 that the penetration values increase as increasing the dosages of WCO and WCO-based bioasphalt, respectively, which implies that WCO and WCO-based bioasphalt can soften the aged asphalt. But the regenerated asphalts containing WCO-based bioasphalt shows lower penetration than the one containing WCO at the same dosages, which is due to the difference components between WCO and WCO-based bioasphalt. Aged asphalt has more resins and asphaltenes but less aromatics content, the main component of the rejuvenator to aged asphalt is aromatics. The SARA fractions of WCO and its bioasphalt show that the aromatics content of WCO higher than WCO-based bioasphalt. However, two different kinds of rejuvenated asphalt can meet the road performance requirements.

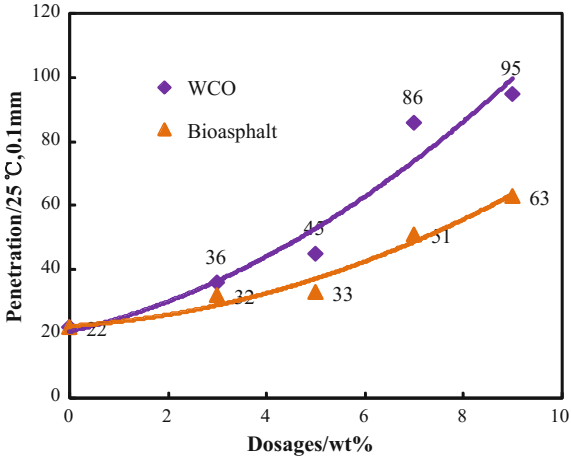

Fig. 3 Penetration of rejuvenated asphalt by WCO and bioasphalt with different dosages

Softening Point. The softening point can reflect the viscosity and the temperature sensitivity of asphalt. The temperature sensitivity increases and the ability to resist high temperature deformation decreases with the softening point decreasing. Figure 4 shows that the effects of WCO and WCO-based bioasphalt on softening point of aged asphalt. Softening point values of asphalts decrease as increasing the dosage of WCO and WCO-based bioasphalt, which indicates that aged asphalt was softened by WCO and WCO-based bioasphalt just like penetration test. However, the ability of resisting high temperature deformation declines. So, the dosage of WCO and WCO-based bioasphalt should to be at a reasonable range. The regenerate asphalts containing WCO shows lower softening point than the one containing WCO-based bioasphalt at the same dosage. This is due to the WCO containing higher aromatics than WCO-based bioasphalt. The main component in the softening effect to aged asphalt is aromatics.

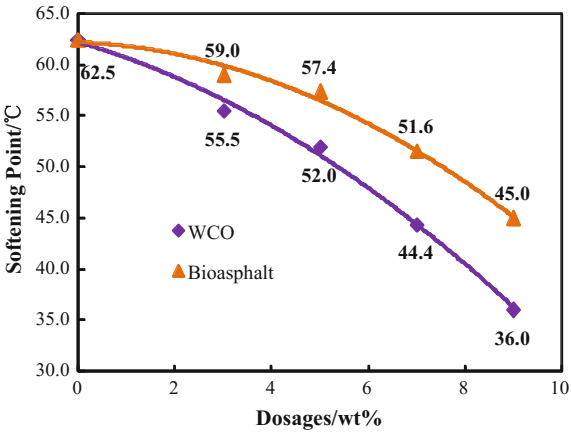

Fig. 4 Softening point of rejuvenated asphalt by WCO and bioasphalt with different dosage

Table 3 Influences of WCO and Bioasphalt on ductility of aged asphalt at 15 °C

Dosage (%)	0	3	5	7	9
WCO (cm)	57	187	>500	>500	>500
Bioasphalt (cm)	57	91.7	111.7	>500	>500

Ductility. Ductility can reflect the ability to resist deformation under external forces of asphalt, which represents the flexibility of asphalt. The ability to resist external force stretching of asphalt is better with the ductility value increasing, which indicates that the flexibility is better. Table 3 shows that the ductility value increases with increasing the dosage of WCO and WCO-based bioasphalt and the ductility is greater than 500 cm when the dosages are 7–9 wt%. There also have different effects between two regenerations. The rejuvenated asphalts containing WCO-based bioasphalt shows lower ductility values than the one containing WCO at the same dosage. The flexibility of the two kinds of rejuvenated asphalts is very well, which indicates that WCO and WCO-based bioasphalt can improve the low temperature crack resistance of asphalt, which is consistent with the experimental results of above.

Viscosity. Viscosity is the characterization of asphalt's ability to resist shear deformation under external force and the viscosity at 135 °C has great significance to the mixing temperature of asphalt. Figure 5. illustrates that the effect of different regenerations and dosages on viscosity of aged asphalt. The viscosity of aged asphalt decreased as the dosages of rejuvenator increased, which indicates that WCO and WCO-based bioasphalt can reduce the mixing temperature and the compaction temperature of the asphalt mixture. This result shows that both WCO and WCO-based bioasphalt can soften the aged asphalt, which is consistent with the experimental results of softening point and penetration. It also can be found that the viscosity values of recycled asphalts by WCO lower than that of recycled by WCO-based bioasphalt. The high temperature performance of rejuvenated asphalts

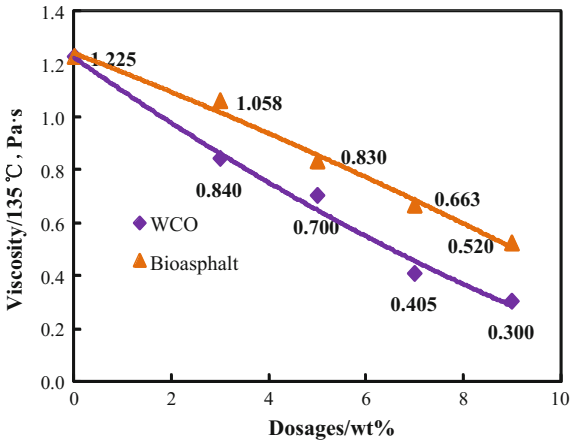

Fig. 5 Viscosity of rejuvenated asphalt by WCO and bioasphalt with different dosage at 135 °C

decreases if the dosage too large. The adhesion between asphalt and aggregate decreases when the dosage too small. The contents of SARS have a proportion, the viscosity content will be too much if the content of light component is too high. So, the dosage of WCO and WCO-based bioasphalt should be controlled in 7 and 9 wt%, respectively.

Rheological Properties

High Temperature Rutting Resistance Factor (G*/sin δ). Rutting resistance factor (G*/sin δ) reflects the unrecoverable deformation of asphalt [14]. The ability of the asphalt to resist deformation at high temperatures increases with the rutting factor increasing. Figure 6 indicates that the rutting factor of aged asphalt is the highest at the same temperature, which indicates that asphalt aging is beneficial to resist rutting performance and also can improve the ability of asphalt to resist high temperature deformation in summer. The rutting factor declined when the WCO and WCO-based bioasphalt were added. Besides, when the temperature is less than 50 °C, the rutting factor declines faster while this trend gentle at the higher temperature. The regenerated asphalt containing WCO shows lower rutting resistance factor than the ones containing WCO-based bioasphalt at the same dosage, which indicates that the ability to resistant rutting declines with adding the WCO and WCO-based bioasphalt. So, the content of WCO and WCO-based bioasphalt should to be at a reasonable range.

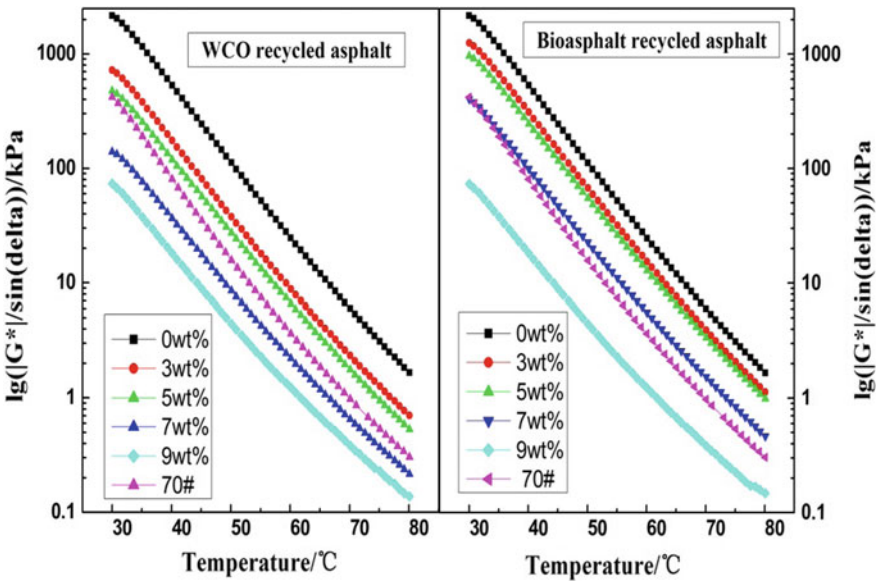

Fig. 6 lg(|G*|/sin δ) versus temperature for asphalt with different rejuvenators and different dosages

High Temperature Phase Angle. The high temperature phase angle obtained from temperature sweep tests at the temperature range from 30 to 80 °C. The phase angle value indicates that the content of the viscosity components and the elastic components of asphalt. The viscosity components increase and the elastic components decrease with the phase angle values increasing, which indicates that the asphalt has more opportunity to occur permanent deformation. Figure 7 indicates that the phase angle of aged asphalt decreases obviously, which indicates that the elastic components increase. The phase angle increased when the WCO and WCO-based bioasphalt were added and it was higher with the dosage increasing, which indicates that the viscosity composition increase and the elasticity components reduce. Figure 7 also illustrates that the phase angle of the rejuvenated asphalts are always lower than that of original asphalt when the dosage of WCO and WCO-based bioasphalt are 3–9 wt%. However, the phase angle values of rejuvenated asphalts are closed to that of the original asphalt when the dosage is 9 wt%. In a word, WCO and WCO-based bioasphalt can increase the viscosity component of aged asphalt and decrease the high temperature performance, which is consistent with the previous experimental results.

High Temperature Complex Modulus. The complex shear modulus (G*) can be considered as the asphalt sample's total resistance to deformation when repeatedly sheared [15]. The greater the complex modulus values, the better elasticity of asphalt. Figure 8 illustrates that aged asphalt has the largest complex modulus,

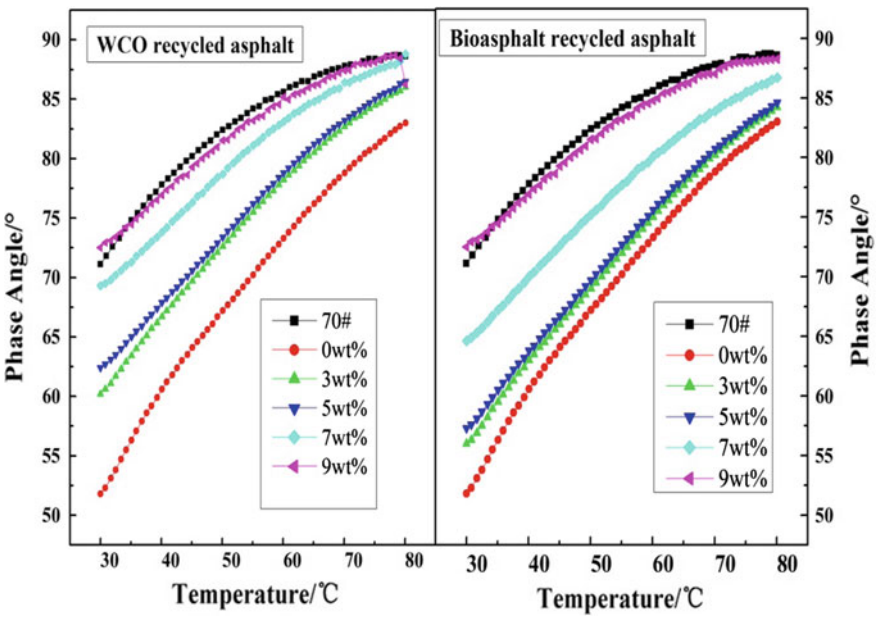

Fig. 7 δ values versus temperature for asphalt with different rejuvenators and different dosages

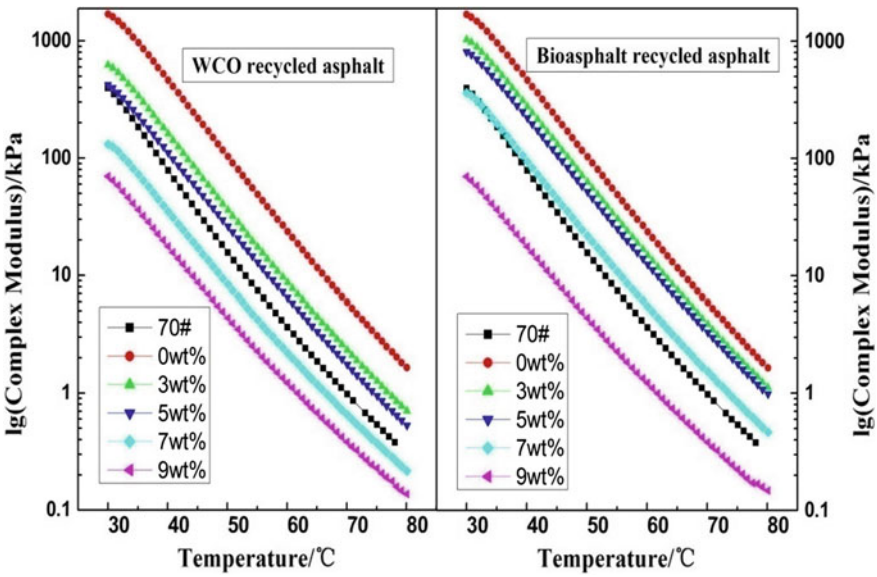

Fig. 8 lg(G*) values versus temperature for asphalt with different rejuvenators and different dosages

which indicates that the elastic recovery performance increases and the anti-rutting performance improves with the aging of asphalt. Figure 8 also shows that the complex modulus values of asphalt decrease with addition the WCO and WCO-based bioasphalt. The values of rejuvenate asphalts are closed to that of the virgin asphalt when 5 wt% WCO or 7 wt% WCO-based bioasphalt was added, respectively. Besides, the regenerated asphalts containing WCO shows lower complex modulus values than the ones containing WCO-based bioasphalt at the same dosages, which indicates that WCO can soften the asphalt and the ability of regenerate asphalts to resist high temperature deformation decline.

Low Temperature Phase Angle. The low temperature phase angle obtained from temperature sweep tests at the temperature range from −10 to 30 °C. Figure 9 illustrates that the phase angle value of aged asphalt is the lowest at the same temperature and the value gradually increases with addition the WCO or the WCO-based bioasphalt. At the same time, the phase angle increases more obvious when the dosages increase. Otherwise, the phase angle values of rejuvenated asphalts were lower than that of original asphalt when 3–7 wt% WCO or 3–9 wt% WCO-based bioasphalt was added. The rejuvenated asphalts containing WCO-based bioasphalt show lower phase angles than the ones containing WCO at the same dosage. Thus, the elastic recovery performance of asphalt with WCO-based bioasphalt is better than that of asphalt containing WCO at a low temperature. Obviously, phase angle values of this rejuvenate asphalts are dependent on the rejuvenator types and components.

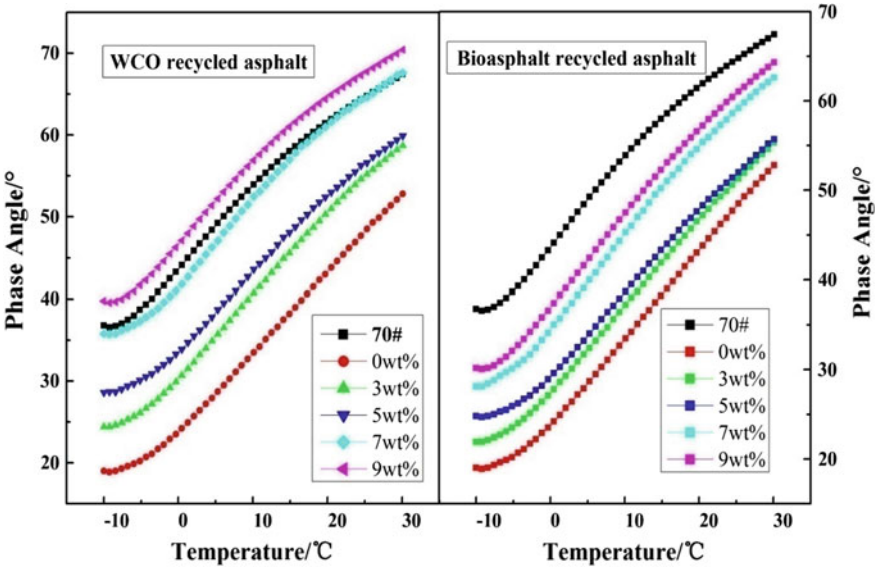

Fig. 9 δ values versus temperature for asphalt with different rejuvenators and different dosages

Low Temperature Complex Modulus. Figure 10 illustrates that the complex modulus values of aged asphalt increase obviously compared with the virgin asphalt. The complex modulus values obviously decreased when WCO and WCO-based bioasphalt were added and this trend gradually reduces as the temperature increases. The complex modulus values of rejuvenated asphalts are larger than that of aged asphalt and it is more obvious as the WCO and WCO-based bioasphalt dosages increasing. The regenerate asphalts containing WCO-based bioasphalt shows larger complex modulus than the ones containing WCO as the same content. In addition, rejuvenator components can remarkably affect the complex modulus value of asphalt in this study.

BBR Test for Evaluating Low-Temperature Performance. For BBR test a small creep load was applied to a binder beam specimen and the creep stiffness (S) and creep rate (m-value) were measured [16]. There are less the elastic components and more viscous components of asphalt with the increasing of S values, which indicates that it is prone to crack and occurring brittle fracture at the low temperatures. The larger of m values of asphalt shows that it has a better crack resistance and the brittleness changed for the better.

Figure 11 illustrates that the S value of aged asphalt is significantly higher than that of virgin asphalt, which indicates that the ability to resist crack decreases and become more brittle as the asphalt aging. This is due to the light components reduction when the asphalt aged. S value was significantly reduced when the WCO or WCO-based bioasphalt was added and this trend decrease with the dosage

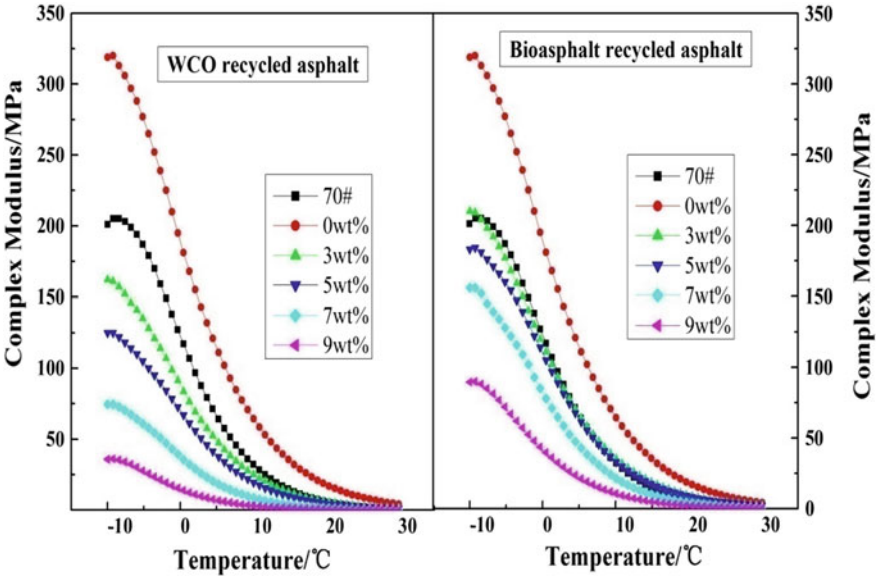

Fig. 10 G*values versus temperature for asphalt with different rejuvenators and different dosages

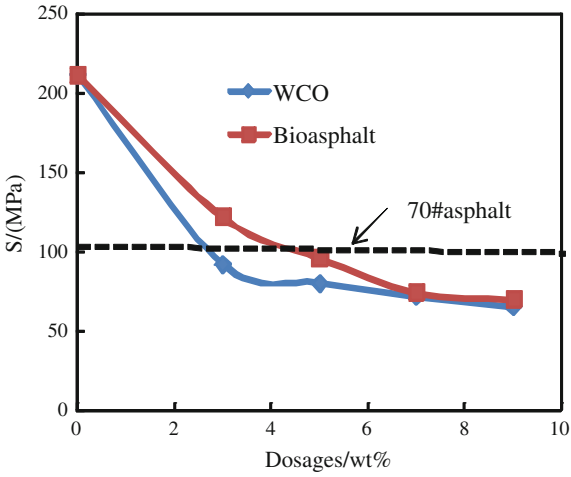

Fig. 11 Influences of WCO and bioasphalt on S value of aged asphalt at −12 °C

increasing, which indicates that the WCO and WCO-based bioasphalt can soften the aged asphalt and make it less prone to brittle fracture at low temperature.

Figure 12 illustrates that the creep rate of aged asphalt is smaller than that of virgin asphalt, which indicates that the strain stability of aged asphalt decreases and it becomes brittle. The creep rate of aged asphalt increased when the WCO or WCO-based bioasphalt was added, which indicates that both the WCO and

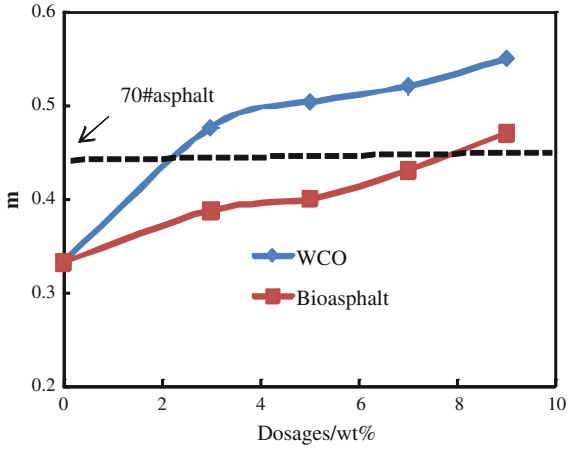

Fig. 12 Influences of WCO and bioasphalt on m value of aged asphalt at −12 °C

WCO-based bioasphalt can increase the flexibility of asphalt and the ability of resistance low-temperature cracking was improved. This result is consistent with the creep stiffness.

Fourier Transform-Infrared Spectroscopy (FTIR). Infrared spectroscopy can characterize the functional groups and molecular structures of asphalt and regeneration. In this study, the Fourier Transform Infrared (FTIR) Spectroscopy tests were used to evaluate the influence of regeneration contents and types on the microstructure of recycled asphalt, which can help us understanding the regeneration mechanism.

Figure 14 shows that rejuvenated asphalts have two new peaks, which appear at 1746 and 1166 cm^{-1} compared with virgin and aged asphalts, which is the C=O stretching of carbonyl and it is also the characteristic peak of oil. From the Fig. 13,

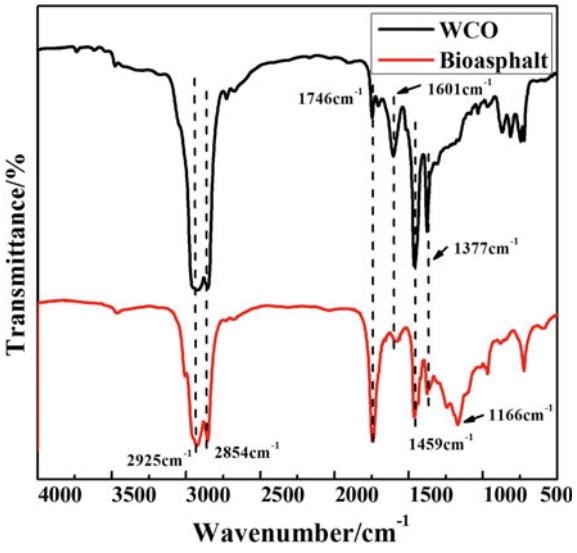

Fig. 13 Infrared spectra of WCO and bioasphalt

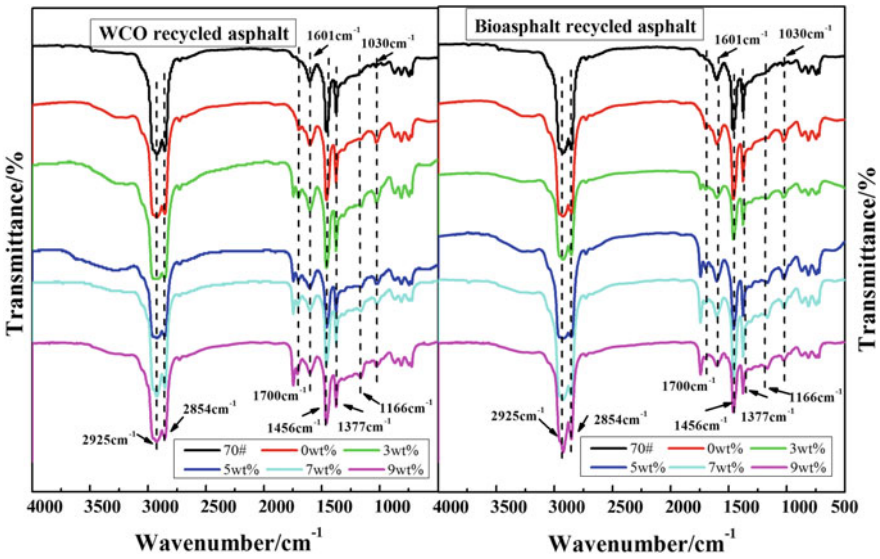

Fig. 14 Infrared spectra of asphalt aging before and after regeneration by bioasphalt or WCO

1746 and 1166 cm^{-1} can be seen in infrared spectroscopy of WCO and WCO-based bioasphalt, which indicates that the rejuvenated asphalts by WCO and WCO-based are physical blended rather than chemical reaction. The bands at 1700 and 1030 cm^{-1} correspond to C=O carbonyl and S=O sulphoxide compounds modes of vibration, respectively [5]. Figure 14 illustrates that aged asphalt appears the new peak at 1700 cm^{-1} compared with the origin asphalt, which is due to the presence of carbonyl, and it is the unique peak of aged asphalt. At the same time, the peak of aged asphalt at 1030 cm^{-1} also reinforces, which indicates that the large molecular weight increase.

The 1746 and 1030 cm^{-1} are closely related to the aging asphalt. The carbonyl peak shows that there are a series of oxidation reactions in aging process of asphalt. The sulphoxide peak improved shows that the oxidation of sulfur also occurred in the aging process and had a significant influence on aging degree.

The carbonyl index ($I_{C=O}$) and sulfoxide index ($I_{S=O}$) were used to evaluate the degree of asphalt aging. Two functional group peaks increase with the aging of asphalt. The peak at 1700 and 1030 cm^{-1} were reduced when WCO and WCO-based bioasphalt were added. The carbonyl index and sulfoxide index can be calculated according to the Eqs. 1 and 2.

$$I_{s=o} = \frac{\textit{Sulfoxide}\ \text{peak area}\ (1030\,\text{cm}^{-1})}{\text{Peak area}\ (\sum 2000\ \text{and}\ 600\,\text{cm}^{-1})} \tag{1}$$

Table 4 Sulfoxide index and carbonyl index of rejuvenated asphalts

Types	$I_{(S=O)}$	$I_{(C=O)}$
WCO	0.003	0.002
Bioasphalt	0	0
70#	0	0.0033
70#PAV	0.02	0.0068
70#PAV + 3% WCO	0.019	0.0054
70#PAV + 5% WCO	0.015	0.004
70#PAV + 7% WCO	0.014	0.0037
70#PAV + 9% WCO	0.013	0.0031
70#PAV + 3% Bioasphalt	0.016	0.0052
70#PAV + 5% Bioasphalt	0.014	0.0032
70#PAV + 7% Bioasphalt	0.011	0.0031
70#PAV + 9% Bioasphalt	0.010	0.0018

$$I_{c=o} = \frac{Carbony\,peak\,area\,(1700\,\mathrm{cm}^{-1})}{Peak\,area\,(\sum 2000\,\mathrm{and}\,600\,\mathrm{cm}^{-1})} \tag{2}$$

Table 4 shows that the carbonyl index and sulfoxide index of rejuvenated asphalt. Carbonyl index and sulfoxide index of virgin asphalt are smaller and the WCO-based bioasphalt are zero. However, the sulfoxide index and carbonyl index decreased when the WCO or WCO-based bioasphalt was added and this trend increase with the content increasing, which indicates that WCO and WCO-based bioasphalt can regenerate the aged asphalt. Otherwise, the regenerative asphalts containing WCO-based bioasphalt show lower carbonyl index and sulfoxide index than the ones containing WCO at the same dosage, which may be difference with the result of physical properties. Nevertheless, both WCO and WCO-based bioasphalt can decrease the carbonyl and sulfoxide. The rejuvenator performance cannot be only evaluated by carbonyl and sulfoxide.

Conclusions

Based on the study of above, the results show that the WCO and its bioasphalt have great influence to age asphalt and the following conclusions can be drawn:

(1) Both WCO and WCO-based bioasphalt can rejuvenate the asphalt and meet the requirements of road performance. The effect of WCO to physical properties are better than WCO-based bioasphalt on the performance of the aged asphalt, which is due to the light components contents of WCO are higher than WCO-asphalt.
(2) Adding the WCO and WCO-based bioasphalt to aged asphalt can improve the low temperature brittleness. And the temperature sensitivity of rejuvenated

asphalts is improved, which is detrimental to the high temperature stability of asphalt. Thus, the high temperature performance needs to be further improved.

(3) The FTIR test results show that carbonyl index and sulfoxide index of aged asphalt declines when the WCO and WCO-based bioasphalt are added, which indicates that the aging degree of asphalt significantly reduces. At the same time, the new peaks of rejuvenated asphalt appear at 1746 and 1166 cm^{-1} compared with virgin and aged asphalts, which indicate that the rejuvenated asphalts by WCO and WCO-based are physical blended rather than chemical reaction.

References

1. F. Dong et al., Comparison of high temperature performance and microstructure for foamed WMA and HMA with RAP binder. Constr. Build. Mater. **134**, 594–601 (2017)
2. M. Zaumanis et al., Influence of six rejuvenators on the performance properties of Reclaimed Asphalt Pavement (RAP) binder and 100% recycled asphalt mixtures. Constr. Build. Mater. **71**, 538–550 (2014)
3. H. Asli et al., Investigation on physical properties of waste cooking oil—Rejuvenated bitumen binder. Constr. Build. Mater. **37**, 398–405 (2012)
4. J. Su et al., Investigation the possibility of a new approach of using microcapsules containing waste cooking oil: in situ rejuvenation for aged bitumen. Constr. Build. Mater. **74**, 83–92 (2015)
5. M. Chen et al., Physical, chemical and rheological properties of waste edible vegetable oil rejuvenated asphalt binders. Constr. Build. Mater. **66**, 286–298 (2014)
6. W. Luo, Y. Zhang, P. Cong, Investigation on physical and high temperature rheology properties of asphalt binder adding waste oil and polymers. Constr. Build. Mater. **144**, 13–24 (2017)
7. M. Chen et al., High temperature properties of rejuvenating recovered binder with rejuvenator, waste cooking and cotton seed oils. Constr. Build. Mater. **59**, 10–16 (2014)
8. D. Sun et al., Evaluation of optimized bio-asphalt containing high content waste cooking oil residues. Fuel **202**, 529–540 (2017)
9. M. Gong et al., Evaluation of bio-binder modified asphalt's adhesion behavior using sessile drop device and atomic force microscopy. Constr. Build. Mater. **145**, 42–51 (2017)
10. Z. Han et al., Study on the optimum rice husk ash content added in asphalt binder and its modification with bio-oil. Constr. Build. Mater. **147**, 776–789 (2017)
11. H. Zhu et al., Recycling long-term-aged asphalts using bio-binder/plasticizer-based rejuvenator. Constr. Build. Mater. **147**, 117–129 (2017)
12. X. Xu et al., Structure and performance evaluation on aged SBS modified bitumen with bi- or tri-epoxy reactive rejuvenating system. Constr. Build. Mater. **151**, 479–486 (2017)
13. J. Ji et al., Effectiveness of vegetable oils as rejuvenators for aged asphalt binders. J. Mater. Civil Eng. **29**, D40160033 (2017)
14. M.H. Gong et al., Physical-chemical properties of aged asphalt rejuvenated by bio-oil derived from biodiesel residue. Constr. Build. Mater. **105**, 34–45 (2016)
15. P. Li et al., Analysis of viscous flow properties of asphalt in aging process. Constr. Build. Mater. **124**, 631–638 (2016)
16. Z. Lei et al., Effects of refined waste and bio-based oil modifiers on rheological properties of asphalt binders. Constr. Build. Mater. **148**, 504–511 (2017)

Mineralography and Comprehensive Utilization of Highly Activity Steel Slag

Ying Xu, Zizi Zhang, Yanqing Cai, Bian Wang and Chenguang Hu

Abstract The traditional technical constraints made low utilization of the steel slag, which caused a waste of resources and polluted the environment, therefore, new methods are urgently needed to make full use of the waste steel slag. In this paper, quicklime, fly ash and slag were added to steel slag according to the proportioning principle of cement, and then reconstructed by high temperature calcination, finally the steel slag with highly activity was obtained. The study of comprehensive utilization of highly activity steel slag could reduce the accumulation of steel slag and improve the environmental quality. The theoretical contents of minerals in highly activity steel slag were calculated, and the XRD and mineragraphy were performed to analyze the reasons for the increased activity of steel slag. The results showed that there were more tricalcium silicate generated as the improving of calcium-silicate ratio, and there were more liquid phase and calcium aluminoferrite as the improving silica-alumina ratio, the increase of cementitious activity minerals in the steel slag made the cementitious activity improve in the steel slag. Wherein, the crystal defect made the minerals activity improve in the steel slag, and to further improve the cementitious activity of steel slag.

Keywords Steel slag · Utilization · Highly activity · Mineralography Environmental quality

Y. Xu · Z. Zhang · Y. Cai (✉) · B. Wang · C. Hu
College of Material Science and Engineering, North China University of Science and Technology, Tangshan, China
e-mail: caiyanqing126@126.com

Y. Xu
e-mail: xuying9940@126.com

Z. Zhang
e-mail: zhangzhang0115@163.com

B. Wang
e-mail: 1130409940@qq.com

C. Hu
e-mail: huchenguang00ts@163.com

Y. Han (ed.), *Advances in Energy and Environmental Materials*,
Springer Proceedings in Energy, https://doi.org/10.1007/978-981-13-0158-2_62

Introduction

The utilization of steel slag has reached balance in developed countries, however, the utilization ratio in China is only 20% [1]. The large amount of steel slag not only cause serious pollution to the environment, but also bring great waste as the massive accumulation. It can solve the environmental problems as well as bring good benefits if the steel slag was made full use of as a second precious resources [2]. The unstable chemical composition, low cementitious activity and poorly soundness are the main reasons for causing low utilization of steel slag [3]. Therefore, improving the cementitious activity and stability of steel slag is one of the effective ways to solve the low comprehensive utilization rate of steel slag.

The purpose of the experiment in this paper is to improve the cementitious activity and stability by changing the chemical composition of the steel slag according to the proportioning principle of cement clinker [4, 5], which by means of adding quicklime, fly ash, slag as conditioning components. Then the composition and mineralogical character of the steel slag were also referred, which provide a theoretical basis for improving the cementitious activity of steel slag. It will realize the resource utilization of steel slag gradually, and promote the development of the industry as well as reduce environmental pressure.

Experiment

Experimental Materials. The steel slag is obtained from a converter steel slag factory in Tangshan. The cement is Portland cement, and the mainly conditioning components are quicklime, fly ash, and slag. The chemical compositions are shown in Table 1.

The XRD pattern of raw steel slag is shown in Fig. 1. From Fig. 1 we can see that the mainly minerals in steel slag are Fe_2O_3, tricalcium silicate (C_3S), dicalcium silicate (C_2S), calcium aluminoferrite (C_4AF), and RO phase. The XRD pattern of cement is shown in Fig. 2, and from Fig. 2 we can see that the mainly minerals in cement are tricalcium aluminate (C_3A), calcium aluminate (CA), C_2S, C_3S, needle-shaped calcium ferrite ($Ca_5Si_2(FeAl)_{18}O_{36}$), and skarms ($Ca_{54}MgAl_2Si_{16}O_{90}$). The XRD patterns of quicklime, fly ash, slag are shown in Fig. 3, and from which

Table 1 Chemical compositions of raw materials

Name	CaO	SiO_2	Al_2O_3	Fe_2O_3	MgO	K_2O	Na_2O	Others
Steel slag	41.40	14.96	0.84	7.90	5.49	0.12	0.14	29.15
Cement	62.60	21.35	4.67	3.31	3.08	0.54	0.21	4.24
Quicklime	94.45	–	–	–	–	–	–	5.55
Fly ash	6.82	51.41	26.74	5.29	0.87	1.18	0.71	6.98
Slag	38.20	28.64	14.60	0.42	10.82	0.44	0.32	6.56

we can see that the mainly mineral in quicklime is CaO, the mainly minerals in fly ash are mullite ($Al_6Si_2O_{13}$) and SiO_2, and the mainly materials in slag are glassy state.

Formula Design and Minerals Content. As the reason of steel slag and conditioning components are natural mineral materials, and the content of iron element in steel slag is higher than that of cement clinker, the chemical composition of the reconstructed steel slag cannot be completely consistent with cement clinker. In this experiment, quicklime and fly ash were added to the steel slag according to the chemical composition of cement clinker [6], and then the silica-alumina ratio was changed by adding quicklime and slag to the steel slag, which made the content of two or three chemicals of CaO, SiO_2 and Al_2O_3 in the reconstructed steel slag the same as that of cement clinker, and the ratio of the experimental is shown in Table 2.

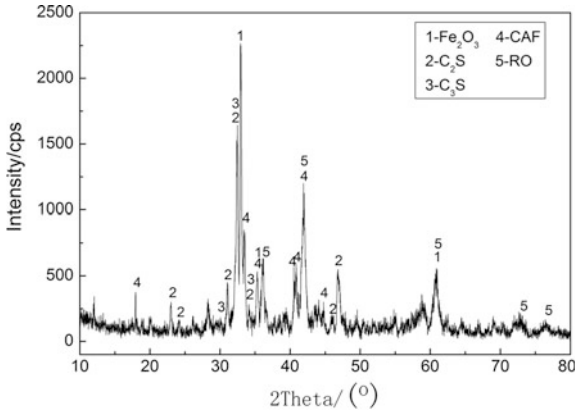

Fig. 1 XRD pattern of raw steel slag

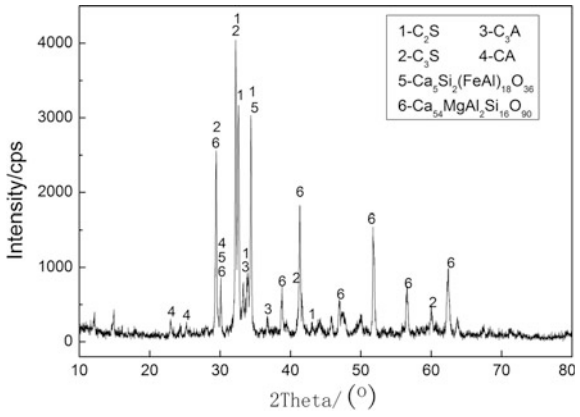

Fig. 2 XRD pattern of cement

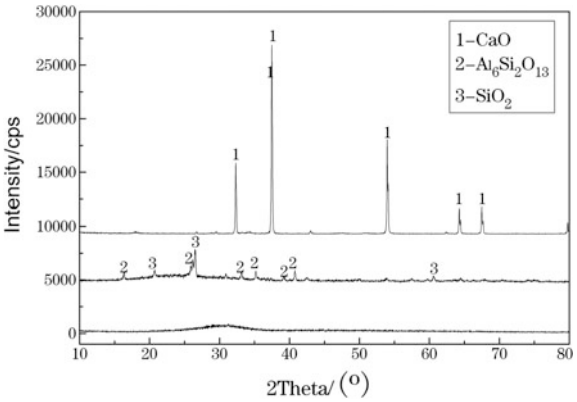

Fig. 3 XRD patterns of quicklime, fly ash and slag

Table 2 Ratio of the experimental table (%)

Number	Steel slag	Quicklime	Fly ash	Slag
0#	100	0	0	–
1#	87	10	3	–
2#	85	10	5	–
3#	82	10	8	–
4#	80	10	10	–
5#	77	10	13	–
6#	95	5	–	–
7#	88	5	–	7
8#	81	5	–	14
9#	83	2	–	15
10#	76	1	–	23

Generally speaking, the content of minerals in clinkers can be calculated with the R. H. Bogue Equation, and use C_3S, C_2S, C_3A, C_4AF as well as CaO, SiO_2, Al_2O_3, Fe_2O_3 to represent the minerals and the part of oxides in the clinkers. And the percentages of the chemical constituents of the four minerals are shown in Table 3.

The following Eqs. (1)–(4) can be listed according to Table 3:

$$\mathrm{CaO} = 0.7369\mathrm{C_3S} + 0.6512\mathrm{C_2S} + 0.6227\mathrm{C_3A} + 0.4616\mathrm{C_4AF} \quad (1)$$

Table 3 Percentages of the chemical constituents of the four minerals (%)

Oxide	C_3S	C_2S	C_3A	C_4AF
CaO	73.69	65.12	62.27	46.16
SiO_2	26.31	34.88	–	–
Al_2O_3	–	–	37.73	20.98
Fe_2O_3	–	–	–	32.86

$$SiO_2 = 0.2631C_3S + 0.3488C_2S \tag{2}$$

$$Al_2O_3 = 0.3773C_3A + 0.2098C_4AF \tag{3}$$

$$Fe_2O_3 = 0.3286C_4AF \tag{4}$$

According to the equation mentioned above, the Formula (5)–(8) of percentage content of each mineral can be calculated:

$$C_3S = 4.07CaO - 7.6SiO_2 - 6.72Al_2O_3 - 1.43Fe_2O_3 \tag{5}$$

$$C_2S = 8.60SiO_2 + 5.07Al_2O_3 + 1.07Fe_2O_3 - 3.07CaO \tag{6}$$

$$C_3A = 2.65Al_2O_3 - 1.69Fe_2O_3 \tag{7}$$

$$C_4AF = 3.04Fe_2O_3 \tag{8}$$

The Al_2O_3 will preferentially react with Fe_2O_3 to generate C_4AF in the steel slag, and then react with CaO to generate C_3A. Thus, there is no C_3A formation in the reconstructed steel slag because of the less Al_2O_3, and Fe_2O_3 in the reconstructed steel slag cannot be totally converted into C_4AF, the redundant Fe_2O_3 can be translated into C_2F and other ferrites. That is to say, the content of C_4AF calculated by *R. H. Bogue* is actually the total content of C_4AF, C_2F and other ferrite. Therefore, it can be calculated the content of C_4AF and C_2F by the method of lime saturation factor. It is assumed that all Fe_2O_3 in steel slag was converted to C_4AF and C_2F, and $\frac{M_{C_4AF}}{M_{Al_2O_3}} = 4.76$ in the C_4AF, $\frac{M_{C_2F}}{M_{Fe_2O_3}} = 1.7$ in the C_2F, the content of C_4AF can be calculated directly by Al_2O_3 content, that is, $C_4AF = 4.76Al_2O_3$. The Fe_2O_3 which calculated content of C_2F should first be subtracted from the total Fe_2O_3 to form the amount of Fe_2O_3 consumed by C_4AF, and the content of Fe_2O_3 consumed by C_4AF is the content of Al_2O_3 divided by 0.64. Besides, we can calculate the amount of C_2F with the remaining Fe_xO_y (Fe_2O_3 and FeO), that is, $C_2F = 1.7\left(Fe_xO_y - \frac{Al_2O_3}{0.64}\right)$.

Experimental Method. First of all, making the *Blain* specific surface of original steel slag reached 410 m^2/Kg by crushing and milling. Then well-mixed the steel slag with quicklime, fly ash and slag in the corundum crucible. Finally, put the corundum crucible into the electric furnace and heated up to 1400 °C, kept the thermal insulation for 30 min, and cooled to 1000 °C to obtain the reconstructed steel slag by water quenching.

In order to further explore the cementitious activity of reconstructed steel slag, the steel slag and cement in the ratio of 30:70 is prepared into a paste test block. After that, used press machine to test the compressive strength of the steel slag in 3d, 7d and 28d. Then the cementitious activity of reconstructed steel slag was analysed according to the regulations of (GB/T20491-2006) “Steel Slag Powder Used for Cement and Concrete”, and the concrete calculation is shown in Formula (9):

$$A = \frac{R_t}{R_0} \times 100\% \tag{9}$$

where, "A" is the activity index of "steel slag–cement", "R_t" is the compressive strength of "steel slag–cement", "R_0" is the compressive strength of pure cement paste. Therefore, the greater compressive strength in "steel slag–cement", the better activity index in "steel slag–cement", which makes the best cementitious activity of the steel slag.

According to the GB/T1346-2011 test method to measure the soundness of reconstructed steel slag.

Results and Discussion

Study on the Properties of Highly Activity Steel Slag. The compressive strength and the activity index of reconstructed steel slag are shown in Figs. 4 and 5. It can be seen that the compressive strength and the activity index of the reconstructed slag are higher than the raw steel slag. Wherein, there are the lowest compressive strength and the activity index of the reconstructed steel slag with the number of 6#, and there are the highest compressive strength and the activity index of the reconstructed steel slag with the number of 3#. The "Steel Slag Powder Used for Cement and Concrete" (GB/T20491-2006) shows that when the activity index reached above 80% after 28d, the steel slag will have highly activity, that is to say, the reconstructed steel slag we obtained are belong to the range of highly activity steel slag. After the test of soundness, the results showed that the soundness of the reconstructed steel slag is qualified, that is, the highly activity soundness steel slag is obtained.

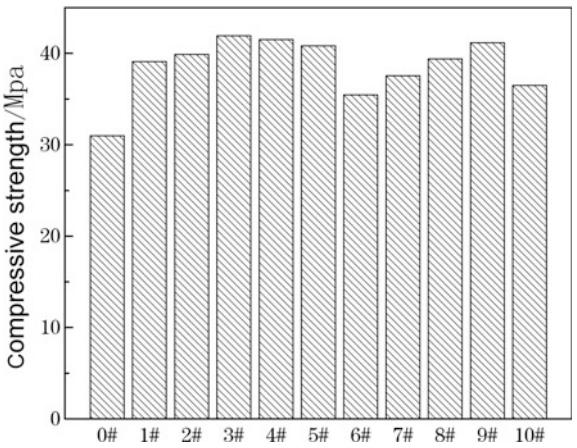

Fig. 4 Compressive strength of reconstructed steel slag

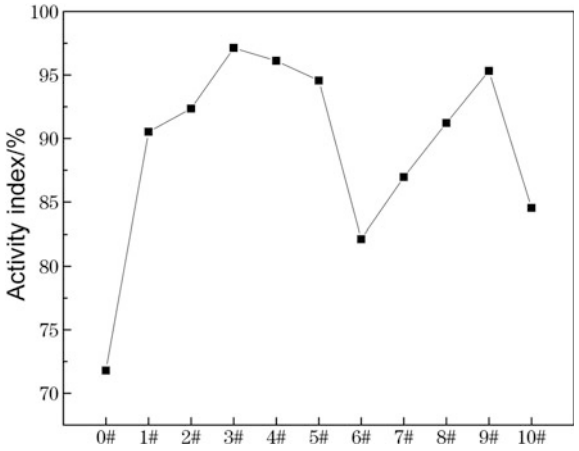

Fig. 5 Activity index of reconstructed steel slag

In order to further analyse the results of the study, the XRD analyses for the four groups of the highest activity index of steel slag was conducted, as shown in Fig. 6. It can be seen from the diagram, the main minerals are C_2S, C_3S, C_4AF, calcium ferrite (C_2F) and magnesioferrite in activity steel slag. The diffraction peaks of C_2S in highly activity steel slag are better than that of the original steel slag, it shows that the number of C_2S are increased with the addition of conditioning materials. The ratio of calcium to silicon is decreased with the addition of conditioning materials, and the content of C_3S is decreased, wherein, the mainly content of the highly activity steel slag is C_2S. Compared with the original steel slag, the RO phase peak of highly active slag is gradually weakened and passivated, the reason is that most of the FeO in the RO phase of steel slag changed into ferrite and aluminoferrite minerals, most of the MgO changed to magnesioferrite, which improved the cementitious activity of steel slag and ensured its stability. It can be seen from the graph that in the case of a certain ratio of calcium to silicon, the compressive strength of the reconstructed steel slag is improved under the reduced ratio of silica-alumina. The main reason is that in a certain ratio of calcium to silicon, the content of aluminoferrite increases with the increases of Al ion content while the decreases of silica-alumina ratio in the reconstructed steel slag. With the increases of silica-alumina ratio, the content of aluminoferrite is decreased as the content of Al ion reduces in the reconstructed steel slag. Meanwhile, the solute diffusion rate will slow down if the viscosity of liquid phase is greater in the system, and it goes against the generation of C_3S, which will decrease the cementitious activity of reconstructed steel slag. There is more generation of C_3A at the low ratio of silicon-aluminum where there are more Al_2O_3, however, the increased content of C_3A caused the quick setting of the mortar, which can seriously affect the compressive strength of the steel slag. Therefore, the silica-alumina ratio of the reconstructed steel slag should be controlled within a certain range.

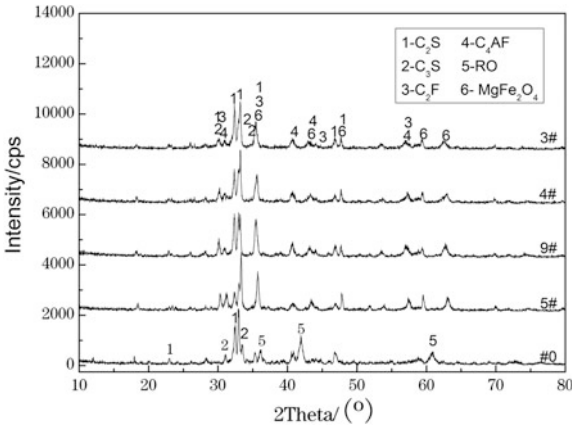

Fig. 6 XRD spectra of highly activity steel slag

Study on the Minerals Composition and Phase of Highly Activity Steel Slag. The composition of minerals in highly activity steel slag is theoretical calculated and the result is shown in Table 4, from which, we can see that the content of C_3S is more than C_2S in the raw steel slag, and the least mineral is C_4AF. The contents of C_3S, C_2S and C_4AF in 3# are more than the original steel slag, however, the content of C_2F is less than the original steel slag. The content of C_2S in 5# is the highest in three kinds of highly activity steel slag, however, there were not any C_3S, and the content of C_4AF is higher than that of original steel slag. The contents of C_2S and C_4AF in 9# are higher than those in original steel slag while the content of C_3S and C_2F are lower than that of original steel slag.

In order to further analyse the morphology of minerals in highly activity steel slag, the mineralography analysis was conducted, as shown in Fig. 7. It is observed that the C_2S in 0# are mainly round and ellipsoidal, the C_3S are mostly hexagonal plates, and there is dendritic ferroaluminate around the C_3S, and the RO phase (solid solution of metal oxides FeO, MgO and MnO and other two price formation) is amorphous. The original steel slag is refractory, and there is less liquid phase, therefore, the amount of C_3S is not as much as calculated. There are more round C_2S and hexagonal plates C_3S in 3#, which the solid solution of these minerals is the best, and its mineral composition is more compact than the raw steel slag, it can be seen from the Figs. 4 and 5 there are best compressive strength and activity index in 3#. There are mainly with metallic granular or elliptical shape C_2S and arborization ferrate in 9#, and the crystal shape of the minerals are relatively clear,

Table 4 Mineral composition of highly activity steel slag

Number	C_3S	C_2S	C_4AF	C_2F
0#	37.86	14.27	4.00	21.13
3#	25.46	27.70	13.46	23.07
5#	–	55.07	19.63	15.66
9#	14.98	36.56	13.74	13.74

the content of C_2S and C_4AF are more over than the original steel slag while the content of C_3S is less, meanwhile, the cementitious activity of 9# steel slag is better than the raw steel slag. The content of C_2S in 5# is the highest in three kinds of highly activity steel slag, and the densities of all minerals are lower than those of 9# and 3#. The theoretical calculation is not C_3S content in 5#, however, a smaller amount of C_3S can be seen from the mineralography map, the main reason is that the formation of minerals are not pure mineral solid solution and it always under the influence of other impurities, while the calculation of chemical composition of clinker mineral composition complete balance of assumed conditions. It will be some errors between the theoretical calculation and the actual calculation, however, the calculated theoretical results can explain the steel slag composition in certain situations. In the end, the reason for the increase of cementitious activity in highly activity steel slag is the combined action of all minerals, and the main minerals are C_3S, C_2S and C_4AF. All in all, it can be increased the content of C_3S, C_2S, C_4AF to improve the cementitious activity of reconstructed steel slag.

Study on the Highly Activity of Steel Slag Comprehensive Utilization. Steel slag with highly activity stability obtained in this experiment can be used as ordinary Portland cement bricks, blocks, plates and other building materials products. It can also be used as a concrete mixture, which with the late strength of concrete and will be significantly improved, and has fine abrasion resistance, dry shrinkage resistance, frost resistance, as well as corrosion resistance to a certain extent. And the concrete product with highly activity steel slag has advantages of high strength,

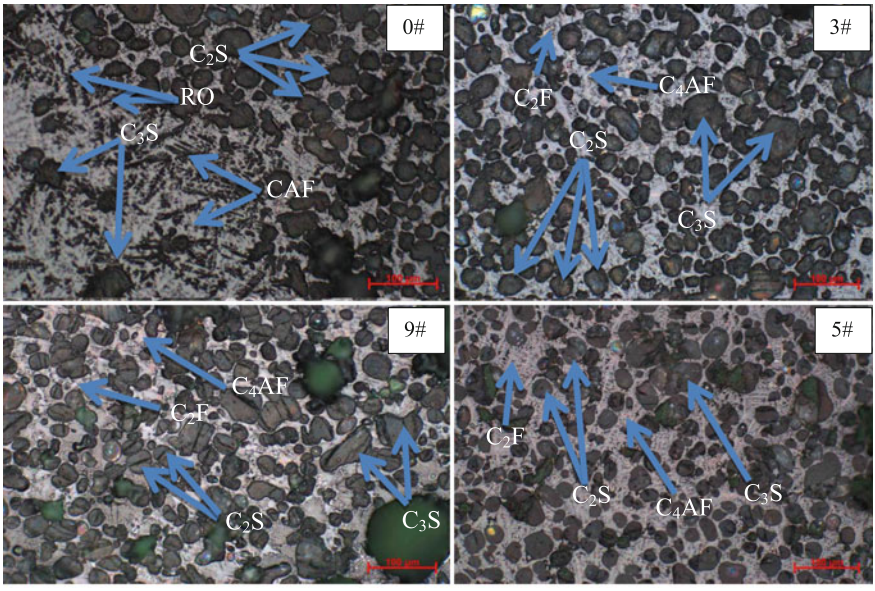

Fig. 7 Mineralography map of highly active steel slag

wear resistance, frost resistance and other characteristics, which can improve engineering quality simultaneously and reduce the engineering cost. Therefore, it can be widely used in the construction of the city.

The utilization ratio of steel slag is improved and a new technology effective way of metallurgical solid waste treatment is explored, relying on scientific and technological progress to constantly optimize the industrial structure, which can reduce the exploitation of natural resources and mining pollution of the source. It can protect the ecological resources and environment as well as the effective use of waste.

Conclusion

(1) When the content of steel slag is 82%, the quicklime is 10% and the fly ash is 8%, the cementitious activity of the reconstructed steel slag is the best.
(2) There are more tricalcium silicate generated as the improving of calcium-silicate ratio, and there are more liquid phase and calcium aluminoferrite as the improving silica-alumina ratio.
(3) There are more round or elliptical shape C_2S and hexagonal plates C_3S in highly activity steel slag, and the arborization ferrate are mainly around other minerals, and the more crystal defect are made the cementtitious of steel slag improve.
(4) It can promote the development of metallurgical industry, reduce the environmental pressure and improve the economic efficiency according to the improvement of comprehensive utilization of highly activity steel slag.

Acknowledgements This research was supported by the financial support of National Natural Science Foundation of China (51574109), and Hebei provincial Key Laboratory of Inorganic Nonmetallic Materials, College of Materials Science and Engineering, North China University of Science and Technology.

References

1. P. Jian, Q. Dao, Y. Juan et al., Status and development of the comprehensive utilization of the steel slag at Baosteel. Baosteel Tech. Res. **5**, 15–19 (2011)
2. W.P. Zhang, S.J. Hao, W.F. Jiang et al., Study of comprehensive utilization on the steel slag. J. Appl. Biomater. **488–489**, 137–140 (2014)
3. X.L Yang, H.X. Dai, X. Li et al., Comprehensive utilization and discussion of iron and steel metallurgical slag. Adv. Mater. Res. **807–809**, 2328–2331 (2013)
4. B. Fronek, P. Brad, N. Delatte, Steel slag aggregate used in Portland cement concrete. Transp. Res. Rec. J. Transp. Res. Board **2267-1**, 37–42 (2012)
5. X.L. Guo, H. Shi, Modification of steel slag powder by mineral admixture and chemical activators to utilize in cement-based materials. Mater. Struct. **46**, 1265–1273 (2013)
6. N. Palankar, A.U.R. Shankar, B.M. Mithun, Durability studies on eco-friendly concrete mixes incorporating steel slag as coarse aggregates. J. Clean. Prod. **129**, 437–448 (2016)

Improvement on Freeze-Thaw Resistance of Cement-Based Materials by Functional Admixtures

Yagang Zha, Jianying Yu, Ruiyang Wang, Guang Zhang and Wei Duan

Abstract The effects of different functional admixtures (F1, F2 and F3) on mechanical property, total porosity and freeze-thaw (F-T) resistance ability of mortars were investigated. The F-T resistance ability of mortars was evaluated by mass loss, compressive strength loss and total porosity increase. The results indicated that the mortars with functional admixtures showed higher compressive strength and lower total porosity. During the F-T cycles, mortars with functional admixtures have a lower mass loss and their compressive strength decline and total porosity increase. Meanwhile, by scanning electron microscope (SEM) analysis it is found that there was a large amount of fibrous crystals formation in the microcracks which is due to the self-healing capability of the functional admixture resistant to damage. Compared with controlling samples without functional admixture, the mass loss, compressive strength decline and total porosity increase of mortars with 0.5 wt% F2 dropped 28.7, 34.2 and 40.7% respectively.

Keywords Cement-based materials · Functional admixtures · Freeze-thaw resistance · Self-healing

Y. Zha · J. Yu (✉) · R. Wang
State Key Laboratory of Silicate Materials for Architectures, Wuhan University of Technology, Wuhan 430070, China
e-mail: jyyu@whut.edu.cn

Y. Zha
e-mail: zhayagang1023@163.com

R. Wang
e-mail: 18202719663@163.com

G. Zhang · W. Duan
Inner Mongolia High-Grade Highway Construction and Development Co. Ltd, Hohhot 010020, China
e-mail: zg4999@163.com

W. Duan
e-mail: 994789168@qq.com

Y. Han (ed.), *Advances in Energy and Environmental Materials*,
Springer Proceedings in Energy, https://doi.org/10.1007/978-981-13-0158-2_63

Introduction

Concrete is essential building material which has been widely used in industrial and civil building, bridge, road engineering and so on. But concrete is prone to generate damage during freeze-thaw (F-T) cycles because of its brittleness and porosity [1]. The damage can accelerate the occurrence of chemical erosion and steel corrosion of the concrete, and seriously impact the durability of concrete [2].

Increased attention has always been given to the improvement on F-T resistance of cement-based materials. Some researchers improved internal pores and capillaries of concrete to enhance F-T resistance by adding mineral admixture and chemical agent. Fan [3] has found that concrete contained nano-kaolinite clay exhibited higher compressive strength, chloride diffusion resistivity, relative dynamic modulus of elasticity, and more electrical resistivity after F-T cycles. Mönnig [4] used super absorbent polymers to increase the F-T resistance of high strength concrete by adjusting porosity and porous connectivity. Hang [5] has revealed that concrete with a suitable air-entraining agent or lower water-cement ratio possessed better F-T resistance.

Although improving the internal structure of the concrete can enhance its F-T resistance, the occurrence of damage is inevitable with the extension of service time. Hence, exploiting a kind of the concrete which has better F-T resistance is very necessary. The functional admixture which has excellent chelate ability could promote concrete itself components to generate some insoluble fibrous crystal in the pores and capillary in concrete [6]. Some researcher used this kind of compound to improve internal pore structure and heal damage by crystalline product [7–10]. But the report about functional admixtures on F-T resistance of cement-based materials was less.

In this paper, the different functional admixtures (F1, F2 and F3) were selected for improving performance of mortars. The effects of functional admixtures on mechanical property, total porosity and F-T resistance ability of mortars were investigated. The F-T resistance of mortars was evaluated by change of compressive strength, quality and total porosity during F-T cycles. Meanwhile, the microstructure of mortars before and after F-T cycles was observed by scanning electron microscope (SEM).

Experimental

Materials. Ordinary Portland cement (CEMI 42.5N) was provided by Huaxin Cement Co. LTD. Medium size sand with a soil and a water amount less than 1% was used. Three kinds of functional admixtures (F1, F2 and F3) are complexes containing unary, binary and ternary carboxyl groups respectively, which made in

our laboratory. And the molecular weight of chemical compositions is 218, 162 and 294 g/mol respectively.

Preparation of Mortars. All formulation design of mortars was a water to cement ratio of 0.50 and sand to cement ratio of 3. The functional admixture was added according to the mass of cement. The controlling sample without functional admixture was called A0. The mortar samples which contained 0.05 wt% F1, 0.50 wt% F2 and 0.05 wt% F3 respectively were labelled A1, A2 and A3. The difference in proportion is due to the longer retarded time of mortars with 0.50 wt% F1 or 0.50 wt% F3. The mortars were cast in molds with a size of 70.7 mm 70.7 mm × 70.7 mm which was used for mass loss, compressive strength and total porosity test. The mortars were demolded after 24 h and subsequently placed in a standard curing room for 28d with a controlled temperature of 20 ± 2 °C and a RH 95%.

F-T Cycles Test. The mortars which standard curing for 24 days and soak for 4 days were placed in −20 ± 2 °C cooler for 4 h, then the samples were moved to 20 ± 2 °C wet curing box for 4 h, keeping a F-T cycle at 8 h. When the F-T cycles reach 0, 25, 50, 75 and 100 cycles respectively, the mortars were taken out from the set-up of F-T cycles, and the relative mass, compressive strength, total porosity and microstructure were determined to evaluate the F-T resistance.

Performance Test

Mass Loss Test. The ratio of mass loss can be calculated via Eq. (1).

$$\Delta W_{ni} = (W_{0i} - W_{ni})/W_{0i} \times 100\%. \quad (1)$$

where ΔW_{ni} the ratio of mass loss; W_{0i} is the initial mass of samples and W_{ni} is the mass of mortars after different number of F-T cycles. The number of F-T cycles is called N.

Compressive strength loss test. The percentage of compressive strength loss can be calculated via Eq. (2).

$$\Delta f_c = (f_{c0} - f_{cn})/f_{c0} \times 100\%. \quad (2)$$

where Δf_c is the percentage of compressive strength decreased; f_{c0} is the initial compressive strength of samples and f_{cn} is the compressive strength of mortars after different N.

Total Porosity Test. According to the method as content of evaporative water [11, 12], the total porosity includes porosity, coarse and fine wool stoma. The greater total porosity, the more loose the internal structure of material. The total porosity by fully saturated specimens under 105 °C drying (12–14 h) to constant weight is obtained, which can be calculated via Eq. (3).

$$\rho = (M_0 - Mn)/\rho_w V \times 100\%. \quad (3)$$

where ρ is total porosity; M_0 is quality of mortar under fully saturated water; Mn is the quality of the specimen after drying to constant weight; V is the volume of mortar specimen; ρ_w is the density of water. Moreover, the percentage of total porosity growth can be calculated via Eq. (4).

$$\rho^* = (\rho_n - \rho_0)/\rho_0 \times 100\%. \quad (4)$$

where ρ_0 is the initial total porosity; ρ_n is the total porosity during different N; ρ^* is the percentage of total porosity growth.

SEM Observation. The QUANTA FEG 450 scanning electron microscope (SEM) was used to investigate the microstructure of mortars before and after F-T cycles. Small pieces of mortar specimens with the dimension of 5 mm × 5 mm 5 mm were stored in 105 °C oven for a day to remove moisture. The specimen was sputter coated with Pt, and the prepared specimens were observed by SEM.

Results and Discussions

Influence of Functional Admixtures on Compressive Strength of Mortars. Figure 1 shows the compressive strength of mortars without or with functional admixture at standard curing 28 days. It is found that mortars with functional admixtures have higher compressive strength. The compressive strength of A0 without functional admixtures is 34.0 MPa. Comparing with A0, compressive strength of A1, A2 and A3 has increased 20.6, 26.5 and 23.5% respectively which indicates that functional admixture can make a contribution for improving the mechanical properties of mortars at a certain extent.

Influence of Functional Admixtures on Microstructure of Mortars.

SEM of mortars. Figure 2 shows the SEM images of mortars with or without various functional admixtures after 28d standard curing. As can obviously see from Fig. 2, the microstructure of the A1, A2 and A3 is very dense and the pores of mortars with functional admixture are less than A0. SEM images of the mortars with different functional admixtures shows that a large quantity of fibrous crystal grew in the pores, which contribute to the significant increase of the impermeability of the mortars. Compared with A1 and A3, a large number of fibrous crystals grow in microcracks of A2, and the filling effect is the best.

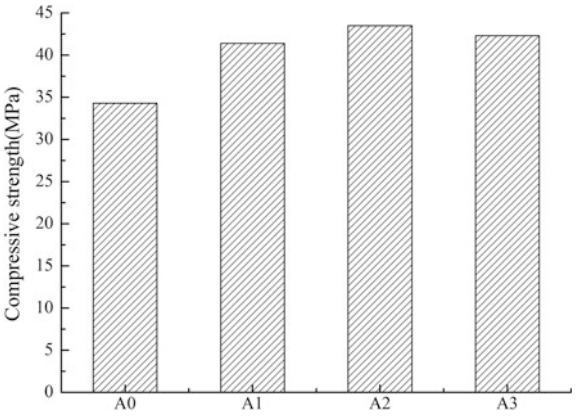

Fig. 1 Compressive strength of mortars with functional admixtures

Total Porosity of Mortars. The total porosity of mortars after standard curing 28 days is presented in Fig. 3. As can see from Fig. 3, the A0 without functional admixtures has the highest total porosity which was 17.1%. Furthermore, the total porosity of A1, A2 and A3 drops to 14.5, 14.0 and 14.4% respectively. This result confirms that the functional admixtures can improve microstructure of materials.

Effect of Functional Admixtures on F-T Resistance of Mortars.

Mass Loss of Mortars. Figure 4 shows the mass change of mortars without or with functional admixture during 100 F-T cycles. Before 25 F-T cycles, the difference between the samples seems very slight in the aspect of mass loss. However, the mass loss rate grows quickly after 25 F-T cycles because damage slowly accumulates with the increase of F-T cycles. The mass loss rate of A0 without functional admixtures has declined 11.5% on 100 F-T cycles. However, mass loss rate of A1, A2 and A3 with functional admixtures has decreased 8.8, 8.2 and 8.6% respectively on 100 F-T cycles. Comparing with control sample A0, the mass loss rate of A2 has reduced 28.7%.

Compressive Strength Loss of Mortars. The compressive strength change of mortars during 100 F-T cycles is presented in Fig. 5. With increase of F-T cycles, the difference of mortars in compressive strength loss is obvious. The compressive strength of A0 has reduced 33.9%, A1, A2 and A3 has declined 24.6, 22.3 and 23.5% respectively on 100 F-T cycles.

Total Porosity Change of Mortars. The total porosity change of mortars during F-T cycles is shown in Fig. 6. As can see from Fig. 6, the first 50 F-T cycles results in relatively small change in porosity. However, the total porosity of A0, A1, A2 and A3 has increased 18.2, 12.2, 10.8 and 11.3% on 100 F-T cycles. The A1, A2 and A3 have declined obviously in 33.0, 40.7 and 37.9% in total porosity relative to A0 on 100 F-T cycles. Total porosity would increase because the micro pore water of cement-base material form fatigue stress which is synergistic effect of ice bulge

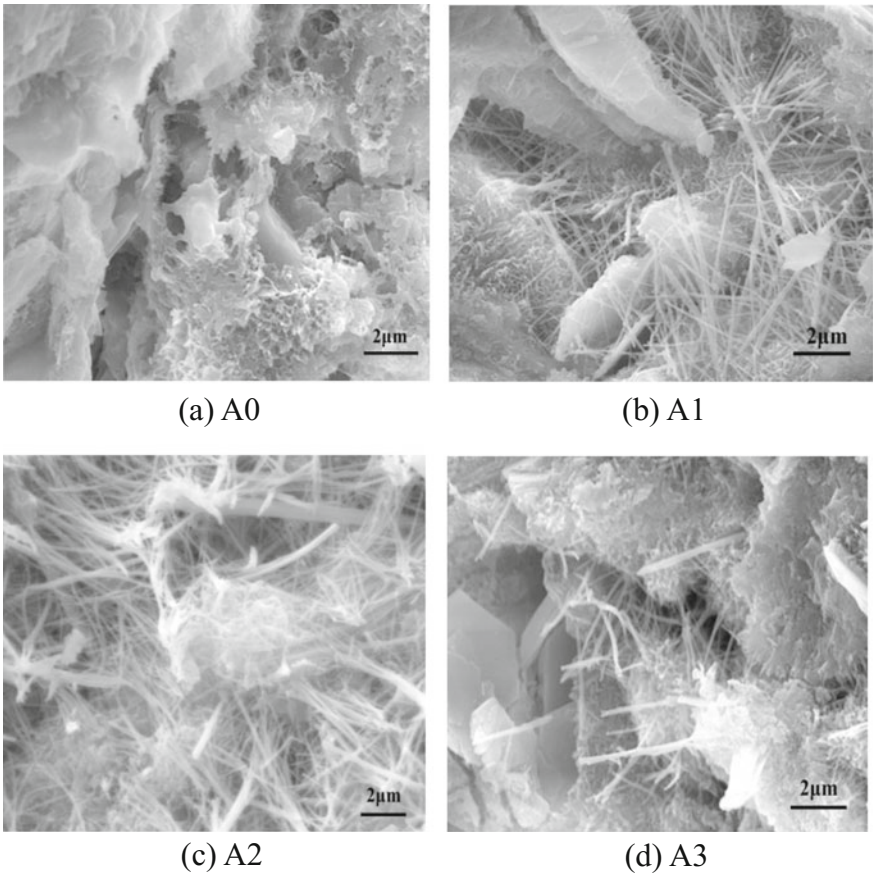

Fig. 2 SEM images of mortars with functional admixtures

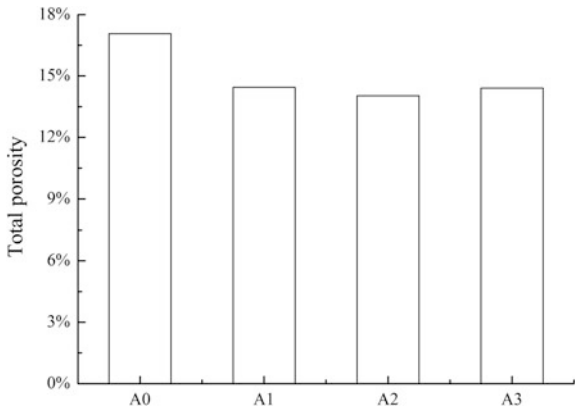

Fig. 3 Total porosity of mortars with different functional admixtures

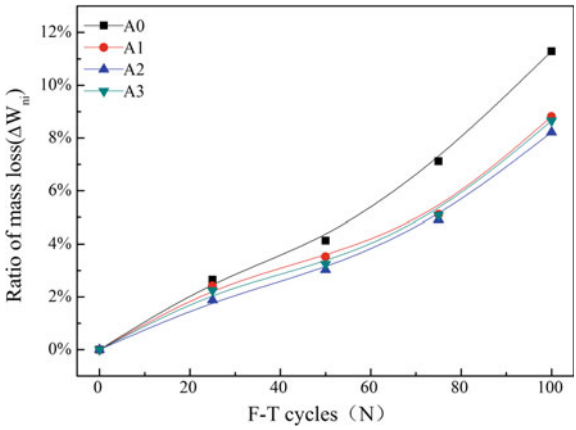

Fig. 4 Mass loss of mortars during F-T cycles

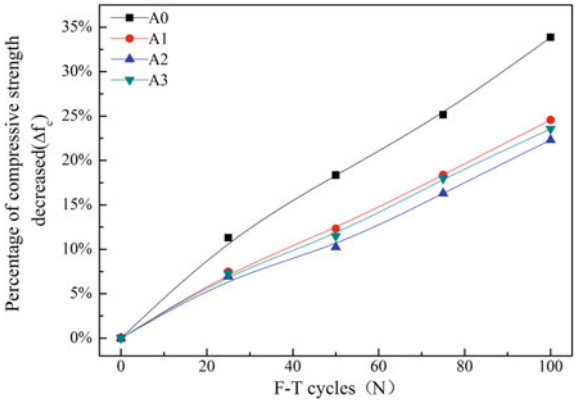

Fig. 5 Percentage of compressive strength decreased of mortars during F-T cycles

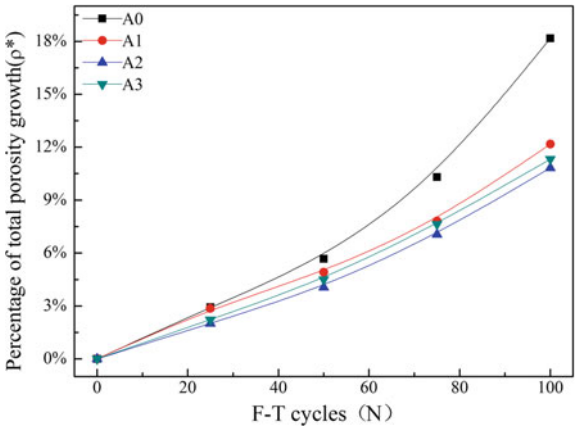

Fig. 6 Percentage of total porosity growth of mortars during F-T cycles

and water penetration pressure under positive and negative temperature alternating effect [13].

From the loss rate of mass, percentage of compressive strength decline and total porosity growth, the functional admixtures can enhance F-T resistance of mortars by the improvement of the internal pore structure.

Microstructure of Mortars after F-T Cycles. The SEM images of mortars on 100 F-T cycles are shown in Fig. 7. As can be seen in, the mortars have produced more visible cracks and large pores because of F-T cycles damage. The A0 without functional admixtures has appeared a clear and smooth crack with nothing in the middle of it. As seen from Fig. 7b, c, d, there have been smaller cracks internal of mortars and the fibrous material is formed to repair the cracks, but fibrous crystals of A1 and A3 is not as well as dense of A2. This phenomenon indicated that the micro-cracks of mortars with functional admixtures during F-T cycles can be self-healed through the formation of fibrous crystals.

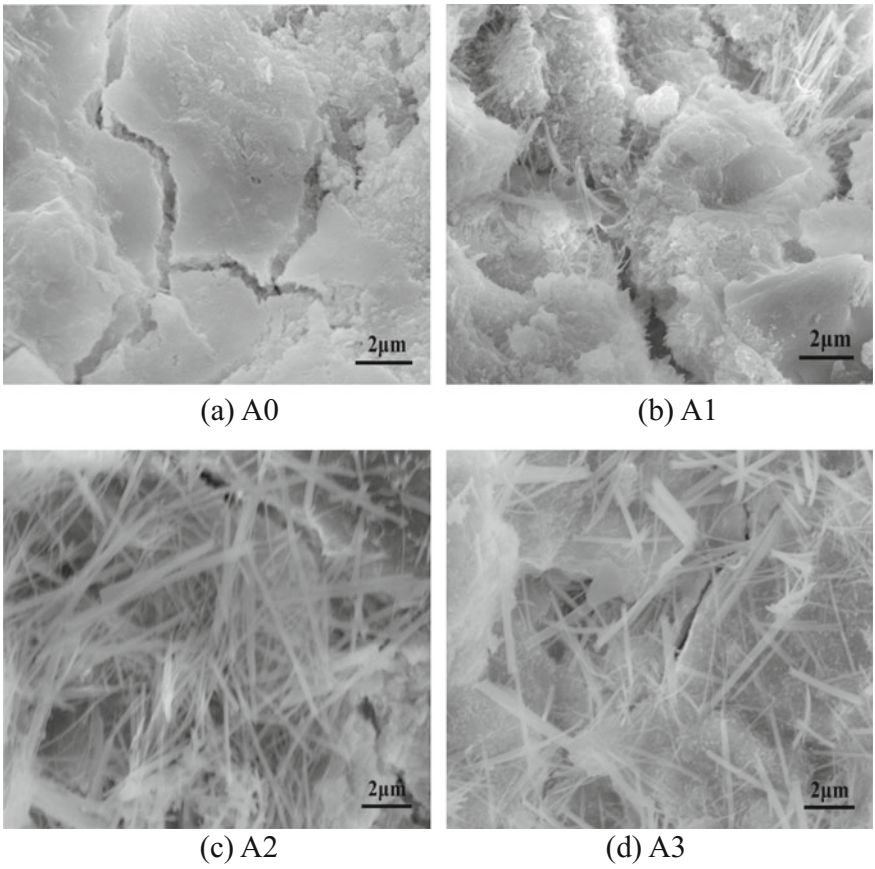

Fig. 7 SEM images of mortars after 100 F-T cycles

Conclusions

Results of the tests on mortars during F-T cycles indicate that the functional admixtures could improve F-T resistance of cement-based materials.

Comparing with controlling mortar A0, compressive strength of A1, A2 and A3 has increased 20.6, 26.5 and 23.5%, respectively. Moreover, the total porosity of A0 is 17.1%, but the total porosity of A1, A2 and A3 is 14.5, 14.0 and 14.4% respectively.

By mass loss, compressive strength decline and total porosity increase during 100 F-T cycles, the mortars with functional admixtures has a better F-T resistance. As for A2, the mass loss, compressive strength decline and augment of total porosity has dropped 28.7, 34.2 and 40.7% respectively relative to A0.

SEM analysis showed that the functional admixtures improve the microstructure of mortars by forming a large amount of fibrous crystal to make a denser interior structure of the mortar. During F-T cycles, the microcracks on the mortars with functional admixtures can be self-healed through the formation of fibrous crystals.

Acknowledgements This work is supported by the National Key R & D Program of China (No. 2017YFB0309905). The authors gratefully acknowledge financial support.

References

1. M. Hori, H. Morihiro, Micromechanical analysis on deterioration due to freezing and thawing in porous brittle materials. Int. J. Eng. Sci. **36**(4), 511–522 (1998)
2. J. Yuan, Y. Liu, H. Li et al., Experimental investigation of the variation of concrete pores under the action of freeze-thaw Cycles. Procedia Eng. **161**(6), 583–588 (2016)
3. Y. Fan, S. Zhang, Q. Wang et al., Effects of nano-kaolinite clay on the freeze-thaw resistance of concrete. Cem. Concr. Compos. **62**, 1–12 (2015)
4. S. Mönnig, P. Lura, Superabsorbent polymers-an additive to increase the freeze-thaw resistance of high strength concrete. in *Advances in Construction Materials 2007*, pp. 351–358 (2007)
5. M.Y. Hang, W. Zhang, Efficiency air-entraining water-reducing agent in concrete study on the freeze-thaw resistance. Appl. Mech. Mater. **71–78**, 3566–3571 (2011)
6. M.C.G Juenger, H.M. Jennings, New insights into the effects of sugar on the hydration and microstructure of cement pastes. Cem. Concr. Res. **32**(3), 393–399 (2002)
7. G.M. Wang, J.Y. Yu, Self-healing action of permeable crystalline coating on pores and cracks in cement-based materials. J. Wuhan Univ. Technol. Mater. Sci. Ed. **20**(1), 89–92 (2005)
8. M. Roig-Flores, S. Moscato, P. Serna et al., Self-healing capability of concrete with crystalline admixtures in different environments. Constr. Build. Mater. **86**(6), 1–11 (2015)
9. A. Alotoom, A.K. And, A. Shawaqfeh, Crystallization technology for reducing water permeability into concrete. Ind. Eng. Chem. Res. **46**(16), 5463–5467 (2007)
10. K. Sisomphon, O. Copuroglu, E.A.B. Koenders, Self-healing of surface cracks in mortars with expansive additive and crystalline additive. Cem. Concr. Compos. **34**(4), 566–574 (2012)

11. V.T. Ngala, C.L. Page, L.J. Parrott et al., Diffusion in cementitious materials: II, further investigations of chloride and oxygen diffusion in well-cured OPC and OPC/30% PFA pastes. Cem. Concr. Res. **25**(4), 819–826 (1995)
12. V.T. Ngala, C.L. Page, Effects of carbonation on pore structure and diffusional properties of hydrated cement pastes. Cem. Concr. Res. **27**(7), 995–1007 (1997)
13. B. Zhang, P. Su, L.T. Dong, The researches on the mechanism of the concrete under low temperature frost injury. Adv. Mater. Res. **838–841**, 846–849 (2013)

Preparation of Manganese Sulfate by Reduction of Electrolytic Manganese Mud with Corn Straws

Yujiang Teng, Fenglan Han, Shizheng Zhao and Yaguang Wang

Abstract In this paper, manganese was recovered from electrolytic manganese anode mud by using the wet-method reducing technique. Manganese sulfate was prepared using corn stover as a reducing agent, dilutes sulfuric acid as the leaching agent, and removal of heavy metals with sodium dimethyl dithiocarbamate (SDD) to recover manganese anode mud. The effects of straw dosage, sulfuric acid concentration, aging time, curing temperature, pH value of leaching solution and the amount of magnesium on the leaching rate and recovery rate of manganese were considered by orthogonal and single factor experiments. The method of ferrous ammonium sulfate titration and inductively coupled plasma atomic emission spectrometry (ICP) were used to identify the content of manganese and other elements. The results show that optimum conditions are corn straw dosage of 7 g, liquid-to-solid ratios to 6:1 and 7.35 wt% H_2SO_4, aging time is 80 min, ripening temperature is 350 °C, leaching solution pH is 5.5 and SDD dosage is of 3.5 g. The leaching efficiency of manganese reaches 99.85%, recovery efficiency of manganese reaches 94.06% under the optimum conditions.

Keywords Manganese anode mud · Manganese sulfate · Leaching rate

Introduction

With the depletion of manganese resources, it is very important to strengthen the recycling of secondary resources of manganese [1, 2]. In the process of electrolytic manganese inevitably produces, the content of manganese anode mud is up to 40% or more, and manganese anode mud has a higher content of lead and arsenic. Manganese anode mud improper handling is a nasty business, and will lead to leading pollution, arsenic pollution and other heavy metal pollution. At present, most of the manganese plants choose to store the anode mud or sell cheaply. From

Y. Teng · F. Han (✉) · S. Zhao · Y. Wang
North Minzu University, Yinchuan 750021, China
e-mail: 625477897@qq.com

Y. Han (ed.), *Advances in Energy and Environmental Materials*,
Springer Proceedings in Energy, https://doi.org/10.1007/978-981-13-0158-2_64

the perspective of environmental protection and rational utilization of resources, comprehensive utilization of manganese anode mud is of great importance.

The main components of the manganese anode mud are the hydrate oxides of Mn^{4+} produced by oxidation of the partial Mn^{2+} in the electrolytic solution and the hydrate oxides of heavy metals such as Pb, Sn and Sb produced by the anode mud and electrolytic solution [3]. Most of the Pb and Sn have the close relation ship with the manganese hydrate oxide, they cannot be deleted by the method of simple mechanical dressing [4, 5]. The recycling treatment of manganese anode mud mainly used the method of special selection of manganese, the reduction leaching and direct leaching can be used as the treatment method of this aspect of research. Huang, et al. [6] used dilution heats from concentrated sulfuric acid to quickly hydrolyze wood chips and reduce the manganese dioxide from manganese anode mud. The manganese leaching rate of manganese anode mud from an electrolytic plant in Hubei is above 99.5%, the recovery rate is over 98%. Niu, et al. [7] used orange peel as a reducing agent in the sulfuric acid system to decrease leaching of electrolytic manganese anode slag. The manganese leaching rate was owned by 96%, and lead leaching rate less than 0.2%. Therefore, it effectively achieved lead and manganese separation.

The objective of the present works a methodology for recovery and utilization of manganese anode mud. Manganese anode mud was supplied by Ningxia Tianyuan manganese Industry (Group) Co., Ltd., and its composition was analyzed. Depending on the results of the analysis, corn straw was selected as the reducing agent, manganese sulfate and sodium dimethyl dithiocarbamate (SDD) were prepared for leaching manganese by wet reduction leaching method as the remover of heavy metal impurities. Low-temperature waters bath method and high-temperature aging process, obtained a higher manganese leaching rate, decreasing the process of impurity production. Selecting SDD in addition to heavy metals, which improve the recovery of manganese and streamline the process of removing impurities. This method has a great prospect in terms of economy and energy consumption, which provides a feasible reference to the recycling of electrolytic manganese anode mud in Ningxia area.

Experiment

Raw Materials and Reagents. Manganese anode mud is from Ningxia Tianyuan Manganese Industry (Group) Co., Ltd., and corn stalks are from Ningxia Zhongwei suburbs. Concentrated sulfuric acid (AR), calcium carbonate (AR), sodium dimethyl dithiocarbamate (SDD)-Industrial graded.

Reaction Principle. The leaching process of manganese anode mud belongs to the heterogeneous redox reaction. The cellulose, $(C_6H_{10}O_5)_n$, which is rich in corn stalks, is oxidized under the action of dilute sulfuric acid, and hydrolyzed to produce reducing sugar [8]. Under acidic conditions, the reducing sugar reacts with

manganese dioxide to produce soluble manganese sulfate. Removal process: the use of neutralization method is to remove Fe and Al. As a heavy metal collector, SDD reacts with heavy metal to form the complex precipitation, then the complex precipitation are filtered. The main reactions are:

(1) The reaction formula for the leaching process involves [9].

$$(C_6H_{10}O_5)_n + nH_2SO_4 \rightarrow n(C_6H_{11}O_5)HSO_4. \quad (1)$$

$$n(C_6H_{11}O_5)HSO_4 + nH_2O \rightarrow n(C_6H_{12}O_6) + nH_2SO_4. \quad (2)$$

$$(C_6H_{12}O_6) + 12H_2SO_4 + 12MnO_2 \rightarrow 12MnSO_4 + 6CO_2 + 18H_2O. \quad (3)$$

$$Mn^{2+} + SO_4^{2-} \rightarrow MnSO_4. \quad (4)$$

$$2H_2SO_4 + 2MnO_2 + C(\text{Carbon or organic matter}) \rightarrow 2MnSO_4 + CO_2 + 2H_2O. \quad (5)$$

$$C + O_2 \rightarrow CO_2. \quad (6)$$

(2) The reaction formula for the removal processes to involve [10].

$$2C_3H_6NS_2Na(H_2O)_2 + M^{2+} \rightarrow C_3H_6NS_2 - M - S_2NC_3H_6 + 2Na^+ + 4H_2O. \quad (7)$$

$$C_3H_6NS_2Na(H_2O)_2 + M^+ \rightarrow C_3H_6NS_2 - M + Na^+ + 2H_2O. \quad (8)$$

Experimental Method. Weigh a certain amount of manganese anode mud placed in the beaker, according to the solid liquid ratio of water manganese anode slime 1:1, adding distilled water, stirring for 15 min, filtration, filtrate retention. The residue and a certain amount of straw powder placed in the ceramic crucible, according to the solid liquid ratio of manganese sulfate anode slime 6:1 with dilute sulfuric acid solution, the reaction rate was 180 min at a certain concentration and water bath at 70 °C, and the solid liquid ratio remained unchanged during the reaction. The crucible is placed in an oven to dry the material at a temperature not exceeding 80 °C. The crucible is placed on the electric heating plate for 2 h, the temperature does not exceed 300 °C, with the process of the periodic stirring, after that put it in a muffle the furnace at a certain temperature in the heating time. Add a certain amount of distilled water to dissolve, filter the slurry, after filtration, the leachate was added to the 1:1 leaching process. Adjust to the pH of the filtrate, add a certain amount of sodium dimethyl dithiocarbamate (SDD), stir well, standing

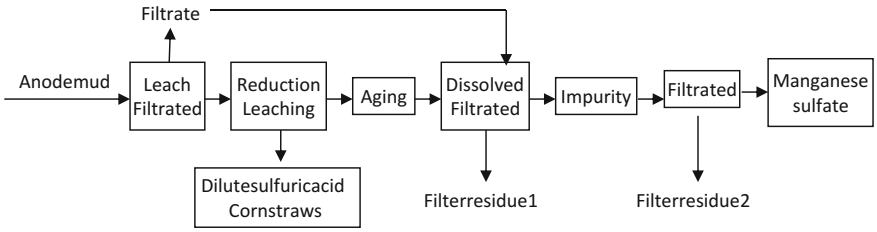

Fig. 1 Experimental flow chart

reaction 24 h. The filtrate was filtered, the filtrate was evaporated to give primary manganese sulphate.

Experimental Process. The experimental variables and the range of variables are determined by orthogonal experiment and theoretical calculation. The optimal process conditions are explored by a single factor experiment. The specific experimental process is as follows [10] (Fig. 1):

Detection Method. In this experiment, the phase analysis of the samples was analyzed by XRD to determine the main phase composition of the material [11–13]. The titration method of the manganese content of the substances which have more than 5% manganese contents is based on ammonium ferrous sulfate titration [14], and the titration method of the manganese content of the substances which have less than 5% manganese contents are being based on Inductively Coupled High Frequency Plasma Emission Spectrometer ICP (ICP-7000) [10].

Results and Analysis

Phase Analysis of Manganese Anode. The main chemical constituents of the manganese anode muds were determined by ammonium ferrous sulfate titration and ICP. The results are shown in Table 1. The content of Mn in the manganese anode mud is high. Indicated in Table 1, the content of Mn is around 42.1%. The remaining components are Mg and Pb, the contents of heavy metals such as Fe and Cr are low.

Table 1 Chemical composition analysis results in manganese anode mud [10]

Element	Content (%)	Element	Content (%)
Mn	42.1	Ag	6.6×10^{-4}
Pb	0.7	Se	4.5×10^{-4}
Mg	4.6	As	0.1×10^{-4}
Fe	5.3×10^{-2}	Sb	9.5×10^{-3}
Cr	5.9×10^{-3}	Cu	2.6×10^{-3}

The Effect of Straw Consumption of Manganese Leaching Rate and Manganese Recovery. Manganese exists mainly on the form of MnO_2 in electrolytic manganese anode mud. Reductant is required during leaching. The leaching rate of manganese increases from the increment of reducing agent dosage. That makes no sense to raise the dosage of reducing agent. The leaching rate of manganese attains a maximum until the reducing agent is sufficient. In this paper, the reducing agent that is corn straw to make high-priced manganese in the manganese anode mud to cut back to Mn^{2+}. On the leaching rate of manganese and manganese recovery rate, effect of reducing agent consumption as show in Fig. 2. As showed in Fig. 2, the leaching rate of manganese reaches 99.04% and recovery rate of manganese reaches 89.75%, the dosage of corn straw has been 14%. It sets out the amount of reducing agent is sufficient, after the increase in corn straw consumption, the increase in manganese leaching rate is not significant. With the increase in straw consumption, the number of carbides which can have not yet been fully burnt after aging has increased. Residue 1 will absorb more manganese ions in the process of filtration. Therefore, augmenting the consumption of straw will result in a slight decrease in leaching rate of manganese.

The Effect of Sulfuric Acid Concentration on Manganese Leaching Ratio. The hydrolysis of corn straw into monosaccharide in the leaching process, what the anode mud of the high manganese reduction needed is simple sugar. A hydrogen ion and high temperature conditions, the catalysis of monosaccharide which can continue to break with. Corn straw breaks down for organic, sugar acid and other products, that does not contribute to manganese leaching. Secondly, (3) type is mainly reactive in stage of hydrolysis reaction. The process of leaching should be avoided straw carbonization. Straw is carbonized in sulfuric acid, reducing the rate of hydrolysis reaction. With increases in sulfuric acid straw carbonation degree increases the leaching rate of decline.

The effect of sulfuric acid concentration on manganese leaching rate is significantly showed in Fig. 3. The leaching rate of manganese rises from the increase in

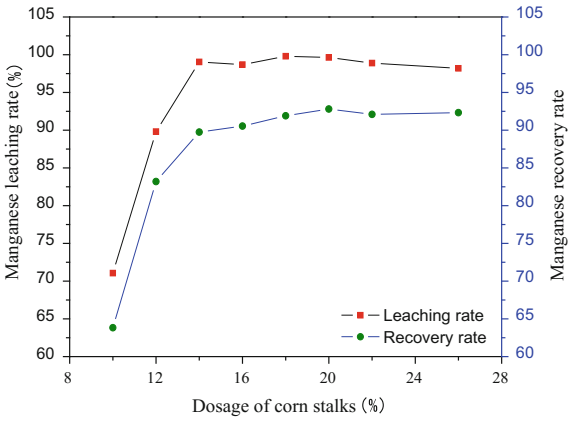

Fig. 2 Effect of straw consumption of manganese leaching rate and manganese recovery

sulfuric acid concentration, during the reaction period of 180 min. The concentration of sulfuric acid is 7.35%, the leaching rate of manganese can reach 99.30%.

The Effect of Aging Time and Temperature on Manganese Leaching Rate. Some corn straw cannot be completely hydrolyzed to further reaction coke. The surface is under a dense layer of carbon membrane in the process of sulfuric acid and corn straw. This will lead to incomplete hydrolysis of corn straw, namely reducing the reducing agent required, the carbon layer on the surface of corn straw has a strong adsorption capacity, will absorb some manganese, affect the leaching rate of manganese. In addition, some organic compounds, such as pigments, which are difficult to decompose, are involved in (5) type reaction by high temperature curing process. The leaching rate of manganese is further improved. Therefore, the influence of aging time and aging temperature on the leaching rate of manganese was studied. Figure 4 indicates the effect of aging time for the leaching rate of manganese. Figure 5 indicates the effect of aging temperature on the leaching rate of manganese. As showed in Fig. 4, the leaching rate of manganese increases first after that it goes down with the increase in aging time. In the aging times reaches 80 min. The leaching rate of manganese can reach more than 99.40%. The leaching rate of manganese increases from the increase in aging temperature, and tends to be gentle after 350 °C. The extraction rate of manganese is above 99.40% in the range of 325–425 °C.

The Effect of Sodium Dimethyl Dithiocarbamate (SDD) on the Recovery of Manganese. Figure 6 indicates the effect of sodium dimethyl dithiocarbamate (SDD) on the recovery of manganese. Sodium dimethyl dithiocarbamate ($C_3H_6NS_2Na{\cdot}2H_2O$) is one kind of heavy metal collector. It responds to heavy metals in the leachate to form precipitates and flocculent complexes that are filtered out of the residue. As showed in Fig. 6, the recovery rate of manganese increases first, after that it goes down with the increase in dosage of SDD. In the amount of SDD reaches 7%, the recovery of manganese is quite high. The dosage of the SDD

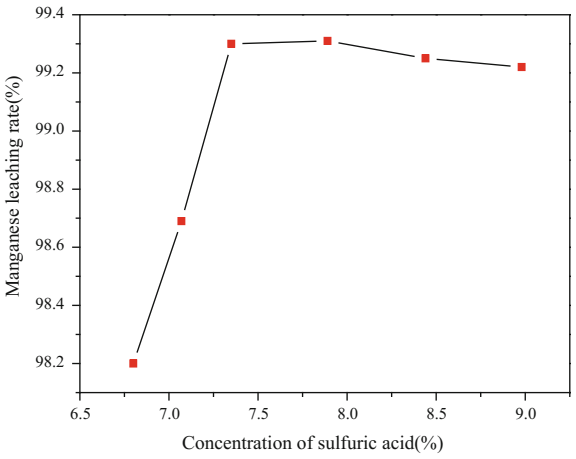

Fig. 3 Effect of sulfuric acid concentration on manganese leaching rate

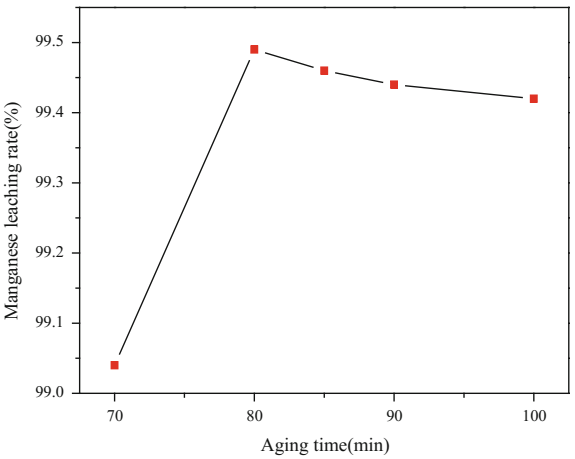

Fig. 4 Effect of aging times on leaching rate

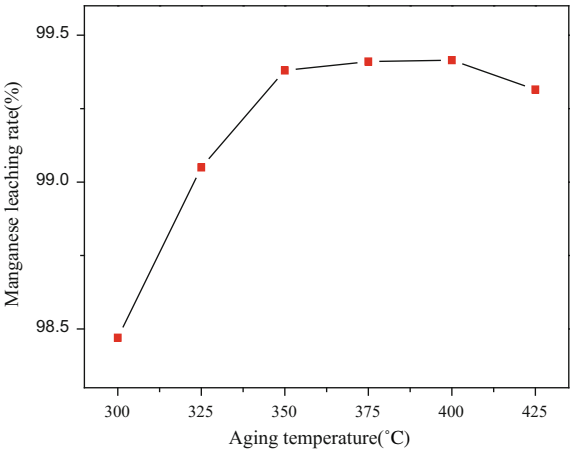

Fig. 5 Effect of aging temperature on leaching rate

is sufficient. With the increase in the amount of SDD, excessive SDD combined with Mn^{2+} deposits formed. Results the manganese recovery rates to decrease.

The Effect of pH on Recovery of Manganese. Figure 7 indicates the effect of the pH of the solution to the recovery of manganese. The pH of the solution is adjusted to neutralize the precipitate and remove Fe and Al. The proper pH allows the SDD to reach the optimum reaction environment. As showed in Fig. 7, the recovery rate of manganese increases at first, after that it goes down with the increase in pH. The pH value of the solution reaches 5.5, the recovery rate of manganese is relatively high. Since the pH greater than six, SDD combined with Mn^{2+} rate is greater than other metal ion, the rate of manganese recovery rate decreased significantly.

Slag Materials. The slag materials in the whole recovery process are obtained by the leaching process and the impurity removal process, that is, the residue obtained by the filtration of impurity after the aging and dissolution. The amount of slag in

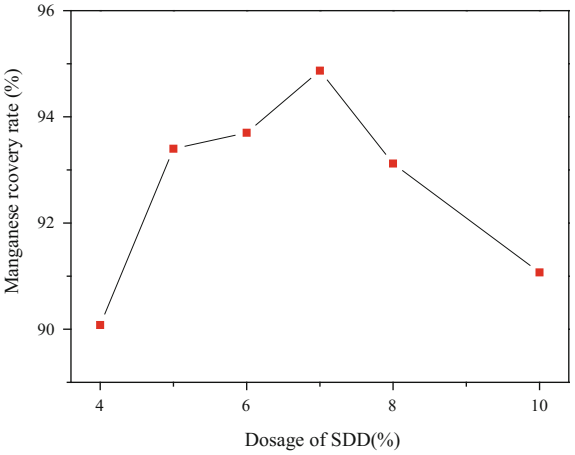

Fig. 6 Effect of SDD on the recovery of manganese

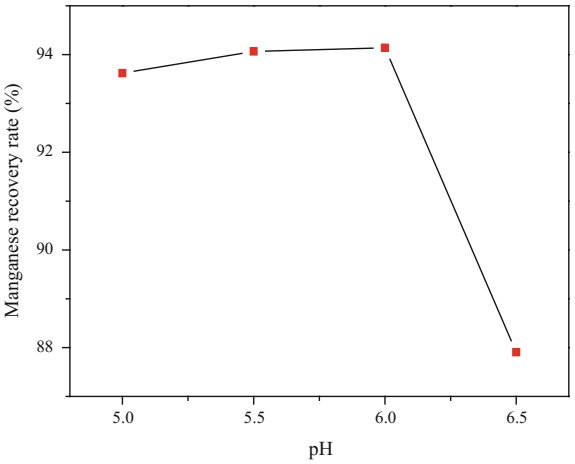

Fig. 7 Effect of pH on recovery of manganese

the leaching process is 4.63 g. The mass of the slag produced during the remove impurity process is 11.35 g. The total mass of the whole process slag are equal to the mass of the waste produced by the two processes. The amount of total slag is 15.98 g. The rate of slag production is the proportion of total slag and the addition of manganese anode mud and corn stalk. The slag production rate was 28.03%.

Experimental Products. XRD is used to analyze the phase of the experimental sample. The chemical composition are given in ferrous ammonium sulfate titration and ICP. The results are shown in Fig. 8 and Table 2. Table 2 shows toppers results from the chemical composition of the experimental sample. Figure 8 shows the XRD analysis spectrum. Table 2 demonstrates that the content of manganese is 28.10%, that is, the content of manganese sulfate is 85.48%, the content of other heavy metal is 4.62%. It can be observed in Fig. 8 that the chemical composition

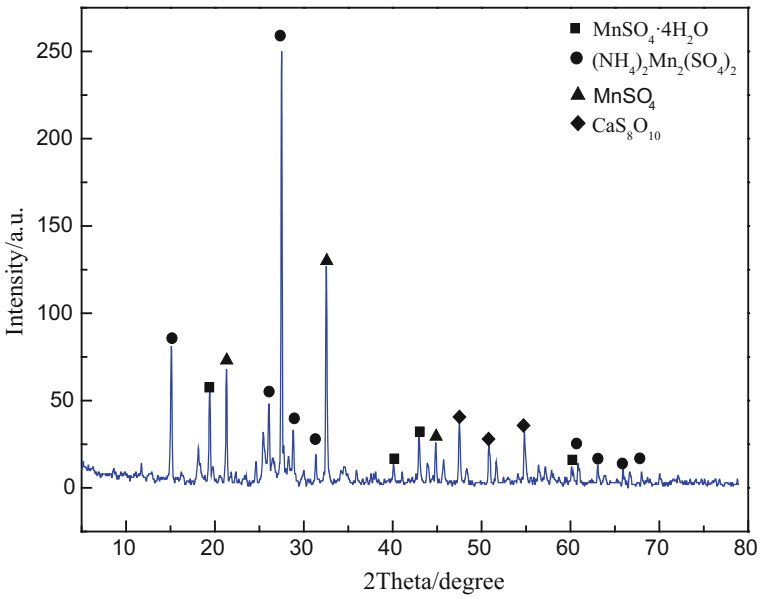

Fig. 8 Product XRD analysis spectrum

Table 2 Analysis results of chemical components of products

Element	Content (%)	Element	Content (%)
Mn	28.1	Ag	0.4×10^{-4}
Pb	0	Se	0.3×10^{-4}
Mg	4.6	As	0.01×10^{-4}
Fe	9.7×10^{-3}	Sb	2.0×10^{-4}
Cr	9.9×10^{-4}	Cu	0

are mainly manganese sulfate and calcium sulfate. The manganese in the experimental product is present in the form of $MnSO_4 \cdot 4H_2O$, $MnSO_4$, (NH_4) $Mn(SO_4)_2$, which is different to the expected sample $MnSO_4 \cdot H_2O$. However, Mn in the sample mainly exists on the form of $MnSO_4$, which basically achieves the experimental purpose.

Conclusions

Using wet-method reducing technique, the amount of manganese increases from electrolytic manganese anode mud. The corn straw was used as reducing agent, dilute sulfuric acid as leaching agent, and sodium dimethyl dithiocarbamate (SDD) as heavy metal excipient in this study. The optimal technological conditions

for the leaching and eliminating manganese were through orthogonal and single factor variable experimental acquisition. Optimum technological conditions are corn straw dosage of 7 g, liquid-to-solid ratios to 6:1 and 7.35 wt% H_2SO_4, aging time is 80 min, ripening temperature is 350 °C, leaching solution pH is 5.5, SDD dosage is of 3.5 g. Under the optimum conditions, the leaching efficiency of manganese reaches 99.85%, recovery efficiency of manganese reaches 94.06%. The content of manganese sulfate in the experimental sample in excess of 85%, the content of heavy metal is less than 5%.

Acknowledgements Thanks to China EU International Cooperation Project (SQ2013ZOG300003) and Ningxia Hui Autonomous Region science and technology support project (2014ZYH50). Thanks to the support of the national international science and technology cooperation base (2015D01016).

References

1. Z.N. Liu, H. Xu, Q.S. Wang et al., China's manganese supply-demand actuality and its sustainable development. Res. Ind. **06**, 38–43 (2015)
2. P. Lin, F.Z. Chen, The demand situation and utilization strategy of China's manganese resources. Chin. Mark. **40**, 20–22 (2007)
3. S.Y. Xiong, Z.F. Zhang, Existing problems and countermeasure of Chinese market of EMM. China's Manganese Ind. **5**, 14–16 (2005)
4. G.Y. Liu, *Research on Comprehensive Recycling of Manganese Anode Slime*. (D. Guangxi University, 2013)
5. Y.Q. Shen, Z.R. Fu, Y.F. Huang, The research on manganese anode slime recycle to produce into chemical manganese dioxide. China's Manganese Industry. **25**, 14–16 (2007)
6. Q.M. Huang, C.P. Wang, H. Zhou et al., The research on manganese anode slime recycle to produce manganese sulfate. Chin. Nonferrous Met. **06**, 6–8 (2010)
7. S.S. Niu, Z.X. Wang, H.J. Guo et al., Reductive leaching of manganese from manganese anode slag. Chin. J. Nonferrous Met. **09**, 2662–2666 (2012)
8. J.G. Tang, Z.C. Han, Investigation on process mineralogy of manganese anode slime and impurity removal. J. Min. Metall. **03**, 75–78 (2005)
9. J.B. Liu, S. Chen, Preparation of manganese sulfate using anode slurry from electrolytic manganese production and industrial exhaust gas containing SO_2. Environ. Prot. Chem. Ind. **06**, 538–540 (2009)
10. S.Z. Zhao, F.L. Han, Y.J. Teng et al., Study on preparation of manganese sulfate by reduction electrolytic manganese anode slime from wood fiber. Inorg. Chemicals Ind. **49**, 63–65 (2017)
11. X.B. Zeng, The development trend of electrolytic manganese industry in China. Technol. Chin. Manganese Ind. pp. 1–4 (2014)
12. L.Q. Huang, Y.F. Bi, L.L. Mu et al., The process and mechanism of electrolytic manganese anode slime lead removal. Adv. Mater. Res. **878**, 163–170 (2014)
13. H.B. Zhang, Y.F. Bi, X.F. Chen et al., Treatment and characterization analysis of electrolytic manganese anode slime. Procedia Environ. Sci. **31**, 683–690 (2016)
14. GB, *Manganese ores—Determination of manganese content—Potentiometric method and ammonium iron (II) sulphate titrimetric method*. (S. People's Republic of China, 2002)

Influence of Diffusion Annealing and Subsequent Deformation on Bonding Strength of Cu/Al Bimetallic Strips

Zhi Qin, Weifeng Peng, Jing Zhang, Donghui Xie, Min Yu and Kaihong Cai

Abstract To implement the spirit of the State Council's document on resolving the serious excess capacity contradiction, at the same time, to solve the problem of welding between copper and aluminum in the electricity, a bimetallic strip with Al–Cu–Al sandwich structure has been developed, of which copper accounts for nearly 80%. The solid phase rolling process was adopted for the strip. The interface and bonding strength of copper aluminum clad were studied by different diffusion annealing process and subsequent cold rolling deformation, and the conductivity of the laminated clad strip was tested. The results show that, the critical reduction rate to combine copper and aluminum together is 40%; the diffusion annealing temperature at 300 °C can be achieved with copper and aluminum metallurgy combination; the subsequent cold rolling deformation run up to 50%, which can increase the bonding strength of copper and aluminum clad strip; the conductivity of the copper/aluminum bimetallic strip are between the value of pure copper and pure aluminum. Welding adverse contradictions of copper and aluminum can be solved by cold rolling bonding at room temperature.

Keywords Interface · Heat treatment · Bond strength · Aluminum Copper · Bimetal

Introduction

With the development of modern industry and more severe energy saving and environmental protection requirements, the State Council called for the use of more aluminum instead of copper to reduce costs and digest capacity. At the historic moment, clad materials arise because industrial production requires not only to save costs, as much as possible to dilute the precious metals, but also to maintain a certain performance of materials. The copper, aluminum clad material combines the chemical and physical properties of aluminum and copper, and makes up for the

Z. Qin (✉) · W. Peng · J. Zhang · D. Xie · M. Yu · K. Cai
No. 1 Xiaoying East Road, Beijing 100192, China

Y. Han (ed.), *Advances in Energy and Environmental Materials*,
Springer Proceedings in Energy, https://doi.org/10.1007/978-981-13-0158-2_65

deficiency of a single material. Moreover, the price is complementary, which helps to save the cost and improve the production efficiency, and has a good application prospect. Bimetal joints made of copper and aluminum have been of great interest in various disciplines of engineering, especially for electrical applications such as new energy automotive field. A two layer Al/Cu clad sheet can reduce its nearly 40% weight by keeping the conductivity and thermal conductivity close to that of pure copper, at the same time saves 60% of the cost [1]. Electric vehicle weight reduced by 10%, the mileage increased 5.5%, so light weight of an electric vehicle is of great significance.

In recent years, explosive welding, rolling bonding, diffusion bonding, extrusion and friction-stir welding are developed as the production techniques of clad strips [2–8]. Cold roll bonding technique has been extensively investigated and most widely used, because it is the most efficient and economical one, and it avoids the generation of the brittle intermetallic compounds which will be made between copper and aluminum when the temperature is higher than 120 °C [9–11]. Roll bonding can join two or more dissimilar metals in the solid state, which needs to guarantee a basic parameter is the critical reduction rate [12–14]. Different metals could bond together only the deformation exceeding this value. The interfacial microstructure of Cu/Al interface can be improved due to the large interfacial plastic deformation caused by the different rotation speeds of roll in the asymmetrical roll bonding process [15]. The threshold reduction between 40 and 80% has been reported for Cu/Al clad sheets [16, 17]. Moreover, it is equally important to remove the contamination layers from the surfaces by chemical and mechanical treatments [18]. After that the heat treatment for diffusion would enhance the interfacial adhesion, but for the interface between copper and aluminum improper heat treatment processes is detrimental to the interface [19, 20].

In recent years, great progress has been made in the research of copper/aluminum clad materials, and many achievements have been made in the process of solid phase clad rolling and post rolling heat treatment [20–23]. However, many problems have not been solved for interface control and mechanical properties of Cu/Al multilayer sheets. Problems such as the interfacial morphology controlling, the interfacial compounds inhibiting, the relationship between interfacial structure and properties, etc. These problems have not been solved properly, which will seriously restrict and become a great barrier to the application of Cu/Al cold rolled bimetallic strip. Therefore, in the present study, a three-layer clad strip comprised of Al (1060), Cu (TU1) and Al (1060) was manufactured by solid phase rolling at room temperature. The effect of diffusion treatment and subsequent deformation on the bonding strength of the three layer clad strip were investigated.

Table 1 Specification of aluminum and copper in investiture used in the investigation

Cu and Al grade	Chemical composition (wt%)	Temper	Hardness (HV)	Yield strength (MPa)	Tensile strength (MPa)
Cu-TU1	≥ 99.9 Cu	Annealed	60	360	380
Al-1060	≥ 99.6 Al	H12	58	180	192

Materials and Experiments

In this investigation, the annealed electrical grade of copper strips (TU1) and aluminum strips (1060) with thickness of 6.0 mm and 0.75 mm were rolling welded at room temperature (20–25 °C). The composition and properties of the Cu and Al are summarized in Table 1.

Firstly, cleaning the materials in a powerful solvent then dried up. Carrying out the surface treatment of both Al and Cu to remove surface contamination. Scratch brushes on both surfaces of the Cu and Al after abrasive belt grinding. The bristles of the brush were made of stainless steel wire. After that aligning and fixing the aluminum, copper and aluminum strips in a pack. After surface preparation a fixed pack of aluminum and copper was made in order that the pack passes uniformly and adjustable through the roller gap. It has been reported that the oxide layer is formed very rapidly on the surface of the aluminum and copper and acts as a barrier to the formation of a metallurgical bond [24]. Therefore, the interval time between the surface preparation and rolling was kept less than 30 min to avoid the formation of a thick and continuous oxide layer on the surfaces of the strips.

The last step of making the tri-layer bimetal was to cold roll of the pack to produce a metallic continuity between Cu and Al at the interface. For roll welding of Al to Cu, a roll force between 190 to 220 t and reduction between 40 and 60% has been applied in total thickness of the pack, a sound metallurgical bond between Cu and Al strip was made.

The produced bimetal samples were heat treated at 300–600 °C per 50 °C for 2 h. Subsequent deformation mostly to 90% reduction applied to the sample after 60% reduction roll welding and heat treatment at 300 °C for 2 h. Microstructure observation and bending test were carried out to all the samples.

Results and Discussion

Diffusion Annealing. When the cold rolling reduction rate reached 40%, the three layers of metal begin to stick together. The metal bond became stronger as the reduced rate increased. As known from the previous studies on the effect of reduction of the cold roll bonding, bond strength improved when the reduction increased because of the enhancement of the rolling pressure, surface expansion and

area fraction of cracks, as well as the greater percentage of the bonded areas at the bond interface [25]. More fresh metal surfaces were brought together within a very close distance and the welded area becomes larger, this extension of the area available for an atom to an atom bonding results in a stronger bonding. Furthermore, when deformation is less than the threshold deformation, only a few surface cracks results, and therefore, the amount of virgin metals in contact with each other at the interface is very low so that fresh metal surfaces cannot bond together strongly. This threshold reduction is greatly depending on surface treatment and the numerous rolling parameters such as diameter, rigidity and surface roughness of the roll, preliminary thickness of each layer before rolling and geometry of deformation zone.

Repeated bending to fracture is a kind of method to measure bonding strength of multilayer composite metals. The result of bending tests of samples of various heat treatment temperature is showed in Fig. 1, the toughness of the clad strip first increased with the annealing temperature, and reached the maximum at 450 °C and then decreased. Unfortunately, all samples showed delamination after bending to fracture. The heat treatment after rolling can improve bond strength even at low times. There were three ways to influence the bonding process. First the strip hardness was decreased by the annealing that means the bond toughness was increased. So the force required for crack propagation increased. Thereby the bond strength increased. Second, the heat treatment could accelerate the atomic motion, be attributed to the atomic diffusion phenomenon at the interface and thermally activated short range atomic movements. Post-rolling annealing was also known as diffusion annealing. The diffusion layer thickness depending on the temperature and time of the annealing. As showed in Fig. 2, the thickness increased with the increase of annealing temperature, because the higher temperatures made atoms more active which conformed to the diffusion law. It's reasonable for the diffusion layer around 5 μm in bimetal strips, so 300 °C is a reasonable heat treatment temperature for post-cold roll bonding of copper and aluminum. Third, the residual stresses between the solid state bonded materials which induced by cold rolling will be removed or reduced through heat treatment. The post-rolling annealing will improve bonding which was partially bonded during the rolling.

Furthermore, when the temperature of post-rolling annealing is increased, for some copper and aluminum, the intermetallic or other brittle phases may be formed at the interface, as same as titanium alloy [26–28]. Delamination after bending to fracture can be attributed to the generation of the intermetallic compounds. After the heat treatment at 600 °C for 2 h, the interface between copper and aluminum showed a transition layer which was not a single structure, but a multi-layered structure as shown in Fig. 3. From the point of view of the welding process, Al and Cu are incompatible metals because they have a high affinity to each other at temperatures greater than 120 °C and produce brittle, low strength and high electrical resistance intermetallic on their interface [9, 11]. Priority of formation of intermetallic phases was such that the intermetallic compounds Cu_3Al, Cu_4Al_3, saturated solid solution of 9–13% Al in Cu, CuAl, and $CuAl_2$ [19]. Al and $CuAl_2$ are next to each other make the phase interface is not straight because Al and the

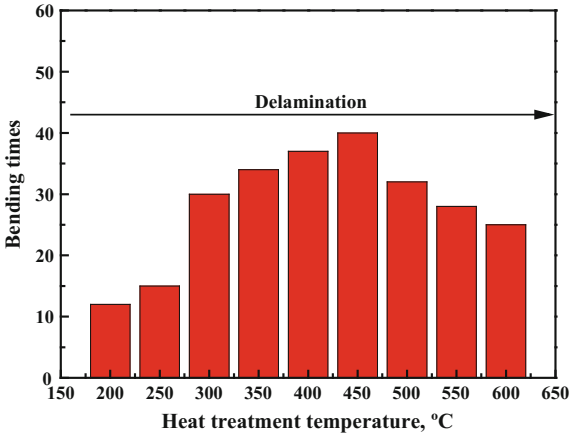

Fig. 1 Results of the bending test for various heat treatment temperature

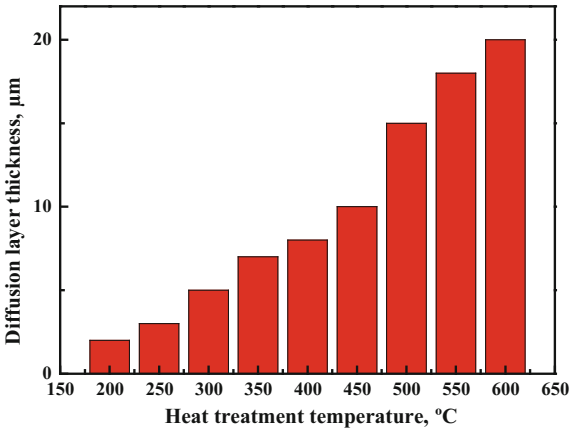

Fig. 2 Diffusion layer thickness after various heat treatment temperature

$CuAl_2$ crystal structure are both along the [0 0 1] direction, but in a different form. The $CuAl_2$ phase has a tetragonal crystal structure with a = 0.6067 nm and c = 0.4887 nm, while Al has a Face center crystal structure with a = 0.4049. The lattice parameters of Al and $CuAl_2$ are quite different along the [0 0 1] crystal direction. A weak transition layer would be formed along the Al and $CuAl_2$ interface to reduce the influence of lattice difference. Meanwhile, little oxygen was found on the tear surface on one side of aluminum. The surface treatment of the Al may not get a new metal surface, a thin oxide film covered. That is because Al is extremely reactive, $4Al + 3O_2 \rightarrow 2Al_2O_3$, the standard molar enthalpy of formation is −1582 kJ/mol. This also makes the bonding weak.

Subsequent Deformation. The result of bending tests of samples of various reduction rate after 300 °C annealing is shown in Fig. 4, the toughness of the clad strip first increased with the annealing temperature, and reached the maximum at

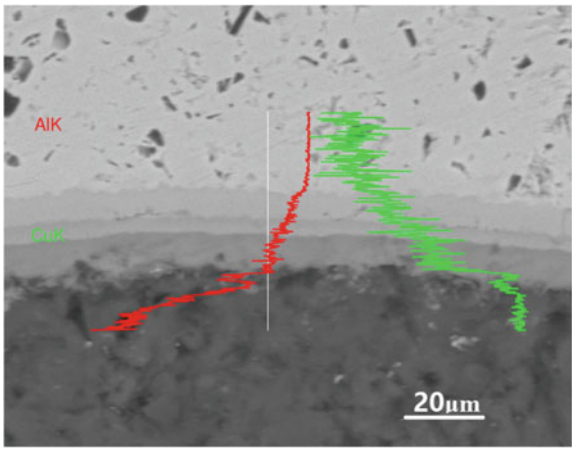

Fig. 3 Interfacial morphology and SEM energy spectrum line sweep of Al, Cu elements with 600 °C heat treatment

60% reduction rate and then decreased rapidly because of the work hardening. Before the reduction rate got 50%, delamination happened to all the samples, but when reaching and exceeding 50% non-delamination occurred. Post-annealing rolling enhanced bonding strength. Generally, the higher thickness reduction during cold roll will produce greater metal flow, and a new, stronger bonding will be formed by the more intense interracial interaction. The intermetallic compounds and alumina originally existed at the interface which will be segmented into pieces during deformation. More new bonding without substance that weakens the interface has been created.

Electrical Conductivity. The electrical conductivity of the clad strip was shown in Fig. 5. The electrical conductivity of the copper/aluminum bimetallic strip is between the value of pure copper and pure aluminum. The resistivity was relatively stable and showed a slight fluctuation with the change of the reduction rate. For

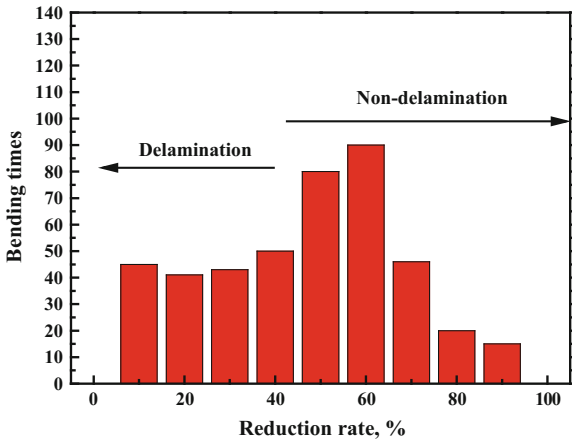

Fig. 4 Results of the bending test for various post-annealing reduction rate

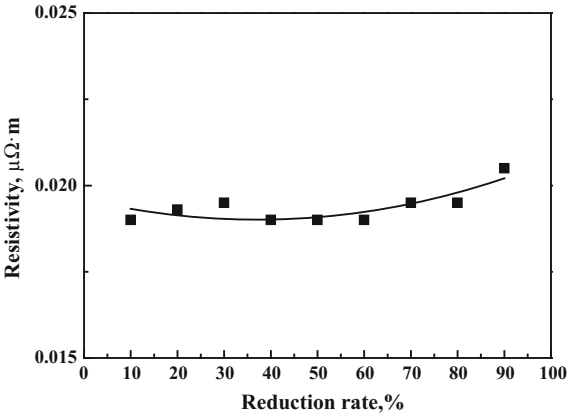

Fig. 5 Resistivity at different rates of reduction

multilayer materials, their resistivity can be considered as a parallel resistance of multilayer metal, so satisfy the formula:

$$\frac{h}{\rho} = \frac{h_{\mathrm{u}}}{\rho_u} + \frac{h_{\mathrm{m}}}{\rho_{\mathrm{m}}} + \frac{h_{\mathrm{l}}}{\rho_{\mathrm{l}}} \tag{1}$$

In which h, h_u, h_m and h_l represented the thickness of clad material, upper layer, middle layer and lower layer respectively.

ρ, ρ_u, ρ_m and ρ_l represented the resistivity of clad material, upper layer, middle layer and lower layer respectively.

Conclusion

1. Copper and aluminum can be combined by cold roll bonding with the threshold deformation 40%;
2. Metallurgy combination between copper and aluminum will be achieved with the diffusion annealing at 300 °C;
3. The subsequent cold rolling deformation increased the bonding strength of copper and aluminum clad strip when reduction rate reaching and exceeding 50%;
4. The conductivity of the copper/aluminum bimetallic strip is between the value of pure copper and pure aluminum.

References

1. M. Eizadjou, A.K. Talachi, H.D. Manesh, H.S. Shahabi, K. Janghorban, Investigation of structure and mechanical properties of multi-layered Al/Cu composite produced by accumulative roll bonding (ARB) process. Compos. Sci. Technol. **68**(9), 2003–2009 (2008)
2. Y. Yang, Z. Xinming, L. Zhenghua, L. Qingyun, Adiabatic shear band on the titanium side in the Ti/mild steel explosive cladding interface. Acta Materialia. **44**(2), 561–565 (1996)
3. J.H. Han, J.P. Ahn, M.C. Shin, Effect of interlayer thickness on shear deformation behavior of AA5083 aluminum alloy/SS41 steel plates manufactured by explosive welding. J. Mater. Sci. **38**(1), 13–18 (2003)
4. F. Yoshida, R. Hino, Forming limit of stainless steel-clad aluminium sheets under plane stress condition. J. Mater. Process. Technol. **63**(1), 66–71 (1997)
5. T. Mori, S. Kurimoto, Press-formability of stainless steel and aluminum clad sheet. J. Mater. Process. Technol. **56**(1), 242–253 (1996)
6. M. Abbasi, A. Karimi Taheri, M.T. Salehi, Growth rate of intermetallic compounds in Al/Cu bimetal produced by cold roll welding process. J. Alloy Compd. **319**(1), 233–241 (2001)
7. P. He, X. Yue, J.H. Zhang, Hot pressing diffusion bonding of a titanium alloy to a stainless steel with an aluminum alloy interlayer. Mater. Sci. Eng. A. **486**(1), 171–176 (2008)
8. W.-B. Lee, K.-S. Bang, S.-B. Jung, Effects of intermetallic compound on the electrical and mechanical properties of friction welded Cu/Al bimetallic joints during annealing. J. Alloy. Compd. **390**(1), 212–219 (2005)
9. M. Braunovic, N. Aleksandrov, in *Effect of Electrical Current on the Morphology and Kinetics of Formation of Intermetallic Phases in Bimetallic Aluminum-Copper Joints*. Proceedings of the Thirty-Ninth IEEE Holm Conference on Electrical Contacts (1993), pp. 261–268
10. S. Mróz, P. Szota, A. Stefanik, S. Wąsek, G. Stradomski, Analysis of Al-Cu bimetallic bars properties after explosive welding and rolling in modified passes. Arch. Metall. Mater. **60**(1), 427–432 (2015)
11. R. Uscinowicz, Impact of temperature on shear strength of single lap Al–Cu bimetallic joint. Compos. B. Eng. **44**(1), 344–356 (2013)
12. D. Pan, K. Gao, J. Yu, Cold roll bonding of bimetallic sheets and strips. Mater. Sci. Technol. **5**(9), 934–939 (1989)
13. H.D. Manesh, A.K. Taheri, Study of mechanisms of cold roll welding of aluminium alloy to steel strip, Materials Science & Technology. 20(8) (2004) 1064–1068
14. A. Yahiro, T. Masui, T. Yoshida, D. Doi, Development of nonferrous clad plate and sheet by warm rolling with different temperature of materials. ISIJ Int. **31**(6), 647–654 (2007)
15. X.-B. Li, G.-Y. Zu, P. Wang, Asymmetry in interface and bending property of Al/Cu/Al bimetallic laminates. Rare Metals. **33**(5), 556–562 (2014)
16. N. Bay, Cold Welding: Part 1. Characteristics, Bonding mechanisms, Bond Strength. Br. Marit. Technol. **18**, 369–372 (1986)
17. C. Clemensen, O. Juelstorp, N. Bay, Cold Welding. Part 3: Influence of Surface Preparation on Bond Strength. **18**, 625–629 (1986)
18. H.R. Le, M.P.F. Sutcliffe, P.Z. Wang, G.T. Burstein, Surface oxide fracture in cold aluminium rolling. Acta Materialia. **52**(4), 911–920 (2004)
19. M. Abbasi, A.K. Taheri, M.T. Salehi, Growth rate of intermetallic compounds in Al/Cu bimetal produced by cold roll welding process. J. Alloy. Compd. **319**(1–2), 233–241 (2001)
20. L.Y. Sheng, F. Yang, T.F. Xi, C. Lai, H.Q. Ye, Influence of heat treatment on interface of Cu/Al bimetal composite fabricated by cold rolling. Composites B Eng. **42**(6), 1468–1473 (2011)
21. Y.S. Yang, D.D. Yang, Processing method and application of copper aluminum composite plate. Hot Working Process. **40**(12), 107–110 (2011)
22. L. Lu, *Influence of Diffusion Process on Structure of Cu/Al Composite Interface Layer* (Shenyang University of Technology, 2012)

23. L. Sun, *Study on Rolling Process of Three Metal Composite Plate—Copper/Aluminum/Stainless Steel* (Xi'an University Of Architecture and Technology, 2014)
24. W. Zhang, N. Bay, *Influence of Different Surface Preparation Methods on the Bond Formation in Cold Pressure Welding*, pp. 379–388 (1994)
25. R. Jamaati, M.R. Toroghinejad, Effect of Al2O3 nano-particles on the bond strength in CRB process. Mater. Sci. Eng. A. **527**(18), 4858–4863 (2010)
26. J.-G. Luo, V.L. Acoff, Using cold roll bonding and annealing to process Ti/Al multi-layered composites from elemental foils. Mater. Sci. Eng A. **379**(1), 164–172 (2004)
27. P. Qu, L. Zhou, H. Xu, V.L. Acoff, Microtexture development of niobium in a multilayered Ti/Al/Nb composite produced by accumulative roll bonding. Metall. Mater. Trans. A. **45**(13), 6217–6230 (2014)
28. G.P. Chaudhari, V.L. Acoff, Titanium aluminide sheets made using roll bonding and reaction annealing. Intermetallics. **18**(4), 472–478 (2010)

Effect of Waste Cooking Oil Viscosity on Basic and Rheological Properties of Aged Asphalt

Dong Zhang, Meizhu Chen, Shaopeng Wu, Siqing Liu and Jingxiang Liu

Abstract Waste cooking oil (WCO) can be used to rejuvenate aged asphalt and restore its properties. However, the influence of WCO properties on rejuvenating behavior of aged asphalt is still unknown. The objective of this study is to investigate the effect of WCO viscosity on basic and rheological properties of aged asphalt. The materials used for this study included eight kinds of WCO (fabricated by fresh soybean oil in the laboratory) and one aged asphalt (AH-90). The basic properties of rejuvenated asphalt were characterized by penetration value, softening point and ductility, then the influence of WCO viscosity on rheological properties of rejuvenated asphalts were evaluated by rotational viscosity, rutting parameter, complex modulus and phase angle master curves, and creep recovery ratio. The experimental results indicate that WCO viscosity has a great influence on the properties of rejuvenated asphalt, and different aged asphalts require WCOs with different viscosity to achieve the desirable rejuvenation effects. Basic and rheological properties of aged asphalt can be restored to some extent but there are still gaps between the basic performances of WCO rejuvenated asphalts and virgin asphalt. WCOs with too high or too low viscosity values would have an adverse impact on the performance recovery of rejuvenated asphalt. WCO with viscosity ranging from 420–700 mm^2/s are preferable to restore the properties of rejuvenated asphalt in this research.

D. Zhang · M. Chen (✉) · S. Wu · S. Liu · J. Liu
State Key Laboratory of Silicate Materials for Architectures, Wuhan University of Technology, Wuhan 430070, China
e-mail: chenmzh@whut.edu.cn

D. Zhang
e-mail: pytmac@whut.edu.cn

S. Wu
e-mail: wusp@whut.edu.cn

S. Liu
e-mail: liusiqing@whut.edu.cn

J. Liu
e-mail: liujingx@whut.edu.cn

Y. Han (ed.), *Advances in Energy and Environmental Materials*,
Springer Proceedings in Energy, https://doi.org/10.1007/978-981-13-0158-2_66

Keywords Waste cooking oil · Viscosity · Aged asphalt · Rejuvenation Properties

Introduction

Reclaimed asphalt pavement (RAP) contains many value aggregates and asphalt binders, and the recycling of these raw materials in pavement construction can benefit both environment and economy [1, 2]. Generally, asphalt recycling can be classified into three major categories, namely hot, warm and cold, based on the condition of the deteriorated pavement, construction procedure, equipment availability, and cost. Hot recycling is the most commonly process due to the similar performance to newly-built pavement as well as demonstrating cost effectiveness of the recycled materials, and the recycling agents are critical to that achievement.

Conventional recycling agents are called as rejuvenators, which are usually comprised of low viscosity components, asphaltenes and other additives that could improve the performance of asphalt binders [3]. However, the application of rejuvenators are limited because of their expensive price and high dosage in use, which elevates the construction budget and difficulty. In order to meet the high demand for asphalt recycling agent, recycled oils were researched and applied owing to the similar chemical constituent with rejuvenator. Romera verified the feasibility of applying recycled motor oil to rejuvenate aged asphalt [4]. Asli and Zargar evaluated the effects of waste cooking oil (WCO) on the physical and rheological properties of aged asphalt [5, 6]. Chen studied the influence of WCO categories on physical, chemical and rheological properties of rejuvenated asphalt binders [7]. Zhang evaluated the low temperature performance of asphalt binder containing bio-based and refined waste oil [8].

Some studies have shown that WCO is one of rejuvenating agents that possibly restore the aged asphalt properties to the similar level of the virgin asphalt. However, no research was found to evaluate the relationship between WCO property and asphalt rejuvenation effect. The standard of American Society for Testing and Materials (ASTM) [9] suggested that the viscosity at 60 °C is suitable for classifying hot-mix asphalt (HMA) recycling agents. Therefore, the objective of this paper is to investigate the effect of WCO viscosity on basic and rheological properties of aged asphalt, and thusly raising a quality standard to identify the WCO that can be used for recycling asphalt mixture. Penetration, softening point and ductility tests were performed to investigate the influence of WCO viscosity on conventional physical performance of rejuvenated asphalt. Rotational viscosity, rutting parameter, complex modulus and phase angle master curves, creep recovery curves were tested to evaluate the rheological properties of WCO rejuvenated asphalt.

Materials and Methods

Raw Materials. An AH-90 asphalt binder (referred as A_0) that has been widely used in China was used as control asphalt in this research, and its conventional properties were tested and presented in Table 1 along with the performances of laboratory aged asphalts.

Restaurant-recycled WCO was selected in most studies to investigate the influence of WCO on asphalt performance, however the qualities of these WCO, like viscosity, density, acid value, impurity content, water content are uncontrollable, and thus the experimental results are subject to uncertainty. Therefore, fresh soybean oil (referred to as W_0) was selected and heated continuously to produce quality controllable WCO in this research. The WCO sample was fabricated at a temperature of 270 °C and the stirring rate of 1200 rpm for 2, 4, 6, 8, 10, 12, 14 and 16 h respectively, the obtained WCOs were referred to as W_1–W_8, respectively. The viscosity of WCO was tested according to ASTM D4552 [9], and the results are shown in Fig. 1. It can be noticed that the viscosity of WCO increases with the heating time distinctly, which proves that the viscosity of WCO can be regulated in the laboratory, and a prolonged heating time means a lower quality of WCO.

Table 1 Basic Properties of Asphalt Binders

Asphalt Categories	Softening Point [°C]	Penetration [0.1 mm, 25°C]	Ductility [cm, 15°C]	Viscosity [Pa·s, 135°C]
AH-90 asphalt (A_0)	45.1	83.7	> 150	0.45
AH-90 + RTFOT	49.9	53.4	129	0.57
AH-90 +RTFOT + PAV (A_1)	58.5	32.7	10	0.99

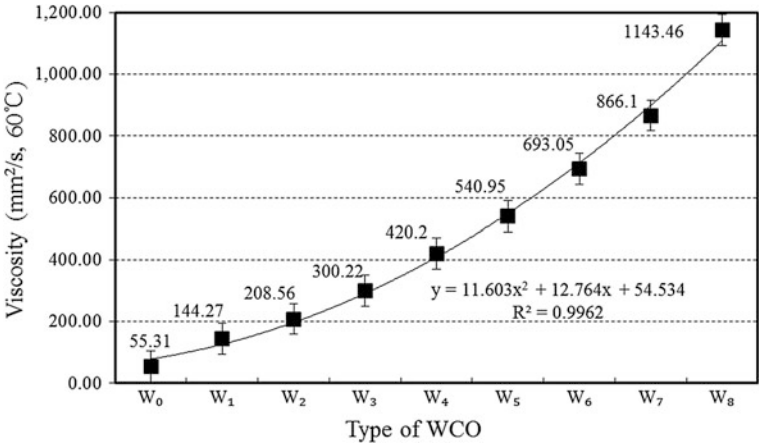

Fig. 1 Viscosity of WCO at 60°C with different heating time

Experimental Methods

Preparation of Aged Asphalt Binder. Laboratory accelerated ageing was applied to prepare aged asphalt binder in this research. Rolling thin film oven test (RTFOT) was firstly used to simulate the ageing process of binders in asphalt mixtures paving (ASTM D2872) [10]. Then, the pressure ageing vessel (PAV) was applied to simulate the long-term ageing effects of climate on asphalt mixtures after the RTFOT (ASTM D6521) [11]. The basic properties of short-term and long-term ageing asphalt binders are shown in Table 1.

Preparation of Rejuvenated Asphalt Binders. Rejuvenated asphalt binders were prepared by means of mixing laboratory accelerated ageing asphalt (referred as B_0) with different WCOs (W_1–W_8). The blending process was conducted by a propeller mixer at a constant speed of 1200 rpm for 15 min, and the experimental temperatures are 130 °C. The proportion of WCO is 6.0 wt% of aged asphalt binder B_0 based on the published article [12]. The rejuvenated asphalt binders were referred to as A_1–A_8, respectively.

Basic Property Tests. To evaluate the effect of WCO viscosity on basic properties of rejuvenated asphalt, conventional methods such as penetration (ASTM D5) [13], ductility (ASTM D113) [14], ring and ball softening point (ASTM D36) [15] were selected in this research.

Rheological Property Tests. Dynamic Shear Rheometer (DSR) was applied to investigate the influence of WCO viscosity on rheological properties of WCO rejuvenated binders based on ASTM D7175 [16]. DSR temperature sweep tests from 30 to 80 °C were performed to study the permanent deformation resistance of rejuvenated asphalts by means of the construction of parameter curves. DSR frequency sweep tests from −10 to 60 °C at 10° °C intervals with frequencies from 0.1 to 100 rad/s were conducted, and the time-temperature superposition principle (TTSP) was used to construct master curves for complex modulus G^* and phase angle δ at a reference temperature of 20 °C. To study the response of binders to creep loading, creep recovery tests were performed by DSR at 10 °C and a fixed shear stress of 2 kPa, an experimental condition that represents the high stress level on pavement services.

Experimental Results and Discussion

Basic Properties.

Penetration Values. Figure 2a is the statistical results of penetration test of rejuvenated asphalt binder with different WCOs incorporated. As can be seen in Fig. 2a that the penetration values of rejuvenated asphalt binders are significantly higher than that of aged asphalt B_0, which has verified the feasibility of using WCO to

rejuvenate aged asphalt. On the other hand, an obvious trend is manifested when the results of rejuvenated asphalts with different WCOs are taken into consideration: with the increase of WCO viscosity, the penetration values have decreased gradually. Therefore, from the results point of view, the aged asphalt can be softened by adding WCO and the efficiencies of softening are varied with the viscosity of WCO. The cause may be the content difference of light component in different WCOs.

Softening Point Values. Softening point is a measurement of the temperature sensitivity of asphalt. Figure 2a also shows the influence of WCO viscosity on the softening point values of rejuvenated asphalt binders. It can be seen from the histogram that the softening point values of rejuvenated binders are obviously lower than that of the aged binder, which means the viscous behavior of aged asphalt has been enhanced. Besides that, the softening point values of rejuvenated binders increase gradually with the viscosity of WCO. The experimental results are consistent with the penetration test results.

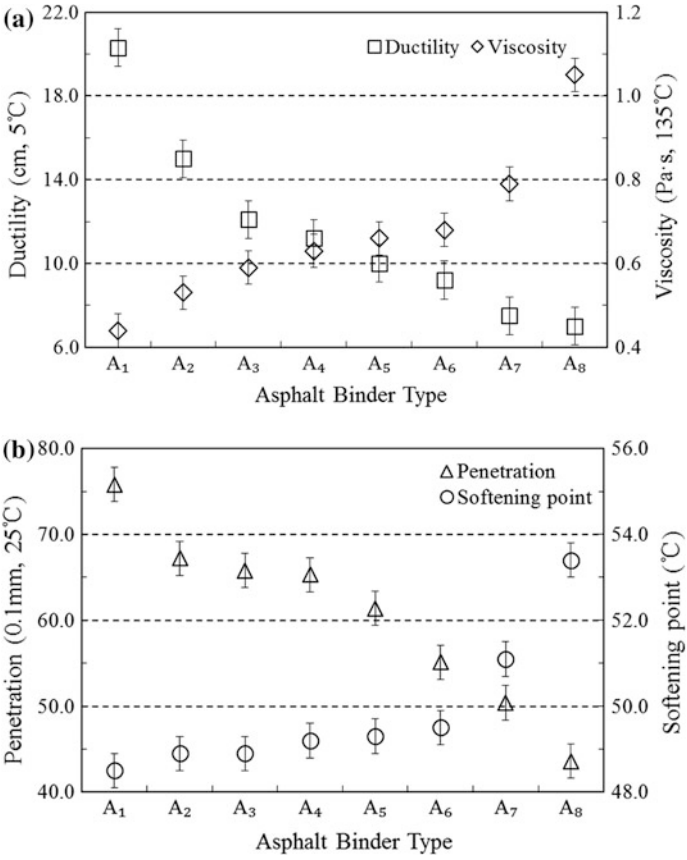

Fig. 2 Conventional property versus different kinds of asphalt binders

Ductility Values. Ductility is usually tested to illustrate the plasticity and ductility of asphalt at low temperatures. As shown in Fig. 2b, the trend is of ductility values is similar to that of penetration values. These results indicate that the addition of WCO can enhance the ductility behavior of aged asphalt. Nonetheless, the ductility decreasing with the increasing of WCO viscosity means the ductility improvements of aged asphalt are controlled by the quality of WCO.

The above results indicate that the basic properties of aged asphalt can be restored due to the addition of WCO, and the efficiency improves with the decreasing of WCO viscosity. However, there are still gaps between the basic performance of WCO rejuvenated asphalts and virgin asphalt. Therefore, DSR tests were performed subsequently to study the effect of WCO viscosity on the rheological properties of rejuvenated asphalts.

Rheological Properties.

Rotational Viscosity Results. Viscosity can characterize the resistance to shear deformation of asphalt under an external force. The viscosity at 135 °C is normally used to represent the compacting temperature of asphalt mixture. Figure 2b shows the effect of WCO viscosity on aged asphalt viscosity. It can be seen that the viscosity values of rejuvenated asphalt increase gradually with the increase of WCO viscosity, and the rejuvenated asphalt A8 has a higher viscosity value than the aged asphalt B_0. This result indicates that using WCO with viscosity lower than 1150 mm^2/s can improve the fluidity of aged asphalt as well as the construction temperature and energy consumption of HMA. On the other hand, it is notable that the viscosity value of virgin asphalt A_0 is between that of rejuvenated asphalts A_1 and A_2, which means that the WCO with viscosity around 100 mm^2/s can restore the viscosity of aged asphalt to the level of virgin asphalt. Therefore, it can be concluded that using WCO with viscosity ranges from 100–1150 mm^2/s can achieve the purpose of restoring aged asphalt viscosity in this case. Normally, WCO with lower viscosity can also be selected for asphalt rejuvenation, and the obtained viscosity values may be even lower than that of virgin asphalt. However, an excessively low viscosity of asphalt would lead to the adhesion reduction and thus the performance degradation of asphalt mixture. Consequently, it is advisable to keep the viscosity of WCO in a reasonable range.

Temperature Sweep Results. Rutting parameter ($G^*/\sin\delta$) reflects the unrecoverable deformation of asphalt binders during loading process [17]. Asphalt binder with higher $G^*/sin\delta$ but lower flow deformation at high temperatures are desirable. Figure 3 illustrates the $G^*/sin\delta$ of virgin, aged and WCO rejuvenated binders. It can be observed that the $G^*/sin\delta$ values of rejuvenated binders are obviously dependent on the viscosity of WCO and the test temperatures. Generally, the $G^*/sin\delta$ values of rejuvenated asphalts decrease with the increase of test temperature and the decrease of WCO viscosity. To be specific, the $G^*/sin\delta$ values of rejuvenated asphalts containing different WCO are lower than that of the aged asphalt B_0 but higher than that of the virgin asphalt A_0. However, the rejuvenated asphalts A_1 and A_2 shows lower $G^*/sin\delta$ than the virgin asphalt at the intermediate temperatures (30–80 °C),

while the $G^*/sin\delta$ of rejuvenated asphalt A_1 is higher than that of the aged asphalt. Therefore, the WCO with viscosity ranging from 200–700 mm^2/s is recommended in this research to restore the high-temperature properties of aged asphalt.

Frequency Sweep Results. Frequency sweep tests were conducted and the master curves were constructed to fully investigate the influence of WCO viscosity on rheological properties of rejuvenated asphalt. The frequency dependence of complex modulus (G^*) and phase angle (δ) for virgin, aged and rejuvenated binders with different WCO have been assessed in Fig. 4, by producing their master curves using the time-temperature superposition principle [18, 19].

The complex modulus master curves are illustrated in Fig. 4a. It can be noticed that at low frequencies (high temperatures), the G^* values of WCO rejuvenated asphalts are lower than that of aged asphalt (B_0) except for A_8, which indicates that the viscosity of WCO has a great impact on the permanent deformation resistance restoration of aged asphalt, and the WCOs with viscosity higher than 1150 mm^2/s is inapplicable for the high-temperature properties recovery. Moreover, the high-temperature rheological properties of rejuvenated asphalts are varied with different WCO applied. With the decreasing of WCO viscosity, the complex modulus master curves of rejuvenated asphalts are approaching to the master curve of virgin asphalt, which can be considered as the recovery efficiency increases with the WCO qualities improving.

The master curves of phase angle δ are shown in Fig. 4b. As illustrates in the graph that the δ values of WCO rejuvenated asphalts are lower than that of virgin asphalt (A_0) but higher than that of the aged asphalt (B_0), which indicates that the addition of WCO can replenish the viscous components in aged asphalt but the replenishments are limited. It can also be noticed that the rejuvenated binder with lower viscosity WCO has closer δ value with the virgin asphalt. These results are coincident with the complex modulus analyses that the recovery efficiency of WCO increases with the qualities improving.

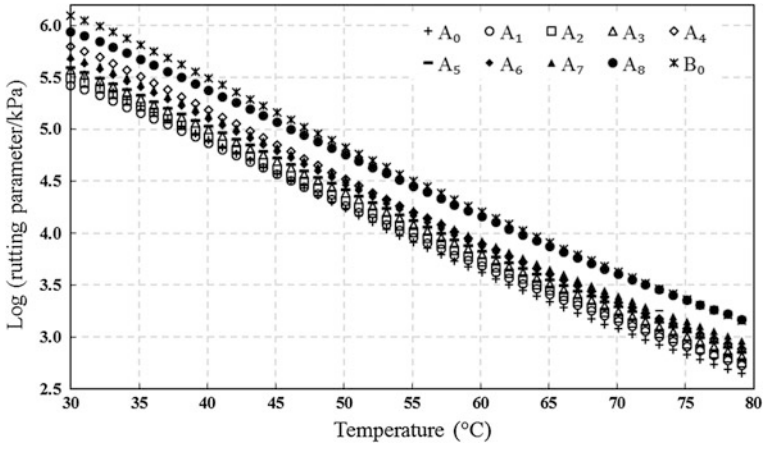

Fig. 3 Rutting parameter $G^*/\sin\delta$ versus temperature for different kinds of asphalt binders

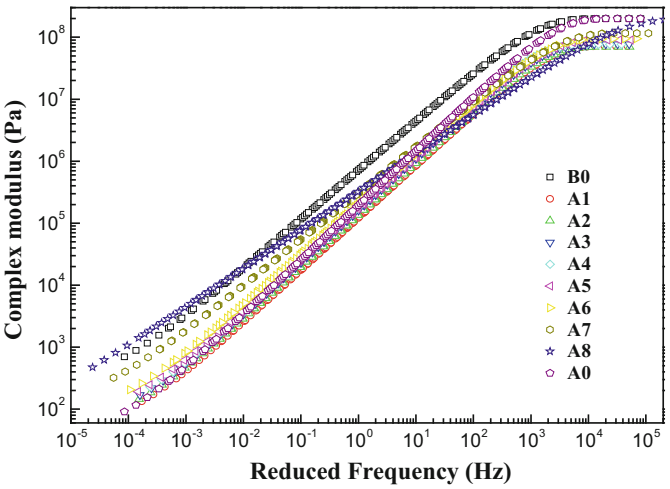

(a) Complex modulus (G^*)

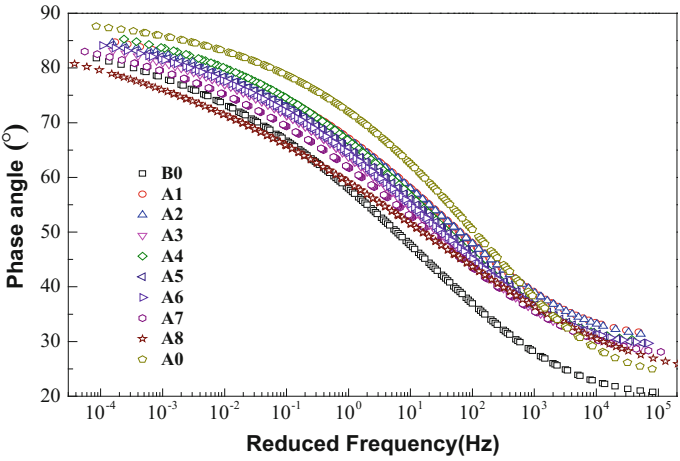

(b) Phase angle (δ)

Fig. 4 Master curve at 20°C for different kinds of asphalt binders

Creep Recovery Results. Creep is a phenomenon that strain increasing gradually over time when stress at a fixed value [20]. Typically, asphalts with lower maximum and permanent deformation have greater creep recovery. Figure 5 shows the influence of WCO viscosity on creep recovery of rejuvenated binders at 10 °C. It can be observed that the rejuvenated asphalt binders have greater maximum and permanent deformation than the aged asphalt B_0 except for A_8. These results indicate that the addition of WCO could increase the thermal cracking resistance of aged binder. Besides that, the maximum and permanent deformation of rejuvenated

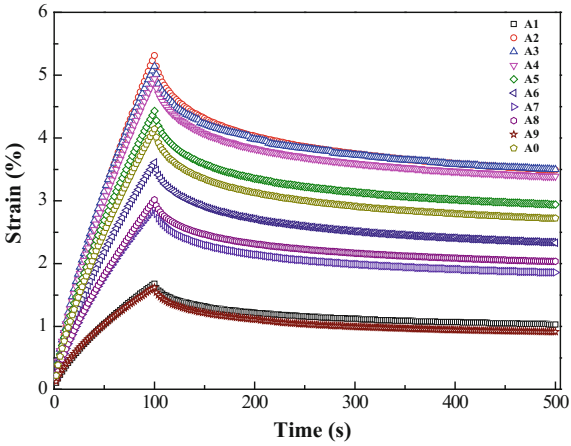

Fig. 5 Creep recovery at 10°C for different kinds of asphalt binders

binders increase with the viscosity of WCO decreases, and the rejuvenated binders A_1, A_2, A_3 and Aa show lower creep recovery performance than its virgin binder. The results indicates that WCO with extremely low viscosity would impair the low-temperature rheological property of rejuvenated binder. In this research, the WCOs with viscosity range from 420 to 870 mm^2/s are desirable for restoring the rheological property of aged asphalt at low temperatures particularly.

Conclusions

Based on the experimental results from the rejuvenated asphalts with different kinds of WCO in terms of a series of basic and rheological tests, the following conclusions can be drawn:

(1) WCO viscosity has a great influence on the properties of rejuvenated asphalt, and different aged asphalt requires WCO with different viscosity to achieve the desirable rejuvenation effects.
(2) Basic properties of aged asphalt can be restored due to the addition of WCO, and the rejuvenation efficiency improves with the decreasing of WCO viscosity. However, there are still gaps between the basic performance of WCO rejuvenated asphalts and virgin asphalt.
(3) The results of rotational viscosity test indicate that the WCO with viscosity ranging from 100–1150 mm^2/s can restore the viscosity as well as the shear deformation resistance of aged asphalt in this case.
(4) DSR tests indicate that the WCO with viscosity ranging from 420–700 mm^2/s are preferable to restore the rheological properties of rejuvenated asphalt. WCOs with too high or too low viscosity values would have an adverse impact on the performance recovery of rejuvenated asphalt.

References

1. R. Taha, A. Al-Harthy, K. Al-Shamsi, Cement stabilization of reclaimed asphalt pavement aggregate for road bases and subbases.J. Mater. Civ. Eng. **14**, 239–245 (2002)
2. G. Valdés, F. Pérez-Jiménez, R. Miró, Experimental study of recycled asphalt mixtures with high percentages of reclaimed asphalt pavement (RAP). Constr. Build. Mater. **25**, 1289–1297 (2011)
3. J. Shen, S. Amirkhanian, B. Tang, Effects of rejuvenator on performance-based properties of rejuvenated asphalt binder and mixtures. Constr. Build. Mater. **21**, 958–964 (2007)
4. R. Romera, A. Santamaría, J.J. Peña, Rheological aspects of the rejuvenation of aged bitumen. J. Rheol. Acta. **45**, 474–478 (2006)
5. H. Asli, E. Ahmadinia, M. Zargar, M.R. Karim, Investigation on physical properties of waste cooking oil-rejuvenated bitumen binder. Constr. Build. Mater. **37**, 398–405 (2012)
6. M. Zargar, E. Ahmadinia, H. Asli, M.R. Karim, Investigation of the possibility of using waste cooking oil as a rejuvenating agent for aged bitumen, J. Hazard. Mater. **233**, 254–258 (2012)
7. M. Chen, B. Leng, S. Wu, Y. Sang, Physical, chemical and rheological properties of waste edible vegetable oil rejuvenated asphalt binders. Constr. Build. Mater. **66**, 286–298 (2014)
8. Z. Lei, H. Bahia, T. Yi-qiu, Effect of bio-based and refined waste oil modifiers on low temperature performance of asphalt binders. Constr. Build. Mater. **6**, 95–100 (2015)
9. ASTM D4552/D4552 M-10(2016)e1, *Standard practice for classifying hot-mix recycling agents.* (ASTM International, West Conshohocken, PA, 2016), www.astm.org
10. ASTM D2872-12e1, *Standard test method for effect of heat and air on a moving film of asphalt (Rolling thin-film oven test).* (ASTM International, West Conshohocken, PA, 2012), www.astm.org
11. ASTM D6521-13, *Standard practice for accelerated aging of asphalt binder using a pressurized aging vessel (PAV).* (ASTM International, West Conshohocken, PA, 2013), www.astm.org
12. M. Chen, F. Xiao, B. Putman, B. Leng, S. Wu, High temperature properties of rejuvenating recovered binder with rejuvenator, waste cooking and cotton seed oils. Constr. Build. Mater. **59**, 10–16 (2014)
13. ASTM D5/D5 M-13, *Standard test method for penetration of bituminous materials*. (ASTM International, West Conshohocken, PA, 2013), www.astm.org
14. ASTM D113-07, *Standard test method for ductility of bituminous materials.* (ASTM International, West Conshohocken, PA, 2007), www.astm.org
15. ASTM D36/D36 M-14e1, *Standard test method for softening point of bitumen* (*Ring-and-Ball apparatus).* (ASTM International, West Conshohocken, PA, 2014), www.astm.org
16. ASTM D7175-15, *Standard test method for determining the rheological properties of asphalt binder using a dynamic shear rheometer*. (ASTM International, West Conshohocken, PA, 2015), www.astm.org
17. J. Shen, S. Amirkhanian, F. Xiao, B. Tang, Constr. Build. Mater. **23**, 304–310 (2009)
18. L. Hillstrom, M. Mossberg, B. Lundberg, J. Sound. Vib. **230**, 689–707 (2000)
19. J.D. Ferry, *Viscoelastic Properties of Polymers* (New York, 1980)
20. F. Xiao, V.S. Punith, S. Amirkhanian, Fuel. **94**, 144–155 (2011)

Acid Leaching Process of Waste Power Lithium Ion Battery

Zhengzheng Zhang, Liwen Ma, Xiang Zhang, Yuehua Wang, Yuanyuan Cai and Xiaoli Xi

Abstract The power lithium ion battery has been widely used for its excellent performance, with the waste batteries increased yearly and causing environmental pollution and resource waste. The problem must be solved immediately. In this paper, through the "alkaline separation-roasting-acid leaching" process, spent lithium ion battery anode is handled so that to achieve the extraction of valuable metals in the anode. The results show positive active material can separate from the aluminum foil by means of the using of NaOH solution. Under the process of 700 °C high-temperature roasting for 2 h, active substances Li (Ni_xCo_{1-x}) O_2 transform into NiO, CoO, etc., and it is conducive to subsequent acid leaching. After roasting, the acid leaching of active substance is conducted through respectively using hydrochloric acid and sulfuric acid. The leaching rate of Li, Ni, Co are 99.9, 99.5, 99.2% under the optimum conditions in hydrochloric acid system respectively: the concentration of the acid 2 mol/L, the ratio of solid-liquid 60 mg/ml, leaching temperature 90 °C and leaching time 50 min. In sulfuric acid system, the leaching rate of Li, Ni, Co are all closer to 100% under the optimum conditions: the concentration of the acid 2 mol/L, the S/L 75 mg/ml, leaching temperature 85 °C leaching time 50 min and volume ratio of hydrogen peroxide is 5%. Through the fitting calculation, acid leaching is applied to the nuclear reaction model and leaching

Z. Zhang · L. Ma (✉) · Y. Wang · Y. Cai · X. Xi
Beijing University of Technology, Chaoyang District, Beijing, China
e-mail: maliwen@bjut.edu.cn

Z. Zhang
e-mail: zhangzhengzheng@bjut.edu.cn

Y. Wang
e-mail: wangyuehua@bjut.edu.cn

Y. Cai
e-mail: caiyuanyuan@bjut.edu.cn

X. Xi
e-mail: xixiaoli@bjut.edu.cn

X. Zhang
GEM Co., Ltd, Shenzhen, China

Y. Han (ed.), *Advances in Energy and Environmental Materials*,
Springer Proceedings in Energy, https://doi.org/10.1007/978-981-13-0158-2_67

of lithium nickel and cobalt are controlled by chemical reaction. Two kinds of acid system all have good results for metal extraction from waste lithium ion battery cathode material. Considering recycling cost and environmental impact, sulfuric acid system is better.

Keywords Lithium ion battery · Alkaline separation · Roasting
Acid leaching

Introduction

With the rapid development of domestic automotive industry, environmental pollution and energy development issues such as shortage of resources caused by the traditional car is increasingly serious. The proportion of new energy vehicles in China gradually improve. Lithium ion battery does not contain toxic heavy metals such as mercury, cadmium and so on, but the anode materials and electrolyte solution has a great impact on the environment and the anode material contains a large number of valuable metal elements such as nickel and cobalt, causing a certain amount of wasting of resources. The Analysis result indicates that the lithium battery contains Li5–7%, Ni5–10% and Co5–20% [1, 2]. Therefore, our country of lithium ion battery recycling is imminent.

At present, the recycling of waste lithium ion battery at home and abroad mainly concentrated in the recycling of marketable scarce metal cobalt, nickel and lithium. It have high recovery value compared to other metals [3]. Hydrometallurgy is an important way to recycle the valuable metal. Hydrometallurgy method is going to convert the metal ions in the electrode material to leach liquor based on all kinds of transfer medium such as acid, alkaline solution. Then extracting the metal ions from a solution in the form of salts and oxides extracted through the means such as ion exchange, precipitation, adsorption [4]. The method is adopted wildly by researchers at home and abroad because the recovery rate of method to valuable metals is higher, operating condition is milder, and the pollution to the environment is less. Acid leaching as the key technology of hydrometallurgy has been widely research. The cathode active material of the spent lithium ion battery can be leached out by using inorganic acid (such as hydrochloric acid [5], sulfate [6], nitrate [7]), and a variety of organic acids, such as ascorbic acid [8], citric acid [9, 10], malic acid [9, 11] oxalate to aspartic acid [9], oxalic acid [12], DL—maleic acid [11, 13], succinic acid [14], tartaric acid [15] iminodiacetic acid [13] and glycine acid [16]. The acid leaching process is different because of using different acid. For example In the reaction of cobalt acid lithium in sulfuric acid, the value of the presence of hydrogen peroxide can response to Co–O–Co from the $LiCoO_2$, weakening bond energy of Co–O, reducing the activation energy of leaching process, promoting the decomposition of cobalt acid lithium and the presence of hydrogen peroxide is conducive to leaching [17]. Although there is a production of harmful gases such as Cl_2, SOx, NO_X, etc. it will increase the cost of recycling if use the exhaust gas

recovery device in the process of recycling, the price of inorganic acid is lower, the time is shorter and the Leaching efficiency is higher compared with the organic acid. The inorganic acid is more suitable for acid leaching of the positive active material in the factory. This paper studies the acid leaching of the cathode active material using hydrochloric acid and sulfuric acid, studies the acid leaching process, the cost of leaching and the effect of environmental.

Experimental

Experimental Material. The waste cathode material from the S400 Hybrid power lithium-ion batteries.

Methods. Dealing with positive plate by using 2 mol/L NaOH solution. To make the black substance pulled away from aluminum foil carrier fluid through by using NaOH solution with stirring constantly in the process of reaction. The black material pulled away from the aluminum foil, after the reaction. Making XRD, XRF testing to black material.

Putting black substance into the muffle furnace after the separation, drying Roasting for 2 h under high temperature at 700 °C, cooling in the air and recycling black material after roasting. Making XRD testing of phase after roasting.

Acid leaching to black material after roasting at high temperature respectively by using sulfuric acid and hydrochloric acid. Using ICP-AES to detect the concentration of the ions in the solution.

Result and Discussion

Separation of the Positive Active Material and Aluminum Foil and Roasting. To come true the separation of the cathode active material and carrier fluid-aluminum foil through using 2 mol/L NaOH solution along with stirring constantly in the process of reaction. Reaction time is short, fluid aluminum foil is not fully reacted, preserved in the form of aluminium foil together with less consumption of sodium hydroxide; Reaction time is long, carrier fluid aluminum foil react completely, the consumption of sodium hydroxide is morer. After react completely, adding 1 mol/L H_2SO_4 into filtering medium, generating white precipitate $Al(OH)_3$. The XRF of active material show in the Table 1. It contain three element Li, Ni, Co and impurity element Al, Cu.

Table 1 XRF analysis of positive active material

Elements	Ni	Co	Al	Cu	Na
wt/%	80.82	13.38	1.92	1.50	0.27

The cathode active material after alkali separation is $Li(Ni_xCo_{1-x})O_2$. After roasting at 700 °C for 2 h, the cathode active material decompose, the layered structure is destructed, and it transform into the NiO, CoO, etc.

Acid Leaching.

Hydrochloric Acid Leaching.

(1) Experimental condition optimization

As shown in Fig. 1, when the concentration of acid is 2 mol/L, and ratio of solid-to-liquid is 6 g/100 ml, the temperature is 90 °C, with the increasing of time of acid leaching, leaching rate of Li, Ni, Co is increasing and when the time is 50 min, the leaching rate arrive to 100%. With the increasing of the acid concentration, the ratio of solid-to-liquid, temperature and time, the leaching efficiency of Li, Ni, Co is keep growing. When the acid concentration is 2 mol/l, the leaching efficiency of Li, Ni, Co arrive to maximum, even close to 100%, If continue to increase the acid concentration, the leaching efficiency is not increasing. Thus, the optimum conditions of acid concentration is 2 mol/L. While the temperature increased from 40 to 90 °C,the leaching efficiency of Li, Ni, Co increase. When the number of cathode active material in every 100 ml hydrochloric acid solution increase, the leaching efficiency of Li, Ni, Co is increasing, and the optimum ratio of solid-to-liquid is 6 g/100 ml. To further increase the amount of the cathode active material, its leaching rate is not increasing. When the ratio of liquid-to-solid increases, the volume that dissolving a certain amount of solid solution increases, but the concentration of products in the solution also decreases. The diffusion rate of new generation products can improve as concentration gradient of the reaction products decreases in the solution, so as to benefits the dissolution of powder. If the rate of liquid—solid is too high, the reaction container is larger and it increasing the burden of the leaching process, At the same time, inevitably reduces the solubility of lixiviant, adverse to the recycling process. So choosing 6 g/100 ml is the best ratio. When the temperature is 90 °C, the leaching rate of maximum, close to 100%.

Based on analysis, the cathode active material after roasting can be leached by using hydrochloric acid, the best technology of hydrochloric acid leaching can be obtained: 2 mol/L, 6 g/100 ml, 90 °C, 50 min. The leaching rate of Lithium, nickel, cobalt is respectively 99.1, 99.2, 99.5%.

(2) Leaching kinetics of hydrochloric acid

Acid leaching process of lithium ion battery anode materials is liquid—solid reaction, applying to nuclear reaction mode, the relevant mathematical expressions as shown in the table where X as the leaching rate, t for the reaction time. This article based on sulphuric acid leaching kinetics in the leaching system study the process of lithium ion battery anode materials.

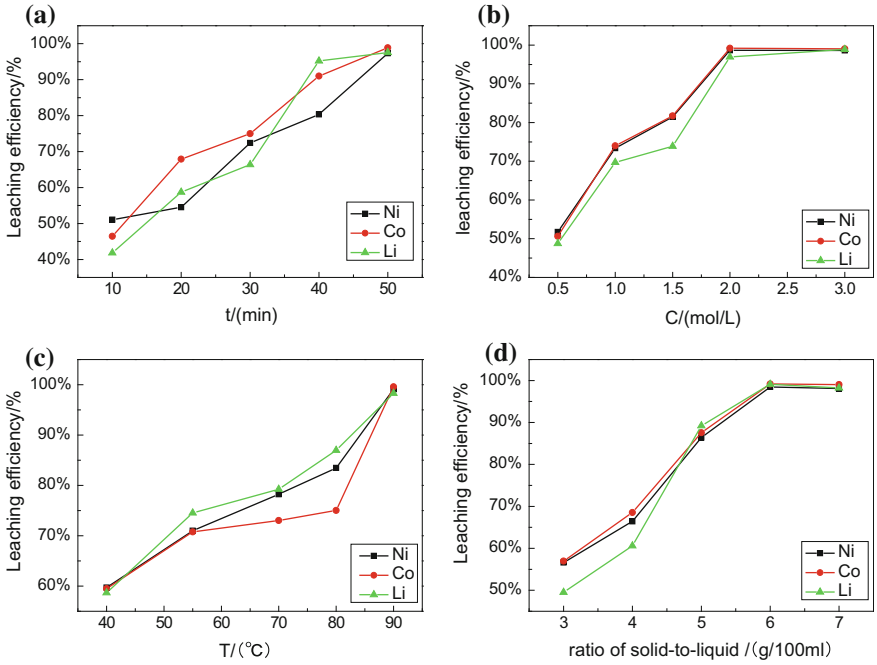

Fig. 1 Effect of time (**a**), acid concentration (**b**), ratio of solid-to-liquid (**c**), temperatures (**d**) on leaching efficiency

$$(1)\ \text{diffusion control} \quad X = K_1 t \tag{1}$$

$$(2)\ \text{internal diffusion control} \quad 1 - 2/3X - (1 - X)^{2/3} = K_2 t \tag{2}$$

$$(3)\ \text{the chemical reaction control} \quad 1 - (1 - X)^{1/3} = K_3 t \tag{3}$$

By mathematical fitting, as shown in Fig. 2, the positive active material hydrochloric acid leaching process is suitable for the nuclear reaction contraction model. The fitting results of three elements have good linear correlation and they both are controlled by the interfacial chemical reaction. The leaching kinetics of lithium, nickel, cobalt in the positive active material in the Hydrochloric acid system at 363 K follows the nuclear reaction model.

Sulfuric Acid Leaching.

(1) Experimental condition optimization

The Fig. 3 show a significant impact of acid concentration, the ratio of solid-to-liquid, temperature, time and volume ratio of hydrogen peroxide to leaching rate of lithium, nickel and cobalt. With the extension of time, the leaching rate of lithium, nickel and cobalt greatly improve. When the leaching time is 50 min, leaching rate up to

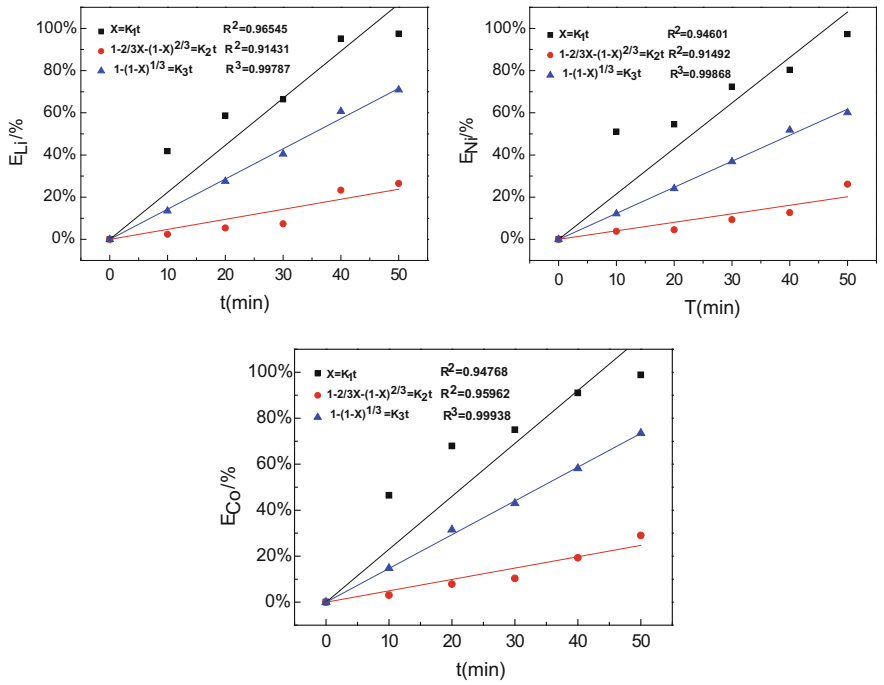

Fig. 2 Dynamics computation of hydrochloric acid leaching

maximum. With the concentration of hydrochloric acid increasing, leaching rate of three elements increase significantly. When the concentration increase from 1 to 2 mol/L, the leaching rate increases and When the concentration is 2 mol/L, the leaching rate arrive to maximum, and to further increase the concentration of acid, leaching rate is not increasing. The leaching rate of lithium, nickel, cobalt increases when increasing the solid-liquid ratio in the system of Sulfuric acid leaching of the cathode material. When the ratio of solid-to-liquid is 7.5 g/100 ml, the leaching rate of maximum. Raise the temperature of reaction system, the leaching rate of three kinds of elements shows a trend of rising. On the one hand, this is because the chemical reaction activity of leaching agent increasing as the temperature increase, On the other hand, temperature will speed up the transfer of diffusion in the reaction system, the reaction of sulfuric acid and the cathode active material is more easier and quicker. Considering the actual situation, 85 °C is the best. Hydrogen peroxide in the sulfuric acid leaching system have significantly influence on leaching. When the volume ratio of hydrogen peroxide is 5%, the leaching rate of elements arrive to the maximum value, close to 100%.

The best technology of sulfuric acid leaching is: 50 min, 2 mol/L, 7.5 g/100 ml, 85 °C, $V_{H_2O_2}$ = 5%. Under the process, the leaching rate of lithium, nickel and cobalt up to maximum, close to 100%, to came true 100% acid leaching of cathode active material.

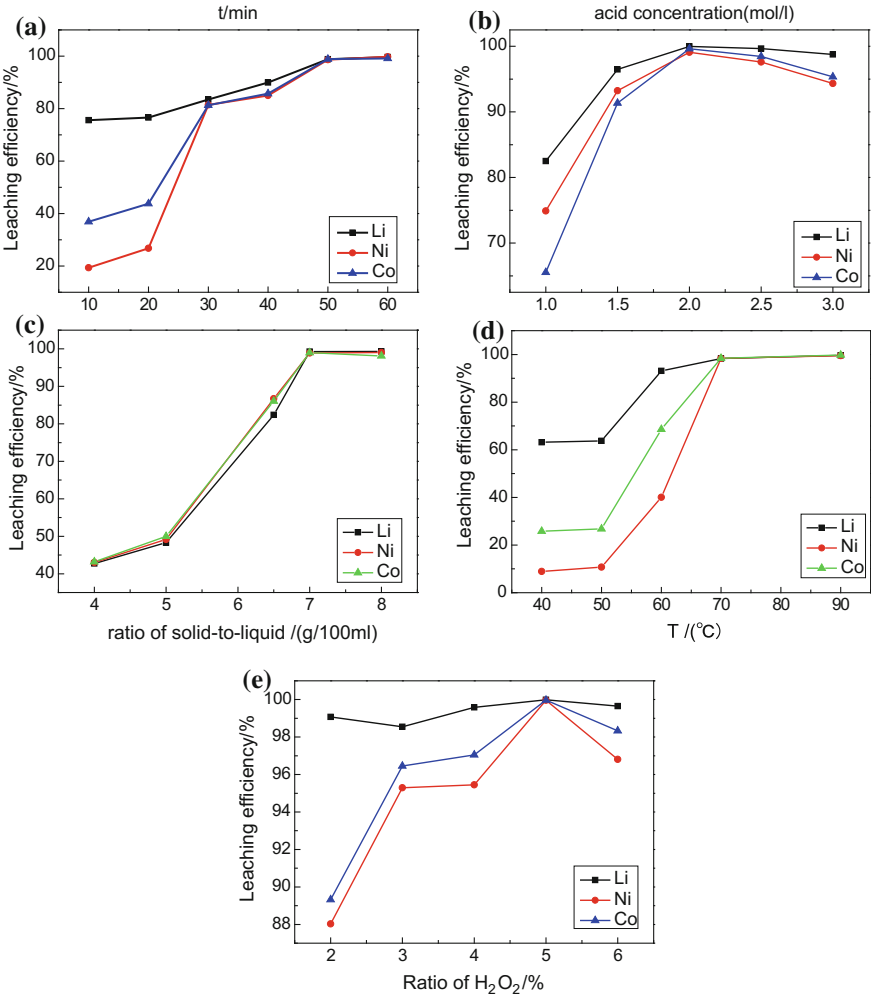

Fig. 3 Effect of time (**a**), acid concentration (**b**), ratio of solid-to-liquid (**c**), temperatures (**d**), $V_{(H2O2)}$ (**e**) on leaching efficiency

(2) Leaching kinetics of sulfuric acid

This article based on sulfuric acid leaching kinetics in the leaching system study the process of lithium ion battery anode material

By mathematical fitting, as shown in Figs. 3 and 4, the positive active material hydrochloric acid leaching process is suitable for the nuclear reaction contraction model. The fitting results of three elements have good linear correlation and The acid leaching of Li, Ni and Co is controlled by the chemical reaction control. The leaching kinetics of lithium, nickel, cobalt in the positive active material in the sulfuric acid system at 363 K follows the nuclear reaction model.

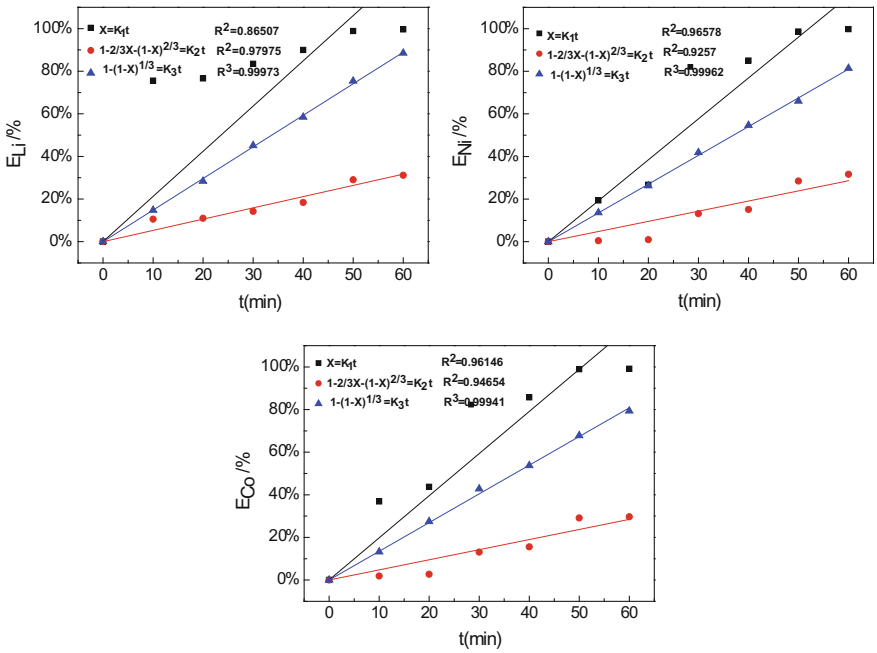

Fig. 4 Dynamics computation of sulfuric acid leaching

Table 2 Materials consumption of leaching

Seagant	V (L)	$V_{(H2O2)}$ (L)	Cost (Yuan)
Sulfuric acid	1.44	0.665	59.16
Hydrochloric acid	2.78	0	83.4

The Comparison of Two Kinds of Acid Leaching. From the perspective of process, the temperature of sulfuric acid is lower than hydrochloric acid, the quantity of the positive active material of the sulfuric acid leaching is more than hydrochloric acid.

From the perspective of consumption, two kinds of acid leaching of the positive active material, can recycling elements, close to 100% (Table 2), but the consumption of materials consumption is smaller than hydrochloric acid. In conclusion, the best choice is sulfuric acid.

Summary

Lithium ion batteries positive plate transform into the positive active material and aluminum foil by 2 mol/L NaOH solution, adding 1 mol/L into filtered fluid, aluminum ions separated form solution.

After Separation and drying, the positive active material roasting for 2 h under 700 °C and the layered structure is destroyed, the positive active material decomposition into NiO, CoO etc. The particles is smaller after roasting, the roasting process in favour of follow-up acid leaching.

After roasting, the positive active material respectively leaching in hydrochloric acid, sulfuric acid. And in the acid leaching, the best technology of hydrochloric acid leaching is 2 mol/L, 6 g/100 ml, 90 °C, 50 min. The best technology of sulfuric acid leaching is: 2 mol/L, 7.5 g/100 ml, 85 °C, 50 min, the volume ratio of hydrogen peroxide is 5%. Through dynamics calculation, the leaching of Li, Ni, Co are both controlled by the chemical reaction control. The leaching process apply to the nuclear reaction model. Considering the material consumption and the influence of the environment, the best choice is sulfuric acid solution.

Acknowledgements This work was supported by National Natural Science Foundation of China (51422401), Beijing Municipal Science and Technology Project (Z151100003415008) and Beijing municipal science & technology commission project (D161100002416001).

References

1. S.M. Shin, N.H. Kim, J.S. Sohn, D.H. Yang, Y.H. Kim, Development of a metal recovery process from Li-ion battery wastes. Hydrometallurgy **79**(3/4), 172–181 (2005)
2. C.K. Lee, E.I. Rhee, Preparation of $LiCoO_2$ from spent lithium ion batteries. J. Power Sources. **109**(1), 17–21 (2002)
3. Y. Wu, F. Pei, L. Jia, X. Liu, W. Zhang, P. Liu, Waste Manage. **32**, 1275–1582 (2011)
4. Y. Zhao, M. Xia, Y. Yu, Y. Wang, C. Ji, Y. Sun, Study on the reuse and valuable metals recovery of spent power lithium-ion batteries. 1674-0912 (2014) 07-0027-05
5. D.P. Mantuano, G. Dorella, R.C.A. Elias, M.B. Mansur, J. Power Sources **159**, 1510–1518 (2006)
6. M.K. Jha, A. Kumari, A.K. Jha, V. Kumar, J. Hait, B.D. Pandey, Waste Manage. **33**, 1890–1897 (2013)
7. C.K. Lee, K.I. Rhee, Preparation of $LiCoO_2$ from spent lithium-ion batteries. J. Power Sources **109**, 17–21 (2002)
8. L. Li, J. Lu, Y. Ren, X.X. Zhang, R.J. Chen, F. Wu, K. Amine, J. Power Sources **218**, 21–27 (2012)
9. L. Li, J.B. Dunn, X.X. Zhang, L. Gaines, R.J. Chen, F. Wu, K. Amine, J. Power Sources **233**, 180–189 (2013)
10. G.P. Nayaka, J. Manjanna, K.V. Pai, R. Vadavi, S.J. Keny, V.S. Tripathi, Hydrometallurgy **151**, 73–77 (2015)
11. L. Li, J. Ge, R. Chen, F. Wu, S. Chen, X. Zhang, Waste Manage. **30**, 2615–2621 (2010)
12. L. Sun, K. Qiu, Waste Manage. **32**, 1575–1582 (2012)
13. G.P. Nayaka, K.V. Pai, J. Manjanna, S.J. Keny, Use of mild organic acid reagents to recover the Co and Li from spent Li-ion batteries. Waste Manage. **51**, 234–238 (2016)
14. L. Li, W. Qu, X. Zhang, J. Lu, R. Chen, F. Wu, K. Amine, J. Power Sources **282**, 544–551 (2015)
15. G.P. Nayaka, K.V. Pai, G. Santhosh, J. Manjanna, Dissolution of cathodic active material of spent Li-ion battery using tartaric acid and ascorbic acid mixture to recover Co. Hydrometallurgy **161**, 54–57 (2016)
16. G.P. Nayaka, K.V. Pai,, G. Santhosh, J. Manjanna, Recovery of cobalt as cobalt oxalate spent lithium ion batteries by using glycine as leaching agent. J. Environ. Chem. Eng. **4**, 2378–2383 (2016)
17. Z. Zhan, Study of recycling of spent Lithium ions batteries. Waste Manage. **32**, 1574–1582 (2012)

Physical and Chemical Properties of Asphalt Binders Modified with Waste Engine Oil

Liu Siqing, Chen Meizhu, Wu Shaopeng, Liu Jingxiang, Zhang Dong and Wan Guiwen

Abstract Waste engine oil (WEO) modified asphalt was prepared by melt blending. The objective of this paper is to investigate the influence of WEO on the physical properties, chemical compositions and microstructure of asphalt. Penetration, softening point and ductility were tested to evaluate the effect of WEO on basic properties of asphalt. Then the rheological properties of modified asphalts were characterized based on rotational viscometer (RV), bending beam rheometer (BBR) and dynamic shear rheometer (DSR) tests. Finally, SARA (saturates, aromatics, resins and asphaltenes) fractions, Pyrolysis-gas chromatography (PyGC) and Fourier transform infrared spectroscopy (FTIR) tests were carried out to investigate the influence of WEO on chemical properties of asphalt. The experimental results indicate that the chemical compositions of WEO is similar to asphalt with similarity-intermiscibility characteristics, and both are mainly physical blending rather than chemical reaction. The addition of WEO can reduce the viscosity, the colloidal instability index (I_c) value, the Carbonyl (C=O) and Sulfoxide (S=O) indexes of asphalt. Moreover, the viscous components of asphalt are significantly increased in low temperature. It is beneficial to the anti-aging properties and low-temperature crack resistance of asphalt, while the temperature sensitivity and high-temperature stability of asphalt remains to be further improved.

L. Siqing · C. Meizhu (✉) · W. Shaopeng · L. Jingxiang · Z. Dong · W. Guiwen
State Key Laboratory of Silicate Materials for Architectures, Wuhan University of Technology, Wuhan 430070, China
e-mail: chenmzh@whut.edu.cn

L. Siqing
e-mail: liusiqing@whut.edu.cn

W. Shaopeng
e-mail: wusp@whut.edu.cn

L. Jingxiang
e-mail: liujingx@whut.edu.cn

Z. Dong
e-mail: pytmac@whut.edu.cn

W. Guiwen
e-mail: wanguiwen@whut.edu.cn

Y. Han (ed.), *Advances in Energy and Environmental Materials*,
Springer Proceedings in Energy, https://doi.org/10.1007/978-981-13-0158-2_68

Keywords Waste engine oil · Modified asphalt · Property research
Chemical composition · Microstructure

Introduction

In recent years, with the rapid development of transportation industry, the performances of asphalt binders are required to be better [1, 2]. Modified asphalt binders can serve several purposes, such as a pavement carrying a high traffic volume or an extreme climate [3, 4]. The common modifiers are rubbers, resins, high-molecular polymers, native bitumen, polyphosphoric acid [5].

The weather of extremely cold and high-altitude areas are very horrible, with low temperature all the year, large temperature difference and strong ultraviolet radiation [6, 7]. The asphalt concrete paving in such areas is very difficult, some diseases such as crack, loose and dry will appear quickly, which seriously shorten the road service life. Therefore, it's significant to develop modified asphalt materials for extremely cold and high-altitude areas [8–10].

Styrene-butadiene rubber (SBR) and styrene-butadiene-styrene block copolymer (SBS) are widely used in the world for their excellent performances, such as high-temperature stability, fatigue resistance and low-temperature crack resistance [11–14]. However, the anti-aging performance and compatibility of polymers are poor, and the cost of engineering is raised. Meanwhile, the waste engine oil (WEO) is an effective modifier to improve the low-temperature performances of asphalt binders [15]. By the end of 2016, the number of vehicles in China is over 3000 million, and the car need to replace the oil every 5000–10,000 km [16]. According to the statistics, the annual production of WEO is more than 19 million tons. Nowadays, the main ways to deal with WEO is discard, fuel and recycling. However, the utilization rate is less than 20% [17]. If the WEO as a modifier added to asphalt, it will be significant for environmental protection and economical saving.

According to the investigation, lots of research findings have been achieved by foreign and domestic scholars on the WEO modified asphalts. Aaron Villanueva [18] found that the used oil is useful to improve the low-temperature performance, but at the expense of high-temperature PG grade. Zhao [19] indicated that a small amount of WEO is beneficial to the anti-aging properties and low-temperature crack resistance, while the high-temperature rutting resistance remains to be further improved. Jia [20] verified that infrared spectra and rheological properties of asphalt will be significantly altered when the WEO content up to 5%. Simon [21] indicated that zinc is a universal additive in engine oil through X-ray fluorescence (XRF), which promotes the hardening of asphalt. Borhan [22] found that some chemical interaction occur when the used cylinder oil (UCO) is mixed into the asphalt concrete.

From the above literature review, there are a few articles discussing the WEO as a modifier to improve the low-temperature and rheological properties of asphalt. However, the comprehensive physical and chemistry properties of WEO modified asphalt binder remain to be further researched. Therefore, the objective of this study

is to investigate the effect of WEO on physical, chemical and micro-structure of asphalt binder. A series of laboratory experimental including basic tests, rotational viscosity, dynamic shear rheometer (DSR), bending beam rheometer (BBR), SARA (saturates, aromatics, resins and asphaltenes) fractions, Pyrolysis-gas chromatography (PyGC) and Fourier transforms infrared (FTIR) spectra were carried out to systematically study the influence of WCO on properties of asphalt binder.

Materials

Asphalt. The penetration grade 60/80 of asphalt was used in this study and supplied from Taizhou, China. The basic properties and SARA (saturates, aromatics, resins and asphaltenes) fractions of asphalt binders were shown in Tables 1 and 2.
Waste Engine Oil. A collective blend of waste engine oil from auto workshops showed similar properties based on FTIR and rheological analyses, which may be due to similar statistical distributions of different automobiles used in US [23].The waste engine oil (WEO) in this study was obtained from an automobile sales service shop 4S, and the test results of WEO were illustrated in Tables 3 and 4.

Experimental Methods

Preparation of Modified Asphalt. Modified asphalts were produced by mixing virgin asphalt with six contents (1, 3, 5, 7, 10 and 15 wt%, by mass of binders) of waste engine oil (WEO), respectively (referred to W_1–W_6). Firstly, these materials were diffused in propeller mixer at a constant speed of 1200 rpm for 20 min at 135 °C, then stirred in a high speed shearing machine at a stable speed of 4000 rpm for 40 min at 135 °C.
Preparation of Aged Asphalt. Rolling thin film oven test (RTFOT) is used to simulate the aging process of asphalt during plant mixing, transportation and paving. In this article, asphalts were heated in an oven for 85 min at 163 °C, respectively (according to ASTM D2872).

Table 1 Basic properties of asphalt binders

Asphalt categories	Softening Point (°C)	Penetration (0.1 mm, 25°C)	Ductility (cm, 5°C)	Viscosity (Pa·s, 135°C)	Mass loss (%)
AH-70 (W_0)	49.4	68.3	>100	0.48	–
AH-70 RTFOT (A_0)	54.8	40	125	0.61	0.07

Table 2 SARA fractions of AH-70 asphalt

Content	Saturates (%)	Aromatics (%)	Resins (%)	Asphaltenes (%)
Percent (%)	16.74	37.75	32.37	13.14

Table 3 Basic properties of WEO

Content	Appearance	Acid value (mg KOH.g^{-1})	Specific gravity (g/cm^3)	Viscosity (Pa·s, 60 °C)	Flash point (°C)	RTFOT	
						Viscosity ratio (%)	Mass loss (%)
WEO	Black	3.7	0.835	0.021	7.5	1.2	0.8

Table 4 SARA fractions of WEO

Content	Saturates (%)	Aromatics (%)	Resins (%)	Asphaltenes (%)
Percent (%)	81.78	13.51	2.89	1.92

Basic Properties. Basic characteristics of asphalt binders include penetration, softening point and ductility. Penetration test was applied to evaluate the consistency an deformation resistance of asphalt binder, and the samples were implemented with a standard load of 100 g for 5 s at 25 °C (ASTM D5). Softening point test is a method to denote the temperature sensitivity of asphalt binder, and the experiment was conducted with a steel ball weighs 3.5 g at a constant heating rate of 5 °C/min (ASTM D36). Ductility test is a way to evaluate the tensile deformation and flexibility at a low temperature, and the test was conducted at an elongation rate of 5 cm/min at 5 °C (ASTM D113).

Rheological Properties. The rheological behavior of asphalt was studied by rotational viscometer (RV), bending beam rheometer (BBR) and dynamic shear rheometer (DSR). BBR test was conducted at −18 °C to study the low-temperature crack resistance (ASTM D6648). High-temperature sweep test is from 30–80 °C, which is performed to study the ability of high-temperature permanent deformation resistance. The sweep test from −10 to 30 °C was researched to evaluated the low-temperature rheological properties of asphalt (ASTM D7175).

Chemical Properties. The SARA (saturates, aromatics, resins and asphaltenes) fractions, chemical compounds and molecule structure were measured by thin-layer chromatography with flame ionization detection (TLC-FID), Pyrolysis-gas chromatography (PyGC) and Fourier transform infrared spectroscopy (FTIR) spectra. The specific experimental technological process was illustrated in Fig. 1.

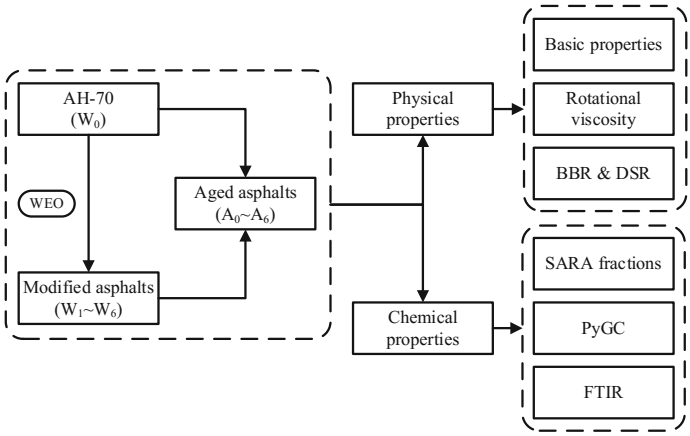

Fig. 1 Experimental technological process

Physical Properties

Basic Properties. The basic properties of modified asphalts including penetration, softening point and ductility, which are shown in Fig. 1a, b, c, respectively. Penetration Retention Rate (PRR), Softening point increment (SPI) and Ductility Retention Rate (DRR) are used to reflect the aging properties of asphalt binders. The equations are as follows:

$$\mathrm{PRR} = \frac{\mathrm{P}}{\mathrm{P}_0} * 100\% \tag{1}$$

$$\mathrm{SPI}(^{\circ}\mathrm{C}) = \mathrm{SP} - \mathrm{SP}_0 \tag{2}$$

$$\mathrm{DRR}(\%) = \frac{D}{D_0} * 100\% \tag{3}$$

where P_0 and P are the penetration of asphalt before and after aging, respectively. SP_0 and SP are the softening point of asphalt before and after aging, separately. D and D_0 are the aged and unaged ductility of asphalt binder, respectively.

As Fig. 2 shows, with the increase of waste engine oil (WEO) content, the penetration and ductility values of asphalt binders increase, while the softening point decrease. Meanwhile, the PRR and DRR of modified asphalts show a trend that increase firstly and then decrease. However, the SPI values of modified asphalts show a contrary law. It implies that the addition of WEO can soften asphalt binders, enhance the flexibility and improve the anti-aging properties of asphalt. However, WEO has an adverse effect on the temperature sensibility, which reduces the heat resistance of asphalt.

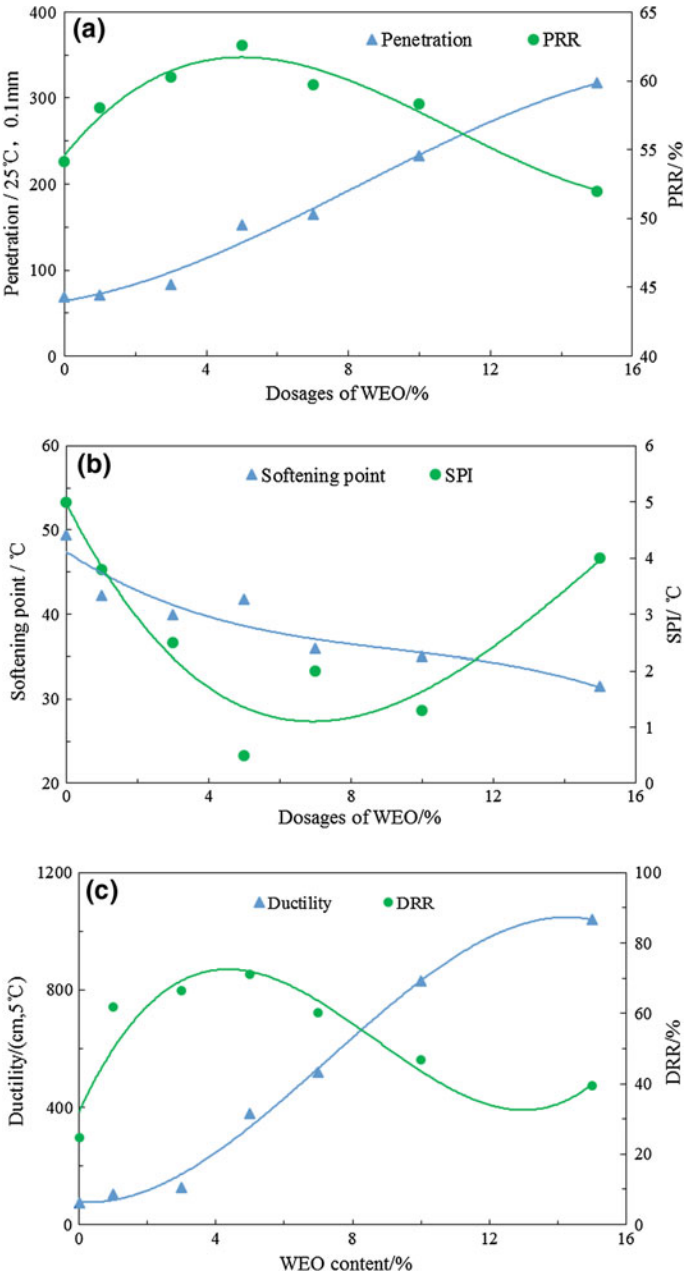

Fig. 2 Basic properties of modified asphalt binders with WEO

Rotational Viscosity. Rotational viscosity is a flow characteristic index of fluid, which reflects the frictional resistance when the fluid undergoes a flow deformation. The modified asphalts with different contents of WEO (1, 3, 5, 7, 10 and 15 wt%, by mass of binders) are referred to W_1–W_6.

Figure 3 illustrates the viscosity of asphalt binders at different temperatures. As the figure shows, it can be noted that the viscosity values of asphalt decrease rapidly with the temperature increasing. Meanwhile, with the WEO content increase, the viscosity value of modified asphalt decreases at the same temperature. WEO is oil with low viscosity, which can increase the flowing properties of asphalt. Moreover, the molecular motion rate is accelerated at the high temperature. Furthermore, the asphalt with a low viscosity has a lower construction temperature. However, an excessive low viscosity of asphalt will lead to adhesion reduction, which will damage the performance of asphalt mixture.

BBR Test. Bending beam rheological (BBR) test is used to evaluate the low-temperature rheological properties of asphalt. The creep stiffness (S) can reflect the deformation resistance capacity, the higher the S value, the greater the elastic component of material is. The creep rate (m-value) is used to characterize the stiffness changing rule of asphalt, which shows the stress relaxation ability.

Figure 4 illustrates the stiffness and m-value of virgin and modified asphalts. It can be found that the virgin asphalt has the maximum S value and the minimum m-value. At the same time, with the WEO content increasing, the S value decrease while the m-value increase, and all meet the relevant specific standards ($S \leq 300$ MPa, $m \geq 0.3$). It can be speculated that WEO can enhance the viscous compositions of asphalt and stress relaxation ability, which is beneficial to the low-temperature crack resistance of asphalt binders.

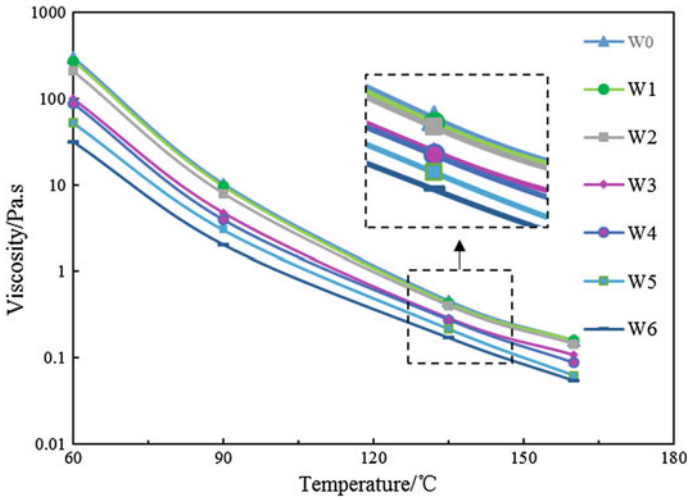

Fig. 3 Viscosity of asphalt binders at different temperatures

DSR Test. DSR test was used to characterize fully the asphalt's rheological properties with the change of load and temperature. Complex modulus (G*) represents the total resistance during the repeated shear loading. Phase angle (δ) reflects the lag between the stress and the corresponding strain. Rutting factor (G*/sin δ) is chosen to characterize the deformation resistance in high temperature.

Figure 5a, b, c illustrates the complex modulus, phase angle and rutting factors of asphalts in high temperature. It can be noticed that the virgin asphalt (W_0) has the maximum values of G* and G*/sin δ, and the minimum δ value compared with the modified asphalts. Meanwhile, with the increase of WEO content, the G* and G*/sin δ values decrease while the δ values increase. It can be explained that W_0 has more elastic components compared with modified asphalts. When the same shear deformation occurs, W_0 needs a larger stress. The addition of WEO is harmful to the permanent deformation resistance at a high temperature.

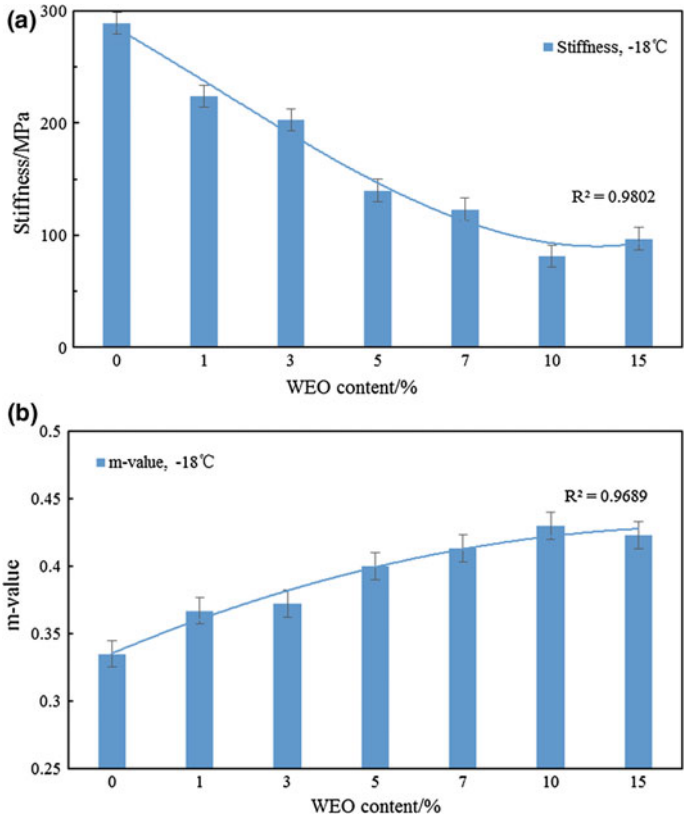

Fig. 4 Stiffness and m-value of virgin and modified asphalts

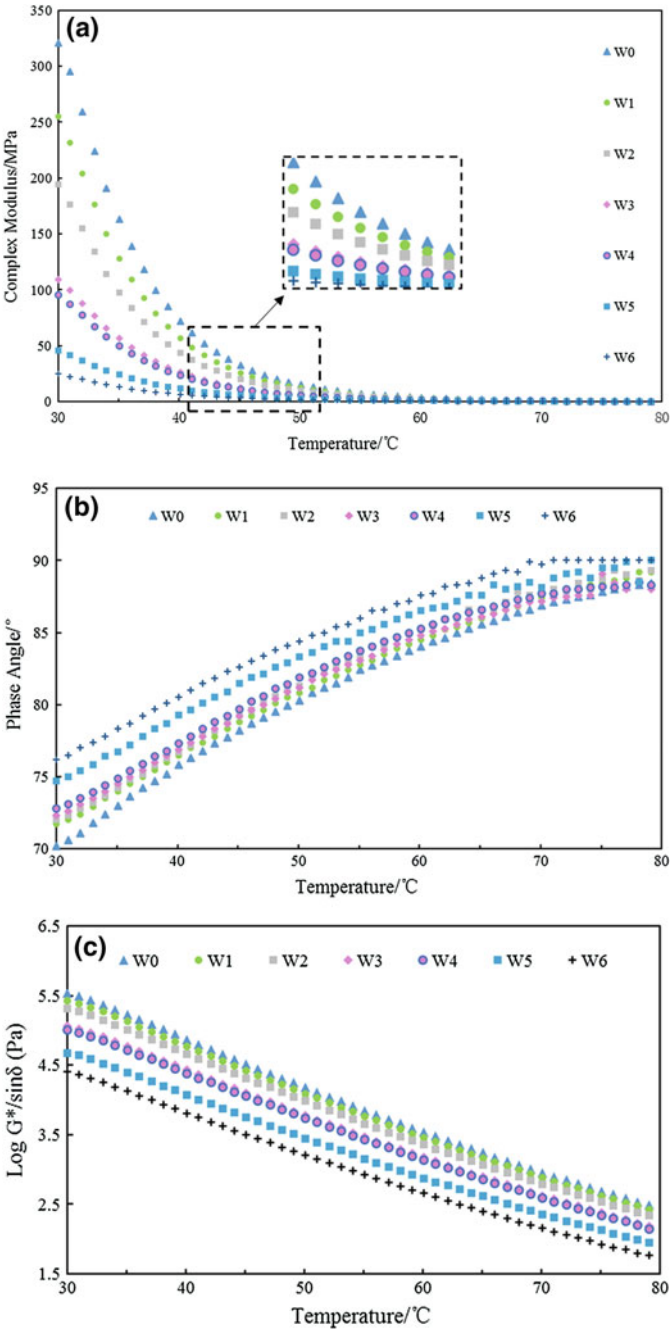

Fig. 5 Complex modulus, phase angle and rutting factors of asphalts at high temperature

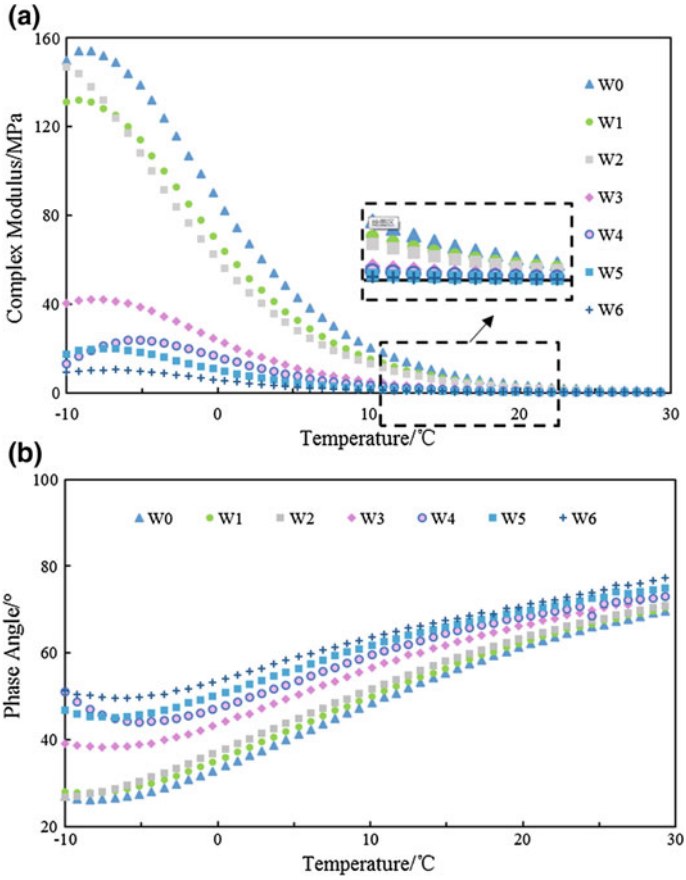

Fig. 6 Complex modulus and phase angle of asphalts in low-temperature

Figure 6a, b illustrates the complex modulus and phase angle of asphalts at low temperature. It's easy to find that the changing rule of asphalts is the same as Fig. 5. As the temperature increases, the G* values decrease gradually whereas the δ values increase. Meanwhile, with the increase of WEO content, the G* values decrease, while the δ values increase. These changes illustrate that WEO can enhance the viscous compositions of asphalt in low temperature, which improves the flowing properties and crack resistance.

Chemical Properties

SARA Fractions. Asphalt is conventionally considered as a colloidal system, which is consisted of asphaltenes with high weight and high polarity, and low

molecular weight solute. The asphaltenes molecule acts as the colloidal nucleus, which absorbs some large polar solutes such as resins and aromatics. According to the colloidal state, the asphalt can be divided into "sol" type and "gel" type. The colloidal instability index (I_c) is a ratio of the sum amount of asphaltenes and saturates to the sum amounts of aromatics and resins. It can reflect the changes of the colloidal structure during aging period.

Figure 7 shows the SARA (saturates, aromatics, resins and asphaltenes) fractions of virgin and modified asphalts. Compared with the constituents of virgin asphalt (W_0), modified asphalts have more saturates but less aromatics and asphaltenes contents. What's more, with the increase of WEO content, the saturates increase while the aromatics and asphaltenes decrease gradually. The reason might be that the WEO is abundant of saturates while has a spot of asphaltenes, which changes the relative content of asphalt.

Table 5 illustrates the I_c values of aged asphalt binders. A_0 is aged asphalt, A_1–A_6 are referred to the modified asphalts (W_1–W_6) after aging. It can be found that with the increase of WEO, the I_c values of aged asphalts show a trend that decrease firstly and then increase. Meanwhile, A_4 (the modified asphalt with 7% WEO after aging) has the minimum I_c value. It indicates that moderate content of WEO is beneficial to the SARA fractions of asphalt, and the colloidal systems are transformed from gel-type to sol type. However, an excessive amount of WEO promotes the agglomeration of the micelle, which is harmful to the colloidal structure.

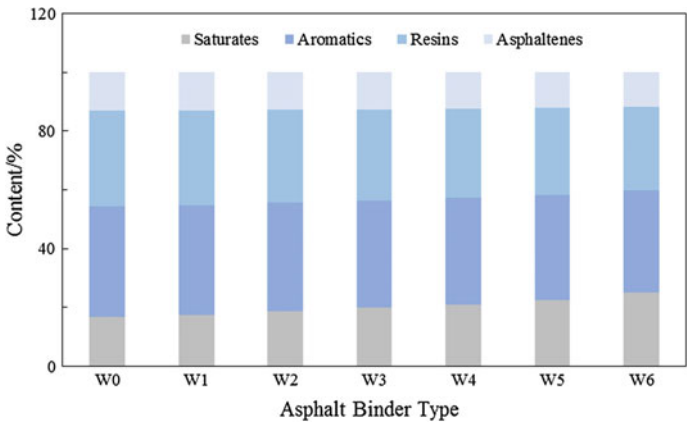

Fig. 7 SARA fractions of virgin and modified asphalt binders

Table 5 I_c values of aged asphalt binders

Type	A_0	A_1	A_2	A_3	A_4	A_5	A_6
I_c	0.49	0.47	0.43	0.39	0.37	0.45	0.58

PyGC. Asphalt is a complicated mixture of different macromolecules hydrocarbons and their nonmetallic derivatives. In order to explore the specific substances of asphalt, Pyrolysis-gas chromatography (PyGC) is used in this article. PyGC is a combination of both pyrolysis and gas chromatography, which reveals the process of converting the sample into several substances by heat. The specific principle is that different substances can be separated because of different distribution coefficient in two phases. the time and size of the peak can be utilized for qualitative and quantitative analysis.

Figure 8 illustrate the PyGC results of WEO. It's clear to find that the most abundant peaks of WEO are located between 17–19 min and 25–27 min. Likely compounds are identified as Naphthalene, Alkenes and Olefins. Figure 9 illustrates the PyGC results of modified asphalts. It's noted that with the increase of WEO, the position of the strongest peak of asphalt has turned right, and formed more long-chain alkanes. Table 6 shows the chemical compositions and relative amount of WEO and asphalts. It indicates that the chemical compositions of WEO are similar to asphalt, and both are mainly physical blending rather than chemical reaction.

FTIR Analysis. Infrared absorption spectroscopy is widely used in the qualitative analysis of organic compounds, especially in determining the functional groups. The infrared spectrum and the structure of the material has a strict correspondence. In the same time, the various functional groups, atomic mass and chemical bond isomers have an important influence on the position and strength of the peak. The characteristic absorption peaks at 1030 and 1700 cm^{-1} are the telescopic vibration of Sulfoxide (S=O) and Carbonyl (C=O), respectively. Carbonyl is the formation marker of carbonyl acid or ketone. The changes of the functional groups of carbonyl and sulfoxide can show the aging degree of asphalt, which can be calculated as Eqs. (4)–(5).

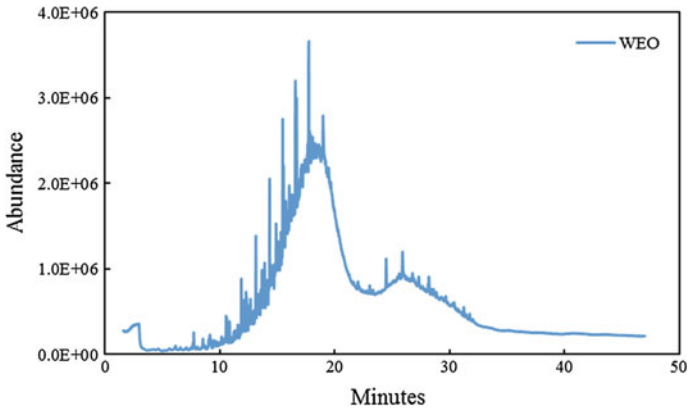

Fig. 8 PyGC results of WEO

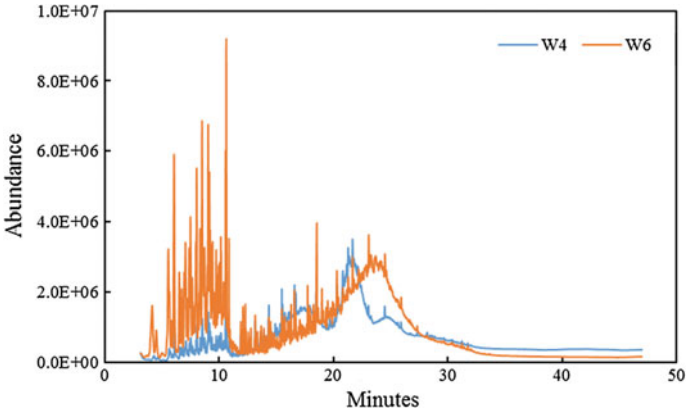

Fig. 9 PyGC results of modified asphalts

Table 6 Chemical compositions and relative amount of WEO and asphalts

Type	Alkanes	Naphthalene	Cyclobutanol	Benzenes	Phenols	Olefins	Ketones	Tin chloride
WEO	57.40	5.97	3.94	3.56	3.42	3.42	5.45	1.22
W_0	47.40	2.61	2.42	2.77	1.29	9.77	1.56	–
W_4	49.37	3.35	2.73	2.93	1.49	3.96	1.80	–
W_6	53.26	3.94	3.45	3.24	1.73	4.54	2.75	–

$$I_{c=0} = \frac{\text{Carbonyl peak area (centered around 1699 cm}^{-1})}{\text{Peak area } (\sum 2000 \text{ and } 600 \text{ cm}^{-1})} \quad (4)$$

$$I_{s=0} = \frac{\text{Sulfoxide peak area (centered around 1030 cm}^{-1})}{\text{Peak area } (\sum 2000 \text{ and } 600 \text{ cm}^{-1})} \quad (5)$$

WEO is composed of base oil and additive decomposition products. The FTIR spectrum of the WEO is shown in Fig. 10. It's easy to find that the strong absorption peak is at 2955–2854 cm^{-1}, 1464–1377 cm^{-1}, which is corresponding to the stretching vibration of CH_3, CH_2 and C–H. It indicates that there is a large number of hydrocarbon substances in WEO. The slight absorption peak at 1700 cm^{-1} shows that the WEO has undergone an oxidation process. It shows that there are ketones, carboxylic acid and other substances in WEO. Peaks at 1304–999 cm^{-1} are corresponding to the additive decomposition products, such as viscosity index improver, cleaning agent and antioxidant. It is worth mentioning that there is no absorption peak at 3400 cm^{-1}, which indicates that there is no water in WEO.

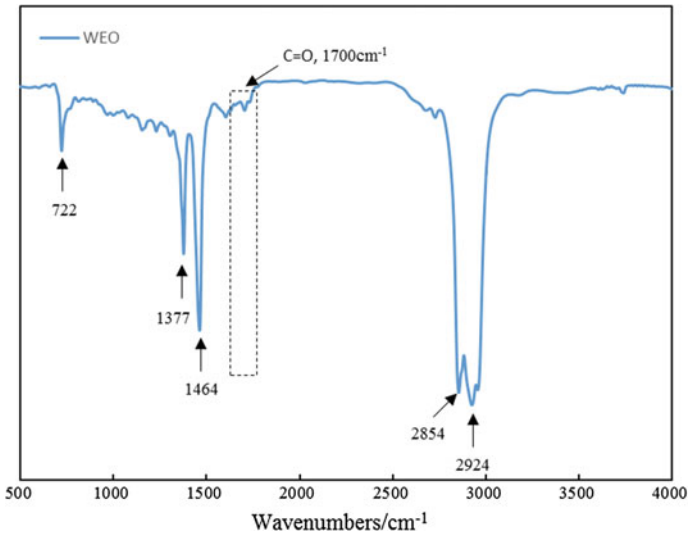

Fig. 10 FTIR spectra of WEO

Figure 11 illustrates the FTIR spectra of virgin and modified asphalt. It's clear to find there is no peak at 2955 cm^{-1} in asphalt, which can be explained that the chemical reaction has taken place rather than simply physical mixing. Compared with the modified asphalts after aging (referred to as A_1–A_6), the aged asphalt (A_0) shows a notable increasing in C=O and S=O peak areas. As for the modified

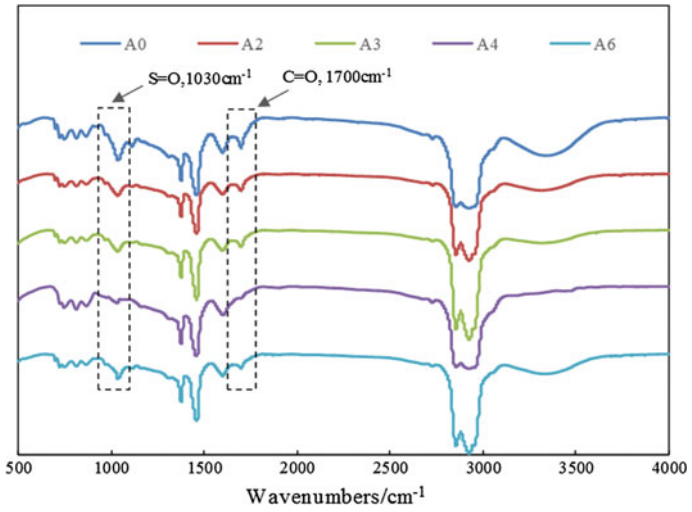

Fig. 11 FTIR spectra of aged asphalts

Table 7 Functional group indexes of WEO, virgin asphalt and aged asphalts

Asphalt	WEO	W_0	A_0	A_1	A_2	A_3	A_4	A_5	A_6
$I_{c=o}$	0.033	0	0.109	0.084	0.083	0.065	0.048	0.057	0.087
$I_{s=o}$	0	0.032	0.172	0.153	0.138	0.128	0.107	0.113	0.124

asphalts after aging, the C=O and S=O peak areas decrease firstly and then increase with the applied WEO qualities increase. Moreover, the values of C=O and S=O peak areas reach the minimum when WEO content is 7%. It indicates that an appropriate content of WEO can relieve the aging degree of asphalt.

The functional group indexes of WEO, virgin asphalt (W_0) and aged asphalts (A_0–A_6) are presented in Table 7. It can be observed that the $I_{s=o}$ value of WEO is zero while the $I_{c=o}$ value is 0.033. The presence of carbonyl peak in WEO can make the $I_{c=o}$ value of aged asphalt larger than the real situation. Moreover, the $I_{c=o}$ and $I_{s=o}$ values of aged asphalt (A_0) is far more than modified asphalts after aging (A_1–A_6). With the increase of WEO content, the $I_{c=o}$ and $I_{s=o}$ values show a trend that decrease firstly and then increase and lower than aged asphalt. When the WEO content is 7 wt%, the $I_{c=o}$ and $I_{s=o}$ values of A_4 reached the minimum ($I_{c=o}$ = 0.048, $I_{s=o}$ = 0.107). From the above results, appropriate content of WEO can relieve the aging degree of aged asphalt. However, an excessive WEO has an adverse effect on the anti-aging performance of asphalt.

Conclusions

Based on the experimental results mentioned above, in terms of a series of basic, rheological and chemical properties tests, the following conclusions can be drawn:

1. WEO can effectively reduce the viscosity and enhance the viscous compositions of asphalt. It's beneficial to improve the flexibility and low-temperature crack resistance of asphalt. However, the temperature sensitivity and high-temperature rutting resistance remain to be further improved.
2. The chemical compositions of WEO are similar to asphalt, and both are mainly physical blending rather than chemical reaction. A small amount of WEO can improve the colloidal structure of asphalt and reduce the indexes of carbonyl (C=O) and sulfoxide (S=O) of asphalt.
3. To summarize, WEO can be used to improve the low temperature properties and anti-aging properties of asphalt, and the WEO content should be less than 7%. However, the correlation between the improvement effect and the quality of WEO, the impact of WEO modified asphalt on the environment, and the high-temperature properties of asphalt remain to be further researched.

References

1. J.S. Zhang, *Asphalt Materials* (Chemical Industry Press, 2009)
2. J.S. Zhang, A.Q. Zhang, M.T. Li et al., Research progress of nano-modified asphalt. Mater. Rev. **10**, 87–90 (2005)
3. P. Gang, X.Y. Cheng, X. Bo et al., Effects of two warm mix agents on high and low temperature performance of SBS modified asphalt binder. J. East Chin. Jiaotong Univ. (2014)
4. X.M. Huang, S.P. Wu, Y.L. Zhao, *Asphalt and Asphalt Mixture* (Southeast University Press, 2002)
5. J.S. Zhang, *Road Bituminous Materials* (Harbin Institute of Technology Press, 2013)
6. Y.J. Qiu, C.F. Ai, B. Huang et al., The adaptability of asphalt pavement structure in alpine region. J. Southwest Jiaotong Univ. **44**(2), 147–154 (2009)
7. C.F. Ai, B. Huang, Q.Y. Song et al., Investigation and analysis of dominant diseases of asphalt pavement in alpine region. J. Chongqing Jiaotong Univ. (Natural Science) **26**(3), 73–77 (2007)
8. W.G. Li, Y.H. Duan, L.K. Yan et al., Research of some asphalt pavement preventive maintenance materials' performance in high and cold area. J. Wuhan Univ. Technol. (2012)
9. H. Liu, Y. Qiu, C.F. Ai, Study on applicability of flexible base of asphalt pavement in high-cold area. J. Highw. Transp. Res. Dev. **26**(9), 21–25 (2009)
10. Q. Zhou, Temperature design of asphalt pavement at cold area. J. Changan Univ. (2007)
11. J. Zhang, J. Wang, Y. Wu et al., Preparation and properties of organic palygorskite SBR/organic palygorskite compound and asphalt modified with the compound. Constr. Build. Mater. **22**(8), 1820–1830 (2008)
12. G. Wen, Y. Zhang, Y. Zhang et al., Rheological characterization of storage-stable SBS-modified asphalts. Polym. Test. **21**(3), 295–302 (2002)
13. H. Fu, L. Xie, D. Dou et al., Storage stability and compatibility of asphalt binder modified by SBS graft copolymer. Constr. Build. Mater. **21**(7), 1528–1533 (2007)
14. B.M. Yvonne, A.J. Müller, Y. Rodriguez, Use of rheological compatibility criteria to study SBS modified asphalts. J. Appl. Polym. Sci. **90**(7), 1772–1782 (2003)
15. M. Ragab, M. Abdelrahman, Investigation of the physical and molecular properties of asphalt binders processed with used motor oils. J. Mater. **2015**(3), 1–9 (2015)
16. X.Y. Hong, The problems you need to pay attention to about raising a car. Financ. World **19**, 18 (2015)
17. J.T. Cui, Research on regeneration process of waste lubricating oil, China University of Petroleum (East China), 2012
18. A.V. Villanueva, S.H. Ho, L.Z. Zanzotto, Asphalt modification with used lubricating oil. Can. J. Civ. Eng. **35**(35), 148–157 (2008)
19. S.P. Zhao, Performance evaluation of waste oil modified asphalt based on anti-aging and high temperature rheological analysis. Road Constr. **41**(3), 154–157 (2016)
20. X. Jia, B. Huang, B.F. Bowers et al., Infrared spectra and rheological properties of asphalt cement containing waste engine oil residues. Constr. Build. Mater. **50**(1), 683–691 (2014)
21. S.A.M. Hesp, H.F. Shurvell, X-Ray fluorescence detection of waste engine oil residue in asphalt and its effect on cracking in service. Int. J. Pavement Eng. **11**(6), 541–553 (2010)
22. M.N. Borhan, F. Suja, A. Ismail et al., Used cylinder oil modified cold-mix asphalt concrete. J. Appl. Sci. **7**(22) (2007)
23. E. Dominguez-Rosado, J. Pichtel, Chemical characterization of fresh, used and weathered motor oil via GC/MS, NMR and FTIR techniques. Indian Acad. Sci. **112**(2) (2003)

Effect of Sintering Temperature on Preparation of W–La_2O_3–Y_2O_3–ZrO_2 Rare Earth Tungsten Electrode by Spark Plasma Sintering

Tu Zhang, Jiancan Yang, Peng Wang and Peng Li

Abstract The rare earth tungsten electrode was prepared by spark plasma sintering (SPS) with W–La_2O_3–Y_2O_3–ZrO_2 composite powders synthesized by second-time reduction as raw materials. And the effects of SPS sintering temperature on the microstructure and hardness of sintered rare earth tungsten electrode were studied. The structure and morphology were investigated by metallographic microscope, scanning electron microscopy and Vickers Indenter, and the density degree of rare earth tungsten electrode sintered sample were analyzed based on Archimedes Principle. Sintering process was performed at a temperature range of 1200–1500 °C for a dwell time of 5 min under an external pressure of 50 MPa in vacuum, the optimum sintering temperature of sintered rare earth tungsten electrode was 1450 °C; with the increase of sintering temperature, the tungsten grains in the microstructure of the sintered sample grew gradually, the relative density and the hardness of the sintered sample also increased. Tungsten grain growth can be effectively inhibited by spark plasma sintering, which prompts fine grain strengthening of the tungsten electrode, and it is possible to prepare a high densification and fine grain structure rare earth tungsten electrode.

Keywords Spark plasma sintering · Rare earth tungsten electrode
Sintering temperature · Densification

T. Zhang (✉) · J. Yang · P. Wang · P. Li
College of Material Science and Engineering, Beijing University of Technology, Beijing 100124, China
e-mail: zhangtu@emails.bjut.edu.cn

J. Yang
e-mail: yjcan@bjut.edu.cn

P. Wang
e-mail: 1262269308@qq.com

P. Li
e-mail: 1369014792@163.com

Y. Han (ed.), *Advances in Energy and Environmental Materials*,
Springer Proceedings in Energy, https://doi.org/10.1007/978-981-13-0158-2_69

Introduction

Owing to its high melting point, high strength, low vapor pressure, low sputter etching rate, good thermal stability and high strength ductility and excellent comprehensive properties, tungsten alloys were widely used in national defense, aerospace, metallurgy, electronics and other fields [1, 2].

Tungsten electrode is an important functional material used in inert gas shielded welding, plasma cutting, spray melting and other fields and so on [3, 4]. With the extensive application of rare earth tungsten electrodes, people put forward higher requirements for the stability and high temperature erosion of rare earth tungsten electrodes, Materials workers are committed to researching and developing various new electrode materials.

Traditionally, tungsten electrode powder is processed by powder metallurgy route such as vertical melting sintering and medium frequency induction sintering [5, 6], which requires high sintering temperatures and long soaking times, and produces coarse microstructure often. Thus, more efficient sintering techniques have been pursued for consolidating tungsten electrode.

Spark plasma sintering is a fast sintering technique for consolidation of powders utilizing uniaxial force and pulsed direct electric current under low atmospheric pressure [7–9]. Wide range of materials (metals, composites, ceramics) can be compacted using spark plasma sintering at few hundred Kelvin lower processing temperature than in conventional sintering process [10–12]. As an innovative sintering technology, Spark plasma sintering(SPS) makes it possible to enhance the densification of sintered samples in a very short period of time because of its a number of advantages, such as lower sintering temperature and voltage, rapider heating rate and shorter holding time [13–15]. Therefore, SPS is quite suitable for producing of various difficult-to-cult materials and refractory metal, especially tungsten with high density and fine grained microstructures [16, 17].

For Spark plasma sintering, there are many factors that affect the performance of the material, such as sintering temperature, sintering pressure, holding time and heating rate, etc. A review of the available literature shows that one of the factors that have the greatest impact on material properties is the sintering temperature. The working stability and corrosion resistance is the property of this electrode material, and in the past study we found such a phenomenon: high density and fine grain structure of the tungsten electrode material often have a good resistance to burning capacity.

The samples were spark plasma sintered at seven designated temperatures of 1200, 1250, 1300, 1350, 1400, 1450 and 1500 °C with a heating rate of 100 °C/min through increasing the direct current. Applied external pressure during the sintering process was 50 MPa in vacuum condition of ≤ 10 Pa. Isothermal dwelling at the sintering temperature was 5 min. And we studied the effects of SPS sintering temperature on the microstructure and hardness of sintered rare earth tungsten electrode were investigated by metallographic microscope, scanning electron

microscopy and Vickers Indenter, and analyzes density degree of rare earth tungsten electrode sintering sample based on Archimedes principle.

Experimental Procedure

Tungsten electrode powder with a mass ratio of W–1.5% La_2O_3–0.08% Y_2O_3–0.08% ZrO_2 were used in SPS process, and the average particle size of the ranges were about 2.78 μm respectively through calculation. An SPS-3.2-MV sintering apparatus (Sumitomo Corporation Industrial Co., Ltd., Japan) and graphite die (50 mm height) with an internal diameter of 20.4 mm and an external diameter of 40 mm were employed, and graphite paper of 0.2 mm thickness was placed between graphite punches and the powder to prevent sticking during the sintering process. prepared composite powders were first pre-compacted under a pressure of 5 MPa, and then sintered by SPS at a temperature of 1200,1250,1300,1350,1400,1450,1500 °C under a pressure of 50 MPa for 5 min, and heating rate was 100 °C/min. Sintering was performed in vacuum (residual pressure ≤ 10 Pa). And after Sintering, the furnace was cooled to room temperature and the sintered sample was taken out.

Microstructural characterization of the samples surface were observed by scanning electron microscopy (SEM), density of the sintered samples were determined though Archimedes method by using an electronic balancer, relative density is the ratio of the measured density to the theoretical density. The Vickers hardness was measured by hardness tester with the load of 0.5 kg for 15 s after polished, and the average value of each specimen was gained by evaluating 7 points. The sintered samples were vertically cut and polished to a 1.0 μm finish. The microstructures of the samples were observed under a scanning electron microscope without chemical etching in order to obtain more reliable grain size data. The average grain size of a cross-section was measured using analytical software. At least 1000 grains were examined for each sample with different fields and averaged. The three-dimensional average grain size was obtained from the measured two-dimensional data by multiplying the latter by 1.5, and are presented as the grain size data.

Results and Discussion

Figure 1 shows the relationship between relative density and temperature of rare earth tungsten electrode for sintered samples by SPS. Microstructural analysis was carried out to study the development of the microstructure and the evolution of the porosity. The representative scanning electron microscopy of the polished surfaces of spark plasma sintered tungsten electrode samples are shown in Figs. 2 and 3. It can be seen that the relative density of rare earth tungsten electrode is increasing with the sintering temperature rising, and the grains of tungsten electrode sintered

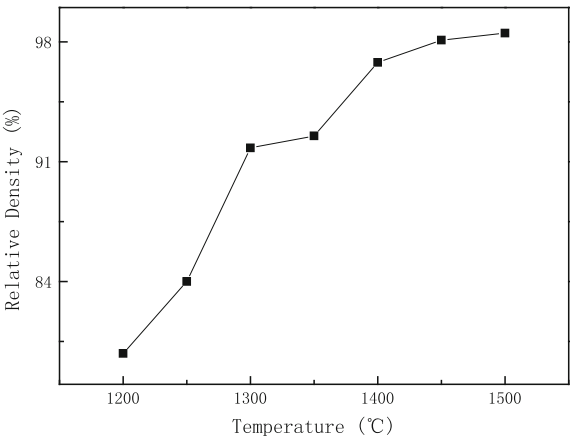

Fig. 1 Relationship between relative density and temperature for samples sintered by SPS

samples continue to grow, the organization of the pores in the sintered samples is decreasing gradually.

When the sintering temperature is 1200 °C, the relative density of the rare earth tungsten electrode sintered sample is 79.8%, the average grain sizes of the tungsten electrode sintered sample are about 0.8 μm, the grain is not fully grown, and there are also many holes in the sintered sample after sintering process. It seems that the SPS temperature of 1200 °C is not enough to reach a dense material. At this point the dominant mechanism of sintering densification is surface diffusion, which can effectively reduce and eliminate holes in the tungsten electrode sintered sample.

With the increasing of temperature, the relative density of tungsten electrode sintered samples is greatly improved, the tungsten grains in the microstructure of the sintered sample grow gradually. At 1300 °C, the densification degree of the sintered sample is relatively large, the relative density of the sintered sample is increased to 92.1%. The grain size grows to 1.4 μm, and the crystal grain morphology does not change too much. The pores inside the tungsten electrode sintered sample gradually decrease and disappear. This show that the increase of the density in the sintering densification process has a great relationship with the disappearance of the connection hole inside the tungsten electrode sintered sample, and the inside of the sintered sample will form a closed hole, and the effect of surface diffusion on the densification of the sintered sample will gradually decrease.

As the sintering temperature rises to 1450 °C, the relative density of tungsten electrode sintered sample has reached 98.05%. The number of pores in the tungsten electrode sintered sample has been greatly reduced, and the grain size is 3.5 in the case of high density, which is inseparable from the characteristics of spark plasma sintering. The current and temperature of particles increased rapidly due to strong spark discharge effect, and the bonding between particles was facilitated by the softening of the particle surface [18, 19]. The current passed directly through the sintering neck when the two particles connected, and Joule heating became a main heating mode to make particles connect together replacing the spark discharge

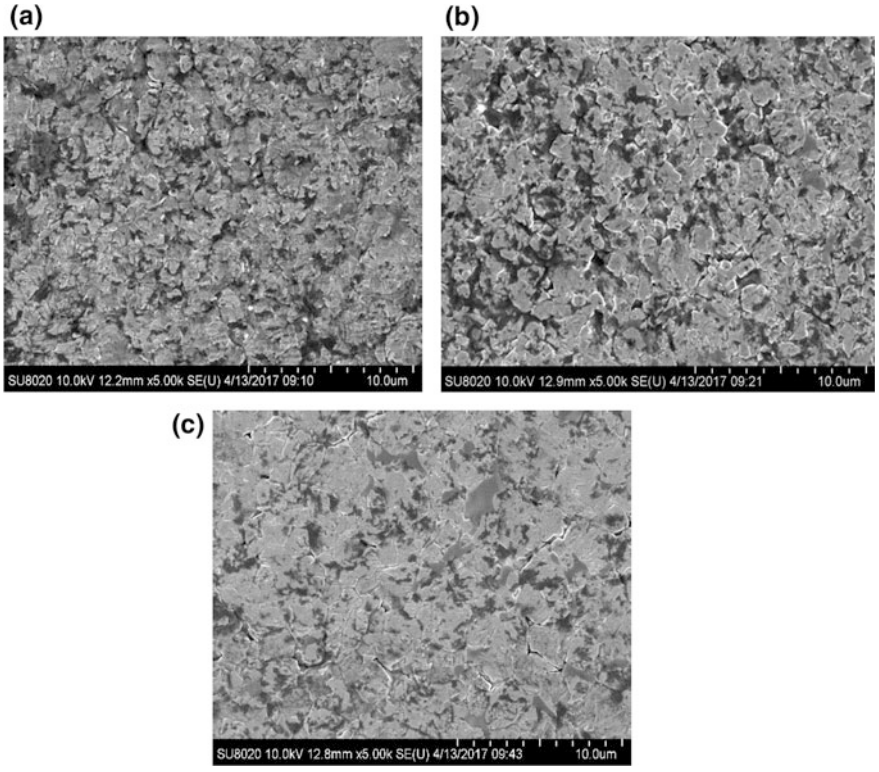

Fig. 2 SEM of the sintered samples with different temperatures **a** 1200 °C, **b** 1250 °C, **c** 1300 °C

effect [12]. The increase of temperature also promoted the rapid transformation of the densification mechanism in the sintered sample from the surface diffusion to the volume diffusion, and the volume diffusion promotes the sintering neck growth in the sintered sample while also reducing and eliminating the enclosed holes and pores in the sintered sample, thereby further promoting the densification of the sintered sample.

As can be seen from the analysis of Fig. 4, the hardness of the rare earth tungsten electrode prepared by SPS preparation was enhanced with the increase of sintering temperature, and the porosity of the sintered sample was decreased with the increase of sintering temperature. When the sintering temperature is 1450 °C, the sintered sample reaches the maximum hardness of 496.7 HV. Despite that, other samples, which were sintered at 1500 °C, the hardness was reduced to 444.5 HV, and the porosity of the sintered sample increases a little. There may be two reasons to account for this case: one is with the sintering temperature rise, the grain size of sintered sample grows obviously, the increment of residual fine porosities caused by the grain growth at the highest sintering temperature designated and the effect of fine grain strengthening inside the sintered sample will be reduced; the other is that

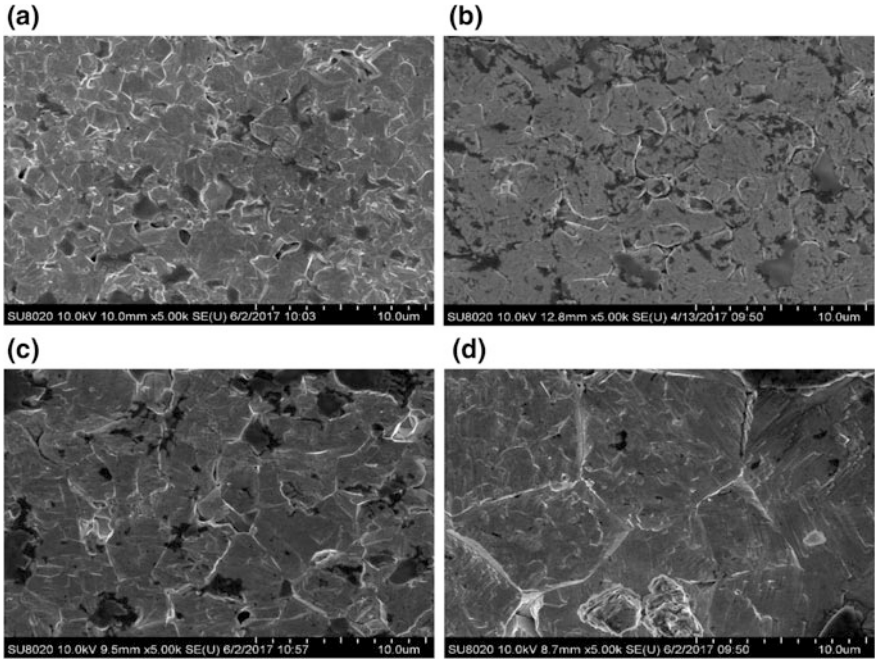

Fig. 3 SEM of the sintered samples with different temperatures **a** 1350 °C, **b** 1400 °C, **c** 1450 °C, **d** 1500 °C

the rare earth component has low melting point, the rare earth in the sintered sample will evaporate with the rising of temperature, this factor will also reduce the role of fine grain strengthening for the sintered sample, and resulting in the decrease for hardness.

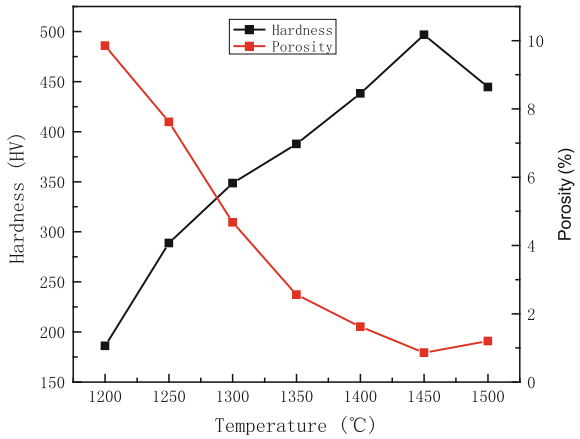

Fig. 4 Effect of different temperatures on hardness and of porosity of reaction products

Based on the above analysis, when the sintering temperature is 1450 °C, the grain size of the sintered sample prepared by SPS is 3.5 μm, the grain distribution is uniform and the grain shape is regular. At this time, the hardness is the highest and the porosity is the lowest, and the density of the sintered sample has also been basically completed.

Summary

The rare earth tungsten electrode with high densification and fine grain structure can be successfully prepared by using spark plasma sintering. The density and hardness of rare earth tungsten electrode prepared by SPS sintering are higher than it prepared by intermediate frequency sintering, and the micro-organizational of sintered sample is uniform and the grain size is small, which is beneficial to improve the anti-burning performance of the rare earth tungsten electrode.

Under the condition of sintering pressure of 50 MPa, sintering holding time of 5 min and heating rate of 100 °C/min, the optimum sintering temperature of sintered rare earth tungsten electrode is 1450 °C, the relative density of the tungsten electrode is 98.05%, and the hardness of the tungsten electrode is 496.7 HV.

With the increase of the sintering temperature, the grain size of the rare earth tungsten electrode sintered with SPS increases. At the best sintering temperature of 1450 °C, the sintered rare earth tungsten electrode grain size is 3.5 μm.

Acknowledgements The project was financed by National key research and development program of China, the subject code is 2017YFB0305601. The authors gratefully acknowledge the supports of School of Materials Science and Engineering, Beijing University of Technology.

References

1. Y. Chen, Y.C. Wu, *Preparation and Properties of the Tungsten Matrix Composites Face to the Plasma* (Hefei University of Technology Press, Hefei, 2008)
2. S. Wang, M. Xie, Research status and development trend of high-density tungsten alloy. Rare Met. Mater. Eng. **41**(2), 145 (2012)
3. L. Peng, S.K. Li, H.N. Cai, X.Q. Zhou, Influence of deformation ratio on microstructure and adiabatic shear banding in tungsten heavy alloy processed by rotary swaging. Chin. J. Rare Met. **3**(2), 218 (2011)
4. Y.T. Cui, S.G. Zhang, M. Wang et al., Study on rare earths doped tungsten cathode for high performance plasma spray torch. Therm. Spray Technol. (2014)
5. R. Bollina, R.M. German, Heating rate effects on microstructural properties of liquid phase sintered tungsten heavy alloys. Int. J. Refrac. Met. Hard Mater. **22**(2–3), 117–127 (2004)
6. K. Liu, L.H. Zhu, Y.J. Sui et al., Effect of medium frequency induction sintering and electric resistance sintering of tungsten billet on its microstructure and fabrication behavior. Shanghai Nonferrous Met. (2010)
7. R.S.S. Maki, S. Mitani, T. Mori, Effect of spark plasma sintering (SPS) on the thermoelectric properties of magnesium ferrite. Mater. Renew. Sustain. Energy. **6**(1), 2 (2017)

8. D. Chakravarty, A.H. Chokshi, Direct characterizing of densification mechanisms during spark plasma sintering. J. Am. Ceram. Soc. **97**, 765–771 (2014)
9. X. Song, X. Liu, J. Zhang, Neck formation and self-adjusting mechanism of neck growth of conducting powders in spark plasma sintering. J. Am. Ceram. Soc. **89**, 494–500 (2006)
10. O. Guillon, J. Gonzalez-Julian, B. Dargatz et al., Field-assisted sintering technology/spark plasma sintering: mechanisms, materials, and technology developments. Adv. Eng. Mater. **16**(7), 830–849 (2014)
11. D. Chakravarty, A.H. Chokshi, Direct characterizing of densification mechanisms during spark plasma sintering. J. Am. Ceram. Soc. **97**(3), 765–771 (2014)
12. X. Song, X. Liu, J. Zhang, Neck formation and self-adjusting mechanism of neck growth of conducting powders in spark plasma sintering. J. Am. Ceram. Soc. **89**(2), 494–500 (2006)
13. S.H. Risbud, Y.H. Han, Preface and historical perspective on spark plasma sintering. Scripta Materialia **69**(2), 105–106 (2013)
14. M. Gendre, A. Maître, G. Trolliard, A study of the densification mechanisms during spark plasma sintering of zirconium (oxy-)carbide powders. Acta Materialia **58**(7), 2598–2609 (2010)
15. Y. Wang, S. Li, F. Wang et al., Effects of spark plasma sintering temperature on microstructure and dynamic mechanical properties of 93 W-4.9Ni-2.1Fe Alloy. Rare Met. Mater. Eng. **39**(10), 1807–1810 (2010)
16. Z.A. Munir, U. Anselmi-Tamburini, M. Ohyanagi, The effect of electric field and pressure on the synthesis and consolidation of materials: a review of the spark plasma sintering method. J. Mater. Sci. **41**(3), 763–777 (2006)
17. S. Deng, T. Yuan, R. Li et al., Spark plasma sintering of pure tungsten powder: Densification kinetics and grain growth. Powder Technol. **310**, 264–271 (2017)
18. C.S. Bonifacio, J.F. Rufner, T.B. Holland et al., In situ transmission electron microscopy study of dielectric breakdown of surface oxides during electric field-assisted sintering of nickel nanoparticles. Appl. Phy. Lett. **101**(9), 132 (2012)
19. Z. Zhang, F. Wang, L. Wang et al., Sintering mechanism of large-scale ultrafine-grained copper prepared by SPS method. Mater. Lett. **62**(24), 3987–3990 (2008)

Effect of Non-functional Additives on Performance of Internal Combustion Engine Lubricating Oil

Jingqiu Mu, Jinlong Wu, Fenglan Han, Jingjing Li and Liqing Su

Abstract In order to improve the quality of lubricants and prolong the life of oil products, additives should be added to the base oil. The non-functional additives of lubricating oil are mainly included: viscosity index improver, pour point depressant, anti-foam agent. In a certain ratio, the viscosity index improver, pour point depressant, and anti-foam agent have a synergistic or inhibitory effect. This experiment aims to explore the synergistic and inhibitory effects of non-functional additives and the effect of different dosage of additives on the performance of internal combustion engine lubricants. Certain amount of additives are added to the base oil for testing. Viscosity index improver T613, pour point depressant T803B, anti-foam agent T901 were selected as non-functional additives in the experiment. An orthogonal experiment was used to design the scheme. The performance of compound non-functional additives on lubricating oil was determined by means of oil kinematic viscosity measurement, foam property measurement and petroleum pour point measurement. The results of orthogonal design show that: the addition of anti-foaming agent is in the range of 5–20 ppm/100 g, and the viscosity index improver is inhibited. When the pour point depressant is 0.2–0.3 wt%, it has synergistic effect with viscosity index improver, but more than 0.3 wt% after the viscosity index improver to produce inhibitory effect. The anti-foaming agent content has a synergistic effect on the pour point depressant in the range of 5–20 ppm/100 g; the viscosity index improver has a synergistic effect on the pour point depressant in the range of 5–6.5 wt%. The content of the pour point depressant in the range of 0.2–0.3 wt% synergies with the anti-foaming agent, the content of more than 0.3% after the inhibition effect; adding viscosity index improver in the range of 5–6.5 wt% with the anti-foam agent inhibition. The optimum process was as follows: viscosity index improver T613 was 6.0 wt%, pour point depressant T803B was 0.3 wt%, and anti-foam agent T901 was 5 ppm/100 g.

Keywords Lubricants · Nonfunctional additives

J. Mu · J. Wu · F. Han (✉) · J. Li · L. Su
North Minzu University, Yinchuan 750021, China
e-mail: 625477897@qq.com

Y. Han (ed.), *Advances in Energy and Environmental Materials*,
Springer Proceedings in Energy, https://doi.org/10.1007/978-981-13-0158-2_70

Introduction

Lubricating oil is described as the blood that maintains the normal operation of the machine [1]. About 90% of the lubricating oil as the base oil, the rest are additives which play a major role in the physical and chemical properties of lubricants [2]. There are many types of additives, it mainly divided into functional additive and non-functional additive. Non-functional additives play an important role [3, 4]. There are two effects in the study of lubricating oil additives: synergistic effect and inhibitory effect. Synergistic effect refers to not less than two kinds of the same type or different types of lubricant additives used together, and its various aspects of the effect is significantly better than the effect of individual use of the phenomenon [5]. The inhibitory effect is harmful to some additives because of different chemical properties and chemical activity and surface energy, and it will cause the effect of the additive to be reduced or even disabled [6]. The production process of the compound is not simply a mixture of functional additives. Because of the high concentration of additives in the compound, the physical and chemical properties of additives can greatly affect the application of the compound.

Ma et al. [7] introduces the composite effect of extreme pressure anti-wear additives and the status of synergistic interaction with solid lubricant and surface modification layer respectively, and puts forward some research contents worthy of attention. Qiao and others [8] use of HQ-1-type friction and wear tester to observe the commonly used extreme pressure anti-wear additives vulcanized olefin and di-n-butyl phosphide vinegar system of lubricating properties, and micro-analysis of the test method used in the complex Synergistic mechanism. So far, the synergistic or inhibitory effects on non-functional additives of the same type or different types of lubricants have not been taken into account and have not been explained in great detail.

Synergistic and inhibitory effects are essential for the reconciliation of lubricants and are easily overlooked in the application process [9]. In the study of the compound non-functional additive of internal combustion engine, attention should be paid to the balance between the performance of each additive, and all the indexes of the compound formula should be met [10, 11].

In this study, the internal combustion engine commonly used additives (viscosity index improver T613, pour point depressant T803B, anti-foam agent T901) as experimental non-functional additives. The effects of different amounts on the kinematic viscosity (100 °C), viscosity index, pour point and foam stability of lubricating oil were investigated. The purpose of this experiment is to explore the synergistic and inhibitory effects of non-functional additives and provide reference data for the application of these three non-functional additives.

Experimental Methods

Major Reagents. Base oil 400SN, base oil 150BS, base oil 250 N were obtained from Shenzhen Zhongrun Tong Chemical Co. Ltd; viscosity index improver T613, pour point depressant T803B, anti-foam agent T901 were obtained from Jinzhou Baxter Chemical Co. Ltd.

Non-functional Additives Single Agent Experiment. Three non-functional additives (T613, T803B, T901) were added to the internal combustion engine base oil according to the mass or mass fraction gradient. The basic physical and chemical properties are determined of the lubricating oil: kinematic viscosity (at 40, 100 °C), pour point and foam stability (at 24, 93.5 °C). The optimal range of a single additive is determined through the physical and chemical properties.

Composite Non-functional Additives Orthogonal Design Test. Orthogonal design of three non-functional additives is designed in accordance with optimal use range. Then the basic physical and chemical properties of lube are tested in turn. In the process of additive compounding, the additive that can reduce the performance should be added simultaneously or adjacently. According to the performance requirements of internal combustion engine lubricants, the adding order of additive compound is: base oil-viscosity index improver-pour point depressant-antifoamer.

Results and Discussion

Adding Non-functional Additives Single Test Results. With the increase of pour point depressant T803B, the change of the pour point is shown in Fig. 1. The change of kinematic viscosity and viscosity index with the increase in the viscosity index improver T613 is shown in Fig. 2. As well as with the anti-foam agent T901 increase in the amount of foam stability changes as shown in Table 1 below. The increase in foam stability with the addition of anti-foam agent T901 is shown in Table 1.

As can be seen from Fig. 1, with the increase of the addition of the pour point depressant T803B, the pour point of the lubricating oil is reduced to −30 °C by −15 °C. According to the internal combustion engine lubricants use standard and combined with economic effects, adding 0.2–0.35 wt% of the T803B to meet the demand. It can be seen from Fig. 2, the viscosity index improver T613 added, the lubricating oil kinematic viscosity and viscosity index are increased. The range of the kinematic viscosity (at 100 °C) of standard internal combustion engine oil is 12.5–16.3, and the viscosity index is greater than or equal to 110. Based on the standard and economic requirements, the viscosity index improver is 5–6.5%. As can be seen from Table 1, with the increase of the anti-foaming agent, the stability of the foam is improved and then decreased. According to the standard of internal combustion engine lubricants, the content of anti-foaming agent is 5–20 ppm/100 g.

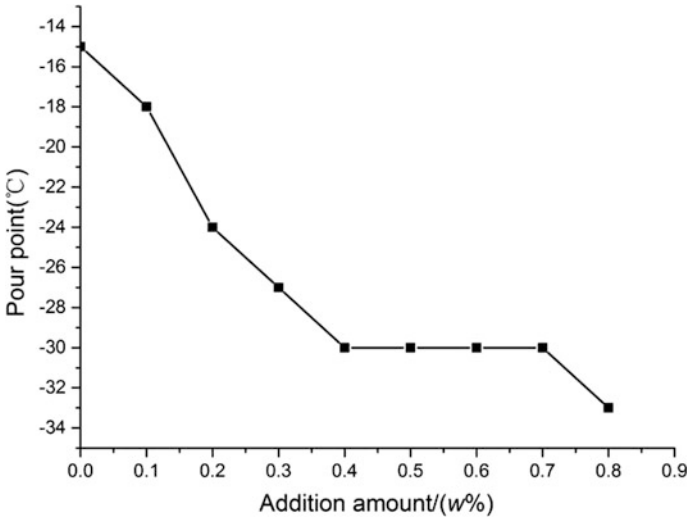

Fig. 1 Increasing the pour point of the lubricant with the addition of T803B

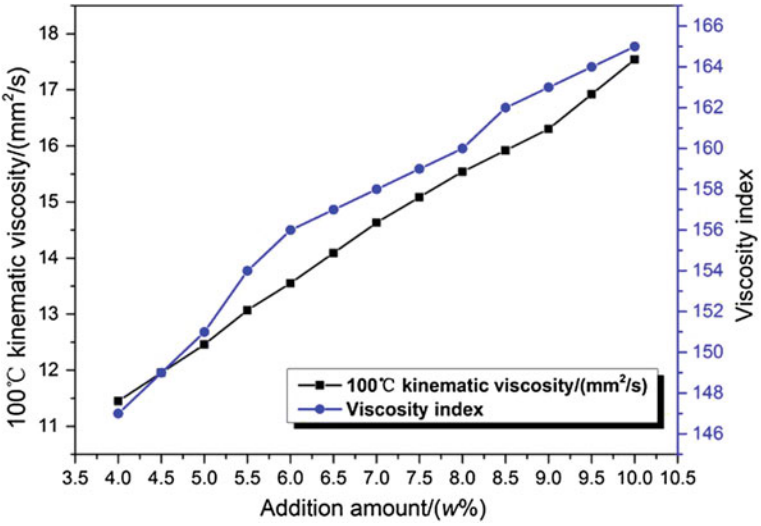

Fig. 2 Lubricant 100 °C kinematic viscosity and viscosity index with the increase in the amount of T613 increase

Table 1 Lubricant foam stability increases with the addition of T901

T901 added (ppm/100 g)	0	10	25	50	75	100
Foam stability at 93.5 °C (ml/ml)	10/0	8/0	12/0	15/0	16/0	18/0
Foam stability at 24 °C (ml/ml)	30/0	5/0	8/0	10/0	15/0	18/0

Table 2 Horizontal table of all formulas for orthogonal design

Level	T613 added amount (wt%)	T803B added amount (wt%)	T901 added amount (ppm/100 g)
1	5.0	0.20	5
2	5.5	0.25	10
3	6.0	0.30	15
4	6.5	0.35	20

Composite Non-functional Additive Orthogonal Test Results Analysis. In this paper, the addition of viscosity index improver, pour point depressant, anti-foam agent are three factors of orthogonal test design. Each factor takes four levels, each of which is the optimal use range for the single agent. Full formulation of the orthogonal test design of the factors and test the design of the table as shown in Table 2.

The viscosity index defines the molecular structure, it is an accurate description of the definition of the molecule, so the viscosity index of the base oil of the internal combustion engine oil is analyzed only. The effect of the composite non-functional additive on the viscosity index is shown in Table 3.

From Table 3, it can be seen that when the content of the depressant is constant, the viscosity index becomes smaller, followed by 147, 138, 136, 132. This indicates that there is a certain inhibitory effect between anti-foam agent and viscosity index improver for oil viscosity.

From Table 4, the content of the anti-foaming agent is unchanged. When the pour point depressant increases with the increase of the viscosity index improver, the viscosity index increases first and then decreases, followed by 147, 154, 183, 152. The results showed that the pour point depressant had synergistic effect with the viscosity index improver when the content of oil depressant was in the range of

Table 3 Effect of T901 on viscosity index in composite nonfunctional additives

Level	T613 added amount (wt%)	T803B added amount (wt%)	T901 added amount (ppm/100 g)	Viscosity index
1	5.0	0.20	5	147
2	5.5	0.20	10	138
3	6.0	0.20	15	136
4	6.5	0.20	20	132

Table 4 Effect of T803B on viscosity index in composite nonfunctional additives

Level	T613 added amount (wt%)	T803B added amount (wt%)	T901 added amount (ppm/100 g)	Viscosity index
1	5.0	0.20	5	147
5	5.5	0.25	5	154
9	6.0	0.30	5	183
13	6.5	0.35	5	152

Table 5 Effect of T901 on pour point in composite nonfunctional additives

Level	T613 added amount (wt%)	T803B added amount (wt%)	T901 added amount (ppm/100 g)	Pour point(°C)
1	5.0	0.20	5	−24
6	5.0	0.25	10	−27
11	5.0	0.30	15	−30
16	5.0	0.35	20	−30

Table 6 Effect of T613 on pour point in composite nonfunctional additives

Level	T613 added amount (wt%)	T803B added amount (wt%)	T901 added amount (ppm/100 g)	Pour point(°C)
1	5.0	0.20	5	−24
5	5.5	0.25	5	−27
9	6.0	0.30	5	−30
13	6.5	0.35	5	−30

0.2–0.3 wt%, but the content of pour point depressant was more than 0.3 wt%, and the viscosity index improver to suppress the effect.

From Table 5, the amount added of viscosity index improver does not change, When the anti-foaming agent increases with the increase of the pour point depressant, the pour point of the lubricating oil decreases, followed by −24, −27, −30, −30 °C, the low temperature fluidity of oil is enhanced, that is, for the low temperature fluidity of oil, the anti-foam agent and the pour point depressant synergies.

From Table 6, it can be seen that when the content of the anti-foaming agent is constant, when the viscosity index improver increases with the increase of the pour point depressant, the pour point of the lubricating oil is −24, −27, −30, −30 °C. The low temperature fluidity of the oil is enhanced, indicating that the viscosity index improver has synergistic effect with the pour point depressant for oil flow.

In the case of high temperature access to the air more prone to air bubbles, where only the analysis of additives after the internal combustion engine oil base oil 93.5 °C when the impact of oil anti-foam.

Table 7 Effect of T803B on the stability of foam at 93.5 °C in composite nonfunctional additives

Level	T613 added amount (wt%)	T803B added amount (wt%)	T901 added amount (ppm/100 g)	Foam stability
1	5.0	0.20	5	10/0
6	5.0	0.25	10	20/0
11	5.0	0.30	15	20/0
16	5.0	0.35	20	15/0

Table 8 Effect of T613 on foam stability in composite nonfunctional additives

Level	T613 added amount (wt%)	T803B added amount (wt%)	T901 added amount (ppm/100 g)	Foam stability
1	5.0	0.20	5	10/0
2	5.5	0.20	10	15/0
3	6.0	0.20	15	20/0
4	6.5	0.20	20	20/0

From Table 7, it can be seen that when the content of viscosity index improver does not change and the pour point depressant increases with the increase of the anti-foaming agent content, the stability of the oil foam is decreased by 10/0 to 20/0 and then to 15/0. This indicates that in terms of the anti-foaming properties of oil, the pour point depressant content is synergistic with anti-foaming agent in the range of 0.2–0.3%, and the inhibition effect is generated after the content exceeds 0.3%.

It can be seen from Table 8 that the content of pour point depressant is certain and that when the viscosity index improver increases with the content of anti-foaming agent, the stability of oil foam is reduced. This indicates that the viscosity index improver and anti-foaming agent have inhibitory effect on oil resistance.

Conclusion

For the oil viscosity index change, the anti-foam agent T901 added in the range of 5–20 ppm/100 g, the viscosity index improver T613 inhibition, pour point depressant T803B added 0.2–0.3 wt%, the viscosity index modifier T613 has a synergistic effect, but after the addition of the pour point depressant T803B exceeds 0.3 wt%, the viscosity index improver T613 is inhibited.

For the low temperature fluidity of the oil, the anti-foaming agent T901 is added in the range of 5–20 ppm/100 g, the anti-foaming agent T901 has synergistic effect on the pour point depressant T803B, the viscosity index improver T613 is added in the range of 5–6.5 wt% within the scope of the synergistic effect on the pour point depressant T803B.

In the case of oil anti-foaming, the amount of pour point depressant T803B added in the range of 0.2–0.3 wt% synergistic effect with anti-foaming agent T901, the addition of more than 0.3 wt%, the inhibitory effect, adding viscosity index improver T613 content in the range of 5–6.5 wt% with the anti-foam agent T901 inhibition.

The optimum process is as follows, the viscosity index improver T613 is 6.0 wt %, the amount of pour point depressant T803B is 0.3 wt%, and the anti-corrosion resistance of the internal combustion engine is the same as that of the non-functional additive. The amount of foam T901 added is 5 ppm/100 g.

References

1. G. Wu, Performance Study and Preparation of Anti Wear Additive for Lubrication Oil, Harbin Engineering University, 2004
2. W.Q. Yao, Y.L. Wu, J.Y. Liu, Base oil and additives for modern gasoline engine lube. J. Chang'an Univ. (Natural Science Edition) **3**, 71–74 (2003)
3. H. Wang, Study on the LNG Engine Lubricant of Heavy-duty Truck, Chang'an University, 2015
4. S. Liang, J. Fan, J. Zhang, L. Ding, Research progress in lubricating oil detergent metalation process. Chem. Ind. Eng. Prog. **8**, 1451–1456 (2010)
5. Z. Xu, Study on CNG Engine Lubricating Oil Composite Additive for City Bus, Chang'an University, 2015
6. X. Zhang, The current situation and development trend of lubricant additives at home and abroad. Lubricating Oil **2**, 1–4 (2012)
7. Y.S. Ma, J.J. Liu, B.L. Zhu, L.Q. Zheng, R.L. Wang. Combatic effect of lubricating oil extreme pressure antiwear additives and its synergistic effect with solid lubricants and surface modified layers. Tribology **3**, 270–278 (1994)
8. Y. Qiao, X. Fang, H. Dang, Co synergistic mechanism of two typical sulfur-containing phosphorus additive systems in lubricating oil. Tribology **1**, 29–38 (1995)
9. W. Wang, W. Li, Y. Dong, X. Zhang, Effect of additives blending process on CNG engine oils performance. Lubr. Sealing **11**, 134–137 (2015)
10. F.G. Jiang, The development status and trend of lubricating oil in automobile internal combustion engine. Chin. Pet. Chem. Ind. Stan. Qual. **8**, 101 (2011)
11. H.X. Zhao, in *Application and Development of Lubricating Oil in Internal Combustion Engine*. China Automotive Engineering Society Automotive Fuel and Lubricating Oil Branch. China Automotive Engineering Society Fuel and Lubricant Branch of the 13th Annual Conference Proceedings. China Society of Automotive Engineers With Lubricants Branch, (2008) 5

Application of Phosphate-Solubilizing Bacteria Activating Phosphate Materials in Solidification of Soil Heavy Metal

Yibin Li, Mingjiang Zhang and Xingyu liu

Abstract Removal of heavy metals by phosphate-solubilizing bacteria (PSB) activating phosphate materials in simulated heavy metal liquid environment was studied. Calcium phosphate was a kind of functional carrier material under action of PSB, accelerating the reaction to form phosphate precipitation of heavy metal. The results indicated that the removal of heavy metals with activated phosphate materials by PSB occurred within 15 days, and achieved high removal rates of Pb^{2+}, Cu^{2+}, Zn^{2+} and Cd^{2+} comparing with the phosphate materials inactivated. Therefore the activated phosphate materials by PSB could be a functional material for efficiently removing heavy metal from contaminated soil.

Keywords Heavy metals · Immobilization · Phosphate-solubilizing bacteria Phosphate materials

Introduction

The soil heavy metal pollution increases rapidly in the past few decades, especially heavy metals in soil serious exceeded the standard near the smelter which referred to lead, zinc, copper, and cadmium etc. Latest survey of soil pollution in country, the exceed the standard rate of national soil is 16.1% and at the same time one eighth of country existence of heavy metal pollution [1]. Heavy metal contamination can affect grain yield and indirectly affect human health.

Y. Li · M. Zhang · X. liu (✉)
National Engineering Laboratory of Biohydrometallurgy, General Research Institute for Nonferrous Metals, No. 2 Xinjiekouwai Street, Beijing 100088, China
e-mail: wellwoodliu@163.com

Y. Li
e-mail: zndxlyb@126.com

M. Zhang
e-mail: zmj0603@163.com

Y. Han (ed.), *Advances in Energy and Environmental Materials*,
Springer Proceedings in Energy, https://doi.org/10.1007/978-981-13-0158-2_71

At present, many different remediation methods can be applied to alleviate the toxic metal pollution, for instant, physical, chemical and biological-chemical ones. The study show biochemical methods remediation method is an effective and environmentally friendly method. A number of activated phosphate materials as hydroxyapatite have been proved to effectively immobilize toxic heavy metals in contaminated soil [2].

The mechanisms of metal immobilization by phosphate material include: (a) ion exchange process at the surface, (b) surface complexation, (c) dissolution of the original phosphate minerals and formation of new metal phosphate minerals, (d) substitution of Ca in phosphate material by other metals during recrystallization (coprecipitation) [3]. According to previous study results, acid pH condition increases phosphate solubility, what is the necessary prerequisite to activated phosphate materials.

At present, the more effective phosphorus is released when 2% citric acid is used as a release agent, which means the greater the amount of soil dissolved in it. The addition of citric acid is exogenous, so that the formation of slightly acidic soil condition [4]. However, there are many microorganisms that can dissolve insoluble phosphate in soil environment, because of secretion of multiple organic acids during metabolism process lowers the environmental pH value [5]. It can maintain pH values in the 4.5–6.5 range and it can convert insoluble forms of phosphorus into an accessible form to promote the immobilization of heavy metal. Eighteen strains of phosphate solubilizing microorganisms were isolated from soil. Named of Pantoea sp. and Enterobacter sp. were used for immobilization in lead contaminated soil. The result showed that they had a great application prospect in soil remediation [6]. Enterobacter sp. did not enhance Pb immobilization in solution because of acidification of bacterial medium, thereby inhibiting the formation of P-induced Pb precipitation. The immobilization of Pb in Pb-spiked soils was attributed to pyromorphite formation as indicated by XRD analysis [7].

The role of microorganisms in the solidification of heavy metals is not very clear, which accelerates the curing process or not. These factors limit the further development of phosphate-solubilizing bacteria activated phosphate materials. Therefore, it is necessary to do further research in this field. The aim of the study was to evaluate the effectiveness of phosphate-solubilizing bacteria activated phosphate material on Cd, Cu, Pb and Zn immobilization in simulation heavy metal contaminated conditions.

Materials and Methods

Materials. Phosphate-solubilizing bacteria activated phosphate materials mainly consisted of phosphate-solubilizing bacteria and high pure calcium phosphate. The phosphate-solubilizing bacteria of our research was preserved in Institute of Microbiology, Chinese Academy of Sciences, which derived from soil, obtained

after dissolution, dilution and coating. The analytically pure calcium phosphate was purchased at reagent company whose calcium content was between 34 and 40%.

The condition of calcium phosphate was prepared in the laboratory which comprised of 140.41 mg/L Cu^{2+}, 262.32 mg/L Pb^{2+}, 136.88 mg/L Zn^{2+} and 487.39 mg/L Cd^{2+}. These heavy metal ions were rooted in exogenous heavy metal nitrates. The content of heavy ions was based on molar ratio of phosphate to heavy metal.

Methods. Cultivation of phosphate-solubilizing bacteria. phosphate-solubilizing bacteria (PSB) was cultured at 30 °C for 3 days in 500 mL Erlenmeyer flask and the culture medium was carried out using National Botanical Research Institute's phosphate growth (NBRIP) fluid medium, the composition of NBRIP was shown in Table 1. The initial pH value was 7.51. Every three days, we observed PSB by microscope and counted the quantity of bacteria.

Whether the existence of PSB played a role in the NBRIP medium when the removal rate of heavy metals was studied in this paper. In 300 mL calcium phosphate solution, 3 g of calcium phosphate mentioned above was soaked. The effectiveness of heavy metal ions was compared in the solution with or without bacteria.

Analytical Methods. All solid samples are weighed by a scale. The test of solution was filtered through 0.22 μm filter before analyzed. The concentrations of heavy metal ions were determined by ICP-OES. The pH value of the solution was measured with a pH meter. The solid residues after chemical reaction were examined with an X-ray diffractometer.

Results and Discussion

In presence or absence of PSB, during different period the main heavy metal concentration and the value of pH were determined. There were differences of chemical properties between the both solutions, which were shown in Figs. 1, 2, 3, 4, 5, 6, 7 and 8.

From the figure as we could see, the pH value of PSB solution decreased from 7.51 to 3.46 in 21 days, while from 7.51 to 4.47 in sterility solution. The results indicated that nitrates of heavy metals caused decrease of pH value in the solution. Another factor was the produce of acid by PSB, which caused by metabolism of phosphate-solubilizing bacteria.

In the PSB solution, the concentration of bacteria increased first, then decreased. The highest concentration occurred on the sixth day, then decreased rapidly. Maybe

Table 1 Solution composition [g/L]

Composition	Glucose	$MgCl{\cdot}6H_2O$	$MgSO_4{\cdot}7H_2O$	KCl	$(NH_4)_2SO_4$	$Ca_3(PO_4)_2$
Concentration	10.0	5.0	0.25	0.2	0.1	5

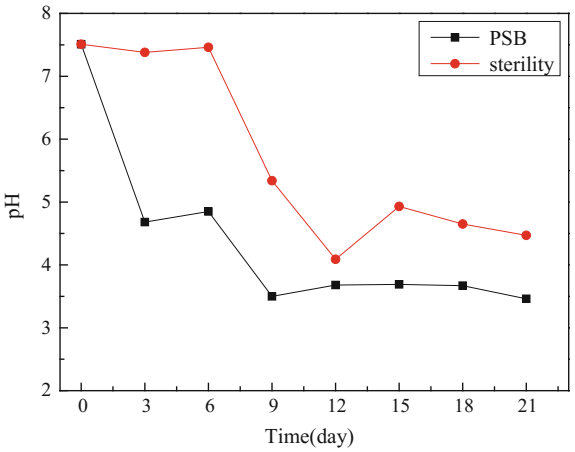

Fig. 1 Regulation of pH value changes over the time

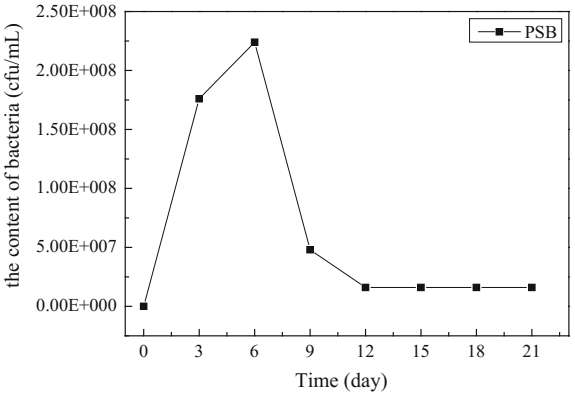

Fig. 2 Regulation of the concentration of bacteria changes over the time

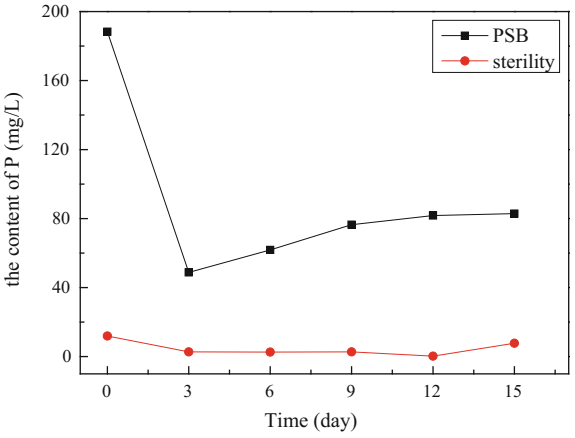

Fig. 3 Regulation of the concentration of P changes over the time

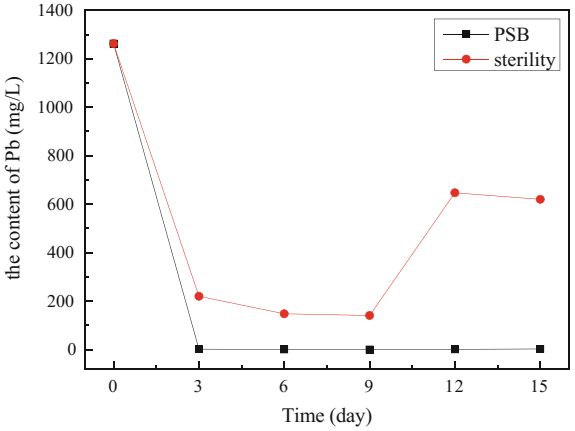

Fig. 4 Regulation of the concentration of Pb changes over the time

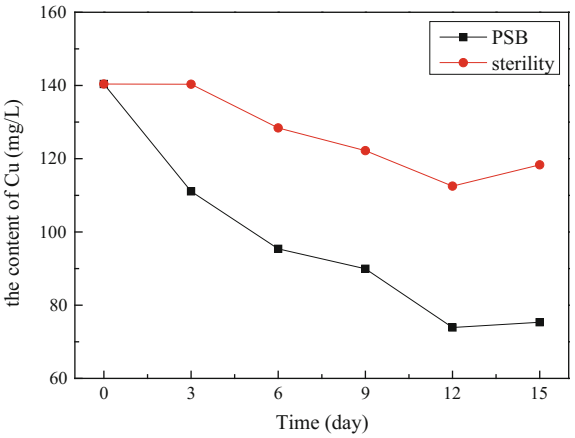

Fig. 5 Regulation of the concentration of Cu changes over the time

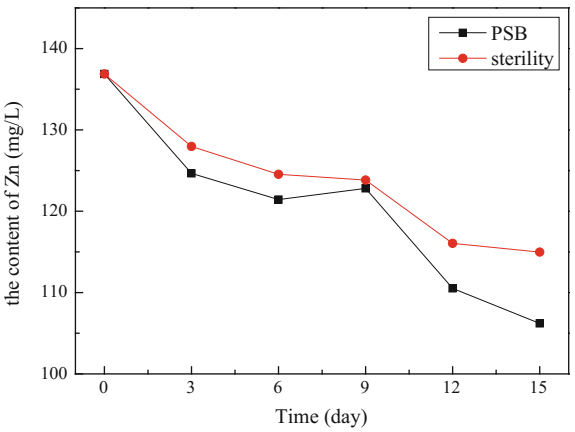

Fig. 6 Regulation of the concentration of Zn changes over the time

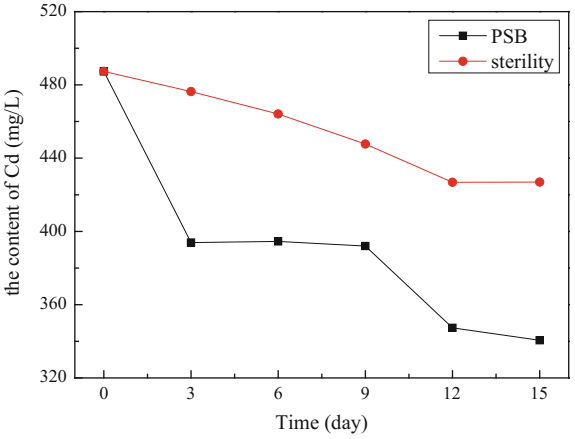

Fig. 7 Regulation of the concentration of Cd changes over the time

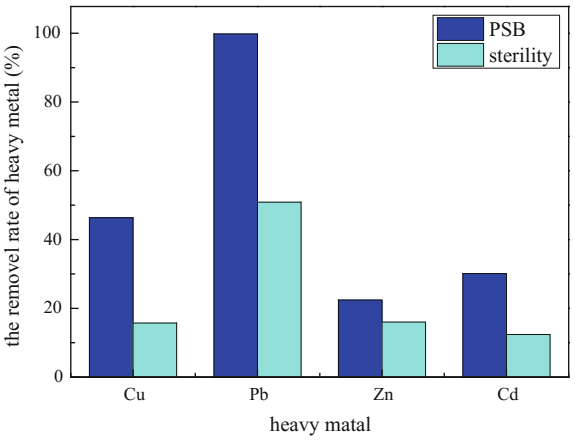

Fig. 8 Regulation of the removal rate changes of heavy metal over the time

bacteria died. But bacteria continued existence in the solution. The bacteria were not well suited to the condition of high concentrations of heavy metals.

In the sterility solution, the concentration of trace P almost stayed in the same, while from 188.32 to 82.91 mg/L in PSB solution. There was a large different between PSB and sterility solution. Because of PSB was the main form to promote the dissolution of phosphorus. These rhizosphere microorganisms could convert insoluble calcium phosphate into soluble form constantly.

The concentration of Pb in PSB solution rapid declined from 1262.32 to 2.71 mg/L, while declined to 140.72 mg/L, increased to 619.91 mg/L. According to solubility product constant of lead phosphate, chloropyromorphite would be formed. However, in the sterility solution, lead may be adsorbed on the surface of phosphate and desorption as pH changed.

The concentration of Cu ion in the solution declined over the time, from 140.41 to 75.33 mg/L in PSB solution and from 140.41 to 118.33 mg/L in sterility solution. By literature we could know it may be caused by decreased of pH value and copper occurred replacement reaction on the surface of phosphate. According to the analysis result, copper sulfide precipitation was formed under the action of PSB. The reason may be that PSB converted sulphate radical into sulfide ion with the process of metabolism.

The concentration of Zn changed little in two different solutions, while PSB played a limited role in removal of zinc. According to the result of measure, the deposition of zinc sulfide was found in solid residues under action of PSB. The reason may be occurred replacement reaction on the surface of phosphate.

The concentration of Cd ion in the solution declined over the time, from 487.39 to 340.53 mg/L in PSB solution and from 487.39 to 426.92 mg/L in sterility solution. The reason was caused by the produce of sulfide ion. Cadmium occurred replacement reaction on the surface of phosphate.

The removal rate of heavy metal was 46.35, 99.79, 22.41 and 30.13% for Cu, Pb, Zn and Cd in the PSB solution, respectively. It was more better than in sterility solution, which value of removal rate was 15.73, 50.89, 16.00 and 12.41% for Cu, Pb, Zn and Cd, respectively. From the figure, we could know that the binding force between metal element were in the order: Pb > Cd > Cu > Zn.

Conclusions

Calcium phosphate is a kind of functional carrier material under action of PSB, the removal efficiency of heavy metal is better with activated phosphate materials than that not activated. Because of high bacterial activity accelerated the reaction to form precipitation, PSB activating phosphate materials is useful to solidified heavy metal.

The binding force between metal element and phosphate ion is in the order: Pb > Cd > Cu > Zn, which the concentration of these elements in the PSB solution will become lower with the generation of phosphate ion.

Acknowledgements This work was supported by the National Natural Science Foundation of China under grant numbers U1402234, 41573074, 50904011, and 31300025; the nation high-level youth talents special support plan; the Guangxi scientific research and technology development plan under grants GuikeAB16380287 and Guikegong14124004-3-1; the public welfare fund of the Ministry of Environmental Protection of People's Republic of China under grant number 201509049; and Program of International S & T Cooperation S2016G2135.

References

1. Ministry of environmental protection, Ministry of land and resources, National survey of soil pollution survey. China Environ. Prot. Ind. **5**, 10–11 (2014)
2. S. Mignardi, A. Corami, V. Ferrini, Evaluation of the effectiveness of phosphate treatment for the remediation of mine waste soils contaminated with Cd, Cu, Pb, and Zn. Chemosphere **86**(4), 354 (2012)

3. X. Cao, A. Wahbi, L. Ma et al., Immobilization of Zn, Cu, and Pb in contaminated soils using phosphate rock and phosphoric acid. J. Hazard. Mater. **164**(2–3), 555–564 (2009)
4. R.X. Cao, L.Q. Ma, M. Chen et al., Phosphate-induced metal immobilization in a contaminated site. Environ. Pollut. **122**(1) 19–28 (2003)
5. L. Hui, W.U. Xiao-Qin, J.H. Ren et al., Isolation and identification of phosphobacteria in poplar rhizosphere from different regions of China. Pedosphere **21**(1), 90–97 (2011)
6. H.P. Jin, N. Bolan, M. Megharaj et al., Isolation of phosphate solubilizing bacteria and their potential for lead immobilization in soil. J. Hazard. Mater. **185**(2–3), 829–836 (2011)
7. J.H. Park, N. Bolan, M. Megharaj et al., Concomitant rock phosphate dissolution and lead immobilization by phosphate solubilizing bacteria (Enterobacter sp.). J. Environ. Manage. **92**(4), 1115 (2011)

Property and Mechanism of Immobilization of Cd(II) in Fly Ash Based Geopolymers

Yaguang Wang, Fenglan Han, Jingqiu Mu and Shizhen Zhao

Abstract Due to their special three-dimensional structure, geopolymers have a good effect in immobilizing heavy metal ions. At present, there is very little research that heavy metal ion[Cd(II)] are immobilized by fly ash geopolymers. Therefore, in this study, with the addition amounts of Cd(II) 1, 1.5, 2, 3, 4 and 5 wt%, respectively added into fly ash geopolymers, the immobilization effect of Cd(II) was tested and the immobilization mechanism was analyzed. The immobilization results were explained by XRD, SEM-EDS, compressive strength and leaching. It was found that fly ash geopolymers were effective for immobilizing Cd(II). Cd(II) (1 wt%) is beneficial to improve the compressive strength of geopolymers, reached 38.55 MPa at 7d. But the compressive strength of samples after more than 1 wt%[Cd(II)] is reduced. According to results of XRD, SEM-EDS and leaching, Cd(II) is considered to balance the negative charge of tetrahedral[AlO_4] in geopolymer frameworks. The more Cd(II) immobilized in the geopolymers, the more exchangeable ions (Na or Ca) is replaced during this work. The leaching shows that the Cd(II) is highly immobilized, and the immobilize rate of Cd(II) can reach 99%.

Keywords Fly ash · Geopolymers · Immobilization · Cd(II)

Introduction

Environmental problem is one of the important topics for human sustainable development in this century. The contamination by heavy metals is a major environmental problem in urban areas near mines [1]. Heavy-metal pollution in soils is very common at home and abroad. Heavy metals pollution in soil is more hidden, hysteretic, cumulative and irreversible than in the air and water pollution, not easily found directly by senses [2]. Soil contamination by heavy metals, especially by cadmium (Cd), has been one of the worldwide environmental hot issues in recent

Y. Wang · F. Han (✉) · J. Mu · S. Zhao
North Minzu University, Yinchuan 750021, China
e-mail: 625477897@qq.com

Y. Han (ed.), *Advances in Energy and Environmental Materials*,
Springer Proceedings in Energy, https://doi.org/10.1007/978-981-13-0158-2_72

years [3]. There is an increasing threat of heavy metal cadmium pollution for human health. It has complex binding modes, it is not only hard to be decomposed by microorganism, but also easy to chemically generate in organisms and become more toxic compounds, and Cd can cause serious health hazards to animals and humans through the food chain due to easy accumulation toxicity, refractory and other characteristics. Meanwhile, With the continues development of industrial production, increasing coal consumption, a large number of solid waste fly ash has not been timely and efficiently disposed in our country every year, which is great harm to the atmosphere, water, soil and even human life [4]. Recently, annual production of fly ash in the world is about 800 million tons, and dramatically increases due to the large demand of power in China and India since 2004 [5]. Fly ash is rich SiO_2 and Al_2O_3 which is potential to be prepared as geopolymers.

The terms immobilization and stabilization were used interchangeably to refer to a process that involves the mixing of a perilous waste with a binder to reduce the leaching of the contaminant by both physical (encapsulation or adsorption) and chemical (fixation) means [6]. The final aim was to convert this hazardous waste into an environmentally acceptable waste form for land disposal or construction use [7]. Thus, immobilization/stabilization is an excellent method to treat the waste for ultimate disposal [8]. Immobilization/stabilization of heavy metal contaminated soil is an important way to heavy metal pollution control, making use of the methods of extraction of the metals and stabilization/immobilization technique to restore heavy metal contaminated soil was two important aspects in this field [9]. Because of the first was extraction of the metals. This is an energy and time consuming process. The second was abating the mobility of metal ions by ions immobilization technique which was much more cost effective for heavy metal contaminated environment [10].

Traditional cementitious materials were recognized as immobilize materials in the past, but the disadvantage of traditional cementitious materials immobilized bodies are heavy metals leaching concentration, because they are characterized by high permeability and poor durability [11]. J. Davidovits et al. supposed that other traditional inorganic cementitious materials were not appropriate to deal with solid wastes contained heavy metal ions [12]. Geopolymers are new generation of aluminosilicate inorganic cementitious materials. They are generally synthesized by activation of an aluminosilicate source (natural mineral, artificial silicon aluminum compound and solid wastes) with an alkaline hydroxide or silicate solution [13]. Due to the “coop” structure of the geopolymer gel like zeolite, so heavy metals were locked in the structure of the geopolymer gel, and they have great advantages in immobilizing heavy metals. Geopolymerization is recognized as occur through dissolution, migration and polymerization of Al and Si precursor species (from metakaolin or fly ash) as well as surface reaction on surface of undissolved particles [14]. In the geopolymer frameworks, aluminum is four coordinated to oxygen atoms, therefore, a negative charge is created and the presence of cations such as Na, K, Li, Ca, and NH_4 is essential to balance the negative charge of Al [15]. Over the years, immobilization of heavy metals using geopolymers have been investigated [6, 16, 17].

This work is aimed at dealing with the practical problem of fly ash accumulation and heavy metal ion Cd(II) pollution. In order to high efficiently and comprehensively using fly ash from Ningxia province, fly ash geopolymers have been prepared. The study on immobilization of heavy metal ion Cd(II) has been done. The products and microstructures of the geopolymers were analyzed by X-ray diffraction (XRD) and scanning electron microscopy (SEM).

Experiment

Fly ash was obtained from a power plant in Ningxia (China). NaOH (AR) and $Cd(NO_3)_2 \cdot 4H_2O$ (AR) were obtained from Tianjin Kermel Chemical Reagent Co. Ltd. Sodium silicate solution was obtained from Panyu chemical plant (sodium silicate solution with a composition of 8 wt% Na_2O, 25 wt% SiO_2, 67 wt% H_2O).

The fly ash powder was dried in the oven (DHG-9070A) at 105 °C for 2 h, and the oven was closed into the sealed sample mill (HFZY-F4) when the oven was cooled to room temperature. The powder obtained after grinding for 20 min was experimental fly ash samples, and the particle size distribution was measured by laser particle size distribution instrument (Microtrac-X-100). The test results were shown in Fig. 1 and d_{50} was 28.32 μm. X-ray Diffraction (XRD) test were conducted to assess mineralogy of fly ash, as shown in Fig. 2. The XRD patterns of fly ash (Fig. 2) showed broad reflection between 15 and 40 (2θ) which an amorphous structure with a dominant phase of quartz, mullite. Analysis of the main component of fly ash by chemical analysis, the main chemical component shown in Table 1. According to Table 1, the major elements of the fly ash are SiO_2 (52.78%), Al_2O_3 (20.97%) and CaO (7.01%).

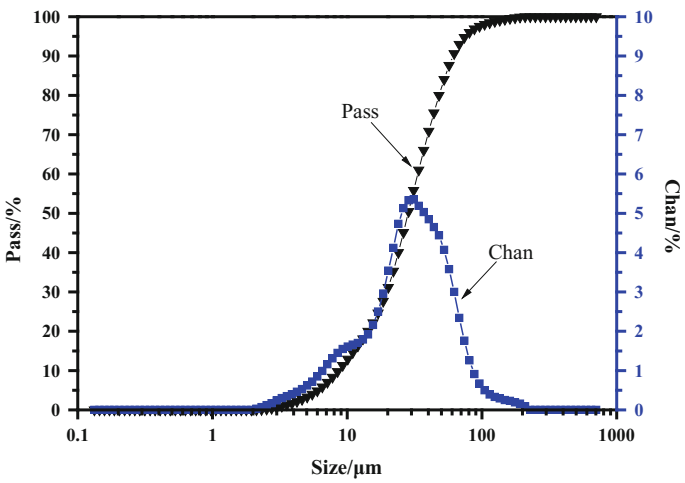

Fig. 1 Particle size distribution of fly ash

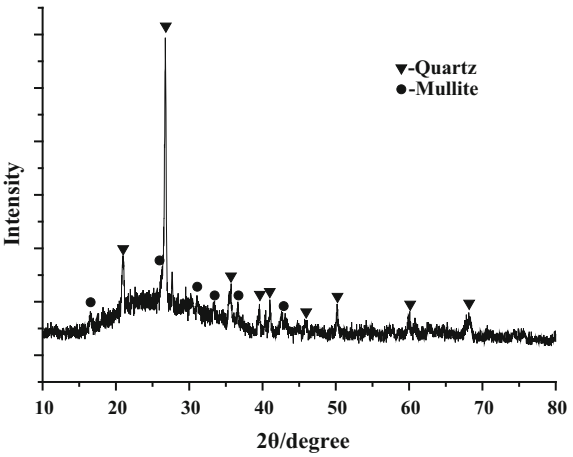

Fig. 2 XRD pattern of fly ash

Table 1 Chemical composition of fly ash

Oxide/wt%	CaO	SiO_2	Al_2O_3	MgO	Fe_2O_3	TiO_2	Other
Fly ash	7.01	52.78	20.97	3.35	8.04	0.93	6.92

Preparation of Geopolymer Samples. Geopolymer batches of different compositions were prepared according to the proportions listed in Table 2. Each geopolymer batch in Table 2 was prepared by first mixing the sodium silicate with sodium hydroxide, then dissolved in the specified amount of water. Then the resultant solution was mixed with solid fly ash and heavy metal salt in mixer (Bomann) for 5 min at 200 rpm. The produced slurry was cast into a steel plate containing 6 molds with cube shape (The size is 40 × 40 × 40 mm). After the vibration was to eliminate the bubble and then wrapped samples in a plastic wrap, and cured at 80 °C for 12 h in an oven (DHG-9070A). The samples were left at room temperature for 7 days after demoulding and subjected to characterization assays. Geopolymer samples prepared in the presence of heavy metal salt were given the code FA-G-Cd-X where X = Cd-1, Cd-1.5, Cd-2, Cd-3, Cd-4 and Cd-5 wt%. On the other hand, reference geopolymer samples prepared in the absence of Cd(II) was given the code FA-G.

Characterization of Synthesized Geopolymer Samples. The X-ray diffractometer (XRD-6000, Shimadzu, Japan) with Cu Kα radiation in a scanning range of 10°–80° was used for phase analysis of samples. The microstructures of Samples were analyzed by scanning electron microscopy (KYKY-2800B). Characterization of the effectiveness of immobilization treatment should be based on determining the environmental impact of the treated waste after it is disposed or reused. One method to succeed this is to estimate the amount of contaminant that might be released to the environment, using tests under specific conditions.

Table 2 Composition of batches used in preparation of geopolymer samples

Sample code	Fly ash/g	NaOH/g	Sodium silicate/g	Water/g	Reagent	Heavy metal ion (wt/%)
FA-G	325	12.05	69.20	34	–	–
FA-G-Cd-1 wt%	325	12.05	69.20	34	$Cd(NO_3)_2{\cdot}4H_2O$	1
FA-G-Cd-1.5 wt%	325	12.05	69.20	34	$Cd(NO_3)_2{\cdot}4H_2O$	1.5
FA-G-Cd-2 wt%	325	12.05	69.20	34	$Cd(NO_3)_2{\cdot}4H_2O$	2
FA-G-Cd-3 wt%	325	12.05	69.20	34	$Cd(NO_3)_2{\cdot}4H_2O$	3
FA-G-Cd-4 wt%	325	12.05	69.20	34	$Cd(NO_3)_2{\cdot}4H_2O$	4
FA-G-Cd-5 wt%	325	12.05	69.20	34	$Cd(NO_3)_2{\cdot}4H_2O$	5

Leaching tests were conducted by using horizontal vibration extraction procedure based on Chinese National Standard (HJ 557-2009). The ground samples, 100 g for each, were placed in 2 L glass bottles with a solid/water mass ratio of 1:10, respectively. After vibrating for 8 h at a frequency of 115 min^{-1} and setting for 16 h, the samples were filtered and stored for Inductively Coupled Plasma-Atomic Emission Spectrometry (ICP-AES) tests.

For the purpose of measuring compressive strength, samples of geopolymer with cubic shapes (40 × 40 × 40 mm) were prepared. Compression strength was performed using controls testing machine (YAW-300C), where the load was applied and increased by displacement rate of 1 mm/min. Each numbered geopolymer were tested for 3–6 samples, and the test data were averaged as final test results.

Results and Discussion

X-Ray Diffraction Analysis. The X-ray diffraction patterns of FA-G, FA-G-Cd-1, FA-G-Cd-2, FA-G-Cd-3, FA-G-Cd-4 and FA-G-Cd-5 wt% samples were given in Fig. 3. Geopolymers were known to be amorphous and the major feature of powder XRD patterns was a hump (broad band) between 20° and 40° (2θ) with a center at 28° [18]. There were unreacted quartz and mullite in all samples. Compared with the FA-G, some new peaks appeared on the XRD patterns of the samples containing Cd (II). At the same time, with the increased of Cd(II), the peaks near 29° were gradually strengthened. This was the result of the Cd(II) effects. In the blank sample, the reaction produced C(N)–A–S–H gel phase. After added to Cd(II). Cd(II) were replaced Na or Ca, which was immobilized in the three-dimensional structure of the geopolymers. This is in agreement with the results of J. Zhang et al. [19].

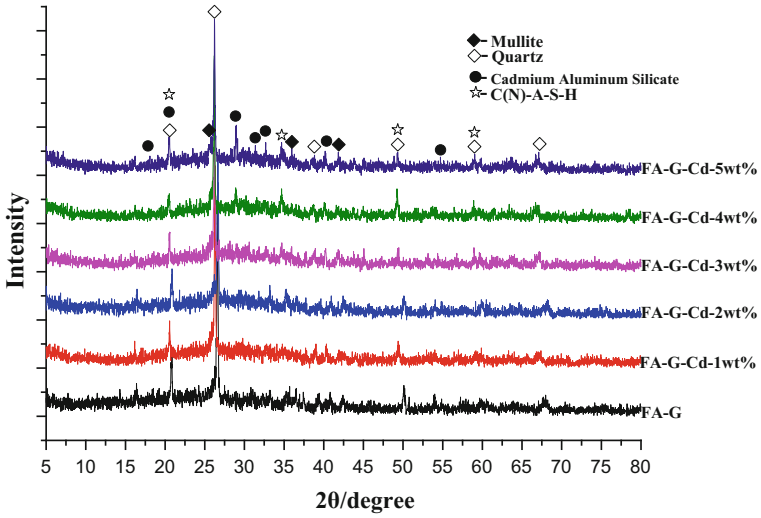

Fig. 3 XRD patterns of geopolymer sample

SEM Analysis. Figure 4 is SEM-EDS figures about immobilized bodies with Cd (II) after leaching. Table 3 is the data of energy spectra of A, B, and C. As can be seen from Fig. 4, FA-G-Cd-1, FA-G-Cd-1.5 wt% is similar in microstructure to FA-G, and the structure was quite dense. Dense structure could prevent external liquid penetration, so the Cd(II) did not leach out to the outside. The A and C phases were mainly composed of Si, Al, Na and Ca, and Si: Al was close to 2: 1, which was similar to the Si–Al network structure of typical PSS (Davidovits described the geopolymer as polysialate, which is divided according to Si/Al. When the Si/Al = 1, the structure name is Polysialate (PS). When the Si/Al = 2, the structure name is Polysialate-siloxo (PSS). When the Si/Al = 3, the structure name is Polysialate-disiloxo (PSDS) [20]). The Si: Al = 1.5: 1 in the B phase, and the monomer structure and the three-dimensional network structure of the geopolymer were between PS (Si: Al = 1: 1) and PSS. From the comparison of Cd(II) content in Table 3, it was found that most of the Cd(II) was immobilized by the special structure of the geopolymer, and we speculated that the Cd(II) participated in the formation of geopolymer structure. Moreover, the zeolite-like structure of reaction products also had a strong adsorption capacity, and Cd(II) could be encapsulated in the polymer structure. However, as the number of Cd(II) increases, the micro-structure of C was not as dense as that of A and B. This is why the compressive strength of the sample decreases with the increase of Cd(II).

Compressive Strength. Table 4 is the compressive strength of the geopolymer immobilized body. Compressive strength was to reduce along with increased of Cd (II). FA-G-Cd-1 wt% had the highest compressive strength. When the amount of

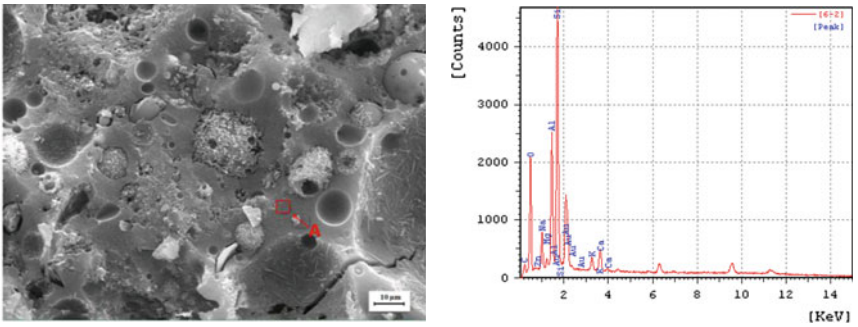

(a) SEM-EDS images of FA-G.

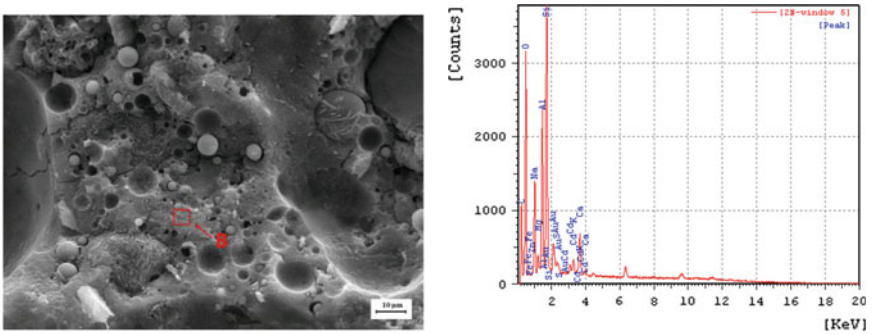

(b) SEM-EDS images of FA-G-Cd-1wt%.

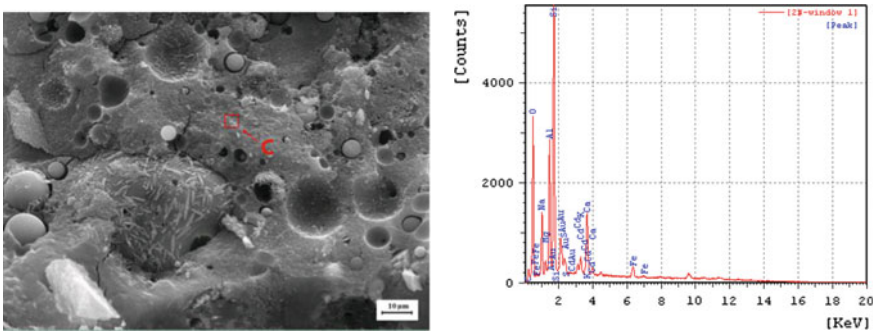

(c) SEM-EDS images of FA-G-Cd-1.5wt%.

Fig. 4 SEM-EDS images of FA-G, FA-G-Cd-1, FA-G-Cd-1.5 wt%

Cd(II) was 1 wt%, the compressive strength of the immobilized body increased slightly, and the addition of Cd(II) was raised, and the strength of the immobilized body decreased rapidly. In the polymerization reaction system, heavy metal ions were reacted with hydroxide ions to form hydroxyl ions, which caused the alkalinity and viscosity to decrease, and stopped Si and Al to dissolve in fly ash. At the same time, heavy metal hydroxyl complex ions could interfere with the

Table 3 Energy spectrum analysis of FA-G(A), FA-G-Cd-1 wt%(B) and FA-G-Cd-1.5 wt%(C) (w/%)

Number	Si	Al	Cd	O	Na	Ca	Others
A	21.817	11.130	–	45.553	3.973	2.478	15.049
B	8.085	5.347	0.960	52.786	5.020	1.689	26.113
C	12.424	6.683	1.453	56.514	4.957	4.198	13.771

Table 4 Compressive strength of the geopolymers

Name	Compressive strength/ MPa	
	3d	7d
FA-G	35.98	37.44
FA-G-Cd-1 wt%	36.69	38.55
FA-G-Cd-1.5 wt%	35.42	36.97
FA-G-Cd-2 wt%	30.43	33.33
FA-G-Cd-3 wt%	24.48	26.47
FA-G-Cd-4 wt%	16.05	17.16
FA-G-Cd-5 wt%	10.46	11.58

condensation reaction of [SiO_4] and [AlO_4] tetrahedrons. Heavy metal hydroxide complex ions also prevented the growth of the network of silicon aluminum skeleton and reduced the system's gel structure. This may be the principal factor leaded to the decrease of compressive strength of samples.

Immobilized Effect of Cd(II). According to GB5085.3-2007 "Identification standards for hazardous wastes-Identification for extraction toxicity" [21], the upper limit of heavy metal element concentration in toxic leaching test Cd(II) is 1.0 mg/L. The immobilize rate was calculated according to the leaching results. The immobilize rate was calculated from the following relationship:

$$\text{immobilize rate} = W_1/W_0 \tag{1}$$

where:

W_1 is the mass fraction of heavy metals in the immobilized body after leaching.
W_0 is the mass fraction of heavy metals in the immobilized body before leaching.

Table 5 is the result of leaching tests of samples. Leaching toxicity of FA-G-Cd-1, FA-G-Cd-1.5, FA-G-Cd-2, FA-G-Cd-3, FA-G-Cd-4 and FA-G-Cd-5 wt% were 0.23, 0.72, 1.28, 2.39, 4.98 and 10.94 mg/L. Their immobilize rate were reached 99%. It indicated that geopolymers have a great advantage in immobilizing Cd(II). The leaching results of 4 wt% Cd(II) were still below the specified value. However, the leaching results of 5 wt% Cd(II) were much higher than the standard. Still and all, the result of this study are worthy of our reference, and the geopolymers show great value in immobilizing Cd(II).

Table 5 Effect of fly ash geopolymer on the immobilization of Cd(II)

Name	Ion species	Leaching value (mg/L)	Immobilize rate (%)
FA-G	Cd(II)	–	–
FA-G-Cd-1 wt%	Cd(II)	0.23	99.9977
FA-G-Cd-1.5 wt%	Cd(II)	0.72	99.9952
FA-G-Cd-2 wt%	Cd(II)	1.28	99.9936
FA-G-Cd-3 wt%	Cd(II)	2.39	99.9921
FA-G-Cd-4 wt%	Cd(II)	4.98	99.9876
FA-G-Cd-5 wt%	Cd(II)	10.94	99.9781

Conclusion

Based on this study, the following conclusions were drawn:

The high addition of Cd(II) can also be successfully immobilized in the fly ash geopolymer matrices. Depending on the XRD, SEM-EDS and leaching studies, Cd(II) is considered to balance the negative charge of tetrahedral[AlO_4] in geopolymer frameworks. The more Cd(II) immobilized in the geopolymers, the more exchangeable ions (Na and Ca) is released during this work. Since compressive strength of geopolymers is affected by incorporation of Cd(II). A small amount of Cd(II) is added to increase the compressive strength of samples, but the compressive strength of samples after more than 1 wt% [Cd(II)] is reduced. Leaching results show that 99% of Cd(II) are immobilized in the fly ash geopolymers. This will provide the valuable reference for the study of Cd(II) environmental pollution.

Acknowledgements Thanks to the support of the National International Science and Technology Cooperation Base (2015D01016) and China EU International Cooperation Project (SQ2013ZOG300003).

References

1. L.I. Xiao-Hu, Z.L. Tang, F.Y. Chu, Chemical speciation and distribution of heavy metals in different environmental mediums around Ni–Cu mine area [J]. J. Jilin Univ. **38**, 847–853 (2008)
2. C. Candeias, R. Melo, P.F. Avila, E.F.D. Silva, A.R. Salgueiro, Heavy metal pollution in mine-soil-plant system in S. Francisco de Assis-Panasqueira mine (Portugal). J. Appl. Geochem. **44**, 12–26 (2014)
3. Z.Q. Zhao, X.I. Mei-Zhu, Advances in research on mechanisms of Cd-induced oxidative stress in plants [J]. J. Agro-Environ. Sci. **26**, 47–51 (2007)
4. Z. Tang, Q. Huang, Y. Yang, PCDD/Fs in fly ash from waste incineration in China: a need for effective risk management. Environ. Sci. Technol. **47**, 5520–5521 (2013)
5. X. Guo, L. Zhang, J. Huang, H. Shi, Detoxification and solidification of heavy metal of chromium using fly ash-based geopolymer with chemical agents. J. Constr. Build. Mater. **151** (1), 394–404 (2017)

6. C. Shi, A. Fernandez-Jimenez, Stabilization/solidification of hazardous and radioactive wastes with alkali-activated cement. J. Hazard. Mater. B **137**, 1656–1663 (2006)
7. B.I. El-Eswed, R.I. Yousef, M. Alshaaer, I. Hamadneh, F. Khalili, Stabilization/solidification of heavy metals in kaolin/zeolite based geopolymers [J]. Int. J. Mineral. Process. **137**, 34–42 (2015)
8. B.I. El-Eswed, Omar M. Aldagag, F.I. Khalili, Efficiency and mechanism of stabilization/solidification of Pb(II), Cd(II), Cu(II), Th(IV) and U(VI) in metakaolin based geopolymers. J. Appl. Clay Sci. **140**, 148–156 (2017)
9. D. Dermatas, X. Meng, Utilization of fly ash for stabilization/solidification of heavy metal contaminated soils. J. Eng. Geol. **70**(3–4), 377–394 (2003)
10. G.M. Gadd, International leader Head deputy research director Professor Fellow president convener. 14. In *Remediation of Metal-Contaminated Soils: An Overview. Biophysico-Chemical Processes of Heavy Metals and Metalloids in Soil Environments* (Wiley, 2007), pp. 565–605
11. J.G. Jiang, X.U. Xin, Y. Zhang, Investigation of leaching characteristics of heavy metals during cement stabilization of fly ash from municipal solid waste incinerator. Environ. Sci. **27** (12), 2564–2569 (2007)
12. J. Davidovits, D.C. Comrie, J.H. Paterson, D.J. Ritcey, Geopolymeric concretes for environmental protection Concr. J. Int. **12**(7), 30–40 (1990)
13. J. Davidovits, Geopolymers and geopolymeric materials. J. Therm. Anal. **35**(2), 429–441 (1989)
14. H. Xu, J.S.J.V. Deventer, Factors Affecting the Geopolymerization of Alkali-Feldspars. J. Miner. Metall. Proc. **19**(4), 209–214 (2002)
15. H. Rahier, J. Wastiels, M. Biesemans, R. Willem, G. Van Assche, B. Van Mele, Reaction mechanism, kinetics and high temperature transformations of geopolymers. J. Mater. Sci. **42**, 2982–2996 (2007)
16. J.G.S. van Jaarsveld, J.S.J. van Deventer, A. Schwartzman, The potential use of geopolymeric materials to immobilize toxic metals: part II. material and leaching characteristics. J. Miner. Eng., 75–91 (1999)
17. J. Sun, X. Chen, C. Lei, Zhou Detoxification and immobilization of chromite ore processing residue with metakaolin-based geopolymer. J. Environ. Chem. Eng. **2**, 304–309 (2014)
18. P.D. Silva, K. Sagoe-Crenstil, The role of Al_2O_3, SiO_2 and Na_2O on the amorphous to crystalline phase transformation in geopolymer systems. J. Aust. Ceram. Soc. **45**, 63–71 (2009)
19. J. Zhang, J.L. Provis, D. Feng, J.S.J. van Deventer, The role of sulfide in the immobilization of Cr(VI) in fly ash geopolymersCem. J. Concr. Res. **38**(5), 681–688 (2008)
20. J. Davidovits. Process for the fabrication of sintered panels and panels resulting from the application of this process. U. S. Patent, 3,950,470. (1976)
21. GB. Identification standards for hazardous wastes-identification for extraction toxicity, S. People's Republic of China (2007)

Influence of Bio-rejuvenator on the Rheological Properties of Aged Asphalt Binder

Yao Zhang, Shaopeng Wu and Gang Liu

Abstract In this paper, the organic compounds with aromatic odor in waste peel were extracted by steam distillation in the laboratory, and then were analyzed by techniques of gas chromatography-mass spectrometry. The waste peel extract with different dosages were added to the aged asphalt to produce the recycled asphalt binders. The rheological properties of base asphalt, aged asphalt and recycled asphalt were tested. The results showed that the main chemical compositions of the waste peel extract are light oil which similar to the aromatic component of asphalt. Penetration, softening point, viscosity, complex modulus, phase angle and low temperature stiffness of recycled asphalt can be fully restored to the level of base asphalt with the addition of the waste peel extract. The research of this paper provides a new idea for the treatment of waste peel, and the waste peel extract can be used as a kind of bio-rejuvenator for the recycling of asphalt pavement.

Keywords Bio-rejuvenator · Aged asphalt binder · Rejuvenation Rheological properties

Y. Zhang · G. Liu (✉)
School of Materials Science and Engineering, Wuhan University of Technology, Wuhan 430070, China
e-mail: liug@whut.edu.cn

Y. Zhang
e-mail: zy2016@whut.edu.cn

S. Wu
State Key Laboratory of Silicate Materials for Architectures, Wuhan University of Technology, Wuhan 430070, China
e-mail: wusp@whut.edu.cn

Y. Han (ed.), *Advances in Energy and Environmental Materials*,
Springer Proceedings in Energy, https://doi.org/10.1007/978-981-13-0158-2_73

Introduction

The physical and chemical characteristics of asphalt binders get worse when suffer from the aging process during storage, mixing, transportation and in-service life [1, 2]. Aged asphalt binders is more brittle and stiffer than fresh asphalt and noticeable changes in its composition which is mainly caused by the decrease of aromatic oil and increase of asphaltene [3]. The existence of aged asphalt can result in serious properties deterioration of pavement [4, 5]. Therefore, rejuvenators are widely used to restore the properties of aged asphalt and have been achieved excellent effect [6, 7].

There are more and more reports about the influence of asphalt rejuvenator on the properties of aged asphalt with the development of asphalt recycling technology, and various types of asphalt rejuvenators are emerging. With the addition of the rejuvenators, the stiffness of aged asphalt can be lower and the cracking resistance be improved [8–10]. Therefore, the rheological properties of aged asphalt binder are effectively improved [11, 12]. However, most of asphalt rejuvenators are kinds of mixtures of resin compounds and synthetic oils in petroleum industry, which are non-renewable, harmful to human body and restricted by petroleum energy. It is necessary to explore a non-petroleum base substitute as asphalt rejuvenator, which is environmental, renewable, and harmless to the human body. Citrus peel is rich in pigment, aromatic oil, pectin, bioflavonoid, etc. These organic compounds can be extracted and are similar to asphalt rejuvenator.

This study investigated using the waste peel extract to recycle the aged asphalt binder. The extraction process was carried out by steam distillation in laboratory, and the constituents of waste peel extract were analyzed by techniques of gas chromatography-mass spectrometry (GC-MS). Penetration, softening point, viscosity of cone/plate rheometer method, dynamic shear rheometer method and bending beam rheometer method was test to examine the rejuvenation effect of waste peel extract.

Experimental

Raw Materials.

Laboratory Aged Asphalt Binders. Virgin asphalts binders, base70$^{\#}$ and base90$^{\#}$, from Ezhou City, Hubei Province, China, was treated by thin film oven test (TFOT) to imitate the short-term aged process, then was aged by pressure aging vessel test (PAV) to imitate the long-term aged process.

The TFOT test and PAV test were performed in accordance with the standards ASTM D1754 and ASTM D6521. The 70$^{\#}$ short-term aging asphalt and 90$^{\#}$ short-term aging asphalt was marked as T_1 and T_2; the 70$^{\#}$ long-term aging asphalt and 90$^{\#}$ long-term aging asphalt was marked as P_1 and P_2; the virgin asphalt binders, base70$^{\#}$ and base90$^{\#}$ was marked as V_1 and V_2.

Waste Peel Extract. The waste peel, come from fresh citrus produced in Yi Chang City, Hubei province, China, was cut into pieces and mashed into the distillation flask, with the addition of appropriate amount of NH_4Cl and was then subjected to steam distillation. The organic compounds with aromatic odor in waste peel was extracted and prepared for the following recycling process.

Recycled Binders. Four realistic ratios, 1, 3, 5 and 7% by mass of waste peel extract were chosen to recycle the 70# long-term aging asphalt binder and 90# long-term aging asphalt binder by using laboratory shear mixer.

In total, 2 virgin binders, 4 aged binders and 8 recycled binders were prepared and their codes are given in Table 1.

Methods. GC-MS, which is an analytical method that combines the features of Gas Chromatography and Mass Spectrometer to carried out a qualitative and quantitative analysis of the components in mixture, was conducted in this research to analysis the components of waste peel extract.

Empirical rheological properties (Pen. And S.P.) were measured according to ASTM D5 and ASTM D26.

The viscosity was determined at three temperature 60, 100, and 150 °C. A cone/plate rheometer, with a cone angle of 1° and plate diameter of 25 mm, was used to characterize the viscosity of virgin, short-time aged, and long-term aging asphalt binders, at a shear rate of 0.05 s^{-1} under 60 °C and at a shear rate of 500 s^{-1} under both 100 and 150 °C.

The dynamic shear rheometer tests were used according to AASHTO T315. The parameters of the dynamic shear rheometer test are given in Table 2.

Low temperature creep response properties of base, aged and recycled asphalt were measured by bending beam rheometer following ASTM D6648. This test was performed at –12 °C and at a constant bending load of 978 mN.

Table 1 Codes of different types of asphalt binders

Codes	Label	Codes	Label
Virgin70#	V_1	Virgin90#	V_2
TFOT70#	T_1	TFOT90#	T_2
PAV70#	P_1	PAV90#	P_2
1% essential oil + PAV70#	A_1	1% essential oil + PAV90#	A_2
3% essential oil + PAV70#	B_1	3% essential oil + PAV90#	B_2
5% essential oil + PAV70#	C_1	5% essential oil + PAV90#	C_2
7% essential oil + PAV70#	D_1	7% essential oil + PAV90#	D_2

Table 2 Parameters of dynamic shear rheometer test

Device	Diameter, R	Temperature	Gap	Angular frequency
	[mm]	[°C]	[mm]	[rad/s]
DSR	25	30,40,50,60	1	0.1–400

Results and Discussion

Chemical Analysis of Waste Peel Extract. The total ion chromatogram of GC-MS is shown in Fig. 1. The corresponding organic compounds were retrieved according to NIST 05 standard spectrogram and shown in Table 3. A total of 21 main organic compounds were detected from the waste peel extract, and the relative content could be represented by the ratio of peak area of each component to the total peak area.

The major components of waste peel extract are monocyclic monoterpenes, the others are aromatic hydrocarbons containing benzene ring. Monoterpene is a kind of the terpenoids, which polymerized by isoprene, and their oxygenated derivatives and unsaturated derivatives. Monocyclic monoterpenes are obtained by chain monoterpenes cyclization, and are the main sources of aromatic odor in the waste peel. The aromatic hydrocarbons measured in this paper are mainly m-xylene and m-cymene, polycyclic aromatic hydrocarbons were not detected. The chromatogram peaks of aromatic hydrocarbons have a smaller abundance and fewer species compared with monoterpenes. And the chemical structure of m-xylene and m-cymene are more similar to the aromatic component of asphalt compared with monoterpenes. The chemical construction of the components of waste peel extract are similar to the light oil, which consist of saturates and aromatics and lost during the asphalt aging process.

Empirical Rheological Properties. The penetration and softening points of 70# and 90# base, aged and recycled asphalt binders are shown in Tables 4 and 5. As we can seen from Table 4, the penetration decreased from 60.1 to 39.4 (dmm), softening point increased from 47.8 to 53.1°C after a short-term aging process. Then after a long-term aging, the penetration reduced to 24.2 (dmm), softening point increased to 60.8 °C. This is because the light oil lost and the colloidal structure changed during the aging process, and resulted in hardened asphalt, reduced penetration and increased softening point. After adding the waste peel extract to the

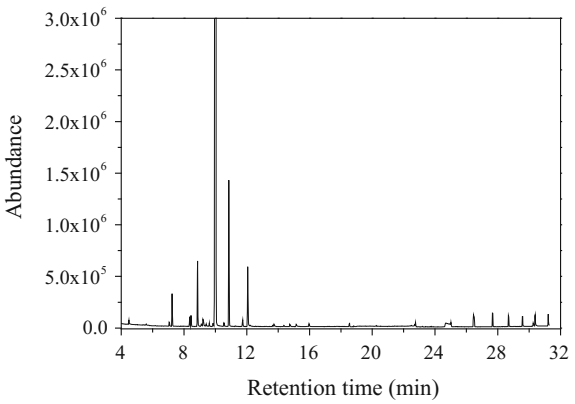

Fig. 1 Total ion chromatogram of GC-MS

Table 3 The main chemical component of waste peel extract

Number	Name	Content (%)
1	m-Xylene	15.11
3	Thujene	0.12
4	alpha-Pinene	0.80
5	2-p-menthadiene	0.25
6	(1_S)-(1)-beta-Pinene	0.30
7	Myrcene	2.07
9	Octanal	0.35
10	3-carene	0.10
11	Terpilene	0.11
12	M-cymene	0.12
13	D-Limonene	69.25
14	Ocimene	5.14
15	g-Terpinene	3.96
16	Terpinolene	0.22
17	Linalool	1.75
19	Alpha-Terpineol	0.12
20	Decanal	0.12
21	2-methoxy-4-methyl-1-(1-methylethyl)-Benzene	0.11

long-term aging asphalt, the penetration increased in a certain degree and the softening point decreased. When 5% of waste peel extract was added, the penetration and softening points can be fully restored to the level of base asphalt, which indicated that the waste peel extract can significantly improve the empirical rheological properties. As can be seen from Table 5, the change rule of empirical rheological properties of $90^{\#}$ asphalt are similar to those of $70^{\#}$ asphalt, which shows that the waste peel extract has similar effect on different types of asphalt. The waste peel extract can increase the penetration and reduce the soft point of aged asphalt. This is because that the chemical components of the waste peel extract are similar to saturates and aromatics, which can improve the aged asphalt from gel colloidal structure to sol colloidal structure.

Table 4 Empirical rheological properties of $70^{\#}$ base, aged and recycled binders

Binders	Penetration [dmm]	Softening point [°C]
V_1	64.1	47.8
T_1	39.4	53.1
P_1	24.2	60.8
A_1	25.7	52.7
B_1	46.5	50.2
C_1	73.7	48.0
D_1	82.7	40.5

Table 5 Empirical rheological properties of 90# base, aged and recycled binders

Binders	Penetration [dmm]	Softening point [°C]
V_2	90.9	40.5
T_2	57.6	44.7
P_2	34.6	50.7
A_2	44.2	46.8
B_2	79.7	42.7
C_2	95.7	39.7
D_2	107.6	32.2

Viscosities. The viscosity can reflect an ability of binders to resist shear deformation, and is one of the most relevant properties with mechanical behavior of asphalt pavement. The viscosity of 70# and 90# base, aged and recycled asphalt at 60, 100 and 150 °C was measured by a cone/plate rheometer and shown in Tables 6 and 7. Due to aging process, the viscosity significantly increased at each temperature. The viscosity of aged binder decreases with the addition of waste peel extract. After adding 7% of the waste peel extract, the value was fully restored to the level of base asphalt. We can found that there was a similar change rule in viscosity when using the 90# asphalt as the base asphalt. The viscosity of asphalt binders has a great influence on workability and compaction of asphalt mixture during mixing and paving. Aged asphalt can't satisfy the performance requirements of binders because a very high viscosity caused by long-term ageing process, and the engineering

Table 6 Viscosities of 70# base, aged and recycled binders at three temperatures

Binders	Viscosity [Pa s]		
	[60 °C]	[100 °C]	[150 °C]
V_1	360.4	5.35	0.314
T_1	618.4	7.36	0.430
P_1	1708.0	13.93	0.518
A_1	1491.0	11.58	0.494
B_1	857.2	8.27	0.442
C_1	609.5	7.28	0.405
D_1	318.7	4.45	0.306

Table 7 Viscosities of 90# base, aged and recycled binders at three temperatures

Binders	Viscosity [Pa s]		
	[60 °C]	[100 °C]	[150 °C]
V_2	165.0	2.66	0.226
T_2	286.4	4.16	0.325
P_2	959.9	6.94	0.412
A_2	451.1	5.42	0.296
B_2	362.6	4.56	0.272
C_2	303.0	3.96	0.258
D_2	237.0	2.97	0.236

application of asphalt mixture can be significantly affected. Therefore, it is necessary to use the rejuvenator to decrease the viscosity. The waste peel extract can restore the viscosity of aged binder, and the recycled asphalt binders can satisfy the requirement of viscosity of binders during the asphalt mixture mixing and paving process.

Master Curves. Asphalt is a kind of typical viscoelastic material. It produces both elastic deformation and viscous flow deformation under the state of force. The complex shear modulus of asphalt are used to reflect the ability to resist the shear deformation. It consists of two parts, an elastic recoverable part and a viscous unrecoverable part. Phase angle is the relative index of recoverable and unrecoverable deformation.

The master curves of 70# and 90# base, aged and recycled asphalts were shown in Figs. 2 and 3. The long-term aging asphalt has the highest complex modulus than others. The complex modulus of recycled asphalt decreased after adding 1% of the waste peel extract, but is still bigger than that of the short-term ageing asphalt. The value of recycled asphalt with 3% of the waste peel extract is similar to short-term ageing asphalt. When the content of waste peel extract reached 5%, the value almost restored to the level of base asphalt, and the value is far smaller than that of base asphalt with the content of 7%. The phase angle shows completely different rule. The long-term aging asphalt has the smallest phase angle and the value of recycled asphalt with 1, 3 and 5% of the waste peel extract have a litter enhancement. The recycled asphalt with the addition of 7% of the waste peel extract has a smaller phase angle than base asphalt. The results shows that the complex modulus of aged asphalt can be reduced with adding the waste peel extract. The recycled asphalt has a smaller phase angle when has the same complex modulus with base asphalt. This indicates that the recycled asphalt have the more obvious elastic properties than base asphalt, and is easier to recover the deformation after the load is removed. This will be beneficial for the ability to resist permanent deformation, and makes the asphalt binder have a excellent high temperature stability.

Low Temperature Cracking Resistance. The low temperature stiffness modulus S and creep rate m-value represent the ability of asphalt to resist the low temperature cracking. Bending beam rheometer can accurately evaluate the creep stiffness modulus S and creep rate m-value of asphalt at low temperature. The measured stiffness modulus and creep rate m-value at –12 °C are shown in Tables 8 and 9. Due to the aging of asphalt, the stiffness modulus increased significantly, the rate m-value decreased. The more serious aging happened, the more seriously the stiffness modulus S increased and the rate m-value decreased. After adding the waste peel extract to aged asphalt, the stiffness modulus decreased and the rate m-value increased gradually with the increase of the amount of the waste peel extract. When 5% of waste peel extract was added, the stiffness modulus S and creep rate m-value of the recycled asphalt were restored to the level of the base asphalt. Table 9 shows that there is a same change rule of low temperature properties between the 70# asphalt binder and the 90# asphalt binder when added with the waste peel extract. And the change rule of low temperature properties is similar

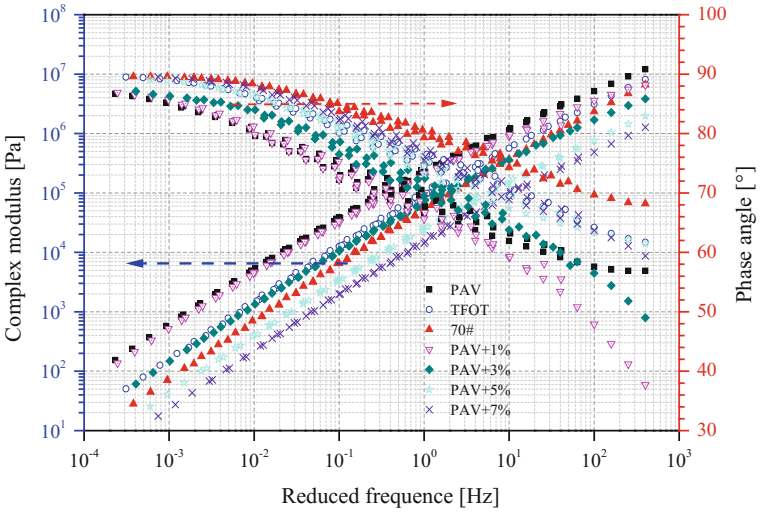

Fig. 2 Master curves of 70# base, aged and recycled binders

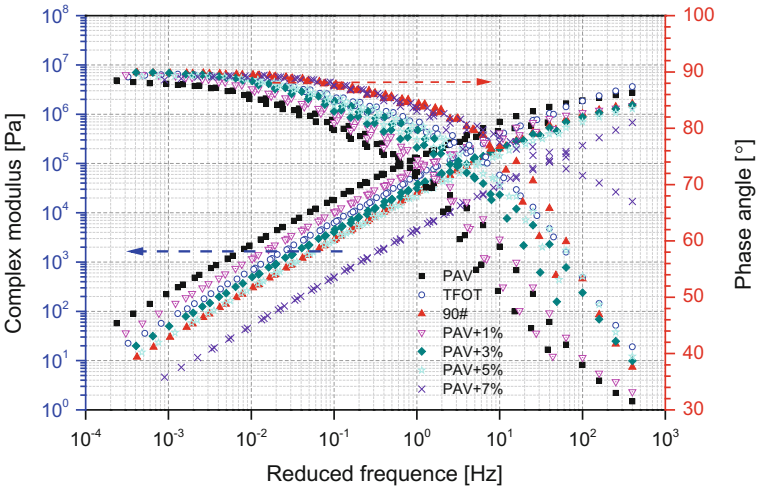

Fig. 3 Master curves of 90# base, aged and recycled binders

to that of regular rheological properties, complex modulus and phase angle. This indicated that there is a good correlation between each rheological property indexes.

At low temperature, a very high creep stiffness modulus S caused by ageing process can lead to asphalt brittleness, which makes the pavement easy to crack, thus the service life of asphalt pavement reduce. A bigger m-value means a better low temperature performance of the asphalt. This is because the response of asphalt

Table 8 Stiffness and m-value of 70# base, aged and recycled binders

Binders	Stiffness [MPa]	m-value
V_1	97	0.474
T_1	115	0.435
P_1	156	0.374
A_1	116	0.429
B_1	113	0.406
C_1	91	0.477
D_1	83	0.493

Table 9 Stiffness and m-value of 90# base, aged and recycled binders

Binders	Stiffness [MPa]	m-value
V_2	73	0.614
T_2	97	0.482
P_2	117	0.468
A_2	93	0.454
B_2	83	0.523
C_2	71	0.579
D_2	64	0.663

binders will be similar to that of the material with lower stiffness when the temperature drops and pavement contraction. Consequently, the tensile stress in the asphalt mixture decreases, thus the possibility of cracking at low temperature of asphalt pavement decreases. Otherwise, the asphalt pavement is more easily to crack with a smaller m-value. The temperature cracking of asphalt pavement is usually caused by constantly increases of stiffness modulus S and decreases of m-value during asphalt aging process. Tables 8 and 9 shows that the waste peel extract can obviously improve the ability of asphalt to resist the crack at low temperature, and thus improve the service life of asphalt pavement.

Conclusions

In this study, the organic compound in waste peel was extracted and analyzed in laboratory. Recycled asphalt binder was prepared by using the waste peel extract as the bio-rejuvenator, and the rheological properties of base, aged and recycled asphalt were investigated. Three main results are found:

1. The main chemical compositions of the waste peel extract are light oil that similar to the aromatic component of asphalt.

2. After adding the waste peel extract to long-term aging asphalt, penetration, softening point, viscosity, complex modulus, phase angle, low temperature stiffness modulus and m-value, can be effectively improved.
3. The rheological properties of recycled asphalt can be fully restored to the level of base asphalt with adding the waste peel extract as bio-rejuvenator.

Acknowledgements This work was supported by National Natural Science Fund for Young Scholars of China (grant numbers. 51608411) and the Fundamental Research Funds for the Central Universities of China (WUT: 173101004 and 173201002).

References

1. F.P. Xiao, S. Amirkhanian, Laboratory investigation of utilizing high percentage of RAP in rubberized asphalt mixture. Mater Struct. **43**, 223–333 (2010)
2. F.P. Xiao et al., Model developments of long-term aging asphalt binders. Constr. Build. Mater. **37**, 248–256 (2012)
3. H. Asli, E. Ahmadinia, M. Zargar, M.R. Karim, Investigation on physical properties of waste cooking oil—rejuvenated bitumen binder, Constr. Build. Mater **37**, 398–405 (2012)
4. F.P. Xiao, S.N. Amirkhanian, C.H. Juang, S.W. Hu, J.N. Shen, Model developments of long-term aging asphalt binders. Constr. Build. Mater. **37**, 248–256 (2012)
5. J. Wang, L. Pang, S.P. Wu, Q.T. Liu, Z. Chen, Effect of ageing on fatigue properties of asphalt. J. Cent. South Univ. Technol. **15**, 111–114 (2008)
6. T. Ma, B.U. Hussain, M. Enad, E.Y. Hajj, Estimating allowable RAP in asphalt mixes to meet target low temperature PG requirements. J. Assoc. Asphalt Paving Technol. **79**, 473–495 (2010)
7. Z. Luo, F.P. Xiao, S.W. Hu, Y.S. Yang, Probabilistic analysis on fatigue life of rubberized asphalt concrete mixtures containing reclaimed asphalt pavement. Constr. Build. Mater. **41**, 401–410 (2013)
8. H.M.R.D. Silva, J.R.M. Oliveira, C.M.G. Jesus, Are totally recycled hot mix asphalts a sustainable alternative for road paving? Resour. Conserv. Recycl. **60**, 38–48 (2012)
9. J.J. Shen, S. Amirkhanian, J.A. Miller, Effects of rejuvenating agents on superpave mixtures containing reclaimed asphalt pavement. J. Mater. Civ. Eng. **19**, 376–384 (2007)
10. A. Dony, J. Colin, D. Bruneau, I. Drouadaine, J. Navaro, Reclaimed asphalt concretes with high recycling rates: changes in reclaimed binder properties according to rejuvenating agent. J. Constr. Build. Mater. **41**, 175–181 (2013)
11. H. Asli, E. Ahmadinia, M. Zargar, M.R. Karim, Investigation on physical properties of waste cooking oil—rejuvenated bitumen binder. J. Constr. Build. Mater. **37**, 398–405 (2012)
12. J.J. Shen, S. Amirkhanian, B. Tang, Effects of rejuvenator on performance-based properties of rejuvenated asphalt binder and mixtures. J. Constr. Build. Mater. **21**, 958–964 (2007)

Evolution of the Chemical Valence on the Surface of the Cerium—Tungsten Electrode

Peng Wang, Jiancan Yang, Tu Zhang and Zhikun Gao

Abstract Cerium tungsten electrode was heated in the analysis chamber of X-ray photoelectron spectroscopy (XPS) system at different temperatures. The evolution of the valence state of the main elements on the surface of the cerium tungsten electrode material was monitored by in suit XPS. It was found that the cerium on the surface of the sample in the initial state was mainly in the form of Ce^{4+} and Ce^{3+}. During the heating process, Ce 3d core energy level spectrum changed. With the temperature rised, the content of Ce^{4+} in the samples decreased gradually. It can be seen that a part of Ce^{4+} is converted to Ce^{3+} during the heating process of the cerium tungsten electrode material. That means cerium in the cerium tungsten electrode material has a tendency to be restored, this will promote the electron emission and enhance the performance of the electrode material.

Keywords Tungsten cathode · X-ray photoelectron spectroscopy (XPS) Cerium · Reduction

Introduction

Pulsed xenon lamp can achieve periodic instantaneous luminescence. It has the characteristics of strong load capacity, high pump efficiency, good laser beam quality and long service life. Hot cathode is regarded as the core component in this kind of electronic devices, whose performance directly determines the working characteristics of electronic components and service life. The development of hot

P. Wang · J. Yang (✉) · T. Zhang · Z. Gao
College of Material Science and Engineering, Beijing University of Technology, Beijing, China
e-mail: yjcan@bjut.edu.cn

P. Wang
e-mail: michael_jz@emails.bjut.edu.cn

T. Zhang
e-mail: zhangtu@emails.bjut.edu.cn

Y. Han (ed.), *Advances in Energy and Environmental Materials*,
Springer Proceedings in Energy, https://doi.org/10.1007/978-981-13-0158-2_74

cathode can be divided into three stages: Pure metal cathode, Oxide cathode and Diffusion cathode [1]. The W-Ce electrode studied in this paper belongs to the oxide cathode, which formed by adding rare earth oxide cerium in the tungsten matrix. Such cathode will be accompanied by elemental valence and content changes in use, this has always been a concern for the experts of the cathode [2]. Cerium is a variable rare earth element, its valence state usually presents both +3 and +4 [3]. The change of valence state of rare earth cerium ion in electrode can affect the physical and chemical properties of the material. Therefore, it has a guiding significance for performance improvement to carry out the judgment and analysis of the valence state of the cerium tungsten electrode material.

For this kind of electron emission materials, the surface-active component has strong influence on the emission property of the hot cathode. Cathode materials interact with their surroundings through their surfaces. The change of physical and chemical composition of these surfaces determines the nature of the interactions. XPS is a kind of surface sensitive analysis techniques, so we applied XPS techniques in this study. It would be a useful analysis of the changes of valence state of the cerium tungsten electrode surface.

Experiment and Methodology

Sample Preparation. An electrode used in xenon lamp with a diameter of 6 mm was selected for the experiment, in which the content of ceria is 2.2 wt%. A sample with a thickness of 1 mm was fabricated using a wire cutting process, then we use different types of sandpaper to polish the surface smooth. Fill the sample with an organic solvent and clean the sample using an ultrasonic cleaner. The order of addition of organic solvents is ethanol, acetone, ethanol. Dried the sample after cleaning in Vacuum oven, then loaded the sample into the sample stage. By means of sample transfer system, transfer the sample from fast entered lock chamber into the main analysis chamber of XPS device.

X-ray Photoelectron Spectroscopy. In XPS we are concerned with a special form of photoemission, i.e., the ejection of an electron from a core level by an X-ray photon of energy hυ. The energy of the emitted photoelectrons is then analyzed by the electron spectrometer and the data presented as a graph of intensity (usually expressed as counts or counts/s) versus electron energy—the X-ray induced photoelectron spectrum [4]. The kinetic energy (E_k) of the electron is the experimental quantity measured by the spectrometer, but this is dependent on the photon energy of the X-rays employed and is therefore not an intrinsic material property. The binding energy of the electron (E_b) is the parameter which identifies the electron specifically, both in terms of its parent element and atomic energy level. The relationship between the parameters involved in the XPS experiment is:

$$Eb = h\upsilon - E_k - W. \quad (1)$$

where hυ is the photon energy, E_k is the kinetic energy of the electron, and W is the spectrometer work function. As all three quantities on the right-hand side of the equation are known or measurable, it is a simple matter to calculate the binding energy of the electron. In practice, this task will be performed by the control electronics or data system associated with the spectrometer and the operator merely selects a binding or kinetic energy scale whichever is considered the more appropriate.

The XPS spectra in this study were obtained with a modified Omicron photoelectron spectrometer equipped with both A1 and Mg anodes at a power of 280 W (14 kV, 20 mA). The angle between the X-ray direction and the emitted electron direction was 60°. The analyzed area was about 16 mm^2. Kinetic energies of photoelectrons were measured using a hemispherical electrostatic analyzer working in the constant pass energy mode, and the analysis pressure was better than 1e-8 mbar. The instrument was interfaced to an PC compatible for data collection and subsequent data analysis. The binding energy scale was established by referencing the C 1 s value of adventitious carbon (284.8 eV). For calefaction experiments, there is a specialized high temperature heater stage in this XPS system, using the resistance wire to heat the sample, which can achieve up to 800 °C at the sample.

Deconvolution. Deconvolution is the removal of broadening effects from a spectrum. An XPS spectrum is broadened by convolution of the intrinsic signal with several broadening functions that are either Gaussian or Lorentzian in nature. Examples of these broadening functions include the natural linewidth, the exciting x-ray line shape, the detection system and any broadening due to charging. In order to achieve a successful deconvolution, each spectrum must be pretreated. Pretreatment includes background removal and spectral smoothing. The backgrounds were removed using a Shirley-type integral and spectral smoothing was carried out using a cubic spline [5]. All the data were processed using the software package CasaXPS (computer aided surface analysis for X-ray photoelectron spectroscopy; Casa Software Ltd., UK).

Calefaction Experiments. In order to simulate the high temperature environment of the W-Ce electrode during operation, the sample will be heated in this experiment. By means of the device's high-temperature heating stage in ultra-high vacuum chamber, the sample will be heated to the following temperature: 100, 200, 300, 600, 700, 800 °C. After reaching the preset temperature, keep the temperature on sample for 30 min and then stop heating. Then the sample was allowed to cool naturally to room temperature, gathered the survey spectra of the surface and narrow scan spectra of W 4f, Ce 3d, O 1 and C 1 s.

Results and Discussion

Quantitative Analysis. XPS technology can effectively collect the element chemical state information on sample surface, and make a quantitative analysis of the content of each element [6]. Figure 1 shows the survey spectra of the sample surface before the sample experience the heat treatment. The main constituent elements are W, Ce, O, C. Due to the residual solvent and the reasons for the adsorption of some gases when the sample is treated, the C 1 s peak and O 1 s peak had a higher intensity.

When the sample is heated to the preset temperature, in order to stabilize the surface composition of the sample, the heating device parameters will be maintaining for 30 min to keep the preset temperature. After this process is over, collect the relevant energy spectrum data when the sample is cooled to room temperature. By collecting the energy spectrum data of each heating temperature, the content of each element varies with temperature can be obtained. Table 1 summarizes the changes in the elements of the sample surface, which experienced a serious of heating process.

We found that the content of the W on surface changed from 29.52 to 51.05 at. %, at the same time, the cerium content changes from 2.62 to 6.68 at. %. The content of these two elements shows a rising trend. The content of the O changed from 38.17 to 22.9 at. %, the content of the C changed from 29.69 to 19.37 at. %. Compared to W and Ce, the contents of these two components have different degrees of reduction.

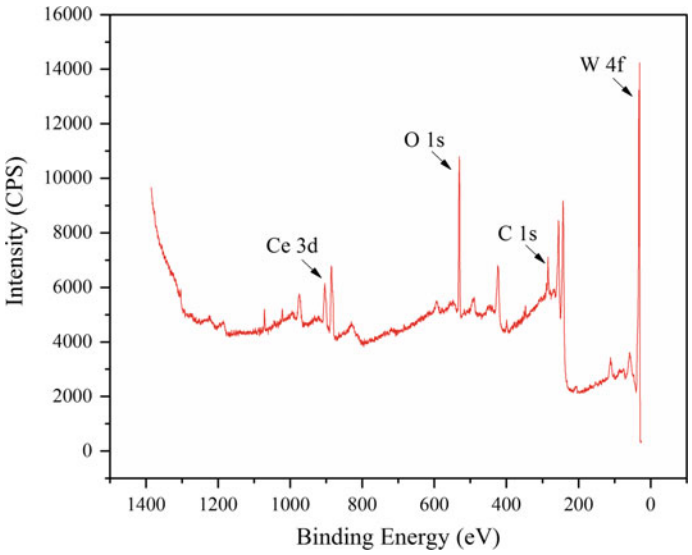

Fig. 1 Survey spectra of the sample surface

Table 1 Atomic compositions (at. %) change of main element

Element	Temperature						
	28 °C	100 °C	200 °C	300 °C	600 °C	700 °C	800 °C
W	29.52	33.83	34.72	35.35	40.41	46.16	51.05
Ce	2.62	3.25	3.22	3.35	3.72	4.62	6.68
O	38.17	39.62	38.19	36.58	27.59	21.66	22.9
C	29.69	23.3	23.88	24.72	28.28	27.56	19.37

This is due to the fact that Some organic solvents will remain on the sample surface when the sample is processed early before enters the vacuum chamber, in addition, some gases will also remain on the surface of the sample due to physical adsorption. In the process of heating the sample in ultra-high vacuum environment, these surface contaminants and adsorbed gases leave from the sample surface Constantly. In addition, part of the adsorbed oxygen in the rare earth oxide also disengaged the sample surface at high temperatures. As a result of the combined effect of these two reasons, the relative contents of the four elements show different trends.

By further analyzing the full spectrum data at each temperature, we obtained the change in the value of Ce/W at each temperature. This will further reveal the change in the relative content of W and Ce during the heating process. As can be seen from Fig. 2, the Ce/ W ratio on the surface shows a rising trend during heating process. Especially after 600 °C, this change is more obvious. For W-Ce electrodes, the W element as a matrix, its content can be assumed to be constant. The rise in Ce/ W value illustrates that the content of rare earth oxides on the surface of the material increases. This indicates that rare earth cerium oxide migrate from the inside to the surface of the material during the heating process.

Interpretation of W 4f. As shown in Fig. 3, the positions of the four peaks appearing in the initial spectrum are 37.3, 35.2, 32.9, 30.8 eV, respectively. The peaks at 35.2 and 30.8 eV belong to W 4f5/2 of W6+ and W^0 [7]. While the peak at 37 eV belongs to W 5p3/2 [8].

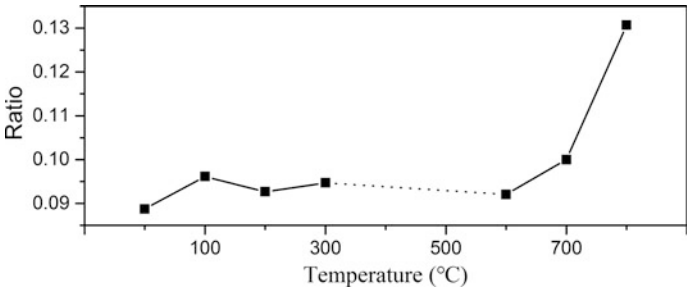

Fig. 2 Ce/W ratio on the surface

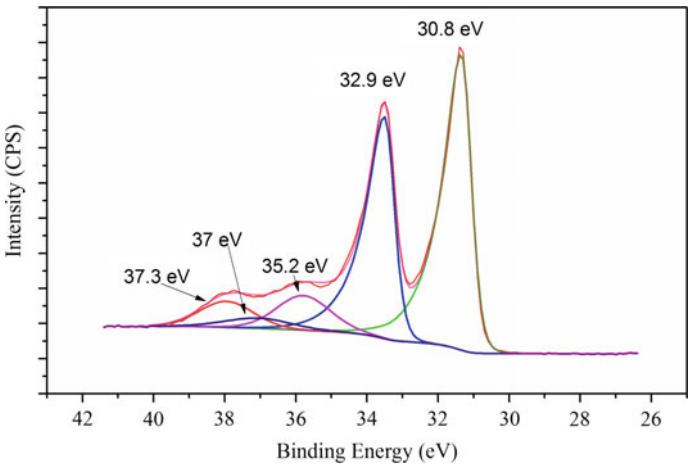

Fig. 3 Narrow scan spectra of W 4f

W^{6+} comes from compound WO_3, which accounted for 16.30 at. % of the total content of tungsten elements at room temperature. WO_3 is one of the intermediates in the electrode preparation process. So the presence of a small amount of WO_3 is due to imperfect manufacturing process of tungsten electrode, in which the intermediate product was not completely restored.

Figure 4 shows a series of W 4f narrow scan spectra at different temperatures. It is obvious that one of the composition decreases or even disappears when the heating temperature changes from 600 to 700 °C. Compared the narrow scan spectra of W4f at 600 and 700 °C, we found that the reduced components have the peak positions of 37.3 and 35.2 eV. This should be W6+, corresponding to a small amount of WO_3 in the matrix material. Figure 5 shows that only W^0 peaks are present in the w4f spectrum after the heating temperature reaches 700 °C. It can be seen that the valence composition of the W element changes when the sample heating temperature rises above 600 °C. The content of W^{6+} decreases until it completely disappears. All the WO_3 leave the sample surface by the sublimation under the effect of heating in the vacuum chamber between 600 to 700 °C. For W elements, only the metal W is present in the subsequent heating process.

Interpretation of O 1 s. By the process of peak fitting of the O 1 s peak at room temperature, we found two main types of oxygen on the surface of the sample. As shown in Fig. 6, there are two kinds of oxygen species on W-Ce cathode at room temperature, e. g, the lattice oxygen species with lower binding energy (Eb = 530.80 eV) and the adsorbed (chemisorbed) oxygen species with higher binding energy (Eb = 532.5 eV) [2].

The O 1 s peak for each heating stage is plotted in Fig. 7, it can be seen that the intensity of the adsorbed oxygen is gradually reduced during the subsequent heating process. The proportion of adsorbed oxygen in the O1 s peak decreased gradually,

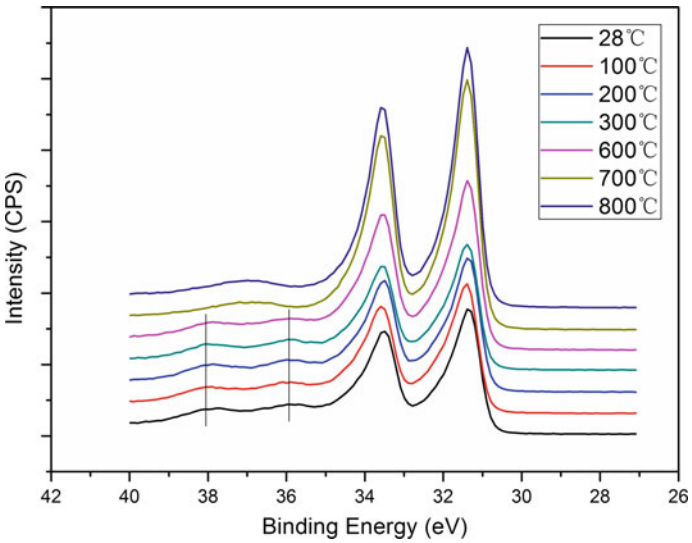

Fig. 4 W 4f spectra at different temperature

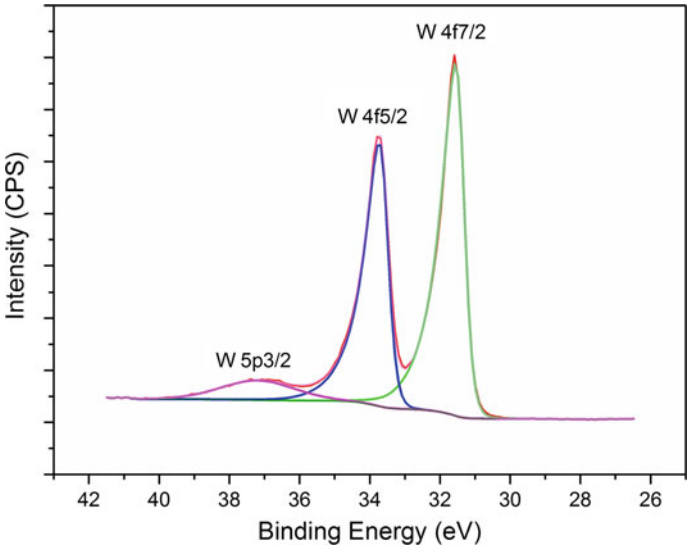

Fig. 5 W 4f spectra at 700 °C

and finally became stable. From Table 1 we can see the changes in the O element content on the surface of the sample during the heating process, which decreased from 38.17 to 22.9 at. %. At the beginning of the heating, the decrease in the O element content can be considered to be the separation of the surface adsorbed gas.

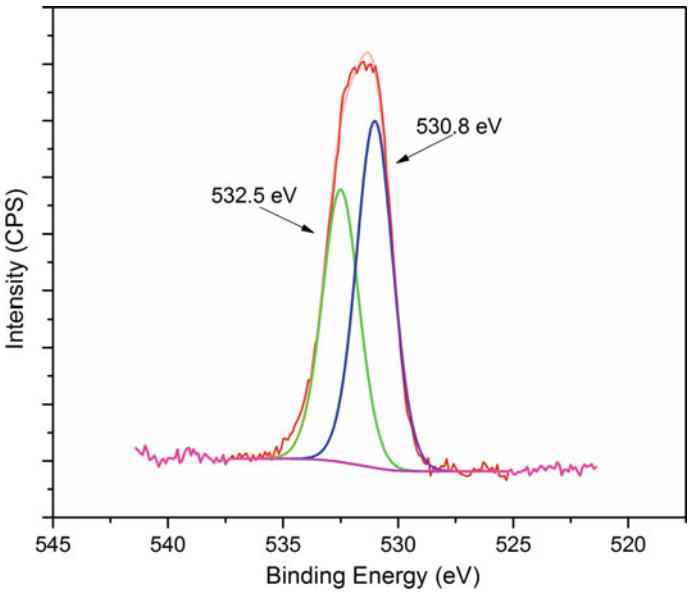

Fig. 6 O 1 s spectra at room temperature

When heated to higher temperatures, the oxygen content continued to decrease, may indicating that the Ce^{4+} on the surface of the sample tends to be reduced. This results in the reduction of Ce^{4+} in CeO_2 to Ce^{3+} and the release of oxygen, which in turn reduces the oxygen content of the sample surface.

Interpretation of Ce 3d. XPS core-level spectra of the stoichiometric oxides CeO_2 and Ce_2O_3 can be individually resolved into up to five features grouped as u and v lines to depict the electronic transitions in Ce^{3+} and Ce^{4+}, respectively. For Ce^{4+}, v_0 and v_2 components represent the intense peaks, and v_1 a weak satellite, in the Ce $3d_{5/2}$ spin-orbit split doublet. Correspondingly, v, 0 and v, 2 components characterize the Ce $3d_{3/2}$ doublet intense peaks, and v, 1 the associated weak satellite. For the valence state +3, the main components, u_0 (respectively, u, 0) and associated shake-down peaks, u_1 (respectively, u, 1) characterize the Ce $3d_{5/2}$ (respectively, Ce $3d_{3/2}$) contribution. In this study, Ce^{4+} has been fitted with six peaks: v_0 (BE≈882.2 eV), v_1 (BE≈888.6 eV), v_2 (BE≈898 eV), v, 0 (BE≈900.7 eV), v, 1 (BE≈907.2 eV), v, 2 (BE≈916.15 eV). Ce^{3+} has been fitted with four peaks: u_0 (BE≈884.4 eV), u_1 (BE≈880.6 eV), u, 0 (BE≈903.9 eV), and u, 1 (BE≈899.3 eV) [9], According to the parameters described above, we fitted the spectrum data of Ce 3d transition.

Figure 8 showed the spectrum obtained at room temperature, along with their fitted six components for Ce^{4+} and four components for Ce^{3+}. They belong to two rare earth oxides: ceria and cerium oxide, respectively. Figure 9 illustrates the change in the ratio of Ce^{3+} and Ce^{4+} for each stage of heating. As we can see from the Fig. 9, before the heating experiment, there are two valence states of cerium on the sample

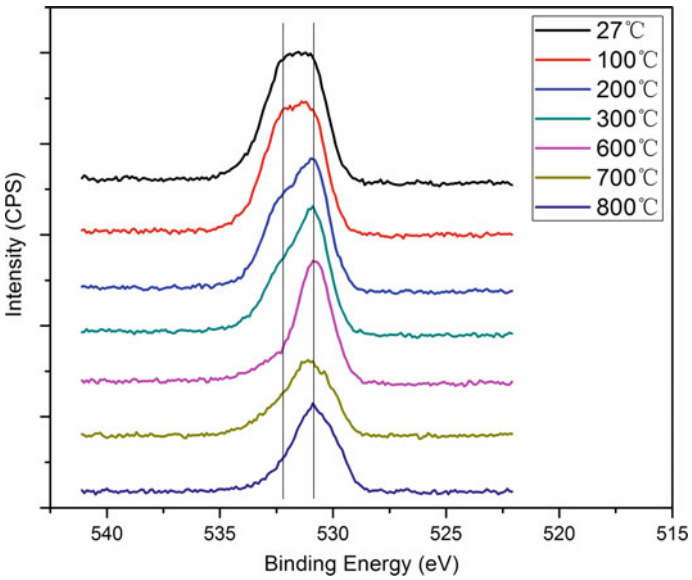

Fig. 7 O 1 s spectra at different temperature

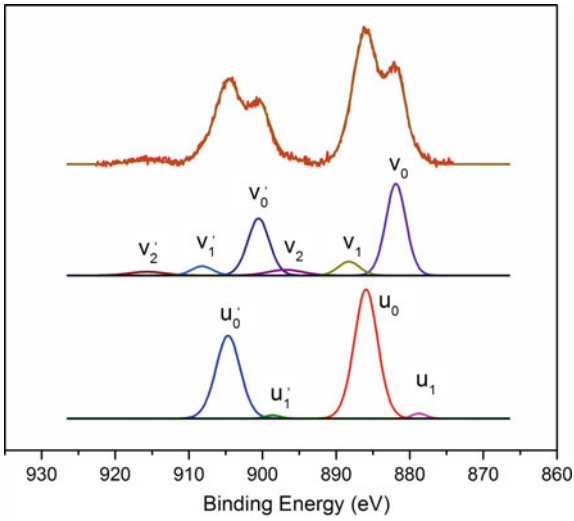

Fig. 8 Ce 3d spectra at room temperature

surface, of which the proportion of Ce^{3+} is 56.16%. At the first heating stage (28–100 °C), we found that the content of Ce^{3+} reduced to 50.34%, this is the result of the interaction between Ce_2O_3 and absorbed oxygen ions. Because the content of absorbed oxygen ions in the initial stage is very high, it provided the conditions for the oxidation reaction of Ce^{3+}. In the subsequent heating stage, with the consumption

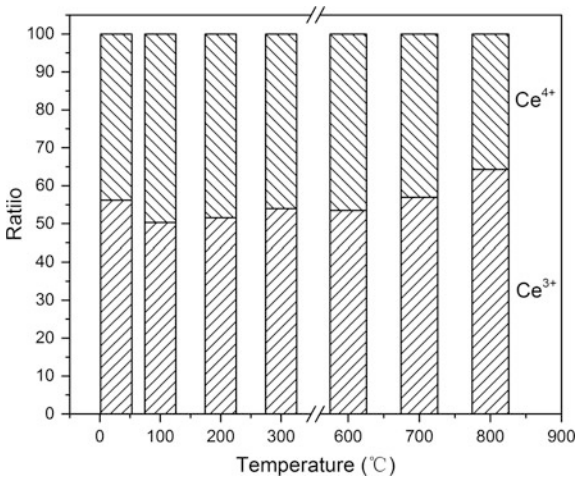

Fig. 9 Ratio of $Ce^{4+/}$ Ce^{3+}

and detachment of absorbed oxygen ions, the effect of oxidation on Ce^{3+} is weakened, accompanied by the content of Ce^{3+} tends to be stable. When the heating temperature rises to 600 °C, the ratio of Ce^{3+} to Ce^{4+} is noticeably changed: the content of Ce^{3+} increased from 53.49 to 64.28%, while the content of Ce^{4+} from 46.51 to 35.72%. This result shows that during this heating reaction phase, the valence states of cerium ion changed from +4 to +3, it means that CeO_2 has a reduction reaction. At the same time, oxygen content on the sample surface is also declining. This reduction reaction, on the one hand, avoids the risk of oxidation of other elements, on the other hand, forming more oxygen vacancies in rare earth oxide, enhanced the ionic properties of REO, this will be beneficial to the electron emission of the material.

Conclusion

1. The contents of Ce on the sample surface are increasing gradually, it shows that rare earth elements migrate from the inside of the material to the surface. While the contents of C and O are decreasing.
2. Due to electrode manufacturing process limitations, there is a small amount of WO_3 in this kind of electrode product. This component on the surface disappears by the sublimation at a sufficiently high temperature.
3. There exists two kinds of oxygen ions: the lattice oxygen and the adsorbed oxygen. The content of the adsorbed oxygen is reduced gradually, and ultimately maintains at a low level.
4. The cerium element undergoes a reduction reaction at a higher temperature, this will contribute to the electron emission of such materials.

Acknowledgements This work was supported by The National Key Research and Development Program of China (2017YFB0305601).

References

1. Lin Zulun, Wang Xiaoju, *Cathode Electronics* (National Defense Industry Press, Beijing, 2013)
2. Nie Zuoren, Zuo Tieyong, Zhou Meiling, Wang Yiman, Wang Jinshu, Zhang Jiuxing, High temperature XPS/AES investigation of Mo–La_2O_3 Cathode-I. species and properties of oxygen on surface[J]. J. Rare Earths **04**, 267–270 (1999)
3. Mei Yan, Yan Janping, Nie Zuoren, Study on the effect of roasting conditions on the valence of Ce Ion[J]. Spectro. Spectr. Anal. **01**, 270–273 (2010)
4. J.F. Watts, J. Wolstenholme, An introduction to surface analysis by XPS and AES[J] (2003)
5. C. De Boor, C. De Boor, E.U. Mathématicien et al., *A practical guide to splines[M]* (Springer, New York, 1978)
6. S. Hüfner, *Photoelectron spectroscopy: principles and applications[M]* (Springer Science & Business Media, 2013)
7. Information on https://srdata.nist.gov/xps/Default.aspx
8. F.Y. Xie, L. Gong, X. Liu et al., XPS studies on surface reduction of tungsten oxide nanowire film by Ar^+ bombardment[J]. J. Electron Spectrosc. Relat. Phenom. **185**(3), 112–118 (2012)
9. F. Larachi, J. Pierre, A. Adnot et al., Ce 3d XPS study of composite $Ce_xMn_{1-x}O_{2-y}$ wet oxidation catalysts[J]. Appl. Surf. Sci. **195**(1), 236–250 (2002)

Comparison of Climate Change Impact Between Power System of Electric Vehicles and Internal Combustion Engine Vehicles

Xudong Zhang, Feng Gao, Xianzheng Gong, Zhihong Wang and Yu Liu

Abstract The substitution of electric vehicle (EV) for conventional gasoline vehicles is a promising new way to reduce greenhouse gases (GHG) emission in China. This study compared the environmental impact on climate change between electric vehicle power system and internal combustion engine vehicle (ICEV) power system. A life cycle analysis model was built with the GaBi software to analyze the GHG emission with IPCC methodology. The life cycle of vehicle was divided into four phases including raw material production phase, auto parts production and assembly phase, transportation phase and use phase. Three scenarios of the electric power mix were carried out for the sensitivity analysis. Overall, the global warming potential (GWP) of ICEV was reduced by 69.8% compared with that of EV. However, when considering the whole vehicle use phase, EV provided 45% benefits of carbon reduction than ICEV. The results of sensitivity analysis showed that GHG emission decreased with improving of cleaner energy utilization. The results concluded that EV can reduce GHG emission compared to ICEV. Electricity consumption in the use stage, raw materials stage and production stage were the key processes for controlling GHG emission during EV management.

Keywords Life cycle assessment · Electric vehicles · Internal combustion engine vehicles · Power system · Climate change

X. Zhang (✉) · F. Gao · X. Gong · Z. Wang · Y. Liu
College of Materials Science and Engineering, Beijing University of Technology, No.100 Ping Le Yuan, Chaoyang District, Beijing 100124, China
e-mail: zhangxudong@emails.bjut.edu.cn

F. Gao
e-mail: gaofeng@bjut.edu.cn

X. Gong
e-mail: gongxianzheng@bjut.edu.cn

Z. Wang
e-mail: wangzhihong@bjut.edu.cn

Y. Liu
e-mail: liuyu@bjut.edu.cn

Y. Han (ed.), *Advances in Energy and Environmental Materials*,
Springer Proceedings in Energy, https://doi.org/10.1007/978-981-13-0158-2_75

Introduction

In recent years, "environmental protection", "new energy" and "smart travel" have become hot issues. At the end of 2015, China had 583.2 thousand electric vehicles in total, of which 332 thousand were pure electric vehicles [1]. China will build the largest market for global carbon trading. The objective of "13th five-year plan" is a 18% decrease in carbon intensity [2].

Even though EVs are cleaner vehicles because of zero emissions during the driving process, the environmental impacts in their full life cycles are still controversial. Since the 1990s, researchers focused on the environmental impacts of electric vehicles. Previous studies showed that the environmental impacts from EVs were transferred from use phase to production phase of vehicles and electricity consumption [3]. The main research scales included the fuel life cycle, the engine life cycle, the vehicle key parts life cycle and the vehicle full life cycle [4–7]. Due to limitations and shortages of the collection of automobile inventory data with time and place, most of the data used in domestic research have adopted the European or international average data. In our study, the data of electric power generation and fuel production were based on the local database. Therefore, we aimed to build a life cycle model for the power system of EV and ICEV, and calculated the life cycle inventory and analyzed the GHG emission.

Data Sources and Method

Boundary and Data Sources. The EV and ICEV were manufactured in a same factory and basically have the same manufacturing process and structure except the power system [8]. The research boundary is shown in Fig. 1. It consisted of raw materials production, parts production and assembly, transports, and use phase. As data limitation, our study did not include maintenance, sales and end of life. The function unit in our research was one power system. The lifetime of vehicles is 300,000 km.

The components that less than 0.5 kg were omitted. In this study, internal combustion engine power system and electric vehicle power system are defined as follows: The internal combustion engine power system is a combination of a gasoline engine and a gearbox. The electric vehicle power system is composed of a permanent magnet brushless DC motor reducer, a lithium-ion battery and a motor. The main parameters of the two vehicles are shown in Table 1.

The input and output data were based on enterprise investigation, literature survey, database and industrial reports [9]. The data of battery compositions including polypropylene, ethylene emulsion and carbon black were from the Ecoinvent dataset. The data of main raw materials production and transportation

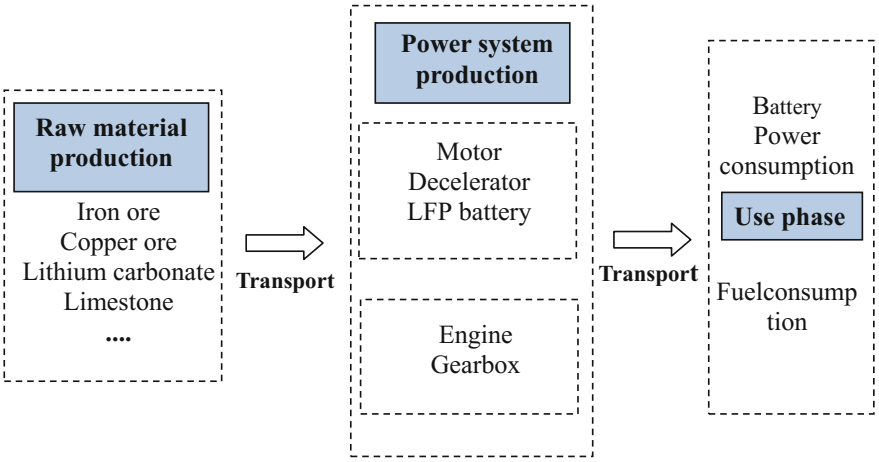

Fig. 1 system boundary

Table 1 EV and ICEV specifications

Item	ICEV	EV
Mass of vehicle	1100 [Kg]	1260 [Kg]
Mass of power system	110 [Kg]	270 [Kg]
Maximum power	73 [kW]	27 [kW]
Maximum RPM	6500 [r·min^{-1}]	6000 [r·min^{-1}]
Fuel (energy) consumption per 100 km	7.6 [L]	15 [kWh]
Lifetime	300,000 [Km]	300,000 [Km]

were based on the database of CNMLCA [10], certain data in production of parts and final assembly processes were estimated by the "mass ratio".

For the manufacturing process of engine and gearbox, the data was from the reference [11, 12].

Environmental Impact Model. The GHGs include carbon dioxide, methane and nitrous oxide in this paper. The GHG emission was indexed by CO_2 equivalency published in the IPCC report 2007 [13]. GHGs including carbon dioxide, methane and nitrous oxide were considered in this paper. Inventory analysis included collecting and calculating data of resource consumption throughout the life cycle of the product, as well as detailed data on solid, liquid and gaseous waste discharged into the environment. In this paper, the life cycle model of the EV and ICEV was established in the GaBi software.

Processes

Material Production. Most data were collected in China, it covered the majority of constituents of the powertrain, including material loss during manufacturing phase [14].

Parts Production and Assembly. The power consumption of main engine parts, other parts and the assembly process were 63.88, 94 and 41 kWh, respectively, aggregated 198.88 kWh. Inventory of gear box came from the GREET database.

In the manufacturing phase of lithium battery, the processing and assembling of Cathode, Anode, Separator, battery shell and battery modules are mainly considered. The entire process discharged 161.6 kg CO_2 eq. and consumed 856 kWh electricity [15]; The process of motor included processing and assembling of stator winding, core, stator manufacturing, permanent magnet rotor, drive electric shaft, shell and base of drive motor, bringing about 216 kWh power consumption in a total. GaBi database was used for reducer and for a total power consumption of 190 kWh.

Transports. The transportation of power systems involved mining to raw materials factories and raw materials factories to parts manufacturing plants, and then to the assembly plant. The transportation distance is about 1600 km by truck transportation, engine emissions comply with Euro III emission standards.

Use Phase. In this stage, the power consumption for EV power system and the fuel consumption for ICEV power system are included in the use phase. They are determined by Eqs. 1 and 2.

$$E_{EV} = \frac{\mathrm{e}}{\eta} \times \mathrm{L_{EV}} \times \frac{\mathrm{m_{EV}}}{\mathrm{M_{EV}}}. \tag{1}$$

$$E_{ICEV} = \circ \times \mathrm{L_{ICEV}} \times \frac{\mathrm{m_{ICEV}}}{\mathrm{M_{ICEV}}}. \tag{2}$$

where $\mathrm{E_{EV}}$ stands for the power consumption of the EV power system (kWh); e is electric power consumption of EV per 100 km (kWh), which is 15 kWh in this study; *O* is fuel consumption of ICEV per 100 km (7.6 L), these data represent the average parameter of the two vehicles;η represents the charging efficiency of the battery, $\mathrm{L_{EV}}$ and $\mathrm{L_{ICEV}}$ is the total driving distance(300,000 km); $\mathrm{m_{EV}}$ and $\mathrm{m_{ICEV}}$ is the mass of power system for EV and ICEV, respectively, $\mathrm{M_{EV}}$ and $\mathrm{M_{ICEV}}$ represent the total mass of EV and ICEV.

In this study, the charging efficiency of EV battery is 90%, the actual consumption of EV comes to 16.7 kWh/100 km. Allocation was set according to "mass ratio" principle [16], which is 110/1100 for ICEV and 270/1260 for EV, then energy consumption is 0.76 L/100 km and 3.214 kWh/100 km for ICEV and EV

with regard to power system; Through Eqs. 1 and 2, it can be concluded that the total power consumption of the power system is 9643 kWh and 2280 L for EV and ICEV at the use phase, respectively.

Results and Interpretation

Results and Discussion. The characterization results of GWP were shown in Fig. 2. The results illustrated that the powertrain of EV represents larger impact than that of ICEV in each phase with regard to GWP. The gap between EV and ICEV in raw materials production phase and production phase were much bigger than use phase. However, the use phase was responsible for the majority of the GWP impact, either directly through fuel combustion or indirectly during electricity production. Production phase impact was more significant in ICEV than in EV.

For full life cycle of power systems, the value of GHG emissions was 1.34×10^4 CO_2 eq. for EV and 7.92×10^3 CO_2 eq. for ICEV as shown in Fig. 3. ICEV was found to reduce GWP by 69.8% compared to EV. In another literature the reduction is 23%, we considered the difference was most from the selection of different databases. For ICEVs in our study, the majority GHG emissions were from fuel usage, which account for 82.9% of its full life cycle. For EVs, it's 64.1%.

From "mass ratio", EVs' Power system account for a larger proportion of the whole vehicle mass when compared to ICEVs', the higher ratio leads to a higher environmental impact. Therefore, the environmental impact of the whole vehicle cannot be judged only from the power system.

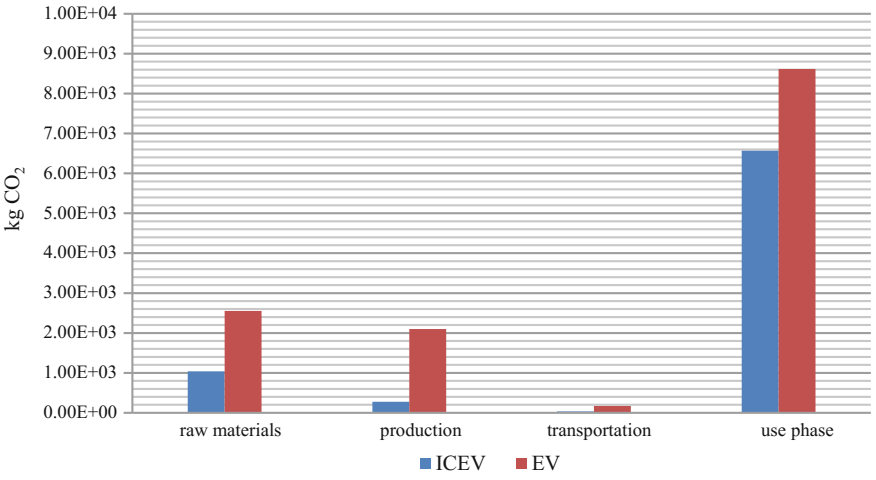

Fig. 2 GHG emissions at each phase

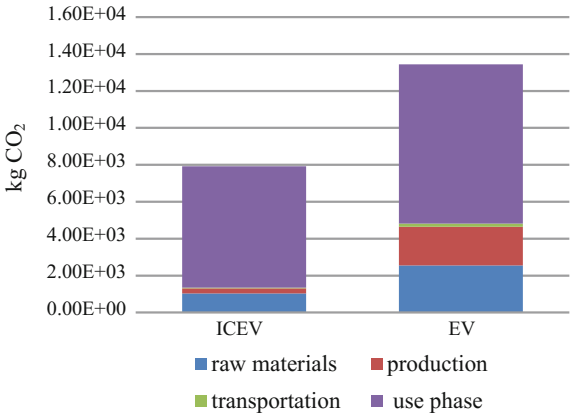

Fig. 3 GHG emissions in full life cycle

As we define above, the electric vehicle and internal combustion engine vehicle were basically the same expect their power system. So we define the same part as B, it includes every part of the vehicle except power system. Based on this point, part B of the two versions had same raw material production phase, production phase and transportation phase, the difference between them was that one consumes electricity and the other consumes fuel in the use phase, we considered Part B had same life cycle processes except use phase.

The GWP impact of part B during use phase was added to the power system, and then the results can reflect the relative GWP impact between EV and ICEV. According to Eqs. 1 and 2, greenhouse gas emission was 3.30×10^4 kg for EV and 5.90×10^4 kg for ICEV in terms of part B during use phase, the total GWP impact with part B is shown in Fig. 4.

Without considering the raw material production, production and transportation of part B, the GWP impact of electric vehicle was 45% lower than that of internal

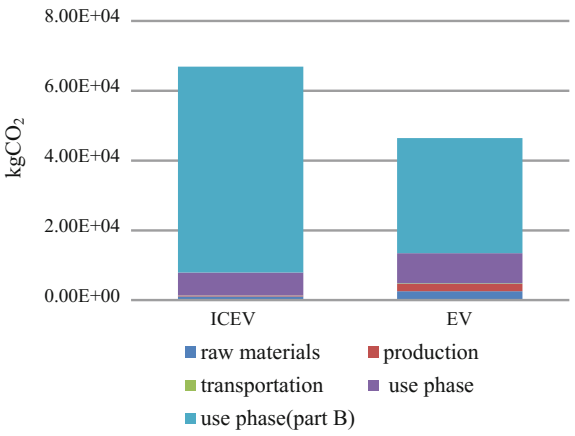

Fig. 4 GHG emissions with part B

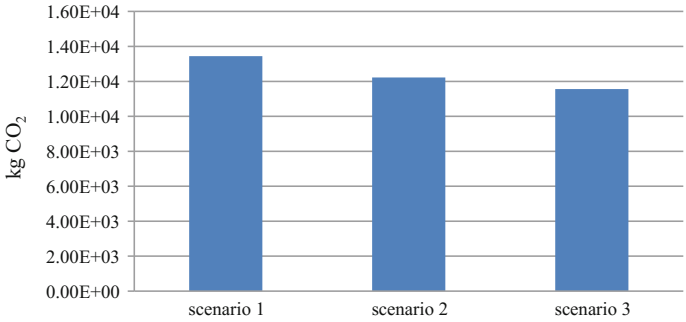

Fig. 5 GHG emissions change from Scenario 1 to Scenario 3

combustion engine vehicle. When taking the full life cycle of part B into account, the difference will be less than 45%, but generally, electric vehicles still provide benefits of carbon reduction.

Sensitive Analysis. The power system of EV consumeda large amount of power during the manufacturing process and power generation process of the use phase. While almost 75% of Chinese electricity comes from coal-fired power. It is clear that the GHG emission from EVs were transferred from use phase to production phase of vehicles and electricity consumption.

The electricity structure was a key factor that affects the GHG emissions of EV power system. In order to know how much benefit will electricity structures affect EV, three scenarios of the electric power structure for the sensitivity analysis were set up as follow:

1) Scenario 1: thermal power account for 75% of the whole electricity generation
2) Scenario 2: thermal power account for 67% of the whole electricity generation
3) Scenario 3: thermal power account for 61% of the whole electricity generation

The cleaner energy proportion increased and coal power proportion decreased from Scenario 1 to Scenario 3. In Fig. 5, the results that GHG emission decreased to 91% in Scenario 2 and to 86% in Scenario 3 when compared to Scenario 1. Therefore, it was concluded that improving the cleaner energy was beneficial to increase the benefit of GHG reduction of EV.

Conclusion

The analysis of the contributions of the different phases to GWP showed that for the powertrain of ICEVs, the majority GHG emissions were from fuel usage, which was as high as 82.9%. For the powertrain of EVs, emissions partly transferred to upstream, but the main impact phase remained the use phase, which was 64.1%, followed by raw material production, by 19% and production, by 15.6%. Because

of their lower "mass ratio", ICEVs allocated few shares to their powertrain, therefore, ICEV was found to reduce GWP by 69.8% compared to EV in terms of powertrain.

However, when taking use phase of the whole vehicle into account, the situation was, instead, rather different, EVs provided 45% benefits of carbon reduction compared to ICEVs. We speculate that considering the vehicle full life cycle, EVs can bring less than 45% benefits compared to ICEVs.

Sensitivity analysis indicate that with the expected increase of the renewable share for electricity production, the switch from ICEV to EV will be more favorable for global warming. Thus, if electricity production becomes free of fossil carbon on a global scale, great improvement can reach for EVs in mitigating global warming.

It is also concluded that the electricity production in the use stage and parts production in the production stage are the key processes for controlling GHG emission during EV management.

Acknowledgements This study was supported by the grant from National Natural Science Foundation of China (NSFC, Project No. 51304009), and Beijing municipal science & technology commission project (D161100002416001), and National Key Research and Development Program (2016YFF0201501), and Science-Technology foundation of Beijing University of Technology (ykj-2016-00687).

References

1. Yang Guofeng, Analysis of China's electric vehicles and its prospect. J. Int. Pet. Econ. **04**, 59–65 (2017)
2. B. Wang, China will build the largest market for global carbon emissions trading. J. Energ. Res. Inf. **32**(4), (2016)
3. Ai Jianghong, Analysis on impact of electric vehicle on environment in total life-cycle. J. Tech. Econ. **03**, 35–39 (2010)
4. Bunyamin, Assessment of electrically-driven vehicles in terms of emission impacts and energy requirements: a case study for Istanbul, Turkey. J. Clean. Prod. **96**, 486–492 (2015)
5. Boya Zhou, Energy real-world performance of battery electric buses and their life-cycle benefits with respect to energy consumption and carbon dioxide emissions. J. Energ. **96**, 603–613 (2016)
6. M. Singh, Total energy cycle assessment of electric and conventional vehicles: an energy and environmental analysis, Tech. Rep (ANL/ES/RP–96387-Vol. 3, Argonne National Lab., IL, USA, 1998)
7. S. Campanari, G. Manzolini, F.G. de la Iglesia, Energy analysis of electric vehicles using batteries or fuel cells through well-to-wheel driving cycle simulations. J. Power Sources **186**, 464–477 (2009)
8. L.C. Casals, E. Martinez-Laserna, B.A. García, N. Nieto, Sustainability analysis of the electric vehicle use in Europe for CO_2 emissions reduction. J. Clean. Prod. **127**, 425–437 (2016)
9. H. Michael, B. Michael, Assessment of the environmental impacts of electric vehicle concepts. J. Life Cycle Assess. **22**, 138–147 (2017)
10. CNMLCA (Centre of National Material Life Cycle Assessment) Material life cycle assessment databased-sinocenter. (Beijing University of Technology (BJUT), Beijing, China, 2013). http://cnmlca.bjut.edu.cn/database. (in Chinese, Accessed 20 Dec 2016)

11. Chen Yisong, Liu Zongwei et al., Study on impact assessment of life cycle environment of automobile engine considering scrap recycling. J. Environ. Sci. Technol. **39**(12), 189–193 (2016)
12. X. Sun, P. Zhang, M.N. Zhao, Life cycle energy consumptions and environmental impact assessment of the gasoline engine, [J]. Acta Scientiae Circumstantiae **36**(8), 3059–3065 (2016)
13. A.J. Mark, Huijbregts, ReCiPe2016: a harmonised life cycle impact assessment method at midpoint and endpoint level. Int J. Life Cycle Assess. **22**, 138–147 (2017)
14. L. Zhang, Z.F. Liu, J.J. Wang, Comparative analysis of life cycle environmental impact between power system of electric and internal combustion engine vehicles, J. Acta Scientiae Circumstantiae **33**(3), 931–940.56 (2013)
15. Mats Zackrisson, Life cycle assessment of lithium-ion batteries for plug-in hybrid electric vehicles-critical issues. J. Clean. Prod. **18**(15), 1519–1529 (2010)
16. Xiaoqing Shi, Xue Wang, Jianxin Yang, Zhaoxin Sun, Electric vehicle transformation in Beijing and the comparative eco-environmental impacts: A case study of electric and gasoline powered taxis. J. Clean. Prod. **137**, 449–460 (2016)

Effect of Conductivity and Radiation on Heat Dissipation Performance of Coating

Qianjin Mao, Yue Gao, Nairimudele, Wenwen Wu, Ziming Wang, Mingzhang Lan and Suping Cui

Abstract Aiming at the problem of heat dissipation of electronic devices in low temperature environment, the effect of thermal conductivity and emissivity of coating on its heat dissipation performance was studied by theoretical calculations and experiments in this study. The results show that the heat dissipation performance of organic coating with emissivity of 0.7–0.95 is improved as its thermal conductivity increasing. And temperature difference between inside and surface of object is inversely proportional to thermal conductivity. That is, when thermal conductivity exceeds a certain value, it will no longer affect heat dissipation performance of coating. In addition, emissivity of coating directly affects its cooling performance, and the proper matching interaction between thermal conductivity and emissivity of coating can enhance heat dissipation effects. In the case of non-forced convection cooling, the thermal conductivity of the organic coating is preferably 2–10 W/m·K.

Keywords Cooling coatings · Thermal conductivity · Emissivity
Heat dissipation performance

Introduction

Electronic device, the LED lamp, transformers and others in the long hours of work, will rise temperature caused by accumulated heat, affecting their operating stability and longevity. In recent years, researchers have proposed the application of coating technology to solve the problem of device heat-dissipation [1–3]. The surface of

Q. Mao (✉) · Y. Gao · Nairimudele · W. Wu · Z. Wang · M. Lan · S. Cui
Department of Materials Science and Engineering, Beijing University of Technology, Beijing, China
e-mail: maoqj@bjut.edu.cn

Q. Mao · Y. Gao · Nairimudele · W. Wu · Z. Wang · M. Lan · S. Cui
Key Laboratory of New Functional Materials, Ministry of Education, Beijing University of Technology, Beijing, China

Y. Han (ed.), *Advances in Energy and Environmental Materials*,
Springer Proceedings in Energy, https://doi.org/10.1007/978-981-13-0158-2_76

device is coated with a cooling coating, the heat is first transmitted to the surface by conduction, then radiated into atmosphere by the high emissivity of the coating, thus removing heat from surface and internal so as to achieve the purpose of cooling. Hence, the ideal cooling coating has the characteristics of high thermal conductivity and high radiation.

In the case where the coating covers the metal surface, the emissivity of the coating is higher than that of the metal, and the heat dissipation of the electronic device, the radiator or the like is facilitated [4]. Researchers improve their thermal performance by increasing the emissivity of the coating [5]. Nano-carbon ball, carbon nanotubes and other filler added in the organic coating, the coating emissivity can be increased to 0.95, and the heat dissipation is enhanced [6–8]. There are also researchers to improve the thermal conductivity of organic materials such as modified polyester, epoxy and other organic materials to improve the heat dissipation capacity of organic materials [9, 10].

However, the thermal cooling capacity of organic coatings is the result of the combination of heat conduction and radiation. The matching problem of coating conduction and radiation should be considered. In addition, the electronic devices in the low temperature, the radiation effect is much weaker than the high temperature. So, how much impact does the coating emissivity have on heat dissipation? Similarly, the thickness of the coating material is small compared to the bulk material, and how does its thermal conductivity affect heat transfer? For the development of thermal coatings, these problems need to be resolved. In this paper, the influence of thermal conductivity and emissivity on the heat dissipation performance of organic coatings at electrical working temperature is studied by means of theoretical calculation and experiment. And the influence of the conduction and radiation synergistic effect of the coating on the heat dissipation was discussed. Therefore, in the design of the coating, it is possible to optimize the thermal conductivity and emissivity of the coating in order to obtain a better cooling effect.

Experimental

Coating and Sample Preparation. First, according to certain proportion, the filler, coupling agent and dispersant was added in the NMP solvent and kept ultrasonic for 5 min in ultrasonic cell disruptor to get mixed solution A, fluorocarbon resin was diluted to a certain concentrations mixed solution B. Then, solution A was added to solution B at the speed of 10,000 r/min using a FA-25 high shear dispersion emulsifying machine at room temperature, stirring for 10 min. Next, add 1 wt% (relative to fluorocarbon resin) curing agent and other additives, the mixture continue stirring at high-speed for 5–7 min to obtain the heat dissipative coating. Finally, heat dissipative coating was printed on aluminum which was treated by polishing, cleaning and drying, then solidified in drying oven at 90 °C.

Test Instruments and Method

Test Instruments. Coating thickness was measured by ultrasonic coating thickness gauge (PosiTector 200CS, DeFelsko, USA). Thermal conductivity was measured by thermal conductivity measuring instrument (DRL-III, Xiangtan City Instruments and Meters Co. Ltd, China). Specimen size is diameter of 30 mm, thickness range 0.02–20 mm. The thermal conductivity that can be measured by this method is 0.05–45 W/m·K. Emissivity was tested with hemispherical emissivity detector of China Building Material Research Institute, which showing the hemispherical emissivity of the coating at room temperature.

Test Method. At present, there is not yet a perfect or standard method for characterizing the heat dissipation performance of coating. And the representative method adopted in most literatures is based on the Conservation Law of Energy, as shown Eq. (1).

$$Q_A = Q_H + Q_L \tag{1}$$

where Q_A is the amount of heat absorbed by the aluminum plate per unit time (W), Q_H is the amount of heat stored by the aluminum plate per unit time (W), and Q_L is the amount of heat loss per unit time (W), which includes thermal conduction, thermal convection and thermal radiation.

With the increase of Q_L, the heat dissipation performance of coating is improved. When Q_A is certain, Q_L can be indirectly characterized by Q_H according to Eq. (1), which is indicated through measuring the temperature reduction of aluminum plate. That is to say, the low temperature tested of aluminum plate means the small Q_H, this indirectly shows that Q_L is large that the heat dissipation of the coating is efficient.

According to principle mentioned above, the instrument for testing heat dissipation of coating was homemade. The test procedure is as follows: The heat sink (80 mm*100 mm*2 mm) were prepared using two pieces of aluminum plate, which their material, size, thickness and surface condition should be consistent. One piece is painted with coating prepared, recorded as sample A, and another piece as sample B that no brushed do blank contrast. Sample A and sample B were placed on a hot plate and heated at 90 °C for 30 min. Then, the samples were removed and placed quickly in the incubator made of foam plastics. The temperature measured by the thermocouple thermometer was recorded at regular intervals to evaluate the effect of cooling and cooling.

Results and Discussion

There are three basic modes of heat dissipation, namely conduction, convection and radiation. Atmospheric convection cooling is largely influenced by the external environment and is therefore not considered in material research. The material itself

mainly relies on conduction and radiation for heat dissipation. For the cooling coating, the thermal conductivity of coating affects the heat transfer from interior to surface of coating, that is, affects temperature difference of device surface and inside. And the emissivity of the coating directly affects the heat dissipation, heat through the coating radiation to the atmosphere. In the following sections, a series of coatings with controllable thermal conductivity and emissivity were obtained by adjusting the type and proportion of the fillers. Then, the influences of the thermal conductivity and emissivity of the coating on the heat dissipation were studied respectively.

Effect of Emissivity on Heat Dissipation. The emissivity of the coating directly affects the cooling performance. Three sets of samples which thermal conductivity close to 1.2 W/m·K, were prepared with emissivity of 0.91, 0.75 and 0.48, respectively. The cooling curves of the coatings were measured as shown in Fig. 1.

As shown in Fig. 1, when the thermal conductivity of the coating is close, the temperature of the aluminum sheet covered with the high emissivity coating is lower than that of covered with the low emissivity coating. This indicates that high emissivity coatings can radiate heat quickly, resulting in faster temperature drop. It is interesting to note that since the emissivity of aluminum is only 0.15, even if the thermal conductivity of aluminum is as high as 240 W/m·K, the cooling rate is still lower than that of the coated aluminum plates.

Based on the theory of radiant heat dissipation, the radiant heat of different emissivity materials at different temperatures is calculated by Eq. (2).

$$q_a = \varepsilon\sigma(T^4 - T_0^4) \tag{2}$$

Where ε is the emissivity of materials, σ is the Stefan–Boltzmann constant $\left(5.67 \times 10^{-8}\mathrm{W}/(\mathrm{m}^2{\cdot}\mathrm{K}^4)\right)$, T is the substrate surface temperature (K), and T_0 is the ambient (air) temperature (K).

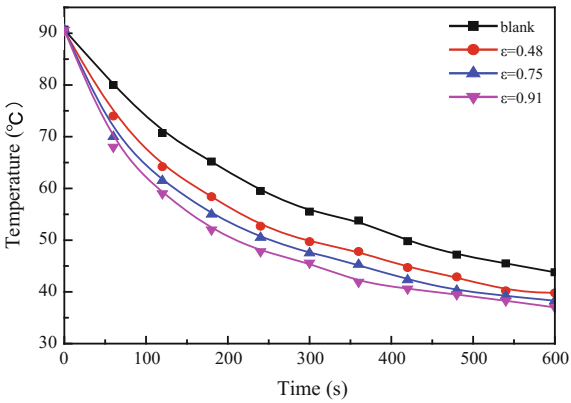

Fig. 1 Cooling curves of the coatings at different emissivity

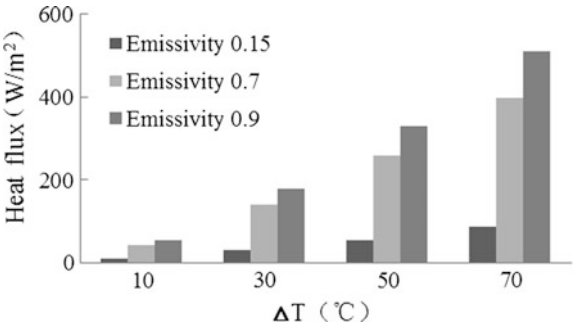

Fig. 2 Radiation heat of materials with different emissivity at different temperature

Setting ambient temperature of 20 °C, radiation heat per unit area were calculated by Eq. (2) when the emissivity were 0.15, 0.7, 0.9 and the temperature difference between the surface of the object and the environment were 10, 30, 50, 70 °C. The calculation results are shown in Fig. 2.

As shown in Fig. 2, with the emissivity improved, the radiation heat increases. When the emissivity from 0.15 to 0.9, the radiant heat increased by 6 times. With the increase of the temperature difference between the object and the environment, the radiant heat also increases. At ambient temperatures of 20 °C, when the temperature difference increases from 10 to 70 °C, the radiant heat increases by nearly 10 times.

In addition to radiant, there is a way to conduct heat to air. Nevertheless, due to the air thermal conductivity of only 0.024 W/m·K, heat dissipated caused by air conduction is much less than that of radiation in small temperature difference and non-forced convection environment.

In summary, in non-forced convection environment, the emissivity of coating directly affects its cooling effect. The emissivity of organic coatings is usually between 0.7–0.95. In general, the metal plate covered with organic coating is conducive to improving its cooling effect.

Effect of Thermal Conductivity on Heat Dissipation. Thermal conductivity of coating affects the heat transfer from interior to surface of coating, that is, affects temperature difference of device surface and inside, thus affecting the heat dissipation performance. A series of samples with emissivity of 0.91 were prepared, that the thermal conductivity respectively was 0.258, 0.554, 0.815, 1.201 and 1.344 W/m·K. The cooling curves of coating were measured as shown in Fig. 3. Figure 4 presents temperature difference between the aluminum plate painted with varying thermal conductivity coatings and the blank aluminum plate after cooling for 240 s.

As shown in Fig. 3 and 4, when the coating emissivity is the same, the temperature of the aluminum plate decreases with the increase of the thermal conductivity of the coating, which indicates that the heat dissipation effect of the coating is enhanced. The increase in the thermal conductivity of the coating helps to enhance heat dissipation. Cooling for 240 s, the temperature of the aluminum plate coated *with* a thermal conductivity of 1.344 W/m·K is 9.7 °C lower than that of the

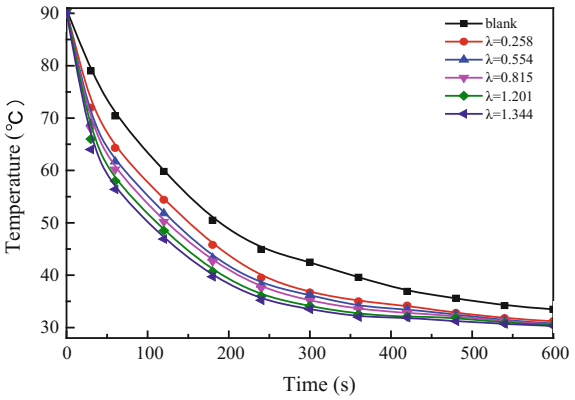

Fig. 3 Cooling curves of the coatings with different thermal conductivity

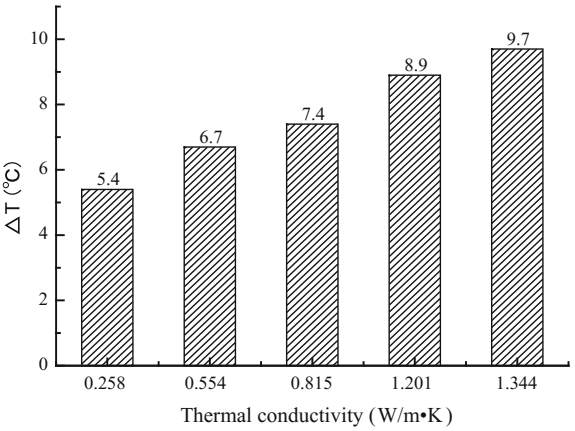

Fig. 4 Temperature difference of the coatings at different thermal conductivity after 240 s

blank aluminum plate. The difference between the aluminum plate with the coating thermal conductivity of 0.258 W/m·K and the blank aluminum plate is only 5.4 °C. The increase in the thermal conductivity of the coating can accelerate the heat transfer, so that the surface of the object and the internal temperature difference is reduced, while the higher surface temperature favors heat loss of radiation. Thus, the coating with high thermal conductivity enhances heat dissipation.

The total conduction heat per unit area transferred from aluminum plate to the coating surface is calculated as follows Eq. (3).

$$q_b = \frac{\lambda}{\delta}(T_1 - T) \tag{3}$$

Where λ is the thermal conductivity of coating (W/m·K), δ is the thickness of coating (m), T_1 is the aluminum plate temperature (K), and T is the coating surface temperature (K).

The coating thickness is small, about 80 μm in this study. Thermal conductivity of aluminum plate (240 W/m·K) is much higher than that of the organic coating, it can be considered that the internal temperature of the aluminum plate is evenly distributed. So the temperature difference between the inner and outer of the coating is the temperature difference between the aluminum plate and the outer surface of the coating. Suppose that air convection and heat conduction are not considered, then $q_a = q_b$. Derived from the Formulas 2 and 3, the temperature difference (ΔT) is inversely proportional to the thermal conductivity: $\Delta T \propto 1/\lambda$.

When the coating thickness is 80 μm, the emissivity is 0.91, the ambient temperature is 20 °C, the outer surface temperature of the coating is 90, 70, 50 and 30 °C respectively, the corresponding relationship of the coating temperature difference ΔT and its thermal conductivity is given in Fig. 5.

As shown in Fig. 5, coating temperature difference decreases with the thermal conductivity increasing. When the thermal conductivity of the coating reaches 10 W/m K, the temperature difference has dropped to near zero. And then continue to improve the thermal conductivity of the coating will no longer affect the coating heat. In this case, the cooling effect of the coating is only related to its emissivity.

However, the actual situation is much more complex than the above calculation. Taking into account the air convection heat, air heat conduction, etc., the coating conduction heat is greater than its radiant heat, that is, the temperature difference between the inner and outer surface is greater than the calculated value in actually. If the thickness of the coating increases, especially when the air convection cannot be ignored, the role of coating thermal conductivity will be more important.

Synergistic Heat Dissipation of Thermal Conductivity and Emissivity. In the absence of convection, the cooling capacity of the coating is the result of its heat conduction and radiation. The thermal conductivity and emissivity of the four coatings were listed in Table 1. The temperature difference between the aluminum plate and the blank aluminum sheet, which is not coated with the cooling coating, is shown in Fig. 6.

As shown in Fig. 6, the temperature difference between the four samples was C4 > C3 > C1 > C2. The thermal conductivity of C1 and C2 coatings is far less to

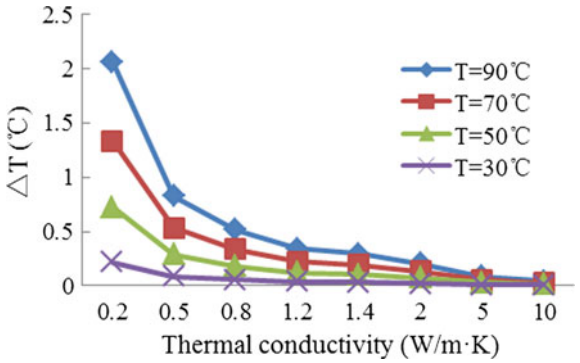

Fig. 5 Temperature difference of different thermal conductivity coatings at different temperature

Table 1 Thermal conductivity and emissivity of different coatings

Group	Thermal conductivity(W/m·K)	Emissivity
C1	0.272	0.90
C2	0.266	0.89
C3	0.841	0.735
C4	1.911	0.78

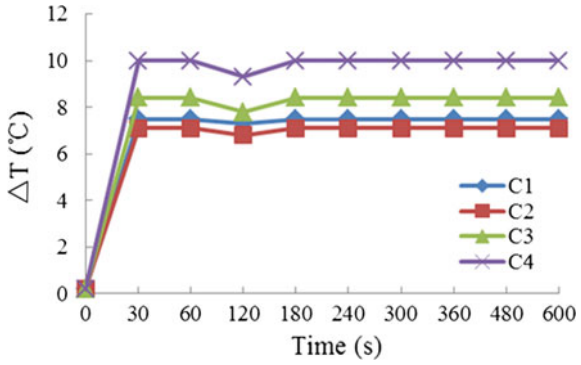

Fig. 6 Temperature difference of coatings with time

C3 and C4 as shown in Table 1, even though emissivity of the first two is higher than the latter, the heat dissipation of C1 and C2 are still weak. The reason is that the low thermal conductivity of the coating hinders heat transfer from interior to surface, the surface temperature decreases and the radiant heat decreases, so that the cooling effect of the coating is deteriorated. Thus, increasing the thermal conductivity of the coating, even if the emissivity is reduced, still contributes to improved coating cooling properties such as C3 and C1. It can be inferred that the thermal conductivity of the coating has a certain matching relationship with the emissivity. So we can optimize the coating to improve the cooling performance.

In summary, for organic coating, because of its high emissivity (0.7–0.95) and low thermal conductivity, increasing thermal conductivity will improve its cooling properties. More attention should be paid to improving thermal conductivity of cooling coating for low temperature. The heat dissipation performance of materials is closely related to its thermal conductivity and emissivity, and there exists a matching relationship between the two in this study. In the case of non-forced convection cooling, the thermal conductivity of the organic coating is preferably 2–10 W/m·K.

Conclusions

(1) In non-forced convection environment, the emissivity of coating directly affects its cooling effect. Organic coating emissivity is generally between 0.7–0.95, so the metal surface covered with organic coating can improve heat dissipation.

(2) Heat dissipation performance of coating is enhanced with the increase of thermal conductivity. Temperature difference between inside and surface of object is inversely proportional to the thermal conductivity in this study. As the thermal conductivity of the coating increases, the temperature difference between the inner and outer surfaces of the object decreases until it approaches zero. In this case, the thermal conductivity no longer affects the coating's thermal performance.
(3) For organic coating, which with the emissivity of 0.7–0.95 and low thermal conductivity, more attention should be paid to improve thermal conductivity of cooling coating. And there exists a matching relationship between thermal conductivity and emissivity of coating. In the case of non-forced convection cooling, the thermal conductivity of the organic coating is preferably 2–10 W/m·K.

Acknowledgements This research was financially supported by Funding Project for Academic Human Resources Development in Institutions of Higher Learning Under the Jurisdiction of Beijing Municipality.

References

1. S. Wijewardane, D.Y. Goswami, A review on surface control of thermal radiation by paints and coatings for new energy applications. Renew. Sustain. Energy Rev. **16**, 1863–1873 (2012)
2. J. Wu, S. Li, W. Yang et al., Study on heat sinks for high power LEDs. Semicond. Technol. **35**, 964–967, 1027 (2010)
3. Zihui Lang, Effect of composite surface treatment on CPU radiator performance. Autom. Instrum. **155**, 155–157 (2011)
4. S. Kim, J. Kim, J.H. Kim, Fabrication of insulated metal substrates with organic ceramic composite films for high thermal conductivity. Ceram. Int. **43**, 8294–8299 (2017)
5. K. Zhao, K.H. Hua, A.Z. Shui, Application of infrared radiation coating in LED heat dissipation. Bull. Chin. Ceram. Soc. **34**, 172–176 (2015)
6. Y.J. Nie, L.J. Jin, J.Z. Hang, et al., Preparation and properties of waterborne nano-composite heat dissipative coating. J. Funct. Mater. **44**, 736–739, 743 (2013)
7. X. Han, X. Cui, K. Ma et al., Carbon nano-capsule coating for high-power LED thermal management. Mater. Res. Innovations **19**, 1112–1116 (2015)
8. H. Zhang, P. Lou, F.W. Liu et al., Effect of carbon nanotube structure on properties of infrared radiation heat sink coatings. Shanghai Coat. **54**, 1–5 (2016)
9. J. Li, J. Liang, Y. Liu, High-thermal conductive coating used on metal heat exchanger. Chin. J. Chem. Eng. **22**, 596–601 (2014)
10. H. Im, J. Kim, The effect of Al_2O_3 doped multi-walled carbon nanotubes on the thermal conductivity of Al_2O_3/epoxy terminated poly(dimethyl siloxane) composites. Carbon **49**, 3503–3511 (2011)

Adsorption of Cd (II) Ion on Aragonite Calcium Carbonate Crystals

Yiqi Yang, Zhenping Qin, Yu Qian, Hongxia Guo and Shulan Ji

Abstract Calcium carbonate was prepared with urea hydrolytic method, and was characterized by Scanning electron microscopy (SEM), Fourier transform infrared spectroscopy (FTIR), X-ray diffract meter (XRD) and Ratio of surface area porosity analyzer. It is revealed that the Calcium carbonate obtained here is aragonite calcium carbonate crystals. The adsorption of Cd (II) ion onto aragonite calcium carbonate crystals were studied via investigating parameters as effect of contact time, dosage of aragonite calcium carbonate crystals and initial heavy metal concentration using static batch adsorption experiments. The results reveal that the removal rate of Cd (II) ion is 83% under the following conditions: temperature as 25 °C, contact time as 120 min, initial concentration of the Cd (II) ion as 100 mg/L, and dosage of aragonite calcium carbonate crystals as 0.6 g/L. The adsorption capacity reaches 200 mg/g. Meanwhile the results suggest that the adsorption of the Cd (II) ion by the aragonite calcium carbonate crystals well follows the pseudo-second-order kinetics model, and the Langmuir isotherm model provides a good fit to the experimental data.

Keywords Aragonite calcium carbonate crystals · Cd (II) ion · Adsorption

Y. Yang · Z. Qin (✉) · S. Ji
Beijing Key Laboratory for Green Catalysis and Separation, College of Environmental and Energy Engineering, Beijing University of Technology, Beijing 100124, China
e-mail: zhenpingq@bjut.edu.cn

Y. Yang
e-mail: samanthayang1986@hotmail.com

Y. Qian
Environmental Protection Research Institute of Light Industry, Beijing 100089, China

H. Guo
College of Material Science and Engineering, Beijing University of Technology, Beijing 100124, China

Y. Han (ed.), *Advances in Energy and Environmental Materials*,
Springer Proceedings in Energy, https://doi.org/10.1007/978-981-13-0158-2_77

Introduction

With the development of industry, great amount of cadmium-polluted wastewater generated from metallurgy, electroplate and mining etc. poses great threat to environment [1]. Cadmium is of heavy toxicity, non-biodegradable in water, and accumulative in soil and living body, Cadmium is absorbed by the body, selectively accumulate in the liver and kidney, can cause diarrhea, anemia and Itai Itai disease. Consequently leading to severe impacts both to ecosystem and human health. Hence, the discharge of wastewater containing chromium ion has been strictly restricted [2]. Presently, methods commonly used to remove heavy metals from water are adsorption [3], ion-exchange [4], chemical precipitation [5] and reverse osmosis [6] etc. Among these methods, adsorption has advantages, such as wide application, efficient and avoidance of secondary pollution etc. Recent years, research in removing of heavy metal ions from wastewater with Calcium carbonate is gradually developed. There are three kinds of calcium carbonate crystal contains calcite, aragonite and vaterite, Calcite is one of the most abundant and stable structures in nature, and aragonite and vaterite are mostly synthetic.

Different crystal types of calcium carbonate have been used as adsorbents to remove contaminants in water, The aragonite and vaterite has better adsorption properties, but the adsorption capacity is about 2–150 mg/g [7, 8]. Therefore, the preparation of special morphology of calcium carbonate by synthetic method can improve its adsorption performance. In this study, aragonite calcium carbonate crystals was prepared with urea hydrolytic method, and was used to adsorb Cd (II) ion in water. Effect of factors such as contacting time, dosage of aragonite calcium carbonate crystals and initial heavy metal concentration on adsorption of cadmium were investigated. Pseudo-second-order kinetics model and the Langmuir isotherm model were also studied. This work provides basis on adsorption of Cd (II) ion by bio-mineral aragonite calcium carbonate crystals.

Experimental

Materials. Starting materials, calcium acetate, and urea, were of analytical reagent grade and obtained from Sinopharm Chemical Reagent Co., Ltd. in China. Cadmium nitrate was provided by Shanghai Jinshan Tingxin Chemical Co. in China. All chemicals were used as received. Filter paper was purchased from Hangzhou Special Paper Co. Ltd. in China.

Preparation of Aragonite Calcium Carbonate Crystals. Weigh 14.0952 g of calcium acetate powder and 28.8288 g of urea accurately and (Calcium acetate and Urea Mole ratio: 1:6) and dissolve them in 60 mL of ultrapure water to form 41.7% solution. Put the aqueous solution into a 200 mL glass test tube and covered by a rubber stopper with three syringe-needle penetration. The tube was then statically

placed in a forced convection oven at 90 °C or for 24 h. Subsequently, the solution was cooled to ambient temperature. The precipitate was collected by filtration through a 0.2 μm cellulose acetate membrane filter and rinsed with deionized water. The products were dried at 60 °C in a vacuum oven and then stored in a desiccator before characterization.

Characterizations. SEM image was obtained with an S-3400 N scanning electron microscope (Hitachi High-Technologies Co., Japan) at an accelerating voltage of 20 kV after sputtering the precipitates with gold. Powder XRD pattern was obtained with an XRD-7000 X-ray diffractometer (Shimadzu Co., Japan) equipped with Cu-Kα radiation (λ = 1.5405 Å) at a scanning rate of 10° per minute. Infrared spectra were collected with a Vertex-70 FTIR spectrometer (Bruker Optics Co., Germany) on KBr pellets.

Adsorption Experiment. The adsorption experiment was carried out with static batch adsorption method. Add accurately a certain quantity of the prepared aragonite calcium carbonate crystals powder into in a certain concentration of cadmium (II) solution containing in an Erlenmeyer flask. After shaking in 150 rpm for fixed time, the supernatant was extracted by centrifugal filtration. The Cd (II) ion concentration in the supernatant was measured by ICP-OES spectrophotometer. The removal rate R (%) and the adsorption capacity Q_e (mg/g) were calculated according to Eq. (1) and (2), respectively.

$$\mathrm{R}(\%) = \frac{(C_0 - C_e)}{C_0} \cdot 100\%. \tag{1}$$

$$\mathrm{Q}_e(mg/g) = \frac{(C_0 - C_e) \cdot V}{m}. \tag{2}$$

where, R (%) is the removal rate, Q_e (mg/g) is adsorption capacity, C_0 (mg/L) is the initial concentration of cadmium before adsorption, C_e (mg/L) is the concentration of cadmium after adsorption, m (g) is the added quality of aragonite calcium carbonate crystals powder prepared, V (L) is the volume.

Results and Discussions

Characterization of the Prepared Aragonite Calcium Carbonate Crystals. The SEM image of the prepared aragonite calcium carbonate crystals was shown in Fig. 1a. It can be seen that the prepared aragonite calcium carbonate crystals were rod-like sticks with an average aspect ratio of 2.6 ± 0.2 (defined as the ratio of length to diameter), which was the typical morphology of aragonite. XRD pattern in Fig. 1b indicated the obvious diffraction peak appearing at 2θ of 26.2, 27.2, 33.1, 37.9, 45.8, which was consistent with the diffraction absorption peak of the aragonite calcium carbonate crystals, according to the standard JCPDS card [9].

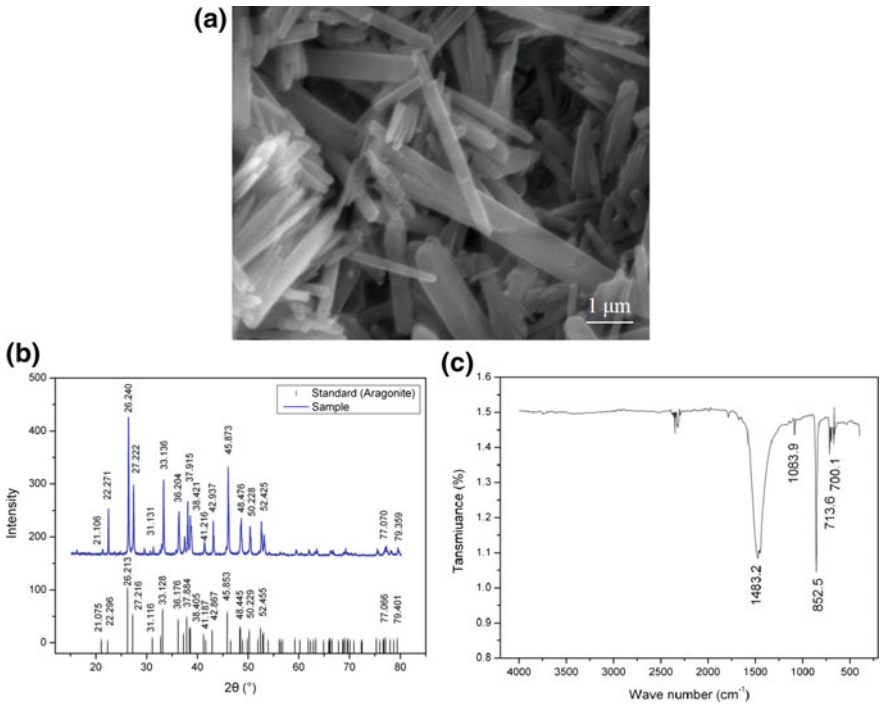

Fig. 1 **a** SEM image, **b** XRD pattern and **c** FTIR of the prepared aragonite calcium carbonate crystals

The peaks in Fig. 1b exhibited strong intensity, indicating that the prepared aragonite calcium carbonate crystals powder was of good purity and in complete crystal structure. This result can be further demonstrated by FTIR spectroscopy in Fig. 1c, which appeared peaks at 1483.2, 1083.9, 852.5, 713.6, 700.1 cm^{-1} respectively, corresponding to the characteristic absorption peak of aragonite calcium carbonate crystals [10].

Adsorption of Cd (II) Ion by Aragonite Calcium Carbonate Crystals. The adsorption capacity of the prepared aragonite calcium carbonate crystals for Cd (II) ion with different contact time was shown in Fig. 2 (temperature as 25 °C, contact time as 10 to 240 min, initial concentration of the Cd (II) ion as 100 mg/L, and dosage of aragonite calcium carbonate crystals as 0.2 g/L). It can be seen that the adsorption capacity of aragonite calcium carbonate crystals for Cd (II) ion increased from 32 to 191 mg/g with increasing contact time from 10 to 120 min. 120 to 240 min the adsorption capacity tends to moderate, adsorption equilibration is reached. When the adsorption time reaches 240 min, the adsorption capacity reached 200 mg/g.

The removal rate of Cd (II) ion in the supernatant with the dosage of aragonite calcium carbonate crystals powder was shown in Fig. 3 (temperature as 25 °C,

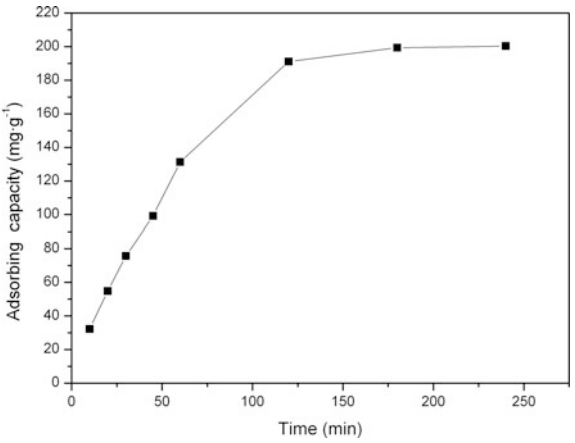

Fig. 2 Effect of contact time on the Cd (II) ion adsorption capacity by the aragonite calcium carbonate crystals

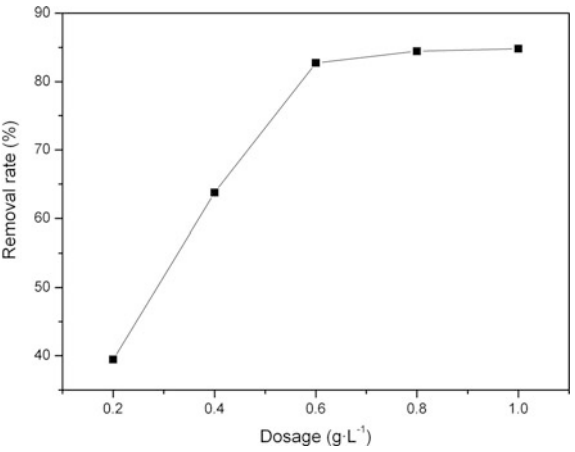

Fig. 3 The influence of aragonite calcium carbonate crystals dosage on removal rate

contact time as 120 min, initial concentration of the Cd (II) ion as 100 mg/L, and dosage of aragonite calcium carbonate crystals as 0.6 g/L). It can be seen that when the dosage increased from 0.2 to 0.6 g/L, the removal rate increased from 39 to 83%. It is shown that increasing the dosage of calcium carbonate provides more adsorption sites, which is beneficial to increase adsorption capacity and removal rate rapidly. However, the content of cadmium ion decreased when the dosage is up to a certain level, this leads to the decrease of diffusion velocity and the increase of removal rate.

Adsorption Isotherm of Aragonite Calcium Carbonate Crystals for Cd (II) Ion. The effects of Cd (II) concentrations on the adsorption of aragonite calcium carbonate crystals powder measured at 25 °C were shown in Fig. 4. Accordingly, the equilibrium adsorption capacity was calculated according to Langmuir model [11]

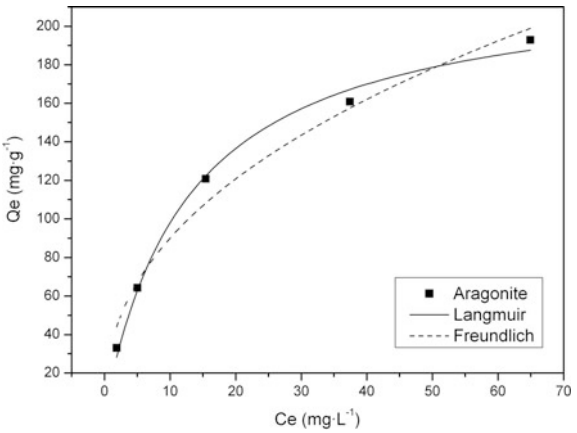

Fig. 4 Langmuir and Freundlich adsorption isotherms of Cd (II) ion on aragonite calcium carbonate crystals

Table 1 Fitness of isotherm models and corresponding parameters

Langmuir			Freundlich		
Qm (mg/g)	K_L (L/g)	R^2	K_F ($mg^{(1-1/n)}$ $L^{1/n}$/g)	1/n	R^2
225.0034	0.0772	0.9925	29.6941	0.4238	0.9745

and Freundlich model [12] by Origin software [13]. The fitting result was depicted in Fig. 4, and the fitting parameters were shown in Table 1. The results indicated that the two models all well characterize the adsorption process of aragonite calcium carbonate crystals on cadmium ion, but the relevance presented by Langmuir model was better than Freundlich model being closer to 1, which suggested that the adsorption process of aragonite calcium carbonate crystals on Cd (II) ion can be better described with Langmuir model. Langmuir model is a typical monolayer adsorption model, consequently, adsorption of aragonite calcium carbonate crystals of Cd (II) ion mainly is monolayer adsorption [14]. The range of adsorption equilibrium constant K_L falls in 0 to 1, it indicates that the adsorption was favorable adsorption [15]; The measured adsorption capacity is close to the theoretical value.

Adsorption Kinetics of Aragonite Calcium Carbonate Crystals on Cd (II) Ion. To determine the adsorption kinetics of aragonite calcium carbonate crystals on Cd (II) ion, were used the Lagergren pseudo-first-order kinetics and pseudo-second-order kinetics model to fit the experiment data of effect of contact time on Cd (II) ion adsorption respectively. The fitting results are depicted in Fig. 5 and Fig. 6, respectively. It can be seen that fitting result of pseudo-second-order kinetics ($R^2 = 0.9825$) is better than that of pseudo-first-order kinetics ($R^2 = 0.9316$), suggesting that the adsorption happened mainly is chemical adsorption, which is in consistent with conclusion of related researchers [16].

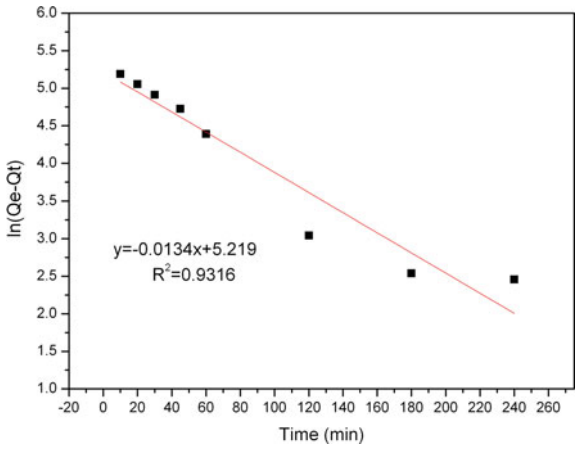

Fig. 5 Pseudo-first-order kinetic fitting curve for adsorption of Cd (II) ion on aragonite calcium carbonate crystals

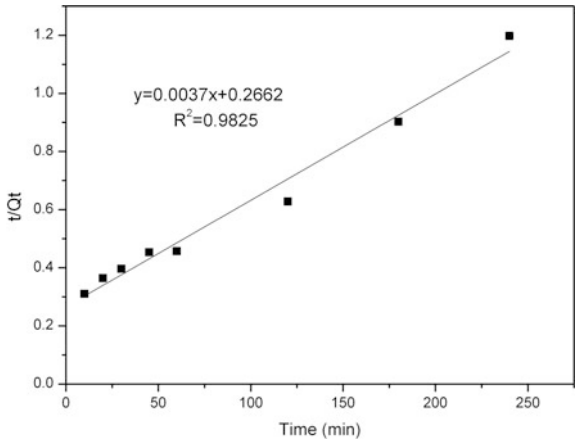

Fig. 6 Pseudo-second-order kinetic fitting curve for adsorption of Cd (II) ion on aragonite calcium carbonate crystals

Conclusion

In this work, the rod-like aragonite calcium carbonate crystals were prepared by urea hydrolytic method. The average aspect ratio is about 2.6 ± 0.2 (defined as the ratio of length to diameter) while the Mole ratio of Calcium acetate and Urea is 1:6. The aragonite calcium carbonate crystals exhibit the highest adsorption capacity of 191 mg/g under Cd (II) ions concentration of 100 mg/L and dosage of 0.2 mg/L for 2 h, and removal rate of 83% under Cd (II) ions concentration of 100 mg/L and dosage of 0.6 mg/L for 2 h. The theoretical adsorption value is more than 225 mg/g. The adsorption kinetics and isotherms indicate that the adsorption process is very consistent with the pseudo-second-order and Langmuir models. The aragonite

prepared by this method can be used to adsorb Cd (II) ion with large adsorption capacity, which is simple and easily operated. It is considered to be a good application prospect as an adsorbent for water treatment.

Acknowledgements This work was supported by the National Natural Science Foundation of China (21476005, 21176005), and the Fund from Beijing Municipal Selected Excellent Overseas Scholars Project.

References

1. T.A. Davis, B. Volesky, R.H.S.F. Vieira, Sargassum seaweed as biosorbent for heavy metal. Water Res. **34**, 4270–4278 (2000)
2. M. Xu, P. Hadi, G. Chen et al., Removal of cadmium ions from wastewater using innovative electronic waste-derived material. J. Hazard. Mater. **273**, 118–123 (2014)
3. D. Enshirah, Adsorption of heavy metals on functionalized-mesoporous silica: a review. Microporous Mesoporous Mater. **145**, 145–157 (2017)
4. D. Pathania, G. Sharma, R. Thakur, Pectin @ zirconium (IV) silicophosphate nanocomposite ion exchanger: photo catalysis, heavy metal separation and antibacterial activity. Chem. Eng. J. **267**, 235–244 (2015)
5. Y. Guo, Z. Fang, J. Hu et al., Research development of treating wastewater containing heavy metals by chemical precipitation process. Ind. Water. Treat. **31**, 9–13 (2012)
6. C. Nithinart, M. Scott, Husson. High-capacity, nanofiber-based ion-exchange membranes for the selective recovery of heavy metals from impaired waters. Sep. Purif. Technol. **179**, 94–103 (2017)
7. E. Pehlivan, A.M. Ozkan, S. Dinç et al., Adsorption of Cu^{2+} and Pb^{2+} ion on dolomite powder. J. Hazard. Mater. **167**, 1044–1049 (2009)
8. S.J. Köhler, P. Cubillas, J.D. Rodriguez-Blanco, C. Bauer, M. Prieto, Removal of cadmium from wastewaters by aragonite shells and the influence of other divalent cations. Environ. Sci. Technol. **41**, 112–118 (2007)
9. Faculty of Mineral and Petrology, Department of Geology, Nanjing University, *Powder crystal X ray phase analysis* (The Geological Publishing House, Beijing, 1980). (in Chinese)
10. G.T. Zhou, Q.Z. Yao, J. Ni, G. Jin, Formation of aragonite mesocrystals and implication for biomineralization. Am. Mineral. **94**, 293–302 (2009)
11. S.J. Allen, Q. Gan, R. Matthews et al., Kinetic modeling of the adsorption of basic dyes by kudzu. J. Colloid. Interface Sci. **286**, 101–109 (2005)
12. I. Langmuir, The adsorption of gases on plane surfaces of glass, mica and platinum. J. Am. Chem. Soc. **40**, 1361–1403 (1918)
13. H.M.F. Freundlich, Over the adsorption in solution. J. Phys. Chem. A **57**, 358–471 (1906)
14. Y. Xia, L. Meng, Y. Jiang et al., Facile preparation of MnO_2 functionalized baker's yeast composites and their adsorption mechanism for Cadmium. Chem. Eng. J. **259**, 927–935 (2015)
15. A.H. Chen, S.M. Chen, Biosorption of azo dyes from aqueous solution by glutaraldehyde-crosslinked chitosans. J. Hazard. Mater. **172**, 1111–1121 (2009)
16. Z. Ma, W. Di, S. Wang et al., Thermodynamic process of Zn^{2+} adsorbed on humic acid extracted from albic soil fitted by the non-linear curve from the Origin 7.0 software. Chin. Agr. Sci. Bull. **30**, 159–164 (2014)

The Influence of Volume Changes in Portland and Calcium Sulfoaluminate Binary Cement

Yan Zheng, Suping Cui, Yali Wang, Gao Feng, Ziming Wang and Qianjin Mao

Abstract The long-term volume changes of Portland-Calcium sulfoaluminate cement systems has been studied for samples cured under different conditions. Three curing conditions were chosen in this study and the composite cement systems showed different results with different CSA dosages. Progressively higher amount of CSA was added to the composite cement system and it was found that there was a critical dosage of CSA leading to unstable expansion and failure of the samples by curing under water. But in drying condition, the systems showed shrinkage and the degree of volume changes were similar than expansion by curing under water. By selecting the composition of CSA-PC systems and curing conditions, the volume stability of composite cement could be controlled.

Keywords Calcium sulfoaluminate cement · Binary cement · Ettringite Volume change

Introduction

Concrete, mainly based on Portland cement, is the most used material worldwide, with a production of about seventeen billion tons per year [1, 2]. However, cementitious materials undergo volumetric changes during their hydration and special binders based on calcium sulfoaluminate cements (CSA)-calcium sulfate can be deliberately formulated to expand and to compensate the shrinkage. Usually about 15–25 wt% of gypsum is interground with the clinker for optimum setting

Y. Zheng (✉) · S. Cui · Y. Wang · G. Feng · Z. Wang · Q. Mao
Department of Materials Science and Engineering, Beijing University of Technology, Beijing 100124, China
e-mail: zhengyan2012@emails.bjut.edu.cn

S. Cui
e-mail: cuisuping@bjut.edu.cn

Y. Wang
e-mail: wangyali1978@bjut.edu.cn

Y. Han (ed.), *Advances in Energy and Environmental Materials*,
Springer Proceedings in Energy, https://doi.org/10.1007/978-981-13-0158-2_78

time, strength development and volume stability [3]. The hydration of the calcium sulfoaluminate cements obtained depends mainly on the amount and reactivity of the added calcium sulfate [4, 5] as well as on the kind and amount of minor phases present. Some factors as lime content and calcium carbonates are also critical have been proved in many studies [6]. In this paper the main research is ettringite and calcium sulfoaluminate cement content.

Microstructural investigations [7–11] revealed mainly the formation of large space filling ettringite needles, together with monosulfate, aluminium hydroxide and calcium silicate hydrates, leading to a very dense, low-porosity microstructure, according to Eqs. (1), (2) and (3).

$$C_4A_3\bar{S} + 2C\bar{S}H_2 + 34H = C_3A \cdot 3C\bar{S} \cdot H_{32} + 2AH_3 \quad (1)$$

$$C_3A + 3C\bar{S}H_2 + 26H = C_3A \cdot 3C\bar{S} \cdot H_{32} \quad (2)$$

$$C_4AF + 3C\bar{S}H_2 + 21H = C_6(A,F)\bar{S} \cdot H_{32} + (A,F)H_3 \quad (3)$$

In order to understand better the hydration mechanisms of PC-CSA composite cements and theories of expansion, the CSA/PC ratio and the volume changes curing in different conditions were determined in this study.

Materials and Methods

Materials. Two commercial cements were used. CSA produced by Polar Bear Building Materials Co.; Ltd and a Portland cement. Table 1 shows the oxides composition of the cements (by XRF) and Table 2 shows the composition of CSA-PC systems.

Methods. All the experiments were carried out at 20 °C. Cement pastes were prepared with a constant water/binder ratio of 0.35 (preparation of pastes at higher w/c ratios would lead to bleeding). CSA was first added to Portland cement which was then added to water and mixed for 2 min using a paddle mixer (1100 rpm).

For the expansion test [12], the cement paste was cast in steel moulds of $10 \times 10 \times 40$ mm^3 with end pieces for the measurement of the length evolution. The samples were then cured for 1 day in the moulds in a high humidity environment (96% R.H.) and unmoulded after 24 h to start the measurements. The samples (6 prisms) were then submerged into 60–70 g of deionised water. The length of the

Table 1 Oxides composition of CSA and Portland cements [wt%]

	CaO	Al_2O_3	SiO_2	Fe_2O_3	K_2O	Na_2O	TiO_2	MgO	SO_3
CSA	57.21	9.46	3.35	0.53	0.1	0.05	0.44	2.42	23.48
PC	64.48	4.39	20.45	3.01	0.89	0.24	0.34	1.66	2.83

Table 2 Design the composition of CSA-PC systems

No.	Mixture [wt%]	
	CSA	OPC
P1	1	99
P2	2	98
P3	3	97
P5	5	95
P6	6	94
P7	7	93
P9	9	91

samples (~40 mm) was measured regularly with an extensometer having a precision of ±1 μm. The expansion values result from the average of 3 measures. In this study, three curing condition were chosen, water condition, drying condition and drying condition after curing water in different days.

Result and Discussion

Expansion Curing Under Water. In order to show the different of volume changes of OPC and CSA-OPC system more clearly, the cement expansion curing under water have been tested. Figure 1 shows the expansion as a function of time for CSA-OPC systems by curing under water. Expansion increases with the CSA content. Macro-cracks appear after 0.7% of expansion, leading to cracks of the samples. So only the sample of P9 system (the dosage of CSA is 9%) has the cracks. For P7 system, there is rapid initial expansion, which slows to a much lower

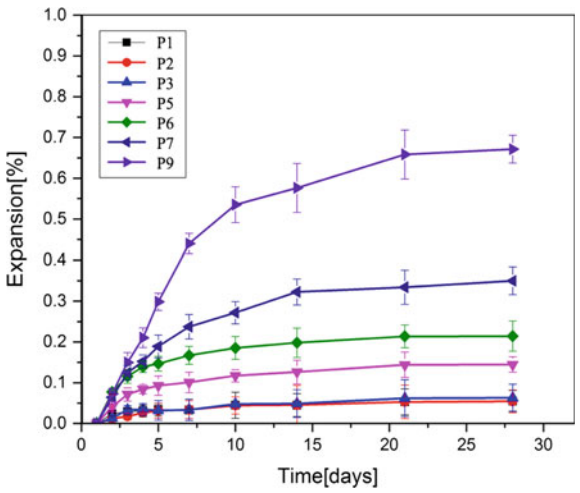

Fig. 1 Expansion profiles as a function of time for different CSA-OPC systems

rate after a few days. It was found that there is a critical dosage between the systems with 7 and 9% of CSA leading to unstable expansion and failure of the samples by curing under water.

Shrinkage in Drying Condition. In order to study the effects of curing conditions of cement in depth, the volume change of cement by curing in drying condition also be studied. Figure 2 shows the shrinkage as a function of time for Portland-Calcium sulfoaluminate cement systems by drying condition. In drying condition, the systems show shrinkage and the degree of volume changes are similar than expansion by curing under water. There is no clear relationship between the amount of CSA and shrinkage. For the two systems with highest CSA dosage, a small expansion happened in first measure day, maybe because of more ettringites growing at early ages.

Volume Changes of Composite Cement Systems by Curing in Different Conditions. According to the results of expansion and shrinkage in different curing condition, we can know that curing condition is the main influence of volume change in composite cement systems.

The expansion result of Portland and CSA-PC (P3) system cured under water for different times are shown in Fig. 3. The systems show shrinkage and the degree of volume changes are similar than expansion by curing under water. After curing in water condition, the samples in three systems all appear rapid initial shrinkage. The degree of shrinkage in OPC-CSA systems is lower than that in Portland cement.

SEM and Porosity Results of OPC and Calcium Sulfoaluminate Binary Cement. According to the results of above studies on volume change of Portland and CSA-PC system, we found that the trend of volume change of cement tends to be gentle after hydration 7 days. For a clear comparison and show the different of OPC and CSA-PC systems on volume change at early age, the morphology of pore structure in OPC and P6 system during hydration 7 days have been tested. The results show as Fig. 4.

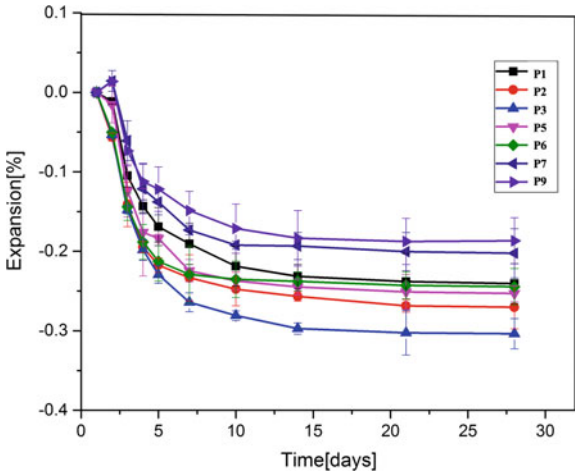

Fig. 2 Drying shrinkage as a function of time for different CSA-OPC systems

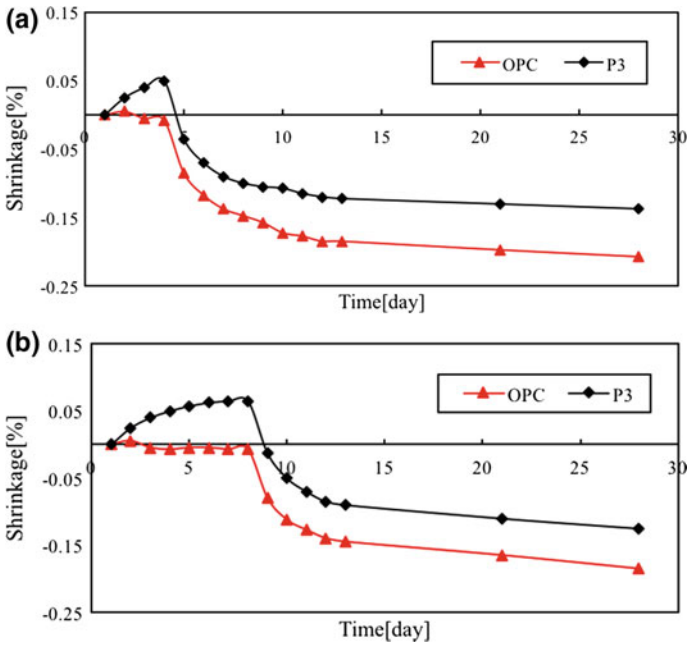

Fig. 3 Expansion of different composite cement systems cured under water for different times (**a** curing in water for 3 days, **b** curing in water for 7 days)

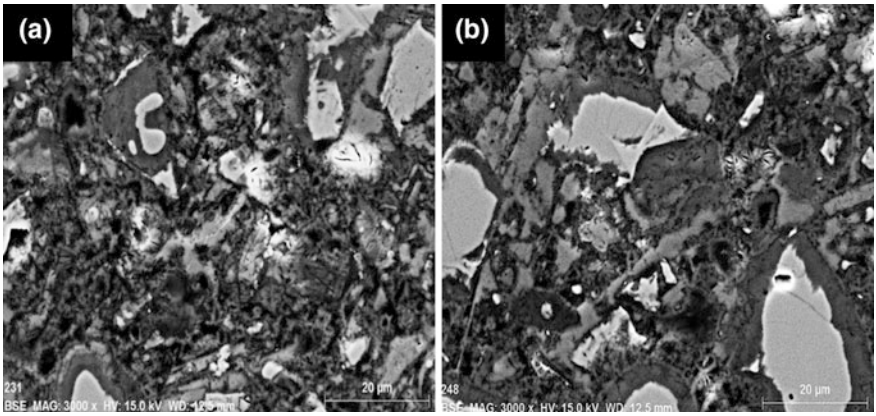

Fig. 4 Morphology of pore structure in OPC and P6 system during hydration 7 days (**a** OPC porosity = 14.35, **b** P6 porosity = 12.55)

After hydration 7 days, the porosity of OPC is 14.35 and the porosity of P6 is 12.55. Combined with the results of SEM we can verified that compare with OPC more abundant ettringite needles growth in CSA-PC system at early age. The different of porosity also proved CSA content lead to the further expansion.

Conclusion

Curing condition and the CSA content in composite systems are the most important influence of volume changes in Portland and Calcium sulfoaluminate composite cement. There is a critical dosage between the systems with 7 and 9% of CSA leading to unstable expansion and failure of the samples by curing under water. By selecting the composition of CSA-PC systems and curing conditions, the volume stability of composite cement can be controlled.

Acknowledgements This research was supported by Beijing Natural Science Foundation of China Project-Research on the key issues of the environmental performance of new energy-saving building materials evaluation and design (Grant No. 2141001) and PHR (IHLB) Funding Project for Academic Human Resources Development in Institutions of Higher Learning Under the Jurisdiction of Beijing Municipality.

References

1. E. Gartner, Industrially interesting approaches to "low-CO_2" cements. Cem. Concr. Res. **34** (9), 1489–1498 (2004)
2. C.W. Hargis, A.P. Kirchheim, P.J.M. Monteiro, E.M. Gartner, Early age hydration of calcium sulfoaluminate (synthetic ye'elimite,) in the presence of gypsum and varying amounts of calcium hydroxide. Cem. Concr. Res. **48**, 105–115 (2013)
3. F.P. Glasser, L. Zhang, High-performance cement matrices based on calcium sulfoaluminate-belite compositions. Cem. Concr. Res. **21**(12), 1881–1886 (2001)
4. S. Sahu, J. Havlica, V. Tomkova, J. Majling, Hydration behaviour of sulphoaluminate belite cement in the presence of various calcium sulphates. Thermochim. Acta **175**(1), 45–52 (1991)
5. G. Bernardo, A. Telesca, G.L. Valenti, A porosimetric study of calcium sulfoaluminate cement pastes cured at early ages. Cem. Concr. Res. **36**(6), 1042–1047 (2006)
6. C.W. Hargis, A. Telesca, P.J.M. Monteiro, Calcium sulfoaluminate (Ye'elimite) hydration in the presence of gypsum, calcite, and vaterite. Cem. Concr. Res. **65**, 15–20 (2014)
7. C. Yu, K.L. Scrivener, Mechanism of expansion of mortars immersed in sodium sulphate solution. Cem. Concr. Res. **43**, 105–111 (2013)
8. L. Zhang, F.P. Glasser, Hydration of calcium sulfoaluminate cement at less than 24 h. Adv. Cem. Res. **14**(4), 141–155 (2002)
9. M. Andac, F.P. Glasser, Pore solution composition of calcium sulfoaluminate cement. Adv. Cem. Res. **11**(1), 23–26 (1999)
10. L. Zhang, F.P. Glasser, Investigation of the microstructure and carbonation of CSA-based concretes removed from service. Cem. Concr. Res. **35**(12), 2252–2260 (2005)
11. F. Winnefeld, B. Lothenbach, Hydration of calcium sulfoaluminate cements—Experimental findings and thermodynamic modelling. Cem. Concr. Res. **40**, 1239–1247 (2005)
12. J. Bizzozero, C. Gosselin, K.L. Scrivener, Expansion mechanisms in calcium aluminate and sulfoaluminate systems with calcium sulfate. Cem. Concr. Res. **56**, 190–202 (2014)

Effects of Chain Transfer Agent on the Performances of Branched Polycarboxylate Superplasticizer

Xiao Liu, Guanghong Lai, Yunsheng Zheng, Jianan Guan, Ziming Wang and Wenbo Xi

Abstract A branched polycarboxylate superplasticizer (BPCE) was synthesized via copolymerization of polymerizable active center, isobutenyl polyethylene glycol (IPEG) and acrylic acid (AA). To investigate the effects of chain transfer agent on the performances of BPCE, a series of BPCEs with different molecular weights were further synthesized by changing the addition amount of chain transfer agent, i.e., thioglycolic acid (TGA). The characteristic molecular structures of BPCEs were determined by Infrared Spectroscopy (IR) and viscosity method. Furthermore, the dispersing capacities and adsorption behaviors of BPCEs in cement pastes were probed. The result showed that, the paste fluidity and adsorption amount both presented a trend of first increase and then decrease with the increase of TGA/IPEG proportion, and the maximum appeared at the TGA/IPEG proportion of 0.15 (M = 96314 g/mol). The hydration products of cement pastes containing BPCEs at different curing ages were measured by X-Ray Diffraction (XRD), showing that the introduction of BPCE caused the delay of initial hydration which presented some retardation, and this trend was shown most significantly at the TGA/IPEG

X. Liu (✉) · G. Lai · J. Guan · Z. Wang · W. Xi
College of Materials Science and Engineering, Beijing University of Technology, Beijing 100124, China
e-mail: liux@bjut.edu.cn

G. Lai
e-mail: laiguanghong@yeah.net

J. Guan
e-mail: jiananguan@yeah.net

Z. Wang
e-mail: wangziming@bjut.edu.cn

W. Xi
e-mail: xwboliver123@163.com

Y. Zheng
State Key Laboratory of Solid Waste Reuse for Building Materials, Beijing 100041, China
e-mail: zhengyunsheng@outlook.com

Y. Han (ed.), *Advances in Energy and Environmental Materials*,
Springer Proceedings in Energy, https://doi.org/10.1007/978-981-13-0158-2_79

proportion of 0.15. The aim of this study is to suggest that moderate dosage of chain transfer agent for the synthesis of BPCE is beneficial to achieve good dispersing and adsorption effectiveness.

Keywords Branched structure · Polycarboxylate superplasticizer
Effectiveness · Characterization · Chain transfer agent

Introduction

Nowadays, the rapid development of cities results in an increased demand of constructions such as infrastructure, road, hydropower dam, building and so on [1]. Consequently, the natural coarse/fine aggregates with good qualities are consumed considerably to be exhausted. Besides, it is too difficult to exploit high-quality raw materials from the limited natural resources.

To solve the above problem, some builders employ the inferior aggregates instead of high-quality aggregates [2], leading to a large increase in admixture amount to achieve equal performances. This is detrimental to the development of construction industry. Based on this, some researchers consider to develop novel superplasticizer to achieve certain characteristics of concrete [3, 4]. Therefore, it is urgent to prepare a novel polycarboxylate superplasticizer (PCE) with advanced performances by structural design, which can exhibit good environmental adaptability.

In this study, a series of novel BPCEs were synthesized by polymerizable active center, IPEG and AA as monomers. The molecular structure were confirmed and the effects of chain transfer agent on the dispersion capacity and adsorption amount in cement pastes were investigated. Compared with conventional PCE, BPCE exhibits higher dispersion capacity to cement paste due to its branched structure. Employing appropriate dosage of chain transfer agent can achieve the effectiveness optimization.

Experimental

Materials. Ammonium persulfate (APS), AA, TGA and sodium hydroxide (NaOH) were purchased from Tianjin Fuchen Chemical Reagents Factory (Tianjin, China). IPEG was received from Liaoning Oxiranchem, Inc (Liaoning, China). The polymerizable active center was self-made in our laboratory. Reference cement was supplied by China Building Materials Research Institute (Beijing, China), which chemical and mineral compositions are illustrated in Table 1.

Table 1 Chemical and mineral compositions of reference cement (%)

Composition	SiO_2	Al_2O_3	Fe_2O_3	CaO	MgO	SO_3	Na_2Oeq	f-CaO	C_3S	C_2S	C_3A	C_4AF
Reference cement	22.93	4.29	2.89	66.23	1.92	0.35	0.7	0.64	58.78	21.38	6.49	8.77

Preparation. The polymerizable active center and IPEG aqueous solution were mixed in a four-neck round-bottom flask which was placed in a constant temperature bath at 65 ± 1 °C with stirring. Then, AA, APS and TGA aqueous solutions were dropwise added to the flask. The reaction lasted for 5 h, and then NaOH aqueous solution was added to adjust pH value to 6–7 followed by cooling to room temperature, thus yielding the final product, i.e., BPCE. Furthermore, the conventional PCE was synthesized by the same process without adding polymerizable active center.

Characterizations and Measurements. The solid PCE was mixed with KBr and pressed into a disk before IR measurement. The IR spectra of PCEs were detected on a TENSOR27 Fourier transform infrared spectrometer at 25 °C by scanning the sample disks. In all cases, 32 scans under the transmission mode were used to record the spectra. The scanning range was from 4000 to 450 cm^{-1} with a resolution of 4 cm^{-1}. The characteristic molecular properties were determined by viscosity method. The flow times of solvent (t_0) and solution (t) were determined and used to calculate relative viscosity ($\eta_r = t/t_0$), specific viscosity ($\eta_{sp} = \eta_r - 1$), reduced viscosity (η_{sp}/c), inherent viscosity ($\ln\eta_r/c$), and intrinsic viscosity ($[\eta] = \eta_{sp}/c = \ln\eta_r/c$) [5]. The relationship between viscosity and molecular weight is $[\eta] = 3.83 \times 10^{-4}M^{0.61}$, where M is the molecular weight. The fluidities of fresh cement pastes containing PCEs were tested according to the standard method GB/T 8077-2012 [6] described in the National Standards of the People's Republic of China. The PCE solution was generally added to the mixing water, and the amount of water contained in the PCE solution was subtracted from the amount of mixing water required for a water-cement ratio (W/C) ratio of 0.29. The adsorption amounts of PCEs on the surfaces of cement particles were evaluated. The non-adsorbed portion of polymer remaining in solution at equilibrium condition was determined by analyzing the total organic carbon (TOC) content of the solution. Cement, deionized water and the PCE to be tested (remaining the same concentration as in cement paste) were filled into a centrifuge tube and then centrifuged for 5 min to 160 min at 6000 rpm. The supernatant was diluted 30 times with deionized water. Measurements were generally repeated three times and the average was reported as the adsorption amount. Hydrated phase development of hardened pastes containing PCEs (W/C = 0.29, PCE = 0.20%) at curing ages of hydrated 1d, 3d and 7d was determined by XRD patterns recorded at room temperature on a Shimadzu XRD-6000 diffractometer utilizing CuKα radiation at 40 kV and 100 mA. The scan range was set from 5° to 70° (2θ) with a step size of 0.01°.

Results and Discussion

IR Spectra. The IR spectra of the branched polycarboxylate superplasticizer and conventional comb-shaped polycarboxylate superplasticizer are shown in Fig. 1. By comparison, the main characteristic peaks with different intensity for two PCEs all appear at around 1081, 1631 and 2700–3200 cm^{-1}, which are symmetric vibration peak of $-(CH_2–CH_2–O)_n–$, symmetric vibration peak of C = O bond of carboxyl and stretching vibration peak of $-(CH_2–CH_2–O)_n–$, respectively. It is interesting that a peak appears at around 1718 cm^{-1} corresponding to the ester groups for BPCE, but no peak at this position for comb-shaped PCE. These results thus show that BPCE involves common polyethylene glycol and carboxyl groups as well as exclusive ester groups. This confirms the achievement of target structure for our synthesized products.

Molecular Weight Characteristics. To characterize the molecular weights of PCEs, ubbelohde viscometer was used to measure their viscosities, and then their molecular weights were calculated according to the equation mentioned above. The calculated molecular weights for two PCEs as a function of the proportion of TGA/IPEG are shown in Fig. 2. It can be seen that the molecular weights for two PCEs both decrease with the increase of the proportion of TGA/IPEG, indicating that the chain growth for macromolecules correspondingly declines when the amount of chain transfer agent increases. Also from Fig. 2, the molecular weight of BPCE is closed to that of comb-shaped PCE under the condition of same amount of chain transfer agent, demonstrating the sum of branch length for BPCE is identical to the backbone length for comb-shaped PCE. This result proves that the molecular weights of these PCEs can be regulated by the introduced amount of chain transfer agent during the synthesis process, and presents an inverse proportion to the amount of chain transfer agent.

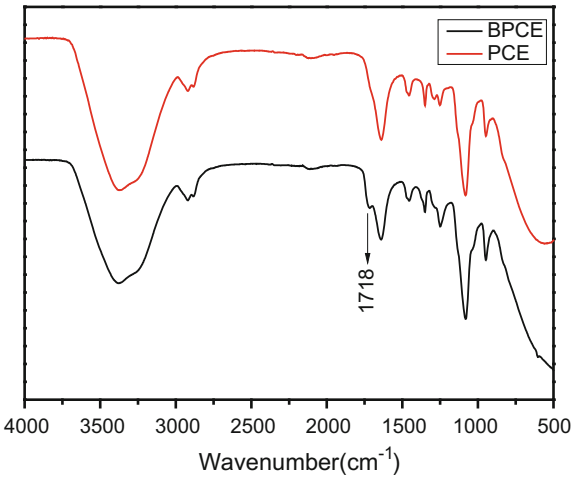

Fig. 1 IR spectra of PCE and BPCE

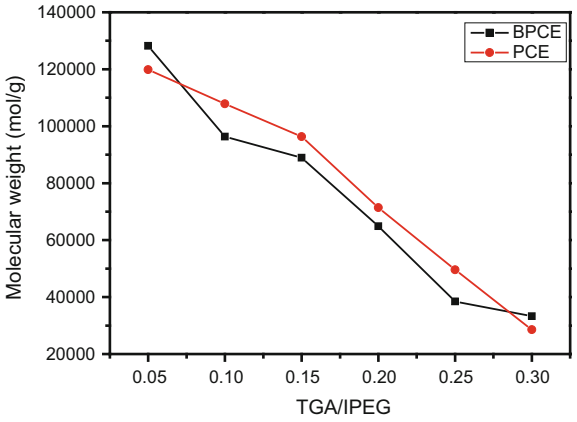

Fig. 2 Molecular weights of PCEs and BPCEs

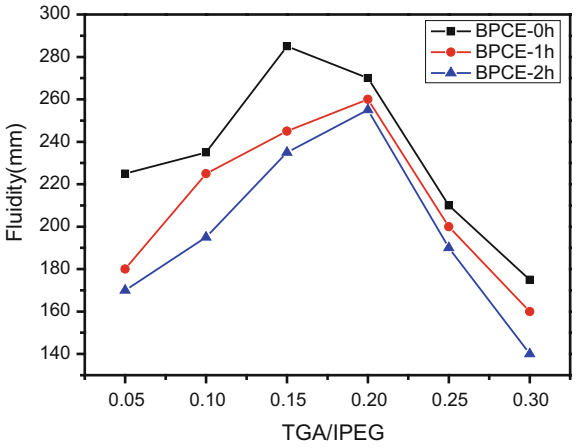

Fig. 3 Fluidities of cement pastes containing BPCEs

Dispersing Capacity. To investigate the effects of chain transfer agent on the dispersing capacities of BPCE, the fluidity and fluidity retention measurements for cement pastes containing BPCEs synthesized at different TGA/IPEG proportion were carried out. The fluidities at 0, 1 and 2 h of fresh cement pastes containing BPCE or comb-shaped PCE (dosage = 0.2%) at the TGA/IPEG proportion from 0.05 to 0.30 with an interval of 0.05 are shown in Fig. 3.

From Fig. 3, the fluidities at 0, 1 and 2 h of fresh cement pastes for BPCEs all present a trend of first increase and then decrease with the increase of TGA/IPEG proportion. The initial fluidities of cement pastes containing BPCE at the TGA/IPEG proportion of 0.15 and 0.20 are entirely higher than those at other proportions; besides, this trend is also reflected in the fluidities at 1 and 2 h of fresh cement pastes. This result indicates that the optima of TGA/IPEG proportions are 0.15

and 0.2, at which the optimal paste fluidity and paste fluidity retention can be achieved. This is because the increased length of branched molecules increases the probability of molecular entanglement when the TGA/IPEG proportion is low, leading to the reduction of anchoring points on the surfaces of cement particles. Likewise, when the TGA/IPEG proportion is high, the decreased length of macromolecules can weaken the steric hindrance effect, resulting in the decrease of dispersing capacity. Overall, the moderate TGA/IPEG proportion can contribute to achieving good dispersing capacity for BPCE in cement paste.

Adsorption on Cement Particles. The adsorption behavior of PCE on cement paste is related to the structural characteristics of PCE [7]. The molecular structure type of PCE can significantly influence its adsorption mode in the cement paste. The time-dependent adsorption amount in cement paste for BPCEs synthesized at different TGA/IPEG proportion is shown in Fig. 4.

From Fig. 4 for both BPCE and comb-shaped PCE, the adsorption amounts increase over time, presenting that the curves reach to the maximum in first 5 min and then gradually reach to equilibrium. With the increase of TGA/IPEG proportion, the adsorption amount at equilibrium increases firstly and then decreases when it exceeds 0.15. The reason is that, when the TGA/IPEG proportion is low, the long branched length is apt to be entangled, leading to low adsorption amount; when the TGA/IPEG proportion is high, the short branched length caused by hindered chain growth brings the reduced amount of carboxylic acid ion which can chelate with calcium ion on the surfaces of cement particles to form complex, also leading to low adsorption amount.

Compared with comb-shaped PCE, BPCE exhibits more adsorption amounts on cements, possibly because the stronger steric hindrance effect and higher content of absorbable polar groups leads to higher probability of adsorption on cement particles. During the hydration process, the failure of comb-shaped PCE caused by the coverage of hydrated products is observed; on the other hand, due to the branched structure, there are still free side chains of BPCE in the pore solution which can

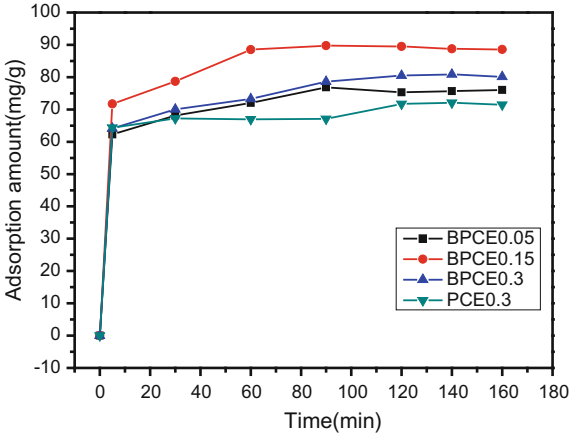

Fig. 4 Adsorption amounts of PCEs on cements

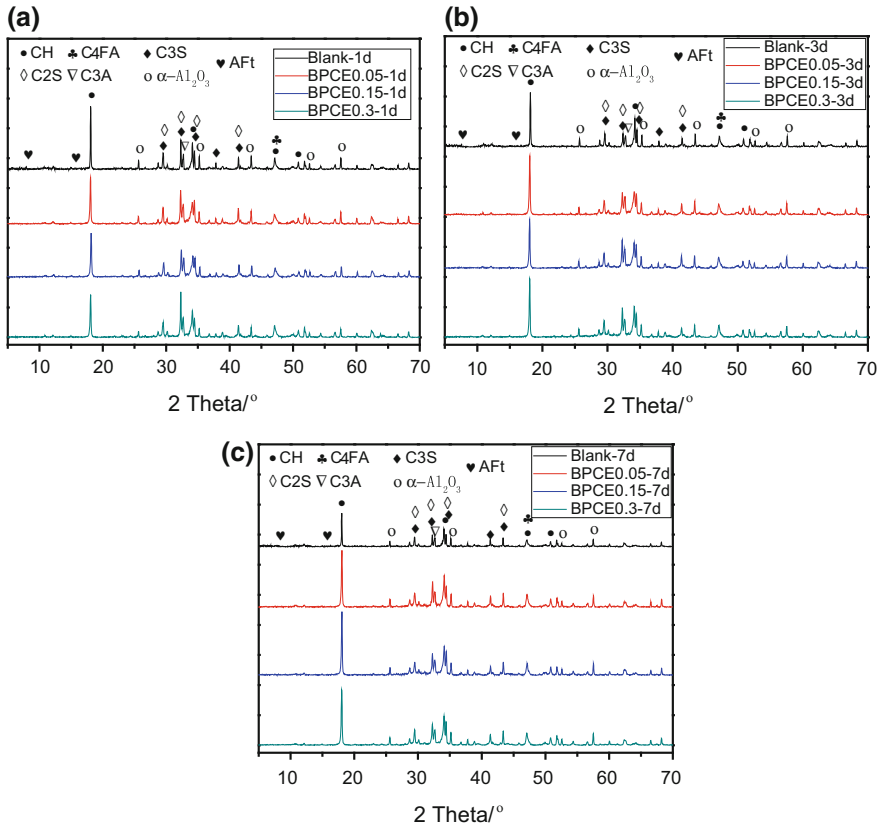

Fig. 5 XRD patters of cement pastes in absence of presence of BPCE at **a** 1d. **b** 3d. **c** 7d

further adsorb on the surfaces of cement particles. This is well correlated to the fluidity results.

XRD Analysis. XRD patterns of cement pastes in absence or presence of BPCE at different curing ages are shown in Fig. 5.

It is clearly seen that the intensity of $Ca(OH)_2$ peak in presence of BPCE is found to be lower than that in absence of PCE, indicating a significant retardation effect. It is mainly because the formed calcium chelated complexes decrease the production of hydrated $Ca(OH)_2$. This effect is more prominent at the TGA/IPEG proportion of 0.15. However, the intensity of $Ca(OH)_2$ peak in absence or presence of BPCE seems to be identical at the hydration age of 7d, showing that the inhibition of hydration for BPCE is mainly reflected at early hydration ages. This is also in line with the fluidity results.

Conclusion

(1) A series of BPCE with different molecular weights were synthesized by polymerizable active center, IPEG and AA, by means of changing the amount of chain transfer agent in the polymerization stage.
(2) The results of IR spectra confirm the existences of branched structure and characteristic functional groups, and the results of molecular weight shows that BPCE processing different molecular weights can be synthesized through changing the proportion of TGA/IPEG.
(3) With the increase of TGA/IPEG proportion from 0.05 to 0.30, the paste fluidity and adsorption amount for BPCE both show a trend of first increase and then decrease, and reach a maximum at the TGA/IPEG proportion of 0.15, which corresponds the molecular weight of 96314 g/mol.
(4) The introduction of BPCE can strongly retard the cement hydration, but only be limited at early hydration ages. It is more noticeable at the TGA/IPEG proportion of 0.15, which is well consistent with the above results.

Acknowledgements The authors would like to acknowledge the National Natural Science Foundation of China (Grant number: 51578025), Beijing Natural Science Foundation (Grant number: 2162007), Project of Science and Technology Plan of Beijing Municipal Commission of Education (Grant number: KM201510005003) and Rixin Talent Development Project of Beijing University of Technology (Grant number: 2015-RX-L09) for financing this research work.

References

1. P.C. Aïtcin, Cements of yesterday and today: concrete of tomorrow. Cem. Concr. Res. **30**(9), 1349–1359 (2000)
2. W.G. Shen, Y. Liu, L.H. Cao, X.J. Huo, Z.G. Yang, C.C. Zhou, P.T. He, Z.L. Lu, Mixing design and microstructure of ultra high strength concrete with manufactured sand. Constr. Build. Mater. **143**, 312–321 (2017)
3. H. Uchikawa, Approaches to ecologically benign system in cement and concrete industry. J. Mater. Civ. Eng. **12**(4), 320–329 (2000)
4. Y.F. Houst, P. Bowen, F. Perche, A. Kauppi, P. Borget, L. Galmiche et al., Design and function of novel superplasticizers for more durable high performance concrete (superplast project). Cem. Concr. Res. **38**(10), 1197–1209 (2008)
5. J. Yamanaka, H. Matsuoka, H. Kitano, Revisit to the intrinsic viscosity-molecular weight relationship of ionic polymers: I. Viscosity behavior of dilute suspensions of ionic polymer latices. J. Colloid Interface Sci. **134**(1), 92–106 (1990)
6. GB/T 8077-2012, Method for testing uniformity of concrete admixture, 2012. http://cx.spsp.gov.cn/
7. A. Zingg, F. Winnefeld, L. Holzer, Adsorption of polyelectrolytes and its influence on the rheology, zeta potential, and microstructure of various cement and hydrate phases. J. Colloid Interface Sci. **323**(2), 301–312 (2008)

Influence of Synthesis Temperature on MnOx/TiO_2 SCR DENOx Catalyst Prepared with Acidolysis Residue

Suping Cui, Yeqiang Wan, Hongxia Guo, Yali Wang and Guolan Tian

Abstract This paper focused on MnOx/TiO_2 SCR DENOx catalytic materials prepared with acidolysis residue (a solid waste which was generated during the sulfate process of the titanium oxide industry), and investigated the influence of synthesis temperature on catalytic properties and microstructure of the catalytic materials. Two different synthesis temperatures including ambient temperature and 80 °C were employed to prepare the catalytic materials. The modifications of textural, surface properties and catalytic activity of catalyst prepared at different temperatures were compared. Results showed that the catalyst prepared by precipitation method at room temperature (ammonia-hydrogen peroxide was used as precipitant and the calcination temperature is 250 °C), leads to a higher NOx conversion rate. The NOx conversion at 100 °C is 80%, even 95% at 130 °C. Results from XRD analysis indicate that the catalyst synthesized at room temperature results in a less sharp peak of Mn_3O_4. The active substances of manganese oxides are highly dispersed on the surface of the catalytic materials in amorphous state. Furthermore, H_2-TPR demonstrates that the catalyst synthesized at room temperature has a higher redox activity and the MnO_2 phase occupies the leading position of MnOx, which contributes to the excellent NOx conversion rate of the catalytic.

Keywords Acidolysis residue · SCR · MnOx/TiO_2 · Synthesis temperature

S. Cui (✉) · Y. Wan · H. Guo · Y. Wang · G. Tian
College of Materials Science and Engineering, Beijing University of Technology, Beijing 100124, China
e-mail: cuisuping@bjut.edu.cn

Y. Wan
e-mail: 717251961@qq.com

Y. Han (ed.), *Advances in Energy and Environmental Materials*,
Springer Proceedings in Energy, https://doi.org/10.1007/978-981-13-0158-2_80

Introduction

Selective catalytic reduction (SCR) is an efficient environmental protection technology in the industry of NOx emission reduction field, and making the proper low temperature catalytic materials is the core mission of SCR technology. MnOx/TiO_2 catalysts have good low temperature activity of denitration, generally using titanium dioxide as raw material. Due to the process is not mature and the cost is high, therefore has not been applied to practical engineering. And the production of titanium dioxide is a process that needs constant purification, which consuming a large amount of energy, also producing much waste and environmental pollution (the production of 1 t titanium dioxide will generate 8–10 t waste sulfuric acid and the total theoretical energy consumption is 1.6619×10^7 kJ) [1, 2], so the acidolysis residue utilization and treatment are of great importance to the protection of the environment.

The research on manganese-based low-temperature SCR catalysts at home and abroad is mainly focused on manganese-based composite oxide catalysts or supported manganese-based catalysts with manganese oxide as active components. The studies of Min et al. [3] have shown that Cu oxide can improve the specific surface area of the catalytic material, and then improve its low temperature denitrification activity. Li et al. [4], Ettireddy et al. [5] prepare the MnOx/TiO_2 catalysts by impregnation method have a denitrification efficiency of 80% or more at a low temperature of about 150 °C, and the manganese oxide in the catalytic material is mainly in the form of MnO_2 and Mn_2O_3.

In this study, acidolysis residue was used as raw material. The MnOx/TiO_2 catalyst was prepared by using the co-precipitation method [6] with simple process and preparation conditions without strict control. The effect of synthesis temperature on the denitrification activity of MnOx/TiO_2 catalyst and its microstructure were studied.

Experimental

Catalyst Preparation. The supporter is industrial grade raw materials acidolysis residue, take from Panzhihua Titanium Science and Technology Co., Ltd, its chemical composition is shown in Table 1. The test reagents are manganese acetate ($C_4H_6MnO_4{\cdot}4H_2O$), aqueous ammonia, 30% hydrogen peroxide, anhydrous ethanol.

Table 1 The chemical composition of acidolysis residue

	TiO_2	SO_3	MnO	Fe_2O_3	SiO_2	CaO
(wt%)	22.2370	18.8343	0.9559	8.8500	34.0827	8.4181

In this study, the catalysts were prepared at room temperature and 80 °C by a co-precipitation method. The acidolysis residue was grinded for 45 min with the addition of grinding agent triethanolamine. Finally, it is screened through mesh size of 200. After suspension of acidolysis residue and aqueous solution of manganese acetate were mixed (the mole ratio of Mn/(Ti + Si) was 0.6), aqueous ammonia was added to the mixed solution slowly, control the pH of the solution reached 10–11. After 30 min of stirring, 30% hydrogen peroxide was added to the solution until the color uniform and no longer change. The resulting precipitate was aged for 0.5 h, filtered and washed several times with distilled water and anhydrous ethanol. The cake was dried in air at 90 °C for 12 h and calcined at 250 °C for 3 h.

Catalyst Characterization. XRD spectra was measured with a XRD-7000 diffractometer using CuK-α radiation. Full scans of 20–80° were measured with a scan rate of 1 deg/min. The surface atomic state of every catalyst prepared at different temperature was demonstrated by X-ray photoelectron spectroscopy (XPS). The reducibility of catalysts was determined by the Temperature Programmed Reduction (H_2-TPR) experiment. The catalysts were pretreated at 250 °C in a N_2 stream (100 ml/min) for 1 h. Then the TPR experiment was performed from 100 to 700 °C in a mixed flow of 50% H_2, and the heating rate was 5 °C min^{-1}.

Activity Measurements. The denitrification activity of the catalytic material was tested using a self-designed SCR reactor and detection device. The prepared powdered catalytic material was pelletized: using a tabletting machine under a pressure of 5 MP, after crushing into pellets, selected the particles between 40 and 80 mesh sieve for testing, take 3 ml of the sample for SCR reaction. Simulated flue gas and testing conditions were as follows: The reaction temperature was generally 90–350 °C, the total flow rate was 2000 ml/min, airspeed was 27000 h^{-1}, NO concentration was 1000 ppm, NH_3 concentration was 1000 ppm, 5% O_2, N_2 as balance. The NOx conversion was calculated according to Eq. (1).

$$\text{NOx conversion} = \frac{([\text{NOx}]\text{in} - [\text{NOx}]\text{out})}{[\text{NOx}]\text{in}} \times 100\% \quad (1)$$

The $[NOx]_{in}$ and $[NOx]_{out}$ are the NOx concentration at the inlet and outlet respectively.

Result and Discussion

Catalytic Performance. Figure 1 shows the NOx conversion over $MnOx/TiO_2$ catalysts prepared at different temperatures with increasing temperature in NH_3–SCR reaction. As can be seen from Fig. 1, the synthetic temperature can significantly effect the SCR activity of $MnOx/TiO_2$ catalyst. The $MnOx/TiO_2$ catalyst prepared at room temperature shows the highest activity and selectivity in a

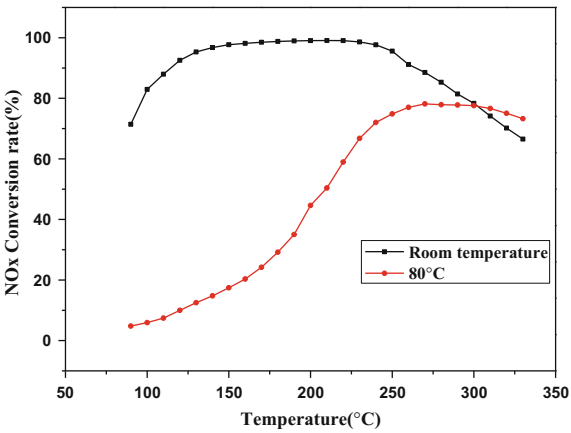

Fig. 1 The influence of synthesis temperature to SCR activity of catalysts

wide temperature range with NOx conversion above 95% from 150 to 250 °C. However, the NOx conversion of the catalyst prepared at 80 °C is much smaller than that of the catalysts prepared at room temperature. In the denitrification reaction, with the increase of the reaction temperature, on the one hand, the denitration activity of the catalyst is improved and the NOx conversion rate is increased, on the other hand, the oxidation reaction of NH_3 is increased and the N_2 selectivity is decreased, resulting in the decrease of NOx conversion [7].

X-Ray Diffraction. Powder XRD patterns of various MnOx/TiO_2 catalysts samples are shown in Fig. 2. As we can see, Fe_2O_3 and rutile TiO_2 can be detected, and accompanied by weak diffraction peaks of anatase TiO_2, SiO_2 and Mn_3O_4. It is found that the catalysts prepared at room temperature have a weak diffraction peak of Mn_3O_4. Indicating that the active material MnOx is more likely to exist in an amorphous state, which play a greater role in denitrification [8]. The increase in

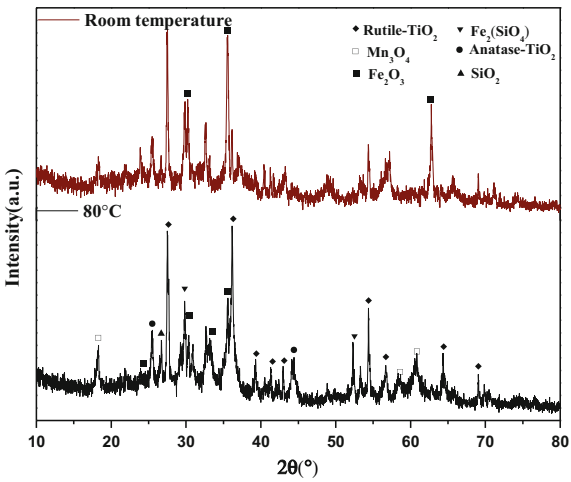

Fig. 2 XRD patterns of catalysts by acidolysis residue

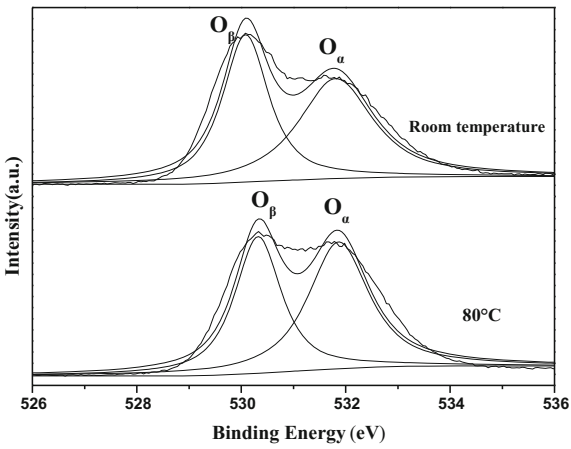

Fig. 3 O1s-XPS spectra of catalysts by acidolysis residue

oxygen vacancy is due to the highly dispersed of MnOx, leads to a higher NOx conversion rate [9]. This also explains that the catalytic material produced at room temperature has a higher activity. The weak peaks of Mn_3O_4 are due to the oxidation of hydrogen peroxide, and the catalytic material may also have other amorphous states of MnOx.

X-Ray Photoelectron Spectroscopy. XPS spectra of O1 s for the various MnOx/TiO_2 catalysts prepared at different temperature are presented in Fig. 3. It can be seen that the intensity of the peaks around O1 s decrease greatly with the improvement of preparation temperature. Oxygen on the surface of the catalytic material can be divided into the lattice oxygen O^{2-} (denoted as Oα) and surface chemisorbed oxygen (denoted as Oβ) [10]. The ratio of Oα/(Oα + Oβ) for catalyst prepared at room temperature is higher than catalyst prepared at 80 °C, suggesting that the lower temperature make the catalyst has more surface chemisorbed oxygen. A large number of chemical adsorption oxygen on the surface of the catalytic material can lead to the formation of Brønsted acid sites. The high concentration ratio of Oα/(Oα + Oβ) on the catalyst surface can be associated with high SCR activity [11].

X-ray photoelectron spectroscopy (XPS) was used to detect the elemental concentration on the surface of catalytic materials synthesized at room temperature, the results are showed in Table 2. The molar ratios of Mn/Ti in catalytic materials prepared at room temperature and 80 °C were 27.94 and 9.84, respectively, indicating that Mn atoms in the catalysts prepared at room temperature are easy to disperse on the surface of the catalysts.

H_2-TPR Analysis. To investigate the reducibility of MnOx/TiO_2 catalysts, H_2-TPR experiments were conducted and the results are shown in Fig. 4. As we can see, there are three peaks of the reduction process, corresponding to 359, 457 and 530 °C, respectively. These three reduction peaks corresponding to the reduction process of $MnO_2 \rightarrow Mn_2O_3$, $Mn_2O_3 \rightarrow Mn_3O_4$ and $Mn_3O_4 \rightarrow MnO$ [12, 13]. And it can be seen that the area of $MnO_2 \rightarrow Mn_2O_3$ reduction peak of catalytic material prepared

Table 2 Atom concentrations on the surface of catalysts determined by XPS

Catalyst	Metal content (at%)				
	Mn	Ti	Mn/Ti	O_t	O_α/O_t
Room temperature	19.00	0.68	27.94	80.32	54.63
80 °C	19.68	2.00	9.84	68.32	52.02

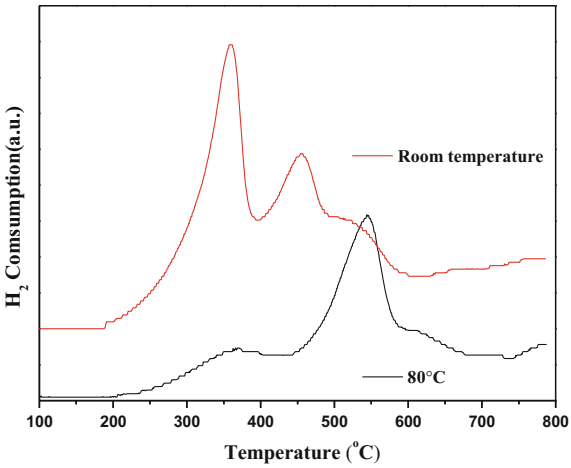

Fig. 4 H_2-TPR of catalysts by acidolysis residue

at room temperature is the largest, indicating that MnO_2 is mainly composed of MnO_2. Previous study shows that the order of activity of manganese oxide in different valence states is: $MnO_2 > Mn_5O_8 > Mn_2O_3 > Mn_3O_4 > MnO$. This should be the main reason that the catalytic material has low temperature and high SCR denitration catalytic activity, not only Mn of the redox ability to increase, more importantly, but MnO_2 phase occupy the dominant position.

Conclusions

In this study, the $MnOx/TiO_2$ catalyst prepared at room temperature exhibited excellent catalytic activity compared to the catalytic material prepared at 80 °C. The activity of the catalysts can achieve nearly 95% at the temperature range of 150–250 °C. The Mn_2O_3 and MnO_2 in the catalysts material prepared at room temperature might be in amorphous form. MnO_2 plays a major role in the NOx removal process. The lower synthesis temperature is favorable to increase the proportion of MnO_2 in the manganese oxide while increasing the dispersion of the manganese oxide on the surface of the carrier, thereby improving the catalyst activity.

References

1. W.Q. Tang, J.B. Zhang et al., Energy consumption analysis and comments of manufacturing titanium dioxide by sulfuric acid process and chloride process. Inorg. Chem. Ind. **43**(6), 7–9 (2011)
2. J.W. Wang, X.L. Ren, Q.F. Wei et al., Current research situation and prospect for comprehensive utilization of waste acid from titanium dioxide production. Inorg. Chem. Ind. **41**(9), 4–7 (2009)
3. K. Min, E.D. Park, M.K. Ji et al., Cu–Mn mixed oxides for low temperature NO reduction with NH_3. Catal. Today **111**(3–4), 236–241 (2006)
4. J.H. Li, J.J. Chen, R. Ke et al., Effect of precursors on the surface Mn species and the activities for NO reduction over MnOx/TiO_2 catalysts. Catal. Commun. **8**(12), 1896–1900 (2007)
5. P.R. Ettireddy, N. Ettireddy, S. Mamedov et al., Surface characterization studies of TiO_2 supported manganese oxide catalysts for low temperature SCR of NO with NH_3. Appl. Catal. B **76**, 123–134 (2007)
6. C. Liang, J.H. Li, M.F. Ge et al., Mechanism of selective catalytic reduction of NOx with NH_3 over CeO_2–WO_3 catalysts. Chin. J. Catal. **32**(5), 836–841 (2011)
7. F. Liu, H. He, C. Zhang et al., Selective catalytic reduction of NO with NH_3 over iron titanate catalyst: catalytic performance and characterization. Appl. Catal. B **96**(3–4), 408–420 (2010)
8. G. Qi, R.T. Yang, Performance and kinetics study for low-temperature SCR of NO with NH_3 over MnOx–CeO_2 catalyst. J. Catal. **217**(2), 434–441 (2003)
9. S.M. Saqer, D.I. Kondarides, X.E. Verykios, Catalytic oxidation of toluene over binary mixtures of copper manganese and cerium oxides supported on γ-Al_2O_3. Appl. Catal. B **103**(3–4), 275–286 (2011)
10. L.J. Zhang, S.P. Cui, H.X. Guo et al., The influence of K^+ cation on the MnOx–CeO_2/TiO_2 catalysts for selective catalytic reduction of NOx with NH_3 at low temperature. J. Mol. Catal. A: Chem. **390**, 14–21 (2014)
11. M. Kang, E.D. Park, J.M. Kim et al., Manganese oxide catalysts for NOx reduction with NH_3 at low temperatures. Appl. Catal. A **327**(2), 261–269 (2007)
12. A. Gil, L.M. Gandía, S.A. Korili, Effect of the temperature of calcination on the catalytic performance of manganese and samarium–manganese-based oxides in the complete oxidation of acetone. Appl. Catal. A **274**(1–2), 229–235 (2004)
13. T. Mishra, P. Mohapatra, K.M. Parida, Synthesis, characterisation and catalytic evaluation of iron–manganese mixed oxide pillared clay for VOC decomposition reaction. Appl. Catal. B **79**(3), 279–285 (2008)

Mechanism of SO_2 Influence on Mn/TiO_2 for Low Temperature SCR Reaction

Lu Wei, Suping Cui, Hongxia Guo, Xiaoyu Ma and Boxue Sun

Abstract Mn-based catalysts extremely restricted with the deactivation by SO_2. In this paper, catalysts of Mn/TiO_2 prepared by co-precipitation method for low temperature selective catalytic reduction (SCR) of NO with NH_3 under the influence of SO_2. For Mn/TiO_2, NO conversion decreased rapidly from 90% to about 55% at 200 °C in the presence of SO_2. We reveal the mechanism of SO_2 effect on the adsorption of NH_3 and NO based on DRIFT and TPD. The result show that SO_2 can reduce the adsorption amount of NH_3 on the Lewis acid sites and react with NH_4^+ to form NH_4HSO_3 on the Brønsted acid sites. In the meantime, SO_2 can inhibit the adsorption of NO took part in the SCR reaction on the surface of catalyst due to the mechanical of competitive adsorption. These poisoning phenomenon of SO_2 hinder the proceeding of SCR reaction.

Keywords Low temperature SCR · $MnOx/TiO_2$ · SO_2 · DRIFT · TPD

Introduction

Selective catalytic reduction (SCR) of nitrogen oxide with ammonia has already been considered the major technology for the removal of nitrogen oxide [1]. The activity of SCR catalyst is one of the most key factors in the process of NO_x reduction [2]. The conventional SCR catalyst is mainly based on V_2O_5/TiO_2, which have to be placed upstream of particulate control device to meet its high operating temperature.

L. Wei · S. Cui (✉) · H. Guo · X. Ma · B. Sun
Beijing University of Technology, Beijing 100124, China
e-mail: cuisuping@bjut.eedu.cn

L. Wei
e-mail: weilu0529@emails.bjut.edu.cn

H. Guo
e-mail: hxguo@bjut.edu.cn

Y. Han (ed.), *Advances in Energy and Environmental Materials*,
Springer Proceedings in Energy, https://doi.org/10.1007/978-981-13-0158-2_81

Mn-based catalysts are expected to be applied for removing NO_x in cement industry due to its better low-temperature activity. Wu et al. [3] reported that Mn/TiO_2 catalysts appeared high activity at low temperature and the higher N_2 selectivity. Our previous study showed that the NO conversion of Mn/TiO_2 catalyst near at 150 °C could obviously increase to 87% [6]. However, there is still certain amount of SO_2 in the flue gas, which could have a serious poisoning effect on SCR catalytic activity in the low temperature. Kijlstra et al. [4] have reported that the poisoning SO_2 can weakened the activity of Mn/TiO_2 catalysts. Therefore, improving sulfur tolerance of Mn-based catalysts is significant for its practical usage. There were few reports on this issue. We aim to solve the problem. In our previous studies [5], it was found that the difference adsorption strength of NH_3 and NO_x on the catalytic reaction plays an important role, which has provided the basis for further exploring the reaction rate. Therefore, in this paper, we explore the SO_2 effect on adsorption of NH_3 and NO_x for the low temperature SCR reaction based on Diffuser Reflection Infrared Fourier Transform (DRIFT) and Temperature Programmed Desorption (TPD). We expect that the results present herein will be helpful in promoting sulfur-resistant of Mn-based catalysts.

Experimental

Catalytic Preparation. The Mn/TiO_2 catalysts were prepared by the co-precipitation method as we previously reported [6]. After aqueous solutions of titanium sulfate, manganese acetate were pre-mixed under vigorous stirring at 60 °C, carbamide solution, ammonia (25 wt%), hydrogen peroxide was continuously added to the mixed nitrate solution. The precipitates were collected by centrifugation and washed using distilled water for two times and ethanol for two times. The mixture was dried at 100 °C for 24 h to remove residual water and ethanol, and then, the solid were calcined at 400 °C for 6 h in air in a tubular furnace after that the solid was crushed and sieved to 40–60 mesh.

Catalytic Activity Measurement. SCR reaction was performed on a fixed-bed quartz tube reactor. The thermocouple was projected directly into the center of the reactor to measure the reaction temperature. The total flow rate was 200 ml min^{-1}. The reactant gas condition was: 1000 ppm NH_3, 1000 ppm NO, 200 ppm SO_2 5% O_2 and N_2 balance. The corresponding gas hourly space velocity (GHSV) was 40 000 h^{-1}, and the range of reaction temperature was controlled by a tubular furnace from 90 to 300 °C with a step of 30 °C. The concentrations of NO, NO_2, NH_3, SO_2 were continually monitored by an FTIR spectrometer (Bruker, Germany). The percent conversion of NO was calculated as follows:

$$\text{NO conversion} = 100 \times ([NO]_{in} - [NO]_{out})/[NO]_{in} \quad (1)$$

where $[NO]_{in}$ is the inlet concentration of NO, and $[NO]_{out}$ is the outlet concentration of NO.

Catalyst Characterizations. FTIR spectra were acquired using in situ DRIFT cell equipped with gas flow system. The DRIFT measurements were performed whit KaBr windows coupled to BRUKE VERTER 72 spectrometers. Prior all experiments, the sample was treated at 400 °C in He stream for 2 h, then cooled to 180 °C. All the spectra were recorded at this temperature. In DRIFT cell, the gas flow rate was 30 mL/min. The background spectrum was recorded with the flowing of He and was subtracted from the sample spectrum.

Temperature programmed desorption (TPD) were carried out on the 1100 Series TPDRO (Thermo USA) instrument. For NH_3–TPD experiments, after pretreated in N_2 at 500 °C for 1 h, catalysts were saturated with anhydrous NH_3 (4% in N_2) at a flow rate of 30 ml min^{-1} for about 30 min. Desorption was performed by heating the sample in N_2 (30 ml/min) from 100 to 800 °C (5 °C min^{-1}).

Results and Discussion

Effect of SO_2 on NO Conversion. The effect of SO_2 on SCR activity of Mn/TiO_2 is illustrated in Fig. 1. When SO_2 did not exist in the system, Mn/TiO_2 catalysts had considerable activity that NO conversion could be approximately 90% at 200 °C. After 200 ppm SO_2 was introduced into reactor, NO conversion decreased rapidly from 90% to about 55% at 200 °C. This result indicated that the presence of SO_2 showed an apparent deactivation of the SCR reaction for two Mn/TiO_2 catalysts. According to Tang [7], the deactivation mechanism of SO_2 on the SCR reaction could be mainly due to the sulfation of active phase. Some authors have

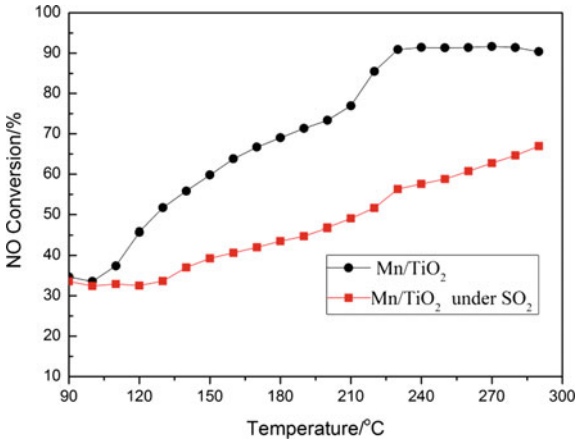

Fig. 1 Effect of SO_2 on NO conversion for Mn/TiO_2 catalyst

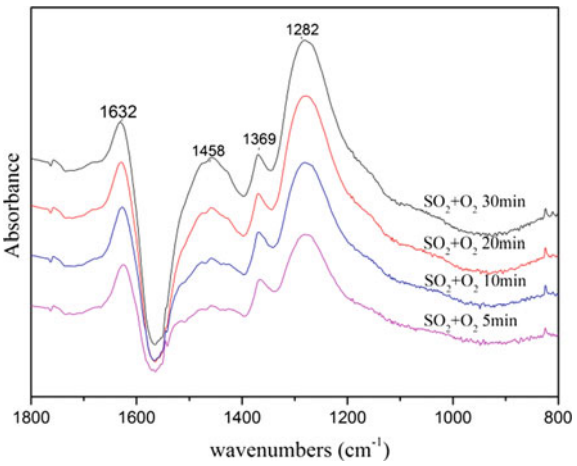

Fig. 2 DRIFT spectra of Mn/TiO_2 catalyst in the flow of 200 ppm SO_2 at 180 °C for different times

reported that a SO_2 deactivation mechanism for NH_3-SCR catalysts was due to the deposition of ammonium sulfate. In this paper, DRIFT and TPD was used to study the mechanism of SO_2 poisoning.

Sulfur Dioxide Adsorption. To investigate the existence states of sulfates for understanding the interaction between sulfates and sample, SO_2 adsorption on Mn/TiO_2 catalysts in the presence of O_2 was observed first. Figure 2 shows the DRIFT spectra when the sample was exposed to SO_2 + O_2/He for different times. Several bands at 1282, 1369, 1458 and 1632 cm^{-1} were detected for SO_2 adsorption on the Mn/TiO_2 catalysts. The band at 1282 cm^{-1} was assigned to the stretch motion of bulk-like sulfates and the intensity increased with time. We suspect that bulk-like sulfates was due to the sulfation of manganese oxides. The band at 1369 cm^{-1} was assigned to asymmetric vibration of surface sulfate species with covalent S=O=S [8]. Bands at 1458 cm^{-1} was result of SO_3 species absorbed on surface of catalyst. The band at 1632 cm^{-1} was attributed to absorption of HSO_4^- due to the reaction of SO_2 and surface hydroxyl groups [9].

Effect of SO_2 on NH_3 Adsorption. In this part of the study, the catalyst was first treated by 500 ppm of SO_2 and 3% of O_2 for 30 min followed by He purging for 30 min. This method was used to simulate the sulfuration process of Mn/TiO_2 catalysts. The NH_3 adsorption on pre-treated Mn/TiO_2 catalysts was compared with that of fresh sample to investigate the influence of sulfation on NH_3 adsorption.

Figures 3 and 4 show in situ DRIFT spectra of adsorption of NH_3 on Mn/TiO_2 and pre-treated Mn/TiO_2 at 180 °C, respectively. After the adsorption of NH_3 over Mn/TiO_2, several characteristic band at 1171, 1602, 3259, 3378 cm^{-1} were detected. the band at 1171 cm^{-1} were attributed to the formation of coordinated NH_3 on Lewis acid sites [10], while the band at 1602 cm^{-1} was attributed to ionic NH_4^+ bound to Brønsted acid sites [11]. The band at 3259 cm^{-1} was attributed to symmetric stretching of NH_3 bound to Lewis acid sites, while the band at 3378 was

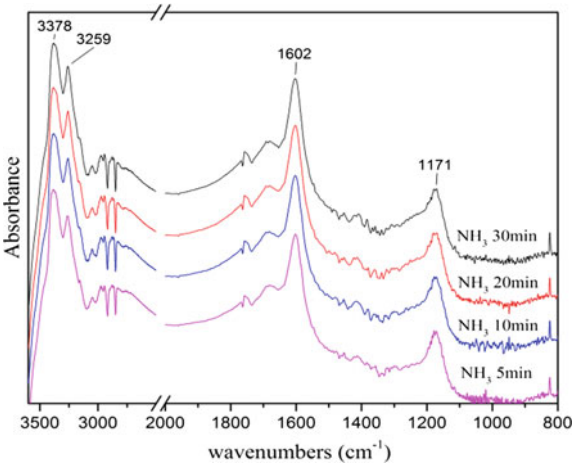

Fig. 3 DRIFT spectra of NH_3 on fresh Mn/TiO_2 catalyst at 180 °C for different times

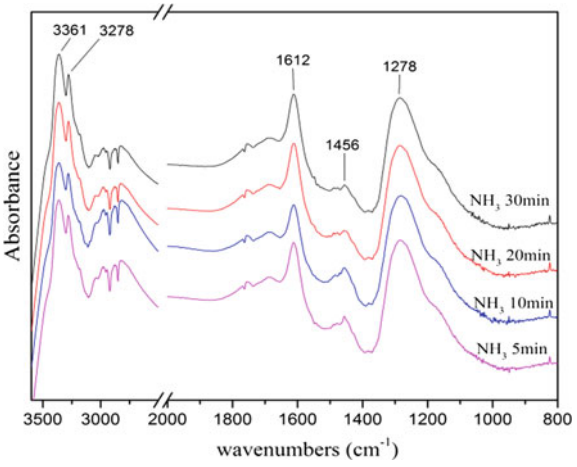

Fig. 4 DRIFT spectra of NH_3 pre-treated Mn/TiO_2 catalyst at 180 °C for different times

assigned to asymmetric stretching of NH_3 coordinated to Lewis acid sites [12]. Therefore, there were two NH_3 adsorption methods for this catalysts, coordinated NH_3 formed on the manganese (Lewis acid sites) and NH_4^+ formed on the oxygen surface groups (Brønsted acid sites). As compared with Fig. 4 the introduction of NH_3 onto pre-treated Mn/TiO_2, the initial peak at 1171 cm^{-1} due to Lewis acid sites vanished, and new band at 1278 and 1456 cm^{-1} was formed. The two new peak corresponded to bidentate sulfate and NH_3 adsorbed on Brønsted acid sites respectively [13] assigned to Brønsted acid sites were sharply weakened. These implied that the formed sulfate species on Mn/TiO_2 surface could sharply weakened the Lewis acid sites and produce new Brønsted acid sites.

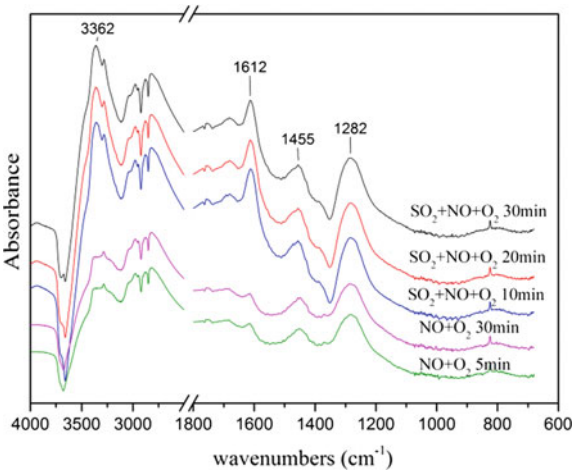

Fig. 5 DRIFT spectra of Mn/TiO_2 exposed to 1000 ppm NO followed by the introduce of 200 ppm SO_2 at 180 °C

Competitive Adsorption Between SO_2 and NO. Figure 5 shows the competitive adsorption between SO_2 and NO on Mn/TiO_2. When the catalyst was exposed to 1000 ppm NO + 2% O_2 for 30 min, the band at 1282, 1455, 1612, 3362 cm^{-1} appeared. The band at 1282, 1455 cm^{-1} could be attributed to monodentate nitrate on catalyst surface [14]. The band at 1612 cm^{-1} was attributed NO_2, which was due to NO oxidized by catalyst. The negative band around 3709 cm^{-1} appeared, which could assign to the surface hydroxyl. As we mentioned above, the band at 1282, 1455, and 1612 cm^{-1} were assigned to the stretch motion of bulk-like sulfates, SO_3 species and HSO_4^- respectively. We could find that the characteristic peaks of NO adsorption are similar with SO_2. After the introduction of SO_2, the intensity of the main characteristic peaks (1282, 1455, 1612 cm^{-1}) was larger than before. The reason of this result might be that both of SO_2 and NO were apt to be adsorbed on the same active sites on catalysts surface and the adsorption ability of SO_2 was much higher than NO. Consequently, we can propose that the adsorption capacity of NO on the Mn/TiO_2 surface would be declined significantly in the presence of SO_2.

NH_3-TPD Analysis. Figure 6 shows the NH_3-TPD curves for fresh and pre-treated Mn/TiO_2 catalysts. The acid sited in which NH_3 was adsorbed was significant in the SCR reaction. For fresh catalysts, the peak in 200–400 °C were assigned to NH_3 desorbed by Brønsted acid sites. With increasing desorption temperature, one broad desorption was present in 590–690 °C, which was attributed to NH_3 molecules adsorbed by Lewis acid sites. The NH_3 desorption curve of pre-treated Mn/TiO_2, which was first exposed to 500 ppm SO_2 for 30 min, was much different with fresh simple. Although the main NH_3 desorption peaks of two simple were at the same positions, the intensity of the peaks was different obviously. Comparing with fresh catalyst, the pre-treated catalyst showed the stronger peak at low temperature and weaker peak at high temperature, which implied that SO_2 poisoning improved the quantity of weak acid sites (Brønsted acid sites) and reduced the quantity of strong acid sites (Lewis acid sites). We get the similar result in the part of DRIFT study.

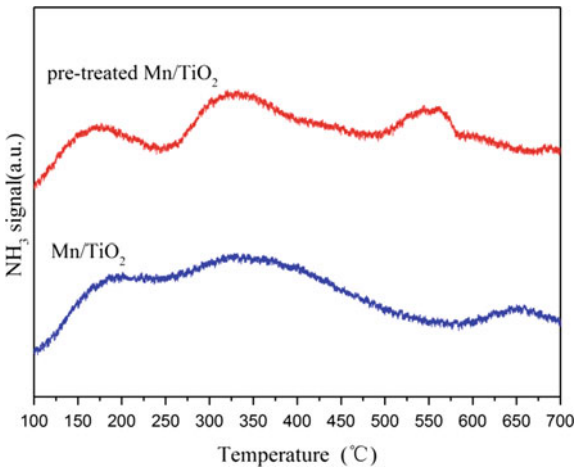

Fig. 6 TPD patterns of Mn/TiO_2 catalysts

The results above could be explained as follows: SO_2 were more capable of occupying the Lewis acid sites than NH_3, which inhibited the adsorption of NH_3 in the SCR reaction. NH_3 could react with SO_2 to form NH_4HSO_3 on the Brønsted acid sites, which led to increase of NH_3 adsorbed on Brønsted acid sites.

Conclusions

SO_2 can react with manganese oxides to form sulfate on the surface of Mn/TiO_2 catalyst. For NH_3 adsorption, the presence of SO_2 can reduce the adsorption amount of NH_3 on the Lewis acid sites due to the sulfation of active components manganese. Simultaneously, SO_2 is adsorbed on Brønsted acid sites form HSO_3^-, which can react with NH_4^+ to form NH_4HSO_3 and results in the blocking of microfiltration. For NO adsorption, SO_2 is more capable of occupying the active site than NO, which inhibit the adsorption of NO in the SCR reaction. For that reason, Mn/TiO_2 catalyst shows lower NO conversion in the low temperature SCR reaction under effect of SO_2.

Acknowledgements The project of financially supported by the National Natural Science Foundation of China (Grand No. 51502008).

References

1. Z.G. Huang, Z.P. Zhu, Z.Y. Liu, Q.Y. Liu, J. Catal. **214**, 213–219 (2003)
2. L.Z. Zhang, S.P. Cui, H.X. Guo, X.Y. Ma, X.G. Luo, J. Mol. Catal. A. Chem. **390**, 14–21 (2014)
3. Z.B. Wu, R.B. Jin, Y. Liu, H.Q. Wang, Catal. Commun. **9**, 2217–2220 (2008)

4. W.S. Kijlstra, M.B. Biervliet, E.K. Poels, A. Bliek, Appl. Catal. B **16**, 327–337 (1998)
5. L.J. Zhang, S.P. Cui, H.X. Guo, X.Y. Ma, L. Wei, Comp. Mater. Sci **112**, 238–244 (2016)
6. L.J. Zhang, S.P. Cui, H.X. Guo, X.Y. Ma, X.G. Luo, Appl. Surf. Sci. **355**, 1116–1122 (2015)
7. X. Tang, J. Hao, H. Yi, J. Li, Catal. Today. **126**, 406–411 (2007)
8. F.D. Liu, K. Asakura, H. He, W.P. Shan, X.Y. Shi, C.B. Zhang, Appl. Catal. B. **103**, 369–377 (2011)
9. W. Xu, H. He, Y. Yu, J. Phys. Chem. C. **113**, 4426–4432 (2009)
10. M.A. Larrubia, G. Ramis, G. Busca, Appl. Catal. B. **27**, 145–151 (2000)
11. S.D. Lin, A.C. Gluhoi, B.E. Nieuwenhuys, Catal. Today **90**, 3–14 (2004)
12. S. Sayan, M. Kantcheva, S. Suzer, D. Uner, J. Mol. Struct. **480–481**, 241–245 (1990)
13. S.D. Lin, A.C. Gluhoi, B.E. Nieuwenhuys, Catal. Today **90**, 3–14 (2004)
14. J.C.S. Wu, Y.T. Cheng, J. Catal **237**, 393–404 (2006)

Preparation of Micro-porous Chitosan Membrane and Its Adsorption Property for Cr(VI) Ions

Bingyang Sun, Zhenping Qin, Suping Cui, Yali Wang, Xiaoyu Ma and Hongxia Guo

Abstract Chitosan (CS) micro-porous membranes were prepared by blending-phase inversion method using chitosan as film-forming polymer, polyethylene glycol (PEG) as porogen and glycerol as plasticizer. Adsorption experiments were conducted under varied Cr(VI) ions concentration, pH values, contact time and temperature. The results indicated that when the ratio of chitosan to polyethylene glycol and glycerol was 1:0.5:0.5 at pH of 2.79, the prepared CS membrane exhibited the highest adsorption capacity of 168.41 mg g^{-1} under Cr(VI) ions concentration of 100 mg L^{-1}, contact time of 4 h, and membrane dosage of 10.0 mg. Langmuir and Freundlich adsorption models were applied to describe the equilibrium isotherms at different Cr(VI) ions concentrations. The equilibrium data was found to be fitted well to the Langmuir isotherm. Pseudo-first-order and pseudo-second-order kinetics models were used to describe the membrane adsorption.

Keywords Chitosan · Adsorption · Kinetics · Cr(VI) ions

Introduction

Chromium (Cr) and its compounds are important raw materials for metallurgical, metal processing, electroplating, printing and tanning industries. The waste emissions Cr-containing can't be degraded in the environment, and is only changed into

B. Sun · S. Cui · Y. Wang · X. Ma · H. Guo (✉)
College of Material Science and Engineering, Beijing University of Technology, Beijing 100124, China
e-mail: hxguo@bjut.edu.cn

B. Sun
e-mail: sunbingyang@emails.bjut.edu.cn

Z. Qin
Beijing Key Laboratory for Green Catalysis and Separation, College of Environmental and Energy Engineering, Beijing University of Technology, Beijing 100124, China

Y. Han (ed.), *Advances in Energy and Environmental Materials*,
Springer Proceedings in Energy, https://doi.org/10.1007/978-981-13-0158-2_82

other form, posing a serious threat the environment and human health [1]. The disposals and emissions of waste Cr-containing are strictly managed and controlled in Chinese "*national list of hazardous waste*". Thus, the effective methods to treat chromium-containing wastewater have attracted much attention.

The techniques to remove heavy metal ions from wastewater include chemical precipitation/ coagulation, ion exchange [2], membrane technology [3], electrolytic reduction [4] and adsorption [5]. Among them, the adsorption method showed advantages, such as simple operation, easy to use and unnecessary for complex equipment [6]. Typical adsorbents including chitosan beads, rubber wood activated carbon and cerium oxide have been explored for use in chromium removal [7–9]. However, the adsorption capacity of these adsorbents is too low due to their nonporous state. Chitosan (CS), the second most abundant biopolymer after cellulose, contains a large number of reactive groups, such as hydroxyl (–OH) and amine ($–NH_2$) groups, which has been utilized to remove dyes, metal ions, and proteins [10].

In this work, the micro-porous chitosan membrane was prepared by blending-phase inversion method using polyethylene glycol (PEG) as the porogen and glycerol (Gl) as the polyol plasticizer. The separation properties of the micro-porous membrane on Cr(VI) ions was evaluated under different conditions. Also, the adsorption isotherms and kinetics was investigated. This work would provide a new strategy with porous CS membrane for both efficiently adsorption and filtration of heavy metal ions.

Experimental

Materials. Chitosan (Mw 100 000–300 000 g/mol) obtained from Beijing Yi Nuokai Technology Co., Ltd. Polyethylene glycol (PEG, Mw 10,000) were purchased from Tianjin Guangfu Fine Chemical Research Institute. Glycerol, acetic acid and potassium dichromate were obtained from Beijing chemical plant.

Preparation of Chitosan Micro-porous Membrane. The aqueous PEG and glycerol solution was prepared by dissolving 0.5 g PEG in 50 mL of 2% (v/v) acetic acid solutions. After stirring for an hour, 1.0 g of chitosan was added into the solution, and then stirred at 50 °C for 24 h, and was degassed at room temperature for 3 h. Then, the solution were poured onto a glass plate to form a flat membrane. Next, the membrane was heated at 40 °C for 5 h and soaked in 4.0 wt% aqueous NaOH for 1 h. After that, the membranes were placed into distilled water at about 80 °C for over 12 h to dissolve the PEG component. Finally, the micro-porous chitosan membrane was obtained.

Evaluation on Adsorption Performance of Micro-porous Chitosan Membrane. Added 10.0 mg of the micro-porous chitosan membrane into 20 mL of different concentrations of Cr(VI) ions solution containing in an Erlenmeyer flask. After shaking in 150 rpm for fixed time, the membrane was taken out, and the Cr(VI)

ions concentration in the supernatant was measured by UV-visible spectrophotometer. The adsorption capacity was calculated according to the following equation:

$$q_e = \frac{(C_0 - C_e)V}{M}. \quad (1)$$

$$\eta = \frac{C_0 - C_e}{C_0} \times 100\%. \quad (2)$$

where Q (mg g^{-1}) is the amount of Cr(VI) ions adsorbed on the membrane, C_0 (mg L^{-1}) is the initial Cr(VI) ions concentration, C_e (mg L^{-1}) is the equilibrium Cr (VI) ions concentration in the solution, V (mL) is the volume of the used Cr(VI) ions solution, M (g) is the weight of the used membrane, and η is the Cr(VI) ions removal rate by the membrane.

Based on the measurement, the adsorption were further carried out at different temperatures (25, 35, 45 °C) to give the kinetic result.

Results and Discussion

The Morphology and Adsorption of the Chitosan Membrane. Figure 1 showed the SEM images of the prepared chitosan membranes. It can be seen that the chitosan membrane without PEG of pore former is much denser (Fig. 1a). After addition of PEG, with the ratio of chitosan to polyethylene glycol and glycerol is 1:0.5:0.3 ($CS_{0.3}$), a number of pores were observed on the membrane surface (Fig. 1b). The average pore size was about 0.3 μm; while the deeper pores formed and the pore size was about 0.6 μm (Fig. 1c) with the ratio of chitosan to polyethylene glycol and glycerol is 1:0.5:0.5 ($CS_{0.5}$). If further increase the ratio of chitosan to polyethylene glycol and glycerol, the obtained membrane become brittle

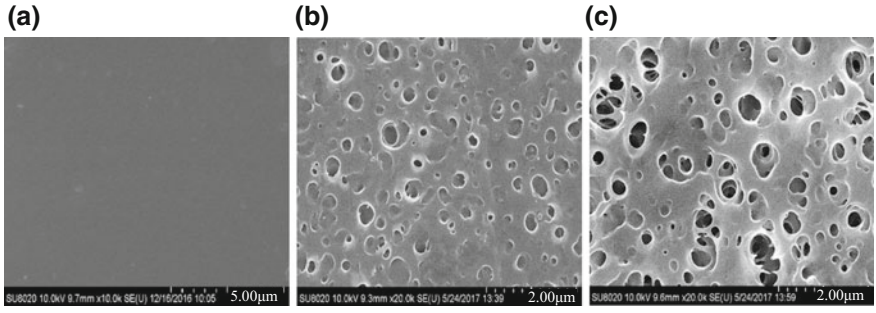

Fig. 1 SEM images of **a** the chitosan membrane, **b** micro-porous chitosan membrane ($CS_{0.3}$) and **c** micro-porous chitosan membrane ($CS_{0.5}$)

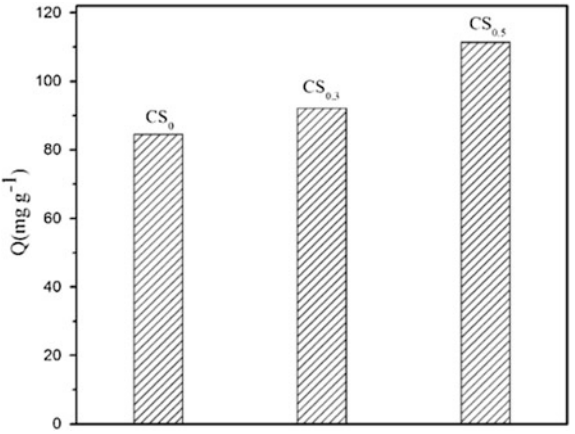

Fig. 2 The adsorption capacity of chitosan micro-porous membrane with different PEG content on chromium ions in one hour

due to serious phase separation of the blends lead to extremely weak mechanical properties of membranes.

The adsorption properties of the membrane shown in Fig. 2 indicated that within 1 h, the adsorption capacity of the nonporous dense membrane to Cr(VI) ions was 84.56 mg g^{-1}. While the adsorption capacity of the porous membrane with pore size of 0.6 μm was 111.44 mg g^{-1} under the same condition. This result showed that the micro-porous chitosan membrane showed a relatively higher adsorption of Cr(VI) ion due to its higher specific surface area.

Influence of pH Value of the Solution on Adsorption. The variation of Cr(VI) adsorption capacity with pH value were shown in Fig. 3. It can be seen that Cr(VI) adsorption capacity increased and then decreased with increasing pH value of the solution. The maximum adsorption of 168.41 mg g^{-1} and removal rate of 84.21% appeared at pH of 2.79, then the adsorption capacity decreased with increasing pH. This is attributed to that there is a balance between $HCrO^{4-}$ and $Cr_2O_7^{2-}$ under

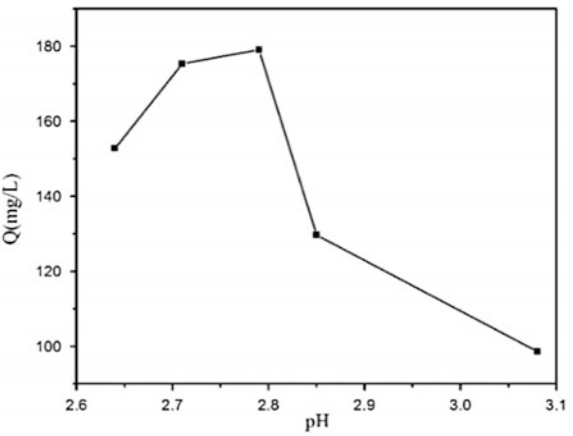

Fig. 3 Effect of pH value on Cr(VI) ions adsorption (Cr(VI) ions concentration: 100 mg L^{-1}, dosage of the membrane to solution: 10 mg/20 mL)

acidic condition. When the pH value increased, the equilibrium moved to $Cr_2O_7^{2-}$. When the protonated chitosan interact with Cr(VI), one adsorption site can adsorb one Cr(VI) in $HCrO^{4-}$ form; while if the protonated chitosan interact with CrO_4^{2-}, it is equivalent to adsorption half of Cr(VI) at the same adsorption site. Therefore, in the more acidic condition, the adsorption efficiency of the chitosan membrane was relatively higher than that on basic condition.

Adsorption Isotherms. The effects of Cr(VI) concentrations on the adsorption measured at 25 °C were shown in Fig. 4. Accordingly, the equilibrium concentration and the isothermal adsorption curve were calculated as shown in Fig. 5. The Langmuir and Freundlich adsorption of CS micro-porous membrane for Cr(VI) ions were showed in Fig. 5, respectively. Then, the isothermal parameters of the Langmuir and Freundlich equations calculated according to Ref. [11] were shown in Table 1. It can be seen that the linear R^2 coefficients for the Langmuir and

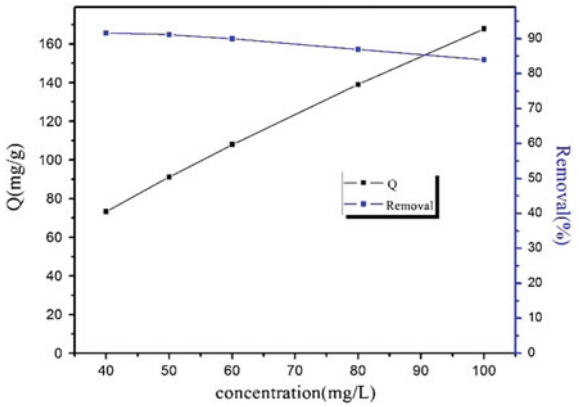

Fig. 4 Effect of initial concentration on Cr(VI) ions adsorption onto the $CS_{0.5}$ micro-porous membrane (contact time = 240 min, pH = 2.79 $CS_{0.5}$ dosage = 10 mg/20 mL)

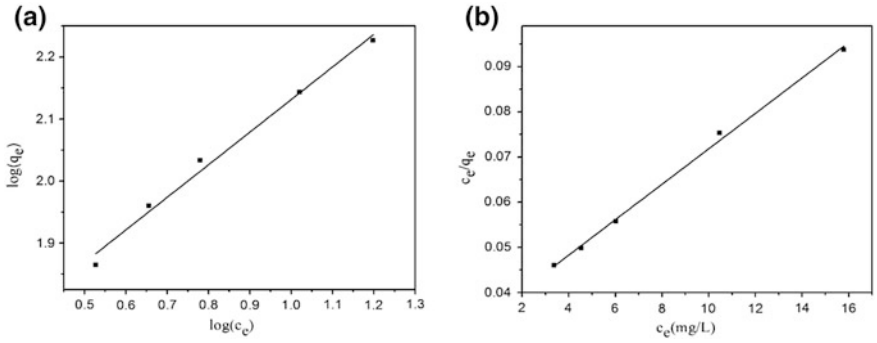

Fig. 5 Adsorption isotherms plot for Cr(VI) ions removal by $CS_{0.5}$ membrane: **a** Freundlich isotherm and **b** Langmuir isotherm

Table 1 Freundlich and Langmuir constants for the adsorption of Cr(VI)

Freundlich constants			Langmuir constants		
1/n	K_F (mg g^{-1})	R^2	q_m (mg g^{-1})	K_L (L mg^{-1})	R^2
0.5254	40.36	0.9899	256.41	0.1196	0.9976

Table 2 Comparison of adsorption capacities for Cr(VI) in aqueous solution with other works

Adsorbents	Sorption capacity (mg/g)	Solution pH	Reference
Hybrid membrane of carboxymethyl Chitosan and silicon dioxide	80.7	5.0	[12]
Magnetic chitosan resin	51.813	2.0	[13]
Chitosan/poly(vinyl alcohol)/yttrium(III) membrane	38.48	4.0	[14]
Micro-porous chitosan membrane	168.41	2.79	This work

Freundlich isotherms were 0.9976 and 0.9899, respectively. Hence, the Langmuir isotherm model was more suitable on Cr(VI) ions adsorption than Freundlich isotherm. The maximum adsorption capacity of Cr(VI) ions in the Langmuir isotherm is 256.41 mg g^{-1} (Table 2).

Adsorption Kinetics. The effect of contact time on Cr(VI) ions adsorption was investigated at Cr(VI) ions concentration of 100.0 mg L^{-1} and pH of 2.79 for 240 min. As shown in Fig. 6, at temperatures range from 25 to 45 °C, the adsorption capacity of chitosan to Cr(VI) ions increased with contact time. The maximum adsorption capacity appeared at 25 °C, because The hydrolysis reaction is an endothermic reaction, with the reaction of the temperature increasing towards $HCrO^{4-}$.

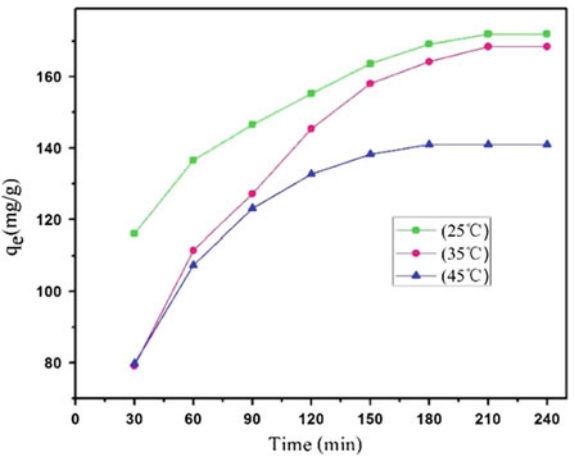

Fig. 6 Kinetic curves of Cr (VI) ions adsorption on chitosan micro-porous membrane

Table 3 Kinetic parameters for Cr(VI) ions adsorption onto $CS_{0.5}$ membrane

Temperature (K)	Pseudo-first-order		Pseudo-second-order	
	R^2	K_1 (min^{-1})	R^2	K_2 (g (mg min)$^{-1}$)
298	0.9455	0.01888	0.9983	2.3253×10^{-4}
308	0.9660	0.02004	0.9976	8.6802×10^{-5}
318	0.9826	0.02533	0.9997	1.8960×10^{-5}

The associated kinetics parameters were presented in Table 3. The correlation of the Pseudo-second order kinetics model is larger than that of the Pseudo-first order kinetic model. This indicated that the kinetics behavior within the whole adsorption process could be predicted by pseudo-second-order model. And the decreased k_2 as the temperature increase indicated that the adsorption reaction was exothermic reaction. Thus, increasing temperature was not favor to the adsorption reaction.

Conclusions

In this work, the micro-porous chitosan membrane was prepared by polyethylene glycol (PEG) as porogen. The pore size is about 0.6 μm with the ratio of chitosan to polyethylene glycol and glycerol is 1:0.5:0.5. The chitosan micro-porous membrane exhibits the highest adsorption capacity of 168.41 mg g^{-1} and removal rate of 84.21% under chromium (VI) ions concentration of 100 mg L^{-1} and membrane dosage of 10 mg for 4 h. The adsorption kinetics and isotherms indicate that the adsorption process best fits the pseudo-second-order and Langmuir models.

Acknowledgements This work was supported by the National Natural Science Foundation of China (21476005, 21176005), and the Fund from Beijing Municipal Selected Excellent Overseas Scholars Project.

References

1. Z. Guo, D.D. Li, X.K. Luo, Simultaneous determination of trace Cd(II), Pb(II) and Cu(II) by differential pulse anodic stripping voltammetry using a reduced graphene oxide-chitosan/poly-l-lysine nanocomposite modified glassy carbon electrode. J. Colloid & Interface Sci. **490**, 11 (2016)
2. F. Fu, Q. Wang, Removal of heavy metal ions from wastewaters: a review. J. Environ. Manag. **92**(3), 407–418 (2011)
3. S.S. Madaeni, Y. Mansourpanah, COD removal from concentrated wastewater using membranes. Filtr. Sep. **40**(6), 40–46 (2003)
4. N. Kongsricharoern, C. Polprasert, Chromium removal by a bipolar electro-chemical precipitation process. Water Sci. Technol. **34**(9), 109–116 (1996)
5. G. Crini, Recent developments in polysaccharide-based materials used as adsorbents in wastewater treatment. Prog. Polym. Sci. **30**(1), 38–70 (2005)

6. D.W. O'Connell, C. Birkinshaw, T.F. O'Dwyer, Heavy metal adsorbents prepared from the modification of cellulose: a review. Bioresour. Technol. **99**(15), 6709 (2008)
7. G.N. Kousalya, G.M. Rajiv, S. Meenakshi, Sorption of chromium(VI) using modified forms of chitosan beads. Int. J. Biol. Macromol. **47**(2), 308–315 (2010)
8. T. Karthikeyan, S. Rajgopal, L.R. Miranda, Chromium(VI) adsorption from aqueous solution by Hevea Brasilinesis sawdust activated carbon. J. Hazard. Mater. **124**(1–3), 192 (2005)
9. S. Recillas, J. Colón, E. Casals et al., Chromium VI adsorption on cerium oxide nanoparticles and morphology changes during the process. J. Hazard. Mater. **184**(1–3), 425 (2010)
10. X.J. Wu, J.D. Wang, L.Q. Cao, Characterization and adsorption performance of chitosan/diatomite membranes for Orange G removal. e-Polymers **16**(2), 99–109 (2016)
11. X. Zhao, L. Song, J. Fu, et al. Adsorption characteristics of Ni(II) onto MA–DTPA/PVDF chelating membrane[J]. J. Hazard Mater. **189**(3), 732 (2011).
12. Y. Deng, N. Kano, H. Imaizumi, Adsorption of Cr(VI) onto hybrid membrane of carboxymethyl chitosan and silicon dioxide. J. Chem. (2017)
13. X.J. Hu, J.S. Wang, Y.G. Liu, Adsorption of chromium (VI) by ethylenediamine-modified cross-linked magnetic chitosan resin: isotherms, kinetics and thermodynamics. J. Hazard. Mater. **185**(1), 306–314 (2011)
14. F. Wang, M. Ge, Organic-inorganic hybrid of chitosan/poly (vinyl alcohol) containing yttrium (III) membrane for the removal of Cr(VI). Fibers Polym. **14**(1), 28–35 (2013)

Pore Structural Evolution and Properties of Active CaO Blocks Prepared from Carbide Slag

Jianwei Cao, Hang Yang, Zhi Wang, Shifu Shen and Xuzhong Gong

Abstract The CaO block with high strength and high activity was prepared from waste carbide slags, which were by-product in the process of acetylene production using calcium carbide method, as raw materials. The results show that the CaO block prepared from the carbide slag at 1100 °C has the highest activity. With the increase of sintering temperature, the average pore diameter of CaO block increases gradually and the uniformity of pore structure increases as well, while the total pore area decreases. The pore structure of CaO block is controlled by both the decomposition of $Ca(OH)_2$ and $CaCO_3$ and sintering crystallization of CaO. The compressive strength of CaO decreases with increasing of porosity, showing a good semi logarithm linear relationship: $\ddot{y}_s = {}_0e^{-bP}$. For the sintered CaO block, the higher the porosity is, the higher the activity is. Under the same porosity, the larger the pore diameter is, the higher CaO block activity is. With increasing average diameter of the pores, the sintering neck of CaO crystalline grains and the connection effect of the main and collateral channels between the holes becomes bigger and stronger, thus the thermal shock resistance of CaO block increases.

J. Cao · Z. Wang (✉) · X. Gong
National Engineering Laboratory for Hydrometallurgical Cleaner Production Technology, Key Laboratory of Green Process and Engineering, Institute of Process Engineering, Chinese Academy of Sciences, Beijing 100190, China
e-mail: bjhdcjw@163.com

J. Cao
e-mail: yangfqh@aliyun.com

H. Yang · S. Shen
State Key Laboratory of Science and Technology of Mineral Processing, Beijing General Research Institute of Mining and Metallurgy, Beijing 100044, China
e-mail: yanghang@bgrimm.com

Y. Han (ed.), *Advances in Energy and Environmental Materials*,
Springer Proceedings in Energy, https://doi.org/10.1007/978-981-13-0158-2_83

Graphical Abstract

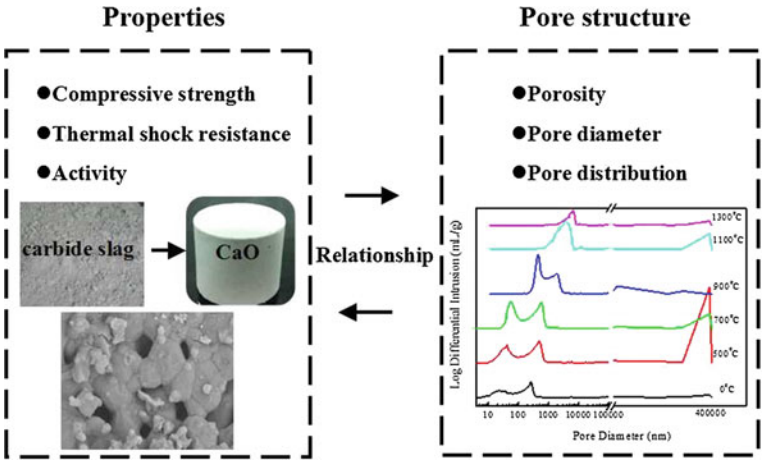

Keywords Carbide slag · CaO blocks · Structural evolution · Compressive strength · Activity · Thermal shock resistance

Introduction

The carbide slag containing $Ca(OH)_2$ as the main composition is a kind of hard-disposal industrial waste produced in the preparation process of acetylene using calcium carbide method process PVC [1]. It can produce about 1.2 t of carbide slag per ton of calcium carbide production [2]. Carbide slag, with strong alkalinity and the pH value of its slag liquid being above 12, takes up a lot of land resources and causes huge environmental pollution at the same time. However, the content of calcium hydroxide in the calcium carbide slag can reach up to 70.0–85.0%, thus the calcium carbide slag has a large potential resource reuse value. Comprehensive utilization of carbide slag and environmental governance will be the key for the sustainable development of calcium carbide acetylene method PVC enterprises in China [3, 4].

At present, carbide slag utilization factor is less than 10% in China [5]. Given this situation, the purified carbide slag will firstly be burnt into calcium oxide block with highly activity and certain intensity as the basic raw material for calcium carbide production. Its process route of calcium circulation is shown in Fig. 1, The reaction process is shown as Eq. 1 [6]:

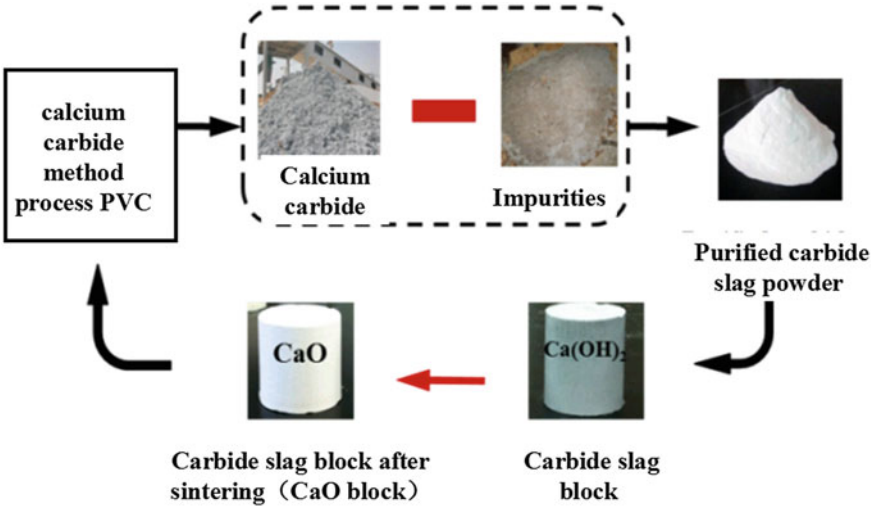

Fig. 1 Process route of calcium circulation

$$CaO + 3C = CaC_2 + CO \quad (1)$$

Not only the high porosity of the highly active calcium oxide blocks effectively promote solid-solid reaction process between the calcium oxide and the coke, but certain strength and good thermal shock resistance avoid the damage to calcium carbide production equipment from the pulverization burst of the blocks during the process of high-temperature feeding as well. It has been widely reported that the effects of different temperature, time and atmosphere on the high temperature sintering characteristics and microscopic structure change in the process of sintering limestone into calcium oxide [7, 8]. However, in the production of calcium carbide, the mechanism of microstructure change in the sintering and sintering process with calcium carbide slag as raw materials is not clear. In this study, as the burnt products, the calcium oxide blocks are porous and the pore structural evolution of calcium oxide block in the process is closely related to its activity and the intensity. R.S. Mikhail, D.Alvarez etc. [9, 10] studied the microstructure and thermal decomposition characteristics of calcium carbide slag in the dynamic sintering of the calcium carbide slag powder and sintering process. But there is no literature report about the related mechanism between the organization structure of carbide slag blocks sintering process and the block performance. The calcium oxide blocks need not only high activity but also the high strength and good thermal shock resistance at the same time. So it is necessary to conduct further study for the associated mechanism of the organizational structure with strength, activity and thermal shock performance, and thus provide beneficial reference work for the comprehensive utilization of carbide slag.

Therefore in the present work, the pore structure evolution and change in the sintering process of CaO blocks in the preparation of carbide slag were investigated. Meanwhile, the relationship among porosity, pore size and pore distribution and the compressive strength, the activity were analyzed with the change of sintering temperature systematically.

Experimental

Materials. The carbide slag used in this study was obtained from China's Inner Mongolia and calcium carbide used in the experiment was purified by hydrocyclone [11, 12] with compositions shown in Table 1. XRD phase composition analysis is shown in Fig. 2 and the main phase of the carbide slag is the $Ca(OH)_2$.
Experimental Procedure. The preparation of CaO blocks is shown in Fig. 3. Carbide slag powder was mixed with 15% water to a mixture, which then was loaded into the stainless steel mould of Φ20 mm and compressed into a green body by embedded prototype under the pressure of 35 MPa with a dwelling time of 3 min. The green body weighed 10 g with an aspect ratio of 1:1 and was dried at 100 °C for 12 h. The dynamic sintering experiments were conducted in the muffle furnace with the sintering temperature increasing up to 500, 700, 900, 1100, 1300 °C at the speed of 5 °C/min. After sintered at each temperature with a furnace cooling the sample was analyzed. The online analysis of phase in the process of dynamic sintering was conducted by X-ray diffractometer with a Cu-Kα radiation

Table 1 Chemical contents of carbide slag (wt%)

CaO	SiO_2	Al_2O_3	Fe_2O_3	MgO	Others	LOI
64.497	3.738	2.033	0.203	0.188	2.553	26.66

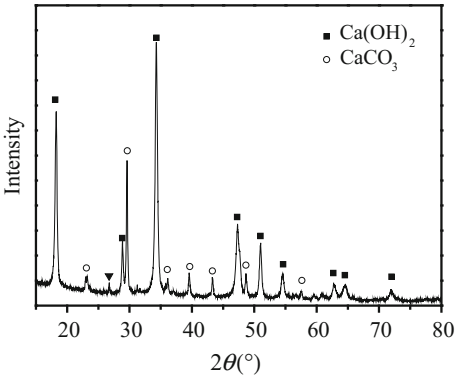

Fig. 2 XRD phase compositions of molding material

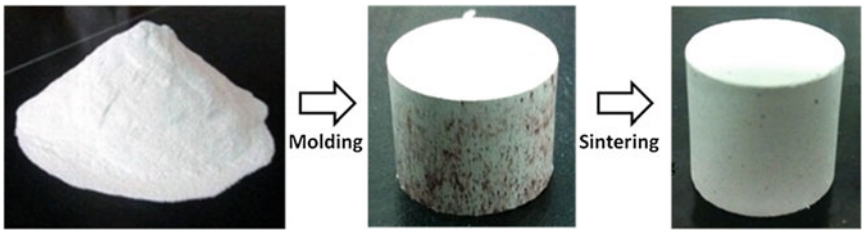

(a) Purified carbide slag powder (b) Carbide slag block (c) Carbide slag block after sintering (CaO block)

Fig. 3 Block molding and sintering process

and the power of 40 kV × 40 mA in the 2θ range of 10–80°. The scanning speed and step length were 8°/min and 0.02°, respectively. The specific surface area, porosity, pore volume and pore size distribution of CaO blocks in the dynamic sintering and samples sintering process were tested by the mercury injection apparatus, in which the mercury has the contact angle of 140° to solid materials and the surface tension of the mercury of 450 × 105 N cm^{-1}. The surface morphology of carbide slag samples before and after sintering was analyzed by the SEM and EDS. Before tested, the sample surface was treated using gold spray processing with the accelerating voltage of 25 kV. The compressive strength of CaO block was tested with GB/T50081. The test piece was placed in the lower platen center of the testing machine and the bearing surface of the test piece was perpendicular to the top surface of the molding. A pressure of 0.3–0.5 MPa was loaded to the specimen continuously and uniformly with the compression speed of 30 mm/min until the specimen was damage and then the failure load was recorded. An average of three measured values (accurate to 0.l MPa) was defined as the strength value of the testing group. HCl titrimetry (Physics detection methods of national metallurgical lime) was employed as the activity test of CaO block.

The powder sample with a particle size of 15 mm and a weight of 25 g was prepared. 1000 ml water was poured into a 200 ml cylinder with 1000 ml water at 40 ± 1 °C and stirred at a stirring speed of 250–300 r/min using a stirring apparatus. At the same time, a thermometer was used to measure the temperature. 10 drips of phenolphthalein indicator solution with a concentration of 10 g/L were dropped into the cylinder, and then the CaO particles were added into in the water. A timer was used to record time. When the CaO particles started dissolving and the solution turned red, the HCL solution with a concentration of 4 mol/L was added until the red disappeared. When the red reappeared, the HCL solution was added again until the red mixture disappeared. The HCl consumption after 10 min was taken as the characterization of CaO block activity.

Analysis and Characterization Methods. The pore arrangement parameters were detected by Mercury Injection Apparatus (Model: AutoPoreIV9510). The phase composition of the products was characterized by X-ray diffraction (XRD) using D/MPax-2400 Multi-crystal Diffractometer (X' Pert PRO MPD, Holland) with a

Cu-Kα radiation in the 2θ range of 10°–90°. Chemical components were evaluated by X-ray fluorescence spectrum analyzer (AXIOS, Panalytical. B.V). The morphology and elemental chemical compositions of the dissociative residue were examined respectively by scanning electronic microscopy (SEM) (JSM-7001F type) combined with energy dispersive X-ray analysis (EDS) (INCA X-MAX, Oxford Instruments, UK).

Results and Discussion

Pore Structural Evolution in the Sintering Process of CaO Blocks. There are two decomposition reactions in the sintering process. One is the decomposition of $Ca(OH)_2$ and the other is decomposition of $CaCO_3$. A large amount of pores could be produced in the sintering process of the bulk. The produced porous CaO is featured with different pore structures under different conditions. The presence of pore structure is mainly due to the following two respects. On the one hand, the molar volume of $Ca(OH)_2$, $CaCO_3$ and CaO is 33.0, 37.0 and 16.9 cm^3 mol^{-1} respectively, from which it can be deduced that the volume of crystal grain of Ca $(OH)_2$ and $CaCO_3$ is twice that of CaO. Therefore, $Ca(OH)_2$ and $CaCO_3$ as the main composition can produce a large amount of pores when they subjected to thermal decomposition and transformed into CaO. On the other hand, the escape of the decomposition products of $Ca(OH)_2$ and $CaCO_3$, that are H_2O and CO_2, can also make some contribution to the formation of pores [13]. The change of the pore size distribution in the sintering process of bulk at 0–1200 °C is shown in Fig. 4.

It can be observed that there is certain variation trend not only for the shape and location of the peaks in the range of pore size but also for the pore distribution, indicating that the pores in the bulk develop mainly around these initial pores.

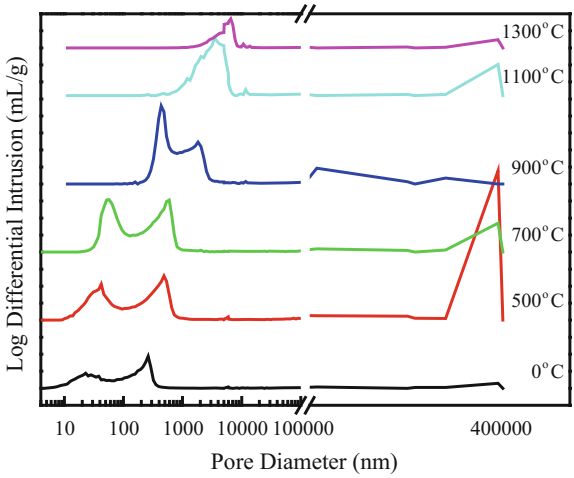

Fig. 4 Pore size distribution of CaO block during sintering process

Table 2 Pore structure parameters of CaO block during sintering process

Temperature/°C	Average pore diameter/nm	Porosity/%	Total intrusion volume ml/g	Total pore area m^2/g	Apparent (skeletal) density g/mL	Bulk density g/mL
0	47.6	48.5833	0.3110	26.140	3.0384	1.5622
500	65.3	72.14	0.5919	36.273	4.3760	1.2188
700	105.2	73.61	0.66	25.10	4.23	1.1151
900	233.3	66.3	0.64	11.004	3.07	1.0331
1100	892.3	71.6	0.51	2.272	4.97	1.4118
1300	1728.5	39.23	0.17	0.403	3.71	2.252

Figure 4 shows that the pore structure in the CaO bulk can be classified into two types according to the size: one is the micro pore in the range of 10–10,000 nm and the other is the macro pore at scale of 40,000 nm. The formation of these pores with different sizes and types is closely related to the phase transformation and crystalline grain growth in the CaO bulk. Before sintering, the pore size mainly ranges from 10 to 400 nm with an average pore size of 47.6 nm, total pore area of 26.140 m^2/g and total pore volume of 0.3110 ml/g (Table 2). These initial gaps are mainly caused by the residual gas that does not discharge in the process of pore forming. After carbide slag was sintered at 500 °C, the range of the bulk is 20–800 nm, larger than the distribution range before sintering. The large pores with a size of 40,000 nm are formed for the first time. $Ca(OH)_2$, as the main ingredients of CaO bulk, has completed decomposition at 500 °C. The main reason for the increase of pore size is the decomposition of $Ca(OH)_2$. On the one hand, the escape of water, as the breakdown products, plays a role, which can be confirmed by the porosity increase from 48.58 to 72.14%. On the other hand, the $Ca(OH)_2$ decomposition caused the shrink and rupture in the original solid particles, which explains the sudden appearance of a large number of macro pores of 40,000 nm after sintering [14]. After sintering of carbide slag in 700 °C, the average pore size increased from 47.6 nm to 105.2 nm in the range of 10–1000 nm, whereas porosity increased only 1.5% (Table 2). The main change is that after the sintering at a certain temperature, pores of 40,000 nm decreases because the highly active CaO and CO_2 react to produce $CaCO_3$ that dominates this process and the product of $CaCO_3$ that has a similar molar volume with $Ca(OH)_2$ plays a repair effect to the fragmentation caused by the $Ca(OH)_2$. After sintering at 900 °C, the average pore diameter doubles compared to that at 700 °C and the pore size of the CaO bulk distributes in the range of 200–2000 nm. At this temperature, the cause of pore size increase is the escape pore-forming role of the product CO_2 from $CaCO_3$ decomposition. When the temperature further increased up to 1100 °C, CaO crystalline grains started sintering and growing up, which cause the average pore diameter to increase to 892.3 nm. The change in peaks of pore distribution from bimodal to unimodal indicates that as CaO grain size becomes uniform, pore size distribution gradually gets even, sintering effect is still to be mild at this time, and many holes and big hole has not yet been squeezed in the sintering

of carbide slag. When the sintering temperature gets to 1300 °C, the increase of crystal grains and the densified combination of particles decrease the gap so sharply that it causes the porosity rapidly decline from 71.6 to 39.23% and the bulk density increase to 2.25 g/mL (Table 2).

In the sintering process, the total pore area gets smaller as the temperature rises because the area specific surface of micro pores is considerably larger than that of medium and macro pores under the same volume of the pore. In a preliminary analysis, the reason for the increase of the uniformity of pore structure may be that in the microstructure of porous ceramics there is an optimum pore diameter, which can make the ceramic particles maintain the lowest energy state in the sintering process. With the increase of temperature, the crystal grains consisting of the small pores aperture begins softening, mass transfer and transforms to the morphology that constitute the optimal pore size [15]. Similarly, the crystal grains that constitute the large pore size transform with this kind of change. The overall result is that the small pores get larger, while the large pore becomes small and there is almost no change near optimal pore size with the final peak position changeless, but the pore size distribution (peak width) narrows and the accommodated volume (peak area) is also reduced.

The SEM of the CaO block before sintering is shown in Fig. 5, indicating that the surface is composed of $Ca(OH)_2$ and $CaCO_3$ block particles, which distributed messily, have obvious particle size difference, and the CaO blocks integrate with density.

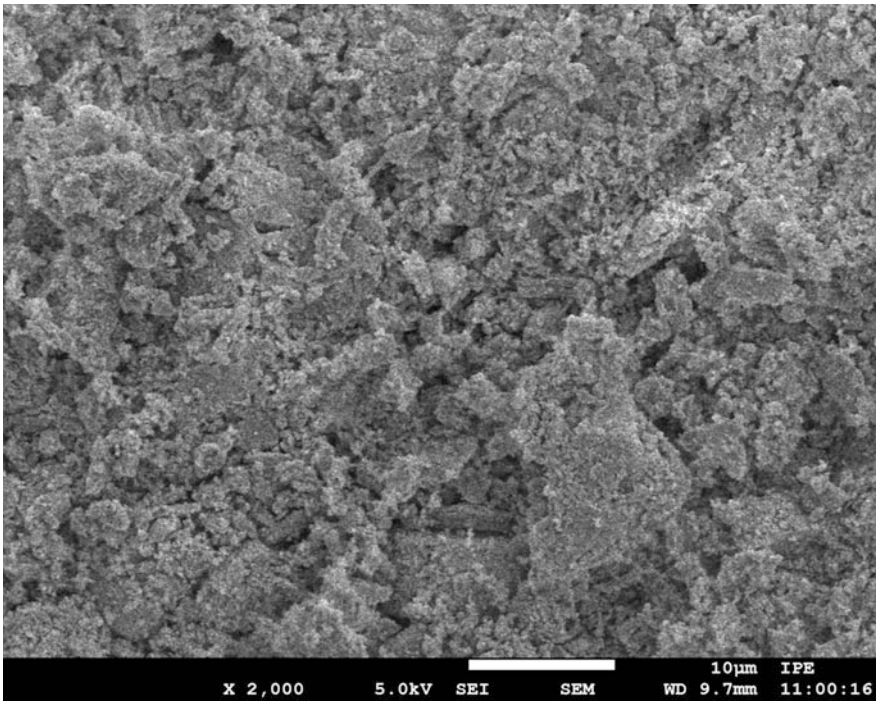

Fig. 5 SEM images of CaO block before sintering

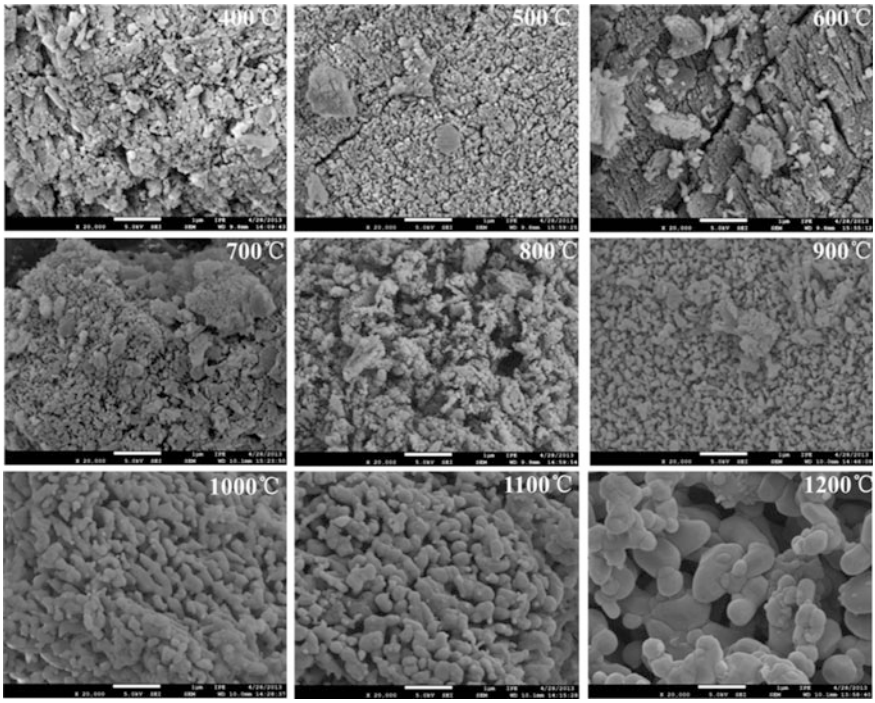

Fig. 6 SEM images of CaO block during sintering process

The SEM morphology evolution of CaO blocks in the dynamic sintering is shown in Fig. 6.

After the sintering at 400 °C, the escape of water, as the decomposition product of $Ca(OH)_2$, causes the appearance of parts of small pores in the surface of CaO blocks. At 500–600 °C, the cracks formed by the shrinkage and rupture of the original solid particles because of the decomposition of $Ca(OH)_2$ observed on the surface. The further increase of small gaps confirms the sudden appearance of a large amount of macro-pores of 40000 nm after sintered at 500–600 °C. The decomposition of $CaCO_3$ into CaO at 700–900 °C can produce smaller pores compared to the morphology at 700–900 °C, which indicates that the CaO crystal grains are all discomposed into CaO with smaller molar volume after sintering at 900 °C with an increase of porosity. The CaO crystallization begins at 1000–1200 °C. With the increase of temperature, the sintering of CaO crystal grains in the CaO blocks intensifies gradually at 900 °C. The crystal grains begin to grow up and the size of pore increases correspondingly because of the gradual expansion. The pore connectivity between particles improves and the crystal grains within a small distance adhere to each other.

After the sintering of blocks at 1200 °C, the surface is composed of well-developed CaO crystal grains with uniform particle sizes and regular distribution. These sintering and expanding crystal grains are featured with about 1 μm in length and 0.6 μm in width. After sintered at high temperature, despite CaO grains grew up after a long time, the grain boundary is still well-distinguished, pores of about 1.4 μm is still uniformly distributed between particles and the grains do not aggregate. The pore structure of CaO blocks prepared by carbide slag is a kind of cylindrical pore, and the pore structure is mainly controlled by the reaction process because the intergranular accumulation state is suffered from complex decomposition and phase change process of $Ca(OH)_2$ and $CaCO_3$.

Effects of Pore Structure of CaO Block on the Strength. The effects of sintering temperature on porosity, average pore size and the compressive strength is shown in Fig. 7, demonstrating that the porosity of porous CaO block increase first, and then decreased with the increase of temperature. The main composition of CaO block is $Ca(OH)_2$ before the sintering and is featured with porosity of 48.58%, average pore size of 47.6 nm and block volume density of 1.56 g/mL.

The green-pressing of carbide slag is featured with a high intensity up to 18 MPa. After sintering at 400–900 °C, the porosity of CaO block begins to increase and fluctuates in the range of 66.3–73.61% with the exponential increase of the average pore diameter. When calcinated at up to 900 °C, the average pore diameter is nearly four times that before sintering, up to 233 nm. In the temperature range, the decomposition of $Ca(OH)_2$ and $CaCO_3$ mainly dominates the process. On the one hand, the escape of H_2O and CO_2 as the decomposition products produces a large number of pores. On the other hand, the transformation to CaO of small molar volume from $Ca(OH)_2$ and $CaCO_3$ of large molar volume can contribute to the formation of many gaps between the particles. Although main ingredient of the bulk is CaO at this time, grain boundary is still not clear and the structure of $CaCO_3$ is still kept. There are many pores with a diameter size being 100 nm in the bulk profile and the pore shape is not regularly rounded. Many pores are the slender and coherent cracks between the irregular grains and the block volume density of CaO blocks within the range of 400–900 °C is lower than that before calcining with only

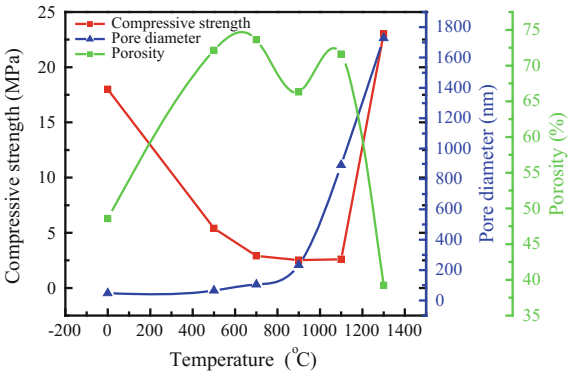

Fig. 7 Relationship between pore parameters and compressive strength of CaO block

1.0331–1.2188 g/mL (Table 2), thus reducing the mass density of blocks. So the compressive strength of CaO blocks is small, between 2.2 and 2.5 MPa. When the sintering temperature is increased to 1100 °C, porosity of the bulk is 71.6% and the average pore size sharply increases to 892.3 nm while the increase of compressive strength is not obvious, mainly because CaO began to grow up after the begin of sintering and crystallization and the morphology of CaO begins to develop into the regularly spherical, then some small irregular pore mutually swallows up to form larger pores leading to the increase of grain gaps. The phenomenon that the sharp increase of pore size did not cause the sharp fell of compressive strength of CaO block is mainly due to two aspects: on the one hand, the increase of particle size makes the intergranular pore volume reduced from 0.64 ml/g to 0.51 ml/g; On the other hand, the 1100 °C sintering of CaO grains has begun to already form the sintering neck, with the contact points between grain increased, and compensate reduction of the strength by the increase of the pore size [16]. When the temperature is further raised to 1300 °C, porosity has fallen sharply from 71.6 to 39.23%, while the grain size increases significantly with the average pore diameter increases to 1728.5 nm. At this time strength sharply ascends to 23 MPa and volume density of CaO block reached a maximum of 2.25 g/mL, showing that CaO block is dense and significant increase of sintering rate. The CaO block markedly sinters to shrink because sintering shrinkage effect exceeds the solid thermal expansion. The shrinkage and densification of sample strongly cause the surge of strength. To sum up, the compressive strength and porosity of porous CaO present the opposite regularity on the whole, showing that porosity is the main factor affecting the compressive strength of CaO block [17]. The change of the pore size is caused by the growth of grain size which has little effect on the CaO block strength and the increase of porosity significantly reduces the compressive strength of CaO block.

Where σ_s is the strength, σ_0 is the strength when the porosity decreases to 0. p denotes the porosity and b is an experienced constant which is mainly determined by the accumulation way of equal-diameter balls in porous medium. The relationship between the strength and porosity is analyzed by modeling in this article through the above empirical formula.

Figure 8 is the compressive strength and porosity data fitting using Eq. 2 [18].

$$\sigma_s = \sigma_0 e^{-bP} \tag{2}$$

The data fitting result shows good fitness with Eq. 2 and the compressive strength of CaO block is in good half logarithm linear relationship with porosity.

Effects of the pore structure of CaO block on the activity. The high porosity of the highly active CaO block effectively promotes the transfer process in solid-solid reaction, significantly increase the reaction ability with coke which mainly depends on that CO molecules fully spread to inside of the pore in the reaction process and have a full contact to react. The structure characteristics, the pore size, pore size distribution and pore length of CaO internal pores will directly affect the rate of gas-solid reaction [19]. So this article focuses on the relationship between the

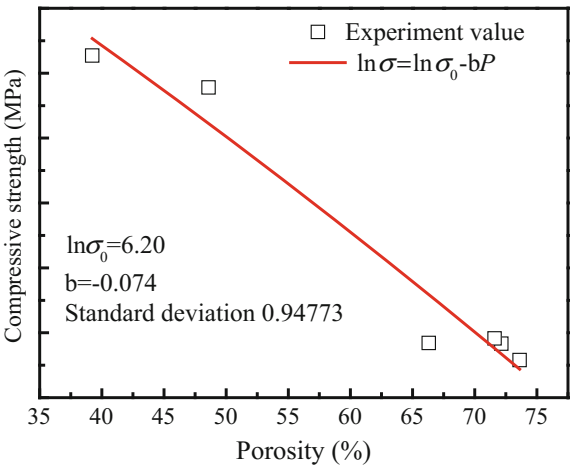

Fig. 8 Fitting results comparing the measured values with the compressive strength and porosity

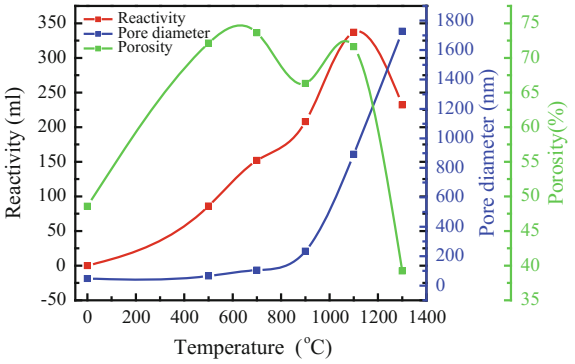

Fig. 9 Relationship between pore parameters and reacticity of CaO block

microscopic pore structure parameters of CaO block and its reactivity. Given the high temperature of 2100–2200 °C brings great difficulty in testing CaO and coke reaction ability, the reaction activity of CaO is generally tested by HCl titration to measure the CaO hydration ability in the metallurgical lime industry.

The relationship between porosity, average pore size and activity of CaO block with the temperature is shown in Fig. 9.

It can be seen that the porosity, average pore size and activity of CaO block all increase with the increase of temperature, indicating that high porosity and large pore size are in favor of promotion of the activity of CaO block. The main composition of CaO before sintering is the $Ca(OH)_2$, that does not have activity. When the CaO block is calcinated at up to 500 °C, the produced CaO by decomposition of $Ca(OH)_2$ begins to produce activity. Though the porosity of block can get up to more than 70% at 500–700 °C, the activity is less than 150 mL because the $Ca(OH)_2$, and $CaCO_3$ are not decomposed completely. When the temperature gets to

900 °C, the $Ca(OH)_2$, and $CaCO_3$ are decomposed completely and the activity can reaches to about 200 mL because of the high CaO content. When the sintering temperature is 1100 °C, the activity of CaO block gets to its maximum, 330 mL with it corresponding porosity larger than the 66.3% of 900 °C. But the average pore size increases to 892.3 nm, nearly four times as 233.3 nm of 900 °C, which demonstrates that under the similar porosity, the activity of CaO is mainly determined by the size of porosity. When the temperature gets to 1300 °C, the pore size increases to 1728.5 nm whereas the porosity declines to 39.23% significantly. At this point the activity of CaO block decreases sharply indicating that the porosity play a more significant role than the average pore size among these two factors.

The experiments show that hydration rate of CaO is closely related to the condition of sintering, which is also the environment of crystal formation and growth. The nature of crystal grow is the atomic transition where the growth driving force is ascribed to the higher free energy in the crystal grain surface, interface and the interior lattice. If the structure is located in the unstable state, the large hydration activity will be shown once in contact with water. The microstructure of the formed CaO crystals will be different under different calcinating condition which can cause the difference of hydration activity. The reasons for the above phenomenon are analyzed. On the one hand, under the same porosity, the larger is the pore size, the smaller is the resistance that water molecules encounter and it will be more likely to fully spread to the interior of the pore and react with CaO [19]. The CaO block is porous in 900 °C, but CaO still maintains the diamond structure of $CaCO_3$ with small grain size and no-obvious boundaries. Although it also has high porosity with small pore size, the hole size being 11.004 (Table 2) and a lot higher than 2.272 at 1100 °C, CaO has not started sintering. The crystallization and microstructure of CaO bulk has not developed the regular face-centered cubic structure of NaCl. The atomic arrangement in CaO bulk is irregular. The connectivity of the corresponding pores by the accumulation of grains is bad and the effective contact area with the water molecules is not big. As a result, the activity of CaO bulk is poor. At 1100 °C, CaO preliminary begins to sinter with its grains arranged regularly and the connectivity of pores increase. The pore diameter further increases with growth of the crystal grains, which improves of the activity of CaO bulk. The significant sintering of CaO causes the abnormal growth of crystal grains [20]. Lattice distortion becomes smaller. The crystal structure tends to be dense with smaller grain boundary surface area and surface free energy. Thus the hydration activity of CaO bulk gets lower.

Effects of pore structure of CaO block on thermal shock resistance. The percentage change of compressive strength before and after thermal shock experiments was evaluated in this study. The compressive strength loss rate of pore structure of CaO block of three different pores sintered at 900, 1100 and 1300 °C under quenching temperature difference of ΔT = 500 °C, 700 °C, 900 °C and 1100 °C is shown in Fig. 10.

It can be found that the compressive strength of three kinds of CaO blocks all have a certain degree of decline compared to that before the thermal shock experiments. The compressive strength loss rate of three kinds of CaO blocks all

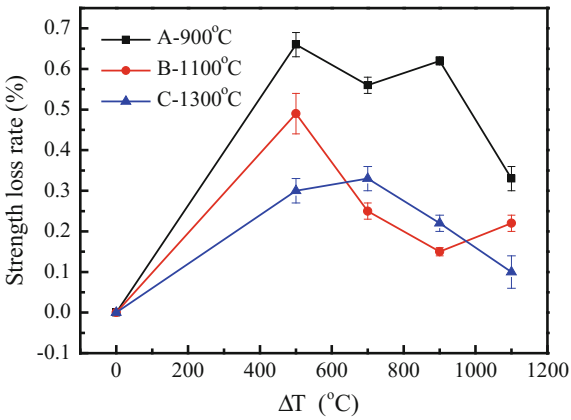

Fig. 10 Thermal shock resistance of CaO block in different quenching temperature

reaches maximum values especially at ΔT = 500 °C. Combined with the coefficients of thermal expansion of CaO block under different temperatures, the coefficients are all larger than zero, indicating that the block are expanding all the time in this temperature range. After the expansion reaches its maximum at 200 °C, the coefficient begins to decrease. When the temperature is 500 °C, the block begins to shrink to its minimum value and then the shrinkage decreases. It can be seen that 500 °C is a turning point of thermal expansion and shrinkage, which indicates that at the temperature of mutation for coefficient of thermal expansion, the thermal stress reaches its maximum, which causes the decrease of thermal shock compressive strength and the strength loss rate after quenching.

The thermal expansion curve of CaO block is shown in Fig. 11, showing that CaO block has obvious thermal expansion and shrinkage behavior in the sintering process.

The sintering process can be divided into three stages. At the first stage, the sample presents a certain expansion and shrinkage fluctuation with the increase of

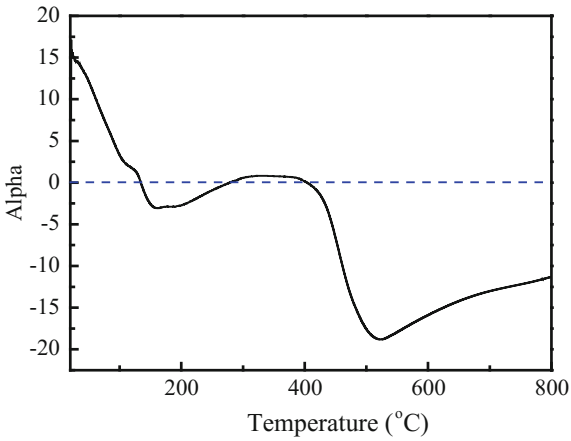

Fig. 11 Thermal expansion curve of CaO block during sintering process

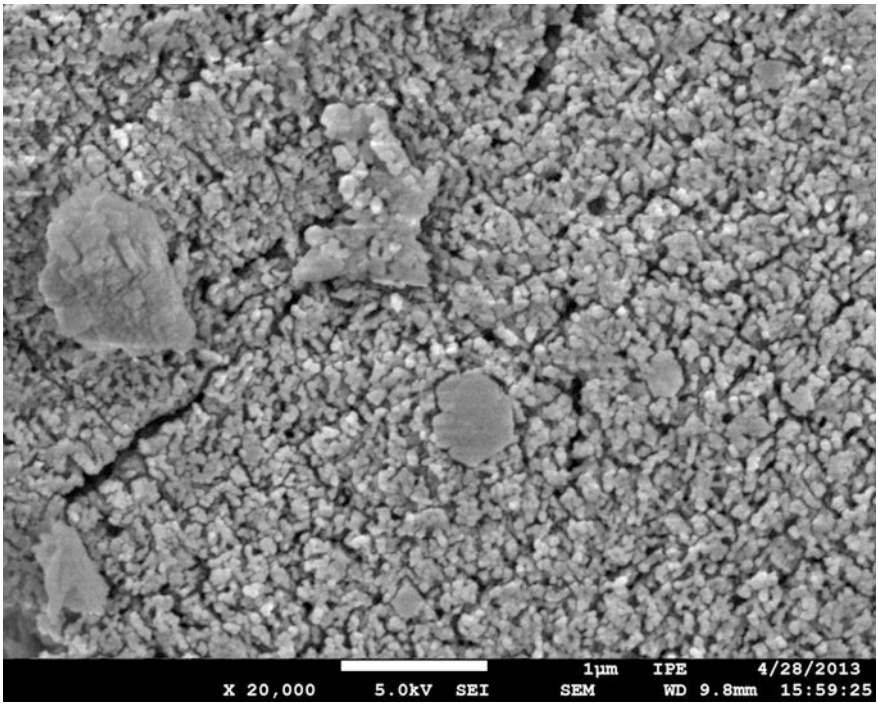

Fig. 12 SEM images of CaO block at 500 °C

temperature (<400 °C) because the volatilization of free water and combined water. At the second stage, when the temperature gets to 400–500 °C, the coefficient of thermal expansion decrease from 0 to −20. The shrinkage of blocks is caused by the decomposition of $Ca(OH)_2$ and the loss of water. $Ca(OH)_2$ with large molar volume (33.0 cm^3 mol^{-1}) decomposes into CaO with small molar volume (16.9 m^3 mol^{-1}), resulting in the original solid particles to shrink and rapture as shown in Fig. 12.

At 550–700 °C, the sample shows small thermal expansion with continuous increase of sintering temperature. Meanwhile, the highly active CaO reacts with CO_2 to form $CaCO_3$. It is the transformation from CaO with small molar volume (16.9 cm^3 mol^{-1}) to $CaCO_3$ with larger molar volume (37.0 cm^3 mol^{-1}) that causes a small thermal expansion of CaO block. At the third stage, with the increase of temperature to 900 °C, CaO enters the sintering stage. The surface of the particles begins to soften and sinter, resulting in shrinkage of the sample. Thermal expansion rate begins to decrease significantly because the shrinkage effects offset most of the thermal expansion, even with the appearance of zero expansion. Therefore, in the range of 900–1100 °C, there is no obvious thermal shrinkage behavior of CaO block.

Performance optimization of CaO block. The dependence of both compressive strength and reactivity of CaO block on temperature is shown in Fig. 13.

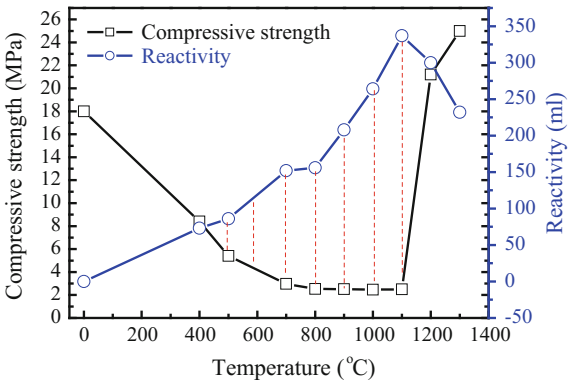

Fig. 13 Compressive strength and reactivity of CaO block with different temperature

It is found that the strength of CaO block has an initial reduction followed by an increase with the increase of sintering temperature, whereas the variation of activity with temperature shows a totally opposite trend. The shaded area in the figure is the main range for adjustment of activity and intensity in this study. When the temperature is less than or equal to 400 °C, the main ingredient of CaO block is still Ca $(OH)_2$ without the production of CaO, therefore no activity occurs. When the temperature is above or equal to 1200 °C, CaO block will be sintered rapidly, demonstrating that CaO grains grow up and aggregate. The block trends to become dense with the porosity declining. Although the block strength is improved, there is a significant reduction in the activity. In the temperature range of 400–1200 °C, the temperature corresponding to the maximum reactivity is 1100 °C. However, the strength in this temperature range decreases gradually even though the decrease is not obvious. As a result, the performance of CaO block can be adjusted flexibly according to the industrial applications to reach a dynamic balance of strength and reactivity. In the temperature range of 900–1300 °C, the thermal shock resistance of CaO block increases with the increase of temperature. Considering the three main physical and chemical properties of CaO block, such as the strength, activity and thermal shock resistance, the temperature that corresponds to the best performance of CaO block is 1100–1200 °C. In this temperature range, the required reactivity and thermal shock resistance of CaO block can be reached using reinforcement binder to improve the strength according to the technical requirements.

Conclusions

The microstructure change in the sintering process of carbide slag was investigated. The dependence of porosity, pore size and distribution, the compressive strength and the activity on the sintering temperature were analyzed. The following conclusions have been made:

(1) The CaO block prepared by carbide slag has the highest reactivity and the maximum strength after sintered at 1100 and 1200 °C, respectively. Given the priority principle of the reactivity, the optimized sintering temperature can be 1100 °C.
(2) With the increase of sintering temperature, the average pore diameter of CaO block increases gradually and the uniformity of pore structure increases as well, while the total pore area decreases. The pore structure of the CaO block is simultaneously controlled by the escape of H_2O and CO_2 as the products in the decomposition process and the change of crystal grain size of CaO in the sintering process.
(3) The increase of porosity can significantly decrease the compressive strength of CaO. The change of pore size is induced by the growth of crystalline grains, which has little effect on strength of CaO block. The compressive strength of CaO block has a half logarithm linear relationship with porosity, i.e. $\sigma_s = \sigma_0 e^{-bP}$.
(4) Under a fixed porosity, the larger the pore size is and the more regular the crystal grains arrangement is, the higher the sintering reactivity of the CaO block is. The excessive sintering will cause abnormal growth of grains. The more dense crystal structure is, the less the grain boundary surface area is and the lower surface free energy is, thus the lower the hydration activity is.
(5) 500 °C is a turning point of thermal expansion and shrinkage, at which the coefficient of thermal expansion changes drastically and the thermal stress gets the maximum value, resulting in a decrease of thermal shock compressive strength. The increase of particle size will improve the thermal shock compressive strength. The strengthening of "network" connection among pores can improve the thermal shock performance. The larger the sintering neck of CaO crystalline grains is, the stronger the "network" connection among pores gets.

Acknowledgements The research of this paper was supported by Natural Science Foundation for Young Scholars of China (51604029) (51404225) and the National Science Fund for Outstanding Young Scholars of China (51422405).

References

1. P. Ramasamy, A. Periathamby, S. Ibbrahim, Carbide sludge management in acetylene plants by using vacuum filtration. Waste Manage. **20**, 536 (2002)
2. W. Zhang, H. Pan, H. Zheng, T. Liu, Study of the process of preparing the high purity calcium oxide by using carbide residue. J. Northeast Dianli Univ. **34**, 48–51 (2014)
3. C. Liu, Current state and reservation direction of industrial wastes–calcium carbide sludge. Cem. Technol. **6**, 60–62 (2005)
4. H. Wang, J. Tong, L. Shen, Resourcification utilization routes for carbide slag. Chem. Prod. Technol. Surg. **14**, 47–51 (2007)
5. S. Wang, J. Gao, M. Lin, Research of reclaiming calcium oxide from carbide residue. Mod. Chem. Eng. **27**, 153–155 (2007)

6. J. Cheng, J. Zhou, J. Liu, Z. Zhou, X. Cao, Dynamic sintering carbide slag and microstructure analysis of the sintering process]. J. Chem. Ind. Eng. (China) **54**, 984–988 (2003)
7. Z. Ma, G. Wei, Study on the characteristics of decomposition of dry discharged carbide slag. J. Cem. **4**, 1–6 (2011)
8. X. Wu, L. Liu, C. Cao, Mechanical properties of calcium carbide slag. Silicate Bulletin. **28**, 235–238 (2009)
9. R.S. Mikhail, Activation and sintering behavior of calcium oxide—the effect of hydration on the surface area of the oxide produced by thermal Decomposition. J. Phys. Chem. **67**, 2050–2054 (1963)
10. D. Alvarez, J. Abanades, Pore-size and shape effects on the recarbonation performance of calcium oxide submitted to repeated sintering recarbonation cycles. Energy Fuels **19**, 270–278 (2005)
11. H. Yang, J. Cao, Z. Wang, Enrichment of high Ca-containing phases in calcium carbide hydrolysis slag with hydro-cyclone method. Chin. J. Process Eng. **03**, 369–376 (2014)
12. H. Yang, J. Cao, Z. Wang et al., Discovery of impurities existing state in carbide slag by chemical dissociation. Int. J. Miner. Process. **130**, 66–73 (2014)
13. M. Mai, T. Edgar, Surface area evolution of calcium hydroxide during sintering and sintering. AIChE J. **35**, 30–36 (1989)
14. J. Han, C. Hong, X. Zhang et al., Highly porous ZrO_2 ceramics fabricated by acamphene-based freeze-casting route: microstructure and properties. Eur Ceram. Soc. **30**, 3–60 (2010)
15. F. Knudsen, Dependence of mechanical strength of brittle polycrystal lines pecimens on porosity and grainsize. J. Am. Ceram. Soc. **42**, 376–387 (1959)
16. N. Nomura, T. Kohama, I. Oh et al., Mechanical properties of porous Ti-15Mo-5Zr-3Al compact sprepared by powder sintering. Mater. Sci. Eng., C-BioS **25**, 30–335 (2005)
17. R. Millington, permeability of porous media. Nature **183**, 387–388 (1959)
18. R. Dias, C. Fernandes, J. Teixeira et al., Permeability analysis in bisized porous media: wall effect between particles of different size. J. Hydrol. **349**, 470–474 (2008)
19. T. Isobe, Y. Kameshima, A. Nakajima et al., Gas permeability and mechanical properties of porous alumina ceramics with unidirectionally aligned pores. J. Eur. Ceram. Soc. **27**, 53–59 (2007)
20. M. Haji-Sulaiman, A. Scaroni, The sintering and sulphation behaviour of sorbents in fluidized bed combustion. Fuel **70**, 169–176 (1991)

Preparation and Modification of Ceramic Membrane and Its Application in Oil/Water Wastewater Treatment

Yongqing Wang, Xuebing Hu, Qibing Chang, Xiaozhen Zhang, Yulong Yang, Ke Yang and Jianer Zhou

Abstract Using the alumina powders with different average particle sizes as main raw materials, the tubular ceramic membrane support was prepared by extrusion method, and the membrane interlayer (thickness ~20 μm) and top layer (thickness ~5 μm) were deposited on the membrane support surface by dip coating process. In order to improve the separation performance of the membrane, it was modified with FAS, nano metal oxide or graphene oxide, respectively. During the oil/water treatment, the water flux of the modified membrane is higher about 27.8–43% than that of the original membrane. The modified membrane has higher oil rejection (99%) than that of the original membrane. The results show the modification has an important role on the oil/water separation performance of the membrane.

Keywords Ceramic membrane · Modification · Separation performance Oil/water

Introduction

As one of the membrane materials, ceramic membrane has attracted more attention compared with organic membrane [1]. Generally, ceramic membrane, including Al_2O_3, TiO_2, ZrO_2, etc., has an asymmetric structure containing macroporous support and several porous thin layers for the separation function [2, 3].

Nowadays, ceramic membrane has been put into use in wastewater treatment especially the oily wastewater [4]. The oily wastewater has an important attention because of its harmfulness to the environment [5]. Compared with the conventional

Y. Wang (✉) · X. Hu (✉) · Q. Chang · X. Zhang · Y. Yang · K. Yang · J. Zhou
Key Laboratory of Inorganic Membrane, Jingdezhen Ceramic Institute, Jingdezhen 333001, China
e-mail: wyq8248@126.com

X. Hu
e-mail: xuebinghu2010@gmail.com

Y. Han (ed.), *Advances in Energy and Environmental Materials*,
Springer Proceedings in Energy, https://doi.org/10.1007/978-981-13-0158-2_84

techniques, membrane separation technology shows an amazing perspective as it is more effective, low cost, and environmental friendly [6, 7].

However, membrane fouling is still a major obstacle in the oily wastewater treatment [8]. Recently, many technologies, including the preparation of the membrane with different materials and the membrane modification, have been adopted to reduce membrane fouling [9, 10]. Especially, some modification methods have been widely applied to enhance the oil/water separation performance of ceramic microfiltration membrane [11, 12].

In this work, we report an efficient and feasible method to prepare the multilayer ceramic membrane following the modification with different materials. During the oily wastewater treatment, the modified membrane shows an excellent separation performance, such as higher permeate flux and higher oil rejection. Our study will be helpful to improve the performance of ceramic membrane and expand its applications.

Experimental Procedure

Preparation of Ceramic Membrane. Alumina powders (purity of 99.5%, Henan Baige Group, China) with different average particle sizes (37, 8.2 and 1.6 μm) were mixed in a definite ratio by ball milling for 2 h at 150 rpm. To prepare the membrane support, the above-mentioned alumina powders, plastering agent and pore former were mixed by ball milling for 24 h at 150 rpm. 3 wt% lubricant and 20 wt % water of the dry alumina powders were added. After mixed, aged and then extruded in the form of 19-channel tubular with diameter 32 mm. The tubular membrane support sample was dried at 20 °C and then sintered at 1640 °C for 240 min.

The interlayer and top layer of the membrane were deposited on the support by dipping the tubular membrane support into the alumina suspension with different average particle sizes (1 and 5 μm). The thickness of the membrane interlayer is 20 μm. The top layer (thickness 5 μm) is also obtained via dip coating technique. All these samples were dried at 20 °C and then sintered at 1450–1550 °C for 120 min.

Membrane Modification. In our work, three methods were used to obtain the modified membrane. (1) Homogenous precipitation method [7]. Membrane is firstly immersed in the precursor solution, and then the precipitation deposits on the pore surface using precipitator. After calcination, the coating consisting of the nano metal oxide (NMO) grains on the membrane pore surface is formed. For example, $TiO(SO_4)_2$ and urea were dissolved into distilled water and mixed at 20 °C. The ceramic membrane was saturated with the mixed solution. And then, the wet membrane was dried at 85 °C for 3 h. The membrane was washed and dried at 110 °C for 10 h. Finally, the dried membrane was calcined at 950 °C for 120 min. (2) Grafting method [13]. Firstly, the surface of the membrane was eroded by

3 M NaOH for 5 min, and then cleaned and dried. The tridecafluoroctyltriethoxysilane ($C_8F_{13}H_4Si(OCH_2CH_3)_3$, FAS) solution was prepared by dispersion FAS in hexane under strong stirring for 12 h at 20 °C. Secondly, the precleaned membrane was immersed in the FAS solution for 24 h, and then rinsed by hexane. At last, the samples were heated at 100 °C for 12 h. (3) Transfer via vacuum method [3]. The membrane was immersed into graphene oxide (GO) aqueous dispersion under vacuum at 20 °C for 60 min. After rinsed, the membrane coated GO was heated at 100 °C for 120 min.

Oil/Water Treatment of Ceramic Membrane. Filtration experiments were carried out in a cross-flow membrane module. The flow velocity was 5 ms^{-1} and transmembrane pressure was controlled by the flow valve. Permeate samples were continuously collected. The oil content of samples was also measured. The permeate flux and oil rejection were calculated using the equations had reported in the previous reference [3].

Characterization and Measurement Methods. The microstructure of the sample was observed by transmission electron microscopy (TEM, JEM-200CX, Japan) and field emitting scanning electron microscope (FE-SEM, JSM-6700F, Japan). The pore size distribution of the sample was measured by mercury intrusion porosimeter (Autopore IV9500, Micromeritics, USA). The wetting performance of the sample was evaluated with water contact angle instrument (SL200B, China). The oil content of permeate was tested by UV-spectrophotometer (Rayleigh, UV-9200) at a wavelength of 256 nm.

Results and Discussion

Microstructure of Ceramic Membrane. Figure 1 displays the obtained composite membrane can be categorized as a typical asymmetric multilayer membrane. Figure 1a, b show the surface and cross section morphology of the membrane top layer. As displayed in Fig. 1a, b, it is observed the surface and cross section of the membrane top layer is uniform and flawless. The thickness of the top layer is about 5 μm. From Fig. 1c, d, it also is found the surface and cross section of the membrane interlayer is uniform and the thickness is about 20 μm. Figure 1e, f display the cross section of the membrane support with different magnifications. It can be observed the microstructure of the support is continuous and porous. Figure 1 also appears the penetration of the top layer into the interlayer pores and the interlayer into the support pores is successfully prevented, and the top layer has been coated on the surface of membrane interlayer homogeneously.

Figure 2 displays the pore size distribution of the top layer, interlayer and support of the ceramic membrane. From Fig. 2, we can find the membrane has a narrower pore size distribution, and the average pore size of the top layer, interlayer and support of the membrane are 0.6, 0.8 and 3.8 μm, respectively. All these results show the membrane has an excellent microstructure and continuous pore gradient structure.

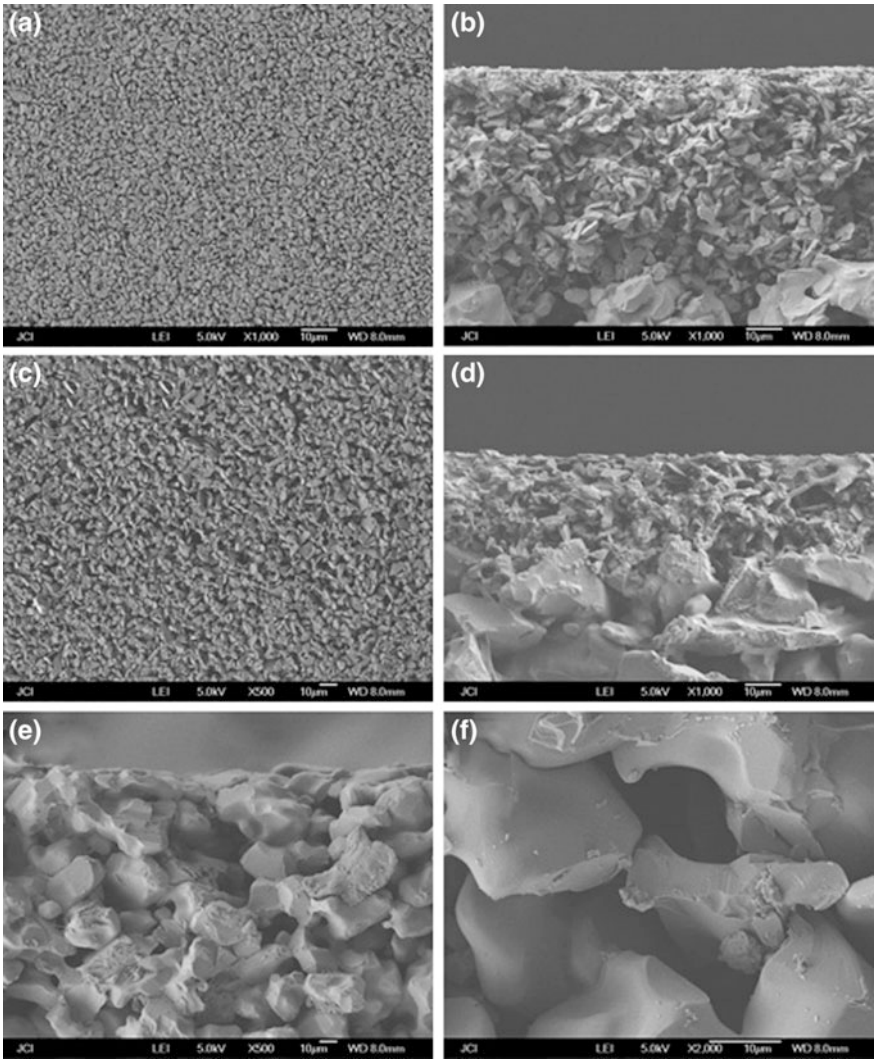

Fig. 1 SEM images of membrane. Surface of top layer (**a**) and interlayer (**c**), cross section of top layer (**b**), interlayer (**d**) and support with various magnification (**e**) and (**f**)

Microstructure and Wetting Performance of Modified Ceramic Membrane. The membrane is modified by FAS, NMO or GO, respectively. Figure 3 displays the microstructure of original and modified membrane. From Fig. 3b, FAS has been coated on the surface of the membrane and the modified membrane is superhydrophobic (the water contact angle is 164°). TEM images of the samples (Fig. 3c, d)

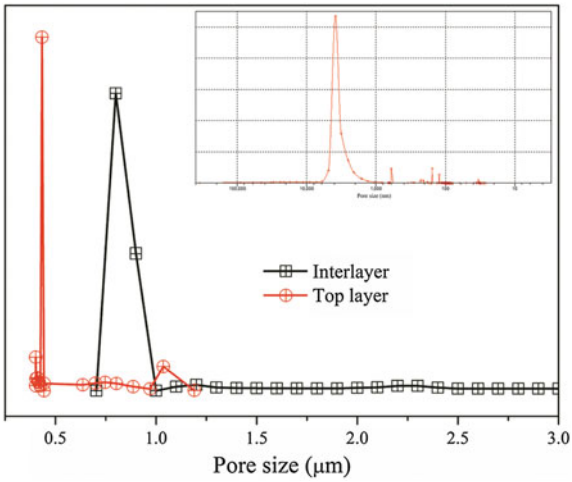

Fig. 2 Pore size distribution of top layer, interlayer and support (inset) of membrane

display NMO and GO has been coated on the pore surface of membrane, and the thickness of NMO and GO coating is ~20 nm and 3 nm, respectively.

From the insets of Fig. 3, it should also be noted that the wetting performance of the membrane changes significantly with the modification. Compared with the

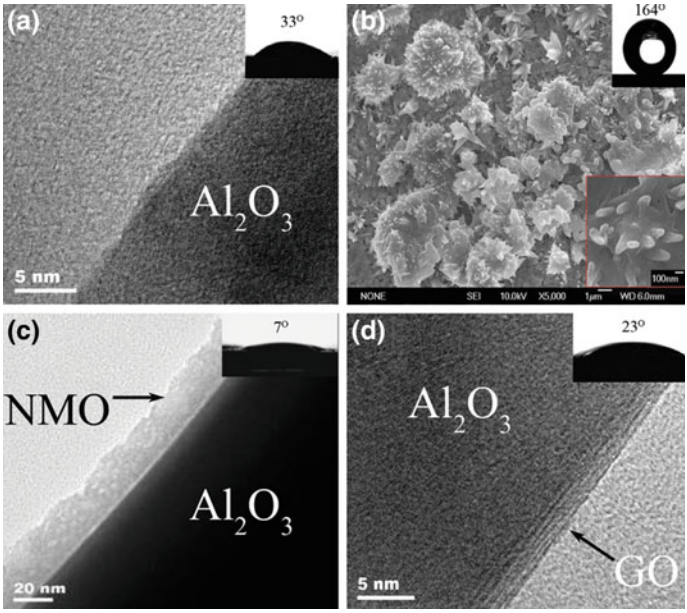

Fig. 3 TEM and SEM images of membrane. Unmodified membrane (**a**), and FAS (**b**), NMO (**c**) and GO (**d**) modified membrane. The inset shows the water contact angle of the membrane

unmodified membrane (the water contact angle is 33°), the water contact angle of the membrane modified with NMO and GO are 7° and 23°, respectively. It shows the NMO and GO modification can improve the hydrophilicity of the membrane, which is helpful to promote the membrane performance.

Oil/Water Separation Performance of Ceramic Membrane. The oil/water separation experiments were carried out for treating a lab-made oily wastewater with the different membranes, and the oil concentration is 1 g L^{-1}. As shown in Fig. 4a, the modified membrane exhibits higher permeate flux than the original membrane. The stable permeate flux of the modified membrane is higher about 27.8% than that of the original membrane. The oil content of permeate of modified and original membranes is shown in Fig. 4b, it is found the oil content of the permeate for different membranes, ranging between 12.8 and 25.5 mg L^{-1}. The permeate of modified membrane has a lower oil content compared with that of the original membrane, and the oil rejections for the original and modified membranes are 98.1 and 98.7% after 120 min, respectively. These results show the modified membrane has a higher oil rejection than the original membrane. Figure 4c indicates the permeate of the modified membrane is transparent, implying a lower oil content in the permeate.

In this work, the oily wastewater coming from automobile company was also investigated. The oil concentration of the wastewater is 1.69 g L^{-1}. As shown in Fig. 5a, the modified membrane exhibits a higher permeate flux than original membrane. The stable permeate flux of the modified membrane is higher about 43%

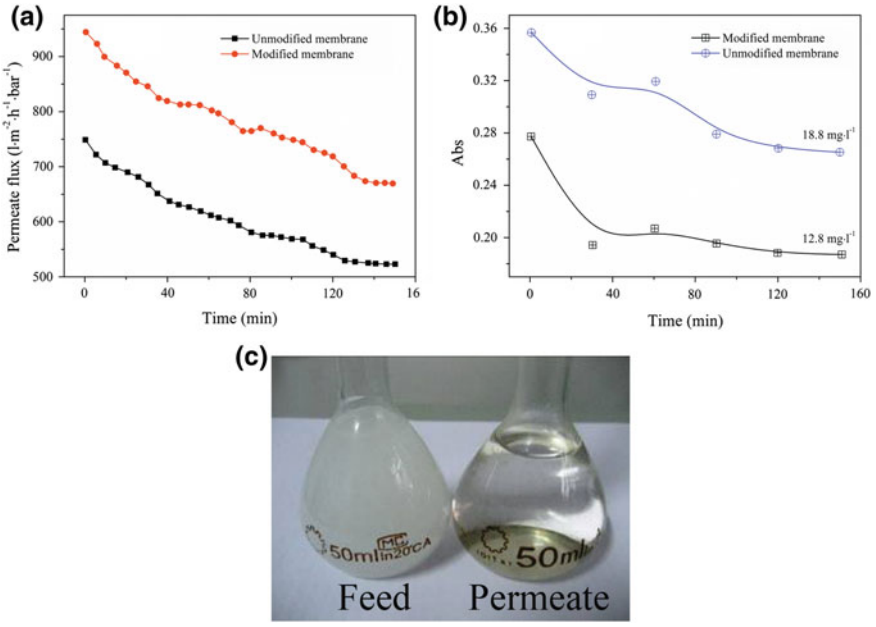

Fig. 4 The permeate flux (**a**) and, oil rejection (**b**) and photos of feed and permeate for membrane (**c**) for treating a lab-made oily wastewater

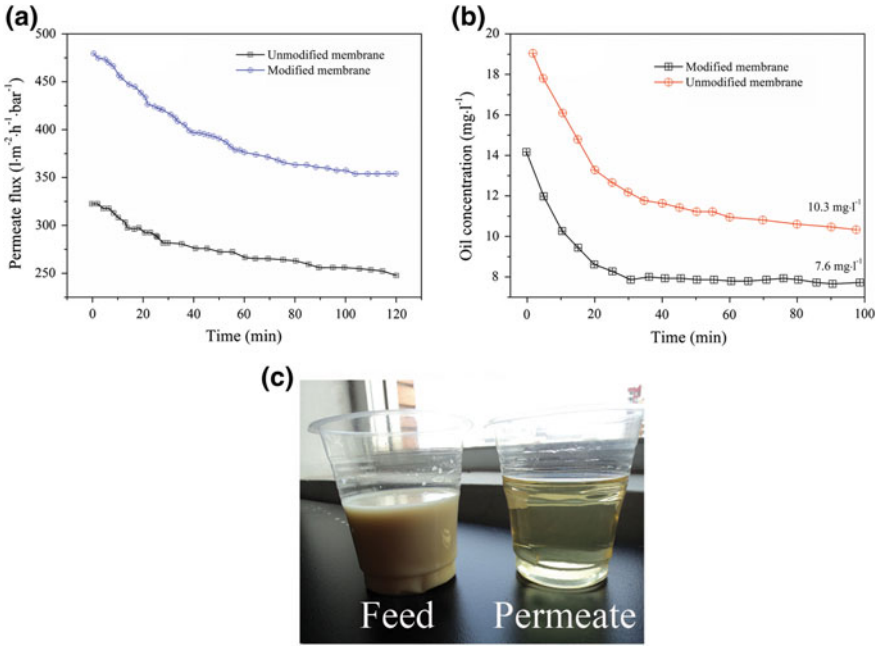

Fig. 5 The permeate flux (**a**) and, oil rejection (**b**) and photos of feed and permeate for membrane (**c**) for treating an automobile company oily wastewater

than that of the original membrane. The oil content of permeate of the modified and original membranes is shown in Fig. 5b. The permeate of the modified membrane has a lower oil content compared with that of the original membrane, and the oil rejections for the original and modified membranes are 99% and 99.3% after 100 min, respectively. Especially, the oil content of the permeate for the modified membrane is less than 10 mg L^{-1} after 20 min. These results indicate the modified membrane has higher oil rejection than the original membrane. The membrane performance is superior to those reported literatures [4, 9]. From Fig. 5c, the permeate for modified membrane is relatively clear. The results display the modified membrane has an improved separating efficiency of the oil/water emulsion treatment. The possible reasons that the modified membrane indicates better performance have been explained in our pervious literatures [3, 6, 11].

Conclusions

A feasible method is developed to prepare ceramic composite membrane with a uniform multilayer structure and a narrower pore size distribution by the extrusion and dip coating methods using alumina powders as the main raw material. The thickness of the top layer and membrane interlayer is about 5 and 20 μm,

respectively. The average pore size of the top layer, interlayer and support of the membrane are 0.6, 0.8 and 3.8 μm, respectively. With the modification of FAS, NMO or GO, the water contact angle of the modified membrane can vary from 7° to 164°, and the oil/water separation performance of the modified membrane is significantly improved.

Acknowledgements The authors gratefully acknowledge the financial support of this research by the National Science Foundation of China (Nos. 51662019, 51662020, 51362015) and the research projects of Jiangxi department of Science and Technology (Nos. 20161ACB21008, 20143ACB21022) and Jiangxi department of Education (No. GJJ150929).

References

1. S. Tang, Z. Zhang, J. Liu, X. Zhang, Double-win effects of in-situ ozonation on improved filterability of mixed liquor and ceramic UF membrane fouling mitigation in wastewater treatment. J. Membr. Sci. **533**, 112–120 (2017)
2. Q. Chang, Y. Wang, S. Cerneaux, J. Zhou, X. Zhang, X. Wang, Y. Dong, Preparation of microfiltration membrane supports using coarse alumina grains coated by nano TiO_2 as raw materials. J. Eur. Ceram. Soc. **34**, 4355–4361 (2014)
3. X. Hu, Y. Yu, J. Zhou, Y. Wang, J. Liang, X. Zhang, Q. Chang, L. Song, The improved oil/water separation performance of graphene oxide modified Al_2O_3 microfiltration membrane. J. Membr. Sci. **476**, 200–204 (2015)
4. L. Zhu, M. Chen, Y. Dong, C.Y. Tang, A. Huang, L. Li, A low-cost mullite-titania composite ceramic hollow fiber microfiltration membrane for highly efficient separation of oil-in-water emulsion. Water Res. **90**, 277–285 (2016)
5. S. Jamaly, A. Giwa, S.W. Hasan, Recent improvements in oily wastewater treatment: Progress, challenges, and future opportunities. J. Environ. Sci. **37**, 15–30 (2015)
6. Q. Chang, J. Zhou, Y. Wang, J. Liang, X. Zhang, S. Cerneaux, X. Wang, Z. Zhu, Y. Dong, Application of ceramic microfiltration membrane modified by nano-TiO_2 coating in separation of a stable oil-in-water emulsion. J. Membr. Sci. **456**, 128–133 (2014)
7. Q. Chang, X. Wang, Y. Wang, X. Zhang, S. Cerneaux, J. Zhou, Effect of hydrophilic modification with nano-titania and operation modes on the oil-water separation performance of microfiltration membrane. Desalin. Water Treat. **57**, 4788–4795 (2016)
8. D. Lu, T. Zhang, J. Ma, Ceramic membrane fouling during ultrafiltration of oil/water emulsions: roles played by stabilization surfactants of oil droplets. Environ. Sci. Technol. **49**, 4235–4244 (2015)
9. D. Vasanth, G. Pugazhenthi, R. Uppaluri, Cross-flow microfiltration of oil-in-water emulsions using low cost ceramic membranes. Desalination **320**, 86–95 (2013)
10. T. Meng, R. Xie, X.J. Ju, C.J. Cheng, S. Wang, P.F. Li, B. Liang, L.Y. Chu, Nano-structure construction of porous membranes by depositing nanoparticles for enhanced surface wettability. J. Membr. Sci. **427**, 63–72 (2013)
11. J. Zhou, J. Wu, Y. Wang, J. Liang, X. Zhang, R. Cao, Modification of Al_2O_3 Microfiltration Membrane by Nano-crystalline TiO_2 Coating. J. Inorg. Mater. **21**, 725–730 (2016)
12. Y. Yu, W. Hou, X. Hu, Y. Yu, L. Mi, L. Song, Superhydrophobic modification of an Al_2O_3 microfiltration membrane with TiO_2 coating and PFDS grafting. RSC Adv. **4**, 48317–48321 (2014)
13. J. Lu, Y. Yu, J. Zhou, L. Song, X. Hu, A. Larbot, FAS grafted superhydrophobic ceramic membrane. Appli. Surf. Sci. **255**, 9092–9099 (2009)

Application of Carbide Slag in Autoclaved Aerated Concrete

Han Fuqiang, Tan Xing and Zhao Fengqing

Abstract Carbide slag is a solid waste which is difficult to handle. When it is used to substitute for lime to produce autoclaved aerated concrete (AAC) block without necessary treatments, the aeration efficiency is low and density of the AAC block is high. Besides, the initial mechanical strength of the block is lower because of lower curing temperature in static placing stage. The influence of hot water and pre-curing process (50 °C, 5 h) before static placing phase were investigated in this paper. The results show that when the substitution ratio of carbide slag for lime is below 50%, the performance of the AAC block is good enough to reach the level of standard GB11968-2006. As the substitution ratio is 38%, the compressive strength is 5.55 MPa with a dry density of 620 kg/m^3. The application of carbide slag as substitution for lime is realized in production of AAC block and the production cost is well reduced.

Keywords Solid waste · Carbide slag · Autoclaved aerated concrete
Pre-curing process

H. Fuqiang · T. Xing · Z. Fengqing (✉)
Hebei University of Science and Technology, Shijiazhuang 050018, China
e-mail: zhaofq3366@126.com

H. Fuqiang
e-mail: 568197188@qq.com

T. Xing
e-mail: 1067233667@qq.com

Z. Fengqing
Hebei Engineering Research Center of Solid Wastes Utilization,
Shijiazhuang, China

Y. Han (ed.), *Advances in Energy and Environmental Materials*,
Springer Proceedings in Energy, https://doi.org/10.1007/978-981-13-0158-2_85

Introduction

Carbide slag is the solid waste produced in PVC production by calcium carbide acetylene method. Because of large amount of emissions and high transport cost, it is mostly treated in disorderly stacking and landfill. The main component of calcium carbide slag is calcium hydroxide. If not treated properly, it will cause the land and ground water pollution, endangering people's health as well as resulting in waste of resources [1].

Production of construction and building material is an important approach for solid waste utilization. Fly ash, a common industrial waste, is often used to produce AAC by autoclaved hydration with lime and gypsum [2–5]. Aluminum is used as foam agent in this process. When carbide slag is used to substitute lime partly, the temperature of slurry will be lowered, thus influencing foaming performance. Besides, the initial mechanical strength of the block will also be reduced. Therefore, the slurry temperature is an important factor in forming and thickening process [6]. If it is solved, the lime uses will be reduced and thus the carbon dioxide associated with this process is also reduced [7]. The key in calcium carbide slag substitute for lime is how to guarantee the foaming efficiency and hydration temperature of initial process.

To meet this end, hot water is used for mixing raw materials and pre-curing stage is adopted before autoclaved curing process, in which, waste steam form autoclave process is used to provide the energy needed in order to save energy. The object of this work is to use carbide slag substitute for lime partly for hydration with siliceous material to produce AAC, realizing utilization of carbide slag, and therefore reducing energy consumption and carbon dioxide emissions associated with AAC production.

Materials and Methods

Materials. Compositions of various materials are listed in Table 1. Cement gypsum, aluminum powder and water reducing agent are commercially available.

Foaming Performance Test and Evaluation. Pour the slurry containing aluminum and alkali material into molds, the original height of the slurry is measured

Table 1 Chemical composition of main raw materials (wt%)

Raw material	CaO	MgO	SiO_2	Fe_2O_3	Al_2O_3	SO_3	LOI
Fly ash	4.66	0.83	49.43	5.40	36.51	0.74	6.28
Lime	84.80	7.11	2.68	0.78	1.41	2.58	6.44
Carbide slag	93.79	0.21	3.34	0.31	1.72	0.50	–

and remarked as h; and then pre-cure at certain temperature in the curing box and the slurry begin to foam. When finished, the final height of the block is marked as H. The difference between H and h is the foaming height. See Fig. 1. According to experiments, when the difference is not less than 3.0, the density of the block can meet the requirement of GB11968-2006. The evenness of the foam is another evaluation index.

Preparation Method of AAC Samples. Fly ash, carbide slag, lime and water are mixed well. Lime accounts for 24% of the total solid of the samples. Then add aluminum powder and water. In order to compensate for the temperature decrease because of the substitution of carbide slag for lime, hot water of 70 °C is used. Samples of 70 × 70 × 70 mm are prepared, pre-curing at 50 °C for 5 h. The energy of the hot water and the pre-curing stage can be provided by the waste heat of the autoclaved curing process. The samples are autoclaved then at 180 °C for 4 h. Figure 2 shows the process of AAC production from fly ash and carbide slag.

Product Performance Test. Density and strength performance of AAC samples were tested in accordance with GB11968-2006 (Autoclaved aerated concrete performance test method, China National Standard). The samples were dried and weighed, obtaining the density of the block. The mechanical strength values were tested on NYL-300A. The results are the average of every three samples.

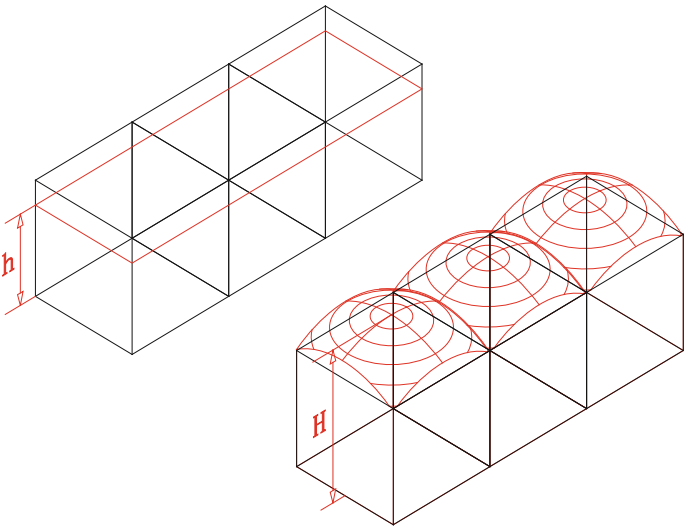

Fig. 1 Schematic foaming performance test

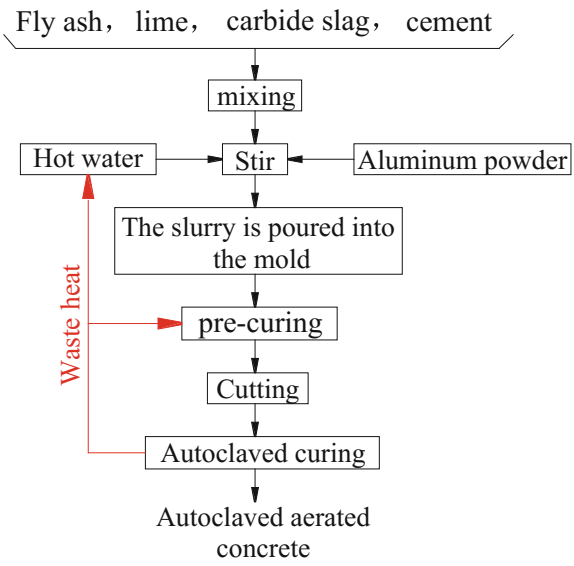

Fig. 2 Workflow of producing AAC from fly ash and carbide slag

Results and Discussion

Foaming Effect. Hot water 70 °C and the pre-curing process (50 °C, 5 h) is used before autoclaved process. The waste heat from autoclave process is used without increasing additional energy consumption. The foaming performance of slurry at various replacement ratio of carbide slag for lime is shown in Table 2.

It can be seen from Table 2 that the foaming efficiency are good at the replacement ratio of carbide slag for lime is 13, 25, 38%. With the increase in the replacement ratio, the maximum temperature of the slurry shows a decreasing trend. When the content of the carbide slag is 13%, the foam height of the slurry reaches relative highness of 3.5 cm. With the increase in the amount of carbide slag, the effective calcium oxide content in slurry is lower, and the digestion heat is less. In such case, the temperature of the slurry is reduced, therefore decreasing the foaming

Table 2 Different content of carbide slag

Experiment	Replacement ratio of carbide slag for lime (%)	Foaming height (cm)	Maximum temperature (°C)	Foaming state
1	0	3.4	73	Good
2	13	3.5	72	Good
3	25	3.3	70	Good
4	38	3.0	65	Good
5	50	3.1	62	Qualified
6	>50	<3.1	<62	Poor

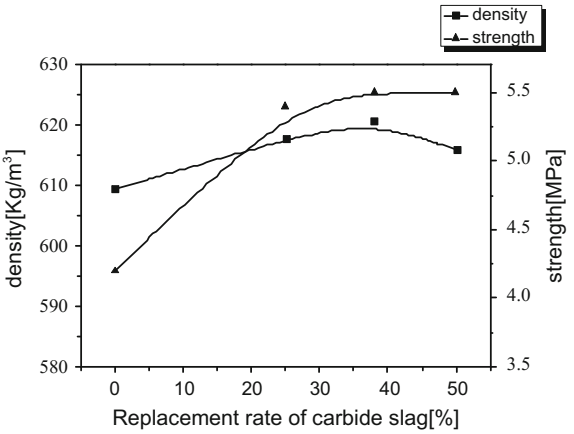

Fig. 3 Effect of replacement ratio of calcium carbide slag on the density and strength of AAC

performance of aluminum. The foam is good even the replacement ratio is 50%. That is to say, the use of hot water and pre-curing process is effective for AAC production when carbide slag is used to replace lime partly.

Density and Strength of Autoclaved Test Pieces. Density and mechanical strength are the main characteristics of AAC products. The Performance of AAC samples at various replacement ratio of carbide slag for lime is shown in Fig. 3.

It can be seen from Fig. 3 that the density and strength of the test piece tend to increase as the replacement ratio of carbide slag increases. This is because with the increase in the ratio of carbide slag replacement, the effective CaO content decreases, lowering the temperature of the paste, weakening the foaming ability, and therefore the density and strength of the products increases.

Anyway, with the replacement ratio below 50%, the density and compressive strength of all the blocks conform to GB11968-2006. When the replacement ratio of carbide slag is 38%, the compressive strength of the test piece reaches a maximum of 5.5 MPa.

Conclusions

(1) The use of carbide slag instead of lime to produce AAC reduces not only the energy consumption of lime production, but also the environmental pollution and waste of resources. The product produced here is environment-friendly material, achieving the best use of solid wastes as well.

(2) Replacing lime with calcium carbide slag directly have adverse effects on foaming performance of slurry and initial strength of the block. This problem is solved by mixing raw material with hot water and a pre-curing stage before autoclaving process. The results showed that when the replacement ratio of lime with calcium carbide slag falls the range of 0–50%, the density and the mechanical strength of the AAC block conform to GB11968-2006.

(3) With the increase of replacement ratio of calcium carbide slag for lime, the heat generated by calcium oxide hydration decreases and the temperature inside the test block is reduced, which affects the foaming of slurry. When the replacement ratio of carbide slag is 38%, the density of AAC is 621 kg/m^3, and the compressive strength reaches up to 5.5 MPa.

References

1. J.T. Hao, X.F. Jiang, H.W. Yang, et al., Research progress and application of carbide slag. J. Guangzhou Chem. Ind. **8**, 45–46, 122 (2013)
2. Y. Zhang, X.W. Gong, W.W. Duan, Economy analysis on the application of autoclaved aerated concrete blocks. J. China Concr. Cem. Prod. **5**, 60–62 (2010)
3. C.W. Du, G.Z. Li, Preparation and modification of fly ash aerated concrete block. J. Fly Ash. **4**, 21–23 (2013)
4. C.X. Cao, Application on carbide slag in autoclaved fly ash aerated concrete. J. Zhuanwa. **5**, 42–44 (2016)
5. F.Q. Zhao, J.Q. Liu, Q. Li et al., Study of foamed concrete from activated ash/slag blended cement. J. Adv. Mater. Res. **160–162**, 821–826 (2010)
6. H.-H. Feng, Q. Huang, S.-H. Qu, The application study of fly ash content light foam concrete. J. Appl. Chem. Ind. **45**(3), 520–524 (2016)
7. B. Cai, C. Dong, L. Liu, Z. Zhang, Analysis of lime production and energy consumption in China. J. Environ. Eng. **1**, 124–127, 131 (2012)

Hydrothermal Synthesis of Manganese-Containing Hydrochars for Lead Ion Removal

Can Wang, Jia Li, Xixi Liu, Shengtao Xing and Zichuan Ma

Abstract Manganese-containing hydrochars were synthesized by hydrothermal carbonization process of *Fraxinus mandshurica* sawdust in the presence of $KMnO_4$ or $MnSO_4$. The products were characterized by X-ray diffraction (XRD), field emission scanning electron microscope (FESEM), X-ray photoelectron spectroscopy (XPS), Fourier transform infrared spectroscopy (FTIR), energy dispersive X-ray spectroscopy (EDS) and N_2 adsorption–desorption isotherms. The characterization results indicated that the structure, composition and surface properties of the products were dependent on the type of manganese compounds. The introduction of Mn into hydrochar increased its surface area and pore volume. The manganese-containing hydrochar (M7HC) prepared with $KMnO_4$ was a mixture of Mn_3O_4, $MnCO_3$ and carbon with low graphitization degree. Adsorption experiments were carried out to investigate the effect of various factors such as pH, contact time and initial concentration on the adsorption of Pb(II). The kinetic data and the thermodynamic data were well fitted by the pseudo-second order model and Langmuir model, respectively. The maximum adsorption capacity of Pb(II) on M7HC was found to be 95.05 mg/g. The results showed that M7HC could be effectively used as a promising cheap adsorbent to remove heavy metal ions from aqueous solution.

C. Wang · J. Li · X. Liu · S. Xing · Z. Ma (✉)
College of Chemistry and Material Science, Hebei Normal University, Shijiazhuang 050024, China
e-mail: mazc@vip.163.com

C. Wang
e-mail: wangcan15@163.com

J. Li
e-mail: 1126120755@qq.com

X. Liu
e-mail: 1031697824@qq.com

S. Xing
e-mail: stxing07@sina.com

Y. Han (ed.), *Advances in Energy and Environmental Materials*,
Springer Proceedings in Energy, https://doi.org/10.1007/978-981-13-0158-2_86

Keywords Manganese-containing hydrochar · Hydrothermal carbonization
Lead ions · Adsorption

Introduction

Heavy metal pollution is a serious environmental problem attracting much more attention. Heavy metals (e.g. Pb^{2+}, Cd^{2+} and Ni^{2+}) are mostly toxic even at extremely low concentration and cannot be biodegraded [1]. Adsorption has been proved to be an efficient technology for heavy metals removal from contaminated water. Carbon materials such as activated carbons, carbon nanotubes and graphene exhibit high adsorption capacity for heavy metals due to their unique surface property and porous structure [2, 3]. However, the high cost limits their application, especially in developing countries [4, 5]. Therefore, the development of low-cost and efficient adsorbents is highly desirable for removing heavy metals from contaminated water.

Biochar is a kind of solid materials derived from the carbonization of carbon-rich biomass such as crop straw, sludge and wood residues by different methods [1, 6]. Biochar with various degrees of carbonization has a wide range of potential applications including fuel, carbon capture, soil amendment and adsorbent. Recently, many studies have focused on the synthesis of biochar for water treatment. The results suggest that biochar is a promising cheap adsorbent for water purification [7]. The adsorption ability of biochar towards contaminants depends on its physicochemical properties, which are associated with the raw materials and preparation conditions. Moyo et al. found that the biochar derived from the maize cob exhibited excellent ability to remove Cd(II) from aqueous solution [8].

In order to improve the adsorption capacity of biochar, some methods including hydrothermal precipitation, microwave irradiation, chemical precipitation and simultaneous carbonization have been used for the fabrication of biochar-based composites with different inorganic components [9–11]. Manganese oxides have been extensively used as adsorbents for heavy metals due to their environment-friendly properties and strong affinity for heavy metals [12]. Therefore, the composites composed of manganese oxide and porous biochar probably have excellent performances for heavy metal removal. Song et al. reported that the MnO_x-loaded biochars exhibited much higher adsorption capacity for Cu^{2+} than the original one, which was mainly due to the formation of inner-sphere complexes of Cu^{2+} with MnO_x and oxygen-containing groups on the surface [4]. Wang et al. found that the introduction of manganese oxide onto the biochar resulted in an increase of the surface hydroxyl density and a decrease of pH_{PZC} (pH at the point of zero charge), which has favored the adsorption of Pb(II) [13]. However, the previous syntheses usually required a high-temperature treatment or a sophisticated procedure. Moreover, the influence of inorganic components on the adsorption ability of biochar could be further investigated.

Because of the energy shortage and environmental concerns, hydrothermal carbonization (HTC) of biomass, which is a thermochemical treatment of an aqueous solution with a dispersion of biomass, is receiving an increasing attention [14, 15]. During the HTC process, the biosolids (such as plant biomass, woody biomass, food wastes, and algae) could be converted into valuable carbon materials (i.e., hydrochar) [16]. In this work, manganese-containing hydrochars were prepared by HTC of *Fraxinus mandshurica* sawdust (a waste material from the wood working industry) in the presence of $KMnO_4$ or $MnSO_4$. The pH change, volume of gaseous products, and yield of hydrochar in different systems (pure water, $MnSO_4$ aqueous solution and $KMnO_4$ aqueous solution) were examined. The physicochemical properties of Mn(II)-modified, Mn(VII)-modified and unmodified hydrochars were investigated by different characterization methods, and their corresponding adsorption capacities towards lead ions were also evaluated.

Materials and Methods

Hydrochars Preparation. *Fraxinus mandshurica* is one of the most common deciduous trees and distributed widely around the world. Therefore, it was chosen as representative woody feedstock for hydrochar preparation in this study. The hydrochars used in this study were prepared by HTC of *Fraxinus mandshurica* sawdust. All the solutions applied in this work were prepared with deionized water, which was also used to rinse and clean the samples. The sawdust was ground to pass through a 0.83 mm sieve. 15 g of the sawdust was mixed with 100 mL water and then the mixture was transferred into a 250 mL stainless steel autoclave equipped with a mechanical stirrer. Prior to the reaction, the biomass was stirred manually for 30 min to ensure complete wetting and the initial solution pH was determined. Under stirring (200 r/min) at the autogenic pressure, the autoclave was heated to 220 °C, and then held continuously for 2 h. During this process, the volume of gaseous products was determined by a drainage method. After that, the autoclave was cooled down to room temperature naturally and the solution pH was determined. The black solid product, which was just the hydrochar needed to prepare in this study, was collected by filtration, then washed with acetone and water for several times in sequence, and dried at 105 °C in an oven. Finally the dried sample was then ground to pass through a 0.25 mm sieve. The sample prepared with pure water, $MnSO_4$ aqueous solution and $KMnO_4$ aqueous solution were designated as HC, M2HC and M7HC, respectively. In this study, the hydrochar yield was calculated by the following equation:

$$\text{Yield}(\%) = \frac{w_t}{w_0} \times 100 \quad (1)$$

where w_t is the dry weight in gram of the hydrochar after water wash, and w_0 is the dry weight of the raw biomass.

Characterization. The bulk contents of C, H and N in the three samples were determined using an elemental analyzer (Vario MICRO, Elementar, Germany). Their ash contents were measured by heating the samples at 750 °C for 4 h in open crucibles. The oxygen contents were calculated based on mass difference (100%–C, H, N and ash %). The other trace inorganic elements in the samples were determined by inductively-coupled plasma emission spectroscopy (ICP-OES, Optima 2300, PerkinElmer, USA) after digesting with a mixture of HNO_3 and $HClO_4$. Surface chemical composition was determined by X-ray photoelectron spectrometer (XPS, AXIS-Ultra, Kratos, UK), using monochromatic Al Kα radiation (225 W, 15 mA, 15 kV). The morphology of the samples was examined by a field emission scanning electron microscope at 3 kV (HitachiS-4800, Japan), and the localized elemental information on the chosen region was viewed with an energy dispersive X-ray spectroscopy (EDS, EDAX PV9900) in conjunction with FESEM. The phase identification was carried out by X-ray diffraction (XRD) with a Bruker D8-Advance at 40 kV/40 mA using Cu Kα radiation (λ = 0.154 nm). XRD patterns were recorded by the step scanning from 10° to 70° (2θ angular range). Their functional groups were characterized using Fourier transform infrared spectroscopy (FTIR) (Nexus 870, Nicolet, USA). The Brunauer-Emmett-Teller surface area (S_{BET}), total pore volume (V_{tot}), and pore size distribution of the hydrochars were obtained by N_2 adsorption–desorption at 77 K using an Automated Gas Sorption Analyzer (NOVA 4000e, Quantachrome, USA). pH_{PZC} was determined using the pH drift method [17].

Adsorption Experiments. The adsorption isotherms were studied using batch tests in 50 mL polypropylene tubes containing 30 mL of the aqueous solution. The pH of the solution was controlled at pH 5.5 by addition of HCl or NaOH dilute solutions. The dosage of the hydrochars as adsorbents was 1 g/L, and the initial concentrations of Pb^{2+} were in the range of 2–100 mg/L, which was chosen according to the preliminary experiments. The tubes were then put into a gas bath constant temperature oscillator (HZQ-F160, China) maintained at 150 r/min and 25 °C for 20 h. After reaching the equilibration, the samples were taken and filtered through a Millipore filter (pore size 0.22 μm) for analysis. The adsorption kinetic study was carried out with a fixed Pb^{2+} concentration (50 mg/L) at pH 5.5. The effects of solution pH on the adsorption of Pb^{2+} were investigated by varying the solution pH. The concentrations of Pb^{2+} were determined using an atomic absorption spectrometer (180-70, Hitachi, Japan).

Results and Discussion

Effects of Mn(VII)/Mn(II) Compounds on HTC Processes. The effects of Mn compounds on HTC processes were investigated under the same conditions (reaction temperature, HTC holding time, water to biomass ratio, and biomass particle size). As shown in Table 1, the added Mn compounds significantly affected

Table 1 Effects of Mn(VII)/Mn(II) compounds on HTC processes

Sample	pH_{ini}	pH_{fin}	Q_H (mmol)[a]	V_g (mL)	Yield (%)
HC	5.20	3.46	0.034	370	41.1
M2HC	4.30	2.40	0.39	340	46.1
M7HC	8.55	6.37	4.3×10^{-5}	1100	38.2

[a]$Q_H = (10^{-pH_{fin}} - 100^{-pH_{ini}}) \times 100$

the pH (including the initial pH and final pH), the H^+ amount released from the HTC process Q_H, the volume of gaseous products V_g and the hydrochar yield, suggesting that they might participate in the thermochemical conversion of the sawdust such as hydrolysis, dehydration, decarboxylation, condensation, polymerization, and aromatization reactions [18]. Comparing to the process without addition of Mn compound (HC), the solution pH and V_g was decreased, but the yield was increased in the presence of $MnSO_4$ (M2HC). However, the addition of $KMnO_4$ (M7HC) had the opposite effect with $MnSO_4$. As known from the literature [19], CO_2 was the dominant gaseous species in all HTC experiments, and most of the remainder was CO. In addition, the trace amount of hydrogen and low-molecular-weight hydrocarbons might be produced. Therefore, it is speculated that the addition of a strong oxidant ($KMnO_4$) significantly increased the amount of CO_2 produced. The decrease of pH in all HTC experiments suggests the formation of acidic substances. Hoekman et al. reported that aqueous products obtained from HTC treatments of woody and herbaceous biomass were quite acidic, which was attributed to the production of a large number of organic acids including formic acid, acetic acid, levulinic acid, and lactic acid [19]. The amounts of released H^+ (Q_H in Table 1) were quite different in the three HTC experiments, and followed the order of M2HC > HC > M7HC, matching well with the yields. On the contrary, the volume of gaseous products followed the order of M7HC > HC > M2HC. It is assumed that $MnSO_4$ accelerate the formation of organic acids while $KMnO_4$ has the opposite effect. Because much more gaseous products were observed for M7HC, the produced organic acids might be further oxidized into CO_2 by $KMnO_4$. The literature showed that the mass yield was negatively related to the carbonization degree, and temperature was a significant factor in HTC [20]. The results indicate that the addition of $KMnO_4$ could promote the carbonization of biomass.

Characterization of Mn-Modified Hydrochars. The bulk elemental compositions (C, H, N and O) and ash contents of three hydrochars were listed in Table 2. For three hydrochars, the contents of the above basic components were obviously different. In comparison with HC, the contents of C and ash in M7HC were increased, especially the ash content, while the contents of O and H were decreased. On the contrary, the modification with $MnSO_4$ markedly decreased the C content, but increased greatly the O content. The N contents of M2HC and M7HC were slightly higher than that of HC. The H/C atomic ratio reflects the condensation degree of hydrochar structure. The low H/C rate suggests a highly condensed structure, and an H/C rate of ≥ 0.7 indicates non-condensed aromatic structures

Table 2 Physico-chemical characteristics of the hydrochars

Properties of hydrochar	HC	M2HC	M7HC
Bulk element composition (wt%)			
C	63.92	53.86	65.20
H	5.31	4.95	5.16
N	0.012	0.021	0.033
O	30.33	40.39	18.00
Ash	0.43	0.78	11.6
Atomic ratio			
H/C	1.00	1.10	0.95
O/C	0.36	0.56	0.21
Content of the mineral elements (mg/g)			
Na	0.039	0.027	0.056
K	0.015	0.009	0.577
Mg	0.112	0.042	0.120
Ca	0.621	0.19	0.726
Fe	0.369	0.13	0.139
Mn	0.106	1.20	36.28
Surface element composition (wt%)[a]			
C	66.12	66.62	57.91
O	33.88	33.14	35.05
Mn	–	0.12	7.04
S_{BET} (m^2/g)[b]	2.22	3.67	3.59
V_{tot} (cm^3/g)[c]	0.002	0.009	0.006
Pore diameter (nm)	3.70	5.27	4.62
pH_{PZC}	≤ 4.0	≤ 4.0	7.0

[a]Determined by EDS; [b]S_{BET} BET-N_2 specific surface area; [c]V_{tot} total pore volume

such as lignin [21, 22]. In the present study, the H/C ratios of the three products were all above 0.7, indicating that some lignin fractions still remained unchanged. The H/C ratio of M7HC was lower than that of HC, while the H/C ratio of M2HC was higher than that of HC. It means that the condensation degree of hydrochar can be modified by different Mn compounds. On the other hand, the introduction of $KMnO_4$ reduced the polar functional groups, resulting in a low polarity index (the O/C ratios in Table 2).

The contents of inorganic mineral elements in the hydrochars were also given in Table 2. The Mn content in M7HC was much higher than that in M2HC and HC, which was in line with its highest ash content. EDS analysis results (Table 2) showed that the relative surface contents of O and Mn in M7HC were 35.05 and 7.04%, while their bulk contents were 18.00% and 3.63%, respectively. This result indicates that most of the manganese oxides were dispersed on the surface of M7HC.

The crystallinity and phase of the samples were further examined by XRD. As shown in Fig. 1, all the samples presented a poor crystallinity. The broad and weak

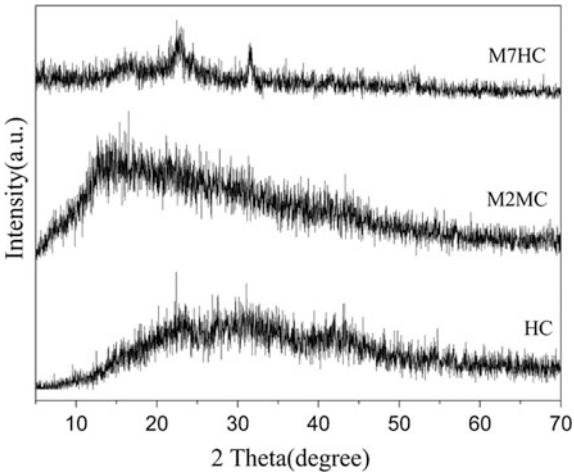

Fig. 1 XRD patterns of different hydrochars

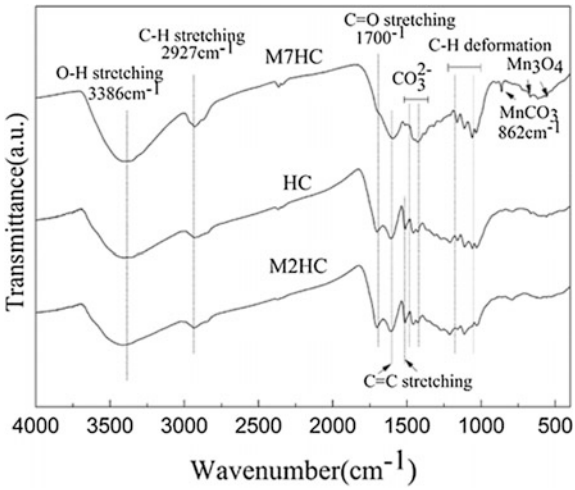

Fig. 2 FTIR spectra of different hydrochars

peaks located between 10° and 40° for HC and M2HC could be ascribed to amorphous graphitic carbon [23–25]. For M7HC, the peaks at 24.3°, 31.5° and 52° were indexed to Mn_3O_4 (JCPDS 24-0734), while the peak at 16.5° was assigned to $MnCO_3$ (JCPDS 86-0173). Additionally, the broad peak in range of 20.5–24.5° could be indexed as the (002) crystal plane of graphitic and turbostratic carbon [25]. The hydrothermal treatment of biomass with $KMnO_4$ gave a mixture of Mn_3O_4, $MnCO_3$ and carbon with a low graphitization.

The FTIR spectra of different samples were shown in Fig. 2. The bands at 3386 and 2927 cm^{-1} were assigned to the stretching vibrations of O–H and aliphatic C–H, respectively, while the band at 1700 cm^{-1} was attributed to the vibration of aromatic C=O (carbonyl/carboxyl) [24]. The peak intensity of M7HC at 1700 cm^{-1}

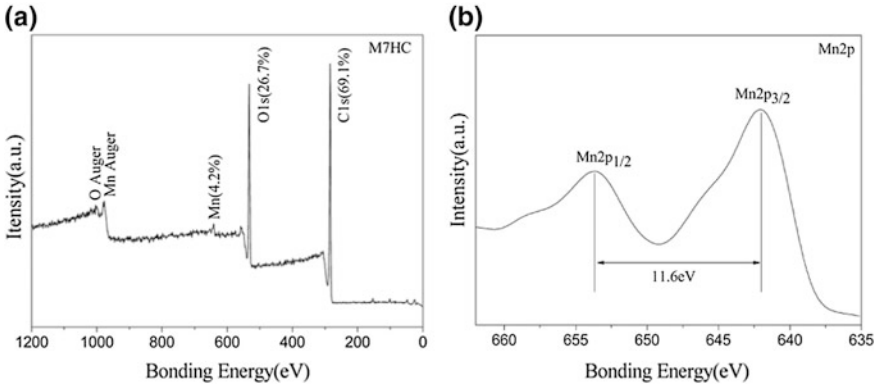

Fig. 3 XPS spectra of M7HC: **a** survey scan, **b** Mn 2p high-resolution spectra

was much weaker than that of HC and M2HC, which may be due to that $KMnO_4$ promoted the decarboxylation of biomass. The bands at 1603 and 1510 cm^{-1} were assigned to the aromatic C=C vibration, while signals at 1180–1030 cm^{-1} might arise from the C–H deformation of cellulose-derived substituted aromatics, demonstrating the presence of aromatic rings in these hydrochar samples [26, 27]. In addition, two peaks were observed in the range of 1420–1480 cm^{-1}, which might be due to the formation of the carbonates (Mn^{2+}, Fe^{2+}, Ca^{2+} and Mg^{2+}) on the surface of the hydrochar [28, 29]. For M7HC, a sharp peak at 862 cm^{-1} appeared, which was consistent with that reported in the literature for $MnCO_3$ [30]. Meanwhile, two weak peaks at 642 and 530 cm^{-1} confirmed the formation of Mn_3O_4. The surface species of M7HC were further investigated by XPS (Fig. 3). The contents of C, O and Mn on the surface were 69.1, 26.7 and 4.2%, respectively, which were consistent with the EDS analysis results. The binding energies of Mn 2p1/2 (653.7 eV) and Mn 2p3/2 (642.1 eV) were similar to that of $MnCO_3$ and Mn_3O_4 [31, 32]. The results further demonstrate that $MnCO_3$ and Mn_3O_4 were formed on the surface of M7HC.

The SEM images in Fig. 4 showed that the morphologies of the samples were irregular and the size of M7HC was much smaller than that of HC and M2HC, which might be associated with the strong oxidation ability of $KMnO_4$. The N_2 adsorption–desorption isotherms for the prepared hydrochars were shown in Fig. 5. According to the IUPAC classification, the isotherms were type II, which accounts for macroporous surfaces. The introduction of Mn increased the surface area and pore volume of the hydrochars to some extent (Table 2), which could be attributed to the $MnCO_3$ and Mn_3O_4 microcrystalline formed over the surfaces.

Adsorption Properties of Pb^{2+} on the Mn-Modified Hydrochars. As shown in Fig. 6a, the adsorption capacities of HC and M2HC decreased dramatically with the decreasing pH, and the removal efficiencies of Pb(II) were less than 30% even at pH 6.5, while M7HC presented excellent adsorption capacities, and the Pb(II) ions were almost totally removed over a wide pH range of 3.0–7.0. Normally, the charge

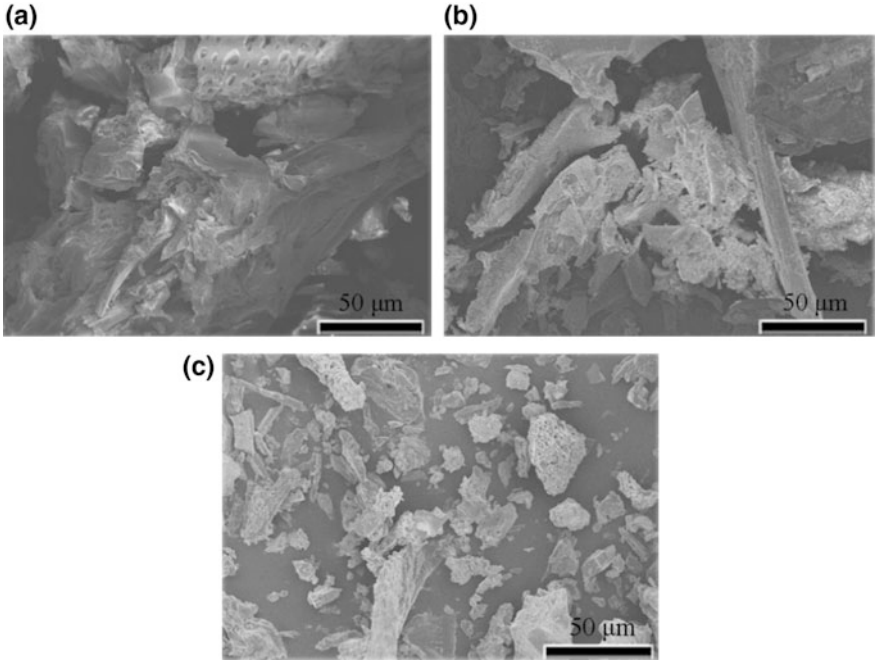

Fig. 4 FESEM images of different hydrochars: **a** HC, **b** M2HC, and **c** M7HC

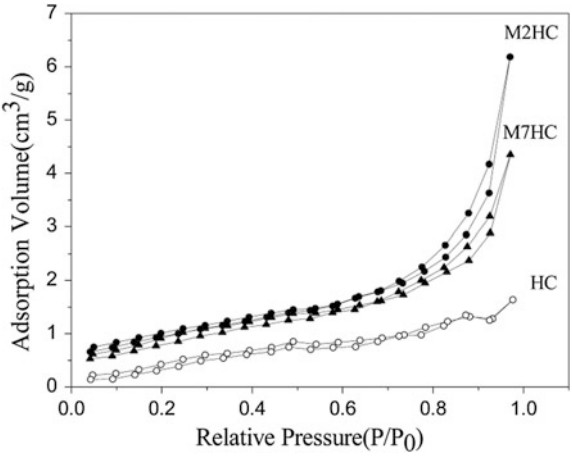

Fig. 5 N_2 adsorption-desorption isotherms at 77 K for different hydrochars

property of adsorbents surface is very important for adsorption. In an aqueous system, an adsorbent surface tends to protonate or deprotonate, which is dependent on the solution pHs. At being lower than pH_{PZC}, the surface is positively charged; on the contrary it has negative charges. Therefore, the pH_{PZC} of the hydrochars

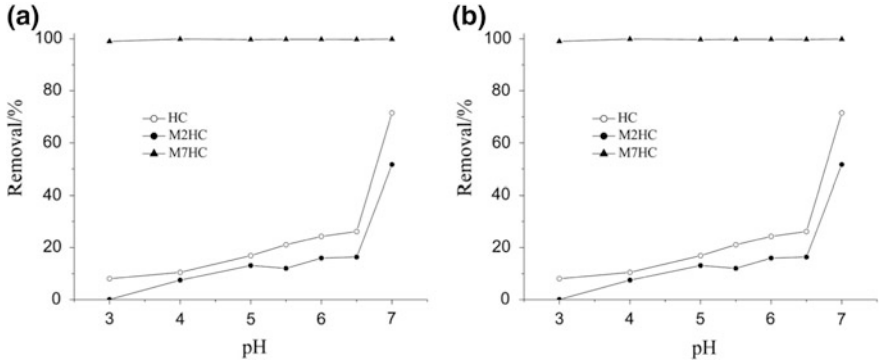

Fig. 6 **a** Effect of pH on Pb^{2+} adsorption at 298 K, and **b** $\Delta pH \sim$ initial pH curves for different hydrochars

were determined by the pH drift method (Fig. 4b). The pH_{PZC} of HC and M2HC were determined to be about 4, while that of M7HC was about 7, which could be attributed to the formation of Mn_3O_4 on the surface [3]. In the tested pH range (pH 2–7), the surface of M7HC was positively charged. Therefore, the adsorption of Pb (II) cation was not attributed to the electrostatic attraction. It is deduced that cation exchange between the protonated surface and Pb^{2+} is the main driving force for Pb (II) adsorption onto M7HC. The adsorption process can be illustrated as follows. It can be seen that much more H^+ ions were released in the Pb^{2+}-M7HC adsorption system, matching well with the experimental result.

$$2\,\text{-Mn-OH}_2^+ + Pb^{2+} \longrightarrow \text{-Mn-O-Pb-O-Mn-} + 4H^+ \quad (2)$$

$$\text{-Mn-OH}_2^+ + Pb(NO_3)^+ \longrightarrow \text{-Mn-O-Pb(NO}_3) + 2H^+ \quad (3)$$

The adsorption kinetics of Pb(II) were fitted by the pseudo-first order equation (Eq. 4), pseudo-second order equation (Eq. 5) and Weber's intra-particle diffusion model (Eq. 6) [33].

$$\ln(q_e - q_t) = \ln q_e - k_1 t \quad (4)$$

$$\frac{t}{q_t} = \frac{1}{k_2 q_e^2} + \frac{t}{q_e} \quad (5)$$

$$q_t = k_{id} t^{1/2} + C \quad (6)$$

where q_t and q_e (mg/g) are the uptake of Pb(II) at time t (h) and equilibrium, respectively. k_1, k_2 and k_{id} are the pseudo-first order rate constant (h^{-1}), the pseudo-second order rate constant (g/(mg^{-1} h^{-1})), and the intra-particle diffusion rate constant (mg/(g $h^{1/2}$)), respectively. C is the intercept of Weber's equation,

Table 3 Kinetic parameters and correlation coefficients (R^2) for adsorption of Pb(II) on different hydrochars at 298 K and pH 5.5

Sample	Pseudo-first order			Pseudo-second order			Intra-particle diffusion		
	q_e	k_1	R^2	q_e	k_2	R^2	k_{id}	C	R^2
HC	6.490	0.123	0.746	17.702	0.139	0.998	1.889	9.978	0.785
M2HC	2.097	0.093	0.846	10.461	0.739	1.000	0.527	8.343	0.641
M7HC	7.164	0.543	0.577	50.787	0.061	0.999	7.350	23.966	0.493

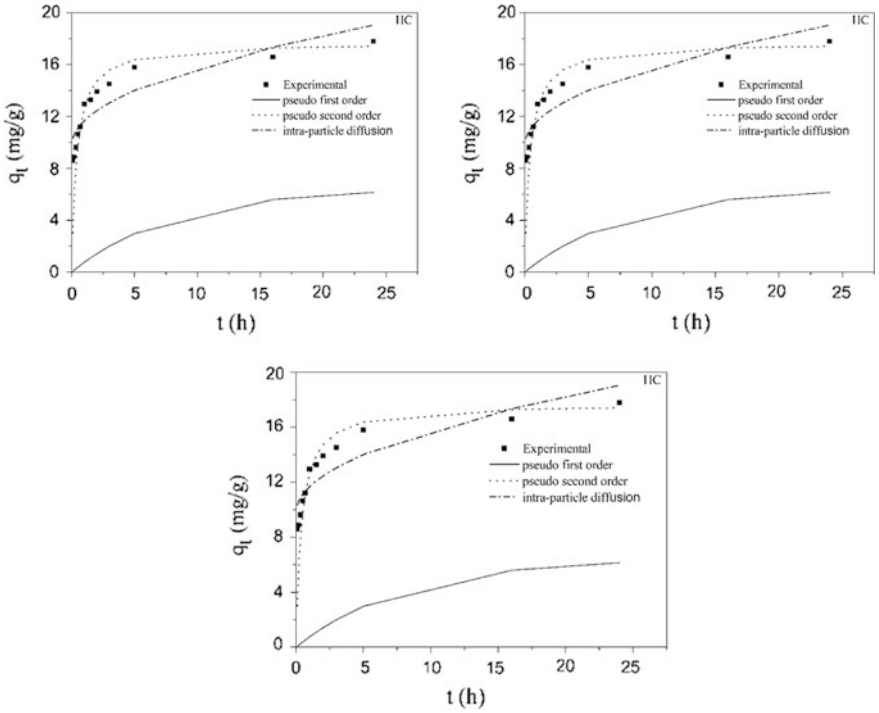

Fig. 7 Adsorption kinetics of Pb^{2+} on different hydrochars at pH 5.5

which can provide information about the thickness of the boundary layer,as the larger the interception the greater the boundary layer effect [34].

The obtained kinetic model parameters and correlation coefficients were given in Table 3. The fitting curves were also illustrated in Fig. 7. The data were well fitted by the pseudo-second order equation over the whole time range, and the correlation coefficients R^2 were high ($R^2 > 0.99$). The correlation coefficients for the pseudo-first order equation and Weber's intra-particle diffusion model were low ($R^2 < 0.85$). The results suggest that the adsorption kinetics of Pb(II) on the hydrochars were described precisely by the pseudo-second order kinetic model. Moreover, the k_2 value followed the order of M7HC > HC > M2HC, indicating that the adsorption rate of M7HC was higher than that of M2HC and HC.

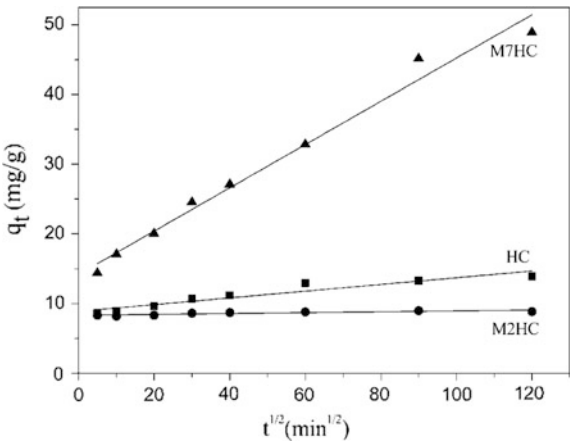

Fig. 8 Intra-particle diffusion kinetics for Pb^{2+} adsorption onto different hydrochars

Table 4 Intra-particle diffusion parameters and correlation coefficients for lead adsorption onto different hydrochars

Sample	Intra-particle diffusion		
	k_{id}	C	R^2
HC	5.168	6.980	0.962
M2HC	0.676	8.043	0.908
M7HC	32.126	2.896	0.972

In addition, the adsorption kinetics of Pb(II) reached equilibrium after 5 h. Although the Weber's model was not well fitted to the data over the whole time range, it is necessary for the kinetic analysis before equilibrium. The mechanisms and rate controlling steps affecting the kinetics of adsorption can be further understood by this model. The plot of q_t against $t^{1/2}$ would result in a straight line if the rate limiting is the intra-particle diffusion. Moreover, the line would pass through the origin if the intra-particle diffusion is the only rate controlling step [5]. Otherwise, some other mechanism along with intra-particle diffusion is also involved [33, 34]. The result of linearity test of q_t against $t^{1/2}$ was shown in Fig. 8, and k_{id} and C obtained from the plot slopes and intercepts were given in Table 4. As can be seen from the results, the correlation coefficients were higher ($R^2 > 0.90$) and the straight lines did not pass through the origin. This means that the pore diffusion is not the only rate limiting step in the adsorption process. It may be concluded that the surface adsorption and the intra-particle diffusion are concurrently operating during the Pb(II)-hydrochar interactions [5, 33].

The adsorption isotherms of Pb(II) on the hydrochars at 298 K and pH 5.5 were shown in Fig. 6. To estimate the maximum adsorption capacity and evaluate the adsorption intensity of Pb(II) onto the hydrochars, Langmuir and Freundlich models were used to fit the experimental data. The two models' equations are expressed as following:

Table 5 Isotherm constants and correlation coefficients (R^2) for the adsorption of Pb(II) on different hydrochars at 298 K and pH 5.5

Sample	Langmuir			Frundlich		
	q_m	K_L	R^2	K_F	n	R^2
HC	24.28	0.41	0.949	17.03	0.17	0.903
M2HC	21.52	0.37	0.952	14.95	0.19	0.859
M7HC	95.05	0.012	0.985	42.97	0.33	0.862

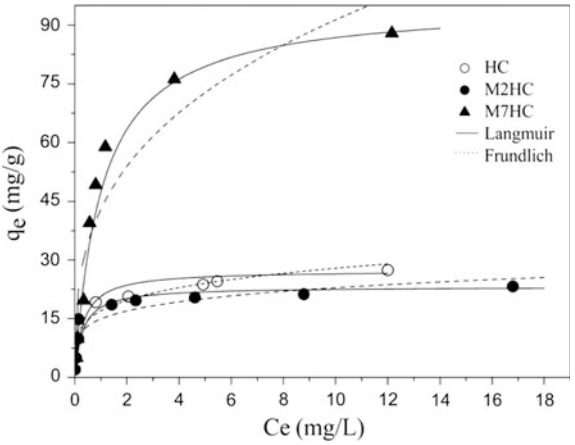

Fig. 9 Langmuir and Freundlich adsorption isotherms of Pb^{2+} on different hydrochars at 298 K and pH 5.5

$$\text{Langmuir model: } q_e = \frac{K_L q_m C_e}{1 + K_L C_e} \tag{7}$$

$$\text{Freundlich model: } q_e = K_F C_e^{1/n} \tag{8}$$

where q_e (mg/g) and q_m (mg/g) are the equilibrium and maximum adsorption amount of Pb(II), respectively; K_L (L/mg) and K_F ($mg^{1-n}\ L^n/g$) denote the Langmuir and Freundlich adsorption affinity parameters, respectively; n is nonlinear coefficient (unit less) [13]. The fitted values of the Langmuir and Freundlich parameters as well as R^2 were presented in Table 5. It can be seen that the experimental data could be well fitted by the Langmuir model. The maximum adsorption capacity of M7HC was 95.05 mg/g, 3.9 and 4.4 times were larger than that of HC and M2HC. On the basis of the characterization results, the appropriate surface loading of Mn_3O_4 on the hydrochar was one of the critical factors in improving the adsorption capacity of Pb(II) on M7HC. The loaded Mn_3O_4 promoted the protonation of the hydrochar and increased the cation exchange capacity of M7HC for Pb(II). Moreover, the introduction of $KMnO_4$ increased the surface area and pore volume of the hydrochar to some extent, facilitating the adsorption of Pb(II). The result indicates that M7HC is an effective adsorbent for Pb(II) removal from aqueous solutions (Fig. 9).

Conclusions

Manganese-containing hydrochars (M7HC and M2HC) were successfully synthesized by HTC of *Fraxinus mandshurica* sawdust in the presence of $KMnO_4$ or $MnSO_4$. The hydrochar yield followed the order of M2HC > HC > M7HC. The addition of $KMnO_4$ could promote the carbonization of biomass and increase the ash content. M7HC was a mixture of Mn_3O_4, $MnCO_3$ and carbon with low graphitization. The adsorption kinetics was best described by the pseudo-second order kinetic model and the adsorption isotherms could be well fitted by the Langmuir model. The maximum lead adsorption capacities were 24.28, 21.52 and 95.05 mg/g onto HC, M2HC and M7HC at 298 K, respectively. M7HC exhibited much higher adsorption capacity than HC and M2HC due to its unique structure and composition. This approach offers a novel and low-cost adsorbent with potential applications in wastewater treatment and immobilization of heavy metals in contaminated soils.

Acknowledgements This work is supported by the National Natural Science Foundation of China (No. 21677046), the Natural Science Foundation of Hebei Province of China (No. B2017205146), and Hebei province in 2016 college students' innovative training program (201610094011).

References

1. J. Jiang, R.K. Xu, T.Y. Jiang, Z. Li, Immobilization of Cu(II), Pb(II) and Cd(II) by the addition of rice straw derived biochar to a simulated polluted Ultisol. J. Hazard. Mater. **229–230**, 145–150 (2012)
2. H.H. Cho, K. Wepasnick, B.A. Smith, F.K. Bangash, D.H. Fairbrother, W.P. Ball, Sorption of aqueous Zn[II] and Cd[II] by multiwall carbon nanotubes: the relative roles of oxygen-containing functional groups and graphenic carbon. Langmuir **26**, 967–981 (2010)
3. D.A. Shaughnessy, H. Nitsche, C.H. Booth, D.K. Shuh, G.A. Waychunas, R.E. Wilson, H. Gill, K.J. Cantrell, R.J. Serne, Molecular interfacial reactions between Pu(VI) and manganese oxide minerals manganite and hausmannite. Environ. Sci. Technol. **37**, 3367–3374 (2003)
4. Z.G. Song, F. Lian, Z.H. Yu, L.Y. Zhu, B.S. Xing, W.W. Qiu, Synthesis and characterization of a novel MnOx-loaded biochar and its adsorption properties for Cu^{2+} in aqueous solution. Chem. Eng. J. **242**, 36–42 (2014)
5. Z.G. Liu, F.S. Zhang, Removal of lead from water using biochars prepared from hydrothermal liquefaction of biomass. J. Hazard. Mater. **167**, 933–939 (2009)
6. X.C. Chen, G.C. Chen, L.G. Chen, Y.X. Chen, J. Lehmann, M.B. McBride, A.G. Hay, Adsorption of copper and zinc by biochars produced from pyrolysis of hardwood and corn straw in aqueous solution. Bioresour. Technol. **102**, 8877–8884 (2011)
7. M.S.U. Rehman, I. Kim, N. Rashid, M.A. Umer, M. Sajid, J.-I. Han, Adsorption of Brilliant Green dye on biochar prepared from lignocellulosic bioethanol plant waste. Clean Soil. Air Water **44**(1), 55–62 (2016)
8. M. Moyo, S.T. Lindiwe, E. Sebata, B.C. Nyamunda, U. Guyo, Equilibrium, kinetic and thermodynamic studies on biosorption of Cd(II) from aqueous solution by biochar. Res. Chem. Intermed. **42**, 1349–1362 (2016)

9. M. Zhang, B. Gao, Y. Yao, Y.W. Xue, M. Inyang, Synthesis of porous MgO-biochar nanocomposites for removal of phosphate and nitrate from aqueous solutions. Chem. Eng. J. **210**, 26–32 (2012)
10. M. Zhang, B. Gao, S. Varnoosfaderani, A. Hebard, Y. Yao, M. Inyang, Preparation and characterization of a novel magnetic biochar for arsenic removal. Bioresour. Technol. **130**, 457–462 (2013)
11. X.D. Zhu, Y.C. Liu, F. Qian, C. Zhou, S.C. Zhang, J.M. Chen, Preparation of magnetic porous carbon from waste hydrochar by simultaneous activation and magnetization for tetracycline removal. Bioresour. Technol. **154**, 209–214 (2014)
12. D.L. Zhao, X. Yang, H. Zhang, C.L. Chen, X.K. Wang, Effect of environmental conditions on Pb(II) adsorption on β-MnO_2. Chem. Eng. J. **164**, 49–55 (2010)
13. M.C. Wang, G.D. Sheng, Y.P. Qiu, A novel manganese-oxide/biochar composite for efficient removal of lead(II) from aqueous solutions. Int. J. Environ. Sci. Technol. **12**, 1719–1726 (2015)
14. A.B. Fuertes, M. Camps Arbestain, M. Sevilla, J.A. Maciá-Agulló, S. Fiol, R. López, R. J. Smernik, W.P. Aitkenhead, F. Arce, F. Macias, Chemical and structural properties of carbonaceous products obtained by pyrolysis and hydrothermal carbonisation of corn stover. Aust. J. Soil. Res. **48**, 618–626 (2010)
15. M. Sevilla, A.B. Fuertes, R. Mokaya, High density hydrogen storage in superactivated carbons from hydrothermally carbonized renewable organic materials. Energy Environ. Sci. **4**, 1400–1410 (2011)
16. C. Falco, J.P. Marco-Lozar, D. Salinas-Torres, E. Morallón, D. Cazorla-Amorós, M.M. Titirici, D. Lozano-Castelló, Tailoring the porosity of chemically activated hydrothermal carbons: influence of the precursor and hydrothermal carbonization temperature. Carbon. **62**, 346–355 (2013)
17. X.D. Zhu, Y.C. Liu, C. Zhou, S.C. Zhang, J.M. Chen, Novel and high-performance magnetic carbon composite prepared from waste hydrochar for dye removal. ACS Sustain. Chem. Eng. **2**, 969–977 (2014)
18. M.T. Reza, M.H. Uddin, J.G. Lynam, S.K. Hoekman, C.J. Coronella, Hydrothermal carbonization of loblolly pine: reaction chemistry and water balance. Biomass. Convers. Biorefinery **4**, 311–321 (2014)
19. S.K. Hoekman, A. Broch, C. Robbins, B. Zielinska, L. Felix, Hydrothermal carbonization (HTC) of selected woody and herbaceous biomass feedstocks. Biomass. Convers. Biorefinery **3**, 113–126 (2013)
20. J.G. Lynam, M.T. Reza, W. Yan, V.R. Vásquez, C.J. Coronella, Hydrothermal carbonization of various lignocellulosic biomass. Biomass. Convers. Biorefinery **5**, 173–181 (2015)
21. H. Knicker, K.U. Totsche, G. Almendros, F.J. González-Vila, Condensation degree of burnt peat and plant residues and the reliability of solid-state VACP MAS ^{13}C NMR spectra obtained from pyrogenic humic material. Org. Geochem. **36**, 1359–1377 (2005)
22. K. Hammes, R.J. Smernik, J.O. Skjemstad, A. Herzog, U.F. Vogt, M.W.I. Schmidt, Synthesis and characterisation of laboratory-charred grass straw (*Oryza sativa*) and chestnut wood (*Castanea sativa*) as reference materials for black carbon quantification. Org. Geochem. **37**, 1629–1633 (2006)
23. S.M. Kang, X.L. Li, J. Fan, J. Chang, Characterization of hydrochars produced by hydrothermal carbonization of lignin, cellulose, D-xylose, and wood meal. Ind. Eng. Chem. Res. **51**, 9023–9031 (2012)
24. L.L. Wang, Y.P. Guo, Y.C. Zhu, Y. Li, Y.N. Qu, C.G. Rong, X.Y. Wang, Z.C. Ma, A new route for preparation of hydrochars from rice husk. Bioresour. Technol. **101**, 9807–9810 (2010)
25. X.Y. Chen, C. Chen, Z.J. Zhang, D.H. Xie, J.W. Liu, Nitrogen/manganese oxides doped porous carbons derived from sodium butyl naphthalene sulfonate. J. Colloid. Interf. Sci. **398**, 176–184 (2013)

26. K. Sun, K. Ro, M.X. Guo, J. Novak, H. Mashayekhi, B.S. Xing, Sorption of bisphenol A, 17α-ethinyl estradiol and phenanthrene on thermally and hydrothermally produced biochars. Bioresour. Technol. **102**, 5757–5763 (2011)
27. L.M. Wu, C.H. Zhou, D.S. Tong, W.H. Yu, H. Wang, Novel hydrothermal carbonization of cellulose catalyzed by montmorillonite to produce kerogen-like hydrochar. Cellulose. **21**, 2845–2857 (2014)
28. X.Y. Xu, X.D. Cao, L. Zhao, H.L. Wang, H.R. Yu, B. Gao, Removal of Cu, Zn, and Cd from aqueous solutions by the dairy manure-derived biochar. Environ. Sci. Pollut. Res. **20**, 58–368 (2013)
29. X.D. Cao, L.N. Ma, B. Gao, W. Harris, Dairy-manure derived biochar effectively sorbs lead and atrazine. Environ. Sci. Technol. **43**, 3285–3291 (2009)
30. L.X. Yang, Y. Liang, H. Chen, Y.F. Meng, W. Jiang, Controlled synthesis of Mn_3O_4 and $MnCO_3$ in a solvothermal system. Mater. Res. Bull. **44**, 1753–1759 (2009)
31. L.K. Zhou, X.H. Kong, M. Gao, F. Lian, B.J. Li, Z.F. Zhou, H.Q. Cao, Inorg. Chem. **53**, 9228–9234 (2014)
32. J.W. Lee, A.S. Hall, J.D. Kim, T.E. Mallouk, Chem. Mater. **24**, 1158–1164 (2012)
33. A.C.A. de Lima, R.F. Nascimento, F.F. de Sousa, J.M. Filho, A.C. Oliveira, Chem. Eng. J. **185–186**, 274–284 (2012)
34. V.O. de Sousa Neto, D.Q. Melo, T.C. de Oliveira, R.N.P. Teixeira, M.A.A. Silva, R.F. do Nascimento, J. Appl. Polym. Sci. **40744**, 1–11 (2014)

Physico-Chemical Characteristics of Greening Substrate Used in Mining Slope Restoration and Its Optimum Mixture Ratio

Xiaoming Guo, Tongqian Zhao, Wenke Chang, Bingmei Li, Chunyan Xiao, Yuxiao He and Fuling Zhao

Abstract China has abundant limestone mineral resources, which covers the areas of 13×10^5 km^2. The intensive exploitation of limestone causes large area of mining wasteland, such as rock slope, and causes eco-environmental damages, such as soil degradation and vegetation destruction. Greening substrate is a kind of "artificial soil", which is suitable for plant growth and succession and is significantly important for vegetation restoration in the rock slope. The purpose of this paper was to study the physical and chemical characteristics of greening substrates and its optimum mixture ratio. Based on the principle of "waste control by waste", 49 groups of greening substrates with different mixture ratios were made from coal ash, soil, activated sludge, slag, super absorbent polymers, urea and wheat straw using the orthogonal test (L_{49} 7^5). *Festuca arundinacea* was used as an experimental plant, and soils from an artificial forest were used as a reference. Results indicated that the greening substrate contained lower contents of pH and bulk

X. Guo · T. Zhao (✉) · W. Chang · B. Li · C. Xiao · Y. He
Institute of Resources and Environment, Henan Polytechnic University, Jiaozuo 454000, China
e-mail: zhaotq@hpu.edu.cn

X. Guo
e-mail: guoxiaoming@hpu.edu.cn

W. Chang
e-mail: 734097558@qq.com

B. Li
e-mail: 1129459768@qq.com

C. Xiao
e-mail: 184154055@qq.com

Y. He
e-mail: 121239516@qq.com

F. Zhao
Environmental Supervision Group, Jiaozuo Demonstration Area of Urban and Rural Integration, Jiaozuo 454000, China
e-mail: 125565451@qq.com

Y. Han (ed.), *Advances in Energy and Environmental Materials*,
Springer Proceedings in Energy, https://doi.org/10.1007/978-981-13-0158-2_87

density but higher contents of water, electrical conductivity, organic matter, total phosphorus, total potassium, available phosphorus and available potassium than the control soils. Compared to the control soils, the greening substrate had more obvious aggregate structures according to the analysis of scanning electron microscope. The content of sludge in the greening substrate significantly affected the characteristics of water and fertilizer condition, acidity and alkalinity, salt density and seed germination. The optimum mixture ratio of greening substrate is super absorbent polymers (0.7%), sludge (9.7%), coal ash (38.9%), soil (38.9%), slag (9.7%), urea (0%) and wheat straw (1.9%) according to the range analysis. These results suggested that the greening substrates with reasonable mixture ratio can supply good condition of water and fertilizer, and are suitable for plant growth.

Keywords Mining slope · Vegetation restoration · Greening substrate
Fertility · Scanning electron microscope

Introduction

Limestone is an important mineral resource for architecture, metallurgy, food, chemical engineering, agriculture, light industry and petroleum. China has abundant limestone mineral resources, which covers the areas of 13×10^5 km^2 (13.5% of the national territory area). The intensive exploitation of limestone for several successive years causes large area of wasteland, such as rock slope, and causes eco-environmental damages, such as vegetation deterioration, land degradation, and landscape destruction. Furthermore, it is rather difficult for vegetation restoration in the rock slope, which seriously influences the local socio-economic development [1].

Salonen and Setala [2] showed that the soil plays an important role in the ecological rehabilitation of mining wasteland. Greening substrate is one kind of "artificial soil", which is suitable for plant growth and succession and is mainly mixed by super absorbent polymers, fertilizer and soil. It can be successfully applied to vegetation restoration in the rock slope, because it can provide reasonable physical structure and appropriate contents of water and nutrients for plant growth. Many studies of ecological restoration in the slope mainly focus on restoration strategy [3, 4], artificial soil properties [5, 6], vegetation restoration [7], substrate improvement [8, 9] and selection of plant species [10, 11]. However, there is little research on physico-chemical characterization of greening substrate and its optimum mixture ratio.

The objective of the present study was to assess the characterization of water and fertility in greening substrate based on 10 different physical and chemical attributes, and suggested the optimum mixture ratio according to the orthogonal test.

Materials and Methods

Source of Raw Materials. The greening substrate was made from the raw materials including coal ash, soil, activated sludge, slag, super absorbent polymers, urea and wheat straw. The coal ash, soil, activated sludge, slag and wheat straw were collected from the heating boiler factory, the artificial forest, the sewage treatment plant, the heating boiler factory and the corn field, respectively. All of these materials were from Jiaozuo city, which is located at Henan province of China. It has a warm continental monsoon climate with an average annual temperature of 14 °C, a mean annual rainfall of 658 mm, and an annual evaporation of 2039 mm. The urea and super absorbent polymers were purchased from a reagent company. To mix the raw materials, the sludge, coal ash, slag and straw were air-dried for 14 days, sieved with a 1-cm screen, and stored in sealed plastic bags.

Orthogonal Test Design. Orthogonal test was designed as follows: five factors (super absorbent polymers, mixture of sludge and coal ash, mixture of soil and slag, urea and wheat straw) and 7 levels in each factor. According to the orthogonal test (L_{49} 7^5, see Table 1), 49 groups of greening substrates (see Table 2) with different mixture ratios was made.

Pot Experiment Design. 49 groups of greening substrates and one CK soil were taken into the 50 flowerpots, respectively. In each flowerpot, we plant 30 seeds of *Festuca arundinacea*, which were purchased from a flower market and used as an experimental plant. *Festuca arundinacea* is a species of grass commonly known as tall fescue. It is an important forage grass, and many cultivars have been used in agriculture. It is also an ornamental grass in gardens, and a ecological phytoremediation plant. Until the *Festuca arundinacea* were grown for 30 days, the rate of seed germination was investigated and calculated.

Analysis Method. Contents of water, bulk density, potential of hydrogen (pH), electrical conductivity, organic matter were determined using the drying method, the metal-core sample method, pH electrodes in soil/water (1:5) suspension, conductivity meter and dichromate oxidation technique, respectively [12]. Contents of available phosphorus, total phosphorus, available potassium, total potassium were

Table 1 Factor and level in the orthogonal test (unit: g)

Level	Factor A (super absorbent polymers)	Factor B (sludge: coal ash)	Factor C (soil: slag)	Factor D (urea)	Factor E (wheat straw)
1	0	0:750	0:750	0	0
2	1	150:600	150:600	1	5
3	3	300:450	300:450	2	10
4	5	375:375	375:375	3	15
5	8	450:300	450:300	5	20
6	11	600:150	600:150	7	25
7	15	750:0	750:0	10	30

Table 2 49 groups of greening substrate with different mixture ratios according to orthogonal test

Number	A	B	C	D	E	Number	A	B	C	D	E	Number	A	B	C	D	E
1	5	7	7	1	2	18	1	3	5	4	7	34	5	6	5	3	6
2	5	5	3	5	3	19	1	7	6	3	5	35	7	7	4	7	4
3	2	3	7	7	1	20	7	2	1	3	3	36	1	1	1	1	1
4	4	1	7	3	4	21	7	6	2	2	1	37	7	5	7	4	5
5	6	7	2	4	3	22	1	4	7	2	3	38	6	6	7	6	7
6	1	2	3	6	4	23	3	2	7	5	6	39	2	1	3	4	2
7	4	5	1	2	2	24	6	2	6	7	2	40	5	1	2	6	5
8	7	3	3	1	6	25	2	6	6	1	3	41	2	2	5	2	5
9	3	1	5	7	3	26	3	4	4	1	5	42	4	7	5	5	1
10	6	5	5	1	4	27	6	4	3	3	1	43	5	3	6	2	4
11	6	3	1	5	5	28	3	5	6	6	1	44	2	4	2	5	4
12	3	7	3	2	7	29	4	2	2	1	7	45	4	6	3	7	5
13	3	6	1	4	4	30	5	4	1	7	7	46	6	1	4	2	6
14	1	5	2	7	6	31	7	1	6	5	7	47	4	3	4	6	3
15	4	4	6	4	6	32	2	7	1	6	6	48	7	4	5	6	2
16	3	3	2	3	2	33	5	2	4	4	1	49	2	5	4	3	7
17	1	6	4	5	2												

measured with dicarbonate extraction, sodium hydroxide fusional, ammonium acetate extraction and sodium hydroxide fusional methods, respectively [12]. The characteristics of microstructure were observed according to the scanning electron microscope (SEM).

Results and Analysis

Physico-Chemical Characterization. The physical and chemical characteristics of greening substrate are presented in Fig. 1. The greening substrate contained lower bulk density and pH values than the CK soil (see Fig. 1a, b). The bulk density of substrate decreased with the increasing straw content, while it increased with the increasing slag content. The substrate contained relatively low bulk density when the straw content was 30 g or the slag content was 750 g, which showed that the straw and slag obviously reduced bulk density and improved gas permeability of substrate. The pH values in the substrate decreased with the increase of sludge content, which significantly affected the acidity and alkalinity of substrate. The substrate contained significantly higher contents of water, electrical conductivity, organic matter, available phosphorus, total phosphorus, available potassium and total potassium than the CK (see Fig. 1c–i). The contents of these properties

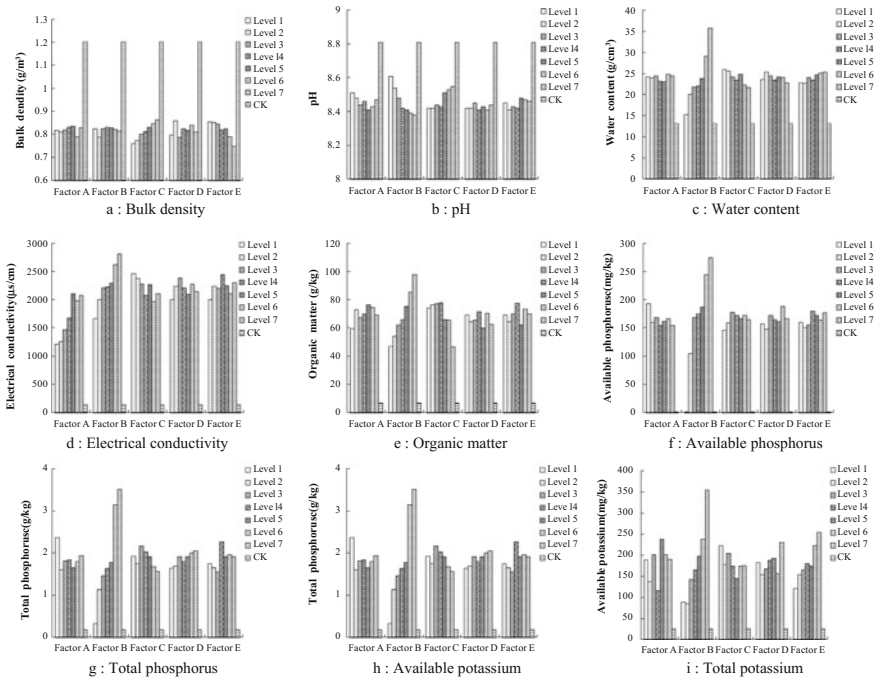

Fig. 1 Physical and chemical characteristics of greening substrate

increased with the increase of sludge content, which distinctly influenced the condition of water, salt and fertilizer in the substrate.

Microstructure Characterization. Scanning electron microscope (SEM) images of greening substrates are shown in Fig. 2. The CK soil with a close-packed

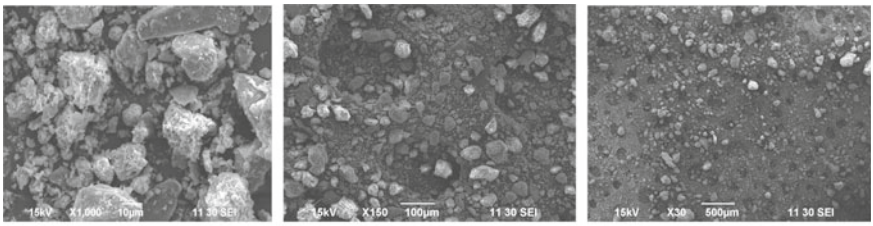

a : CK

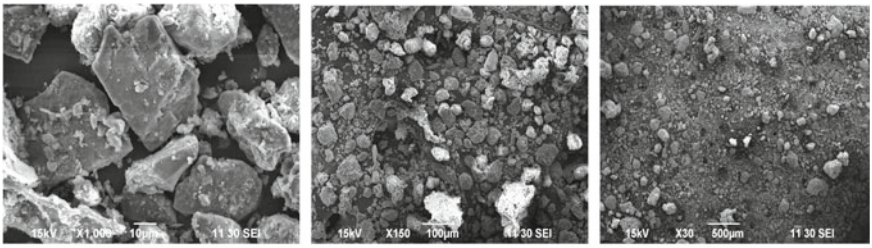

b: Coal ash (0g), Soil (750g), Sludge (750g), Slag (0g), Super absorbent polymers (8g), Urea (0g) and Straw (5g)

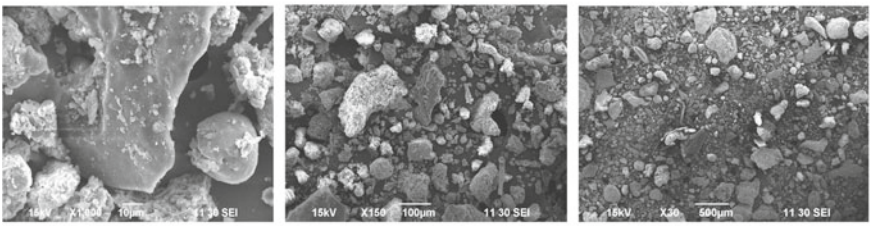

c: Coal ash (600g), Soil (150g), Sludge (150g), Slag (600g), Super absorbent polymers (5g), Urea (0g) and Straw (30g)

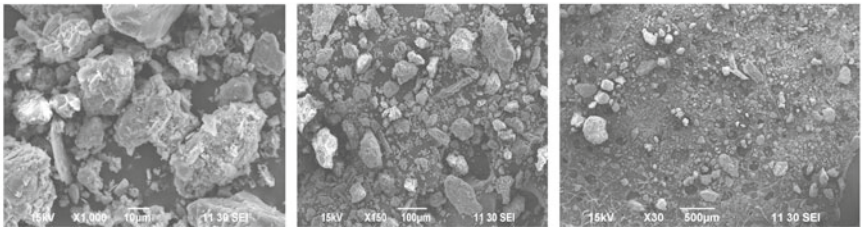

d: Coal ash (450g), Soil (300g), Sludge (300g), Slag (450g), Super absorbent polymers (15g), Urea (0g) and Straw (25g)

Fig. 2 SEM of greening substrate under increasing resolution (*Note* The resolution increases from 500 to 10 μm)

structure had relatively small pores (see Fig. 2a). The particles in the CK were single grains, and the aggregate had seldom been seen according to the SEM. The substrate contained larger pores than the CK when a large amount of sludge was added in the substrate (see Fig. 2b). The particles in this substrate loosely arranged, and the structure of aggregate had been seen. The pores in the substrate were larger than that in the CK when a large amount of coal ash and slag was added in the substrate (see Fig. 2c). The particles in this substrate were large and can cohere to the fine particles on their surface, which can generate aggregate structures. The aggregate can be also produced when the coal ash, slag and sludge were simultaneously added in the substrate (see Fig. 2d). These results showed that the substrate with good structure had low compaction and a large amount of pore space, which was better than the CK.

Germination Rate. The germination rates of *Festuca arundinacea* in the substrate are presented in Fig. 3. The value of germination rate was maximum when the substrate had sludge content of 150 g. On the contrary, there was the minimum value when the substrate had sludge content of 750 g. It indicated that low content of sludge was beneficial to the plant germination, while the high content of sludge was harmful to it. Similarly, the urea content had negative effects on the rate. The reason may be that adding urea caused excessive nutrients and was against seed germination due to adequate nutrients provided by the sludge. The germination rate increased with the increase of straw content, which showed that the straw can promote plant germination. It was because the straw can increase porosity and content of organic matter and avoid compaction in the substrate. The substrates contained higher germination than the CK when there had reasonable ratio of soil to slag, namely, 450:300 or 600:150. It was because the environment of soil was helpful for plant growth and slag was used to prevent soil hardening and ensure large pores and high air permeability in the substrate, both of which were useful for the germination. The super absorbent polymers had no apparent effects on the germination rate. The reason may be that there was adequate water in the substrate due to continuous irrigation during the early periods of plant growth.

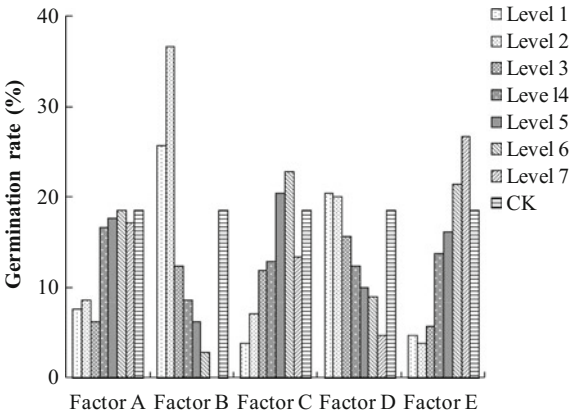

Fig. 3 Germination rate of *Festuca arundinacea* in the substrate

Table 3 Range analysis of germination rate

Items	Germination rate				
	A	B	C	D	E
K_1	7.62	25.7	3.81	20.5	4.76
K_2	8.57	36.7	11.9	20	3.81
K_3	16.6	12.3	7.14	15.7	5.71
K_4	17.6	8.57	12.8	10	13.8
K_5	6.19	6.19	20.4	9.05	16.2
K_6	18.5	2.86	22.8	4.76	21.4
K_7	17.1	0	13.3	12.3	26.6
R	12.4	36.7	19.1	15.7	22.86

Optimum Mixture Ratio. Table 3 shows the range analysis results of germination rate. The effects of five factors on the germination rate were in the following order: the ratio of sludge to coal ash, straw content, the ratio of soil to slag, urea content and super absorbent polymers, and the optimum mixture ratio was $A_6B_2C_6D_1E_7$. Based on the water-fertilizer characteristics, structural characteristics and germination rate of *Festuca arundinacea* in the substrate, the optimum mixture ratio of greening substrate was suggested, namely, super absorbent polymers (0.7%), sludge (9.7%), coal ash (38.9%), soil (38.9%), slag (9.7%), urea (0%) and wheat straw (1.9%).

A-E represent the factor of super absorbent polymers, mixture of sludge and coal ash, mixture of soil and slag, urea and wheat straw, respectively. K_i represents the average germination rate under the specific level. R represents the range.

Conclusions

This paper was conducted to study the reasonable ratio of greening substrate used in the rock slope restoration. Seven materials including coal ash, soil, activated sludge, slag, super absorbent polymers, urea and wheat straw were used to make the substrate. We found that the greening substrate had more obvious aggregate structures according to the analysis of scanning electron microscope when compared to the control soils. The content of sludge in the greening substrate significantly affects the characteristics of water and fertilizer condition, acidity and alkalinity, salt density and seed germination. The optimum mixture ratio of greening substrate is super absorbent polymers (0.7%), sludge (9.7%), coal ash (38.9%), soil (38.9%), slag (9.7%), urea (0%) and wheat straw (1.9%) according to the range analysis. Although the greening substrate can supply sufficient water and fertility for the plant, it still needs further research to assess the sustainability on plant growth.

Acknowledgements This study was financially supported by the National Natural Science Foundation of China (No. 41371501, No. 41502241), Doctor Program Foundation of Henan Polytechnic University Grant (No. B2013-069), Science and Technology Research Project of Henan Province (No. 172102310354) and Technological Innovation Team of Colleges and Universities in Henan Province of China (No. 15IRTSTHN027).

References

1. L.P. Qiu, S.C. Li, H.L. Sun, Models of nitrogen, phosphorus and potassium losses in rock slope matrix-vegetation system. Chin. J. Ecol. **33**, 3164–3168 (2014). (in Chinese)
2. V. Salonen, H. Setala, Plant colonization of bare peat surface relative—importance of seed availability and soil. Ecography **15**, 199–204 (2010)
3. J.A.A. Meira-Neto, A. Clemente, G. Oliveira, A. Nunes, O. Correia, Post-fire and post-quarry rehabilitation successions in Mediterranean-like ecosystems: implications for ecological restoration. Ecol. Eng. **37**, 1132–1139 (2011)
4. A. Medl, S. Mayr, H.P. Rauch, Microclimatic conditions of 'green walls', a new restoration technique for steep slopes based on a steel grid construction. Ecol. Eng. **101**, 39–45 (2017)
5. S.N. Chen, X.Y. Ai, T.Y. Dong, B.B. Li, R.H. Luo, Y.W. Ai, A.Q. Chen, C.R. Li, The physico-chemical properties and structural characteristics of artificial soil for cut slope restoration in Southwestern China. Sci. Rep. **6**, 20565 (2016)
6. Z.Y. Huang, J. Chen, X.Y. Ai, The texture, structure and nutrient availability of artificial soil on cut slopes restored with OSSS—influence of restoration time. J. Environ. Manage. **200**, 502–510 (2017)
7. G. Oliveira, A. Nunes, A. Clemente, O. Correia, Effect of substrate treatments on survival and growth of Mediterranean shrubs in a revegetated quarry: an eight-year study. Ecol. Eng. **37**, 255–259 (2011)
8. G. Maisto, A. de Marco, F. de Nicola, C. Arena, L. Vitale, A.V. de Santo, Suitability of two types of organic wastes for the growth of sclerophyllous shrubs on limestone debris: a mesocosm trial. Sci. Total Environ. **408**, 1508–1514 (2010).
9. G. Marando, P. Jiménez, A. Hereter, M. Julià, M. Ginovart, M. Bonmatí, Effects of thermally dried and composted sewage sludges on the fertility of residual soils from limestone quarries. Appl. Soil Ecol. **49**, 234–241 (2011)
10. Z.Q. Wang, L.H. Wu, T.T. Liu, Revegetation of steep rocky slopes: planting climbing vegetation species in artificially drilled holes. Ecol. Eng. **35**, 1079–1084 (2009)
11. B. Beikircher, F. Florineth, S. Mayr, Restoration of rocky slopes based on planted gabions and use of drought-preconditioned woody species. Ecol. Eng. **36**, 421–426 (2010)
12. S.D. Bao, *Soil Agro-Chemical Analysis*, 3rd edn. (China Agricultural Press, Beijing, 2000). (in Chinese)

Synthesis of Mesoporous Calcium Silicate by Ultrasonic-Assisted Template Method and Evaluation of Its Adsorption Characteristics for Cd(II)

Lihua Liu, Tong Li, Jinyan Liu, Yifeng Wang, Boqiang Hu, Zhihua Zhou and Anping Tang

Abstract Mesoporous calcium silicate (MCS) was prepared from calcium nitrate and sodium silicate by ultrasonic-assisted template method. The effects of different templates (sodium dodecyl sulfate, cetyl trimethyl ammonium bromide, P123, and cetyl trimethyl ammonium bromide–tetramethyl ammonium hydroxide) on the pore size and surface topography of MCS were investigated. Calcium silicate synthesized was characterized by X-ray diffraction, scanning electron microscopy, the Brunauer–Emmett–Teller method, and Fourier transform infrared spectroscopy. The adsorption performances of the MCS synthesized for Cd^{2+} were also investigated. Results showed that the MCS synthesized using cetyl trimethyl ammonium bromide as template under ultrasonic treatment acquired a mesoporous slit-pore structure with a

L. Liu (✉) · T. Li · J. Liu · Y. Wang · B. Hu · Z. Zhou · A. Tang
School of Chemistry and Chemical Engineering, Hunan University of Science and Technology, Xiangtan 411201, China
e-mail: llh213@163.com

T. Li
e-mail: 1546044226@qq.com

J. Liu
e-mail: 870512305@qq.com

Y. Wang
e-mail: 735857488@qq.com

B. Hu
e-mail: 501306287@qq.com

Z. Zhou
e-mail: zhou7381@126.com

A. Tang
e-mail: anpingxt@126.com

L. Liu · Z. Zhou · A. Tang
Key Laboratory of Theoretical Organic Chemistry and Function Molecule, Ministry of Education, Xiangtan 411201, China

L. Liu · Z. Zhou · A. Tang
Hunan Province Key Laboratory of Controllable Preparation and Function Application of Fine Polymer, Xiangtan 411201, China

Y. Han (ed.), *Advances in Energy and Environmental Materials*,
Springer Proceedings in Energy, https://doi.org/10.1007/978-981-13-0158-2_88

specific surface area of 244.32 $m^2\ g^{-1}$ and pore size (D_{BJH}) of 11.2 nm. MCS showed extremely high adsorption capacity for Cd^{2+} at pH 5.0–7.5, and the adsorption capacity for Cd^{2+} was 509.91 mg g^{-1} at 293 K, which was much higher than those of the adsorbents in literature. The equilibrium adsorption data of MCS for Cd^{2+} all fitted the Langmuir and Redlich–Peterson models, and more closely with the Redlich–Peterson model. The adsorption of MCS toward Cd^{2+} was a spontaneous endothermic reaction driven by increased entropy involving both physical and chemical modes. The adsorption of MCS for Cd^{2+} was better described by the pseudo-second-order model than by the pseudo-first-order model, with an activation energy of 13.4327 kJ mol^{-1}. Thus, it is evident that MCS can be a promising excellent adsorbent for the treatment of Cd^{2+}-containing wastewater.

Keywords Mesoporous calcium silicate · Ultrasonic-assisted template synthesis method · Cd^{2+} · Adsorption charateristics

Introduction

Cadmium pollution not only affects the growth of plants and animals but also enriches in their bodies and enters the human body through the food chain. Subsequently, cadmium accumulates in the human liver, kidney, and bone and easily damages these organs as well as the reproductive system, disturbs the enzyme systems, instigates functional imbalance in internal organs, promotes cancerous distortions, and eventually causes death [1, 2]. Cadmium is regarded as the sixth most poisonous substance to the human body by the Poison and Disease Registry (ATSDR). Therefore, an efficient treatment method to control cadmium pollution is urgently needed.

Many treatment methods have been developed to alleviate cadmium pollution. Examples of these approaches include chemical precipitation, the ion exchange method, flocculation method, flotation, nanofiltration, and adsorption treatment methods [3–8]. However, these strategies hold some disadvantages [2], which limit their practical applications. Among these methods, adsorption offers a high processing efficiency, easy operation, low processing cost, and low sludge disposal amounts [2, 8] and has thus become the top application prospect. The key factor in treating cadmium-containing wastewater is the adsorbent performance. Among the reported adsorbents, the natural mineral, industrial, or municipal waste (e.g., red mud, and natural diamond zeolite) holds advantages of low cost and high accessibility [9, 10]. However, their structural defects also cause some limitations, such as low adsorption capacity for Cd^{2+}, low selectivity, regeneration difficulty, considerable production of Cd^{2+}-containing wastes, and secondary pollution. By contrast, synthetic adsorption materials are gradually becoming a research hot spot because they can satisfy adsorption requirements through structural design and controllable preparation. Examples of these materials are biochar, TMU-16-NH_2 metal organic framework complexes, and molecularly imprinted polymer [11–13].

Among synthetic adsorption materials, inorganic porous materials hold advantages of ion exchange adsorption; shape-selective adsorption; high chemical and biological stability; controllable structure, size, and composition; and modifiable microchannels. As such, these porous materials have attracted increasing attention in heavy-metal wastewater treatment. The inorganic porous materials presently used to treat Cd^{2+} mainly include powder-activated carbon-impregnated calcium alginate beads [14], ethylenediamine-functionalized SBA-15 [15], and mesoporous silica and activated carbon [16]. However, these materials are difficult to popularize in practical wastewater treatment because of their complex synthetic processes, high costs, and mass-production difficulty. Porous calcium silicate is a type of porous inorganic silicate material prepared from calcium hydroxide or calcium salt and silicate under certain conditions. This silicate exists in different whiteness degrees and possesses a high specific surface area, high porosity, and negative strength [17]. Moreover, the raw material can be obtained from a wide range of sources, is easily prepared, costs cheaply. Given these benefits, porous calcium silicate has aroused attention in water treatment. At present, the material is mainly applied in the adsorption treatment of wastewaters containing low-concentration phosphorus [18], low-concentration nutrients (N, P) [19], and coking material [20]. Less commonly, the silicate is also used to treat heavy-metal wastewater [21, 22].

In this paper, mesoporous calcium silicate (MCS) was synthesized using nitrate calcium and sodium silicate as raw materials through the ultrasonic-assisted template synthesis method. The effects of various template agents on the pore size and surface topography of MCS were investigated. Their structures were also characterized by X-ray diffraction (XRD), scanning electron microscope (SEM), Brunauer–Emmett–Teller (BET) surface analysis, and Fourier transform infrared (FT-IR) spectroscopy. The materials' adsorption performance for Cd^{2+} in the wastewater was then evaluated systematically. The adsorption thermodynamics and kinetic characteristics were also explored. This study provided an excellent adsorption material for treating Cd^{2+}-containing wastewater.

Experimental

Reagents. Calcium nitrate tetrahydrate was purchased from Tianjin Fengchuan Chemical Reagent Technology Co., Ltd., whereas sodium metasilicate nonahydrate was purchased from Shantou Xilong Chemical Co., Ltd. Cetyl trimethyl ammonium bromide (CTMAB) and tetramethyl ammonium (TMAH) were purchased from Sinopharm Group Chemical Reagent Co., Ltd. P123 was purchased from Aladdin. Sodium dodecyl sulfate (SDS) and anhydrous ethanol were obtained from Tianjin Kermel Chemical Reagent Co. Ltd. Cadmium sulfate was obtained from Shanghai Aibi Chemical Co., Ltd. Triethylene tetramine, nitric acid and sodium hydroxide were purchased from Tianjin Damao Chemical Reagent Co., Ltd. All these reagents were of analytical grade and used as purchased. Deionized water was used in the experiments.

Synthesis of MCS. Calcium nitrate tetrahydrate (14.16 g) was added in a 250 mL three-necked flask with 88 mL of deionized water, stirred for 1 h for complete dissolution, and then placed in a KQ-100DB ultrasonic cleaning machine (100 W; Kunshan Ultrasonic Instrument Co., Ltd.). Under ultrasonic conditions, 0.73 g of template agent, such as SDS, P123, CTMAB, or CTMAB–TMAH (mass ratio *m*[CTMAB]:*m*[TMAH] = 4:1), was added to the above solution. Then, the solution was stirred for 1 h at 120 r min^{-1} and 45 °C, and a white gel was gradually formed. Afterward, 17.04 g of sodium metasilicate nonahydrate was dissolved in 40 mL of deionized water (in accordance with a molar ratio of calcium nitrate tetrahydrate and sodium metasilicate nonahydrate = 1:1) was slowly dripped into the above-mentioned mixture. With the addition of sodium metasilicate nonahydrate, a white glue gradually formed. After reacting for 5 h, the reaction mixture was aged for 24 h at room temperature. Then, the mixture was washed with deionized water and extracted for 24 h with anhydrous ethanol to remove the template agent. The products (MCS) were then placed in a vacuum dryer to dry to a constant weight under 40 °C.

Adsorption Experiments. To evaluate the adsorption performance of MCS for Cd^{2+}, simulated Cd^{2+} wastewater samples containing 25, 50, 75, 100, 125, and 150 mg L^{-1} Cd^{2+} were initially used as test samples.

Adsorption Conditions

(1) Effect of adsorbent dosage

Initially, 50 mL of 100 mg L^{-1} Cd^{2+} simulation solution was added to a series of 250 mL conical flasks. Then, different amounts of MCS were added individually to the flasks, which were placed in a KYC-111-type thermostatic water bath shaker at 200 r min^{-1} for 10 h at 293 K. The conical flasks were then obtained from the shaker, and the supernatant solution was separated from the adsorbent by centrifuging for 30 min after standing for 10 min in an Eppendorf 5430 centrifuge. The residual Cd^{2+} concentration in the supernatant solution was determined using an atomic absorption spectrometer. The adsorption ratio φ and the equilibrium adsorption amount q_e were calculated by Eqs. (1) and (2), respectively. Then, a $\varphi(q_e)$–dosage diagram was plotted, and suitable adsorbent dosages may be determined in accordance with the variation trend of the curve as follows:

$$\varphi = \frac{(c_0 - c_e)}{c_0} \times 100 \tag{1}$$

$$q_e = \frac{(c_0 - c_e)v}{m} \tag{2}$$

where $\varphi(\%)$ is the adsorption ratio; c0 and ce are the initial and equilibrium concentrations (mg L^{-1}) of Cd^{2+} in solution, respectively; q_e (mg g^{-1}) is the equilibrium adsorption amount of Cd^{2+}; ν (L) is the solution volume; and m (g) is the adsorbent mass.

(2) Effect of contact time

Initially, 50 mL aliquots of 100 mg L^{-1} Cd^{2+} simulation solution were individually added to a series of 250 mL conical flasks. Then, suitable dosages of MCS

determined by the above experiments were added, and then the conical flasks were placed in a KYC-111 type thermostatic water bath shaker at 200 r min^{-1} for different times at 293 K. Afterward, the conical flasks were obtained from the shaker, and the residual Cd^{2+} concentrations in the supernatant solution were determined by the above same method. The φ was calculated through Eq. (1), and φ was plotted against time (t). The suitable contact time may be determined from the change trend of the curve.

(3) Effect of the initial pH value

The pH values of the simulated Cd^{2+} wastewaters were adjusted with 0.1 mol L^{-1} HNO3 or NaOH solution to 3.5, 4, 4.5, 5, 5.5, 6, 6.5, 7, and 7.5. Then, the above-mentioned procedures were applied to investigate the effect of the initial pH value on the adsorption ratio under the determined optimal adsorbent dosage and contact time.

Isothermal Adsorption Experiment. Isothermal adsorption experiments were carried out in accordance with the method and steps steps of **Adsorption conditions**, including the determined suitable dosage, contact time, and initial pH. The concentrations of the simulated Cd^{2+} solutions were 25, 50, 75, 100, 125, and 150 mg L^{-1}, and the test solution volumes were all 50 mL. The adsorption temperatures were 293, 303, 313, and 323 K. The adsorption isotherms at different temperatures were obtained by plotting the equilibrium adsorption amount for Cd^{2+} (q_e) against the equilibrium concentration of Cd^{2+} in solution (c_e) in accordance with the variation of Cd^{2+} concentration at pre- and post-adsorption.

Adsorption Thermodynamic Parameters. The relationship between an adsorbent and adsorbate is described by adsorption isotherms, and the isothermal adsorption data usually employ the Langmuir model (Eq. 3), Freundlich model (Eq. 4), and Redlich–Peterson model (Eq. 5) [23]. In this work, the three models were employed to fit the adsorption experimental data (**Isothermal adsorption experiment**) and obtain the thermodynamic parameters. The adsorption process is further discussed.

$$q_e = \frac{Qbc_e}{1 + bc_e} \tag{3}$$

$$q_e = K_F c_e^{\frac{1}{n}} \tag{4}$$

$$q_e = \frac{K_{R-P} c_e}{1 + \alpha c_e^{\beta}} \tag{5}$$

where q_e is the amount of adsorbed Cd^{2+} per weight unit of MCS at equilibrium (mg g^{-1}); b is a constant related to the affinity of the binding sites (L mg^{-1}); Q is the maximum amount of Cd^{2+} per weight unit of MCS (mg g^{-1}); c_e is the concentration of Cd^{2+} in solution at equilibrium (mg L^{-1}); K_F is the Freundlich constant; n is a constant, usually above 1; and K_{R-P}, α, and β are the Redlich–Peterson constants, where β lies between 0 and 1.

The logarithmic function $\ln K_d$ of the distribution coefficient K_d (described by Eq. 6) was then plotted against the reciprocal of temperature $1/T$. By linear fitting,

the enthalpy change ΔH and entropy change ΔS of the adsorption process were obtained from the linear slope and intercept, respectively (Eq. 7). Then, the Gibbs free energy of ΔG was calculated through Eq. (8) and indicated the adsorption reaction type and reaction degree [24].

$$K_d = \frac{x/m}{y/v} \tag{6}$$

$$\ln K_d = \frac{\Delta S}{R} - \frac{\Delta H}{RT} \tag{7}$$

$$\Delta G = \Delta H - T\Delta S \tag{8}$$

where x and y are the masses (mg) of Cd^{2+} adsorbed and in solution, respectively; m is the mass of the adsorbent in g; and v is the volume of the solution in mL. Therefore, x/m and y/v are the solid-phase concentration q_e (mg g^{-1}) and the equilibrium concentration in solution c_e (mg L^{-1}) at equilibrium, respectively.

Adsorption Kinetics Experiment. After 50 mL aliquots of 100 mg L^{-1} Cd^{2+} simulation solution was individually added to a series of 250 mL conical flasks. Afterward, 10 mg of MCS was added to each flask, which was then placed in a thermostatic water bath shaker under 293 K to oscillate at a speed of 200 r min^{-1} for 0–180 min. A conical flask was removed from the shaker at certain intervals, and the supernatant solution was separated from the adsorbent by centrifuging for 30 min after standing for 10 min. The Cd^{2+} concentration in the supernatant solution was determined using an atomic absorption spectrometer, and the adsorption amounts (q_t) at different times were calculated from the results. The adsorption rate curve was acquired by plotting q_t against time (t).

The adsorption kinetics information in the MCS–cadmium system is crucial to the thorough understanding of the adsorption process and adsorbent performance. The experimental adsorption kinetic data were analyzed by applying pseudo-first-order and pseudo-second-order kinetic models expressed below. The equation for the pseudo-first-order kinetic model is given by

$$q_t = q_e(1 - e^{-k_1 t}) \tag{9}$$

where q_t (mmol g^{-1}) is the amount of Cd^{2+} adsorbed per unit mass of adsorbent at t (time); q_e (mmol g^{-1}) is the amount of Cd^{2+} adsorbed per unit mass of adsorbent at equilibrium; and k_1 (min^{-1}) is the pseudo-first-order kinetic constant.

By contrast, the pseudo-second-order kinetic model is represented by

$$q_t = \frac{k_2 q_e^2 t}{1 + k_2 q_e t} \tag{10}$$

where q_t (mmol g^{-1}) is the amount of metal adsorbed per unit mass of adsorbent at t (time); q_e (mmol g^{-1}) is the amount of metal adsorbed per unit mass of adsorbent at equilibrium; and k_2 (g $mmol^{-1}$ min^{-1}) is the pseudo-second-order kinetic constant. The adsorption rate constant at 303, 313, and 323 K can be determined through the same method. The logarithm of the adsorption rate constant (ln$k$) can be calculated, and curve of the variation of the adsorption rate constant with temperature was obtained by plotting ln$k$ against 1/T. The curve can then be fitted by linear regression, and the adsorption activation energy (Ea) can be calculated from the slope of the regression line in accordance with the Arrhenius equation (Eq. 11). The adsorption type can be determined further as shown below:

$$\ln k = -\frac{E_a}{RT} + B \tag{11}$$

where k is the adsorption rate constant, R is the molar gas constant 8.314 J mol^{-1} K^{-1}, T is the absolute temperature (K), Ea is the activation energy of adsorption in kJ mol^{-1}, and B is the constant.

Regeneration Investigation. MCS (30 mg) was added into a 100 mL conical flask with 50 mL of 100 mg L^{-1} Cd^{2+} solution. Then, the conical flask was sealed and placed in a thermostatic shaker at 200 r min^{-1} for 10 h at 293 K. The supernatant solution was separated from the adsorbent by filtering after standing for 20 min, and the Cd^{2+} concentrations in the filtrate were measured. The adsorbents were withdrawn from the solution, and then 100 mL of 0.1 mg L^{-1} of triethylene tetramine solution was applied as elution agent to regenerate the adsorbents for 6 h. The regenerated adsorbents were obtained by filtering, washing with deionized water three times, and then drying to a constant weight in a vacuum oven at 60 °C. Afterward, the MCS obtained after regeneration was employed for repeated adsorption experiments to measure the variation in adsorption properties for Cd^{2+}.

Analytical Method. XRD patterns were obtained with a D8 advance type X-ray diffractometer (Bruker Co., Germany) and were used to identify the phase structures of the samples. FT-IR spectroscopy was then performed by the KBr pellet method on a Spectrum One (B) FT-IR spectrophotometer (Perkin Elmer Co., America) between 400 and 4000 cm^{-1}. The N_2 adsorption–desorption isotherms were determined by a specific surface area and pore volume analyzer (BEL SORP II, BELSOKP, Japan) at 77 K, and a specific surface area was then calculated on the basis of the BET method. The morphologies of samples were tested by S-4800 field emission SEM (Hitachi Co., Japan), and the Cd^{2+} concentration was measured using an A-Analyst 300 atomic absorption spectrometer (Perkin Elmer Co., America).

Results and Discussion

Characterization of the Synthesized Samples. Figures 1, 2, 3 and 4 give XRD patterns, infrared spectrum, SEM images, nitrogen adsorption–desorption isotherms, and pore size distribution curves of the synthetic products. MCS_S, MCS_C,

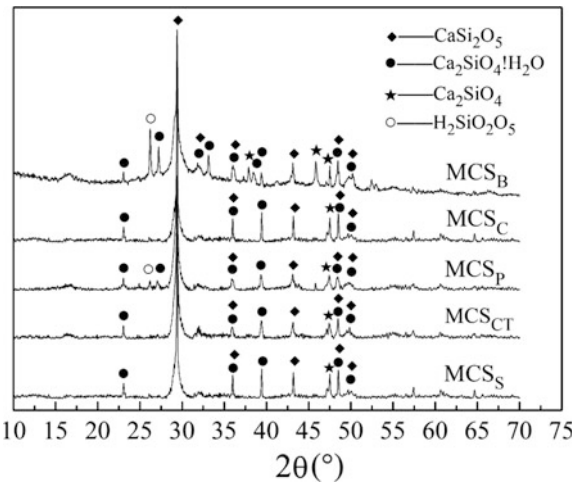

Fig. 1 XRD patterns of the synthetic samples

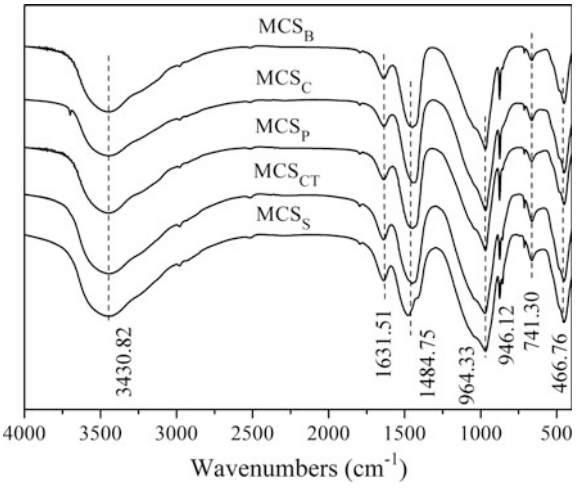

Fig. 2 Infrared spectra of the synthetic samples

MCS_{CT}, and MCS_P represent the synthetic calcium silicates that employed SDS, CTMAB, CTMAB–TMAH, and P123 as template agents, respectively, whereas MCS_B represents the calcium silicate synthesized without a template agent.

In Fig. 1, the main diffraction peaks of the samples synthesized with and without template agent are basically similar, and strong diffraction peaks are present at 2 theta = 29.5°. Compared with the standard JCPDS card, the above-mentioned five kinds of calcium silicate contained $CaSi_2O_5$ (PDF# 51-0092), $Ca_2SiO_4{\cdot}H_2O$ (PDF# 29-0373), and Ca_2SiO_4 phases (PDF# 49-1672). Moreover, the samples synthesized without template agent and with P123 as template agent contained the $H_2Si_2O_5$ phase (PDF# 27-0606). The diffraction peaks elsewhere are diffuse, which signify the low crystallinity of the sample.

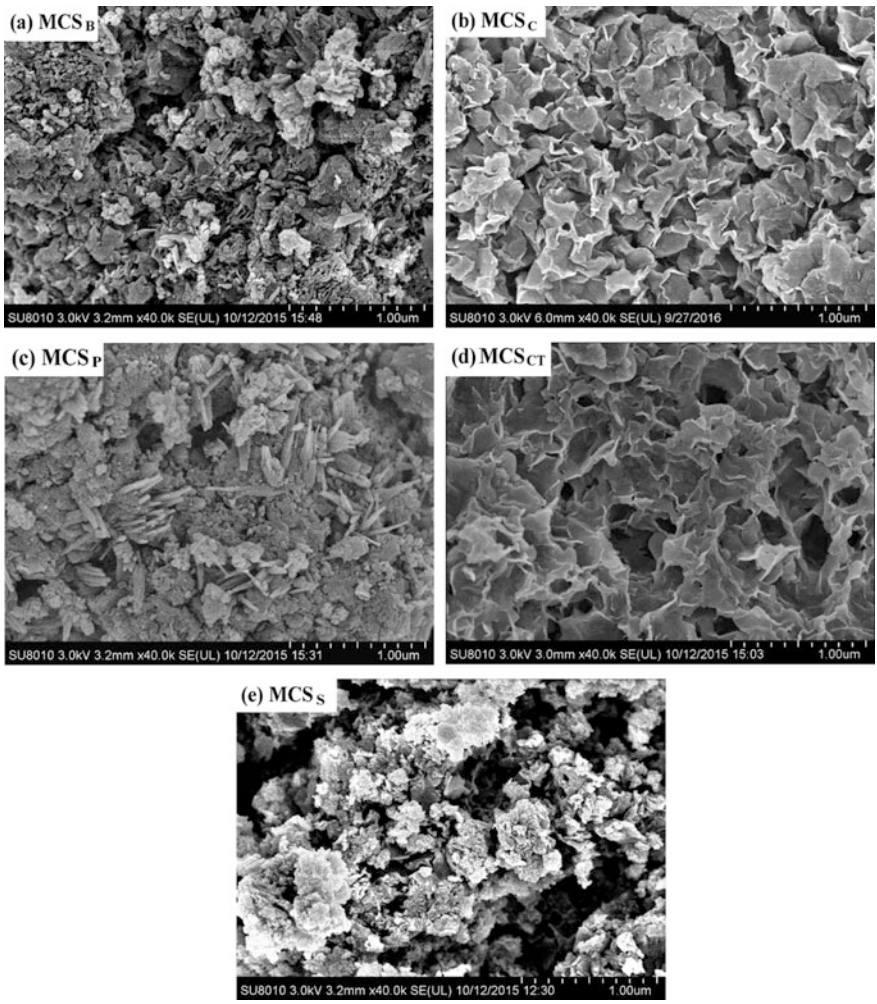

Fig. 3 SEM images of the synthetic samples

The infrared spectra of the four kinds of calcium silicate that used template agents are basically identical to that of the calcium silicate synthesized without a template agent (MCS_B) (Fig. 2). This result was achieved because the main phases and functional groups of the five kinds of calcium silicate were basically consistent (Fig. 1). The absorption peaks were assigned as follows [25, 26]. The peaks around 3430 cm^{-1} correspond to the water molecules and the asymmetric stretching vibration of surface –OH. Meanwhile, the peaks around 1630 cm^{-1} refer to the bending vibration of the water molecules adsorbed and the surface –OH and indicate the abundant presence of reactive group –OH on the surface of the synthetic samples. The peaks at about 964 cm^{-1} represent the stretching vibrations of

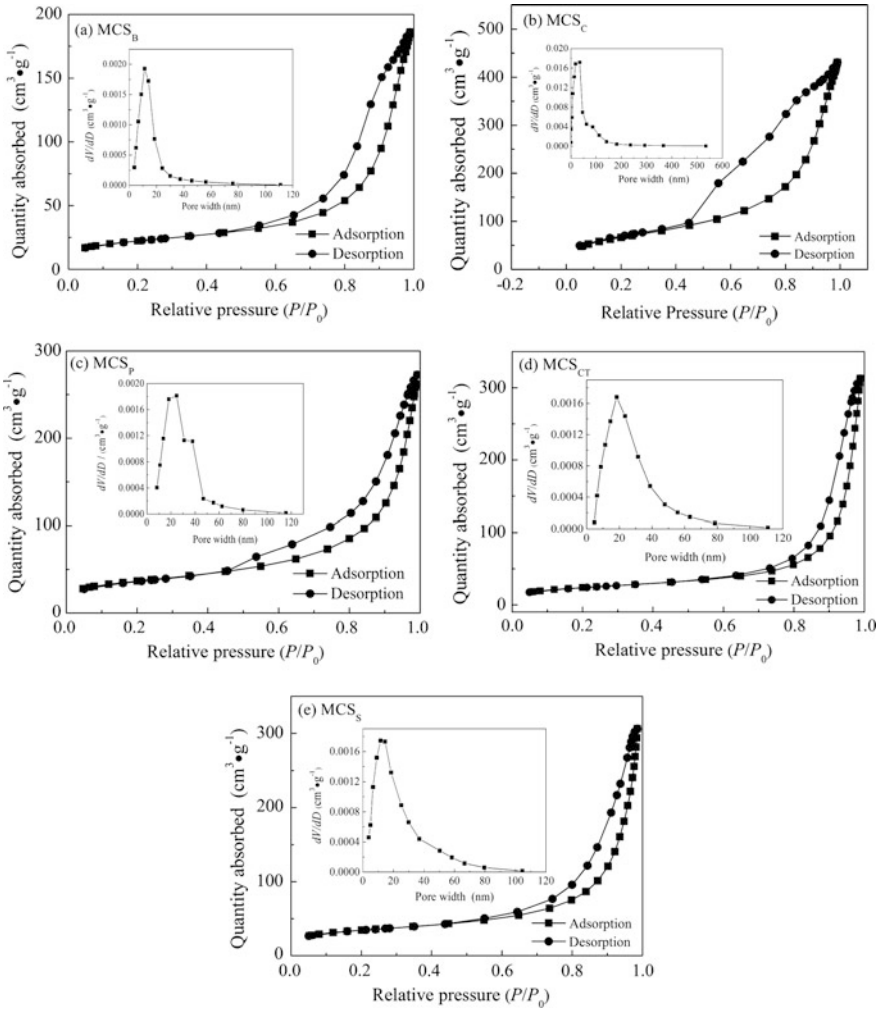

Fig. 4 Nitrogen adsorption–desorption isotherms and pore size distribution curves of the synthetic samples

Si–OH and belong to the SiO_4 tetrahedron's characteristic peak. The peaks at about 741 and 466 cm^{-1} correspond to the stretching vibrations of Si–O–Si. The characteristic absorption peak assigned to SiO_3^{2-} emerged at about 1484 cm^{-1}. The infrared spectra further confirmed that calcium silicate was synthesized successfully.

Figures 1 and 2 showed that the different template agents did not substantially affect the XRD patterns and infrared spectra of the synthetic products. However, the morphologies under SEM (Fig. 3) were highly variable and indicated the tremendous influence of the template agent on the morphology of synthetic calcium

silicate. All the synthetic calcium silicates were composed of many irregular particles with slit-pore accumulation and exhibited uneven surfaces. The calcium silicate (a) synthesized without any template agent formed by accumulating irregular granules and flakes and presented a highly uneven surface. The calcium silicate (b) synthesized using CTMAB as template agent formed by accumulating uniform thin flakes, whereas that synthesized using P123 (c) formed by accumulating irregular particles with many columnar grains, which were highly uneven. The calcium silicate (d) synthesized using CTMAB–TMAH exhibited a similar tremella shape. Finally, the calcium silicate (e) synthesized using SDS formed by accumulating numerous irregular particles and few flakes.

The nitrogen adsorption–desorption isotherms (Fig. 4) of the five kinds of synthetic calcium silicates belong to the V category of nitrogen adsorption stripping curves for perforated materials set by IUPAC. This curve exhibited a H3 type hysteresis loop, and the pore canal formed by accumulating flakes into slit shape channels. Hence, the synthesized calcium silicate was basically amorphous, consistent with the XRD analysis results. As shown by the pore size distribution in Fig. 4, the pore sizes of the mesoporous silicate synthesized using the template agents SDS, CTMAB–TMAH, P123, and CTMAB, as well as without template agent lay in the range of 5–80 nm (mainly concentrating at 18 nm), 5–80 nm (mainly at 21 nm), 8–60 nm (mainly at 25 nm), 3–60 nm (mainly at 11 nm), and 5–50 nm (mainly at 16 nm), respectively. Meanwhile, the corresponding proportions with pore sizes above 50 nm were 11.82, 13.42, 10.31, 10.21, and 7.89%. The pore size distributions of the synthesized silicates lay mainly in the range of 3–50 nm, mainly concentrating at 11–25 nm, and the proportions with sizes beyond 50 nm were low, which confirm the fabrication of MCS.

Under the BET method, the specific surface area (S_{BET}) and pore size (D_{BJH}) of the calcium silicates synthesized using different template agents were calculated (Table 1).

As shown, the pore sizes (D_{BJH}) of the synthetic calcium silicate lay in the range of 11–25 nm and belong to mesoporous materials. The template agent only modestly affected the pore sizes but highly influenced the specific surface areas of the calcium silicates. That is, the specific surface areas of the calcium silicates that used template agents were larger than that without template agent. The order of pore size was $MCS_C > MCS_{CT} > MCS_S > MCS_P > MCS_B$. Along with Fig. 3, Table 1 indicates that the calcium silicates synthesized using CTMAB and CTMAB–TMAH as template agents not only acquired large specific surface areas and but also uniform particles and a neat appearance. All of these attributes contribute to the

Table 1 Specific surface area and pore size of the synthetic samples

Sample	S_{BET} (m^2 g^{-1})	D_{BJH} (nm)
MCS_S	123.64	18
MCS_{CT}	131.22	20
MCS_P	86.68	25
MCS_C	244.32	11.2
MCS_B	79.32	16

efficient adsorption of heavy-metal ions. Notably, the specific surface area of the calcium silicate synthesized using CTMAB was higher than that of the calcium silicate synthesized using CTMAB–TMAH. Thus, using the auxiliary template TMAH may be omitted, which lowers the production cost. Therefore, the subsequent studies only investigated the adsorption properties, thermodynamics, and kinetic characteristics of MCS_C.

Adsorption Properties of Mesoporous Silicate

Effect of Adsorption Conditions on the Adsorption Efficiency. Figure 5 showed the effects of adsorbent dosage, contact time and initial pH on the adsorption of Cd^{2+} solution. With increased adsorbent dosage, the adsorption ratio of MCS_C for Cd^{2+} first rose rapidly, whereas the adsorption amount unit mass adsorbent (q_e) for Cd^{2+} declined gradually (Fig. 5a). When the dose reached 200 mg L^{-1}, the adsorption ratio of Cd^{2+} tended to stabilize, and the adsorption ratio increased only modestly even with the continuously rising dosage. Therefore, the suitable MCS dosage was 200 mg L^{-1}, and the adsorption ratio reached 92.51%. Figure 5b shows the change in adsorption ratio of Cd^{2+} with time (at the MCS_C dosage of 200 mg L^{-1}). When the adsorption time reached 60 min, the adsorption ratio increased to 92.49%. The adsorption ratio tended to stabilize, and the adsorption ratio increased very slowly even with continuously extending contact time. The above results revealed that the adsorption of MCS_C for Cd^{2+} can reached the adsorption equilibrium more quickly. To ensure a full adsorption balance, we selected 10 h as the contact time. Figure 5c presents the change in adsorption ratio of Cd^{2+} with the initial pH (at the MCS_C dosage of 200 mg L^{-1} and contact time of 10 h). When the initial solution pH was 5.0–7.5, the adsorption ratio of MCS_C for Cd^{2+} was high. At pH less than 5, the adsorption ratio increased rapidly with rising pH. When the initial pH reached 5, the adsorption ratio of MCS_C for Cd^{2+} was 89.69% and began to stabilize with small changes. When the initial pH was not adjusted (the pH of 100 mg L^{-1} Cd^{2+} solution was 6.17), the adsorption ratio was 92.51%. Therefore, except to investigate the influence of pH on the adsorption ratio, we did not adjust the pH of the Cd^{2+}solution (pH 6.17) for the subsequent experiments.

Effect of Adsorption Temperature on the Adsorption Efficiency. Figure 6 displays the adsorption isothermal curves of MCS_C for Cd^{2+}. The adsorbent dosage was 200 mg L^{-1}, the contact time was 10 h, and the Cd^{2+} solution pH was not adjusted.

The adsorption ratio of Cd^{2+} increased rapidly with solution concentration when the Cd^{2+} solution concentration was less than 100 mg L^{-1} (fourth experimental point) at the same temperature. Beyond 100 mg L^{-1}, and the adsorption amount increased only slightly even with continuously increasing Cd^{2+} solution concentration. The adsorption isotherm of MCS_C for Cd^{2+} also rose with temperature elevation. This result indicates that the adsorption amount increases with

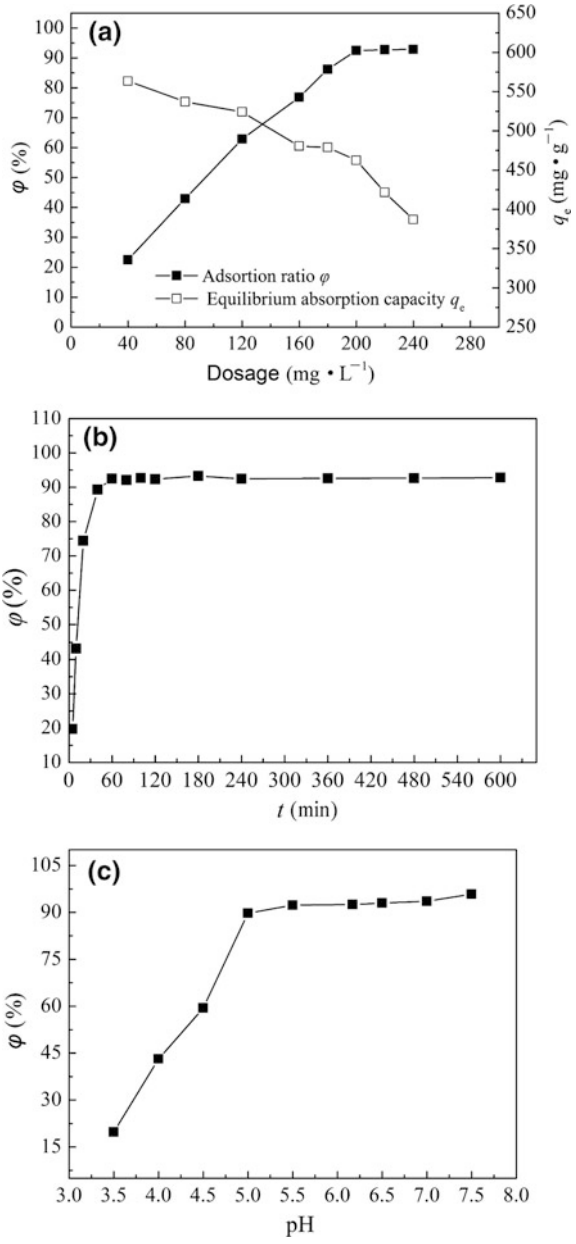

Fig. 5 Effects of MCS_C dosage, contact time, and initial pH of Cd^{2+} ion solution on the removal ratios for Cd^{2+}

temperature. However, the increased amplitude of the adsorption amount from 313 to 323 K was obviously lower than those of the temperatures below 313 K. This effect proves that increasing the adsorption temperature would increase the adsorption of Cd^{2+}, and that the adsorption was an endothermic reaction.

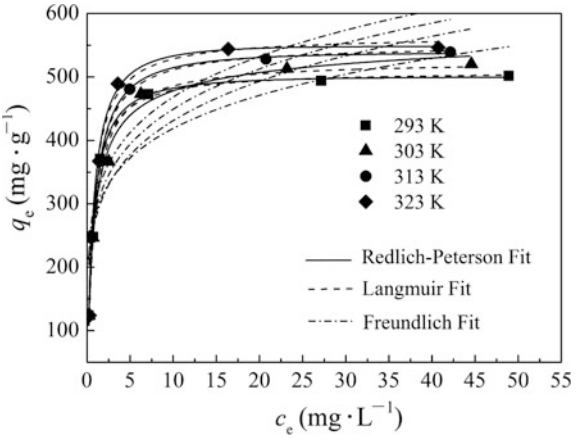

Fig. 6 Adsorption isotherms of MCS_C for Cd^{2+}

The decreased rise in amplitude at high temperature (323 K) was achieved potentially because the adsorption was not merely a simple chemical adsorption process, but also included physical adsorption. The physical adsorption amount decreased, whereas the chemical adsorption amount increased, with temperature rise. Furthermore, the increase in adsorption amount by chemical adsorption dominated at lower temperatures, whereas the decreased adsorption amount by physical adsorption was more apparent at high temperatures. Hence, amplitude increase of the adsorption amount decreased obviously at high temperatures.

The data in Fig. 6 were then fitted by the Langmuir, Freundlich, and Redlich–Peterson models, and the results are shown in Table 2 The correlation coefficient fitted by the Redlich–Peterson model was highest, followed by the Langmuir model, and then by the Freundlich model. Both the Redlich–Peterson and Langmuir models can fit the experimental data well. However, the Redlich–Peterson model was more accurate because the Redlich–Peterson model combined the success of the Langmuir and Freundlich models and was not bound by the ideal monolayer assumption of the Langmuir model [23]. Under the Langmuir adsorption model, the maximum adsorption capacity of MCS_C for Cd^{2+} was 509.91 mg g^{-1} at 293 K. This value was far higher than those of common adsorbents reported in literature (Table 3). This is because that apart from the high specific surface area and abundant pore canals, abundant active groups, such as –OH and –O– were present on the surface of MCS_C [17, 20], which is beneficial to complex with Cd^{2+}.

Adsorption Thermodynamic Characteristics of MCS_C for Cd^{2+}. Figure 7 shows the relationship curve between the logarithm ln K_d of the Cd^{2+} distribution coefficient K_d at adsorption equilibrium and the reciprocal of temperature ($1/T$). The solid line refers to the fitted curve of the four temperatures of 293, 303, 313, and 323 K, whereas the dotted line corresponds to the fitted curve of the former three temperatures. Given the intercept and slope of the fitted line, the adsorption thermodynamic parameters, such as ΔS, ΔH, and ΔG, were calculated in accordance with Eqs. (7) and (8) (Table 4).

Table 2 Nonlinear fitting parameters of MCS for Cd^{2+}

Temperature (K)	Langmuir			Freundlich			Redlich-Peterson			
	Q (mg g^{-1})	b (L mg^{-1})	R^2	K_F	n	R^2	K_{R-P}	α	β	R^2
293	509.91	1.5619	0.9919	283.89	5.9184	0.7810	757.85	1.4358	1.0106	0.9923
303	525.22	1.2352	0.9859	275.99	5.1608	0.8445	778.26	1.6768	0.9595	0.9887
313	551.25	1.2781	0.9987	290.04	5.2591	0.7931	672.47	1.1726	1.0125	0.9990
323	564.83	1.4543	0.9587	306.15	5.4134	0.7364	765.62	1.2782	1.0192	0.9648

Table 3 Adsorption capacities of adsorbents for Cd^{2+} in literature

Adsorbent	Adsorption capacity (mg g^{-1})	Ref.	Adsorbent	Adsorption capacity (mg g^{-1})	Ref.
Activated carbon	10.3	[1]	TMU-16-NH_2 metal–organic framework	126.6	[12]
Chitosan biosorbent	10		PF-Cd(II)-SPANDS	270	[13]
Chitosan/activated carbon composite	52.63		Powdered activated carbon impregnated alginate beads (ABPAC)	149.32	[14]
Phosphoricacid-impregnated mesoporous activated carbon	227.27	[8]	Ethylenediamine functionalized SBA-15	100.0 ± 0.6	[15]
Granular red mud	38.2	[9]	Mesoporous silica (mono-amino-)	28.10	[16]
Natural chabazite	120	[10]	Mesoporous silica (mercapto-groups)	14.61	
Ipomoea Biochar	41.67–72.43	[11]	Activated carbon (carboxylic group)	12.37	

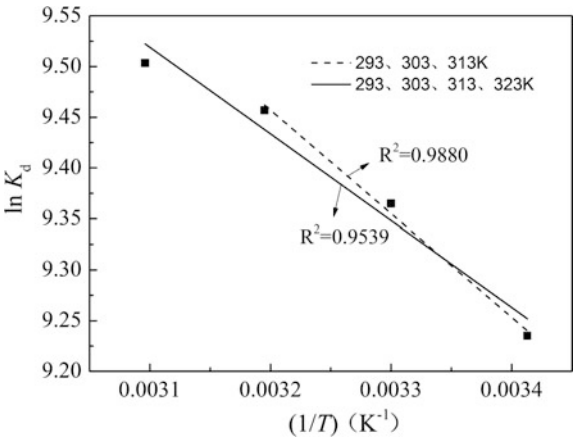

Fig. 7 ln K_d versus 1/T for Cd^{2+} adsorption onto MCS_C

Table 4 Thermodynamic parameters of Cd^{2+} adsorption on MCS_C

ΔH(kJ mol^{-1})	ΔS (J mol^{-1} K^{-1})	ΔG/(kJ mol^{-1})			
		293 K	303 K	313 K	323 K
7.098	101.145	−22.537	−23.549	−24.560	−25.572

Evidently, the correlation coefficient of the fitted line for the former three temperature points was higher than that for the four temperature points (Fig. 7). This result indicates that the adsorption of MCS_C for Cd^{2+} closely follows Eq. (5) when the temperature was below 313 K. When the temperature was 323 K, the adsorption of MCS_C for Cd^{2+} significantly deviated from the relationship law (Eq. 7). This effect was achieved because the adsorption of MCS_C for Cd^{2+} included chemical and physical adsorption; at the high temperature of 323 K, the decrement caused by physical adsorption was larger than the increment from chemical adsorption.

The ΔH and ΔS of the adsorption process of MCS_C for Cd^{2+} were above zero, and ΔG was less than zero (Table 4). Hence, the adsorption process was a spontaneous endothermic process with entropy increase. The adsorption of MCS_C for Cd^{2+} primarily involved chemical adsorption caused by the coordination effect of the active groups of –OH and –O– with Cd^{2+}. Therefore, the process needed to absorb a certain amount of energy to overcome the activation energy and exhibited the heat absorption phenomenon. The chemical adsorption contributed only partly to the adsorption; thus, the heat absorption amount was not large. The increase in adsorption entropy of MCS_C for Cd^{2+} may be due to the Cd^{2+} ions in the aqueous solution are solvated, and the adsorbents may have adsorbed a certain amount of solvent molecules in the preparation process. When the Cd^{2+} ions adsorbed onto the MCS_C surface, the Cd^{2+} ions were constrained to the surface, and the entropy of the adsorption process decreased. Meanwhile, the solvent molecules that were adsorbed onto the adsorbent surface and the solvent layer were partly released from the MCS_C surface and the solvent layer of Cd^{2+} and lead to entropy increase. Furthermore, the entropy decrement from Cd^{2+} constrained to the surface of MCS_C is lower than the entropy increment from the release of solvent molecules and hence increased the entropy.

Adsorption Kinetic Characteristics. Figure 8 reveals the change in adsorption amount q_t with time (t) at different temperatures. The kinetic fitting parameters are shown in Table 5.

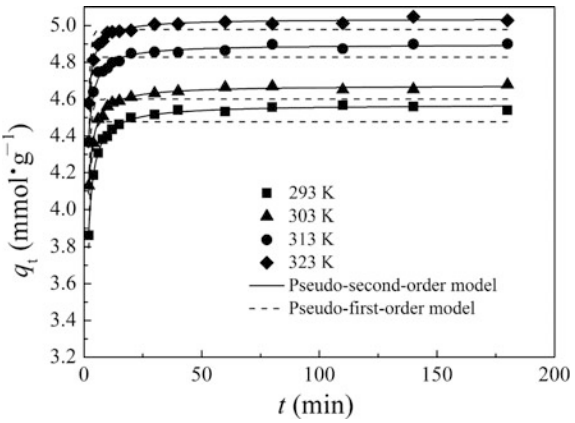

Fig. 8 Change in adsorption amount (q_t) with time (t)

Table 5 Kinetic fitting parameters

Temperature (K)	Pseudo-first-order kinetics model			Pseudo-second-order kinetics model			Experimental value q_e (mmol g^{-1})
	q_e (mmol g^{-1})	k_1 (min^{-1})	R^2	q_e (mmol g^{-1})	k_2 (mmol mg^{-1} min^{-1})	R^2	
293	4.4764	0.9405	0.7544	4.5714	0.5972	0.9971	4.5361
303	4.5998	1.0945	0.7166	4.6748	0.7974	0.9938	4.6723
313	4.8282	1.1408	0.7696	4.8972	0.8642	0.9866	4.9039
323	4.9781	1.2327	0.7753	5.0373	1.0242	0.9884	5.0247

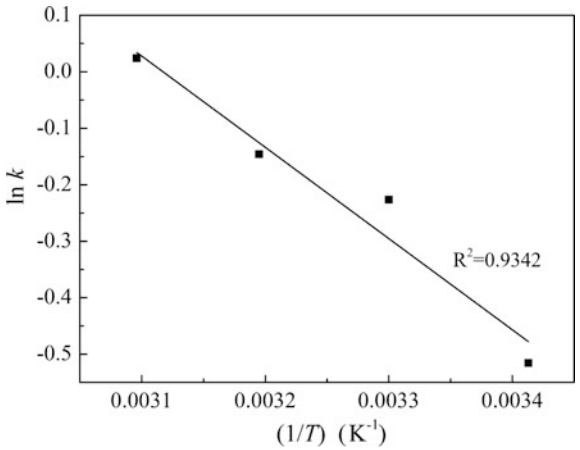

Fig. 9 ln k versus $1/T$ for Cd^{2+} adsorption onto MCS_C at different temperatures

Table 6 Regeneration of MCS_C from Cd^{2+} adsorption

Regeneration times	0	1	2
Equilibrium adsorption value q_e (mmol g^{-1})	4.47	3.65	3.09
Decreasing percent (%)		18.34	30.87

As displayed in Fig. 8 and Table 5, the adsorption of MCS_C for Cd^{2+} fitted well with the pseudo-second-order kinetic model. The fitted values were also very close to the experimental values. The logarithm of the secondary adsorption rate constant (Table 5) ln k was plotted against the reciprocal of temperature ($1/T$) (Fig. 9). A good correlation between ln k at different temperatures and $1/T$ was notable (Fig. 9). The activation energy of the adsorption process was calculated from the slope of the fitted curve to be 13.4327 kJ mol^{-1} on the basis of Eq. (11).

Regeneration of MCS_C. Table 6 gives the regeneration of the MCS_C-adsorbed Cd^{2+} by using 0.1 mol L^{-1} triethylene tetramine elution. As can be seen from Table 6, triethylene tetramine is an effective eluent for the MCS_C-adsorbed Cd^{2+}; after the first elution–regeneration, the decreasing percent of equilibrium adsorption values was evident at 18.34%, and increase to 30.87% after the second elution–regeneration; therefore, continuous elution–regeneration is unnecessary.

Conclusion

(1) MCS was successfully synthesized using calcium nitrate and sodium silicate as raw materials through the ultrasonic-assisted template method. The pore is a slit-pore measuring 3–50 nm in size (mainly at 11–25 nm). The specific surface area of the MCS_C prepared using CTMAB reaches as high as 244.32 m^2 g^{-1}.

(2) MCS_C exhibites a good adsorption efficiency for Cd^{2+}; the adsorption capacity of Cd^{2+} reaches up to 509.91 mg g^{-1}, which is far higher than those of the adsorbents reported in literature. The experimental data agree with the Langmuir model and more closely with the Redlich–Peterson model. The adsorption is a spontaneous endothermic process with entropy increase involving physical and chemical modes.
(3) The adsorption process of MCS_C for Cd^{2+} follows the pseudo-second-order kinetic model, and the adsorption activation energy is calculated to be 13.4327 kJ mol^{-1}. MCS_C possesses a high adsorption capacity for Cd^{2+} in the pH range of 5.0–7.5. Therefore, MCS_C exhibites an excellent adsorption performance and is an outstanding adsorption material for Cd^{2+}.

Acknowledgements This research was supported by the National Nature Science Foundation of China (Grant No. 51378201) and the Key Scientific Research Program of Hunan Education Department (Grant No. 16A069).

References

1. S. Hydari, H. Sharififard, M. Nabavinia, M. Reza Parvizi, A comparative investigation on removal performances of commercial activated carbon, chitosan biosorbent and chitosan/activated carbon composite for cadmium. Chem. Eng. J. **193–194**, 76–282 (2012)
2. D. Purkayastha, U. Mishra, S. Biswas, A comprehensive review on Cd(II) removal from aqueous solution. J. Wat. Proc. Eng. **2**, 105–128 (2014)
3. X. Lin, R.C. Burns, G.A. Lawrance, Heavy metals in wastewater: the effect of electrolyte composition on the precipitation of cadmium(II) using lime and magnesia. Water Air Soil Pollut. **165**(1–4), 131–152 (2005)
4. C.W. Wong, J.P. Barford, G. Chen, G. McKay, Kinetics and equilibrium studies for the removal of cadmium ions by ion exchange Resin. J. Environ. Chem. Eng. **2**, 698–707 (2014)
5. M. Kobya, E. Demirbas, N.U. Parlak, S. Yigit, Treatment of cadmium and nickel electroplating rinse water by electrocoagulation. Environ. Technol. **31**(13), 1471–1481 (2010)
6. M.R. Mahmoud, N.K. Lazaridis, K.A. Matis, Study of flotation conditions for cadmium (II) removal from aqueous solutions. Process Saf. Environ. Prot. **94**, 203–211 (2015)
7. E. Saljoughi, S.M. Mousavi, Preparation and characterization of novel polysulfone nanofiltration membranes for removal of cadmium from contaminated water. Sep. Purif. Technol. **90**, 22–30 (2012)
8. I.A.W. Tan, J.C. Chan, B.H. Hameed, L.L.P. Lim, Adsorption behavior of cadmium ions onto phosphoricacid-impregnated microwave-induced mesoporous activated carbon. J. Wat. Process Eng. **14**, 60–70 (2016)
9. C.L. Zhu, Z.K. Luan, Y.Q. Wang, X.D. Shan, Removal of cadmium from aqueous solutions by adsorption on granular red mud (GRM). Sep. Purif. Technol. **57**, 161–169 (2007)
10. S.M. Yakout, E.H. Borai, Adsorption behaviour of cadmium onto natural chabazite: batch and column investigations. Desalin. Water Treat. **52**(22–24), 4212–4222 (2014)
11. R. Goswami, J. Shim, S. Deka, D. Kumari, R. Kataki, M. Kumar, Characterization of cadmium removal from aqueous solution by biochar produced from Ipomoea fistulosa at different pyrolytic temperatures. Ecol. Eng. **97**, 444–451 (2016)
12. M. Roushani, Z. Saedi, Y.M. Baghelani, Removal of cadmium ions from aqueous solutions using TMU-16-NH2 metal organic framework. Environ. Nanotechnol. Monit. Manage. **7**, 89–96 (2017)

13. D.K. Singh, S. Mishra, Synthesis, characterization and removal of Cd(II) using Cd(II) ion imprinted polymer. J. Hazard. Mater. **164**, 1547–1551 (2009)
14. A. Sigdel, W. Jung, B. Min, M. Lee, U. Choi, T. Timmes, S.J. Kim, C.U. Kang, R. Kumar, B. H. Jeon, Concurrent removal of cadmium and benzene from aqueous solution by powdered activated carbon impregnated alginate beads. Catena **148**, 101–107 (2017)
15. L. Hajiaghababaei, A. Badiei, M.R. Ganjali, S. Heydari, Y. Khaniani, G.M. Ziarani, Highly efficient removal and preconcentration of lead and cadmium cations from water and wastewater samples using ethylenediamine functionalized SBA-15. Desalination. **266**, 182–187 (2011)
16. M. Machidaa, B. Fotoohi, Y. Amamb, T. Ohba, H. Kanoh, L. Mercier, Cadmium(II) adsorption using functional mesoporous silica and activated carbon. J. Hazard. Mater. **221–222**, 220–227 (2012)
17. M. Mehrali, S.F.S. Shirazi, S. Baradaran, M. Mehrali, H.S.C. Metselaar, N.A.B. Kadri, N.A. A. Osman, Facile synthesis of calcium silicate hydrate using sodium dodecyl sulfate as a surfactant assisted by ultrasonic irradiation. Ultrason. Sonochem. **21**, 735–742 (2014)
18. K. Okano, M. Uemoto, J. Kagami, K. Miura, T. Aketo, M. Toda, K. Honda, H. Ohtake, Novel technique for phosphorus recovery from aqueous solutions using amorphous calcium silicate hydrates (A-CSHs). Water Res. **47**, 2251–2259 (2013)
19. C.J. Li, Y. Dong, Y.H. Lei, D.Y. Wu, P. Xu, Removal of low concentration nutrients in hydroponic wetlands integrated with zeolite and calcium silicate hydrate functional substrates. Ecol. Eng. **82**, 442–450 (2015)
20. T. Guo, J.H. Han, P. Liu, Pretreatment of COD and NH3-N of coking wastewater by calcium silicate adsorption method. Environ. Chem. **32**(1), 168–169 (2013)
21. J. Wu, Y.J. Zhu, F. Chen, Ultrathin calcium silicate hydrate nanosheets with large specific surface areas: synthesis, crystallization, layered self-assembly and applications as excellent adsorbents for drug, protein, and metal ions. Small. **9**(17), 2911–2925 (2013)
22. G.X. Qi, X.F. Lei, L. Li, C. Yuan, Y.L. Sun, J.B. Chen, Y. Wang, J.M. Hao, Preparation and evaluation of a mesoporous calcium-silicate material (MCSM) from coal fly ash for removal of Co(II) from wastewater. Chem. Eng. J. **279**, 777–787 (2015)
23. O. Redlich, D.L. Peterson, A useful adsorption isotherm. J. Phy. Chem. **63**(6), 1024 (1959)
24. D. Ghosh, K.G. Bhattacharyya, Adsorption of methylene blue on kaolinite. Appl. Clay Sci. **20**, 295–300 (2002)
25. M.L. Zhang, J. Chang, Surfactant-assisted sonochemical synthesis of hollow calcium silicate (CSH) microspheres for drug deliver. Ultrason. Sonochem. **17**(5), 789–792 (2010)
26. N.Y. Mostafa, E.A. Kishar, S.A. Abo-El-Enein, FTIR study and cation exchange capacity of Fe^{3+}- and Mg^{2+}-substituted calcium silicate hydrates. J. Alloys Compd. **473**, 538–542 (2009)

Removal of Hexavalent Chromium from Aqueous Using Biochar Supported Nanoscale Zero-Velent Iron

Weilin Shi and Xue Song

Abstract A novel biochar carried nanoscale zero-valent iron (NZVI) particles were synthesized by means of liquid phase reduction method that can overcome the aggregation of NZVI particles. The Composite material of the biochar-NZVI can effectively improve the removing rate of hexavalent chromium Cr(VI) in the application of water treatment. The experimental results showed that the remove rate of Cr(VI) was up to 96.8% by using biochar-NZVI when the mass ratio of biochar and NZVI was of 5:1, the rate was enhanced by about 35.9% than that of the same dose pure NZVI. The analyzed results of TEM and BET showed that the biochar-NZVI had higher dispersion and specific surface area than pure NZVI, which was the key reason for biochar-NZVI with high removing efficiency of Cr(VI). The apparent rate constant k_{obs} decreases from 0.1041 to 0.0235 min^{-1} as the initial concentration of Cr(VI) increased from 25 to 125 mg/L in the solution, indicating that the reaction velocity decreases with the increased initial concentration of Cr(VI) in the solution. The removal efficiency reached to 92.1% when the pH value of the solution containing biocha-NZVI treating Cr(VI) increased from 4.48 to 8.36, showing that the biochar carried NZVI has high removing rate of Cr(VI) in a wide range of pH value.

Keywords Biochar · Nanoscale zero-valent iron · Hexavalent chromium Removal

W. Shi (✉) · X. Song
School of Environmental Science and Engineering, Suzhou University of Sciences and Technology, Suzhou 215011 China
e-mail: goldlionwl@163.com

X. Song
e-mail: 331677126@qq.com

Y. Han (ed.), *Advances in Energy and Environmental Materials*,
Springer Proceedings in Energy, https://doi.org/10.1007/978-981-13-0158-2_89

Introduction

Nanoscale zero-valent iron (NZVI) with a larger specific surface area and a high reactivity, can effectively remove heavy metal pollutants. Recently years, it reported that nanoscale zero-valent iron (NZVI) attached on montmorillonite [1], bentonite [2], activated carbon and other materials maintain its strong reduction characteristics in the field of environmental remediation, and enhance its stability and suitable for engineering operation. Compared with above carriers, biochar is a kind of a easy to gat raw material, low cost, superior adsorption performance and environmentally friendly materials [3]. At the same time, it has not only good pore structure and large specific surface area, which easily disperse NZVI particles. Obviously, NZVI carried by biological carbon may have good engineering application prospects [4]. However, the studies and related reports on biological carbon carrying NZVI and the research on removal of heavy metals are few.

Six valence chromium Cr(VI) is a common pollutants in water environment, which can easily invade into human body through the digestive tract, respiratory tract and skin contacts, harm to human health. With the development of economy and the change of consumption structure, more and more chromium wastewater discharged into the environment through tanning, electroplating, metallurgy and other industries. Therefore, The effectively removing methods of Cr(VI) in water received wide attention [5, 6]. NZVI is an efficient reducing agent have got much attention because can effectively reduce Cr(VI) to trivalent chromium Cr(III) that is of low toxicity. In the present study, we studied the properties of biological carbon carried NZVI to remove Cr(VI) in solution using liquid phase reduction method. The results will provide some theoretical basis for engineering application.

Materials and Methods

Materials Preparation. The prepared biochar was over a 100 mesh screen, immersed in 1.0 mol/L hydrochloric acid 12 h to remove impurities, and washed it with deionized water to neutral water, then dried for use. The preparing and attaching of NZVI on the cleaned biochar was operated under anaerobic conditions. 1.0 g nano zero valent iron was made by solving 5 g $FeSO_4{\cdot}7H_2O$ in a 100 mL ethanol and deionized water intermixture with the alcohol water ratio of 4:1 (*v/v*), and dropping 50 mL 20 g/L KBH_4 solution one by one with stirring under nitrogen protection. Then 5.0 g biochar was soaked in $FeSO_4{\cdot}7H_2O$ solution 60 min with stirring velocity 200 r/min to fully mixed. The remaining steps the same as above. Finally, 6.0 g biochar carried NZVI with a carbon iron mass ratio of 5:1 was made. The chemical equation of the reaction as

$$2Fe^{2+} + BH_4^- + 2H_2O = 2Fe + BO_2^- + 2H_2 + 4H^+ \quad (1)$$

After the reaction, washing the obtained material a few times with deionized water and absolute ethanol, which were purged nitrogen 1 h to remove oxygen before using, finally dried it under nitrogen protection.

Material Characterization. Biochar-NZVI mixed with 2.0 mol/L hydrochloric acid and hydroxylamine hydrochloride solution, dissolved iron and the solution heated in a water bath at 100°C, then filtered with 0. 22 μm membrane. The filtrate was measured with phenanthroline colorimetric method to determination the content of ferrous ion, and converted to the mass of NZVI. The mass ration of iron and carbon in the biochar was obtained by compared the dried filter residue with the mass of NZVI.

The size of the material particles was observed by Hitachi HT7700 transmission electron microscope (TEM) under 100 kV operating voltage. The surface functional groups of biochar were measured using NICOLET iN10 MX Fourier transform infrared spectrometer (FT-IR); the crystal structure was analyzed using thermo ARL X'TRA X-ray differaction (XRD), and the specific surface area and aperture parameters of material were measured by ASAP 2020 surface area meter.

Experiment Methods. The Cr(VI) water samples used in the experiment were prepared using $K_2Cr_2O_7$ to a stock solution with a concentration of 150 mg/L. First, the removing effect to Cr(VI) in solution was investigate by comparing the results of biochar, nano zero valent iron, and biochar-NZVI with the mass ration of iron and carbon of 3:1, 5:1, 7:1, noted as 3BC-Fe, 5BC-Fe and 7BC-Fe, respectively. The initial concentration of Cr(VI) used in the experiment was 50 mg/L, the average mass of NZVI in various materials is 0.5 g/L,the reaction temperature was 25 °C, and the solution initial pH was 4.5.

The influence of the initial concentration of Cr(VI) on the removing effect of biochar-NZVI to Cr(VI) was analyzed using 5BC-Fe solution. The initial concentration of Cr(VI) was set as 25, 50, 75, 100 and 125 mg/L; the amount of biochar-NZVI was 3.0 g/L, the reaction temperature was 25°C,and the solution initial pH was 4.5.

The influence of the initial pH in the solution to the remove effect of Cr(VI) was selected 5BC-Fe solution. The initial pH was set as 4.5, 6.5, 7.0, 8.5, and 10.5; the amount of biochar-NZVI was 3.0 g/L, and the reaction temperature was 25 °C.

Third, the effect of temperature on remove Cr(VI) was selected 5BC-Fe solution. The temperature was set as 15, 25, 35, 45 and 55 °C, The initial concentration of Cr (VI) was 50 mg/L; the amount of biochar-NZVI was 3.0 g/L, and the solution initial pH was 4.5.

Each experiment was carried in a 250 mL conical flask stirred by amagnetic stirrer with a speed of 200 r/min. Samples was took in the set time point and filtered using 0.22 μm membrane. The concentration of Cr(VI) was determined using two benzoyl hydrazine spectrophotometry by means of Alpha-1106 spectrophotometry of 540 nm wavelength light.

Result and Discuss

Materials Characterization. First, we validate the mass ration of iron and carbon in biochar-NZVI. The results show that the mass ration of iron and carbon was 1: 6.84, 1:4.92 and 1: 2.88 in the 7BC-Fe, 5BC-Fe and 3BC-Fe samples, basically consistent with the mass ratio of iron carbon settled in the original experimental. Figure 1a–c are the appearance pictures observed in biochar, NZVI, and BC-Fe by TEM. We can see that biochar takes the shape of flakes, NZVI is of spherical particles with a size about 30–70 nm. In Fig. 1c shows that many NZVI particles are attached on the surface of biochar, indicating that biochar successfully carried NZVI partiles. The shape of NZVI is characteristic of a chain because of their larger specific surface area leading to a large attraction between particles [7]. In the TEM picture we observed that almost each the biochar flake is attached on NZVI particles. The measured specific surface area for biochar, NZVI Fe, 3BC-Fe, 5BC-Fe and7BC-Fe is 205.4, 20.9, 138.1, 142.8 and 126.6 m^2/g, respectively. The decrease of the specific surface area of biochar may be related to the holes and channels of biochar filled up by NZVI particles.

Figure 2 shows the spectrum of Fourier transform infrared spectroscopy. The absorption peak at 3400 cm^{-1} is attributed to the stretching vibration caused by –OH group; the peak at 1710 cm^{-1} is caused by the vibration of C=O band in carboxyl group; and the peak at 1103 cm^{-1} corresponding to the stretching vibration of C=O bands in phenol, alcohol and other substances [8]. In the preparation of biochar-NZVI, these groups can absorb Fe(II) of the solution, which help to the carrying of NZVI.

Figure 3 shows the XRD spectrum of the three kinds samples [9]. Obviously, there is a main peak at 44.5° from NZVI Fe, corresponding to the characteristic diffraction peak of α-Fe [10, 11], indicating that the main form of iron in the samples is α-Fe. The peak at $2\theta = 22.7°$ is characteristics a amorphous structure of carbon from the characteristic peak of the biochar samples [12]. The two characteristic peaks of the biochar-NZVI samples in the XRD spectrum shows that NZVI Fe and biochar both exist simultaneously in the samples.

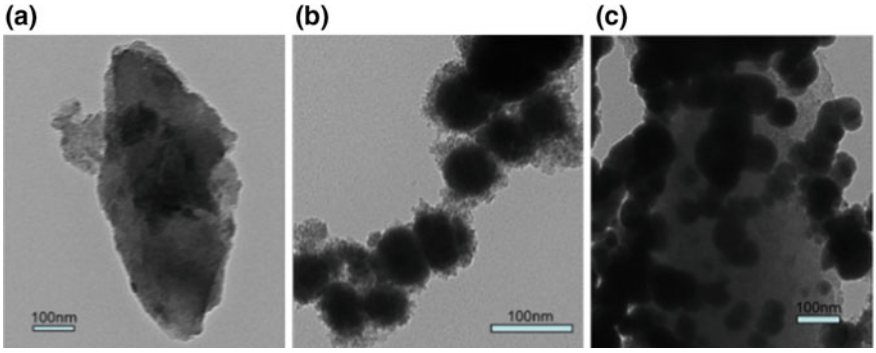

Fig. 1 TEM images of samples. **a** BC; **b** NZVI; **c** BC-Fe

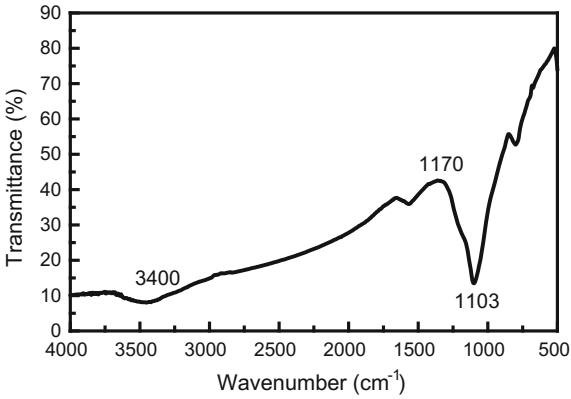

Fig. 2 FT-IR spectra of biochar

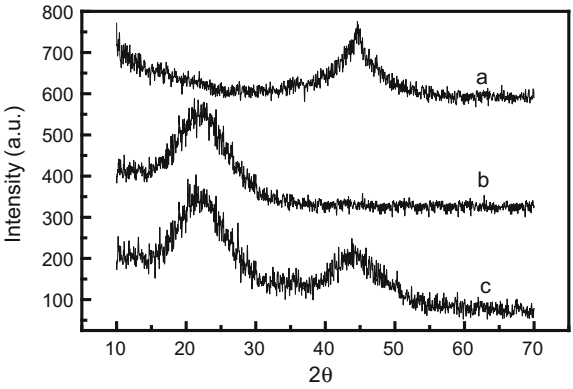

Fig. 3 X-ray diffraction (XRD) spectra of the samples. **a** NZVI; **b** BC; **c** 5BC-Fe

Biochar-NZVI removing Cr(VI). Figure 4 shows the remove behaviors of the NZVI and biochar-NZVI materials to Cr(VI). It is seen that the removal reaction to Cr(VI) basically achieves to a balance about 120 min. In 120 min, the removing effect of biochar with mass concentration of 2.5 g/L to Cr(VI) is not obvious. The removal rate is only about 16.1%. This because Cr(VI) in the solutions exists in the forms of $HCr_2O_7^-$, $Cr_2O_7^{2-}$ and CrO_4^{2-} etc. anionics. Although biochar has porous structure and large specific surface area, the carried surface negative charges are mutually exclusive with $HCr_2O_7^-$, $Cr_2O_7^{2-}$ and CrO_4^{2-} etc. anionics, leading to low removing efficiency to Cr(VI).

The removing efficiency of NZVI sample to Cr(VI) is about 60.9% in 120 min. Clearly, biochar-NZVI sample significantly increases the removal capacity of Cr (VI). The removing efficiency of Cr(VI) enhanced from 60.9 to 92.0, 96.8 and 85.0% for 3BC-Fe, 5BC-Fe and 7BC-Fe samples, respectively. This because NZVI particles attached on biochar can effectively overcome the defects of NZVI, increasing the removing efficiency of biochar-NZVI to Cr(VI). At the same time,

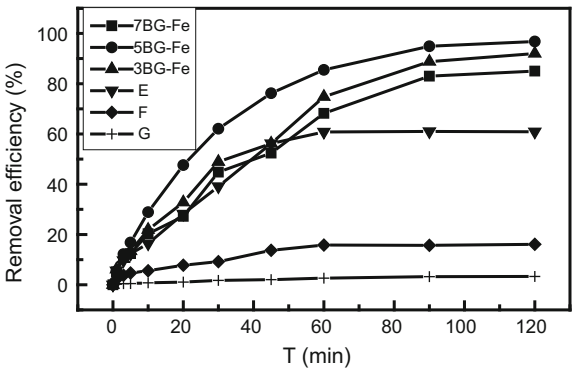

Fig. 4 The removing curves of Cr^{6+} under different composites

biochar has a certain adsorption capacity to Cr(VI), which can adsorb Cr(VI) on the surface of it. The larger concentration of NZVI is the fast the remove reaction does.

The result of Fig. 4 shows that the ratio of carbon and iron in biochar-NZVI has influence the removing effect to Cr(VI). Compared the removal efficiency of the biochar-NZVI samples to Cr(VI), we found that the efficiency of 5BC-Fe sample is larger about 4.8% than that of 3BC-Fe sample. However, it reduced about 11.8% for 7BC-Fe than that of 5BC-Fe. As a carrier biochar can overcome the aggregation defect of NZVI, then increases the reaction rate. But too much biochar will lead reunion between biochars [13] that lows the specific surface area of material, finally leading to low the removal efficiency of Cr(VI). Chen et al. [14] thought that the reaction rate reduced because too much biochar will occupy the activity position of NZVI. Therefore, there is an optimum proportion of iron and crrbon in the biochar-NZVI material. The results found that the removal effect of biochar-NZVI Fe to Cr(VI) is better than that of other materials when the ration of iron and carbon is 5:1.

The Influence Factors of Biochar-NZVI Fe to Cr(VI). Figure 5 shows the relationship of removal effect with the initial concentration of Cr(VI). In 120 min reaction time, the removal rate of Cr(VI) in solution decreases with the initial concentration increasing of Cr(VI). The rate is 100, 96.8, 92.8, 83.7 and 78.8% when the initial concentration is 25, 50, 75, 100 and 125 mg/L, respectively. The removing process of biochar-NZVI to Cr(VI) can be divided into two stages: in the first 60 min the removing speed is very fast. In this case Cr(VI) ions in the solution were quickly absorbed on the adsorption sites of the material surface. With the reaction proceeding, Cr(VI) began to diffuse into the pores of biochar because the surface adsorption site decreases gradually. Since the iron oxide formed in previous reaction might block the pores, leading to the removing speed to Cr(VI) decreases in the second stage. Zhu [15] found the similar result in the supported nano iron removing As(V) in drinking water.

Generally, the process of removing Cr(VI) using NZVI or bimetallic materials took place on the surface of materials is a heterogeneous reactions. The Kinetic

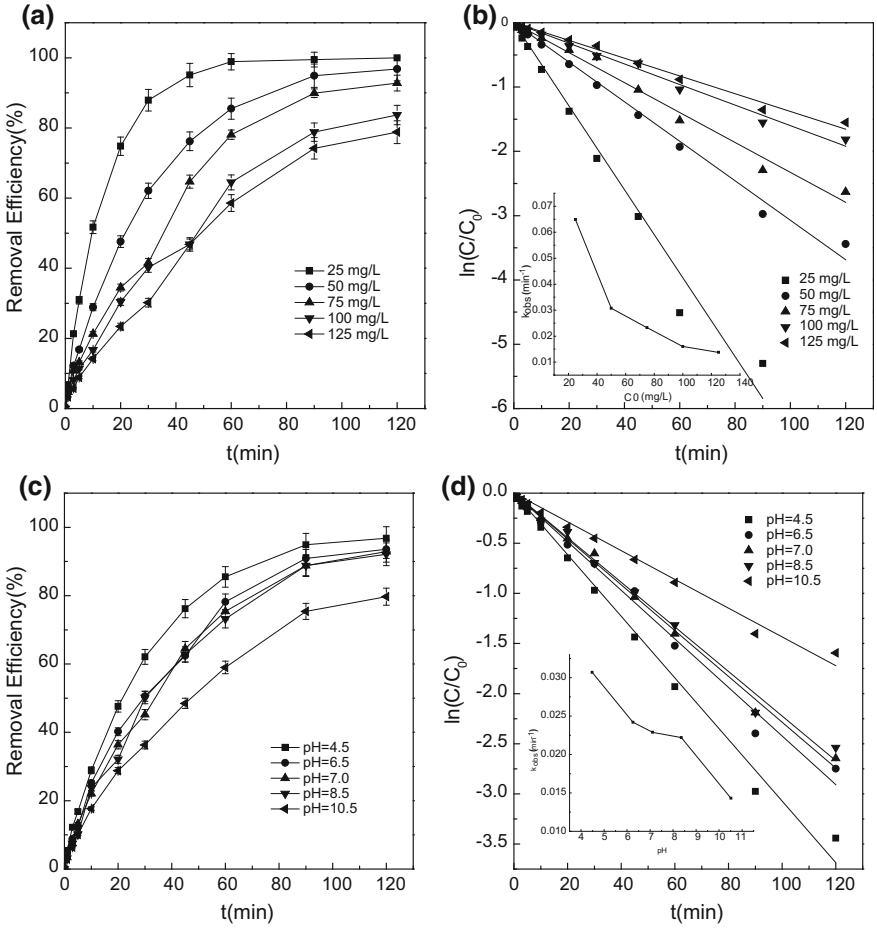

Fig. 5 **a** The influence of the initial concentration of Cr^{6+} on the removing efficiency of Cr^{6+} by BC-Fe; **b** The pseudo-first-order kinetics fitting for different initial concentration of the Cr^{6+} reduced by BC-Fe; **c** The influence of the initial pH on the removing of Cr^{6+} by BC-Fe; **d** The pseudo-first-order kinetics fitting of the reduction Cr^{6+} by BC-Fe in different initial pH; **e** The influence of temperature on the removing of Cr^{6+} by BC-Fe; **f** The pseudo-first-order kinetics fitting of the reduction of Cr^{6+} by BC-Fe at different temperature

process can be well fitted using the pseudo first order reaction kinetics model. The pseudo first order reaction as

$$\ln(c/c_0) = -k_{\text{obs}} \times t. \tag{2}$$

where, c is the concentration (mg/L) of Cr(VI); c_0 is the initial concentration of Cr (VI) (mg/L); k_{obs} is the apparent rate constant, it can be obtained by linear fitting to ln (c/c_0) and t.

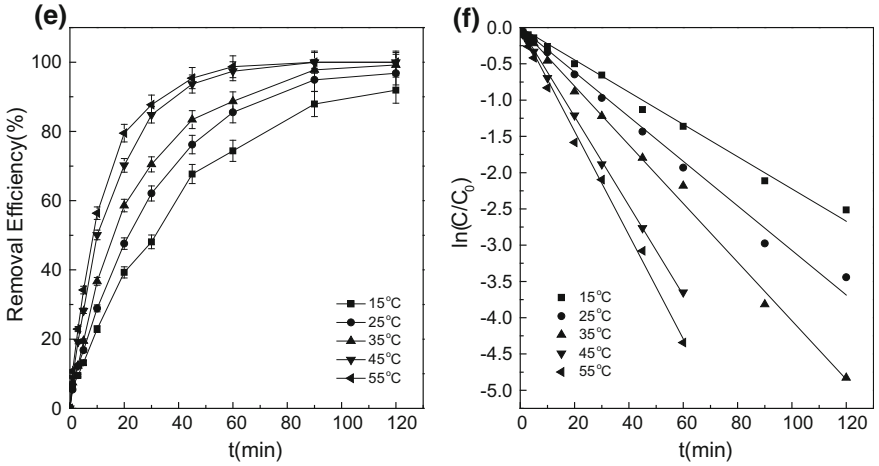

Fig. 5 (continued)

Figure 5b is the fitting results using pseudo first order kinetic each reaction for different initial concentration of Cr(VI). k_{obs} is 0.1041, 0.0584, 0.0449, 0.0306 and 0.0235 min^{-1} when initial concentration of Cr(VI) is 25, 50, 75, 100 and 125 mg/L, respectively. Clearly, k_{obs} decreases with the increasing of the initial concentration of Cr(VI). This because NZVI deduction Cr(VI) is a surface controlled reaction process. The reaction speed has related to the number of surface active sites of NZVI as it is not affected by the mass transfer. At a low concentration of Cr(VI) in the solution, the surface active sites of NZVI are not saturated, the reaction speed is larger. With the increasing concentration of Cr(VI), the surface active sites of NZVI tends saturate, the reaction near zero order kinetics and the reaction rate declines [16]. It can be seen that k_{obs} has a good linear relationship with Cr(VI) concentration when the concentration is between 50 and 125 mg/L.

k_{obs} increase sharply when the initial concentration of Cr(VI) is 25 mg/L that is smaller about 10 times than that of the concentration of NZVI. This because Cr(VI) is reduced to Cr(III) when Cr(VI) reacts with NZVI carried by biochar. At the same time, NZVI is reduced to Fe(III). Cr(III)-Fe(III) co-deposition were created, which hinder the reaction continually when they attached on the surface of NZVI [16]. Melitas et al. [17] found that the increasing concentration of Cr(VI) will promote the formation of passivation layer, thereby reduced the reaction rate.

Figure 5c shows that the relationship between the removal efficiency and the initial pH value in the solution. The removal rate of Cr(VI) by biochar-NZVI is 96.8, 93.692.992.1 and 79.7% when the pH value is 4.5, 6.5, 7.0, 8.5 and 10.5 in 120 min. Obviously, the removal rate decreases gradually with the increasing PH. Comparing the removal rate of the four groups, we found that removal rate biochar-NZVI have good removal effect when PH is from acidic to weakly alkaline range.

Figure 5d shows that the pseudo first order kinetic fitting relationship between the removal effect and the initial pH of the solution. The five groups show a better

linear correlation (the correlation coefficient r^2 over 97%). It is found that the initial PH has some influence to the apparent rate constant. k_{obs} researches the maximum when pH = 4.5, and it has the best removal effect. The removal rate of Cr(VI) drops gradually when k_{obs} decreases from 0.0307 to 0.0143 min^{-1}, and the initial pH increases from 4.5 to 10.5.

The removal effect of pH to Cr(VI) is related to the reaction process. The reaction equation of Cr(VI) reduced to low toxicity Cr(III) by Fe as following

$$Cr_2O_7^{2-} + 3Fe^0 + 14H^+ \rightarrow 2Cr^{3+} + 3Fe^{2+} + 7H_2O. \quad (3)$$

where, Fe^{2+} still has reducibility, it can continually reduced Cr(VI) to Cr(III), that is,

$$Cr_2O_7^{2-} + 6Fe^{2+} + 14H^+ \rightarrow 2Cr^{3+} + 6Fe^{2+} + 7H_2O. \quad (4)$$

Combined the two reaction equations as

$$Cr_2O_7^{2-} + 2Fe^0 + 14H^+ \rightarrow 2Cr^{3+} + 2Fe^{3+} + 7H_2O. \quad (5)$$

From the above analysis, we can get the main reason of pH effect to the remove reaction of Cr(VI) is that Fe(III)–Cr(III) hydroxide co-precipitation were formed on surface of NZVI, which blocked the internal electron of NZVI transfer to outward [4] when PH is too high. In addition, Cr(VI) exists in a $Cr_2O_7^{2}$ negatively charge form in the solution, high PH will lead to the increase of the negative charge on the surface of NZVI. It will generate a rejection to Cr_2O7_2 that is unfavorable to the reaction. At the same time, too high PH will prevent zero valent iron from turning to Fe (II) (etching process), thus inhibiting the reduction of Cr(VI).

The removal reaction of biochar-NZVI to Cr(VI) is well accordance with the pseudo first order kinetics. According to the theory of chemical reaction dynamics, temperature can affect the rate of first order reaction kinetics, as shown in Fig. 5e. The removal rate of Cr(VI) reaches 91.9, 96.8, 99.2, 100 and 100% when the reaction temperature is 15, 25, 35, 45 and 55 °C, respectively. In Fig. 5f the apparent rate constant increases from 0.0222 to 0.0715 min^{-1} when the reaction temperature increases from 15 to 55 °C. It shows that the thermal motion of molecules increases that makes the number of activated molecules increase also, thus the reaction is speed up [18].

Summary

The removal effect of biochar-NZVI to Cr(VI) by biochar carried NZVI using liquid phase reduction preparation was investigated. The results showed that biochar-NZVI has better dispersion and higher specific surface area than that of pure NZVI, and overcomes the agglomeration defects of NZVI Fe. The removal

rate of 5BC-Fe sample to Cr(VI) reached 96.8% at the initial concentration of Cr (VI) 50 mg/L and in the same initial concentration of NZVI. It was about 35.9% higher than that of the pure NZVI dosage, indicating that biochar-NZVI has better removal effect to Cr(VI) that favors to engineering application

The removal of biochar-NZVI to Cr(VI) accords with the pseudo first order kinetics. The study of the theory of chemical reaction dynamics shows that the removal rate of biochar-NZVI to Cr(VI) in solution decrease with the increase of initial concentration and initial pH value. In addition, the increase of reaction temperature can improve the removal rate of biochar-NZVI to Cr(VI) in the solution.

The removal rate of biochar-NZVI samples to Cr(VI) in the solution is all over 92.1% when the initial pH of the reaction solution is between 4.48 and 8.36, indicating that the synthesized materials have good removal effect on Cr(VI) in acidic to weakly alkaline pH conditions.

Acknowledgements This work is supported in parts by the National Natural Science Foundation of China (No. 31570515) and the Scientific Project Program of Suzhou City (No. SYN201511).

References

1. G. Quan, J. Zhang, J. Guo, Y. Lan, Removal of Cr (VI) from aqueous solution by nanoscale zero-valent iron grafted on acid-activated attapulgite. Water Air Soil Pollut **225**, 1979–1989 (2014)
2. C. Yan, W. Chen, L. Pan, Q. Wang, Removal of lead in water by nano zero valent iron loaded on bentonite. J. Water Resour Water Eng (in Chinese), **24**, 20–24 (2013)
3. Q. Zhao, Q. Zhao, H. Wang, H. Yu, Z. Hui, Review of biochar soil improvement mechanism and the application prospect in our country tropical area. Chin. J. Trop. Agric. (in Chinese), **34**, 53–57 (2014)
4. Y. Zhou, B. Gao, A.R. Zimmerman, H. Chen, M. Zhang, X. Cao, Biochar-supported zero valent iron for removal of various contaminants from aqueous solutions. Bioresour Technol **152**, 538–542 (2014)
5. M. Avila, T. Burks, F. Akhtar, M. Göthelid, P.C. Lansåker, M.S. Toprak, M. Muhammed, A. Uheida, Surface functionalized nanofibers for the removal of chromium (VI) from aqueous solutions. Chem. Eng. J. **245**, 201–209 (2014)
6. Y. Wang, Z. Fang, B. Liang, E.P. Tsang, Remediation of hexavalent chromium contaminated soil by stabilized nanoscale zero-valent iron prepared from steel pickling waste liquor. Chem. Eng. J. **247**, 283–290 (2014)
7. H. Jabeen, V. Chandra, S. Jung, J.W. Lee K.S. Kim, S.B. Kim, Enhanced Cr(VI) removal using iron nanoparticle decorated graphene. Nanoscale **3**, 3583–3585 (2011)
8. Z. Liu, F. Zhang, J. Wu, Characterization and application of chars produced from pinewood pyrolysis and hydrothermal treatment. Fuel **89**, 510–514 (2010)
9. J. Yan, L. Han, W. Gao, S. Xue, M. Chen, Biochar supported nanoscale zerovalent iron composite used as persulfate activator for removing trichloroethylene, Biores Technol **175**, 269–274 (2015)
10. Q. Wang, S. Snyder, J. Kim, Aqueous Ethanol modified nanoscale zerovalent iron in bromate reduction: synthesis, characterization, and reactivity. Environ. Sci. Technol. **43**, 3292–3299 (2009)

11. X. Wang, C. Chen, H. Liu, J. Ma, Characterization and evaluation of catalytic dechlorination activity of Pd/Fe bimetallic nanoparticles. Indus. Eng. Chem. Res. **47**, 8645–8651 (2008)
12. Z. Dai, J. Meng,. N. Muhammad, X. Liu, H. Wang, Y. He, P.C. Brookes, J. Xu, The potential feasibility for soil improvement, based on the properties of biochars pyrolyzed from different feedstocks. J. Soils Sed. **13**, 989–1000 (2013)
13. J. Chen, J. Zhu, Z. Da, H. Xu, J. Yan, H. Ji, H. Shu, H. Li, Improving the photocatalytic activity and stability of graphene-like BN/AgBr composites. Appl. Surf. Sci. **313**, 1–9 (2014)
14. Z. Chen, Y. Cheng, Z. Chen, M. Mallavarapu, N. Ravendra, Kaolin-supported nanoscale zero-valent iron for removing cationic dye-crystal violet in aqueous solution. J. Nanoparticle Res. **14**, 899 (2012)
15. H. Zhu, Y. Jia, X. Wu, H. Wang, Removal of arsenic from water by supported nano zero-valent iron on activated carbon. J. Hazard. Mat. **172**, 1591–1596 (2009)
16. R. Venkatapathy, D.G. Bessingpas, S. Canonica, J.A. Perlinger, Kinetics models for trichloroethylene transformation by zero-valent iron. Appl. Catal B: Environ. **37**, 139–159 (2002)
17. N. Melitas, J.P. Wang, C.M. Peggy, F. James, Understanding soluble arsenate removal kinetics by zerovalent iron media. Environ. Sci. Technol. **36**, 2074–2081 (2002)
18. X. Li, J. Cao, W. Zhang, Stoichiometry of Cr (VI) immobilization using nanoscale zerovalent iron (nZVI): a study with high-resolution X-ray photoelectron Spectroscopy (HR-XPS). Indus. Eng. Chem. Res. **47**, 2131–2139 (2008)

Isolation, Identification and Characteristics of an Efficient PCBs-Degrading Strain

Hui Cai, Qiu Yue Sheng, Zhi Gang He and Wei Lin Shi

Abstract An efficient polychlorinated biphenyls (PCBs)-degrading bacteria named ZW was cultivated and isolated from soil suffering from long-term PCBs contamination. The strain was identified as *Pseudomonas aeruginosa* through 16S rDNA sequence analysis. Experiments were conducted to study the degradation characteristics of the bacteria for PCBs. The study revealed that the strain ZW could grow with PCB77 as the only carbon source and its best 7-day degradation rate in 2 mL culture (OD_{600} = 1.0) was 50.1%, with the PCB77 concentration at 1.0 mg L^{-1}, pH 7.5, 30 °C and rotating speed 150 r min^{-1} in a Thermostatic Vibrating Incubator. The influence of additives, including four organic matters and five heavy metals, on the degradation rate was also studied. It was indicated that the degradation rates changed to 65.2, 59.58, 52.3 and 39.8%, respectively, when the same concentration (i.e. 1.0 mg L^{-1}) of Tween-80 or biphenyl or phthalic acid or benzoic acid was introduced. The presence of Cd^{2+}, Cu^{2+}, Ni^{2+}, Cr^{6+} and Pb^{2+} had inhibiting effect on the biodegradation rate in a descending order $Cd^{2+} > Cu^{2+} > Cr^{6+} > Ni^{2+} > Pb^{2+}$ with the same heave metal ion concentration, and the higher the concentration, the more significant the inhibitory effect was. As the number of chlorine atoms in PCB congeners (PCB18, PCB77, PCB101) increased, the degradation rate changed to 89.6, 49.6 and 23.5%, respectively. The toxicity of PCBs biodegradable system decreased over time and the drop rate showed negative correlation with the number of chlorine atoms in PCBs.

Keywords Polychlorinated Biphenyls-degrading bacteria · Degradation characteristics · Heavy metals · Biotoxicity

H. Cai · Q. Y. Sheng · Z. G. He · W. L. Shi (✉)
Suzhou University of Science and Technology, Suzhou 215101, China
e-mail: 196131182@qq.com

H. Cai
e-mail: hcai531@126.com

Q. Y. Sheng
e-mail: 372489877@qq.com

Z. G. He
e-mail: 1365003463@qq.com

Y. Han (ed.), *Advances in Energy and Environmental Materials*,
Springer Proceedings in Energy, https://doi.org/10.1007/978-981-13-0158-2_90

Introduction

Polychlorinated biphenyls (PCBs) have been confirmed to be harmful substances that may lead to carcinogenesis, teratogenesis and mutagenesis. They are recalcitrant, bio-toxicant, bio-accumulative, and long-distance migratory, and have posed a serious threat to the survival, reproduction, and sustainable development of human beings [1, 2]. Although the production and utility of PCBs have been prohibited in China, some regions are still severely polluted by PCBs because of extensive usage and disposal in the early days [3].

Biological treatment is a method low-cost and easy to operate to restore the soil polluted by PCBs, and the pollution can be degraded thoroughly without any secondary pollution [4–6]. Studies show that the 6-day degradation rate is up to 77.4% when the bacterial strain Sinorhizobium meliloti is used to degrade 2,4,4′-trichloro-2′-hydroxydiphenyl ether (TCPE), and the 7-day degradation rate of 2,2′,5,5′-tetrachlorobiphenyl PCB52 is 52.9% using the bacterial strain *Stenotrophomonas maltophilia* [7, 8]. However, the pollution of PCBs in soil is usually accompanied by heavy metal contamination, which may restrain the biochemical degradation of PCBs [9–11].

In this paper, native microorganism was chosen and trained, and their ability in degrading PCBs and the influencing factors were investigated, along with the study of the variations of the biotoxicity microbial degradation system.

Materials and Methods

PCB77 (3,3′,4,4′-Tetrachlorobiphenyl) is the main research subject studied in this paper. Through separation/preconcentration, one bacterial strain, which can feed on PCB77 as the only carbon source and has broad environmental adaptability and high degradation rate, was selected from the soil chronically polluted by organic pollutants. It was identified as *pseudomonas sp.* by 16S rDNA, and was named as ZW. Biphenyl was used as the substrate to domesticate its capacity in degrading PCB77 and the effect of its growth and properties in PCB77 degradation are investigated under different conditions in this paper. At the same time, the ability of ZW in degrading PCB congeners (PCB18, PCB101) was also investigated.

Main Instruments and Samples. The samples used in the experiments were PCB18 (2,2′,5-Trichlorobiphenyl), PCB77 and PCB101 (2,2′,4,5,5′-Pentachlorobiphenyl) from Accustandard Inc. (New Haven CT, USA); n-Hexane is chromatographic pure, and other reagents are analytical pure. Main instruments used were GC-MS (Agilent, Technologies Inc., Santa Clara, CA, USA), biotoxicity analyzer (Macherey-Nagel, Düren, Germany), incubator-shaker, laminar flow clean bench and electric sterilizer.

Main Solution and Nutrient Medium. The nutrient solution for preliminary domestication were compounded with 5 g of glucose, 1 g of mono-potassium phosphate, 2 g of urea, 10.0 g of biphenyl, and 10 L of distilled water.

The enrichment medium (EM) was compounded in the environment of pH = 7.0 with 5.0 g of beef extract, 10.0 g of peptone, 5.0 g of NaCl and 1000 mL of distilled water; the solid version was based on the same recipe, with 15 g L^{-1} of agar added in, and was sterilized at 121 °C for 30 min for further use.

The nutrient medium of minimum salt media (MSM) was compounded in the environment of pH = 7.0 with 0.5 g of dipotassium phosphate, 0.5 g of mono-potassium phosphate, 1.0 g of ammonium sulfate, 0.2 g of magnesium sulfate, 0.1 g of NaCl and 1000 mL of distilled water; the solid version was based on the same recipe, with 15 g L^{-1} of agar added in, and was sterilized at 121 °C for 30 min for further use.

Selection, Identification and Domestication of Polychlorinated Biphenyl-Degrading Bacteria

Preliminary Domestication and Separation of Degrading Bacteria. A self-made 50 cm × 50 cm × 30 cm plexiglass box was used for preliminary domestication. A 5-cm thick layer of sand was bedded in the bottom, above which was a 5-cm thick layer of gravel, and then a 15-cm thick layer of organically contaminated soil taken from a chemical plant. Nutrient medium, which was compounded with 1000 mg L^{-1} of biphenyl was added in regularly, and the soil was stirred regularly to keep a constant humidity and pH value (PH = 6–8). The preliminary domestication was continued for a month, and then 1 g of the domesticated soil was taken out and cultivated in a 100 mL conical flask, along with 50 mL of the sterilized solution of the enrichment medium, under the conditions of 30 °C and 150 r min^{-1}. After the enrichment medium became turbid, single colonies were separated.

Enhanced Domestication and Separation of Degrading Bacteria. The single colonies and 50 mL of the sterilized MSM which contained a certain concentration of PCB77 were mixed into a 100 mL conical flask, and were cultivated under shaking cultivation at 30 °C and 150 r min^{-1}. Then the transferred 5 mL of cultured medium was pipetted to new one every 5–7 days and sub-cultured for 2 months under the same conditions, and the concentration of PCB77 in the MSM was increased at the same time to domesticate the PCB77 degrading capacity of the strain ZW. The domesticated bacterial suspension was then taken, followed by streaking separation and purification on the solid MSM. The strain ZW with high degradation capacity was selected and stored at 4 °C on the slant of the test-tube.

Identification of the Degrading Bacteria and Measurement of its Physiochemical Properties. The 16S rDNA sequences of ZW were sequenced by Sangon Biotech (Shanghai) Co. Ltd., and then compared with that of other strains in GenBank. The phylogenetic tree of the strain ZW was drawn based on deduced

amino acids by bio-software (MEGA5.0). Referring to the < Bergey's Manual of Systematic Bacteriology > and relevant literature, the bacterial strain ZW was identified according to morphology, physiology and biochemistry.

Measurement of Growth Curve of Strain ZW. The purified bacteria strains were inoculated into the liquid enrichment medium, the MSM that contained 1000 mg L^{-1} biphenyl, and the MSM that contained 1 mg L^{-1} PCB77, respectively, and then cultivated at 30 °C and 150 r min^{-1}. Next, 2 mL of the nutrient solution was taken out every certain time, and the UV mini-1240 SHIMADZU was used to measure the absorbance at 600 nm, which was used to represent the concentration of the thalli inside the solution.

Influencing Tests on Degradation Rate of Bacteria ZW

Preparation of Bacteria Solution. The separated bacteria strains were inoculated into the liquid enrichment medium, and were cultivated at 30 °C and 150 r min^{-1} for exponential phase. They were centrifuged for 10 min at 3500 r min^{-1}; the supernatant was discarded; the sediments were washed for 3 times with phosphoric acid buffer solution (pH = 7.2), and were re-suspended into the same nutrient solution so as to make the final OD_{600} equal to 1.0.

Impact of External Carbon Source on Degradation of PCB77. TW-80, benzoic acid, phthalic acid, and biphenyl were chosen as the external carbon sources. The degradation system was a 50-mL conical flask with 20 mL of MSM that contains PCB77 at a concentration of 1 mg L^{-1}. The first set was the control, the second was with 1000 mg L^{-1} biphenyl, the third was with 1000 mg L^{-1} benzoic acid, and the fourth was with 1000 mg L^{-1} phthalic acid. They were cultivated at 30 °C and 150 r min^{-1} for 7 days and then the samples were taken for the measurement of the degradation rate.

Impact of pH on Biodegradation. The pH of the MSM was adjusted to 3, 4, 5, 6, 6.5, 7, 7.5, 8, and 9, respectively; 2 mL (OD_{600} = 1.0) of the degrading bacterial suspension was inoculated; the concentration of PCB77 in the system was maintained at 1 mg L^{-1}; they were cultivated at 30 °C and 150 r min^{-1} for 7 days and then the samples were taken for the measurement of the degradation rate.

Impact of Temperature on Biodegradation. The culture temperature of the degradation system was adjusted to 15, 20, 25, 30, 35, 40, 45 and 50 °C, respectively; 2 mL (OD_{600} = 1.0) of the degrading bacterial suspension was inoculated; the concentration of PCB77 in the system was maintained at 1 mg L^{-1}; they were cultivated with pH = 7.5 and at 150 r min^{-1} for 7 days, and then the samples were taken to measure the degradation rate.

Impact of Initial Concentration on Biodegradation. Under aseptic condition, a certain amount of PCB77 mother liquor was put into the 50 mL conical flask. After the n-hexane was volatilized completely, the sterilized MSM was added and 2 mL of the bacterial suspension was inoculated and the concentration of PCB77 in the system was adjusted to 0, 1.0, 2.0, 3.0, 4.0, 5.0 mg L^{-1}, respectively. They were

cultivated at 30 °C and 150 r min^{-1} for 7 days, and then the samples were taken to measure the degradation rate.

Impact of Microorganism Inoculum Size on Biodegradation. Under aseptic condition, 0.5, 1.0, 2.0, 4.0, 5.0, 6.0, 7.0 and 8.0 mL, respectively, of the bacteria suspension were fetched and transferred into MSM with a pipette. They were cultivated at 30 °C and 150 r min^{-1} for 7 days, and then the samples were taken to measure the degradation rate, so as to determine the optimal inoculum size.

Impact of Heavy Metal on Biodegradation. Cu^{2+}, Cr^{6+}, Ni^{2+}, Cd^{2+} and Pb^{2+} were used as impressed heavy metals to study their impact on the degradation of PCB77 by the bacteria strain ZW. Under aseptic condition, 2 mL of the PCB77 mother liquor with a concentration of 10 mg L^{-1} was fetched accurately and transferred into a 50 mL conical flask. After the n-hexane was volatilized completely, certain amount of one of the five heavy metals was added in, and 2 mL of the bacteria suspension was inoculated and the concentration of the heavy metal in the system was adjusted to 0, 0.1, 1, 5, 10, 20 mg L^{-1} and PCB77 with the same concentration of 1 mg L^{-1}. They were cultivated at 30 °C and 150 r min^{-1} for 7 days, and then the samples were taken to measure the degradation rate.

Degradation Performances of ZW With PCB Congeners. The ability to degrade PCB congeners (PCB17, PCB77, PCB101) by strain ZW was tested in the paper. Under aseptic condition, 2 mL of PCB18, PCB77, PCB101 mother liquor at a concentration of 10 mg L^{-1} were fetched accurately and transferred into a 50-mL conical flask, respectively. After the n-hexane was volatilized completely, 2 mL of the bacteria suspension and 20 mL of the sterilized MSM was inoculated to maintain the concentration of PCB congeners at 10 mg L^{-1}. They were cultivated at 30 °C and 150 r min^{-1} for 7 days, and then the samples were taken to measure the degradation rate.

Biotoxicity Variation of the Biodegradation System. Under aseptic condition, a certain amount of PCB18, PCB77 and PCB101 mother liquor, respectively, were fetched accurately and transferred into a 50 mL conical flask. After the n-hexane was volatilized completely, 2 mL of the bacteria suspension and 20 mL of the sterilized MSM was inoculated. They were cultivated at 30 °C and 150 r min^{-1} for 12 days, and then the samples were taken to measure the degradation rate.

The degradation rate above refers to that of substrate by growing cells, and the 7 days degradation rate measured when 2 mL bacteria suspension, which was in exponential phase, was inoculated into the 20 mL different degrading systems. Each experiment had three parallel tests, and deviations were calculated.

Extraction and Measurement of PCBs. The n-hexane (20 mL) was added into the degradation system, followed by ultrasound-assisted extraction for 10 min [12]. The mixed liquor was then transferred into a separating funnel, and let stand for stratification after intensive mixing. After the liquor was stratified, the upper and lower layer were separated and extracted for three times. The extracted n-hexane were then merged and spin-dried to 3–5 mL after the treatment with sodium sulphate anhydrous and then dried to 5 mL by nitrogen blowing. The solution was

intensively mixed with vortex vibration, and measured with GC-MS. The condition of analysis was 30 m × 0.25 mm HP-5MS chromatographic column, programmed ion source temperature of 230 °C and MS quadrupole temperature of 150 °C, and the sample size of 1 μL without shunt [13].

Results and Discussion

Biological Characteristics of Strain ZW. An efficient PCBs-degrading bacteria strain ZW was isolated from soil suffering from long-term PCBs contamination, followed by enrichment and domestication. Strain ZW can feed on PCB77 as the only carbon source and has high capacity of degrading PCB77.

The characteristics of the bacteria strain ZW on the inorganic salt solid board were observed. The bacterial colony was flat-shaped, opaque and small with diameter about 1 mm; it had a smooth surface with regular boundaries; it was light yellow at the beginning of the inoculation and green secretions were generated afterwards. In the liquid medium selection, the nutrient solution was first transparent and light yellow and then became green and muddy with the time of cultivation, and finally it became brownish red. Under the optical microscope, the cell was in the shape of a short bar. It was identified as negative bacterium by gram staining. The results of the biochemical experiments on the strain ZW are listed in Table 1.

The 16S rDNA sequencing of the strain ZW was delegated to Sangon Biotech (Shanghai) Co. Ltd. (Shanghai, China). The results are shown in Fig. 1. By contrasting the experimental atlas and control atlas, it shows only one band in agarose gel electrophoresis, which suggests no impurity. Besides, by polymerase chain reaction (PCR) amplification with the universal primer (7F, 1540R), PCR products about 1300–1500 pb were taken, which can be used to estimate the species of strain ZW.

Based on the Blast database in GenBank, the 16S rDNA homology of the strain ZW was studied. The comparison indicated that the 16S rDNA sequence of ZW had

Table 1 Physiological and biochemical characteristics of strain ZW

Experiment items	Experiment results
Oxidase test	+
Starch hydrolysis test	–
Gelatin liquefaction test	+
Indole test	+
Methyl red test	–
Cysteine hydrogen sulfide test	+
Citrate utilization test	+
Nitrate reduction test	+
V.P. test	–

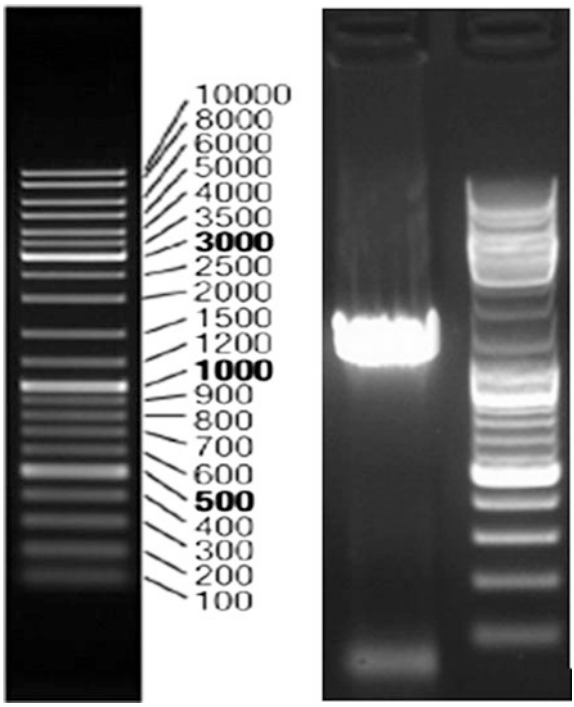

Fig. 1 PCR products of ZW. *Note* PCR, polymerase chain reaction: ZW

high similarity (99%) with that of *pseudomonas aeruginosa*. The 16S rDNA fragments which have high similarity with the strain ZW were searched and downloaded from the GenBank database. The phylogenetic tree was plotted using MEGA5.0. A preliminary conclusion can be made from Fig. 2 that ZW is a kind of *pseudomonas aeruginosa*.

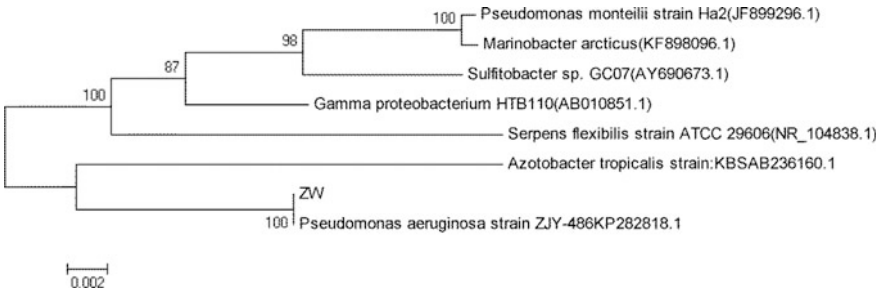

Fig. 2 Phylogenetic tree of strain ZW

Impact of Different Culture Conditions

Growth Curves of Bacteria Strain ZW. The growth curves of bacteria strain ZW in different media are depicted in Fig. 3. It can be seen that under the same culture condition (30 °C, 150 r min^{-1}), the enrichment medium can give ZW the best growth vigor and enter into the exponential phase within 24 h. The amount of microorganism decreased slightly and became stable then. Since biphenyl and PCB77 are toxic, when MSM contains them, the adjustment phase of ZW was obviously extended [14]. After about 90 h, ZW grew fast, and the growth rate increased significantly.

Impact of External Carbon Source on Biodegradation. The impact of ZW on the degradation rate of PCB77 (1 mg L^{-1}) with different external carbon sources was studied. As shown in Fig. 4, the addition of TW-80, biphenyl and phthalic acid raised the degradation rate of PCB77 by ZW, while the addition of benzoic acid restrained the degradation to some extent. The promotion effects by TW-80 was the most significant, and the 7-day degradation rate was 65.2%; biphenyl had the second most significant promotion effects with the 7-day degradation rate as 59.8%; phthalic acid followed with the 7-day degradation rate as 52.3%. The microorganism took advantages of external carbon sources and raised the degradation rate through co-metabolism [15].

The inhibiting effect by the addition of benzoic acid may be related to its acidity in water solution, which can change the pH condition of the system and made the ZW grow in an environment that was not the best for the growth and the 7-day degradation rate as 39.8%. A single variable analysis was applied to analyze the results. Each group had significant difference with 95% confidence interval, thus it can be concluded that the type of external carbon sources has significant impact on the degradation of PCB77 by the microorganism.

Impact of Temperature and pH on Biodegradation. The growth of different microorganisms varies with different conditions of pH and temperature. When the

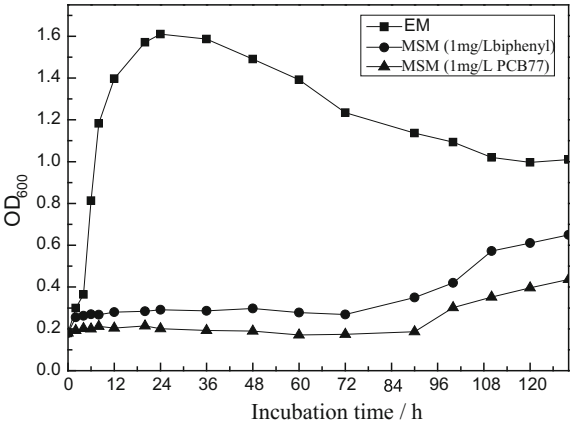

Fig. 3 Growth curve of strain ZW in different media

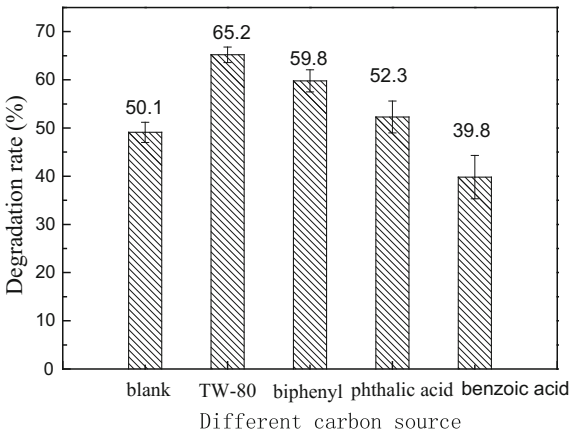

Fig. 4 Effect of different carbon sources on the degradation of PCB77

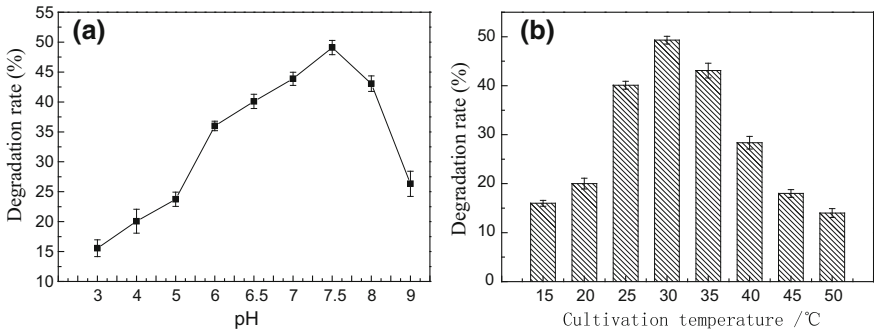

Fig. 5 Effect of different culture conditions on the degradation of PCB77

pH of the culture system changes, the bioavailability of the nutriment and the biotoxicity of the pollutant will change, too, hence the activity of the microorganism will be influenced and finally the growth rate of the microorganism and the degradation rate of the pollutant will be changed [16]. Figure 5a indicates that ZW can grow fast when the pH of the degradation system is between 6 and 8, and the degradation rate hence maintains a high level. When the pH is 7.5, the 7-day degradation rate is as high as 50.1%. Therefore, it can be seen that a neutral or slightly alkaline environment is suitable for the growth of ZW, while an overly acidic or overly alkaline environment has side-effect to the degradation ability.

The growth of microorganism requires an appropriate temperature condition. If the temperature is comparatively low at first, the activity of the microorganism and its enzyme will be improved along with the increase of the degradation rate when the temperature rises; when the temperature surpasses the optimal point, the activity of the microorganism will decrease or may even die, and the degradation rate of

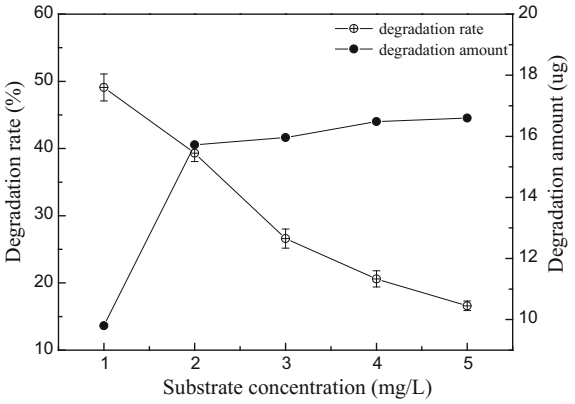

Fig. 6 Effect of different PCB77 concentrations on the degradation of PCB77

PCB77 decreases significantly. It can be seen from Fig. 5b that the culture temperature has considerable impact on the degradation of PCB77 by ZW. The strain can degrade PCB77 within a wide range of temperature, and the appropriate range is 25–40 °C with the optimal point at 30 °C.

Impact of Initial Concentration on Biodegradation. Figure 6 reveals the impact of the initial concentration of PCB77 on its degradation. When the initial concentration of the substrate was low, the 7-day degradation rate of PCB77 by ZW was comparatively high. When the initial concentration of the substrate increased from 1 mg L^{-1} to 5 mg L^{-1}, the degradation rate decreased from 50.1 to 16.6%. It may be explained by that a high concentration of the substrate has inhibiting effect on the activity of the microorganism and hence has influence on the enzyme catalysis, which restrains the degradation of the pollutants by the microorganism [17]. On the other hand, when the concentration of the substrate increased from 1 to 2 mg L^{-1}, the degradation amount increased from 9.86 to 15.72 μg because the biotoxicity of the substrate is insignificant when its concentration is low, and the increase of its concentration can improve the probability of the utilization of the substrate by the microorganism and hence increase the degradation amount. When the concentration of the substrate increased continually, the 7-day degradation amount of PCB77 was almost invariant. That is because the addition of carbon sources has limited auxo-action on the biological metabolism, and a high concentration of the substrate has certain inhibiting effect on the activity of the microorganism. It can be seen that the microorganism has certain degradation ability with respect to PCB77; however, it is usually effective to low-concentration pollution, and the degradation process is slow.

Impact of Inoculum Size on Biodegradation. The initial inoculum size of the microorganism has significant impact on the growth of the thallus. Within certain limits, with the increase of the initial inoculation size, the degradation rate also increases gradually. That is because when the inoculum size increases, the thallus will accelerate the process of adaption to the new environment through synergistic mechanism, which increases the degradation efficiency with the total amount of the

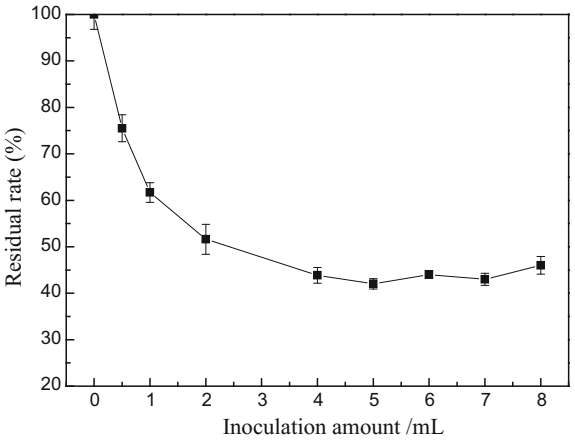

Fig. 7 Effect of microbial inoculation size on the degradation of PCB77

microorganism increasing. Figure 7 shows the impact of inoculum size on the degradation of PCB77. It can be seen that when the inoculum size increased, the residual rate of PCB77 in the degradation system decreased accordingly; when the inoculum size is 0.5 mL, the 7-day residual rate is 75.5%, which is 1.72 times of that when the inoculum size is 4 mL (43.8%). Because of the nutritional competition, the degradation rate is not obviously increased with further increase of the inoculum size.

Impact of Impressed Heavy Metals on Biodegradation. When copper, lead, nickel, hexavalent Chromium and cadmium, five common heavy metals, were added to the biodegradation system, the 7-day degradation rate of PCB77 by ZW remarkably differed. When the concentration of the added heavy metals is the same, the inhibiting effect on biodegradation was in a descending order: $Cd^{2+} > Cu^{2+} > Cr^{6+} > Ni^{2+} > Pb^{2+}$ (Fig. 8). When the concentration of the added heavy metals is low, the inhibiting effects of Ni^{2+}, Pb^{2+} and Cr^{6+} were limited, and

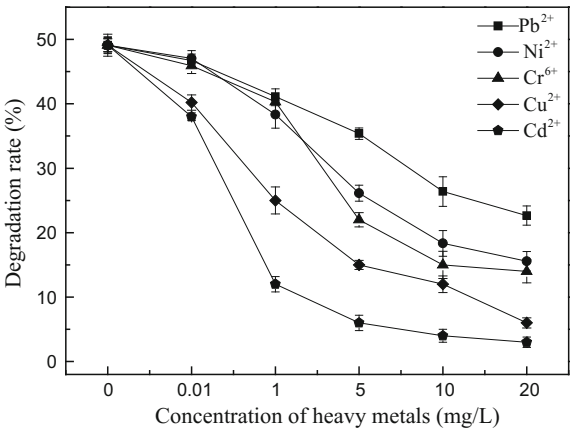

Fig. 8 Effect of different heavy metal ions on the degradation of PCB77

the 7-day degradation rate by ZW maintained at a high level. When the concentration of the added heavy metals was 0.01 mg L^{-1}, the inhibiting effect was ignorable; and when the concentration of the added heavy metal increased, the degradation rate by ZW decreased dramatically.

Of all of the heavy metals that we studied, Pb^{2+} showed the weakest inhibitory effect. The degradation rate when the concentration of Pb^{2+} was 10 mg L^{-1} was half as high as that when the concentration was 0.01 mg L^{-1}. Under the same condition, when Cr^{6+} was impressed, the degradation rate maintained 60% of the original one. Cd^{2+} is the most toxic and causes the death of degrading bacteria sharply when the concentration was 5 mg L^{-1}. The above results indicate that the toxicity of different heavy metal ions that restrains the growth of the bacteria may be related to the affinity to the cell wall, and the negative charge above the cell wall has affinity to the metal ion which has positive charge, and the stronger the affinity, the stronger the biotoxicity [18].

It can be seen that when different heavy metals are impressed, the impact on the growth of ZW and the biodegradation of pollutants is variant. A high concentration of heavy metals always has certain inhibiting effect on ZW, thus ZW is effective in degrading pollutants appropriately in the environment with low-concentration heavy metals and PCBs.

Degradation Performances of ZW With PCB Congeners. Under the same concentration, there was a significant difference in biodegradation ability of ZW with PCB congeners. With the increase of the number of Chlorine atoms in PCBs (PCB18, PCB77, PCB101), the 7-day biodegradation rate by strain ZW declines sharply. The biodegradation ability with PCB18 was the most significant, and the 7-day degradation rate was 90.3%; PCB77 had the second most significant biodegradation rate with the 7-day degradation rate as 49.1%; PCB101 is one of the most toxic organic pollutants and is difficult to be degraded among the three PCB congeners. The 7-day biodegradation rate of PCB101 was 20.5%. The results indicated that the biotoxicity of PCB congeners was enhanced with the increase of the chlorine atoms and decrease of the biodegradation ability at the same time, which was consistent with the results of previous research (Fig. 9).

Biotoxicity Variation of the Biodegradation System. With the increase of the incubation time, the inhibitory rate of luminescence fall fell off at the same time, which means the toxicity of the biodegradation system was reduced. That is because the bacteria ZW were growing on PCB congeners (PCB18, PCB77, PCB101) as carbon and energy sources. The benzene ring structure of PCB congeners were broken through due to the biochemistry effect and the toxicity of reaction products were below than that of the PCB congeners. In addition, the inhibitory rates of luminescence decreased slowly with increasing number of Chlorine atoms in PCBs (PCB18, PCB77, PCB101), which suggested that the more chlorine atoms in PCBs, the higher the biotoxicity was. After a period of cultivation, the inhibitory rate of luminescence became stable. The biodegradation system with PCB18 took 15 days and finally the inhibitory rate of luminescence reached 0; the biodegradation system with PCB77 took 20 days and finally the inhibitory rate of luminescence reached 10; the biodegradation system with PCB101 showed the

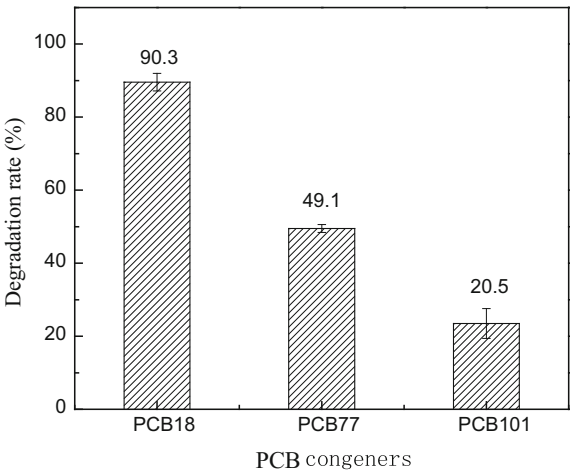

Fig. 9 Effect of different chlorinated congeners of PCBs on the degradation of PCB77

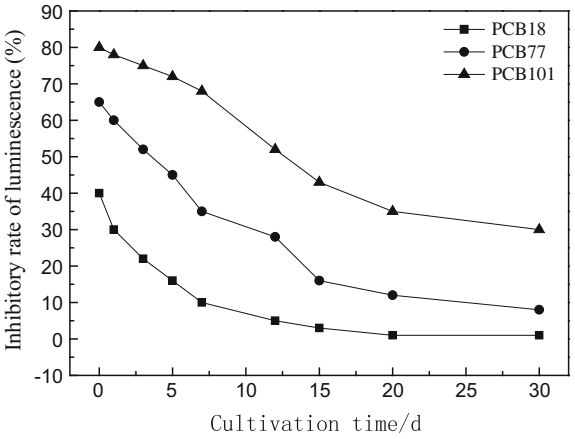

Fig. 10 Inhibitory rate of luminescence at different time points of PCB18, PCB77 and PCB101

highest toxicity and the inhibitory rate of luminescence still kept in 32 after 30 days cultivation; the results are shown in Fig. 10.

As shown in Fig. 11, with the same concentration of PCB congeners, the inhibitory rate of luminescence increased with the increase of the number of Chlorine atoms in PCBs (PCB18, PCB77, PCB101), which was more obvious at higher concentration. It can be explained by that the more chlorine atoms in PCBs, the greater harm to bacteria, which resulted in better inhibition level. When using the same PCBs, the inhibitory rate of luminescence significantly rose with increasing concentration. It is because the PCBs molecules were easier to contact with luminous bacteria, which caused higher toxicity and better inhibition level.

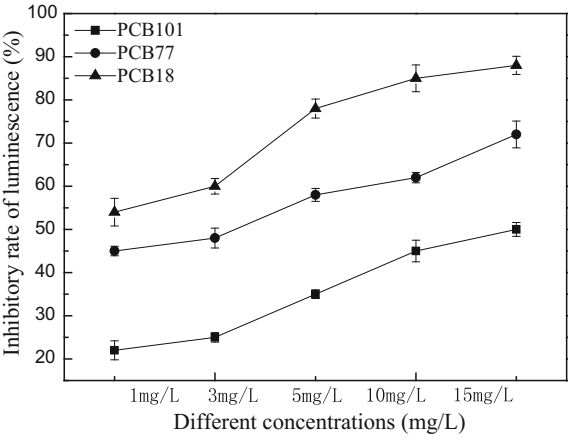

Fig. 11 Inhibitory rate of luminescence of PCB18, PCB77 and PCB101

Conclusion

A PCBs-degrading bacteria ZW was firstly isolated from soil suffering from long-term PCBs contamination and then cultivated, which was identified as *Pseudomonas aeruginosa* by 16S rDNA sequence analysis. The study revealed that the strain ZW could grow with PCB77 as the only carbon source and its best 7-day degradation was 50.1% on the optimal conditions when the PCB77 concentration is 1.0 mg L^{-1}, pH = 7.5, temperature at 30 °C, rotating speed at 150 r min^{-1}, and in a Thermostatic Vibrating Incubator with 2 mL (OD_{600} = 1) bacteria solution. The degradation of ZW varies under different conditions of carbon sources. The degradation rate is increased with the addition of Tween-80, biphenyl, or phthalic acid as the impressed carbon source, and Tween-80 is more effective; however, the degradation rate is constrained with the addition of benzoic acid (i.e. 1.0 mg L^{-1}) with the same concentration. Moreover, the strain ZW has tolerability to heavy metals at certain concentration. Cd^{2+}, Cu^{2+}, Ni^{2+}, Cr^{6+} and Pb^{2+} have inhibiting effect on the biodegradation rate in a descending order $Cd^{2+} > Cu^{2+} > Cr^{6+} > Ni^{2+} > Pb^{2+}$ at the same concentration. Additionally, ZW can biodegrade PCB congeners. With increasing number of chlorine atoms in PCB congeners (PCB18, PCB77, PCB101), the biodegradation rate declines sharply and changes to 89.6, 49.6 and 23.5%, respectively. Finally, the toxicity of the PCBs biodegrading system decreases over time and the drop rate shows negative correlation with the number of chlorine atoms in PCBs.

References

1. S. Lucile, P. Sophie, F. Mathieu, et al., Autochthonous ascomycetes in depollution of polychlorinated biphenyls contaminated soil and sediment. Chemosphere **110**, 62–69 (2014)
2. T. Zhang, S.J. Chen, N. Li, et al., Current situation and ecological risk of typical pops in the surface sediments of Taizhou water system. Res. Environ. Sci. **27**(12), 1540–1548 (2014)
3. Y. Yang, Z.Q. Wang, Q. Wang, et al., Characteristics and environment risk assessment of PCBs in multi-media environment of the electronic waste dismantling venues. Asian J. Ecotoxicol. **9**(1), 133–144 (2014)
4. K. Furukawa, H. Fujihara, Microbial Degradation of polychlorinated biphenyls: Biochemical and molecular features. Journal of Bioscience and Bioengineering, **105**(5) (2008) 433–449.
5. O.I. Matthew, K.R. Gary, A.A. Sunday, Degradation and mineralization of 2-chloro-, 3-chloro- and 4-chlorobiphenyl by a newly characterized natural bacterial strain isolated from an electrical transformer fluid-contaminated soil. J. Environ. Sci. **20** 1250–1257 (2008)
6. B.A. Rasulov, A.A. Kim, A. Lorenz, et al., Biodegradation of tritium labeled polychlorinated biphenyls (PCBs) by local salt tolerant mesophylic bacillus strains. J. Environ. Protect. **1**, 420–425 (2010)
7. T. Chen, T. Ying, M.L. Yong, et al., Potential for biodegradation of polychlorinated biphenyls (PCBs) by *Sinorhizobium meliloti*. J. Hazard. Mat. **186**(2–3), 1438–1444 (2011)
8. S.Y. Shi, L. Feng, J. Gong, Isolation and degradation characteristics of PCB-degrading strain. Environ. Sci. **33**(10), 3627–3633 (2012)
9. M. Liu, B. Huang, X.H. Bi, et al., Heavy metals and organic compounds contamination in soil from an e-waste region in South China. Environ. Sci. Processes Impacts **15**, 919–929 (2013)
10. T.R. Sandrin, D.R. Hoffman, Bioremediation of organic and metal co-contaminated environment: effects of metal toxicity, speciation, and bioavailability on biodegradation. Environ. Bioremediat. Technol. 1–34 (2007)
11. T. Valentina, V.S. Catefina, F. Stefano, et al., Tolerance of *Pseudomonas pseudoalcaligenes* KF707 to metals, polychlorobiphenyls and chlorobenzoates: effects on chemotaxis, biofilm-and planktonic-grown cells. FEMS Microbiol. Ecol. **74**, 291–301 (2010)
12. B.L. Wang, X.L. Zhang, Q. Zhang, et al., Determination of 39 polychlorinated biphenyls in indoor dust using ultrasonic extraction and gas chromatography-tandem mass spectrometry. Chin. J. Chromatogr. **32**(1), 74–80 (2014)
13. Y.F. Shi, Y.Q. Cai, H.J. Yu, et al, Identification of polychlorinated biphenyls in water products by gas chromatography-mass spectrometry. Chin. J. Anal. Chem. **42**(11), 1640–1645 (2014)
14. D.M. Su, Z.G. Miao, X.P. Song, et al., Optimization of liquid growth conditions and determination of growth curves for *bartonella* species. Microbiol. China **39**(11), 1695–1702 (2012)
15. F.H. Li, L. Xu, T.H. Zhang, et al., Degradation characteristics and fermentation conditions optimization of a PCBs-degrading strain. Microbiol. China, **41**(7), 1299–1307 (2014)
16. S.C. Xiong, H. Yin, B.Y. He, et al., Enzymatic degradation of decabromodiphenyl ether by white rot fungi. Environ. Chem. **31**(5), 615–619 (2012)
17. Y.M. Cao, L. Xu, L.Y. Jia, Analysis of PCBs degradation abilities of biphenyl dioxygenase derived from *Enterobacter* sp. LY402 by molecular simulation. New Biotechnol. **29**(1), 90–98 (2011)
18. Y. Xu, G. D. Sun, J.H. Jin, et al., Successful bioremediation of an aged and heavily contaminated soil using a microbial plant combination strategy. J. Hazard. Mat. **264**, 430–438 (2014)

A New Photosynthetic Bacteria Consortium and Treatment of Low-COD Wastewaters

Boyuan Ma, Guangming Zhang, Huan Song, Yi Zhang, Zhiguo Zou and Meng Peng

Abstract Photosynthetic bacteria consortium was isolated from sediment of black odorous river and was named HJ-1. The main pigments were bacteriochlorophyll *a* and carotenoid. Fructose, mannosej, ethanol, sorbitol, and sodium acetate could be used as carbon source. 16S rDNA gene sequence analysis showed that the dominant strains were *Rhodovulum strictum* and *Thiococcus pfennigii*. Its organics-degrading capability was tested using low COD soybean wastewater, low COD brewery wastewater, low COD sugar wastewater and municipal wastewater. Results showed that the COD in all wastewater reached under 100 mg/L within 72 h. COD removal and biomass accumulation were realized. This study suggested the feasibility of COD degradation and resource recovery by HJ-1 in low COD wastewater.

Keywords Photosynthetic bacteria · Low COD wastewater · Feasibility Resource recovery

B. Ma · G. Zhang (✉) · H. Song · M. Peng
School of Environment and Natural Resources, Renmin University of China, Beijing 100872, China
e-mail: zgm@ruc.edu.cn

B. Ma
e-mail: 1359721515@qq.com

H. Song
e-mail: songhuan199510@163.com

M. Peng
e-mail: mvponesky@ruc.edu.cn

Y. Zhang · Z. Zou
Shandong Public Holdings Limited, Jining 272000, China
e-mail: 13608916070@vip.163.com

Z. Zou
e-mail: 4808954@qq.com

Y. Han (ed.), *Advances in Energy and Environmental Materials*,
Springer Proceedings in Energy, https://doi.org/10.1007/978-981-13-0158-2_91

Introduction

Food processing industry has rapidly developed in China, correspondingly, wastewater production is also high. The treatment and resource recovery of wastewater are important. Activated sludge is extensively used, but the process generates a lot of waste sludge. Photosynthetic bacteria (PSB) can grow and metabolize by absorbing organic matter in wastewater, and can adapt to various environmental changes by changing metabolic way [1, 2]. The cells of PSB are rich in carotenoids, coenzyme Q10, polyhydroxyalkanoates, 5-aminolevulinic acid and other high-value substances [1–3]. For wastewater with high COD (>2000 mg/L), the COD removal reached 80–98% after PSB treatment [3, 4]. Continual addition of PSB could not boost COD degradation [3–5]. To compensate this deficiency, researchers had tried many physical and chemical methods to post-treatment the effluent to the discharging standard. But these methods are complex, and increasing the operation difficulty and energy consumption. Therefore, it is of great practical significance to explore the feasibility of PSB treatment and resource recovery of low COD (200–1000 mg/L) wastewater.

Previous research mainly focused on screening, separation, identification and degradation characteristics of pure PSB. However, pure PSB were susceptible to be restrained by other bacteria in wastewater treatment, so that the treatment efficiency greatly declined. If PSB consortium is used, synergistic effect between the species can promote cell growth and wastewater treatment.

Therefore, a group of photosynthetic bacteria was isolated and used for the degradation and resource recovery feasibility of low-COD soybean wastewater, brewery wastewater, sugar wastewater and municipal wastewater in this work.

Materials and Methods

Industrial wastewaters were obtained from local plants. Municipal wastewater was obtained from campus municipal collection pipeline. River sediment was obtained from River Xiaolong, Beijing. Culturing medium was obtained from Sinopharm Group Chemical Reagent Co.

River sediment was inoculated in ATYP enrichment medium in 100 ml stoppered flasks at 28 °C, light intensity 3000 lx for 7 d. The process repeated 4 times and the obtained PSB consortium was dark red and named HJ-1.

Bacteria consortium gene extraction, amplification and sequencing were completed by Shanghai Meiji Biomedical Technology Co. The specific steps were as follows [6]: bacteria consortium DNA was extracted by OMEGA-soil DNA kit, 16S rDNA universal primers (338F:5′-ACT CCT ACG GGA GGC AGC AG-3′; 806R: 5′-GGA CTA CHV GGG TWT CTA AT-3′) were used to expand target segment. The reaction parameters were as follows: pre-denaturation at 95 °C for 3 min, denaturation at 95 °C for 30 s, annealing at 55 °C for 1 min, extension at

72 °C for 45 s, 27 cycles, extension at 72 °C for 10 min. The PCR product was digested with 2% agarose gel electrophoresis and recovered using the Axy Prep DNA Gel Recovery Kit (AXYGEN). The sequences were compared in the NCBI gene pool and the phylogenetic tree was constructed by MEGA 5.0.

For wastewater treatment, the PSB inoculation was 5% (v/v). According to previous studies, natural light-oxygen condition was chosen, temperature was 22–25 °C, and initial pH was controlled to 7–9 [7, 8]. The bacteria solution was diluted to OD660 = 0.4 with sterile water, and was scanned by UV-Vis spectrophotometer from 190 to 900 nm to record the peaks. COD was measured with rapid digestion method, and biomass production was measured with colorimetric method.

Results and Discussion

Physiological Properties of Consortium HJ-1. The absorption peaks of the bacteria solution appeared at 860, 800, 590, 480, 380 and 355 nm (Table 1). These peaks indicated the presence of bacteriochlorophyll *a* and carotenoids [1, 2]. The results of absorption indicated the main pigments of HJ-1 were bacteriochlorophyll *a* and carotenoid, which proved HJ-1 could contain photosynthetic bacteria [2, 3].

Utilization of carbon source experiments showed that fructose, mannose, ethanol, sorbitol and sodium acetate were used by consortium HJ-1, while glucose, mannitol and glycerol were not used.

According to 16S rDNA sequence data, BAC-1 and BAC-2 were dominant strains in consortium HJ-1. BAC-1 had the closest relationship to *Rhodovulum strictum* MB-G2 (NR 025,845.1) and BAC-2 had the closest relationship to *Thiococcus pfennigii* strain 4250 (NR 036,977.1), with sequence similarities of 99 and 97% respectively (Fig. 1). BAC-1 accounted for 30.65% and BAC-2 accounted for 29.24% in consortium HJ-1. *Rhodobacter*, *Rhodopseudomonas*, *Rhodospirillum*, *Rhodocyclus* were mostly used in conventional PSB wastewater treatment [1–5]. *Thiococcus* was hardly used in PSB wastewater treatment. Therefore it is meaningful for increasing PSB species fitted in wastewater treatment to investigate consortium HJ-1.

Treatment and resource recovery of four low-COD wastewater by HJ-1. Figure 2 shows that HJ-1 had a good degradation effect on low-COD soybean wastewater. The wastewater COD declined to 85.31 mg/L at 48 h and the highest

Table 1 Characteristic absorption peaks of bacteria solution

No.	Wave length (nm)/OD					
	860	800	590	480	380	355
1	0.462	0.443	0.6	0.808	1.206	1.182
2	0.425	0.404	0.548	–	1.137	1.111
3	0.477	0.456	0.61	0.818	1.22	1.187

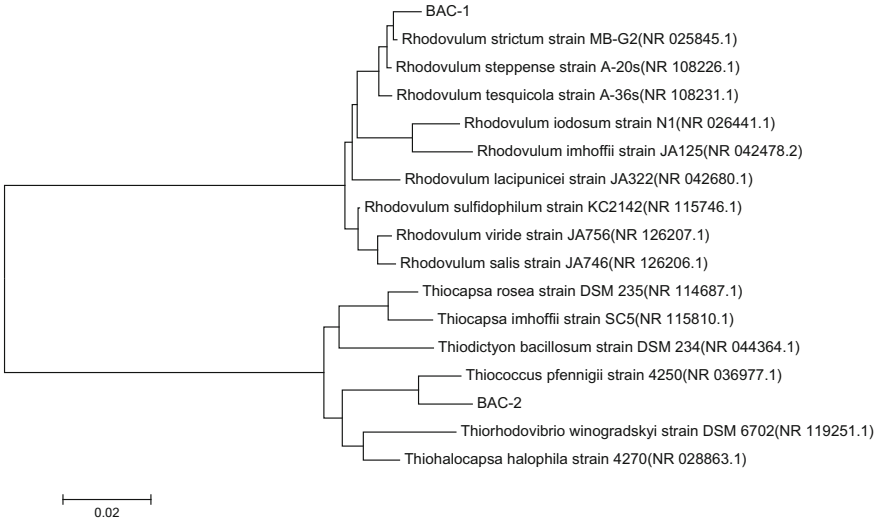

Fig. 1 Phylogenetic tree of photosynthetic bacteria BAC-1 and BAC-2

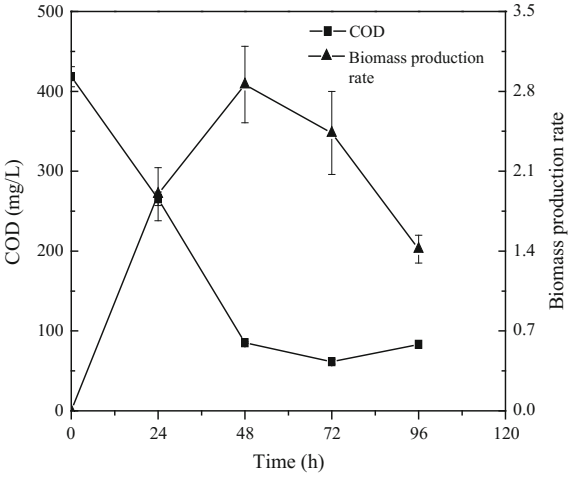

Fig. 2 HJ-1 treatment of soybean wastewater

degradation rate was 85.28%. Lu et al. [4] verified direct degradation of soybean wastewater by PSB [3]. The COD declined from 12,000 to 300 mg/L by PSB Z08, however, it could not decline any more. In this work, the soybean wastewater with a low COD of about 400 mg/L reached COD of 61.58 mg/L after treatment, showing high degrading capability of HJ-1. The difference was mainly due to the fact that PSB Z08 was a pure strain while HJ-1 was PSB consortium. Synergistic effect among different strains helped the degradation of low-COD soybean wastewater. Further, the biomass production increased 2.86 times.

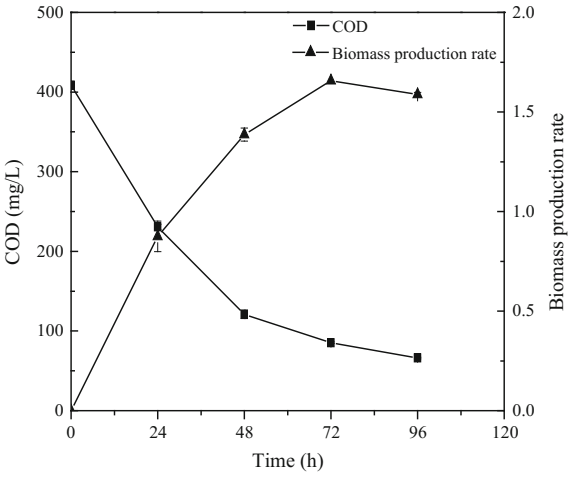

Fig. 3 HJ-1 treatment of brewery wastewater

Figure 3 shows that COD of brewery wastewater declined to 66.02 mg/L. Brewery wastewater with COD between 8000 and 10,000 mg/L could be degraded to 500–2000 mg/L by PSB Z08 [9]. Consortium HJ-1 could continue to metabolize organic matter in the wastewater, reduce COD to below 100 mg/L to meet the discharge standard. Meanwhile, biomass production was growing fast in the first 48 h and increased by 1.66 times at 72 h.

Figure 4 shows that HJ-1 treated sugar wastewater well and the COD declined to 57.86 mg/L at 96 h, with the highest degradation rate of 86.53%. In addition, natural light—micro-oxygen condition used in this study was no need for aeration, thus saving energy and simplifying the device. Biomass grew during the first 72 h, increasing by 0.95 times.

Figure 5 shows that the COD of municipal wastewater degraded from 192.1 to 90.50 mg/L at 24 h and to 83.09 mg/L at 72 h. It indicated that treatment time could be less than 24 h if HJ-1 were applied in continuous flow treatment of

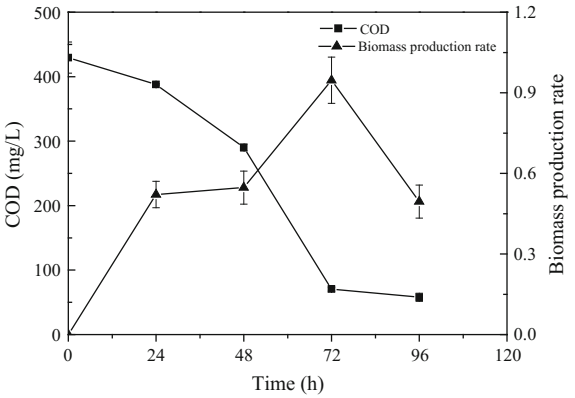

Fig. 4 COD and HJ-1 biomass production in low-COD sugar wastewater

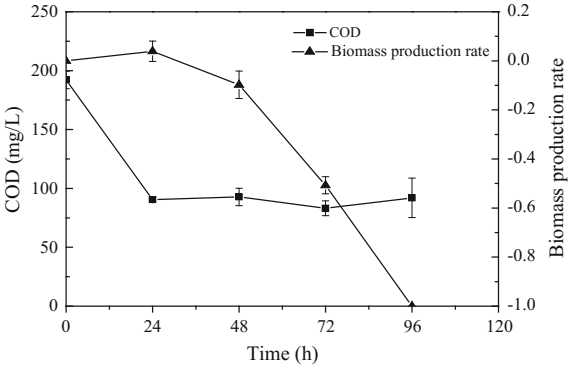

Fig. 5 COD and HJ-1 biomass production in municipal wastewater

municipal wastewater. Due to low initial COD of municipal itself, there was no promotion for growth of bacteria.

Clearly, the degradation rate of COD was all above 80% in the three low-concentration nutritive wastewater, indicating HJ-1 had a quite high degradation efficiency for these kinds of wastewater. Besides, the HRT of the three was all within 72 h, which was shorter than that in PSB high-concentration nutritive wastewater of 72–120 h. Although the degradation rate of municipal wastewater was not as high as the previous three ones, the effluent COD was also less than 100 mg/L. In addition, the HRT of municipal wastewater was only 24 h.

Soybean wastewater was rich in nutrients (vitamins, amino acids, etc.) and small molecule carbon sources fit for PSB growth [10], so the biomass production rate was up to 285.91%. In sugar wastewater and brewery wastewater, biomass production also increased to a high degree. As for municipal, on the one hand there was no much carbon sources available for PSB, on the other hand other strains might compete with PSB and inhibit the growth of HJ-1.

Conclusion

PSB consortium HJ-1 was isolated and purified from river sediment. Fructose, mannose, ethanol, sorbitol, sodium acetate could be used as carbon source by HJ-1, while glucose, mannitol and glycerol could not be utilized. The dominant strains of HJ-1 were Rhocovulum strictum and *Thiococcus pfennigii*, accounting for about 60%. Low-concentration soybean wastewater, low-concentration brewery wastewater, low-concentration sugar wastewater and municipal wastewater could be degraded to below COD 100 mg/L under the conditions of natural light in the daytime, dark at night, room temperature and 5% dosage. At the same time, biomass production increased obviously in the first three kinds of wastewater. It confirmed the feasibility of the treatment and resource recovery of low-concentration nutrient wastewater by HJ-1.

Acknowledgements This work is supported by special fund of State Key Joint Laboratory of Environment Simulation and Pollution Control (17K09ESPCT) and Key Research& Development Plan of Shandong Province (2017CXGC1005).

References

1. X. Chen, R. Zhang, High concentration organic wastewater treatment with photosynthetic bacteria and resource recovery. J. Agro-environ. Sci. **10**, 122–124 (1991)
2. S. Liu, G. Zhang, X. Li, J. Zhang, Microbial production and applications of 5-aminolevulinic acid. Appl. Microbiol. Biotechnol. **98**, 7349–7357 (2014)
3. H. Lu, G. Zhang, W. Zhao, Photosynthetic bacteria wastewater treatment technology. Beijing: Chin. Build. Indust. Press. 10–12 (2014)
4. H. Lu, G. Zhang, X. Dai, C. He, Photosynthetic bacteria treatment of synthetic soybean wastewater: direct degradation of macromolecules. Bioresour. Technol. **101**, 7672–7674 (2010)
5. L. Xie, R. Yang, Y. Hu, Application of photosynthetic bacteria in treatment of organic wastewater. Environ. Pollut. Control. **22**, 36–38 (2000)
6. H. Zhou, F. Liu, G. Qiu, Isolation, identification and characterization of a photosynthetic bacterium strain. Ecol. Environ. **15**, 901–904 (2006)
7. H. Xie, S. Wang, R. Chu, Treatment of brewery wastewater with photosynthetic bacteria. Indust. Water Waste. **37**, 38–40 (2006)
8. Q. Zhou, P. Zhang, G. Zhang, Biomass and carotenoid production in photosynthetic bacteria wastewater treatment: effects of light intensity. Bioresour. Technol. **171**, 330–335 (2014)
9. X. Dai, G. Zhang, Brewery wastewater treatment and resource recovery by photosynthetic bacteria Z08. J. Harbin Inst. Technol. **42**, 937–940 (2010)
10. R. Liu, Application of photosynthetic bacteria in organic wastewater treatment. Environ. Sci. **12**, 63–67 (1991)

Preparation of Ceramics Added Tailings and Electromagnetic Properties

M. M. Wang, Z. L. Zhang, Z. J. Xin, L. Fan, R. Li and M. Q. Peng

Abstract Electromagnetic functional ceramics added iron tailings were prepared using the burning method, and the EMWA properties were tested through the arch testing method at 2–18 GHz. It was found that the minimum reflection loss (*RL*) peak was −16.0 dB at 17.0 GHz, and that the thickness of ceramics was 2.00 cm. With the thickness increasing, the *RL* value went up, and the *RL* peak number also increased. The magnetic and dielectric losses of tailing powders acting as an absorbent were the main mechanisms of EMWA properties for ceramics, which could be used for electromagnetic radiation protection of architectural spaces.

Keywords Tailings · Ceramics preparation · Electromagnetic properties
Electromagnetic wave absorption (EMWA) analysis

Introduction

With the rapid development and popularization, electronic products have provided significant convenience for users, such as telecommunication base stations, high-voltage power lines and broadcast television transmission equipment, and mobile phones, but they have also caused some problems, such as generating a large number of electromagnetic radiations in the environment. The electromagnetic pollution of the indoor environment of buildings also appears at the same time. If people study and live in the polluted environment for a long time, they will suffer from serious damages to their physical and mental health. To solve these problems, more and more researchers have been involved in the development of electromagnetic protection materials. Among them, the electromagnetic wave absorption functional building materials have become a research focus in recent years. These

M. M. Wang (✉) · Z. L. Zhang · Z. J. Xin · L. Fan · R. Li · M. Q. Peng
China Building Materials Academy, Beijing, China
e-mail: christineming@126.com

Y. Han (ed.), *Advances in Energy and Environmental Materials*,
Springer Proceedings in Energy, https://doi.org/10.1007/978-981-13-0158-2_92

materials can be applied in many fields apart from the basic function in architecture, such as eliminating radiation in buildings and containing electromagnetic pollution of the building spaces [1–7]. The electromagnetic functional ceramics have been widely studied [8, 9], mostly through adopting traditional absorbents as the annexing agent, such as flaky graphite, carbon black and ferrite. There were some tests on glass-ceramic with iron ore tailings, of which the electromagnetic loss properties need improvement [10, 11]. In this paper, electromagnetic functional ceramics were prepared by adding iron tailing to improve the EMWA performance. It then studied the feasibility of tailing as an absorbing reagent, and the structure and electromagnetic properties of the ceramic in detail. Based on the transmission line theory, the ceramic could be simulated as the monolayer absorbent when further studying the EMWA properties and used for architectural radiation protection to make the architectural electromagnetic space safer and more reliable.

Experimental Materials and Characterization

In the experiment, iron tailing powders were supplied by one of the diggings in Chengde city, Hebei Province, of which the iron content is about 26–30%. Feldspar is a raw material from Yantai district. Clay including burning coke, iron mouth soil, Wenzu stone and Hainan mud was purchased from Zibo district in Shandong province. Quartz sand was supplied from Mengyin district in Shandong province as well, and the silicon dioxide content is 80–90% approximately.

The crystallite structure was confirmed using X-ray diffraction (XRD, Bruker). The micrography and EDS spectrum were characterized using Quanta 250 FEG Field emission environmental scanning electron microscope (SEM, FEI Company). And the chemical ingredients were tested using X-ray fluorescence (XRF, Panalytical Company). The relative complex permittivity ($\varepsilon_r = \varepsilon' - j\varepsilon''$) and permeability ($\mu_r = \mu' - j\mu''$) were measured using a vector network analyzer (AV3629D) at 2–18 GHz.

Preparation of electromagnetic functional ceramics. Electromagnetic functional ceramics were prepared using the burning method and carried out as follows [12]. First, various materials at a certain ration were mixed uniformly according to the body formulation and processed in wet ball-milling to get the sizing agent of which the fineness was 3.0–4.5%, the moisture content 35 ± 1% and the flow velocity 30–60 s/cup. Afterwards, the sizing agent went through sieving and was placed in the storage pool. After 12 h, the agent was put into a drying tower for the powdering process. Then the powders were placed in a press machine to form the ceramic body. At last, the surface of the body underwent glazing and printing using a conventional method in the ceramic field, and was sent to be burned in the kilns to obtain the electromagnetic functional ceramics successfully.

Results and Discussions

Feasibility of tailing as absorbing reagent. To realize the feasibility of iron tailing as ceramic materials, the XRF of tailing powders was tested by means of the melting method firstly. From Table 1, it is observed that the content of main ingredients is over 80% including Fe_2O_3, Al_2O_3 and SiO_2. Among them, the content of Fe_2O_3 is about 30%, and the tailing contains a little CaO, MgO, K_2O, Na_2O and TiO_2. XRF analysis can only identify the elements, but not their exact composition modes and existing forms. As a result, further analyses are needed. The XRD spectra exhibited that the Fe element main existed as Fe_2O_3 and the major ingredients were Hematite, Corundum and Diopside, which were somewhat magnetic in the tailing [13]. In general, when the temperature was within 1150–1270 °C, Fe^{3+} oxide would start to resolve and turn into Fe^{2+} oxide, giving out O_2. Fe_2O_3 content was relatively higher in the ceramic body, making it more likely to blister in the burning process and have a big influence on its performance [13]. The burning temperature was controlled at 1200 °C according to the Fe_2O_3 content, which could prepare high performance ceramic products.

Crystalline structure analysis. The sample was prepared at 1200 °C burning temperature, of which the tailing mixing amount was 28%. It is observed from the sample's XRD spectra in Figs. 1 and 2 that the characteristic peaks of Hematite, Quartz and Cristobalite are obvious except that of Mullite, due to the complex ingredients of tailing powders. Therefore, the main crystallines of tailing ceramics are Hematite, Quartz, Cristobalite and a little Mullite, which make up the ceramic body skeleton together, and help enhance its body strength. Meanwhile, the tailing

Table 1 The tailing ingredient (%)

Ingredient	SiO_2	Al_2O_3	Fe_2O_3	CaO	MgO	K_2O	Na_2O	TiO_2	Ignition lost
Tailing	37.47	20.88	28.05	0.66	0.42	1.89	1.55	2.25	3.79

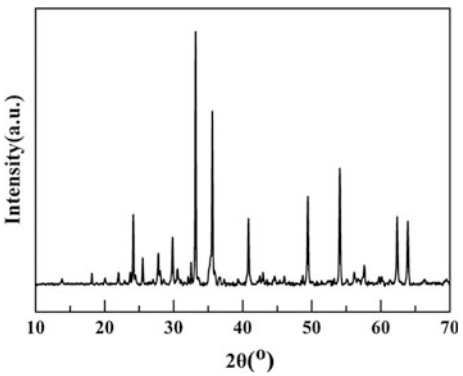

Fig. 1 XRD spectra of tailing powders

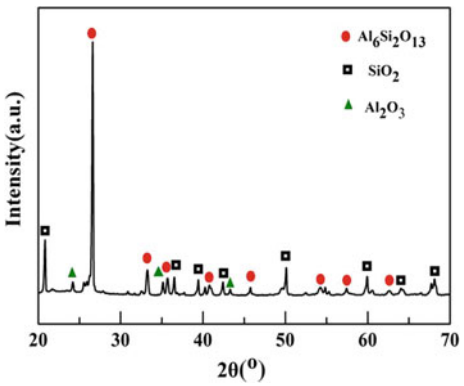

Fig. 2 XRD spectra of ceramic

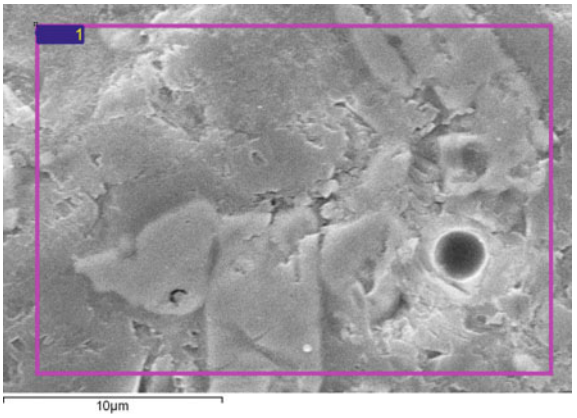

Fig. 3 SEM spectra of ceramic

content makes the ceramic display brown colour. To further confirm the crystalline structure of the ceramic body, the SEM/EDS spectrum was measured and showed in Figs. 3 and 4. The SEM/EDS analysis indicates that the surface of the tailing ceramic body is smooth and dense, and has a few pores and a lot of fake and bulk particles closely bonded together that are surrounded by glass phase to form the dense whole [14].

As shown in Fig. 3, the selected region contains Al, Si, Fe, K and Ti obviously. And it is identified that the main crystallines are Hematite and Quartz and very little Mullite. The little Mullite is mainly originated from the more alkali metal and alkaline-earth metal ions. The ions have stronger fluxing actions, and Fe^{3+} and Fe^{2+} coming into being at a high temperature promote Quartz fusing liquation [13]. The formed Hematite makes the ceramic body display brown colour.

Complex permittivity and permeability spectrum. Figures 5 and 6 show the complex permittivity (ε' and ε'') and the complex permeability (μ' and μ'') spectra of ceramics at 2–18 GHz frequency respectively. From Fig. 5, it can be seen that the real permittivity ε' and imaginary permittivity ε'' are all increasing, and that there are

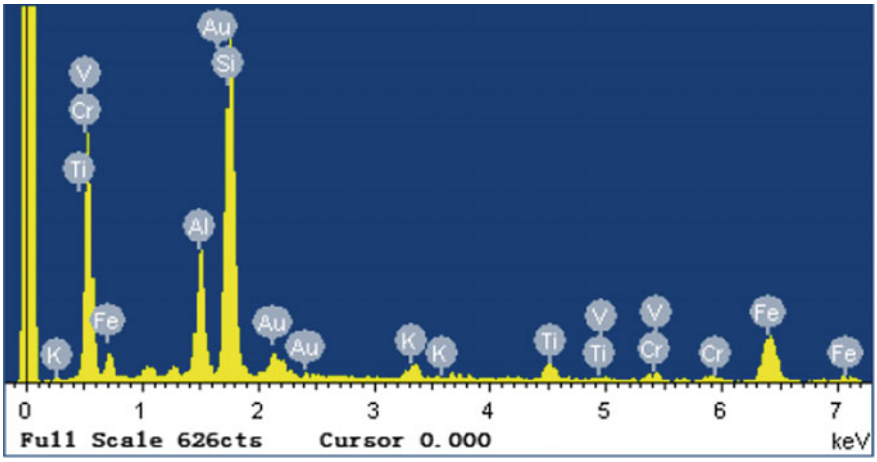

Fig. 4 EDS spectra of ceramic

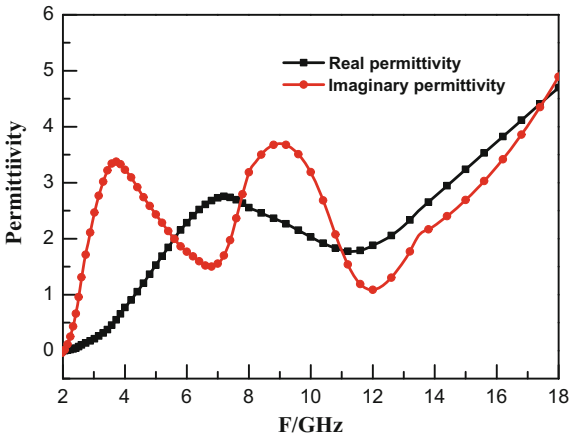

Fig. 5 Complex permittivity spectrum

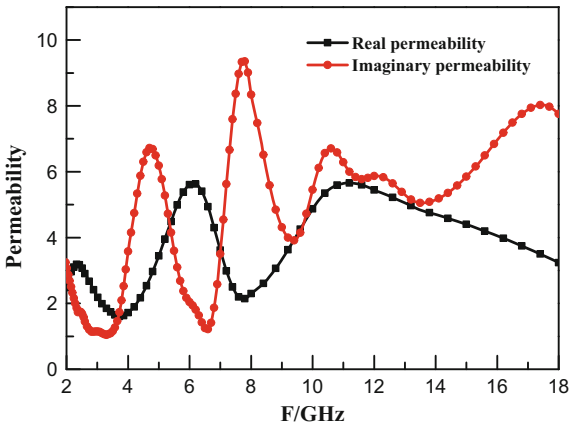

Fig. 6 Complex permeability spectrum

resonance peaks. The permittivity explains that tailing powders have a certain dielectric performance, due to the more content of iron which exists as Hematite. Meanwhile, the ceramics own several kinds of electric dipoles at the inherent vibration frequency. In the effect of the external electric field, the ε'' would display characteristic peaks and provide ceramics with dielectric loss ability. The high ε'' represents high conductivity, mainly because Hematite forms the electric channel in ceramic and effectively reduces the reflection to electromagnetic waves. At the same time, the real permeability and imaginary permeability also show obvious resonance peaks at 2–18 GHz. In the dynamic magnetizing process, there are some kinds of energy losses caused by magnetic hysteresis loss, eddy-current loss, domain wall resonance and natural resonance, embedding the ceramics with a certain magnetic loss ability [15–17].

Electromagnetic wave absorption properties. Figure 7 shows the monolayer absorber structural model, in which the thickness of the dielectric layer is d_2. Dielectric layer and metal plate are fastened using a binder, where d_0 and d_1 are the thickness, respectively. Incidence direction of the electromagnetic wave is from the dielectric layer. It can design the EMWA building coating using the monolayer absorber model. According to the transmission line theory, the *RL* can be calculated using the ε_r and μ_r at a given thickness, whose relations are described as follows [18]:

$$Z_{in} = Z_0 \sqrt{\frac{\mu_r}{\varepsilon_r}} \tanh\left[j\frac{2\pi fd}{c}\sqrt{\mu_r \varepsilon_r}\right]. \tag{1}$$

$$RL = 20\log_{10}|(Z_{in} - Z_0)/(Z_{in} + Z_0)|. \tag{2}$$

$$Z_0 = \sqrt{\frac{\mu_0}{\varepsilon_0}}. \tag{3}$$

where Z_{in} is the input impedance, Z_0 is the impedance of the free space, ε_r and μ_r are the complex permittivity and permeability, *RL* (dB) is the reflection loss of monolayer absorber, *f* is the frequency of microwave, d is the simulated thickness of the absorber and *c* is the velocity of the light in the free space.

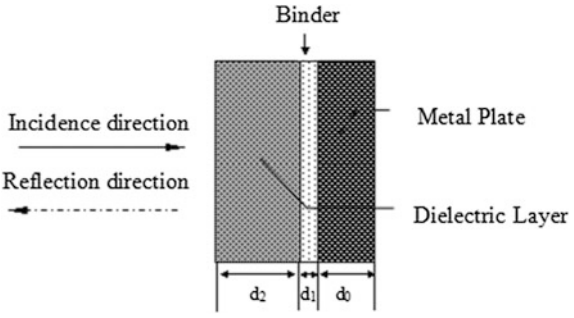

Fig. 7 Monolayer absorber structure

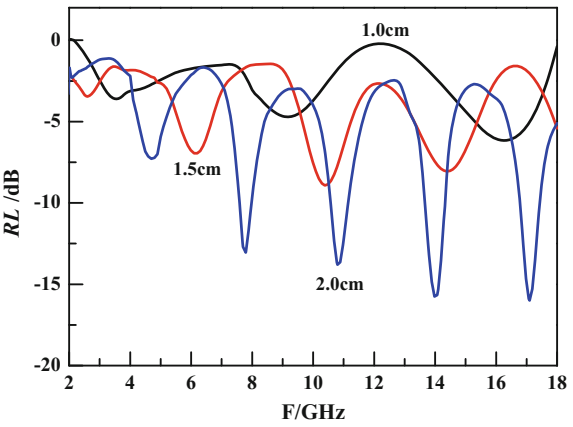

Fig. 8 Reflection loss of ceramic

It can be seen that the tailing ceramics are both dielectric and magnetic losses materials, consisting of some Quartz, Cristobalite and Mullite wave-transparent contents. To improve materials to the EMW impedance and further prepare electromagnetic wave absorption (EMWA), materials should meet certain requirements [19]. Based on the EMWA theory, the tailing could be used to prepare EMWA building ceramic tile according to the monolayer design (Fig. 7). Assuming that the monolayer absorber is 1, 1.5, and 2 cm thick, the theoretical simulation results with frequency is showed in Fig. 8. With the thickness increasing, the *RL* peaks also increase and the EWMA performance is enhanced. When the monolayer abosorber is 2 cm thick, the minimum *RL* value is −16.0 dB at 17.0 GHz, and there are five *RL* peaks at 2–18 GHz. The added thickness changes ceramic tile's wave impedance as well as the reflection to incident wave on the surface, thus having an effect on the loss performance.

Conclusion

By analyzing the chemical ingredient, crystalline structure, complex permittivity and permeability of iron tailing, the feasibility of using tailing powders as an absorbing reagent was identified. The ceramic-added iron tailings were successfully prepared using the burning method, of which the mechanical properties were excellent. Meanwhile, theoretical simulation results exhibited that, when the thickness of the monolayer ceramic tile absorber was 2 cm, the *RL* value was minimum, which was −16.0 dB at 17.0 GHz. Due to the complex content effects, the ceramic tiles had a better EWMA performance, suggesting that it could be used for architectural radiation protection to make architectural electromagnetic space safer and more reliable.

References

1. S.H. Liu, J.M. Liu, X.L. Dong, *Electromagnetic Wave Shielding and Absorbing Materials* (Chemical Industry Press, 2007), pp. 20–40
2. A.J. Douglas, et al., IEEE Transac. Microw. Theory Techn. **50**, 721 (2002)
3. S.H. Wang, et al., Environ. Sci. Technol. **29**, 96–98 (2006)
4. W.J. Hao, Sci. Technol. Foreign Building Mat. **25**, 74–76 (2004)
5. T. Simizu, Absorb and shield of electromagnetic wave. Econ. Technol. Book 150–180 (1989)
6. W. Wang, The micro-structure and electromagnetic property study of anti-EMI FeSiAl soft magnetic flakes (Zhejiang University, Hangzhou, 2007)
7. Y.D. Zhou, Studies on preparation, structures and characteristics of FeSiAl flaky powders (University of Electronic Science and Technology of China, Chengdu, 2004).
8. X.Z. Che, Elelctromagnetic shield and decorative function ceramic and its preparation method. CN 1699272A, China, 2005-11-23
9. C. Gao, Q. Xu, P. Ji, A kind of electromagnetic protective artificial stone. CN 103951316A, China, 2014-04-15
10. R. Yao, et al., Effects of ZnO and NiO on material properties of microwave absorptive glass-ceramic tile derived from ion ore tailings. Ceram. Int. **42**(2016), 8179–8189 (2016)
11. R. Yao, et al., Preparation and characterization of novel glass-ceramic tile with microwave absorption properties from iron ore tailings. J. Magn. Mag. Mat. **378**, 367–375 (2015)
12. H.B. Li, A.X. He, T.X. Deng, et al. Research on the proportioning schedule and sintering - shaping process of ceramic tile with the tailings of V-bearing titanonmagenitite. China Ceram. **35**, 31–33 (1999)
13. L. Ning, *Preparation and Properties of Antistatic Ceramics with High Fe_2O_3 Content* (South China University of Technology, Guangzhou, 2013)
14. T.L. Chen, *Preparation and Mechanism of Fired Bricks and Titles with Low-Silicon Iron Tailings from Western Hubei* (Wuhan University of Science and Technology, 2012)
15. Y.J. Guan, The preparation and electric-magnetic properties of the multiferroic composite ceramics. Ceramics **7**, 24–28 (2016)
16. C.Y. Yang, *Preparation, Microstructure, Electrical and Magnetic Properties of $YMnO_3$ Based Multiferroic Ceramics* (Wuhan University of Science and Technology, 2014)
17. J.Y. Zhang, *Study on the Properties of High Iron Fly-Ash and the Absorption of Cement-Based Composites Materials* (Chongqing University, 2010)
18. M. Toru, et al., J. Magn. Magn. Mater. **281**, 195–205 (2004)
19. Y.T. Zhu, *Synthesis and Microwave Absorption Properties of Ferric Oxide/Graphene (Polyaniline) Composite Materials* (Anhui University of Science and Technology, 2016)

Effect of Calcination Temperature on the SCR Activity of Fe–S/TiO_2 Catalysts

Fengxiang Li, Junlin Xie, Pijun Gong, Kai Qi, De Fang and Feng He

Abstract A series of Fe–S/TiO_2 catalysts were prepared at different calcination temperatures by impregnation method and its performance of selective catalytic reduction (SCR) of NO with NH_3 was investigated at temperatures ranging from 200 to 400 °C. Fe–S/TiO_2-300 °C catalyst showed the highest activity, the NO conversion reaching over 80% in the range of 280–400 °C. With the help of XRD, H_2-TPR and NH_3-TPD, the structures and properties of catalysts were characterized. With the increase of calcination temperature, the $Fe(OH)SO_4$ content in the catalyst decreased gradually. In addition, When the calcination temperature was below 400 °C, the main crystal phase in the catalyst is $Fe(OH)SO_4$ and $FeSO_4$. However, when it was 500 °C, the crystal phase of the active material became

F. Li · J. Xie · P. Gong · K. Qi · D. Fang · F. He
State Key Laboratory of Silicate Materials for Architectures, Wuhan University of Technology, Wuhan 430070, China
e-mail: lifx@whut.edu.cn

J. Xie
e-mail: xjlclxy@126.com

P. Gong
e-mail: gpjwhut@163.com

K. Qi
e-mail: 18271391373@163.com

D. Fang
e-mail: fangde0914@whut.edu.cn

J. Xie · D. Fang
Center for Materials Research and Analysis, Wuhan University of Technology, Wuhan 430070, China

F. Li · P. Gong · K. Qi · F. He (✉)
School of Materials Science and Engineering, Wuhan University of Technology, Wuhan 430070, China
e-mail: he-feng2002@163.com

Y. Han (ed.), *Advances in Energy and Environmental Materials*,
Springer Proceedings in Energy, https://doi.org/10.1007/978-981-13-0158-2_93

$Fe_2(SO_4)_3$ and $FeSO_4$. What's more, the reduction ability of several catalysts showed no much difference, but the surface acidity was quite different, as the acidity of the Fe–S/TiO_2-300 °C catalyst was the strongest.

Keywords NH_3-SCR · Fe–S/TiO_2 catalysts · Calcination temperature

Introduction

Nitrogen oxide has caused serious harm to the environment and become the primary governance target [1, 2]. Selective catalytic reduction with NH_3 (NH_3-SCR) has been proved to be an effective and reliable way to control NO_x emission [3, 4]. Nowadays, V_2O_5–WO_3 (MoO_3)/TiO_2 catalysts have been used in many industrial flue gas treatments. However, those working temperature must be in the 300–400 °C range [5]. In recent years, many medium and low temperature catalysts have become the focus of research. However, these catalysts often exhibit low activity and poor resistance to sulfur poisoning [6]. In order to solve this problem, some sulfur-containing catalysts have been studied. Such as $CuSO_4/TiO_2$ [7], $CuSO_4$–CeO_2/TiO_2–SiO_2 [8], $CuSO_4/ZrO_2$ [9]. The S in the catalyst help to resist SO_2 and increase the acidity of the catalyst.

In this paper, TiO_2 was used as the carrier, various Fe–S/TiO_2 catalysts were prepared by impregnation method, and its performance was studied at the range of 200–400 °C. The properties of the catalysts were evaluated by physicochemical analyses, including X-ray diffraction (XRD), hydrogen temperature programmed reduction (H_2-TPR) and ammonia temperature programmed desorption (NH_3-TPD)

Experiment

Preparation of Catalysts. A series of Fe–S/TiO_2 catalysts were prepared by impregnation method with TiO_2 powder (P25, Degussa, 80%), TiO_2 used as the support and $FeSO_4{\cdot}7H_2O$ used as precursors of Fe-S were dissolved in distilled water. Then stirred for 2 h at room temperature. Subsequently, the mixed solution dried in air at 110 °C. Finally, the prepared products were calcined at different temperature for 3 h to obtain the catalysts. In addition, the molar ratio of Fe/Ti was kept at 0.13 in the process of preparation. The Fe–S/TiO_2 catalysts were denoted as Fe–S/TiO_2–X °C, where X represents the calcination temperature.

NH_3-SCR Activity. Catalytic activity test of catalysts were tested in the fixed bed reactor at a space velocity of 30,000 h^{-1} with simulated reaction gas composition of 720 ppm NO, 800 ppm NH_3, 3 vol% O_2 and N_2 as balance. About 3 g catalysts were pressed into tablets and put in fixed bed reactor. In the test, through adjusting

the temperature step by step, the initial NO concentration ($[NO]_{in}$) and the outlet concentration of NO ($[NO]_{out}$) that could indicate the reaction level of the corresponding temperature were recorded with an online offgas analyzer. The temperature of reaction bed was controlled ranging from 200 to 400 °C, and the denitration rate calculation formula is:

$$NO\ conversion\ [\%] = \frac{[NO]_{in} - [NO]_{out}}{[NO]_{in}} \times 100\% \quad (1)$$

Physico-Chemical Characterization. The powder X-ray diffraction (XRD) patterns were obtained on a Bruker D8 Advance diffractometer (Bruker, Germany) using Cu Kα (λ = 0.15406 nm) with an angle of 2θ from 10° to 80° to explore the presence of crystalline material in the catalysts. In order to characterize the ability of chemisorption for NH_3, NH_3-TPD was performed using an automated catalyst characterization system (TPDRO1100, Thermo, USA). 150 mg sample was pretreated for 1.5 h in He (20 mL/min) at appropriate temperature in which catalysts could not be damaged and cooled to room temperature afterwards. Next, the sample was fluxed with 10% NH_3/He (40 mL/min) for 30 min, and then purged the physically adsorbed NH_3 at 100 °C for 30 min. Finally, the samples were tested by increasing the temperature from 373 to 1073 K at the heating rate of 5 °C/min, at the same time. H_2-TPR was performed using an automated catalyst characterization system (TPDRO1100, Thermo, USA) to characterize the reducing ability of catalysts and interaction between the components. Prior to the analysis, 50 mg catalyst samples were pretreated at 200 °C for 1.5 h in helium (20 sccm) and cooled to room temperature afterwards. Then the samples were purged with 5 vol% H_2 in N_2. The samples were tested by increasing the temperature from 100 to 800 °C at the heating rate of 10 °C/min, recording the amount of H_2 consumption by a TCD.

Results and Discussion

NH_3-SCR Activity. NH_3-SCR activities for Fe–S/TiO_2 Catalysts with different calcination temperatures are shown in Fig. 1. When the calcination temperature was lower (such as Fe–S/TiO_2-no roasted catalyst and Fe–S/TiO_2-200 °C catalyst), the activity of the catalyst was relatively lower. Overall, when the calcination temperature was 300 °C, the Fe–S/TiO_2 catalyst exhibited the highest catalytic activity, the NO conversion could reach over 80% in the range of 280–400 °C. When the calcination temperature rised, the activity of the catalyst did not continue to rise, but rather decreased in the high temperature region.

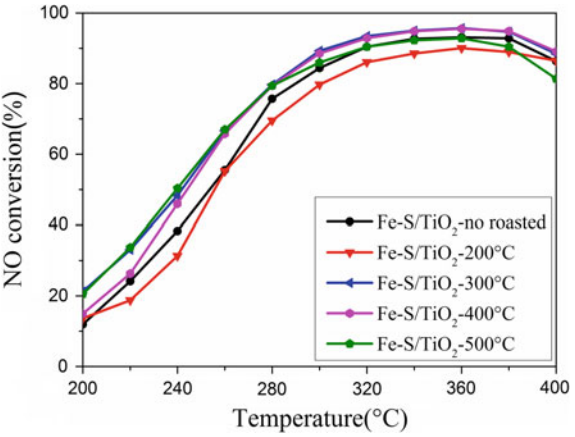

Fig. 1 NH_3-SCR catalytic activity of Fe–S/TiO_2 Catalysts with different calcination temperatures. Reactions: 720 ppm NO, 800 ppm NH_3 and 3 vol% O_2, and in a N_2 stream. GHSV = 30,000 h^{-1}

X-Ray Diffraction. The XRD patterns of Fe–S/TiO_2 catalysts with different calcination temperatures are shown in Fig. 2. For various catalysts, the diffraction peaks of anatase TiO_2 and rutile TiO_2 were detected, it was also the main crystal diffraction peaks in the catalysts. In addition, when the calcination temperature was lower than 400 °C, the diffraction peaks of $Fe(OH)SO_4$ and $FeSO_4$ appeared in the diffraction patterns of the catalysts. When the calcination temperature was 500 °C, the crystal phase of the active material detected in the catalyst became $Fe_2(SO_4)_3$ and $FeSO_4$, suggesting that $Fe(OH)SO_4$ decomposed into $Fe_2(SO_4)_3$ at 500 °C. This may be one of the reasons for the decreasing of activity for Fe–S/TiO_2-500 °C catalyst.

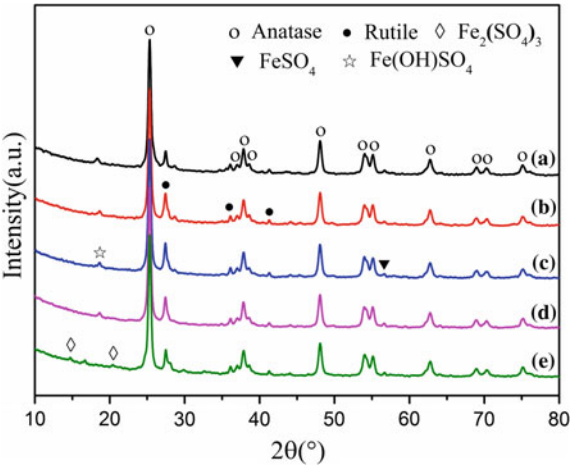

Fig. 2 Powder XRD patterns of Fe–S/TiO_2 Catalysts with different calcination temperatures. **a** Fe–S/TiO_2-no roasted catalyst; **b** Fe–S/TiO_2-200 °C catalyst; **c** Fe–S/TiO_2-300 °C catalyst; **d** Fe–S/TiO_2-400 °C catalyst; **e** Fe–S/TiO_2-500 °C catalyst

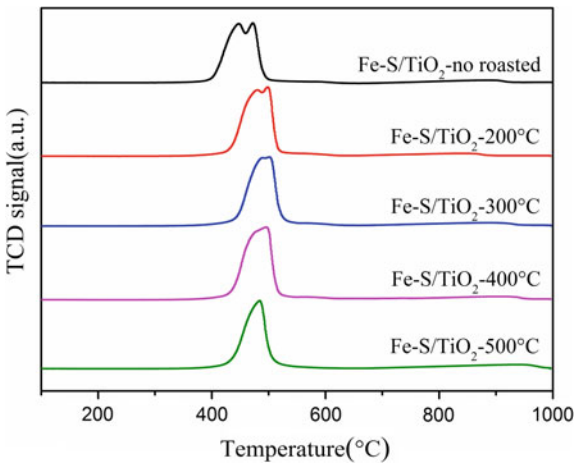

Fig. 3 H_2-TPR profiles of Fe–S/TiO_2 Catalysts with different calcination temperatures

H_2-TPR. H_2-TPR was used to investigate the amount of hydrogen consumption and reduction ability of the catalysts. The H_2-TPR curves of the catalysts in the range of 100–1000 °C are illustrated in Fig. 3. For Fe–S/TiO_2-no roasted catalyst, three reduction peaks were observed at 447, 472 and 890 °C, could be attributed to the reduction of $Fe(OH)SO_4$ to $FeSO_4$, $Fe_2(SO_4)_3$ to $FeSO_4$ and $FeSO_4$ to Fe_2O_3, respectively [10]. The temperature range of the last reduction peak was wide, mainly due to the fact that the $FeSO_4$ at this stage was composed of three parts: the conversion of $Fe(OH)SO_4$, the conversion of $Fe_2(SO_4)_3$ and the catalyst itself. When the calcination temperature continued to rise, the first reduction peak was becoming smaller, indicating that the content of $Fe(OH)SO_4$ in the catalyst was decreasing, which was consistent with the XRD results. In addition, to a certain extent reduction peak position could reflect the redox ability of catalysts, the lower the temperature was, the stronger the oxygen redox ability of the catalyst had [11]. But it can be found from the figure that with the increase of calcination temperature, the reduction peak moved first to the high temperature region and then to the low temperature zone, but the temperature difference was small. Indicating the reduction ability of several groups of catalysts was not much difference, not the main factor affecting the activity of the catalysts.

NH_3-TPD. In order to explore the adsorption ability of NH_3 and the amount of surface acid sites of catalysts with different calcination temperatures, the NH_3-TPD analysis was performed, the results are shown in Fig. 4. the total acidity of Fe–S/TiO_2-no roasted, Fe–S/TiO_2-200 °C, Fe–S/TiO_2-300 °C, Fe–S/TiO_2-400 °C, Fe–S/TiO_2-500 °C catalysts was found to be 77,800, 78,412, 79,240, 45,261, 55,309 μmol/g, respectively. And Fe–S/TiO_2-300 °C catalyst hold the strongest acidity, this facilitates the catalytic reaction to proceed with a higher catalyst activity. In addition, for Fe–S/TiO_2-300 °C catalyst, there were three distinct peaks

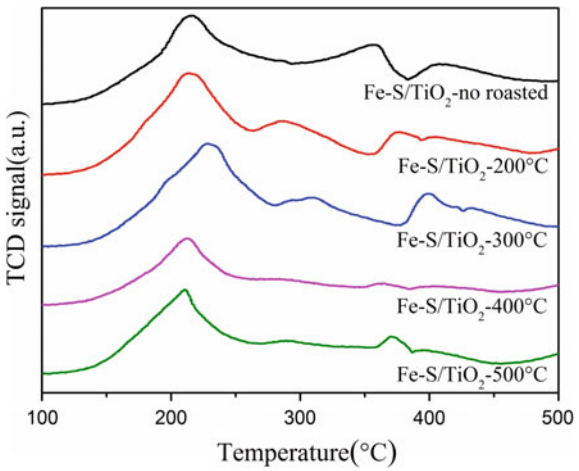

Fig. 4 NH_3-TPD profiles of Fe–S/TiO_2 Catalysts with different calcination temperatures

on the desorption curve, which were assigned to weak, middle and strong acid sites, respectively. What's more, the weak acid site corresponded to the Lewis acid sites of the catalyst surface, so the catalysts surface was predominantly present as a Lewis acid [12].

Conclusions

In summary, a series of Fe–S/TiO_2 catalysts with different calcination temperature were prepared by impregnation method. Overall, when the calcination temperature was 300 °C, the Fe–S/TiO_2 catalyst exhibited the highest catalytic activity, could reach over 80% NO conversion in the range of 280–400 °C. According to XRD studies, the active substances in the catalysts were different at different calcination temperatures. The $Fe(OH)SO_4$ and $FeSO_4$ appeared in catalysts when the calcination temperature was below 400 °C, while $Fe_2(SO_4)_3$ and $FeSO_4$ appeared in catalysts when it was 500 °C. H_2-TPR revealed that with the increase of calcination temperature, the $Fe(OH)SO_4$ content in the catalyst decreased gradually. But the reduction ability of several groups of catalyst showed no much difference. NH_3-TPD results illustrated that Fe–S/TiO_2-300 °C catalyst hold the strongest acidity, which was favorable for its catalytic activity.

Acknowledgements This work was financially supported by "the Fundamental Research Funds for the Central Universities" (2017-YB-012). And the tests of XRD were supported by Research and Test Center of Materials, Wuhan University of Technology. H_2-TPR and NH_3-TPD tests were supported by State Key Laboratory of Silicate Materials for Architectures, Wuhan University of Technology.

References

1. E.Y. Fan, P.B. Wei, G.R. Sui, H. Ji, Preparation of Mn–Ce–O_x denitration catalyst and its Regeneration performance. Environ. Sci. Technol. **35**, 40–44 (2012)
2. Q. Yang, Y. Wang, C. Zhao, Z. Liu, W.I. Gustafson Jr., M. Shao, NOx emission reduction and its effects on ozone during the, Olympic games. Environ. Sci. Technol. **45**(2011), 6404–6410 (2008)
3. W.K. Dong, K.H. Park, S.C. Hong, Influence of VO_x surface density and vanadyl species on the selective catalytic reduction of NO by NH_3 over VO_x/TiO_2 for superior catalytic activity. Appl. Catal. A: Gen. **499**, 1–12 (2015)
4. T. Yu, D. Fan, D., Hao, T., Wang, J., Shen, M., Li, W., The effect of various templates on the NH_3-SCR activities over Cu/SAPO-34 catalysts. Chem. Eng. J. **243**, 159–168 (2014)
5. S. Bröer, T. Hammer, Selective catalytic reduction of nitrogen oxides by combining a non-thermal plasma and a V_2O_5-WO_3/TiO_2 catalyst. Appl. Catal. B: Environ. **28**, 101–111 (2000)
6. F. Li, J. Xie, D. Fang, F. He, K. Qi, P. Gong, Mechanistic study of Ce-modified MnO_x/TiO_2, catalysts with high NH_3-SCR performance and SO_2 resistance at low temperatures. Res. Chem. Intermed. 1–20 (2017)
7. Y. Yu, J. Miao, J. Wang, C. He, Chen, J., Facile synthesis of $CuSO_4/TiO_2$ catalysts with superior activity and SO_2 tolerance for NH_3-SCR: physicochemical properties and reaction mechanism. Cataly. Sci. Technol. **7**, 1590–1601 (2017)
8. Y. He, H. Tong, Z.Q. Tong, Y. Huang, B. Xia, Performance of a novel $CuSO_4$–CeO_2/TiO_2–SiO_2 catalyst for NO reduction with NH_3 at low temperature. Chin. J. Process Eng. **9**, 360–367 (2009)
9. D. Pietrogiacomi, D. Sannino, A. Magliano, P. Ciambelli, S. Tuti, V. Indovina, The catalytic activity of CuSO/ZrO for the selective catalytic reduction of NO_x with NH_3 in the presence of excess O. Appl. Catal. B: Environ. **36**, 217–230 (2002)
10. L. Ma, J. Li, R. Ke, L. Fu, Catalytic performance characterization and mechanism study of $Fe_2(SO_4)_3/TiO_2$ catalyst for selective catalytic reduction of NOx by Ammonia. J. Phys. Chem. C **115**, 7603–7612 (2011)
11. D. Fang, J. Xie, H. Hua, Y. Hu, H. Feng, Z. Fu, Identification of MnO_x species and Mn valence states in MnO_x/TiO_2 catalysts for low temperature SCR. Chem. Eng. J. **271**, 23–30 (2015)
12. W. Mu, J. Zhu, S. Zhang, Y. Guo, L. Su, X. Li, Novel proposition on mechanism aspects over Fe–Mn/ZSM-5 catalyst for NH_3-SCR of NO_x at low temperature: rate and direction of multifunctional electron-transfer-bridge and in-situ DRIFTs analysis. Cataly. Sci. Technol. **6**, 7532–7548 (2016)

The Integrative Process of Flocculation and Submerged Membrane Filtration for Drinking Water Supply

Lei Zhang, Leitao Zhang and Yuzhong Zhang

Abstract Submerged membrane filtration process (SMF) is considered as the core of the third-generation water treatment process, so it is necessary to study SMF process to optimize the quality of drinking water. Here, an integrative process of flocculation pretreatment and SMF process is investigated on a pilot test. The results show that the removal rate for turbidity and bacteria is more than 99% and the water quality of production water meet the China's standards for drinking water (GB 5749-2006). Less than 50% TOC and COD_{Mn} is reduced by the integrative process, while only 24.50% of COD_{Mn} and 15.40% of TOC in a single SMF process. A slow increase of transmembrane pressure (TMP) appears in the filtration flux range of from 30 to 50 L/m^2 h, but a sudden increase is observed at the flux of 60 L/m^2 h. This pilot study identifies an integrative process for clean water supply and the SMF process function as a vital role in the integrative process.

Keywords Drinking water · Flocculation · SMF · Integrative process

Introduction

Water is indispensable for daily life and industrial development. About 70.9% of the Earth's surface is covered with water, however, only 3% of water is freshwater and around 99% exists in form of polar ice and groundwater. Therefore, less than

L. Zhang · L. Zhang · Y. Zhang
School of Materials Science and Engineering,
Tianjin Polytechnic University, Tianjin 300387, China
e-mail: aeilonx@163.com

L. Zhang
e-mail: zgtjtjpu2011@hotmail.com

L. Zhang · L. Zhang · Y. Zhang (✉)
State Key Laboratory of Separation Membranes and Membrane Processes,
Tianjin Polytechnic University, Tianjin 300387, China
e-mail: zhangyz2004@vip.163.com

Y. Han (ed.), *Advances in Energy and Environmental Materials*,
Springer Proceedings in Energy, https://doi.org/10.1007/978-981-13-0158-2_94

1.0% of freshwater is available for people and ecosystems [1]. Despite this, most of the limited freshwater resources deteriorated seriously due to excessive human activities. Organic impurities had always been one of major concerns in drinking water treatment, particularly in developing countries [2]. In China, for example, it had been estimated that more than half of the major surface water resources had been polluted by sewage organics to a level that has a 5-day biochemical oxygen demand (BOD_5) of 5 mg/g or higher and an ammonia nitrogen (NH_3–N) level of more than 3 mg/L [3].

The coagulation precipitation, filtration and disinfection of drinking water are the core processes in conventional water treatment process, and its purpose of the conventional water treatment process is to decrease water turbidity and remove bacteria [4]. However, the conventional process is difficulty to meet latest national water standards (GB 5749-2006) and drinking water treatment presented great difficulties and challenges in terms of the capability and performance of conventional water treatment processes [5].

Membrane separation technologies had been identified as one of the possible solutions to meet the future demands with regard to water supply and sanitation [6, 7]. Submerged membrane filtration process (SMF) is a special operation mode of ultrafiltration membrane technology, which involves the process where ultrafiltration membrane is submerged in water and water can permeate the membrane with the help of suction [8]. There are so many advantages that SMF becomes the potential candidate for drinking water treatment, such as good water quality, anti-pollution, small footprint and compact structure so on. Nevertheless, the inefficiency for organic matter removal has limited its application of SMF process in actual operation [9]. To overcome this defect, some literatures reported that the couple of the partial conventional water treatment process could alleviate SMF "pain and suffering". Zhang Wei et al. confirmed that enhanced coagulation as pretreatment could increase the removal rate of humic acid in the water by hybrid process of UF efficiently, and 10 mg/L dosage of coagulant could make the removal rate of UV_{254} and COD up to 85.7 and 69.0%, respectively [10]. M. Simonič et al. found that the hybrid flocculation/UF process had good efficiency for a real dye-house effluent [11]. Liv Fiksdal et al. used the MF as the pretreatment process for UF to deal with virus in water and found this hybrid process could remove virus efficiently [12].

Despite so much data had evidenced the combination process to gain drinking with much better water quality in lab-scale tests, there still lack straightforward information for the pilot-scale application of this combination process. Here, a pilot-scale study about the integrative process where the flocculation process is selected as the pretreatment step and SMF is choose as the core course is carried out to explore the potentiality for large-scale application of this integrative process in Dongying Water Supply Company. Turbidity, COD_{Mn}, TOC, total bacteria and the trans-membrane pressure is taken as probe to evaluate the feasibility of this integrative process. The results show that the SMF plays a key role and the flocculation

process acts a helpful role for drinking water treatment. The pilot-scale study with the combination of SMF and flocculation will lay a solid foundation for SMF practical applications.

Materials and Methods

Experimental Apparatus and Process

Pretreatment Units. In this study, flocculation process is taken as the core pretreatment process. Flocculation process could decrease partially turbidity, organic substance and bacteria in water and this would be helpful for Submersed Membrane Filtration (SMF) process. Figure 1 depicts the drinking water process. The high-level tank, dosage system, flocculation tank and tube settler are the key components in the pretreatment units. Raw water is pumped into the raw water feed tank with the help of pump. The flux of raw water is about 3 m^3/h. After a short stay in the raw water feed tank, the water is pumped to the flocculation basin and mix with the flocculants, which are injected with the dose of 6 mg/L. In fact, there are four flocculation basins in pretreatment process to regrow the flocculating agent particles. Then the mixture of water and flocculants is pumped to the tube settler to remove suspended particles. The settled water will feed into solution tank for the SMF process.

Submerged Membrane Filtration System Setup. In this pilot-scale test, the core unit was the SMF process and the schematic diagram is shown in Fig. 2 The water stored in the solution tank is pumped to the SMF tank and permeates the SMF membrane by suction. There were two assistant systems (aeration system and backwash system) to maintain the whole process better operation. These two

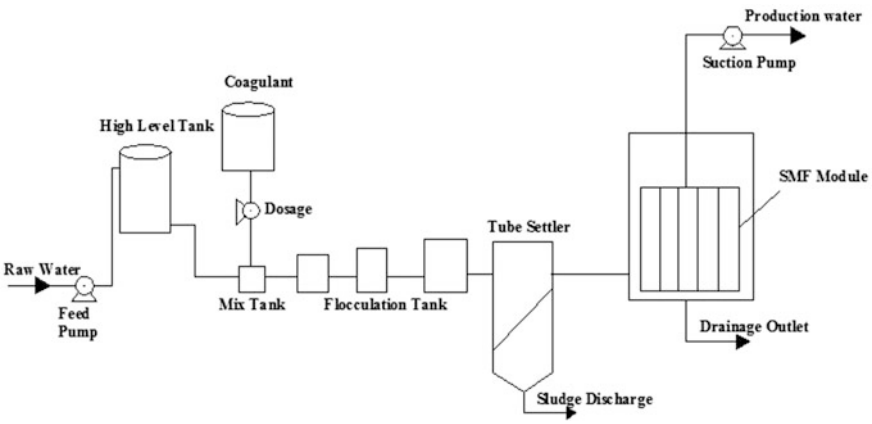

Fig. 1 Schematic diagram of the drinking water treatment process

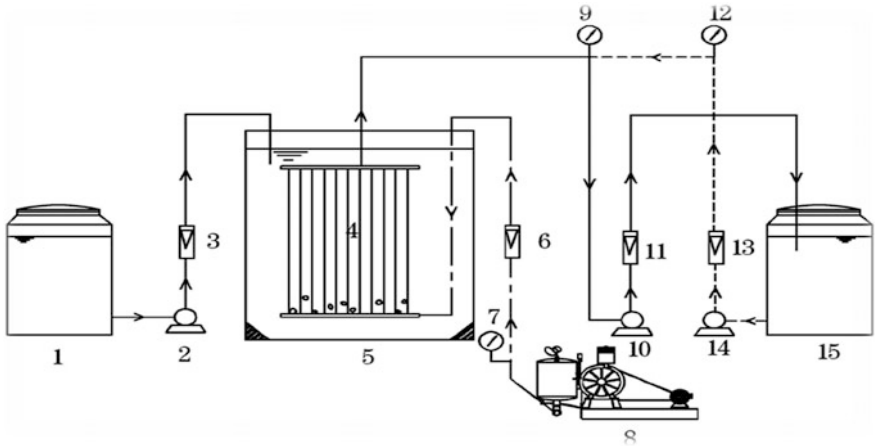

Fig. 2 Schematic diagram of SMF process. 1—solution tank; 2—pump; 3—11,13-liquid flow meter; 4—SMF membranes; 5—SMF tank; 6—gas flow meter; 7—gas-gauge; 8—air blower; 9—vacuum manometer; 10—suction pump; 12—backwash pressure gauge; 14—pump; 15—production water container

systems work simultaneously every one hour and the duration time of backwashing is 30 s. The backwash flow rate is twofold of the production water flow rate. Bubbling system controlled by adjustable air flow regulator continuously supplied air bubbles within the fibers network at the bottom of membrane module to provide a continuous up-flow circulation of micro-flocs suspension for hindering any micro-particles settlement. In particular a constant air scouring bubble of 0.2 m^3/(m^2 min) is applied to exert shear stress to suppress potential particles deposition on the membrane surface [13]. Table 1 shows the SMF process operating parameters.

The SMF Membrane Characteristics. The SMF membrane was provided by the SENUO filtration technology (Tianjin) Co. Ltd (Fig. 3). The specific parameter is shown in the Table 2.

The Quality of Raw Water. Raw water comes from the reservoir in the southern suburbs of Dongying in Shandong province. The reservoir locates in the lower

Table 1 Operating parameters of SMF process

Items	Plan A	Plan B	Plan C	Plan D
Volume of membrane poll (m^3)	0.6	0.6	0.6	0.6
Operation period (Days)	26	6	6	7
Flux rate (L/m^2 h)	30	40	50	60
Recovery rate of SMF system (%)	95	90	90	90
Backwash flow (L/m^2 h)	60	60	80	100
Backwash period (h)	1	1	1	1
Backwashing time (s)	30	30	30	30

Table 2 SMF membrane specification

Items	Parameter
Membrane type	Hollow fiber (SN-MBR I)
Dimension(a × b × c) [mm]	530 × 450 × 1010
Membrane material	Polyvinylidene fluoride (PVDF)
Adhesive material	Epoxy resin/polyurethane
Internal diameter [μm]	700
Molecular weight cutoff [kDa]	150
Membrane area [m^2]	25
Effective length of membrane silk [mm]	1000

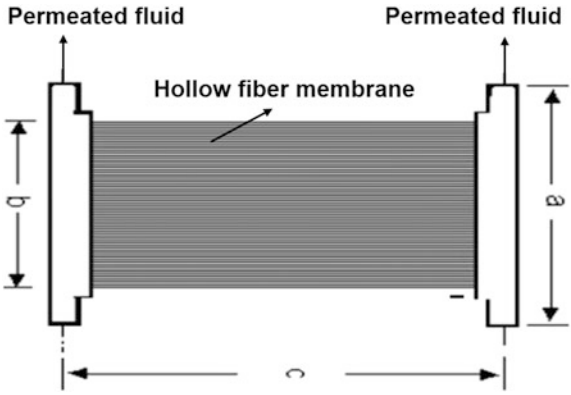

Fig. 3 SENUOFIL curtain type submerged hollow fiber membrane modules

reaches of the Yellow River and the water flow into the reservoir after a grit chamber treatment. Table 3 shows the water main quality indicators in the reservoir every month in past five years. In this pilot test, the Turbidity is from 11 NTU to 29 NTU, the range of COD_{Mn} and TOC is 3.18–5.08 mg/L and 2.08–2.38 mg/L respectively, the total bacterial is 126–364 CFU/L.

Analytical Method. Turb550 (Germany WWT) turbidimeter was used to determine the turbidity of raw water, settled water and production water. Eight number of turbidity was gained every day in our test. COD_{Mn} was obtained through the mutual titration of the potassium permanganate and sodium oxalate.TOC was determined by High-Temperature Combustion Method (Shimadzu 5000 TOC analyzers), where 2 ml of oily sludge were filtered through 0.45 μm-pore-diameters membrane. Filter and filtrate were heated in the oven to 600 °C for 90 min and then was cooled down to 25 °C.

The method of total bacteria measurement was described as follow: first the utensils were sterilized with high temperature and pressure, and then 1 ml of water sample and 25 ml of nutrient agar was added into the utensils. After the agar solidification and being cultured at 37 °C for 48 h in the incubator, the total bacteria were determined by the plate count method.

Table 3 The water quality indicator of reservoir water in 2006–2010

Water indicator	Jan.	Feb.	Mar.	Apr.	May	June	July	Aug.	Sept.	Oct.	Nov.	Dec.
Temperature [°C]	4.8	4.8	7.8	12.6	16.6	24.8	27.2	27.8	23.2	17.2	12.0	4.8
pH	8.06	8.14	7.99	8.11	8.02	7.91	7.89	7.89	7.84	8.01	7.99	8.09
Turbidity [NTU]	2.44	3.15	4.36	12.23	18.83	11.09	13.48	8.00	11.73	16.06	12.73	4.16
COD_{Mn} [mg/L]	3.44	3.21	3.27	3.37	3.62	3.11	3.69	4.14	3.43	3.90	3.57	3.55

Results and Discussion

Turbidity Removal. Turbidity is the probe of the sensory properties in China's national drinking water standards, it is also the indicator of microbiology pollution abroad generally. Turbidity is caused mainly by the presence of the suspended particles, colloids (>0.1 μm) and microbial community in the water. The average turbidity of raw water in this study is about 20.00NTU and the settled water is about 8.00NTU. The average removal rate for turbidity in pretreatment process is 70.00%. The contribution is 70.00% in flocculation process with respect to turbidity and this fact confirms that the flocculation pretreatment process is helpful for the SMF process. After going through the SMF membrane process, with the different filtration flux, the average turbidity of production water is 0.07NTU approximately and the removal rate is more than 99.00% (Fig. 4). As is shown in Fig. 5, the turbidity of production water was less than 0.10NTU and which was below the lowest limit of China's national drinking water standards (GB 5749-2006). Even though the contribution ratio of SMF process is only 30% in turbidity, SMF was indispensable to guarantee the quality of production water and meet the standards of drinking water.

Deep understandings on the filtration mechanism of SMF membrane help explain the reason why the SMF membranes have such a high removal rate for turbidity. There are three situations for the SMF membrane filtration:

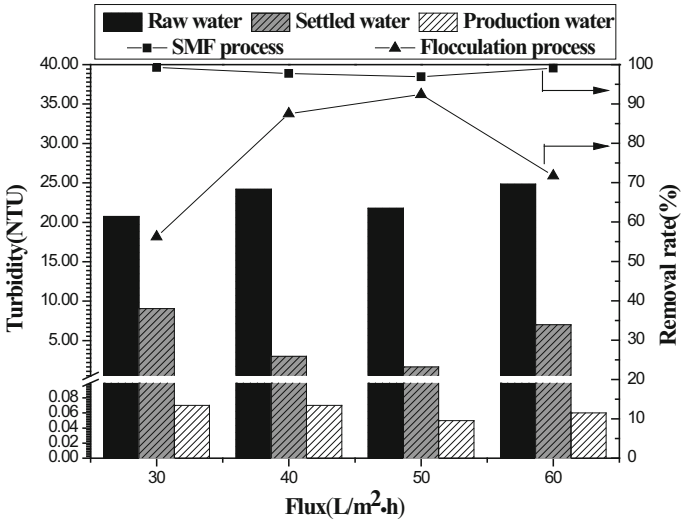

Fig. 4 Turbidity removal by the flocculation and SMF integrative process

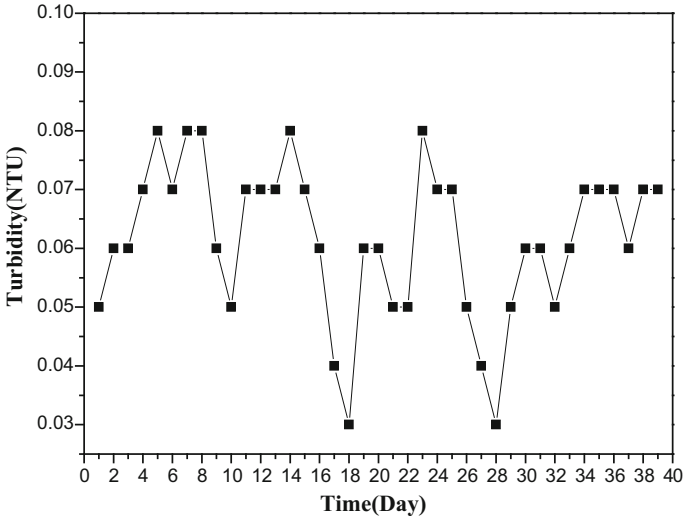

Fig. 5 Turbidity of production water from SMF system

(1) The particle size of the solute is greater than the membrane pore size and the solute will be intercepted on the membrane surface to separate from water.
(2) The particle size of the solute is similar to the membrane pore size and the solute will stay in the hole and cause obstruction.
(3) Solute adsorption on the membrane surface and the walls of the pores.

SMF membrane based these three kinds removal mechanism becomes effective barrier for suspended solids and colloidal particles. The turbidity removal efficiency of SMF membrane is extremely high. It is worth noting that excellent removal efficiency of the SMF membrane system for turbidity reflects its good removal capacity for bacteria and viruses in the raw water. Generally, the high turbidity in the raw water will significantly reduce the effectiveness of the disinfectant for microorganisms. However, low turbidity of SMF treatment influent can effectively improve disinfectant performance in the chlorination and ensure the microbiological safety of drinking water. Therefore, the SMF membrane is a reliable guarantee for the quality of drinking water supplies.

Organic Matter Removal. Chroma is mainly caused by the organic matter which is the disinfection byproduct precursor and leads to the bacterial reproduction in the pipe network. Therefore, the removal of organic matter in water becomes the main task and purpose in current water treatment processes. Due to its wide variety of organic compounds in drinking water, the determination of the overall quantity is feasible, which can reflect the total amount of organic matter in water, such as COD_{Mn} and TOC.

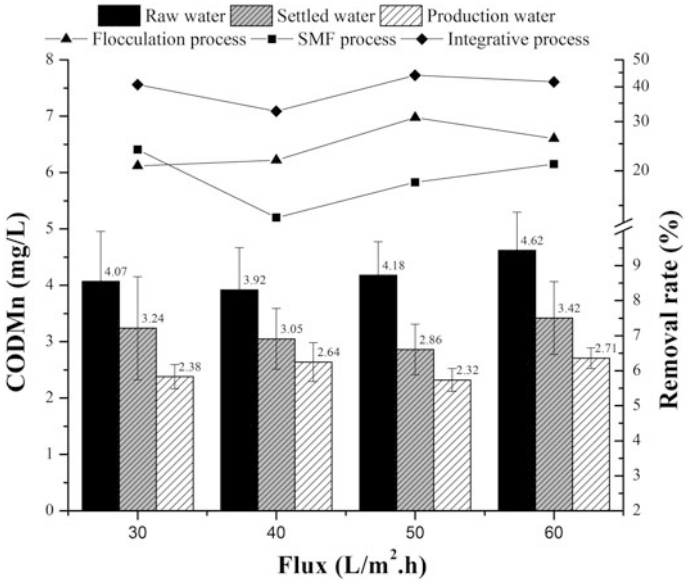

Fig. 6 COD_{Mn} removal by the flocculation and SMF integrative process

COD_{Mn} Removal. Figure 6 indicates COD_{Mn} removal efficiency with different filtration flux for the flocculation and SMF integrative process. The total COD_{Mn} removal rate is less than 50%; the average removal rate of COD_{Mn} is 24.50% for the flocculation process and the average removal rate is 18.64% for the SMF process. In spite of the lower COD_{Mn} removal rate, compared with the high removal rate for turbidity, the COD_{Mn} maximum of production water is less than 3 mg/L, which is the established value of China's national drinking water standards (GB 5749-2006). Of note, the data in continuous 24 days reveals the removal rate of the flocculation process is negative occasionally (Fig. 7). This phenomenon may be due to the misoperation during sludge discharge in the tube settler.

TOC Removal. TOC, based on the carbon content of the organic matter, is an important indicator to evaluate organic contamination in water. As shown in Fig. 8, the total TOC removal rate in the integrative process is 47.46%. The TOC removal rate of the flocculation process is 31.65%, while the average TOC removal rate in SMF is 15.81%.

The phenomena, which the integrative process show lower removal rate for organic compounds, might result from its lower adsorption efficiency. Organic compounds in water exist mainly in the form of small molecules in dissolved state. Parts of organic substance could be cleaned out from the water in SMF process by adsorption on the surface of membrane and particles separated by membrane. Besides this situation, flocculant particles also adsorb organic matter as the particles grow and this lead to the fact that some organic matter could be removed in the

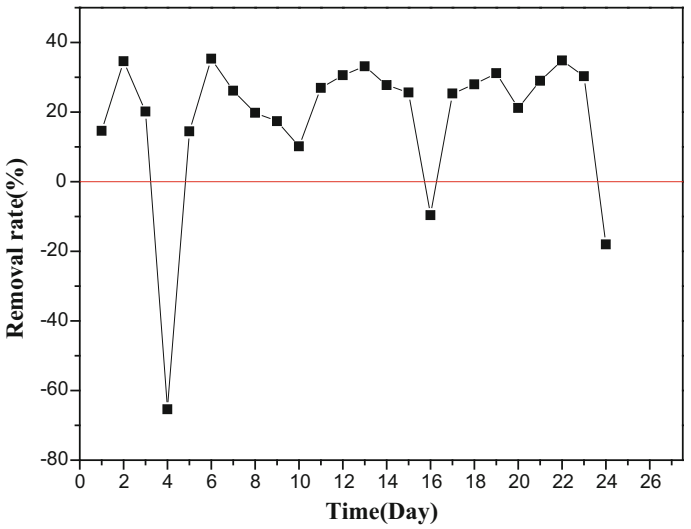

Fig. 7 COD_{Mn} removal in the flocculation process

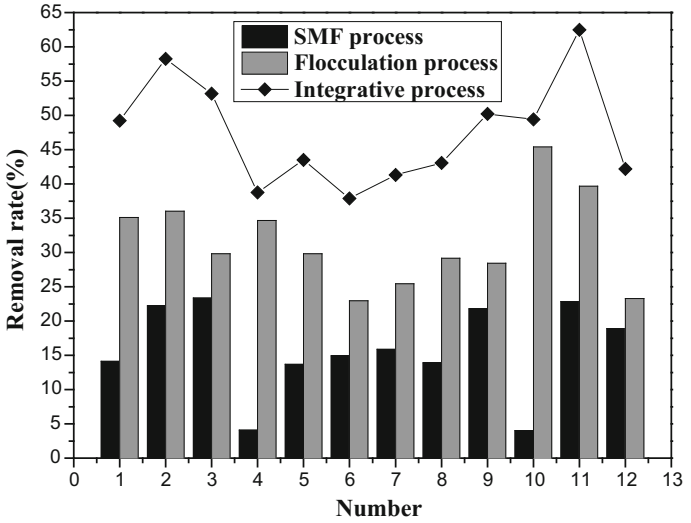

Fig. 8 TOC removal rate by the flocculation and SMF integrative process

Table 4 Total bacteria removal by the pretreatment and SMF integrative process

Number	Total bacteria [CFU/L]			Removal rate [%]		
	Raw water	Settled water	Production water	Integrative process	Flocculation	SMF
1	325±12	102±6	50±4	84.62	68.62	50.98
2	344±10	204±3	56±2	83.72	40.70	72.55
3	324±11	56±4	24±3	92.59	82.72	57.14
4	364±11	68±4	9±1	97.53	81.32	86.76
5	248±11	62±4	18±1	92.74	75.00	70.97
6	200±11	60±4	28±1	86.00	70.00	53.33
7	200±11	68±6	35±4	82.50	66.00	48.53
8	260±13	98±5	0	100.00	62.31	100.00
9	178±11	36±5	5	97.19	79.78	86.11
10	214±12	43±5	1	99.53	79.91	97.67
11	312±11	89±5	1	99.68	71.47	98.88

flocculation process. The above analysis confirms that the pretreatment process was necessary for the SMF membrane process.

Microorganism Removal. In the late of 20th century, some bacteria and new pathogenic protozoan in water emerged and deteriorated the water quality seriously, such as Blue Giardia and Cryptosporidium etc. Because of their strong resistance to chlorine, these organisms were very difficult to remove completely in conventional water treatment process.

Table 4 presents that the total bacteria removal in the pretreatment and SMF integrative process. After this integrative process, the number of total bacteria in production water is less than 100, which meet the china's national standards for drinking water (GB 5749-2006). Theoretically, the SMF membrane (pore size < 30 nm) can hold back all the bacteria (>100 nm). However, parts of bacteria is alive in drinking water after the integrative process and this might be due to bacteria reproduction and growth in the pipe network.

Transmembrane Pressure in SMF Process. Transmembrane pressure (TMP) is the driving force of the membrane separation process. It is an important indicator to reflect the degree of membrane fouling and assess the feasibility of SMF membrane application in actual production process. Figure 9 demonstrates the change of TMP in different filtration flux for SMF system. When the filtration flux is 30L/m^2 h, the 95% recovery rate of production water and tiny TMP difference before and after backwash confirms that a little pollution exists on the membrane surface. As the filtration flux rises, the slow TMP increase indicates that more pollution is on the membrane but the velocity of membrane fouling is relatively low. But with the flux of 60 L/m^2 h, remarkable TMP increase conveys the message that the membrane has been polluted and need the chemical cleaning to remove the pollution.

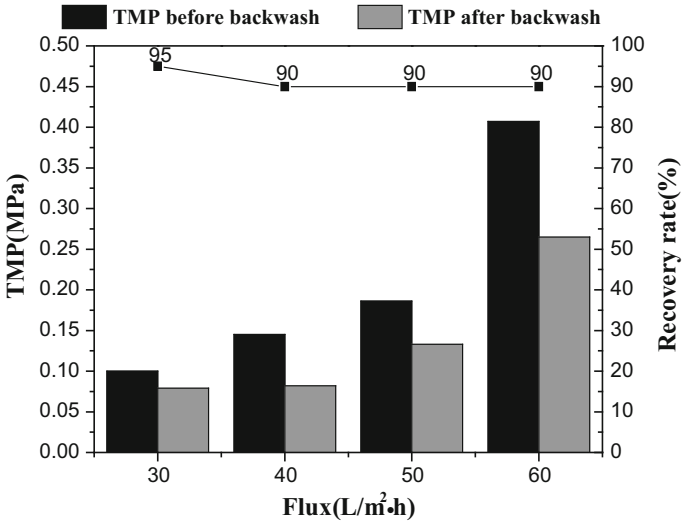

Fig. 9 Transmembrane pressure in different filtration flux for SMF system

Conclusions

In this work, an integrative process with the combination of flocculation pretreatment and SMF is selected for drinking water treatment in a pilot-scale application. In the integrative process, the removal rate of turbidity and bacteria was more than 99% but less than 50% TOC and COD_{Mn} was removed. All the water quality of production water meets the China's National Drinking Water Standards (GB 5749-2006). This suggests that the integrative process is feasible for drinking water treatment.

The results in the SMF process show that removal rate of turbidity and total bacteria is more than 99%, which confirms that SMF process is an efficient process to eliminate turbidity and total bacteria. Despite the SMF membrane has low capacity to remove the organic substance with 18.64% COD_{Mn} and 15.81%. TOC removal rate, the organics in water are still below the national standards and this evidence that SMF can be choose as the core for drinking water treatment. Additionally, the result that parts of turbidity and bacteria, 24.50% for COD_{Mn} and 31.65% for TOC are removed in the flocculation pretreatment process verify that the flocculation pretreatment process is helpful for the SMF process.

Acknowledgements This research was sponsored by the Research Fund for the Doctoral Program of Higher Education (Funding No. 20111201110003, 20091201120002), the open project of State Key Laboratory of Hollow Fiber Membrane Materials and Membrane Processes and Tianjin Natural Science Foundation of China (No. 11JCZDJC21200, 11JCZDJC23700). We thank Dongying water supply Corporation for technical support and Dongying Gongda water environment Technology Corporation for equipment support.

References

1. G. Lean, D. Hinrichsen, *Atlas of the Environment* (Harper Perennml, New York, 1994)
2. E. Drioli, F. Macedonio, Membrane engineering for water engineering. Ind. Eng. Chem. Res. **51**, 10051–10056 (2012)
3. T. Liu, Z.L. Chen, W.Z. Yu, J.M. Shen, J. Gregory, Effect of two-stage coagulant addition on coagulation-ultrafiltration process for treatment of humic-rich water. Water Res. **45**, 4260–4268 (2011)
4. F. Lipnizki, R.W. Field, P.-K. Ten, Pervaporation-based hybrid process: a review of process design, application and economies. J. Membr. Sci. **153**, 183–210 (1999)
5. R.J. Petersen, Composite reverse osmosis and nanofiltration membranes. J. Membr. Sci. **83**, 81–150 (1993)
6. H.-A. Kim, J.H. Choi, S. Takizawa, Comparison of initial filtration resistance by pretreatment processes in the nanofiltration for drinking water treatment. Sep. Purif. Technol. **56**, 354–362 (2007)
7. G.-B. Li, Y.-L. Yang Ultrafiltration–the 3rd generation key water purification technology for city. Water Techn. **1**(1), 1–3 (2007)
8. E. Drioli, A.I. Stankiewicz, F. Macedonio, Membrane engineering in process intensification—an overview. J. Membr. Sci. **380**, 1–8 (2011)
9. S. Sethi, S. Walker, J. Drewes, et al., Existing and emerging concentrate minimization and disposal practices for membrane systems. Florida Water Resour. J. 38–48 (2006)
10. W. Zhang, *Hybrid Process of Immersed Ultrafiltration Applied to Micro-Polluted Surface Water Resource for Rural Drinking Water* (Tsinghua University, 2011)
11. M. Simonič, A. Lobnik, The efficiency of a hybrid flocculation/UF process for a real dye-house effluent using hydrophilic and hydrophobic membranes. Desalination. **271**, 219–224 (2011)
12. L. Fiksdal, T.O. Leiknes, The effect of coagulation with MF/UF membrane filtration for the removal of virus in drinking water. J. Membr. Sci. **279**, 364–371 (2006)
13. A.W. Zularisam, A.F. Ismail, M.R. Salim, M. Sakinah, T. Matsuura, Application of coagulation–ultrafiltration hybrid process for drinking water treatment: optimization of operating conditions using experimental design. Sep. Purif. Technol. **65**, 193–210 (2009)

NH_3-SCR Activity of MnOx/CeO_2 Catalyst at Low Temperature

Junlin Xie, Pijun Gong, Zhe Zhang, Feng He, Fengxiang Li and Kai Qi

Abstract In this paper, CeO_2 was synthesized and used as carrier, meanwhile, MnOx was supported by different methods. The NH_3-SCR activity of MnOx/CeO_2 at low temperature has also been studied. The results show that the performance of the MnO_X/CeO_2 catalyst prepared by hydrothermal deposition method (MC-h) can reach up to 80% at 180 °C, while the impregnation method (MC-i) is only 70% at 180 °C. Testing results indicate that the catalysts synthesized by the hydrothermal deposition method have larger specific surface area and higher reducibility, and manganese oxide existed in the form of nanorods is more favorable for the contact between the active component and the reactive gas. All of these are beneficial to the SCR reaction.

Keywords NH_3-SCR · MnOx/CeO_2 catalyst · Hydrothermal deposit Load

Introduction

Nitrogen oxides are the main components of air pollutants, which will not only lead to acid rain and photochemical smog, but also bring great harm to human health [1, 2]. Selective catalytic reduction (SCR) of NO with NH_3 is the most widely used technique for the abatement of NO emissions. At present, the most widely used

J. Xie · P. Gong · Z. Zhang · F. He (✉) · F. Li · K. Qi
State Key Laboratory of Silicate Materials for Architectures, Wuhan University of Technology, Wuhan 430070, China
e-mail: he-feng2002@163.com

J. Xie
Center for Materials Research and Analysis, Wuhan University of Technology, Wuhan 430070, China

P. Gong · Z. Zhang · F. He · F. Li · K. Qi
School of Materials Science and Engineering, Wuhan University of Technology, Wuhan 430070, China

Y. Han (ed.), *Advances in Energy and Environmental Materials*,
Springer Proceedings in Energy, https://doi.org/10.1007/978-981-13-0158-2_95

commercial catalyst is vanadium titanium tungsten (V_2O_5–WO_3/TiO_2) catalyst [3]. The catalyst has good denitrification effect between 300–400 °C, however it can not play a better catalytic role in the treatment of low temperature kiln exhaust gas (80–200 °C), such as cement kiln. Obviously, it is an urgent problem to study the catalysts with high catalytic activity at low temperature.

In recent years, a great deal of research has been done on low temperature selective catalysts, and it has been found that Mn-based catalysts have good low temperature catalytic activity [4, 5]. However, there are still many defects such as poor resistance to poisoning and easy sintering. CeO_2 has good thermal stability, resistance to sintering and high oxygen storage capacity, which can effectively improve the denitration performance of manganese-based catalyst [6]. Previous research has proved that the MnOx–CeO_2 prepared by co-precipitation is more active than that prepared by impregnation method [7]. In this paper, the NH_3-SCR catalytic activity of MnOx/CeO_2 catalyst was studied by synthesizing CeO_2 and loading MnOx with different methods. We found that the performance of the MnOx/CeO_2 prepared by hydrothermal deposition method (MC-h) is better than that of the impregnation method (MC-i).

Experimental

Catalysts Preparation. 15 g $Ce(NO_3)_3{\cdot}6H_2O$ and 6 g $CO(NH_2)_2$ were dissolved in 40 ml distilled water, the reaction mixture was transferred to a reaction vessel and reacted at 110 °C for 18 h. The precipitate was filtered and washed, then dried 90 °C for 6 h. Finally, the sample was calcined in a muffle furnace at 400 °C for 3 h to obtain CeO_2 carrier. Preparation of MnO_X/CeO_2 catalyst by hydrothermal deposition method (MC-h): Firstly, 2 g CeO_2 were dissolved in 100 ml distilled water, then $KMnO_4$ and 50% $Mn(NO_3)_2$ were add to the above suspension, magnetic stirring for 10 min, dried 90 °C for 24 h. Next, the products were filtered and dried. After grinding and mixing, the MnO_X/CeO_2 catalyst was obtained. Preparation of MnO_X/CeO_2 catalyst by impregnation method (MC-i): 50% $Mn(NO_3)_2$ were added to CeO_2, molar ratios of Mn:Ce were 0.1–0.5, the mixture dried 110 °C for 18 h, then calcined at 500 °C for 3 h.

Catalytic Activity. The activity measurements were performed in a self-designed reactor containing a special glass tube (internal diameter (i.d.) = 20 mm), a temperature programming controller, and the feed gas mixture system. The typical reaction conditions were as follows: [NO] = 720 ppm, [NH_3] = 800 ppm, [O_2] = 3 vol%, N_2 balance, and gas hourly space velocity (GHSV) of 30,000 h^{-1}. In addition, the reaction system was kept at each reaction temperature for 30 min (in a range of reaction temperatures from 80 to 260 °C) to reach a steady state. The concentrations of the feed gases were analyzed continuously by an off-gas analysis spectrometer (Gasboard 3800P) with an on-line detector running; the conversion of

NO_x was calculated as $([NO]_{in}-[NO]_{out})/[NO]_{in}$to evaluate the activity of each catalyst.

Characterization. The powder XRD patterns were obtained using a D8 Advance diffractometer (Bruker, Germany) with Cu Kα radiation (λ = 0.15406 nm) at an angle of 2θ from 10° to 80°. The crystalline phases were identified by comparison with reference data from the International Center for Diffraction Data (ICDD) files. High-resolution scanning electron microscope (JSM-5610LV, Japan) was used to observe the micro morphology of catalysts. Using the thermal analysis-mass spectrometry (TG, STA449, German), TG profiles were carried out for different series of catalysts in N_2 to prevent oxidation. And heating rate were 10 °C/min between 50 and 900 °C. H_2-TPR experiments were performed using an automated catalyst characterization system (TPDRO1100, Thermo, USA) with a thermal conductivity detector (TCD). During H_2-TPR, a flow of 5 vol% H_2 in N_2 was fed to about 50 mg of sample at a rate of 30 mL/min, and sample was tested by increasing the temperature from 100 to 800 °C at a heating rate of 10 °C/min. The amount of H_2 consumed by $MnOx/CeO_2$ in the given temperature range was calculated by TCD.

Results and Discussion

Catalytic Performance Results. In order to explore the application of CeO_2 as a carrier in SCR denitrification, the $MnOx/CeO_2$ catalysts were prepared by impregnation method (1-a) and hydrothermal deposition method (1-b) respectively. The SCR activities of $MnOx/CeO_2$ were tested at the temperature of 80–180 °C. Figure 1 shows that the performance of the $MnOx/CeO_2$ prepared by hydrothermal deposition method (MC-h) is better than that of the impregnation method (MC-i). The denitrification rate of 0.4MC-i is less than 70% at 180 °C, and the denitrification rate of 0.4MC-h can be up to 80%. The $MnOx/CeO_2$ catalyst prepared by two methods showed the best denitrification activity at Mn/Ce ratio of 0.4.

XRD Characterization. Figure 2 shows the XRD spectra of pure CeO_2 and 0.4 $MnOx/CeO_2$ catalysts prepared by two methods. It can be seen from the picture, the nano-CeO_2 prepared in this experiment has an ideal crystal form and the lattice constants were in good agreement with CeO_2 (JCPDS 65-5923). The diffraction peaks corresponding to CeO_2 (JCPDS 65-5923) can only be detected in 0.4MC-i samples. In addition to the diffraction peaks corresponding to CeO_2 (JCPDS 65-5923) in the 0.4MC-h sample, α-MnO_2 (JCPDS 44-0141) was also detected at diffraction angles 2θ of 18.11° (200) and 37.52° (211) [8]. However, the two diffraction peak are not obvious, indicating that although the MnOx will have good dispersion on the catalyst. The results of XRD showed that the crystallinity of Mn was not high in the $MnOx/CeO_2$ catalyst prepared by two methods, the CeO_2 support may lead to the presence of manganese oxides mainly in amorphous form and the amorphous structure have the catalytic activity.

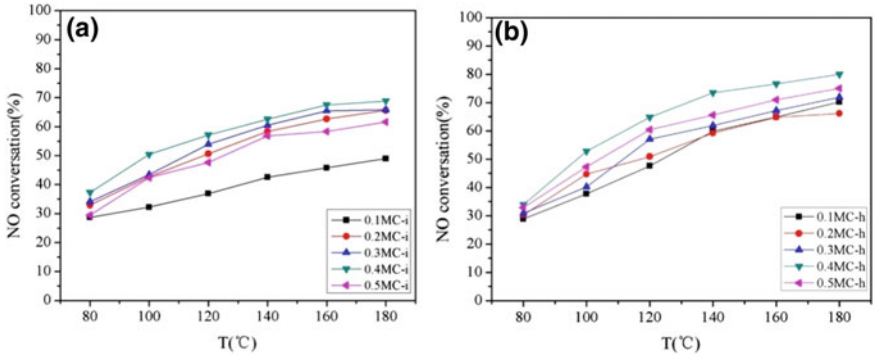

Fig. 1 Catalytic activity of MnOx/CeO_2 catalyst, **a** impregnation method (MC-i); **b** hydrothermal deposition method (MC-h)

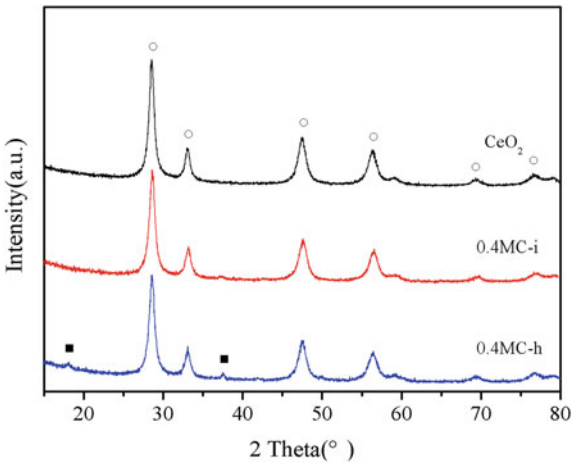

Fig. 2 XRD patterns of MnOx/CeO_2 catalysts, impregnation method (MC-i); hydrothermal deposition method (MC-h), (white circle —CeO_2, black square —α-MnO_2)

Specific Surface Area and Morphology Analysis. The specific surface area of the samples is show in Table 1. The difference of the specific surface area of the three samples is larger, and the aperture gap is not obvious. Where CeO_2 has a large specific surface area when not loaded, the specific surface area of 0.4MC-i is the smallest, indicating that the manganese oxide loading on the CeO_2 will lead to the specific surface area of catalyst lower. And the hydrothermal deposition method can obtain a larger specific surface area than the impregnation method. This is probably because of better dispersion of manganese oxide catalysts prepared by hydrothermal method, which is conducive to the catalyst contact and reaction with active gas, so the catalyst prepared by hydrothermal preparation method (MC-h) showed a relatively good catalytic.

In order to analyze the differences in the morphology of the catalysts obtained by two methods, the samples are analyzed by SEM, and the results are shown in Fig. 3.

Table 1 Specific surface area of MnOx/CeO_2 prepared by different methods

Sample	S_{BET} (m^2/g)	V_P ($\times 10^{-2}$ cm^3/g)
CeO_2	100	4.4
0.4MC-i	58	4.1
0.4MC-h	80	4.2

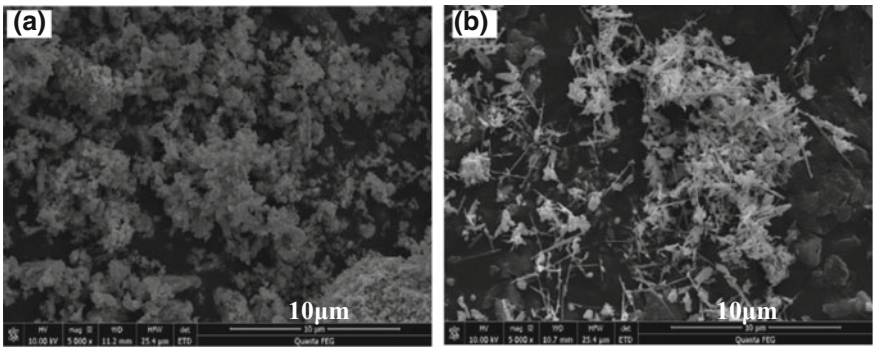

Fig. 3 SEM images of MnOx/CeO_2 prepared by different methods, **a** impregnation method (MC-i); **b** hydrothermal deposition method (MC-h)

It can be seen from the picture that catalysts prepared by impregnation method (0.4MC-i (a)) is mainly distributed on the surface of CeO_2 in granular form; However, the MnOx in the catalyst prepared by hydrothermal deposition (0.4MC-h (b)) is mainly distributed on the surface of CeO_2 in the form of nanorod. BET test results also show that 0.4MC-h (b) has a larger specific surface area. This may be due to the particle morphology is easier to agglomerate, reducing the contact area between the active component and the reaction gas. However, the nanorod has good dispersion, and can reduce the surface energy of the catalyst, which is favorable for the gas-solid reaction, resulting in the better catalytic activity.

TG Characterization. As can be seen from Fig. 4, the three catalysts have a dehydration weight loss process at the temperature of 200 °C. The weightlessness of CeO_2 is not obvious, which shows that CeO_2 has good stability. The weight loss of 0.4MC-i sample at 480–600 °C is attributed to the decomposition of MnO_2 to Mn_2O_3 [9]. The weight loss at 760–850 °C corresponds to the thermal decomposition of Mn_2O_3 to Mn_3O_4, which indicates that there may exit MnO_2 and Mn_2O_3 in the 0.4MC-i catalyst. Similarly, the weight loss of 0.4MC-h sample synthesized by hydrothermal deposition method is a series changes of $MnO_2 \rightarrow Mn_2O_3 \rightarrow Mn_3O_4$ with the increase of temperature [10]. Especially at 550–700 °C, it shows greater weight loss than 0.4MC-i, indicating that there are more amorphous MnO_2 in addition to the MnO_2 crystal phase detected by XRD. Generally speaking, the loss of 0.4MC-i is smaller than that of 0.4MC-h, which may be due to the calcination of the impregnation method.

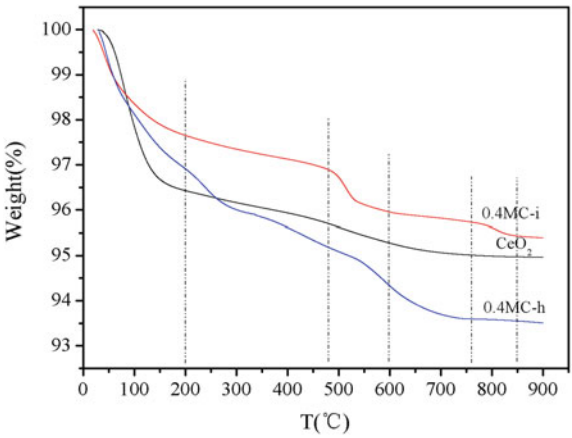

Fig. 4 TG curves of MnOx/CeO_2 catalysts, impregnation method (MC-i); hydrothermal deposition method (MC-h)

H_2-TPR Results. Figure 5 shows that CeO_2 has two distinct reduction peaks. The reduction peak at 450 °C is the surface Ce^{4+} reduced to Ce^{3+}, and the reduction peak at about 850 °C is the bulk phase Ce^{4+} reduced to Ce^{3+} [11]. In addition to Ce^{4+} reduced to Ce^{3+} at 800–850 °C, a series of reduction peaks are observed at 200–400 °C of 0.4MC-i and 0.4MC-h, this is the continuous change of MnOx in the catalyst under the action of H_2. The reduction peak of 0.4MC-i at 240 °C is reduced to Mn_3O_4 by MnO_2 or Mn_2O_3, and the reduction peak at 310 °C is reduced to MnO by Mn_3O_4. The reduction peak of 0.4MC-h at 250 °C is reduced to Mn_3O_4 by MnO_2 or Mn_2O_3, the reduction peak around 360 °C is the Mn_3O_4 reduced to MnO and the reduction of bulk CeO_2. Comparison reduction peak area of 0.4MC-i and 0.4MC-h can be found that the reduction of peak area of 0.4MC-h larger than

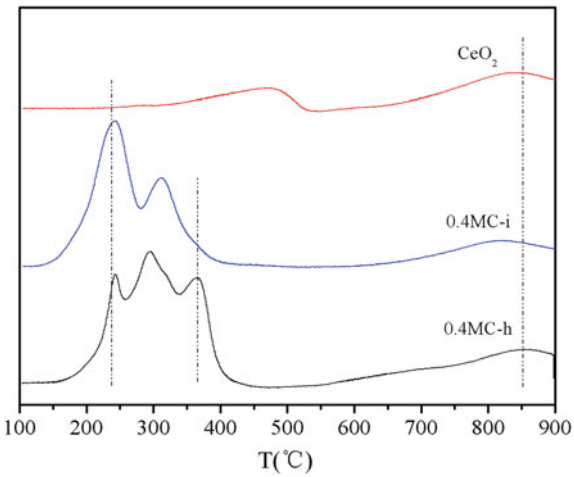

Fig. 5 H_2-TPR profiles of MnOx/CeO_2 catalysts, impregnation method (MC-i); hydrothermal deposition method (MC-h)

0.4MC-i, it can be assumed that the 0.4MC-h has the higher ability to restore. This is also one of the reasons why 0.4MC-h has good denitrification performance.

Conclusion

MnOx was loaded on CeO_2 carrier by impregnation and hydrothermal deposition method. The two methods show the best performance of denitrification at the Mn/Ce molar ratio of 0.4. The denitrification performance of hydrothermal deposition method is better than that of impregnation method. The denitrification rate of 0.4MC-i is less than 70% at 180 °C, and the NOx conversion rate of 0.4MC-h can reach up to 80% at 180 °C. 0.4MC-h has a larger specific surface area and a higher reduction performance than 0.4MC-i. Besides, the nanorod MnOx is more favorable for the active component contact with the reaction gas. All the above reasons are conducive to the promotion of the SCR reaction.

References

1. R.P. Vélez, I. Ellmers, H. Huang, U. Bentrup, V. Schünemann, J. Catal. **316**, 103–111 (2014)
2. M.J. Beier, J.D. Grunwaldt, S. Dahl, Appl. Catal. B: Environ. **93**, 166–177 (2009)
3. M. Li, Y. Yeom, E. Weitz, M.H. Sachtler, Catal. Lett. **112**, 129–136 (2006)
4. R.M. Aguilar, S. Castillo, J. MarIn, V.Z. Gonzale, A. Luz, Fule **198**, 123–133 (2017)
5. F. Kapteljn, L. Smgoredjo, A. Andreml, Appl. Catal. B **3**, 173–189 (1994)
6. M. Kang, T.H. Yeon, E.D. Park, Catal. Lett. **106**, 1–2 (2006)
7. G. Qi, R.T. Yang, J. Catal. **2**(217), 434–441 (2003)
8. D.A. Peña, S.U. Balu, P.G. Smirniotis, J. Catal. **221**, 421–431 (2004)
9. Y.S. Wu, S. Li, Y. Cao, S.T. Xing, Z.C. Ma, Y.Z. Gao, Mater. Lett. **97**, 1–3 (2013)
10. J.L. Xie, D. Fang, F. He, J.F. Chen, Z.B. Fu, X.L. Chen, Catal. Commun. **28**, 77–81 (2012)
11. Q. Zhang, Z.X. Song, P. Ning, X. Liu, H. Lia, J.L. Gu, Catal. Commun. **59**, 170–174 (2015)

A Simplified Ultrasonic Stripping-Chemical Reduction Method for Preparation of Graphene

Lina Shi, Rong Wang, Deguo Zhou, Yan Liu and Yanzong Zhang

Abstract Graphene has been widely used in many fields due to its unique excellent mechanical, optical, thermal and electrical properties. A simple approach for reducing graphene oxide (GO) with Tea polyphenols (TP) (TRG) was developed by ultrasonic stripping-chemical reduction method. The reduction products of TRG were obtained, and Fourier transform infrared spectroscopy (FT-IR), X-ray photoelectron spectroscopy and X-ray-diffraction were introduced to prove the elimination of oxygen-containing groups from GO. It was found that when the weight of TP was 0.225 g, the reduction degree of GO was the highest. Besides, the thermal gravimetric analysis results showed that there was a close relationship between the reduction degree of GO and thermal stability of TRG.

Keywords Graphene oxide · Tea polyphenols · Ultrasonic stripping
Thermal stability · Reduction degree

L. Shi · R. Wang · Y. Liu · Y. Zhang (✉)
College of Environment, Sichuan Agricultural University, Chengdu 611130, Sichuan, China
e-mail: yzzhang@sicau.edu.cn

L. Shi
e-mail: 1048948692@qq.com

R. Wang
e-mail: wr783484590@aliyun.com

Y. Liu
e-mail: liuly6262@hotmail.com

D. Zhou
Befar Group Co., Ltd., Binzhou 256602, Shandong, China
e-mail: zyz1000@163.com

Y. Han (ed.), *Advances in Energy and Environmental Materials*,
Springer Proceedings in Energy, https://doi.org/10.1007/978-981-13-0158-2_96

Introduction

Graphene is a single-atom-thick two-dimensional aromatic sheet composed of sp2-bonded carbon atoms. As a newly discovered allotrope of carbon, is a basic unit to construct the zero dimensional fullerene, one dimensional carbon nanotubes and three dimensional graphite materials [1]. The unique physical properties (such as room temperature quantum Holzer effect [2], ferromagnetic [3], superconductivity [4] and giant magnetoresistance effect [5]), excellent chemical properties and thermodynamic stability results in its outstanding mechanical strength and strain [6], high thermal conductivity [7], electron mobility [8], and chemical inertness [9]. Therefore, graphene has potential applications in the fields of photocatalysis [10, 11], energy storage [12, 13], sensors [14, 15], transistors [16, 17] and polymers [18, 19], etc.

Up to the present, several methods have been utilized to synthesize graphene. Micro-mechanical cleavage [20, 21], chemical vapor deposition (CVD) [22, 23], solvothermal [24, 25], epitaxial growth [26, 27], liquid-phase exfoliation [28, 29] and chemical reduction of graphene oxide (GO) [30, 31] are the main methods employed to prepare graphene. Chemical reduction method has the advantages of low cost, high yield and simple process has been favored by researchers. However, there are too many steps in this method, the cleaning process is repeated and cleaning difficult to lead to the preparation of cumbersome and cumbersome issues. Therefore, simplifying the process of reducing the preparation time is an important way to improve the preparation efficiency of graphene.

In recent years, environmental friendly reducing agent have been attracted much attention. Such as vitamin C [32], amino acid [33], pomegranate juice [34], Colocasia esculenta [35], Mesua ferrea Linn [35], polyphenol alcohol [36], tea solution [37], melatonin [38], bovine serum albumin [39], glucose [40], bacteria [41] and reducing sugar [42] are replacing toxic reducing agents. Among these, tea polyphenols possesses the highest composition of a epigallocatechin gallate compound, which was regarded as an effective reducing agent owing to its ability to donate an electron or hydrogen atom easily [43].

Herein, in this paper, the three processes of traditional chemical oxidation reduction method were decreased to two processes by ultrasonic stripping-chemical reduction method which shortened the preparation time and improved the efficiency. N, N-dimethylacetamide (DMAc) and water mixture were used as reaction solvent and dispersant, respectively. Tea polyphenols (TP) were used as reducing agent to make the reaction process and reaction products more environmental friendly. Moreover, the reduction degree of graphene at various tea polyphenols concentration ranging from 0 to 0.3 g was investigated.

Experimental

Materials. Graphite powder (purity of 99%, 800 mesh) was purchased from the Qingdao Huatai Graphite Co., Ltd., Shandong, China. Tea polyphenols (TP, purity of 98%) were purchased from Zhengzhou Zhongcheng Chemical Co., Ltd., Henan, China. Concentrated sulfuric acid (H_2SO_4, 96–98%), potassium permanganate ($KMnO_4$), hydrogen peroxide (H_2O_2, 30%) and dimethylacetamide (DMAc) were purchased from National Medicines Chemical Corporation, China. All of the chemicals were of analytical grade, and deionized water was used in all experiments.

Preparation of Graphene. Ultrasonic stripping-chemical reduction method was employed to prepare graphene. Firstly, according to modified Hummers method [44], graphite oxide was prepared by using H_2SO_4 and $KMnO_4$ to oxidize the graphite powder. For the ultrasonic stripping-chemical reduction of graphite oxide, in a typical process, 300 mL of dispersion solution with dimethylacetamide and distilled water was prepared according to certain the volume concentrations/ratio at 1, and heated the resulting solution to 60 °C in a water bath. Then, graphite oxide 0.165 g was added to the above solution, and stir well. Meanwhile, TP was added to the foregoing solution. Then, the solution was treated by ultrasonic disrupter at 800 W for 60 min. Finally, the resulting suspension was vacuum filtered with a 0.22 μm membrane, washed with distilled water and dried in a vacuum freeze dryer for 48 h. The produced graphene reduction with TP was referred as TRG. TRG1, TRG2, TRG3 and TRG4 corresponded to the quality of TP is 0.075, 0.15, 0.225 and 0.3 g, respectively.

Characterizations. The chemical state of the elements were evaluated using X-ray photoelectron spectroscopy (XPS, Thermo ESCALAB 250Xi, USA). The binding energy values were calibrated using the contaminant carbon (C 1s = 284.4 eV) as a reference. The thermal stability and the thermal degradation properties of samples were studied by Thermal gravimetric analysis (TGA, TA/TGA Q500, USA) at a heating rate of 10 °C min^{-1}. The Fourier transform infrared spectra (FT-IR, PerkinElmer Spectrum Two, USA) was used to investigated the surface functional groups of samples by using KBr pellets on FT-IR spectrometer in the range of 400–4000 cm^{-1}. The X-ray-diffraction (XRD) measurements were carried out by a PANalyticalX'pert Pro MPD system with a Cu Kα radiation source of wavelength λ = 0.1541 nm and a scanning rate of 0.0334°/s in the range from 5° to 60°.

Results and Discussion

Synthesis and Reduction Degree of TRG. TP plays an important role in the reaction process, it can be seen that no apparently color change in the GO without TP during ultrasonic stripping (Fig. 1a). However, the color of reaction solution changed from brown to black when treating GO dispersions with TP for 30 min

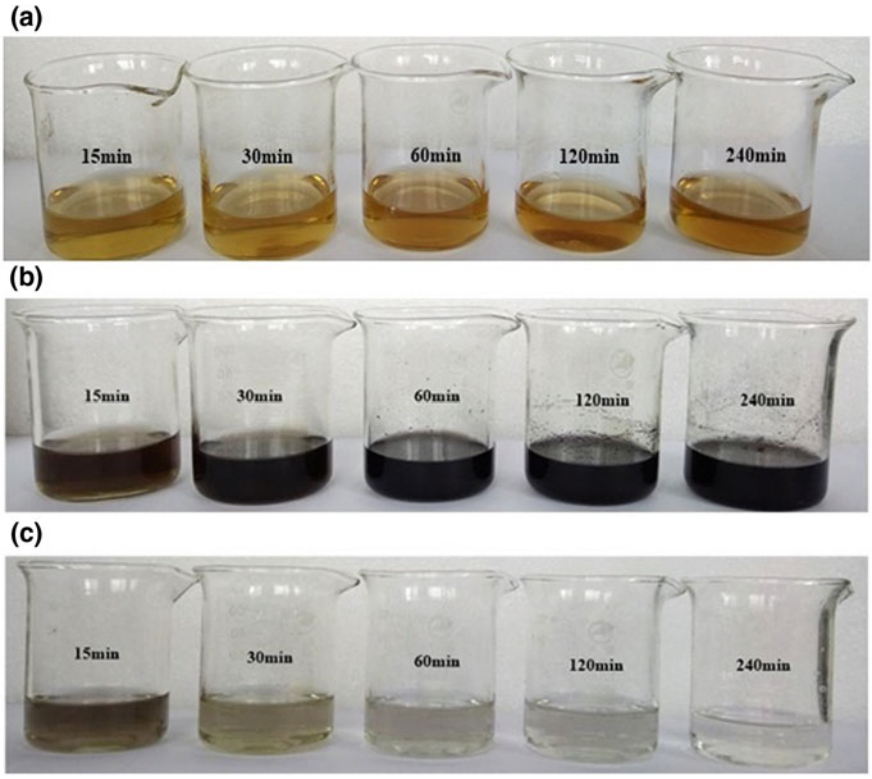

Fig. 1 **a** Images of GO dispersion after ultrasonic stripping for 15, 30, 60, 120 and 240 min, **b** Images of TRG dispersions after reduction by TP for 15, 30, 60, 120 and 240 min, **c** Images of filtrate of TRG after filtration

(Fig. 1b). After filtration of the dispersion, it was observed that the yellow of the filtrate change from the deep to shallow, and close to colorless in 60 min, as shown in Fig. 1c. It indicated that the the longer the time, the higher the degree of reduction of GO.

The functional groups of GO, TRG1, TRG2, TRG3 and TRG4 were studied using FT-IR. As shown in the Fig. 2, there were lots of same characteristic absorption peaks between GO and TRG. Such as the peaks at ~3400, 1720, 1404 and 1049 cm^{-1}, which corresponding to the vibrations of –OH (water molecules), C = O, –OH and C–O/C–O–C, respectively [45–47]. After being reduced by ultrasonic stripping and TP, the characteristic bands of the oxygen functional groups decreased dramatically. And a new peak at 1630 cm^{-1} appeared in TRG, which was attributed to the aromatic skeletal C=C stretching [45]. Moreover, the peak of C=C became more and more prominent with the increasing of reducing agent, conversely others peaks became weak. These phenomena indicated that the oxygen functional groups on GO were mostly removed during the reduction process.

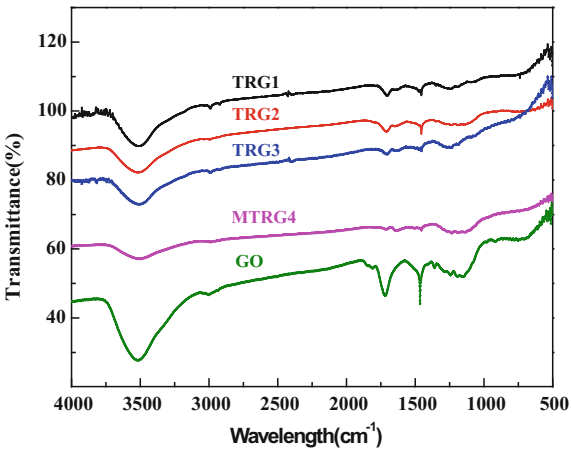

Fig. 2 FT-IR spectra of GO and TRG

The C1 s XPS analysis of GO, TRG1, TRG2, TRG3 and TRG4 are shown in Fig. 3. As is well known, graphene mainly have five types of carbon components. Including the C–C/C=C bond in the aromatic rings, C–O, C–O–C, C=O, and O=C–OH bonds, which are located at the binding energies of 285, 286.8, 287.4, 288.3 and 289.4 eV [48–50]. Figure 3 showed that the peak centered at 285.0 eV was assigned to the sp^2 carbon, the peak centered at 287.0 eV was corresponding to oxygen-containing functional groups. The peak intensity of sp^2 carbon increased with increasing the weight of TPs, but the change trend of oxygen-containing functional groups was opposite.

Based on the previous analysis, the degree of reduction of the TRG sample could reach the maximum at the C/O ratio of 4.9. The XRD features of graphite, GO, and TRG3 is shown in Fig. 4a. In graphite, a high-intensity peak at 26.48° and a small peak at 54.76° was detected, which corresponded to the well-arranged layer

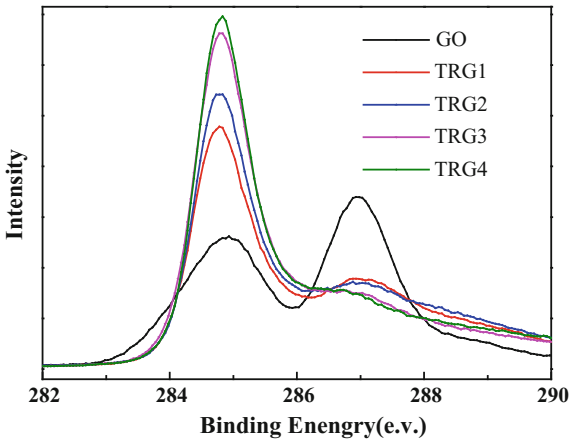

Fig. 3 XPS spectra peaks of GO and TRG

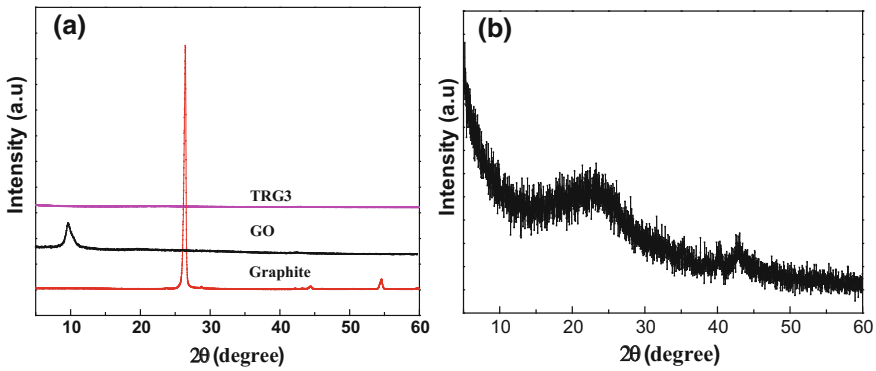

Fig. 4 **a** XRD patterns of Graphite, GO and TRG3, **b** the XRD enlarged drawing of TRG3

structure with d-spacing of 0.218 nm along the (002) and (004) plane respectively. Compared with graphite, the characterized peak of GO was observed at $2\theta = 9.72°$ and the d-spacing increased to 0.909 nm, which suggested the introduced of oxygen containing functional groups and water molecules between the layers of the graphite. After the reduction, it was seen that TRG3 showed two weak peaks in the large version in Fig. 4b. One peak centered at $2\theta = 24.2°$ and the d-spacing decreased to 0.33 nm from 0.909 nm of GO, which indicated that most of the oxygen functional groups had been removed after reduction. Another less intense peak at 43° was ascribed to some restacked graphene layers and turbostratic of disordered graphene.

Thermal Stability of GO and TRG. The thermal stability of GO, TRG1, TRG2, TRG3 and TRG4 was investigated by TGA. The TGA curves (Fig. 5) showed that the thermal degradation was mainly divided into two stage. In the first stage, where the temperature ranged from 100 to 390 °C, GO exhibited a 36 wt% loss while TRG experiences a 6–13 wt% loss because the loss of hydroxyl, epoxy, carboxyl functional groups and residual water molecules. Meanwhile, the mass loss indicated that 36% of the oxygen containing functional groups had been eliminated by reduction. In the second stage at 390–700 °C, the weight decreased to 44 wt% of GO and 56–66 wt% of TRG, which was attributed to the burning of residual oxygen-containing functional groups and ring carbon.

Relationship on Degree of Reduction and Thermal Stability. The C/O ratio represents the degree of reduction and the residual weight of TRG is a symbol of thermal stability. The relationship of the quality of TPs and C/O, thermal stability was shown in Fig. 6. Line A shows the carbon to oxygen (C/O) atomic ratios of samples. The C/O ratio of TRG increased when the quality of TPs ranged from 0 to 0.225 g, while the degree of reduction unchanged and thermal stability decreased as the quality of TP changed from 0.225 to 0.30 g. The results revealed that the

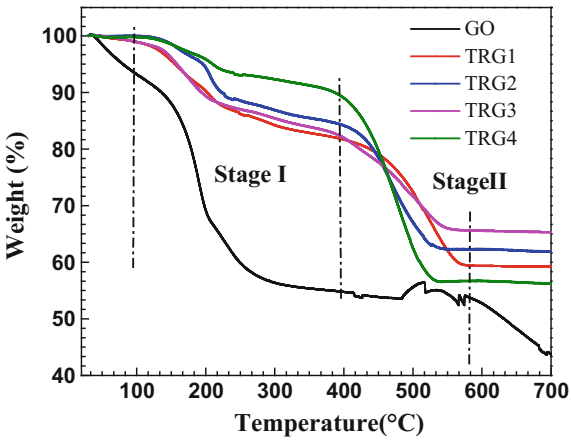

Fig. 5 TGA curves of GO and TRG

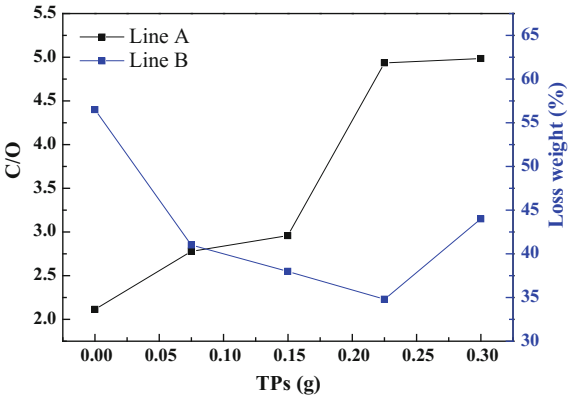

Fig. 6 The relationship of the quality of TPs and C/O, thermal stability

reduction reaction was complete when the quality of TP was added to 0.225 g. That is to say, the higher the degree of reduction is, the better the thermal stability becomes. However, the excess TPs absorbed on the TRG surface was occurred [47, 49, 51], so the burning of the residual TPs weakened the thermal stability of it.

Conclusions

For the preparation of graphene, a green method for the effective reduction of GO by ultrasonic stripping-chemical reduction method was studied. The reduction degree of GO and thermal stability of TRG have positive correlation. The reduction degree of GO reaches the maximum at the quality of TPs is 0.225 g. Besides, the thermal stability of TRG can be weakening by excess of reducing agent.

Acknowledgements This work was supported by the Science and Technology Department of Sichuan Province (2017JZ0021, 2017SZ0039) and the Education Department of Sichuan Province (17ZA0298).

References

1. A.K. Geim, K.S. Novoselov, The rise of graphene. Nat. Mater. **6**, 183–191 (2007)
2. K.S. Novoselov, A.K. Geim, S.V. Morozov, D. Jiang, Y. Zhang, S.V. Dubonos, I.V. Grigorieva, A.A. Firsov, Electric field effect in atomically thin carbon films. Science. **306**, 666–669 (2004)
3. T. Yokoyama, J. Linder, Anomalous magnetic transport in ferromagnetic graphene junctions. Phys. Rev. B. **83**, 3002–3005 (2011)
4. E. Cartlidge, Graphene superconductivity seen. Phys. World **28**, 6–7 (2015)
5. C. Cao, M. Long, X. Mao, Giant magnetoresistance effect, rectifying performance and spin filters in graphene-based heterostructure. J. Comput. Theor. Nanos. **12**, 4849–4854 (2015)
6. C. Androulidakis, G. Tsoukleri, N. Koutroumanis, G. Gkikas, P. Pappas, J. Parthenios, K. Papagelis, C. Galiotis, Carbon **81**, 322–328 (2015)
7. S.N. Leung, M.O. Khan, H. Naguib, F. Dawson, Appl. Phys. Lett. **104**, 081904 (2014)
8. H. Hirai, H. Tsuchiya, Y. Kamakura, N. Mori, M. Ogawa, Electron mobility calculation for graphene on substrates. J. Appl. Phys. **116**, 083703–083706 (2014)
9. A. Deshpande, C.H. Sham, J.M.P. Alaboson, J.M. Mullin, G.C. Schatz, M.C. Hersam, J. Am. Chem. Soc. **134**, 16759–16764 (2012)
10. R.T. Thomas, P.A. Rasheed, N. Sandhyarani, J. Colloid. Interf. Sci. **428**, 214–221 (2014)
11. H.H. Chun, J.Y. Lee, J.H. Lee, W.K. Jo, Ind. Eng. Chem. Res. **55**, 45–53 (2016)
12. M. Pumera, Graphene-based nanomaterials for energy storage. Energy Environ. Sci. **4**, 668–674 (2011)
13. R. Raccichini, A. Varzi, S. Passerini, B. Scrosati, The role of graphene for electrochemical energy storage. Nat. Mater. **14**, 271–279 (2015)
14. R. Stine, S.P. Mulvaney, J.T. Robinson, C.R. Tamanaha, P.E. Sheehan, Fabrication, optimization, and use of graphene field effect sensors. Phys. Rev. C. **85**, 509–521 (2013)
15. S. Wu, Q. He, C. Tan, Y. Wang, H. Zhang, Graphene-based electrochemical sensors. Small **9**, 1160–1172 (2013)
16. D. Reddy, L.F. Register, G.D. Carpenter, S.K. Banerjee, Graphene field-effect transistors. J. Phys. D: Appl. Phys. **44**, 313001 (2011)
17. M. Zhang, C.Z. Liao, Y.L. Yao, Z.K. Liu, F.F. Gong, F. Yan, High-performance dopamine sensors based on whole graphene solution-gated transistors. Adv. Funct. Mater. **24**, 978–985 (2014)
18. H.J. Salavagione, G. Martínez, G. Ellis, Recent advances in the covalent modification of graphene with polymers. Macromol. Rapid. Comm. **32**, 1771–1789 (2011)
19. B.M. Yoo, H.J. Shin, H.W. Yoon, H.B. Park, Graphene and graphene oxide and their uses in barrier polymers. J. Appl. Polym. Sci. **131**, 1–15 (2014)
20. B. Jayasena, S. Subbiah, A novel mechanical cleavage method for synthesizing few layer graphene. Nanoscale Res. Lett. **6**, 95 (2011)
21. R.V. Lapshin, S.T.M observation of a box-shaped graphene nanostructure appeared after mechanical cleavage of pyrolytic graphite. Appl. Surf. Sci. **360**, 451–460 (2016)
22. H. Choi, Y. Lim, M. Park, S. Lee, Y. Kang, M.S. Kim, J. Kim, M. Jeon, Precise control of chemical vapor deposition graphene layer thickness using NixCu1-x alloys. J. Mater. Chem. C. **3**, 1463–1467 (2015)
23. T. Ciuk, P. Caban, W. Strupinski, Charge carrier concentration and offset voltage in quasi-free-standing monolayer chemical vapor deposition graphene on SiC. Carbon **101**, 431–438 (2016)

24. J.J. Ma, Y.S. He, W.M. Zhang, J.L. Wang, X.W. Yang, X.Z. Liao, Z.F. Ma, An experimental insight into the advantages of in situ solvothermal route to construct 3D graphene-based anode materials for lithium-ion batteries. Nano Energy **16**, 235–246 (2015)
25. Y. Lei, J. Xu, R. Li, F.F. Chen, Solvothermal synthesis of CdS-graphene composites by varying the Cd/S ratio. Ceram. Int. **41**, 3158–3161 (2015)
26. N.T. Shelke, B.R. Karche, Ultraviolet photosensor based on few layered reduced graphene oxide nanosheets. Appl. Surf. Sci. **418**, 374–379 (2017)
27. X.F. Li, L. Basile, B. Huang, C. Ma, J.W. Lee, I.V. Vlassiouk, A.A. Puretzky, M.W. Lin, M. Yoon, M.F. Chi, J.C. Idrobo, C.M. Rouleau, B.G. Sumpter, D.B. Geohegan, K. Xiao, Van der waals epitaxial growth of two-dimensional single-crystalline GaSe domains on graphene. ACS Nano **9**, 8078–8088 (2015)
28. S. Haar, A. Ciesielski, J. Clough, H.F. Yang, R. Mazzaro, F. Richard, S. Conti, N. Merstorf, M. Cecchini, V. Morandi, C. Casiraghi, P. Samori, Graphene: a supramolecular strategy to leverage the liquid-phase exfoliation of graphene in the presence of surfactants: unraveling the role of the length of fatty acids. Small **11**, 1691–1702 (2015)
29. A. Ciesielski, P. Samor, Supramolecular approaches to graphene: from self-assembly to molecule-assisted liquid-phase exfoliation. Adv. Mater. **28**, 6030–6051 (2016)
30. S. Gurunathan, J.W. Han, E.S. Kim, J.H. Park, J.H. Kim, Reduction of graphene oxide by resveratrol: A novel and simple biological method for the synthesis of an effective anticancer nanotherapeutic molecule. Int. J. Nanomed. **10**, 2951–2969 (2015)
31. H. Pan, Y.D. Zhang, X.D. Wang, L.G. Yu, Z.J. Zhang, Simultaneous surface modification and chemical reduction of graphene oxide using ethylene diamine. J. Nanosci. Nanotechno. **16**, 2557–2563 (2016)
32. W.C. Ye, J. Yu, Y.X. Zhou, D.Q. Gao, D.A. Wang, C.M. Wang, D.S. Xue, Green synthesis of Pt-Au dendrimer-like nanoparticles supported on polydopamine-functionalized graphene and their high performance toward 4-nitrophenol reduction. Appl. Catal. B-Environ. **28**, 258–263 (2014)
33. D.Z. Chen, L.D. Li, L. Guo, An environment-friendly preparation of reduced graphene oxide nanosheets via amino acid. Nanotechnology **22**, 325601–325607 (2011)
34. M. Salavati-Niasari, M. Ranjbar, M. Sabet, Synthesis and characterization of znin2s4 nanoparticles by a facile microwave approach. J. Inorg. Organomet. Polym. Mater. **23**, 452–457 (2013)
35. S. Thakur, N. Karak, Green reduction of graphene oxide by aqueous phytoextracts. Carbon **50**, 5331–5339 (2012)
36. D.R. Dreyer, S. Murali, Y.W. Zhu, R.S. Ruoff, C.W. Bielawski, Reduction of graphite oxide using alcohols. J. Mater. Chem. **21**, 3443–3447 (2011)
37. K. Kakaei, Palladium silver nanoparticle catalysts synthesis on graphene via a green reduction in tea solution for oxygen reduction reaction in PEM fuel cells. Am. J. Phar. E. **76**, 1203–1214 (2014)
38. O. Akhavan, E. Ghaderi, A. Esfandiar, Wrapping bacteria by graphene nanosheets for isolation from environment, reactivation by sonication, and inactivation by near-infrared irradiation. J. Phys. Chem. B. **115**, 6279–6288 (2011)
39. J.B. Liu, S.H. Fu, B. Yuan, Y.L. Li, Z.X. Deng, Toward a universal "adhesive nanosheet" for the assembly of multiple nanoparticles based on a protein-induced reduction/decoration of graphene oxide. J. Am. Chem. Soc. **132**, 7279–7281 (2010)
40. L.C. Soo, Fabrication of glucose sensor using graphene, University Malaysia Pahang, 2015
41. X.W. Wang, W. Ai, N. Li, T. Yu, P. Chen, Graphene-bacteria composite for oxygen reduction and lithium ion batteries. J. Mater. Chem. A. **3**, 12873–12879 (2015)
42. C.Z. Zhu, S.J. Guo, Y.X. Fang, S.J. Dong, Reducing sugar: new functional molecules for the green synthesis of graphene nanosheets. ACS Nano **4**, 2429–2437 (2010)
43. M.F. Abdullah, R. Zakaria, S.H.S. Zein, Green tea polyphenol-reduced graphene oxide: derivatisation, reduction efficiency, reduction mechanism and cytotoxicity. RSC Adv. **4**, 34510–34518 (2014)

44. H.J. Chu, C.Y. Lee, N.H. Tai, Green reduction of graphene oxide by *Hibiscus sabdariffa* L. to fabricate flexible graphene electrode. Carbon **80**, 725–733 (2014)
45. Y. Feng, N.N. Feng, G.X. Du, A green reduction of graphene oxide via starch-based materials. RSC Adv. **3**, 21466–21474 (2013)
46. J.K. Ma, X.R. Wang, Y. Liu, T. Wu, Y. Liu, Y.Q. Guo, R.Q. Li, X.Y. Sun, F. Wu, C.B. Li, J. P. Gao, Reduction of graphene oxide with l-lysine to prepare reduced graphene oxide stabilized with polysaccharide polyelectrolyte. J. Mater. Chem. A. **1**, 2192–2201 (2013)
47. R.J. Liao, Z.H. Tang, T.F. Lin, B.C. Guo, Scalable and versatile graphene functionalized with the mannich condensate. ACS Appl. Mat. Interfaces **5**, 2174–2181 (2013)
48. J. Li, G.Y. Xiao, C.B. Chen, R. Li, D.Y. Yan, Superior dispersions of reduced graphene oxide synthesized by using gallic acid as a reductant and stabilizer. J. Mater. Chem. A. **1**, 1481–1487 (2013)
49. O. Akhavan, M. Kalaee, Z.S. Alavi, S.M.A. Ghiasi, A. Esfandiar, Increasing the antioxidant activity of green tea polyphenols in the presence of iron for the reduction of graphene oxide. Carbon **50**, 3015–3025 (2012)
50. B.K. Ahn, J. Sung, Y.H. Li, N. Kim, M. Ikenberry, K. Hohn, N. Mohanty, P. Nguyen, T.S. Sreeprasad, S. Kraft, Synthesis and characterization of amphiphilic reduced graphene oxide with epoxidized methyl oleate. Adv. Mater. **24**, 2123–2129 (2012)
51. Y. Wang, Z.X. Shi, J. Yin, Facile synthesis of soluble graphene via a green reduction of graphene oxide in tea solution and its biocomposites. ACS Appl. Mater. Interfaces **3**, 1127–1133 (2011)